Draft version 1.2.1

ATLAS NOTE

July 15, 2014

ATL-COM-2014-051: Search for the Production of a Standard Model Higgs Boson produced in association with a Vector Boson and decaying to a pair of b-quarks

F. Ahmadov [1], Da Palma, A. M.[7], L. Alio[2], B.M.M. Allbrooke[3], T. Bristow[4], D. Buescher[5], A. Buzatu[6], Y. Coadou[2], P. Conde Muio[7], C. Debenedetti[8], Y. Enari[9], G. Facini[10], W. Fisher[11], P. Francavilla[12], G. Gaycken[13], R. Goncalo[7], G. Gonzalez Parra[14], H.M. Gray[15], J.F. Grivaz[16], C. Gwilliam[17], S. Hagebck[13], G. Halladjian[11], M. Jackson[17], D. Jamin[18], R. Jansky[19], K. Kiuchi[20], V. Kostyukhin[13], K. Lohwasser[21], D. Lopez Mateos[22], U. Mallik[23], J. Maneira[7], G. Marchiori[12], M. Martinez Perez[14], A. Mehta[17], K. Mercurio[22], K. Mochizuki[2], N. Morange[23], Y. Ming[24], P. Mullen[6], Y. Nagai[2], J. Nielsen[8], I. Ochoa[25], A. Palma[7], C. Pandini[12], R. Pedro[7], G. Piacquadio[26], M. Proissl[4], T. Ravenscroft[6], P. Rose[8], T. Scanlon[25], E. Schopf[13], S. Shaw[11], B. Smart[4], V. Sorin[14], M. Sousa[7], F. Sforza[27], J. Therhaag[13], P.D. Thompson[3], L. Vacavant[2], J. Wang[21], C. Wang[18,28], S. Wang[18], C. Weiser[5], R. Zaidan[23], L. Zhang[18]

[1] *JINR*
[2] *CPPM Marseille*
[3] *Birmingham*
[4] *Edinburgh*
[5] *University of Freiburg*
[6] *University of Glasgow*
[7] *LIP*
[8] *Santa Cruz*
[9] *University of Tokyo*
[10] *University of Chicago*
[11] *Michigan State University*
[12] *LPNHE*
[13] *Bonn*
[14] *Barcelona*

[15]*CERN*
[16]*LAL*
[17]*Liverpool*
[18]*Academica Sinica*
[19]*Innsbruck*
[20]*Tsukuba*
[21]*DESY*
[22]*Harvard*
[23]*University of Iowa*
[24]*Wisconsin*
[25]*UCL*
[26]*SLAC*
[27]*MPI, Munich*
[28]*Nanjing University*

Abstract

This note describes the dijet mass (cut-based) and multivariate VH(bb) analyses for the ATLAS Run I Publication. It includes discussion of the Monte Carlo simulation samples used, object and event selection, the accuracy to which the backgrounds are modeled, the systematic uncertainties and the statistical treatment used to extract the signal strength.

© Copyright 2014 CERN for the benefit of the ATLAS Collaboration.
Reproduction of this article or parts of it is allowed as specified in the CC-BY-3.0 license.

Contents

1 Introduction **29**

2 Updates since summer 2013 **30**

3 Data selection and event reconstruction **31**
3.1 Introduction on the data and Monte Carlo simulation. . . . 31
3.2 Object Definition . . . 32
3.2.1 Lepton . . . 32
3.2.2 Jet . . . 35
3.2.3 b-Jet . . . 37
3.2.4 $E_{\mathrm{T}}^{\mathrm{miss}}$and track-based missing transverse momentum . . . 37
3.2.5 Overlap Removal . . . 39
3.3 Event Selection . . . 40
3.3.1 Event Cleaning . . . 40
3.3.2 Trigger Selection . . . 41
3.3.3 Lepton Selection . . . 41
3.3.4 Jet Selection . . . 41
3.4 Event Kinematics Selection . . . 44
3.5 Dijet Mass Resolution and the Kinematic Fit . . . 45
3.5.1 Energy corrections to the selected b-jets . . . 45
3.5.2 Kinematic Fit . . . 48

4 VH→bb: Signal Characterization **49**
4.1 Simulation . . . 49
4.1.1 qq and qg Initiated Production . . . 49
4.1.2 NLO Electroweak Differential Correction . . . 50
4.2 Theoretical Uncertainties . . . 51
4.2.1 Inclusive Cross Section . . . 51
4.2.2 Acceptance and p_{T}^{V} . . . 51

5 Backgrounds **55**
5.1 Vector boson+jets . . . 57
5.1.1 Z+jets Modeling, Corrections and Systematic Uncertainties . . . 59
5.1.2 W+jets modeling, correction and systematics . . . 64
5.2 $t\bar{t}$ and single-top . . . 73
5.2.1 $t\bar{t}$ modeling, corrections and systematics . . . 73
5.2.2 Single-top modeling and systematics . . . 81
5.3 Diboson . . . 85
5.3.1 Uncertainties in the Modeling of the Diboson Processes . . . 85
5.4 Multijet and non-collision background . . . 90
5.4.1 0-lepton . . . 90
5.4.2 2-lepton . . . 90
5.4.3 1-lepton . . . 90

6 Multivariate analysis **93**
6.1 Input variables . . . 93
6.2 Boosted Decision Tree: Setup and Training . . . 97
6.2.1 Algorithm Description . . . 97
6.2.2 Boosting . . . 97
6.2.3 Overtraining . . . 98
6.2.4 Parameter Optimization . . . 100
6.3 The correlations between input variables and output variables . . . 102
6.4 MVA for the diboson and for the other mass points . . . 104

7 Experimental Systematic uncertainties **106**
7.1 Experimental Systematics . . . 106
7.1.1 Luminosity and pile up . . . 106
7.1.2 Electrons . . . 106
7.1.3 Muons . . . 106
7.1.4 $E_{\mathrm{T}}^{\mathrm{miss}}$ Trigger . . . 107
7.1.5 Jets . . . 107
7.1.6 Missing Transverse Energy . . . 108
7.1.7 Flavor Tagging . . . 108
7.2 Smoothing . . . 109

8 Statistical model and Systematic Uncertainties **110**
8.1 Likelihood Definition: Variables and Regions . . . 110
8.2 Likelihood Philosophy . . . 112
8.3 Systematics Uncertainties and Nuisance Parameters . . . 113
8.3.1 Naming Conventions . . . 113
8.3.2 Signal Specific Nuisance Parameters . . . 114
8.3.3 V+jets Specific Nuisance Parameters . . . 114
8.3.4 $t\bar{t}$ Specific Nuisance Parameters . . . 115
8.3.5 Single Top Specific Nuisance Parameters . . . 116
8.3.6 Diboson Specific Nuisance Parameters . . . 117
8.3.7 Multijet Specific Nuisance Parameters . . . 118
8.3.8 Experimental Nuisance Parameters . . . 118
8.4 Output Transform . . . 120
8.4.1 General description . . . 120
8.5 Pruning of the Systematic Uncertainties . . . 123
8.6 Understanding the Likelihood . . . 125
8.6.1 Dijet Mass Analysis Fit Studies . . . 125
8.6.2 MVA Analysis Fit Studies . . . 133
8.6.3 Comparison of Dijet Mass and MVA Analysis Fits . . . 141
8.6.4 Nuisance Parameter Ranking Plots . . . 146
8.7 Dijet Mass Analysis Post Fit Plots . . . 151
8.7.1 Normal binning . . . 161
8.7.2 Post fit b-tagging for the m_{jj} shape analysis . . . 171
8.8 MVA background-only post fit plots . . . 173
8.8.1 Post fit b-tagging for the MVA analysis . . . 177
8.9 Studies of the important NP in the fit . . . 179
8.10 Compatibility between the m_{bb} shape analysis and the MVA analysis . . . 180

9 Results **182**
9.1 Diboson observation . . . 182
9.2 Higgs Results . . . 185
9.2.1 Higgs Results Tables . . . 196

A E_T^{miss} trigger **207**
A.1 Emulation of the BGRP7 in the Monte Carlo for the EF_xe80T_tclcw_loose trigger . . . 208
A.2 Trigger efficiency and interdependence with offline variables . . . 210
A.2.1 Dependence of the $E_{\mathrm{T}}^{\mathrm{miss}}$ trigger efficiency on kinematic variables entering in the multivariate analysis . . . 211
A.2.2 Trigger efficiency parametrization . . . 214
A.3 $E_{\mathrm{T}}^{\mathrm{miss}}$trigger data driven scale factors . . . 217

B Delayed stream **218**
B.1 Introduction to delayed stream . . . 218
B.2 Delayed stream $E_{\mathrm{T}}^{\mathrm{miss}}$ trigger efficiency and scale factor . . . 218
B.3 $E_{\mathrm{T}}^{\mathrm{miss}}$ trigger bias . . . 218
B.4 Apply delayed stream in 0-lepton study . . . 219
B.5 Mis–modelling issue in 0–lepton analysis . . . 220

C Low $E_{\mathrm{T}}^{\mathrm{miss}}$ analysis for Zero Lepton Channel **227**
C.1 Event selection . . . 227
C.2 QCD rejection and estimation . . . 227
C.3 Mis-modelings . . . 230
C.4 Sensitivity gain and prospect with delayed trigger . . . 230

D $E_{\mathrm{T}}^{\mathrm{miss}}$ trigger for 1 lepton events **232**
D.1 $E_{\mathrm{T}}^{\mathrm{miss}}$ triggered muon events . . . 232
D.2 $E_{\mathrm{T}}^{\mathrm{miss}}$ trigger efficiency and scale factor . . . 232
D.3 QCD multi-jet background estimation . . . 232
D.4 Sensitivity gain . . . 232

E Electron Isolation **240**
E.1 Tag and Probe Algorithm . . . 240
E.2 Results . . . 241

F Muon isolation **242**
F.1 Results . . . 242

G Global sequential calibration **244**
G.1 GSC validation analysis . . . 244
G.1.1 Monte Carlo samples . . . 244
G.1.2 Event and jet selection . . . 244
G.1.3 Calculation of energy scale and resolution . . . 245
G.2 GSC performance . . . 245
G.2.1 Energy scale of *b*-jets . . . 245
G.2.2 Energy resolution for *b*-jets . . . 246
G.2.3 Closure tests for *b*-jets . . . 246

H Muon-Jet Overlap Removal **249**
H.1 Characterization of the muons overlapping jets . . . 249
H.2 Studies on the strategies to solve the muon-jet overlap . . . 250

I Signal modeling **253**

J Z+jet Modeling **256**
J.1 Effect of Strict Jets Cuts . . . 256
J.2 Determination of the data-driven corrections and systematics . . . 256
J.3 Comparison with other Monte Carlo samples . . . 257

K W+jet Modeling **261**
K.1 $\Delta\phi$Correction Derivation . . . 261
K.2 $\Delta\phi$Correction Usage . . . 261

L W+Heavy-Flavor Modeling **268**
L.1 Monte-Carlo samples . . . 268
L.1.1 aMC@NLO sample . . . 269
L.2 Uncertainties considered in the fit . . . 269
L.3 W+Heavy-Flavor Modeling for MVA variables . . . 273

M Single-top modeling **283**
M.1 t-channel . . . 283
M.2 s-channel . . . 293
M.3 Wt . . . 298

N $t\bar{t}$ modeling **303**
N.1 m_{bb} systematic . . . 303
N.2 $E_{\mathrm{T}}^{\mathrm{miss}}$ systematic . . . 305
N.3 top p_{T} reweighting of ALPGEN+PYTHIA . . . 306
N.4 The 2-to-3-jet and high-to-low-p_{T}^{W} uncertainties . . . 307
N.5 Flavor compositions of the $t\bar{t}$ generators . . . 308
N.6 Generator variations of the BDT input variables . . . 310

O Top Modeling from EPS **319**
O.1 Top Composition . . . 319

P Diboson modeling **320**
P.1 Cross section . . . 320
P.2 Modelling systematic uncertainties . . . 320
P.2.1 Stewart-Tackmann estimate of perturbative uncertainties on the diboson cross-section . . . 321
P.2.2 PDF and α_S uncertainties . . . 323
P.2.3 Parton shower and hadronization model . . . 324

Q Multi-jet background for 0-lepton analysis **341**
Q.1 Introduction: ABCD . . . 341
Q.2 Cross Checks . . . 343
Q.3 Final Product . . . 344

R Multijet background for 1-lepton analysis **347**
R.1 Template Overview . . . 347
R.2 Multijet Rejection . . . 347
R.3 Multijet Template Region . . . 348
R.4 Multijet Normalization . . . 349
R.5 Template Statistics: Using 1 b-tag events for the 2 b-tag regions . . . 350

S Multi-jet background for 2-lepton analysis **369**

T *b*-tagging Related Studies **371**
T.1 Custom *b*-tagging Efficiency Maps . . . 371
T.2 *b*-tagging generator dependence scale factor . . . 377
T.3 truth *b*-tagging efficiency maps closure test . . . 380

U Event-level Kinematic Likelihood Fit **385**
U.1 Likelihood Model . . . 385
U.2 Resolutions . . . 386
U.3 Results . . . 386

V Dijet Mass (m_{jj}) Distributions: Zero Lepton **389**

W Dijet Mass (m_{jj}) Distributions: One Lepton **395**

X Dijet Mass (m_{jj}) Distributions: Two Lepton **400**

Y MVA Input Variable Distributions: Zero Lepton **405**

Z MVA Input Variable Distributions: One Lepton **418**

AA MVA Input Variable Distributions: Two Lepton **451**

AB MVA Training Diagnostics **476**

AC MVA optimization and the transformation D **487**

AD MVA Distributions **490**

AE Correlations between MVA Variables: Zero Lepton **501**

AF Correlations between MVA Variables: One Lepton **512**

AG Correlations between MVA Variables: Two Lepton **533**

AH Pulls for the Individual Channels **542**
AH.1 Dijet Mass Analysis . . . 542
AH.1.1 0-lepton . . . 542
AH.1.2 Pre-fit and Post-Fit for the m_{jj} shape analysis in the 0-lepton fit . . . 547
AH.1.3 1-lepton . . . 554
AH.1.4 Pre-fit and Post-Fit for the m_{jj} shape analysis in the 1-lepton fit . . . 559
AH.1.5 2-lepton . . . 566
AH.1.6 Pre-fit and Post-Fit for the m_{jj} shape analysis in the 2-lepton fit . . . 571

AH.2 MVA . . . 578
AH.2.1 0-lepton pull plots . . . 578
AH.2.2 Pre-fit and Post-Fit for the MVA analysis in the 0-lepton fit . . . 583
AH.2.3 1-lepton pull plots . . . 586
AH.2.4 Pre-fit and Post-Fit for the MVA analysis in the 1-lepton fit . . . 591
AH.2.5 2-lepton pull plots . . . 594
AH.2.6 Pre-fit and Post-Fit for the MVA analysis in the 2-lepton fit . . . 599
AH.3 Dijet Mass versus MVA . . . 602
AH.3.1 0-lepton pull plots . . . 602
AH.3.2 1-lepton pull plots . . . 607
AH.3.3 2-lepton pull plots . . . 612

AI Postfit p_{T}^{V} Spectrums **617**
AI.1 Dijet Mass p_{T}^{V} . . . 617
AI.2 MVA p_{T}^{V} . . . 617

AJ Yield Tables **630**
AJ.1 Dijet Mass Analysis: Prefit . . . 630
AJ.2 Dijet Mass Analysis: Postfit . . . 643
AJ.3 Dijet Mass Analysis: Postfit over Prefit . . . 656
AJ.4 MVA Analysis: Prefit . . . 669
AJ.5 MVA Analysis: Prefit . . . 673
AJ.6 MVA Analysis: Postfit over Preft . . . 677

AKCombining 7 TeV and 8 TeV results **681**
AK.1 Consistency of the results . . . 681
AK.2 Pulls on the combination . . . 684
AK.3 Post-fit 2011 distributions . . . 684

AL Studies for the diboson VZ fit **695**
AL.1 Ranking plots for MVA diboson analysis . . . 695
AL.2 Pulls for MVA diboson analysis . . . 698
AL.3 Correlation Plots for the MVA diboson fit . . . 698
AL.4 Ranking plots for m_{jj} shape diboson analysis . . . 698
AL.5 Pulls for m_{jj} shape diboson analysis . . . 708
AL.6 Correlation Plots for the m_{jj} diboson fit . . . 708
AL.7 Correlation between diboson and Higgs signal strength . . . 716
AL.8 Diboson MVA post fit plots . . . 719
AL.9 Diboson dijet Mass Analysis Post Fit Plots . . . 723

AMImpact of the BCH cleaning on the VH analysis **733**
AM.1BCH cleaning for dummies . . . 733
AM.2Samples used . . . 733
AM.3Impact on selection yield . . . 733
AM.4Impact on distribution shapes . . . 734
AM.5Impact on b-tagging . . . 735
AM.6Conclusion . . . 735

AN Changes in different versions of this note **738**
AN.1 v0.1 . . . 738
AN.2 v0.2 . . . 738
AN.3 v0.3 . . . 738
AN.4 v0.4 . . . 739
AN.5 v0.5 . . . 739
AN.6 v0.6 . . . 740
AN.7 v0.7 . . . 740
AN.8 What we had foreseen from version v0.6 to version v0.7 . . . 740
AN.9 v0.8.1 . . . 741

AO Package List **742**

List of Tables

1 Trigger table used in the 2012 data analysis. . . . 31
2 Electron efficiencies for the cut-based and likelihood definitions. . . . 32
3 Inclusive VH Loose, Medium and Tight lepton definitions. . . . 34
4 Ordered list of jet properties used in the GSC calibration. . . . 36
5 Selection criteria for tracks associated with jets. . . . 36
6 Jet selection definitions. . . . 37
7 MV1c versus MV1 operating points. . . . 38
8 Track selection for $p_{\mathrm{T}}^{\mathrm{miss}}$. . . . 39
9 Overlap hierarchy. . . . 40
10 Signal lepton analysis selection. . . . 41
11 Analysis jet multiplicity requirements. . . . 42
12 Event kinematic selection. . . . 47
13 Muon selection for muon-in-jet correction. . . . 47
14 Inclusive cross sections and related uncertainties for WH production. . . . 51
15 Inclusive cross sections and related uncertainties for ZH production. . . . 51
16 Inclusive cross sections and related uncertainties for qq and gg initiated ZH production. . . . 52
17 Parameters for linear p_{T}^{V} signal shape uncertainty. . . . 52
18 Inclusive acceptance uncertainties derived from scale and PDF variations. . . . 54
19 Monte Carlo programs used. . . . 55
20 Monte Carlo samples and channel numbers and statistics used for the W samples 57
21 Monte Carlo samples and channel numbers and statistics used for the Z samples. . . . 58
22 Simple sample composition for Z+jets modeling studies. . . . 59
23 Summary of Z+jet specific samples used to checks the background modelling 60
24 Normalization change from W+jets $\Delta\phi$ corrections. . . . 65
25 V+jets samples considered for systematic variations. . . . 70
26 Summary of W+jet specific samples used to checks the background modelling 72
27 Monte Carlo samples and channel numbers and statistics used for top samples. . . . 73
28 $t\bar{t}$ jet composition in the 1-lepton analysis. . . . 74
29 $t\bar{t}$ jet composition in the 1-lepton multivariate analysis. . . . 74
30 Summary of $t\bar{t}$ specific samples used to checks the background modelling 80
31 Top samples considered for systematics. . . . 80
32 Top samples considered for systematics. . . . 81
33 Top samples considered for systematics. . . . 82
34 Systematics for the single top 83
35 Monte Carlo generator used for the modelling of the diboson processes and correspondent MC channel number, cross sections and number of generated events. . . . 85
36 Main settings for the MCFM software used to compute the cross-sections for the diboson processes. . . . 87
37 PDF+α_S systematic uncertainties for ZZ, WZ and WW processes, in the 2-jet and 3-jet categories. . . . 87
38 Probative systematics on σ_2 from the C_1 term of the covariance matrix across the different p_T^V bins. . . . 88
39 Perturbative systematics on σ_2 from the C_2 term of the covariance matrix across the different p_T^V bins. . . . 88
40 Perturbative systematics on $\sigma_{\geq 3}$ from the C_2 term of the covariance matrix across the different p_T^V bins. . . . 89

41 Summary of the diboson modelling systematic uncertainties, with the name of the correspondent nuisance parameter. . . . 89
42 Normalization nuisance parameters for multijet entering the fit. The 0-lepton uncertainties are correlated between regions. . . . 90
43 Summary of multijet specific samples used to checks the background modelling 92
44 Normalization nuisance parameters for multijet entering the fit. The 0-lepton uncertainties are correlated between regions. All 2-lepton uncertainties are correlated except for when the top $e-\mu$ control region is included in the standalone fit. . . . 92
45 Variable used to train the multivariate discriminant. . . . 94
46 BDT parameters. . . . 100
47 Regions used in profile likelihood 111
48 Summary of signal specific nuisance parameters. . . . 114
49 Summary of Z+jet specific nuisance parameters. . . . 115
50 Summary of W+jet specific nuisance parameters. . . . 116
51 Summary of $t\bar{t}$ specific nuisance parameters. . . . 116
52 Summary of single top specific nuisance parameters. . . . 117
53 The nuisance parameters used in the fit to parametrize the systematics on the diboson backgrounds. For `VVJetPDFAlphaPt`, the two values represent the normalization change in 2/3Jet region respectively. S="Shape", and SO="Shape Only" meaning explicitly the normalization of each N-jet/M-b-tag/p_{T}^{V} region is preserved while the shape is varied. . . . 117
54 Normalization nuisance parameters for multijet entering the fit. The 0-lepton uncertainties are correlated between regions. †All 2-lepton uncertainties are correlated except for when the top $e-\mu$ control region is included in the 2-lepton standalone fit. . . . 118
55 Summary of Combined Performance and experimental systematics. . . . 119
56 Variable used to train the multivariate discriminant. . . . 122
57 Summary of the important NP for the extraction of the signal μ 179
58 Correlation between the cut-based and MVA analyses 180
59 VZ MVA results. . . . 183
60 VZ m_{jj} results. . . . 184
61 Rescaling factors obtained from the global MVA fit to the 8 TeV data for the normalization of the $t\bar{t}$, Wbb, Wcl, Zbb, and Zcl backgrounds for the 2 jets events. The errors include the statistical and systematic uncertainties. . . . 185
62 The fitted numbers of signal and background events and the observed numbers of events after MVA selection for each lepton channel, in p_{T}^{V} intervals and b-tagging categories. These numbers are for the 8 TeV dataset, corresponding to an integrated luminosity of 20.3 fb^{-1}. The fitted numbers of signal events are shown for WH and ZH production separately for $m_h = 125$ GeV. The quoted errors on the total background correspond to one standard deviation of the fitted nuisance parameters incorporating both the systematic and statistical uncertainties. . . . 185
63 Expected and observed limits, significance and errors on μ for the MVA and m_{jj} shape analyses of the 8 TeV data, in each of the lepton channel, and in the combination for m_h=125 GeV. $\mu_{[\mathrm{x}]\text{-lep}}$ in the combined fit refears to the fit performed with one indipendent μ for each channel in the combined fit. . . . 189
64 Table of limit and p_0 for the m_{jj} 0+1+2 lepton 8 TeV analysis. . . . 196
65 Table of limit and p_0 for the m_{jj} 0-lepton 8 TeV analysis. . . . 196
66 Table of limit and p_0 for the m_{jj} 1-lepton 8 TeV analysis. . . . 197
67 Table of limit and p_0 for the m_{jj} 2-lepton 8 TeV analysis. . . . 197
68 Table of limit and p_0 for the MVA 0+1+2 lepton 8 TeV analysis. . . . 198

69 Table of limit and p_0 for the MVA 0-lepton 8 TeV analysis. . . . 198
70 Table of limit and p_0 for the MVA 1-lepton 8 TeV analysis. . . . 199
71 Table of limit and p_0 for the MVA 2-lepton 8 TeV analysis. . . . 199
72 Table of limit and p_0 for the MVA 0+1+2 lepton 8 TeV analysis. . . . 200
73 Table of limit and p_0 for the MVA 0-lepton 8 TeV analysis. . . . 200
74 Table of limit and p_0 for the MVA 1-lepton 8 TeV analysis. . . . 201
75 Table of limit and p_0 for the MVA 2-lepton 8 TeV analysis. . . . 201
76 E_T^{miss} trigger table used in the 2012 data analysis. . . . 207
77 Summary of $E_{\mathrm{T}}^{\mathrm{miss}}$ triggers used in the analysis. The threshold values are in GeV. . . . 207
78 Data period, integrated luminosity and threshold at each level (in GeV) . . . 218
79 Fitting parameters at each level of trigger for $Z \to \mu\mu$ and $W \to \mu\nu$ samples (MC) . . . 221
80 signal acceptance gain after applying trigger EF_xe60_tclcw_loose_delayed instead of nominal triggers . . . 222
81 Signal significance gain after applying trigger EF_xe60_tclcw_loose_delayed over the trigger EF_xe80_tclcw_loose . . . 223
82 Low $E_{\mathrm{T}}^{\mathrm{miss}}$ 0-lepton selection cuts. . . . 227
83 1 lepton significance with $E_{\mathrm{T}}^{\mathrm{miss}}$ triggered events. . . . 239
84 MC samples used for GSC studies. . . . 244
85 Signal acceptance increase from the improved *muon* overlap removal. . . . 252
86 2-lepton 3-jet yield changes from relaxed jet cuts. . . . 256
87 0-tag yield comparison for 2-lepton events. . . . 257
88 Functions and parameters used for Z+jets data-driven corrections and systematics. . . . 257
89 ALPGEN samples considered for cross-check. . . . 258
90 ALPGEN/SHERPA jet heavy-flavor fraction comparison in 2-lepton 2-tag events. . . . 258
91 ALPGEN/SHERPA heavy-flavor jet multiplicity comparison in 2-lepton 2-tag events. . . . 258
92 Functions and parameters used for W+jets $\Delta\phi$ correction. . . . 261
93 Normalization change for W+jets $\Delta\phi$ corrections. . . . 266
94 MC samples used in the estimation of the modeling uncertainties. All samples were centrally-produced with the exception of aMC@NLO and Sherpa $W + b\bar{b}$. . . . 268
95 MC samples used in the estimation of the flavor composition, at reconstruction-level. . . . 269
96 List of electroweak physical parameters used in the generation of aMC@NLO events with the CT10 PDF set. Dimension quantities given in GeV. . . . 269
97 Top samples considered for systematics. . . . 283
98 $t\bar{t}$ 3-to-2-jet and high-to-lowp_{T}^{W} uncertainties. . . . 310
99 $t\bar{t}$ jet composition of all generators in the 1-lepton analysis. . . . 311
100 $t\bar{t}$ jet composition in EPS. . . . 319
101 Comparison between diboson cross-sections provided by POWHEG and computed with MCFM. . . . 326
102 Relative contribution of $gg \to VV$ processes to WW and ZZ backgrounds. . . . 326
103 Monte Carlo generator used for the modelling of the diboson processes and correspondent cross-sections. . . . 326
104 Main settings for the MCFM software used to compute the cross-sections for the diboson processes. . . . 327
105 Parton-level jet-bins definition applied on the output of the MCFM simulation. The j1 and j2 objects are the two jets originated by the hadronically decaying V boson, while j3 is the extra parton produce by the NLO calculation. . . . 327
106 Perturbative systematics on σ_2 from the C_1 term of the covariance matrix across the different p_T^V bins. . . . 327

107 Perturbative systematics on σ_2 from the C_2 term of the covariance matrix across the different p_T^V bins. . . . 327
108 Perturbative systematics on $\sigma_{\geq 3}$ from the C_2 term of the covariance matrix across the different p_T^V bins. . . . 330
109 PDF+α_S systematic uncertainties for ZZ, WZ and WW processes, in the 2-jet and 3-jet categories. . . . 330
110 0-lepton multijet closure test. . . . 343
111 Event b-tagging rate cross check for 0-lepton multijet. . . . 344
112 0-lepton multijet estimate results for the dijet mass analysis. . . . 346
113 0-lepton multijet estimate results for the MVA analysis. . . . 346
114 Scale factors used for the normalization of the prefit plots 389
115 Variable used to train the multivariate discriminant. . . . 487
116 Table of prefit yields for 0-lepton 2 and 3-jet 1-tag events in the dijet mass selection. . . . 631
117 Table of prefit yields for 0-lepton 2 and 3-jet 2L-tag events in the dijet mass selection. . . . 632
118 Table of prefit yields for 0-lepton 2 and 3-jet 2M-tag events in the dijet mass selection. . . . 633
119 Table of prefit yields for 0-lepton 2 and 3-jet 2T-tag events in the dijet mass selection. . . . 634
120 Table of prefit yields for 1-lepton 2 and 3-jet 1-tag events in the dijet mass selection. . . . 635
121 Table of prefit yields for 1-lepton 2 and 3-jet 2L-tag events in the dijet mass selection. . . . 636
122 Table of prefit yields for 1-lepton 2 and 3-jet 2M-tag events in the dijet mass selection. . . . 637
123 Table of prefit yields for 1-lepton 2 and 3-jet 2T-tag events in the dijet mass selection. . . . 638
124 Table of prefit yields for 2-lepton 2 and 3-jet 1-tag events in the dijet mass selection. . . . 639
125 Table of prefit yields for 2-lepton 2 and 3-jet 2L-tag events in the dijet mass selection. . . . 640
126 Table of prefit yields for 2-lepton 2 and 3-jet 2M-tag events in the dijet mass selection. . . . 641
127 Table of prefit yields for 2-lepton 2 and 3-jet 2T-tag events in the dijet mass selection. . . . 642
128 Table of post unconditional fit yields for 0-lepton 2 and 3-jet 1-tag events in the dijet mass selection. . . . 644
129 Table of post unconditional fit yields for 0-lepton 2 and 3-jet 2L-tag events in the dijet mass selection. . . . 645
130 Table of post unconditional fit yields for 0-lepton 2 and 3-jet 2M-tag events in the dijet mass selection. . . . 646
131 Table of post unconditional fit yields for 0-lepton 2 and 3-jet 2T-tag events in the dijet mass selection. . . . 647
132 Table of post unconditional fit yields for 1-lepton 2 and 3-jet 1-tag events in the dijet mass selection. . . . 648
133 Table of post unconditional fit yields for 1-lepton 2 and 3-jet 2L-tag events in the dijet mass selection. . . . 649
134 Table of post unconditional fit yields for 1-lepton 2 and 3-jet 2M-tag events in the dijet mass selection. . . . 650
135 Table of post unconditional fit yields for 1-lepton 2 and 3-jet 2T-tag events in the dijet mass selection. . . . 651
136 Table of post unconditional fit yields for 2-lepton 2 and 3-jet 1-tag events in the dijet mass selection. . . . 652
137 Table of post unconditional fit yields for 2-lepton 2 and 3-jet 2L-tag events in the dijet mass selection. . . . 653
138 Table of post unconditional fit yields for 2-lepton 2 and 3-jet 2M-tag events in the dijet mass selection. . . . 654
139 Table of post unconditional fit yields for 2-lepton 2 and 3-jet 2T-tag events in the dijet mass selection. . . . 655

140 Table of post unconditional fit over prefit yields for 0-lepton 2 and 3-jet 1-tag events in the dijet mass selection. . . . 657
141 Table of post unconditional fit over prefit yields for 0-lepton 2 and 3-jet 2L-tag events in the dijet mass selection. . . . 658
142 Table of post unconditional fit over prefit yields for 0-lepton 2 and 3-jet 2M-tag events in the dijet mass selection. . . . 659
143 Table of post unconditional fit over prefit yields for 0-lepton 2 and 3-jet 2T-tag events in the dijet mass selection. . . . 660
144 Table of post unconditional fit over prefit yields for 1-lepton 2 and 3-jet 1-tag events in the dijet mass selection. . . . 661
145 Table of post unconditional fit over prefit yields for 1-lepton 2 and 3-jet 2L-tag events in the dijet mass selection. . . . 662
146 Table of post unconditional fit over prefit yields for 1-lepton 2 and 3-jet 2M-tag events in the dijet mass selection. . . . 663
147 Table of post unconditional fit over prefit yields for 1-lepton 2 and 3-jet 2T-tag events in the dijet mass selection. . . . 664
148 Table of post unconditional fit over prefit yields for 2-lepton 2 and 3-jet 1-tag events in the dijet mass selection. . . . 665
149 Table of post unconditional fit over prefit yields for 2-lepton 2 and 3-jet 2L-tag events in the dijet mass selection. . . . 666
150 Table of post unconditional fit over prefit yields for 2-lepton 2 and 3-jet 2M-tag events in the dijet mass selection. . . . 667
151 Table of post unconditional fit over prefit yields for 2-lepton 2 and 3-jet 2T-tag events in the dijet mass selection. . . . 668
152 Table of prefit yields for 0-lepton 2 and 3-jet events in the MVA selection. . . . 670
153 Table of prefit yields for 1-lepton 2 and 3-jet events in the MVA selection. . . . 671
154 Table of prefit yields for 2-lepton 2 and 3-jet events in the MVA selection. . . . 672
155 Table of post unconditional fit yields for 0-lepton 2 and 3-jet events in the MVA selection. 674
156 Table of post unconditional fit yields for 1-lepton 2 and 3-jet events in the MVA selection. 675
157 Table of post unconditional fit yields for 2-lepton 2 and 3-jet events in the MVA selection. 676
158 Table of post unconditional fit over prefit yields for 0-lepton 2 and 3-jet events in the MVA selection. . . . 678
159 Table of post unconditional fit over prefit yields for 1-lepton 2 and 3-jet events in the MVA selection. . . . 679
160 Table of post unconditional fit over prefit yields for 2-lepton 2 and 3-jet events in the MVA selection. . . . 680
161 Impact of BCH cleaning on yield after the full 0-lepton selection in data (last column) and for the signal sample for all triggers. For MC both the medium and tight BCH cleaning are given. . . . 734
162 Impact of BCH cleaning on signal yield after the full 1-lepton selection. . . . 734
163 Impact of BCH cleaning systematic uncertainty on yield after the full 0-lepton selection for the signal sample. The percentages shown correspond to the difference between applying the nominal BCH cleaning and the all-quark or all-gluon BCH mode. . . . 734
164 List of packages . . . 742

List of Figures

1 EM likelihood background rejection comparison. . . . 33
2 Schematic of 1-lepton lepton selection. . . . 35
3 Representative b-tagging scale factors. . . . 38
4 b-tagging categories. . . . 42
5 Truth tagging ΔR correction. . . . 43
6 Generator dependence of flavor tagging for exclusive MV1c 70% OP. . . . 44
7 Motivation for M_{eff} cut over $E_{\mathrm{T}}^{\mathrm{miss}}$ and m_{T}^{W} from the MVA analysis. . . . 46
8 m_{T}^{W} without a cut in the 1-lepton dijet mass analysis for $120 < p_{\mathrm{T}}^{W} < 160$. . . . 46
9 Current p_{T}-reco correction and a comparison to the EM+JES based correction. . . . 48
10 Dijet invariant mass before and after applying a kinematic likelihood fit in $ZH(125)$ simulation. . . . 48
11 Leading order Feynman diagrams for quark-initiated VH production. . . . 49
12 Leading order Feynman diagrams for gluon-initiated ZH production. . . . 50
13 Differential NLO EW VH production correction. . . . 50
14 Normalized p_{T}^{V} distribution for signal QCD scale uncertainty studies. . . . 53
15 Data-driven $\Delta\phi$ correction for Z+jets events . . . 61
16 p_{T}^{Z} for Z+jets events before any corrections have been applied. . . . 62
17 m_{bb} systematics for Z+jets events . . . 63
18 Uncorrected $\Delta\phi$ and p_{T}^{W} distributions in 1-lepton 0-tag and 1-tag events. . . . 66
19 Inclusively corrected $\Delta\phi$ distributions in 1-lepton 0-tag events. . . . 67
20 1-lepton 2-jet 0-tag χ^2 improvements from the $\Delta\phi$ corrections. . . . 68
21 1-lepton 2-jet p_{T}^{W} distribution in 0-tag after $\Delta\phi$ correction. . . . 69
22 1-lepton 2-jet $\Delta\phi$ corrections for low and high p_{T}^{W}. . . . 69
23 W-boson p_T distribution of 2-jet bb events at truth-level. . . . 71
24 Invariant mass distribution of 2-jet bb events at truth-level. The plot on the left compares the generator predictions for the $W + b\bar{b}$ process, and the plot on the right compares the same Sherpa prediction to the nominal B-filtered sample . . . 72
25 ATLAS $t\bar{t}$ p_{T}^{top} unfolded result. . . . 75
26 $t\bar{t}$ m_{bb} systematic. . . . 77
27 $t\bar{t}$ $E_{\mathrm{T}}^{\mathrm{miss}}$ systematic. . . . 78
28 $t\bar{t}$ coverage of systematic effects in the BDT output. . . . 79
29 Shape systematics for the Wt-ch single top . . . 84
30 Stewart-Tackmann method shape pertubative systematics on σ_2 for the $W \to l\nu$ and $Z \to q\bar{q}$ process. . . . 88
31 POWHEG+Pythia8 versus Herwig comparison for the WZ diboson processes. . . . 89
32 MVA Training input plot example. . . . 95
33 Optimization of the input variables for the one Lepton MVA. . . . 96
34 MVA overtraining plot example. . . . 99
35 Optimization of the BDT parameters for the one Lepton MVA. . . . 101
36 Frequency of the input variables . . . 101
37 MVA correlation plot for 2 leptons . . . 102
38 MVA correlation plot for 1 leptons . . . 103
39 MVA optimization for for different Higgs mass for Zero lepton . . . 105
40 2D Expected limit as a function of the z_s and z_b parameters. . . . 122
41 MVA binning transform . . . 122
42 m_{bb}binning transform . . . 122

584 43 0+1+2 lepton MVA fit pulls for b and c-jet tagging. . . . 126
585 44 0+1+2 lepton MVA fit pulls for light-jet tagging and lepton systematics. . . . 127
586 45 0+1+2 lepton MVA fit pulls for JES. . . . 128
587 46 0+1+2 lepton MVA fit pulls for diboson/top and W/Z. . . . 129
588 47 0+1+2 lepton MVA fit pulls for normalization NPs. . . . 130
589 48 0+1+2 lepton MVA fit pulls for the remaining NPs. . . . 131
590 49 Correlation plot for the full dijet masss analysis fit. . . . 132
591 50 0+1+2 lepton MVA fit pulls for b and c-jet tagging. . . . 134
592 51 0+1+2 lepton MVA fit pulls for light-jet tagging and lepton systematics. . . . 135
593 52 0+1+2 lepton MVA fit pulls for JES. . . . 136
594 53 0+1+2 lepton MVA fit pulls for diboson/top and W/Z. . . . 137
595 54 0+1+2 lepton MVA fit pulls for normalization NPs. . . . 138
596 55 0+1+2 lepton MVA fit pulls for the remaining NPs. . . . 139
597 56 Correlation plot for the full MVA analysis fit. . . . 140
598 57 m_{jj} vs MVA pull plots for 0+1+2 fit: b- and c-jet tagging. . . . 141
599 58 m_{jj} vs MVA pull plots for 0+1+2 fit: light-jet tagging and leptons. . . . 142
600 59 m_{jj} vs MVA pull plots for 0+1+2 fit: Jet NPs. . . . 143
601 60 m_{jj} vs MVA pull plots for 0+1+2 fit: Diboson and Top related uncertainties. . . . 144
602 61 m_{jj} vs MVA pull plots for 0+1+2 fit: Normalization and residual uncertainties. . . . 145
603 62 Ranking plots for combined dijet masss analysis. . . . 147
604 63 Ranking plots for 0-lepton , 1-lepton and 2-leptons dijet masss analysis. . . . 148
605 64 Ranking plots for combined MVA analysis. . . . 149
606 65 Ranking plots for 0-lepton , 1-lepton and 2-leptons MVA analysis. . . . 150
607 66 Post-fit dijet mass analysis plots for the 0-lepton 2-jets regions with $p_{\mathrm{T}}^{V} < 200$ GeV. . . . 152
608 67 Post-fit dijet mass analysis plots for the 0-lepton 3-jets regions with $p_{\mathrm{T}}^{V} < 200$ GeV. . . . 153
609 68 Post-fit dijet mass analysis plots for the 0-lepton regions with $p_{\mathrm{T}}^{V} > 200$ GeV. . . . 154
610 69 Post-fit dijet mass analysis plots for the 1-lepton 2-jets regions with $p_{\mathrm{T}}^{V} < 200$ GeV. . . . 155
611 70 Post-fit dijet mass analysis plots for the 1-lepton 3-jets regions with $p_{\mathrm{T}}^{V} < 200$ GeV. . . . 156
612 71 Post-fit dijet mass analysis plots for the 1-lepton regions with $p_{\mathrm{T}}^{V} > 200$ GeV. . . . 157
613 72 Post-fit dijet mass analysis plots for the 2-lepton 2-jets regions with $p_{\mathrm{T}}^{V} < 200$ GeV. . . . 158
614 73 Post-fit dijet mass analysis plots for the 2-lepton 3-jets regions with $p_{\mathrm{T}}^{V} < 200$ GeV. . . . 159
615 74 Post-fit dijet mass analysis plots for the 2-lepton regions with $p_{\mathrm{T}}^{V} > 200$ GeV. . . . 160
616 75 Post-fit dijet mass analysis plots for the 0-lepton 2-jets regions with $p_{\mathrm{T}}^{V} < 200$ GeV. . . . 162
617 76 Post-fit dijet mass analysis plots for the 0-lepton 3-jets regions with $p_{\mathrm{T}}^{V} < 200$ GeV. . . . 163
618 77 Post-fit dijet mass analysis plots for the 0-lepton regions with $p_{\mathrm{T}}^{V} > 200$ GeV. . . . 164
619 78 Post-fit dijet mass analysis plots for the 1-lepton 2-jets regions with $p_{\mathrm{T}}^{V} < 200$ GeV. . . . 165
620 79 Post-fit dijet mass analysis plots for the 1-lepton 3-jets regions with $p_{\mathrm{T}}^{V} < 200$ GeV. . . . 166
621 80 Post-fit dijet mass analysis plots for the 1-lepton regions with $p_{\mathrm{T}}^{V} > 200$ GeV. . . . 167
622 81 Post-fit dijet mass analysis plots for the 2-lepton 2-jets regions with $p_{\mathrm{T}}^{V} < 200$ GeV. . . . 168
623 82 Post-fit dijet mass analysis plots for the 2-lepton 3-jets regions with $p_{\mathrm{T}}^{V} < 200$ GeV. . . . 169
624 83 Post-fit dijet mass analysis plots for the 2-lepton regions with $p_{\mathrm{T}}^{V} > 200$ GeV. . . . 170
625 84 Post-fit unfolded b-tagging scale factors. . . . 172
626 85 Post-fit MVA plots for high p_{T}^{V} 0-lepton events. . . . 174
627 86 Post-fit MVA plots for 1-lepton events. . . . 175
628 87 Post-fit MVA plots for 2-lepton events. . . . 176
629 88 Post-fit unfolded b-tagging scale factors. . . . 178

89 The distribution of the difference of the signal strength for the m_{bb} shape and MVA analyses from the pseudo-data from the bootstrap technique for the combination of the 0, 1, 2 and 0+1+2 lepton channels. . . . 181
90 The relation between the signal strength obtained from the m_{bb} shape and MVA analyses for the combination of the 0- and 2-lepton channels. . . . 181
91 Fitted VZ signal strength for 8 TeV analysis. . . . 182
92 Global $log(s/b)$ ordered distribution from MVA analysis. . . . 186
93 Global $log(s/b)$ ordered distribution from MVA analysis. . . . 187
94 Fitted Higgs signal strength for dijet mass 8 TeV analysis. . . . 187
95 Fitted Higgs signal strength for MVA 8 TeV analysis. . . . 188
96 Fitted Higgs signal strength for combined 7 TeV dijet mass and MVA 8 TeV analysis. . . . 188
97 Left: Expected 95% C.L. upper limits on the normalised signal strength as a function of Higgs boson mass for all channels in 8 TeV data, for m_{bb} shape analysis.The expected upper limit is given for the background-only hypothesis. The green and yellow bands represent the 1σ and 2σ ranges of the expectation in the absence of a signal. Right: The observed local $p0$ as a function of the Higgs boson mass for the m_{bb} shape analysis. The dashed curves shows the expected local $p0$ under the hypothesis of a SM Higgs boson signal at that mass for the analysis of the 8 TeV data. Table 64 contains the exact values at each mass point. . . . 191
98 Left: Expected 95% C.L. upper limits on the normalised signal strength as a function of Higgs boson mass for the different lepton channels in 8 TeV data, for m_{bb} shape analysis.The expected upper limit is given for the background-only hypothesis. The green and yellow bands represent the 1σ and 2σ ranges of the expectation in the absence of a signal. Right: The observed local $p0$ as a function of the Higgs boson mass for the m_{bb} shape analysis. The dashed curves shows the expected local $p0$ under the hypothesis of a SM Higgs boson signal at that mass for the analysis of the 8 TeV data. (a): 0-lepton; (b): 1-lepton; (c): 2-leptons. Tables 65- 67 contain the exact values at each mass point. . . 192
99 Left: Expected 95% C.L. upper limits on the normalised signal strength as a function of Higgs boson mass for all channels in 8 TeV data, for MVA shape analysis.The expected upper limit is given for the background-only hypothesis. The green and yellow bands represent the 1σ and 2σ ranges of the expectation in the absence of a signal. Right: The observed local $p0$ as a function of the Higgs boson mass for the MVA shape analysis. The dashed curves shows the expected local $p0$ under the hypothesis of a SM Higgs boson signal at that mass for the analysis of the 8 TeV data. (a): the MVA has been trained for each mass point (Table 68). (b): the MVA trained for m_h =125 has been used for all the mass point (Table 72). . . . 193
100 Left: Expected 95% C.L. upper limits on the normalised signal strength as a function of Higgs boson mass for the different lepton channels in 8 TeV data, for MVA analysis (the MVA has been trained for each mass point).The expected upper limit is given for the background-only hypothesis. The green and yellow bands represent the 1σ and 2σ ranges of the expectation in the absence of a signal. Right: The observed local $p0$ as a function of the Higgs boson mass for the m_{bb} shape analysis. The dashed curves shows the expected local $p0$ under the hypothesis of a SM Higgs boson signal at that mass for the analysis of the 8 TeV data. (a): 0-lepton; (b): 1-lepton; (c): 2-leptons. Tables 69- 71 contain the exact values at each mass point. . . . 194

101 Left: Expected 95% C.L. upper limits on the normalised signal strength as a function of Higgs boson mass for the different lepton channels in 8 TeV data, for MVA analysis (the MVA trained for m_h =125 has been used for all the mass point).The expected upper limit is given for the background-only hypothesis. The green and yellow bands represent the 1σ and 2σ ranges of the expectation in the absence of a signal. Right: The observed local $p0$ as a function of the Higgs boson mass for the m_{bb} shape analysis. The dashed curves shows the expected local $p0$ under the hypothesis of a SM Higgs boson signal at that mass for the analysis of the 8 TeV data. (a): 0-lepton; (b): 1-lepton; (c): 2-leptons. Tables 73- 75 contain the exact values at each mass point. 195
102 Comparison between the events beloging to the BGRP7 (red) and the rest of th events (blue) in the Monte Carlo simulation for some of the variables (number of jets, inclusive jet p_{T}, inclusive jet ϕ, inclusive jet η). 209
103 selected $W \to \mu\nu$ offline $E_{\mathrm{T}}^{\mathrm{miss}}$ distribution, data(cross points) and MC(colored histogram) 210
104 selected $Z \to \mu\mu$ offline $E_{\mathrm{T}}^{\mathrm{miss}}$ distribution, data(cross points) and MC(colored histogram) 210
105 calculated xe80_tclcw_loose efficiency correlation between $E_{\mathrm{T}}^{\mathrm{miss}}$ (abscissa) and sum of leading two jet p_{T} using Sherpa $Z \to \mu\mu$ Monte Carlo. The four plots, are the L1 (top, left), the L2 (top, right), the EF (bottom left) efficiencies, and the combination of the three (bottom right). 211
106 calculated EF_xe80_tclcw_loose efficiency correlation between $E_{\mathrm{T}}^{\mathrm{miss}}$ (abscissa) and leading jet p_{T} using Sherpa $Z \to \mu\mu$ Monte Carlo. The four plots, are the L1 (top, left), the L2 (top, right), the EF (bottom left) efficiencies, and the combination of the three (bottom right). 212
107 calculated EF_xe80_tclcw_loose efficiency correlation between $E_{\mathrm{T}}^{\mathrm{miss}}$ (abscissa) and 2nd leading jet p_{T} using Sherpa $Z \to \mu\mu$ Monte Carlo. The four plots, are the L1 (top, left), the L2 (top, right), the EF (bottom left) efficiencies, and the combination of the three (bottom right). 212
108 calculated EF_xe80_tclcw_loose efficiency correlation between $E_{\mathrm{T}}^{\mathrm{miss}}$ (abscissa) and important variables (first row: left m_{jj} , right $\min(\Delta\phi(E_{\mathrm{T}}^{\mathrm{miss}}, jet))$; second row: $\Delta\phi(jet, jet)$) for the analysis using Sherpa $Z \to \mu\mu$ Monte Carlo. The plots, showing the combination of the L1, L2, EF efficiencies, are obtained after the selection cut described in this appendix has been applied. 213
109 Comparison of 2012 data and MC $E_{\mathrm{T}}^{\mathrm{miss}}$ distributions. Offline $E_{\mathrm{T}}^{\mathrm{miss}}$ distribution of selected $Z \to \mu\mu$ events (top left). L1 $E_{\mathrm{T}}^{\mathrm{miss}}$ distribution of selected $Z \to \mu\mu$ events (top right). L2 $E_{\mathrm{T}}^{\mathrm{miss}}$ distribution after L1 trigger with 40 GeV threshold (bottom left). EF $E_{\mathrm{T}}^{\mathrm{miss}}$ distribution after L2 trigger with 45 GeV threshold (bottom right). 214
110 EF_xe80_tclcw_loose efficiency calculated using Sherpa $W \to \mu\nu$ MC events. The efficiency is shown for each trigger level: L1 (top left), L2 (top right), EF (bottom left) and for the overall(bottom right). 215
111 Trigger Efficiency turn on estimate using $W(\to \mu\nu) + jets$ and $Z(\to \mu\mu) + jets$ events for data (top left), Alpgen (top right) and Sherpa (bottom). 216
112 Calculated scale factor for EF_xe80_tclcw_loose from the $W \to \mu\nu$, and the $Z \to \mu\mu$ samples. 217
113 Trigger efficiencies for each level and for over all (bottom right) of trigger EF_xe60_tclcw_loose_delayed using $W \to \mu\nu$+ 2 jets Sherpa events. 219
114 Trigger efficiencies for each level and for over all (bottom right) of trigger EF_xe60_tclcw_loose_delayed using $Z \to \mu\mu$+ 2 jets Sherpa events. 220

115 Correlation of trigger efficiencies between $E_{\mathrm{T}}^{\mathrm{miss}}$ and sum of p_T of jets for each level and for over all (bottom right) of trigger EF_xe60_tclcw_loose_delayed using $W \rightarrow \mu\nu$+ 2 jets Sherpa samples. . . . 221
116 Correlation of trigger efficiencies between $E_{\mathrm{T}}^{\mathrm{miss}}$ and sum of p_T of jets for each level and for over all (bottom right) of trigger EF_xe60_tclcw_loose_delayed using $W \rightarrow \mu\nu$+ 3 jets Sherpa samples. . . . 222
117 Scale factor of trigger EF_xe60_tclcw_loose_delayed after applying sum of p_T of jets cleaning cut using $Z \rightarrow \mu\mu$+ 2 jets, $W \rightarrow \mu\nu$ and $t\bar{t}$ events. . . . 222
118 Distribution of mass invariant (top) and $E_{\mathrm{T}}^{\mathrm{miss}}$ (bottom) of two b jets using MV1c tagger with 80 % of working point in $E_{\mathrm{T}}^{\mathrm{miss}}$ bin from 90 to 120 GeV in bin of 2 jet for data and MC samples using delayed stream trigger (left) and nominal triggers (right). . . . 223
119 Distribution of transverse momentum of 4–vector sum of 2 jets (pre b–tagging procedure) in $E_{\mathrm{T}}^{\mathrm{miss}}$ bin 90–120 GeV (left) and $E_{\mathrm{T}}^{\mathrm{miss}}$ bin 120–160 GeV (right) using nominal $E_{\mathrm{T}}^{\mathrm{miss}}$ triggers. . . . 224
120 Distributions of $E_{\mathrm{T}}^{\mathrm{miss}}$ (top), $E_{\mathrm{T}}^{\mathrm{miss}}/\sqrt{J12pT}$ (middle) and $\Delta\phi(jet, jet)$ (bottom) in $E_{\mathrm{T}}^{\mathrm{miss}}$ bin 90–120 GeV for jets (before b–tagging) before (left) and after (right) applying the additional QCD rejection cuts using delayed stream $E_{\mathrm{T}}^{\mathrm{miss}}$ trigger exclusively. . . . 225
121 Distributions of transverse momentum of 4–vector sum of 2 jets (pre b–tagging procedure) in $E_{\mathrm{T}}^{\mathrm{miss}}$ bin 90–120 GeV using delayed stream trigger exclusively (left) and nominal $E_{\mathrm{T}}^{\mathrm{miss}}$ triggers. . . . 226
122 $\Delta\phi(jet_1, jet_2)$ and $E_{\mathrm{T}}^{\mathrm{miss}}$ significance in the 0-lepton low $E_{\mathrm{T}}^{\mathrm{miss}}$ region. . . . 228
123 Input variables for low $E_{\mathrm{T}}^{\mathrm{miss}}$ 0-lepton multijet likelihood ratio discriminant. . . . 229
124 0-lepton low $E_{\mathrm{T}}^{\mathrm{miss}}$ LR output distribution. . . . 229
125 0-lepton low $E_{\mathrm{T}}^{\mathrm{miss}}$ kinematics before and after the LR cut. . . . 230
126 misH_{T} distributions for the low $E_{\mathrm{T}}^{\mathrm{miss}}$ 0-lepton channel. . . . 231
127 Validation of $\Delta\phi(jet_1, jet_2)$ as not source of low $E_{\mathrm{T}}^{\mathrm{miss}}$ mis-modeling in 0-lepton. . . . 231
128 $E_{\mathrm{T}}^{\mathrm{miss}}$ without muon contribution in $120 < p_{\mathrm{T}}^{W} < 160$ GeV1 lepton 2 jet events. . . . 233
129 $E_{\mathrm{T}}^{\mathrm{miss}}$ without muon contribution in $160 < p_{\mathrm{T}}^{W} < 200$ GeV1 lepton 2 jet events. . . . 233
130 $E_{\mathrm{T}}^{\mathrm{miss}}$ without muon contribution in $p_{\mathrm{T}}^{W} > 200$ GeV1 lepton 2 jet events. . . . 234
131 $E_{\mathrm{T}}^{\mathrm{miss}}$ without muon contribution in $120 < p_{\mathrm{T}}^{W} < 160$ GeV1 lepton 3 jet events. . . . 234
132 $E_{\mathrm{T}}^{\mathrm{miss}}$ without muon contribution in $160 < p_{\mathrm{T}}^{W} < 200$ GeV1 lepton 3 jet events. . . . 235
133 $E_{\mathrm{T}}^{\mathrm{miss}}$ without muon contribution in $p_{\mathrm{T}}^{W} > 200$ GeV1 lepton 3 jet events. . . . 235
134 m_{jj} in $E_{\mathrm{T}}^{\mathrm{miss}}$ triggered events with $120 < p_{\mathrm{T}}^{W} < 160$ GeV1 lepton 2 jet events. . . . 236
135 m_{jj} in $E_{\mathrm{T}}^{\mathrm{miss}}$ triggered events with $160 < p_{\mathrm{T}}^{W} < 200$ GeV1 lepton 2 jet events. . . . 236
136 m_{jj} in $E_{\mathrm{T}}^{\mathrm{miss}}$ triggered events with $p_{\mathrm{T}}^{W} > 200$ GeV1 lepton 2 jet events. . . . 237
137 m_{jj} in $E_{\mathrm{T}}^{\mathrm{miss}}$ triggered events with $120 < p_{\mathrm{T}}^{W} < 160$ GeV1 lepton 3 jet events. . . . 237
138 m_{jj} in $E_{\mathrm{T}}^{\mathrm{miss}}$ triggered events with $160 < p_{\mathrm{T}}^{W} < 200$ GeV1 lepton 3 jet events. . . . 238
139 m_{jj} in $E_{\mathrm{T}}^{\mathrm{miss}}$ triggered events with $p_{\mathrm{T}}^{W} > 200$ GeV1 lepton 3 jet events. . . . 238
140 Electron isolation efficiencies and derived scale factors. . . . 241
141 Muon isolation efficiencies and derived scale factors. . . . 242
142 Muon isolation efficiencies as a function of the number of reconstructed vertices (a) and with track isolation probing only (b) as well as a function of close-by jets (c-d). . . . 243
143 b-jet GSC versus EM+JES scale. . . . 245
144 b-jet GSC versus EM+JES resolution. . . . 246
145 b-jet scale as a function of f_{tile0} for the GSC versus EM+JES calibrations. . . . 247
146 b-jet scale as a function of f_{em3} for the GSC versus EM+JES calibrations. . . . 247
147 b-jet scale as a function of n_{trk} for the GSC versus EM+JES calibrations . . . 247
148 b-jet scale as a function of W_{track} for the GSC versus EM+JES calibrations . . . 247

149 Acceptance gain when changing ΔR cuts between μ and jets for overlap removal. 249
150 The scalar p_T sum of charged particle tracks around a μ for various μ types. 250
151 Fraction of jet EM energy as a function of $\Delta R(\mu$,jet). 250
152 $N_t rack$ of jets overlapping prompt μs and μs from semi-leptonic decays. 251
153 Jet vertex fraction when not using *muons*. 252
154 Normalized p_{T}^{V} distribution for signal PDF uncertainty studies. 254
155 PDF re-weighted p_{T}^{V}distribution for ZH events that pass a truth-level event selection. . . 255
156 PDF re-weighted p_{T}^{V}distribution for WH events that pass a truth-level event selection. . . 255
157 p_{T}^{Z} correction for Z+jets events derived for ALPGEN. 259
158 m_{bb} systematics for Z+jets events from ALPGEN. 260
159 Uncorrected $\Delta\phi$ and p_{T}^{W} distributions in 1-lepton 0 tag events. 262
160 Uncorrected $\Delta\phi$ distributions in 1-lepton 1-tag events. 263
161 Inclusively corrected $\Delta\phi$ distributions in 1-lepton 0 and 1-tag events. 264
162 1-lepton 2-jet χ^2 improvements from $\Delta\phi$ corrections. 265
163 1-lepton 2 and 3-jet $\Delta\phi$ corrections. 266
164 Improvement from applying the W+jet $\Delta\phi$ correction to W+jets or W+ll/cl. 267
165 Distribution of number of signal jets in the baseline aMC@NLO sample and in the samples where the μ_R and μ_F parameters have been varied (independently). Normalized to same area. 270
166 W-boson p_{T} distribution of 2-jet bb events at truth-level. The ratio is taken of each sample where the μ_R and μ_F parameters have been varied (independently) with respect to the baseline aMC@NLO sample. Normalized to same area. 270
167 Invariant mass distribution of 2-jet bb events at truth-level as predicted by the available W+bb generators (left) and the Sherpa samples (right). Normalized to same area. 271
168 Fit functions to the ratio plots shown in Figure 167. 271
169 , for $p_T(W) < 120$ GeV (left) and $p_T(W) > 120$ GeV (right). Normalized to same area. . 272
170 Distribution of the number of jets in bb events at truth-level. Comparison between generators (left) and between the different Sherpa samples (right). Normalized to same area. 272
171 Fit function to the observed aMC@NLOto SHERPAratio in the p_{T}^{W}distribution, for 2-jet bb events at truth levee. 273
172 Fraction of events with each flavor label in the 2-jet (left) and 3-jet (right) pre-tag regions, for Alpgen and Sherpa W+jets. Reconstruction-level distribution. Normalized to same area. 273
173 $\min|\Delta\phi(\ell, j)|$ variable in the low and high $p_T(W)$ regions, for the 2- and 3-jet cases. Events with leading jets matched to b-hadrons. 274
174 $|\Delta\phi(V, H)|$ variable in the low and high $p_T(W)$ regions, for the 2- and 3-jet cases. Events with leading jets matched to b-hadrons. 275
175 $\Delta R(b, b)$ variable in the low and high $p_T(W)$ regions, for the 2- and 3-jet cases. Events with leading jets matched to b-hadrons. 276
176 MET variable in the low and high $p_T(W)$ regions, for the 2- and 3-jet cases. Events with leading jets matched to b-hadrons. 277
177 Dijet mass in the low and high $p_T(W)$ regions, for the 2- and 3-jet cases. Events with leading jets matched to b-hadrons. 278
178 $M_T(W)$ in the low and high $p_T(W)$ regions, for the 2- and 3-jet cases. Events with leading jets matched to b-hadrons. 279
179 $p_T(j_1)$ in the low and high $p_T(W)$ regions, for the 2- and 3-jet cases. Events with leading jets matched to b-hadrons. 280

180 $p_T(j_2)$ in the low and high $p_T(W)$ regions, for the 2- and 3-jet cases. Events with leading jets matched to b-hadrons. . . . 281
181 $p_T(j_3)$ in the low and high $p_T(W)$ 3-jet regions. Events with leading jets matched to b-hadrons. . . . 282
182 m_{bbj} in the low and high $p_T(W)$ 3-jet regions. Events with leading jets matched to b-hadrons. . . . 282
183 One Lepton t-channel single top variables in 2 b-tag 2 jet $p_{\mathrm{T}}^{W} < 120$ GeV events. . . . 285
184 One Lepton t-channel single top variables in 2 b-tag 2 jet $p_{\mathrm{T}}^{W} < 120$ GeV events. . . . 286
185 One Lepton t-channel single top variables in 2 b-tag 2 jet $p_{\mathrm{T}}^{W} > 120$ GeV events. . . . 287
186 One Lepton t-channel single top variables in 2 b-tag 2 jet $p_{\mathrm{T}}^{W} > 120$ GeV events. . . . 288
187 One Lepton t-channel single top variables in 2 b-tag 3 jet $p_{\mathrm{T}}^{W} < 120$ GeV events. . . . 289
188 One Lepton t-channel single top variables in 2 b-tag 3 jet $p_{\mathrm{T}}^{W} < 120$ GeV events. . . . 290
189 One Lepton t-channel single top variables in 2 b-tag 2 jet $p_{\mathrm{T}}^{W} > 120$ GeV events. . . . 291
190 One Lepton t-channel single top variables in 2 b-tag 3 jet $p_{\mathrm{T}}^{W} > 120$ GeV events. . . . 292
191 One Lepton s-channel single top variables in 2 b-tag 2 jet $p_{\mathrm{T}}^{W} < 120$ GeV events. . . . 294
192 One Lepton s-channel single top variables in 2 b-tag 2 jet $p_{\mathrm{T}}^{W} > 120$ GeV events. . . . 295
193 One Lepton s-channel single top variables in 2 b-tag 3 jet $p_{\mathrm{T}}^{W} < 120$ GeV events. . . . 296
194 One Lepton s-channel single top variables in 2 b-tag 3 jet $p_{\mathrm{T}}^{W} > 120$ GeV events. . . . 297
195 One Lepton Wt-channel single top variables in 2 b-tag 2 jet $p_{\mathrm{T}}^{W} < 120$ GeV events. . . . 299
196 One Lepton Wt-channel single top variables in 2 b-tag 2 jet $p_{\mathrm{T}}^{W} > 120$ GeV events. . . . 300
197 One Lepton Wt-channel single top variables in 2 b-tag 3 jet $p_{\mathrm{T}}^{W} < 120$ GeV events. . . . 301
198 One Lepton Wt-channel single top variables in 2 b-tag 3 jet $p_{\mathrm{T}}^{W} > 120$ GeV events. . . . 302
199 All generator comparisons for $t\bar{t}$ m_{bb} systematics. . . . 304
200 PowHeg+Pythia and alpgen+Pythia comparisons for $t\bar{t}$ m_{bb} systematics. . . . 305
201 $t\bar{t}$ m_{bb} systematic function. . . . 306
202 All generator comparisons for $t\bar{t}$ $E_{\mathrm{T}}^{\mathrm{miss}}$ systematics. . . . 307
203 PowHeg+Pythia and alpgen+Pythia comparisons for $t\bar{t}$ $E_{\mathrm{T}}^{\mathrm{miss}}$ systematics. . . . 308
204 $t\bar{t}$ $E_{\mathrm{T}}^{\mathrm{miss}}$ systematic function. . . . 309
205 $t\bar{t}$ alpgen+Pythia to PowHeg+Pythia top p_{T} reweighting distribution. . . . 310
206 $t\bar{t}$ difference between alpgen and Pythia for m_{bb} flavor splitted . . . 312
207 $t\bar{t}$ difference between alpgen and Pythia for m_{bb} for bl events . . . 313
208 $t\bar{t}$ generator variations for BDT input variables, 2tag2jet, lpt. . . . 314
209 $t\bar{t}$ generator variations for BDT input variables, 2tag2jet, hpt. . . . 315
210 $t\bar{t}$ generator variations for BDT input variables, 2tag3jet, lpt. . . . 316
211 $t\bar{t}$ generator variations for BDT input variables, 2tag3jet, hpt. . . . 317
212 $t\bar{t}$ generator variations for additional 2tag3jet BDT input variables . . . 318
213 Perturbative systematics on σ_2 for the six diboson processes obtained applying scale variations according to the Stewart-Tackmann method. The solid line corresponds to the errors derived from the C_1 term and the dotted line from the C_2 term of the covariance matrix C. . . . 328
214 Perturbative systematics on $\sigma_{\geq 3}$ for the six diboson processes obtained applying scale variations according to the Stewart-Tackmann method. The solid line corresponds to the errors derived from the C_2 term of the covariance matrix C, while the C_1 term of the matrix does not provide any contribution to the 3-jet errors. . . . 329
215 Systematic uncertainties due to PDF errors on the 2-jet exclusive cross section for the six diboson processes, computed from the CT10 PDF set, across the five p_T(V) bins. . . . 330
216 Systematic uncertainties due to PDF errors on the 3-jet inclusive cross section for the six diboson processes, computed from the CT10 PDF set, across the five p_T(V) bins. . . . 331

217 Systematic uncertainties due to PDF errors on the 2-jet exclusive cross section for the six diboson processes, computed from the MSTW PDF set, across the five p_T(V) bins. . . . 331
218 Systematic uncertainties due to PDF errors on the 3-jet inclusive cross section for the six diboson processes, computed from the MSTW PDF set, across the five p_T(V) bins. . . . 332
219 Systematic uncertainties from α_S on the 2-jet exclusive cross section for the six diboson processes, computed from the CT10 PDF set, across the five p_T(V) bins. The solid line corresponds to the variation of the central value $\alpha_S = 0.117$, while the dotted line corresponds to the variation of $\alpha_S = 0.119$. . . . 332
220 Systematic uncertainties from α_S on the 3-jet inclusive cross section for the six diboson processes, computed from the CT10 PDF set, across the five p_T(V) bins. The solid line corresponds to the variation of the central value $\alpha_S = 0.117$, while the dotted line corresponds to the variation of $\alpha_S = 0.119$. . . . 333
221 Systematic uncertainties from α_S on the 2-jet exclusive cross section for the six diboson processes, computed from the MSTW PDF set, across the five p_T(V) bins. The solid line corresponds to the variation of the central value $\alpha_S = 0.117$, while the dotted line corresponds to the variation of $\alpha_S = 0.119$. . . . 334
222 Systematic uncertainties from α_S on the 3-jet inclusive cross section for the six diboson processes, computed from the MSTW PDF set, across the five p_T(V) bins. The solid line corresponds to the variation of the central value $\alpha_S = 0.117$, while the dotted line corresponds to the variation of $\alpha_S = 0.119$. . . . 335
223 Envelope of the systematic uncertainties from PDF+α_S on the 2-jet exclusive cross section for the six diboson processes. The solid line corresponds to the variations from the CT10 PDF set, while the dotted line from the MSTW PDF set. . . . 336
224 Envelope of the systematic uncertainties from PDF+α_S on the 3-jet inclusive cross section for the six diboson processes. The solid line corresponds to the variations from the CT10 PDF set, while the dotted line from the MSTW PDF set. . . . 337
225 POWHEG+Pythia8 versus Herwig comparison for the WZ diboson processes applying the 0-lepton selection in the 2-tag inclusive (LL+MM+TT) category: the systematic uncertainties from the PS/hadronization model is estimated taking the fit of the ratio of the different MC predictions. . . . 338
226 POWHEG+Pythia8 versus Herwig comparison for the ZZ diboson processes applying the 0-lepton selection in the pre-tag category: the systematic uncertainties from the PS/hadronization model is estimated taking the fit of the ratio of the different MC predictions. . . . 339
227 POWHEG+Pythia8 versus Herwig comparison for the WW diboson processes applying the 0-lepton selection in the pre-tag category: the systematic uncertainties from the PS/hadronization model is estimated taking the fit of the ratio of the different MC predictions. . . . 340
228 $\Delta\phi(E_{\mathrm{T}}^{\mathrm{miss}}, p_{\mathrm{T}}^{\mathrm{miss}})$ and $min|\Delta\phi(E_{\mathrm{T}}^{\mathrm{miss}}, jet)|$ distribution . . . 341
229 Two-dimensional kinematic plane for estimating QCD multi-jet background in the 0-lepton signal region (region A). $dphi(E_{\mathrm{T}}^{\mathrm{miss}}, p_{\mathrm{T}}^{\mathrm{miss}}) > \pi/2$ defines region A/C. . . . 342
230 Correlation test for two variables in 0-lepton multijet ABCD estimate. . . . 342
231 De-correlation check for variables used in 0-lepton MJ estimate. . . . 344
232 Sketch of jets, $E_{\mathrm{T}}^{\mathrm{miss}}$, and $p_{\mathrm{T}}^{\mathrm{miss}}$in the regions used for the 0-lepton multijet estimate. . . . 345
233 Truth label of the jet with $min|\Delta\phi(E_{\mathrm{T}}^{\mathrm{miss}}, jet)|$ . . . 345
234 Shape used for MJ in 0-lepton analysis. . . . 346
235 Motivation for M_{eff} cut over $E_{\mathrm{T}}^{\mathrm{miss}}$ and m_{T}^{W} from the MVA analysis. . . . 348
236 m_{T}^{W} without a cut in the 1-lepton dijet mass analysis for $120 < p_{\mathrm{T}}^{W} < 160$. . . . 349

912 237 Comparison of multijet template in muon 1-tag and 2-tag 2-jet events with $p_{\mathrm{T}}^{W} < 120$ GeV. 351
913 238 Comparison of multijet template in muon 1-tag and 2-tag 2-jet events with $p_{\mathrm{T}}^{W} > 120$ GeV. 352
914 239 Comparison of multijet template in muon 1-tag and 2-tag 3-jet events with $p_{\mathrm{T}}^{W} < 120$ GeV. 353
915 240 Comparison of multijet template in muon 1-tag and 2-tag 3-jet events with $p_{\mathrm{T}}^{W} > 120$ GeV. 354
916 241 Variables used for 1-lepton electron multijet reweight and final variables for 2L tag $p_{\mathrm{T}}^{W} <$
917 120 GeV events. 355
918 242 Variables used for 1-lepton electron multijet reweight and final variables for 2L tag $p_{\mathrm{T}}^{W} >$
919 120 GeV events. 356
920 243 Variables used for 1-lepton electron multijet reweight and final variables for 2M tag
921 $p_{\mathrm{T}}^{W} < 120$ GeV events. 357
922 244 Variables used for 1-lepton electron multijet reweight and final variables for 2M tag
923 $p_{\mathrm{T}}^{W} > 120$ GeV events. 358
924 245 Variables used for 1-lepton electron multijet reweight and final variables for 2T tag $p_{\mathrm{T}}^{W} <$
925 120 GeV events. 359
926 246 Variables used for 1-lepton electron multijet reweight and final variables for 2T tag $p_{\mathrm{T}}^{W} >$
927 120 GeV events. 360
928 247 Reweighted variables for the 1-lepton electron multijet template in 2L tag $p_{\mathrm{T}}^{W} < 120$ GeV
929 events. 361
930 248 Reweighted variables for the 1-lepton electron multijet template in 2L tag $p_{\mathrm{T}}^{W} > 120$ GeV
931 events. 362
932 249 Reweighted variables for the 1-lepton electron multijet template in 2M tag $p_{\mathrm{T}}^{W} < 120$ GeV
933 events. 363
934 250 Reweighted variables for the 1-lepton electron multijet template in 2M tag $p_{\mathrm{T}}^{W} > 120$ GeV
935 events. 364
936 251 Reweighted variables for the 1-lepton electron multijet template in 2T tag $p_{\mathrm{T}}^{W} < 120$ GeV
937 events. 365
938 252 Reweighted variables for the 1-lepton electron multijet template in 2T tag $p_{\mathrm{T}}^{W} > 120$ GeV
939 events. 366
940 253 Comparison of multijet template in electron 1-tag and 2-tag 3-jet events with $ptW >$
941 120 GeV. 367
942 254 Comparison of multijet template in electron 1-tag and 2-tag 3-jet events with $ptW >$
943 120 GeV. 368
944 255 The di-electron invariant mass distribution for (a) 0-tag, (b) 1-tag and (c) 2-tag. The
945 background expectations have been scaled by the results of the fits. The purple distribu-
946 tion is Z+jets, the green is the other non-multijet backgrounds, and the blue histogram is
947 the multijet background. 369
948 256 Distribution of the sum of the MV1c values of the two tagged jets in the 2 tag multijet
949 template (black points). Also shown is the distribution of the multijet template using the
950 truth tagging method (red points). 370
951 257 Comparison of multijet in 2-lepton electron and muon channels 370
952 258 b-jet efficiency maps. 372
953 259 c-jet efficiency maps. 373
954 260 *light*-jet efficiency maps. 374
955 261 τ-jet efficiency maps. 375
956 262 Example of a varied efficiency map. 376
957 263 Impact of varied efficiency map on Zcc in 0-lepton analysis. 376
958 264 Generator dependence of flavor tagging for exclusive MV1c 100% OP. 377
959 265 Generator dependence of flavor tagging for exclusive MV1c 80% OP. 378

266 Generator dependence of flavor tagging for exclusive MV1c 70% OP. . . . 378
267 Generator dependence of flavor tagging for exclusive MV1c 60% OP. . . . 379
268 Generator dependence of flavor tagging for MV1c 50% OP. . . . 379
269 Comparison between truth tagging and direct tagging for V+ll events. . . . 380
270 Comparison between truth tagging and direct tagging for V+cl events. . . . 381
271 Comparison between truth tagging and direct tagging for V+cc events. . . . 382
272 Comparison between truth tagging and direct tagging for WW events. . . . 382
273 Ratio of truth to direct tagged V+cc events. . . . 383
274 Truth tagging ΔR correction. . . . 383
275 Closure test of truth tagging ΔR correction. . . . 384
276 Balance of event from truth using $ZH(125)$ simulation. . . . 387
277 Dijet invariant mass before and after applying a kinematic likelihood fit in $ZH(125)$ simulation. . . . 388
278 Improvement in m_{jj} resolution in $ZH(125)$ simulation according to system balance. . . . 388
279 Zero Lepton m_{jj} distributions in 1 b-tag 2 jet events. . . . 391
280 Zero Lepton m_{jj} distributions in 1 b-tag 3 jet events. . . . 391
281 Zero Lepton m_{jj} distributions in 2L b-tag 2 jet events. . . . 392
282 Zero Lepton m_{jj} distributions in 2L b-tag 3 jet events. . . . 392
283 Zero Lepton m_{jj} distributions in 2M b-tag 2 jet events. . . . 393
284 Zero Lepton m_{jj} distributions in 2M b-tag 3 jet events. . . . 393
285 Zero Lepton m_{jj} distributions in 2T b-tag 2 jet events. . . . 394
286 Zero Lepton m_{jj} distributions in 2T b-tag 3 jet events. . . . 394
287 One Lepton m_{jj} distributions in 1 b-tag 2 jet events. . . . 396
288 One Lepton m_{jj} distributions in 1 b-tag 3 jet events. . . . 396
289 One Lepton m_{jj} distributions in 2L b-tag 2 jet events. . . . 397
290 One Lepton m_{jj} distributions in 2L b-tag 3 jet events. . . . 397
291 One Lepton m_{jj} distributions in 2M b-tag 2 jet events. . . . 398
292 One Lepton m_{jj} distributions in 2M b-tag 3 jet events. . . . 398
293 One Lepton m_{jj} distributions in 2T b-tag 2 jet events. . . . 399
294 One Lepton m_{jj} distributions in 2T b-tag 3 jet events. . . . 399
295 Two Lepton m_{jj} distributions in 1 b-tag 2 jet events. . . . 401
296 Two Lepton m_{jj} distributions in 1 b-tag 3 jet events. . . . 401
297 Two Lepton m_{jj} distributions in 2L b-tag 2 jet events. . . . 402
298 Two Lepton m_{jj} distributions in 2L b-tag 3 jet events. . . . 402
299 Two Lepton m_{jj} distributions in 2M b-tag 2 jet events. . . . 403
300 Two Lepton m_{jj} distributions in 2M b-tag 3 jet events. . . . 403
301 Two Lepton m_{jj} distributions in 2T b-tag 2 jet events. . . . 404
302 Two Lepton m_{jj} distributions in 2T b-tag 3 jet events. . . . 404
303 Zero Lepton MVA input variables in 1 b-tag 2-jet events. . . . 406
304 Zero Lepton MVA input variables in 1 b-tag 2-jet events postfit. . . . 407
305 Zero Lepton MVA input variables in 2 loose b-tags 2-jet events. . . . 408
306 Zero Lepton MVA input variables in 2 loose b-tags 2-jet events postfit. . . . 409
307 Zero Lepton MVA input variables in 2 MM+TT b-tags 2-jet events. . . . 410
308 Zero Lepton MVA input variables in 2 MM+TT b-tags 2-jet events postfit. . . . 411
309 Zero Lepton MVA input variables in 1 b-tag 3-jet events. . . . 412
310 Zero Lepton MVA input variables in 1 b-tag 3-jet events postfit. . . . 413
311 Zero Lepton MVA input variables in 2 loose b-tags 3-jet events. . . . 414
312 Zero Lepton MVA input variables in 2 loose b-tags 3-jet events postfit. . . . 415

313 Zero Lepton MVA input variables in 2 MM+TT b-tags 3-jet events. 416
314 Zero Lepton MVA input variables in 2 MM+TT b-tags 3-jet events postfit. 417
315 One Lepton MVA input variables in 1 b-tag 2-jet $p_{\mathrm{T}}^{W} < 120$ GeV events. 419
316 One Lepton MVA input variables in 1 b-tag 2-jet $p_{\mathrm{T}}^{W} < 120$ GeV events postfit. 420
317 One Lepton MVA input variables in 1 b-tag 2-jet $p_{\mathrm{T}}^{W} > 120$ GeV events. 421
318 One Lepton MVA input variables in 1 b-tag 2-jet $p_{\mathrm{T}}^{W} > 120$ GeV events postfit. 422
319 One Lepton MVA input variables in 2 LL b-tag 2-jet $p_{\mathrm{T}}^{W} < 120$ GeV events. 423
320 One Lepton MVA input variables in 2 LL b-tag 2-jet $p_{\mathrm{T}}^{W} < 120$ GeV events postfit. . . . 424
321 One Lepton MVA input variables in 2 LL b-tag 2-jet $p_{\mathrm{T}}^{W} > 120$ GeV events. 425
322 One Lepton MVA input variables in 2 LL b-tag 2-jet $p_{\mathrm{T}}^{W} > 120$ GeV events postfit. . . . 426
323 One Lepton MVA input variables in 2 MM b-tag 2-jet $p_{\mathrm{T}}^{W} < 120$ GeV events. 427
324 One Lepton MVA input variables in 2 MM b-tag 2-jet $p_{\mathrm{T}}^{W} < 120$ GeV events postfit. . . . 428
325 One Lepton MVA input variables in 2 MM b-tag 2-jet $p_{\mathrm{T}}^{W} > 120$ GeV events. 429
326 One Lepton MVA input variables in 2 MM b-tag 2-jet $p_{\mathrm{T}}^{W} > 120$ GeV events postfit. . . . 430
327 One Lepton MVA input variables in 2 TT b-tag 2-jet $p_{\mathrm{T}}^{W} < 120$ GeV events. 431
328 One Lepton MVA input variables in 2 TT b-tag 2-jet $p_{\mathrm{T}}^{W} < 120$ GeV events postfit. . . . 432
329 One Lepton MVA input variables in 2 TT b-tag 2-jet $p_{\mathrm{T}}^{W} > 120$ GeV events. 433
330 One Lepton MVA input variables in 2 TT b-tag 2-jet $p_{\mathrm{T}}^{W} > 120$ GeV events postfit. . . . 434
331 One Lepton MVA input variables in 1 b-tag 3-jet $p_{\mathrm{T}}^{W} < 120$ GeV events. 435
332 One Lepton MVA input variables in 1 b-tag 3-jet $p_{\mathrm{T}}^{W} < 120$ GeV events postfit. 436
333 One Lepton MVA input variables in 1 b-tag 3-jet $p_{\mathrm{T}}^{W} > 120$ GeV events. 437
334 One Lepton MVA input variables in 1 b-tag 3-jet $p_{\mathrm{T}}^{W} > 120$ GeV events postfit. 438
335 One Lepton MVA input variables in 2 LL b-tag 3-jet $p_{\mathrm{T}}^{W} < 120$ GeV events. 439
336 One Lepton MVA input variables in 2 LL b-tag 3-jet $p_{\mathrm{T}}^{W} < 120$ GeV events postfit. . . . 440
337 One Lepton MVA input variables in 2 LL b-tag 3-jet $p_{\mathrm{T}}^{W} > 120$ GeV events. 441
338 One Lepton MVA input variables in 2 LL b-tag 3-jet $p_{\mathrm{T}}^{W} > 120$ GeV events postfit. . . . 442
339 One Lepton MVA input variables in 2 MM b-tag 3-jet $p_{\mathrm{T}}^{W} < 120$ GeV events. 443
340 One Lepton MVA input variables in 2 MM b-tag 3-jet $p_{\mathrm{T}}^{W} < 120$ GeV events postfit. . . . 444
341 One Lepton MVA input variables in 2 MM b-tag 3-jet $p_{\mathrm{T}}^{W} > 120$ GeV events. 445
342 One Lepton MVA input variables in 2 MM b-tag 3-jet $p_{\mathrm{T}}^{W} > 120$ GeV events postfit. . . . 446
343 One Lepton MVA input variables in 2 TT b-tag 3-jet $p_{\mathrm{T}}^{W} < 120$ GeV events. 447
344 One Lepton MVA input variables in 2 TT b-tag 3-jet $p_{\mathrm{T}}^{W} < 120$ GeV events postfit. . . . 448
345 One Lepton MVA input variables in 2 TT b-tag 3-jet $p_{\mathrm{T}}^{W} > 120$ GeV events. 449
346 One Lepton MVA input variables in 2 TT b-tag 3-jet $p_{\mathrm{T}}^{W} > 120$ GeV events postfit. . . . 450
347 Two Lepton MVA input variables in 1 b-tag 2-jet $p_{\mathrm{T}}^{Z} < 120$ GeV events. 452
348 Two Lepton MVA input variables in 1 b-tag 2-jet $p_{\mathrm{T}}^{Z} < 120$ GeV events postfit. 453
349 Two Lepton MVA input variables in 1 b-tag 2-jet $p_{\mathrm{T}}^{Z} > 120$ GeV events. 454
350 Two Lepton MVA input variables in 1 b-tag 2-jet $p_{\mathrm{T}}^{Z} > 120$ GeV events postfit. 455
351 Two Lepton MVA input variables in 2 LL b-tags 2-jet $p_{\mathrm{T}}^{Z} < 120$ GeV events. 456
352 Two Lepton MVA input variables in 2 LL b-tag 2-jet $p_{\mathrm{T}}^{Z} < 120$ GeV events postfit. 457
353 Two Lepton MVA input variables in 2 LL b-tags 2-jet $p_{\mathrm{T}}^{Z} > 120$ GeV events. 458
354 Two Lepton MVA input variables in 2 LL b-tag 2-jet $p_{\mathrm{T}}^{Z} > 120$ GeV events postfit. 459
355 Two Lepton MVA input variables in 2 MM+TT b-tags 2-jet $p_{\mathrm{T}}^{Z} < 120$ GeV events. 460
356 Two Lepton MVA input variables in 2 MM+TT b-tag 2-jet $p_{\mathrm{T}}^{Z} < 120$ GeV events postfit. 461
357 Two Lepton MVA input variables in 2 MM+TT b-tags 2-jet $p_{\mathrm{T}}^{Z} > 120$ GeV events. 462
358 Two Lepton MVA input variables in 2 MM+TT b-tag 2-jet $p_{\mathrm{T}}^{Z} > 120$ GeV events postfit. 463
359 Two Lepton MVA input variables in 1 b-tag 3-jet $p_{\mathrm{T}}^{Z} < 120$ GeV events. 464
360 Two Lepton MVA input variables in 1 b-tag 3-jet $p_{\mathrm{T}}^{Z} < 120$ GeV events postfit. 465

361 Two Lepton MVA input variables in 1 b-tag 3-jet $p_{\mathrm{T}}^{Z} > 120$ GeV events. 466
362 Two Lepton MVA input variables in 1 b-tag 3-jet $p_{\mathrm{T}}^{Z} > 120$ GeV events postfit. 467
363 Two Lepton MVA input variables in 2 LL b-tags 3-jet $p_{\mathrm{T}}^{Z} < 120$ GeV events. 468
364 Two Lepton MVA input variables in 2 LL b-tag 3-jet $p_{\mathrm{T}}^{Z} < 120$ GeV events postfit. 469
365 Two Lepton MVA input variables in 2 LL b-tags 3-jet $p_{\mathrm{T}}^{Z} > 120$ GeV events. 470
366 Two Lepton MVA input variables in 2 LL b-tag 3-jet $p_{\mathrm{T}}^{Z} > 120$ GeV events postfit. 471
367 Two Lepton MVA input variables in 2 MM+TT b-tags 3-jet $p_{\mathrm{T}}^{Z} < 120$ GeV events. 472
368 Two Lepton MVA input variables in 2 MM+TT b-tag 3-jet $p_{\mathrm{T}}^{Z} < 120$ GeV events postfit. 473
369 Two Lepton MVA input variables in 2 MM+TT b-tags 3-jet $p_{\mathrm{T}}^{Z} > 120$ GeV events. 474
370 Two Lepton MVA input variables in 2 MM+TT b-tag 3-jet $p_{\mathrm{T}}^{Z} > 120$ GeV events postfit. 475
371 MVA Training for 0 lepton, 2 jets, $p_{\mathrm{T}}^{V} > 120$ GeV 477
372 MVA Training for 0 lepton, 3 jets, $p_{\mathrm{T}}^{V} > 120$ GeV 478
373 MVA Training for 1 lepton, 2 jets, $p_{\mathrm{T}}^{V} < 120$ GeV 479
374 MVA Training for 1 lepton, 2 jets, $p_{\mathrm{T}}^{V} > 120$ GeV 480
375 MVA Training for 1 lepton, 3 jets, $p_{\mathrm{T}}^{V} < 120$ GeV 481
376 MVA Training for 1 lepton, 3 jets, $p_{\mathrm{T}}^{V} > 120$ GeV 482
377 MVA Training for 2 leptons, 2 jets, $p_{\mathrm{T}}^{V} < 120$ GeV 483
378 MVA Training for 2 leptons, 2 jets, $p_{\mathrm{T}}^{V} > 120$ GeV 484
379 MVA Training for 2 leptons, 3 jets, $p_{\mathrm{T}}^{V} < 120$ GeV 485
380 MVA Training for 2 leptons, 3 jets, $p_{\mathrm{T}}^{V} > 120$ GeV 486
381 MVA binning optimization 488
382 MVA binning transform 489
383 Zero Lepton MVA distributions. 491
384 Zero Lepton MVA distributions. 492
385 One Lepton MVA distributions $p_{\mathrm{T}}^{W} < 120$ GeV. 493
386 One Lepton MVA distributions $p_{\mathrm{T}}^{W} < 120$ GeV. 494
387 One Lepton MVA distributions $p_{\mathrm{T}}^{W} > 120$ GeV. 495
388 One Lepton MVA distributions $p_{\mathrm{T}}^{W} > 120$ GeV. 496
389 Two Lepton MVA distributions $p_{\mathrm{T}}^{W} < 120$ GeV. 497
390 Two Lepton MVA distributions $p_{\mathrm{T}}^{W} < 120$ GeV. 498
391 Two Lepton MVA distributions $p_{\mathrm{T}}^{W} > 120$ GeV. 499
392 Two Lepton MVA distributions $p_{\mathrm{T}}^{W} > 120$ GeV. 500
393 Zero Lepton Correlation between mva and mBB 502
394 Zero Lepton Correlation between mva and dRBB 503
395 Zero Lepton Correlation between mva and MET 504
396 Zero Lepton Correlation between mva and dPhiVBB 505
397 Zero Lepton Correlation between mBB and dRBB 506
398 Zero Lepton Correlation between mBB and MET 507
399 Zero Lepton Correlation between mBB and dPhiVBB 508
400 Zero Lepton Correlation between dRBB and MET 509
401 Zero Lepton Correlation between dRBB and dPhiVBB 510
402 Zero Lepton Correlation between MET and dPhiVBB 511
403 One Lepton Correlation between mvaWlvH125 and mBB ($p_{\mathrm{T}}^{W} > 120$ GeV) 513
404 One Lepton Correlation between mvaWlvH125 and dRBB ($p_{\mathrm{T}}^{W} > 120$ GeV) 514
405 One Lepton Correlation between mvaWlvH125 and MET ($p_{\mathrm{T}}^{W} > 120$ GeV) 515
406 One Lepton Correlation between mvaWlvH125 and dPhiVBB ($p_{\mathrm{T}}^{W} > 120$ GeV) 516
407 One Lepton Correlation between mBB and dRBB ($p_{\mathrm{T}}^{W} > 120$ GeV) 517
408 One Lepton Correlation between mBB and MET ($p_{\mathrm{T}}^{W} > 120$ GeV) 518

409 One Lepton Correlation between mBB and dPhiVBB ($p_T^W > 120$ GeV) . . . 519
410 One Lepton Correlation between dRBB and MET ($p_T^W > 120$ GeV) . . . 520
411 One Lepton Correlation between dRBB and dPhiVBB ($p_T^W > 120$ GeV) . . . 521
412 One Lepton Correlation between MET and dPhiVBB ($p_T^W > 120$ GeV) . . . 522
413 One Lepton Correlation between mvaWlvH125 and mBB ($p_T^W < 120$ GeV) . . . 523
414 One Lepton Correlation between mvaWlvH125 and dRBB ($p_T^W < 120$ GeV) . . . 524
415 One Lepton Correlation between mvaWlvH125 and MET ($p_T^W < 120$ GeV) . . . 525
416 One Lepton Correlation between mvaWlvH125 and dPhiVBB ($p_T^W < 120$ GeV) . . . 526
417 One Lepton Correlation between mBB and dRBB ($p_T^W < 120$ GeV) . . . 527
418 One Lepton Correlation between mBB and MET ($p_T^W < 120$ GeV) . . . 528
419 One Lepton Correlation between mBB and dPhiVBB ($p_T^W < 120$ GeV) . . . 529
420 One Lepton Correlation between dRBB and MET ($p_T^W < 120$ GeV) . . . 530
421 One Lepton Correlation between dRBB and dPhiVBB ($p_T^W < 120$ GeV) . . . 531
422 One Lepton Correlation between MET and dPhiVBB ($p_T^W < 120$ GeV) . . . 532
423 One Lepton Correlation between mva and mBB ($p_T^Z > 120$ GeV) . . . 534
424 One Lepton Correlation between mva and dRBB ($p_T^Z > 120$ GeV) . . . 535
425 One Lepton Correlation between mva and pTV ($p_T^Z > 120$ GeV) . . . 536
426 One Lepton Correlation between mva and dPhiVBB ($p_T^Z > 120$ GeV) . . . 537
427 Two Lepton Correlation between mva and mBB ($p_T^W < 120$ GeV) . . . 538
428 Two Lepton Correlation between mva and dRBB ($p_T^W < 120$ GeV) . . . 539
429 Two Lepton Correlation between mva and pTV ($p_T^W < 120$ GeV) . . . 540
430 Two Lepton Correlation between mva and dPhiVBB ($p_T^W < 120$ GeV) . . . 541
431 Pull plots for 0-lepton channel: *b*- and *c*-jet tagging. . . . 542
432 Pull plots for 0-lepton channel: light-jet tagging and leptons. . . . 543
433 Pull plots for 0-lepton channel: Jet NPs. . . . 544
434 Pull plots for 0-lepton channel: Diboson and Top related uncertainties. . . . 545
435 Pull plots for 0-lepton channel: Normalization and residual uncertainties. . . . 546
436 Pre-fit dijet mass analysis plots for the 0-lepton 2-jets regions with $p_T^V < 200$ GeV in the 0-lepton fit . . . 548
437 Pre-fit dijet mass analysis plots for the 0-lepton 3-jets regions with $p_T^V < 200$ GeV in the 0-lepton fit. . . . 549
438 Pre-fit dijet mass analysis plots for the 0-lepton regions with $p_T^V > 200$ GeV in the 0-lepton fit. . . . 550
439 Post-fit dijet mass analysis plots for the 0-lepton 2-jets regions with $p_T^V < 200$ GeV in the 0-lepton fit . . . 551
440 Post-fit dijet mass analysis plots for the 0-lepton 3-jets regions with $p_T^V < 200$ GeV in the 0-lepton fit. . . . 552
441 Post-fit dijet mass analysis plots for the 0-lepton regions with $p_T^V > 200$ GeV in the 0-lepton fit. . . . 553
442 Pull plots for 1-lepton channel: *b*- and *c*-jet tagging. . . . 554
443 Pull plots for 1-lepton channel: light-jet tagging and leptons. . . . 555
444 Pull plots for 1-lepton channel: Jet NPs. . . . 556
445 Pull plots for 1-lepton channel: Diboson and Top related uncertainties. . . . 557
446 Pull plots for 1-lepton channel: Normalization and residual uncertainties. . . . 558
447 Pre-fit dijet mass analysis plots for the 1-lepton 2-jets regions with $p_T^V < 200$ GeV in the 1-lepton fit. . . . 560
448 Pre-fit dijet mass analysis plots for the 1-lepton 3-jets regions with $p_T^V < 200$ GeV in the 1-lepton fit. . . . 561

449 Pre-fit dijet mass analysis plots for the 1-lepton regions with $p_{\mathrm{T}}^{V} > 200$ GeV in the 1-lepton fit. . . . 562
450 Post-fit dijet mass analysis plots for the 1-lepton 2-jets regions with $p_{\mathrm{T}}^{V} < 200$ GeV in the 1-lepton fit. . . . 563
451 Post-fit dijet mass analysis plots for the 1-lepton 3-jets regions with $p_{\mathrm{T}}^{V} < 200$ GeV in the 1-lepton fit. . . . 564
452 Post-fit dijet mass analysis plots for the 1-lepton regions with $p_{\mathrm{T}}^{V} > 200$ GeV in the 1-lepton fit. . . . 565
453 Pull plots for 2-lepton channel: *b*- and *c*-jet tagging. . . . 566
454 Pull plots for 2-lepton channel: light-jet tagging and leptons. . . . 567
455 Pull plots for 2-lepton channel: Jet NPs. . . . 568
456 Pull plots for 2-lepton channel: Diboson and Top related uncertainties. . . . 569
457 Pull plots for 2-lepton channel: Normalization and residual uncertainties. . . . 570
458 Pre-fit dijet mass analysis plots for the 2-lepton 2-jets regions with $p_{\mathrm{T}}^{V} < 200$ GeV in the 2-lepton fit. . . . 572
459 Pre-fit dijet mass analysis plots for the 2-lepton 3-jets regions with $p_{\mathrm{T}}^{V} < 200$ GeV in the 2-lepton fit. . . . 573
460 Pre-fit dijet mass analysis plots for the 2-lepton regions with $p_{\mathrm{T}}^{V} > 200$ GeV in the 2-lepton fit. . . . 574
461 Post-fit dijet mass analysis plots for the 2-lepton 2-jets regions with $p_{\mathrm{T}}^{V} < 200$ GeV in the 2-lepton fit. . . . 575
462 Post-fit dijet mass analysis plots for the 2-lepton 3-jets regions with $p_{\mathrm{T}}^{V} < 200$ GeV in the 2-lepton fit. . . . 576
463 Post-fit dijet mass analysis plots for the 2-lepton regions with $p_{\mathrm{T}}^{V} > 200$ GeV in the 2-lepton fit. . . . 577
464 Pull plots for 0-lepton channel: *b*- and *c*-jet tagging. . . . 578
465 Pull plots for 0-lepton channel: light-jet tagging and leptons. . . . 579
466 Pull plots for 0-lepton channel: Jet NPs. . . . 580
467 Pull plots for 0-lepton channel: Diboson/Top and W/Z related uncertainties. . . . 581
468 Pull plots for 0-lepton channel: Other model and normalization uncertainties. . . . 582
469 Pre-fit MVA plots for high p_{T}^{V} 0-lepton events in the 0 lepton fit. . . . 584
470 Post-fit MVA plots for high p_{T}^{V} 0-lepton events in the 0 lepton fit. . . . 585
471 Pull plots for 1-lepton channel: *b*- and *c*-jet tagging. . . . 586
472 Pull plots for 1-lepton channel: light-jet tagging and leptons. . . . 587
473 Pull plots for 1-lepton channel: Jet NPs. . . . 588
474 Pull plots for 1-lepton channel: Diboson/Top and W/Z related uncertainties. . . . 589
475 Pull plots for 1-lepton channel: Other model and normalization uncertainties. . . . 590
476 Pre-fit MVA plots for 1-lepton events in the 1 lepton fit. . . . 592
477 Post-fit MVA plots for 1-lepton events in the 1 lepton fit. . . . 593
478 Pull plots for 2-lepton channel: *b*- and *c*-jet tagging. . . . 594
479 Pull plots for 2-lepton channel: light-jet tagging and leptons. . . . 595
480 Pull plots for 2-lepton channel: Jet NPs. . . . 596
481 Pull plots for 2-lepton channel: Diboson/Top and W/Z related uncertainties. . . . 597
482 Pull plots for 2-lepton channel: Other model and normalization uncertainties. . . . 598
483 Pre-fit MVA plots for 2-lepton events in the 2 lepton fit. . . . 600
484 Post-fit MVA plots for 2-lepton events in the 2 lepton fit. . . . 601
485 Pull plots for 0-lepton channel: *b*- and *c*-jet tagging. . . . 602
486 Pull plots for 0-lepton channel: light-jet tagging and leptons. . . . 603

487 Pull plots for 0-lepton channel: Jet NPs. . . . 604
488 Pull plots for 0-lepton channel: Diboson/Top and W/Z related uncertainties. . . . 605
489 Pull plots for 0-lepton channel: Other model and normalization uncertainties. . . . 606
490 Pull plots for 1-lepton channel: b- and c-jet tagging. . . . 607
491 Pull plots for 1-lepton channel: light-jet tagging and leptons. . . . 608
492 Pull plots for 1-lepton channel: Jet NPs. . . . 609
493 Pull plots for 1-lepton channel: Diboson/Top and W/Z related uncertainties. . . . 610
494 Pull plots for 1-lepton channel: Other model and normalization uncertainties. . . . 611
495 Pull plots for 2-lepton channel: b- and c-jet tagging. . . . 612
496 Pull plots for 2-lepton channel: light-jet tagging and leptons. . . . 613
497 Pull plots for 2-lepton channel: Jet NPs. . . . 614
498 Pull plots for 2-lepton channel: Diboson/Top and W/Z related uncertainties. . . . 615
499 Pull plots for 2-lepton channel: Other model and normalization uncertainties. . . . 616
500 0-Leptons: 1 and inclusive 2-tag postfit p_{T}^{V} plots from m_{jj} analysis. . . . 618
501 0-Leptons: 2-tag postfit p_{T}^{V} plots from m_{jj} analysis. . . . 619
502 1-Leptons: 1 and inclusive 2-tag postfit p_{T}^{V} plots from m_{jj} analysis. . . . 620
503 1-Leptons: 2-tag postfit p_{T}^{V} plots from m_{jj} analysis. . . . 621
504 2-Leptons: 1 and inclusive 2-tag postfit p_{T}^{V} plots from m_{jj} analysis. . . . 622
505 2-Leptons: 2-tag postfit p_{T}^{V} plots from m_{jj} analysis. . . . 623
506 0-Leptons: 1 and inclusive 2-tag postfit p_{T}^{V} plots from MVA analysis. . . . 624
507 0-Leptons: 2-tag postfit p_{T}^{V} plots from MVA analysis. . . . 625
508 1-Leptons: 1 and inclusive 2-tag postfit p_{T}^{V} plots from MVA analysis. . . . 626
509 1-Leptons: 2-tag postfit p_{T}^{V} plots from MVA analysis. . . . 627
510 2-Leptons: 1 and inclusive 2-tag postfit p_{T}^{V} plots from MVA analysis. . . . 628
511 2-Leptons: 2-tag postfit p_{T}^{V} plots from MVA analysis. . . . 629
512 Fitted Higgs signal strength for dijet mass 7 TeV analysis. . . . 682
513 Fitted Higgs signal strength for MVA 8 TeV analysis. . . . 682
514 Fitted Higgs signal strength for combined 7 TeV dijet mass and MVA 8 TeV analysis. . . . 683
515 Expectation for 7 TeV and 8 TeV combination 683
516 0+1+2 lepton MVA fit pulls for b, c and light-jet tagging and lepton systematics. . . . 685
517 0+1+2 lepton MVA fit pulls for JES, diboson/top and W/Z 686
518 0+1+2 lepton MVA fit pulls for normalization NPs and remaining NPs. . . . 687
519 Correlation plot for the full MVA analysis fit in the combined fit 688
520 Post-fit dijet mass analysis plots for 2-jets 0-lepton regions. . . . 689
521 Post-fit dijet mass analysis plots for 3-jets 0-lepton regions. . . . 690
522 Post-fit dijet mass analysis plots for 2-jets 1-lepton regions. . . . 691
523 Post-fit dijet mass analysis plots for 3-jets 1-lepton regions. . . . 692
524 Post-fit dijet mass analysis plots for 2-jets 2-lepton regions. . . . 693
525 Post-fit dijet mass analysis plots for 3-jets 2-lepton regions. . . . 694
526 Ranking plots for combined MVA analysis. . . . 696
527 Ranking plots for 0-lepton , 1-lepton and 2-leptons MVA analysis. . . . 697
528 0+1+2 lepton MVA diboson fit pulls for b and c-jet tagging. . . . 699
529 0+1+2 lepton MVA diboson fit pulls for light-jet tagging and lepton systematics. . . . 700
530 0+1+2 lepton MVA diboson fit pulls for JES. . . . 701
531 0+1+2 lepton MVA diboson fit pulls for diboson/top and W/Z. . . . 702
532 0+1+2 lepton MVA diboson fit pulls for normalization NPs. . . . 703
533 0+1+2 lepton MVA diboson fit pulls for the remaining NPs. . . . 704
534 Correlation plot for the full MVA diboson analysis fit. . . . 705

535 Ranking plots for combined m_{jj} analysis. . . . 706
536 Ranking plots for 0-lepton , 1-lepton and 2-leptons m_{jj} analysis. . . . 707
537 0+1+2 lepton m_{jj} diboson fit pulls for b and c-jet tagging. . . . 709
538 0+1+2 lepton m_{jj} diboson fit pulls for light-jet tagging and lepton systematics. . . . 710
539 0+1+2 lepton m_{jj} diboson fit pulls for JES. . . . 711
540 0+1+2 lepton m_{jj} diboson fit pulls for diboson/top and W/Z. . . . 712
541 0+1+2 lepton m_{jj} diboson fit pulls for normalization NPs. . . . 713
542 0+1+2 lepton m_{jj} diboson fit pulls for the remaining NPs. . . . 714
543 Correlation plot for the full m_{jj} diboson analysis fit. . . . 715
544 Correlation plot between the Higgs and the diboson VZ signal strength in the MVA Higgs fit. 717
545 Correlation plot between the Higgs and the diboson VZ signal strength in the m_{jj} shape Higgs fit. . . . 718
546 Post-fit MVA plots for high p_{T}^{V} 0-lepton events. . . . 720
547 Post-fit MVA plots for 1-lepton events. . . . 721
548 Post-fit MVA plots for 2-lepton events. . . . 722
549 Post-fit diboson dijet mass analysis plots for the 0-lepton 2-jets regions with $p_{\mathrm{T}}^{V} < 200$ GeV. 724
550 Post-fit diboson dijet mass analysis plots for the 0-lepton 3-jets regions with $p_{\mathrm{T}}^{V} < 200$ GeV. 725
551 Post-fit diboson dijet mass analysis plots for the 0-lepton regions with $p_{\mathrm{T}}^{V} > 200$ GeV. . . . 726
552 Post-fit diboson dijet mass analysis plots for the 1-lepton 2-jets regions with $p_{\mathrm{T}}^{V} < 200$ GeV. 727
553 Post-fit diboson dijet mass analysis plots for the 1-lepton 3-jets regions with $p_{\mathrm{T}}^{V} < 200$ GeV. 728
554 Post-fit diboson dijet mass analysis plots for the 1-lepton regions with $p_{\mathrm{T}}^{V} > 200$ GeV. . . . 729
555 Post-fit diboson dijet mass analysis plots for the 2-lepton 2-jets regions with $p_{\mathrm{T}}^{V} < 200$ GeV. 730
556 Post-fit diboson dijet mass analysis plots for the 2-lepton 3-jets regions with $p_{\mathrm{T}}^{V} < 200$ GeV. 731
557 Post-fit diboson dijet mass analysis plots for the 2-lepton regions with $p_{\mathrm{T}}^{V} > 200$ GeV. . . . 732
558 Leading jet p_{T}, m_{bb}, $E_{\mathrm{T}}^{\mathrm{miss}}$, $\phi(E_{\mathrm{T}}^{\mathrm{miss}})$, $\Delta\phi_{min}(E_{\mathrm{T}}^{\mathrm{miss}}, jet)$ and $\Delta R(jj)$ in the 0-lepton signal sample for events passing (black) and failing (red) BCH cleaning. . . . 736
559 Leading jet p_{T}, m_{bb}, $E_{\mathrm{T}}^{\mathrm{miss}}$, $\phi(E_{\mathrm{T}}^{\mathrm{miss}})$, $\Delta\phi_{min}(E_{\mathrm{T}}^{\mathrm{miss}}, jet)$ and $\Delta R(jj)$ in the 0-lepton `JetTauEtMiss` sample for events passing (black) and failing (red) BCH cleaning. . . . 737

1 Introduction

The search for the Standard Model (SM) [1–3] Higgs boson [4–7], is a central component of the physics program at the Large Hadron Collider (LHC). The observation of a narrow resonance decaying to a pair of photons, a pair of Z bosons, or a pair of W bosons has been reported by the ATLAS [8] and CMS [9] collaborations. A Higgs boson with a mass of $\approx$ 125 GeV would be accessible in a number of channels at the LHC. Measurements by ATLAS have thus far demonstrated that this narrow resonance can decay to bosons. Observing the decay to a pair of b quarks would be the first direct observation of the coupling to quarks by ATLAS and CMS. The decay to b quarks plays a particularly important role, as most of the Higgs bosons with a mass of $\approx$ 125 GeV are predicted by the SM to decay to b quarks ($BR \approx 58\%$ [10]) and therefore an observation in this channel is crucial in providing a constraint to the overall Higgs decay width, which is not directly measurable at the LHC. The cross section for associated production is lower than the inclusive Higgs cross section by more than an order of magnitude, however the signature provided by the leptonic decay modes of the associated vector boson is essential to reduce overwhelming multi-jet backgrounds.

We present an update with respect to [11] in the search for the Higgs boson decaying to a pair of b quarks with the Higgs produced in association with a vector boson. This update uses 20.3 fb^{-1} of data at $\sqrt{s}$ = 8 TeV delivered by the LHC in 2012. As of now the 4.7 fb^{-1} of data at $\sqrt{s}$ = 7 TeV delivered by the LHC in 2011 will not be reanalyzed but will be included for the signal strength extraction. The analysis is performed in three categories for events containing zero, one or two leptons. This targets three channels of Higgs production: $ZH \to \nu\bar{\nu}b\bar{b}$, $WH \to \ell\nu b\bar{b}$ and $ZH \to \ell^+\ell^- b\bar{b}$, where ℓ, or the term lepton, is understood to be either an electron or a muon. The 2-lepton category is only sensitive to the ZH production mode and the 1-lepton category is most sensitive to WH production. The 0-lepton category is most sensitive to ZH production, but with a small although not insignificant contribution from WH production.

Two version of the analysis are documented; one using the dijet mass as the final variable used to separate signal from background and another using a multivariate discriminant. The version using the dijet mass is usually referred to as the dijet masss analysis by the analysis team. Referring to this version as the dijet mass analysis helps the reader keep in mind that even though modeling all the variables which are cut on is important, the understanding of the dijet mass shape and the quantities used to calculate it is paramount since the signal extraction is done with a shape comparison. This thought process is not different for a multivariate analysis, only more intricate.

This note presents in parallel both versions of the analysis noting the common elements and the differences. Section 3 discusses the data, triggers, and object definitions which are common to both analysis as well as a side-by-side comparison of the event selection used. The signal samples and are discussed in Section 4 and Section 5 includes a description of the backgrounds. Both sections include information concerning systematic uncertainties specific to the processes discussed within. Section 6 introduces the multivariate techniques used in the analysis. Section 7 briefly notes the systematic uncertainties already discussed in the previous sections and detail those which are common to all (or most) processes. The statistical model is introduced and motivated in Section 8 with the results given in Section 9.

This analysis does not suffer from simplicity and so the documentation follows suit. Related sections are referenced in a hope that if one chooses to not read the note from front to back, the necessary information to understand the piece of the analysis chosen for investigation can be found easily. Enjoy!

2 Updates since summer 2013

Several optimizations and changes in modeling were implemented in the analysis with respect to the previous result reported in [11], in order to improve the search sensitivity. Some of these improvements are briefly summarized in the following list:

- Object selection changes

  The electron quality cuts for the signal have been changed to the likelihood definition;

  Removal of d_0 cut for electron identification;

  The lepton p_{T} used in the lepton veto have been lowered to 7 GeV;

  The Global Sequential Calibration (GSC) calibration is used for jets;

  The p_{T}-reco correction has been updated;

  The calorimeter isolation cut for leptons was tightened;

  The muon-jet overlap was revamped to take into account muons from V decays overlapping jet objects;

  A new heavy flavor tagger, which has a better b-c jet discrimination, has been used (MV1c), and a dedicated pseudo-continuous calibration has been derived;

  A $\sum p_{\mathrm{T}}^{jet}$ cut was introduced in the 0-lepton analysis;

- The Monte-Carlo (MC) samples were updated with more statistics when available.

- A new multi-variate analysis have been produced.

- The cut-based m_{jj} analysis have been updated including new tagging categories.

- A more mature multijet suppression for the 1-lepton analysis have been derived and the multijet model was updated.

- In the 2-leptons analysis, a kinematic likelihood fit have been studied and used to improve the m_{jj} resolution.

- The missing transverse energy (MET) trigger modeling was studied and the efficiency scale factors parametrized as function of the missing transverse energy and a specific cut on $\sum p_{\mathrm{T}}^{jet_i}$ has been used to avoid regions with trigger bias.

- A MET based trigger was implemented to recover sensitivity on the 1-lepton analysis, by triggering on events containing muons which have escaped due to limited acceptance of the L1 trigger muon chambers (30% increase in statistics). MET triggered 1-lepton event have been studied and included in the analysis for the 1-muon channel with $p_{\mathrm{T}}^{V} > 120$ GeV (previously only $p_{\mathrm{T}}^{V} > 160\,GeV$ was included).

- Detailed studies on the 0-lepton final state with 90 GeV $< E_{\mathrm{T}}^{\mathrm{miss}} <$ 120 GeV have been done, with the goal of including this region in the final fit. A dedicated effort have been made to validate the use of the delayed stream in this $E_{\mathrm{T}}^{\mathrm{miss}}$ region.

- Revisit and change of the $\Delta\phi$ corrections to V+jets simulations.

- Every modeling systematic was reevaluated.

3 Data selection and event reconstruction

This section describes the event reconstruction and selection. The signal is characterized by a leptonicly decaying vector boson and a Higgs decaying to a pair of heavy-flavor jets. The selection criteria was designed to maximize the acceptance of the expected signal topology while reducing the multijet and electroweak backgrounds contributions to a minimum. Section 3.1 details the data sets and triggers used. Section 3.2 describes the criteria used to reconstruct objects followed by how the objects are used to optimally select events compatible with the signal topology in Section 3.3.

3.1 Introduction on the data and Monte Carlo simulation.

The data used in this analysis were recorded by the ATLAS experiment during the 2012 LHC runs at a center-of-mass energy of $\sqrt{s}$ = 8 TeV with an integrated luminosity of 20.3 fb^{-1} [12].

The Monte Carlo (MC) samples used in the analysis are generated at the same center-of-mass energy as the corresponding data sample and passed through the ATLAS detector simulation [13] which is based on the GEANT 4 [14] program. In order to have significant amount of MC statistics, the "ATLFast II" simulation [15] is used for almost all the samples (the exceptions are noted in Section 5). Due to the differences in the distribution of pile-up events in the MC simulation with respect to the one measured in data, the standard pile-up re-weighting strategy has been adopted [16].

Event with leptons are primarily selected using the lowest un-prescaled single lepton triggers in addition to dilepton triggers where appropriate from `EGamma` and `Muon` streams in data. The lowest un-prescaled single lepton triggers used include a requirement on track isolation (iso_{track}) to combat the high pile-up conditions in the 2012 LHC data at the cost of a slight trigger inefficiency. To recover the lost events higher threshold triggers without a iso_{track} requirement are considered. To ensure that the trigger efficiency is well-defined, trigger matching is used to ensure that the offline lepton is the same lepton which fired the trigger. Missing transverse energy ($E_{\mathrm{T}}^{\mathrm{miss}}$) triggers in the `JetTauEtmiss` data stream are used to select events where the vector boson decays to neutrinos or charged leptons which are not identified or reconstructed. The full list of triggers considered is given in Table 1.

Trigger Object	Data Period	Trigger Names	iso_{track}	Luminosity (fb−1)
$E_{\mathrm{T}}^{\mathrm{miss}}$< 160 GeV	A-B5	EF_xe80T_tclcw_loose	NA	1.91928
	B6-L	EF_xe80_tclcw_loose		18.132
$E_{\mathrm{T}}^{\mathrm{miss}}$> 160 GeV	A-B5	EF_xe80_tclcw	NA	2.1257
	B6-L	EF_xe80_tclcw_loose		18.132
single electron	A-L	EF_e24vhi_medium1	✓	20.2769
		EF_e60_medium1		
single muon		EF_mu24i_tight	✓	
		EF_mu36_tight		
di-electron	A-L	EF_2e12Tvh_loose1		20.2769
di-muon		EF_2mu13		

Table 1: Trigger table used in the 2012 data analysis. The digits exceed the precision on the measurement of the luminosity, but they are reported here for future reference, since these are the numbers used to normalize the Monte Carlo predictions.

3.2 Object Definition

The following sections outlines the requirements used to select leptons (Section 3.2.1), jets (Section 3.2.2), b-jets (Section 3.2.3), and $E_{\mathrm{T}}^{\mathrm{miss}}$(Section 3.2.4), as well as the overlap removal criteria (Section 3.2.5) used to ensure no object is double counted. More technical information concerning the common performance group packages and tags used is given in Appendix AO.

3.2.1 Lepton

Three inclusive lepton definitions are listed below in increasing order of purity: loose (Section 3.2.1.1), medium (Section 3.2.1.2), and tight (Section 3.2.1.3). As discussed in the next pages, tight leptons are used for the selection of the W events, medium and loose for Z, and loose leptons are also used to veto events with extra leptons (like $t\bar{t}$). A lepton must also pass the overlap removal rules specified in Section 3.2.5 to considered in any analysis. Scale factors to correct for differences in the modeling of the efficiency of the isolation cuts discussed in the following sections have been calculated using tag and probe analysis with the Z boson and are discussed in Appendix E and F for electrons and muons respectively. With respect to the previous analysis [11], using the same calibration **??** the lepton minimum p_{T} requirement for Loose muons was decreased to 7 GeV (from 10 GeV) in order to maximize the 2-lepton signal acceptance and the rejection of $t\bar{t}$ events in the 0 and 1-lepton analyses. The electron quality was also changed to the likelihood definition which provides almost two times larger jet rejection for same electron efficiency compared to the cut-based one [17] [18]. Table 2 is a excerpt from Table 2 in [17] which compares the efficiency of real and fake electrons for the three cut-based definitions used for EPS and the corresponding likelihood definitions used for the current version. Figure 1 shows a similar comparison of the cut-based and likelihood definitions as a function of the electron E_{T}.

Menu	$20 < E_{\mathrm{T}} < 50\ GeV$	
	Data efficiency (%) $Z \to ee$	Data efficiency (%) Background
Loose Cuts	95.68 ± 0.17	5.414 ± 0.025
Very Loose LH	97.77 ± 0.14	3.028 ± 0.019
Tight Cuts	77.48 ± 0.24	0.463 ± 0.008
Very Tight LH	76.97 ± 0.29	0.278 ± 0.006

Table 2: Taken from [17], signal and background efficiencies for likelihood and cut-based menus, averaged over η and E_{T} between 20 and 50 GeV. Both signal and background efficiencies are determined with respect to basic track quality cuts in the denominator and errors on the signal include statistical and systematic uncertainties, while uncertainties in background are statistical only.

3.2.1.1 VH Loose Lepton

The VH loose lepton criteria are defined in Table 3. Calorimeter **??** and stand-alone **??** muons are used to increase the muon acceptance in η. Track isolation is defined as:

$$iso_{track}(\ell) = \frac{1}{p_T^{\ell}} \sum_{trk} p_T^{trk} \text{ for } \Delta R(\ell, trk) < 0.2. \quad (1)$$

The calo-muon candidates within $\Delta R< 0.1$ of a selected combined, segmented tagged or stand-alone muon are rejected to avoid double counting.

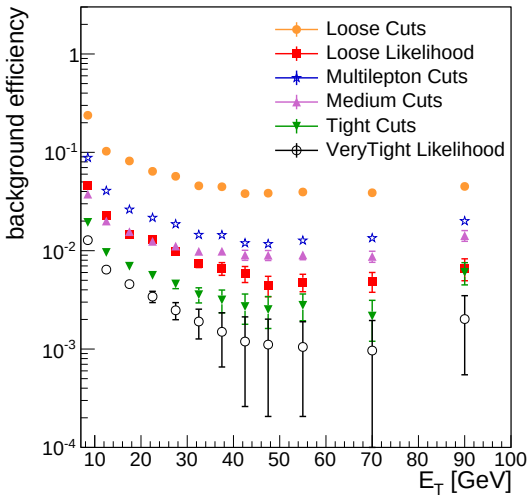

Figure 1: A comparison of the cut and likelihood qualities is shown as a function of the transverse energy of the electron object. This shows the increase in background rejection for the same signal efficiency for the various quality definitions.

3.2.1.2 VH Medium Lepton

VH Medium leptons have additional requirements in addition to those used to define loose leptons. For muons, only combined/segment-tagged muons are considered. Stand-alone and Calo muons are not considered to identify the decay products of the vector boson as this would lead to an increase in the multijet background. The medium lepton cuts are outlined in Table 3.

3.2.1.3 VH Tight Lepton

VH Tight leptons are medium candidates satisfying tight isolation requirements. In addition, tight electrons should pass the very tight LH selection. The VH Tight lepton cuts are defined in Table 3. Calorimeter isolation (iso_{calo}) is defined as:

$$iso_{calo}(\ell) = \frac{1}{p_T^{\ell}} \sum_{TC} E_T^{TC} \text{ for } \Delta R(\ell, TC) < 0.3. \quad (2)$$

where TC stands for topoclusters. The electron isolation is corrected in order to subtract out-of-cluster leakage in the isolation cone, and energy density from underlying event and pileup (using the jet area technique).

The tight lepton selection has been re-optimized in concert with the 1-lepton multijet model lepton selection. In comparison to the EPS result [11] the calorimeter isolation criterion has been tightened from 0.07 to 0.04 in both the electron and muon channel. A loose d_0 significance requirement, $\left(\frac{d_0}{\sigma_{d_0}}\right)$, had been entertained in the muon channel to help reduce the multijet contribution but this cut was shown to be ineffective after applying the event level cuts.

3.2.1.4 Notable Change from EPS

For over two years now the impact parameter (d_0) has been required to be less that 0.1 *mm* for both the electron and muon channel. For electrons, a d_0 cut should be used with assoicated scale factors which do not exist and therefore would have to be derived by this analyis group. With the interest of time, this cut

as been dropped from the electron channel only resulting in an over 10% increase of the 2-electron signal acceptance with the cost of a non-negligible multijet contribution described in detail in Appendix S and summarized in Section 5.4.2. In the 1-electron channel the signal acceptance increased less than 2% as the EM likelihood has a decreased efficiency at larger d_0 values.

3.2.1.5 1-lepton Multijet Model Leptons

Data events are used to estimate the contribution of multijet (MJ) events which satisfy the 1-lepton selection since generating sufficient MC statistics to model this process would be extremely difficult. A MJ model region is defined from which data events are extracted and the electroweak contribution subtracted to obtain the MJ template. The MJ model region is defined as Medium VH leptons with the modification of $0.05(0.07) < iso_{track} < 0.12(0.5)$ in the $e(\mu)$ channel and $iso_{calo} < 0.07$ in both and the quality of MediumPP [19] in the e channel on top of the *VeryLoose* LH criteria. The choice of cuts is motivated in Appendix R but stated briefly the cuts were determined in order to have decent agreement with template sufficient statistics to populate the high p_{T}^{V} regions. All event level cuts are then required. Full details on the MJ estimation including normalization, b-tagging, and systematic uncertainties are given in Section 5.4.3. The template region has changed since EPS [11]. Then the iso_{track} range was changed from $0.04 \leq iso_{track} \leq 0.1$ to reduce the fraction of EW contamination (increase lower cut) and increase the available statistics (increase the upper cut). The VeryTight LH criteria was checked in the electron channel but was shown to produce a template similar to the MediumPP choice but with less statistics. The iso_{calo} cut was not tightened to 0.04 as it was for the signal lepton to maintain more statistics in the template. The details of the studies performed to make these decisions are given in Appendix R but these changes resulted in an increase in the MJ statistics by a factor of 2. Figure 2 shows a schematic of all the lepton selections used for the 1-lepton analysis.

Flavor	Electrons	Muons		
Type	Author 1 or 3	Comb/Seg-Tag	Calo	Stand Alone
VH Loose				
Quality	VeryLoose LH [17] [18]	Tight MuID & MCP hit requirements		
$\lvert\eta\rvert$	< 2.47	< 2.7	< 0.1	in [2.5, 2.7]
E_{T} (GeV)	> 7	> 7	> 20	> 7
$\lvert d_0\rvert$ (mm)	–	< 0.1	< 0.1	NA
$\lvert z_0\rvert$ (mm)	–	< 10	< 10	NA
iso_{track}	< 0.1	< 0.1	< 0.1	NA
VH Medium				
E_{T} (GeV)	> 25	> 25	NU	NU
$\lvert\eta\rvert$	–	< 2.5		
VH Tight				
Quality	VeryTight LH	–		
iso_{track}	< 0.04	< 0.04	NU	NU
iso_{calo}	< 0.04	< 0.04		

Table 3: Inclusive VH Loose, Medium and Tight lepton definitions. NU stands for 'Not Used'. Additional information is given in Sections 3.2.1.1-3.2.1.3.

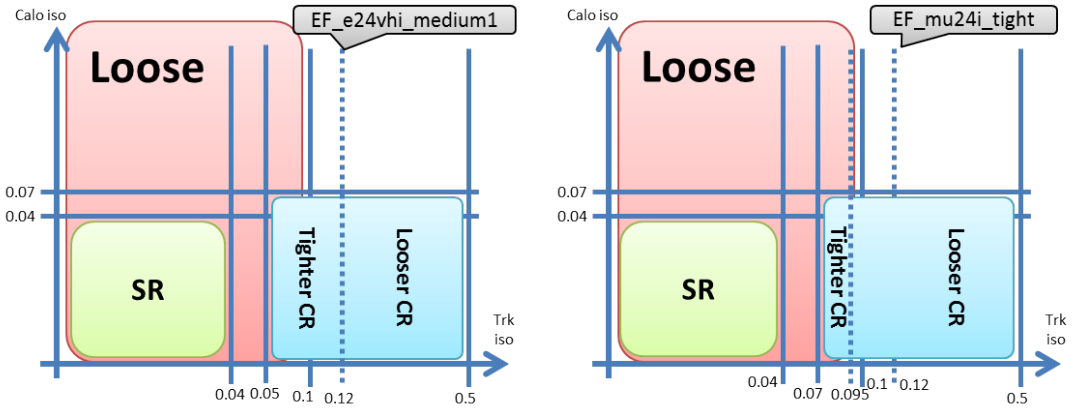

(a) Electron (b) Muon

Figure 2: The 1-lepton selection is shown for electrons (a) and muons (b) in the iso_{track} versus iso_{calo} plane. The red box fills the region used for Loose leptons and the green box fills the Tight lepton region. The blue box represents the region used for the 1-lepton multijet selection. One can clearly see that only some multijet leptons satisfy the loose lepton criteria. For electrons, the Tight CR is used for the nominal template and the loose for the systematic variation. For muons, the inclusive CR is used for the nominal while Tight and Loose are used individually for the Up and Down systematic variation of the iso_{track} cut.

3.2.2 Jet

Jets are reconstructed using the anti-k_T algorithm [20] with a radius parameter $R = 0.4$. The jet energy dependence on in-time pile-up is mitigated by applying two data-derived corrections: one based on the product of the event p_{T} density and the jet area [21], and one that depends on the number of reconstructed primary vertices and the mean number of expected interactions which primarily affects jets in the forward region. The second correction addresses effects due to out-of-time pile-up. After the two corrections, an energy and η-dependent MC-based calibration is applied to all jets. Finally, a residual correction from in situ measurements is applied to data.

Since the previous version of this analysis was released [11] a new calibration known as Global Sequential Calibration (GSC) has been introduced and is applied on top of the EM+JES calibration. GSC was proposed as a way of incrementally improving the jet energy resolution and making the jet response,

$$R =< p_T^{\mathrm{reco}} / p_T^{\mathrm{truth}} >, \tag{3}$$

less dependent whether the jet is more quark-like or gluon-like. In ATLAS, this is referred to as flavor dependence which should not be confused with the quark flavor (b, c, light) assigned to jets. In this note, jet flavor usually refers to the quark flavor and in cases where the terminology is used to denote quark-gluon differences, the meaning of flavor is clarified. Sequential corrections are applied as

$$C(x, p_{\mathrm{T}}) = R^{-1}(x, p_{\mathrm{T}}) \tag{4}$$

where x is the jet property under consideration. This list of jet properties considered can be found in Table 4. Ghost-matched tracks **??** selected by the criteria listed in Table 5 with $p_{\mathrm{T}} > 1$ GeV and associated to the 0^{th} primary vertex are used for the track related properties including the track width, W_{track}, which is defined as

$$W_{track} = \frac{\sum_{\mathrm{trk}} p_{\mathrm{T}} \Delta R(\mathrm{jet}, \mathrm{trk})}{\sum_{\mathrm{trk}} p_{\mathrm{T}}} \tag{5}$$

The W_{track} correction has been shown to be the modification which reduces the difference in response between light-quark and gluon jets. Coincidentally this correction is applied last and can be removed to understand the effect on b-jets. More details about the correction technique can be found in References [22], [23] as well as in Appendix G. The main motivation for using this calibration in a quark-dominated final state analysis such as this one is for the improvement in the dijet mass resolution.

Jet Property	Order	Definition
f_{tile0}	1	fraction of energy deposited in the first layer of the Tile calorimeter
f_{em3}	2	fraction of energy deposited in the third layer of the EM calorimeter
n_{trk}	3	track multiplicity
W_{track}	4	p_T weighted average ΔR of tracks in the jet

Table 4: Ordered list of jet properties used in the GSC calibration. More details are given in Section 3.2.2 including the track selection shown in Table 5.

Observable	Cut
Track Selection Criteria	
p_{T} (GeV)	> 0.5 OR > 1.0
$\lvert\eta\rvert$	< 2.5
pixel hits	> 0
SCT hits	> 5
$\lvert z\rvert$ (mm)	< 200
d_0 (mm)	< 5.0
d_0/σ_{d_0}	< 100
χ^2/DOF	< 5
Track-Vertex$_i$ Association	
d_i (mm)	< 1.0
$z_i \sin(\theta)$ (mm)	< 1.0

Table 5: Selection used for tracks to be associated to jets and vertices. Additional information, including the various p_{T} cuts, is given in Section 3.2.2.

Two orthogonal categories of jets, *signal* and *forward*, are defined by the criteria outlined in Table 6. Only signal jets are considered to potentially have originated from a Higgs decay which motivates the usage of these jets for event kinematics calculations. A jet must also pass the overlap removal rules specified in Section 3.2.5 to considered in any analysis. To suppress the contribution from jet produced by pile-up interactions, a cut on the Jet Vertex Fraction (JVF) is used. Tracks with $p_{\text{T}} > 0.5$ GeV and satisfying the requirements given in Table 5 are used in the JVF definition,

$$\text{JVF}(jet_j, vtx_k) = \frac{\sum_i p_T^{trk_{ijk}}}{\sum_k \sum_i p_T^{trk_{ijk}}}, \tag{6}$$

where trk_{ijk} is the i^{th} track ghost-matched to the j^{th} jet associated to the k^{th} vertex. The JVF used in the analysis is evaluated for the highest $\sum p_T^2$ vertex, or the 0^{th} vertex in the event and is only applied to jets with $p_T < 50$ GeV and $|\eta| < 2.4$. This limited application is because the cut discriminates against

jets which are not produced in the primary interaction, so called pile-up jets, which tend to have a softer spectrum and the cut is not applied unless the jet falls completely within the inner tracker acceptance.

Type	Signal Jet	Forward Jet
p_{T}(GeV)	$\mathrm{jet}_{i=1} > 45$ $\mathrm{jet}_{i>1} > 20$	>30
$\lvert\eta\rvert$	< 2.5	$2.5 < 4.5$
|JVF|	$> 0.5^{\dagger}$	–

Table 6: Selection used to define orthogonal sets of central and forward jets. †The JVF cut if only required for jets with $p_T < 50$ GeV and $|\eta| < 2.4$. More information can be found in Section 3.2.2.

The flavor of reconstructed Monte Carlo jets is determined by the hadrons with $p_T > 5$ GeV within a cone of $R = 0.4$ defined by the jet axis. The flavor hierarchy is b, c, then τ such that the jet is labeled by the highest hadron/lepton within the list found in the jet. The *light*-jet category is used if neither a heavy flavored hadron nor a τ are found.

3.2.3 *b*-Jet

Jets which originate from b quarks are identified using algorithms which exploit the long lifetime of b hadrons. The b-tagging algorithm MV1c [24–26] is used, which combines information from an impact parameter based algorithm, an inclusive secondary vertex finder, and a $b \rightarrow c$ hadron decay chain fit into a single neural network based discriminant, w, such that jets with higher w are more likely to be b-jets. The MV1 algorithm which was used in the EPS result [11] has been abandoned in favor of the MV1c tagger. MV1c has superior c-jet rejection, at the price of a smaller *light*-jet rejection factor in the tighter operating points, achieved by training the discriminant against a mixture of *light* and c-jets[1]. Section 5.2.1.1 motivates the need for enhanced c-jet rejection. A comparison of MV1 and MV1c tagger performance in Table 7. Another change compared to EPS is the fact that the MV1c tagger has been calibrated such that one can apply upper and lower cuts on w which is referred to as *continuous* or *pseudo-continuous tagging*. In other words, the operating points described in Table 7 are inclusive, such that a 'Tight' b-tagged jet will always satisfy the 'Loose' requirement, however the information can be used in an exclusive way, by requesting jets which satisfy 'Medium not Tight' for example. This feature allows for the division of the sample into regions of higher sensitivity through the use of multiple operating points as discussed in Section 3.3.4. For EPS only the 70% operating point was used. These changes improve the 0, 1, and 2-lepton dijet mass analysis *approximately* 7, 15, and 9% respectively without considering systematics.

The w distribution needs to be calibrated such that the efficiency in MC matches that in data. A combinatorial likelihood method [27] has been used in dilepton $t\bar{t}$ events [28] [29] to calibrate the b-jet efficiency. The c and *light* jet efficiencies were calibrated from D^* [30] and dijet [31] samples respectively. The pseudo-continuous calibration is described in [32] from where the Figure 3 showing scale factors for representative jet p_{T} bins was extracted.

3.2.4 $E_{\mathrm{T}}^{\mathrm{miss}}$ and track-based missing transverse momentum

$E_{\mathrm{T}}^{\mathrm{miss}}$ and the track-based missing transverse momentum ($p_{\mathrm{T}}^{\mathrm{miss}}$) are reconstructed using the standard techniques developed in the JetEtMiss performance group. For the $E_{\mathrm{T}}^{\mathrm{miss}}$, the `METRefFinal_Eflow` has

[1] MV1 was trained only against *light* jets

Name	w value	b-jet eff. (%)	c-jet RF		τ-jet RF		l-jet RF	
			MV1c	$\frac{\text{MV1c}}{\text{MV1}}$	MV1c	$\frac{\text{MV1c}}{\text{MV1}}$	MV1c	$\frac{\text{MV1c}}{\text{MV1}}$
80 'Loose' or 'L'	0.4050	79.85	3.04	0.98	6.40	1.13	29.12	1.07
70 'Medium' or 'M'	0.7028	70.00	5.34	1.07	14.90	1.01	135.76	0.91
60	0.8353	59.99	10.45	1.31	33.92	1.35	453.53	0.70
50 'Tight' or 'T'	0.9237	49.99	26.22	1.9	120.33	2.6	1388.28	0.55

Table 7: The efficiencies for the available calibrated operating points for the MV1c algorithm and a comparison to the MV1 algorithm performance. These values have been determined in di-leptonic $t\bar{t}$ events with a jet p_{T} threshold of 20 GeV. RF stands for Rejection Factor which is the reciprocal of the efficiency. These numbers were taken from Reference **??**.

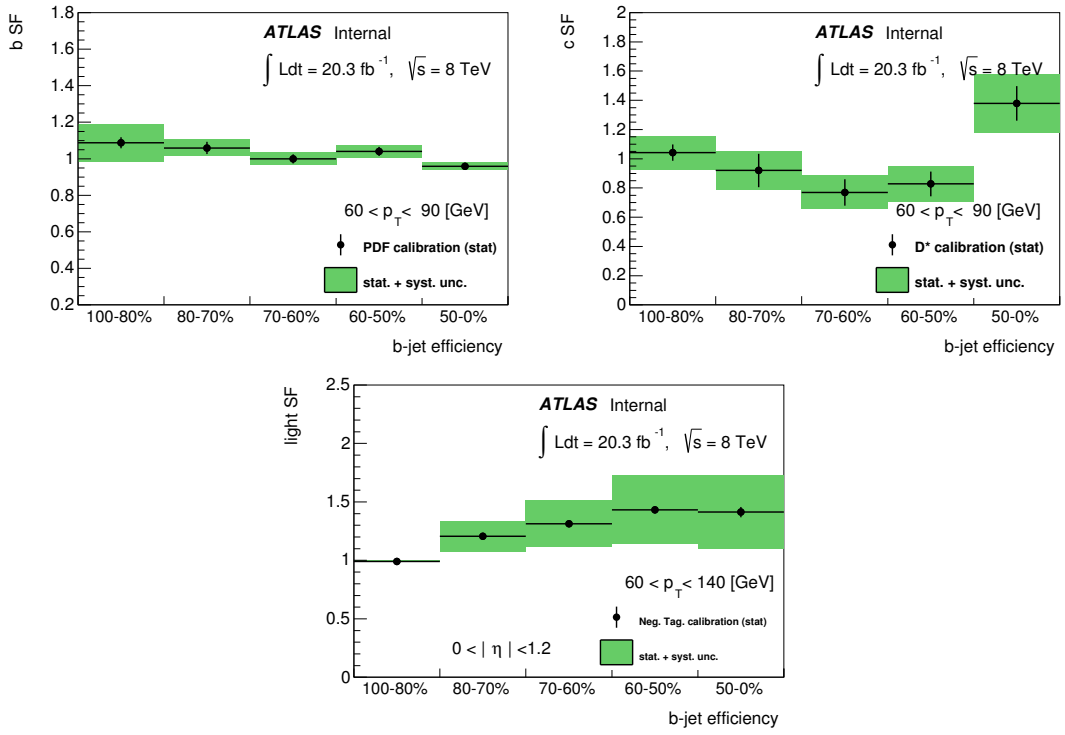

Figure 3: Taken from Ref. [32], the final MC-to-data calibration scale factors for the MV1c b, c-jet and $|\eta| < 1.2$ *light*-jet calibration is shown for a representative jet p_{T} bin. The data results are compared to the MC expectations. Error bars refer to statistical uncertainties, while the total error bands include systematics as well.

been used, while the $p_{\mathrm{T}}^{\mathrm{miss}}$ with no object (cluster or jet) corrections have been used. For consistency with the object definition, in both the `METRefFinal_Eflow` and $p_{\mathrm{T}}^{\mathrm{miss}}$ muID muons have been used.

The `METRefFinal_Eflow` includes all the standard terms: `RefEle`, `RefGamma`, `RefTau`, `RefJet`, `MuonTotal`, and `SoftTerm`. Each of these terms, with the exception of `RefGamma` and `RefTau`, is recalculated from each object, synchronizing all the correction and systematic variations for the objects described above. For `RefGamma` and `RefTau` the pre-calculated terms in the D3PD are used. Specific corrections for the jet-egamma overlap have been used. Due to the $E_{\mathrm{T}}^{\mathrm{miss}}$setup used in the analysis, the jet-egamma overlap correction has an effect between jet and electrons which results in a potential double counting of energy. The impact of the jet-gamma overlap correction has been evaluated to be negligible for the specific selection of the analysis, nevertheless the fix is used. Reference [33] shows the effect of the problem and the solution in a different analysis.

The $E_{\mathrm{T}}^{\mathrm{miss}}$enters in different part of the analysis: as input variable for the multi-variate analysis, and, just to mention some uses, to estimate the p_{T}^{W} in the 1-lepton channel, to estimate the Z p_{T} in the 0-lepton channel, and to suppress the top background in the 2-lepton channel.

On the contrary, the use of the $p_{\mathrm{T}}^{\mathrm{miss}}$ is limited to suppress the non-collision and to extract the estimate of the multi-jet background in the 0-lepton channel. A cut of $p_{\mathrm{T}}^{\mathrm{miss}}$> 30 GeV cleans the non-collision background while avoiding any cuts on the jets (like the cuts on the EM fractions and on the maximum layer fraction, used in other 0-lepton analysis in ATLAS). Since a direct cut on jet variables can cause a bias in both the jet calibration, and the b-tagging calibration with respect to the other channels in this search, the $p_{\mathrm{T}}^{\mathrm{miss}}$cut has been selected. The other $p_{\mathrm{T}}^{\mathrm{miss}}$quantity used is the direction. A coarse cut on the $\Delta\phi(E_{\mathrm{T}}^{\mathrm{miss}}, p_{\mathrm{T}}^{\mathrm{miss}})$ is used in the ABCD method to extract the multijet template and normalization from data for the 0-lepton analysis. The track selection **??** is described in Table 8. No mis-reconstructed tracks removal have been used.

Observable	Cut
p_{T} (GeV)	> 0.5
$\lvert\eta\rvert$	< 2.4
pixel hits	> 0
SCT hits	> 5
d_0 (mm)	< 1.5
$z_0 \sin(\theta)$ (mm)	< 1.5

Table 8: Tracks for $p_{\mathrm{T}}^{\mathrm{miss}}$definition **??**. Additional information is given in Section 3.2.4.

3.2.5 Overlap Removal

To ensure objects are not double counted a hierarchy shown in Table 9 has been established in order to decide which interpretation of the energy deposit in the detector is most likely correct for objects which satisfy the loosest of the above mentioned criteria. The order in which the ambiguities are resolved is given in the table. Already stated previously (Section 3.2.1.1), calo-muons are required to have $\Delta R > 0.1$ from any other muon in the event. N_{trk} is the track multiplicity of ghost-matched tracks with $p_{\mathrm{T}} >$ 0.5 GeV, satisfy the track selection in Table 5, and are compatible with the 0^{th} primary vertex as defined in said table. A complicated muon-jet overlap such as this is motivated by the fact that the muon from the vector boson decay can randomly fall on top of a jet. Removing these muons, as was done for EPS, reduces the 2-lepton signal acceptance 12%. In order to increase the signal acceptance as much as possible as well as avoid counting muons from semi-leptonic b and c decays as signal muons, the N_{trk} cut was adopted. Appendix H details the studies arriving at this conclusion.

Case	Order	Keep μ	Keep e	Keep jet
$\Delta R(jet, e) < 0.4$	1	–	Yes	No
$\Delta R(jet, \mu) < 0.4$	2	$N_{trk} \leq 3$	–	$N_{trk} \geq 4$
$\Delta R(\mu, e) < 0.2$	3	if not Calo μ	if Calo μ	–

Table 9: Overlap hierarchy and the order in which the ambiguity is checked. N_{trk} is the track multiplicity of ghost-matched tracks with $p_{\mathrm{T}} > 0.5$ GeV, satisfy the track selection in Table 5, and are compatible with the 0^{th} primary vertex as defined in said table.

3.3 Event Selection

The following sections outlines how the objects described in Section 3.2 are used to define analysis categories and the event kinematic cuts applied. First event level cleaning cuts are described in Section 3.3.1 then trigger selection is discussed in Section 3.3.2. The use of leptons (Section 3.3.3), and jets (Section 3.3.4) to define analysis categories if followed by the event level kinematic cuts (Section 3.4) to conclude the description of the selection and categorization of events. The final section (Section 3.5) details the improvements to the dijet mass resolution pursued by the analysis group itself.

3.3.1 Event Cleaning

The data are required to satisfy conditions ensuring essential elements of the ATLAS detector were operational with good efficiency while the data were collected. The data quality requirements are implemented using a Good Run List (GRL) based on the ATLAS Data Quality (DQ) flags. The GRL used in this analysis is

```
data12_8TeV.periodAllYear_DetStatus-v61-
pro14-02_DQDefects-00-01-00_PHYS_StandardGRL_All_Good.xml
```

On top of the GRL request, a series of standard cleaning cuts are applied to avoid sporadic event problems in the detector, during reconstruction, or due to activity in the detector from non-collision background. The cuts are as follows:

On data:

Incomplete Events: remove events that have Core EventInfo error flag (`coreFlags`&0×40000! = 0 in D3PD);

LAr Error Flag: remove events that have LAr EventInfo error flag;

TileCal Error Flag: remove events that have Tile EventInfo error flag;

Corrupted Tile Events: remove corrupted tile events using TileTripReader;

Hot Tile Cells: Reject events with jets (after overlap removal and before JVF cut) pointing to the Hot Tile Cell in the runs : 202660, 202668, 202712, 202740, 202965, 202987, 202991, 203027, 203169.

On simulations:

Incomplete Events: reject MC events that have no truth particles ($mc_n == 0$ in D3PDs).

On both data and simulations:

Vertex Selection: Require that the first primary vertex contains at least 3 tracks;

MET Cleaning: Reject any data or MC event containing a looser bad jet **??** with p_{T}> 20 GeV, $|\eta|$ < 4.5 (after overlap removal and before JVF cut).

Recently the BCH cleaning prescription has been modified to remove jets in regions of the detector where entire modules in the tile calorimeter were non-operational during data taking. Most of these modules were not simulated in the MC and a correction derived by the Jet/ETMiss group to correct for these dead modules has been shown to be inaccurate. The result of the detailed studies is discussed in Appendix . No jet or event removal have been adopted in this analysis.

3.3.2 Trigger Selection

This section describes how the triggers noted in Section 3.1 are used in each analysis. The 0-lepton analysis uses all the $E_{\mathrm{T}}^{\mathrm{miss}}$ triggers and the parametrization of these triggers is detailed in Appendix A. 0-lepton events with $p_{\mathrm{T}}^{\mathrm{Z}}$ < 120 GeV were not included in the EPS analysis due to the difficulty of the parametrization of the $E_{\mathrm{T}}^{\mathrm{miss}}$ trigger turn-on. Appendix C details the work done to include as much of the phase space below 120 GeV into the analysis. The 1-lepton analysis uses all the single-lepton triggers and in events with p_{T}^{W} > 120 GeV$E_{\mathrm{T}}^{\mathrm{miss}}$ triggers are used to supplement holes the muon trigger coverage (was 160 GeVfor EPS). The 2-lepton analysis uses the single and dilepton triggers.

3.3.3 Lepton Selection

This section describes how the lepton classifications described in Section 3.2.1 are used in define the three orthogonal analyses. The leptons used to reconstruct the vector boson are given in Table 10. Tighter requirements are used in the 1-lepton analysis to reconstruct the W compared to those used to reconstruct the Z because of the potential of a larger multijet background faking leptonic W-decays. Note events with exactly one VH Loose lepton that fail the VH Tight selection are not used. Preliminary studies not documented here showed that including these events would bring minimal improvement to the sensitivity and are therefore not considered in this analysis.

Analysis	VH Loose	VH Medium	VH Tight
0-lepton	0	–	–
1-lepton	0	0	1
2-lepton	1	1	–

Table 10: Signal lepton selection from the 3 inclusive VH lepton definitions.

3.3.4 Jet Selection

This section describes how the jet classifications described in Section 3.2.2 are used to select events compatible with a Higgs decay and define analysis categories in order to isolate regions with a large signal to background ratio. The analysis jet multiplicity requirements are given in Table 11. Events with forward jets are vetoed in order to reduce contributions from single and pair production of top-quarks which is a major background in the 0 and 1-lepton analysis.

Events are categorized by the number of signal jets present in the event and are further divided by the number of b-jets present as shown in Figure 4. Three exclusive double b-tag categories are used in both the dijet and MVA analyses [2] given criteria but fails the next highe

[2] As explained in Section 3.2.3, an exclusive b-tag means that the jet passes the operating point in question but does not satisfy the adjacet tighter one. Concretely, exclusve Loose, referred to as Loose, is used for jets which pass the Loose cut but

Jet Type	Signal	Forward
0-lepton	2-3	0
1-lepton		
2-lepton		

Table 11: Jet multiplicity requirements for each analysis.

- Two exclusive Loose b-tags: ‘LL’ or ‘2L’
- Two exclusive Medium b-tags: ‘MM’ or ‘2M’
- Two tight b-tags: ‘TT’ or ‘2T’

The single b-tag regions are inclusive in the operating points given. In the fit model, discussed in Section 8, some of the double b-tag regions have been combined for the sake of simplicity. 3-signal jet (or 3-jet) events are vetoed if the the lowest p_{T} jet passes the loose b-tag cut given in Table 7. N.B. in this document, when an event is characterized by a jet multiplicity, it refers only to signal jets furthermore only signal jets are considered for event-level kinematic variables such as M_{eff}, ΔR, m_{jj}, etc. Recall, section 3.2.3 motivated the use of a pseudo-continuous flavor-tagging algorithm (including a pointer to Section 5.2.1.1).

In the 2-lepton channel the strict jet requirements are not completely needed since the main background is not top events and the sensitivity evolves differently in jet multiplicity bins. Since the reader has not been introduced to all the backgrounds, signals, selection etc, a more quantitative discussion is located in Appendix J.1.

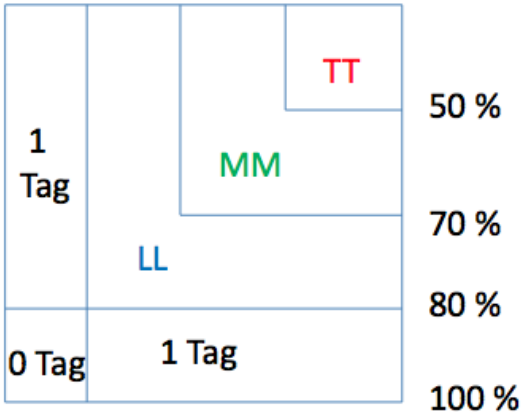

Figure 4: A graphical representation of the exclusive b-tagging categories used.

3.3.4.1 Truth Tagging Versus Direct Tagging

Due to the powerful discrimination of the MV1c algorithm against non-b-jets, it is difficult to produce enough Monte Carlo to have reasonable statistics after requiring 2 b-tags for events without b-jets. A method known as ‘truth tagging’ is therefore used in 2 b-tag events in which neither of the two leading p_{T} jets is a truth-matched b-jet. Truth tagging is a method by which a random MV1c value above the

fail the Medium requirement. Medium is for jets which pass the Medium cut but fail the Tight cut.

loose operating point is generated for a given jet. This is done by creating a 'random efficiency' obtained from sampling a cumulative distribution built from the tagging efficiency above the loose operating point and assigning the MV1c value corresponding to the random efficiency generated to the jet in question. The sample dependent ($t\bar{t}$, W+jets, Z+jets) efficiencies used to build the cumulative distribution are parametrized as a function of the flavor, transverse momentum and pseudo-rapidity of the given jet as well as the process type (see Appendix T.1). After the generation of a random MV1c value every jet will by construction satisfy the loose b-jet cut, so to correct for this bias, the event must be weighed down by the efficiency of the jet to pass the loose operating point. In events where one of the leading two jets is truth-matched to a b-hadron, this procedure is note used, and the original w of each jet is directly cut on; the event is said to have been 'direct tagged'. Full details of the efficiency maps and closure tests can be found in Appendix T.1.

3.3.4.2 Biases from Truth Tagging

Truth-tagging is wonderful in that it dramatically increases the available statistics but this method ignores correlations in the tagging efficiencies of jets in the same event. For events with two c-jets a bias in the tagging efficiency as a function of $\Delta R(cc)$ has been seen and a correction was derived; both are shown in Figure 5. Half the correction is used as a systematic uncertainty (`BTagTruthTagDR`). More details are given in Appendix T.3.

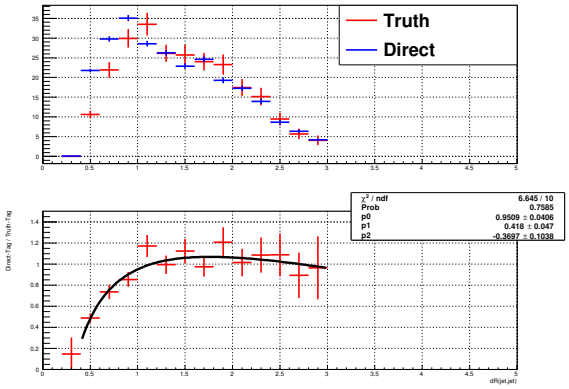

Figure 5: Truth tagging ΔR correction derived from the ratio truth to directed tagged events using W+cc and Z+cc in 2 and 3-jet events (top) in the 0-lepton MVAselection. The correction itself is obtained from a fit to the ratio (bottom): $0.9509 + 0.418 \times \ln(\Delta R) - 0.3697 \times \ln^2(\Delta R)$.

3.3.4.3 Biases from Generators

The data-MC scale factors were derived with respect to PYTHIA6 for b-jets and c-jets alike. As shown in Figure 6 for the exclusive 70% MV1c operating point, the efficiency for jets truth-matched to a b-jet and c-jets different for the three generators used in this analysis (PYTHIA6, PYTHIA8, and SHERPA). A correction is not applied to *light* jets since the effect and the light jet contribution are both small. Half the correction is used as a systematic which is decorrelated for b and c jets as well as for the PYTHIA8, and SHERPA(`BTagBSherpa`, `BTagBPythia8`, `BTagCSherpa`, `BTagCPythia8`). More details are given in Appendix T.2.

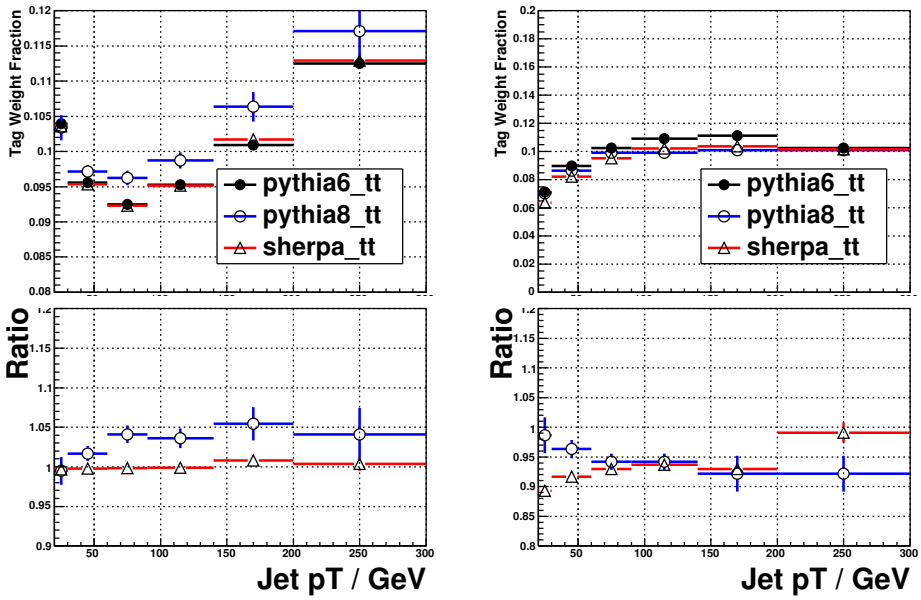

Figure 6: b-jet (left) and c-jet (right) tagging efficiency for the jets between the 70% OP and 60% OP (0.7028<MV1c<0.8353) in $t\bar{t}$ events produced by PYTHIA6 (Black), PYTHIA8 (Blue) and SHERPA (Red). The ratio is the MC-to-MC scale factor. Similar plots for all operating points are shown in Appendix T.2.

3.4 Event Kinematics Selection

After the above mentioned selection, events are classified by the lepton, jet, and b-jet multiplicity. Events are further categorized by the vector boson transverse momentum (p_{T}^{V}) with the higher boost categories having a larger signal to background ratio. The dijet mass analysis has tighter cuts while the multivariate analysis uses a looser selection in order to maximize the information available in the training. Unless a cut is perfectly efficient for the signal it is usually better to loosen or completely release the cut in question and allow the multivariate discriminant training to optimize its usage. This reasoning motivates the absence of the ΔR cuts in the MVA selection as well as other differences. The choice of two p_{T}^{V} bins for the MVA, as apposed to five for the dijet mass, was further motivated by the fact that the performance of any multivariate technique increases with the available training statistics. A fine binning in p_{T}^{V} would not have left sufficient statistics for training. On the other hand, training on the inclusive p_{T}^{V} spectrum has been shown to be sub-optimal since the low p_{T}^{V} statistics dominant preventing the learning algorithm from focusing sufficiently on the higher boost region where the bulk of the sensitivity comes from. This could be avoided if infinite statistics were available. The multivariate discriminant configuration is detailed in Section 6. The full list of event selection criteria is given in Table 12. The cut optimization for both interpretations was done with at least the approximate expected sensitivity[3] Most of the variables used are self-explanatory but a few definition are clarified here:

- V: vector boson constructed from the $E_{\mathrm{T}}^{\mathrm{miss}}$, vectoral sum of $E_{\mathrm{T}}^{\mathrm{miss}}$and p_{T}^{ℓ}, and vectoral sum of $p_{\mathrm{T}}^{\ell_{1,2}}$ in the 0, 1, and 2 lepton analysis respectively.
- H: Higgs constructed from the vectoral sum of the two leading p_{T} jets.

[3] From a binned sum of $s/\sqrt{b}$ to p-value calculations without systematics.

- M_{eff}: scalar sum p_{T} of all the objects in the event, specifically the signal jets, leptons, and $E_{\mathrm{T}}^{\mathrm{miss}}$. In the 1-lepton channel only the two jets used to build the Higgs mass are considered while in the 0-lepton channel the third jet is considered in three jet events. This is clarified by the use of $M_{eff\ 3}$for the later. This difference in definition exists since the variables were optimized in parallel in the different lepton selections and frozen before the subtle difference was noticed.

As stated above, 0-lepton events with $p_{\mathrm{T}}^{Z} < 120$ GeV are difficult to include due to the challenge of modeling the $E_{\mathrm{T}}^{\mathrm{miss}}$ trigger turn-on (Appendix A). Appendix C details the work done to include as many of the events below 120 GeV into the 0-lepton analysis. In the 2-lepton channel, the so called 'e-μ' control region which is dominated by top-pair events is selected with the MVA selection with the additional requirements that the two lepton are of different flavor and opposite sign; the same-sign events are used for the multijet template.

In the previous version of this analysis [11], cuts on the minimum transverse mass of the W (m_{T}^{W}) [4] and $E_{\mathrm{T}}^{\mathrm{miss}}$ were used for p_{T}^{W}< 160 GeV in events with one lepton. From an optimization study performed in the MVA selection, these cuts were dropped in favor of an M_{eff} cut in the low p_{T}^{W} region, p_{T}^{W} < 120 GeV, which increased the statistical sensitivity in that region(s) by 17 (22)% for the MVA (dijet mass) analysis[5] Figure 7 shows an MVA output for the multijet and signal, left and right respectively, for the EPS (optimized) cuts in blue (red). Two different trainings were used but one can clearly see that the change in cuts resulted in a large increase in the signal and no considerable increase of the multijet component in the sensitive region of the MVA output. This optimization study called for a $E_{\mathrm{T}}^{\mathrm{miss}}$cut of 20 GeV for the high p_{T}^{W}region ($p_{\mathrm{T}}^{W} > 120$ GeV). Therefore in the dijet analysis with $120 < p_{\mathrm{T}}^{W} < 200$ GeV the $E_{\mathrm{T}}^{\mathrm{miss}}$cut was reduced to 20 GeV (from 25 GeV [11]). Above p_{T}^{W} of 200 GeV a reduction of the $E_{\mathrm{T}}^{\mathrm{miss}}$cut from 50 GeVdecreases the expected dijet mass sensitivity so the EPS value was maintained. The success of dropping the m_{T}^{W} cut for $p_{\mathrm{T}}^{W} < 120$ GeV prompted a test to abandon it in the region $120 < p_{\mathrm{T}}^{W} < 160$ GeV in the dijet mass analysis which subsequently showed an increase in both the signal and background yield by more than 50% and no large increase in the multijet component was observed as shown in Figure 8. In total these changes increased the expected statistical sensitivity of the 2-jet region in the 1-lepton analysis 5 (8)% in the MVA (dijet) analysis. Note the upper bound of m_{T}^{W} which was present for EPS has been maintained in the dijet mass analysis.

3.5 Dijet Mass Resolution and the Kinematic Fit

Reconstructing the mass of a resonant decay is always a very powerful discriminant against the backgrounds which are either not resonant decays or have a different mass. This analysis is no exception but jets are not the most precise objects available and therefore care has been taken to maximize the dijet mass resolution.

3.5.1 Energy corrections to the selected *b*-jets

Two corrections are applied to selected signal b-jets: the 'muon-in-jets' and 'p_{T}-reco' corrections. With the first, know as the 'muon-in-jets' correction, the jet resolution is improved by adding the 4-vector of muons passing the criteria in Table 13 to the jet 4-vector after subtracting the muon's energy deposit in the calorimeter. If two such muons are found, the closer of the two to the jet is taken.

Furthermore, another correction referred to as 'p_{T}-reco' compensates for the bias in the average migrations of jets due to the underlying jet spectrum has been derived [34]. The current correction is shown in Figure 9.Jets tend to more often migrate down (up) in p_{T} on the rising (falling) part of the truth

[4] $m_{\mathrm{T}}^{W} = \sqrt{2p_{\mathrm{T}}^{\ell}E_{\mathrm{T}}^{\mathrm{miss}}(1-\cos\Delta\phi(\ell, E_{\mathrm{T}}^{\mathrm{miss}}))}$

[5] This difference in the MVA analysis includes the addition of a $|d_0$ significance$| < 3$ cut in the muon channel and tightening the iso_{calo} which decrease the significance 1%.

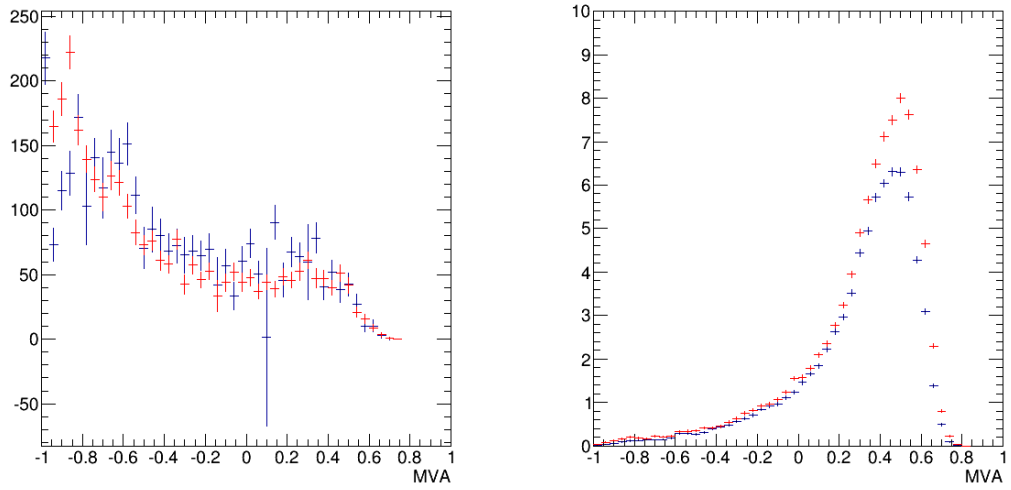

Figure 7: This figure shows an MVA output for the multijet and signal on the left and right respectively for the EPS (optimized) cuts in blue (red) discussed in Section 3.4. The optimized cuts also include the changes to the MJ template selection described in Section 3.2.1.5. Two different trainings were used but one can clearly see that the change in cuts resulted in a large increase in the signal and no considerable increase of the multijet component in the sensitive region of the MVA output. The difference yields a 17% increase in the MVA analysis sensitivity.

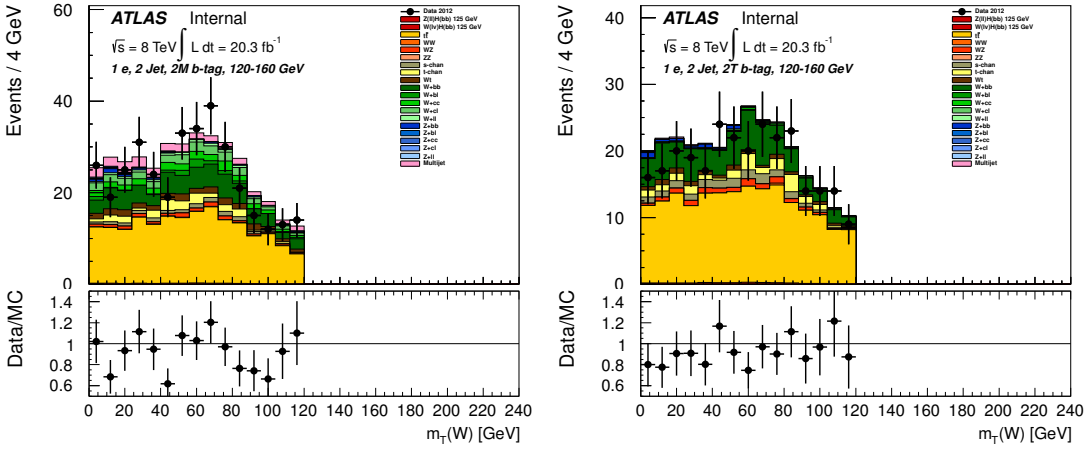

Figure 8: This figure shows the m_{T}^{W} distribution in the for $120 < p_{\mathrm{T}}^{W} < 160$ in the electron channel of the dijet mass analysis after requiring two exclusive medium and tight tags on the left and right respectively. For $m_{\mathrm{T}}^{W} < 40$ GeV, which was excluded previously [11], the agreement is acceptable and the multijet contribution is not significantly more then above 40 GeV. Removing this cut increases the signal and background in this p_{T}^{W} range by 50%.

Variable	Dijet Mass Analysis					Multivariate Analysis	
	Common Selection						
p_{T}^{V} (GeV)	0-90	90-120	120-160	160-200	> 200	0-120	> 120
$\Delta R(jet_1, jet_2)$	0.7-3.4	0.7-3.0	0.7-2.3	0.7-1.8	< 1.4	> 0.7 (p_{T}^{V}<200 GeV)	
	0-Lepton Selection						
$p_{\mathrm{T}}^{\mathrm{miss}}$ (GeV)	NU	App. C	> 30			NU	> 30
$\Delta\phi(E_{\mathrm{T}}^{\mathrm{miss}}, p_{\mathrm{T}}^{\mathrm{miss}})$			$< \pi/2$				$< \pi/2$
$\Delta\phi(E_{\mathrm{T}}^{\mathrm{miss}}, jets)$			> 1.5				> 1.5
$\Delta\phi(V, H)$			> 2.8				-
$\sum p_{\mathrm{T}}^{jet_i}$ $N_{jet} = 2$			> 120				> 120
$\sum p_{\mathrm{T}}^{jet_i}$ $N_{jet} = 3$			> 150				> 150
	1-Lepton Selection						
M_{eff} (GeV)	> 180		–			> 180	–
$E_{\mathrm{T}}^{\mathrm{miss}}$ (GeV)	–		> 20		> 50	–	> 20
m_{T}^{W} (GeV)	< 120					–	
	2-Lepton Selection						
$m_{\ell\ell}$ (GeV)	83-99					71-121	
$E_{\mathrm{T}}^{\mathrm{miss}}$ (GeV)	< 60					–	

Table 12: Event kinematic selection. NU stands for 'Not Used'.

Criteria	Value
Quality	Tight MuID MCP hit requirements
p_{T} (GeV)	> 4
$\Delta R(\mu, jet)$	< 0.4

Table 13: Muon selection for muons reconstructed within a jet cone $\Delta R(\mu, jet) < 0.4$ and then included in the jet. If two such muons are found in a jet, the closer is used.

jet p_{T} spectrum during reconstruction. This correction improves the invariant mass resolution by 8% and even though it also changes the background shape. After this correction is applied, the signal dijet mass resolution improvement from the GSC calibration compared to only using the EM+JES calibration is 3.5% G.

Dedicated systematics have been evaluated to be used with these corrections. They consist of an uncertainty on the b-jet energy scale of 0.4% (`SysJetBE`) and an uncertainty on the b-jet energy resolution, estimated by applying an extra smearing to the jets (`SysBJetReso`). Both are applied before the 'p_{T}-reco' correction have been applied.

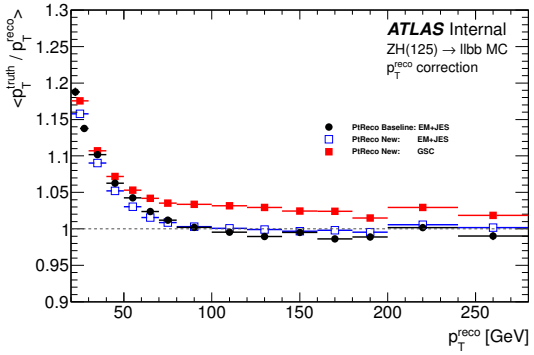

Figure 9: Three versions of the p_{T}-reco correction are shown with the black points showing what was used for EPS [11], the blue uses the updated object selection (except for the GSC calibration) and signal sample with increased statistics, and the red is analogous to the blue but using GSC calibrated jets.

3.5.2 Kinematic Fit

One expects to have fully reconstructed $ZH \to \ell^+\ell^- b\bar{b}$ events in the 2-lepton channel. Since the resolution of the leptons is much better than the resolution of the jets and the entire ZH system has limited if any total transverse momentum, one can adjust the jet energies such that the event is balanced in the transverse momentum. This greatly improves the jet resolution resulting in a $\sim$ 22% improvement in the dijet mass resolution as shown in Figure 10. Further details are given in Appendix U.

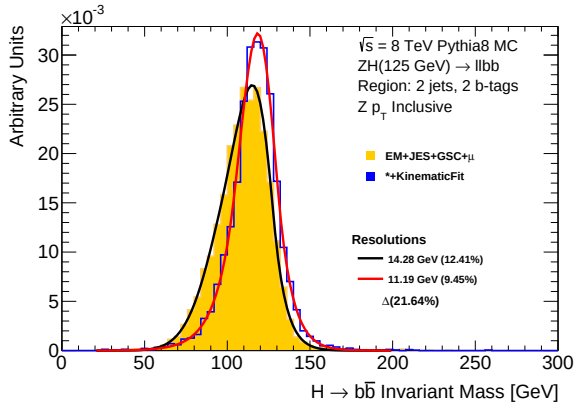

Figure 10: Dijet invariant mass before and after applying a kinematic likelihood fit in ZH $m_H = 125$ GeV signal Monte Carlo events showing a $\sim$ 22% resolution improvement.

4 VH→bb: Signal Characterization

This section details the signal samples themselves. Sample simulation (Section 4.1) as well as theoretical uncertainties (Section 4.2) are discussed. In the description of the systematic uncertainties, `this font is used to note the name of the nuisance parameter` used in the profile likelihood described in Section 8. The reader is encouraged to read Sections 8.1 and 8.2 to better understand how the information here will be used in the profile likelihood.

4.1 Simulation

The VH signals, $ZH \to \nu\bar{\nu}b\bar{b}$, $WH \to \ell\nu b\bar{b}$, and $ZH \to \ell^+\ell^- b\bar{b}$, where $\ell = e, \mu, \tau$ are modeled using Monte Carlo (MC) events produced by the Pythia 8.165 [35] event generator configured with the AU2 tune [36], using the CTEQ6L1 PDF [37], interfaced to PHOTOS [38] for QED final-state radiation, and TAUOLA [39] for the simulation of τ decays. The decay of $V \to \tau\nu$ leptons is simulated to account for the small fraction of additional signal events selected due to the decay $\tau \to \nu_\tau l \nu_l$ where l is either an electron or muon. Samples are generated in the Higgs boson mass range between 100 GeV and 150 GeV at 5 GeV intervals. The same samples which were used for the previous result [11], however since then, the available statistics has increased by a factor of 10 to 3×10^6 events for each of the three channels at the 125 GeV mass point. The additional statistics indeed helps with the training of multivariate discriminants discussed in Section 6. The total cross sections and uncertainties for the Higgs mass productions considered are taken from Reference [10] and the $H \to b\bar{b}$ decay branching ratios come from Reference [10,40] (`TheoryBRbb`). The central values of the cross sections are calculated at next-to-next-to-leading-order (NNLO) in QCD corrections [41] and next-to-leading-order (NLO) in electroweak (EW) corrections [42] assuming factorization between the production of a virtual V^* boson and its decay to VH. The decay branching ratios of $W^\pm$ and Z bosons are taken from the Particle Data Group [43] assuming lepton universality.

4.1.1 *qq* and *gg* Initiated Production

In the Standard Model, VH production is dominated by the quark-initiated process, but in the case of ZH, a significant contribution from the gluon-initiated process contributes. Figures 11 and 12 show the leading order Feynman diagrams for both of these production mechanisms.

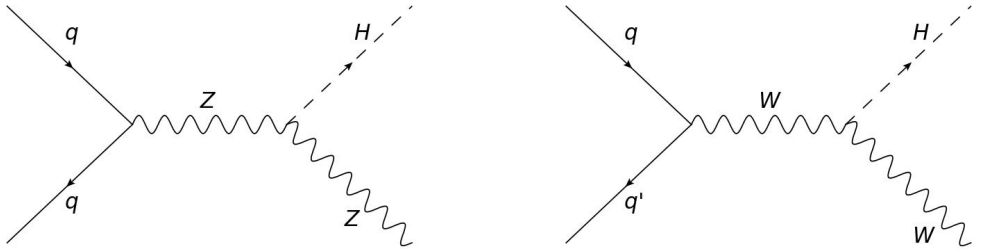

Figure 11: Leading order Feynman diagrams for quark-initiated VH production.

For eps, and therefore what is used for the 7 TeV analysis, the gluon-initiated process was considered as an overall correction to the inclusive ZH cross section with a contribution of approximately 5%. Since then, it was realized that the $gg \to ZH$ contribution is not flat as function of the vector boson p_T due to the top quark loop threshold [44]. Therefore, $gg \to ZH$ events were generated using PowHeg showered with Pythia8 for each of the Higgs boson mass points stated above. The $gg \to ZH$ samples and the $qq \to ZH$ samples are combined using weights derived from their relative cross sections.

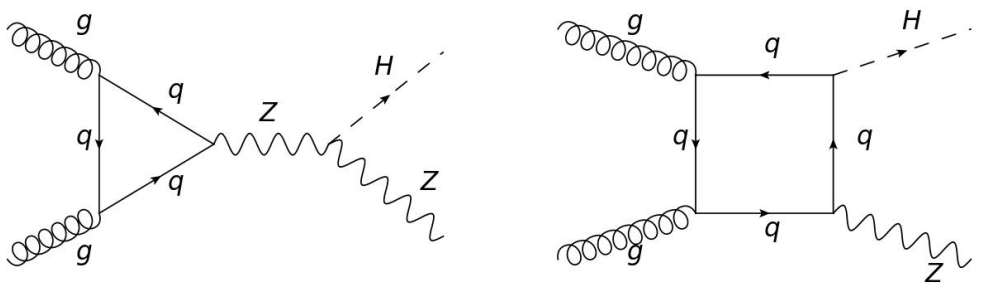

Figure 12: Leading order Feynman diagrams for gluon-initiated ZH production.

4.1.2 NLO Electroweak Differential Correction

The following was considered and documented for the EPS analysis. In the interest of completeness and brevity, this section is includes only the main points. For the details of the correction i.e. the difference between bare and dressed leptons, the reader is encouraged to consult Section 5.3 of Ref. [11].

As stated above the total cross section is calculated to NLO in EW corrections but since these corrections have a strong dependence in p_{T}^{V}, more care must be taken. The HAWK MC program was used to calculate a differential NLO EW cross section correction as a function of p_{T}^{V} [45, 46] shown, along with the associated uncertainty, in Figure 13. Fluctuations due to limited MC statistics are smoothed by fitting the correction above 200 GeV with a first-order polynomial. The correction is applied to qq initiated VH production and is being calculated for the gg initiated processes. The next-order (NNLO) electroweak corrections considering additional α_s vertices are expected to be on the order of the NLO correction squared $\left(\Delta^2_{NLO}\right)$. To ensure the uncertainty does not vanish, $\max\left(2\%, \Delta^2_{NLO}\right)$ is used (`TheoryVHPt`).

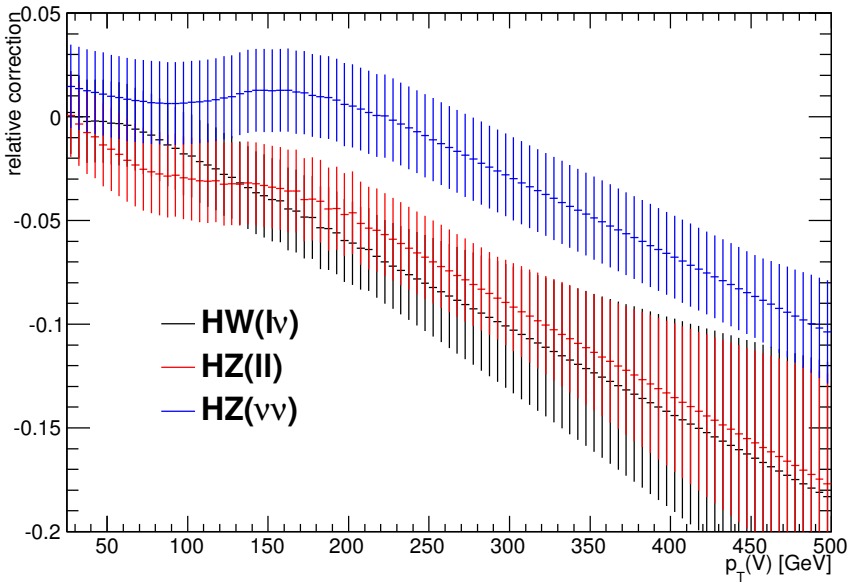

Figure 13: Relative NLO electroweak corrections to signal cross sections and the size of the associated uncertainties is shown as a function of p_{T}^{V} calculated from the HAWK MC generator.

4.2 Theoretical Uncertainties

Theoretical uncertainties on the VH signal can be divided into renormalization/factorization scale uncertainties and PDF uncertainties. For both of these, the uncertainty on the inclusive cross section, acceptance, and differential p_{T}^{V} distribution has been considered.

4.2.1 Inclusive Cross Section

The scale and PDF uncertainties on the inclusive cross sections at $\sqrt{s} = 7$ and 8 TeV are quoted in the CERN Yellow Report [47]. The reported ZH production uncertainties are larger than those for WH production due to the one-loop-induced sub-process $gg \to ZH$. For the 8 TeV analysis, the $qq \to ZH$ uncertainty is assumed to be the same as $qq \to WH$ and the uncertainty on $gg \to ZH$ are chosen such that the total uncertainty of the Yellow Report is preserved. An additional factor is included which accounts for the uncertainty on the ratio of the number of 2 and 3 jet events when scaling the $gg \to ZH$ cross section from LO to NLO. This method produces results that are consistent with an overall 50% uncertainty suggested by theorists in the LHC Higgs Cross Section VH Working Group. These uncertainties are summarized in Tables 14, 15, and 16 (`TheoryQCDscale`).

m_H (GeV)	7 TeV			8 TeV		
	$\sigma(WH)$ (pb)	Scale (%)	PDF+α_s (%)	$\sigma(WH)$ (pb)	Scale (%)	PDF+α_s (%)
115	0.7517	± 0.9	± 2.4	0.9266	± 1.0	± 2.3
120	0.6617	± 0.9	± 2.6	0.8052	± 1.0	± 2.5
125	0.5785	± 0.9	± 2.6	0.7046	± 1.0	± 2.3
130	0.5059	± 0.9	± 2.6	0.6169	± 0.9	± 2.4
135	0.4431	± 1.0	± 2.6	0.5416	± 1.0	± 2.5

Table 14: NNLO QCD + NLO EW inclusive cross sections and related uncertainties for WH production quoted from the CERN Yellow Report [47].

m_H (GeV)	7 TeV			8 TeV		
	$\sigma(ZH)$ (pb)	Scale (%)	PDF+α_s (%)	$\sigma(ZH)$ (pb)	Scale (%)	PDF+α_s (%)
115	0.4345	± 2.6	± 2.7	0.5358	± 2.8	± 2.5
120	0.3808	± 2.8	± 2.8	0.4710	± 3.0	± 2.5
125	0.3351	± 2.9	± 2.7	0.4153	± 3.1	± 2.5
130	0.2957	± 3.0	± 2.8	0.3671	± 3.3	± 2.5
135	0.2616	± 3.2	± 2.8	0.3259	± 3.5	± 2.7

Table 15: NNLO QCD + NLO EW inclusive cross sections and related uncertainties for ZH production quoted from the CERN Yellow Report [47].

4.2.2 Acceptance and p_{T}^{V}

QCD scale uncertainties on the acceptance and p_{T}^{V} distribution shape are evaluated at truth level using privately-made samples generated with PowHeg [48] and showered with Pythia8. The renormalization (μ_R)[1] and factorization (μ_F)[2] scales were varied independently by factors of 2 and 0.5 in all possible combinations whilst maintaining $0.5 \leq \mu_R/\mu_F \leq 2.0$. Each sample was normalized to the nominal

[1] 'renscfact' parameter.
[2] 'facscfact' parameter.

m_H (GeV)	qqZH			ggZH		
	$\sigma(qqZH)$ (pb)	Scale (%)	PDF+α_s (%)	$\sigma(ggZH)$ (fb)	Scale (%)	PDF+α_s (%)
115	0.4995	± 1.0	± 2.3	36.34	± 50.0	± 19.0
120	0.4366	± 1.0	± 2.5	34.39	± 50.0	± 12.8
125	0.3828	± 1.0	± 2.3	32.46	± 50.0	± 16.9
130	0.3365	± 1.0	± 2.4	30.60	± 50.0	± 14.2
135	0.2971	± 1.0	± 2.5	28.79	± 50.0	± 16.4

Table 16: NNLO QCD + NLO EW inclusive cross sections and related uncertainties for $qq \to ZH$ and $gg \to ZH$ production at 8 TeV derived from the CERN Yellow Report [47].

cross section reported above to avoid double counting the inclusive cross section uncertainties. After a full truth-level event selection was performed, the difference in inclusive yields compared to the nominal $\mu_R = \mu_F = 1$ sample is used to determine the acceptance uncertainty. The "Stewart-Tackmann method" [49] [50] is deployed to treat correlations in the acceptance scale uncertainty between the 2 and 3-jet analysis bins. Under this procedure, the uncertainty in the 2-jet bin consists of two components. The first component is the inclusive 2+3 jet acceptance uncertainty (`TheoryAcc_J2`); the second component is the absolute 3-jet exclusive uncertainty relative to the nominal 2-jet acceptance (`TheoryAcc_J3`). This second component acts on the 2 and 3-jet events with an opposite sign creating an anti-correlation in the change in 2-jets versus 3-jets from this single uncertainity. The p_{T}^V uncertainty was taken by comparing the p_{T}^V distribution of the varied and nominal samples plotted with unit normalization. A linear fit was performed to envelope the most discrepant samples as shown in Figure 14 for each $qq \to WH$ (a-b), $qq \to ZH$ (c-d), and $gg \to ZH$ (e-f) for 2 and 3-jet events. The functional form for the linear fit is

$$f\left(p_{\mathrm{T}}^V\right) = 1 \pm \left(a + b\frac{p_{\mathrm{T}}^V}{400\ GeV}\right) \tag{7}$$

with a and b given in Table 17 for each of the processes.

Process	Region	a	b
$qq \to VH$	2 jet	-0.02	0.10
$qq \to VH$	3 jet	-0.03	0.13
$gg \to ZH$	2+3 jet	-0.05	0.25

Table 17: Parameters for the linear fit of Equation 7 for p_{T}^V shape uncertainty for renormalization and factorization scales.

PDF uncertainties on the acceptance and p_{T}^V shape are obtained in a manner similar to that used to evaluate the scale uncertainties. Additional samples are generated with PowHeg and showered with Pythia8 using the MSTW2008nlo68cl [51] and NNPDF23_nlo_as_0120 [52] PDF set central value members, as recommended by the PDF4LHC [53] Working Group. Again, after performing a full truth-level analysis, the varied sample yields are compared to the nominal sample made with the CT10nlo [54] central value PDF set member to derive uncertainties on the acceptance yields stated in Table 18 (`TheoryAccPDF`). PDF uncertainties are considered to be correlated between the 2- and 3-jet bins. Additionally, no evidence for a p_{T}^V shape uncertainty was found. As a cross check to this method, the PDF4LHC re-weighting guidelines were used to re-weight the existing Pythia samples on an event-by-event basis from the cteq6ll central value PDF set member to each of the full PDF sets stated above (central value and

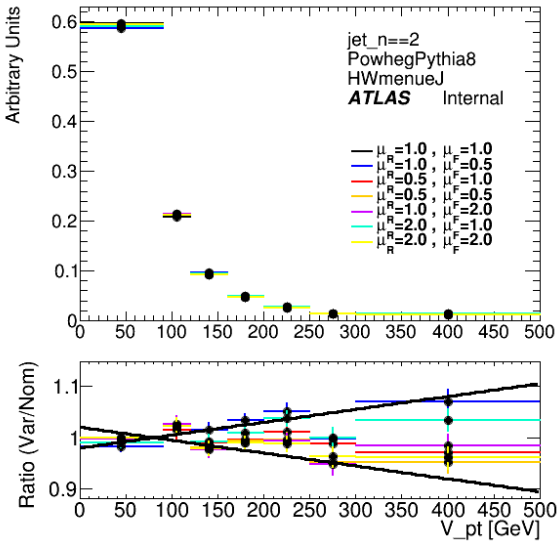

(a) WH 2-jet

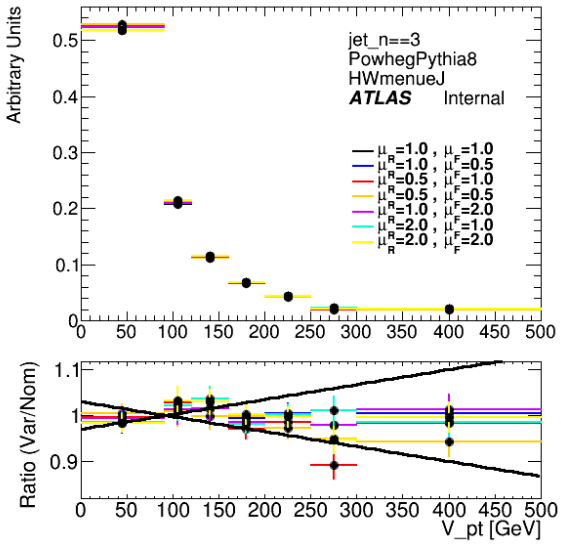

(b) WH 3-jet

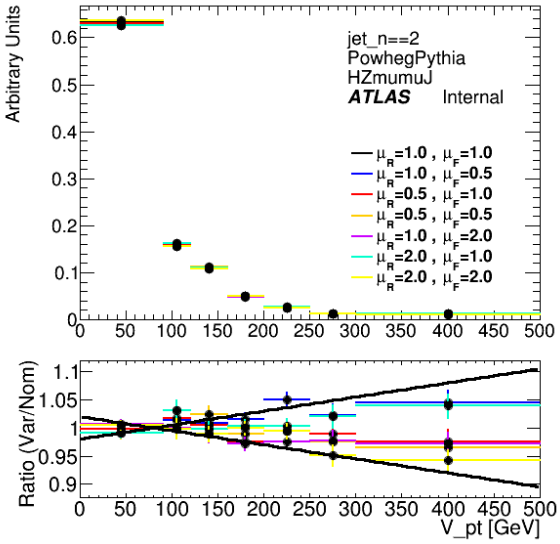

(c) $qq \to ZH$ 2-jet

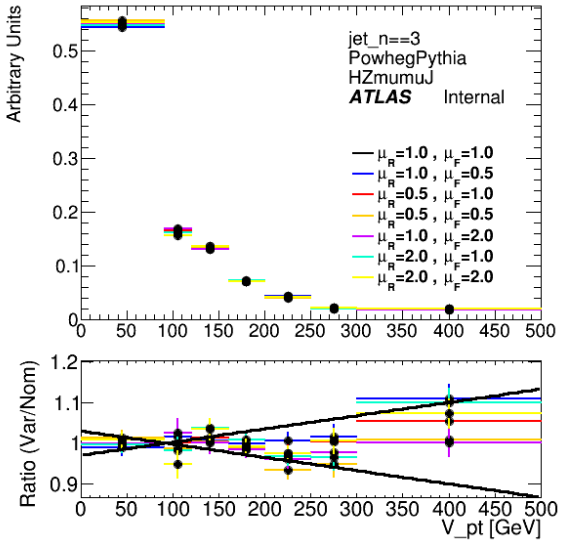

(d) $qq \to ZH$ 3-jet

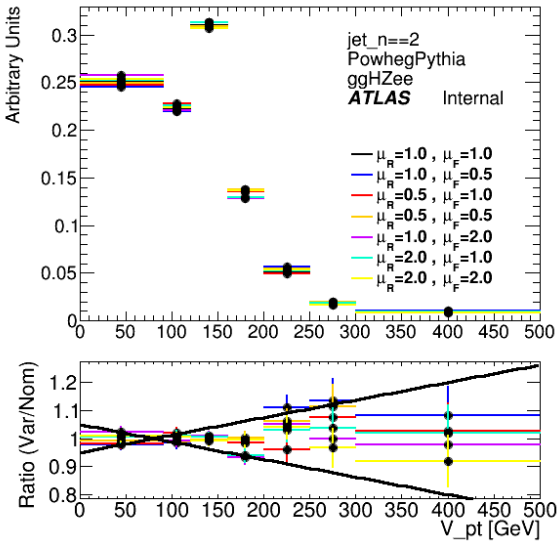

(e) $gg \to ZH$ 2-jet

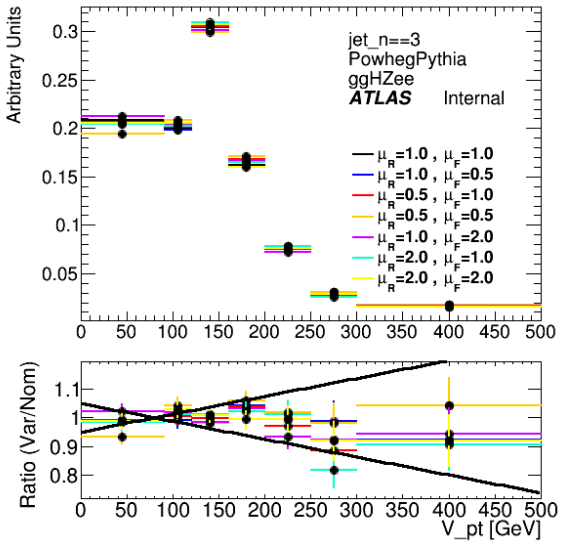

(f) $gg \to ZH$ 3-jet

Figure 14: Normalized p_{T}^{V} distributions after truth-level selection for WH, $qq \to ZH$, and $gg \to ZH$ scale uncertainty studies on the 1^{st}, 2^{nd}, and 3^{rd} row respectively.

error members). The weight applied to each event is calculated as,

$$w = \frac{PDF(x_1, f_1, Q) * PDF(x_2, f_2, Q)}{PDF_0(x_1, f_1, Q) * PDF_0(x_2, f_2, Q)} \tag{8}$$

where $PDF(x, f, Q)$ is the new PDF and $PDF_0(x, f, Q)$ is the original PDF. The results from this weighting method are found to be consistent with those obtained by generating distinct samples with different PDFs (Figure 154) in Appendix I).

Process	PDF		Scale		
	2-jet [%]	3-jet [%]	2+3-jet [%]	3-jet rel. 2-jet [%]	3-jet rel. 3-jet [%]
WH	± 3.5	± 2.8	± 3.0	∓ 1.1	± 4.2
$qq \to ZH$	± 3.0	± 5.0	± 3.4	∓ 0.9	± 3.6
$gg \to ZH$	± 2.1	± 3.4	± 1.5	∓ 1.8	± 3.3

Table 18: Inclusive acceptance uncertainties derived from scale and PDF variations.

The NLO QCD+EWK corrections affect the production of the Higgs boson. This directly changes the boost of the vector boson which then defines the kinematics of the event. Changing the p_{T}^{V} at the truth level will propagate this change to all important observables. The rate of 2 and 3 jet production is covered separately. For the signal it is important to properly parametrize the rate in VpT and jet multiplicities. Changes in the m_{bb} shape due to differences in parton shower are believed to be below the threshold of the sensitivity of this analysis at this time. However, further checks are being done.

5 Backgrounds

The background processes are modeled with several different event generators. This analysis inherits the dedicated campaign of Monte Carlo (MC) production carried out to attempt to reduce the uncertainty due to MC statistics to <5% in the most sensitive bins for the EPS analysis. The increase in statistics was achieved by collaboration with other working groups in producing common samples, making extensive use of the "ATLFastII" [15] simulation and implementing a number of filters on the final state hadrons and leptons to reduce the number of events that required detector simulation. A subset of the V+jets samples (noted in Table 20 and 21) were not produced with the fast simulation; highly boosted samples without b's and those in which the vector boson decays to τs are usually full simulation. Table 19 gives a summary of the different MC samples used for each background process. A detailed discussion of the modeling and systematics for each of the backgrounds considering both the dijet mass and the multivariate analysis follows. V+jets is described in Section 5.1, single and pair production of top quarks in Section 5.2, dibosons in Section 5.3, and finally multijet and non-collision backgrounds in Section 5.4.

In the description of the systematic uncertainties which follow, `this font is used to note the name of the nuisance parameter` used in the profile likelihood described in Section 8. The reader is encouraged to read Sections 8.1 and 8.2 to better understand how the information here will be used in the profile likelihood. The adopted philosophy was to apply a correction if and only if one is obviously needed: it is foolish to apply a correction which has the potential to over-correct a background.

Process	Generator	$\sigma \times BR$	N_{events}
Vector boson + jets			
$W \to \ell\nu$	Sherpa 1.4.1	12.07 nb	390M
$Z/\gamma* \to \ell\ell$	Sherpa 1.4.1		66M
$m_{\ell\ell} > 40$ GeV		1.24 nb	
$Z\gamma* \to \nu\nu$	Sherpa 1.4.1		98M
$m_{\nu\nu} > 5$ GeV		6.71 nb	
Top-quark			
$t\bar{t}$	PowHeg+Pythia	252.89 pb	100M
$t-$channel	AcerMC+Pythia	87.76 pb	9M
$s-$channel	PowHeg+Pythia	5.61 pb	6M
$Wt-$channel	PowHeg+Pythia	22.37 pb	20M
Di-boson (moving to POWHEG)			
WW	PowHeg+Pythia8	52.44 pb	10M
WZ	PowHeg+Pythia8		15M
$m_{\ell\ell} > 20$ GeV and one of the boson hadronically decaying		9.241 pb	
ZZ	PowHeg+Pythia8		15M
$m_{\ell\ell} > 20$ GeV and one of the boson hadronically decaying		3.171 pb	

Table 19: Monte Carlo programs used for modeling signal and background processes and the cross sections times branching ratio (BR) used to normalize the different processes at $\sqrt{s} = 8$ TeV. Branching ratios correspond to the decays shown.

The estimate of the modeling systematic uncertainties are done for each background. When possible, specific control regions have been designed to extract information directly from data. This is the case for the Z+jets, W+light jets, and $t\bar{t}$ backgrounds. In view of the sensitivity of the analysis to $t\bar{t}$ modeling, a detailed study of this background has been completed by using a series of MC generators with different underlying assumption of the $t\bar{t}$ physics in compliance with the Top Group's recommendations. Given the difficulty to design proper control regions with enough statistical power to study processes like single

top, $W + b\bar{b}$ and diboson production, modeling studies are done by comparing different MC predictions. If available, the comparison between different MC was done with fully reconstructed detector objects and the full analysis selection. This is the case of the single top background. For $W + b\bar{b}$ and diboson, the comparisons have been done mostly at the particle or parton level. When different MC predictions are compared to the baseline, the most discrepant is chosen to derive an uncertainty first, then the next on the list is considered. This continues until any discrepancy left between predictions viewed on the final variable is covered by the already considered differences. In order to not put statistical fluctuations from these comparisons into the analysis, a function is fit to the ratio and used to produce the variation.

All Modeling studies have focused on the most relevant variables which are the input variables for the multivariate discriminant described in Section 6, variables strongly related to them, or the variables used to select events (Table 12). The variables of interest can be divided into two categories (with a few exceptions):

- kinematics of b-jet system: This is our Higgs candidate; the description of variables like the jet p_{T} and multiplicity, angles between jets, and the dijet mass (m_{jj}) is critical.

- kinematics of the system recoiling from the Higgs: In this analysis, the recoiling system, formed by the $E_{\mathrm{T}}^{\mathrm{miss}}$, the lepton and the $E_{\mathrm{T}}^{\mathrm{miss}}$, or the dilepton system in the 0, 1 and 2 lepton categories respectively, gives the kinematics of the associated vector boson and is paramount. This is the handle used to reject the potentially overwhelming multijet background and find the region of phase space, the high p_{T}^{V} regime, where the signal-to-background ratio is expected to be maximal.

In the following subsections, each background will be introduced and the corrections and systematics adopted in the analysis will be discussed. The information presented is meant to be enough for the reader to learn what decisions were made. However, not all the details as to why these decisions were made can be put into the main body of the text if there is any hope of presenting a readable document. A complete description is therefore contained in several dedicated appendices which are referred to throughout the following text.

For a clear description on how the systematics described are employed in the profile likelihood i.e. correlations across channels, b-tag categories, etc. the reader should refer to Section 8.

5.1 Vector boson+jets

The $W/Z+\geq 1b$, $W/Z+\geq 1c$ and $W/Z+\geq 1$ light jet events are produced with the SHERPA generator [55] with massive b/c quarks and interfaced with CT10 PDFs. Filters were developed to select events containing b, c and *light* flavored hadrons. This allowed the statistics of the critical V+heavy-flavor samples to be increased with less resources. In addition, filters were developed to select events with high vector boson transverse momentum with division of $p_t^V < 40$, $40 < p_t^V < 70$, $70 < p_t^V < 140$, $140 < p_t^V < 280$, $280 < p_t^V < 500$ and $p_t^V > 500$ GeV allowing for the increase in statistics of the most sensitive high p_{T}^V regions. The detailed list of MC samples for the Vector boson+jets production is listed in Tables 20 and 21. A complexity which is particular to V+jet simulation is the prediction of the relative rates of b, c, and *light* jets, referred to as flavor fractions in the text. Obtaining as much information from the concerning the proportions of the various flavors adds a great deal of complexity to the analysis. The following sections describe the modeling studies used to validated the simulation agreement with data and also derive systematics. More details are given in Appendix J for Z+jets and K-L for W+jets. The reader is encouraged to read the introduction to Section 5 to better understand how the information here will be utilized.

Process	Channel num.	tag	N_events
		$W \to e\nu$, Massive C and B, Sherpa, CT10	
Pt0	167740-2	e1585_a159_a171_r3549_p1328	14997980 / 9998989 / 49885967
Pt40_70	180534-6	e1867_a188_a171_r3549_p1328	2999998 / 4499994 / 16997491
Pt70_140	167761-3	e1620_a159_a171_r3549_p1328	2000000 / 2996497 / 4998998
Pt140_280	167770-2	e1620_a159_a171_r3549_p1328	4998995/ 1999997/ 2000000
Pt280_500	167779	a159_a171_r3549_p1328	899999
Pt280_500†	167780-81	e1714_s1581_s1586_r3658_r3549_p1328	199898 / 499891
Pt500	167788	e1620_a159_a171_r3549_p1328	100000
Pt500†	167789-90	e1620_s1499_s1504_r3658_r3549_p1328	10000 / 10000
		$W \to \mu\nu$, Massive C and B, Sherpa, CT10	
Pt0	167743-5	e1585_a159_a171_r3549_p1328	14989485 / 9992484 / 49846965
Pt40_70	180537-9	e1867_a188_a171_r3549_p1328	2996996 / 4498998 / 16988984
Pt70_140	167764-6	e1714_a159_a171_r3549_p1328	1998999 / 2995999 / 4998992
Pt140_280	167773-5	e1741_a159_a171_r3549_p1328	4983993 / 1995998 / 1723999
Pt280_500	167782	e1714_a159_a171_r3549_p1328	898000
Pt280_500†	167783-4	e1714_s1581_s1586_r3658_r3549_p1328	30000 / 499698
Pt500	167791	e1714_a159_a171_r3549_p1328	90000
Pt500†	167792-93	e1714_s1581_s1586_r3658_r3549_p1328	10000 / 49700
		$W \to \tau\nu$, Massive C and B, Sherpa, CT10	
Pt0	167746-8	e1585_a159_a171_r3549_p1328	14925982 / 9993984 / 49920968
Pt40_70	180540-2	e1867_a188_a171_r3549_p1328	2998997 / 4498999 / 16996492
Pt70_140†	167767-9	e1714_s1581_s1586_r3658_r3549_p1328	1099995 / 2999890 / 4999786
Pt140_280	167776	e1741_a159_a171_r3549_p1328	3998996
Pt140_280†	167777-8	e1714_s1581_s1586_r3658_r3549_p1328	1998688 / 1999994
Pt280_500	167785	e1714_a159_a171_r3549_p1328	898999
Pt280_500†	167786-7	e1714_s1581_s1586_r3658_r3549_p1328	199998 / 499998
Pt500	167794	e1714_a159_a171_r3549_p1328	90000
Pt500†	167795-6	e1714_s1581_s1586_r3658_r3549_p1328	10000 / 49998

Table 20: Monte Carlo samples and channel numbers and statistics used for the W samples. Samples marked with † were made with the full simulation while the rest were made with ATLFastII [15] simulation. More information is given in Section 5.1.

Process	Channel num.	tag	N_events
		$Z \to ee$, Massive C and B, Sherpa, CT10	
Pt0	167749-51	e1585_a159_a171_r3549_p1328	3999000 / 2999995 / 4978999
Pt40_70	180543-5	e1867_a188_a171_r3549_p1328/	1199999 / 600000 / 1399998
Pt70_140	167797-9	e1714_a159_a171_r3549_p1328	1366999 / 999999 / 1999998
Pt140_280	167809-11	e1714_a159_a171_r3549_p1328	999999 / 399999 / 600000
Pt280_500	167821	e1714_a159_a171_r3549_p1328	180000
Pt280_500†	167822-3	e1714_s1581_s1586_r3658_r3549_p1328	49899 / 49999
Pt500	167833	e1714_a159_a171_r3549_p1328	90000
Pt500†	167834-5	e1714_s1581_s1586_r3658_r3549_p1328	10000 / 50000
		$Z \to \mu\mu$, Massive C and B, Sherpa, CT10	
Pt0	167752-4	e1585_a159_a171_r3549_p1328	3997997 / 2937995 / 4993999
Pt40_70	180546-8	e1867_a188_a171_r3549_p1328	1199000 / 599000 / 1398999
Pt70_140	167800-2	e1620_a159_a171_r3549_p1328	1394999 / 1000000/ 1996998
Pt140_280	167812-4	e1620_a159_a171_r3549_p1328	987999 / 399000 / 599500
Pt280_500	167824	e1714_a159_a171_r3549_p1328	175000
Pt280_500†	167825-6	e1714_s1581_s1586_r3658_r3549_p1328	50000 / 50000
Pt500	167836	e1620_a159_a171_r3549_p1328	100000
Pt500†	167837-8	e1620_s1499_s1504_r3658_r3549_p1328	10000 / 139999
		$Z \to \tau\tau$, Massive C and B, Sherpa, CT10	
Pt0	167755-7	e1585_a159_a171_r3549_p1328	3997994 / 2998998 / 4989999
Pt40_70	180549-51	e1867_a188_a171_r3549_p1328	1198999 / 600000 / 1399996
Pt70_140†	167803-5	e1714_s1581_s1586_r3658_r3549_p1328	1399396 / 999998 / 1969693
Pt140_280	167815	e1714_a159_a171_r3549_p1328	798998
Pt140_280†	167816-7	e1714_s1581_s1586_r3658_r3549_p1328	399999 / 598897
Pt280_500	167827	e1714_a159_a171_r3549_p1328	180000
Pt280_500†	167828-9	e1714_s1581_s1586_r3658_r3549_p1328	50000 / 49899
Pt500	167839	e1714_a159_a171_r3549_p1328	90000
Pt500†	167840-41	e1714_s1581_s1586_r3658_r3549_p1328	10000 / 20000
		$Z \to \nu\nu$, Massive C and B, Sherpa, CT10	
Pt0	167758-60	e1585_a159_a171_r3549_p1328	24932972 / 19757479 / 24919979
Pt70_140	167806-8	e1620_a159_a171_r3549_p1328	5998993 / 2998998 / 4999996
Pt140_280	167818-20	e1620_s1499_s1504_r3658_r3549_p1328	10000 / 10000 / 10000
Pt140_280	167818-20	e1620_a159_a171_r3549_p1328	4999995 / 1999998 / 2999999
Pt280_500	167830	e1741_a159_a171_r3549_p1328	1799997
Pt280_500†	167831-2	e1741_s1581_s1586_r3658_r3549_p1328	199999 / 249999 / 999892
Pt500	167842	e1741_a159_a171_r3549_p1328	450000
Pt500†	167843-4	e1741_s1581_s1586_r3658_r3549_p1328	49999 / 50000 / 199699

Table 21: Monte Carlo samples and channel numbers and statistics used for Z samples. Samples marked with † were made with the full simulation while the rest were made with ATLFastII [15] simulation. More details are given in Section 5.1.

5.1.1 Z+jets Modeling, Corrections and Systematic Uncertainties

The following describes the main features of the Z+jets modeling studies and the sources of systematic error. Appendix J contains further details. A summary of the this section is given in Table 23 and a summary of the systematics used in the profile likelihood is given in the statistical model overview (Section 8) in Table 49.

In dilepton events the top background is fairly controllable and a relatively pure Z+jets sample can be obtained. Using the event selection for the MVA analysis given in table given in Table 12, with tighter dijet mass analysis $E_{\mathrm{T}}^{\mathrm{miss}}$ (< 60 GeV) and $m_{\ell\ell}$ (83-99 GeV) cuts, as well as only using the events with $m_{bb} < 100$ GeV or $m_{bb} > 150$ GeV in 2-tag events, a signal-depleted pure Z+jets sample is selected; a breakdown of yields given in Table 22.

process	0-tag (%)	1-tag (%)	2-tag (%)
Z+light	85	46	12
Z+heavy	12	50	69
$t\bar{t}$	0.07	1.5	12

Table 22: Simple sample composition for Z+jets modeling studies using the selection described in Section 5.1.1.

5.1.1.1 Jet multiplicity and flavor fractions

As stated previously, the simulation's predictions of jet multiplicity and flavor fractions in V+jet events cannot be trusted completely. It is not possible to determine everything from data and this ignorance must be properly encapsulated for the profile likelihood described in Section 8. Using the above mentioned selection, data/MC yields were compared in the 0-tag and summarized in Table 87 in Appendix J. From these numbers, a 5% uncertainty has been estimated for both the Z+l normalization (`ZlNorm`) and ratio of 3 to 2 jet production (`ZlNorm_3J`). Both the Z+cl and Z+hf (hf=bb+bl+cc) normalizations are determined from data in the profile likelihood. SHERPA-ALPGEN comparisons after 2-tags shown in Tables 91-90 in Appendix J are used to estimate the uncertainties on the:

- 3/2-jet ratio for the heavy flavor components
  - Z+cl: 26% (`ZclNorm_3J`)
  - Z+hf: 13% (`ZbbNorm_3J`)
- relative heavy flavor composition in Z+2-jet and Z+3-jet events
  - Z+bl to Z+b(b/c): 10% (`ZblZbbRatio`)
  - Z+cc to Z+b(b/c): 20% (`ZccZbbRatio`)

5.1.1.2 $\Delta\phi(jj)$ and p_{T}^{Z}

For the EPS analysis [11], a systematic disagreement in $\Delta\phi(jj)$ was observed and a correction was derived resulting in markedly better agreement of many kinematic variables including p_{T}^{Z} and m_{jj}. For this version of the analysis the correction has been refined. In Figure 15 the $\Delta\phi(jj)$ distribution is shown after the above cuts have been applied. The 0 and 1-tag distributions show a slope in the data/MC ratio which tends to be larger at low p_{T}^{Z} and the slope vanishes after asking for 2-b-tags. This suggests a correction is appropriate for the Z+light background but not the Z+heavy-flavor. Therefore a correction

is derived from 0-tag events applied to only the Z+light background separately for $p_{\mathrm{T}}^{Z} < 120$ GeV and $p_{\mathrm{T}}^{Z} > 120$ GeV by fitting $a(1 + bx)$ to the data minus non-Z background over Z+jets ratio. With this correction applied, the Z+light normalization changes by less than 2% and good data-MC agreement is restored in the 1-tag region, where the contribution from Z+light jets is non-negligible. A systematic of half the correction is applied to Z+light simulation and the full size of the correction to Z+b/c simulation with a de-correlation between Z+l and Z+b/c as well as 2 and 3-jet events (`ZDPhi`). After applying this correction to the Z+light background the agreement in p_{T}^{Z} (Figure 16) was checked for the same selection. Again, there is an obvious slope which *increases* as more b-tags are required. A correction is derived in the 2-tag region by fitting $a + b\log(p_{\mathrm{T}}^{V})$ to the ratio of again, the non-Z background subtracted from the data over the Z+jets background and is applied to Z+b/c events only. Below $p_{\mathrm{T}}^{Z} = 100$ GeV a constant correction is used. A systematic of half the correction is applied to the entire Z+jet simulation but de-correlated between Z+l and Z+b/c (`ZPtV`).

5.1.1.3 m_{jj}

The most important variable in a search such as this is m_{jj}. Using the same selection noted above, the systematic used for EPS [11] was reduced with further study and more statistics. Figure 17 shows the data/MC agreement in the 0, 1 and 2-tag regions. A systematic uncertainty was derived following the functional form of $a(m_{bb} \times 10^{-3} - b)$ and is applied to all Z+jets events with Z+l and Z+b/c de-correlated. A comparison was done between the default generator, SHERPA, and ALPGEN and the difference is covered by this uncertainty (Appendix J).

Description	Samples	Nuissance parameters
Zl Normalization	Data VS. Sherpa	`ZlNorm`
Z 3/2 ratio	Data VS. Sherpa	`ZlNorm_J3`,`ZclNorm_J3`,`ZbbNorm_J3`
Z jet flavour composition	Sherpa VS. Alpgen+Herwig+Jimmy	`ZblZbbRatio`, `ZbcZbbRatio`, `ZccZbbRatio`
$\Delta\phi$ correction and systematics	Data VS. Sherpa	`ZDPhi`
$\Delta\phi$ checks	Data VS. Alpgen+Herwig+Jimmy	
p_{T}^{V} correction and systematics	Data VS. Sherpa	`ZPtV`
p_{T}^{V} checks	Data VS. Alpgen+Herwig+Jimmy	
m_{bb} systematics	Data VS. Sherpa	`ZMbb`
m_{bb} checks	Data VS. Alpgen+Herwig+Jimmy	

Table 23: Summary of the Z+jet specific samples used to checks the background modelling. The list of the nuissance parameters is given for reference, and it will be discussed in Section 8
.

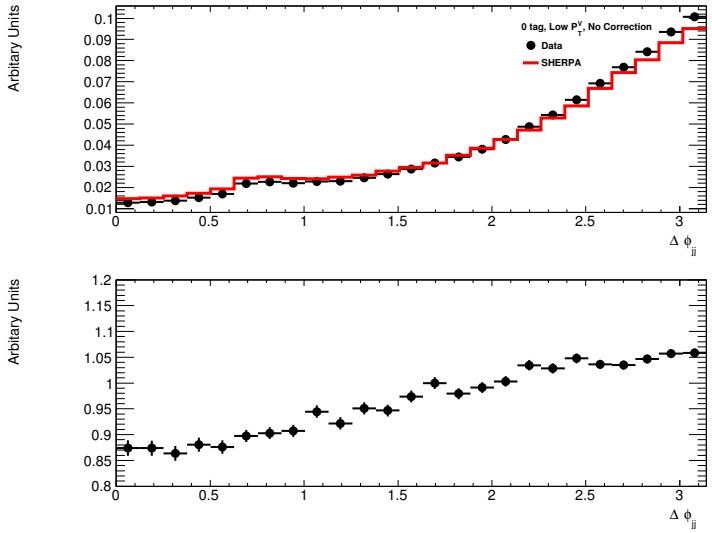

(a) 0-tag p_{T}^{Z}< 120 GeV

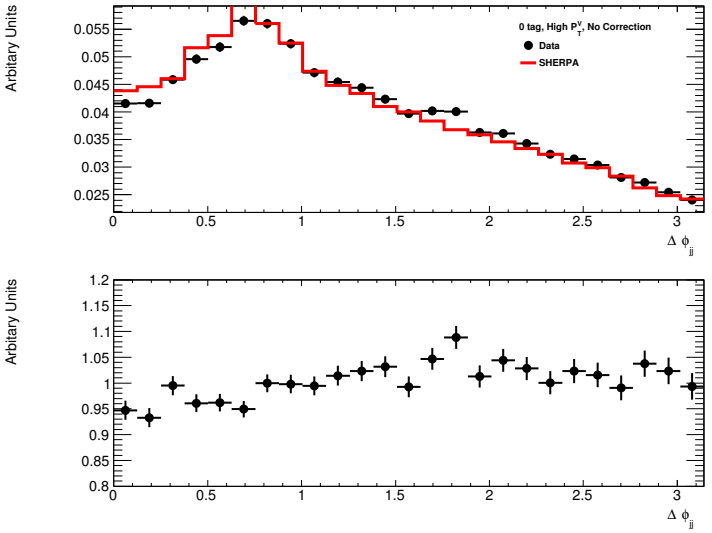

(b) 0-tag p_{T}^{Z}> 120 GeV

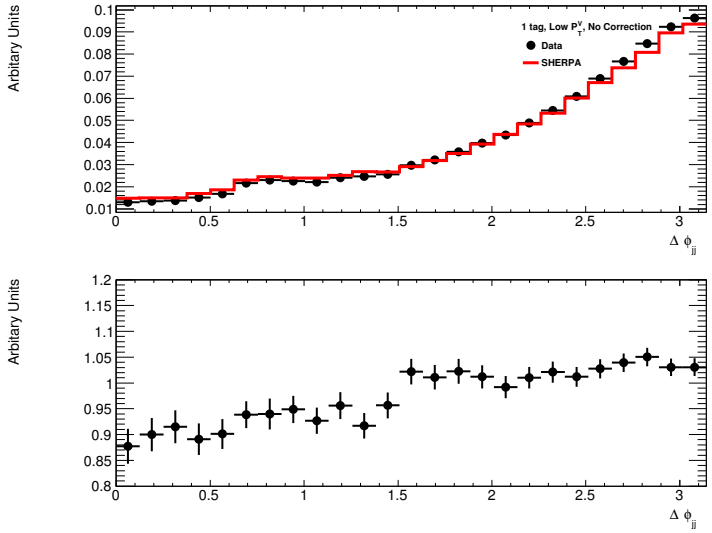

(c) 1-tag p_{T}^{Z}< 120 GeV

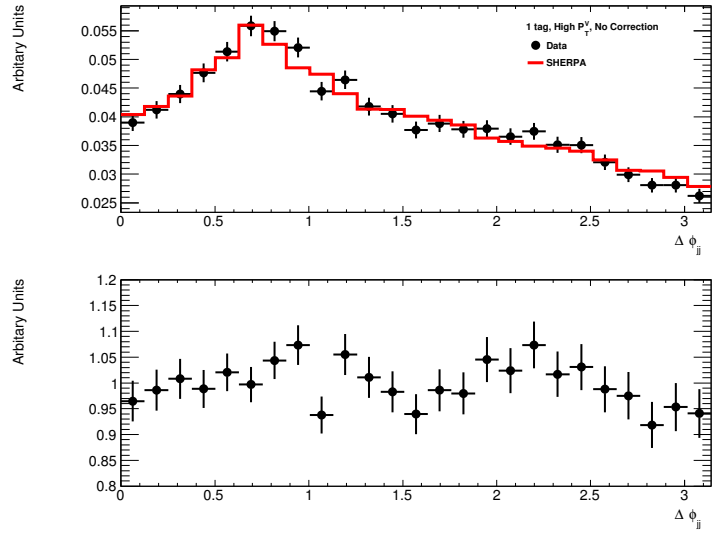

(d) 1-tag p_{T}^{Z}> 120 GeV

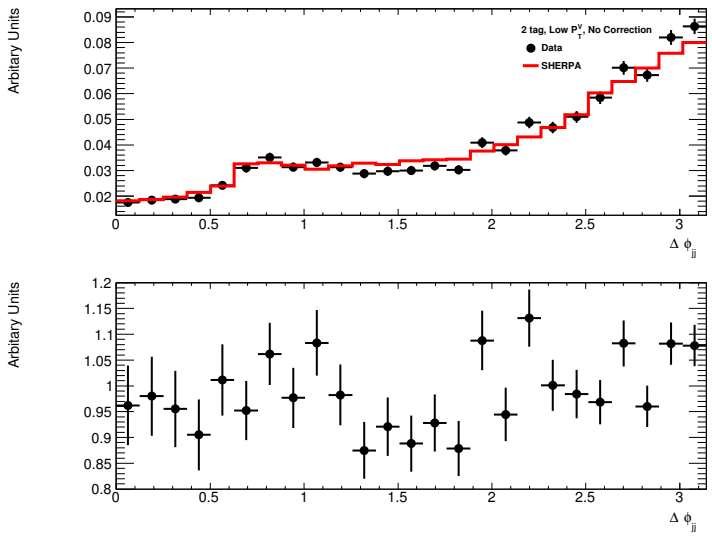

(e) 2-tag p_{T}^{Z}< 120 GeV

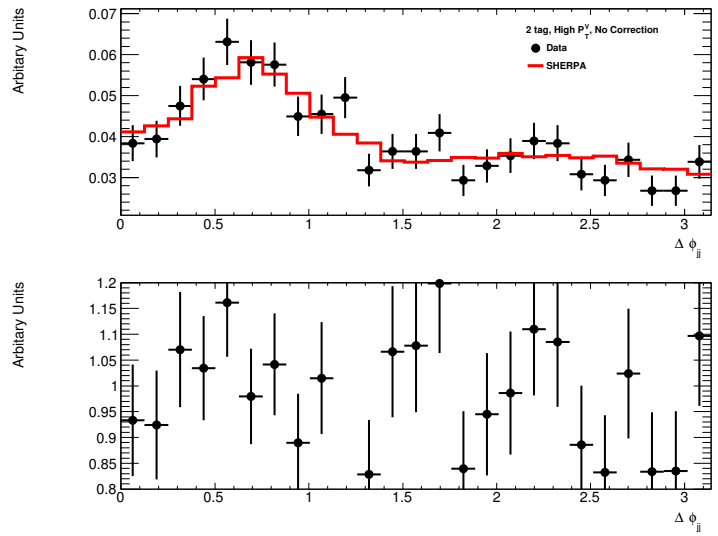

(f) 2-tag p_{T}^{Z}> 120 GeV

Figure 15: A data-driven $\Delta\phi_{jj}$ correction derived from data-MC ratios for Z+light events motivated by the decrease in discrepancy with increased number of b-tags for both $p_{\mathrm{T}}^{V} > 120$ GeV and $p_{\mathrm{T}}^{V} < 120$ GeV.

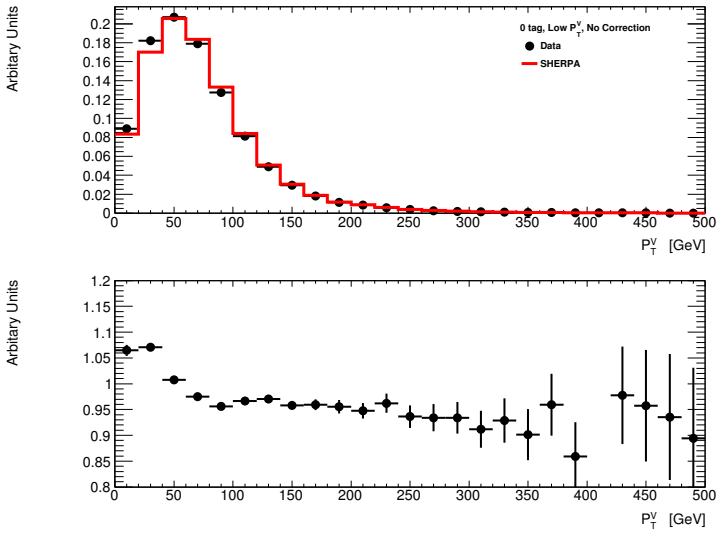

(a) 0-tag

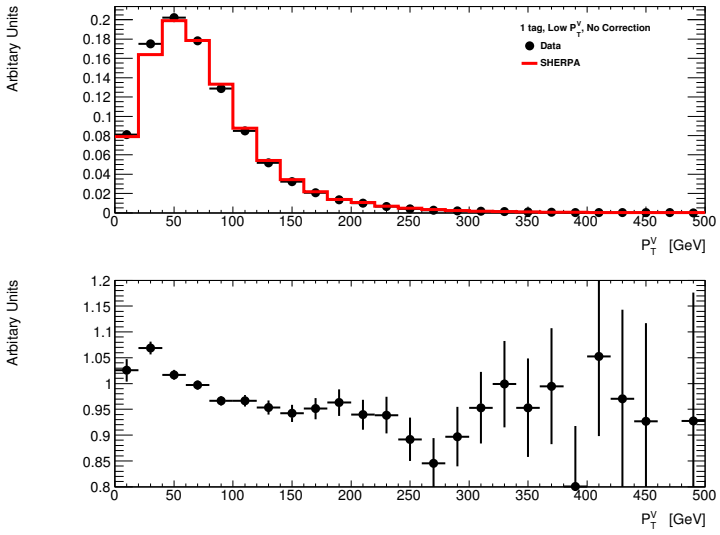

(b) 1-tag

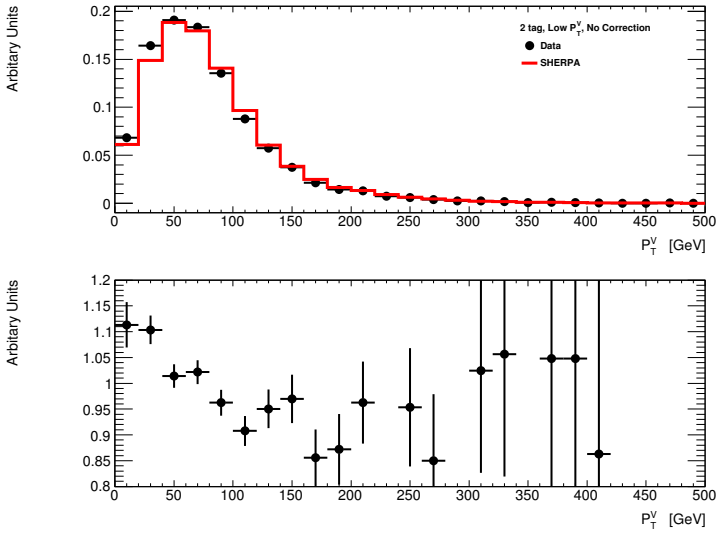

(c) 2-tag

Figure 16: A data-driven p_{T}^{Z} correction derived from data-MC ratios for Z+heavy events motivated by the increase in discrepancy with increased number of b-tags.

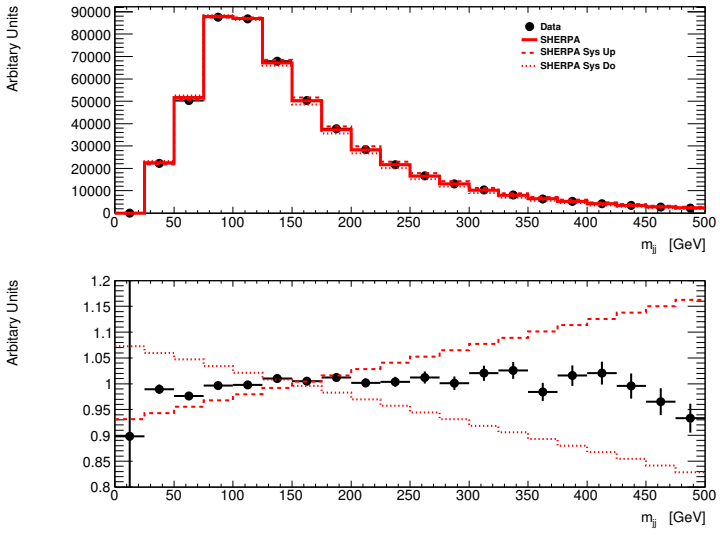

(a) 0-tag

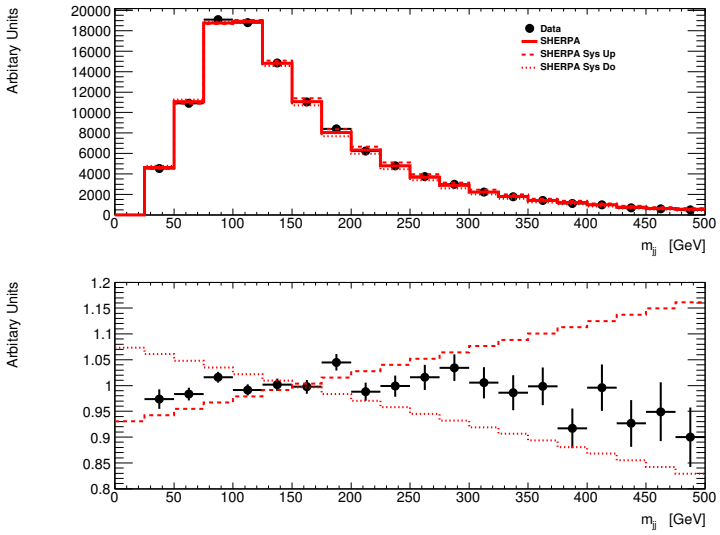

(b) 1-tag

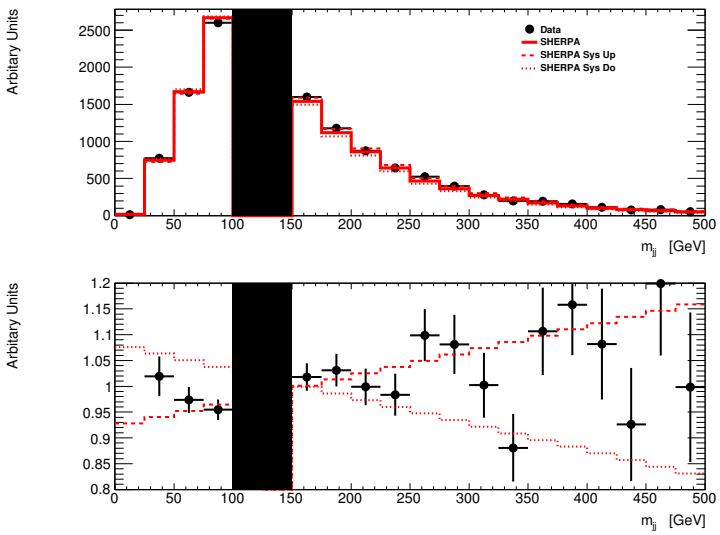

(c) 2-tag

Figure 17: m_{jj} distribution in 2-lepton events from which a systematics uncertainty on the Monte Carlo modeling m_{bb} shape has been derived.

5.1.2 *W*+jets modeling, correction and systematics

1-lepton events with 0 or 1-tag are inundated with W+l/c events but after 2-tags, the $t\bar{t}$ background swamps the W+heavy-flavor (hf=bb+bc+bl+cc) events. Access to the W+jets background in the 0 and 1-tag channels is not problem free since the very difficult multijet background is sizable, especially in the electron channel. In the following, the W+l/c studies from control regions are described in Sections 5.1.2.1-5.1.2.2 (Appendix K) while Sections 5.1.2.3-5.1.2.6 detail the Monte Carlo (MC) studies used to probe the W+hf background (Appendix L). Unless stated otherwise the MVA selection is used for the W+light studies and the dijet mass analysis cuts for the W+hf studies (Table 12). A summary of the this section is given in Table 26 and a summary of the systematics used in the profile likelihood is given in the statistical model overview (Section 8) in Table 50.

5.1.2.1 *W*+light Jet Normalization and Jet Multiplicity

Inherited from EPS, from studies of profile-likelihood fits including the 0-tag region as well from the general agreement the following uncertainties are used:

- normalization of W+ll background: 10% (`WlNorm`)
- 3/2-jet ratio for the light jet production

  W+ll: 10% (`WlNorm_3J`)

  W+cl: 10% (`WclNorm_3J`)

The W+cl and W+hf overall rates are determined from data.

5.1.2.2 *W*+light $\Delta\phi(jj)$ and p_{T}^{W}

Systematic disagreements were observed in 0-tag and 1-tag regions of both the electron and muon selection of the 1-lepton analysis, in particular in the p_{T}^{V} and $\Delta\phi$ of the two leading jets. A pervasive mis-modeling such as this can not be explained by a poor multijet estimate and is similar to features seen in the 2-lepton Z+jets dominated selection (Section 5.1.1). Figure 18 shows the level of agreement of $\Delta\phi(jet_1, jet_2)$ (simply $\Delta\phi$ from now on) and p_{T}^{W} *before* applying any non-standard corrections in 0 and 1-tag events. As was done in EPS (Ref [11] Sections 4.2 and 4.3), a data driven correction is employed. Full details are given in Appendix K. The modeling was studied using bin-to-bin corrections but when the final prescription was chosen, a continuous function was fit to the appropriate ratio. Figure 19 shows when a correction is derived inclusively in p_{T}^{W}, the high p_{T}^{W} region is over-corrected. This motivated a separate correction at low and high p_{T}^{W} which is a change compared to EPS.

It is clear from the shape of the mis-modeling that events should migrate from high to low p_{T}^{W}. Therefore, a normalization change is included in the corrections derived exclusively at high and low p_{T}^{W} to bring the simulation yield to that of the data in each region. Table 24 shows explicitly the change in the simulation yield.

Figure 20 shows the χ^2 value for many kinematic variables without applying a re-weighting, with an inclusive re-weight, and with separate functions at low and high p_{T}^{W} for 2-jet 0-tag events. A dramatic improvement in the modeling is seen.

The flavor composition of the W+jets background is predominantly W+l in 0-tag and W+l and $W+c$l in 1-tag. The contribution from the heavy flavor components in both categories is too small to draw a clear conclusion about whether the same mis-modeling exists. Therefore it was decided to apply the $\Delta\phi$ correction only to the W+l and W+cl backgrounds and to include 50% of the size of the correction as a systematic uncertainty. For the remaining heavy-flavor components, no correction is applied, but the full

Region		Scale Factor (%)
2-jet	$p_{\mathrm{T}}^{W} < 120$ GeV	+0.7
	$p_{\mathrm{T}}^{W} > 120$ GeV	-5.6
3-jet	$p_{\mathrm{T}}^{W} < 120$ GeV	+5.8
	$p_{\mathrm{T}}^{W} > 120$ GeV	-2

Table 24: The normalization changes from the $\Delta\phi$ correction in each of the four regions is show. This is necessary in order to maintain overall agreement while events are migrated between high p_{T}^{W} and low p_{T}^{W}.

size of the correction is taken as a systematic uncertainty (`WDPhi`). Figure 21 shows the improved p_{T}^{W} distribution in the 0-tag after the bin-to-bin correction is applied to the W+l and W+cl backgrounds.

As mentioned above a bin-to-bin correction was used for these studies however the statistical fluctuations of the ratio should not be considered for the correction. Figure 22 shows the function fit used to parametrized the correction derived with respect to W+l and W+cl in 2-jet 0-tag events separately for high and low p_{T}^{W} (3-jet correction is shown in Appendix K Figure 163).

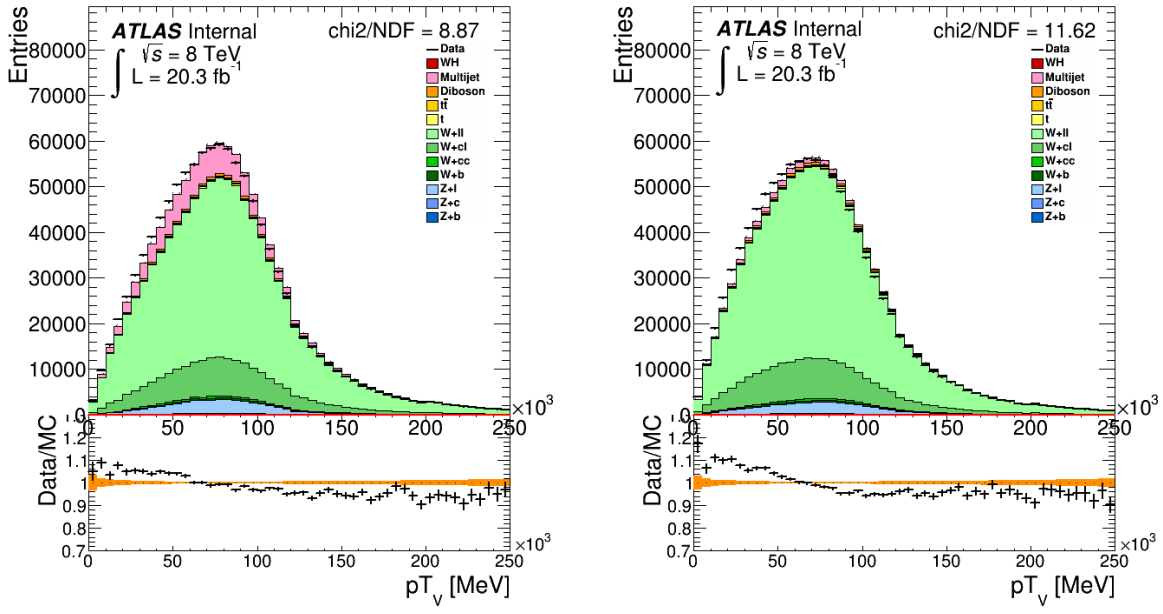

(a) 0-tag uncorrected

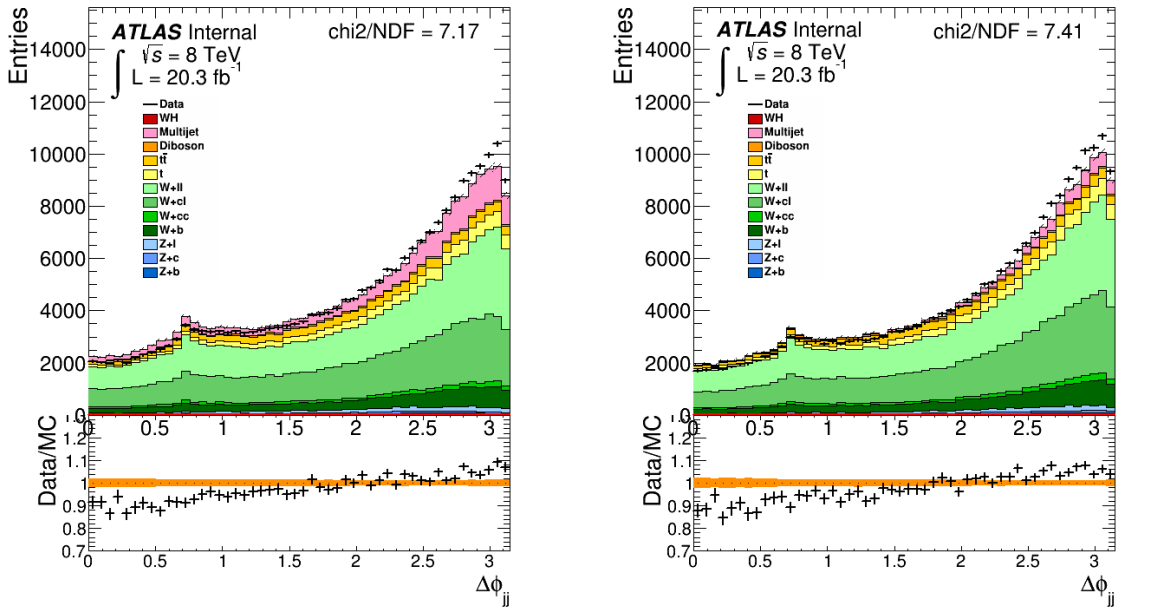

(b) 1-tag uncorrected

Figure 18: 1-lepton 2-jet 0-tag p_{T}^{W} and the 1-tag $\Delta\phi$ distributions before any corrections are applied to the W+jets background. The electron (muon) channel is shown on the left (right).

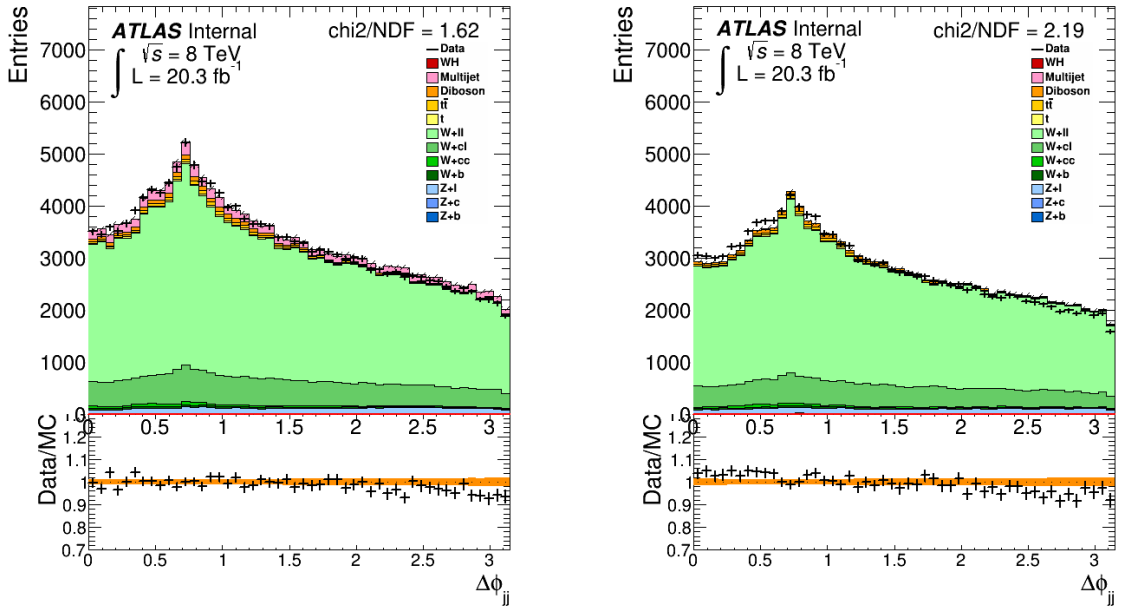

Figure 19: 1-lepton 2-jet 0-tag $\Delta\phi$ distributions using an inclusive $\Delta\phi$ correction similar to the one used for EPS shown in the low ($p_{\mathrm{T}}^{W} < 120$ GeV) and high ($p_{\mathrm{T}}^{W} > 120$ GeV) region on the left and right respectively. Notice the high p_{T}^{W} region is over-corrected. The electron (muon) channel is shown on the left (right).

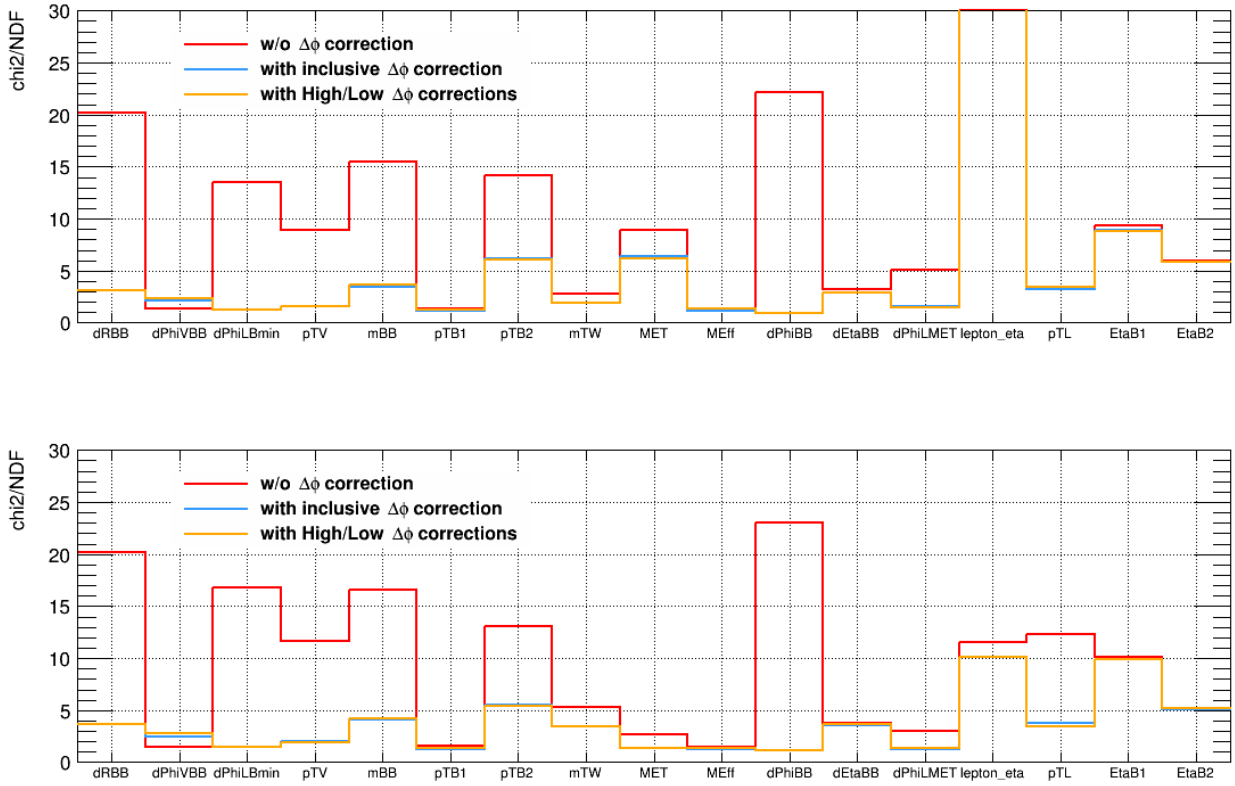

Figure 20: Improvements in the data/MC agreement (χ^2) of many kinematic variables in the 1-lepton 2-jet 0-tag events after various bin-to-bin $\Delta\phi$ corrections derived from the 0-tag region. The electron channel is shown in top half of each plot and the muon channel in the bottom.

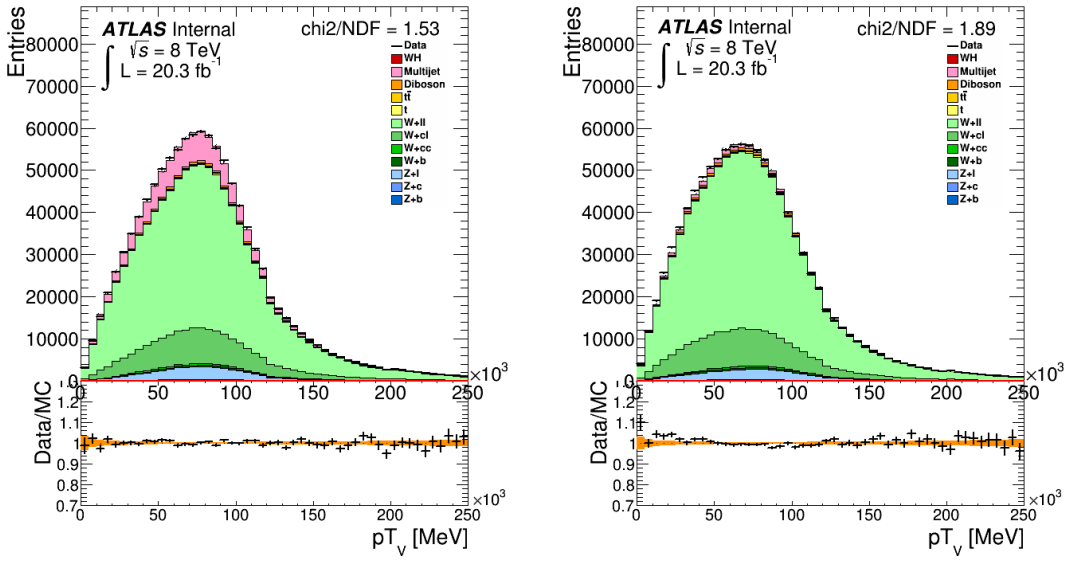

Figure 21: 1-lepton 2-jet 0-tag p_{T}^{W} distribution after a bin-to-bin $\Delta\phi$ correction for $p_{\mathrm{T}}^{W} < 120$ GeV and $p_{\mathrm{T}}^{W} > 120$ GeV separately. The agreement is improved significantly. The electron (muon) channel is shown on the left (right).

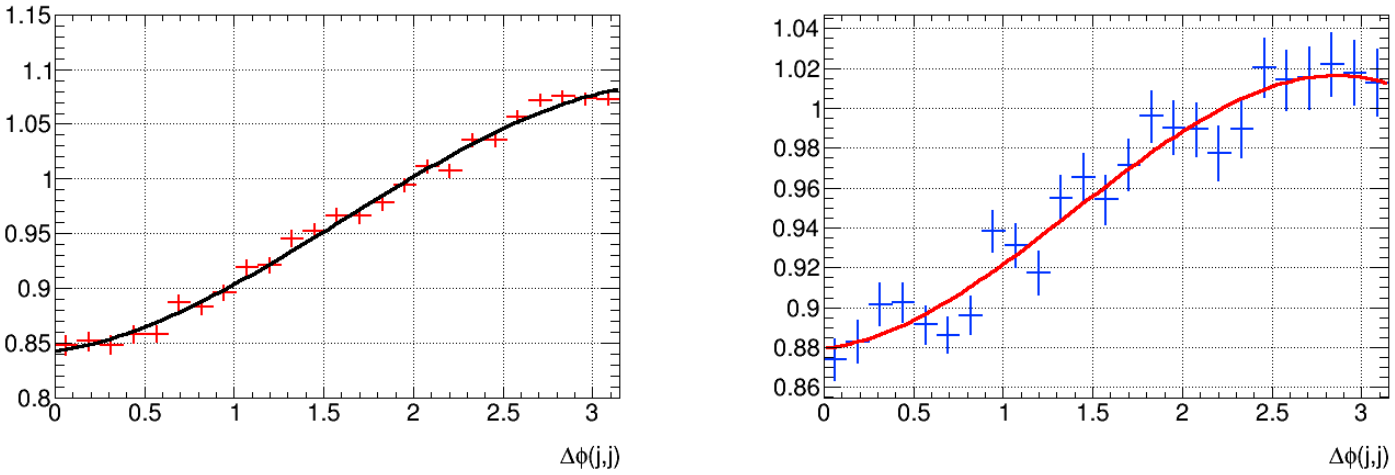

(a) $p_{\mathrm{T}}^{W} < 120$ GeV

(b) $p_{\mathrm{T}}^{W} > 120$ GeV

Figure 22: 1-lepton 2-jet 0-tag $\Delta\phi$ correction for $p_{\mathrm{T}}^{W} < 120$ GeV and $p_{\mathrm{T}}^{W} > 120$ GeV separately.

5.1.2.3 Specific W+Heavy-Flavor Studies

W+heavy-flavor is a tricky background since it can potentially mimic the signal but lacks a good control region. Generator comparisons are therefore utilized to probe the possible variations of the kinematic distributions (at truth-level) and the production rates of the various flavor combinations bb/bc/bl/cc (at reconstruction-level). The following comparisons describe the different aspects studied for the W+hf background:

- *Compare* SHERPA *to* SHERPA. The baseline sample uses a b-filter to create $W+b$ events which include b's from the parton shower. A $W+b\bar{b}$ sample was privately produced where no b's from the parton shower are included.
- *Compare* SHERPA *to a*MC@NLO+HERWIG++ *and* POWHEG. This tests for sensitivity to differences in the matrix element (MX), higher order effects and parton showering. The aMC@NLOsample has been privately produced.

Process	Channel num.	tag	N_events
$W^+ \to e\nu + bb$	167000	evgen.EVNT.e1386	2495000
$W^+ \to \mu\nu + bb$	167001	evgen.EVNT.e1386	2490000
$W^+ \to \tau\nu + bb$	167002	evgen.EVNT.e1386	2500000
$W^- \to e\nu + bb$	167003	evgen.EVNT.e1386	1500000
$W^- \to \mu\nu + bb$	167004	evgen.EVNT.e1386	1500000
$W^- \to \tau\nu + bb$	167005	evgen.EVNT.e1386	1490000

Table 25: Monte Carlo samples and channel numbers and statistics used for centrally produced W samples considered for systematics variations. More information is given in Section 5.1.

Separately, the baseline aMC@NLO sample will be compared to other aMC@NLO samples with varied

- renormalization scale (0.5x,2x).
- factorization scale (0.5x,2x).
- different PDF sets used for the matrix element(NNPDF and MSTW).

More details are contained in Appendix L.

5.1.2.4 Jet multiplicity and flavor fractions

The following normalization systematics have been derived:

- 3/2-jet ratio for the heavy flavor components from SHERPA-aMC@NLO $W + b\bar{b}$ comparisons

  10% (`WbbNorm_J3`)

- relative heavy flavor composition in W+ jet events from SHERPA-ALPGEN comparisons

  W+bl to W+bb: 35% (`WblWbbRatio`)

  W+bc to W+bb: 12% (`WbcWbbRatio`)

  W+cc to W+bb: 12% (`WccWbbRatio`)

An uncertainty on the fraction of gluon splitting to this final state and how it affects the 3/2-jet ratio is estimated by comparing the Sherpa $W + b\bar{b}$ prediction with the baseline Sherpa sample where the heavy flavor also comes from the parton shower (see Appendix L). Half of this uncertainty is considered (2%), which has a negligible impact on the total 3/2-jet ratio uncertainty.

5.1.2.5 $\Delta\phi(jj)$ and p_{T}^{W}

An uncertainty on the p_{T}^{W} shape is estimated from a truth-level study, where the aMC@NLO generator prediction is compared to that of SHERPA $W + b\bar{b}$ (Figure 23).

5.1.2.6 m_{jj}

Two m_{bb}-specific uncertainties were derived from generator differences after a truth-level selection; ALPGEN-SHERPAcomparisons and $W + b\bar{b}$ versus b-filter SHERPA for the fraction of gluon splitting contribution. Figure 24 shows the first (and larger) uncertainty can shift the distribution by ±20% for $m_{b\bar{b}}$ = 50 GeV and ±30% for $m_{b\bar{b}}$ = 200 GeV. The latter has a smaller effect of approximately ±5% across the spectrum since only half of the effect is considered. The choice of half for only the second comparison is motivated, by the nature of the comparison itself. The full difference is to say that gluon splitting does not exist which we know is not true so a fraction (50%) of the difference is applied. Since this last difference can be already be covered by the systematic uncertainty assigned on m_{bb} by comparing different MC generators, the fit will not use it, but detailed studies on its impact have been done while building the final fit model.

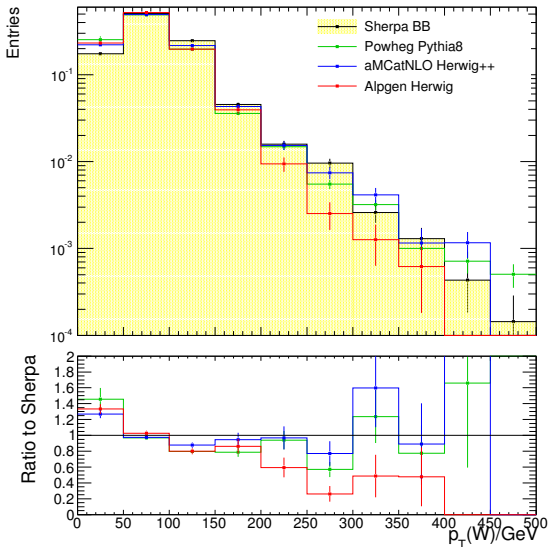

Figure 23: W-boson p_T distribution of 2-jet bb events at truth-level.

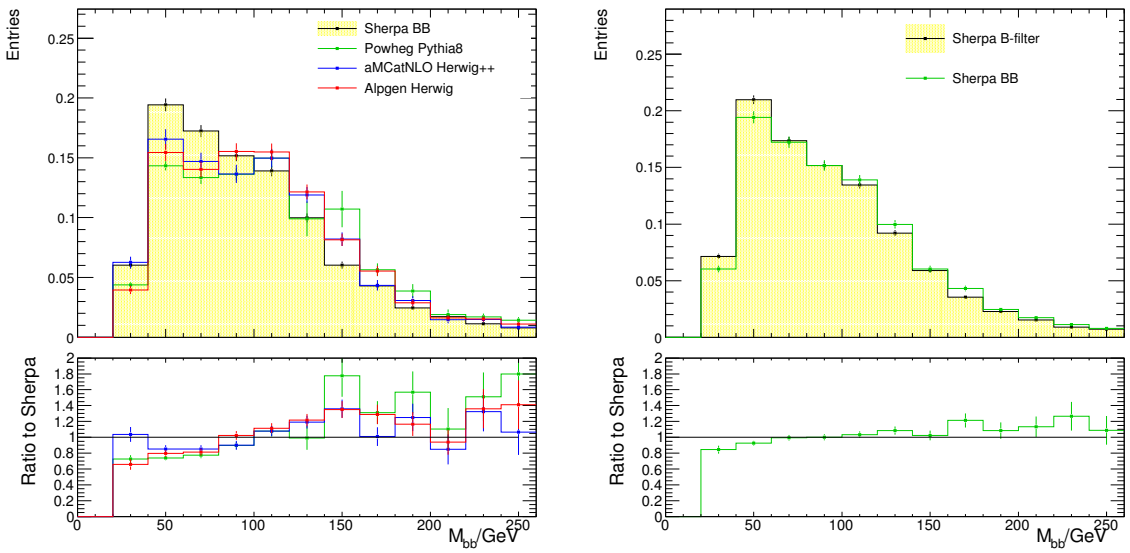

Figure 24: Invariant mass distribution of 2-jet bb events at truth-level. The plot on the left compares the generator predictions for the $W + b\bar{b}$ process, and the plot on the right compares the same Sherpa prediction to the nominal B-filtered sample .

Description	Samples	Nuissance parameters
Wl Normalization	Data VS. Sherpa	`WlNorm`
W 3/2 ratio	Sherpa VS. aMC@NLO	`WlNorm_J3`,`WclNorm_J3`,`WbbNorm_J3`
W jet flavour composition	Sherpa VS. Alpgen+Herwig+Jimmy	`WblWbbRatio`, `WbcWbbRatio`, `WccWbbRatio`
$\Delta\phi$ correction and systematics	Data VS. Sherpa	`WDPhi`
$\Delta\phi$ checks	Data VS. Alpgen+Herwig+Jimmy	
p_{T}^{V} systematics	Sherpa VS. aMC@NLO	`WPtV`
p_{T}^{V} checks	Sherpa VS. Powheg VS. Alpgen+Herwig+Jimmy	
m_{bb} systematics	Sherpa VS. Alpgen+Herwig+Jimmy	`WMbb`
m_{bb} checks	Sherpa VS. Powheg VS. aMC@NLO	
m_{bb} gluon splitting systematics	Sherpa with and without bb from gluon splitting	`WbbMbbGS`

Table 26: Summary of the W+jet specific samples used to checks the background modelling. The list of the nuissance parameters is given for reference, and it will be discussed in Section 8

.

5.2 $t\bar{t}$ and single-top

The top-pair samples are generated with PowHeg [56–58] interfaced to Pythia with a filter which specifies that at least one of W from top decays into charged lepton (e, μ, τ). The parton showering and hadronisation is generated according to the *Perugia2011C* tune which uses CTEQL1 pdf. For the single-top processes, s-channel and Wt-channel are generated with PowHeg+Pythia. and the t-channel simulated with AcerMC+Pythia. All single top channels use the CTEQL1 pdf and the *Perugia2011C* tune. The detailed list of MC samples for the top production is listed in Table 27. The reader is encouraged to read the introduction to Section 5 to better understand how the information here will be utilized.

Process	Channel num.	tag	N_events
Single top, s−ch., PowhegPythia, P2011C			
s−ch.	110119	e1720_a188_a171_r3549_p1328	5995993
Single top, t−ch. and Wt−ch., AcerMCPythia, P2011CCTEQ6L1			
t−ch.	110101	e2096_a188_a171_r3549_p1328	59962956
Wt−ch.	110140	e1743_a188_a171_r3549_p1328	19937980
$t\bar{t}$, PowhegPythia, P2011C			
$t\bar{t}$	117050	e1727_a188_a171_r3549_p1328	99930891

Table 27: Monte Carlo samples and channel numbers and statistics used for the single top and the $t\bar{t}$ samples. More details are given in Section 5.2.

5.2.1 $t\bar{t}$ modeling, corrections and systematics

The $t\bar{t}$ modeling has been explored in depth by other groups within atlas. Given the specific final state selected, of particular interest for this analysis is the $t\bar{t}$ composition and the capability of the MC, to reproduce the top p_{T} observed in data. This section discusses the derivation of systematic uncertainties for the $t\bar{t}$ modeling considering the recommendation and feed-back from the top group. A summary of the this section is given in Table 30 and a summary of the systematics used in the profile likelihood is given in the statistical model overview (Section 8) in Table 51.

5.2.1.1 $t\bar{t}$ Composition

Due to the ΔR cuts placed in the dijet mass analysis the composition of $t\bar{t}$ events evolve as a function of p_{T}^{W} with the leading two jets both being b's at lower p_{T}^{W} values and a b-c pair at high p_{T}^{W}. A similar statement holds for the MVA. The reader should keep this evolution in mind when considering the top-pair modeling and systematic studies in the following sections. The flavor compositions are shown in Appendix O in Table 100 for the eps analysis and in Table 28 for the current 1-lepton analysis[3]. Given that there are exactly two b-tagged jets, the flavor composition for the 1-Lepton MVA input selection is shown in Table 29. For the following comparisons in Section 5.2.1.3 with other generators for $t\bar{t}$ it is important to investigate if these model a similar flavor composition. It was found that the flavor compositions of all of them are as expected. The corresponding studies and their numbers are given in the Appendix Section N.5 in Table 99.

[3]The new object selection was utilized but the eps event selection cuts were used. The table should be updated.

Jet Flavors	p_T^W GeV 0-90	90-120	120-160	160-200	>200
	2T b-tags				
bb	96.0	96.5	94.7	78.8	40.5
bc	3.0	3.1	4.6	18.8	46.8
$b\tau$	<1	<1	<1	1	9.1
	2M b-tags				
bb	79.9	80.2	71.6	46.9	15.0
bc	14.8	14.8	22.2	42.1	63.8
$b\tau$	3.0	5.3	3.3	4.7	7.9
	2L b-tags				
bb	62.3	61.0	51.4	26.4	10.6
bc	19.8	20.5	27.0	38.9	50.1
$b\tau$	5.5	4.9	5.1	6.6	5.3

Table 28: The fraction of jet flavor pairs in the 1-lepton EPS [11] analysis from events with two jets as a function of p_T^W. The new object selection was utilized but the EPS event selection cuts were used. The table should be updated.

Jet Flavors	p_T^W GeV 0-120	>120
bb	79.8	67.3
bc	11.5	20.4
bl	8.5	11.6

Table 29: The fraction of jet flavor pairs in the 1-lepton multivariate analysis from events with two b-tagged jets separated into low and high p_T^W events. The MVA input selection was applied.

The presence of a high fraction of events with bc final state jets at high p_{T}^{V}, and the need to suppress as much as possible the background in this region, are the reasons which guided the decision to move to the mv1c tagging.

5.2.1.2 The p_{T}^{top} correction

A systematic disagreement in $\Delta\phi$ is not observed in the $t\bar{t}$ sample. However it has been noted in the time leading up to EPS that the reconstructed p_{T}^{W} in the 1-lepton top-enriched regions and p_{T}^{Z} in the 2-lepton $e-\mu$ control sample show a disagreement which is consistent with the top p_{T} being too hard in simulation. The ATLAS 7 TeV [59] result shows the same trend so the unfolded measurement shown in Figure 25 was used to reweight the average top p_{T} in MC. Half the reweighting function was used as a systematic (`TopPt`) Further details can be found in Sections 4.4 and 4.5.3 and Appendix J of the EPS note [11].

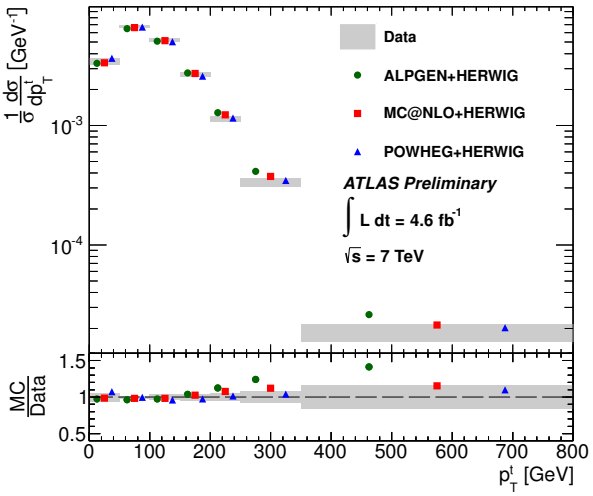

Figure 25: The ATLAS 7 TeV $t\bar{t}$ p_{T}^{top} unfolded result taken from [60] used to reweight the top p_{T} spectrum.

5.2.1.3 Specific $t\bar{t}$ systematics

The $t\bar{t}$ systematic generator variations have been explored in depth by other groups within ATLAS. The baseline approach is to consider all the 'normal' variations which are applicable to this analysis. The list of checks are as follows:

- *Compare to AcerMC with more or less PS.* This will test the effect of the parton showering. The recommendation is to obtain the systematic as (morePS-lessPS)/2. For comparisons with other generators this variation is added to our nominal sample.
- *Compare to PowHeg+Herwig.* This will test different PS and hadronization models. There is some difficulty in that since it is not completely orthogonal to the previous comparison.
- *Compare to Alpgen.* This will show the sensitivity to higher order effects such as gluon radiation since ALPGEN is a LO generator in contrary to POWHEG(NLO).
- *Compare to PowHeg+Pythia with HeraPDFs.* This will test the effect of the PDF set. The HeraPDF set is supposed to describe ATLAS data better especially quantities like top p_{T}. This test will suffer from low statistics since the HeraPDF sample has only 5 million events.

- *Compare to a*MC@NLO. This probes the potential effects from different matrix element calculations.

The top group does recommend several other tests which currently are not planned since they are not considered as having large effects on the analysis. A list of those tests and the reasons for excluding them are given in Appendix N.

Unless directly stated, all systematic samples will be compared to the nominal sample which is PowHeg+Pythia with a dedicated top p_{T} correction applied. Table 31 gives technical details of the samples considered. From the above mentioned comparisons the largest discrepancies between generators were taken as systematic uncertainties.

The effect of different modeling of the BDT input variables between the generators was taken into account as a set of shape uncertainties. These shape uncertainties were derived for the distributions of the input variables from the largest discrepancies between generators . If no significant difference between the generators is observable no dedicated uncertainty will be assigned. For a further reduction of shape systematics advantage was taken of the correlation between the input variables. Therefore a minimal set of shape systematics were chosen which are able to cover the observed differences. For this set it was observed that the largest discrepancy to the nominal is given by alpgen+Pythia. As there was already a systematic uncertainty assigned to the top p_{T} correction double counting of systematic effects was avoided by reweighting alpgen+Pythia to the same top p_{T} in the 7 TeV analysis mentioned above. Details of this study are describes in Appendix Section N.3. After this study shape uncertainties were derived from a fit through the difference between alpgen+Pythia without the top p_{T} reweighting and the nominal sample in the distributions for m_{bb} and $E_{\mathrm{T}}^{\mathrm{miss}}$. Since the shapes for the 2 jet and 3 jet region are similar for the $E_{\mathrm{T}}^{\mathrm{miss}}$ distributions those two regions were merged and a single uncertainty was derived. For m_{bb} a similar merging was not possible. A combination of the high and low p_{T}^{W} region was not possible in both cases due to different shapes originating e.g. from different $E_{\mathrm{T}}^{\mathrm{miss}}$ cuts.

Figure 26 details the m_{bb} systematic for $t\bar{t}$ 2-jet events (`TtbarMBBCont`). Similar plots are shown for 3-jet events along with more details in Appendix Section N.1. The first row shows the comparison of all generators with the most discrepant from the baseline being alpgen+Pythia without the p_{T}^{top} reweight. A fit to the ratio was performed up to 200 GeV as shown in the bottom row. Details of the fit function are described in Appendix Section N.1. Unfortunately, the comparisons with and without the p_{T}^{top} correction shown in the middle row came soon after this systematic was propagated into the analyses. Since no large difference in the ratio is seen in the region used for the systematic derivation, it was decided to not change the prescription.[4] The ratio was different enough in the four regions such that a separate function was fit to each.

The $E_{\mathrm{T}}^{\mathrm{miss}}$ distribution also showed considerable differences, the largest being between alpgen+Pythia and PowHeg+Pythia yet again. Full details are shown in Appendix Section N.2. Figure 27 shows for $p_{\mathrm{T}}^{W} > 120$ GeV the comparison of all the generators in the top row, a specific alpgen+Pythia-PowHeg+Pythia comparison with and without the top p_{T} systematics in the middle row, followed by the systematic used in 2 and 3 jet events alike (`TtbarMetCont`). Again the differences in the systematic after the top p_{T} correction is applied were deemed small enough to avoid. Since the ratios for the 2-jet and 3-jet region were similar for the $E_{\mathrm{T}}^{\mathrm{miss}}$ distributions, these two regions were merged and a single uncertainty was derived.

The functional form used for the systematic is constant above 300 GeVas to maintain a reasonable size in the tail of the $E_{\mathrm{T}}^{\mathrm{miss}}$ distribution. Since the definition and source of $E_{\mathrm{T}}^{\mathrm{miss}}$ is analysis specific, this is only used in the 1-lepton analysis.

The effect of these two systematics were each propagated to the BDT itself and compared to the differences from the full list of generator comparisons. Since the two systematics along with the top

[4] Time dependence is an unfortunate consequence of the complexity of atlas software and this analysis in general.

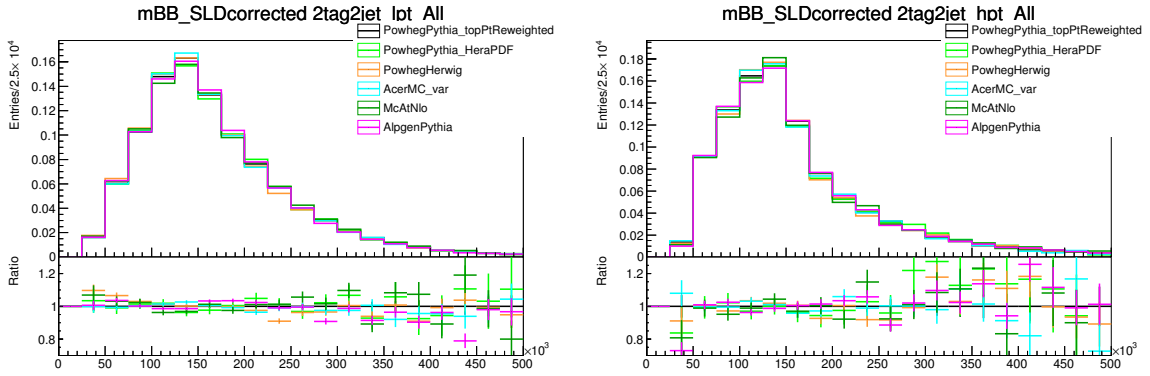

(a) All Generator Comparisons 2-jet events

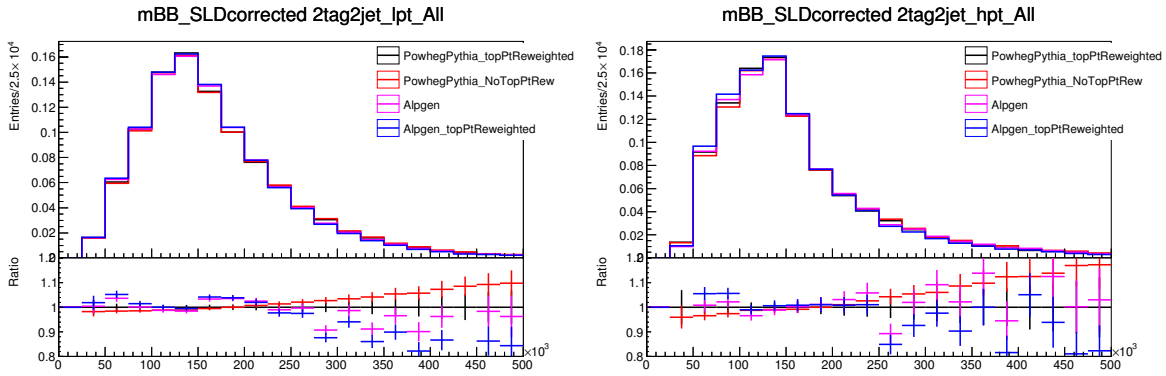

(b) Effect of top p_{T} reweight in 2-jet events

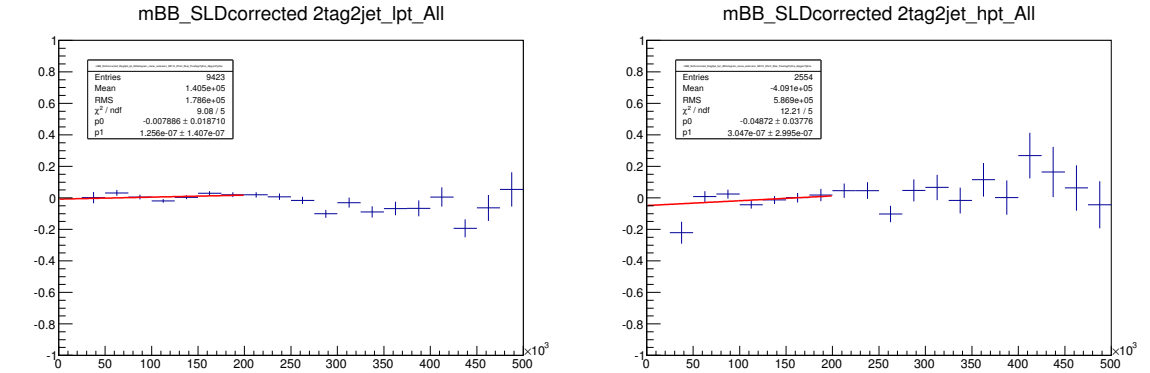

(c) 2-jet m_{bb} systematic fit

Figure 26: m_{bb} systematic for $t\bar{t}$ in 2-jet events (3-jet in Appendix N) $p_{\mathrm{T}}^{W} < 120$ GeV is shown on the left and $p_{\mathrm{T}}^{W} > 120$ GeV is shown on the right. The top row shows the all generator comparison, the middle is a closer look at the most discrepant compared to the nominal, ALPGEN+PYTHIA, with and without the top p_{T} correction, and finally, the systematic itself derived from the ALPGEN+PYTHIA to POWHEG+PYTHIA ratio in the top row of plots.

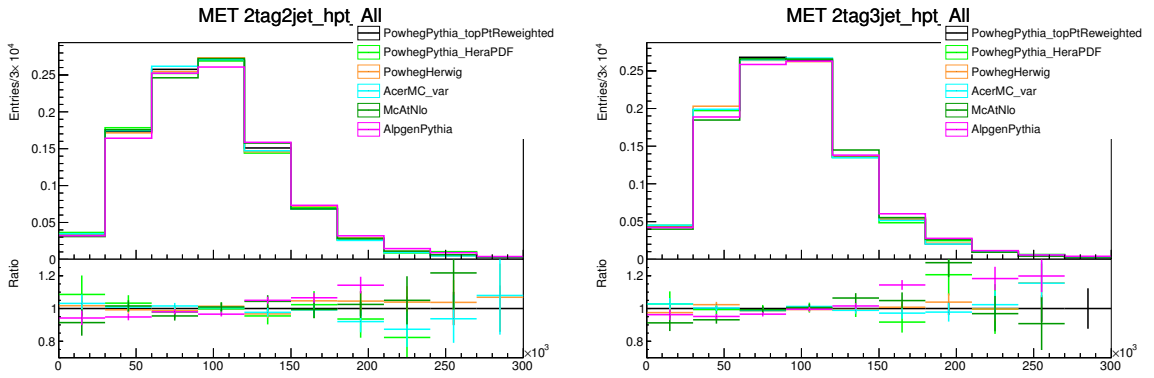

(a) All Generator Comparisons for $p_{\mathrm{T}}^{W} > 120$ GeV

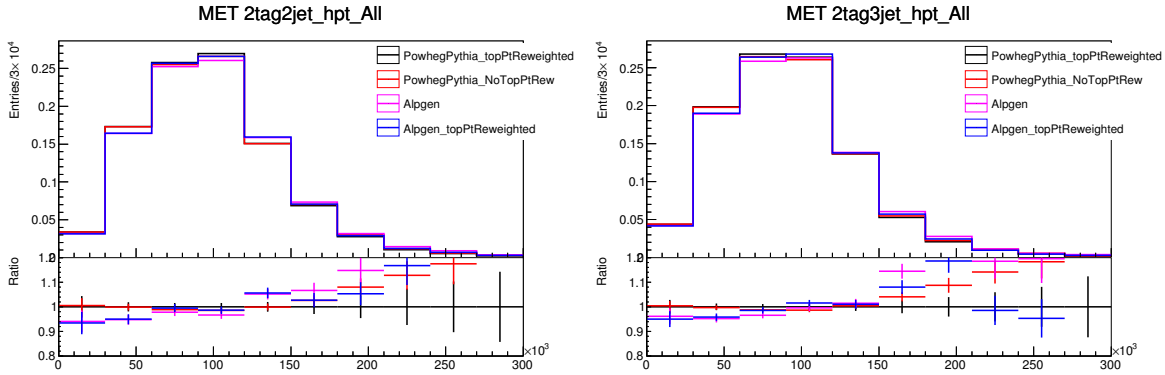

(b) Effect of top p_{T} reweight for $p_{\mathrm{T}}^{W} > 120$ GeV

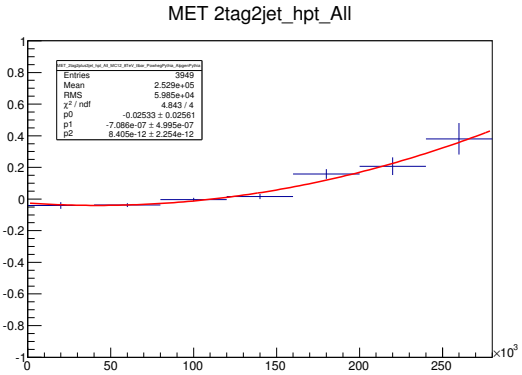

(c) 2+3-jet $p_{\mathrm{T}}^{W} > 120$ GeV systematic

Figure 27: $E_{\mathrm{T}}^{\mathrm{miss}}$ systematic for $t\bar{t}$ events in 2+3-jet events for $p_{\mathrm{T}}^{W} > 120$ GeV the 2 and 3-jet regions on the left and right respectively. These were obtained from a comparison of of ALPGEN+PYTHIA to POWHEG+PYTHIA. More details including the $p_{\mathrm{T}}^{W} < 120$ GeV are given in Appendix N

p_{T} systematic covered all other differences in the BDT input variables, no further modeling systematics were included. The effect of the overall shape systematics (top p_{T}, $E_{\mathrm{T}}^{\mathrm{miss}}$, m_{bb}) on the BDT output for the 2-jet and 3-jet region is shown in Figure 28. Considering the statistical fluctuations the set of shape systematics show a good coverage of systematic effects in the BDT output for the high p_{T}^{W} region. In the low p_{T}^{W} region the coverage in the high BDT output bins is a bit worse but it was decided to not introduce additional systematics.

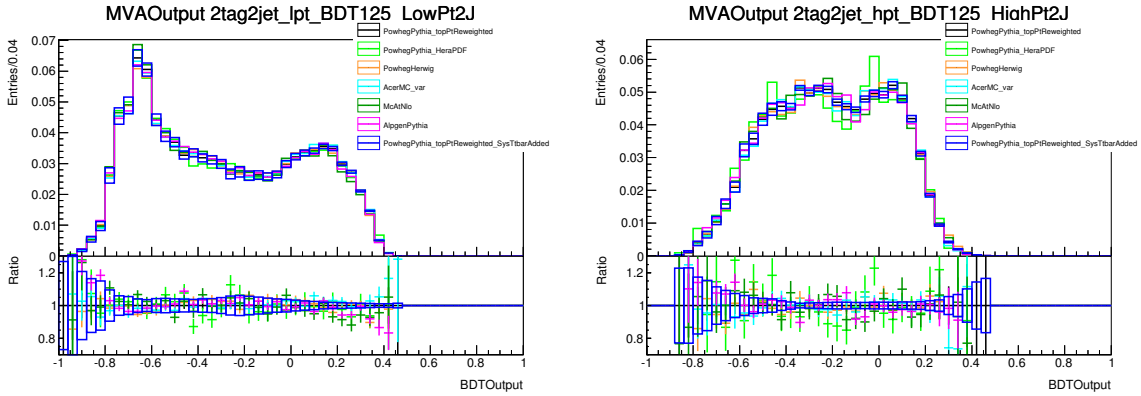

(a) 2-jet

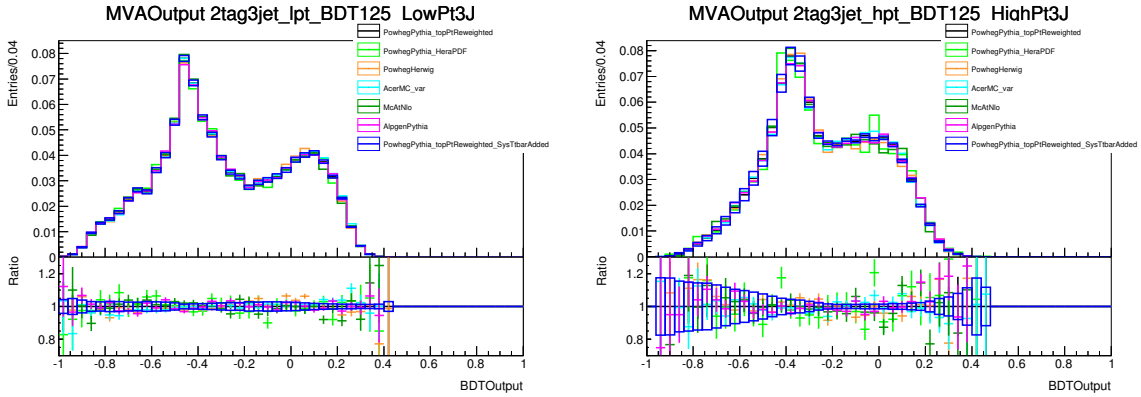

(b) 3-jet

Figure 28: Coverage of systematic effects in the BDT output for $t\bar{t}$, the top p_{T}, m_{bb} and $E_{\mathrm{T}}^{\mathrm{miss}}$ shape systematics were applied.

Since the multivariate analysis is separated into regions with two jets and three jets, always given that there are exactly two b-tagged jets, as well as into regions with a high p_{T}^{W} and a low p_{T}^{W} additional uncertainties have to be assigned which take the differences between the generators regarding this categorization into account. From a comparison of the ratio of high to low p_{T}^{W} events a 7.5% uncertainty was assigned from ALPGEN+PYTHIA which was the most different from the baseline POWHEG+PYTHIA(`ttbarHighPtV`). Similarly a 20% uncertainty was derived for the ratio of 2-to-3 jet production from the comparison to ALPGEN+PYTHIA (`ttbarNorm_J3`). The details of these comparisons are included in Table 98 in Appendix N.

Description	Samples	Nuissance parameters
Systematics on High/low p_{T}^{V} ratio	Powheg VS. Alpgen+Herwig+Jimmy	`ttbarHighPtV`
Systematics on 3/2 jet ratio	Powheg VS. Alpgen+Herwig+Jimmy	`ttbarNorm_J3`
Top p_{T} correction and systematics	Data VS. Powheg	`TopPt`
p_{T}^{V} shape systematics	Powheg VS. Alpgen+Herwig+Jimmy	`TtbarPtWCont`
m_{bb} shape systematics	Powheg VS. Alpgen+Herwig+Jimmy	`TtbarMBBCont`
Leading jet p_{T} shape systematics	Powheg VS. Alpgen+Herwig+Jimmy	`TtbarPtB1Cont`
$E_{\mathrm{T}}^{\mathrm{miss}}$ shape systematics	Powheg VS. Alpgen+Herwig+Jimmy	`TtbarMETCont`
Checks done with :	ALPGEN, POWHEG, AcerMC with more or less PS POWHEG+HERWIG, aMC@NLO.	

Table 30: Summary of the $t\bar{t}$ specific samples used to checks the background modelling. The list of the nuissance parameters is given for reference, and it will be discussed in Section 8.
.

Process	Channel num.	tag	N_{events}
		$t\bar{t}$, aMC@NLO, CT10	
$t\bar{t}$	105200	e1513_s1499_s1504_r3945_r3549	14990603
		$t\bar{t}$, PowhegHerwig, AUET2CT10	
$t\bar{t}$	105860	e1576_a159_a171_r3549	25886964
		$t\bar{t}$, PowhegPythia, P2011CHERAPDF15NLO	
$t\bar{t}$	117001	e2397_a188_a171_r3549	4997997
		$t\bar{t}$, AcerMCPythia, AUET2BMorePSCTEQ6L1	
$t\bar{t}$	117209	e1378_a159_a171_r3549	14040986
		$t\bar{t}$, AcerMCPythia, AUET2BLessPSCTEQ6L1	
$t\bar{t}$	117210	e1378_a159_a171_r3549	14988492
		$t\bar{t}$, AlpgenPythia, P2012	
$t\bar{t}, lnlnNp0$	201020	e2356_s1581_s1586_r3925_r4540	3199485
$t\bar{t}, lnlnNp1$	201021	e2356_s1581_s1586_r3925_r4540	3187981
$t\bar{t}, lnlnNp2$	201022	e2356_s1581_s1586_r3925_r4540	2091691
$t\bar{t}, lnlnNp3$	201023	e2356_s1581_s1586_r3925_r4540	971691
$t\bar{t}, lnlnNp4inc$	201024	e2356_s1581_s1586_r3925_r4540	589998
$t\bar{t}, lnqqNp0$	201220	e2356_s1581_s1586_r3925_r4540	6293873
$t\bar{t}, lnqqNp1$	201221	e2356_s1581_s1586_r3925_r4540	6389459
$t\bar{t}, lnqqNp2$	201222	e2356_s1581_s1586_r3925_r4540	1814984
$t\bar{t}, lnqqNp3$	201223	e2356_s1581_s1586_r3925_r4540	1949886
$t\bar{t}, lnqqNp4inc$	201224	e2356_s1581_s1586_r3925_r4540	1179291

Table 31: Monte Carlo samples and channel numbers and statistics used for the single top and the $t\bar{t}$ systematics. More information is given in Section 5.2.1.

5.2.2 Single-top modeling and systematics

As for the $t\bar{t}$ background, the single top systematic generator variations have been explored in depth by other groups within ATLAS. The baseline approach is to consider all the 'normal' variations which are applicable to this analysis. The single top group has recommended a list of generator comparisons which are summarized in Table 5.2.2. If only one sample is mentioned then a comparison to the baseline sample is implied. Table 97 gives technical details of the samples considered.

A summary of the this section is given in Table 34 and a summary of the systematics used in the profile likelihood is given in the statistical model overview (Section 8) in Table 52.

Process	Samples	Description	Nuisance Parameters
t−ch.	aMCAtNlo	higher order, hadronization and showering	SysTChanPtB2
	AcerMC more vs less PS	parton shower effects	
Wt−ch.	Herwig	hadronization and showering models	SyWtChanPythiaHerwig
	AcerMC	higher order	SyWtChanAcerMC
	PowhegPythia DS	Diagram Removal vs Subtraction	
	MCAtNlo	hadronization and showering models	
	AcerMC more vs less PS	parton shower effects	
s−ch.	AcerMC	higher order effects	SysSChanAcerMC
	MCAtNlo	hadronization and showering models	
	AcerMC more vs less PS	parton shower effects	SysSChanAcerMCPC

Table 32: Monte Carlo samples considered for systematics and what each comparison brings. More information is given in Section 5.2.2.

To perform the study, the events passing the MVA selection for the 1-lepton channel have been used and the shapes of all the relevant variables entering in the multivariate analysis were analyzed. For each of the single top channel ($s-channel$, $t-channel$ and $Wt-channel$) the systematics have been divided into two categories: normalization and shape systematics.

The normalization systematics takes into account the renormalization and factorization scale variation, the α_s uncertainty and the errors on the parton density functions. They are of the order of 3.9%, 6.8% and 3.9% for the $t-channel$, $Wt-channel$ and $s-channel$ respectively.

The second set of errors is coming from the comparisons of the different available Monte Carlo samples. It is estimated for the two analysis signal regions - 2 jets or 3 jets and 2 tags - and in two p_{T}^{V}bins - above and below 120 GeV. Since the different Monte Carlo estimate can differ in the event acceptance and in the shape of the different kinematic variables, a detailed campaign of checks have been carried out for each channel. The strategy adopted in this case was for each of the p_{T}^{V} region, jet multiplicity, and each production channel, to check which Monte Carlo sample shows the worst agreement in terms of acceptance and/or shape of the variables of interest. In this way, a normalization error and a shape variation for specific variables (if needed), have been derived . As a coverage test, the impact of the shape variations have been propagated to the BDT output and compared with the agreement obtained when using the Monte Carlo sample used to derive the systematics.

The major differences are mostly from comparisons of the nominal sample with a next-to-leading order Monte Carlo, or, in the case of the $s-channel$, from the samples with more or less parton shower. This result in the systematics summarized in Table 34. The selected variables and the functions used for the systematics are summarized in the Table 34. Figure 29 show for each production channel, p_{T}^{V}

Process	Channel num.	tag	N_{events}
		Single top, AcerMCPythia, P2011CCTEQ6L1	
$s-$ch.	110102	e2092_a188_a205_r4540_p1328	1199999
$Wt-$ch.	110103	e2092_a188_a205_r4540_p1328	998997
		Single top, PowhegHerwig, AUET2CT10	
Wt-ch	110144	e1743_s1581_s1586_r3658_r3549_p1328	998896
		Single top, PowhegPythia, P2011C, DS	
$Wt-$ch.	110142	e1743_s1581_s1586_r3658_r3549_p1328	994894
		Single top, aMcAtNloJimmy, AUET2CT10	
$t-$ch.	110095	e2240_a188_a205_r4540_p1328	996999
		Single top, McAtNloJimmy, AUET2CT10	
$s-$ch.	108343	e1525_a159_a171_r3549_p1328	999998
	108344	e1525_a159_a171_r3549_p1328	998000
	108345	e1525_a159_a171_r3549_p1328	999998
$Wt-$ch.	108346	e1525_a159_a171_r3549_p1328	4996492
		Single top AcerMCPythia, P2011CMorePSCTEQ6L1	
$t-$ch.	110105	e2092_a188_a205_r4540_p1328	2978000
$s-$ch.	110107	e2092_a188_a205_r4540_p1328	1199999
Wt-ch	110109	e2092_a188_a205_r4540_p1328	998999
		Single top AcerMCPythia, P2011CLessPSCTEQ6L1	
$t-$ch.	110106	e2092_a188_a205_r4540_p1328	2997999
$s-$ch.	110108	e2092_a188_a205_r4540_p1328	1198998
Wt-ch	110110	e2092_a188_a205_r4540_p1328	1000000

Table 33: Monte Carlo samples and channel numbers and statistics used for the single top and the $t\bar{t}$ systematics. More information is given in Section 5.2.2.

region, and number of jets, the selected input variable used to parametrize the systematic uncertainty, and its impact on the BDT output. It must be noted that since the final contribution from the $s-channel$ is negligible, no specific shape systematic uncertainty have been derived. In the case of the $t-channel$, the BDT input variables were found to exhibit no significant shape differences between different Monte Carlo. A detailed description of all the Monte Carlo studies are presented in Appendix M.

Process	Systematic Name	Normalization systematic (%)		Shape systematics
		2 jets, 2 tag p_{T}^{V}< (>)120GeV	3 jets, 2 tag p_{T}^{V}< (>)120GeV	
t−ch.	SysTChanPtB2	52 (25)	12 (-18)	no shape systematic
Wt−ch.	SyWtChanPythiaHerwig	5 (3)	5 (-3)	2 jets, p_{T}^{V}<120 GeV: ±(1.3 - 0.004×$p_{T,b1}$)
	SyWtChanAcerMC	1 (-2)	4 (-15)	2 jets, p_{T}^{V}>120 GeV: ±(0.6 + 0.004×m_{bb})
				3 jets, p_{T}^{V}<120 GeV: ±(1.2 -0.003×$p_{T,b1}$)
				3 jets, p_{T}^{V}>120 GeV: ±(1.4 -0.003×m_{bb})
s−ch.	SysSChanAcerMC	13 (22)	18 (30)	no shape systematic
	SysSChanAcerMCPC	6 (8)	4 (4)	no shape systematic

Table 34: Single-top systematics obtained comparing different Monte Carlo samples. $p_{T,b1}$ and m_{bb} are the p_T of the leading b-jet and the di-bjet invariant mass.

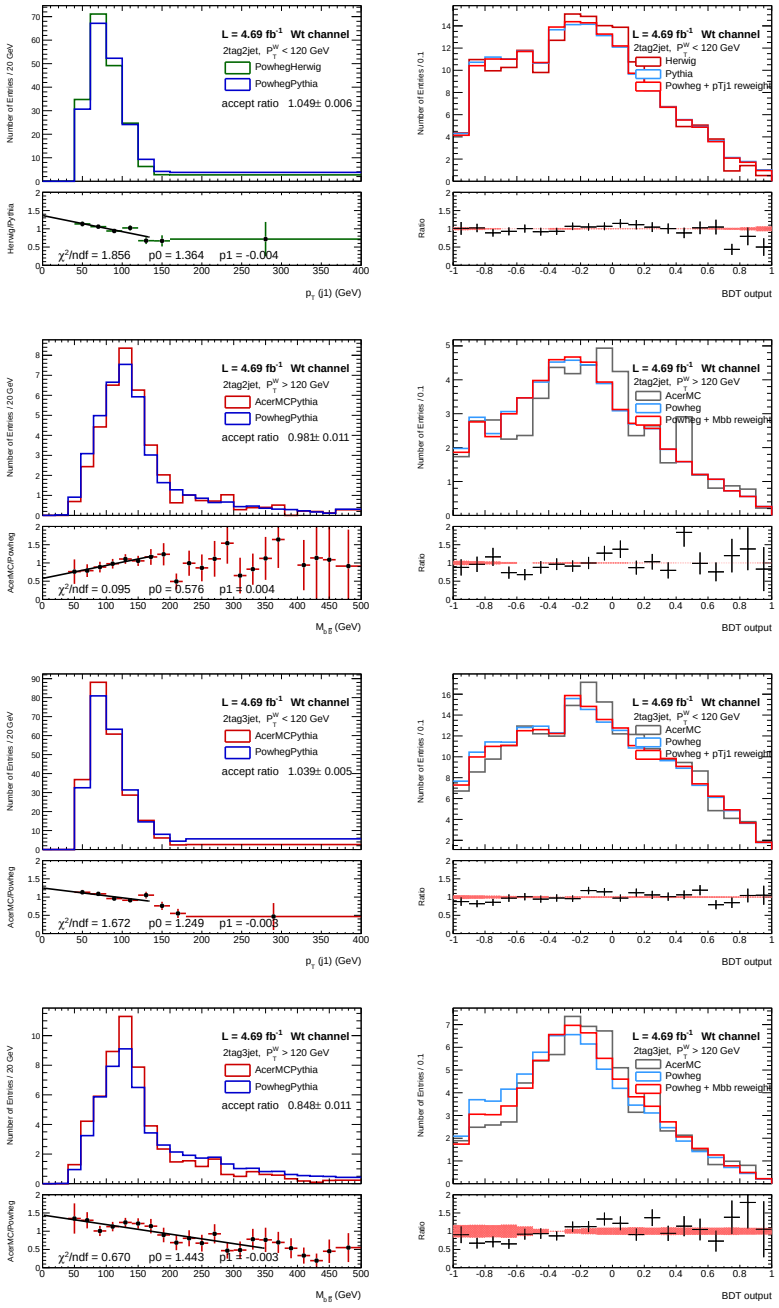

Figure 29: $Wt-$ch. shape systematics, obtained by comparing Herwig with Pythia and AcerMC with Powheg, and its impact on the BDT output. Update BDT output plots.

5.3 Diboson

5.3.1 Uncertainties in the Modeling of the Diboson Processes

The diboson background includes the diboson production processes which originate from a final state with two vector bosons (WW, WZ, ZZ). Several diboson processes give significant contribution in the analysis signal regions: $Z \to \nu\nu$ and $Z \to b\bar{b}$ for the 0-lepton channel, $Z \to ll$ and $Z \to b\bar{b}$ for the 2-lepton channel; $W \to l\nu$ and $Z \to b\bar{b}$ for the 1-lepton channel. Additional processes can give smaller contributions, thanks to the miss-tag of a jet from a W decay or to the failed reconstruction of one of the leptons; $Z \to \nu\nu$ and $W \to q\bar{q}$, $Z \to ll$ and $W \to q\bar{q}$, WW (inclusive) production. The rate of $V(Z \to bb)$ is roughly 5 times that of the signal and so this background provides a great opportunity to validate the analysis against a known process. This is discussed in Section REF. The reader is encouraged to read the introduction to Section 5 to better understand how the information here will be utilized.

The PowHeg generator provides a next-to-leading-order (NLO) estimate, relying on the CT10nlo PDF set and interfacing the Pythia8 parton shower and hadronization model. The MC samples for the diboson processes are listed on Table 35 along with their cross-sections at $\sqrt{s} = 8$ TeV.

Process	Powheg+Pythia8 channel	Cross-Section ($\sqrt{s} = 8$ TeV) [pb]	Nevents
$Z \to \nu\nu\, Z \to q\bar{q}$	181967	1.964	11520000
$Z \to ll\, Z \to q\bar{q}$	181966	1.207	4000000
$W \to l\nu\, Z \to q\bar{q}$	181970	4.870	10000000
$Z \to \nu\nu\, W \to q\bar{q}$	181969	2.777	3000000
$Z \to ll\, W \to q\bar{q}$	181968	1.594	1500000
WW	181971	52.44	10000000

Table 35: Monte Carlo generator used for the modelling of the diboson processes and correspondent MC channel number, cross sections and number of generated events.

Previous studies conducted using the Herwig generator show that the contribution of the diboson processes not listed on Table 35 is less than 1%, and it is thus neglected in the analysis.

The estimated NLO cross-sections quoted in Table 35 are provided directly by the PowHeg samples, and are used to normalize the different processes. For the WW and ZZ processes the PowHeg cross-section does not include the contributions of gluon-gluon initiated processes, which is thus computed and added back to the cross-section value using the MCFM software, set to the configuration outlined in Table 36. In detail the factorization and renormalization scales of the processes are set to half the invariant mass of the bosons decay products, m(3456), and the CT10nlo PDF set is used. For the processes with one leptonicly decaying Z boson a cut on $m_{ll} > 20$ GeV is applied for consistency with the PowHeg samples.

The following sources are considered as a source of systematic uncertainty

- Perturbative uncertainties on the fixed-order NLO cross-section computation
- knowledge of PDF and α_S coupling

and are obtained using the MCFM software.

5.3.1.1 Perturbative uncertainties

Since the analysis requires exactly 2 or 3 jets, the uncertainties are derived separately in the 2-jet and 3-jet bins, which are defined cutting on the transverse momentum and the pseudorapidty of the final state

partons produced by MCFM. Since MCFM does not provide the cross-section computation at higher order than NLO, the 3-jet bin corresponds to the inclusive cross-section $\sigma_{\geq 3}$ for VV+1 jet, while the 2-jet bin corresponds to the exclusive cross-section σ_2 for VV+0 jets.

The uncertainties due to higher-order perturbative corrections to the cross-section are usually estimated through scales variations. To consider a simple scales variation however leads to an underestimation of the uncertainty on exclusive fixed-order cross-sections, due to cancellations occurring between the large corrections to the total cross section and the perturbative corrections from logarithmic dependence on the jet veto. To obtain a robust estimate of these uncertainties, treating properly these cancellations, the "Stewart-Tackmann method" [49] [50] method is applied to derive systematic errors in the 2-jet and 3-jet categories.

According to [49] the covariance matrix for the perturbative uncertainties on the 2-jet and 3-jet categories is built as:

$$\mathrm{C}(\sigma_2, \sigma_{\geq 3}) = \begin{pmatrix} \Delta^2_{\geq 2} + \Delta^2_{\geq 3} & -\Delta^2_{\geq 3} \\ -\Delta^2_{\geq 3} & \Delta^2_{\geq 3} \end{pmatrix},$$

where $\Delta_{\geq 2}$ and $\Delta_{\geq 3}$ are the absolute uncertainties on the inclusive 2-jet cross-section ($\sigma_{\geq 2}$) and the inclusive 3-jet cross-section, derived varying the factorization and renormalization scales down to half and up to double the initial value of m(3456). The covariance matrix C is decomposed in the sum of two matrices,

$$C(\sigma_2, \sigma_{\geq 3}) = \begin{pmatrix} \Delta^2_{\geq 2} & 0 \\ 0 & 0 \end{pmatrix} + \begin{pmatrix} \Delta^2_{\geq 3} & -\Delta^2_{\geq 3} \\ -\Delta^2_{\geq 3} & \Delta^2_{\geq 3} \end{pmatrix} = C_1 + C_2.$$

The first term C_1 results in an absolute systematic error $\Delta_{\geq 2}$ on the 2jet-exclusive cross section σ_2 (`VVJetScalePtST2`), while the second term C_2 has one singular eigenvector (hence no systematic variation) and one non-singular eigenvector which provides an anti-correlated $\Delta_{\geq 3}$ absolute systematic on σ_2 and $\sigma_{\geq 3}$ (`VVJetScalePtST1`). This procedure is applied for each of the diboson processes, obtaining two orthogonal relative uncertainties on σ_2 and one relative systematic uncertainty on $\sigma_{\geq 3}$.

These systematic uncertainties are derived separately in the different p_{T}^V regions used in the analysis: the errors show a non negligible dependence with respect to p_{T}^V, therefore they are treated as normalization and shape systematics, correlated in p_{T}^V, on the cross-sections. Figure 30 shows the two orthogonal shape systematics for the $W \to lv$ and $Z \to q\bar{q}$ process obtained with this procedure on the 2-jet bin cross-section σ_2. Table 38, Table 39 and Table 40 summarize the values of these uncertainties across the 5 p_{T}^V bins for the 6 different diboson processes considered.

5.3.1.2 PDF and α_S uncertainties

The uncertainties on PDF and α_S are evaluated according to the latest prescription from PDF4LHC: the global PDF+α_S uncertainty is derived taking the envelope of the error bands provided by the CT10 and MSTW2008 PDF sets, evaluated for two different α_S central values of 0.117 and 0.119. This set of uncertainties does not show a significant dependence with respect to p_{T}^V, therefore the errors are considered as normalization systematics on the cross-sections of the diboson backgrounds. The systematic errors are derived separately for the 2-jet and 3-jet categories but used in a correlated fashion, and do not depend on the decay of the vector boson but only on the V boson pair produced. The full list of PDF+α_S uncertainties for the diboson processes is quoted on Table 37.

5.3.1.3 Parton shower and hadronization model

To quote a systematic uncertainty on the parton shower and hadronization scheme interfaced with the `Powheg` generator we studied the differences between two different shower models: `Powheg+Pythia8`

MCFM parameter	Value
hmass	126d0
scale:QCD scale choice	+0.5
facscale:QCD fac_scale choice	+0.5
dynamicscale	m(3456)
itmx1, itmx2	10
ncall1, ncall2	500000
LHAPDF group	CT10nlo.LHgrid

Table 36: Main settings for the MCFM software used to compute the cross-sections for the diboson processes.

Process	PDF+α_S (2-jet)	PDF+α_S (3-jet)
ZZ	0.03	0.03
WZ	0.04	0.02
WW	0.03	0.02

Table 37: PDF+α_S systematic uncertainties for ZZ, WZ and WW processes, in the 2-jet and 3-jet categories.

and `Herwig`. `Powheg+Pythia8` is the nominal MC used in the analysis, while `Herwig` provides a LO prediction interfaced with a LL parton shower.
To estimate the systematic errors we considered the distribution of the invariant mass of the jets pair m_{jj}, which is particularly sensitive to hadronization effects, for the two MC generators: since `Herwig` doesn't provide a separate estimate of the different decay modes of the bosons pair, the errors are derived in the inclusive cases WW, WZ and ZZ.
The systematic effect is extracted from the ratio between the shapes of the m_{jj} distribution, therefore the predictions from the two generators are normalized to unit area, applying the full 0-lepton event selection except the b-tagging requirement. The m_{jj} ratio is fitted with a parametric function to reduce the effect of statistical fluctuation; the resulting systematic errors are applied consistently in all the three decay channels.
Figure 31 shows the `Powheg+Pythia8` versus `Herwig` comparison for the WZ processes: the resulting systematic errors range from 10% to about 20% for ZZ, from 10% to 40-50% for WZ and up to about 20% for WW processes. These systematics are included as shape-only nuisance parameters in the fit model.

5.3.1.4 Summary of the systematics

A summary of the systematics used in the fit for the diboson is shown in Table 41.

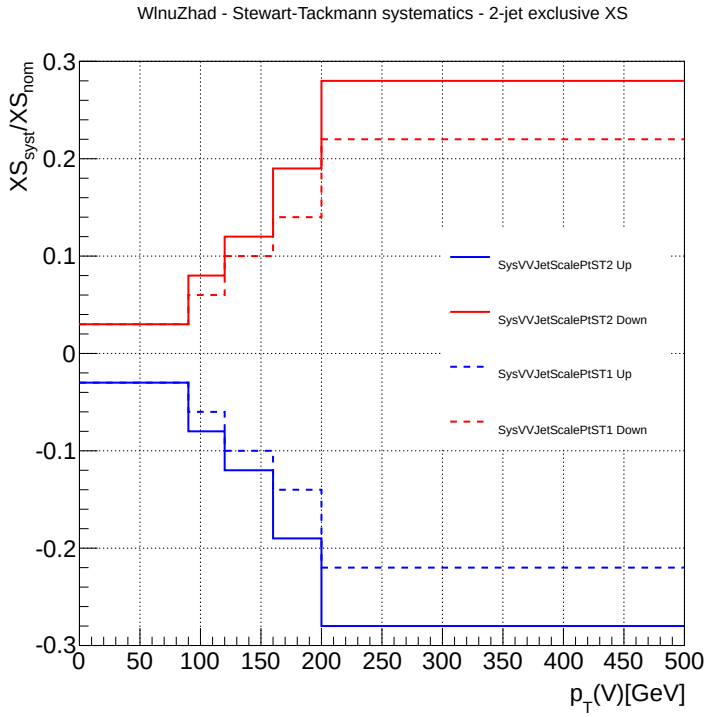

Figure 30: Shape pertubative systematics on σ_2 for the $W \to l\nu$ and $Z \to q\bar{q}$ process obtained applying scale variations according to the Stewart-Tackmann method. The solid line corresponds to the errors derived from the C_1 term and the dotted line from the C_2 term of the covariance matrix C.

p_T^V bins [GeV]	0-90	90-120	120-160	160-200	> 200
$Z \to \nu\nu\ Z \to q\bar{q}$	0.03	0.05	0.07	0.10	0.14
$Z \to ll\ Z \to q\bar{q}$	0.03	0.05	0.07	0.10	0.13
$W \to l\nu\ Z \to q\bar{q}$	0.03	0.08	0.12	0.19	0.28
$Z \to \nu\nu\ W \to q\bar{q}$	0.03	0.07	0.12	0.18	0.28
$Z \to ll\ W \to q\bar{q}$	0.03	0.08	0.13	0.19	0.29
WW	0.03	0.06	0.09	0.13	0.19

Table 38: Probative systematics on σ_2 from the C_1 term of the covariance matrix across the different p_T^V bins.

p_T^V bins [GeV]	0-90	90-120	120-160	160-200	> 200
$Z \to \nu\nu\ Z \to q\bar{q}$	0.02	0.04	0.05	0.07	0.11
$Z \to ll\ Z \to q\bar{q}$	0.02	0.04	0.06	0.08	0.11
$W \to l\nu\ Z \to q\bar{q}$	0.03	0.06	0.10	0.14	0.22
$Z \to \nu\nu\ W \to q\bar{q}$	0.02	0.05	0.08	0.12	0.20
$Z \to ll\ W \to q\bar{q}$	0.02	0.06	0.09	0.13	0.21
WW	0.02	0.04	0.06	0.09	0.13

Table 39: Perturbative systematics on σ_2 from the C_2 term of the covariance matrix across the different p_T^V bins.

p_T^V bins [GeV]	0-90	90-120	120-160	160-200	> 200
$Z \to \nu\nu\, Z \to q\bar{q}$	-0.11	-0.12	-0.13	-0.15	-0.16
$Z \to ll\, Z \to q\bar{q}$	-0.10	-0.12	-0.14	-0.15	-0.16
$W \to l\nu\, Z \to q\bar{q}$	-0.12	-0.13	-0.15	-0.16	-0.17
$Z \to \nu\nu\, W \to q\bar{q}$	-0.11	-0.12	-0.14	-0.15	-0.17
$Z \to ll\, W \to q\bar{q}$	-0.12	-0.13	-0.14	-0.16	-0.18
WW	-0.11	-0.12	-0.14	-0.15	-0.17

Table 40: Perturbative systematics on $\sigma_{\geq 3}$ from the C_2 term of the covariance matrix across the different p_T^V bins.

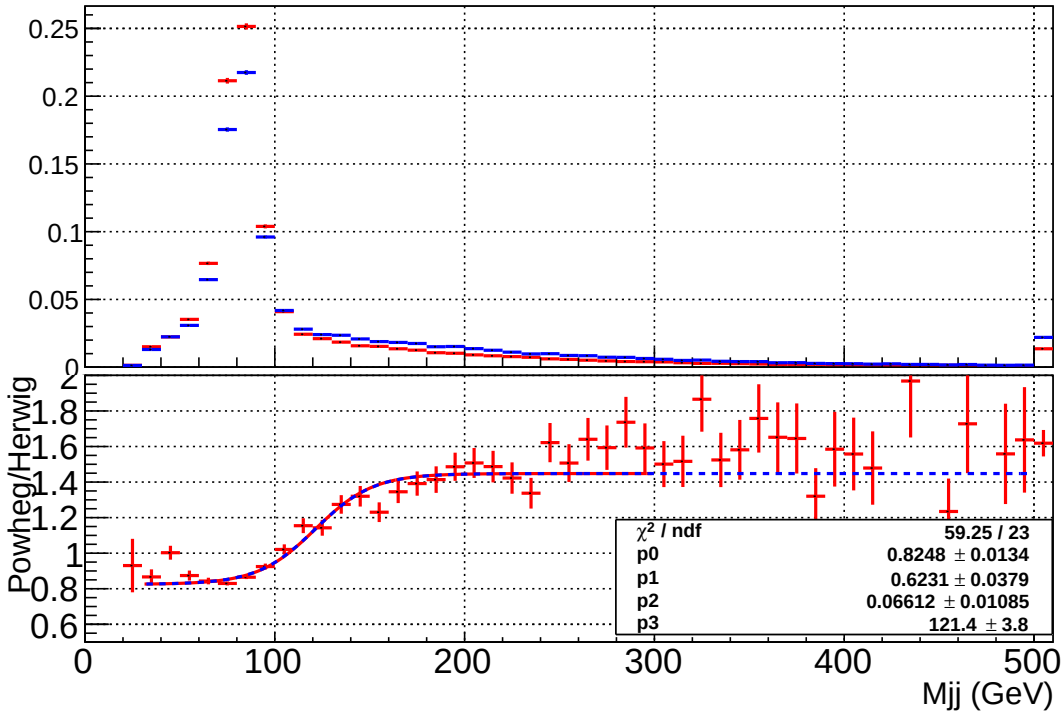

Figure 31: POWHEG+Pythia8 versus Herwig comparison for the WZ diboson processes: the systematic uncertainties from the PS/hadronization model is estimated taking the fit of the ratio of the different MC predictions between.

Description	Samples	Nuisance Parameters
S-T scale p_T(V)-systematic on $\sigma_{2\,jet}$ and $\sigma_{3\,jet}$	`MCFM`	`VVJetScalePtST1`
S-T scale p_T(V)-systematic on $\sigma_{2\,jet}$	`MCFM`	`VVJetScalePtST2`
PDF+α_S normalization-systematic	`MCFM`	`VVJetPDFAlphaPt`
m_{bb} shape-only systematic	`Powheg+Pythia8` vs `Herwig`	`VVMbb`

Table 41: Summary of the diboson modelling systematic uncertainties, with the name of the correspondent nuisance parameter.

5.4 Multijet and non-collision background

The reader is encouraged to read the introduction to Section 5 to better understand how the information here will be utilized. The multijet backgrounds arise from jets faking charged leptons or real $E_{\mathrm{T}}^{\mathrm{miss}}$. The rate of these instrumental effects is never well modeled and they occur so rarely (but during processes with very large cross sections) that a large amount of computing resources would be consumed. Therefore, data driven methods are used. In the following the multijet background of each analysis is described. Only in the 1-lepton channel is this background sizable and is therefore described last.

5.4.1 0-lepton

The method used to estimate the multijet background for the 0-lepton channel is described in Appendix Q. A data driven template from a dedicated control region is normalized via the ABCD method. The contribution from the multijet background range from 0.5-2% in each region. A systematic uncertainty is assessed due to statistical uncertainties and systematic effects. In the fits, a gaussian priors on the multijet normalization is used, with an error of -95% +100% on its normalization. These priors correlate LL, MM, TT categories for the different p_{T}^{V} regions (with the exception of the region with 100< p_{T}^{V} <120 GeV), while it takes non correlated regions with different number of jets and different number of tagged jets (i.e. 1-tag VS. 2-tag). The names used in the fit are summarised in Table 42.

Nuisance Parameter	Description	Region	Value	NP Count
	0-lepton			
`MJ_L0`	normalization	[2,3]-jet [1/2]-tag	100%	4

Table 42: Normalization nuisance parameters for multijet entering the fit. The 0-lepton uncertainties are correlated between regions.

5.4.2 2-lepton

2-lepton channel multijet is described in Appendix S. Events in which the iso_{track} cut for Loose leptons (0.1) is inverted, and therefore dominated by jets faking leptons, are used to extract a template, and the normalization is determined by extrapolating information in the m_{ll} sidebands to the phase space used by the analysis. In the $e-\mu$ control region, the template is obtained from same-sign events. The contribution from the multijet background is small and a systematic uncertainty of 100% is assessed. In EPS the multijet background for the 2-lepton channel was deemed negligible. As stated in Section 3.2.1.4, the $d_0 < 0.1$ *mm* requirement was removed from the definition of a loose electron and therefore the multijet contribution is not longer negligible.

5.4.3 1-lepton

This difficult background is described in more detail in Appendix R. The template definition was refined since EPS in concert with the Tight lepton defintion as described in Section 3.2.1.3. The method to extract the multijet background can be divided into 3 different steps:

- event selection for the template;
- the usage of 1 b-tag events as the 2 b-tag template (so-called *spoofing*)
- normalization

5.4.3.1 Template Selection

The multijet template is described in Section 3.2.1.5. In summary, with all event level cuts applied, data events from an orthogonal region are selected by modifying the signal lepton criteria and the electroweak contribution is subtracted off to create the multijet template. This region is contructed to be orthogonal to the signal region by selecting leptons with inverted track isolation criteria and vetoing any event with multiple leptons (counting both the normal leptons and the leptons used to obtain the multijet template described here). The modified signal lepton selection is given here for convience:

- Medium leptons and in the e channel, passing MediumPP
- inverted iso_{track} cut (compared to Tight leptons): $0.05(0.07) < iso_{track} < 0.12(0.5)$ in the $e(\mu)$ channel (instead of $iso_{track} < 0.04$)
- looser iso_{calo} cut (compared to Tight leptons): $iso_{calo} < 0.07$ (instead of 0.04).

Note, for overlap removal, $0.05(0.07) < iso_{track} < 0.5$ is used in the $e(\mu)$ channel to select multijet leptons. For counting the number of multijet leptons, the iso_{track} range is then modified to the above for the nominal selection and again changed (noted below) for systematic variations.

5.4.3.2 Generation of MV1c Weight

The templates have decent statistics but after 2-tags and in the high p_{T}^{W} region, the events dry up. It has been shown that the kinematics of 1-tag match quite well the kinematic of 2 b-tag events in the muon channel and in 2L tag electron events. The 2T tag events are considerably different from the 1-tag kinematics in the electron channel. A procedure was developed which, given the rank (leading or sub-leading) of the un-tagged jet and the MV1c value of the tagged jet, a MV1c value is generated for the un-tagged jet promoting this event into the 2-tag region. After this redistribution, in 2-jet events in the electon channel, the 1-tag events used in the 2L, 2M, and 2T tagged template are each kinematicly reweighting to match the distribution of the 'real' 2-tag template. The reweighting is performed sequentially on $\Delta R(bb)$ and p_{T}^{W} using using a the ratio of 1-tag to 2-tag events after passing throught the TH1:Smooth alogrithm five times such that the statistical fluctuations of the limited 2-tag events are not encapsulated in the reweighting. 'Real' 2-tag events are not discarded and represent roughly 10% of the events used for the final 2-tag multijet templates. More details of this procedure are given in Appendix R.

5.4.3.3 Normalization

The above template method does not determine the normalization. A fit to data is performed using the $E_{\mathrm{T}}^{\mathrm{miss}}$ distribution. This fit is performed separately for muon and electron events, 2 and 3 jet events, and 1 and 2 b-tag events. The 2 b-tag region is fit inclusively, that is 2L, 2M, and 2T events are all fit with one multijet scale factor. Due to the small contribution of multijet events to the 2T region, this helps stabilize the normalization estimate. Since the multijet normalization is coupled to the electroweak background normalization, a scale factor for the electroweak background is also used. Also, a set of scale factors from the profile likelihood, determined from the ratio of the post-fit yield to the pre-fit yield, are also used to have the electroweak background as close to our best guess as possible. The $E_{\mathrm{T}}^{\mathrm{miss}}$ variable was found to be the most stable interms of template variations. Other variables such as m_{T}^{W} and lepton p_{T} were considered. More details are given in Appendix R.

5.4.3.4 Systematics

To estimate the systematic uncertainity from the tempate choice, the iso_{track} cut is modified. In the electron channel the range $0.12 < iso_{track} < 0.50$ is used and the difference to the nominal is symmetrized

to obtain a symmetric systematic variation (SysMJElTrkIso). For the muon channel, the full range used for the nominal template is divided into two ~equal statistics region $0.07 < iso_{track} < 0.095$ and $0.095 < iso_{track} < 0.50$ which represent the down and up variations respectively (SysMJMuTrkIso). In the electron channel only, it was found that restricting the iso_{calo} to 0.04 thus matching the signal region modifies the template in a different way than the iso_{track} variations due. Therefore, this restricted region is used and the effect is symmetrized for an additional systematic (SysMJElCaloIso). One half of the kinematic reweighting applied in the electron 2-jet 2-tag events is used as shape systematic (SysMJDR and SysMJPtV). The normalization fit is repeated with each variation resulting in a normalization change accompaning the shape change. It should be noted that the template variations change the heavy flavor contribution, therefore altering the ratio of 2L, 2M, and 2T events. The normalization uncertainity (SysMJMuNorm and SysMJElNorm) is derived from two sources added in quadrature. One is the statistical error of the multijet scale factor. The normalization fit is performed inclusively in 2-tag events, but the statistical error is take from the exclusive fits. That is the normalization in each 2L, 2M, and 2T events separtely. Even though the inclusive fit is used to determine the normalization, the statistical error of exclusive fits are used for the systematic to reflect our imperfect knowledge of the heavy-flavor contribution to the multijet template. The second, is the difference in the multijet yield when the EW scale factors are used compared to when they are not used. More details are given in Appendix R. Table 43 summarizes the source of multijet shape and normalization errors while Table **??** explicitly states the values of the normalization errors.

Description	Origin	Nuissance parameters
Normalization	Norm. fit error for 1 and 2 b-tag events	SysMJElNorm SysMJMuNorm
Template iso_{track}	Alteration of iso_{track} range	SysMJElTrkIso
Template iso_{calo}	Alteration of iso_{calo} range	SysMJElCaloIso
$\Delta R(bb)$ reweight for spoofed events	$\frac{1}{2}$ of reweight	SysMJDR
p_{T}^{W} reweight for spoofed events	$\frac{1}{2}$ of reweight	SysMJPtV

Table 43: Summary of the multijet specific samples used to checks the background modelling. The list of the nuissance parameters is given for reference, and it will be discussed in Section 8.

.

Nuisance Parameter	Region	Value	
SysMJMuNorm	normalization	2-jet 1/2L/2M/2T-tag	12/28/42/60%
		3-jet 1/2-tag	11/14%
SysMJElNorm	normalization	2-jet 1/2L/2M/2T-tag	3/11/14/22%
		3-jet 1/2-tag	3/6%

Table 44: Normalization nuisance parameters for multijet entering the fit. The 0-lepton uncertainties are correlated between regions. All 2-lepton uncertainties are correlated except for when the top $e-\mu$ control region is included in the standalone fit.

6 Multivariate analysis

Multivariate techniques become ubiquitous in HEP in recent years. There is rarely one single variable which has the possible maximum separation between signal and background. A multivariate algorithm can learn how to construct such a discriminant from a set of well chosen variables and well optimized algorithm parameters. All multivariate classification methods must be trained and evaluated on separate, independent samples to ensure an unbiased result. The training should be such that the general trends and correlations of a sample and not the random fluctuations dictate the final algorithm. A supervised learning method is one in which the desired output for any input in the training set is known. In general, there is no universal recipe concerning the usage, tuning, and training of multivariate tools. Each case must be considered in the context in which it is needed. However, techniques such as Decision Trees and Neural Networks based techniques generally outperform likelihood-based classifiers in the presence of strong non-linear correlations among the input variables.

6.1 Input variables

The object and event selection criteria are outlined in Section 3.4. The input variables chosen are described in Table 45 and below is a list of those variables which might need further clarification:

- V: vector boson constructed from the $E_{\mathrm{T}}^{\mathrm{miss}}$, vectoral sum of $E_{\mathrm{T}}^{\mathrm{miss}}$and p_{T}^{ℓ}, and vectoral sum of $p_{\mathrm{T}}^{\ell_{1,2}}$ in the 0, 1, and 2 lepton analysis respectively.
- H: Higgs candidate constructed from the vectoral sum of the two leading p_{T} jets.
- M_{eff}: scalar sum p_{T} of all the objects in the event, specifically the signal jets, leptons, and $E_{\mathrm{T}}^{\mathrm{miss}}$. In the 1-lepton channel only the two jets used to build the Higgs mass are considered while in the 0-lepton channel the third jet is considered in three jet events. This is clarified by the use of $M_{eff\ 3}$for the later.
- m_{jj}: dijet mass constructed from the leading two p_{T} signal jets.
- m_{T}^{W}: transverse mass of the W and defined as $m_{\mathrm{T}}^{W} = \sqrt{2p_{\mathrm{T}}^{\ell}E_{\mathrm{T}}^{\mathrm{miss}}(1-\cos\Delta\phi(\ell, E_{\mathrm{T}}^{\mathrm{miss}}))}$.
- *jet*: signal jets are only considered.

Distributions of these variables are shown in Appendix Y, Z, and AA for the 0, 1, and 2-lepton selections respectively. Figure 32 shows the input variables for the high p_{T}^{Z} region of the 0-lepton channel. The signal is shown in red and the background in blue. Both are normalized to the same integral as is done in the training. Similar figures can be found in Appendix AB for all analyses.

Several studies have been done to determine a good set of variables in each of the channel. As a starting point for these studies, a simplified version of the multivariate analysis, with just m_{bb} and ΔR_{bb} as input has been used. These two variables have been selected for the starting point thanks to their discriminator power between signal and background. One-by-one, all the other variables have been tested as a candidate to be the third variable in the multivariate analysis. The variable giving the best significance was selected to join the m_{bb} and ΔR_{bb} in the BDT definition. By using the same algorithm, the fourth, and recursively all the other variables have been studied and selected. As an example, for the Boosted Decision Tree training parameters described in the next section, Figure 33 shows the significance for the 1-lepton 2jets, $p_{\mathrm{T}}^{V}<$ 120 GeV, 1-lepton 2jets, $p_{\mathrm{T}}^{V}>$ 120 GeV, and 0-lepton 2jets, $p_{\mathrm{T}}^{V}>$ 120 GeV for the different studied set of input variables. In 3-jet events, two more variables, m_{jjj} and $p_{\mathrm{T}}^{jet_3}$ were added to improve the 3-jet binned sensitivity by roughly 30% and the total 1-lepton binned sensitivity by slightly less than 3%.

Variable	Name	0-Lepton	1-Lepton	2-Lepton
p_{T}^{V}	pTV		✓	✓
$E_{\mathrm{T}}^{\mathrm{miss}}$	MET	✓	✓	✓
$p_{\mathrm{T}}^{jet_1}$	pTB1	✓	✓	✓
$p_{\mathrm{T}}^{jet_2}$	pTB2	✓	✓	✓
$MV1c(jet_1)$	MV1cB1	✓	✓	✓
$MV1c(jet_2)$	MV1cB2	✓	✓	✓
m_{jj}	mBB	✓	✓	✓
$\Delta R(jet_1, jet_2)$	dRBB	✓	✓	✓
$\lvert\Delta\eta(jet_1, jet_2)\rvert$	dEtaBB	✓		✓
$\lvert\Delta\phi(V, H)\rvert$	dPhiVBB	✓	✓	✓
$\lvert\Delta\eta(V, H)\rvert$	dEtaVBB			✓
$M_{eff}(M_{eff\ 3})$	HT	✓		
$min\lvert\Delta\phi(\ell, jet)\rvert$	dPhiLBmin		✓	
m_{T}^{W}	mTW		✓	
$m_{\ell\ell}$	mLL			✓
	Only in 3 Jet Events			
$p_{\mathrm{T}}^{jet_3}$	pTJ3	✓	✓	✓
m_{jjj}	mBBJ	✓	✓	✓

Table 45: Variables used to train the multivariate discriminant. Additional information can be found in Section 6.1. Distributions are shown in Appendix Y, Z, and AA for the 0, 1, and 2 lepton selections respectively.

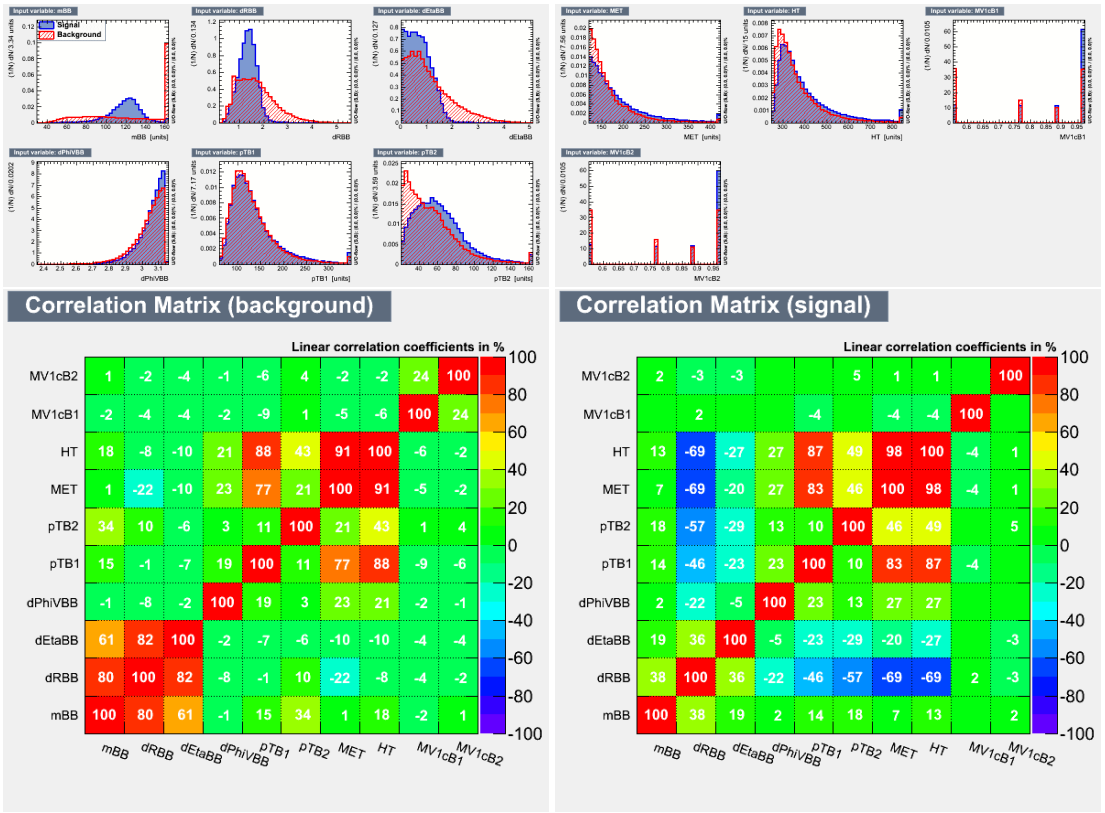

Figure 32: Input variables for the zero lepton analysis, 2 jets final state p_{T}^{V}> 120 GeV shown on the top with red representing the signal and blue the background. The bottom row shows the correlation matrix for the background and signal (left and right respectively). A complete set of such plots is contained in Appendix AB.

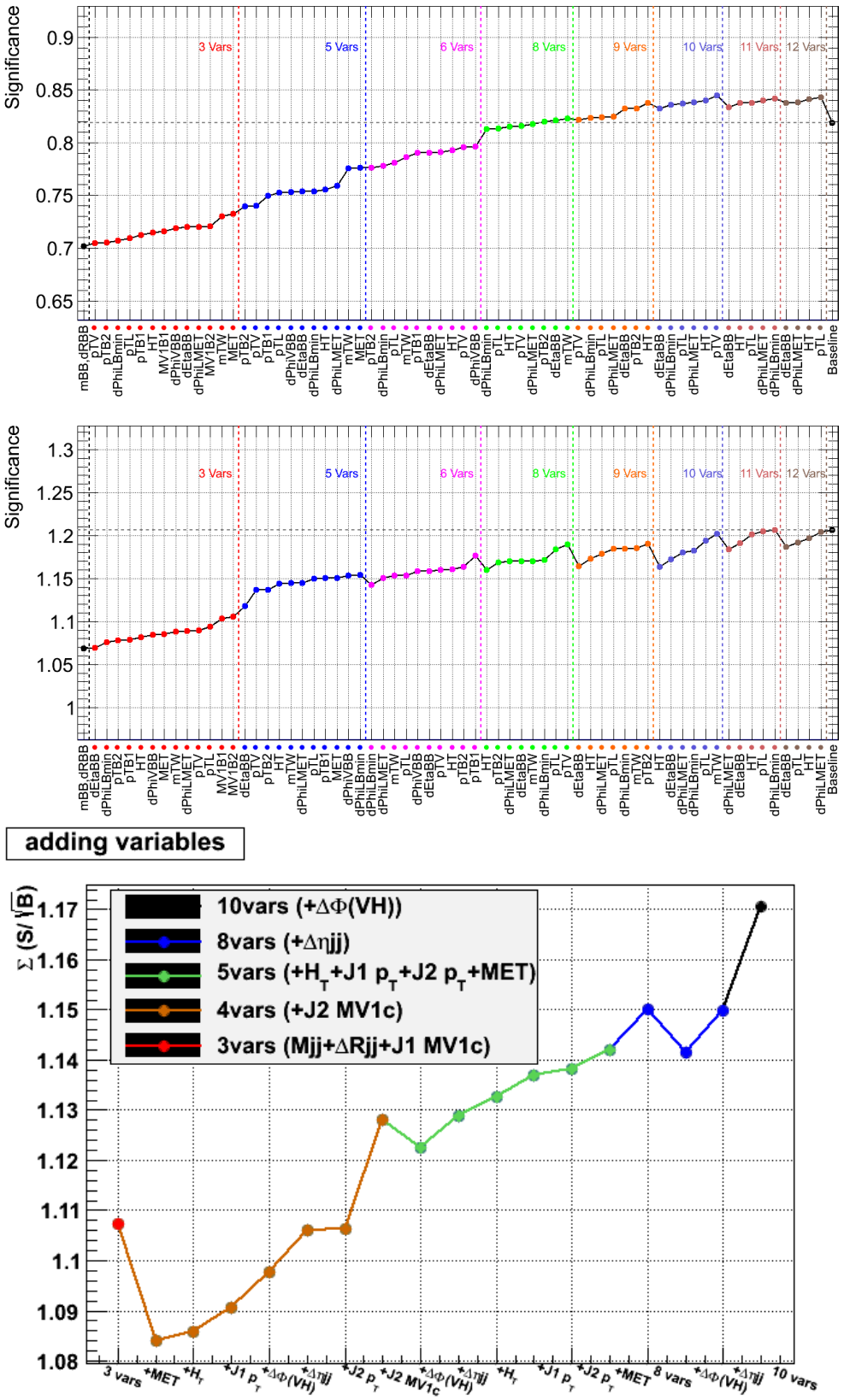

Figure 33: Significance for the 1-lepton 2 jet p_{T}^{V}< 120 GeV (top), 1-lepton 2 jet p_{T}^{V}> 120 GeV (middle), and 0-lepton 2 jet p_{T}^{V}> 120 GeV (bottom) as a function of the input variables using the boosted decision tree discriminant. 'Baseline' in the top two plots refers to the sensitivity before this optimization was done.

6.2 Boosted Decision Tree: Setup and Training

Among the available multivariate techniques available in the Toolkit for Multivariate Data Analysis (TMVA) package [61], a Boosted Decision Tree (BDT) was chosen as similar performance was seen from different techniques and BDTs are in general easy to visualize and train. To maximize the statistics in the training, truth tagging (Section 3.3.4.1) is always applied.

6.2.1 Algorithm Description

A decision tree is a logical extension to a simple dijet masss analysis. It is a rooted binary tree where the root node is the entire training sample consisting of signal (s) and background (b) events. Each variable is scanned with a user defined number of cuts to find the cut which gives the best separation gain. Since the range of the variable by default is determined by the minimum and maximum of the training set and the speed of training is related to the number of cuts chosen, the range of the input variables is restricted to 99% of the signal integrating from the mean outward. This make very little difference in the resultant sensitivity but stabilized the final set of cuts determined by the training. The best separation gain can be measured with various quantities but the most commonly used, and the one used in this analysis, is the Gini-index, $p(1-p)$, where the purity, $p = s/(s+b)$. Since a cut which selects predominantly background is as valuable as a cut which selects signal, the criterion is symmetric with respect to the event class. The maximum, 0.5, is when the samples are fully mixed. If sum of the Gini-index of the two daughter nodes, weighted by their relative fraction of events, is less than that of the parent then the separation of the two populations has increased. This splitting is continued at each node, dividing the training phase space into hypercubes, until a stop criteria is met. Examples of stop criteria are the minimum number of events per node, maximum number of nodes, maximum depth, or when splitting the nodes further does not gain anymore separation. The final nodes are called leaves and are labeled signal (s) or background (b) by the purity. This method is independent of monotonous variable transformations, relatively immune against outliers, and weakly discriminating variables do not deteriorate the performance very much.

6.2.2 Boosting

A single decision tree can be sensitive to statistical fluctuations in the training data. The idea of combining many, or a forest of decision trees was proposed to overcome this stability problem. There are several ways to increase the performance of a forest of DTs. A very powerful technique to improve the performance of any weak classifier by sequentially applying an MVA algorithm to re-weighted versions of the training data and taking a weighted average to produce the final discriminant is known as *boosting*. The most popular boosting algorithm, and the one used in this analysis, is adaptive boosting, known in the literature as 'AdaBoost'. In this method, the original event weights are used for the training of the first tree while subsequent trees are multiplied by a common boost weight give by $\alpha = 1 - \chi$ where χ is the sum of weights of the misclassified events divided by the total sum of weights. The weights of the entire tree are then re-normalized such that the total remains constant.

Let us look at function estimation through boosting in another light, that is by considering a simple additive expansion approach. The function under consideration is assumed to be the weighted sum of parametrized base functions, $f(x; a_m)$, or 'weak learners', such as an individual decision tree or any machine learning technique, where x represents the set of variables for the events in the tree and a_m is the rule used to separate the signal and background populations, which would be the cut at each node for a decision tree. The function is therefore written as the following summation:

$$F(x; P) = \sum_{m=0}^{M} \beta_m f(x; a_m); P \in \beta_m; a_{m0}^{M} \tag{9}$$

where β_m is some multiplicative factor. Boosting adjusts the parameters, P, such that the difference between the response, $F(x;P)$, and the true value y is minimized. The figure of merit for this difference is the loss-function $L(F,y)$. This function fully determines the boosting procedure. AdaBoost is based on exponential loss, $L(F,y) = e^{F(x;P)y}$, which lacks robustness in the presence of outliers or mislabeled data points and thus performance degrades in noisy settings. By choosing a different loss function, such as a binomial log-likelihood,

$$L(F,y) = \ln\left(1 + e^{2F(x;P)y}\right), \tag{10}$$

one can improve on this performance. Since an analytical minimization of some functions is nontrivial the method of steepest-descent is employed. Thus the name, gradient boosting. Robustness is further enhanced by reducing the learning rate of the algorithm, or the step size of the minimization of the loss function. The smaller this number the slower the learning process and hence the more trees that must be grown. Alternative lose functions were tested resulting in similar performance compared to AdaBoost.

6.2.3 Overtraining

Sensitivity to fluctuations in the training data is more commonly know as over-training in the forest application. Over-training occurs when there are too few data points to properly set the model parameters; in other words, there are too many degrees of freedom with respect to the available statistics. The severity of this problem depends on the machine technique used. BDTs usually suffer from at least partial over-training, owing to the large number of nodes in the constituent trees. If over-trained, the DT performance measured in the training sample and an independent test sample will differ considerably. The training (test) sample performance will be better (worse) than the objectively achievable performance. Therefore, a simple way to test for and measure the amount of over-training is to compare the performance results between the independent training and test samples. In the cases where the tree is allowed to grow beyond a handful of nodes, pruning techniques such as removing sub-trees which in total add less improvement than some cut-off can be employed to curb over-training. Another way to avoid over-training is to use a large number of relatively short trees instead of using any of the pruning techniques. Figure 34 shows an example of an overtrainig check for the 1-lepton BDT. Appendix AB contains the same check for all BDTs trained for this analysis. In order to maximize the MC statistics available for the signal extraction all events are used to training and evaluation in an unbiased way. The entire set of event is split into two samples, A and B, with the BDT trained on sample A (B) evaluated by sample B (A). To be clear, an event used to train a BDT is never used to evaluated that same BDT.

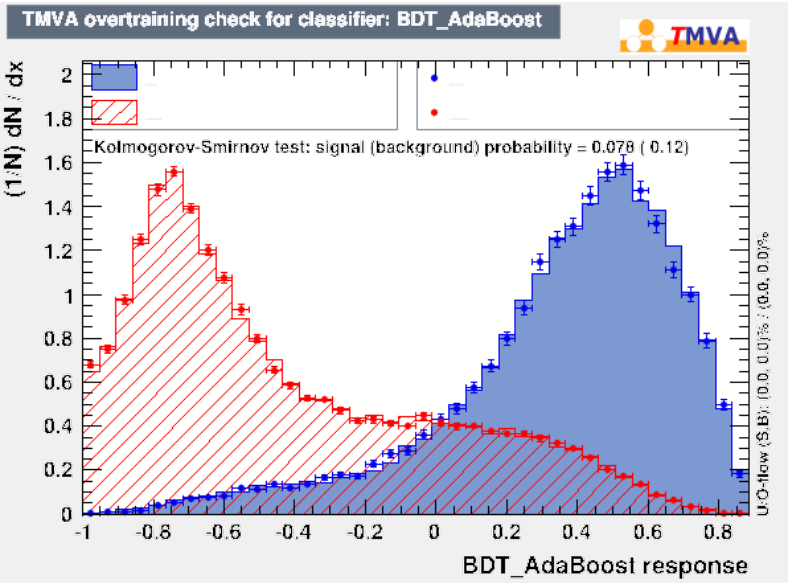

Figure 34: An example of an overtrainig check for the one-lepton analysis, 2 jets final state p_{T}^{V}> 120 GeV. Red represents the signal and blue the background. A complete set of such plots is contained in Appendix AB.

6.2.4 Parameter Optimization

BDTs in general perform well on the first iteration as this simple method only requires a one-dimensional cut optimization. Also the performance is not degraded by the inclusion of poorly discriminating variables as they are largely ignored in favor of the most discriminating variable available at each node. In theory, the given performance should be inferior to other techniques like neural networks but in practice, either because of a lack of training statistics or difficulty in finding the optimal configuration for other classifiers, BDTs often outperform other techniques. A one-dimensional scan of each of the training parameters was performed to arrive at the an optimal set of parameters given in Table 46. As an example, the scans for the 1-lepton channel, in the 2 jet category for p_{T}^{V}> 120 GeV is shown in Figure 35. These plots are obtained with a 2-step procedure. In the first one, a 350 randomly selected configurations have been used to find a first optimal set of parameters. From this first optimal point, a granular one-dimensional scan has been used to optimize the choice for each parameter.

Two-dimensional scans have been produced for some of the training parameters to get a deeper understanding of the combined effect of the two. An example is shown in Figure 35 for the 1-lepton channel, in the 2 jet category for p_{T}^{V}> 120 GeV.

TMVA Setting	Value	Meaning
BoostType	AdaBoost	boost procedure
AdaBoostBeta	0.15	learning rate
SeparationType	GiniIndex	node separation gain
PruneMethod	NoPruning	pruning method
NTrees	200	number of trees
MaxDepth	4	maximum tree depth
nCuts	100	number of equally spaced cuts tested per variable per node
nEventsMin	100	minimum number of events in a node

Table 46: BDT parameters. Additional information is given in Section 6.2.

Dedicated studies have been done on the capability of the BDT to explore all the features of the phase-space with a certain MaxDepth (defined in Table 46). Figure 36, shows for two different MaxDepth settings, the fraction of nodes using a certain variable (weighted by the boost weight of the parent tree) as a function of the depth of the node in its parent tree. One can notice that m_{bb} is the most frequently used variable by the BDT in the first node for both the configurations. In both cases, a good fractions of the input variables have a non negligible frequency from the 3^{rd} node. All variables being used equally below a certain depth is indicative of there being limited discrimination power left in any one variable and fluctuations start to dictate the training. With additional statistics a larger MaxDepth might explore the phase space in a better way. It can be seen that a tree with MaxDepth of four can still use in an efficient way the available information, while maintaining short trees in order to avoid overtraining.

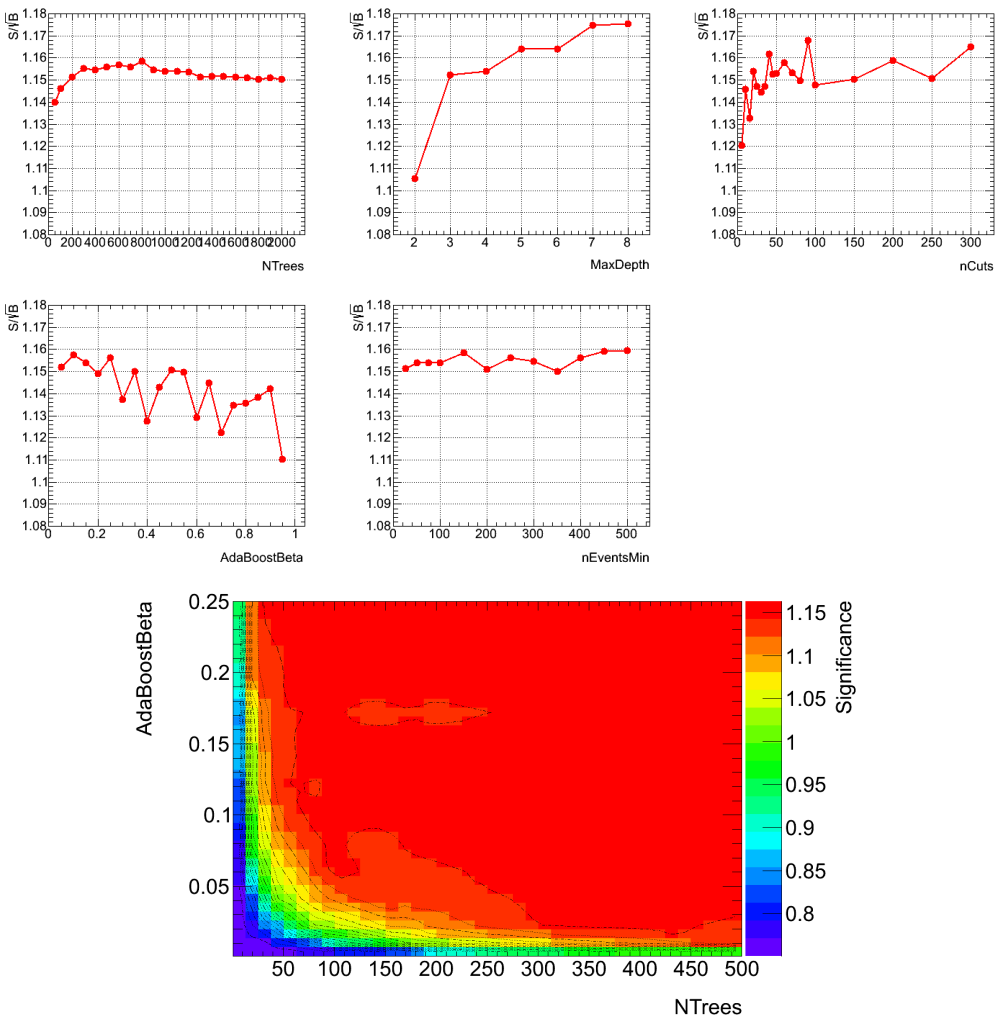

Figure 35: Top: one-dimensional scans of each of the training parameters for the 1-lepton channel, in the 2 jet category for p_{T}^{V}> 120 GeV. Bottom: two-dimensional plot showing the combined effect of changing the number of trees and the AdaBoostBeta on the significance.

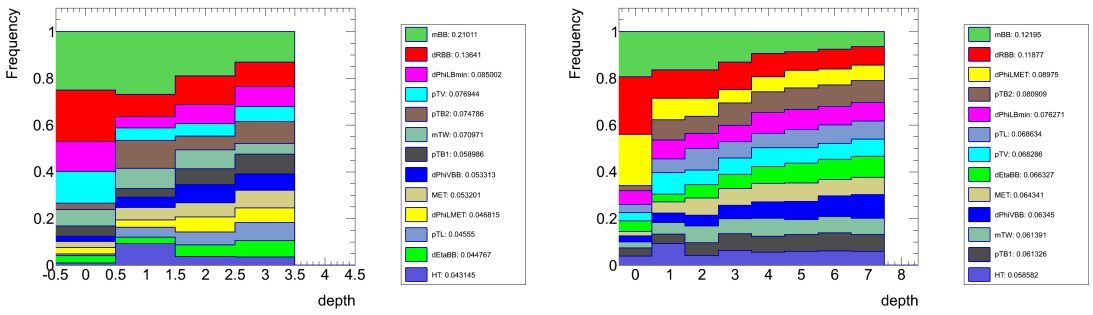

Figure 36: Fraction of nodes using a certain variable (weighted by the boost weight of the parent tree) as a function of the depth of the node in its parent tree. MaxDepth=4 (left); MaxDepth=8 (right).

6.3 The correlations between input variables and output variables

The construction of BDT discriminant relies on the goodness in modeling the properties of the input variables and of their correlations. In this section, we introduce the studies done to ensure the capability of the Monte Carlo simulation to reproduce the correlations present in data. A first way described here is to study the 2 dimensional distribution for all the couple of input variables. For each of these 2-dimensional distributions, 2 projections, one on the horizontal axis, and the other on the vertical axis are done. By comparing these projections on data, and on the sum of all the background, one can check if the Monte Carlo is able to describe some of the underlying relationship between the variables used in the BDT. Figures 37 and 38 show one example. In this case, the 2-dimensional histograms show the distribution of the multivariate output versus the m_{bb} distribution for the sum of all the background. The two projections, along the two axes, are shown, and when allowed by the blinding policy, the data is shown. In this case and in general for the other correlation plots, the data Monte Carlo agreement is good. A complete set of plot for each lepton category has already been prepared in the past and it will be given in a dedicated appendix.

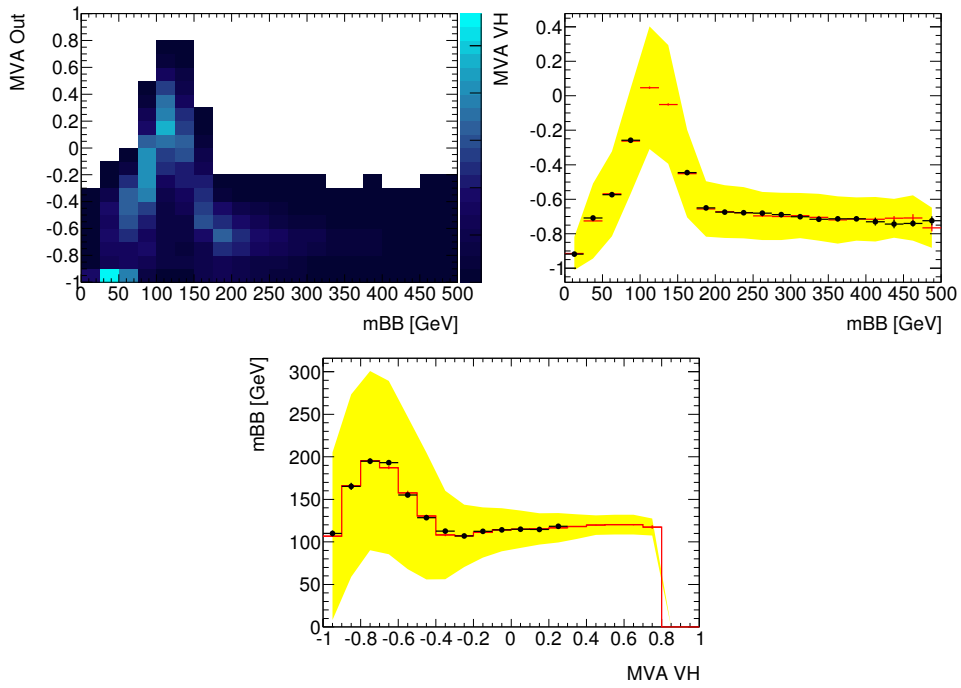

Figure 37: Two dimensional plot showing the BDT output versus the m_{bb}. The projections along the two axis shows the data - Monte Carlo comparison. Distribution for the 2-lepton analysis, for the 2 tagged 2 jet region, p_{T}^{V}> 120 GeV.

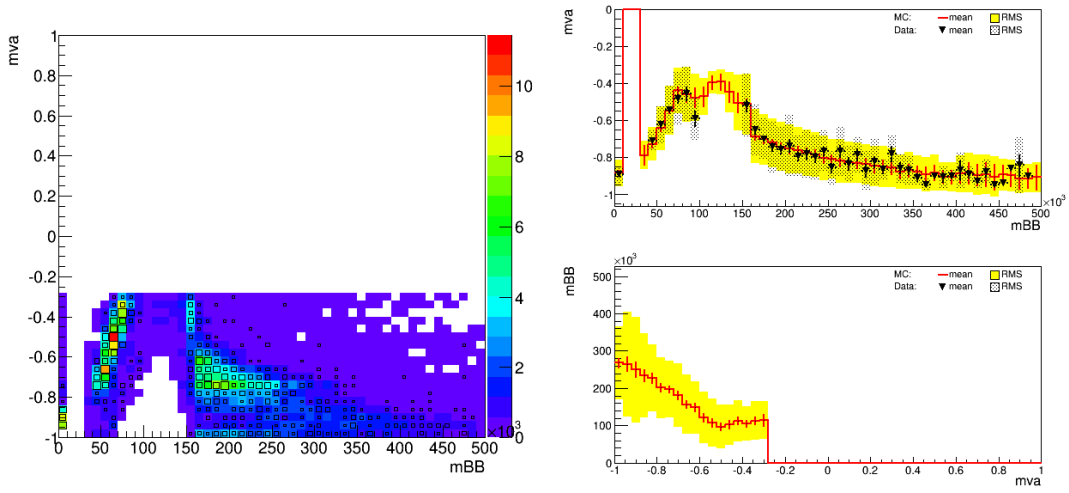

Figure 38: Two dimensional plot showing the BDT output versus the m_{bb}. The projections along the two axis shows the data - Monte Carlo comparison. Distribution for the 1-lepton analysis, for the 2 tagged 2 jet region, p_{T}^{V}> 120 GeV.

6.4 MVA for the diboson and for the other mass points

The MVA studies discussed so far has been performed for the search of a Standard Model Higgs boson with a mass of 125 GeV. This value is of particular interest, given the recent discovery at the LHC, but it is important to explore even other values for the masses. While in the m_{bb} shape analysis, this is obtained in a natural way, the MVA analysis, trained for a specific mass has less discriminating power for other masses if compared with an ad-hoc training. A first preliminary study has been done for the 0-lepton channel. The result of the training for each mass hypothesis in 2 TT b-tagged jets events, with $p_{\mathrm{T}}^{V} > 120$ GeV is shown in Figure 39. In addition, we use the diboson processes $Z \to \nu\nu + Z \to bb$, $W \to l\nu + Z \to bb$ and $Z \to ll + Z \to bb$ as test-bench of the analysis, so an ad-hoc training have been done for these processes (again shown in Figure 39).

The use of these training, improves the expected limit for $m_h\bar{1}20$ GeV and $m_h\bar{1}30$ GeV by almost 20% . So these different trainings will be used to test the search for other Higgs masses.

To check if any simplification is possible, a test which uses the BDT to split the phase space in different categories, containing more and more signal events, and fitting in each category the shape of the m_{bb} have been done. It showd a degradation in the performances, not only for the other mass points, but even for the point at 125 GeV.

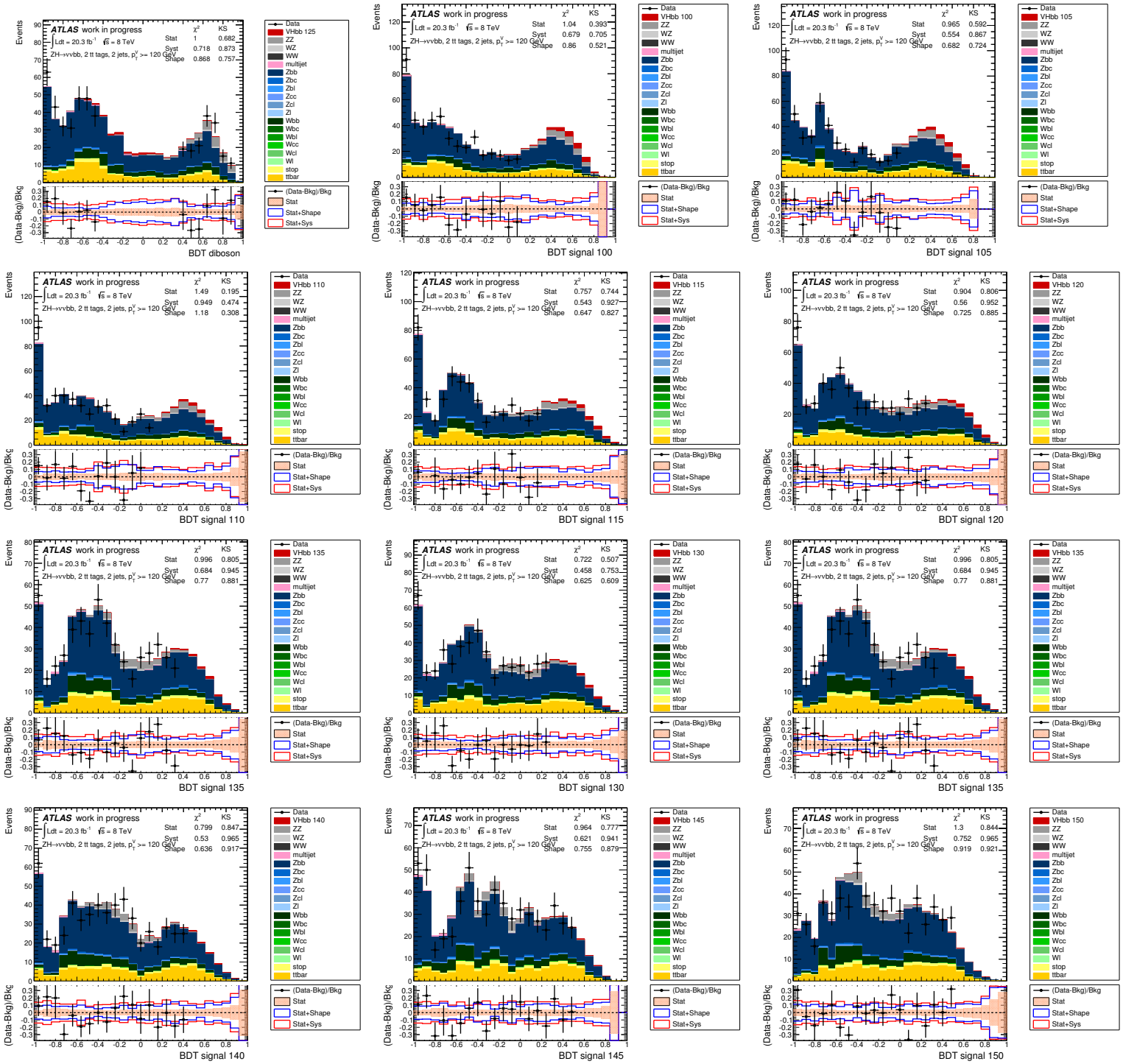

Figure 39: Distribution for the 0-lepton analysis, for the 2 tagged 2 jet region, p_{T}^{V}> 120 GeV.

7 Experimental Systematic uncertainties

In the following section the uncertainty on corrections to the efficiency and/or calibration of simulated objects is described. The majority of these corrections have been provided by the Combined Performance (CP) groups along with several possible configurations for how the error can be treated. The rest have been developed as part of this analysis. An important point to keep in mind is that between low and high p_{T}^{V} regions, light and heavy-flavor jets, and various amounts/types of $E_{\mathrm{T}}^{\mathrm{miss}}$, the phase space of this analysis is tremendous. In a given corner of this phase space a certain *component* of an uncertainty can be dominant while almost negligible in another where a different component is large. If these two components arise from truly different sources then one must be sure to properly decorrelate before ever attempting a profile likelihood maximization such as the one described in Section 8. Maintaining a correlation is an overstatement of knowledge and can lead to unwanted effects such as a bias or a incorrect assessment of precision. When such a decorrelation is done, the components of the uncertainty are briefly described. A summary is contained in Table 55. In Section 7.2 a smoothing procedure is described which is used to minimize the effects of limited MC statistics in the evaluation of systematic uncertainties.

7.1 Experimental Systematics

The leading CP uncertainties are those on the b-tagging efficiency and the jet energy scale (JES). A more precise assessment of the impact of uncertainties can be found in Sections 8.6.4.2 and 8.6.4.1.

7.1.1 Luminosity and pile up

The uncertainty on the integrated luminosity is applied to the signal and backgrounds estimated from MC simulation (all except for the multijet background). The uncertainty on the integrated luminosity is ±2.8%. It is derived, following the same methodology as that detailed in Ref. [12], from a preliminary calibration of the luminosity scale derived from beam-separation scans performed in November 2012. An uncertainty due to the modeling of the additional interactions is applied following [16].

7.1.2 Electrons

The electron trigger [62], reconstruction, and identification [18] efficiencies are corrected and have a relatively small associated error $O(1\%)$. Each efficiency correction weight is shifted coherently to evaluate one systematic variation for the lot (`ElecEffic`). The isolation efficiency correction is described in Appendix E and was done in collaboration with the EGamma group (`LepIso`). Uncertainties on the electron energy and resolution corrections [63] are evaluated separately by shifting the electron energies up and down and re-selecting events and named `ElecE` and `ElecEResol` respectively. In the 0-lepton channel, a systematic uncertainity needs to be evaluated for the lepton veto efficiency - this was done using the 2-lepton selection (`LepVeto`).

7.1.3 Muons

The muon trigger, reconstruction, and identification [64] efficiencies are corrected and have a relatively small associated error $O(1\%)$. Each efficiency correction weight is shifted coherently to evaluate one systematic variation for the lot (`MuonEffic`). The isolation efficiency correction is described in Appendix F and was done in collaboration with the Muon CP group (`LepIso`). Uncertainties on the resolution smearing from the inner detector and muon system component of the muon reconstruction [64] are evaluated separately by shifting the smearing up and down and reselecting events and named `MuonEResolID` and `MuonEResolMS` respectively. In the 0-lepton channel, a systematic uncertainity needs to be evaluated for the lepton veto efficiency - this was done using the 2-lepton selection (`LepVeto`).

7.1.4 $E_{\mathrm{T}}^{\mathrm{miss}}$ Trigger

The full discussion of the $E_{\mathrm{T}}^{\mathrm{miss}}$ trigger parametrization is in Appendix A. The uncertainties have been reduced since [11] as further study showed a significant dependence on the scalar sum of the signal jets p_{T}(JpT_Sum). A cut was introduced on JpT_Sum directly to remove this, which resulted in a significantly reduced uncertainty. One nuisance parameter is used to cover differences seen in the efficiency curve fits: `METTrigZ` for differences between W and Z events. The statistical uncertainty of the efficiency curve fit is represented by `METTrigStat`.

7.1.5 Jets

The experimental uncertainties relating to jets are uncertainties on the energy scale, resolution, and the JVF cut efficiency.

7.1.5.1 The Jet Energy Scale Uncertainty

A detailed discussion of the JES and associated uncertainty is found in [65] and a discussion of the uncertainties can be found in [66]. As discussed in Section 3.2.2, the so-called GSC calibration is used. The jet energy scale has been broken down into 56 nuisance parameters:

- 47 for the various in-situ JES calibration analyses and are combined in an eigenvector decomposition into 6 parameters (`JetNP1-JetNP6_rest`). This does not allow for correlations between 7 TeV and 8 TeV analyses,
- 2 for η inter-calibration, specifically comparisons of Pythia and Herwig and the statistical component of this comparison. It arises from potential mis-modeling of the additional radiation that may affect the p_{T} and η of the dijet system (`JetEtaModel` and `JetEtaStat`),
- 1 for jets with $p_{\mathrm{T}} > 1$ TeV and is ignored for obvious reasons,
- 1 for MC non-closure relative to full simulation MC12a/Pythia8 since other MC do not satisfy closure. The calibration was derived on MC12a and any given MC sample can be classified as MC12a, Pythia8 or AFII (`JetNonClos`),
- 4 for pile-up, 3 of which are mu/N_{PV} dependent and the last is dependent on the event energy density,ρ, (`JetMu`, `JetNPV`, `JetPilePt`, `JetPileRho`),

Additionally, 4 more systematics are included for flavor and topology uncertainties:

- 1 for differences in b-jet response studying the detector response using a variety of different MC simulations, truth b-jets only (`JetFlavB`),
- 1 for μ and ν energies from b-hadron decay [34], truth b-jets only (`JetBE`),
- 1 for the unknown mixture of light-quarks and gluons, non-truth b-jets only (`JetFlavComp_X`),
- 1 for the difference in response between light-quarks and gluons assessed from MC comparisons, non-truth b-jets only (`JetFlavResp_X`).

The b-jet energy scale uncertainty is $\sim$ 1 – 2%. The flavor composition and response above are separated for different processes as the quark/gluon mixture can be different in each. `X` is replaced with `Wjets`, `Zjets`, `Top`, or `VHVV`. The quark/gluon mixture (of non-b-jets) is assumed to be 50% with 100% uncertainty thus the effect of this error is maximal. After including all sources of uncertainty, the total fractional systematic uncertainty on the JES ranges from 3% at 20 GeV to 1% for a 1 TeV jet.

7.1.5.2 Jet Energy Resolution Uncertainty

Two systematics are use - one for all jets and one specifically for b-jets.

- 1 for jet resolution (`JetEResol`),
- 1 for b-jet resolution [34], truth b-jets only (`BJetReso`).

Good jet energy resolution (JER) is crucial for an analysis where the dijet mass is one of the most discriminating variables. The range for the relative JER is from $\sim$ 25% at 20GeV to $\sim$ 5% near 1TeV. The resolution is found to be well described by MC simulation when validated by in-situ analyses using the dijet balance and bisector methods. The relative uncertainty was determined from the *observed differences between data and MC* in the resolution as determined by those in-situ studies *as well as* from uncertainties on the methods themselves. This is known to be an overestimate of the error, therefore constraints in a profile likelihood can be expected. The impact of both JER uncertainties is obtained in this analysis by smearing the jet p_{T} according to a Gaussian distribution centered at 1, with a width equal to the true resolution plus the value of the relative uncertainty given by the jet's p_{T} and for the general JER uncertainty, the η as well. The effect on the final variable is then symmetrized to obtain the a symmetric error.

7.1.5.3 Jet Fraction Uncertainty

The JVF efficiency uncertainty is obtained from the differences between data and simulation in the JVF cut efficiency in Z+jets events. The cut value is nominally 0.5 and varied to 0.47 and 0.53 for the systematic evaluation (`JetJVF`).

7.1.6 Missing Transverse Energy

All systematic variations of object energies is propagated to the $E_{\mathrm{T}}^{\mathrm{miss}}$ calculation which is the reasonable thing to do. Uncertainties on $E_{\mathrm{T}}^{\mathrm{miss}}$ itself is variations of the scale (`METScaleSoftTerms`) and resolution (`METResoSoftTerms`) of energy in calorimeter clusters which have not been associated with a reconstructed object - the *Soft Term*. This systematic has a large impact on the expected signal strength as shown in Section 8.6.4.2.

7.1.7 Flavor Tagging

As discussed in Section 3.2.3, the MV1c discriminant is used to separate light and heavy-flavor jets. In MC, jets are truth labeled as a b, c or *light* and scale factors have been derived for each flavor as a function of jet p_{T} and MV1c output [32] to correct the MC efficiency to that of data. Representative scale factors with the associated uncertainty are shown in Figure 3. The scale factors of course come with an associated error. This error is a mix of experimental errors (i.e. JES), theoretical errors (i.e. the top quark p_{T}spectrum in $t\bar{t}$ events), and statistical errors from the data in each $p_{\mathrm{T}}\times$ MV1c ($\times\eta$ for light jets) bin. To make this suite of errors more manageable, just as with the JES errors an eigenvector decomposition is done only the leading 10 for b-jets, 15 for c-jets and 10 for light jets are applied in the analysis[5]. All other nuisance parameters have been neglected and it was checked that the remaining nuisance parameters have an impact of at most 1% on the analysis. The details of this check can be found in Appendix T. As this analysis is very sensitive to possible p_{T} dependence is it crucial to take care when correlating low and high jet p_{T} effects. The eigenvector decomposition. A generator dependence was

[5] After the eigenvector method is applied, they are ordered from the one corresponding to the bigger error to the smaller one. In the analysis, the top 10/15/10 systematics for b/c/light jets are used out of 24/16/48. The remaining systematic uncertainties correspond to small components or statistical errors from $p_{\mathrm{T}}(\eta)$-$MV1c$ binned scale factor fits.

observed for the b and c jet tagging efficiencies. Scale factors (Section 3.3.4.3 and Appendix T.2) were derived to correct each generator to the PYTHIA6 efficiency which is what the efficiency scale factors are derived with respect to (`BTagBSherpa`, `BTagBPythia8`, `BTagCSherpa`, `BTagCPythia8`).

As discussed in Section 3.3.4.1, truth-tagging is used for samples without a truth-matched b-jet and a bias has been measure as a function of ΔR(jet,jet) for events with two c-jets only. The effect was not seen in *light-light*, nor *c-light* events and truth-tagging is not used in events with a truth-matched b-jet. A correction has been derived and (Section 3.3.4.2 with full details given in Appendix T.3) half the correction is taken as the uncertainty (`BTagTruthTagDR`).

7.2 Smoothing

The uncertainties on CP objects are evaluated in two different way: shifting weights or re-selecting events. For flavor tagging, where a scale factor is used to correct the simulation efficiency to data, this weight is shifted up (down) and the change in the final distribution is noted as the +1 (-1) σ shift. For jet energy scale (JES) uncertainties, the jet energies are shifted and therefore events can migrate in and out of the acceptance. Again the difference in the final variable is noted as the 1 σ error but if the variations are small and/or the sample statistics are small, the 1 σ band can be contaminated with the MC statistical uncertainty. If one has multiple JES errors, which we do, then this MC error should not be include in each one. To mitigate these effects, two algorithms are used to merge consecutive bins in these templates. First, bins from one extremum to the next are merged until no (at most one) local extremum remains in the multivariate (dijet-mass) analysis. If there are more than two extrema, merging is performed at each step of this iterative process where the difference between merged and unmerged templates is smallest. Second, the bins resulting from this first algorithm are sequentially merged, starting from the upper end of the distribution, until the statistical uncertainty in each of the merged bins, calculated in the nominal template, is smaller than 5%.

In the 1-tag regions, it does not make sense to merge neighboring bins as described in Section7.2 since the MV1c distribution is discrete. Therefore in this region, only a pruning is performed which drops one-sided systematics in a given MV1c bin.

8 Statistical model and Systematic Uncertainties

The culmination of this analysis is a complex profile likelihood in which our knowledge is parametrized and tested against the data. This is not simple business since the likelihood is defined in over 100 constrained dimensions and up to 9 free dimensions. The following gives a basic introduction to the procedure followed by a detailed description of the likelihood itself.

8.1 Likelihood Definition: Variables and Regions

The statistical analysis of the data employs a binned likelihood function constructed as the product of Poisson probability terms,

$$\text{Pois}(n|\mu S + B)\left[\prod_{b\in\text{bins}}^{N}\frac{\mu\nu_b^{sig}+\nu_b^{bkg}}{\mu S + B}\right], \tag{11}$$

where μ, a signal strength parameter, multiplies the expected signal yield ν^{sig} in each histogram bin, b, and ν^{bkg} represents the background content per bin. In this analysis the signal is normalized to the Standard Model Higgs boson production cross section so any deviation in the measured μ value is a deviation from the SM. The dependence of the signal and background predictions on the systematic uncertainties is described by a set of nuisance parameters (NP), θ, which are parametrized by Gaussian or log-normal priors. Log-normal priors are used for normalization uncertainties to maintain a positive PDF. The parametrization is chosen such that the rates in each category are log-normally distributed for a normally distributed θ. The expected number of signal and background events in each bin are functions of θ such that the the total number of events for a given process is

$$\nu_{tot}^{p} = \sum_{b\in\text{bins}}^{N} f_b^p(\theta) \tag{12}$$

where p is either the signal or background processes and f_b^p is the number of events in the b^{th} bin as a function of θ. Most NP have been determined from some other dataset and so it not completely unknown. To enforce this knowledge, a so called penalty term or auxiliary measurement is added to the likelihood which will always increase when any nuisance parameter is shifted from the nominal value of zero. Formally the auxiliary measurement is added to the likelihood in a way that emphasises the fact that this NP comes from a measurement in a different dataset:

$$\text{Pois}(m|B_{CR}) \tag{13}$$

where m and B_{CR} are the measured and expected number of events used to determine the nominal value. Some NPs, such as floating normalizations do not have priors and are completely determined from the analysis dataset. The likelihood function is therefore a function of μ and θ and given by

$$\mathcal{L}(\mu,\theta) = \text{Pois}(n|\mu S(\theta) + B(\theta))\left[\prod_{b\in\text{bins}}^{N}\frac{\mu\nu(\theta)_b^{sig}+\nu(\theta)_b^{bkg}}{\mu S(\theta) + B(\theta)}\right]\text{Pois}(m|B_{CR}) \tag{14}$$

The nominal fit result in terms of μ and σ_μ is obtained by maximizing the likelihood function with respect to all parameters. This is referred to as the maximized log-likelihood value MLL. The test statistic q_μ is then constructed according to the profile likelihood:

$$q_\mu = 2\ln(\mathcal{L}(\mu,\hat{\hat{\theta}}_\mu)/\mathcal{L}(\hat{\mu},\hat{\theta})), \tag{15}$$

where $\hat{\mu}$ and $\hat{\theta}$ are the parameters that maximize the likelihood (with the constraint $0 \le \hat{\mu} \le \mu$), and $\hat{\hat{\theta}}_\mu$ are the nuisance parameter values that maximize the likelihood for a given μ. This test statistic is used

to measure the compatibility of the background only model with the observed data and for exclusion intervals derived with the CL_s method [67, 68].

The likelihood function is build based on the expected distributions of either the di-b-jet invariant mass of the two signal jets (in the dijet mass analysis) or of the multi-variate discriminant (BDT) (in the MVA analysis). These variables are used in events with at least 2 b-tagged jets. In both dijet mass and MVA analyses, the 2-tag regions are further subdivided into three flavor categories, LL, MM and TT, as defined in Sec. 3.3.4. In addition, in order to further control the flavor fractions of the W/Z+jet backgrounds, the MV1c distribution of the tagged jet is used in the 1-tag region. The regions entering the fit are summarized in Table 47.

		dijet mass			MVA		
Channel		0 lepton	1 lepton	2 lepton	0 lepton	1 lepton	2 lepton
1-tag	2-jet	MV1c			MV1c		
	3-jet	MV1c			MV1c		
2L-tag		m_{bb}			BDT		
2M-tag	2-jet	m_{bb}			BDT	BDT	BDT
2T-tag		m_{bb}				BDT	
2L-tag		m_{bb}			BDT		
2M-tag	3-jet	m_{bb}			BDT	BDT	BDT
2T-tag		m_{bb}				BDT	

Table 47: The regions entering the likelihood fit for the cut based and MVA analysis and the distributions used. Vertically merged rows should be interpreted as regions treated with one distribution. For example, 2M and 2L are combined for 0-lepton MVA analysis.

The regions described are further subdivided in p_{T}^V bins. The dijet mass 2-tag regions are subdivided into five p_{T}^V bins

$$p_{\mathrm{T}}^V\text{: [0-90), [90-120), [120-160), [160-200), and [200,}\infty\text{) GeV}$$

while the MVA analysis uses the two p_{T}^V bins

$$p_{\mathrm{T}}^V\text{: [0-120) and [120,}\infty\text{) GeV}$$

also detailed in Table 12. For the 1-tag region, in both versions, the two MVA p_{T}^V bins are used. Studies have shown that using two p_{T}^V bins in the 1-tag improves the expected sensitivity by 2% compared to not using the 1-tag region at all. The choice of two p_{T}^V bins differs from the 2-tag region of the dijet mass analysis. It would be quite aggressive to have the MV1c distribution so finely binned in p_{T}^V and would require very careful modeling systematics. This would give access to the jet p_{T} spectrums which the flavor tagging scale factors are parameterized as a function of. A minimal choice of two bins was used in order to have some access to the p_{T}^V spectrum but not to re-fit the scale factors themselves.

In the 0-lepton analysis the low p_{T}^V region of the phase space is not accessible due to the high threshold of the $E_{\mathrm{T}}^{\mathrm{miss}}$ trigger. However, in the dijet mass analysis, a 100 – 120 GeV region has been taken into account, adding a region in which the trigger turn-on curve is well-modeled, as described in Appendix C. In the 1-lepton channel no distinction is made between events triggered by the lepton triggers and by the $E_{\mathrm{T}}^{\mathrm{miss}}$ trigger, which is used to recover muon events outside the muon trigger acceptance, as described in Appendix C.4.

In the fit the dijet mass low-MET 0-lepton region (with p_{T}^V from 100-120 GeV) is also added to the MVA analysis. Therefore the total number of regions for the MVA analysis is 30, while for the dijet

mass analysis the total number of regions is 80. When the 2-lepton channel is considered standalone for validation purposes, the $e-\mu$ region obtained selecting opposite sign and different flavour leptons is added as an additional control region in the fit to constrain the $t\bar{t}$ background normalization. This control region is not included in the combined fit, since the $t\bar{t}$ contribution is already well constrained in the 1-lepton regions for the dijet mass analysis and in the 2-letpon low BDT region in the MVA analysis.

8.2 Likelihood Philosophy

This likelihood is the manifestation of the knowledge accrued by the analysis team. Correlations of NPs across regions is a statement of knowledge - the effect which that particular NP represents has the same source in both regions and therefore a change in one regions dictates the *same* change (in terms of number of sigma) in the other. Priors represent a degree of belief as to where the true value lies for parameters which the model is dependent on. Care must be taken as this analysis covers a tremendous phase space with several different SM processes having yields larger than the expected signal.

One might ask why so many regions are included in the likelihood. Part of the reason is that the flavor fractions (*bb-bc-bl-cc-cl-ll* relative rates) of the V+jet events cannot be trusted from simulation. Therefore the 1-tag is considered. Removing the 1-tag events in the MVA analysis decreases the sensitivity 4% as allows for degeneracies in the shapes of the various flavor productions. The 3-jet region in the 1 and 0-lepton analyses is top-enriched (more so for the 1-lepton) and therefore is needed to constrain the top normalization in a region of phase space that is the odd 1-lepton, 2-tagged jet signal enriched region (Table 28). The signal in the 3-jet region is not negligible. The 3-jet 2-lepton region is very pure in Z+hf and provides a better constraint on the Z+hf production. Using only 2-jet events (discarding 3-jet events) decreases the MVA sensitivity 8% with up to a 14% loss seen in the 2-lepton channel. The low p_{T}^{V} regions are used to get a handle on the modeling. As discussed in the previous sections (Section 5.1 and 5.2), the boost of top-pairs and vector bosons is not well modeled by the MC. One can either remove the low p_{T}^{V} and let the data in the high p_{T}^{V} fix the overall normalizations or fix the normalization at low p_{T}^{V} and propagate that to high p_{T}^{V} very carefully. The later approach is the one chosen here. It is not the easier of the two, but the potentially more informative and fruitful one. On top of that, it is the more sensitive since removing events with $p_{\mathrm{T}}^{V} < 120$ GeV decreases the sensitivity 10%. Once the fit has moved to a point of stability, the exact impact of each of the above claims can be quantified.

In the construction of such a large and powerful likelihood model, choices have to be made consistently and carefully. For V+jets and $t\bar{t}$ the data holds a significant amount of information. In this case we try to minimize the prior knowledge assumed as to not cause an unwanted bias if the knowledge assumed is incorrect. This can come at the price of a larger uncertainty. To be more concrete, a hypothetical situation: Consider a comparison of two generators for W+jets systematics. In this comparison it is noted that both p_{T}^{W} and the ratio of W+bb to W+cc to W+bl (flavor fractions) are different. Both effects can be correlated in one NP. In the dijet mass analysis, with 5 p_{T}^{W} bins, the data contains a lot of clear information of the shape of the p_{T}^{W} spectrum and can fix this NP. Through the correlation *assumed* of the change in p_{T}^{W} and the flavor fractions, this now means that the flavor fractions are known to the same degree as the p_{T}^{W} spectrum – a very aggressive statement. Building on the hypothetical, now consider the addition of MV1c distributions in 1-tag events giving direct access to the flavor fractions. The same NP above which correlated p_{T}^{W} and flavor fraction changes can now be pulled/constrained from the flavor fraction point of view. The correlation derived from the difference between the two generators needs to match exactly the difference between the nominal MC and nature in order to have a 'corret' pull. If the correlation is not correct, unrelated NPs can be pulled to recover any data-MC differences and potentially cause knock-on effects such as biases.

By having separate NPs for p_{T}^{W} and flavor fractions, we allow the data to determine each independently. This is a conservative statement of knowledge. For processes such as single-top and dibosons, where less information is available in data, we chose to correlate more of the differences between gen-

erators. Conflicting information from the data is less likely to occur and the total number of NPs should be maintained at a reasonable level. The expected impact on μ is checked for each NP (Section 8.6). If one of these smaller sample NPs ranks high on the list, then the assumptions are reconsidered before proceeding.

8.3 Systematics Uncertainties and Nuisance Parameters

As stated above, nuisance parameters are used to build a model as a function of information which is not completely known. This is interpreted as systematic and statistical uncertainties in high-energy physics. There are two different types of nuisance parameters used: floating parameters and parameters with priors. A floating normalization is generally associated with the cross section and acceptance where absolute ignorance of the rate is assumed and completely determined from data. When a prior is used, the statement is that the parameter is not known completely nor it is completely unknown but there is a reasonable range within which the true value is believed to lie. The following contains a summary of the 104 constrained modeling nuisance parameters, 8 floating normalization (including μ), as well as the 80 nuisance parameters representing the imperfect knowledge of experimental effects (192 parameters in total).

8.3.1 Naming Conventions

In the following, several formulae illustrate how the nuisance parameters are used to calculate the total number of events which should help the reader build a more clear picture of the complex PDF used in the profile likelihood maximization. Nuisance parameters and changes from them are represented in three ways:

1. ϕ are unconstrained normalization factors
2. $\eta(\alpha)$ represents relative changes in the overall normalization as function of the nuisance parameters, α
3. $\sigma(\alpha)$ parametrizes uncertainties in the shape of the distribution of the discriminating variable as function of the nuisance parameters, α

θ, defined above, represents the set of nuisance parameters and α represents the configuration of these parameters. For example, the nominal expectation is given by all $\alpha = 0$ and a $+1\sigma$ pull for nuisance parameter i is represented by $\alpha_i = 1$.

Nuisance parameters with the same name are correlated. Therefore, to decorrelate NPs across regions or channels a short string is added to the name which represents where that NP acts. These short strings are as follows:

- Lepton Multiplicity: `LX` with `X=0,1,2`
- Jet Multiplicity: `JX` with `X=2,3`
- p_{T}^{V} region (bin): `BX` with `X=0,1,2,3,4` or `X=0,2` for the MVA p_{T}^{V} binning
- b-tagging bin: `TTypeX` with `X='',ll,mm,tt,XX` which represent 1, 2L, 2M, 2T, and 2M+2T b-tag regions

In the following section, other NP specific naming conventions are described where appropriate. In the tables below, the regions listed are the regions where the NP is applied and decorrelated. For example 'all regions' means the NP is applied and correlated everywhere while '2/3 jet, 1/2 tag' means the NP is decorrelated between 2 and 3 jets as well as between 1 and 2-tags. In pull and correlation plots, one should see the basename listed in the table and the appropiate string listed above when applicable.

8.3.2 Signal Specific Nuisance Parameters

Table 48 lists the complete set of nuisance parameters specific to the signal which are described in Section 4.1. The uncertainties have been separately parametrized for the $qq \to WH$, $qq \to ZH$ and $gg \to ZH$ processes. The theory uncertainties on the recently calculated $gg \to ZH$ are significantly larger because it is only calculated at leading order. The nuisance parameters are fully correlated in all regions of phase-space. $qq \to VH$ (denoted with `qqVH`) and $gg \to ZH$ (denoted with `ggZH`) specific errors are never correlated. `TheoryBRbb` is only applied when this analysis is combined with analyses which include Higgs decays besides $H \to bb$.

Nuisance Parameter	Description	qqWH	qqZH	ggZH	NP Count	Section
μ	ratio to SM cross section		float		1	–
`TheoryQCDscale`	Scale Uncertainty	1%	1%	50%	2	4.2.1
`TheoryBRbb`	Branching Ratio	3.3%	3.3%	3.3%	1	
`TheoryVHPt`	NLO EW Correction	S	S	–	1	4.1.2
`TheoryAcc_J2`	Inclusive Acceptance	3.0%	3.4%	1.5%	2	4.2.2
`TheoryAcc_J3`	Scale Acc. 3-jet rel. 2-jet	-1.1%	-0.9%	-1.9%	2	
	Scale Acc. 3-jet rel. 3-jet	4.1%	3.5%	3.3%		
`TheoryAccPDF`	PDF Acc. 2-jet	3.5%	3.0%	2.1%	2	
	PDF Acc. 3-jet	2.8%	5.0%	3.4%		
`TheoryVPtQCD`	QCD Scale	S	S	S	2	
`TheoryPDF`	PDF Sets	2.4%	2.4%	17%	2	
Total	14 with priors, 1 floating					

Table 48: The nuisance parameters used to parametrize the signal-specific systematics. All signal systematics are correlated throughout all phase space regions. All are de-correlated between the $qq \to VH$ (`qqVH`) and $gg \to ZH$ (`ggZH`) processes except for the `TheoryBRbb`, which is fully correlated. S="Shape" and SO="Shape Only" meaning explicitly the normalization of each N-jet/M-b-tag/p_{T}^{V} region is preserved while the shape is varied.

The nuisance parameters used to parametrize our ignorance of each background are listed in Table 50 for the W+jets background, Table 49 for the Z+jets background, Table 51 for the $t\bar{t}$ background, Table 52 for the single-top background, Table 53 for the diboson background, and Table 54 for the multijet backgrounds.

8.3.3 V+jets Specific Nuisance Parameters

Table 49 contains the summary of Z+jets specific nuisance parameters. Due to the different diagrams contributing to Z+jets production compared to that of the W and because of the controllable $t\bar{t}$ background, both Z+light and Z+heavy-flavor modeling checks can be done from data-MC studies. Section 5.1.1 discusses the main results of these studies.

Table 50 contains the summary of W+jets specific nuisance parameters. Section 5.1.2 contains a discussion of W+jets focusing on data-MC comparisons which is the main probe into the W+ll and W+cl modeling. The W+heavy-flavor systematics, which are from generator comparisons, are discussed in Section 5.1.2.3.

It is illustrative to show how the total number of Z and W events are parametrized in terms of nuisance parameters. In the following the convention outlined in Section 8.3.1 is maintained. With V representing

either Z or W, the total number of events is given by

$$N_V = N_{Vl} + N_{Vcl} + N_{Vhf} \quad (16)$$

$$N_{Vl} = \eta(\alpha_{VlNorm})\left(N_{Vl}^{2Jet} + \eta(\alpha_{VlNorm_J3})N_{Vl}^{3Jet}\right) \quad (17)$$

$$N_{Vcl} = \phi_{Vcl}\left(N_{Vcl}^{2Jet} + \eta(\alpha_{VclNorm_J3})N_{Vcl}^{3Jet}\right) \quad (18)$$

$$N_{Vhf} = \phi_{Vbb}\left(N_{Vhf}^{2Jet} + \eta(\alpha_{VbbNorm_J3})N_{Vhf}^{3Jet}\right) \quad (19)$$

where

$$N_{Vhf}^{iJet} = N_{Vbb}^{iJet} + \eta(\alpha_{VblVbbRatio})N_{Vbl}^{iJet} + \eta(\alpha_{VbbVbcRatio})N_{Vbc}^{iJet} \quad (20)$$

with $iJet$ equal to $2Jet$ or $3Jet$.

Nuisance Parameter	Description	Correlation/Samples	Value	NP Count	Section
ZlNorm	Zl normalization	all regions	5%	1	
ZlNorm_J3	Zl 3/2-jet ratio	3Jet regions	5%	1	
norm_Zcl	Zcl norm	all regions	Float	1	
ZclNorm_J3	Zcl 3/2-jet ratio	3Jet regions	26%	1	
norm_Zbb	Zhf normalization	all regions	Float	1	5.1.1.1
ZbbNorm_J3	Zhf 3/2-jet ratio	3Jet regions	20%	1	
ZblZbbRatio	ZblZ/bb ratio	2, 3Jets	12%	2	
ZblZbcRatio	ZbcZ/bb ratio	all regions	12%	1	
ZccZbbRatio	Zcc/Zbb ratio	all regions	12%	1	
ZDPhi	$\Delta\phi$ shape	Z+b/c, Zl × 2, 3Jets	S	4	5.1.1.2
ZPtV	p_{T}^{V} shape	Z+b/c, Zl each in all regions	S	2	5.1.1.2
ZMbb	m_{bb} shape	Z+b/c, Zl each in all regions	SO	2	5.1.1.3
Total	16 with priors, 2 floating				

Table 49: The nuisance parameters used in the fit to parametrize the normalization of the Z+jets backgrounds and the correlation of these parameters between regions. Zhf = Zbb+Zcc+Zbl, Z+b/c=all Z+jets besides Z+ll, S="Shape", and SO="Shape Only" meaning explicitly the normalization of each N-jet/M-b-tag/p_{T}^{V} region is preserved while the shape is varied. Further details are given in Section 5.1.1.

8.3.4 $t\bar{t}$ Specific Nuisance Parameters

Table 51 contains the summary of the $t\bar{t}$ specific nuisance parameters. Section 5.2.1 contains a discussion of the $t\bar{t}$ modeling followed by the method used to determine most of modeling systematics in Section 5.2.1.3.

It is illustrative to show how the total number of $t\bar{t}$ events is parametrized in terms of nuisance parameters. In the following the convention outlined in Section 8.3.1 is maintained. The total number of $t\bar{t}$ events is given by

$$N_{t\bar{t}} = \phi_{t\bar{t}}\left(N_{t\bar{t}}^{2Jet} + \eta(\alpha_{ttbarNorm_J3})N_{t\bar{t}}^{3Jet}\right) \quad (21)$$

where

$$N_{tt}^{iJet} = \left(N_{tt}^{low p_{\mathrm{T}}^{V}} + \eta(\alpha_{ttbarHighPtV})N_{tt}^{high p_{\mathrm{T}}^{V}}\right)^{iJet} \quad (22)$$

with $iJet$ equal to $2Jet$ or $3Jet$.

Nuisance Parameter	Description	Correlation/Samples	Value	Count	Section
WlNorm	Wl normalization	all regions	10%	1	5.1.2
WlNorm_J3	Wl 3/2-jet ratio	3Jet regions	10%	1	
norm_Wcl	Wcl normalization	all regions	Float	1	
WclNorm_J3	Wcl 3/2-jet ratio	3Jet regions	10%	1	
norm_Wbb	Whf normalization	all regions	Float	1	5.1.2.3
WbbNorm_J3	Whf 3/2-jet ratio	3Jet regions	10%	1	
WblWbbRatio	Wbl/Wbb ratio	p_{T}^{V}=[0-90],[90-120],120+GeV^{d}*agger*	35%	3	
WbcWbbRatio	Wbc/Wbb ratio	all regions	12%	1	
WccWbbRatio	Wcc/Wbb ratio	all regions	12%	1	
WDPhi	$\Delta\phi$ shape	Whf, Wcl, Wl × 2, 3Jets	S	6	5.1.2
WMbb	m_{bb} shape	Wbb/cc (p_{T}^{V}=[0-90],[90-120],120+GeV)† Wbc/bl, Wcl, Wl each in all regions	SO	6	5.1.2.3
WPtV	p_{T}^{V} shape	Whf in 2-jet,3jets regions	S	2	
Total	23 with priors, 2 floating				

Table 50: The nuisance parameters used in the fit to parametrize the normalization of the W+jets backgrounds and the correlation of these parameters between regions. Whf = Wbb+Wcc+Wbl, S="Shape", and SO="Shape Only" meaning explicitly the normalization of each N-jet/M-b-tag/p_{T}^{V} region is preserved while the shape is varied. Further details are given in Section 5.1.2 †In the MVA analysis the $90 < p_{\mathrm{T}}^{V} < 120$ GeV NP only pertains to the 0-lepton channel $100 < p_{\mathrm{T}}^{Z} < 120$ GeV events.

Nuisance Parameter	Description	Correlation	Value	NP Count	Section
norm_ttbar	$t\bar{t}$ normalization	3 lepton selections	Float	3	5.2.1.3
ttbarHighPtV	high/low p_{T}^{V}	$p_{\mathrm{T}}^{V} > 120$ GeV	7.5%	1	
ttbarNorm_J3	3/2-jet ratio	3-jet in 2,0+1 lepton	20%	2	
TopPt	top p_{T} corr. variation	all regions	S	1	5.2.1.2
TtbarMBBCont	m_{bb} shape	all regions	SO	1	5.2.1.3
TtbarMetCont	$E_{\mathrm{T}}^{\mathrm{miss}}$ shape	all 1-leptons regions	1	S	
Total	6 with priors, 3 floating				

Table 51: The nuisance parameters used in the fit to parametrize the systematics on the $t\bar{t}$ background. S="Shape" and SO="Shape Only" meaning explicitly the normalization of each N-jet/M-b-tag/p_{T}^{V} region is preserved while the shape is varied.

8.3.5 Single Top Specific Nuisance Parameters

Table 52 contains the summary of the single top specific nuisance parameters. Section 5.2.2 contains a discussion of the single top modeling systematics. Since it is fairly difficult to get a solid control region for any of the three single top production channels, this analysis relies, for better or worse, on MC comparisons. The suite of comparisons contains the list of samples recommended by the single top working group.

Nuisance Parameter	Description	2-jet low p_T^V	2-jet high p_T^V	3-jet low p_T^V	3-jet high p_T^V	Section
s-channel						
stopsNorm	cross section	4%				
SChanAcerMC	AcerMC vs Powheg+Pythia	13%	22%	18%	30%	5.2.2
SChanAcerMCPS	shower uncertainty	6%	8%	4%	4%	
t-channel						
stoptNorm	cross section	4%				5.2.2
TChanPtB2	aMCatNLO vs. AcerMC	52%	25%	12%	-18%	
Wt channel						
stopWtNorm	cross section	7%				
WtChanAcerMC	AcerMC vs Powheg+Pythia	1%	S/-2%	S/4%	S/-15%	5.2.2
WtChanPythiaHerwig	Shower uncertainty	S/5%	3%	5%	-3%	
Total	8 with priors, 0 floating					

Table 52: The nuisance parameters used in the fit to parametrize the systematics on the single top background. All NP are correlated across the full phase-space. The value represents the normalization change in the given region for the given NP while S="Shape" is used to note regions where a shape variation exists. Low $p_T^V$is below 120 GeV and high is above this value.

8.3.6 Diboson Specific Nuisance Parameters

Table 53 contains the summary of the diboson specific nuisance parameters. Section 5.3.1 contains a discussion of the diboson modeling systematics. Since it is fairly difficult to get a solid control region for any of the three diboson production channels with hadronic decays and far enough from the analysis selection to get a control region from the fully leptonic decays, this analysis relies, for better or worse, on MC comparisons and theoretical calculations. Section 5.3.1 contains the most important information.

Nuisance Parameter	Description	Correlation	WW	WZ	ZZ	Section
VVJetScalePtST1	Scale		S	S	S	
VVJetScalePtST2	Scale		S	S	S	
VVJetPDFAlphaPt	PDF, α_S 2-jet	all regions	2%	2%	3%	5.3.1
	PDF, α_S 3-jet		3%	4%	3%	
VVMbb_WW	m_{bb} shape		SO	–	–	
VVMbb_WZ	m_{bb} shape		–	SO	–	
VVMbb_ZZ	m_{bb} shape		–	–	SO	
Total	6 with priors, 0 floating					

Table 53: The nuisance parameters used in the fit to parametrize the systematics on the diboson backgrounds. For VVJetPDFAlphaPt, the two values represent the normalization change in 2/3Jet region respectively. S="Shape", and SO="Shape Only" meaning explicitly the normalization of each N-jet/M-b-tag/p_T^V region is preserved while the shape is varied.

8.3.7 Multijet Specific Nuisance Parameters

The following is a summary of the multijet nuisance parameters. A brief description of the multijet backgrounds is given in Section 5.4 and more in-depth information is available in Appendix Q, R, and S for 0, 1, and 2-lepton respectively.

Nuisance Parameter	Description	Region	Value	NP Count	Secti
		0-lepton			
MJ_L0	normalization	2,3-jet 1/2-tag >,< 120 GeV	100%	6	5.4
		1-lepton			
SysMJMuNorm	normalization	2-jet 1/2L/2M/2T-tag	12/28/42/60%	4	5.4
		3-jet 1/2-tag	11/14%	2	
SysMJElNorm	normalization	2-jet 1/2L/2M/2T-tag	3/11/14/22%	4	5.4
		3-jet 1/2-tag	4/6%	2	
SysMJMuTrkIso	template iso_{track} cut	2/3-jet 1/2-tag	S	4	5.4
SysMJElTrkIso	template iso_{track} cut	2/3-jet 1/2-tag	S	4	5.4
SysMJElCaloIso	template iso_{calo} cut	2-jet 1/2-tag	S	2	5.4
SysMJDR	reweight for spoofed events	(ele) 2-jet 2-tag	S	1	5.4
SysMJPtV	reweight for spoofed events	(ele) 2-jet 2-tag	S	1	5.4
		2-lepton			
MJ_L2	normalization	top e-μ decorrelated†	100%	1	5.4
Total		31 with priors, 0 floating			

Table 54: Normalization nuisance parameters for multijet entering the fit. The 0-lepton uncertainties are correlated between regions. †All 2-lepton uncertainties are correlated except for when the top $e-\mu$ control region is included in the 2-lepton standalone fit.

8.3.8 Experimental Nuisance Parameters

The nuisance parameters used to describe the experimental uncertainties are summarized in Table 55 and described in more detail in Section 7.

Nuisance Parameter	Description	NP Count	Section
	Luminosity (2)		
Lumi	error on total integrated error	1	7.1.1
MuScale	error of profile	1	
	Leptons (8)		
ElecEffic	trigger, reco., and id. efficiencies	1	
ElecE	energy scale	1	7.1.2
ElecEResol	energy resolution	1	
MuonEffic	trigger, reco., and id. efficiencies	1	
MuonEResolID	energy resolution from inner detector	1	7.1.3
MuonEResolMS	energy resolution from muon system	1	
LepIso	isolation scale factors	1	App. E,F
LepVeto	lepton veto efficiency in 0-lepton selection	1	7.1.2, 7.1.3
	$E_{\mathrm{T}}^{\mathrm{miss}}$ Trigger (2)		
METTrigZ	W efficiency curve versus Z curve	1	7.1.4
METTrigStat	statistical uncertainty of efficiency curve fit	1	
	Jet Energy Scale (23)		
JetNPX	eigenvector decomposition of in-situ calibration (X = 1-6rest)	6	7.1.5.1
JetEtaModel	η inter-calibration model	1	
JetEtaStat	statistical error of η inter-calibration	1	
JetNonClos	calibration non-closure	1	
JetMu	μ correction based on average number of pile-up interactions	1	
JetNPV	uncertainty due to N_{PV} correction	1	
JetPilePt	pile-up in jet area correction	1	
JetPileRho	pile-up in jet area correction	1	
JetFlavB†	b-jet energy scale	1	
JetBE†	b-jet scale for μ and ν energy	1	
JetFlavComp_X‡	knowledge of light quark vs gluon fraction	4	
JetFlavResp_X‡	different response of light quarks vs gluon jets	4	
	Jet Energy Resolution (2)		
JetEResol	resolution applied to all jets	1	7.1.5.2
BJetReso†	b-jet specific resolution	1	
	Jet Quality (1)		
JetJVF	jet vertex fraction efficiency	1	7.1.5.3
	$E_{\mathrm{T}}^{\mathrm{miss}}$(2)		
METResoSoftTerms	resolution of soft component	1	7.1.6
METScaleSoftTerms	scale of soft component	1	
	Flavor Tagging (40)		
BTagBNEffic	b-jet uncertainty in 10 eigenvector ($N = 0-9$)	10	7.1.7
BTagCNEffic	c-jet uncertainty in 15 eigenvector ($N = 0-14$)	15	
BTagLNEffic	light-jet uncertainty in 10 eigenvector ($N = 0-9$)	10	
BTagTruthTagDR	correction to ΔR(cc) bias from truth-tagging	1	3.3.4.2
BTagBSherpa	generator dependent heavy flavor tagging efficiecny	1	3.3.4.3
BTagCSherpa		1	
BTagBPythia8		1	
BTagCPythia8		1	
Total	80 with priors, 0 floating		

Table 55: A summary of the names and meaning of systematics from the combined performance tools and other experimental systematics as well as the associated nuisance parameter names. For flavor composition and response systematics, X=Wjets, Zjets, Top, VHVV.
† Applied only to truth-matched b-jets.
‡ Applied only to non-truth-matched b-jets.

8.4 Output Transform

The original BDT distribution is put into a 1000 bin histogram, while the m_{bb} distribution in the dijet masss analysis has 500 bins in the range 0-500 GeV. In both the cases, an algorithm to reduce the number of bins is needed.

Since the BDT is a classification algorithm which maximizes the separation of two populations, for measuring the signal strength, the optimal performance is not necessarily achieved by the default output distribution from TMVA. Furthermore the value of the output distribution itself is essentially meaningless so a remapping of the default MVA output is a reasonable approach to maximizing the analysis potential.

A simple rebin of the m_{bb} distribution of the m_{bb} shape analysis was used in all previous versions. In order to reduce statistical uncertainties in the tails of the dijet mass, wider bins were needed. However this reduces the sensitivity in the signal rich region. A natural conclusion is a variable size binning. To optimize the signal strength while giving stability to the fit, an improved variable size binning has been developed for the distributions entering in the statistical model (for both the m_{bb} shape and the multivariate analysis). A technical note: RooStats cannot handle variable size bins so the output distribution in both cases is mapped to a constant-bin-width histogram. In the case of the m_{bb} this needs to be mapped back to a physically meaningful representation while for the BDT, this is not necessary.

The two figures-of-merit used to optimize the binning are the final expected sensitivity, and the reduction of number of bins. As an example, the total number of bins in the dijet masss analysis, if the m_{bb} distribution has a fixed bins width of 20 GeV (in the range 10 GeV$< m_{bb} <$250 GeV), is almost 1000, and the fits would need to handle all of them, all the errors (including statistical) and the correlations across them.

8.4.1 General description

To remap the histograms entering in the final fit, we define a function:

$$Z(I[k,l]) = Z(z_s, n_s(I[k,l]), N_s, z_b, n_b(I[k,l]), N_b) \tag{23}$$

where

- $I[k,l]$ is an interval of the histograms containing the bins between the bin k and the bin i;
- N_s is the total number of signal events in the histogram;
- N_b is the total number of background events in the histogram;
- $n_s(I[k,l])$ is the total number of signal events in the interval $I[k,l]$;
- $n_b(I[k,l])$ is the total number of background events in the interval $I[k,l]$;
- z_s and z_b are parameters used to tune the algorithm.

Different possible Z functions have been tested. In the following sections, 2 different algorithms will be described: the transformation D and the transformation F[6]:

- **Transformation D** This transformation uses a Z equal to:

$$Z = z_s n_s/N_s + z_b n_b/N_b \tag{24}$$

  where z_s and z_b are parameters, which can be used to optimize the strategy.

[6]NOTE: we keep here the names used in when the studies were performed to keep track of the name convention.

- **Transformation F** This transformation uses a Z equal to:

$$llr_s = \sum_{i \text{ in interval}} s_i \times \log(1 + s_i/b_i) \tag{25}$$

$$Z = \sqrt{z_b n_b / N_b} + \sqrt{z_s llr_s} \tag{26}$$

$$\tag{27}$$

where s_i and b_i are the number of signal and background events in the bin i, and z_s, z_b are parameters which can be used to optimize the strategy.. In addition to the condition on Z, the interval in the general algorithms are requested to satisfy the condition:

$$\sigma_b < 0.10 \tag{28}$$

where σ_b is the relative statistical uncertainty on the background.

While the transformation D was historically used for both the multivariate analysis (see App. AC) and the m_{bb} shape analysis, the transformation F resulted recently in performing better than the D in the multivariate analysis, becoming the default transformation for this analysis.

Both the transformation B and the transformation F share the following steps:

- Starting from the last bin on the right of the original histogram, increase the range of the interval $I(k, last)$ by adding one after the other, the bins from the right to the left;
- Calculate the value of Z at each step;
- Once $Z(I[k_0, last]) > 1$ (let's say for the interval from the bin k_0 to the bin $last$), remap all the bins in the interval $I(k_0, last)$ into a single bin;
- Repeat these last 3 points, starting this time from the last bin on the right, not included in the previous remap (the new $last$ is $k_0 - 1$).

8.4.1.1 MVA Optimization and Transformation F

The optimization for the mva analysis has been evaluated by looking at the dependence of the expected limit and the number of bins as a function of zs and zb (see Figure 40). The selected working point is zs = zb = 4.5. This reduce the number of bins by 53

The optimization for the MVA analysis has been evaluated by looking at the dependence of the expected limit and the number of bins as a function of z_s and z_b(see Figure 40). The selected working point is $z_s = z_b = 4.5$. This reduce the number of bins by 53% and therefore increase the stability of the fit significantly compared to a binning which maps the original 1000 bins to 20 bins of equal size. These choice of parameters reduces the number of bins by 17% with no change in the expected significance compared to transformation D described in Appendix AC.

As an example, one of the MVA distributions, before and after the transform can be seen in Figure 41.

8.4.1.2 m_{bb} shape optimization and the transformation D

For the dijet masss analysis, the optimization has the advantage of increasing the number of bins where signal is expected while avoiding the proliferation of bins in background only regions. The optimized binning for the cut based has been evaluated individually for each lepton channel, resulting in the parameters in Table 56.

The new setup, if compared with the 20 GeV bins in m_{bb} used for EPS reduces the numbers of bins by almost 45% and *improves* the final results by 2% in the total expected sensitivity. As an example, one of the m_{bb} distribution, before and after the transform can be seen in Figure 42.

Cut based :lepton region	2-jets	3 -jets
0 leptons	z_s =6, z_b =2	z_s =4, z_b =2
1 leptons	z_s =6, z_b =2	z_s =4, z_b =2
2 leptons	z_s =4, z_b =4	z_s =2, z_b =2

Table 56: Binning optimization for the cut based analysis

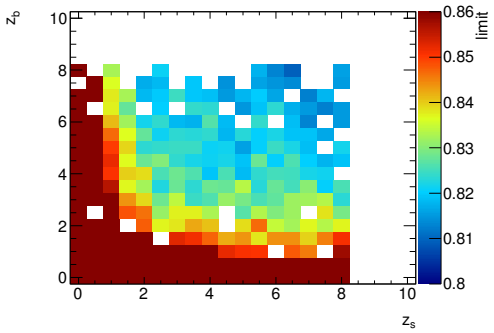

Figure 40: 2D Expected limit as a function of the z_s and z_b parameters.

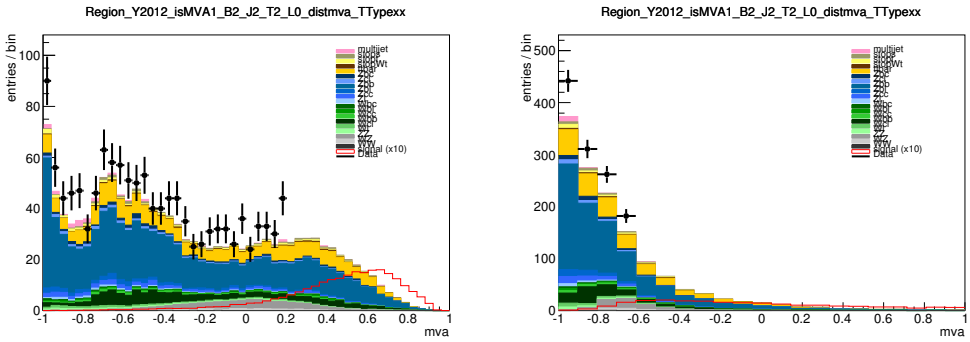

Figure 41: Example of the effect of the binning transform F on the MVAoutput for one of the signal regions. Left: before the binning transform; Right: After the binning Transform.

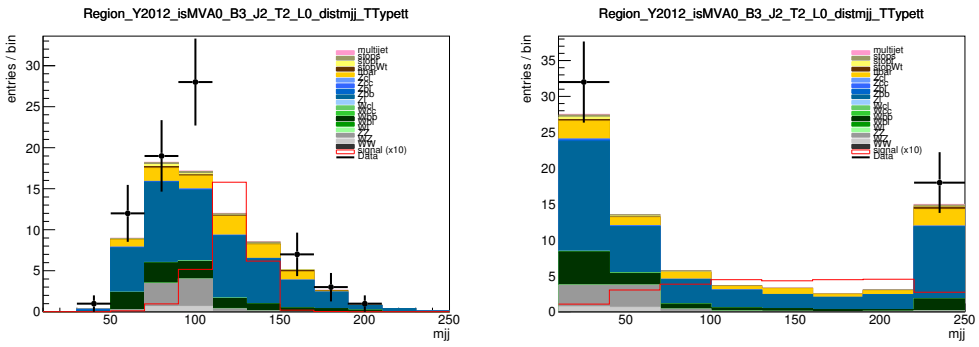

Figure 42: Example of the effect of the binning transform on the m_{bb}output for one of the signal regions. Left: before the binning transform; Right: After the binning Transform. NOTE: The labels on the horizontal axis shown in the plot after the transformation are not anymore meaningful but will be in future versions.

8.5 Pruning of the Systematic Uncertainties

Limited statistics in the MC nominal distributions can produce systematic templates with large fluctuations, introducing noise in the fit. Therefore, the uncertainties are treated according to the following procedure which has an additional step compared to EPS [11] and is carried out for each process in each region after the final distribution is manipulated according to the procedures discussed in Section 8.4:

- reduce statistical fluctuations by the smoothing procedure described in Section 7.2 only to those systematic which require a re-sampling of the events (i.e. JES and not b-tagging)
- neglect the normalization uncertainty if for a given sample in a region either is true:
  - the variation is less than 0.5%
  - both up and down variations have the same sign
- neglect the shape uncertainty if for a given sample in a given region either is true:
  - not one single bin has a deviation over 0.5% after the overall normalization is removed
  - if only up or the down variation is non-zero and passed the previous pruning steps
- neglect the shape and normalization uncertainty for a given sample in a given region if the sample is less than 2% of the total background (new since EPS):
  - if the signal $< 2\%$ of the total background in all bins
    if shape and normalization error are each $< 0.5\%$ of the total background
  - if at least one bin has a signal contribution $> 2\%$ of the total background
    in those bins if the shape and normalization error are each $< 2\%$ of the signal yield

The additional step developed after EPS was tuned to ensure the expected p_0 and $\hat{\mu}$ along with its associated error do not change more than 2% using the EPS workspaces.

The above procedure removed the following systematics completely from the MVA Higgs fit:

- `METTrigZ`
- `METTrigStat`
- `LepIso`

In checking the sizes of the remaining NPs, the following were found to be on very few background and showed evidence of statistical fluctuations so were subsequently removed ‘by hand’ for all analyses:

- `JetNP5`
- `MuonEResolMS`
- `MuonEResolID`
- `ElecEResol`
- `MuScale`

Therefore the total number of parameters in the likelihood is 184 (183 for conditional fits).

For those nuisance parameters remaining after applying this procedure, the normalization uncertainty is taken into account with a log-normal prior and the shape uncertainty with Gaussian prior. Usually the $\pm 1\sigma$ ($\alpha_i = \pm 1$) and the nominal ($\alpha_i = 0$) are known. When the likelihood is constructed, a PDF is created defined from $\alpha_i = \pm 5$ is needed. To do this an extrapolation is needed from the known points out to $\alpha_i = \pm 5$ and an interpolation between the know points as well which should guarantee the PDF is continuous and smooth everywhere (especially if the error is asymmetric). For shape uncertainties a piecewise exponential extrapolation and a 6^{th} order polynomial interpolation are used while a quadratic interpolation and linear extrapolation are used for normalization uncertainties. This is the default configuration in RooStats.

8.6 Understanding the Likelihood

The likelihood can be maximized with respect to the observed data or pseudo data derived from the nominal MC expectation or any variation by created an Asimov data set. When fitting to the nominal MC expectation, the pulls constrained NPs should all remain at 0 and floating normalizations at 1. The post-fit error represents the expected post-fit uncertainty on a given parameter. The post-fit error can be compared to fits to data to check if the constraints from data match the expectation given the size of the error, the samples, and the region(s) on which it acts. Unless otherwise stated, when Asimov data is mentioned it is built from the nominal expectation.

An important tool to understand the important NPs is the so called NP ranking which evaluates the impact of each NP on the expected or measured signal strength. This is discussed in Section 8.6.4 and shown in Section 8.6.4.1 and 8.6.4.2 for the dijet and MVA analysis respectively.

8.6.1 Dijet Mass Analysis Fit Studies

The pull plots for combined fit for the dijet masss analysis are shown in Figures 43-48. Each plot compares the result from a fit to either the Asimov data set (red) or to the observed data (black) on the left, and the result of the fit for each individual lepton channel on the right. The individual channel results are shown in Appendix **??**.

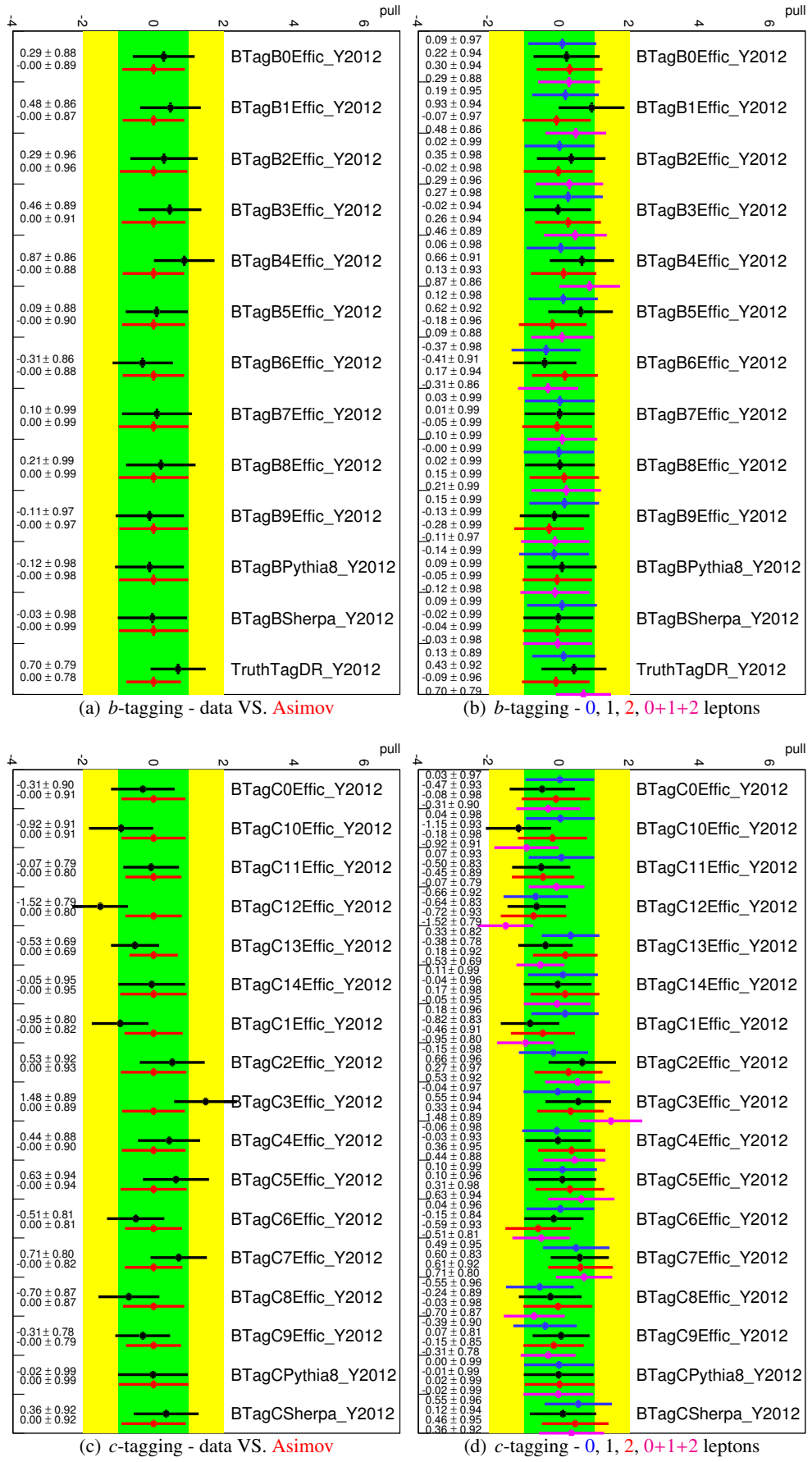

(a) *b*-tagging - data VS. Asimov

(b) *b*-tagging - 0, 1, 2, 0+1+2 leptons

(c) *c*-tagging - data VS. Asimov

(d) *c*-tagging - 0, 1, 2, 0+1+2 leptons

Figure 43: Pull plots for b and c tagging in the 0+1+2 lepton m_{bb} shape fit. The fit to the Asimov data set is shown in red and the fit to the data in black on the left. The fits to 0 lepton (blue), 1 lepton (black) and 2 leptons (red) data and the combined fit to data (magenta) is shown on the right.

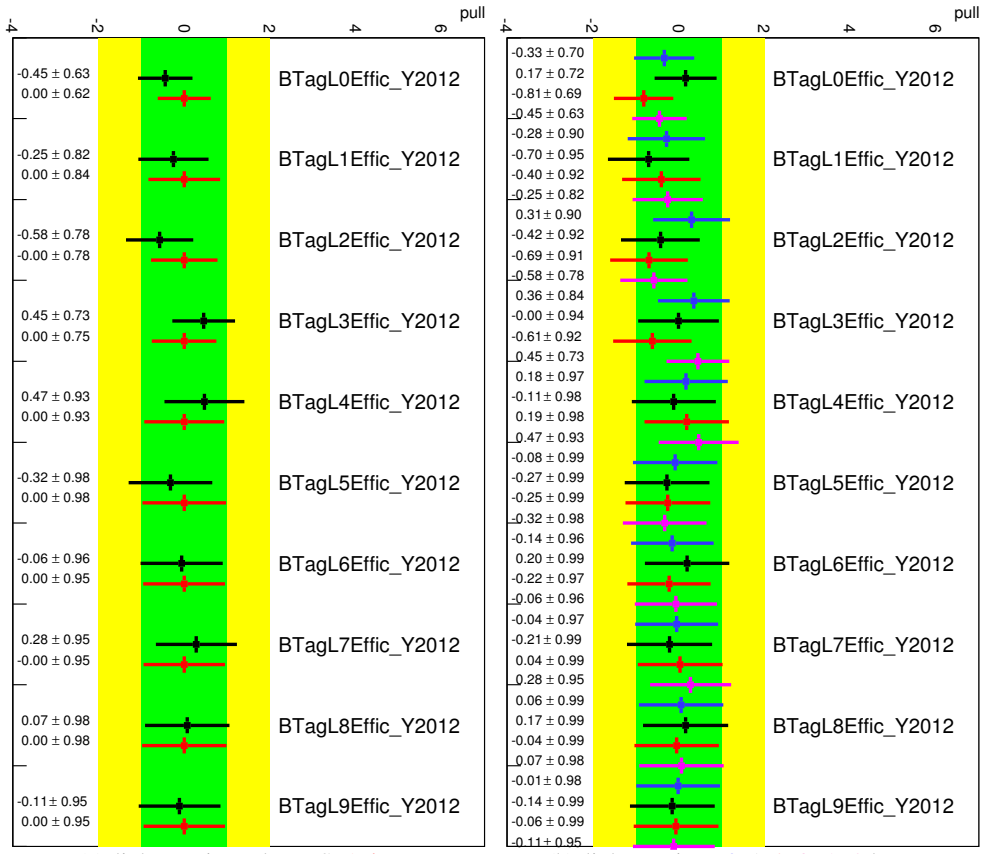

(a) light tagging - data VS. Asimov

(b) light tagging - 0, 1, 2, 0+1+2 leptons

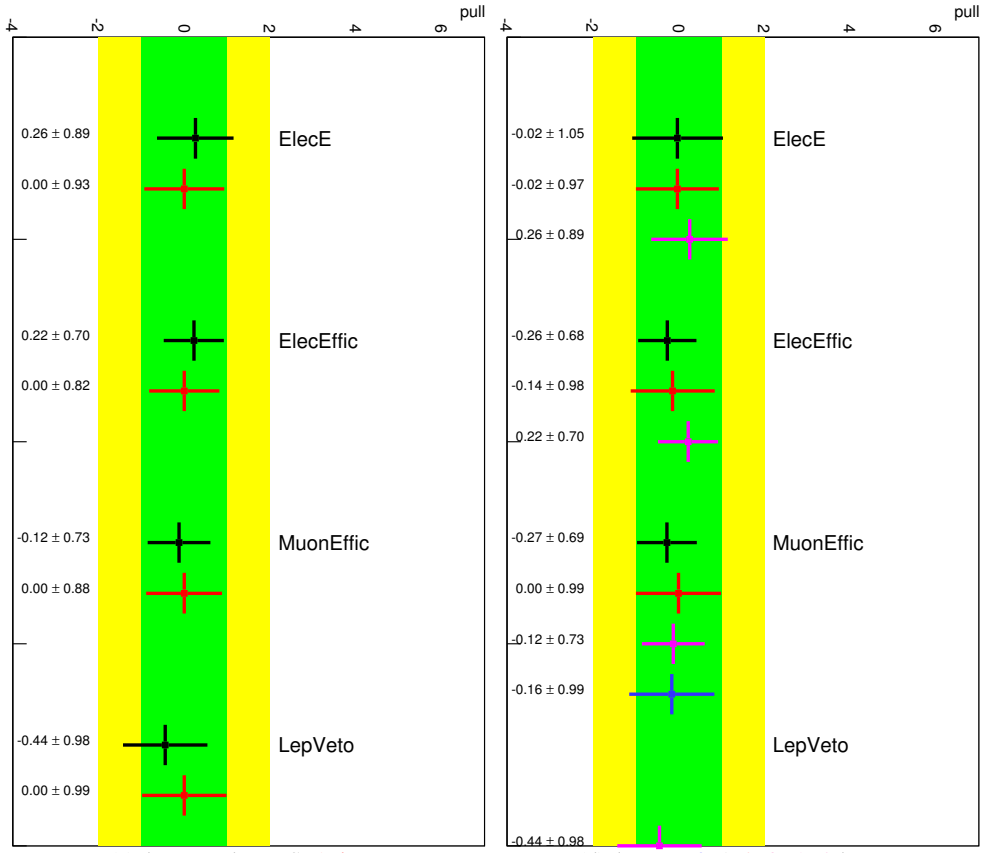

(c) lepton - data VS. Asimov

(d) lepton - 0, 1, 2, 0+1+2 leptons

Figure 44: Pull plots for light-jet tagging and lepton related systematics in the 0+1+2 lepton m_{bb} shape fit. The fit to the Asimov data set is shown in red and the fit to the data in black on the left. The fits to 0 lepton (blue), 1 lepton (black) and 2 leptons (red) data and the combined fit to data (magenta) is shown on the right.

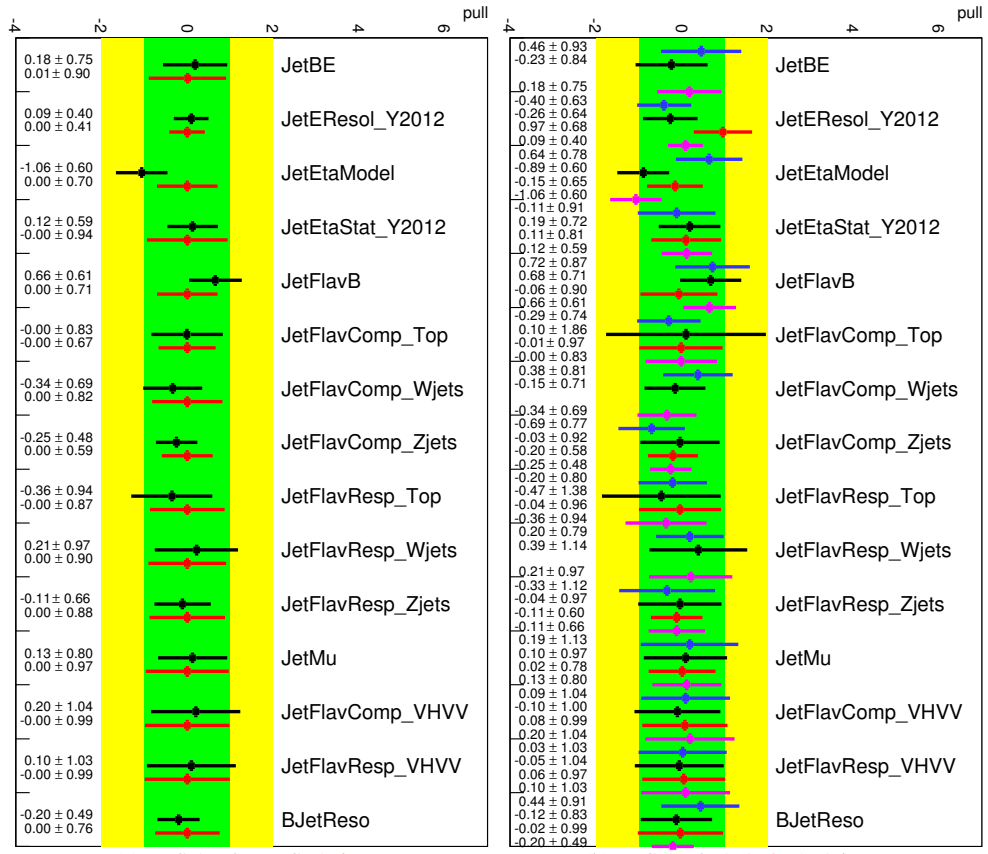

(a) JES 1 - data VS. Asimov (b) JES 1 - 0, 1, 2, 0+1+2 leptons

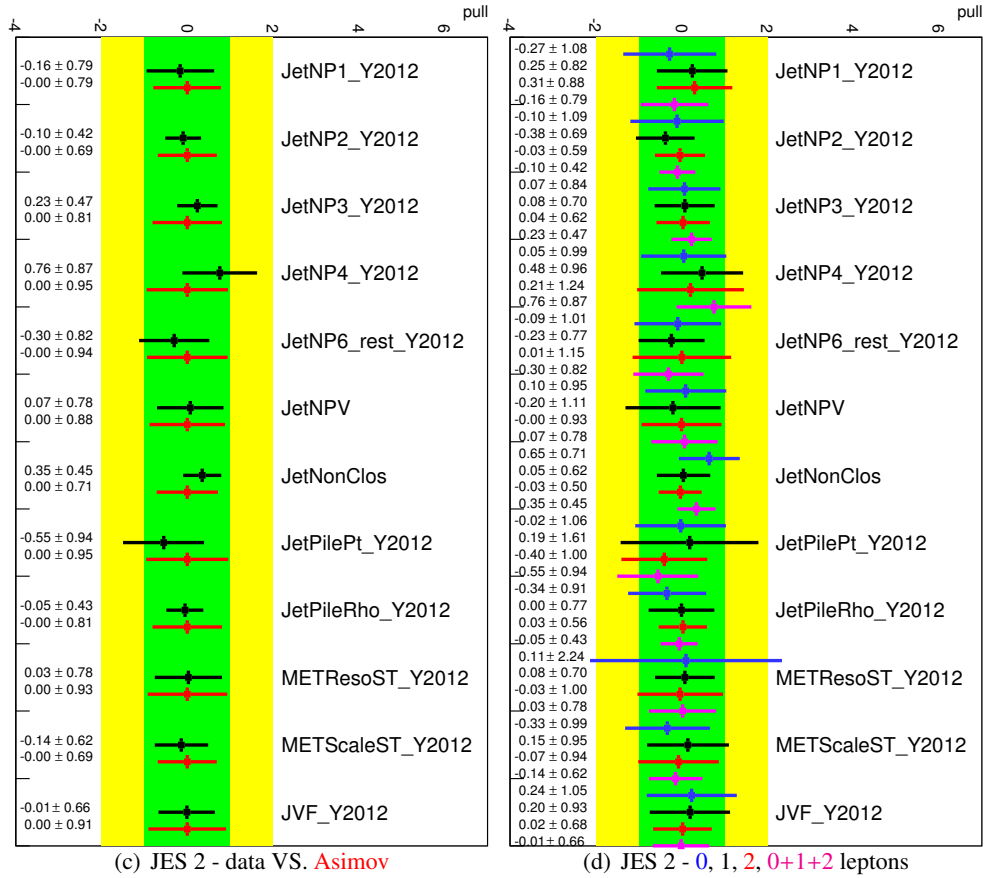

(c) JES 2 - data VS. Asimov (d) JES 2 - 0, 1, 2, 0+1+2 leptons

Figure 45: Pull plots for JES systematics in the 0+1+2 lepton m_{bb} shape fit. The fit to the Asimov data set is shown in red and the fit to the data in black on the left. The fits to 0 lepton (blue), 1 lepton (black) and 2 leptons (red) data and the combined fit to data (magenta) is shown on the right.

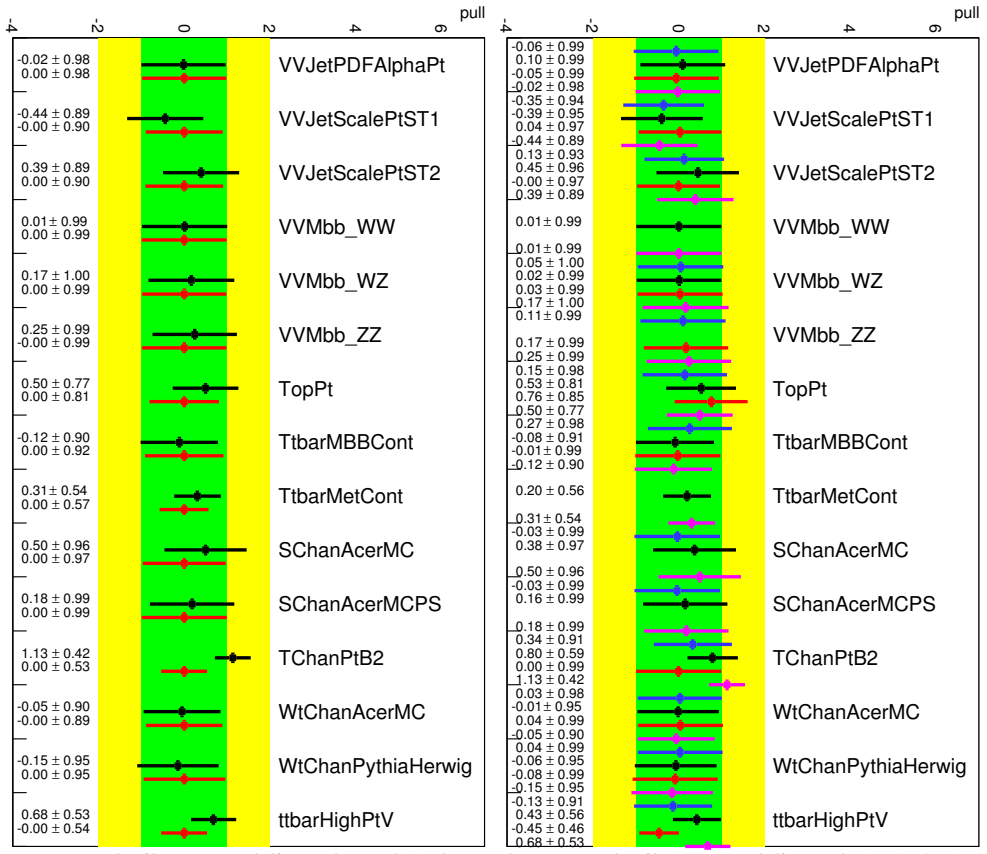

(a) Top and Diboson Modeling - data VS. Asimov (b) Top and Diboson Modeling - 0, 1, 2, 0+1+2 leptons

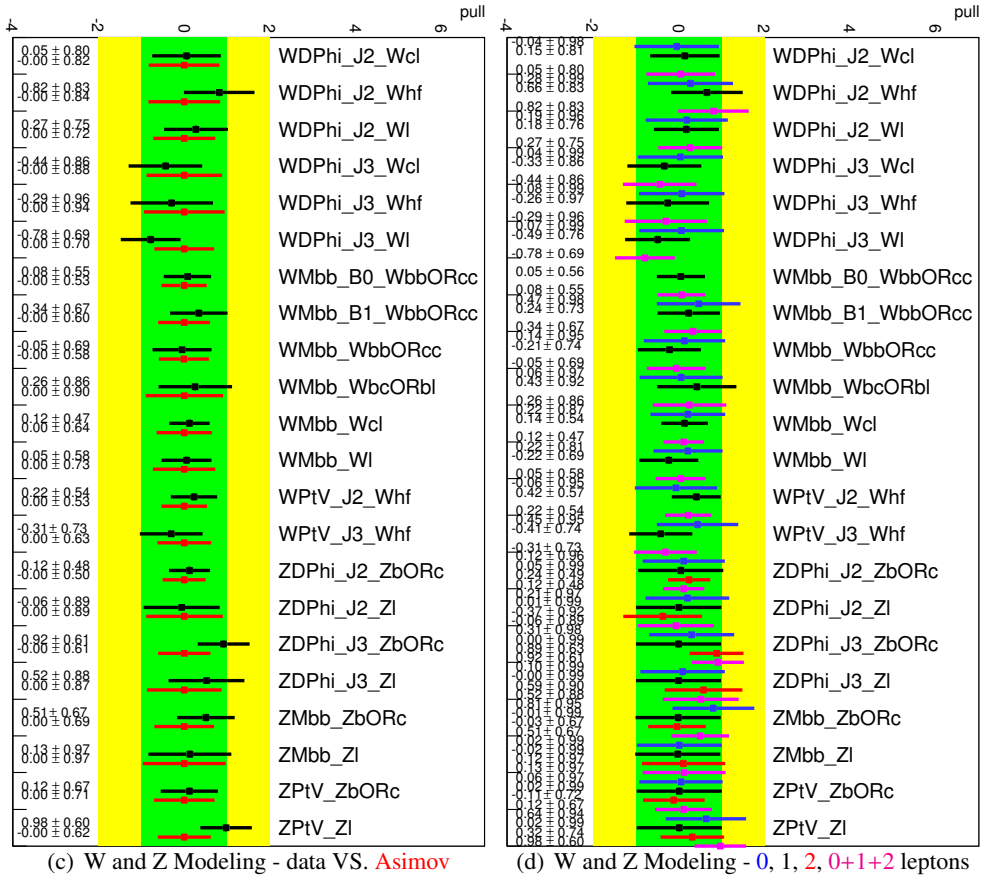

(c) W and Z Modeling - data VS. Asimov (d) W and Z Modeling - 0, 1, 2, 0+1+2 leptons

Figure 46: Pull plots for diboson/top and W/Z systematics in the 0+1+2 lepton m_{bb} shape fit. The fit to the Asimov data set is shown in red and the fit to the data in black on the left. The fits to 0 lepton (blue), 1 lepton (black) and 2 leptons (red) data and the combined fit to data (magenta) is shown on the right.

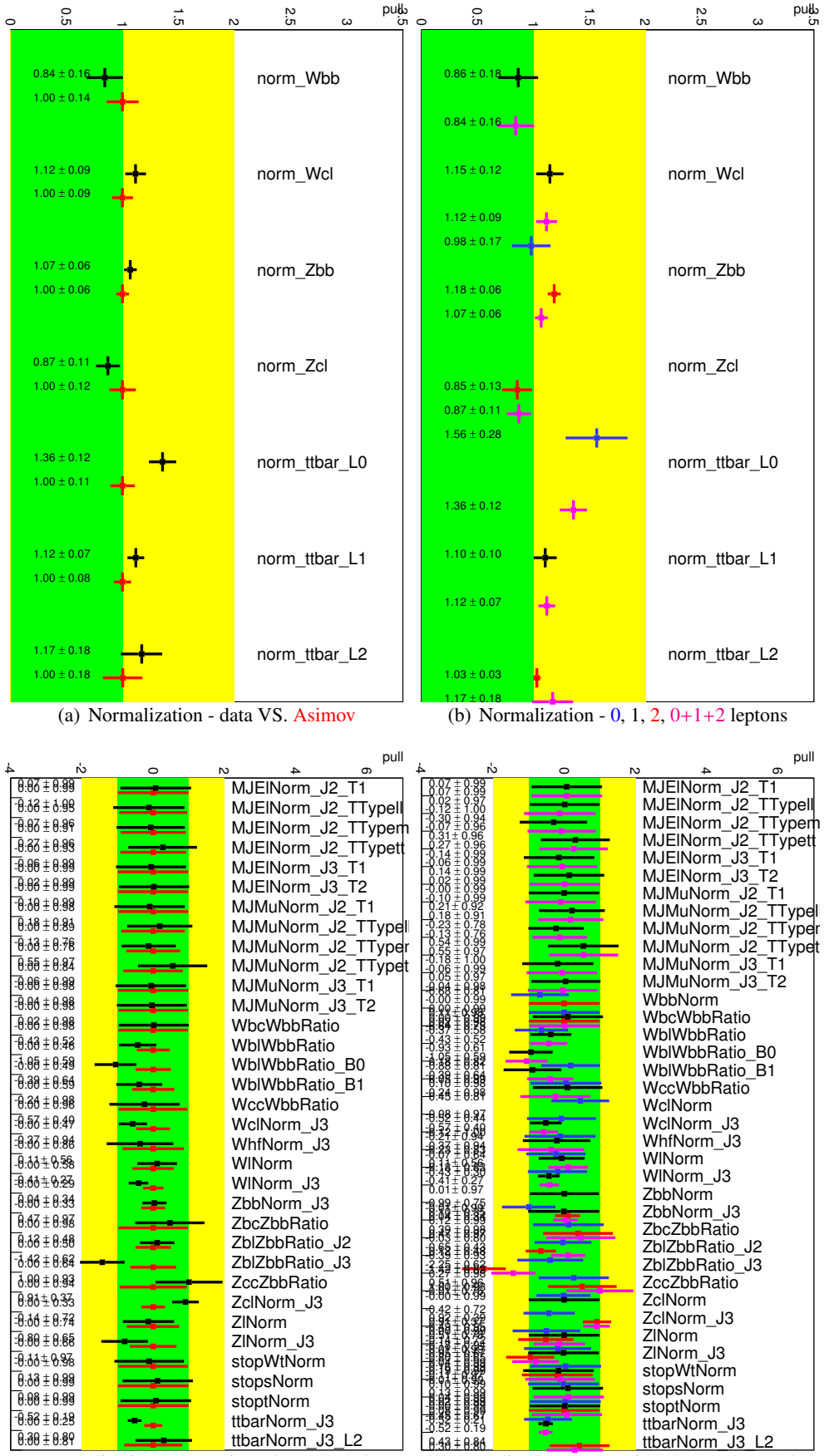

(a) Normalization - data VS. Asimov

(b) Normalization - 0, 1, 2, 0+1+2 leptons

(c) Normalization systematics - data VS. Asimov

(d) Normalization systematics - 0, 1, 2, 0+1+2 leptons

Figure 47: Pull plots for normalization in the 0+1+2 lepton m_{bb} shape fit. The fit to the Asimov data set is shown in red and the fit to the data in black on the left. The fits to 0 lepton (blue), 1 lepton (black) and 2 leptons (red) data and the combined fit to data (magenta) is shown on the right.

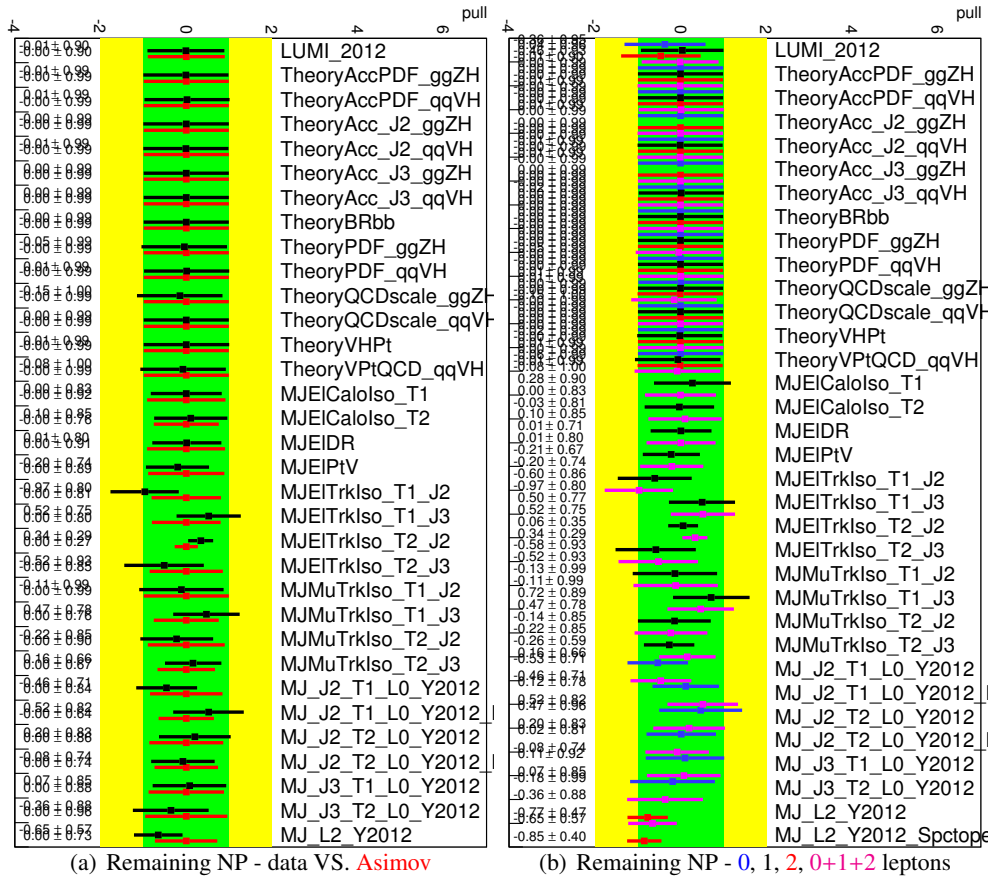

(a) Remaining NP - data VS. Asimov (b) Remaining NP - 0, 1, 2, 0+1+2 leptons

Figure 48: Pull plots for remaining systematics in the 0+1+2 lepton m_{bb} shape fit. The fit to the Asimov data set is shown in red and the fit to the data in black on the left. The fits to 0 lepton (blue), 1 lepton (black) and 2 leptons (red) data and the combined fit to data (magenta) is shown on the right.

8.6.1.1 Correlation Plots

Figure 49 shows the largest correlations in the full dijet masss analysis. This plot is produced by selecting all NP, which have a correlation larger than 20% with any another NP. Note that the parameter of interest, μ has been included by default not because it has particularly large correlations.

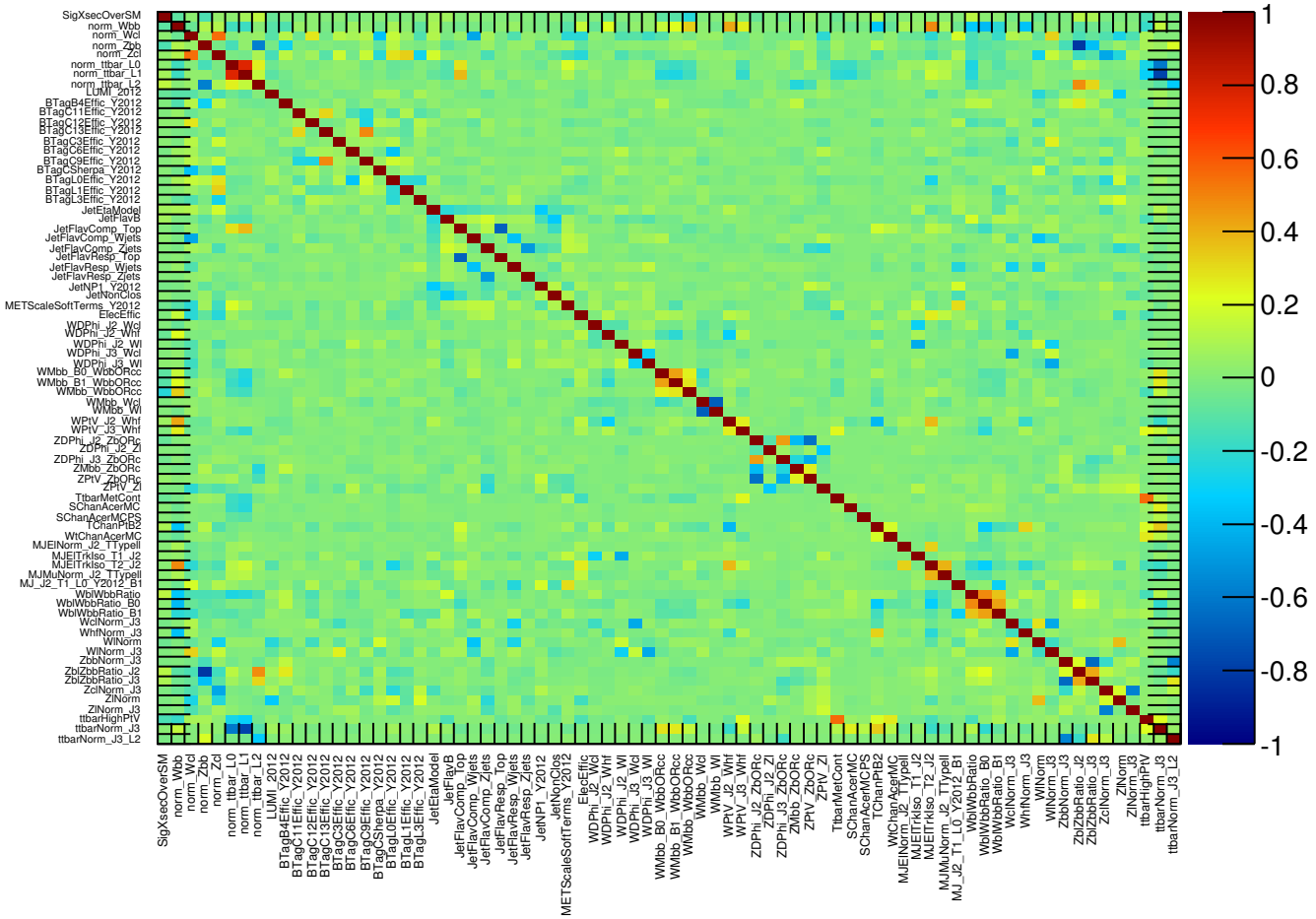

Figure 49: The correlation of all NP with a correlation larger than 20% in the 0+1+2 lepton m_{bb} shape fit. Note that the parameter of interest, μ has been included by default not because it has particularly large correlations.

8.6.2 MVA Analysis Fit Studies

The pull plots for combined fit for the MVA analysis are shown in Figures 50-55. Each plot compares the result from a fit to either the Asimov data set (red) or to the observed data (black) on the left, and the result of the fit for each individual lepton channel on the right. The individual channel results are shown in Appendix **??**.

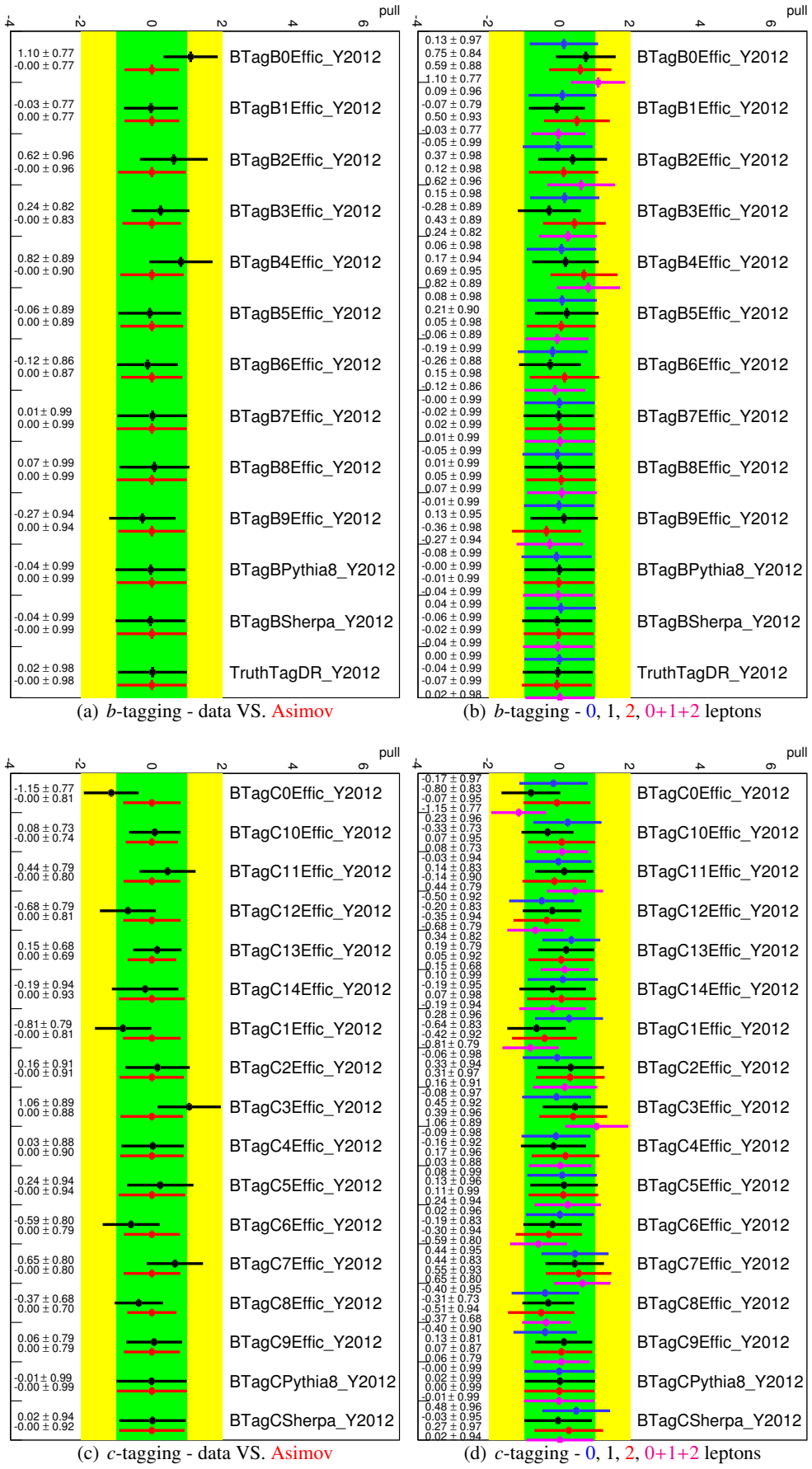

(a) *b*-tagging - data VS. Asimov

(b) *b*-tagging - 0, 1, 2, 0+1+2 leptons

(c) *c*-tagging - data VS. Asimov

(d) *c*-tagging - 0, 1, 2, 0+1+2 leptons

Figure 50: Pull plots for *b* and *c* tagging in the 0+1+2 lepton MVA fit. The fit to the Asimov data set is shown in red and the fit to the data in black on the left. The fits to 0 lepton (blue), 1 lepton (black) and 2 leptons (red) data and the combined fit to data (magenta) is shown on the right.

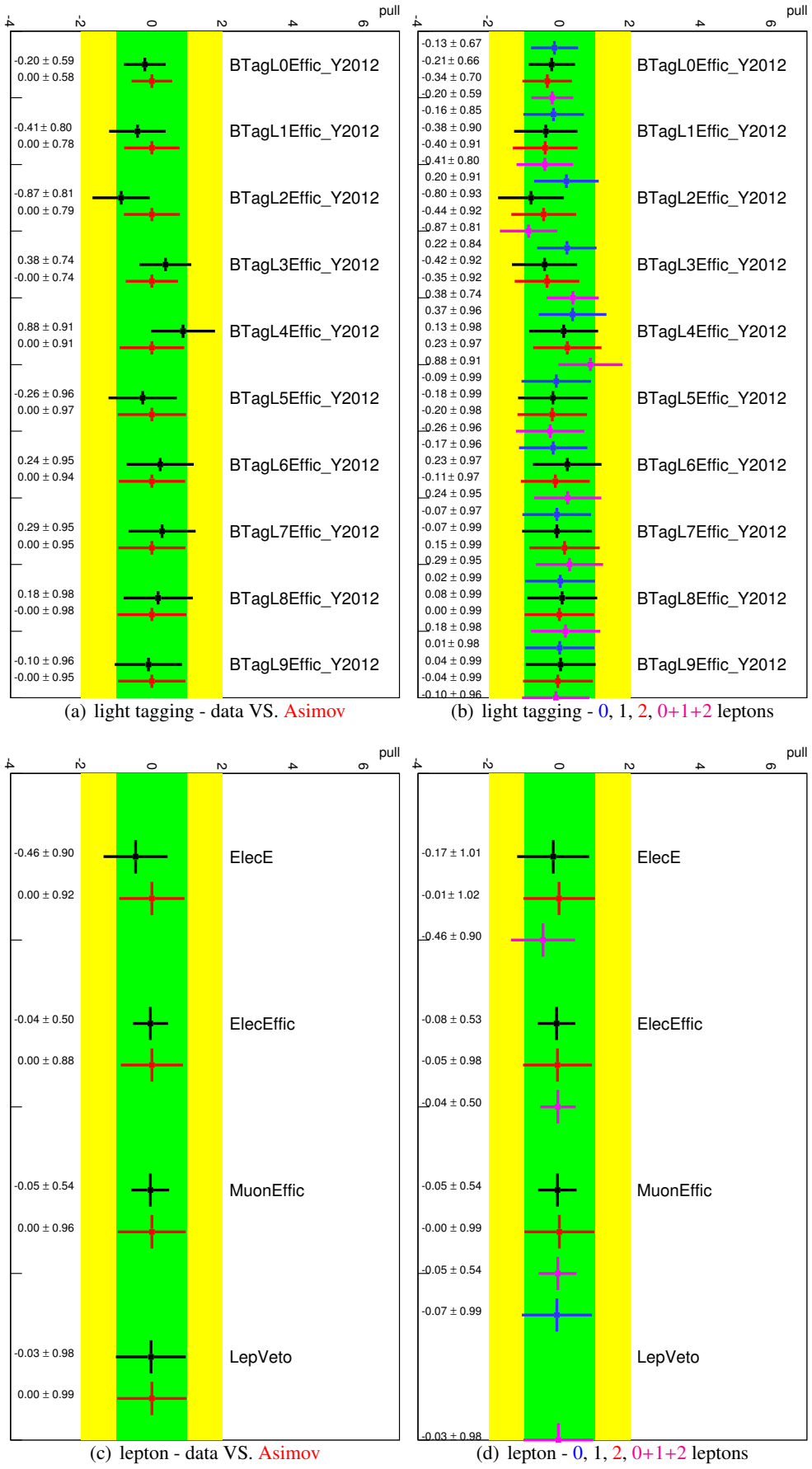

(a) light tagging - data VS. Asimov

(b) light tagging - 0, 1, 2, 0+1+2 leptons

(c) lepton - data VS. Asimov

(d) lepton - 0, 1, 2, 0+1+2 leptons

Figure 51: Pull plots for light-jet tagging and lepton related systematics in the 0+1+2 lepton MVA fit. The fit to the Asimov data set is shown in red and the fit to the data in black on the left. The fits to 0 lepton (blue), 1 lepton (black) and 2 leptons (red) data and the combined fit to data (magenta) is shown on the right.

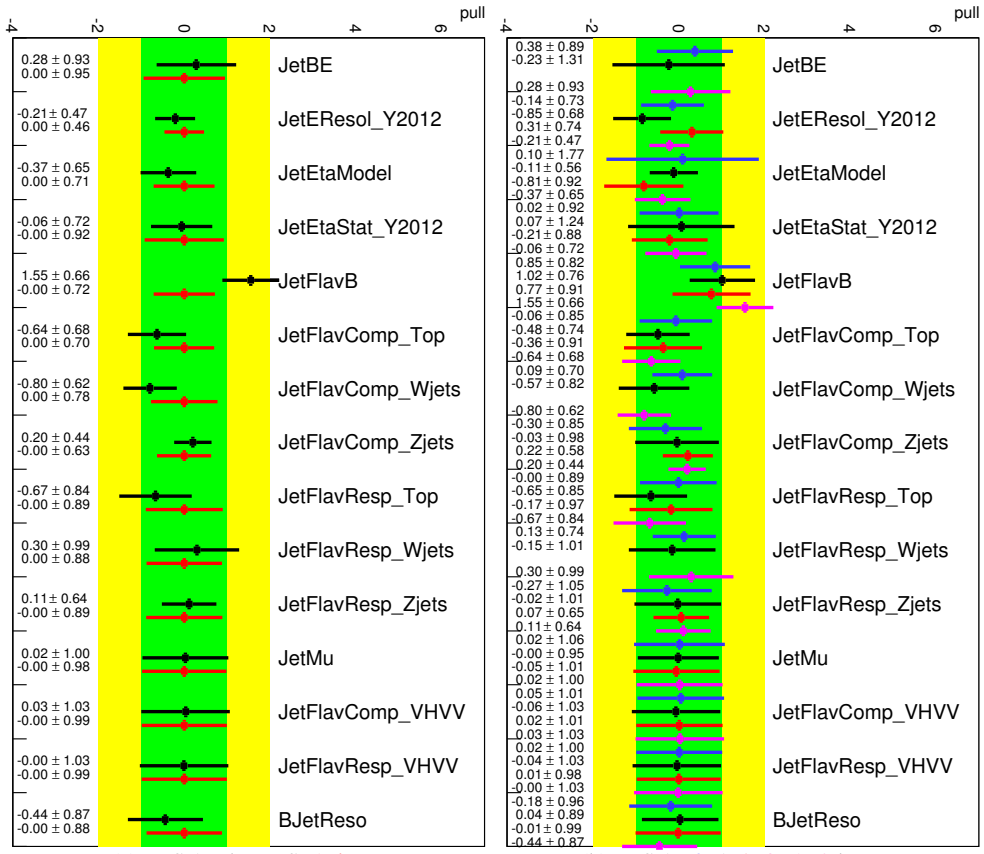

(a) JES 1 - data VS. Asimov (b) JES 1 - 0, 1, 2, 0+1+2 leptons

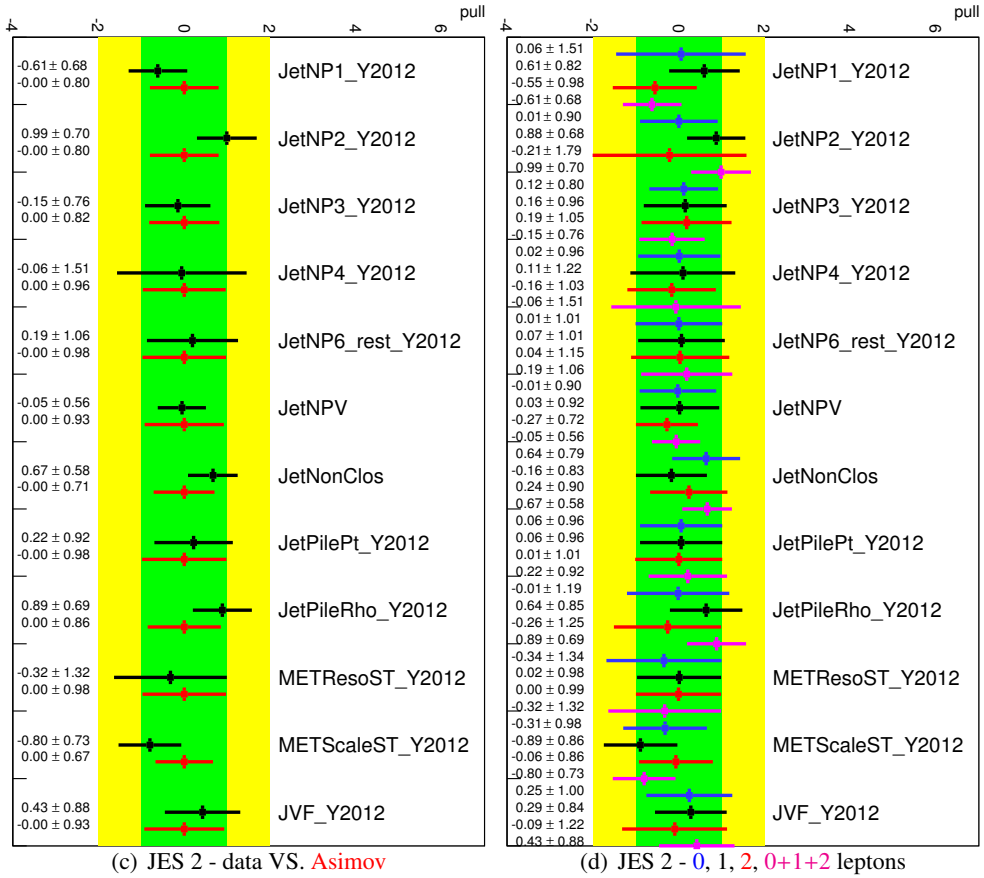

(c) JES 2 - data VS. Asimov (d) JES 2 - 0, 1, 2, 0+1+2 leptons

Figure 52: Pull plots for JES systematics in the 0+1+2 lepton MVA fit. The fit to the Asimov data set is shown in red and the fit to the data in black on the left. The fits to 0 lepton (blue), 1 lepton (black) and 2 leptons (red) data and the combined fit to data (magenta) is shown on the right.

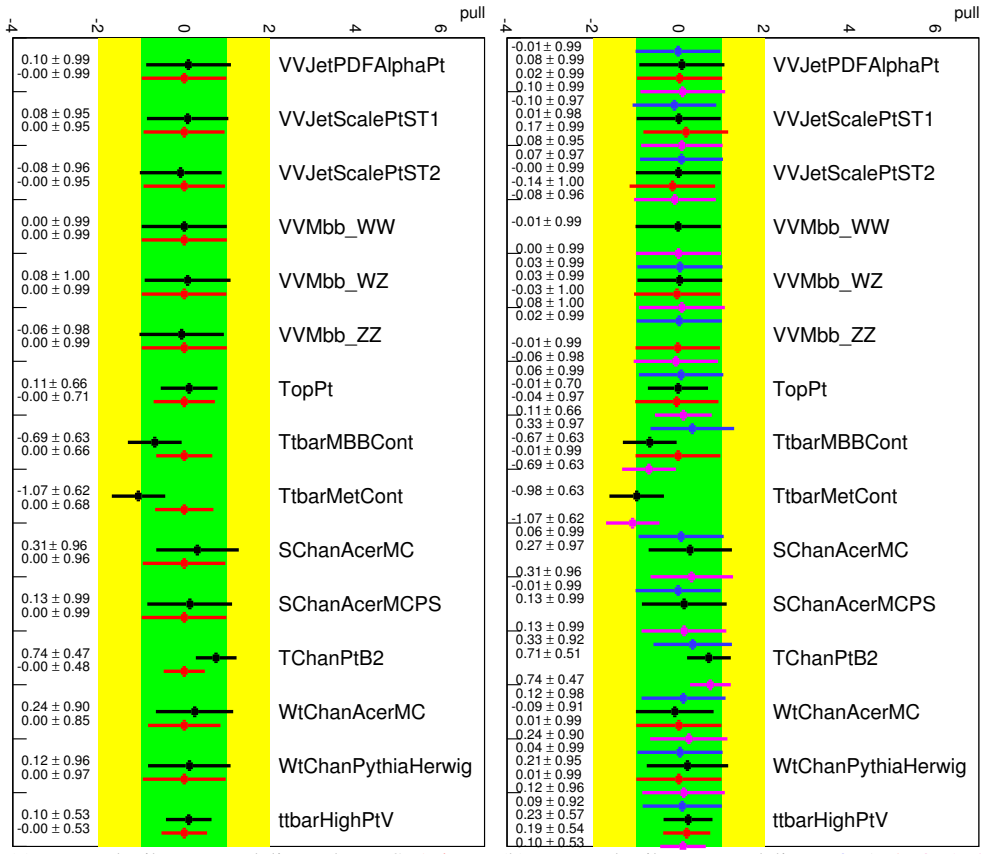

(a) Top and Diboson Modeling - data VS. Asimov (b) Top and Diboson Modeling - 0, 1, 2, 0+1+2 leptons

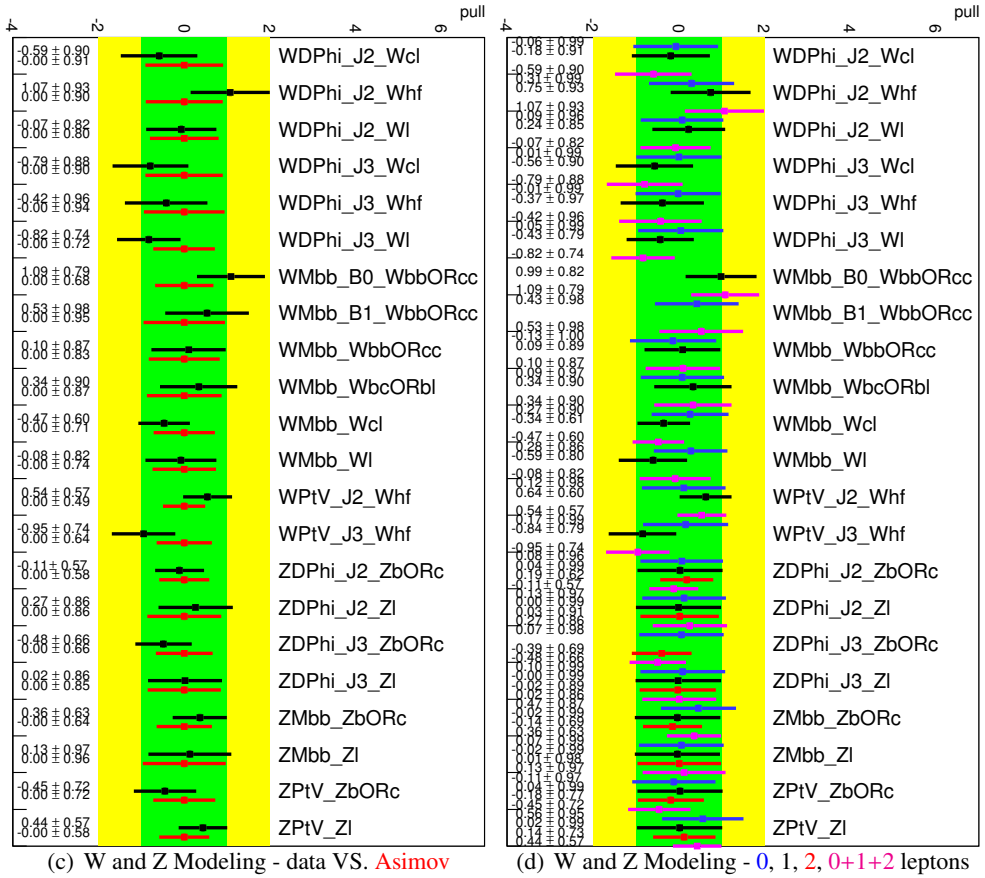

(c) W and Z Modeling - data VS. Asimov (d) W and Z Modeling - 0, 1, 2, 0+1+2 leptons

Figure 53: Pull plots for diboson/top and W/Z systematics in the 0+1+2 lepton MVA fit. The fit to the Asimov data set is shown in red and the fit to the data in black on the left. The fits to 0 lepton (blue), 1 lepton (black) and 2 leptons (red) data and the combined fit to data (magenta) is shown on the right.

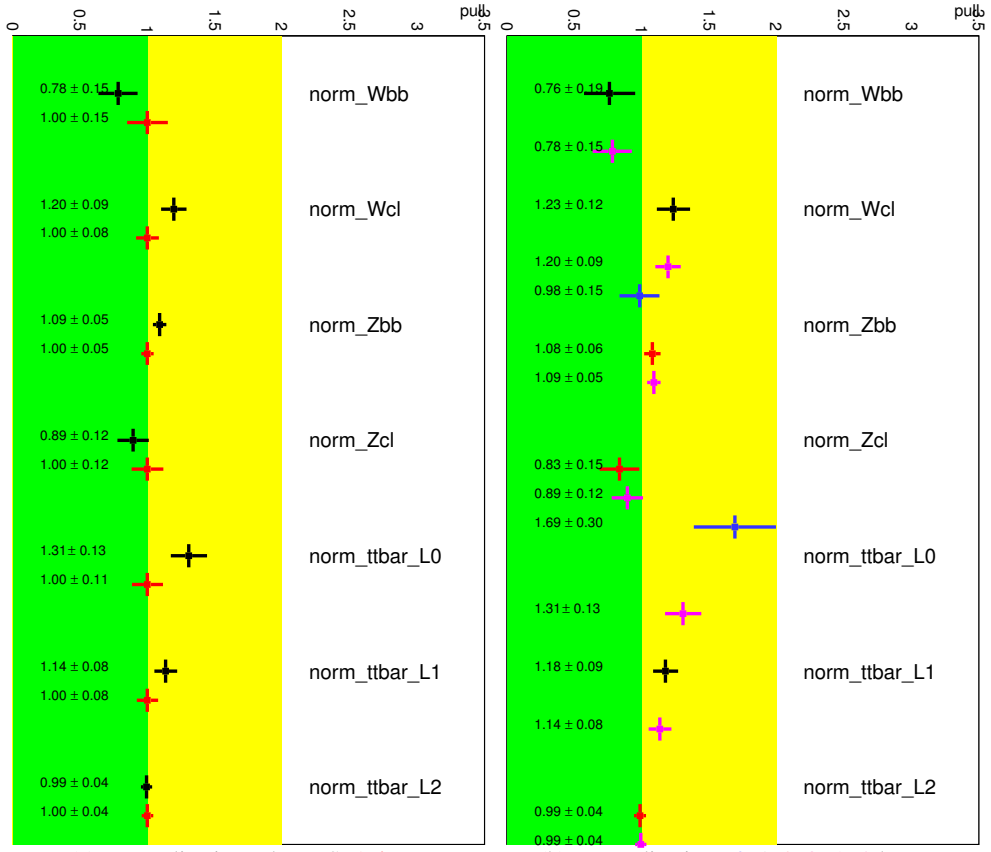

(a) Normalization - data VS. Asimov (b) Normalization - 0, 1, 2, 0+1+2 leptons

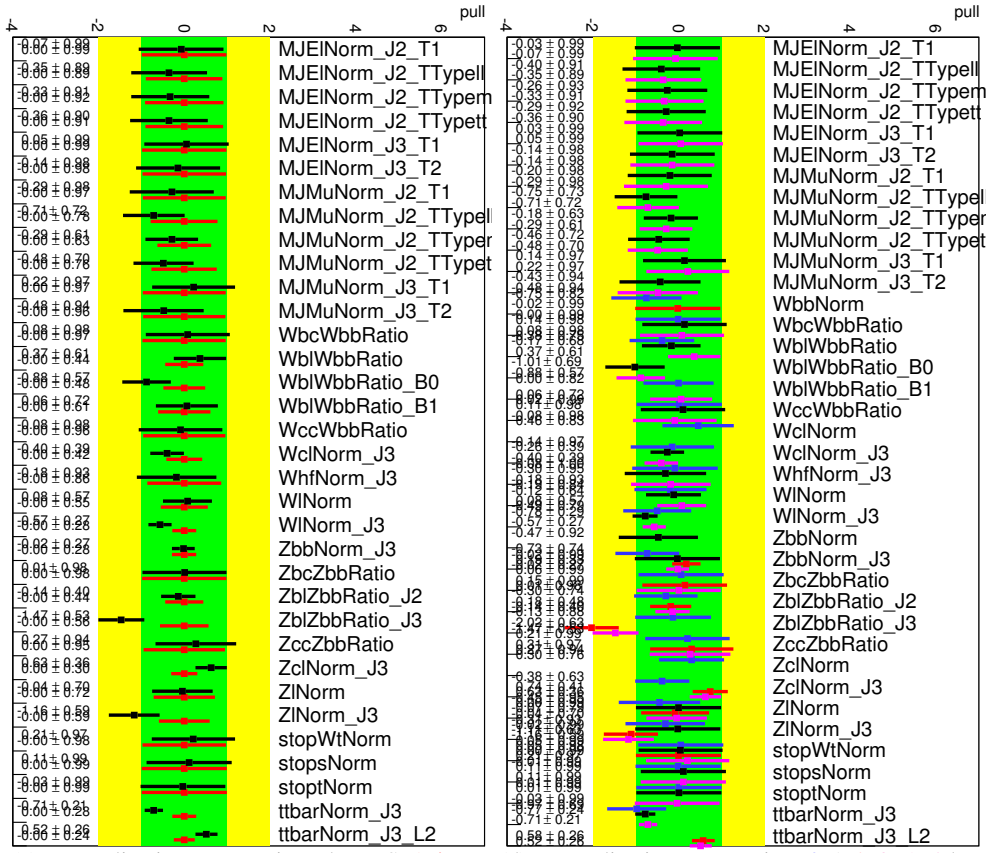

(c) Normalization systematics - data VS. Asimov (d) Normalization systematics - 0, 1, 2, 0+1+2 leptons

Figure 54: Pull plots for normalization in the 0+1+2 lepton MVA fit. The fit to the Asimov data set is shown in red and the fit to the data in black on the left. The fits to 0 lepton (blue), 1 lepton (black) and 2 leptons (red) data and the combined fit to data (magenta) is shown on the right.

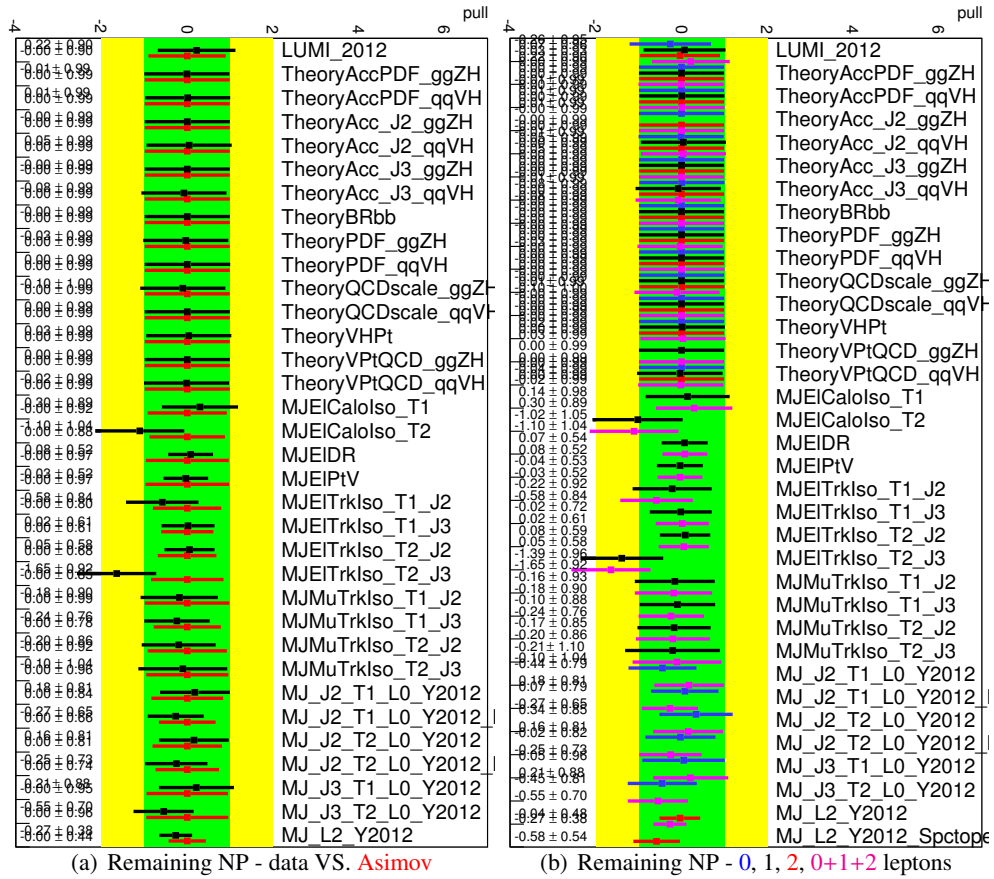

(a) Remaining NP - data VS. Asimov (b) Remaining NP - 0, 1, 2, 0+1+2 leptons

Figure 55: Pull plots for remaining systematics in the 0+1+2 lepton MVA fit. The fit to the Asimov data set is shown in red and the fit to the data in black on the left. The fits to 0 lepton (blue), 1 lepton (black) and 2 leptons (red) data and the combined fit to data (magenta) is shown on the right.

8.6.2.1 Correlation Plots

Figure 56 shows the largest correlations in the full MVA analysis. This plot is produced by selecting all NP, which have a correlation larger than 20% with any another NP. Note that the parameter of interest, μ has been included by default not because it has particularly large correlations.

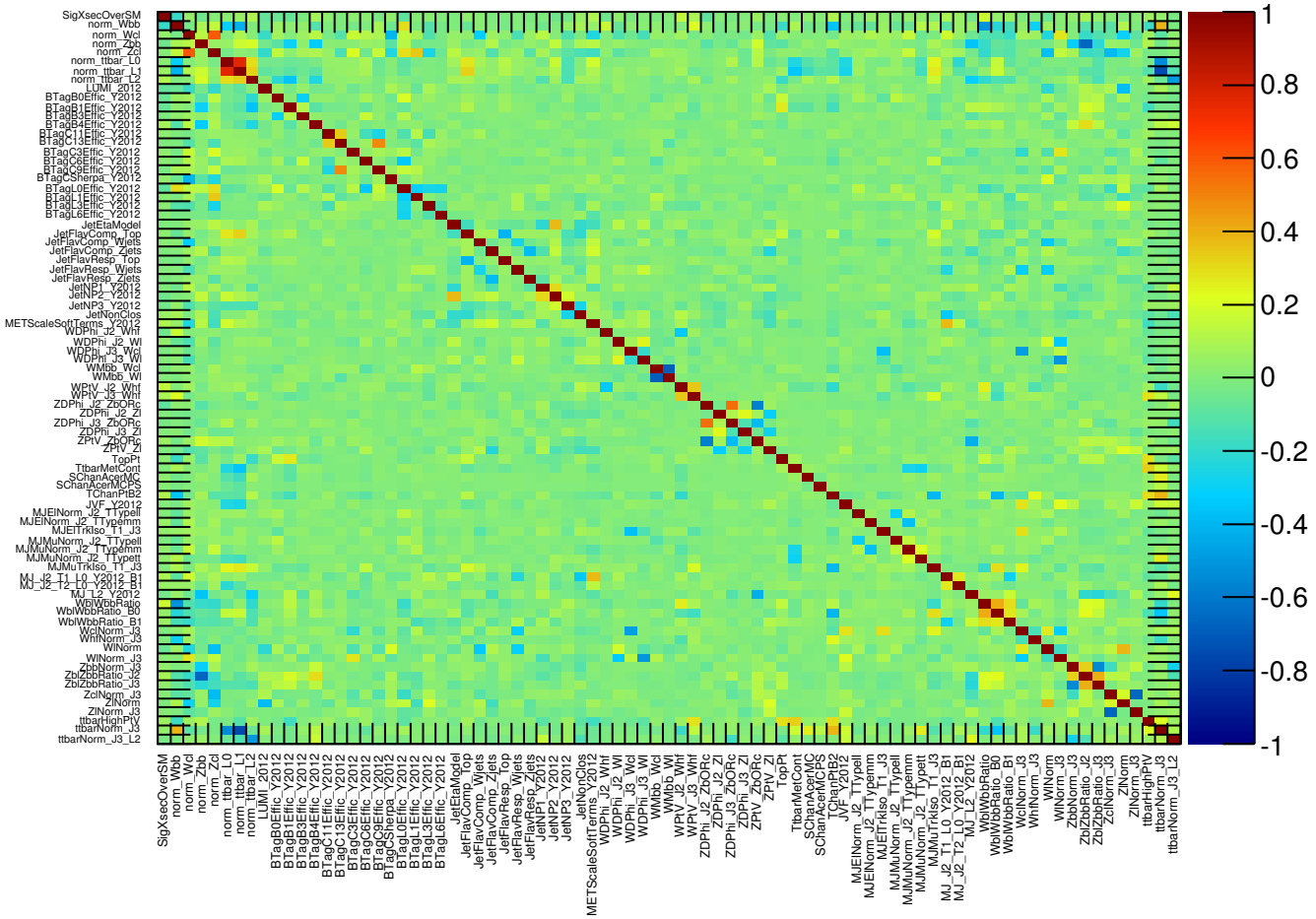

Figure 56: The correlation of all NP with a correlation larger than 20% in the 0+1+2 lepton MVA fit. Note that the parameter of interest, μ has been included by default not because it has particularly large correlations.

8.6.3 Comparison of Dijet Mass and MVA Analysis Fits

The MVA combined fit results are shown in black while the dijet mass analysis pulls are shown in red. A comparison of the individual channels in given in Appendix **??**.

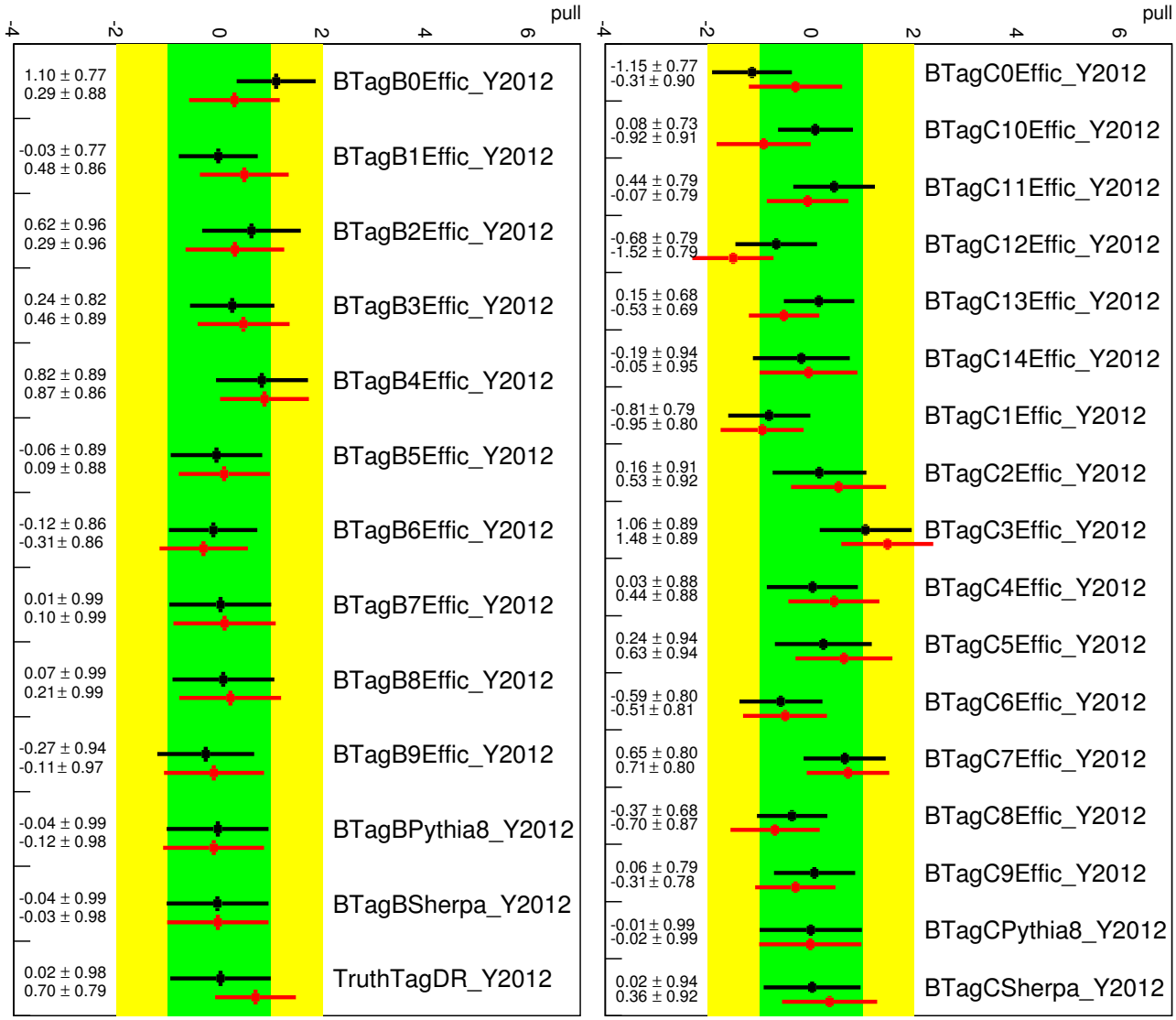

Figure 57: m_{jj} vs MVA pull plots for 0+1+2 fit: b- and c-jet tagging.

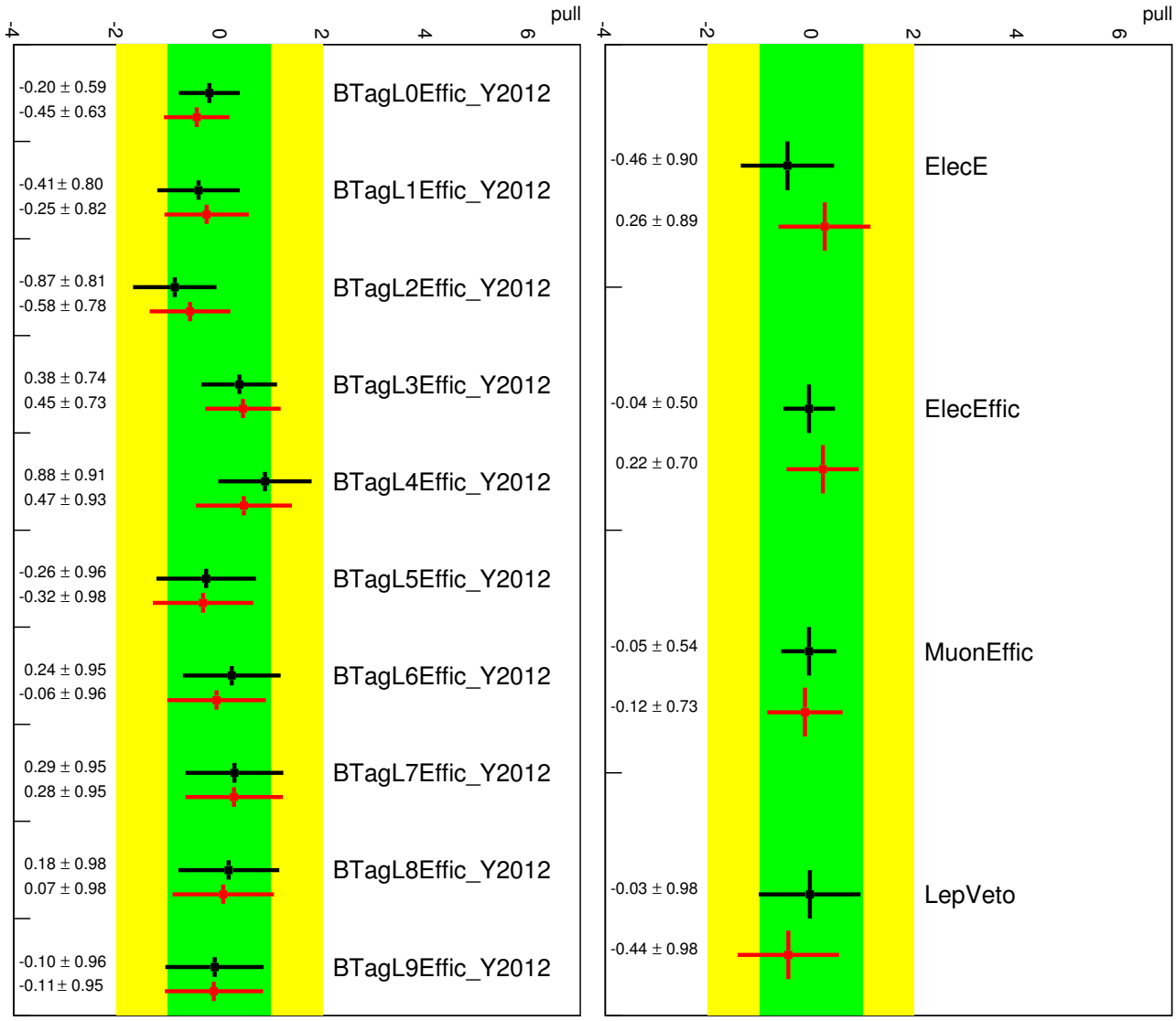

Figure 58: m_{jj} vs MVA pull plots for 0+1+2 fit: light-jet tagging and leptons.

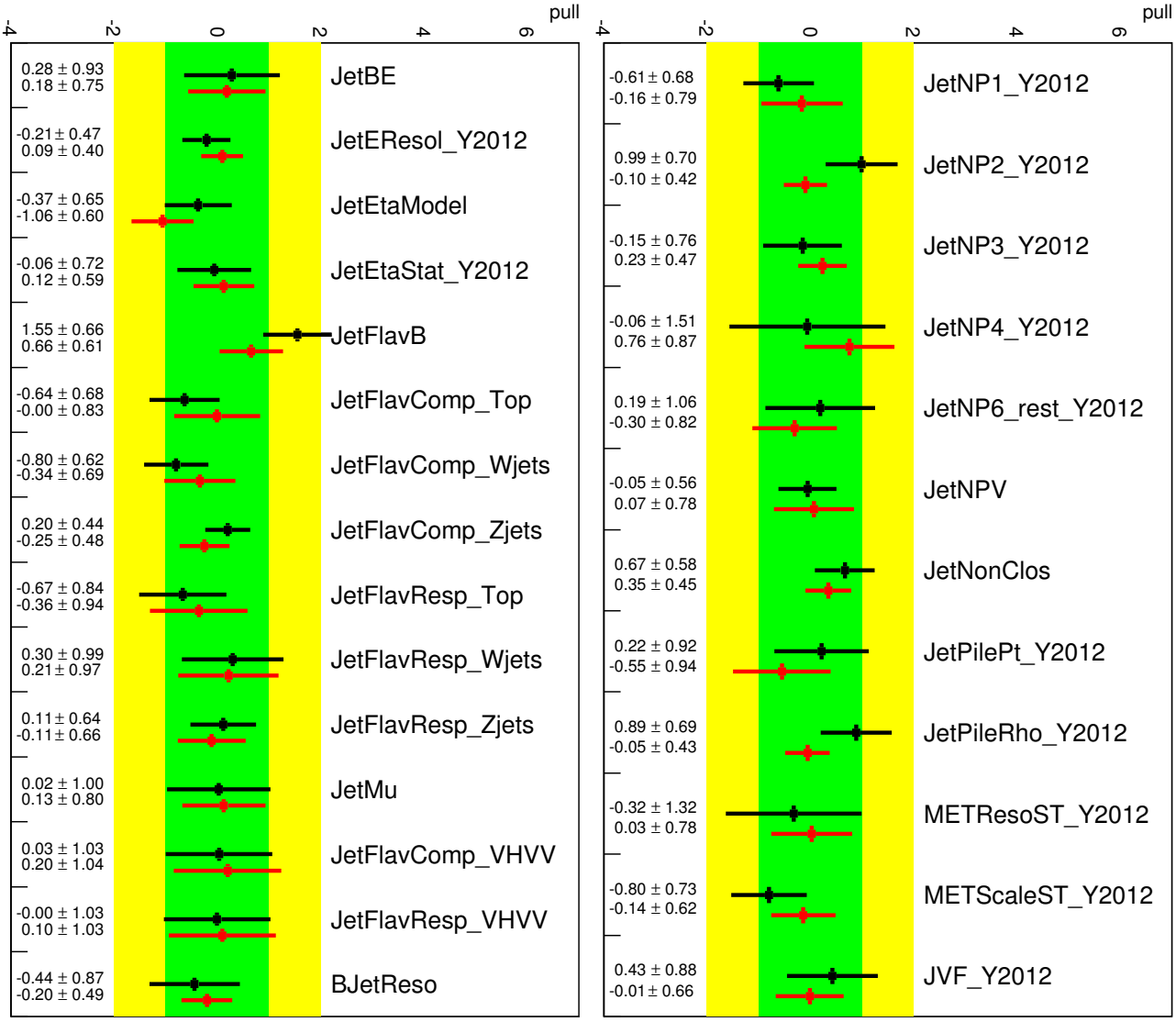

Figure 59: m_{jj} vs MVA pull plots for 0+1+2 fit: Jet NPs.

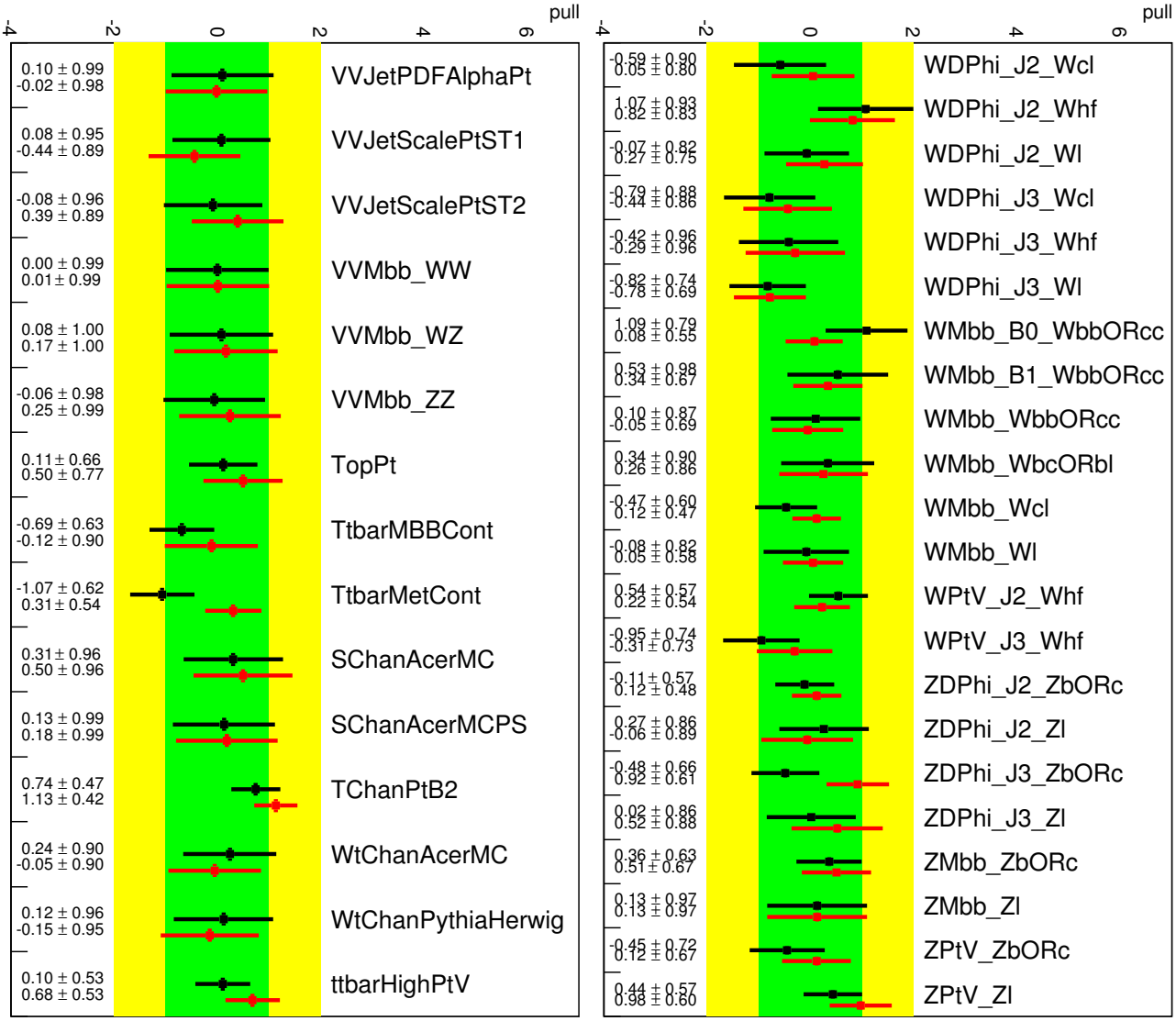

Figure 60: m_{jj} vs MVA pull plots for 0+1+2 fit: Diboson and Top related uncertainties.

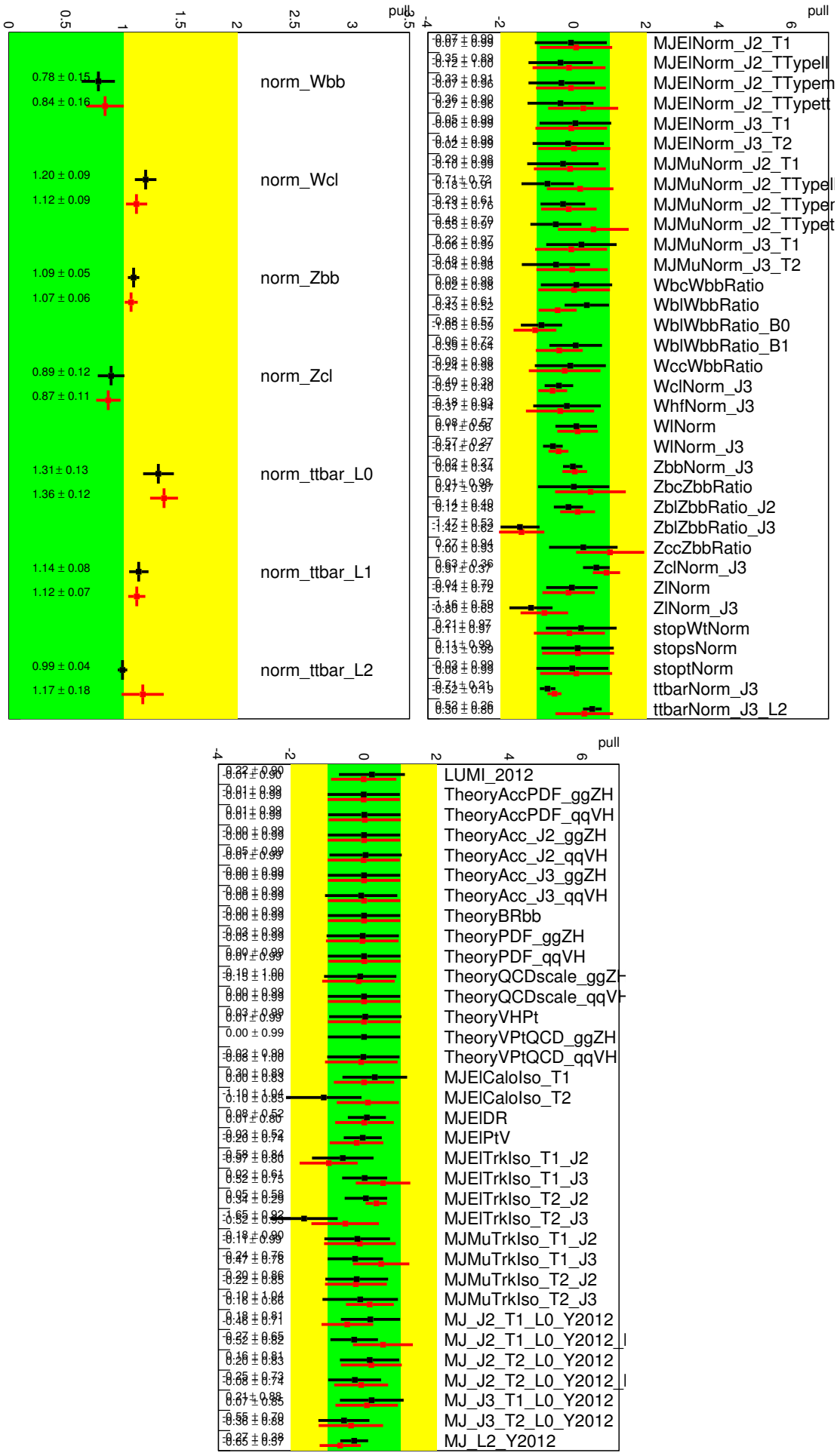

Figure 61: m_{jj} vs MVA pull plots for 0+1+2 fit: Normalization and residual uncertainties.

8.6.4 Nuisance Parameter Ranking Plots

After the MLL value is found, each NP is pulled $\pm 1\sigma$ and the likelihood is maximized again. The change in the best fit μ value gives the inclusive sensitivity of the measured value to the give NP. The impact is judged using fits to data. Figures 62 and 63 show the ranking plots for the full dijet masss analysis, then the 0 through 2-lepton analysis individually. Figures 64 and 65 show the ranking plots for the full MVA analysis, then the 0 through 2-lepton analysis individually. The plots show both pre-fit and post-fit impacts, together with displaying the pulls on the data. All plots are obtained through a fit on the data

8.6.4.1 Dijet Mass Analysis

8.6.4.2 Ranking plots for MVA

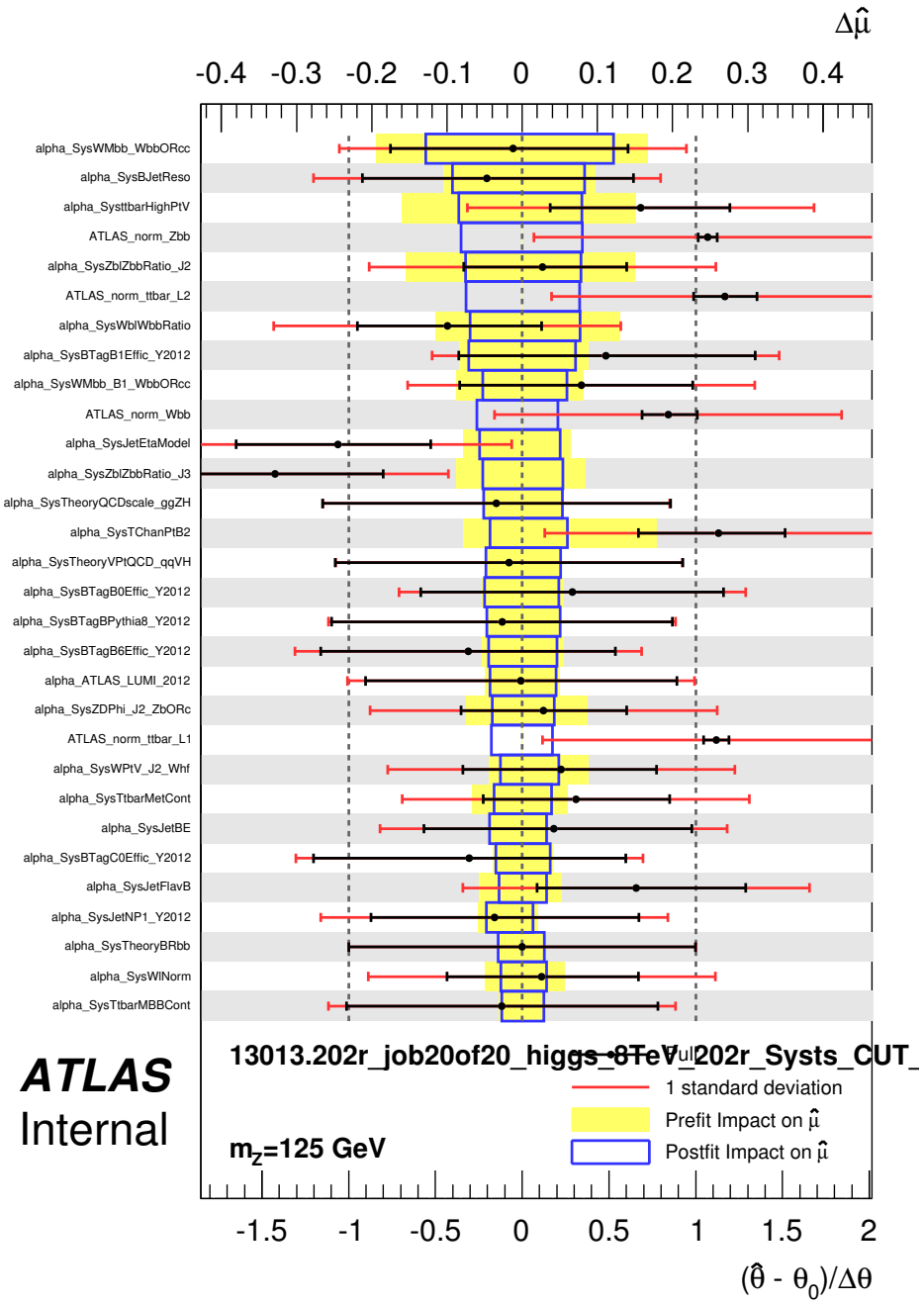

Figure 62: Ranking of systematic uncertainties in the dijet masss analysis for the combined fit.

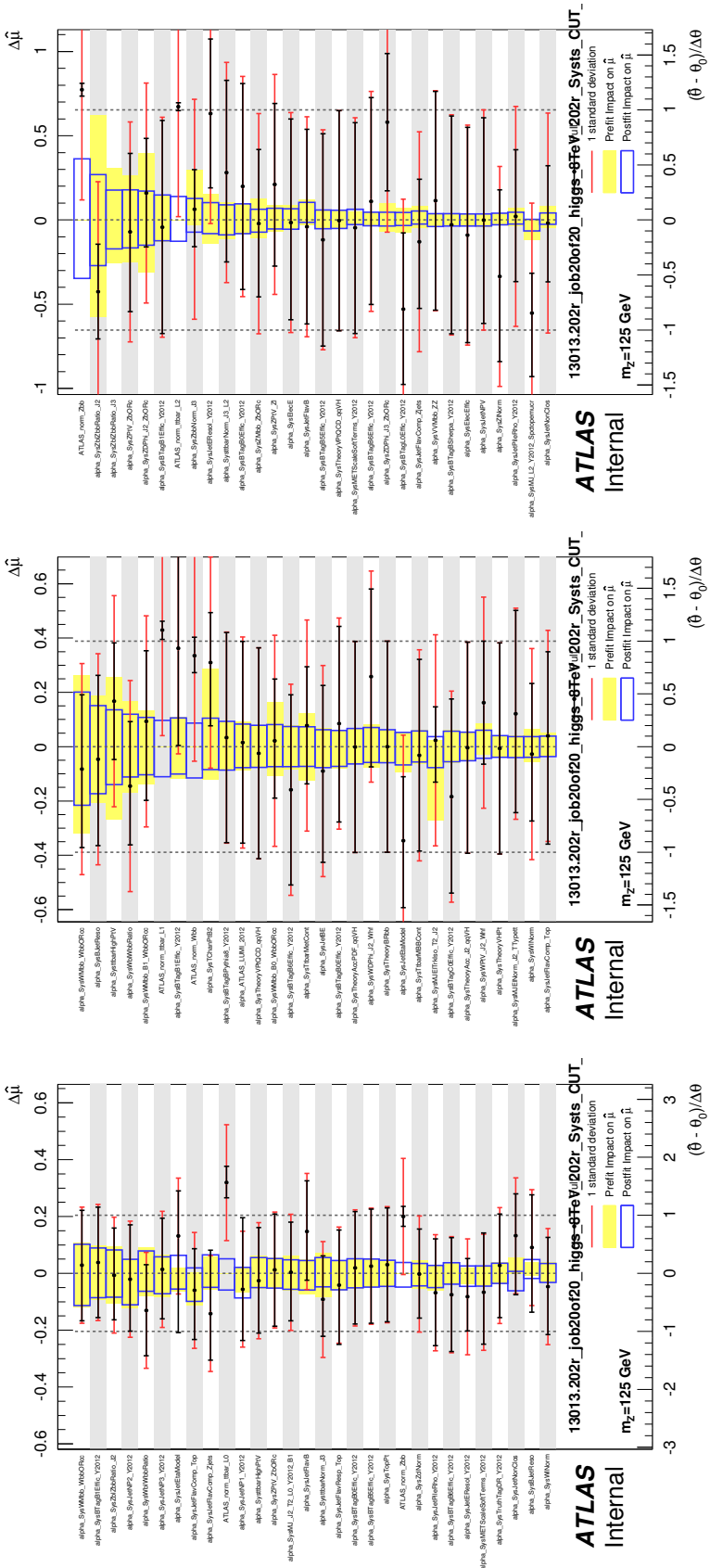

(a) 0-lepton, cut based (b) 1-lepton, cut based (c) 2-leptons, cut based

Figure 63: Ranking of systematic uncertainties in the dijet mass analysis for the , 1 lepton and 2-leptons channels.

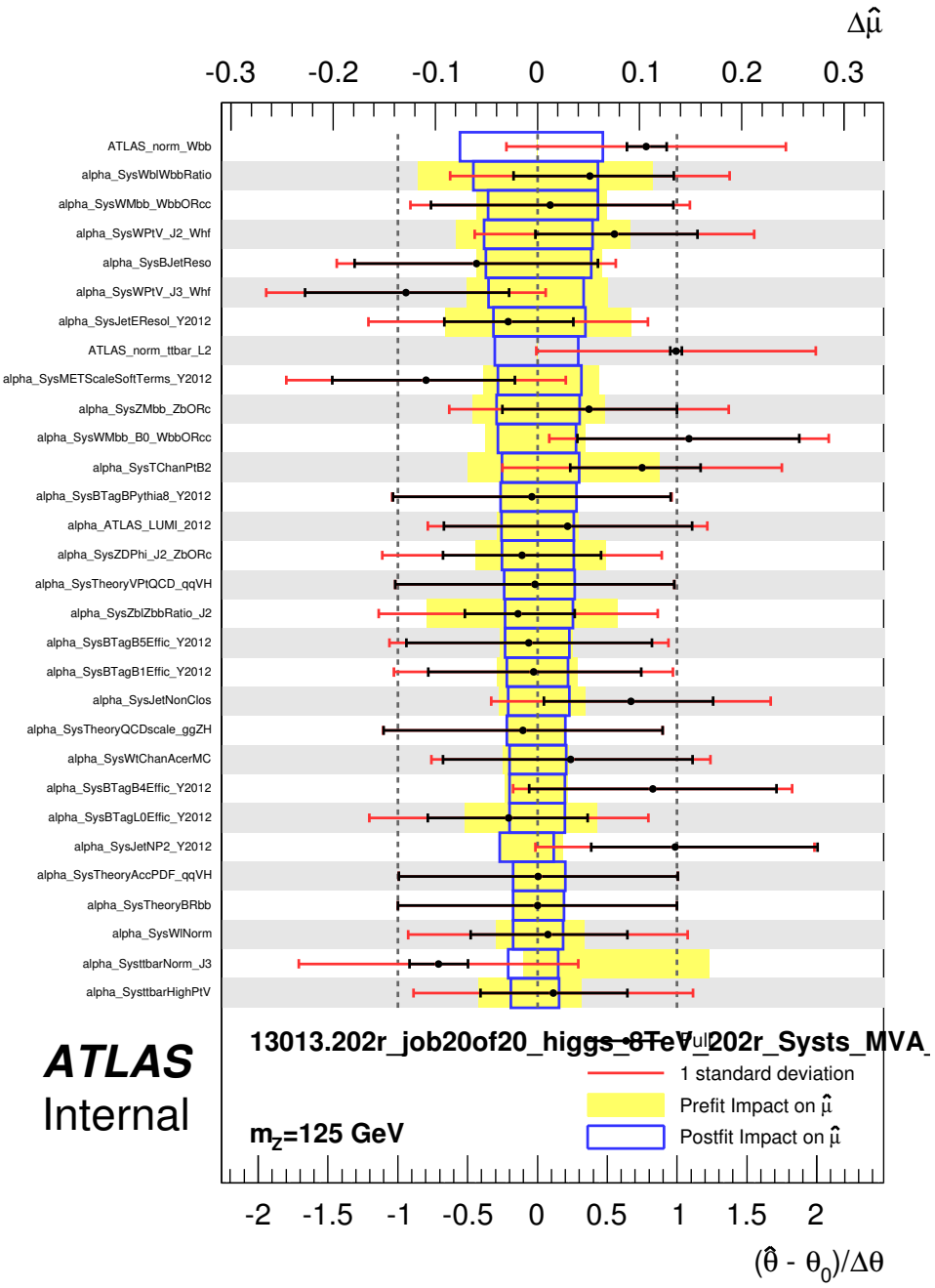

Figure 64: Ranking of systematic uncertainties in the MVA analysis for the combined fit.

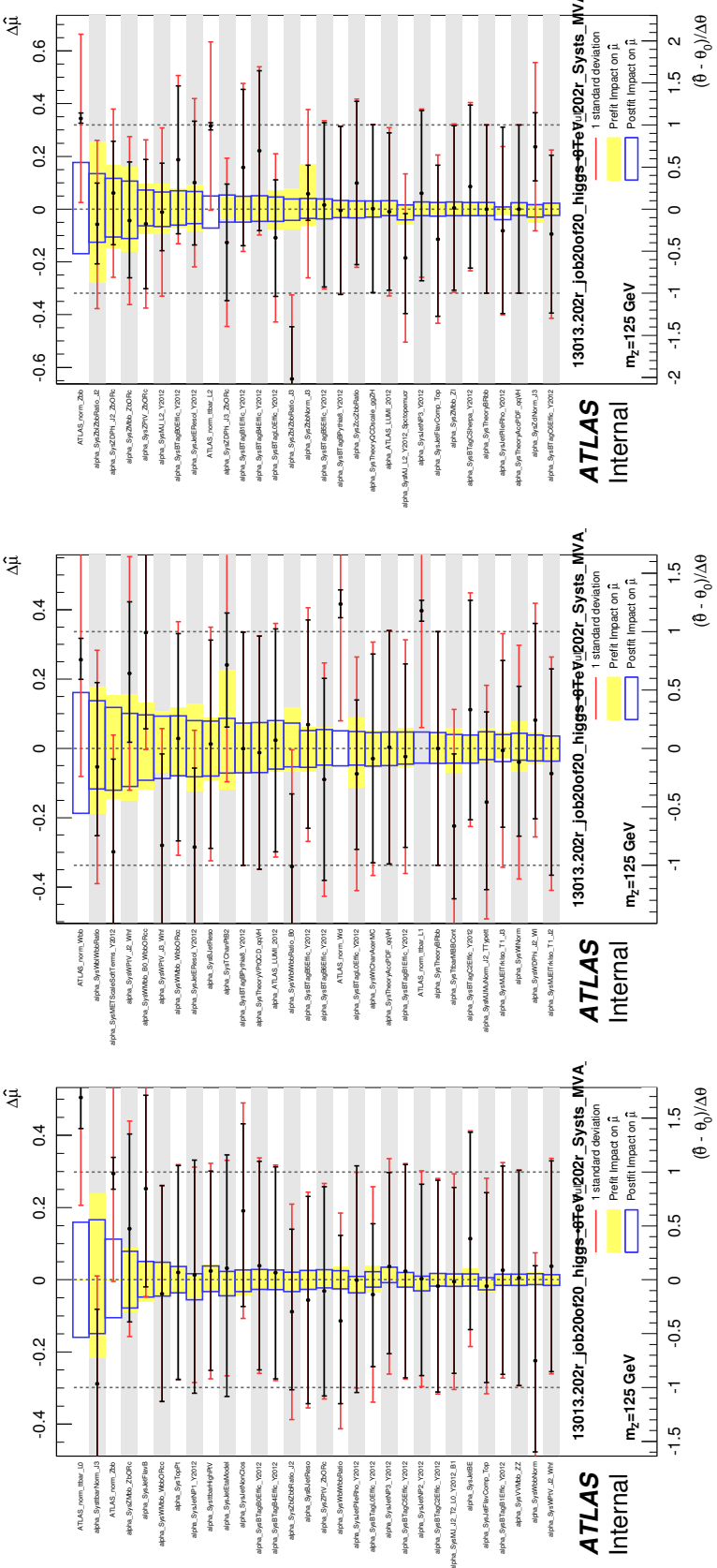

(a) 0-lepton, mva (b) 1-lepton, mva (c) 2-leptons, mva

Figure 65: Ranking of systematic uncertainties in the MVA analysis for the 0-lepton, 1 lepton and 2-leptons channels.

8.7 Dijet Mass Analysis Post Fit Plots

In the following sections post-fit plots corresponding to unconditionnal μ fits to the data for the dijet masss analysis are presented. In all cases the MC expectations have been adapted to the pulls from the data in the combined 0+1+2 lepton fit. As a comparison, the total nominal background prediction is indicated by the dashed blue curve.

In Figures 66 - 68, 69 - 71, 72 - 74 post-fit plots for the m_{bb} shape analysis are shown for the 0, 1 and 2-lepton channel respectively in the various 1-tag and 2-tag categories in different p_{T}^{V} bins.

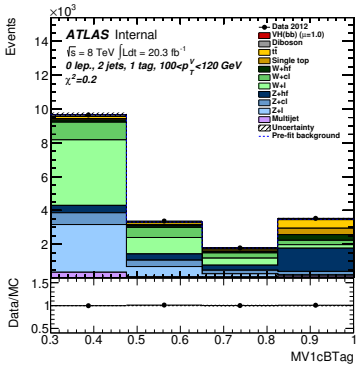

(a) $p_{\mathrm{T}}^{V} < 120$ GeV, 2 jets, 1-tag

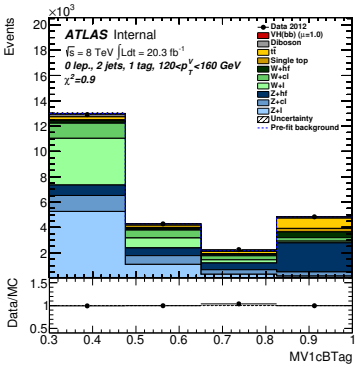

(b) $p_{\mathrm{T}}^{V} > 120$ GeV, 2 jets, 1-tag

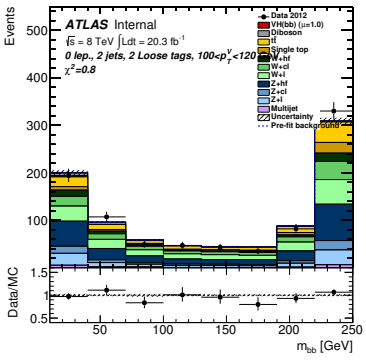

(c) $100 < p_{\mathrm{T}}^{V} < 120$ GeV, 2 jets, LL

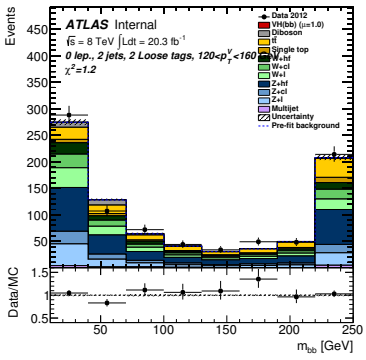

(d) $120 < p_{\mathrm{T}}^{V} < 160$ GeV, 2 jets, LL

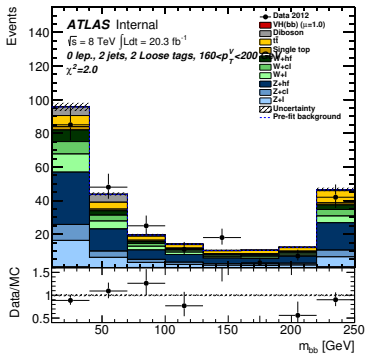

(e) $160 < p_{\mathrm{T}}^{V} < 200$ GeV, 2 jets, LL

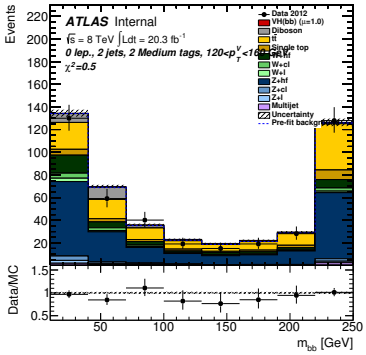

(f) $100 < p_{\mathrm{T}}^{V} < 120$ GeV, 2 jets, MM

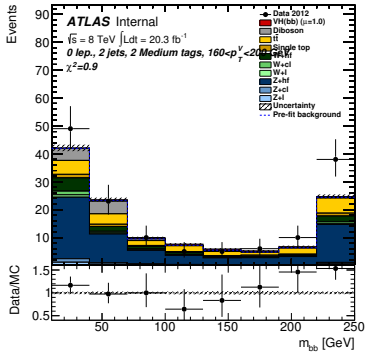

(g) $120 < p_{\mathrm{T}}^{V} < 160$ GeV, 2 jets, MM (h) $160 < p_{\mathrm{T}}^{V} < 200$ GeV, 2 jets, MM

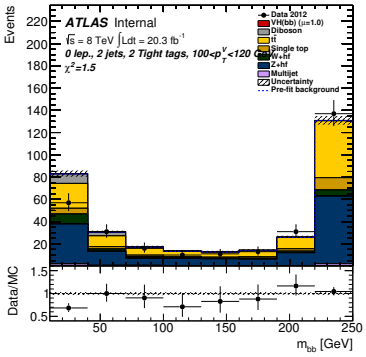

(i) $100 < p_{\mathrm{T}}^{V} < 120$ GeV, 2 jets, TT

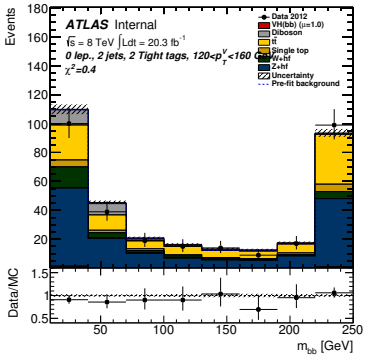

(j) $120 < p_{\mathrm{T}}^{V} < 160$ GeV, 2 jets, TT

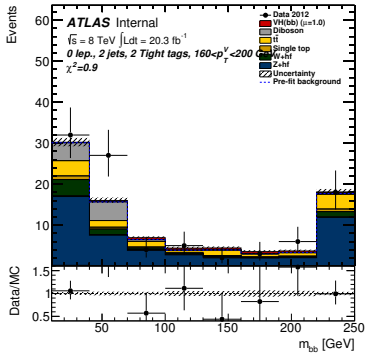

(k) $160 < p_{\mathrm{T}}^{V} < 200$ GeV, 2 jets, TT

Figure 66: Post-fit plots for m_{jj} distribution in 0-lepton events in the 1-tag (where mv1c is used in the fit) *LL*, *MM* and *TT* tag categories for the 2-jets events. Plots are shown for $100 < p_{\mathrm{T}}^{V} < 120$ GeV, $120 < p_{\mathrm{T}}^{V} < 160$ GeVand $160 < p_{\mathrm{T}}^{V} < 200$ GeV. The pre-fit background expectation is indicated by the dashed blue line.

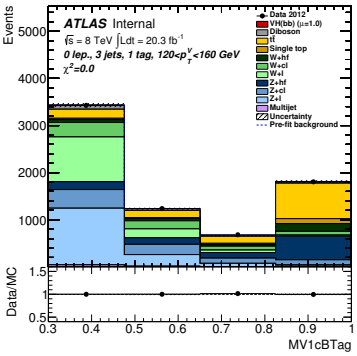

(a) $p_{\mathrm{T}}^{V} > 120$ GeV, 3 jets, 1-tag

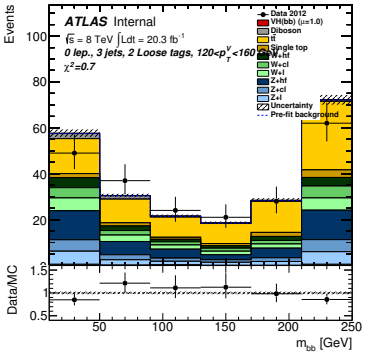

(b) $120 < p_{\mathrm{T}}^{V} < 160$ GeV, 3 jets, LL

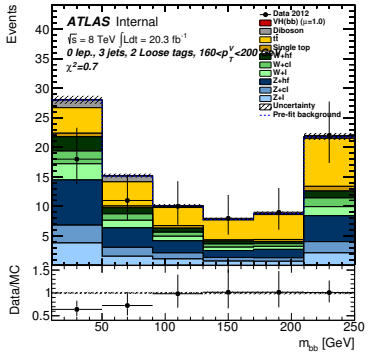

(c) $160 < p_{\mathrm{T}}^{V} < 200$ GeV, 3 jets, LL

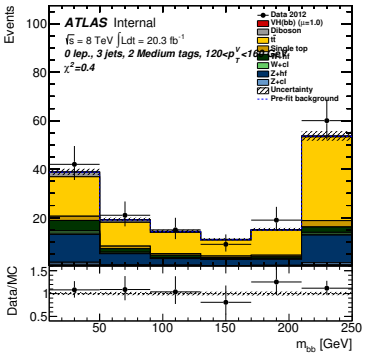

(d) $120 < p_{\mathrm{T}}^{V} < 160$ GeV, 3 jets, MM

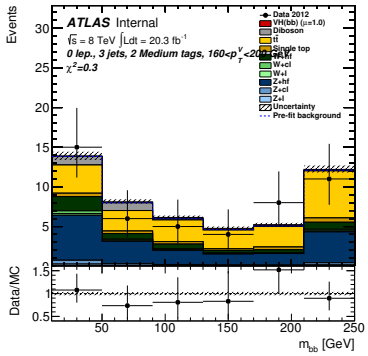

(e) $160 < p_{\mathrm{T}}^{V} < 200$ GeV, 3 jets, MM

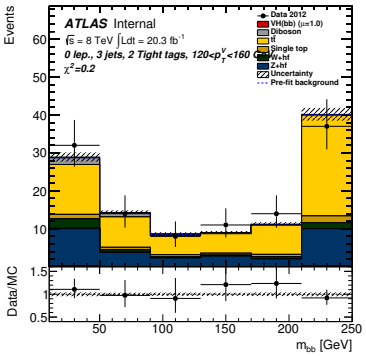

(f) $120 < p_{\mathrm{T}}^{V} < 160$ GeV, 3 jets, TT

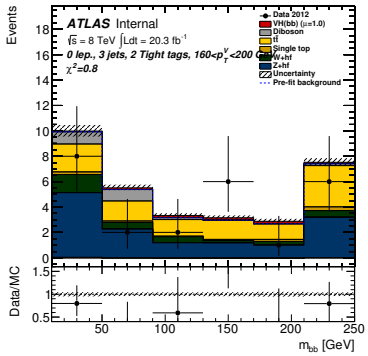

(g) $160 < p_{\mathrm{T}}^{V} < 200$ GeV, 3 jets, TT

Figure 67: Post-fit plots for m_{jj} distribution in 0-lepton events in the 1-tag (where mv1c is used in the fit) LL, MM and TT tag categories for the 3-jets events. Plots are shown for $120 < p_{\mathrm{T}}^{V} < 160$ GeVand $160 < p_{\mathrm{T}}^{V} < 200$ GeV. The pre-fit background expectation is indicated by the dashed blue line.

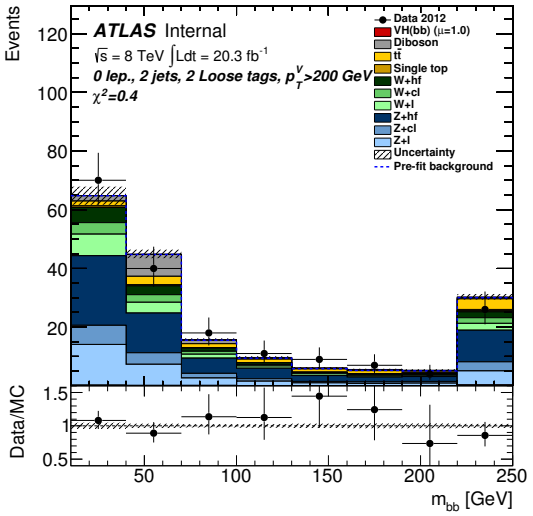

(a) $p_{\mathrm{T}}^{V} > 200$ GeV, 2 jets, LL

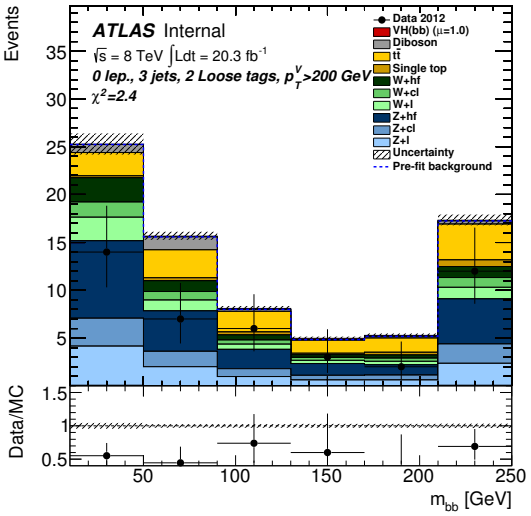

(b) $p_{\mathrm{T}}^{V} > 200$ GeV, 3 jets, LL

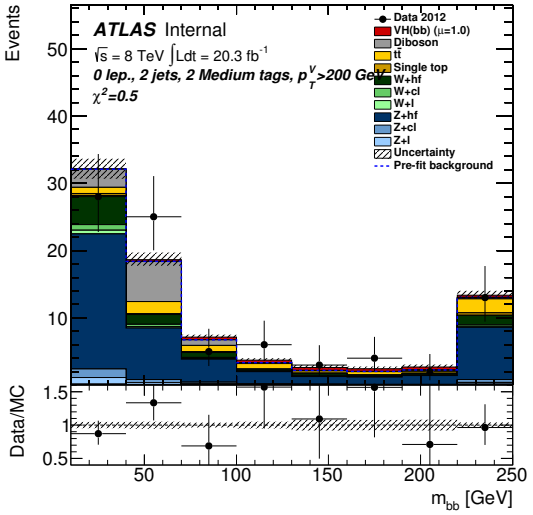

(c) $p_{\mathrm{T}}^{V} > 200$ GeV, 2 jets, MM

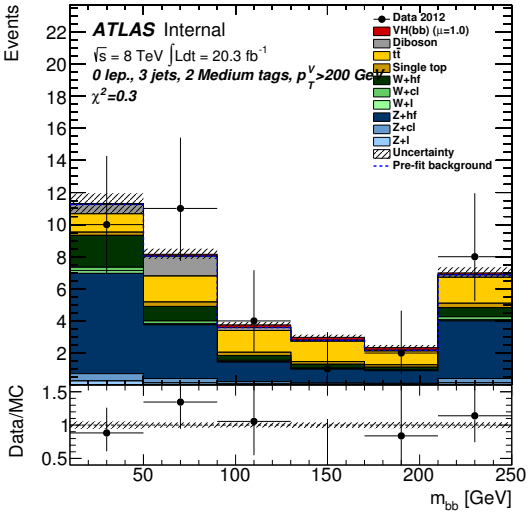

(d) $p_{\mathrm{T}}^{V} > 200$ GeV, 3 jets, MM

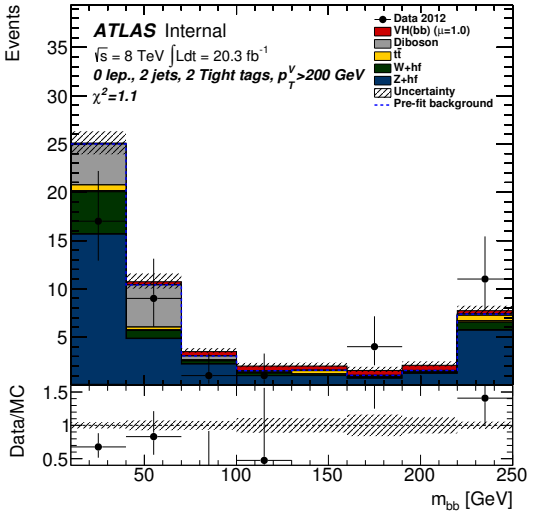

(e) $p_{\mathrm{T}}^{V} > 200$ GeV, 2 jets, TT

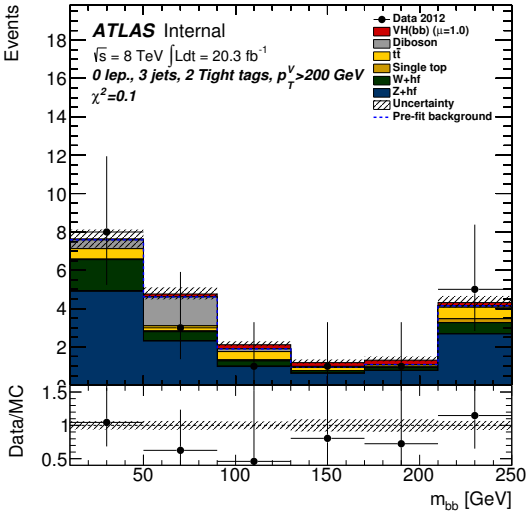

(f) $p_{\mathrm{T}}^{V} > 200$ GeV, 3 jets, TT

Figure 68: Post-fit plots for m_{jj} distribution in 0-lepton events in the LL, MM and TT tag categories for the 2-jets and the 3-jets events. Plots are shown for $p_{\mathrm{T}}^{V} > 200$ GeV. The pre-fit background expectation is indicated by the dashed blue line.

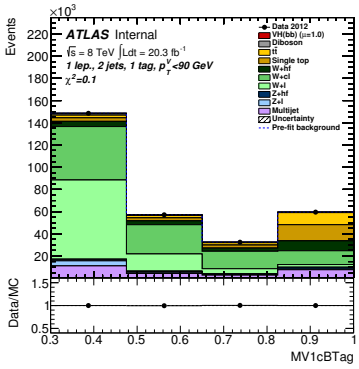

(a) $p_{\mathrm{T}}^{V} < 120$ GeV, 2 jets, 1-tag

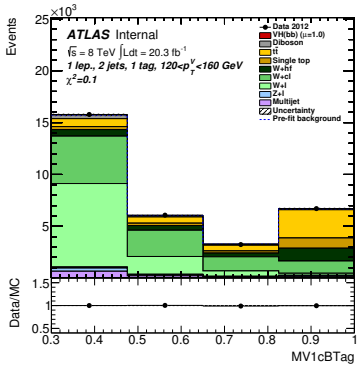

(b) $p_{\mathrm{T}}^{V} > 120$ GeV, 2 jets, 1-tag

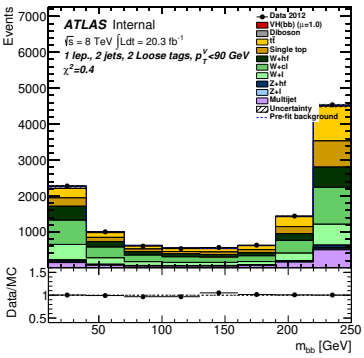

(c) $p_{\mathrm{T}}^{V} < 90$ GeV, 2 jets, LL

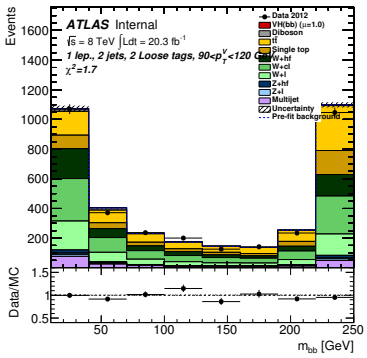

(d) $90 < p_{\mathrm{T}}^{V} < 120$ GeV, 2 jets, LL

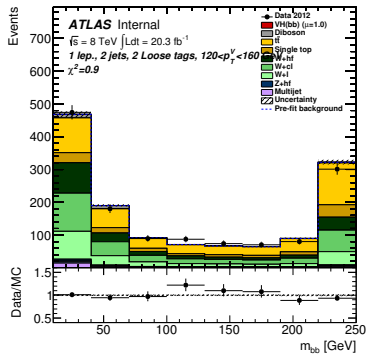

(e) $120 < p_{\mathrm{T}}^{V} < 160$ GeV, 2 jets, LL

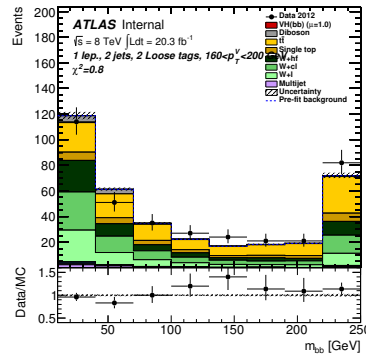

(f) $160 < p_{\mathrm{T}}^{V} < 200$ GeV, 2 jets, LL

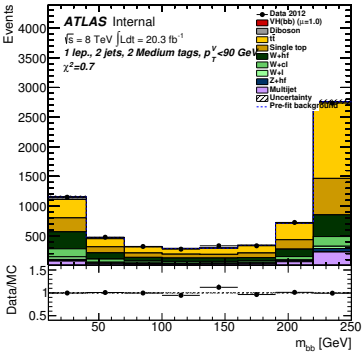

(g) $p_{\mathrm{T}}^{V} < 90$ GeV, 2 jets, MM

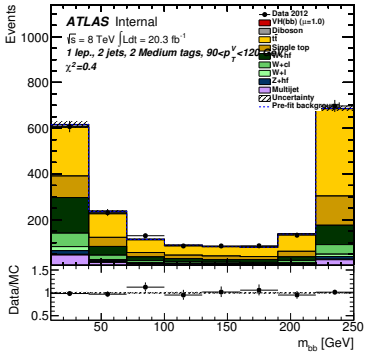

(h) $90 < p_{\mathrm{T}}^{V} < 120$ GeV, 2 jets, MM

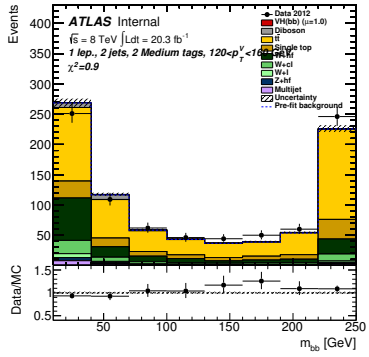

(i) $120 < p_{\mathrm{T}}^{V} < 160$ GeV, 2 jets, MM

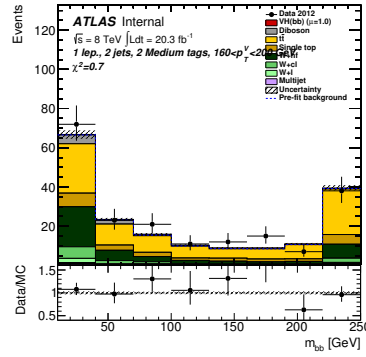

(j) $160 < p_{\mathrm{T}}^{V} < 200$ GeV, 2 jets, MM

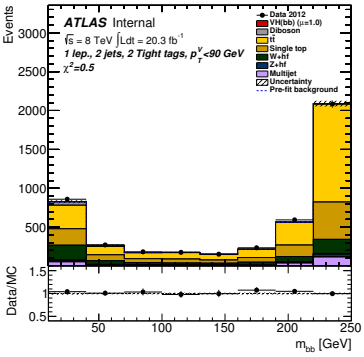

(k) $p_{\mathrm{T}}^{V} < 90$ GeV, 2 jets, TT

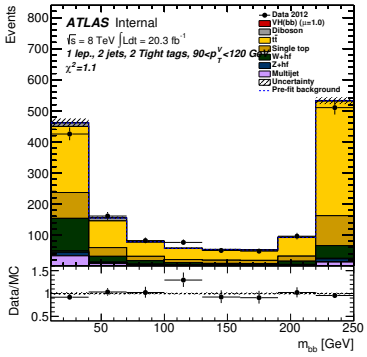

(l) $90 < p_{\mathrm{T}}^{V} < 120$ GeV, 2 jets, TT

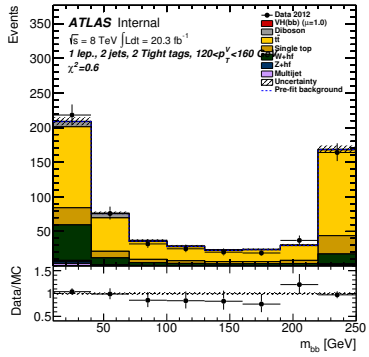

(m) $120 < p_{\mathrm{T}}^{V} < 160$ GeV, 2 jets, TT

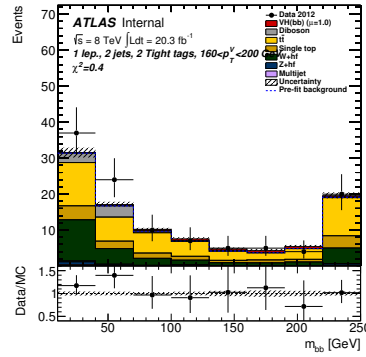

(n) $160 < p_{\mathrm{T}}^{V} < 200$ GeV, 2 jets, TT

Figure 69: Post-fit plots for m_{jj} distribution in 1-lepton events in the 1-tag (where mv1c is used in the fit) *LL*, *MM* and *TT* tag categories for the 2-jets events. Plots are shown for $p_{\mathrm{T}}^{V} < 90$ GeV, $90 < p_{\mathrm{T}}^{V} < 120$ GeV, $120 < p_{\mathrm{T}}^{V} < 160$ GeVand $160 < p_{\mathrm{T}}^{V} < 200$ GeV. The pre-fit background expectation is indicated by the dashed blue line.

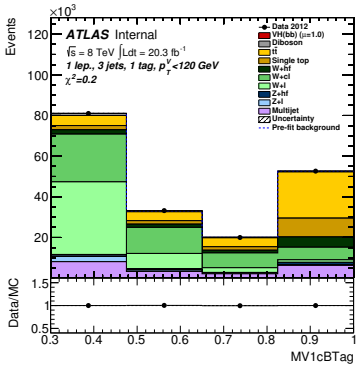

(a) $p_{\mathrm{T}}^{V} < 120$ GeV, 3 jets, 1-tag

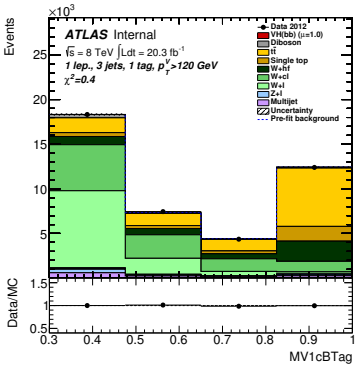

(b) $p_{\mathrm{T}}^{V} > 120$ GeV, 3 jets, 1-tag

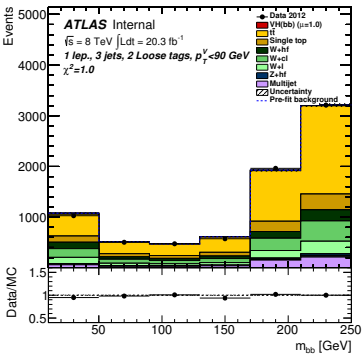

(c) $p_{\mathrm{T}}^{V} < 90$ GeV, 3 jets, LL

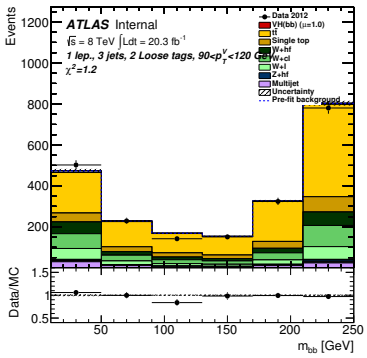

(d) $90 < p_{\mathrm{T}}^{V} < 120$ GeV, 3 jets, LL

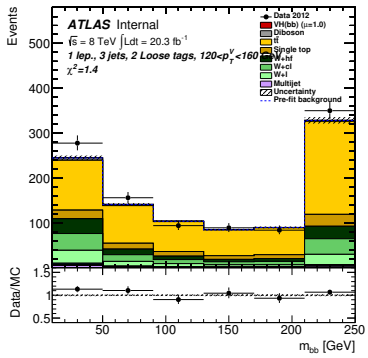

(e) $120 < p_{\mathrm{T}}^{V} < 160$ GeV, 3 jets, LL

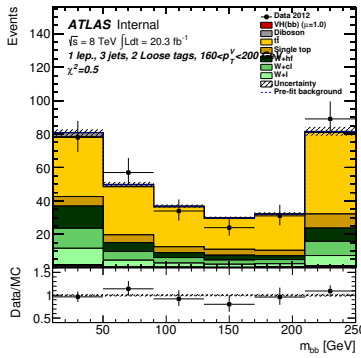

(f) $160 < p_{\mathrm{T}}^{V} < 200$ GeV, 3 jets, LL

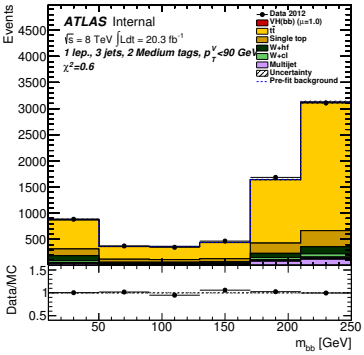

(g) $p_{\mathrm{T}}^{V} < 90$ GeV, 3 jets, MM

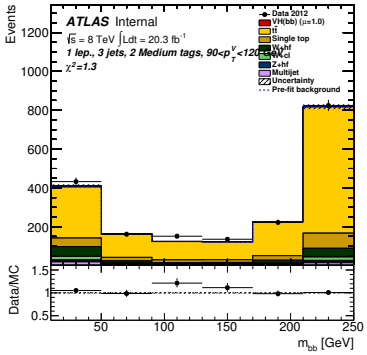

(h) $90 < p_{\mathrm{T}}^{V} < 120$ GeV, 3 jets, MM

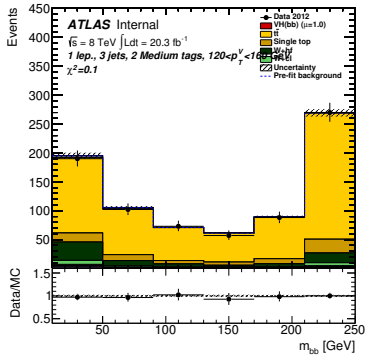

(i) $120 < p_{\mathrm{T}}^{V} < 160$ GeV, 3 jets, MM

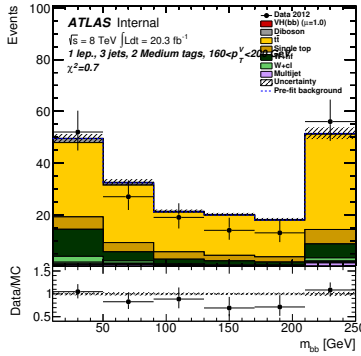

(j) $160 < p_{\mathrm{T}}^{V} < 200$ GeV, 3 jets, MM

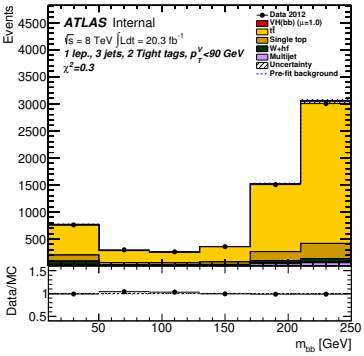

(k) $p_{\mathrm{T}}^{V} < 90$ GeV, 3 jets, TT

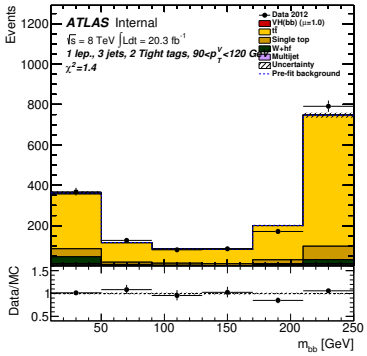

(l) $90 < p_{\mathrm{T}}^{V} < 120$ GeV, 3 jets, TT

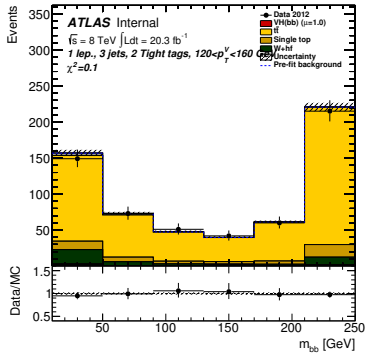

(m) $120 < p_{\mathrm{T}}^{V} < 160$ GeV, 3 jets, TT

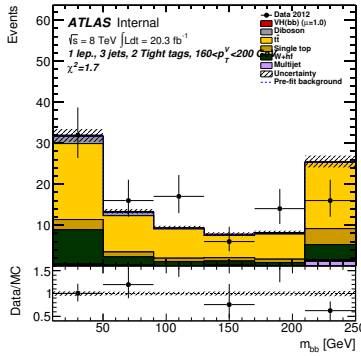

(n) $160 < p_{\mathrm{T}}^{V} < 200$ GeV, 3 jets, TT

Figure 70: Post-fit plots for m_{jj} distribution in 1-lepton events in the 1-tag (where mv1c is used in the fit) *LL*, *MM* and *TT* tag categories for the 3-jets events. Plots are shown for $p_{\mathrm{T}}^{V} < 90$ GeV, $90 < p_{\mathrm{T}}^{V} < 120$ GeV, $120 < p_{\mathrm{T}}^{V} < 160$ GeVand $160 < p_{\mathrm{T}}^{V} < 200$ GeV. The pre-fit background expectation is indicated by the dashed blue line.

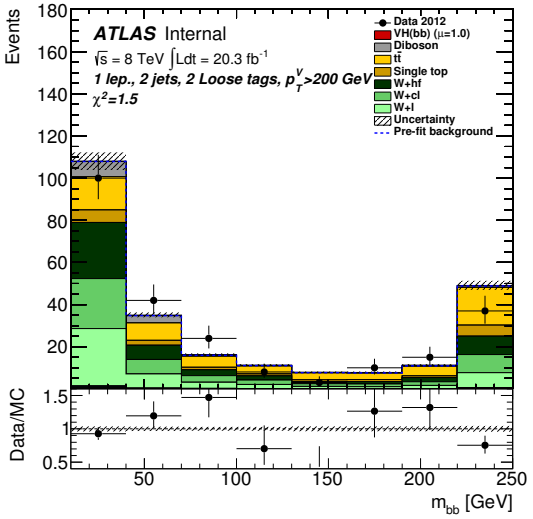

(a) $p_{\mathrm{T}}^{V} > 200$ GeV, 2 jets, LL

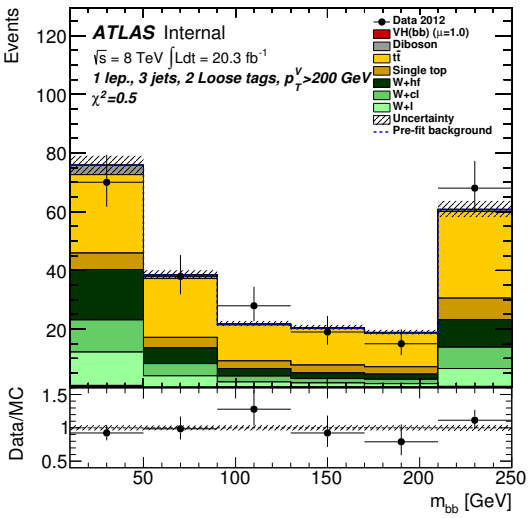

(b) $p_{\mathrm{T}}^{V} > 200$ GeV, 3 jets, LL

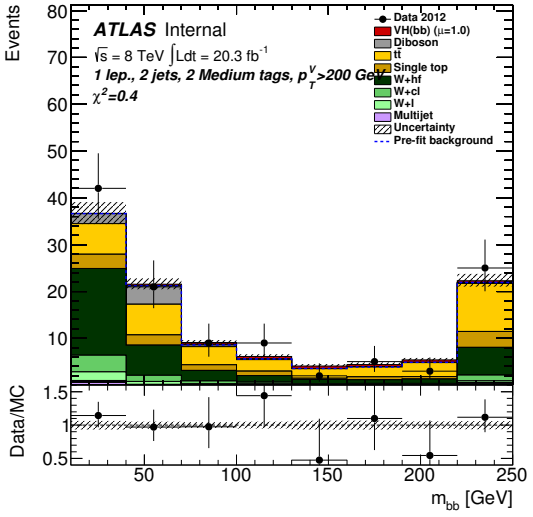

(c) $p_{\mathrm{T}}^{V} > 200$ GeV, 2 jets, MM

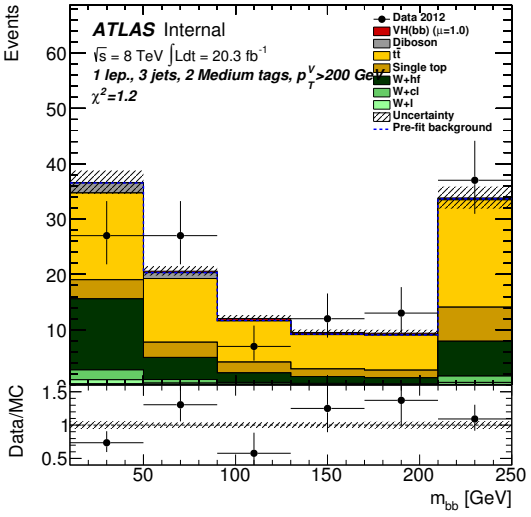

(d) $p_{\mathrm{T}}^{V} > 200$ GeV, 3 jets, MM

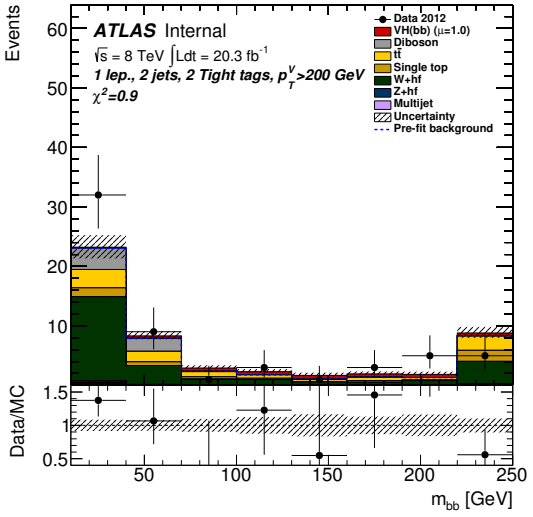

(e) $p_{\mathrm{T}}^{V} > 200$ GeV, 2 jets, TT

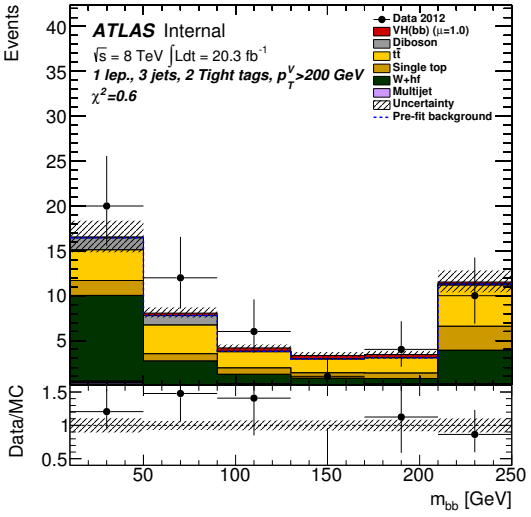

(f) $p_{\mathrm{T}}^{V} > 200$ GeV, 3 jets, TT

Figure 71: Post-fit plots for m_{jj} distribution in 1-lepton events in the LL, MM and TT tag categories for the 2-jets and the 3-jets events. Plots are shown for $p_{\mathrm{T}}^{V} > 200$ GeV. The pre-fit background expectation is indicated by the dashed blue line.

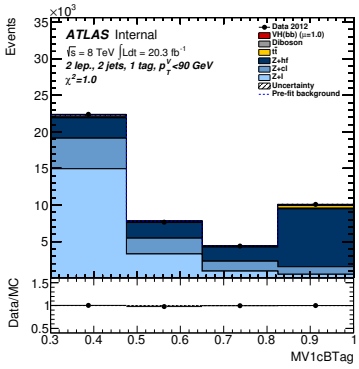

(a) $p_{\mathrm{T}}^{V} < 120$ GeV, 2 jets, 1-tag

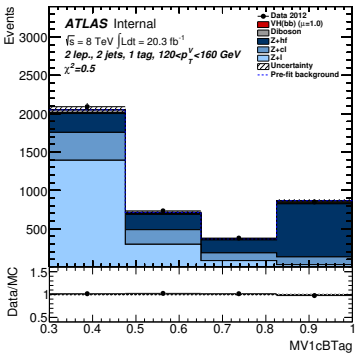

(b) $p_{\mathrm{T}}^{V} > 120$ GeV, 2 jets, 1-tag

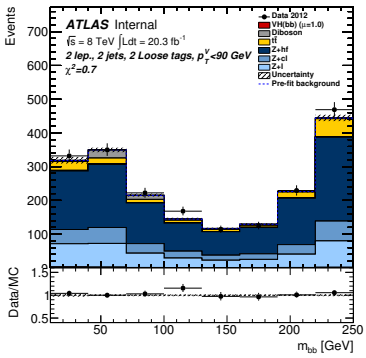

(c) $p_{\mathrm{T}}^{V} < 90$ GeV, 2 jets, LL

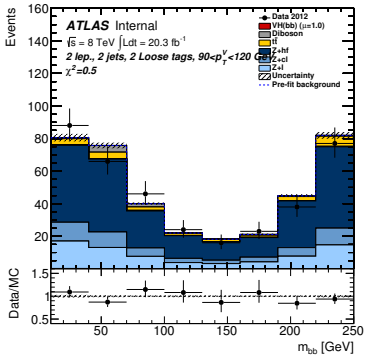

(d) $90 < p_{\mathrm{T}}^{V} < 120$ GeV, 2 jets, LL

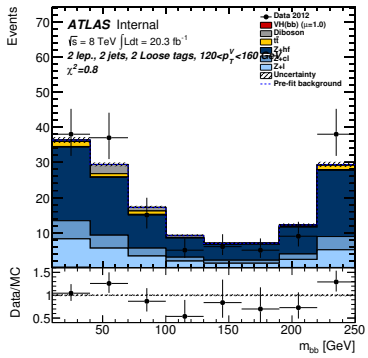

(e) $120 < p_{\mathrm{T}}^{V} < 160$ GeV, 2 jets, LL

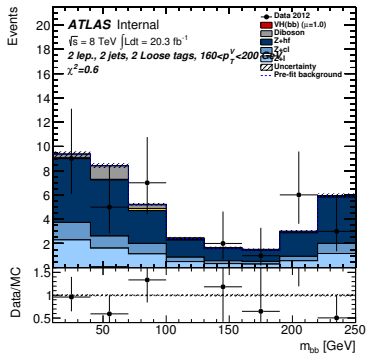

(f) $160 < p_{\mathrm{T}}^{V} < 200$ GeV, 2 jets, LL

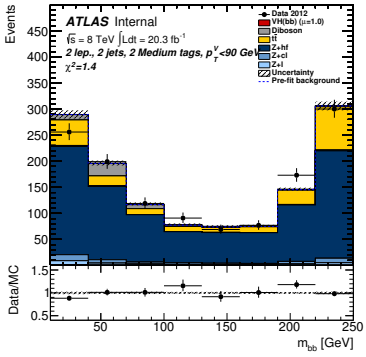

(g) $p_{\mathrm{T}}^{V} < 90$ GeV, 2 jets, MM

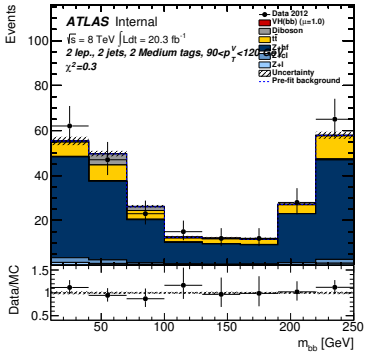

(h) $90 < p_{\mathrm{T}}^{V} < 120$ GeV, 2 jets, MM

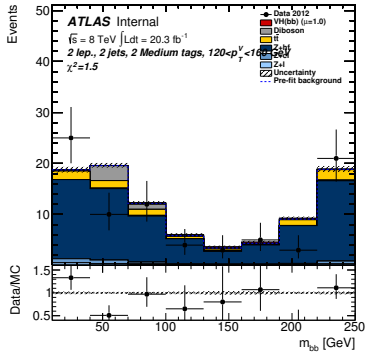

(i) $120 < p_{\mathrm{T}}^{V} < 160$ GeV, 2 jets, MM

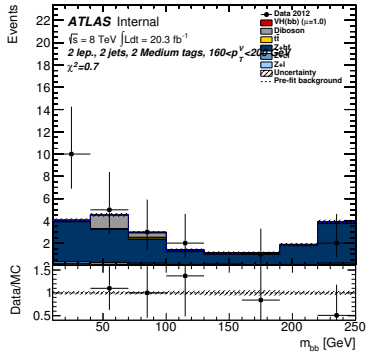

(j) $160 < p_{\mathrm{T}}^{V} < 200$ GeV, 2 jets, MM

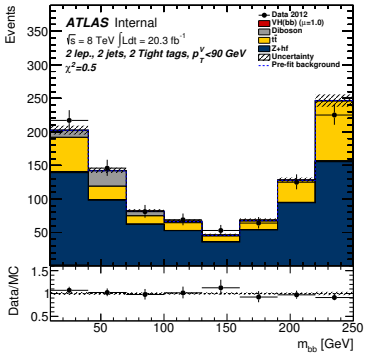

(k) $p_{\mathrm{T}}^{V} < 90$ GeV, 2 jets, TT

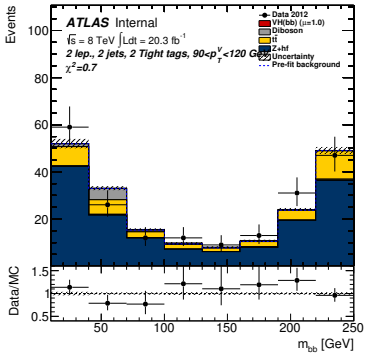

(l) $90 < p_{\mathrm{T}}^{V} < 120$ GeV, 2 jets, TT

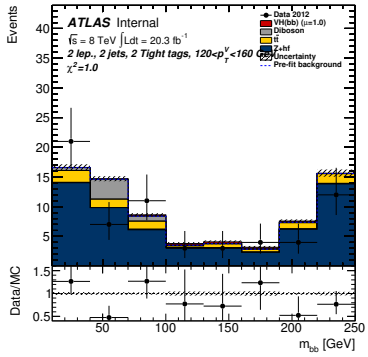

(m) $120 < p_{\mathrm{T}}^{V} < 160$ GeV, 2 jets, TT

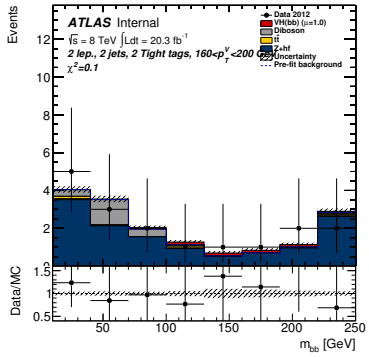

(n) $160 < p_{\mathrm{T}}^{V} < 200$ GeV, 2 jets, TT

Figure 72: Post-fit plots for m_{jj} distribution in 2-lepton events in the 1-tag (where mv1c is used in the fit) *LL*, *MM* and *TT* tag categories for the 2-jets events. Plots are shown for $p_{\mathrm{T}}^{V} < 90$ GeV, $90 < p_{\mathrm{T}}^{V} < 120$ GeV, $120 < p_{\mathrm{T}}^{V} < 160$ GeVand $160 < p_{\mathrm{T}}^{V} < 200$ GeV. The pre-fit background expectation is indicated by the dashed blue line.

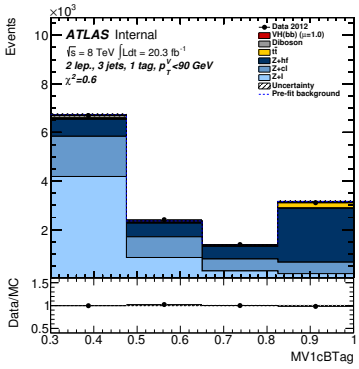

(a) $p_{\mathrm{T}}^{V} < 120$ GeV, 3 jets, 1-tag

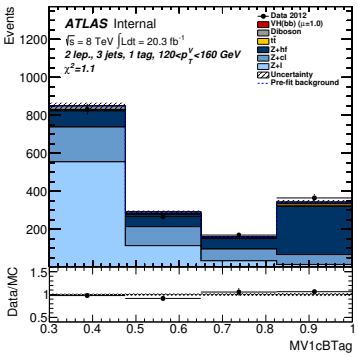

(b) $p_{\mathrm{T}}^{V} > 120$ GeV, 3 jets, 1-tag

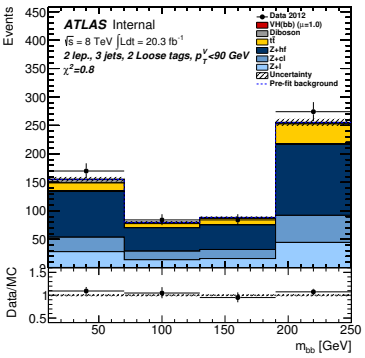

(c) $p_{\mathrm{T}}^{V} < 90$ GeV, 3 jets, LL

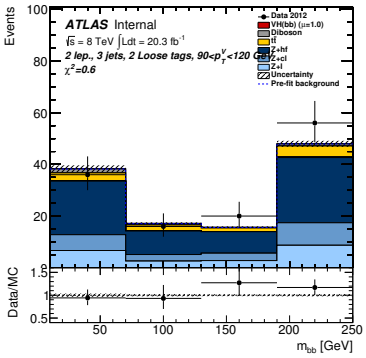

(d) $90 < p_{\mathrm{T}}^{V} < 120$ GeV, 3 jets, LL

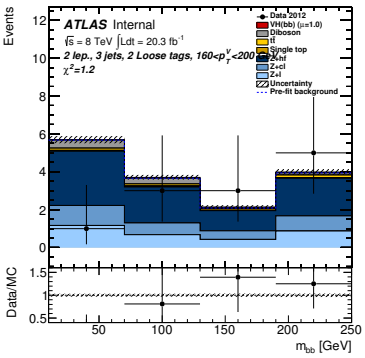

(e) $120 < p_{\mathrm{T}}^{V} < 160$ GeV, 3 jets, LL

(f) $160 < p_{\mathrm{T}}^{V} < 200$ GeV, 3 jets, LL

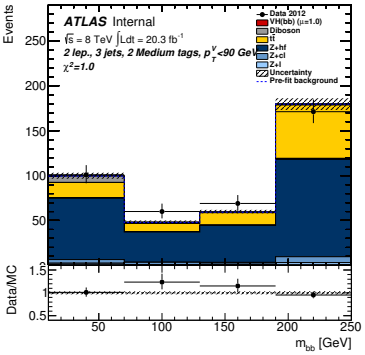

(g) $p_{\mathrm{T}}^{V} < 90$ GeV, 3 jets, MM

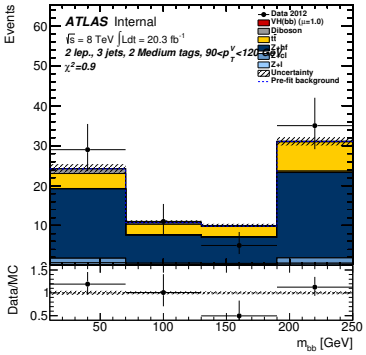

(h) $90 < p_{\mathrm{T}}^{V} < 120$ GeV, 3 jets, MM

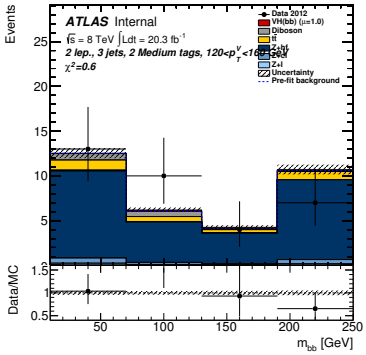

(i) $120 < p_{\mathrm{T}}^{V} < 160$ GeV, 3 jets, MM

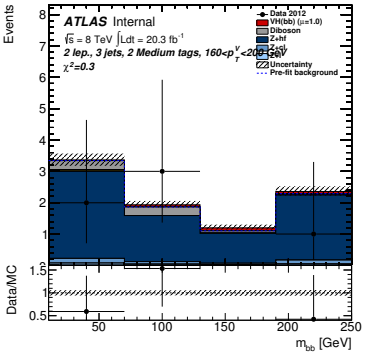

(j) $160 < p_{\mathrm{T}}^{V} < 200$ GeV, 3 jets, MM

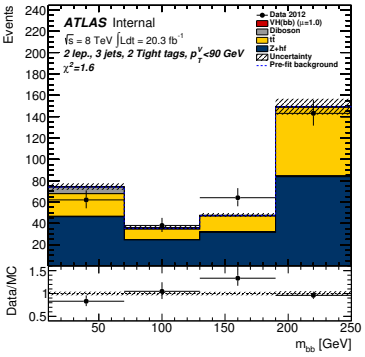

(k) $p_{\mathrm{T}}^{V} < 90$ GeV, 3 jets, TT

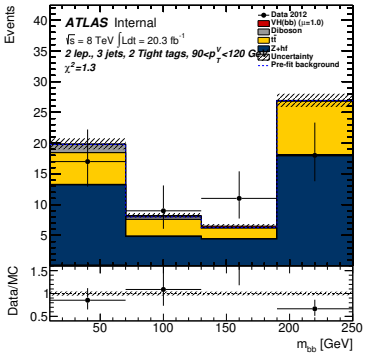

(l) $90 < p_{\mathrm{T}}^{V} < 120$ GeV, 3 jets, TT

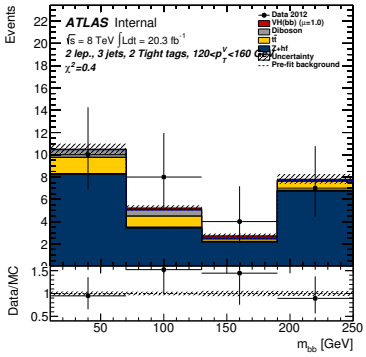

(m) $120 < p_{\mathrm{T}}^{V} < 160$ GeV, 3 jets, TT

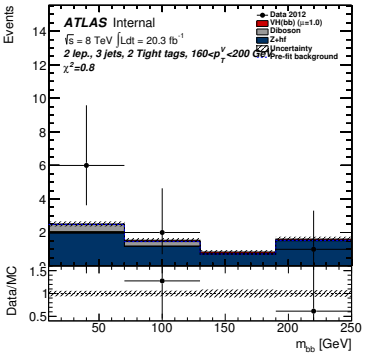

(n) $160 < p_{\mathrm{T}}^{V} < 200$ GeV, 3 jets, TT

Figure 73: Post-fit plots for m_{jj} distribution in 2-lepton events in the 1-tag (where mv1c is used in the fit) *LL*, *MM* and *TT* tag categories for the 3-jets events. Plots are shown for $p_{\mathrm{T}}^{V} < 90$ GeV, $90 < p_{\mathrm{T}}^{V} < 120$ GeV, $120 < p_{\mathrm{T}}^{V} < 160$ GeVand $160 < p_{\mathrm{T}}^{V} < 200$ GeV. The pre-fit background expectation is indicated by the dashed blue line.

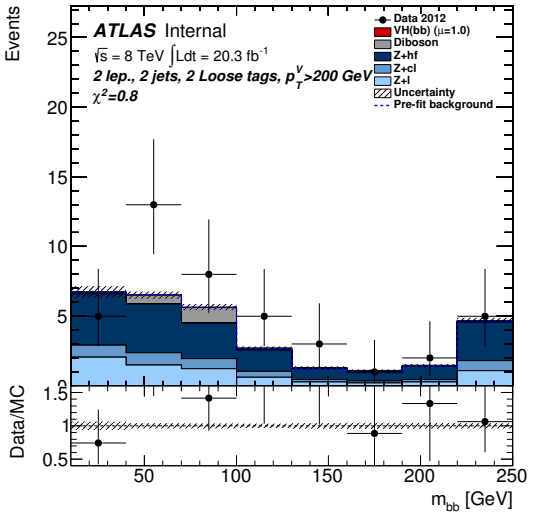

(a) $p_{\mathrm{T}}^{V} > 200$ GeV, 2 jets, LL

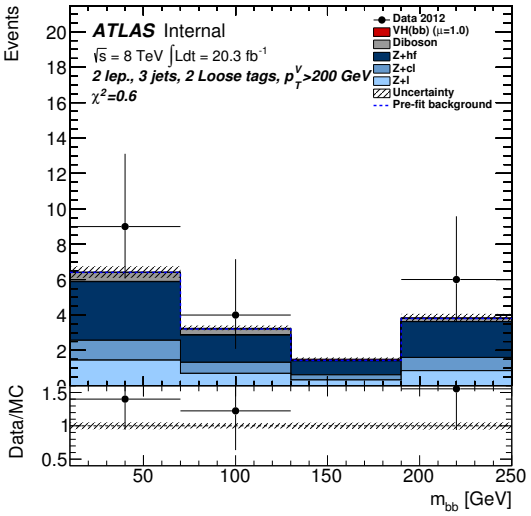

(b) $p_{\mathrm{T}}^{V} > 200$ GeV, 3 jets, LL

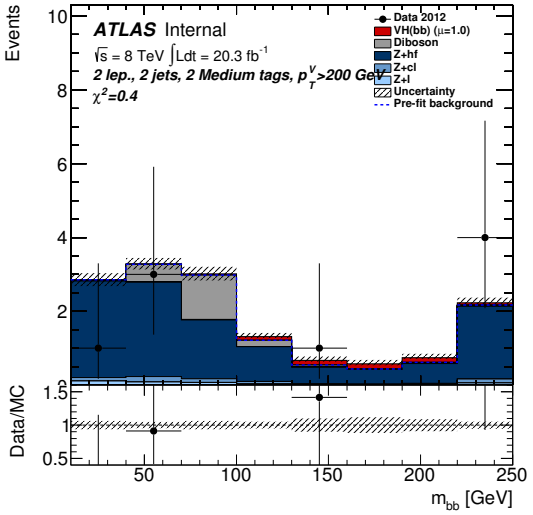

(c) $p_{\mathrm{T}}^{V} > 200$ GeV, 2 jets, MM

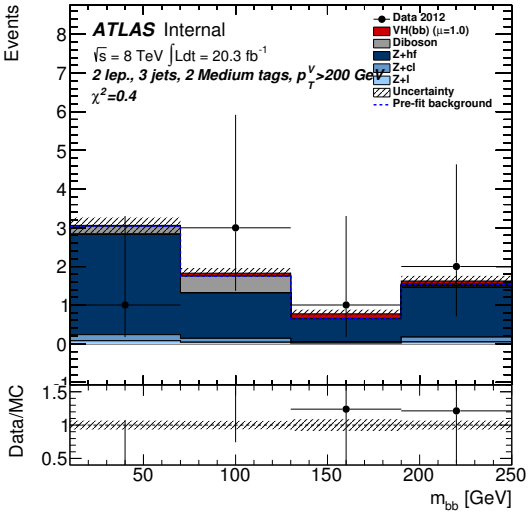

(d) $p_{\mathrm{T}}^{V} > 200$ GeV, 3 jets, MM

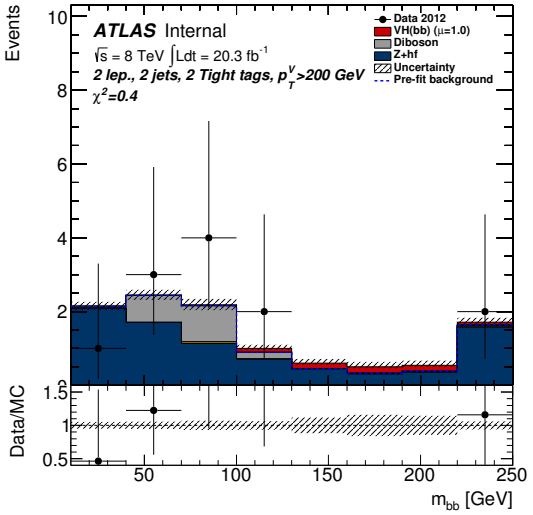

(e) $p_{\mathrm{T}}^{V} > 200$ GeV, 2 jets, TT

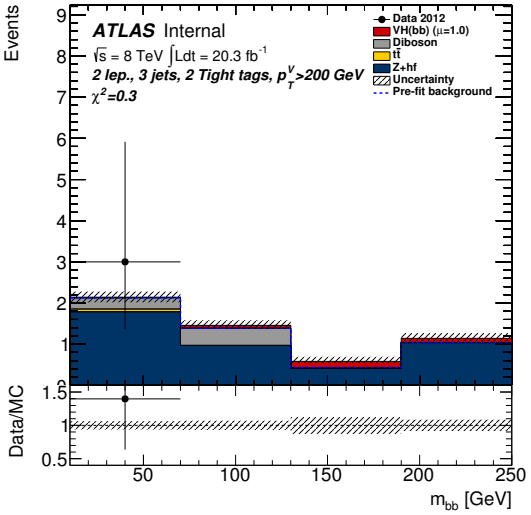

(f) $p_{\mathrm{T}}^{V} > 200$ GeV, 3 jets, TT

Figure 74: Post-fit plots for m_{jj} distribution in 2-lepton events in the LL, MM and TT tag categories for the 2-jets and the 3-jets events. Plots are shown for $p_{\mathrm{T}}^{V} > 200$ GeV. The pre-fit background expectation is indicated by the dashed blue line.

8.7.1 Normal binning

The binning adopted for the fit, coming from the Transformation D, does not allow an easy interpretation of the m_{jj} distribution. The following plots show, the m_{jj} distribution in a fixed bin size.

In Figures 75 - 77, 78 - 80, 81 - 83 post-fit plots for the m_{bb} shape analysis are shown for the 0, 1 and 2-lepton channel respectively in the various 1-tag and 2-tag categories in different p_{T}^{V} bins. They correspond to the plots in Figures 66 - 74.

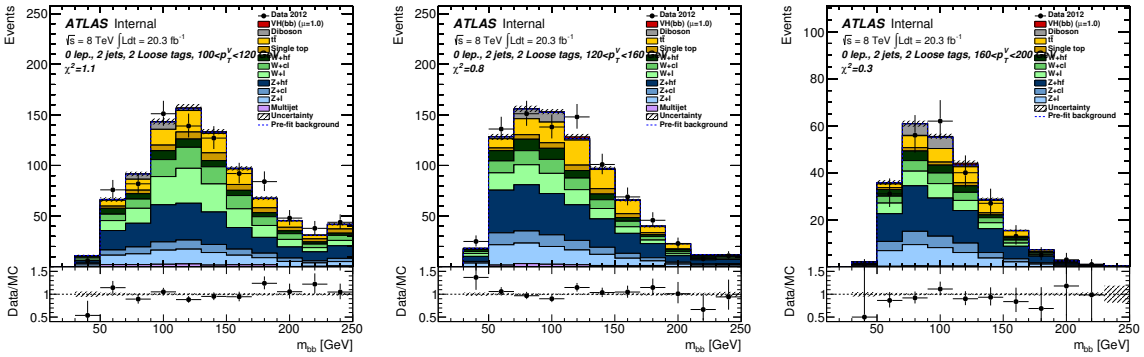

(a) $100 < p_{\mathrm{T}}^{V} < 120$ GeV, 2 jets, LL (b) $120 < p_{\mathrm{T}}^{V} < 160$ GeV, 2 jets, LL (c) $160 < p_{\mathrm{T}}^{V} < 200$ GeV, 2 jets, LL

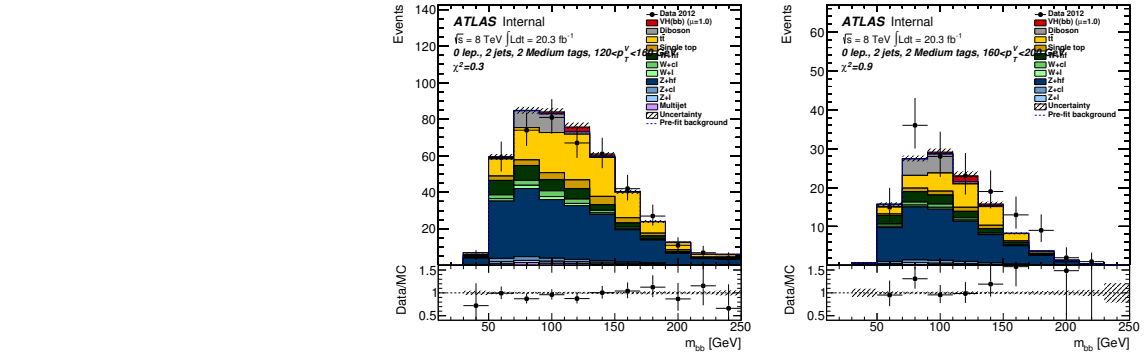

(d) $100 < p_{\mathrm{T}}^{V} < 120$ GeV, 2 jets, MM (e) $120 < p_{\mathrm{T}}^{V} < 160$ GeV, 2 jets, MM (f) $160 < p_{\mathrm{T}}^{V} < 200$ GeV, 2 jets, MM

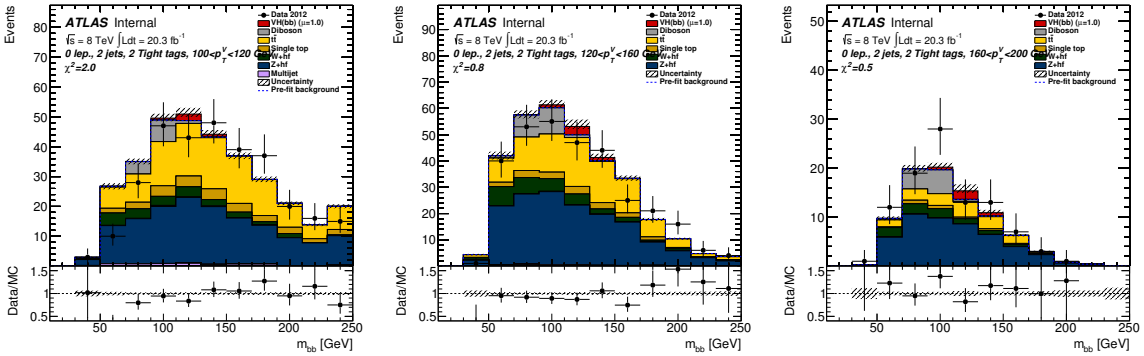

(g) $100 < p_{\mathrm{T}}^{V} < 120$ GeV, 2 jets, TT (h) $120 < p_{\mathrm{T}}^{V} < 160$ GeV, 2 jets, TT (i) $160 < p_{\mathrm{T}}^{V} < 200$ GeV, 2 jets, TT

Figure 75: Post-fit plots for m_{jj} distribution in 0-lepton events in the 1-tag (where mv1c is used in the fit) *LL*, *MM* and *TT* tag categories for the 2-jets events. Plots are shown for $100 < p_{\mathrm{T}}^{V} < 120$ GeV, $120 < p_{\mathrm{T}}^{V} < 160$ GeVand $160 < p_{\mathrm{T}}^{V} < 200$ GeV. The pre-fit background expectation is indicated by the dashed blue line.

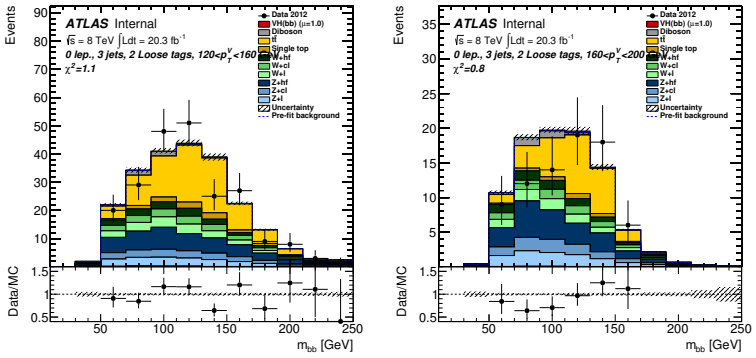

(a) $120 < p_{\mathrm{T}}^{V} < 160$ GeV, 3 jets, LL (b) $160 < p_{\mathrm{T}}^{V} < 200$ GeV, 3 jets, LL

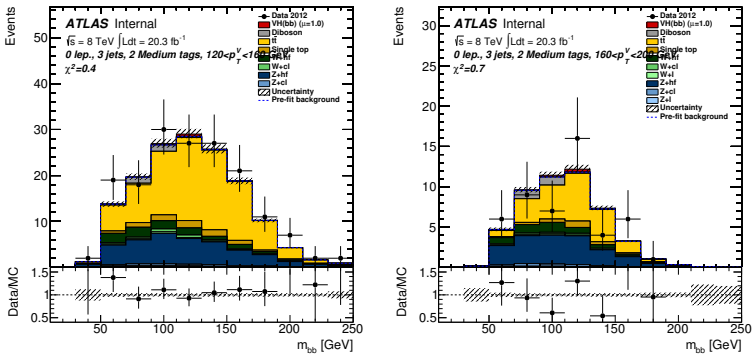

(c) $120 < p_{\mathrm{T}}^{V} < 160$ GeV, 3 jets, MM (d) $160 < p_{\mathrm{T}}^{V} < 200$ GeV, 3 jets, MM

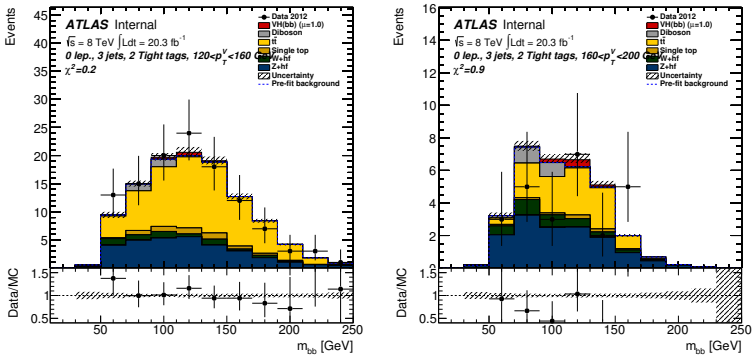

(e) $120 < p_{\mathrm{T}}^{V} < 160$ GeV, 3 jets, TT (f) $160 < p_{\mathrm{T}}^{V} < 200$ GeV, 3 jets, TT

Figure 76: Post-fit plots for m_{jj} distribution in 0-lepton events in the 1-tag (where mv1c is used in the fit) LL, MM and TT tag categories for the 3-jets events. Plots are shown for $120 < p_{\mathrm{T}}^{V} < 160$ GeVand $160 < p_{\mathrm{T}}^{V} < 200$ GeV. The pre-fit background expectation is indicated by the dashed blue line.

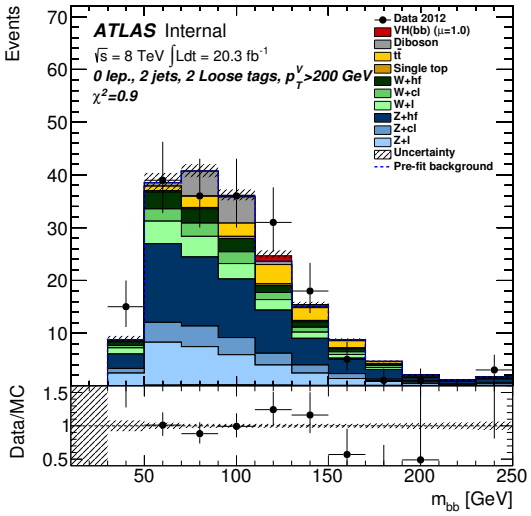

(a) $p_{\mathrm{T}}^{V} > 200$ GeV, 2 jets, LL

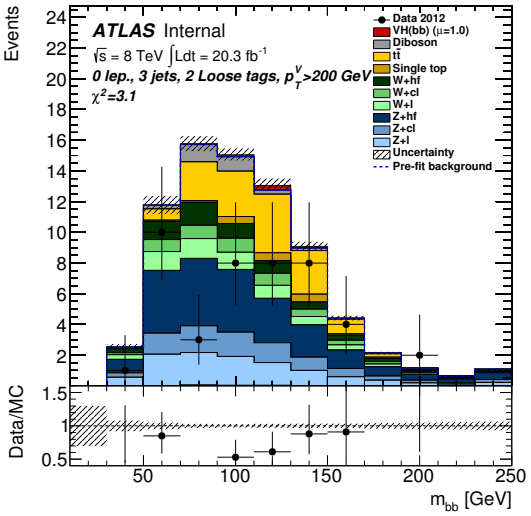

(b) $p_{\mathrm{T}}^{V} > 200$ GeV, 3 jets, LL

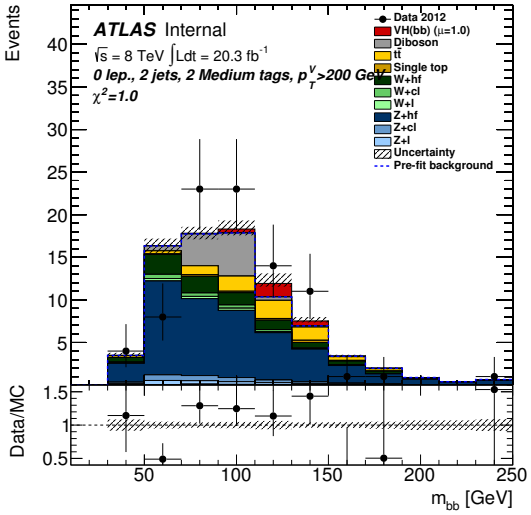

(c) $p_{\mathrm{T}}^{V} > 200$ GeV, 2 jets, MM

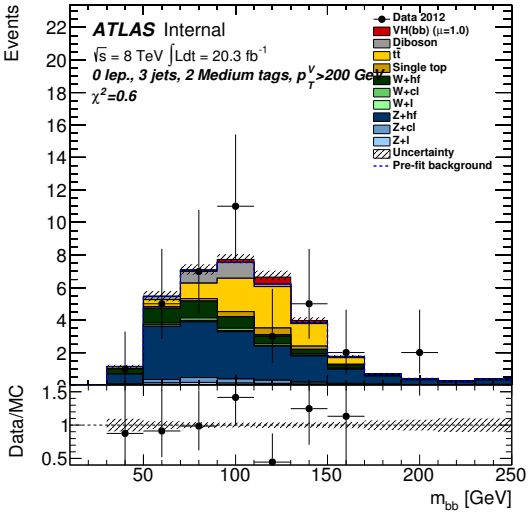

(d) $p_{\mathrm{T}}^{V} > 200$ GeV, 3 jets, MM

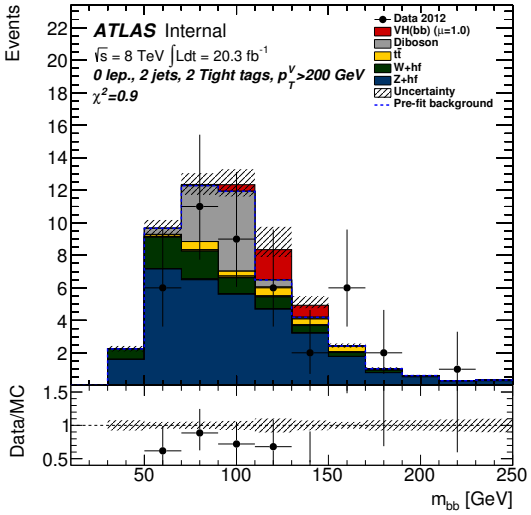

(e) $p_{\mathrm{T}}^{V} > 200$ GeV, 2 jets, TT

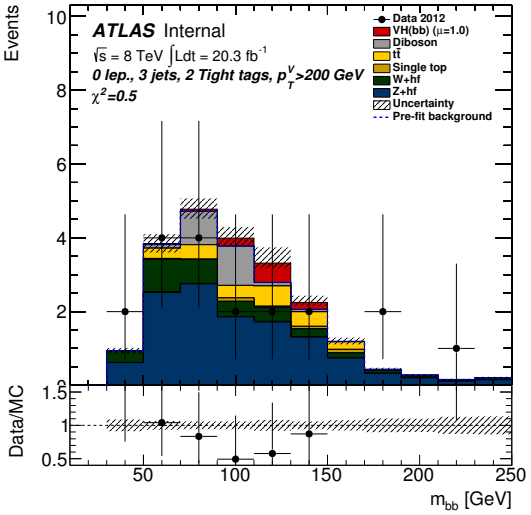

(f) $p_{\mathrm{T}}^{V} > 200$ GeV, 3 jets, TT

Figure 77: Post-fit plots for m_{jj} distribution in 0-lepton events in the LL, MM and TT tag categories for the 2-jets and the 3-jets events. Plots are shown for $p_{\mathrm{T}}^{V} > 200$ GeV. The pre-fit background expectation is indicated by the dashed blue line.

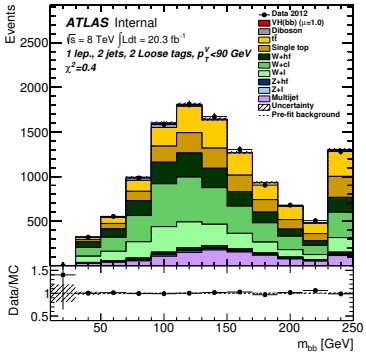

(a) $p_{\mathrm{T}}^{V} < 90$ GeV, 2 jets, LL

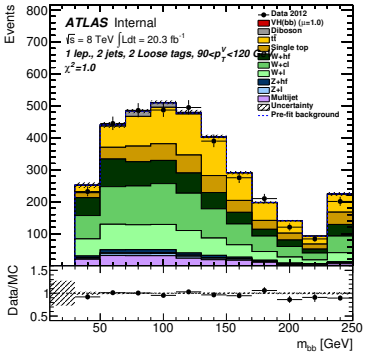

(b) $90 < p_{\mathrm{T}}^{V} < 120$ GeV, 2 jets, LL

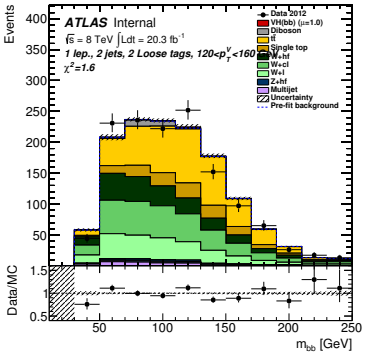

(c) $120 < p_{\mathrm{T}}^{V} < 160$ GeV, 2 jets, LL

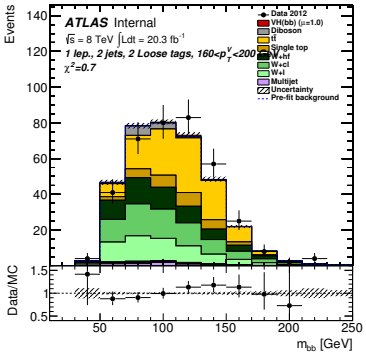

(d) $160 < p_{\mathrm{T}}^{V} < 200$ GeV, 2 jets, LL

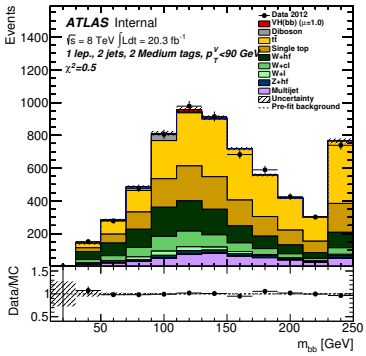

(e) $p_{\mathrm{T}}^{V} < 90$ GeV, 2 jets, MM

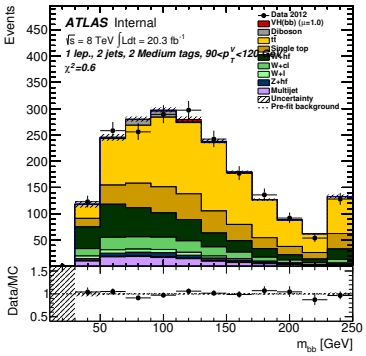

(f) $90 < p_{\mathrm{T}}^{V} < 120$ GeV, 2 jets, MM

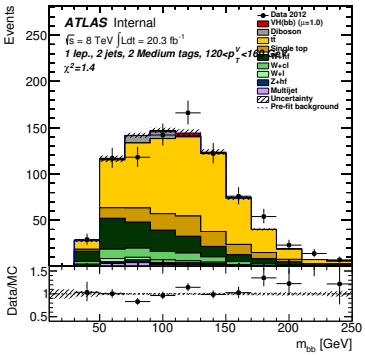

(g) $120 < p_{\mathrm{T}}^{V} < 160$ GeV, 2 jets, MM

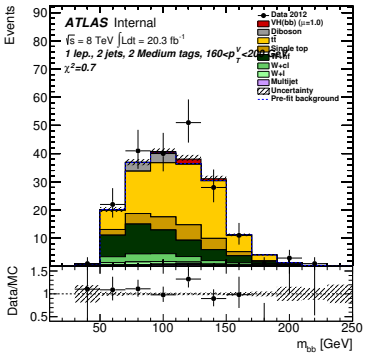

(h) $160 < p_{\mathrm{T}}^{V} < 200$ GeV, 2 jets, MM

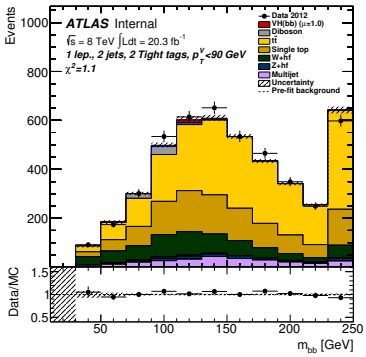

(i) $p_{\mathrm{T}}^{V} < 90$ GeV, 2 jets, TT

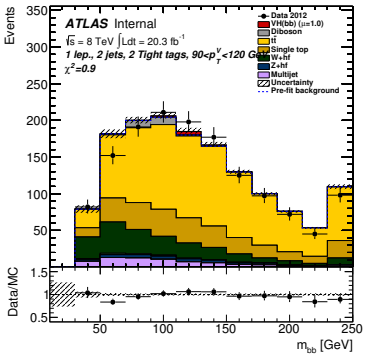

(j) $90 < p_{\mathrm{T}}^{V} < 120$ GeV, 2 jets, TT

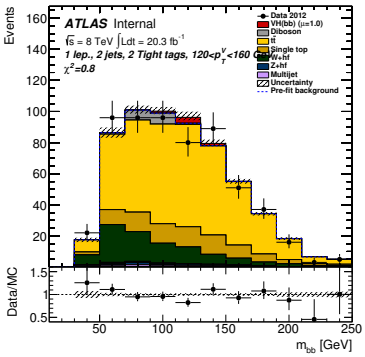

(k) $120 < p_{\mathrm{T}}^{V} < 160$ GeV, 2 jets, TT

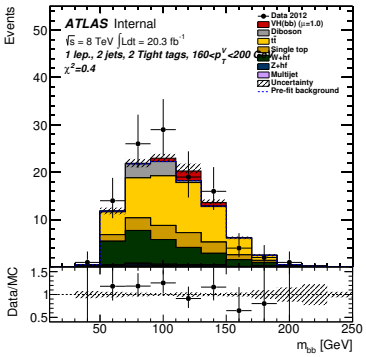

(l) $160 < p_{\mathrm{T}}^{V} < 200$ GeV, 2 jets, TT

Figure 78: Post-fit plots for m_{jj} distribution in 1-lepton events in the 1-tag (where mv1c is used in the fit) *LL*, *MM* and *TT* tag categories for the 2-jets events. Plots are shown for $p_{\mathrm{T}}^{V} < 90$ GeV, $90 < p_{\mathrm{T}}^{V} < 120$ GeV, $120 < p_{\mathrm{T}}^{V} < 160$ GeVand $160 < p_{\mathrm{T}}^{V} < 200$ GeV. The pre-fit background expectation is indicated by the dashed blue line.

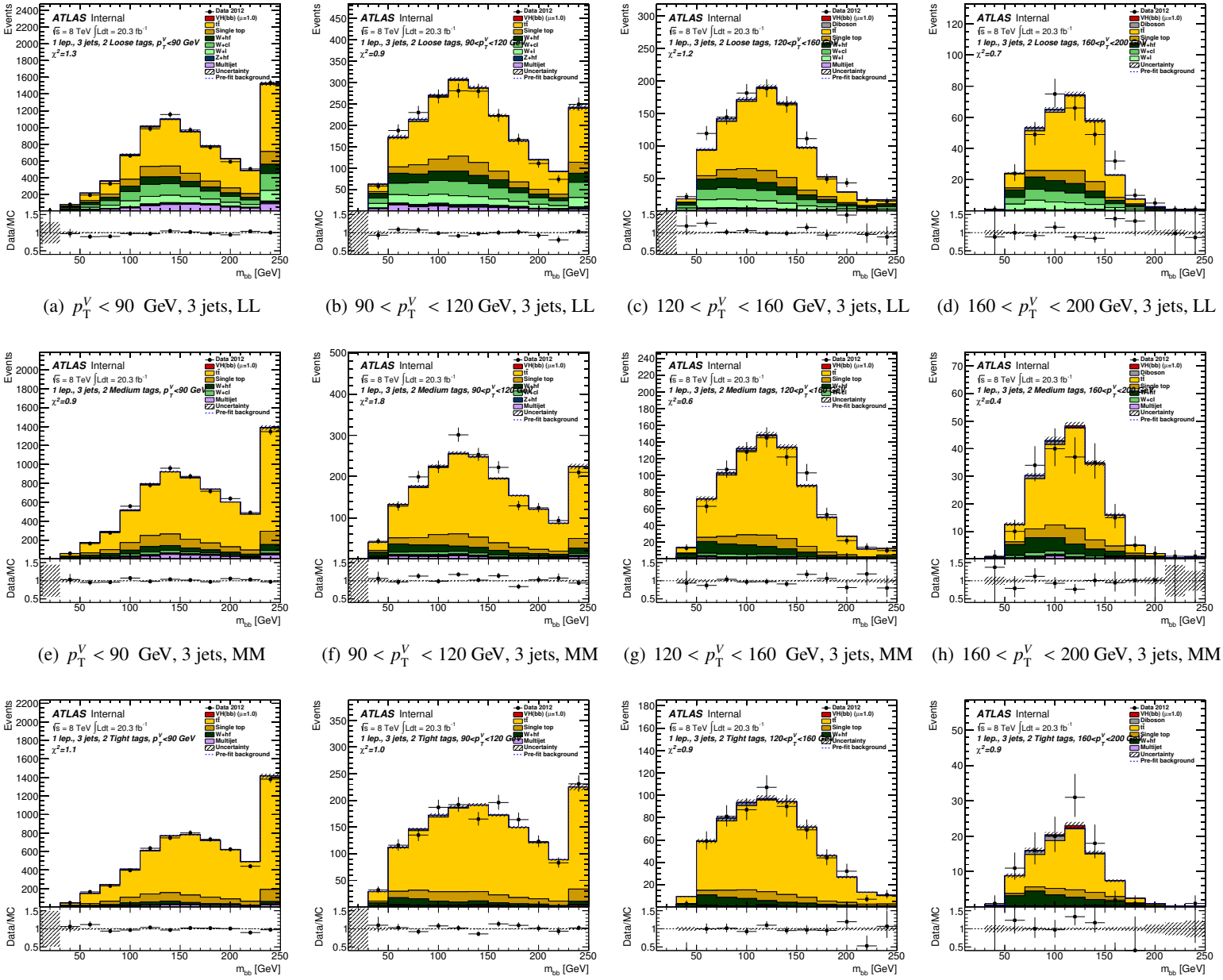

(a) $p_{\mathrm{T}}^{V} < 90$ GeV, 3 jets, LL (b) $90 < p_{\mathrm{T}}^{V} < 120$ GeV, 3 jets, LL (c) $120 < p_{\mathrm{T}}^{V} < 160$ GeV, 3 jets, LL (d) $160 < p_{\mathrm{T}}^{V} < 200$ GeV, 3 jets, LL

(e) $p_{\mathrm{T}}^{V} < 90$ GeV, 3 jets, MM (f) $90 < p_{\mathrm{T}}^{V} < 120$ GeV, 3 jets, MM (g) $120 < p_{\mathrm{T}}^{V} < 160$ GeV, 3 jets, MM (h) $160 < p_{\mathrm{T}}^{V} < 200$ GeV, 3 jets, MM

(i) $p_{\mathrm{T}}^{V} < 90$ GeV, 3 jets, TT (j) $90 < p_{\mathrm{T}}^{V} < 120$ GeV, 3 jets, TT (k) $120 < p_{\mathrm{T}}^{V} < 160$ GeV, 3 jets, TT (l) $160 < p_{\mathrm{T}}^{V} < 200$ GeV, 3 jets, TT

Figure 79: Post-fit plots for m_{jj} distribution in 1-lepton events in the 1-tag (where mv1c is used in the fit) LL, MM and TT tag categories for the 3-jets events. Plots are shown for $p_{\mathrm{T}}^{V} < 90$ GeV, $90 < p_{\mathrm{T}}^{V} < 120$ GeV, $120 < p_{\mathrm{T}}^{V} < 160$ GeVand $160 < p_{\mathrm{T}}^{V} < 200$ GeV. The pre-fit background expectation is indicated by the dashed blue line.

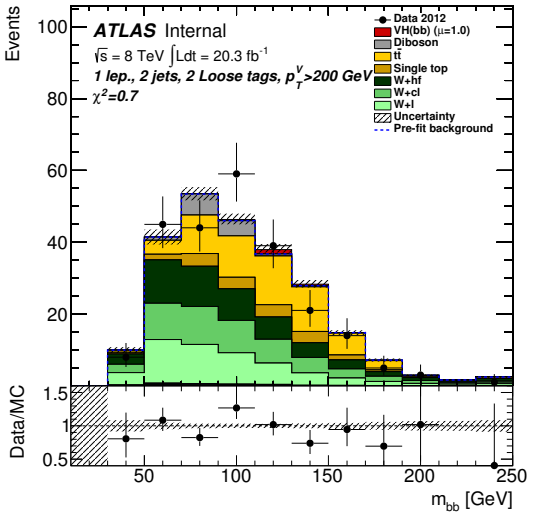

(a) $p_{\mathrm{T}}^{V} > 200$ GeV, 2 jets, LL

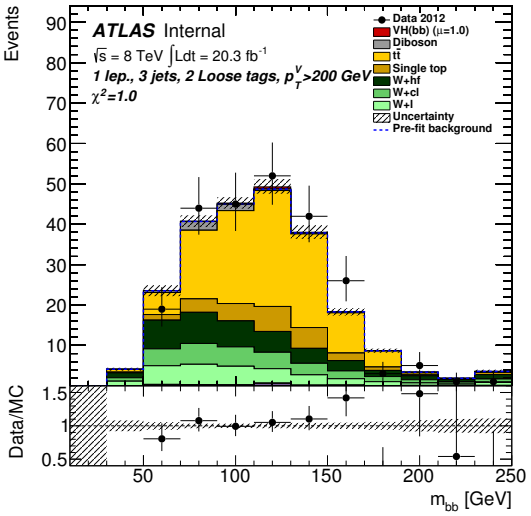

(b) $p_{\mathrm{T}}^{V} > 200$ GeV, 3 jets, LL

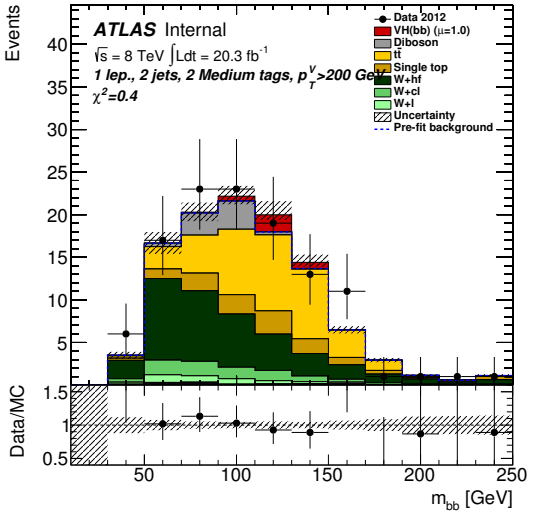

(c) $p_{\mathrm{T}}^{V} > 200$ GeV, 2 jets, MM

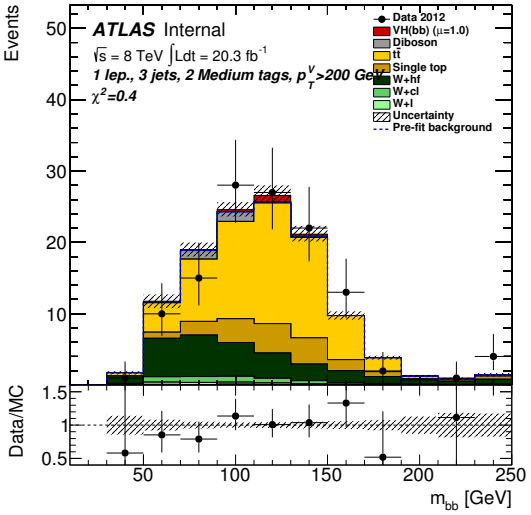

(d) $p_{\mathrm{T}}^{V} > 200$ GeV, 3 jets, MM

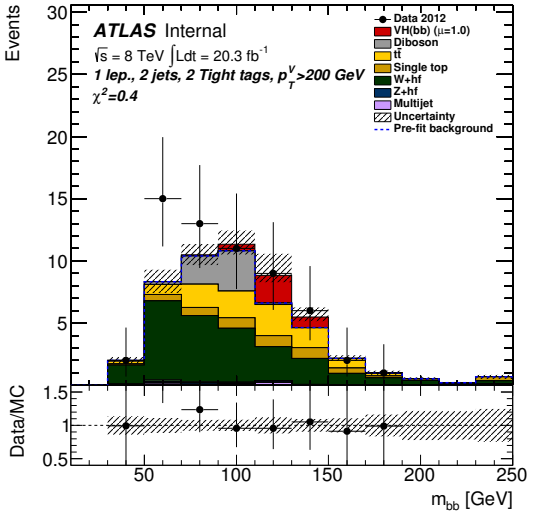

(e) $p_{\mathrm{T}}^{V} > 200$ GeV, 2 jets, TT

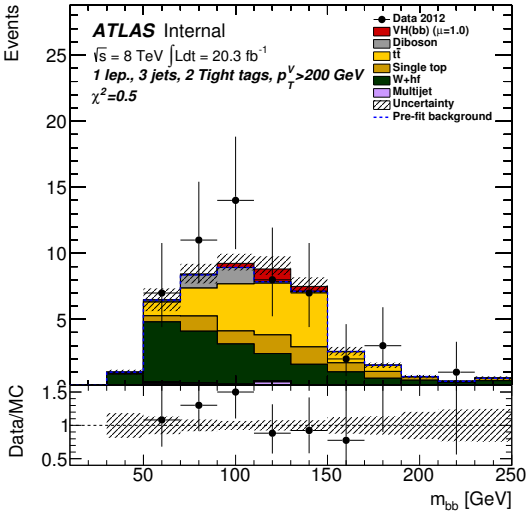

(f) $p_{\mathrm{T}}^{V} > 200$ GeV, 3 jets, TT

Figure 80: Post-fit plots for m_{jj} distribution in 1-lepton events in the LL, MM and TT tag categories for the 2-jets and the 3-jets events. Plots are shown for $p_{\mathrm{T}}^{V} > 200$ GeV. The pre-fit background expectation is indicated by the dashed blue line.

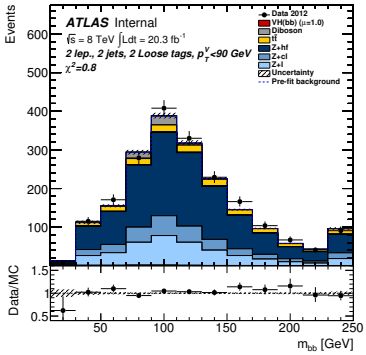

(a) $p_{\mathrm{T}}^{V} < 90$ GeV, 2 jets, LL

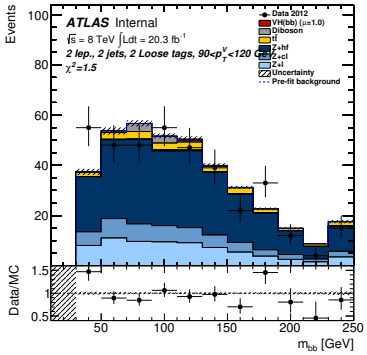

(b) $90 < p_{\mathrm{T}}^{V} < 120$ GeV, 2 jets, LL

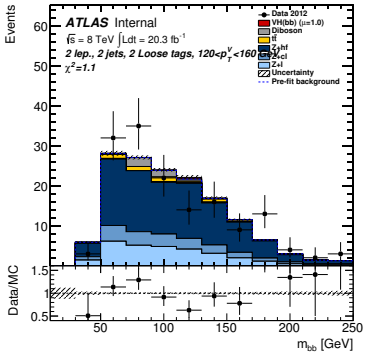

(c) $120 < p_{\mathrm{T}}^{V} < 160$ GeV, 2 jets, LL

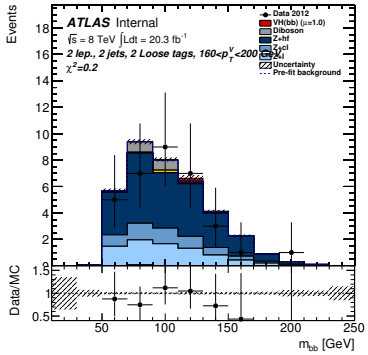

(d) $160 < p_{\mathrm{T}}^{V} < 200$ GeV, 2 jets, LL

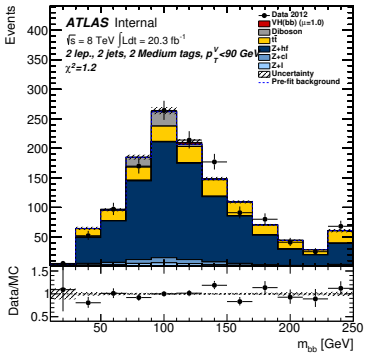

(e) $p_{\mathrm{T}}^{V} < 90$ GeV, 2 jets, MM

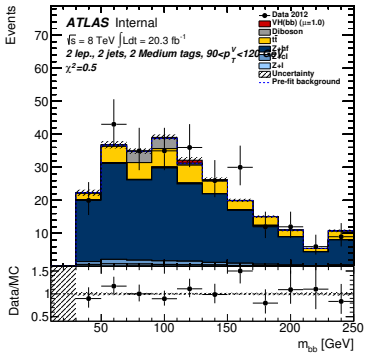

(f) $90 < p_{\mathrm{T}}^{V} < 120$ GeV, 2 jets, MM

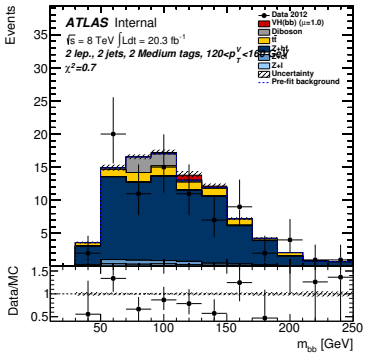

(g) $120 < p_{\mathrm{T}}^{V} < 160$ GeV, 2 jets, MM

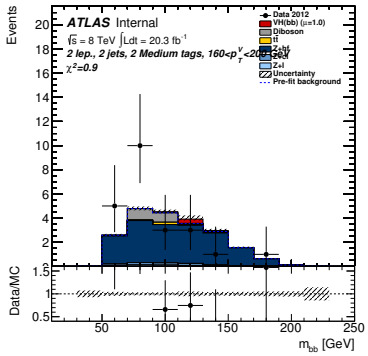

(h) $160 < p_{\mathrm{T}}^{V} < 200$ GeV, 2 jets, MM

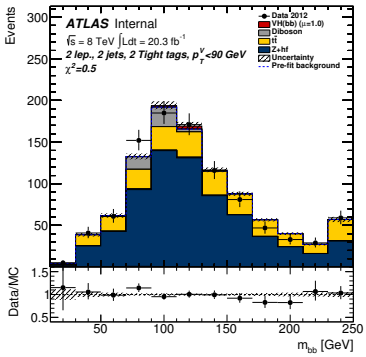

(i) $p_{\mathrm{T}}^{V} < 90$ GeV, 2 jets, TT

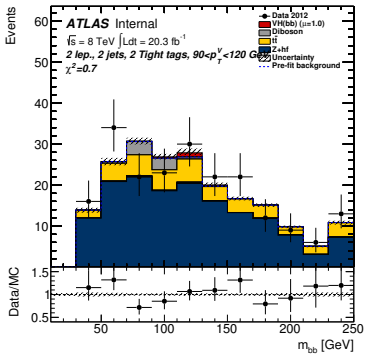

(j) $90 < p_{\mathrm{T}}^{V} < 120$ GeV, 2 jets, TT

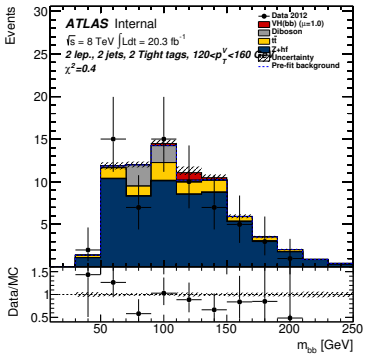

(k) $120 < p_{\mathrm{T}}^{V} < 160$ GeV, 2 jets, TT

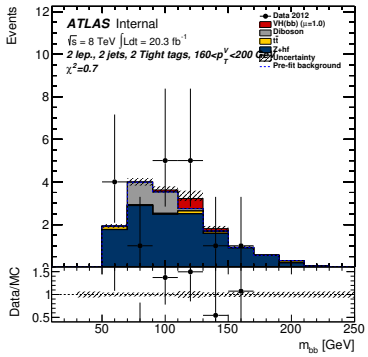

(l) $160 < p_{\mathrm{T}}^{V} < 200$ GeV, 2 jets, TT

Figure 81: Post-fit plots for m_{jj} distribution in 2-lepton events in the 1-tag (where mv1c is used in the fit) LL, MM and TT tag categories for the 2-jets events. Plots are shown for $p_{\mathrm{T}}^{V} < 90$ GeV, $90 < p_{\mathrm{T}}^{V} < 120$ GeV, $120 < p_{\mathrm{T}}^{V} < 160$ GeVand $160 < p_{\mathrm{T}}^{V} < 200$ GeV. The pre-fit background expectation is indicated by the dashed blue line.

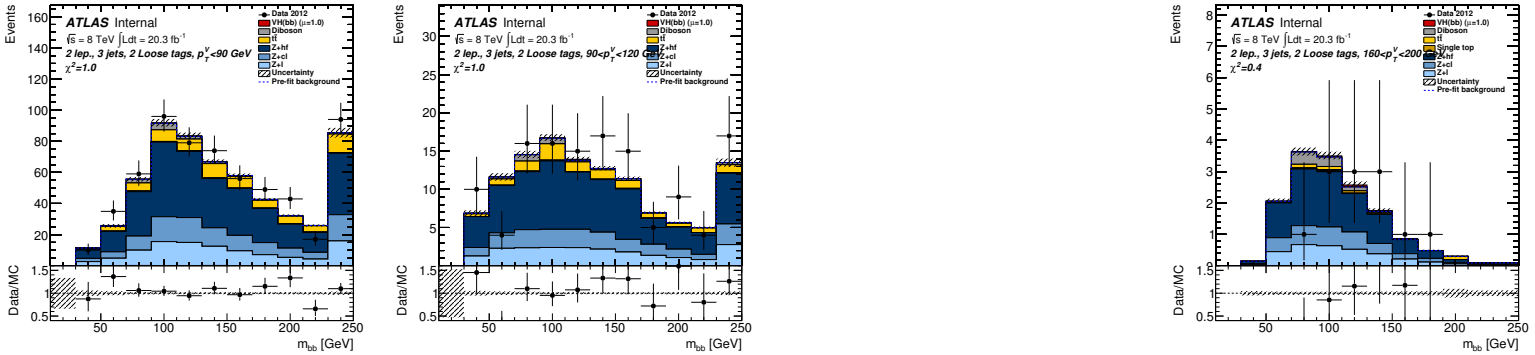

(a) $p_{\mathrm{T}}^{V} < 90$ GeV, 3 jets, LL (b) $90 < p_{\mathrm{T}}^{V} < 120$ GeV, 3 jets, LL (c) $120 < p_{\mathrm{T}}^{V} < 160$ GeV, 3 jets, LL (d) $160 < p_{\mathrm{T}}^{V} < 200$ GeV, 3 jets, LL

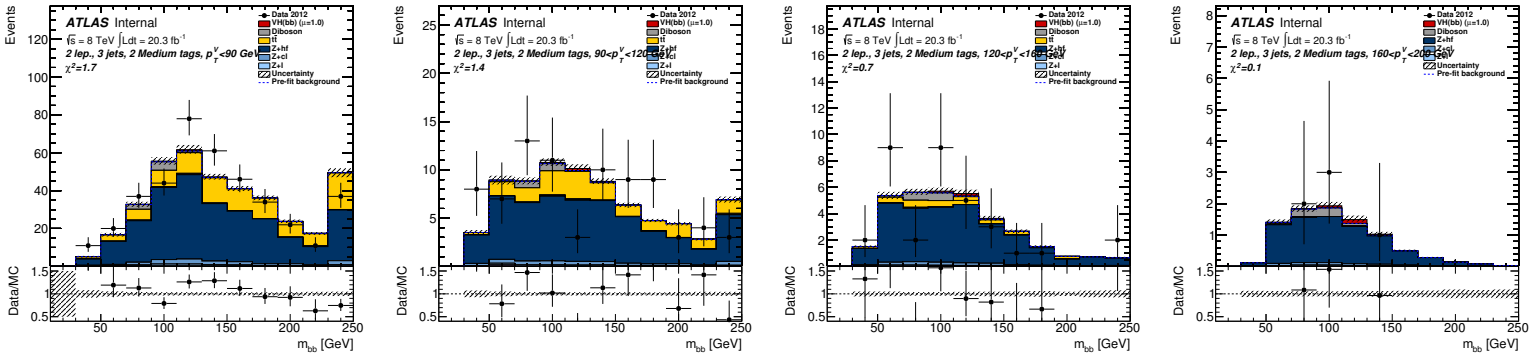

(e) $p_{\mathrm{T}}^{V} < 90$ GeV, 3 jets, MM (f) $90 < p_{\mathrm{T}}^{V} < 120$ GeV, 3 jets, MM (g) $120 < p_{\mathrm{T}}^{V} < 160$ GeV, 3 jets, MM (h) $160 < p_{\mathrm{T}}^{V} < 200$ GeV, 3 jets, MM

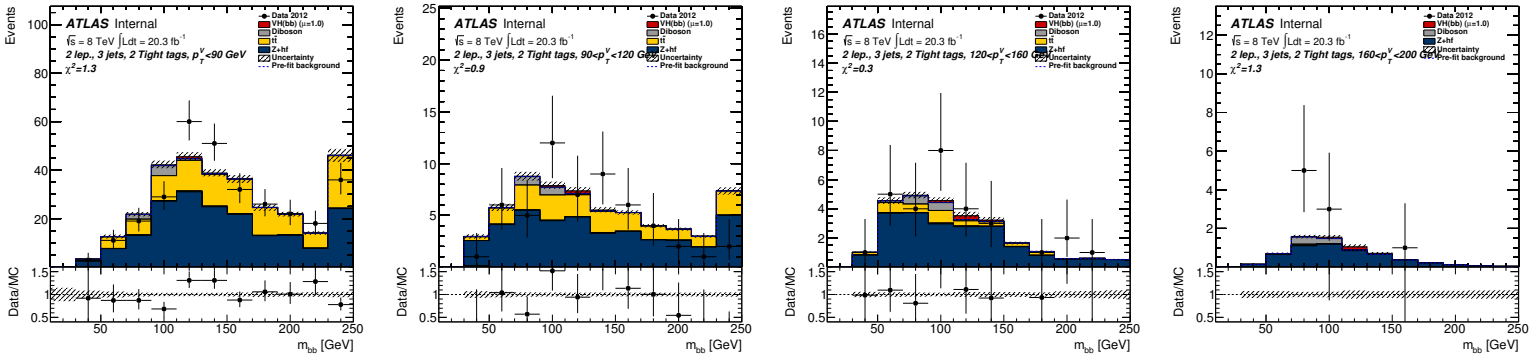

(i) $p_{\mathrm{T}}^{V} < 90$ GeV, 3 jets, TT (j) $90 < p_{\mathrm{T}}^{V} < 120$ GeV, 3 jets, TT (k) $120 < p_{\mathrm{T}}^{V} < 160$ GeV, 3 jets, TT (l) $160 < p_{\mathrm{T}}^{V} < 200$ GeV, 3 jets, TT

Figure 82: Post-fit plots for m_{jj} distribution in 2-lepton events in the 1-tag (where mv1c is used in the fit) LL, MM and TT tag categories for the 3-jets events. Plots are shown for $p_{\mathrm{T}}^{V} < 90$ GeV, $90 < p_{\mathrm{T}}^{V} < 120$ GeV, $120 < p_{\mathrm{T}}^{V} < 160$ GeVand $160 < p_{\mathrm{T}}^{V} < 200$ GeV. The pre-fit background expectation is indicated by the dashed blue line.

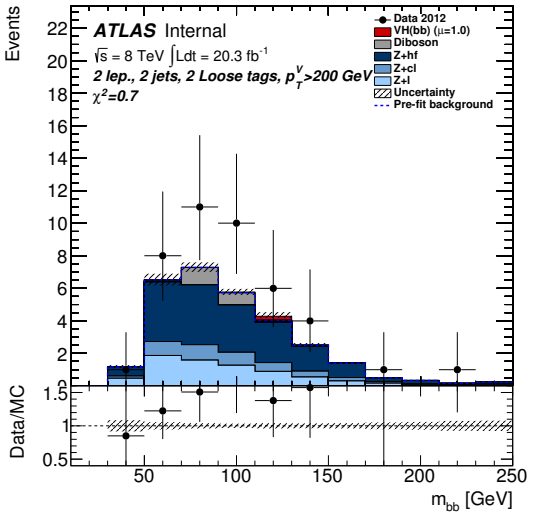

(a) p_{T}^{V} > 200 GeV, 2 jets, LL

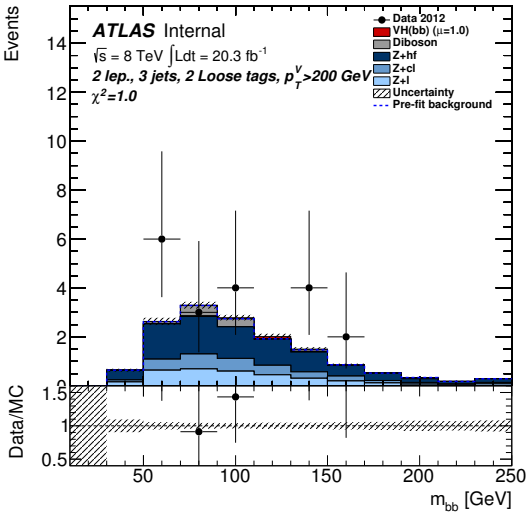

(b) p_{T}^{V} > 200 GeV, 3 jets, LL

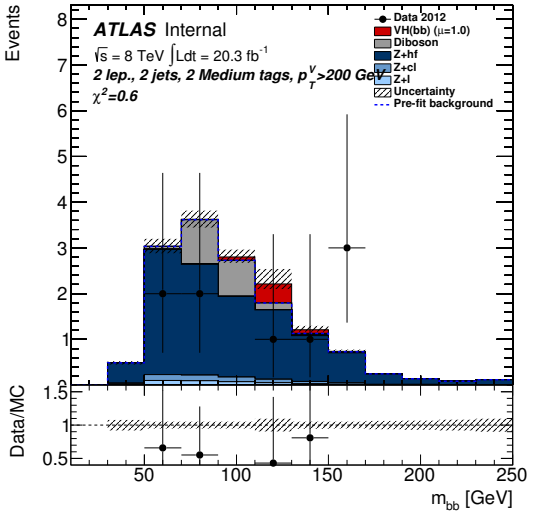

(c) p_{T}^{V} > 200 GeV, 2 jets, MM

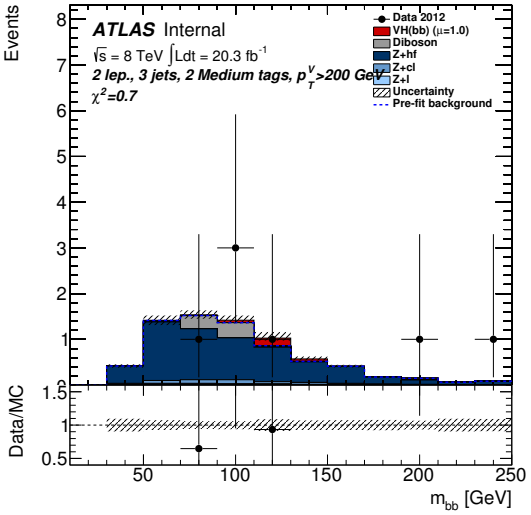

(d) p_{T}^{V} > 200 GeV, 3 jets, MM

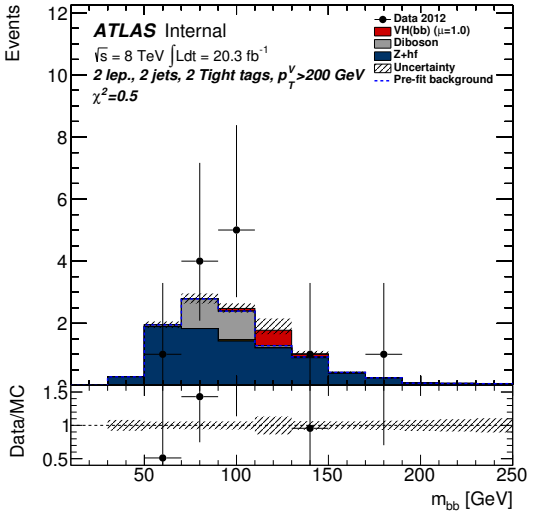

(e) p_{T}^{V} > 200 GeV, 2 jets, TT

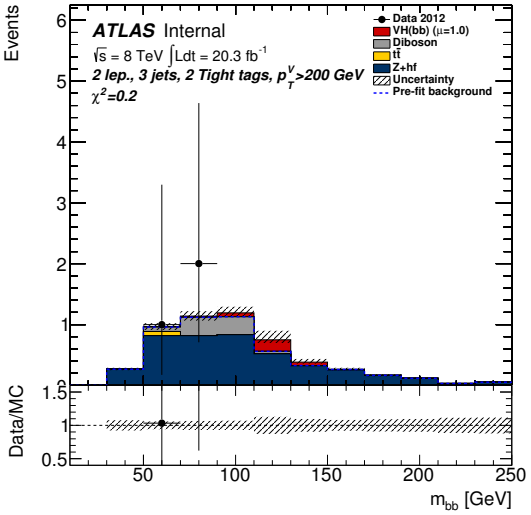

(f) p_{T}^{V} > 200 GeV, 3 jets, TT

Figure 83: Post-fit plots for m_{jj} distribution in 2-lepton events in the LL, MM and TT tag categories for the 2-jets and the 3-jets events. Plots are shown for $p_{\mathrm{T}}^{V} > 200$ GeV. The pre-fit background expectation is indicated by the dashed blue line.

8.7.2 Post fit b-tagging for the m_{jj} shape analysis

In order to understand the effect of the pulls on the b-tagging related parameters the scale factor and related uncertainities are unfold from the fit and shown as a function of jet p_{T}.

As an examples, in Figure 84 we show the plots for the scale factors obtained in the m_{jj} 0+1+2 leptons combined fit .

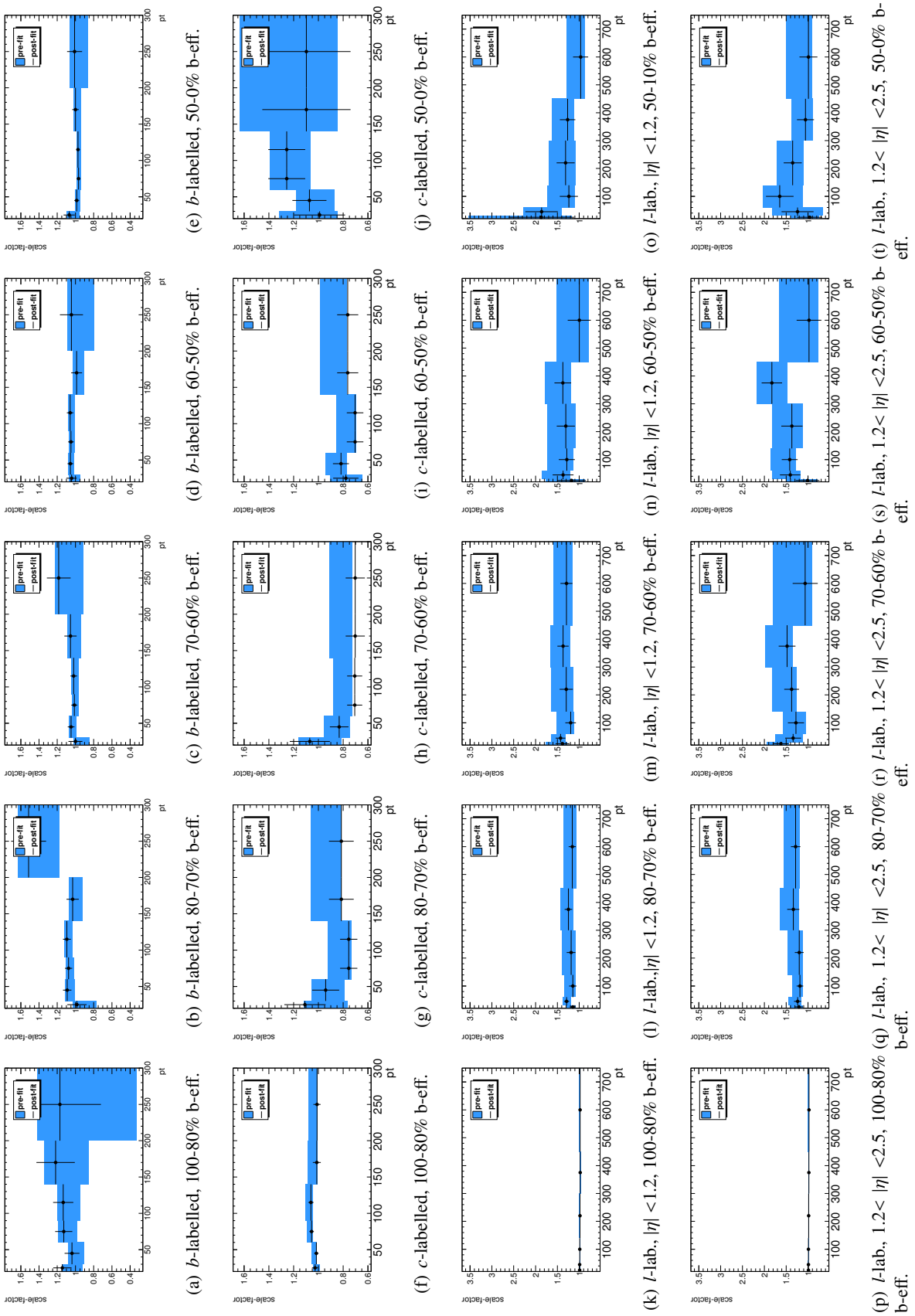

(a) b-labelled, 100-80% b-eff. (b) b-labelled, 80-70% b-eff. (c) b-labelled, 70-60% b-eff. (d) b-labelled, 60-50% b-eff. (e) b-labelled, 50-0% b-eff.

(f) c-labelled, 100-80% b-eff. (g) c-labelled, 80-70% b-eff. (h) c-labelled, 70-60% b-eff. (i) c-labelled, 60-50% b-eff. (j) c-labelled, 50-0% b-eff.

(k) l-lab., $|\eta|$ <1.2, 100-80% b-eff. (l) l-lab.,$|\eta|$ <1.2, 80-70% b-eff. (m) l-lab., $|\eta|$ <1.2, 70-60% b-eff. (n) l-lab., $|\eta|$ <1.2, 60-50% b-eff. (o) l-lab., $|\eta|$ <1.2, 50-10% b-eff.

(p) l-lab., 1.2< $|\eta|$ <2.5, 100-80% b-eff. (q) l-lab., 1.2< $|\eta|$ <2.5, 80-70% b-eff. (r) l-lab., 1.2< $|\eta|$ <2.5, 70-60% b-eff. (s) l-lab., 1.2< $|\eta|$ <2.5, 60-50% b-eff. (t) l-lab., 1.2< $|\eta|$ <2.5, 50-0% b-eff.

Figure 84: The MC-to-data post-fit unfolded calibration scale factors for the MV1c b, c-jet as a function ot the jet p_{T} .

8.8 MVA background-only post fit plots

In the following sections post-fit plots corresponding to background-only fits to the data for the MVA analysis are presented. In all cases the MC expectations have been adapted to the pulls from the data in the combined 0+1+2 lepton fit. As a comparison, the total nominal background prediction is indicated by the dashed blue curve. Only statistical uncertainties are indicated. All the plots do not show the data points in the regions where the signal is expected to be at least 2% of the total background.

In Figures 546, 547 and 548 shown the post-fit distribution for the variables used in the MVA shape analysis for the 0, 1 and 2-lepton channel respectively in the various 2-tag categories in different p_{T}^{V} bins.

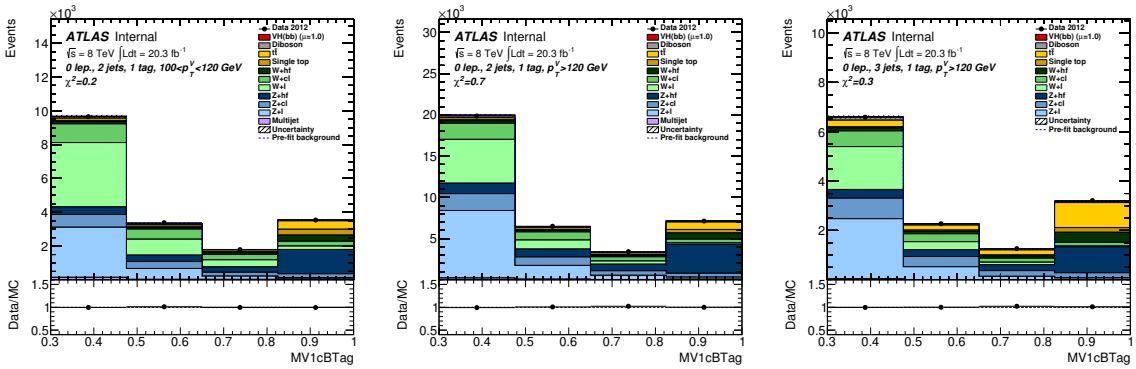

(a) $p_{\mathrm{T}}^{V} < 120$ GeV, 2 jets, 1-tag (b) $p_{\mathrm{T}}^{V} > 120$ GeV, 2 jets, 1-tag (c) $p_{\mathrm{T}}^{V} > 120$ GeV, 3 jets, 1-tag

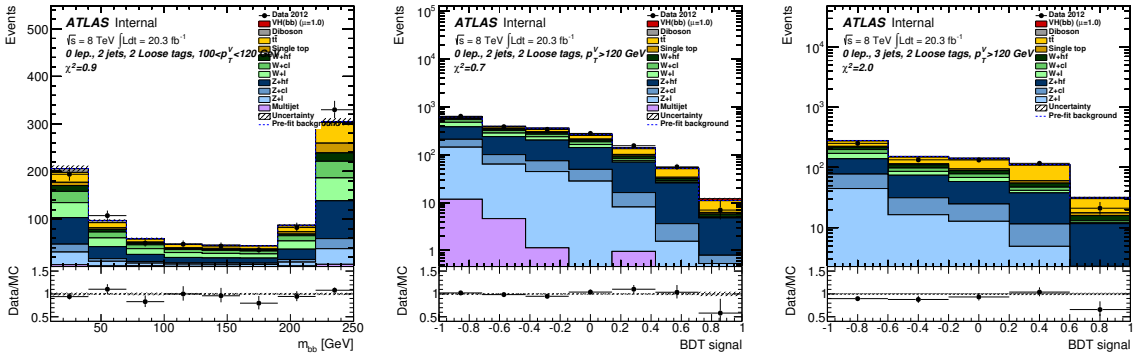

(d) $p_{\mathrm{T}}^{V} < 120$ GeV, 2 jets, LL (e) $p_{\mathrm{T}}^{V} > 120$ GeV, 2 jets, LL (f) $p_{\mathrm{T}}^{V} > 120$ GeV, 3 jets, LL

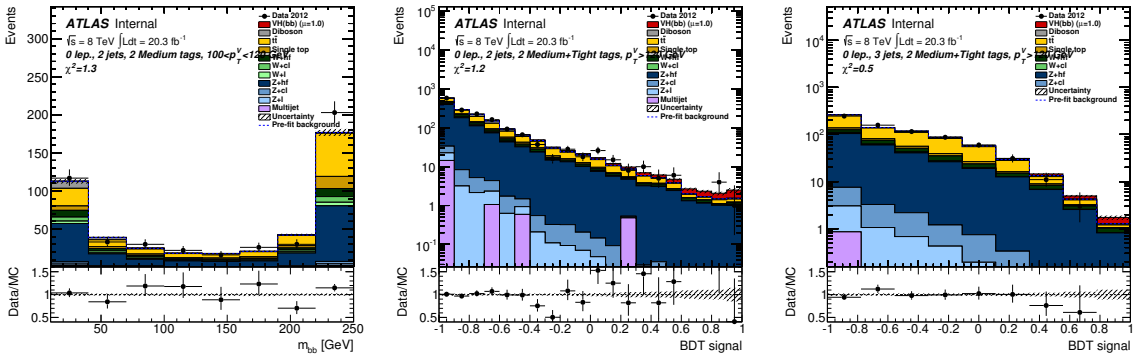

(g) $p_{\mathrm{T}}^{V} < 120$ GeV, 2 jets, MM+TT (h) $p_{\mathrm{T}}^{V} > 120$ GeV, 2 jets, MM+TT (i) $p_{\mathrm{T}}^{V} > 120$ GeV, 3 jets, MM+TT

Figure 85: Post-fit plots for MVA distribution in 0-lepton events with 1 b-tag (MV1c is fit here), *LL* and $MM + TT$ b-tags in the 0+1+2 lepton fit. The pre-fit background expectation is indicated by the dashed blue line. Only statistical uncertainties are indicated.

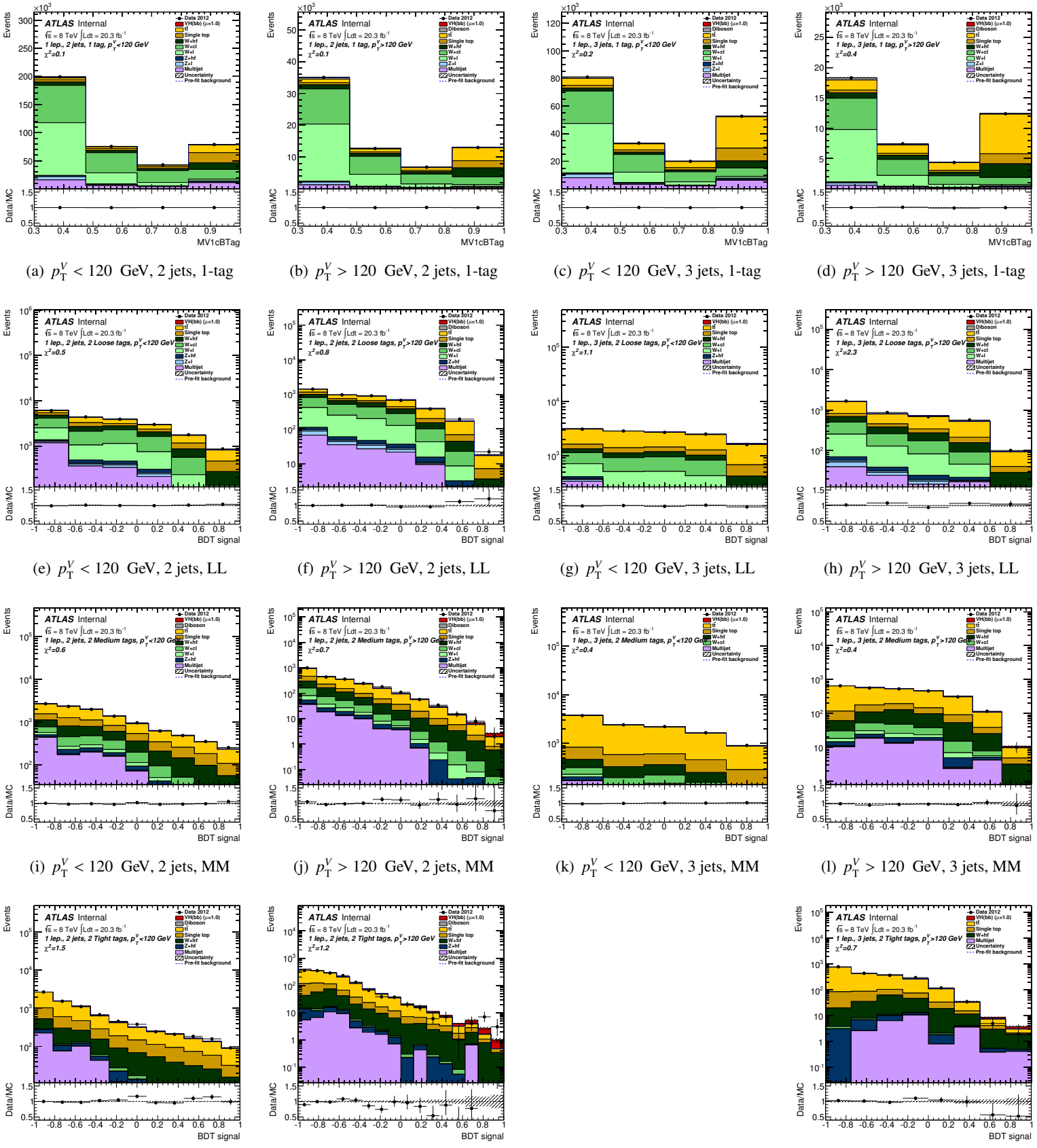

(a) $p_{\mathrm{T}}^{V} < 120$ GeV, 2 jets, 1-tag (b) $p_{\mathrm{T}}^{V} > 120$ GeV, 2 jets, 1-tag (c) $p_{\mathrm{T}}^{V} < 120$ GeV, 3 jets, 1-tag (d) $p_{\mathrm{T}}^{V} > 120$ GeV, 3 jets, 1-tag

(e) $p_{\mathrm{T}}^{V} < 120$ GeV, 2 jets, LL (f) $p_{\mathrm{T}}^{V} > 120$ GeV, 2 jets, LL (g) $p_{\mathrm{T}}^{V} < 120$ GeV, 3 jets, LL (h) $p_{\mathrm{T}}^{V} > 120$ GeV, 3 jets, LL

(i) $p_{\mathrm{T}}^{V} < 120$ GeV, 2 jets, MM (j) $p_{\mathrm{T}}^{V} > 120$ GeV, 2 jets, MM (k) $p_{\mathrm{T}}^{V} < 120$ GeV, 3 jets, MM (l) $p_{\mathrm{T}}^{V} > 120$ GeV, 3 jets, MM

(m) $p_{\mathrm{T}}^{V} < 120$ GeV, 2 jets, TT (n) $p_{\mathrm{T}}^{V} > 120$ GeV, 2 jets, TT (o) $p_{\mathrm{T}}^{V} < 120$ GeV, 3 jets, TT (p) $p_{\mathrm{T}}^{V} > 120$ GeV, 3 jets, TT

Figure 86: Post-fit plots for MVA distribution in 1-lepton 2-jet and 3-jets, $p_{\mathrm{T}}^{V} < 120$ GeV and $p_{\mathrm{T}}^{V} > 120$ GeV events with 1 b-tag (MV1c is fit here), *LL*, *MM* and *TT* b-tags in the 0+1+2 lepton fit. The pre-fit background expectation is indicated by the dashed blue line. Only statistical uncertainties are indicated.

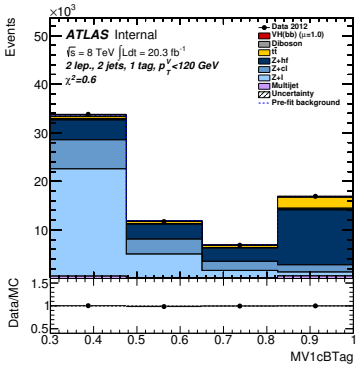

(a) $p_{\mathrm{T}}^{V} < 120$ GeV, 2 jets, 1-tag

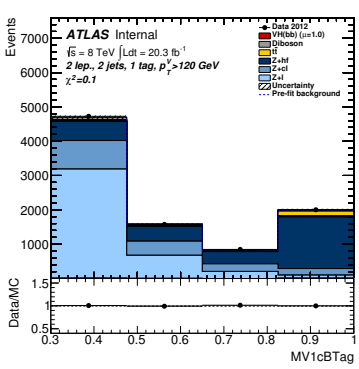

(b) $p_{\mathrm{T}}^{V} > 120$ GeV, 2 jets, 1-tag

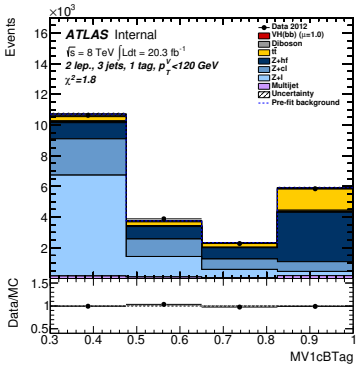

(c) $p_{\mathrm{T}}^{V} < 120$ GeV, 3 jets, 1-tag

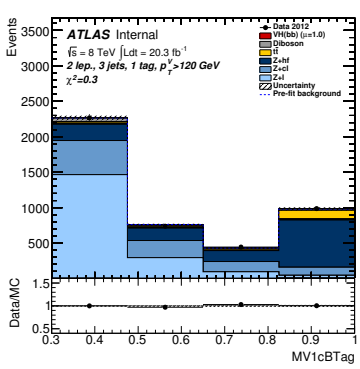

(d) $p_{\mathrm{T}}^{V} > 120$ GeV, 3 jets, 1-tag

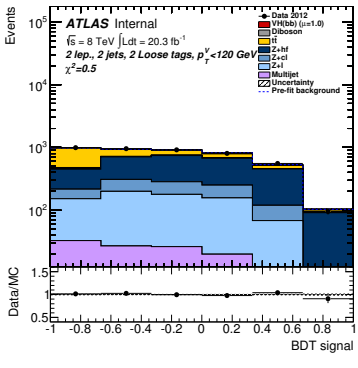

(e) $p_{\mathrm{T}}^{V} < 120$ GeV, 2 jets, LL

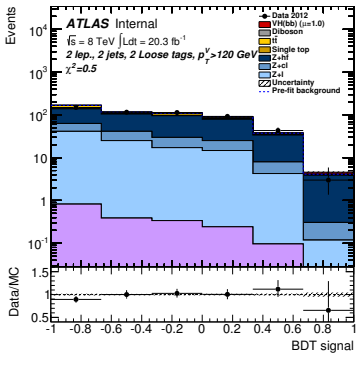

(f) $p_{\mathrm{T}}^{V} > 120$ GeV, 2 jets, LL

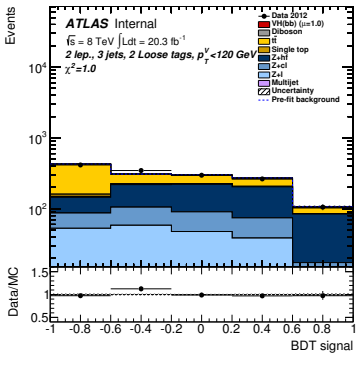

(g) $p_{\mathrm{T}}^{V} < 120$ GeV, 3 jets, LL

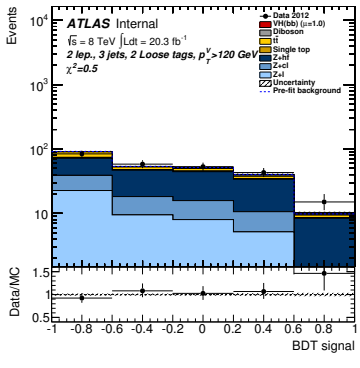

(h) $p_{\mathrm{T}}^{V} > 120$ GeV, 3 jets, LL

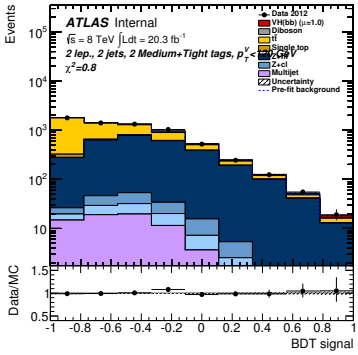

(i) $p_{\mathrm{T}}^{V} < 120$ GeV 2 jets, MM+TT

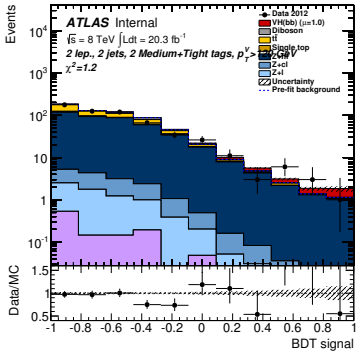

(j) $p_{\mathrm{T}}^{V} > 120$ GeV 2 jets, MM+TT

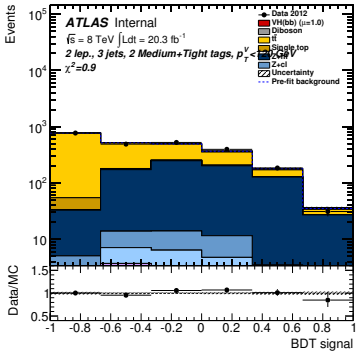

(k) $p_{\mathrm{T}}^{V} < 120$ GeV, 3 jets, MM+TT

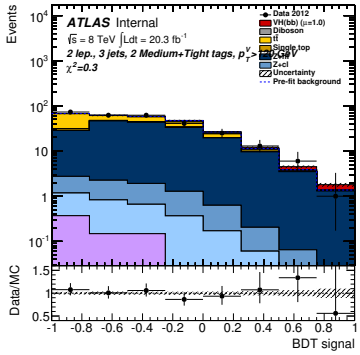

(l) $p_{\mathrm{T}}^{V} > 120$ GeV, 3 jets, MM+TT

Figure 87: Post-fit plots for MVA distribution in 2-lepton 2-jet and 3-jets , $p_{\mathrm{T}}^{V} < 120$ GeV (left) and $p_{\mathrm{T}}^{V} > 120$ GeV (right) events with 1 b-tag (MV1c is fit here), LL and $MM + TT$ b-tags in the 0+1+2 lepton fit. The pre-fit background expectation is indicated by the dashed blue line. Only statistical uncertainties are indicated.

8.8.1 Post fit b-tagging for the MVA analysis

In order to understand the effect of the pulls on the b-tagging related parameters the scale factor and related uncertainities are unfold from the fit and shown as a function of jet p_{T}.

As an examples, in Figure 88 we show the plots for the scale factors obtained in the MVA0+1+2 leptons combined fit .

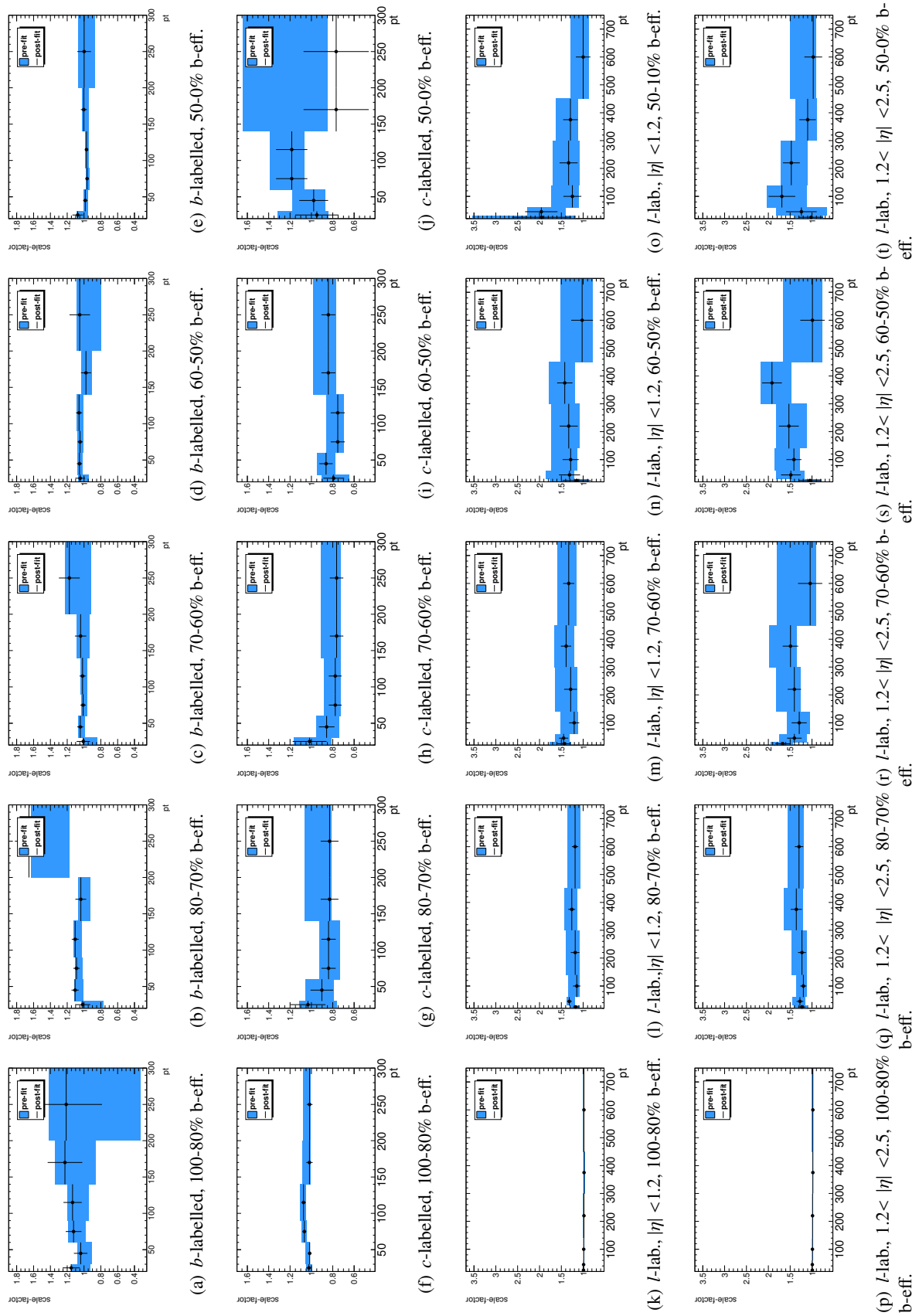

(a) b-labelled, 100-80% b-eff. (b) b-labelled, 80-70% b-eff. (c) b-labelled, 70-60% b-eff. (d) b-labelled, 60-50% b-eff. (e) b-labelled, 50-0% b-eff.

(f) c-labelled, 100-80% b-eff. (g) c-labelled, 80-70% b-eff. (h) c-labelled, 70-60% b-eff. (i) c-labelled, 60-50% b-eff. (j) c-labelled, 50-0% b-eff.

(k) l-lab., $|\eta|$ <1.2, 100-80% b-eff. (l) l-lab.,$|\eta|$ <1.2, 80-70% b-eff. (m) l-lab., $|\eta|$ <1.2, 70-60% b-eff. (n) l-lab., $|\eta|$ <1.2, 60-50% b-eff. (o) l-lab., $|\eta|$ <1.2, 50-10% b-eff.

(p) l-lab., 1.2< $|\eta|$ <2.5, 100-80% b-eff. (q) l-lab., 1.2< $|\eta|$ <2.5, 80-70% b-eff. (r) l-lab., 1.2< $|\eta|$ <2.5, 70-60% b-eff. (s) l-lab., 1.2< $|\eta|$ <2.5, 60-50% b-eff. (t) l-lab., 1.2< $|\eta|$ <2.5, 50-0% b-eff.

Figure 88: The MC-to-data post-fit unfolded calibration scale factors for the MV1c b, c-jet as a function ot the jet p_{T} .

8.9 Studies of the important NP in the fit

We summarize in Table 57 the first NP shown in the ranking plot in Figures 62 and 64. The reader should keep in mind that the systematics for the m_{bb} shape analysis can change, so only the MVA are correct.

In this section, we will discuss each of them, showing plots with the systematics band when relevant for some of the samples, the effect of the smoothing and pruning, the study of which region is determining eventual pulls, and any additional material coming from details studies. Since most of the checks are ongoing, the note will contain this results as soon as available.

Nuisance Parameter	Description	Section, Table	MVA rank	m_{bb} shape rank
norm_Wbb	norm factor on W+hf	–, 50	1 (–, 1, –)	10 (–, 8, –)
WblWbbRatio	Wbl/Wbb ratio for $p_{\mathrm{T}}^{W} > 120$ GeV	5.1.2.3, 50	2 (17, 2, –)	7 (5, 4, –)
WMbb_WbbORcc	Wbb/cc m_{jj} shape error $p_{\mathrm{T}}^{W} > 120$ GeV	5.1.2.3, 50	3 (6, 7, –)	1 (1, 1, –)
WPtV_J2_Whf	W+hf p_{T}^{W} spectrum in 2-jet events	5.1.2.3, 50	4 (30, 4, –)	22 (40, 26, –)
BJetReso	b-jet resolution	7.1.5.2, 55	5 (15, 9, 113)	2 (29, 2, 102)
WPtV_J3_Whf	W+hf p_{T}^{W} spectrum in 3-jet events	5.1.2.3, 50	6 (60, 6, –)	153 (75, 103, –)
JetEResol	jet resolution from JetETMiss	7.1.5.2, 55	7 (31, 8, 8)	58 (25, 105, 9)
norm_ttbar_L2	norm factor on $t\bar{t}$ in 2-lepton	–, 51	8 (–, 9, –)	6 (–, 7, –)
METScaleSoftTerms	Scale of the $E_{\mathrm{T}}^{\mathrm{miss}}$ soft term	7.1.6, 55	9 (53, 3, 63)	32 (26, 36, 18)
ZMbb_ZbORc	Zbb/cc m_{jj} shape error	5.1.1.3, 49	10 (4, 126, 4)	147 (51, 144, 12)
WMbb_B0_WbbORcc	Wbb/cc m_{jj} shape error $p_{\mathrm{T}}^{W} < 120(90)$ GeV for MVA(m_{jj})	5.1.2.3, 50	11 (–, 5, –)	36 (–, 13, –)
TChanPtB2	s-top t-chanel aMC@NLO vs AcerMC	5.2.2, 52	12 (32, 10, –)	14 (33, 9, 111)
BTagBPythia8	b-tagging MC-to-MC SF for b-jets	3.3.4.3, 55	13 (111,11,17)	17 (35,10,56)
LUMI	Luminosity	7.1.1, 55	14 (51, 13, 20)	19 (46, 11, 61)
ZDPhi_J2_ZbOrc	Z+hf $\Delta\phi$ correction in 2-jet events	5.1.1.2, 49	15 (55, 152, 3)	20 (47, 139, 5)

Table 57: The nuisance parameters ranking high in Figures 62 and 64, and their position in each lepton channel for both the m_{bb} shape and the MVA analysis. In parenthesis the breakdown in the 0-lepton, 1-lepton and 2-lepton channels.

Descriptions and explainations are to follow.

8.10 Compatibility between the m_{bb} shape analysis and the MVA analysis

Given the significant but incomplete statistical overlap between the datasets used for the m_{bb} shape and MVA analyses, the correlation between the results needs to be estimated. A modified bootstrap technique was used to assess the correlation due to the statistical overlap. No attempt was made to estimate the correlation due to the systematics.

Synchronised pseudo-datasets for the m_{bb} shape and MVA analyses are produced. These pseudo-datasets are then fit and the correlation between the $\hat{\mu}$ value obtained in each analysis is estimated.

The modified bootstrap technique is implemented technically considering each event from each MC sample used in the analysis. For each event, a number, n is drawn from a Poisson distribution of mean $|w|$, where w is the weight corresponding to the specific MC event. The event is then added n times to the pseudo-dataset with the weight as ± 1. This effectively selects a subsets of the full statistics of the MC sample by weighting each event appropriately. The final events in the pseudo-data are unweighted as a result of the technique. The seeds for the random numbers are determined by the event number such that the selected events are correlated between the pseudo-data for the m_{bb} shape analysis and the MVA analysis.

Figure 89 shows the distribution of the difference of $\hat{\mu}$ obtained for the m_{bb} shape analysis and the MVA analysis respectively using 800 - 900 (285 events for the combined 0+1+2 leptons analysis) events from the pseudo-data for the combination for 0, 1, 2 and 0+1+2 lepton analyses. The relation between $\hat{mu}$ obtained in each analysis is shown in Figure 90. There is a clear relation between the two and the correlation factor was extracted and found to be 0.68. The same study was repeated for fits to each of the individual channels and the results are summarised in Table 58. The correlation is largest for the 0-lepton channel (0.74) and slightly lower for the 2-lepton channel (0.58), as expected because the phase space accessed by the MVA analysis differs more significantly in the 2-lepton channel than the 0-lepton channel.

Channel	Correlation
0-lepton	0.74
1-lepton	0.65
2-lepton	0.58
Combination	0.66

Table 58: The correlation between the measured signal strength in the cut-based and MVA analyses.

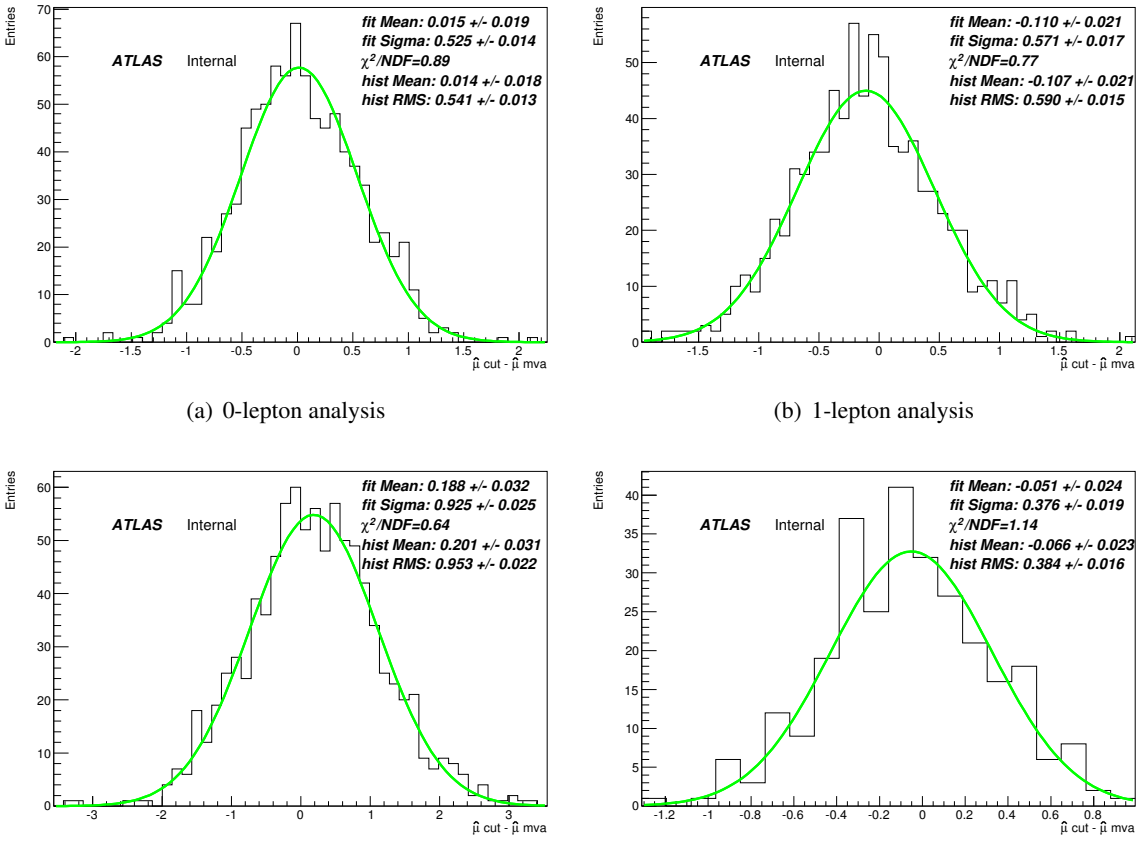

(a) 0-lepton analysis

(b) 1-lepton analysis

(c) 2-leptons analysis

(d) 0+1+2 leptons analysis

Figure 89: The distribution of the difference of the signal strength for the m_{bb} shape and MVA analyses from the pseudo-data from the bootstrap technique for the combination of the 0, 1, 2 and 0+1+2 lepton channels.

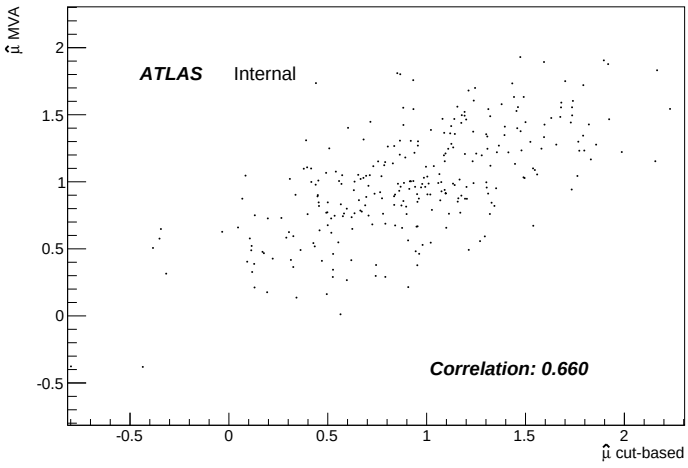

Figure 90: The relation between the signal strength obtained from the m_{bb} shape and MVA analyses for the combination of the 0- and 2-lepton channels.

9 Results

9.1 Diboson observation

The diboson production with a Z boson decaying to a pair of b-quarks and produced in association with either a W or a Z has a very similar signature to the VH process, but with lower p_T^Z and $m_{b\bar{b}}$ peaking at lower values with a cross section $\sim$ 5 times larger than the signal. Therefore, as a validation of this analysis procedure, a separate fit to the diboson process was performed. As the main purpose of this is validation, no attempt was made to optimize the selection towards diboson production.

In the fit the normalization of the diboson contributions is allowed to vary with a multiplicative scale μ_{VZ} with respect to the Standard Model expectation. A Standard Model Higgs boson with $m_H = 125$ GeV is included as a background in the fit.

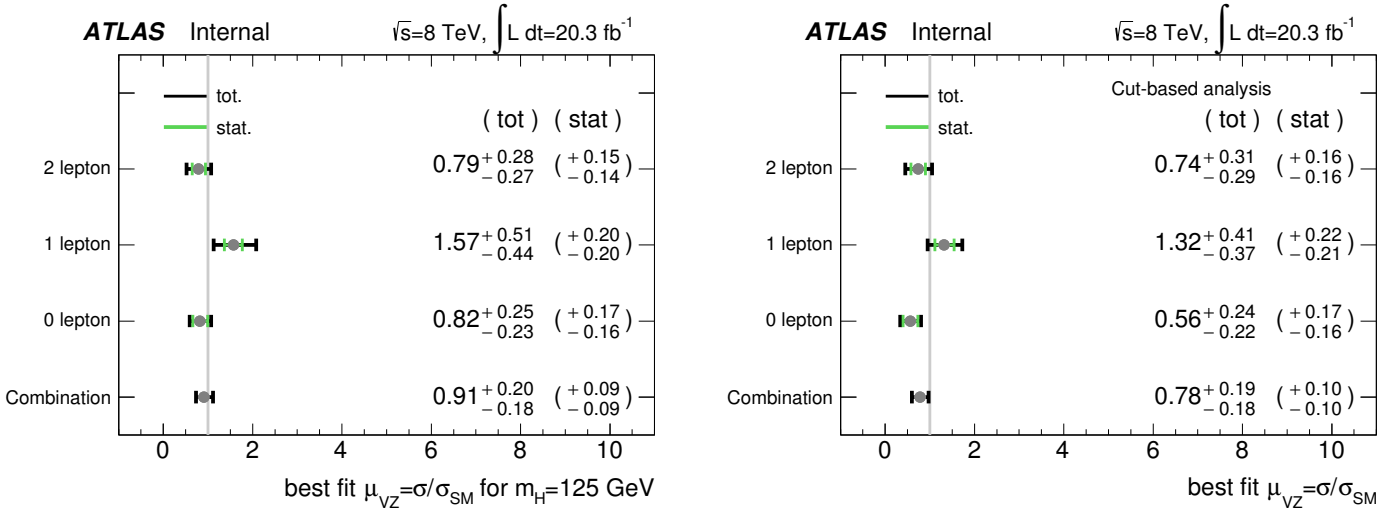

Figure 91: The fitted values of the Higgs-boson signal strength parameter μ for MVA (dijet mass) 8 TeV result one the left (right). Both plot have been created in the context on the full 0+1+2 lepton fit.

The fitted μ_{VZ} values are shown in Fig. 91 for the 8 TeV dataset, and for the three channels separately and combined, as obtained using the MVA and dijet mass analysis for the 8 TeV data. The overall fitted value, $\mu_{VZ} = 0.91^{+0.20}_{-0.18}$. agrees with the SM expectation of $\mu_{VZ} = 1$ and corresponds to an observed significance of 5.8 σ, with an expected significance of 6.19.

In the dijet-mass analysis, a μ_{VZ} value of $\mu_{VZ} = 0.78^{+0.19}_{0.18}$ is obtained. The results of fits performed with both the diboson and Higgs-boson signal-strength parameters μ_{VZ} and μ left freely floating are unchanged with respect to those from the separate fits reported above, and the correlation between the two strength parameters is found to be 0.04% in the Higgs MVA analysis. More details are given in Tables 59 and 60.

Channel	Exp. Lim.	**Obs. Lim.**	Exp. Sig.	**Obs. Sig.**	$\hat{\mu}$	$\sigma_{\hat{\mu}}$
0	0.496	1.354	4.367	4.023	0.89	+0.27 -0.24
1	0.882	2.590	2.493	3.703	1.64	+0.55 -0.49
2	0.557	1.197	3.535	2.423	0.69	+0.30 -0.29
012	0.341	1.245	6.177	5.622	0.91	+0.20 -0.18
					$\hat{\mu}_{0L} = 0.82$ $\hat{\mu}_{1L} = 1.57$ $\hat{\mu}_{2L} = 0.79$	± 0.24 ± 0.47 ± 0.27

Table 59: VZ MVA results.

Channel	Exp. Lim.	**Obs. Lim.**	Exp. Sig.	**Obs. Sig.**	$\hat{\mu}$	$\sigma_{\hat{\mu}}$
0	0.512	1.249	4.021	3.337	0.78	+0.27 -0.25
1	0.718	2.060	2.935	3.748	1.32	+0.43 -0.39
2	0.621	1.106	3.173	1.809	0.55	+0.32 -0.31
012	0.350	1.102	5.761	4.790	0.78	+0.19 -0.18
					$\hat{\mu}_{0L} = 0.56$ $\hat{\mu}_{0L} = 1.32$ $\hat{\mu}_{0L} = 0.74$	± 0.23 ± 0.39 ± 0.30

Table 60: VZ m_{jj} results.

9.2 Higgs Results

The profile likelihood fit with the Higgs boson signal strength μ floating is then performed with the diboson contribution constrained to its SM value within its uncertainty. Results are extracted independently for the dijet-mass and multivariate analyses. Since the MVA has better expected sensitivity to a Higgs-boson signal, it is used for the nominal results, while the dijet-mass analysis provides a cross-check. For the 7 TeV data, however, only a dijet-mass analysis is performed, which is combined with the MVA applied to the 8 TeV data.Unless otherwise specified, all results refer to a Higgs-boson mass of 125 GeV.

The data have sufficient power to constrain the largest background-normalization NPs, which are left free to float in the fit. This applies to the $t\bar{t}$, Wbb, Wcl, Zbb and Zcl processes. The corresponding "rescaling factors", i.e., the factors applied to the background normalizations as resulting from the global fit to the 8 TeV data, are shown in Table 61.

Table 61: Rescaling factors obtained from the global MVA fit to the 8 TeV data for the normalization of the $t\bar{t}$, Wbb, Wcl, Zbb, and Zcl backgrounds for the 2 jets events. The errors include the statistical and systematic uncertainties.

Process	Scale factor
$t\bar{t}_{L0}$	1.36 ± 0.13
$t\bar{t}_{L1}$	1.16 ± 0.07
$t\bar{t}_{L2}$	1.01 ± 0.04
Wbb	0.82 ± 0.16
Wcl	1.14 ± 0.07
Zbb	1.12 ± 0.06
Zcl	0.89 ± 0.11

The fitted numbers of signal and background events after MVA selection are shown in Appendix AJ for each lepton channel, in p_{T}^{V} intervals and b-tagging categories. The numbers of observed events in data are also shown.

Table 62: The fitted numbers of signal and background events and the observed numbers of events after MVA selection for each lepton channel, in p_{T}^{V} intervals and b-tagging categories. These numbers are for the 8 TeV dataset, corresponding to an integrated luminosity of 20.3 fb^{-1}. The fitted numbers of signal events are shown for WH and ZH production separately for $m_h = 125$ GeV. The quoted errors on the total background correspond to one standard deviation of the fitted nuisance parameters incorporating both the systematic and statistical uncertainties.

The fitted μ values for $m_h = 125$ GeV are shown in Fig. **??** for the 7 TeV, 8 TeV and combined datasets, and for the three channels separately and combined, as obtained using the MVA for the 8 TeV data. The fitted value of the signal strength parameter is $\mu = 0.97 \pm 0.42$. In the dijet-mass analysis, a μ value of $1.41 \pm 0.57\pm$ is obtained. Using the "bootstrap" method mentioned in Section 8.10, the results obtained for the 8 TeV data with the dijet-mass analysis and with the MVA are found to be statistically consistent within x.xσ.

Figure 93 shows the data, background and signal yields, where final-discriminant bins in all signal regions are combined into bins of $\log(S/B)$, as obtained using the MVA or the m_{jj}shape analysis for the 8 TeV data. Here, S is the fitted signal yield and B is the fitted background yield.

Impact on μ error (quadratically subtracted from total)

Set of NPs	MVA		CUT	
Data stat	+0.29	−0.25	+0.42	−0.36
Floating norms	+0.10	−0.09	+0.13	−0.12
All norms	+0.12	−0.11	+0.17	−0.15
All other NPs	+0.25	−0.20	+0.36	−0.31
Theory VH	+0.10	−0.055	+0.16	−0.088
Theory VV	+0.036	−0.023	+0.059	−0.041
Total	+0.43	−0.40	+0.59	−0.54

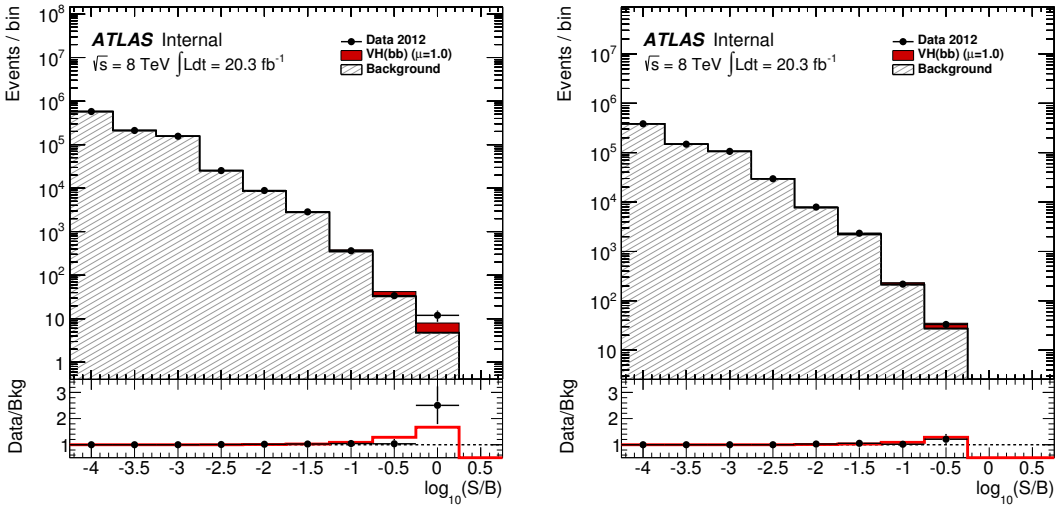

(a) MVA analysis (b) m_{jj} shape analysis

Figure 92: Event yields as a function of $\log(S/B)$ for data, background and Higgs-boson signal for m_h = 125 GeV. Final-discriminant bins in all signal regions are combined into bins of $\log(S/B)$, as obtained using the MVA (left) or m_{jj} shape analysis (right) for the 8 TeV data. The signal yield S corresponds to the best μ value, and B is the background yield evaluated according to the results of the global fit. The Higgs-boson signal contribution is shown both with its fitted signal strength (indicated as "best fit") and as expected for the SM cross section (indicated as $\mu = 1.0$). The background-only distribution (dashed line) is obtained from a global fit unconditional of μ.

Figures **??** and **??** shows the 8 TeV best-fit μ values for the dijet mass and MVA analysis respectively. Figure **??** shows the combination of the 7 TeV dijet mass and 8 TeV MVA analysis described in Appendix AK.

Figure 97 99-(left) shows the 95% CL upper limits on the Higgs-boson production cross section in the mass range 100–150 GeV, as obtained using the m_{bb} shape analysis and the BDTs trained at each individual mass for the 8 TeV data.

The observed limit for m_h = 125 GeV combining 7 TeV and 8 TeV is 1.42 times the SM Higgs-boson production cross section, to be compared to an expected limit, in the absence of signal, of 0.73. If the analysis is restricted to the 7 TeV or 8 TeV dataset, the observed (expected) limits are 1.94 (3.12) and 1.78 (0.76), respectively. Figure 99, show for comparison the expectation for the MVA analysis if the BDT function optimized for m_h 125 GeV is used for all the other mass point.

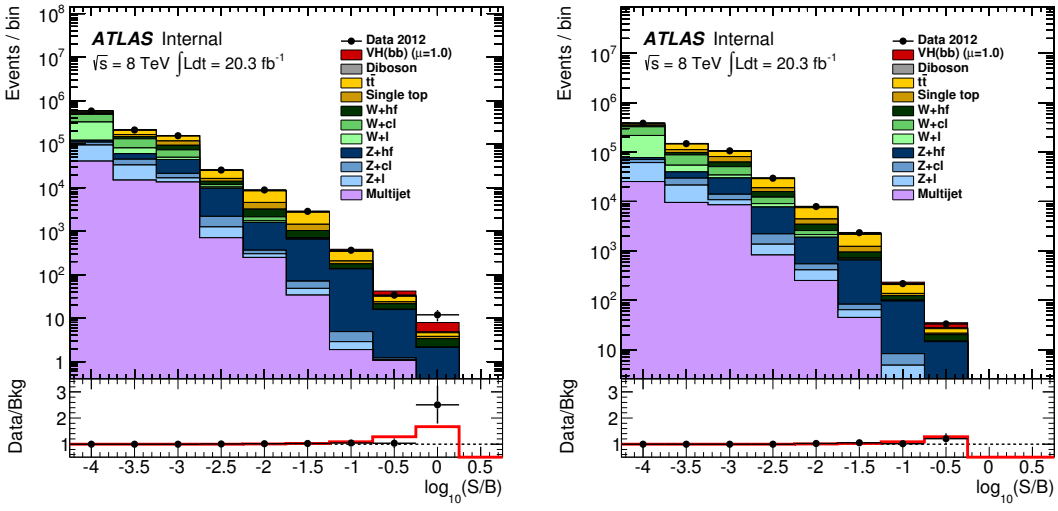

(a) MVA analysis (b) m_{jj} shape analysis

Figure 93: Event yields as a function of $\log(S/B)$ for data, background and Higgs-boson signal for m_h = 125 GeV. Final-discriminant bins in all signal regions are combined into bins of $\log(S/B)$, as obtained using the MVA (left) or m_{jj} shape analysis (right) for the 8 TeV data. The signal yield S corresponds to the best μ value, and B is the background yield evaluated according to the results of the global fit. The Higgs-boson signal contribution is shown both with its fitted signal strength (indicated as "best fit") and as expected for the SM cross section (indicated as $\mu = 1.0$). The background-only distribution (dashed line) is obtained from a global fit unconditional of μ.

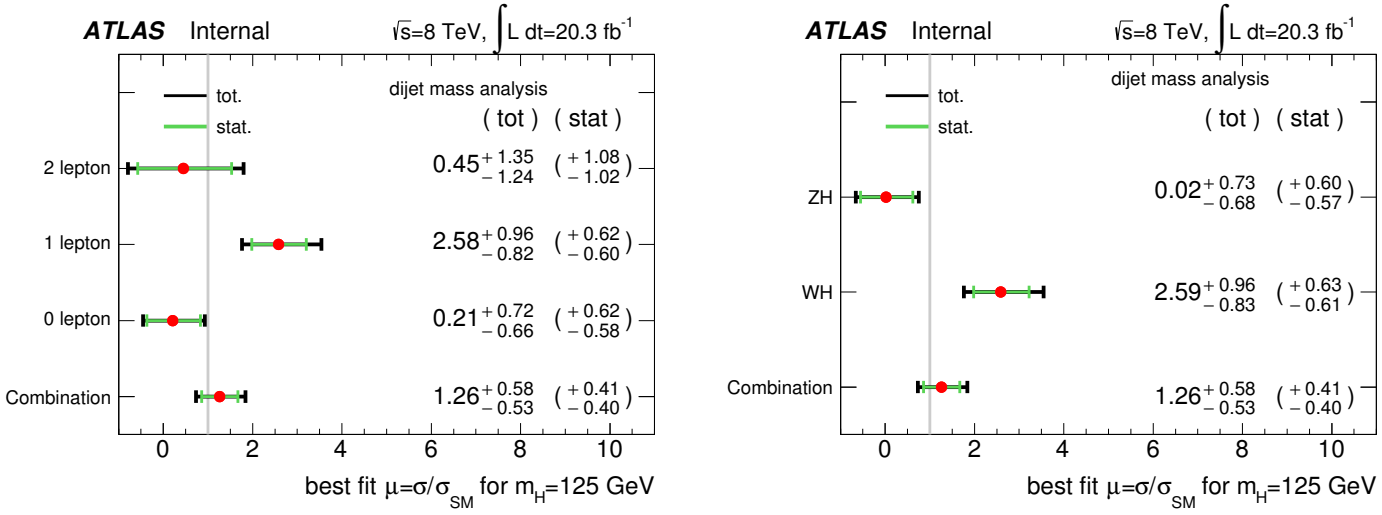

Figure 94: The fitted values of the Higgs-boson signal strength parameter μ for dijet mass 8 TeV result. Both plot have been created in the context on the full 0+1+2 lepton fit. The left plot was made fitting a signal strength in each lepton selection while the right was made fitting a signal strenght for WH and ZH separately.

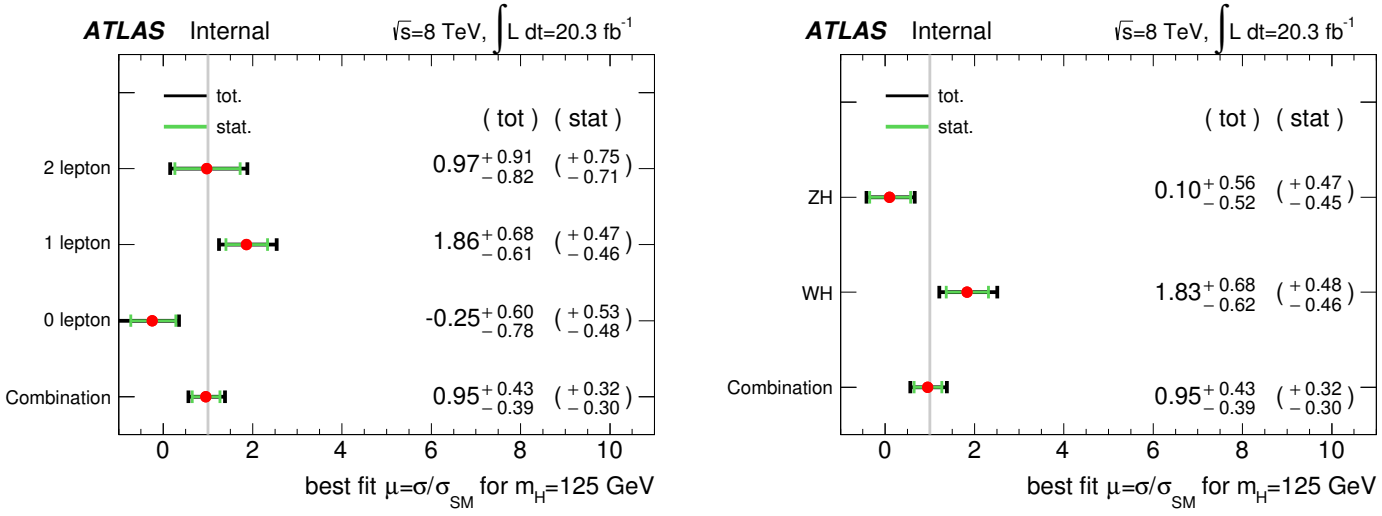

Figure 95: The fitted values of the Higgs-boson signal strength parameter μ for MVA 8 TeV result. Both plot have been created in the context on the full 0+1+2 lepton fit. The left plot was made fitting a signal strength in each lepton selection while the right was made fitting a signal strenght for WH and ZH separately.

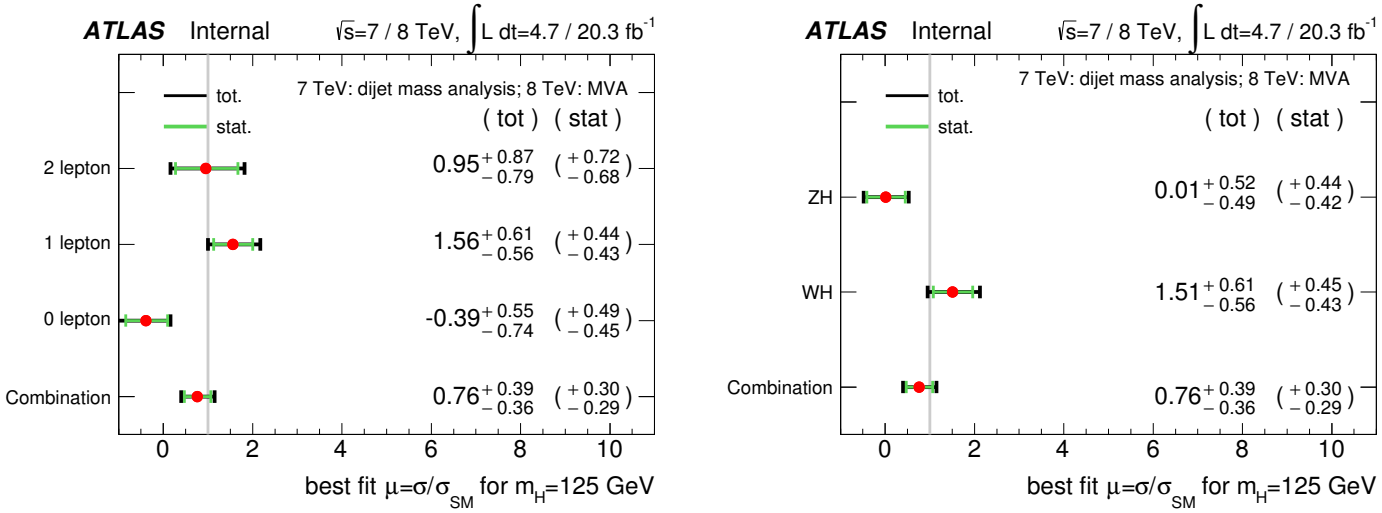

Figure 96: The fitted values of the Higgs-boson signal strength parameter μ for the combination of the 7 TeV dijet mass and MVA 8 TeV result. Both plot have been created in the context on the full 0+1+2 lepton fit. The left plot was made fitting a signal strength in each lepton selection while the right was made fitting a signal strenght for WH and ZH separately.

	MVA	m_{jj} shape
Expected limit	$0.76^{+0.30}_{-0.21}$	$0.99^{+0.39}_{-0.28}$
Observed limit	1.68	2.25
Observed significance	2.54	2.25
μ	$0.95^{+0.43}_{-0.39}$	$1.26^{+0.58}_{-0.53}$
3-μ fit		
	MVA	m_{jj} shape
μ_{WH}	$1.83^{+0.68}_{-0.62}$	$0.21^{+0.72}_{-0.66}$
μ_{ZH}	$2.59^{+0.96}_{-0.83}$	$0.02^{+0.73}_{-0.68}$
$\mu_{\text{0-lep}}$	$-0.25^{+0.60}_{-0.78}$	$0.21^{+0.72}_{-0.66}$
$\mu_{\text{1-lep}}$	$2.86^{+0.68}_{-0.61}$	$2.58^{+0.96}_{-0.82}$
$\mu_{\text{2-lep}}$	$0.97^{+0.91}_{-0.82}$	$0.45^{+1.35}_{-1.24}$
Compatibility		
1-μ vs. 2-μ	3.8%	–%
1-μ vs. 3-μ	4.0%	6.2%

Table 63: Expected and observed limits, significance and errors on μ for the MVA and m_{jj} shape analyses of the 8 TeV data, in each of the lepton channel, and in the combination for m_h=125 GeV. $\mu_{\text{[x]-lep}}$ in the combined fit refears to the fit performed with one indipendent μ for each channel in the combined fit.

Table **??** shows the results for the MVA analysis and m_{bb} shape analysis of the 8 TeV data, for each lepton channel, and for the final combination.

For the full dataset and all channels combined, the probability p_0 of obtaining a result at least as signal-like as observed if no signal is present is 0.0055 (2.54σ), to be compared to an expectation of 0.0039 (2.66σ) for the 8 TeV analysis. in the presence of a SM Higgs boson with a mass of 125 GeV. Similarly, the observed result is 0.07σ from the the SM Higgs boson expectation with $m_h = 125$ GeV. Figure 97 99-(right) shows probability p_0 in the mass range 100–150 GeV, as obtained using the m_{bb} shape analysis and the BDTs trained at each individual mass for the 8 TeV data.

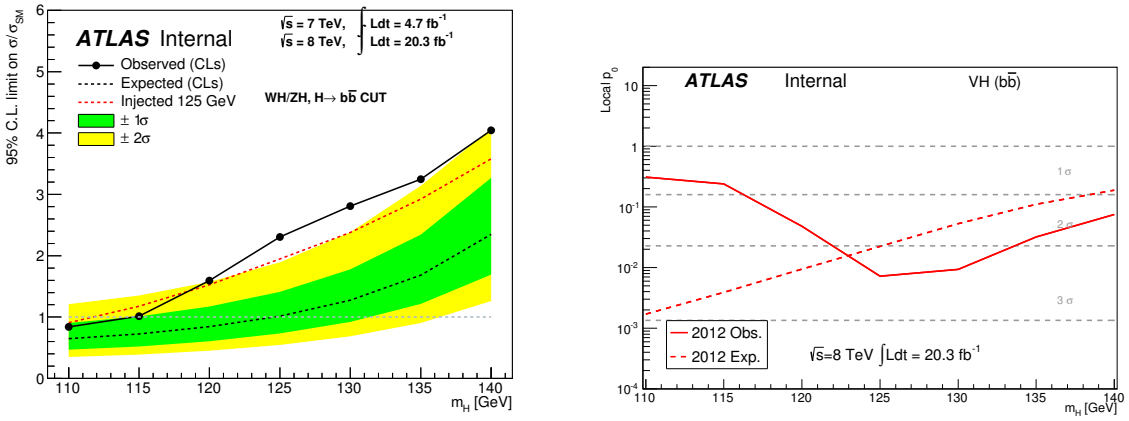

Figure 97: Left: Expected 95% C.L. upper limits on the normalised signal strength as a function of Higgs boson mass for all channels in 8 TeV data, for m_{bb} shape analysis.The expected upper limit is given for the background-only hypothesis. The green and yellow bands represent the 1σ and 2σ ranges of the expectation in the absence of a signal. Right: The observed local $p0$ as a function of the Higgs boson mass for the m_{bb} shape analysis. The dashed curves shows the expected local $p0$ under the hypothesis of a SM Higgs boson signal at that mass for the analysis of the 8 TeV data. Table 64 contains the exact values at each mass point.

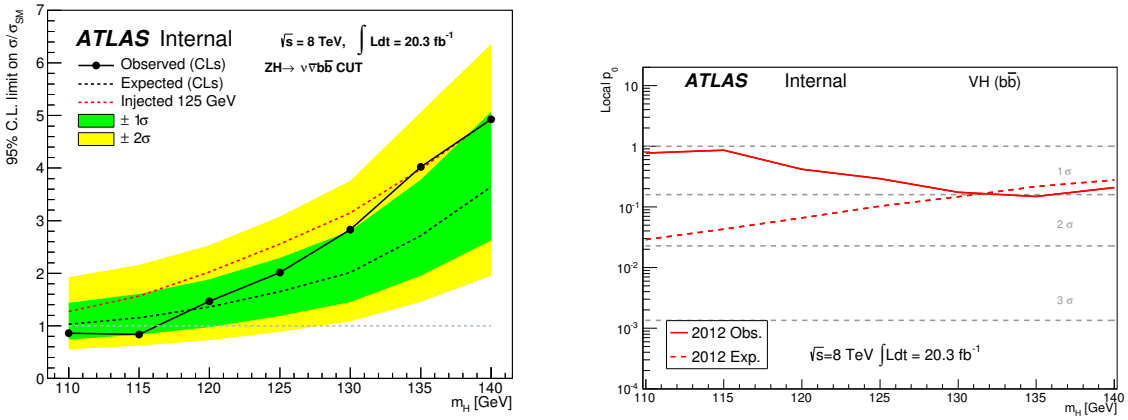

(a) 0-lepton

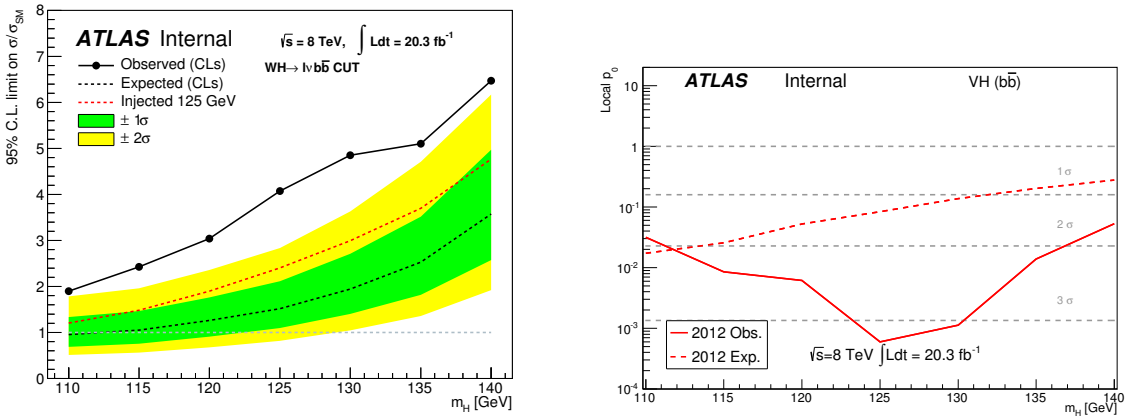

(b) 1-lepton

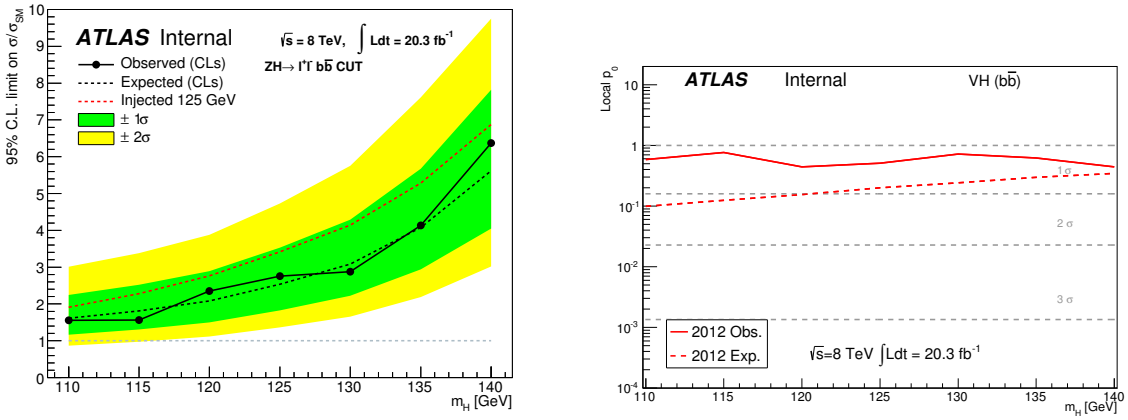

(c) 2-lepton

Figure 98: Left: Expected 95% C.L. upper limits on the normalised signal strength as a function of Higgs boson mass for the different lepton channels in 8 TeV data, for m_{bb} shape analysis.The expected upper limit is given for the background-only hypothesis. The green and yellow bands represent the 1σ and 2σ ranges of the expectation in the absence of a signal. Right: The observed local $p0$ as a function of the Higgs boson mass for the m_{bb} shape analysis. The dashed curves shows the expected local $p0$ under the hypothesis of a SM Higgs boson signal at that mass for the analysis of the 8 TeV data. (a): 0-lepton; (b): 1-lepton; (c): 2-leptons. Tables 65- 67 contain the exact values at each mass point.

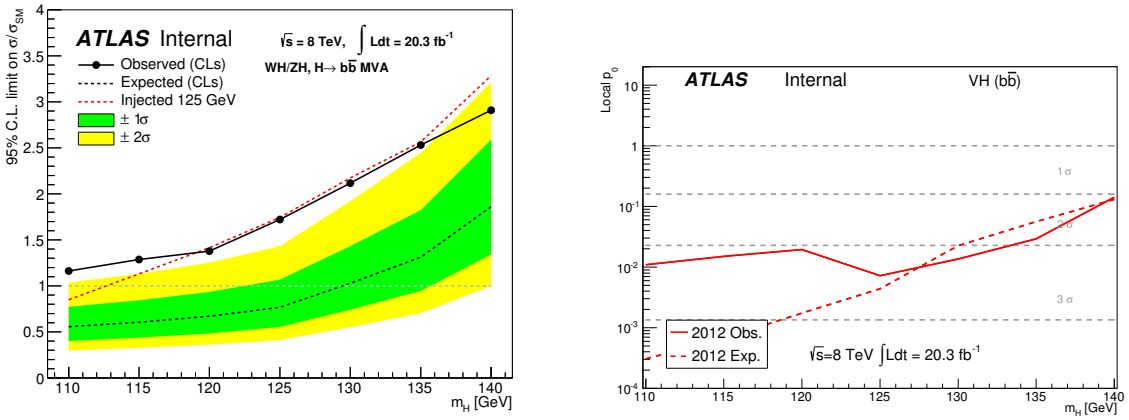

(a) mass point training

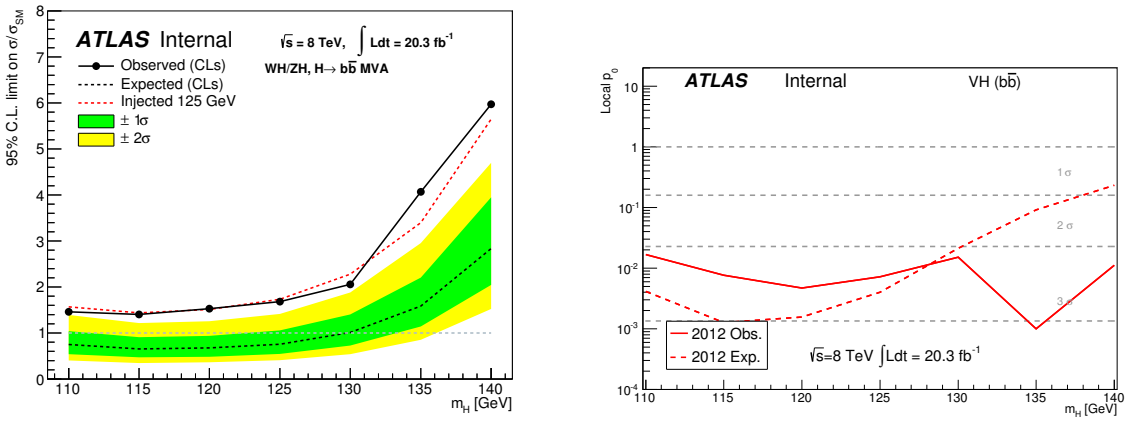

(b) m_H = 125 GeV training

Figure 99: Left: Expected 95% C.L. upper limits on the normalised signal strength as a function of Higgs boson mass for all channels in 8 TeV data, for MVA shape analysis.The expected upper limit is given for the background-only hypothesis. The green and yellow bands represent the 1σ and 2σ ranges of the expectation in the absence of a signal. Right: The observed local $p0$ as a function of the Higgs boson mass for the MVA shape analysis. The dashed curves shows the expected local $p0$ under the hypothesis of a SM Higgs boson signal at that mass for the analysis of the 8 TeV data. (a): the MVA has been trained for each mass point (Table 68). (b): the MVA trained for m_h =125 has been used for all the mass point (Table 72).

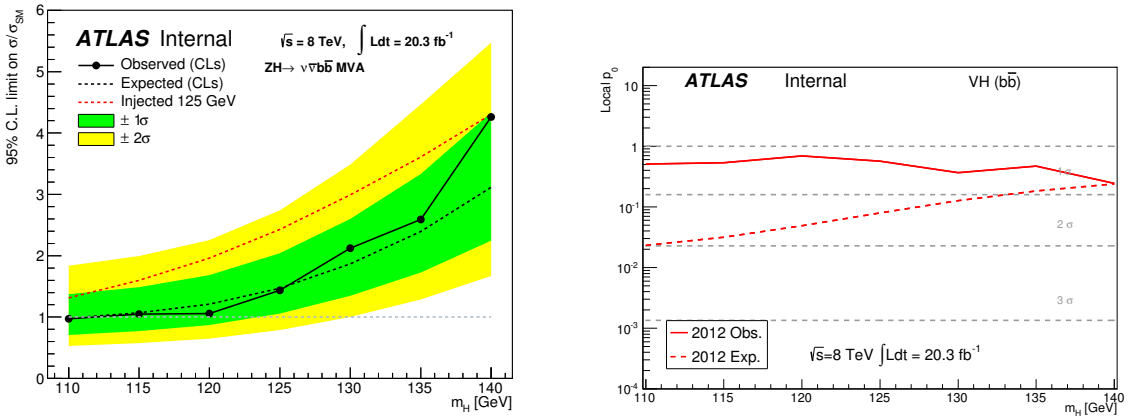

(a) 0-lepton

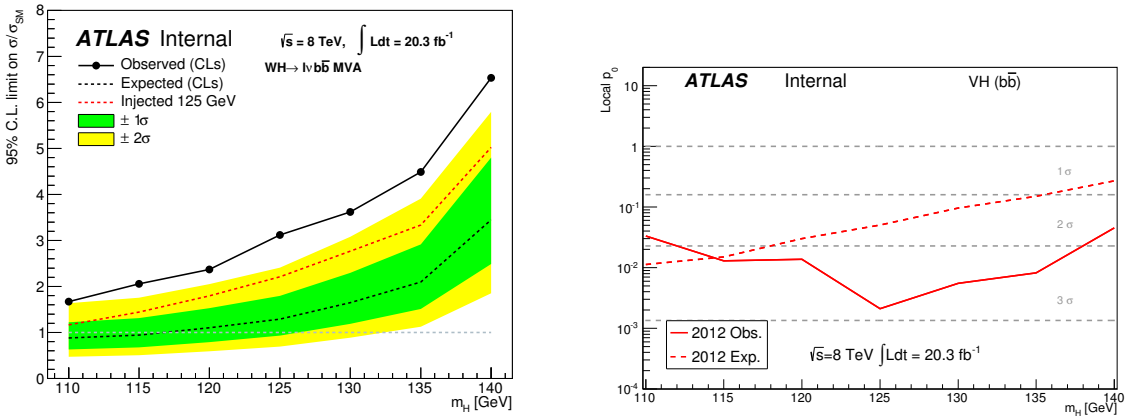

(b) 1-lepton

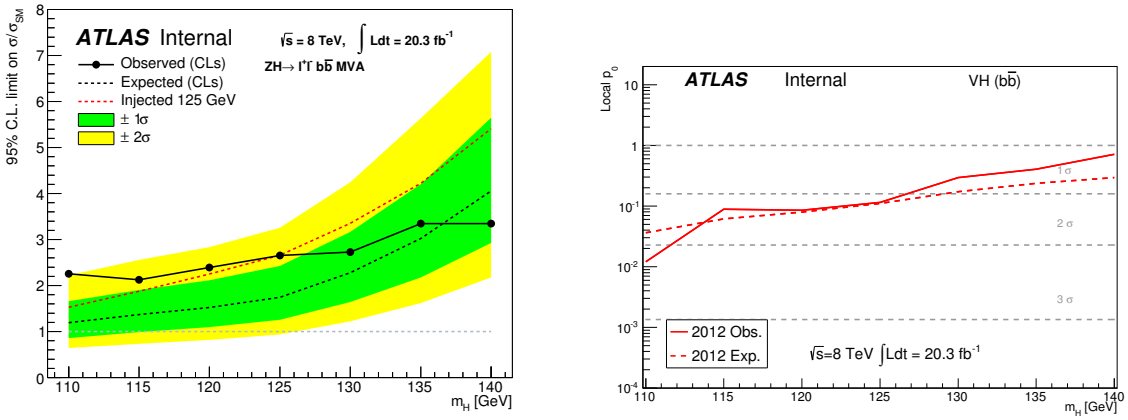

(c) 2-lepton

Figure 100: Left: Expected 95% C.L. upper limits on the normalised signal strength as a function of Higgs boson mass for the different lepton channels in 8 TeV data, for MVA analysis (the MVA has been trained for each mass point).The expected upper limit is given for the background-only hypothesis. The green and yellow bands represent the 1σ and 2σ ranges of the expectation in the absence of a signal. Right: The observed local $p0$ as a function of the Higgs boson mass for the m_{bb} shape analysis. The dashed curves shows the expected local $p0$ under the hypothesis of a SM Higgs boson signal at that mass for the analysis of the 8 TeV data. (a): 0-lepton; (b): 1-lepton; (c): 2-leptons. Tables 69- 71 contain the exact values at each mass point.

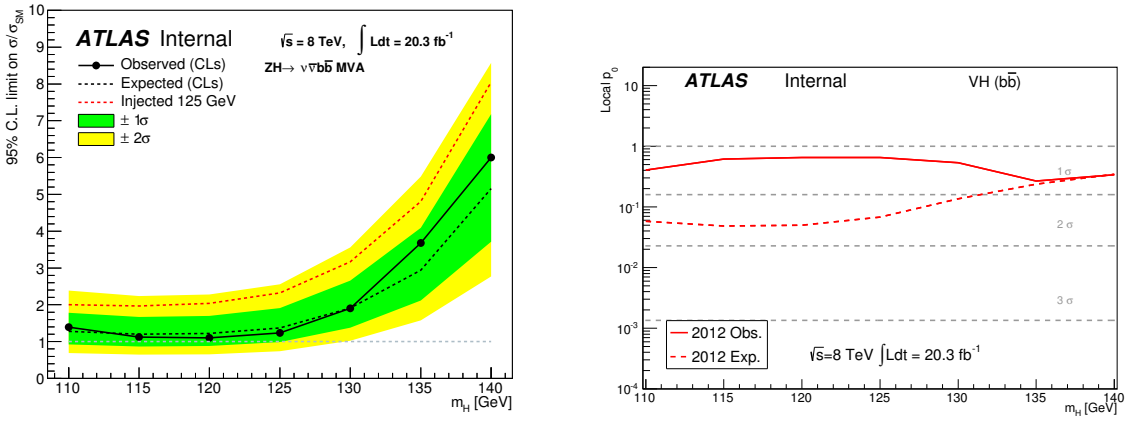

(a) 0-lepton

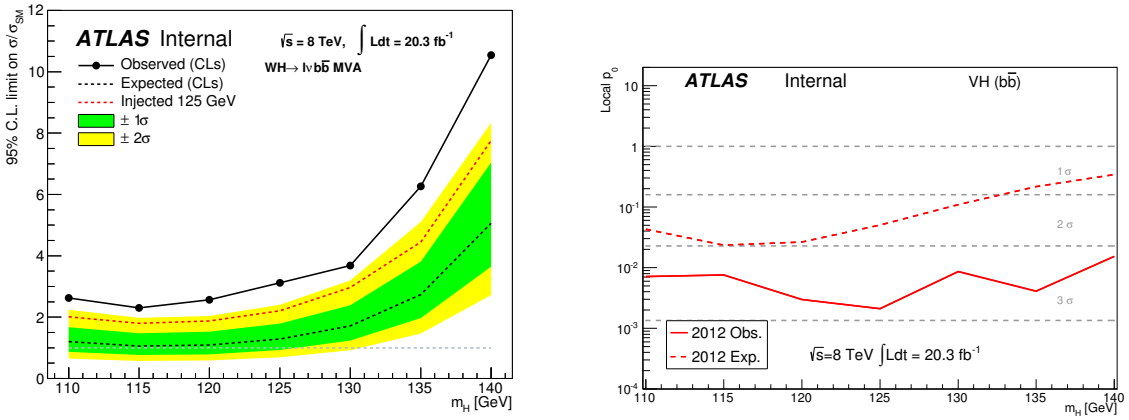

(b) 1-lepton

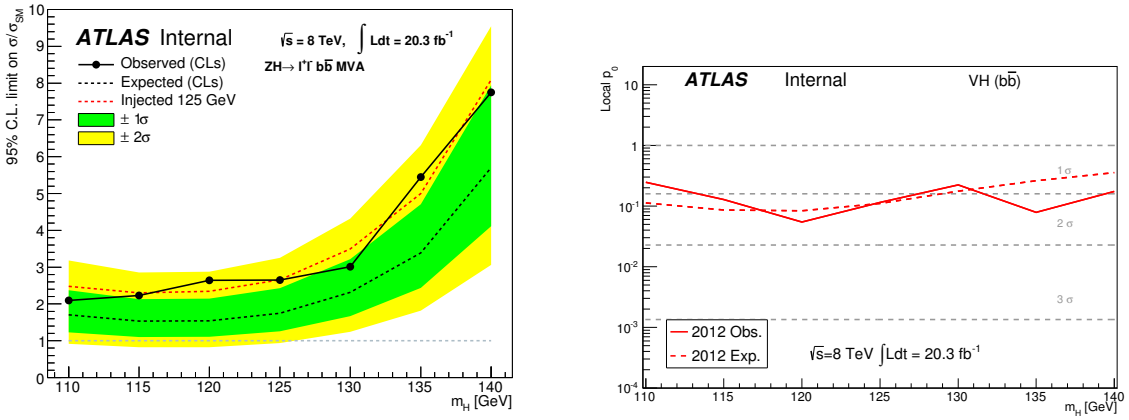

(c) 2-lepton

Figure 101: Left: Expected 95% C.L. upper limits on the normalised signal strength as a function of Higgs boson mass for the different lepton channels in 8 TeV data, for MVA analysis (the MVA trained for m_h =125 has been used for all the mass point).The expected upper limit is given for the background-only hypothesis. The green and yellow bands represent the 1σ and 2σ ranges of the expectation in the absence of a signal. Right: The observed local $p0$ as a function of the Higgs boson mass for the m_{bb} shape analysis. The dashed curves shows the expected local $p0$ under the hypothesis of a SM Higgs boson signal at that mass for the analysis of the 8 TeV data. (a): 0-lepton; (b): 1-lepton; (c): 2-leptons. Tables 73- 75 contain the exact values at each mass point.

9.2.1 Higgs Results Tables

Here is a collection of tables corresponding to the above p_0 and limit plots.

mass	Exp.	$+2\sigma$	$+1\sigma$	-1σ	-2σ	Obs.	Inj.
110	0.65	1.21	0.90	0.47	0.35	0.84	0.91
115	0.72	1.35	1.01	0.52	0.39	1.01	1.18
120	0.84	1.57	1.17	0.61	0.45	1.59	1.52
125	1.01	1.89	1.41	0.73	0.54	2.30	1.95
130	1.28	2.38	1.78	0.92	0.68	2.81	2.38
135	1.68	3.14	2.34	1.21	0.90	3.25	2.92
140	2.35	4.38	3.27	1.69	1.26	4.04	3.58

mass (GeV)	Exp p_0	Obs p_0
110	0.00172	0.31001
115	0.00389	0.23889
120	0.0094	0.0481
125	0.02229	0.00722
130	0.05278	0.00929
135	0.10993	0.03196
140	0.18781	0.07478

Table 64: The limit and p_0 for the m_{jj} 0+1+2 lepton 8 TeV analysis corresponding to Figure 97

mass	Exp.	$+2\sigma$	$+1\sigma$	-1σ	-2σ	Obs.	Inj.
110	1.03	1.92	1.44	0.74	0.55	0.86	1.27
115	1.16	2.16	1.61	0.83	0.62	0.84	1.57
120	1.36	2.53	1.89	0.98	0.73	1.47	2.03
125	1.65	3.08	2.29	1.19	0.88	2.01	2.55
130	2.02	3.76	2.81	1.45	1.08	2.83	3.15
135	2.72	5.07	3.78	1.96	1.46	4.02	3.98
140	3.64	6.80	5.07	2.63	1.96	4.93	4.93

mass (GeV)	Exp p_0	Obs p_0
110	0.02901	0.77017
115	0.04305	0.86258
120	0.06586	0.41575
125	0.10336	0.29178
130	0.14693	0.17409
135	0.21694	0.14824
140	0.2774	0.20915

Table 65: The limit and p_0 for the m_{jj} 8 TeV 0-lepton analysis corresponding to Figure 98 (a).

mass	Exp.	$+2\sigma$	$+1\sigma$	-1σ	-2σ	Obs.	Inj.
110	0.96	1.79	1.33	0.69	0.51	1.90	1.21
115	1.05	1.96	1.46	0.76	0.56	2.43	1.48
120	1.26	2.36	1.76	0.91	0.68	3.04	1.90
125	1.52	2.84	2.12	1.10	0.82	4.07	2.40
130	1.95	3.63	2.71	1.40	1.04	4.86	3.00
135	2.53	4.71	3.52	1.82	1.36	5.10	3.70
140	3.57	6.67	4.97	2.57	1.92	6.47	4.77

mass (GeV)	Exp p_0	Obs p_0
110	0.01719	0.03163
115	0.02555	0.00856
120	0.05227	0.00613
125	0.08359	0.0006
130	0.13794	0.00113
135	0.20205	0.01392
140	0.27732	0.05286

Table 66: The limit and p_0 for the m_{jj} 8 TeV 1-lepton analysis corresponding to Figure 98 (b).

mass	Exp.	$+2\sigma$	$+1\sigma$	-1σ	-2σ	Obs.	Inj.
110	1.61	3.01	2.25	1.16	0.87	1.55	1.91
115	1.81	3.38	2.52	1.31	0.97	1.56	2.28
120	2.08	3.88	2.89	1.50	1.12	2.35	2.76
125	2.54	4.73	3.53	1.83	1.36	2.76	3.42
130	3.08	5.75	4.29	2.22	1.66	2.88	4.14
135	4.08	7.61	5.68	2.94	2.19	4.13	5.28
140	5.62	10.48	7.82	4.05	3.02	6.37	6.88

mass (GeV)	Exp p_0	Obs p_0
110	0.09913	0.58267
115	0.12423	0.76521
120	0.1549	0.44272
125	0.20014	0.50975
130	0.24078	0.71806
135	0.29697	0.61997
140	0.34656	0.44225

Table 67: The limit and p_0 for the m_{jj} 8 TeV 2-lepton analysis corresponding to Figure 98 (c).

mass	Exp.	$+2\sigma$	$+1\sigma$	-1σ	-2σ	Obs.	Inj.
110	0.51	0.96	0.71	0.37	0.28	1.03	0.00
115	0.57	1.06	0.79	0.41	0.31	1.05	0.00
120	0.63	1.17	0.87	0.45	0.34	1.14	0.00
125	0.72	1.35	1.01	0.52	0.39	1.42	0.00
130	0.97	1.82	1.36	0.70	0.52	1.85	0.00
135	1.26	2.34	1.75	0.91	0.67	2.46	0.00
140	1.72	3.21	2.39	1.24	0.92	2.98	0.00

mass (GeV)	Exp p_0	Obs p_0
110	0.00011	0.01447
115	0.00034	0.02987
120	0.00099	0.04992
125	0.00293	0.01789
130	0.01808	0.02475
135	0.04979	0.02527
140	0.11387	0.0769

Table 68: The limit and p_0 for the MVA 0+1+2 lepton 8 TeV analysis where the MVA has been used at each mass point corresponding to Figure 99 (a)

mass	Exp.	$+2\sigma$	$+1\sigma$	-1σ	-2σ	Obs.	Inj.
110	1.28	2.39	1.78	0.92	0.69	1.40	2.00
115	1.20	2.24	1.67	0.87	0.64	1.12	1.97
120	1.22	2.28	1.70	0.88	0.66	1.10	2.04
125	1.37	2.56	1.91	0.99	0.74	1.24	2.33
130	1.91	3.56	2.66	1.38	1.02	1.90	3.17
135	2.94	5.49	4.09	2.12	1.58	3.68	4.81
140	5.16	9.62	7.18	3.72	2.77	6.00	8.05

mass (GeV)	Exp p_0	Obs p_0
110	0.05807	0.40398
115	0.04821	0.61293
120	0.04984	0.6516
125	0.0677	0.6491
130	0.13585	0.53529
135	0.23646	0.26758
140	0.34377	0.33772

Table 69: The limit and p_0 for the MVA 8 TeV 0-lepton analysis where the MVA has been used at each mass point corresponding to Figure 100 (a).

mass	Exp.	$+2\sigma$	$+1\sigma$	-1σ	-2σ	Obs.	Inj.
110	1.20	2.24	1.67	0.87	0.65	2.63	2.01
115	1.06	1.98	1.47	0.76	0.57	2.30	1.80
120	1.09	2.04	1.52	0.79	0.59	2.57	1.88
125	1.29	2.40	1.79	0.93	0.69	3.12	2.21
130	1.72	3.20	2.39	1.24	0.92	3.68	2.96
135	2.74	5.11	3.81	1.97	1.47	6.27	4.45
140	5.06	9.44	7.04	3.65	2.72	10.55	7.76

mass (GeV)	Exp p_0	Obs p_0
110	0.043	0.00717
115	0.02349	0.00756
120	0.02643	0.00299
125	0.05025	0.0021
130	0.10896	0.00861
135	0.21739	0.00411
140	0.34077	0.01529

Table 70: The limit and p_0 for the MVA 8 TeV 1-lepton analysis where the MVA has been used at each mass point corresponding to Figure 100 (b).

mass	Exp.	$+2\sigma$	$+1\sigma$	-1σ	-2σ	Obs.	Inj.
110	1.71	3.18	2.38	1.23	0.92	2.10	2.48
115	1.53	2.86	2.13	1.10	0.82	2.23	2.30
120	1.54	2.88	2.14	1.11	0.83	2.64	2.34
125	1.74	3.26	2.43	1.26	0.94	2.65	2.66
130	2.31	4.32	3.22	1.67	1.24	3.01	3.50
135	3.39	6.32	4.71	2.44	1.82	5.44	5.00
140	5.71	10.65	7.94	4.11	3.06	7.75	8.09

mass (GeV)	Exp p_0	Obs p_0
110	0.11278	0.24549
115	0.08573	0.12774
120	0.08325	0.05482
125	0.11007	0.1144
130	0.17637	0.22373
135	0.26153	0.07884
140	0.35478	0.17493

Table 71: The limit and p_0 for the MVA 8 TeV 2-lepton analysis where the MVA has been used at each mass point corresponding to Figure 100 (c).

mass	Exp.	$+2\sigma$	$+1\sigma$	-1σ	-2σ	Obs.	Inj.
110	0.75	1.39	1.04	0.54	0.40	1.46	1.57
115	0.65	1.22	0.91	0.47	0.35	1.40	1.44
120	0.67	1.26	0.94	0.49	0.36	1.53	1.51
125	0.76	1.41	1.05	0.55	0.41	1.68	1.74
130	1.01	1.88	1.40	0.73	0.54	2.06	2.28
135	1.58	2.96	2.20	1.14	0.85	4.07	3.40
140	2.84	5.29	3.95	2.04	1.52	5.97	5.65

mass (GeV)	Exp p_0	Obs p_0
110	0.00415	0.01673
115	0.00127	0.00767
120	0.00156	0.0047
125	0.00402	0.0072
130	0.02125	0.01514
135	0.09185	0.001
140	0.23306	0.01112

Table 72: The limit and p_0 for the MVA 0+1+2 lepton 8 TeV analysis where the $m_h = 125$ GeV training has been used at each mass point corresponding to Figure 99 (b)

mass	Exp.	$+2\sigma$	$+1\sigma$	-1σ	-2σ	Obs.	Inj.
110	1.28	2.39	1.78	0.92	0.69	1.40	2.00
115	1.20	2.24	1.67	0.87	0.64	1.12	1.97
120	1.22	2.28	1.70	0.88	0.66	1.10	2.04
125	1.37	2.56	1.91	0.99	0.74	1.24	2.33
130	1.91	3.56	2.66	1.38	1.02	1.90	3.17
135	2.94	5.49	4.09	2.12	1.58	3.68	4.81
140	5.16	9.62	7.18	3.72	2.77	6.00	8.05

mass (GeV)	Exp p_0	Obs p_0
110	0.05807	0.40398
115	0.04821	0.61293
120	0.04984	0.6516
125	0.0677	0.6491
130	0.13585	0.53529
135	0.23646	0.26758
140	0.34377	0.33772

Table 73: The limit and p_0 for the MVA 8 TeV 0-lepton analysis where the $m_h = 125$ GeV training has been used at each mass point corresponding to Figure 101 (a).

mass	Exp.	$+2\sigma$	$+1\sigma$	-1σ	-2σ	Obs.	Inj.
110	1.20	2.24	1.67	0.87	0.65	2.63	2.01
115	1.06	1.98	1.47	0.76	0.57	2.30	1.80
120	1.09	2.04	1.52	0.79	0.59	2.57	1.88
125	1.29	2.40	1.79	0.93	0.69	3.12	2.21
130	1.72	3.20	2.39	1.24	0.92	3.68	2.96
135	2.74	5.11	3.81	1.97	1.47	6.27	4.45
140	5.06	9.44	7.04	3.65	2.72	10.55	7.76

mass (GeV)	Exp p_0	Obs p_0
110	0.043	0.00717
115	0.02349	0.00756
120	0.02643	0.00299
125	0.05025	0.0021
130	0.10896	0.00861
135	0.21739	0.00411
140	0.34077	0.01529

Table 74: The limit and p_0 for the MVA 8 TeV 1-lepton analysis where the $m_h = 125$ GeV training has been used at each mass point corresponding to Figure 101 (b).

mass	Exp.	$+2\sigma$	$+1\sigma$	-1σ	-2σ	Obs.	Inj.
110	1.71	3.18	2.38	1.23	0.92	2.10	2.48
115	1.53	2.86	2.13	1.10	0.82	2.23	2.30
120	1.54	2.88	2.14	1.11	0.83	2.64	2.34
125	1.74	3.26	2.43	1.26	0.94	2.65	2.66
130	2.31	4.32	3.22	1.67	1.24	3.01	3.50
135	3.39	6.32	4.71	2.44	1.82	5.44	5.00
140	5.71	10.65	7.94	4.11	3.06	7.75	8.09

mass (GeV)	Exp p_0	Obs p_0
110	0.11278	0.24549
115	0.08573	0.12774
120	0.08325	0.05482
125	0.11007	0.1144
130	0.17637	0.22373
135	0.26153	0.07884
140	0.35478	0.17493

Table 75: The limit and p_0 for the MVA 8 TeV 2-lepton analysis where the $m_h = 125$ GeV training has been used at each mass point corresponding to Figure 101 (c).

References

[1] S. L. Glashow, *Partial Symmetries of Weak Interactions*, Nucl. Phys. **22** (1961) 579–588.

[2] S. Weinberg, *A Model of Leptons*, Phys. Rev. Lett. **19** (1967) 1264–1266.

[3] A. Salam, *Weak and electromagnetic interactions*, Proc. of the 8th Nobel Symposium (1969) 367.

[4] F. Englert and R. Brout, *Broken Symmetry and the Mass of Gauge Vector Mesons*, Phys. Rev. Lett. **13** (1964) 321.

[5] P. W. Higgs, *Broken Symmetries and the Masses of Gauge Bosons*, Phys. Rev. Lett. **13** (1964) 508.

[6] P. W. Higgs, *Broken Symmetries, Massless Particles and Gauge Fields*, Phys. Lett. **12** (1964) 132.

[7] G. Guralnik, C. Hagen, and T. Kibble, *Global Conservation Laws and Massless Particles*, Phys. Rev. Lett. **13** (1964) 585.

[8] ATLAS Collaboration, *Observation of a new particle in the search for the Standard Model Higgs boson with the ATLAS detector at the LHC*, Phys.Lett. **B716** (2012) 1–29, arXiv:1207.7214 [hep-ex].

[9] CMS Collaboration, *Observation of a new boson at a mass of 125 GeV with the CMS experiment at the LHC*, Phys.Lett. **B716** (2012) 30–61, arXiv:1207.7235 [hep-ex].

[10] LHC Higgs Cross Section Working Group, S. Dittmaier, C. Mariotti, G. Passarino, and R. Tanaka (Eds.), *Handbook of LHC Higgs Cross Sections: 1. Inclusive Observables*, CERN-2011-002 (CERN, Geneva, 2011), arXiv:1101.0593 [hep-ph].

[11] ATLAS Collaboration, *Search for the Standard Model Higgs boson in associated production with a vector boson and decaying to bottom quarks with the ATLAS detector*, Tech. Rep. ATL-COM-PHYS-2013-465, CERN, Geneva, Aug, 2013.

[12] ATLAS Collaboration, *Luminosity Determination in pp Collisions at* $\sqrt{s} = 7$ TeV *Using the ATLAS Detector at the LHC*, Eur. Phys. J. C **71** (2011) 1630, arXiv:1101.2185 [hep-ph].

[13] ATLAS Collaboration, *The ATLAS Simulation Infrastructure*, Eur. Phys. J **C70** (2010) 823, arXiv:1005.4568 [physics.ins-det].

[14] GEANT4 Collaboration, S. Agostinelli et al., *GEANT4: A Simulation toolkit*, Nucl.Instrum.Meth. **A506** (2003) 250–303.

[15] "Atlfast ii." Https://twiki.cern.ch/twiki/bin.viewauth/atlas/atlfastii.

[16] "Pile up rescaling." https://twiki.cern.ch/twiki/bin/view/AtlasProtected/InDetTrackingPerformanceGuidelines#Pile_up_rescaling.

[17] J. Alison, K. Brendlinger, S. Heim, J. Kroll, and C. M. Lester, *Description and Performance of the Electron Likelihood Tool at ATLAS using 2012 LHC Data*, Tech. Rep. ATL-COM-PHYS-2013-378, CERN, Geneva, Apr, 2013.

[18] C. Anastopoulos, E. Benhar-Noccioli, A. Bocci, K. Brendlinger, F. Bhrer, L. Iconomidou-Fayard, M. Delmastro, O. Ducu, R. Fletcher, D. Froidevaux, T. Guillemin, S. Heim, F. Hubaut, M. Karnevskiy, J. Kretzschmar, J. Kroll, C. Lester, K. Lohwasser, J. B. Maurer, A. Morley,

3184 G. Psztor, E. Richter-Was, A. Schaffer, T. Serre, P. Sommer, E. Tiouchichine, and H. Williams,
3185 *Supporting document on electron efficiency measurements using the 2012 LHC proton-proton*
3186 *collision data*, Tech. Rep. ATL-COM-PHYS-2013-1295, CERN, Geneva, Sep, 2013.

3187 [19] ATLAS Collaboration, *Electron performance measurements with the ATLAS detector using the*
3188 *2010 LHC proton-proton collision data*, Eur. Phys. J **C72** (2012) 1909, arXiv:1110.3174v2
3189 [hep-ex].

3190 [20] M. Cacciari, G. P. Salam, and G. Soyez, *The anti-k_t jet clustering algorithm*, JHEP **04** (2008) 063,
3191 arXiv:0802.1189 [hep-ph].

3192 [21] "Jet-area-based pile-up subtraction."
3193 Https://twiki.cern.ch/twiki/bin/viewauth/atlasprotected/jetareas.

3194 [22] ATLAS Collaboration, *Jet energy measurement with the ATLAS detector in proton-proton*
3195 *collisions at* $\sqrt{s} = 7$ *TeV*, arXiv:1112.6426 [hep-ex]. Submitted to Eur. Phys. J. C.

3196 [23] ATLAS Collaboration, HSG5, *Invariant Mass Studies for the H→ $b\bar{b}$ Measurements for LHCP*,
3197 Tech. Rep. ATL-COM-PHYS-2013-449, CERN, Geneva, Apr, 2013.

3198 [24] ATLAS Collaboration, *b-jet tagging calibration on c-jets containing D^{*+} mesons*,
3199 ATLAS-CONF-2012-039 (2012), https://cdsweb.cern.ch/record/1435193.

3200 [25] ATLAS Collaboration, *Measurement of the Mistag Rate with 5 fb^{-1} of Data Collected by the*
3201 *ATLAS Detector*, ATLAS-CONF-2012-040 (2012),
3202 https://cdsweb.cern.ch/record/1435194.

3203 [26] ATLAS Collaboration, *Measurement of the b-tag Efficiency in a Sample of Jets Containing Muons*
3204 *with 5 fb^{-1} of Data from the ATLAS Detector*, ATLAS-CONF-2012-043 (2012),
3205 https://cdsweb.cern.ch/record/1435197.

3206 [27] G. Piacquadio, *Calibration of b-tagging using di-leptonic top pair events and a combinatorial*
3207 *likelihood approach*, Tech. Rep. ATL-COM-PHYS-2013-395, CERN, Geneva, Apr, 2013.
3208 b-tagging calibration aiming at being approved in time for analyses to be presented at LHCP.

3209 [28] G. Piacquadio, *Calibration of b-tagging using di-leptonic top pair events applying the*
3210 *combinatorial likelihood approach to 2011 data*, Tech. Rep. ATL-COM-PHYS-2013-1083,
3211 CERN, Geneva, Aug, 2013.

3212 [29] M. zur Nedden, G. Piacquadio, J. Jovicevic, F. Filthaut, T. Scanlon, and F. Parodi, *Calibration of*
3213 *b-tagging using dileptonic top pair events in a combinatorial likelihood approach with the ATLAS*
3214 *experiment*, Tech. Rep. ATLAS-COM-CONF-2014-003, CERN, Geneva, Jan, 2014.

3215 [30] G. Aad, H. Arnold, and C. Weiser, *b-jet tagging calibration on c-jets produced in association with*
3216 *$W^{\pm}$ bosons*, Tech. Rep. ATL-COM-PHYS-2013-1365, CERN, Geneva, Sep, 2013.

3217 [31] I. Burmeister, I. Connelly, A. Ferretto, F. Filthaut, R. Goncalo, R. Hawkings, H. Esch, F. Parodi,
3218 D. Sidorov, C. Schiavi, J. Thomas-Wilsker, J. Yu, and M. Zur Nedden, *Measurement of the*
3219 *b-tagging performance in the 2012 ATLAS data*, Tech. Rep. ATL-COM-PHYS-2013-456, CERN,
3220 Geneva, Apr, 2013.

3221 [32] P. Berta, F. Filthaut, V. Dao, E. Le Menedeu, F. Parodi, G. Piacquadio, T. Scanlon, M. Ughetto,
3222 and L. Zhang, *Continuous b-tagging for the ATLAS experiment*, Tech. Rep.
3223 ATL-COM-PHYS-2014-035, CERN, Geneva, Jan, 2014.

[33] "Elejet overlap removal problem in susy 1/2-lepton analysis." Https://indico.cern.ch/event/242559/material/slides/0?contribid=2.

[34] A. e. a. Buzatu, *Invariant Mass Studies for the $H \to b\bar{b}$ Measurements for HCP*, Tech. Rep. ATL-COM-PHYS-2012-1451, CERN, Geneva, Oct, 2012.

[35] T. Sjostrand, S. Mrenna, and P. Z. Skands, *A Brief Introduction to PYTHIA 8.1*, Comput.Phys.Commun. **178** (2008) 852–867, arXiv:0710.3820 [hep-ph].

[36] *Summary of ATLAS Pythia 8 tunes*, Tech. Rep. ATL-PHYS-PUB-2012-003, CERN, Geneva, Aug, 2012.

[37] J. Pumplin, D. Stump, J. Huston, H. Lai, P. M. Nadolsky, et al., *New generation of parton distributions with uncertainties from global QCD analysis*, JHEP **0207** (2002) 012, arXiv:hep-ph/0201195 [hep-ph].

[38] P. Golonka and Z. Was, *PHOTOS Monte Carlo: A Precision tool for QED corrections in Z and W decays*, Eur.Phys.J. **C45** (2006) 97–107, arXiv:hep-ph/0506026 [hep-ph].

[39] Z. Was, *TAUOLA the library for tau lepton decay, and KKMC / KORALB / KORALZ /... status report*, Nucl.Phys.Proc.Suppl. **98** (2001) 96–102, arXiv:hep-ph/0011305 [hep-ph].

[40] A. Djouadi, J. Kalinowski, and M. Spira, *HDECAY: A program for Higgs boson decays in the Standard Model and its supersymmetric extension*, Comput. Phys. Commun. **108** (1998) 56–74.

[41] O. Brein, A. Djouadi, and R. Harlander, *NNLO QCD corrections to the Higgs-strahlung processes at hadron colliders*, Phys.Lett. **B579** (2004) 149–156, arXiv:hep-ph/0307206 [hep-ph].

[42] M. Ciccolini, S. Dittmaier, and M. Kramer, *Electroweak radiative corrections to associated WH and ZH production at hadron colliders*, Phys.Rev. **D68** (2003) 073003, arXiv:hep-ph/0306234 [hep-ph].

[43] K. e. a. Nakamura, Review of particle physics, J. Phys. G.

[44] C. Englert, M. McCullough, and M. Spannowsky, *Gluon-initiated associated production boosts Higgs physics*, Phys. Rev. D **89** (2014) 013013. http://link.aps.org/doi/10.1103/PhysRevD.89.013013.

[45] A. Denner, S. Dittmaier, S. Kallweit, and A. Muck, *EW corrections to Higgs strahlung at the Tevatron and the LHC with HAWK*, PoS **EPS-HEP2011** (2011) 235, arXiv:1112.5258 [hep-ph].

[46] M. Ciccolini, A. Denner, and S. Dittmaier, *Strong and electroweak corrections to the production of Higgs + 2 jets via weak interactions at the LHC*, Phys. Rev. Lett. **99** (2007) 161803.

[47] LHC Higgs Cross Section Working Group, S. Dittmaier, C. Mariotti, G. Passarino, and R. Tanaka (Eds.), *Handbook of LHC Higgs Cross Sections: 2. Differential Distributions*, CERN-2012-002 (CERN, Geneva, 2012), arXiv:1201.3084 [hep-ph].

[48] G. Luisoni, P. Nason, C. Oleari, and F. Tramontano, *$HW^{\pm}$/HZ + 0 and 1 jet at NLO with the POWHEG BOX interfaced to GoSam and their merging within MiNLO*, JHEP **1310** (2013) 083, arXiv:1306.2542 [hep-ph].

[49] I. W. Stewart and F. J. Tackmann, *Theory uncertainties for Higgs mass and other searches using jet bins*, Phys. Rev. D **85** (2012) 034011. http://link.aps.org/doi/10.1103/PhysRevD.85.034011.

[50] S. Gangal and F. J. Tackmann, *Next-to-leading-order uncertainties in Higgs + jets from gluon fusion*, Phys. Rev. D **87** (2013) 093008. http://link.aps.org/doi/10.1103/PhysRevD.87.093008.

[51] A. Martin, W. Stirling, R. Thorne, and G. Watt, *Parton distributions for the LHC*, Eur.Phys.J. **C63** (2009) 189–285, arXiv:0901.0002 [hep-ph].

[52] R. D. Ball, V. Bertone, S. Carrazza, C. S. Deans, L. Del Debbio, et al., *Parton distributions with LHC data*, Nucl.Phys. **B867** (2013) 244–289, arXiv:1207.1303 [hep-ph].

[53] M. Botje, J. Butterworth, A. Cooper-Sarkar, A. de Roeck, J. Feltesse, et al., *The PDF4LHC Working Group Interim Recommendations*, arXiv:1101.0538 [hep-ph].

[54] H.-L. Lai, M. Guzzi, J. Huston, Z. Li, P. M. Nadolsky, et al., *New parton distributions for collider physics*, Phys.Rev. **D82** (2010) 074024, arXiv:1007.2241 [hep-ph].

[55] T. Gleisberg et al., *Event generation with SHERPA 1.1*, JHEP **02** (2009) 007, arXiv:0811.4622 [hep-ph].

[56] S. Alioli et al., *NLO Higgs boson production via gluon fusion matched with shower in POWHEG*, JHEP **0904** (2009) 002, arXiv:0812.0578 [hep-ph].

[57] P. Nason and C. Oleari, *NLO Higgs boson production via vector-boson fusion matched with shower in POWHEG*, JHEP **1002** (2010) 037, arXiv:0911.5299 [hep-ph].

[58] C. Oleari and L. Reina, $W^{\pm}b\bar{b}$ *production in POWHEG*, JHEP **1108** (2011) 061, arXiv:1105.4488 [hep-ph].

[59] W. e. a. Bell, *Measurement of top quark pair differential cross section with ATLAS in pp collisions at sqrt(s)=7 TeV: Measurement of top quark pair differential cross section with ATLAS using 5/fb of data collected in 2011 and the rel.17 version of the Atlas software* , Tech. Rep. ATL-COM-PHYS-2012-1137, CERN, Geneva, Jul, 2012.

[60] *Measurement of top-quark pair differential cross-sections in the l+jets channel in pp collisions at* $\sqrt{s}$ = 7 *TeV using the ATLAS detector*, Tech. Rep. ATLAS-CONF-2013-099, CERN, Geneva, Sep, 2013.

[61] A. e. a. Hoecker, *TMVA - Toolkit for Multivariate Data Analysis*, ArXiv Physics e-prints (2007), physics/0703039.

[62] D. Damazio, T. Kono, F. Monticelli, and G. Pasztor, *Performance of the ATLAS Electron and Photon Triggers in p-p Collisions at* $\sqrt{s}$ = 8 *TeV in 2012*, Tech. Rep. ATL-COM-DAQ-2013-121, CERN, Geneva, Oct, 2013.

[63] J.-B. Blanchard, J.-B. de Vivie, and P. Mastrandrea, *In situ scales and smearings from Z and J/*Ψ *events*, Tech. Rep. ATL-COM-PHYS-2013-1653, CERN, Geneva, Dec, 2013.

[64] *Preliminary results on the muon reconstruction efficiency, momentum resolution, and momentum scale in ATLAS 2012 pp collision data*, Tech. Rep. ATLAS-CONF-2013-088, CERN, Geneva, Aug, 2013.

[65] ATLAS Collaboration, *Jet energy scale and its systematic uncertainty in proton-proton collisions at $\sqrt{s}$ = 7 TeV with ATLAS 2011 data*, ATLAS-CONF-2014-004 (2013), http://cds.cern.ch/record/1509552.

[66] "Jes uncertainity twiki." Https://twiki.cern.ch/twiki/bin/viewauth/atlasprotected/jetuncertainties2012.

[67] A. L. Read, *Presentation of search results: The CL(s) technique*, J.Phys. **G28** (2002) 2693–2704.

[68] G. Cowan et al., *Asymptotic formulae for likelihood-based tests of new physics*, Eur. Phys. J. **C71** (2011) 1554, arXiv:1007.1727 [physics.data-an].

[69] K. Arnold, L. d'Errico, S. Gieseke, D. Grellscheid, K. Hamilton, et al., *Herwig++ 2.6 Release Note*, arXiv:1205.4902 [hep-ph].

[70] S. Frixione and B. R. Webber, *Matching NLO QCD computations and parton shower simulations*, JHEP **0206** (2002) 029, arXiv:hep-ph/0204244 [hep-ph].

[71] V. H. et al., *Automation of one-loop QCD corrections*, JHEP **05** (2011) 044, arXiv:1103.0621 [hep-ph].

[72] R. Frederix, S. Frixione, F. Maltoni, and T. Stelzer, *Automation of next-to-leading order computations in QCD: The FKS subtraction*, JHEP **0910** (2009) 003, arXiv:0908.4272 [hep-ph].

[73] F. e. a. Ahmadov, *Search for the Standard Model Higgs Boson in the ZH→nunubb Channel with the ATLAS Detector at the LHC*, Tech. Rep. ATL-COM-PHYS-2012-062, CERN, Geneva, Jan, 2012. Intended as support material for the expected H-¿bb publication of the Higgs search results using 2011 LHC data.

[74] ATLAS Collaboration, HSG5, *B-tagging for VH, with $H \to b\bar{b}$*, Tech. Rep. ATL-COM-PHYS-2013-697, CERN, Geneva, May, 2013.

[75] G. Unal, *Electron and Photon energy resolutions and their uncertainties for run-1 calibration*, Tech. Rep. ATL-COM-PHYS-2013-1651, CERN, Geneva, Dec, 2013.

[76] a. many, *Electron and photon energy calibration with the ATLAS detector using LHC Run 1 data*, Tech. Rep. ATL-COM-PHYS-2013-1652, CERN, Geneva, Dec, 2013.

[77] K. Ecker, M. Goblirsch-Kolb, and O. Kortner, *Muon Response Modelling for the Measurement of the Mass of the Higgs Boson Candidate in 4l Final State*, Tech. Rep. ATL-COM-PHYS-2012-1736, CERN, Geneva, Nov, 2012.

A E_T^{miss} trigger

As introduction to the use of the $E_{\mathrm{T}}^{\mathrm{miss}}$ trigger in the analysis, we report here in Table 76 part of the table shown in section 3.1. The analysis used the $E_{\mathrm{T}}^{\mathrm{miss}}$ triggers (the EF_xe80 family) for both the 0-lepton channel and the 1-lepton channel.

Trigger Object	Data Period	Trigger Names	Luminosity (fb−1)
$E_{\mathrm{T}}^{\mathrm{miss}}$< 160 GeV	A-B5	EF_xe80T_tclcw_loose	1.91928
	B6-L	EF_xe80_tclcw_loose	18.132
$E_{\mathrm{T}}^{\mathrm{miss}}$> 160 GeV	A-B5	EF_xe80_tclcw	2.1257
	B6-L	EF_xe80_tclcw_loose	18.132

Table 76: E_T^{miss} trigger Trigger table used in the 2012 data analysis.

This complex use of the trigger is the result of the attempt to maximize the event acceptance for 2012 data. Thanks to the successful L1Calo noise suppression in the forward region of the calorimeter, EF_xe80_tclcw_loose was installed from period B6 on. Before period B6, two $E_{\mathrm{T}}^{\mathrm{miss}}$ triggers with different threshold were available:

- The trigger EF_xe80T_tclcw_loose has a lower threshold, but it vetoed the first 3 bunches (BGRP7) in a bunch train. This BGRP7 mask is intended to suppress spurious high trigger rate bunches in $E_{\mathrm{T}}^{\mathrm{miss}}$ trigger due to the relatively long calorimeter response affecting the L1Calo. The details for the three triggers are shown in Table 77.
- The trigger, xe80_tclcw, has a higher threshold without this bunch mask.

Trigger Name	Start Date	VBGRP7	L1	L2	EF
EF_xe80_tclcw	period A	No	50	55	80
EF_xe80T_tclcw_loose	period A	Yes	40	45	80
EF_xe80_tclcw_loose	period B6	No	40	45	80

Table 77: Summary of $E_{\mathrm{T}}^{\mathrm{miss}}$ triggers used in the analysis. The threshold values are in GeV.

The EF_xe80T_tclcw_loose and EF_xe80_tclcw triggers have been used in this analysis up to period B6, to cover different $E_{\mathrm{T}}^{\mathrm{miss}}$regions (as summarised in Table 76).

To maximize the performance of the analysis, part of the phase space is in a region where the triggers are not completely efficient (in the turn-on). It is important to study in detail the trigger efficiency and to check the interdependencies with the offline reconstructed variables entering in the multivariate analysis. The final goals are:

- to avoid phase spaces with non trivial interependencies between efficiency, $E_{\mathrm{T}}^{\mathrm{miss}}$and other reconstructed variables,
- to derive data driven corrections and systematic uncertainties to be applied to the Monte Carlo simulation.

Since we use three different triggers, the studies have been done for each trigger individually.

An extra study has been done to check the level of detail simulated for the EF_xe80T_tclcw_loose trigger in the Monte Carlo sample. This appendix has been divided in three different parts:

- Emulation of the BGRP7 in the Monte Carlo for the EF_xe80T_tclcw_loose trigger;
- Trigger efficiency and interdependence with offline variables;
- Data driven scale factors and systematics.

A.1 Emulation of the BGRP7 in the Monte Carlo for the EF_xe80T_tclcw_loose trigger

Despite the fact that the EF_xe80T_tclcw_loose trigger is present in the Monte Carlo samples, it is not actively removing events in the 3 first bunches of the trains in the simulations. A detailed study of the offline kinematic properties of these events, compared with the events in the other bunches, have been done on the $ZH \rightarrow \nu\bar{\nu}b\bar{b}$ signal Monte Carlo sample. Given the fact that no significant differences have been found (i.e. Fig. 102), the BGRP7 events have not been removed when analyzing the Monte Carlo samples, but the proper luminosity calculation and PU profile have been adopted.

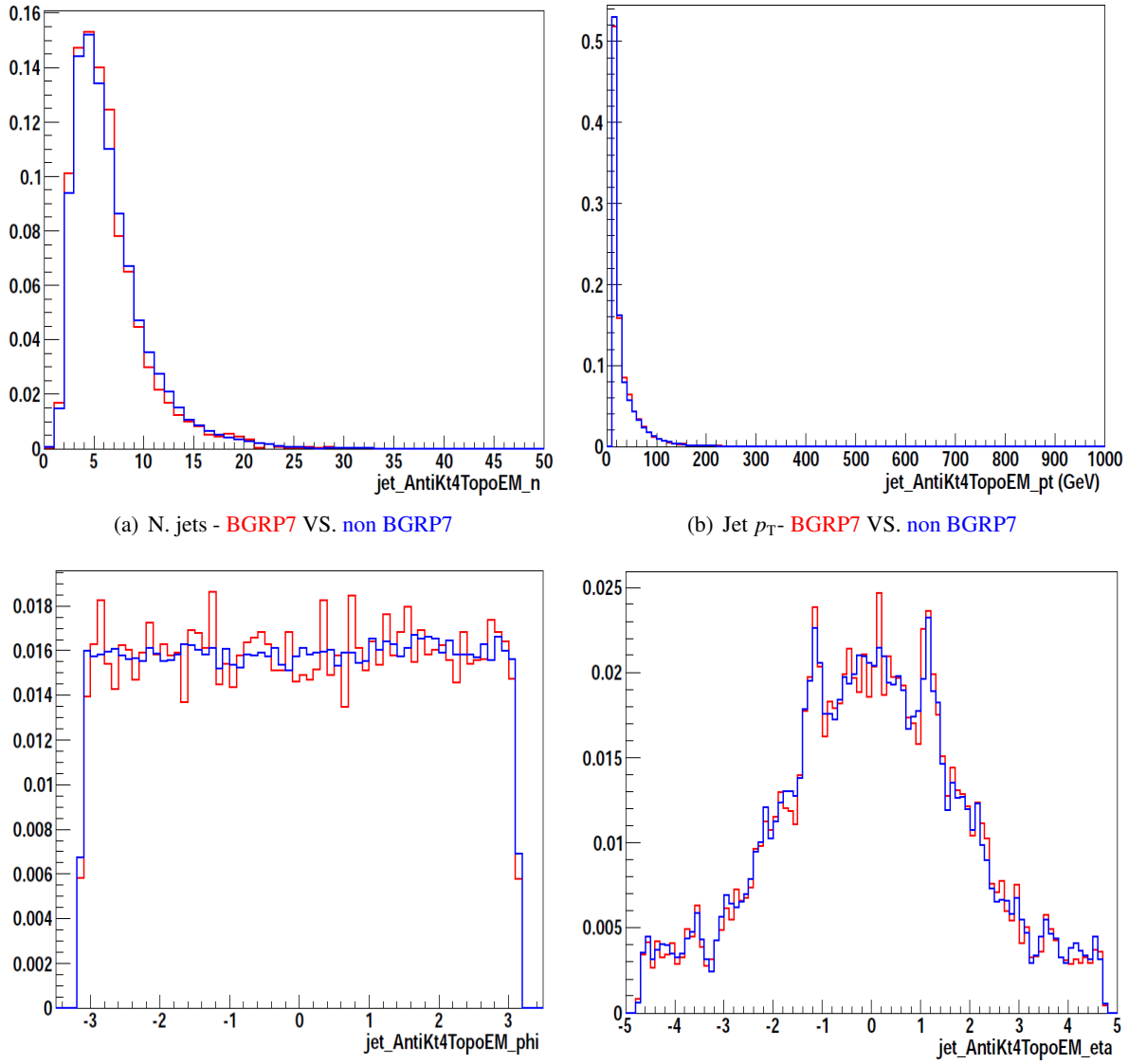

(a) N. jets - BGRP7 VS. non BGRP7

(b) Jet p_{T}- BGRP7 VS. non BGRP7

(c) Jet ϕ - BGRP7 VS. non BGRP7

(d) Jet η - BGRP7 VS. non BGRP7

Figure 102: Comparison between the events beloging to the BGRP7 (red) and the rest of th events (blue) in the Monte Carlo simulation for some of the variables (number of jets, inclusive jet p_{T}, inclusive jet ϕ, inclusive jet η).

A.2 Trigger efficiency and interdependence with offline variables

The final trigger efficiency is the production of the trigger efficiency in the three different trigger levels (L1, L2, Event-Filter). It is defined at each level as follow:

$$Efficiency_{L1} = L1\ passed\ /\ Total \quad (29)$$
$$Efficiency_{L2} = L2\ passed\ /\ L1\ passed \quad (30)$$
$$Efficiency_{EF} = EF\ passed\ /\ L2\ passed \quad (31)$$
$$Efficiency_{Total} = Efficiency_{L1} \times Efficiency_{L2} \times Efficiency_{EF} \quad (32)$$

To measure it on data, orthogonal samples acquired by the muon trigger (in the muon triggered data stream) have been used. Since the on-line trigger $E_{\mathrm{T}}^{\mathrm{miss}}$ does not contain inner detector and muon spectrometer information, the muon momentum is not counted in the on-line trigger $E_{\mathrm{T}}^{\mathrm{miss}}$calculation (apart the energy loss in the calorimeter). This makes from the point of view of the $E_{\mathrm{T}}^{\mathrm{miss}}$trigger, $W \to \mu\nu$ and $Z \to \mu\mu$ very similar to $Z \to \nu\nu$. To study the trigger efficiency, we selected $W(\to \mu\nu) + jets$ or $Z(\to \mu\mu) + jets$ events in the lowest non pre-scaled muon triggers, and check how many of them pass the L1, the L2 and the EF for the $E_{\mathrm{T}}^{\mathrm{miss}}$triggers. In this way we can calculate the efficiencies in the formulas above.

The event selection (for $W(\to \mu\nu) + jets$ and $Z(\to \mu\mu) + jets$) processes) are quite similar to the common VH analysis selections. The presence of exactly one muon or two muons defines if one event belongs to the $W \to \mu\nu$ or $Z \to \mu\mu$ sample. In order to be as close to the analysis phase space as possible, two signal jets with leading jet p_{T} greater than 45 GeV are required. Tight multi-jet rejection cuts(trkIso < 0.03 and $m_T^W > 60$ GeV) and b-jet veto are applied for $W \to \mu\nu$ events, to remove residual multi-jet and $t\bar{t}$ backgrounds. With the above selections applied, $W \to \mu\nu$ and $Z \to \mu\mu$ events are selected at almost 100% purity, see Figs. 103 and 104. These plots show the offline $E_{\mathrm{T}}^{\mathrm{miss}}$distribution, calculated

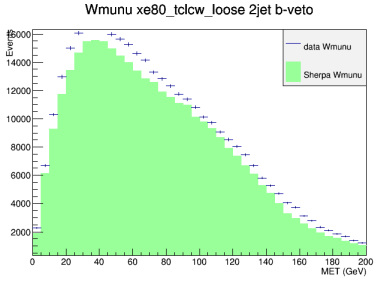

Figure 103: selected $W \to \mu\nu$ offline $E_{\mathrm{T}}^{\mathrm{miss}}$ distribution, data(cross points) and MC(colored histogram)

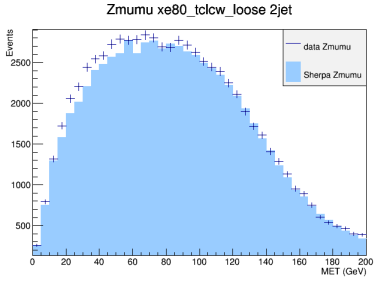

Figure 104: selected $Z \to \mu\mu$ offline $E_{\mathrm{T}}^{\mathrm{miss}}$ distribution, data(cross points) and MC(colored histogram)

by subtracting the muon contributions for the $W \to \mu\nu$ and $Z \to \mu\mu$ cases. These subtracted versions of the $E_{\mathrm{T}}^{\mathrm{miss}}$, used only in this context, have similar kinematic properties (with some approximation) to the $E_{\mathrm{T}}^{\mathrm{miss}}$in $Z \to \nu\nu$ events. Note: no normalization factors have been used, so the data-Monte Carlo difference is partially coming from them.

A.2.1 Dependence of the $E_{\mathrm{T}}^{\mathrm{miss}}$ trigger efficiency on kinematic variables entering in the multivariate analysis

We expect a clear dependence between the efficiency and the offline $E_{\mathrm{T}}^{\mathrm{miss}}$(in this case, for the $Z \rightarrow \mu\mu$ and $W \rightarrow \mu\nu$ events, the muon contributions have been subtracted from the offline $E_{\mathrm{T}}^{\mathrm{miss}}$). To model these, we extract data driven scale factors and systematic uncertainties. It can be more difficult to study all the needed details of the Monte Carlo modeling if we have additional dependencies between the trigger efficiency and other variables O entering in the multivariate analysis. For this reason, we studied several 2-dimensional efficiency scans (efficiency in the 2-D plan $E_{\mathrm{T}}^{\mathrm{miss}}$vs O).

The scalar sum of jet p_{T}(JpT_Sum) and leading jet p_{T} have a strong correlation with the $E_{\mathrm{T}}^{\mathrm{miss}}$ trigger efficiency (Fig. 105), while the others variables O have almost no bias in the signal region (Fig. 106, 107.

These studies highlight a non-trivial dependence of the trigger efficiency on jet activity. We adopted an extra cut on JpT_Sum to avoid any trigger bias induced by this dependence. This was decided because the jet activity in the Monte Carlo simulation can depend on several different aspects (i.e. pile-up, perturbation order of the calculation, parton shower algorithm,....), making harder, in case of data-Monte carlo differences, their traceability to the real source. Here JpT_Sum is defined as follow:

$$JpT_Sum = p_T^{j1} + p_T^{j2} \; for \; 2 - jets \; events \tag{33}$$

$$JpT_Sum = p_T^{j1} + p_T^{j2} + p_T^{j3} \; for \; 3 - jets \; events \tag{34}$$

$$\tag{35}$$

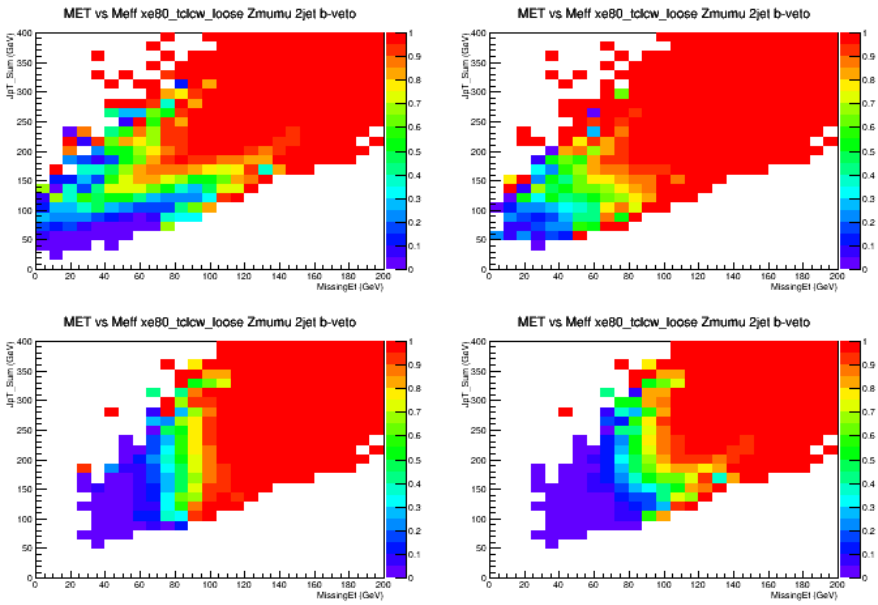

Figure 105: calculated xe80_tclcw_loose efficiency correlation between $E_{\mathrm{T}}^{\mathrm{miss}}$ (abscissa) and sum of leading two jet p_{T} using Sherpa $Z \rightarrow \mu\mu$ Monte Carlo. The four plots, are the L1 (top, left), the L2 (top, right), the EF (bottom left) efficiencies, and the combination of the three (bottom right).

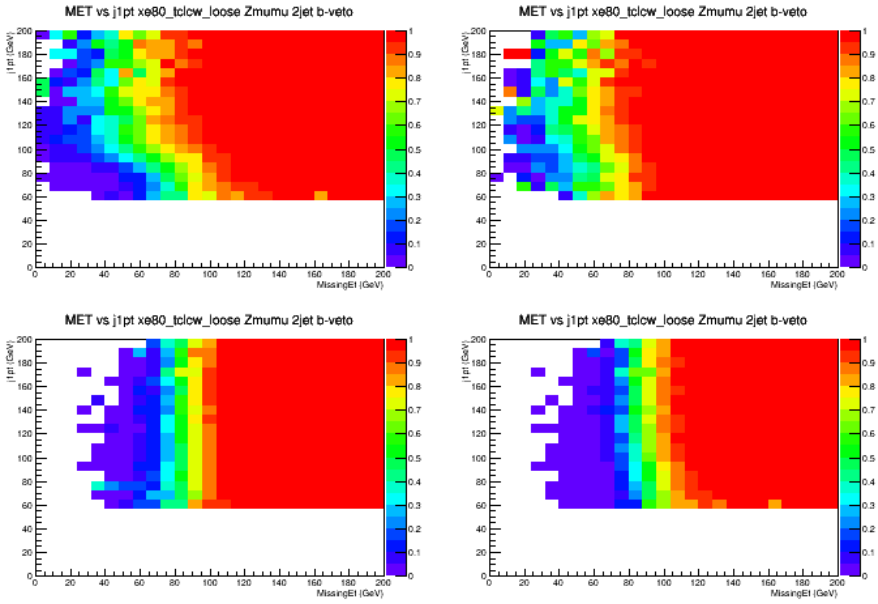

Figure 106: calculated EF_xe80_tclcw_loose efficiency correlation between $E_{\mathrm{T}}^{\mathrm{miss}}$ (abscissa) and leading jet p_{T} using Sherpa $Z \rightarrow \mu\mu$ Monte Carlo. The four plots, are the L1 (top, left), the L2 (top, right), the EF (bottom left) efficiencies, and the combination of the three (bottom right).

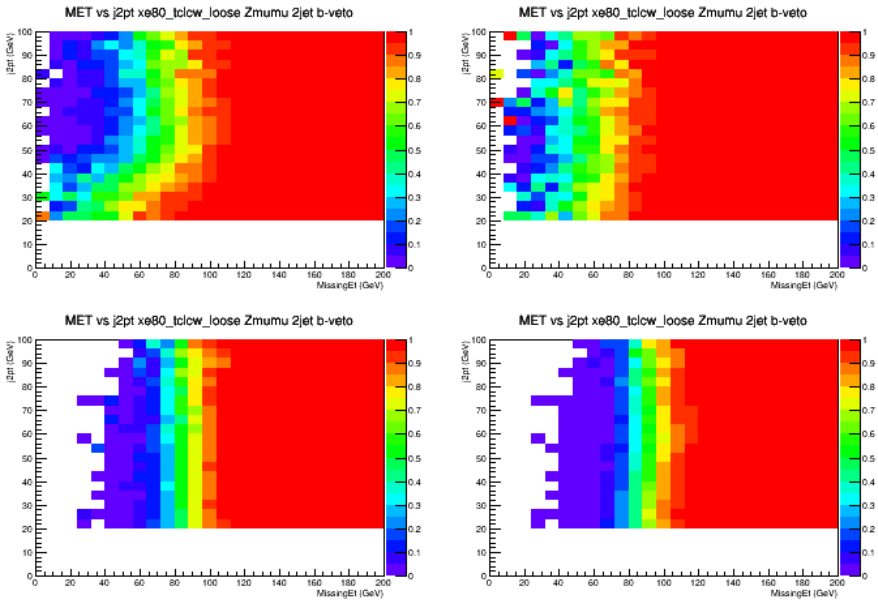

Figure 107: calculated EF_xe80_tclcw_loose efficiency correlation between $E_{\mathrm{T}}^{\mathrm{miss}}$ (abscissa) and 2nd leading jet p_{T} using Sherpa $Z \rightarrow \mu\mu$ Monte Carlo. The four plots, are the L1 (top, left), the L2 (top, right), the EF (bottom left) efficiencies, and the combination of the three (bottom right).

For the 2-jets case, the lowest threshold on JpT_Sum to remove the biased region is 120 GeV. This cleaning cut slightly improves the sensitivity for $E_{\mathrm{T}}^{\mathrm{miss}}$< 120 GeV and has almost no effect for $E_{\mathrm{T}}^{\mathrm{miss}}$> 120 GeV.
For the 3-jets events, the optimization of the cut on JpT_Sum is 150 GeV for $E_{\mathrm{T}}^{\mathrm{miss}}$> 120 GeV and 170 GeV for $E_{\mathrm{T}}^{\mathrm{miss}}$< 120 GeV. The cleaning cut for the 3jet region kills half the sensitivity in the 3 jet events with 100 GeV <$E_{\mathrm{T}}^{\mathrm{miss}}$< 120 GeV, but this region does not enter in the final fit due to very low sensitivity. The effect of the cleaning cut for 3 jet events is negligible in the other p_{T}^{V} regions. Once these cuts are applied, the non trivial dependence of the trigger efficiency by the jets activity is drastically reduced, and the MET trigger efficiency has a dependence only on the reconstructed $E_{\mathrm{T}}^{\mathrm{miss}}$. To complete the study, some other important variables have been shown in Figure 108.

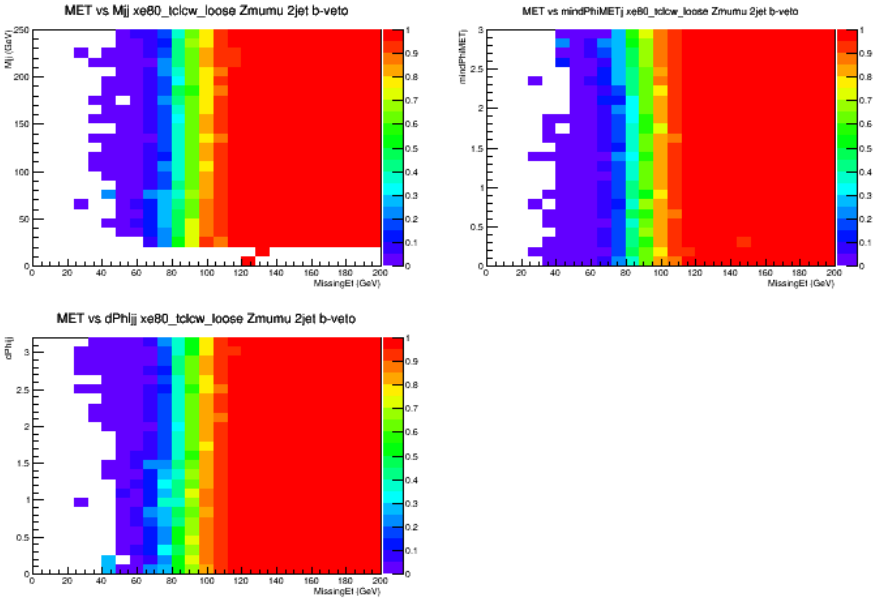

Figure 108: calculated EF_xe80_tclcw_loose efficiency correlation between $E_{\mathrm{T}}^{\mathrm{miss}}$ (abscissa) and important variables (first row: left m_{jj} , right min($\Delta\phi(E_{\mathrm{T}}^{\mathrm{miss}}, jet)$); second row: $\Delta\phi(jet, jet)$) for the analysis using Sherpa $Z \rightarrow \mu\mu$ Monte Carlo. The plots, showing the combination of the L1, L2, EF efficiencies, are obtained after the selection cut described in this appendix has been applied.

A.2.2 Trigger efficiency parametrization

The selection of $Z \rightarrow \mu\mu$ and $W \rightarrow \mu\nu$ events allow us to study the dependence of the trigger efficiency as a function of the offline $E_{\mathrm{T}}^{\mathrm{miss}}$ at each level of the trigger. As shown in Figure 109, while the $E_{\mathrm{T}}^{\mathrm{miss}}$ distribution before any trigger selection shows a good data-Monte Carlo agreement, each trigger level induces a change in the shape of the distribution. It is than crucial to study in detail the shape of the trigger turn on, and to derive data driven corrections.

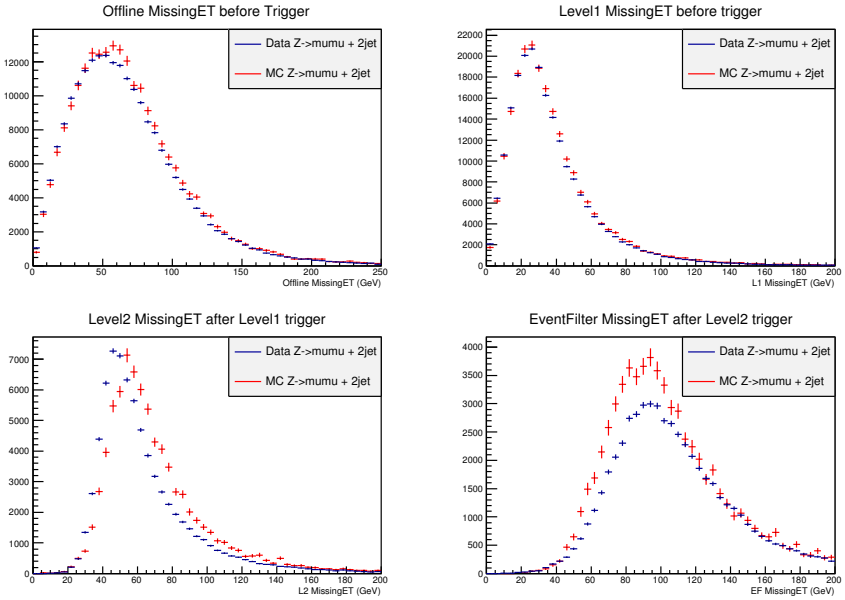

Figure 109: Comparison of 2012 data and MC $E_{\mathrm{T}}^{\mathrm{miss}}$ distributions. Offline $E_{\mathrm{T}}^{\mathrm{miss}}$ distribution of selected $Z \rightarrow \mu\mu$ events (top left). L1 $E_{\mathrm{T}}^{\mathrm{miss}}$ distribution of selected $Z \rightarrow \mu\mu$ events (top right). L2 $E_{\mathrm{T}}^{\mathrm{miss}}$ distribution after L1 trigger with 40 GeV threshold (bottom left). EF $E_{\mathrm{T}}^{\mathrm{miss}}$ distribution after L2 trigger with 45 GeV threshold (bottom right).

The efficiencies in Formula 32 has been plotted as a function of the offline $E_{\mathrm{T}}^{\mathrm{miss}}$, and each efficiency has been fitted using the error function:

$$Efficiency \;=\; 0.5 \times \left(1 + Erf\left(\frac{E_{\mathrm{T}}^{\mathrm{miss}} - threshold}{\sqrt{2} \times width}\right)\right) \tag{36}$$

The fit range for each level is 80-250 GeV. The threshold (50% efficiency point) and the width of the turn on curve are estimated by the fit. Fig. 110 is a result using Sherpa $W \rightarrow \mu\nu$ events.

The Figure 111 shows the comparison of trigger turn-on curves between two different physics processes: $W(\rightarrow \mu\nu) + jets$ and $Z(\rightarrow \mu\mu) + jets$. We can clearly see in both data and MC, the good agreement between the $W(\rightarrow \mu\nu) + jets$ process and the $Z(\rightarrow \mu\mu) + jets$ process.

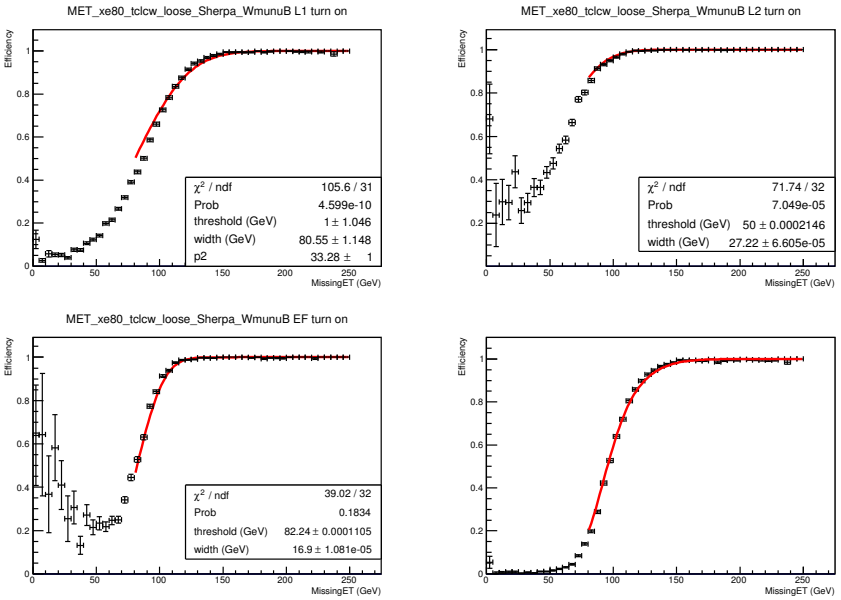

Figure 110: EF_xe80_tclcw_loose efficiency calculated using Sherpa $W \rightarrow \mu\nu$ MC events. The efficiency is shown for each trigger level: L1 (top left), L2 (top right), EF (bottom left) and for the overall(bottom right).

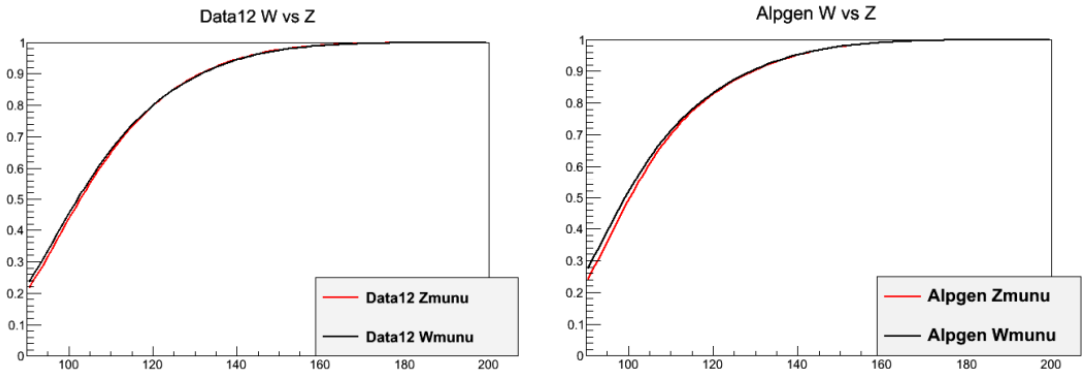

(a)

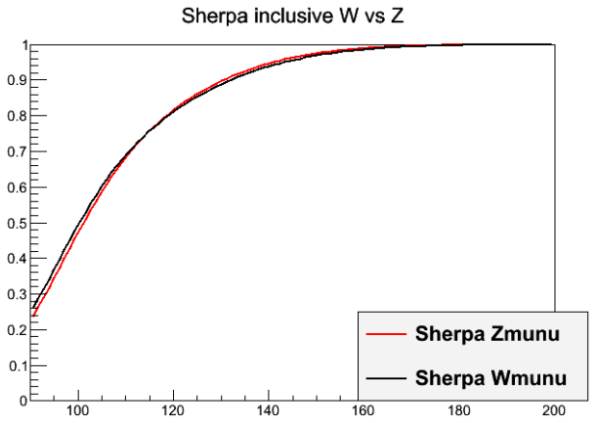

(b)

Figure 111: Trigger Efficiency turn on estimate using $W(\rightarrow \mu\nu)$ + $jets$ and $Z(\rightarrow \mu\mu)$ + $jets$ events for data (top left), Alpgen (top right) and Sherpa (bottom).

A.3 $E_{\mathrm{T}}^{\mathrm{miss}}$ trigger data driven scale factors

The $E_{\mathrm{T}}^{\mathrm{miss}}$ trigger scale factor is calculated using the fitted efficiency curve obtained by the method described above:

$$SF = \frac{Turn-On^{Data}_{W(\rightarrow\mu\nu)+jets/Z(\rightarrow\mu\mu)+jets}}{Turn-On^{MC}_{W(\rightarrow\mu\nu)+jets/Z(\rightarrow\mu\mu)+jets}} \tag{37}$$

Even if the shape of turn on curves depends on the number of jets, the calculated scale factors do not significantly depends to the number of jets, meaning that Monte Carlo is able to properly simulate part of the relevant correlations entering in the trigger decision. The comparison of the scale factors for the $W(\rightarrow \mu\nu)$ and for the $Z(\rightarrow \mu\mu)$ (SF_W and SF_Z) shows a good agreement within 3% (Fig. 112): `METTrigZ`. This small difference is considered as a systematic uncertainty in the analysis . Statistical errors are calculated from the fit error (Fig. **??**) and are taken into account as a separate systematics (`METTrigStat`). Additional studies and comparisons with the top samples, show statistically coherent scale factors.

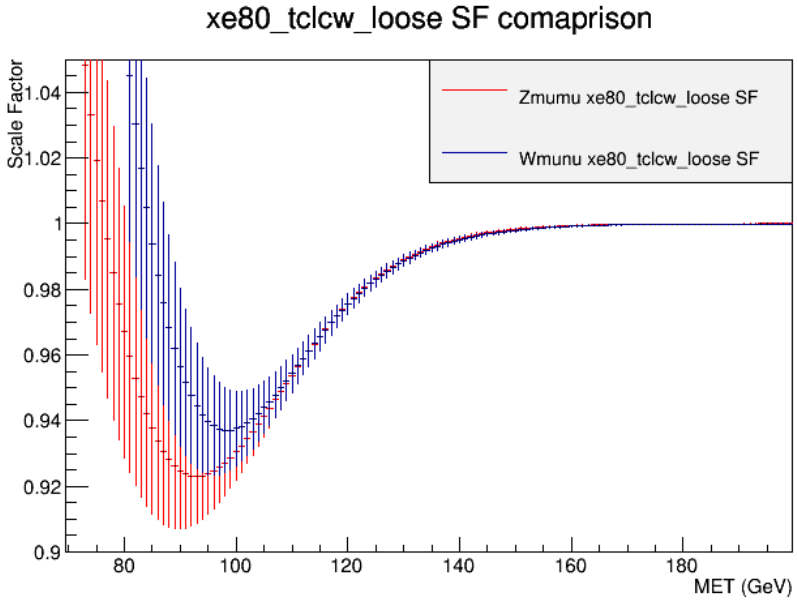

Figure 112: Calculated scale factor for EF_xe80_tclcw_loose from the $W \rightarrow \mu\nu$, and the $Z \rightarrow \mu\mu$ samples.

B Delayed stream

B.1 Introduction to delayed stream

The delayed stream of 2012 data (HadDelayed) is taken from period E1 to the end of the year. It corresponds to data collected on top of regular data taking and processed later, depending on available computing resources. This stream is inclusive in the total data of 2012 with an integrated luminosity of 7.29 fb^{-1}. Apart from the nominal triggers (EF_xe80_tclcw, EF_xe80T_tclcw_loose, EF_xe80_tclcw_loose), there is another $E_{\mathrm{T}}^{\mathrm{miss}}$ trigger which is only available in delayed stream that can be used in the analysis named EF_xe60_tclcw_loose_delayed (see Table 78). This trigger has lower threshold than the nominal triggers, which is useful if we want to analyze the low $E_{\mathrm{T}}^{\mathrm{miss}}$ region (less than 120 GeV) in 0-lepton study. However this trigger is off if the instantaneous luminosity is greater than 5.77×10^{33}.

Table 78: Data period, integrated luminosity and threshold at each level (in GeV)

Trigger Name	Data period	$\int \mathcal{L}dt[\mathrm{fb}^{-1}]$	L1	L2	EF
EF_xe80_tclcw_loose	B6-L3	18.1	40	45	80
EF_xe60_tclcw_loose_delayed	E1-L3	7.29	35	40	60

B.2 Delayed stream $E_{\mathrm{T}}^{\mathrm{miss}}$ trigger efficiency and scale factor

Like the method we use to measure the trigger turn-on of the nominal triggers, we can parameterize the trigger of delayed stream EF_xe60_tclcw_loose_delayed by the following method: first measure the trigger turn-on curves and then, calculate the trigger scale factor using $Z \to \mu\mu$ and $W \to \mu\nu$ events (with the same selection as in App. A). Due to the trigger availability on data, in order to measure the trigger turn-on using data, events where the delayed stream trigger is off should be removed, this can be done using lumiblock information. The trigger turn-on fitting is done by using error function, the fit range (for each level) is from 40 to 200 GeV. Fit results using Sherpa $W \to \mu\nu$ and $Z \to \mu\mu$ events are shown in Fig. 113, 114, respectively. The result for $W \to \mu\nu$ is used as central value while the result for $Z \to \mu\mu$ is used as systematic variation.

We also check the dependence of trigger turn-on and scale factor on the following categories of selection:

- QCD rejection cuts: $E_{\mathrm{T}}^{\mathrm{miss}}$ >90 GeV, $p_{\mathrm{T}}^{\mathrm{miss}}$ >30 GeV, $\Delta\phi(E_{\mathrm{T}}^{\mathrm{miss}}, p_{\mathrm{T}}^{\mathrm{miss}}) < \frac{\pi}{2}$, $\Delta\phi(V, H) > 2.8$, $0.7 < \Delta R(jet, jet) < 3$
- 3-jet events versus 2-jet events
- Studied samples: $Z \to \mu\mu$, $W \to \mu\nu$ or $t\bar{t}$ (for cross–check purpose).

The results obtained from these categories of selection yield a little difference from the original selection ($W \to \mu\nu$ with 2 jets and no QCD cuts). (Table 79)

B.3 $E_{\mathrm{T}}^{\mathrm{miss}}$ trigger bias

Trigger efficiency bias is observed from variables sum of 2 leading jets J12pT (or sum of 3 jets J123pT in 3-jet bin) (Fig. 115, 116) and p_T of leading jet as in nominal triggers, but as already mentioned in the App. A, a cut on J12pT/J123pT is applied in order to avoid this bias while maintaining high signal significance without losing much signal acceptance.

The same cleaning cuts for sum of p_T of jets as in $E_{\mathrm{T}}^{\mathrm{miss}}$ trigger section are used:

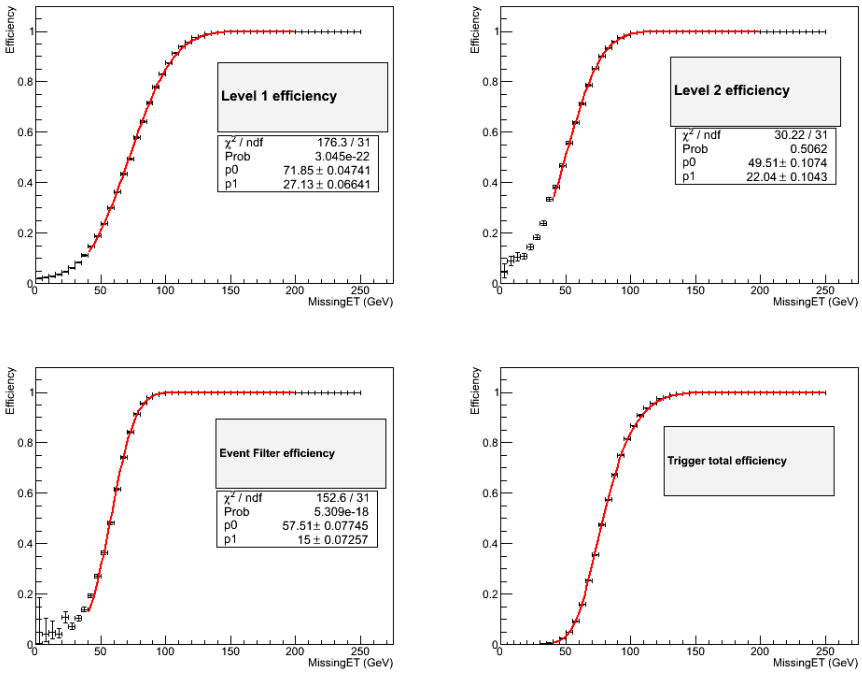

Figure 113: Trigger efficiencies for each level and for over all (bottom right) of trigger EF_xe60_tclcw_loose_delayed using $W \to \mu\nu$+ 2 jets Sherpa events.

- for 2 jets: J12pT > 120 GeV
- for 3 jets and $E_{\mathrm{T}}^{\mathrm{miss}}$ < 120 GeV: J123pT > 170 GeV
- for 3 jets and $E_{\mathrm{T}}^{\mathrm{miss}}$ > 120 GeV: J123pT > 150 GeV.

For $E_{\mathrm{T}}^{\mathrm{miss}}$ > 200 GeV, the trigger scale factor is consistent with 1. The scale factor for $E_{\mathrm{T}}^{\mathrm{miss}}$ < 200 GeV is calculated from the trigger turn-on parameters of data and MC, obtained from the fits. The trigger uncertainties are composed of two parts: one is error of the fit from statistical fluctuations, the other uncertainty is obtained from the difference between the scale factor of $W \to \mu\nu$ events and $Z \to \mu\mu$ events. The scale factor of $t\bar{t}$ events is for cross-checking the consistency with the others only, as the $t\bar{t}$ sample is statistically limited.

The scale factors obtained from $Z \to \mu\mu$, $W \to \mu\nu$ samples are consistent within statistical uncertainty (Fig. 117), the scale factor for $t\bar{t}$ is also compatible with the two former scale factors. The total uncertainty of trigger is small, about 1% at $E_{\mathrm{T}}^{\mathrm{miss}}$=90 GeV, which is small compared to other uncertainties.

B.4 Apply delayed stream in 0-lepton study

In 0-lepton study, the delayed stream and its trigger can be used in order to gain more events in the low $E_{\mathrm{T}}^{\mathrm{miss}}$ region. For this study we apply the 0-lepton selection with lepton veto plus 2 or 3 jets selection with exactly 2 b-tagged jets. The nominal $E_{\mathrm{T}}^{\mathrm{miss}}$ triggers and EF_xe60_tclcw_loose_delayed are used, cleaning cuts on sum of jet p_T for 2 and 3 jets bin are also applied to avoid trigger biases. The QCD rejection cuts are also applied to reduce the QCD contribution (more at App. C).

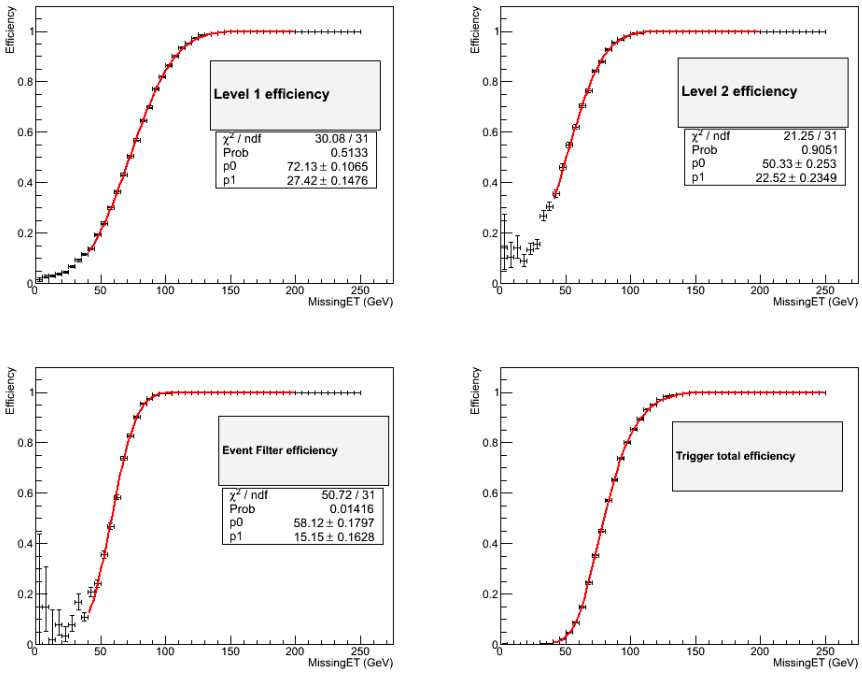

Figure 114: Trigger efficiencies for each level and for over all (bottom right) of trigger EF_xe60_tclcw_loose_delayed using $Z \rightarrow \mu\mu$+ 2 jets Sherpa events.

Due to the delayed stream trigger availability, the delayed stream can be used as following: for data periods A to D, nominal triggers and nominal data stream are used (As in App. A), from period E1 onward, if the delayed stream trigger is available, the delayed trigger and data stream will be used in the analysis, else, use the nominal triggers and nominal stream instead. Figure 118 shows the data points and MC distribution for invariant mass of two b-tagged jets and $E_{\mathrm{T}}^{\mathrm{miss}}$ of two b-jets after applying 0-lepton selection using delayed stream trigger and nominal triggers.

Using delayed stream trigger in the analysis can help us gaining a total 4% of signal acceptance and 2% of signal significance in the lowest $E_{\mathrm{T}}^{\mathrm{miss}}$ bin (Tables 80, 81), the higher $E_{\mathrm{T}}^{\mathrm{miss}}$ bins do not benefit from the delayed stream.

The delayed stream implementation and its trigger usage is included in the TrigMETEfficiency package (version 00-00-13).

B.5 Mis–modelling issue in 0–lepton analysis

(This part make the section C–4 of App. C obsoleted...) In 0–lepton channel of Higgs analysis, at the lowest $E_{\mathrm{T}}^{\mathrm{miss}}$ bin (90–120 GeV), a mis–modelling issue is observed in the distribution of p_T of vector sum of two leading jets while no significant mis–modelling observed at higher $E_{\mathrm{T}}^{\mathrm{miss}}$ bin (Figure 119, more details are in App. C–3). This issue may be from the bias of trigger modelling, so we can check if this bias still exist with the delayed stream trigger since the thresholds of this trigger are lower than the ones of nominal triggers.

To check this mis–modelling, we will only interest in the exclusive part of data that delayed stream trigger is available. The event selection for this check is as for 0–lepton one, except the trigger requirement, that we require only the delayed stream trigger. We also apply other cuts: $\Delta\phi(jet, jet) < 2.0$ and

Table 79: Fitting parameters at each level of trigger for $Z \to \mu\mu$ and $W \to \mu\nu$ samples (MC)

$Z \to \mu\mu$	without QCD cuts		with QCD cuts	
	Mean value (GeV)	Width	Mean value (GeV)	Width
Level 1	72.13±0.11	27.42±0.15	73.66±0.18	27.7±0.24
Level 2	50.33±0.25	22.52±0.23	51.1±0.48	22.24±0.39
Event Filter	58.12±0.18	15.15±0.16	56.24±0.41	15.81±0.32
$W \to \mu\nu$	without QCD cuts		with QCD cuts	
	Mean value (GeV)	Width	Mean value (GeV)	Width
Level 1	71.85±0.11	27.13±0.07	73.4±0.08	27.23±0.11
Level 2	49.51±0.11	22.04±0.1	51.57±0.2	20.8±0.17
Event Filter	57.51±0.08	15±0.07	55.72±0.18	15.59±0.14

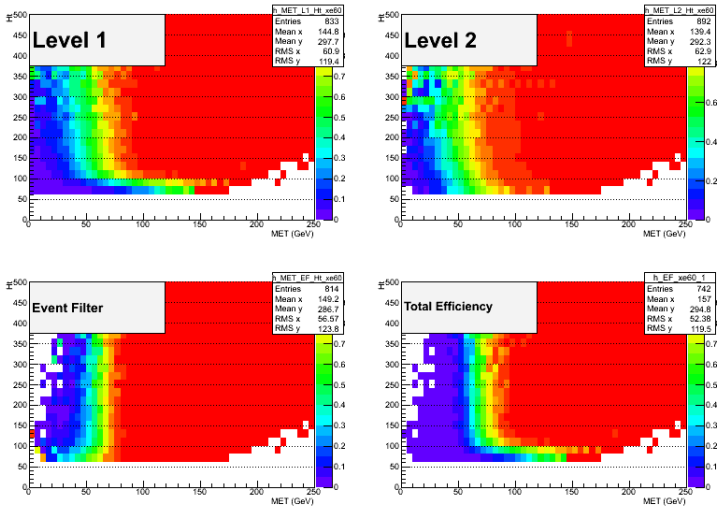

Figure 115: Correlation of trigger efficiencies between $E_{\mathrm{T}}^{\mathrm{miss}}$ and sum of p_T of jets for each level and for over all (bottom right) of trigger EF_xe60_tclcw_loose_delayed using $W \to \mu\nu$+ 2 jets Sherpa samples.

$E_{\mathrm{T}}^{\mathrm{miss}}/\sqrt{J12pT} > 9.0$ to reject more QCD contributions (Figure 120).

Figure 121 show the distributions of transverse momentum of vector sum of 2 jets using delayed stream trigger and nominal trigger under the new selection. The results shows that the mis–modelling issue still exist if the nominal triggers are used while applying delayed stream trigger shows almost no mis–modelling. This may come from the reason that the mis–modelling issue comes from the higher thresholds of nominal triggers while delayed stream trigger has smaller ones. This resolve the mis–modelling issue and the nominal $E_{\mathrm{T}}^{\mathrm{miss}}$ triggers still can be used normally in the Higgs analysis.

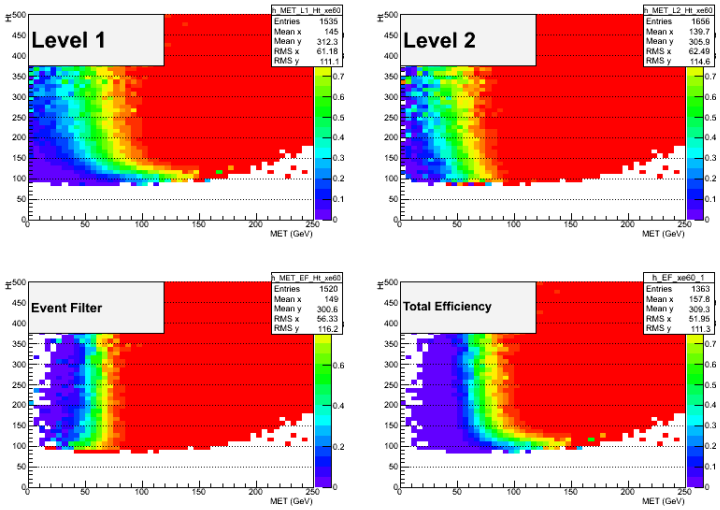

Figure 116: Correlation of trigger efficiencies between $E_{\mathrm{T}}^{\mathrm{miss}}$ and sum of p_T of jets for each level and for over all (bottom right) of trigger EF_xe60_tclcw_loose_delayed using $W \rightarrow \mu\nu$+ 3 jets Sherpa samples.

Table 80: signal acceptance gain after applying trigger EF_xe60_tclcw_loose_delayed instead of nominal triggers

Number of jets	$E_{\mathrm{T}}^{\mathrm{miss}}$ bin 0	$E_{\mathrm{T}}^{\mathrm{miss}}$ bin 1
2 jets	1.04 (4 %)	1.02 (2 %)
3 jets	1.03 (4 %)	1.02 (2 %)
2 or 3 jets	1.04 (4 %)	1.02 (2 %)

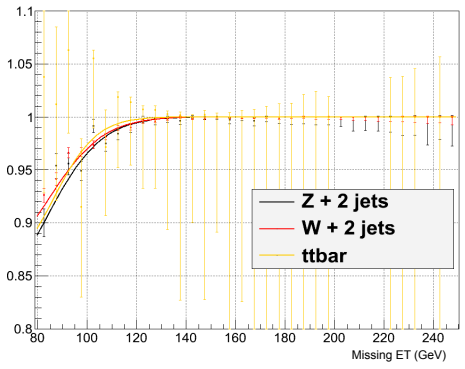

Figure 117: Scale factor of trigger EF_xe60_tclcw_loose_delayed after applying sum of p_T of jets cleaning cut using $Z \rightarrow \mu\mu$+ 2 jets, $W \rightarrow \mu\nu$ and $t\bar{t}$ events.

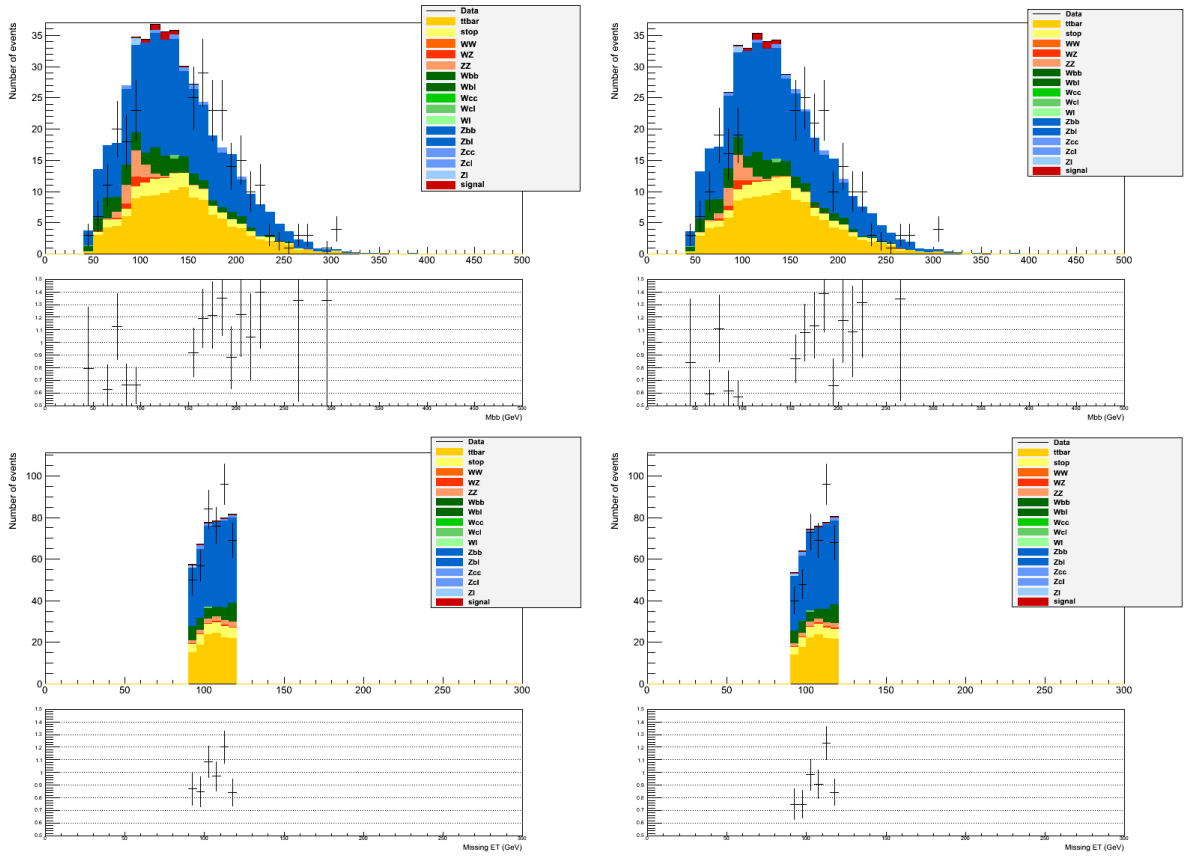

Figure 118: Distribution of mass invariant (top) and $E_{\mathrm{T}}^{\mathrm{miss}}$ (bottom) of two b jets using MV1c tagger with 80 % of working point in $E_{\mathrm{T}}^{\mathrm{miss}}$ bin from 90 to 120 GeV in bin of 2 jet for data and MC samples using delayed stream trigger (left) and nominal triggers (right).

Table 81: Signal significance gain after applying trigger EF_xe60_tclcw_loose_delayed over the trigger EF_xe80_tclcw_loose

$E_{\mathrm{T}}^{\mathrm{miss}}$ bin + N_{jets} bin	Use delayed stream	Use nominal triggers	% gain
bin 0 + 2 jets	0.308	0.302	2 %
bin 0–3 + 2 jets	0.861	0.857	< 1 %
bin 1–3 + 2/3 jets	0.874	0.872	< 1 %
bin 1–3 + 2/3 jets and bin 0 + 2 jets	0.927	0.923	< 1 %

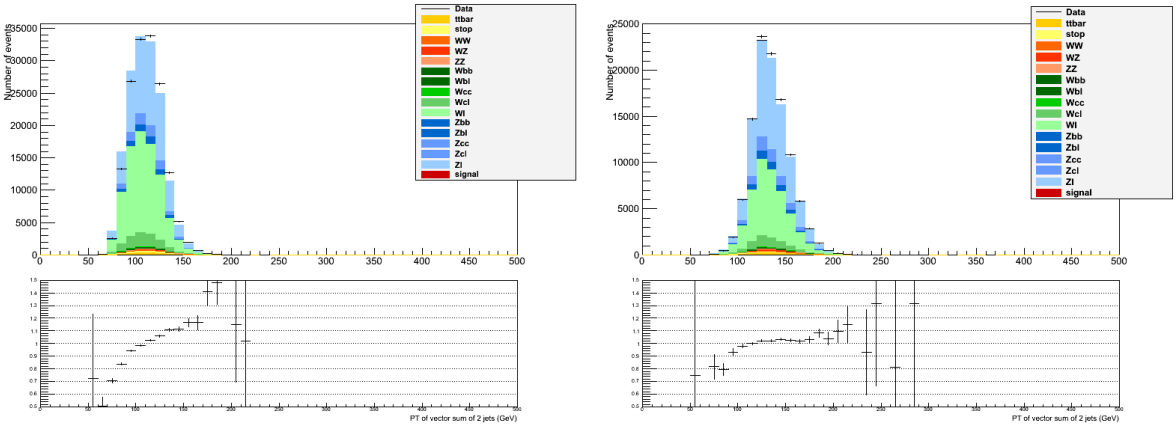

Figure 119: Distribution of transverse momentum of 4–vector sum of 2 jets (pre b–tagging procedure) in $E_{\mathrm{T}}^{\mathrm{miss}}$ bin 90–120 GeV (left) and $E_{\mathrm{T}}^{\mathrm{miss}}$ bin 120–160 GeV (right) using nominal $E_{\mathrm{T}}^{\mathrm{miss}}$ triggers.

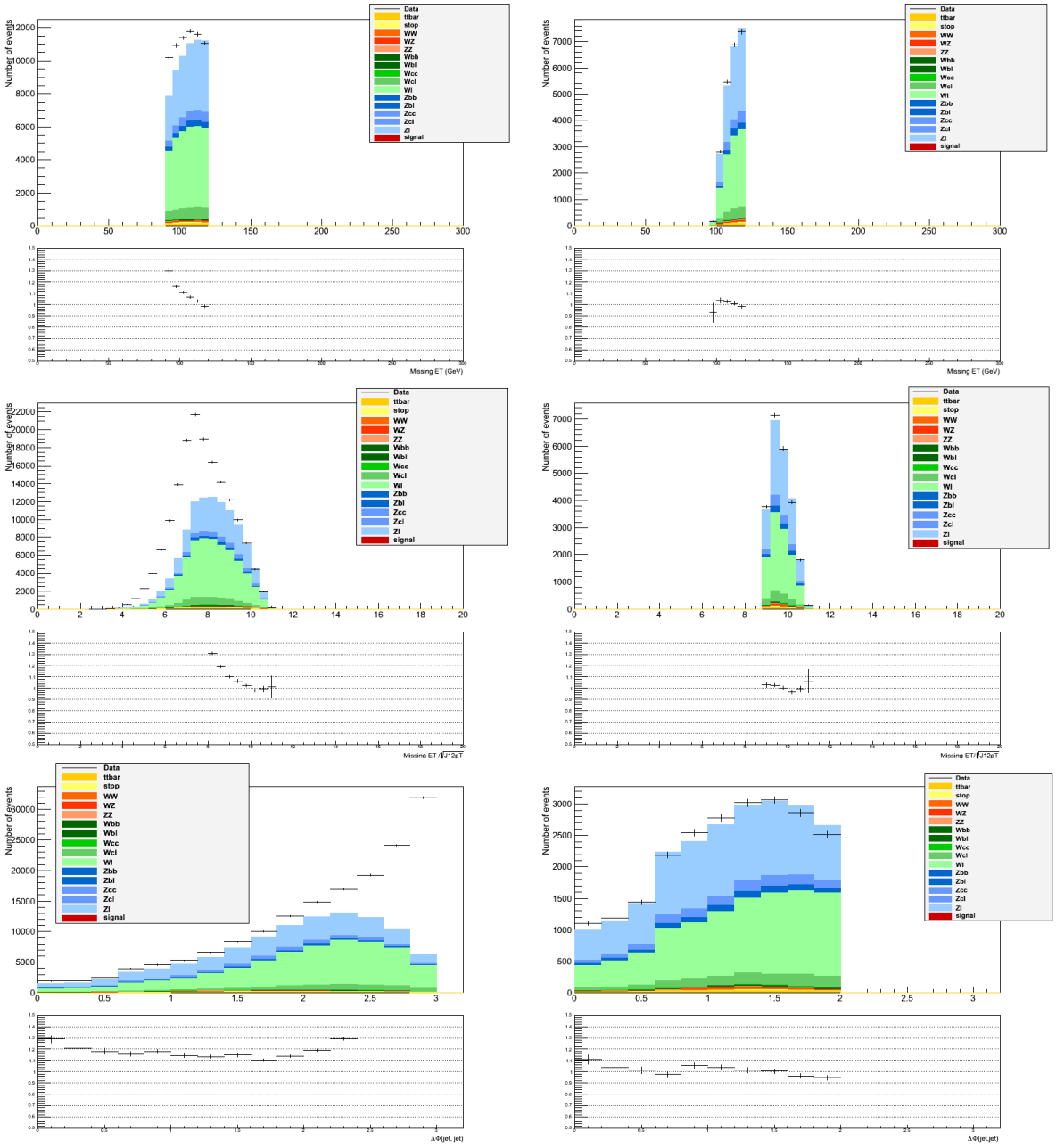

Figure 120: Distributions of $E_{\mathrm{T}}^{\mathrm{miss}}$ (top), $E_{\mathrm{T}}^{\mathrm{miss}}/\sqrt{J12pT}$ (middle) and $\Delta\phi(jet, jet)$ (bottom) in $E_{\mathrm{T}}^{\mathrm{miss}}$ bin 90–120 GeV for jets (before b–tagging) before (left) and after (right) applying the additional QCD rejection cuts using delayed stream $E_{\mathrm{T}}^{\mathrm{miss}}$ trigger exclusively.

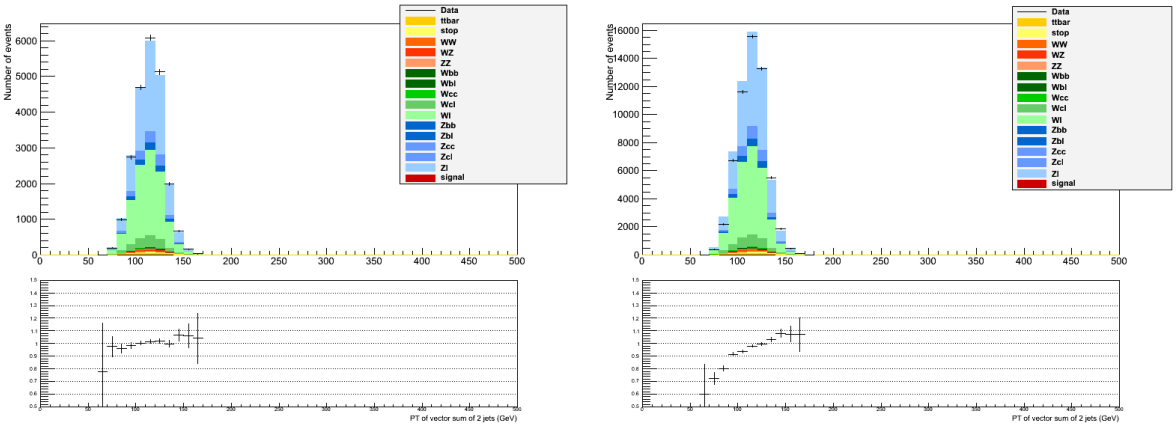

Figure 121: Distributions of transverse momentum of 4–vector sum of 2 jets (pre *b*–tagging procedure) in $E_{\mathrm{T}}^{\mathrm{miss}}$ bin 90–120 GeV using delayed stream trigger exclusively (left) and nominal $E_{\mathrm{T}}^{\mathrm{miss}}$ triggers.

C Low $E_{\mathrm{T}}^{\mathrm{miss}}$ analysis for Zero Lepton Channel

The former $ZH \to \nu\bar{\nu}b\bar{b}$ analysis [11] only considered $E_{\mathrm{T}}^{\mathrm{miss}} > 120$ GeV mainly because it is difficult to parametrize the complete turn on of a $E_{\mathrm{T}}^{\mathrm{miss}}$ trigger. For this round of analysis, thanks to the new trigger parametrization detailed in Appendix A, it is possible to lower the $E_{\mathrm{T}}^{\mathrm{miss}}$threshold down to 90 or 100GeV and to gain $ZH \to \nu\bar{\nu}b\bar{b}$ signal acceptance.

Section C.1 describes event selection for low $E_{\mathrm{T}}^{\mathrm{miss}}$ regions and shows kinematic distributions which have been introduced for low $E_{\mathrm{T}}^{\mathrm{miss}}$ region specifically. Section C.2 presents the rejection of QCD multijet background and its estimation using a likelihood ratio technique. Section C.3 discusses observed mis-modelings and further studies. Finally, Section C.4 discusses the expected sensitivity gain from the low $E_{\mathrm{T}}^{\mathrm{miss}}$ regions and what is expected once the delayed stream trigger (see Appendix B.5) is implemented into low $E_{\mathrm{T}}^{\mathrm{miss}}$ region analysis as well.

C.1 Event selection

The kinematic cuts outlined in Section 3.4 are not fully efficient for this region so the selection cuts were re-optimized. The $min\Delta\phi(E_{\mathrm{T}}^{\mathrm{miss}}, jets)$ cut is very efficient at rejecting the multijet background but in this lower boost region this cuts removes a large fraction of the $ZH \to \nu\bar{\nu}b\bar{b}$ signal. Instead, $\Delta\phi(jet_1, jet_2)$ and $E_{\mathrm{T}}^{\mathrm{miss}}$ significance defined as

$$E_{\mathrm{T}}^{\mathrm{miss}}\ Sig = E_{\mathrm{T}}^{\mathrm{miss}} / \sqrt{p_{T,j1} + p_{T,j2}} \tag{38}$$

are used to reject the QCD multijet background. The remaining multijet background after these cuts is further reduced using a multivariate Likelihood-based technique as described in following. Although the second $p_T(V)$ bin for the one lepton and two lepton channels is defined between 90-120GeV, in the 0-lepton low $E_{\mathrm{T}}^{\mathrm{miss}}$ region it was decided to tighten the lower $E_{\mathrm{T}}^{\mathrm{miss}}$ threshold to 100GeVto avoid possible modeling problem due to the trigger bias. This is further discussed in Section C.3. A summary of the event selection cuts is given in Table 82. The main differences compared to other signal regions are summarized in the Table 82.

3-jet low $E_{\mathrm{T}}^{\mathrm{miss}}$region does not dramatically increase the sensitivity but it does provide a region to test the background modeling with higher statistics, especially for $t\bar{t}$ background.

$E_{\mathrm{T}}^{\mathrm{miss}}$ (GeV)	100-120	100-120
N_{jet}	2	3
$\Delta\phi(V, H)$	>2.2	>2.8
$min\Delta\phi(E_{\mathrm{T}}^{\mathrm{miss}}, jets)$	–	>1.5
$\Delta\phi(jet_1, jet_2)$	<2.7	–
$E_{\mathrm{T}}^{\mathrm{miss}}$ Sig	>7.0	–
Likelihood	>0.5	–

Table 82: Event selection for the 0-lepton analysis between low $E_{\mathrm{T}}^{\mathrm{miss}}$ region (100-120GeV) Only cuts optimized or newly implemented are shown.

Figure 122 shows $E_{\mathrm{T}}^{\mathrm{miss}}$ Sig and $\Delta\phi(jet_1, jet_2)$ distributions and demonstrate the fact that the multijet background is controlled with this set of cuts.

C.2 QCD rejection and estimation

After applying cuts discussed in the previous section, the multijet background is not the predominant background but is still sizable contribution (5-10% depending on the b-tag category within the 100-

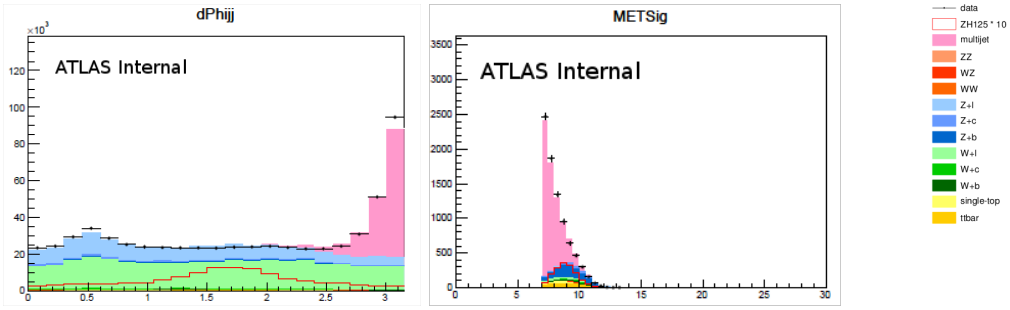

Figure 122: Pre b-tag low $E_{\mathrm{T}}^{\mathrm{miss}}$ region kinematics before applying cuts. (left) $\Delta\phi(jet_1, jet_2)$ (right) $E_{\mathrm{T}}^{\mathrm{miss}}$ significance.

150GeVMbb mass window). Since the multijet background is hard to precisely estimate a new multivariate Likelihood-based multijet rejection technique was developed to further to specifically reject the multijet background.

A likelihood ratio (LR) is defined as: $LR = LH^{signal}/(LH^{signal} + LH^{QCD})$, $LH^{signal} = \Pi_{i=1}^{n_{kin}} P_i^{signal}$ and $LH^{QCD} = \Pi_{i=1}^{n_{kin}} P_i^{QCD}$, where $P_i^{signal}(P_i^{QCD})$ is probability obtained from PDF distribution constructed from Z+jets (multijet data using the side-band of $\Delta\phi(E_{\mathrm{T}}^{\mathrm{miss}}, p_{\mathrm{T}}^{\mathrm{miss}}) > \pi/2$) pretag events. To produce the PDF templates, the $\Delta\phi(jet_1, jet_2)$ cut is not applied. The kinematic variables used to build the discriminant are:

- $\Delta\phi(jet_1, jet_2)$
- $\Delta\phi(V, H)$
- misH_{T}
- mist$H_{\mathrm{T}}/H_{\mathrm{T}}$

Access to the tool used to apply this likelihood in the analysis is documented in Appendix AO.

Figure 123 shows the PDF distributions used to construct Likelihood function and Figure 124 shows output distributions of the LR. We found that using Z+jets template as the signal PDF does not degrade QCD rejection performance compared to the PDF from $ZH \to \nu\bar{\nu}b\bar{b}$ itself. Furthermore, Z+jets PDF templates make it is possible to be Higgs mass independent and to avoid introducing bias due to $ZH \to \nu\bar{\nu}b\bar{b}$ MC usage. Therefore Z+jet events are used instead of the actual signal to construct the Likelihood.

Figure 125 to Figure 125 shows kinematic distributions before and after applying LR cut.

To estimate the multijet background after applying every cuts, the so-called ABCD method similarly to that discussed in Section 5.4 However, $min\Delta\phi(E_{\mathrm{T}}^{\mathrm{miss}}, jets)$ cannot be used for the ABCD method since it is not used in the this low $E_{\mathrm{T}}^{\mathrm{miss}}$ region. Instead, LR is used to construct ABCD 2-D plane together with $\Delta\phi(E_{\mathrm{T}}^{\mathrm{miss}}, p_{\mathrm{T}}^{\mathrm{miss}})$.

Multijet shapes are obtained from data after subtracting the small electroweak background contributions using the 'C'-region defined as $\Delta\phi(E_{\mathrm{T}}^{\mathrm{miss}}, p_{\mathrm{T}}^{\mathrm{miss}}) > \pi/2$. For 2 b-tagged events, statistics of data side-band 'C' is very limited, therefore shapes are obtained from 1 b-tagged events.

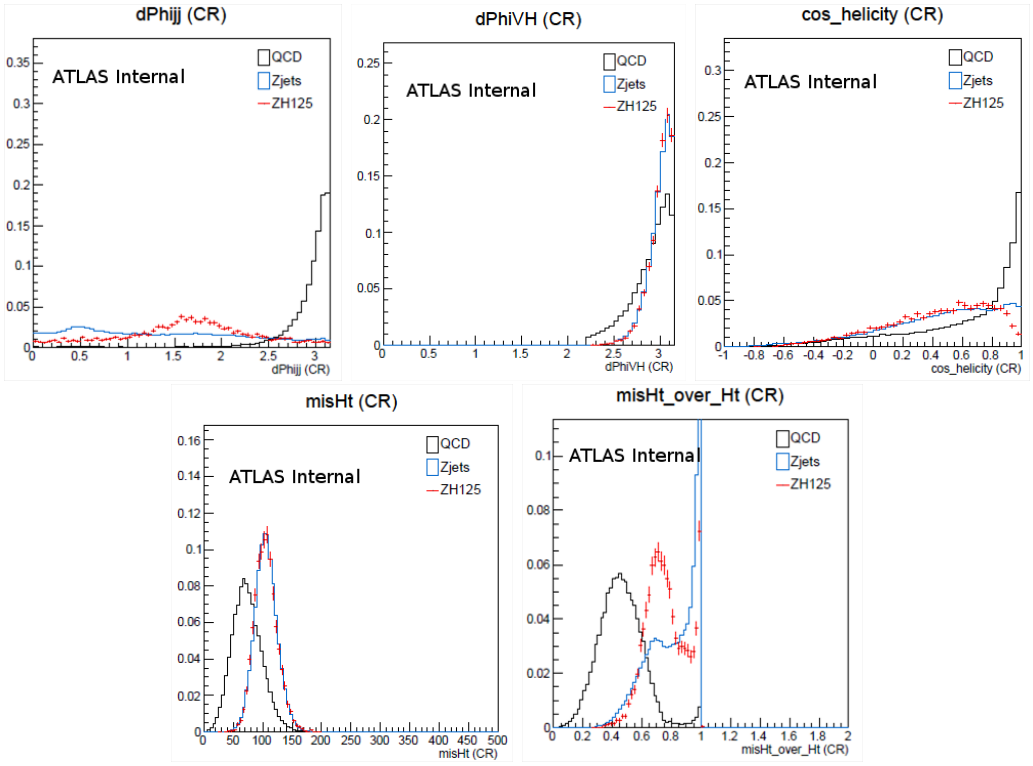

Figure 123: Likelihood PDF kinematics. From top left to bottom right, $\Delta\phi(jet_1, jet_2)$, $\Delta\phi(V,H)$, cos(helicity), misH_T and misH_T/H_T, respectively. Black line shows QCD template and light blue line shows Z+jets template. As a reference, ZH (125 GeV) signal is shown in red line.

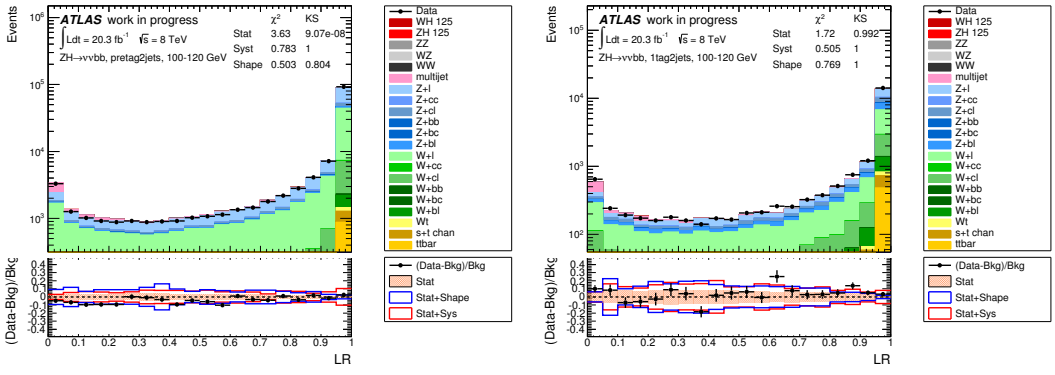

Figure 124: *LR* distributions. (Left) pretag. (Right) 1-tag.

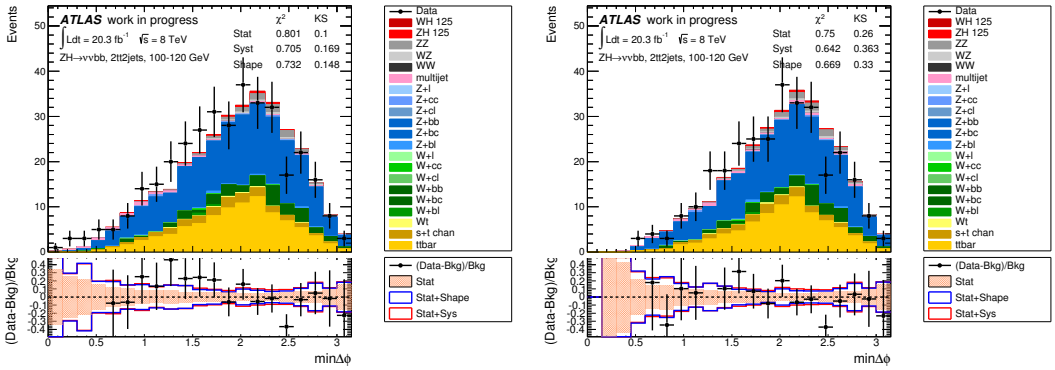

Figure 125: Kinematics before and after applying *LR* QCD rejection cut. (Left) 2-tt tag plot for $min\Delta\phi(E_{\mathrm{T}}^{\mathrm{miss}}, jets)$ before applying *LR* cut. (Right) 2-tt tag plot for $min\Delta\phi(E_{\mathrm{T}}^{\mathrm{miss}}, jets)$ after applying *LR* cut.

C.3 Mis-modelings

It was found that the possible mis-modeling of the vector sum of two leading jet p_{T} (misH_{T}) in the low $E_{\mathrm{T}}^{\mathrm{miss}}$ region, could possibly originated from the bias in the $E_{\mathrm{T}}^{\mathrm{miss}}$ trigger modeling. Figure 126 shows data-MC agreement for misH_{T} for the $E_{\mathrm{T}}^{\mathrm{miss}}$region: $90 < E_{\mathrm{T}}^{\mathrm{miss}} < 100$ GeV, $100 < E_{\mathrm{T}}^{\mathrm{miss}} < 120$ GeV, and $120 < E_{\mathrm{T}}^{\mathrm{miss}} < 160$ GeV. While the $90 < E_{\mathrm{T}}^{\mathrm{miss}} < 100$ GeVregion shows possible modeling problems, modeling is improved once the $E_{\mathrm{T}}^{\mathrm{miss}}$ lower cut threshold is raised to 100 GeV. The agreement is then on a similar level as the $120 < E_{\mathrm{T}}^{\mathrm{miss}} < 160$ GeVregion.

To further check and understand the source of this mis-modeling the following checks have been done.

1. Effect from $\Delta\phi(jet_1, jet_2)$ correction for W/Z+jets.
2. Validation using $W \to \mu\nu$+jets and $Z \to \mu\mu$+jets events.
3. JES systematic covers the disagreement.

Figure 127 shows comparisons among lepton categories on misH_{T} distribution with and without the $\Delta\phi(jet_1, jet_2)$ correction applied. There is no reason to believe this is the source of the mis-modeling. For the second test, events which fires $E_{\mathrm{T}}^{\mathrm{miss}}$ trigger and and request $W \to \mu\nu$ or $Z \to \mu\mu$ candidates, similarly to the $E_{\mathrm{T}}^{\mathrm{miss}}$ trigger parametrization measurement described in Appendix A. No evidence of a source of the mis-modeling was seen from this study.

C.4 Sensitivity gain and prospect with delayed trigger

Studies ongoing, an estimate will be added soon.

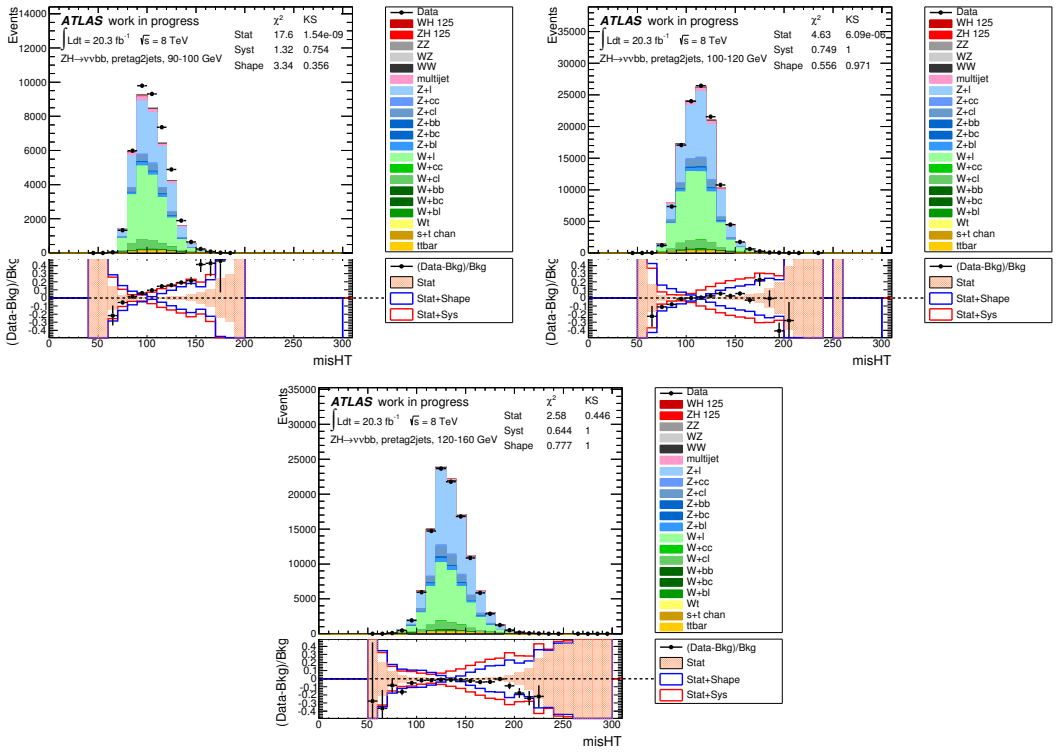

Figure 126: Pretag misH_T distributions for low $E_{\mathrm{T}}^{\mathrm{miss}}$ region. From left to right, $90 < E_{\mathrm{T}}^{\mathrm{miss}} < 100$ GeV, $100 < E_{\mathrm{T}}^{\mathrm{miss}} < 120$ GeV, $120 < E_{\mathrm{T}}^{\mathrm{miss}} < 160$ GeV, respectively.

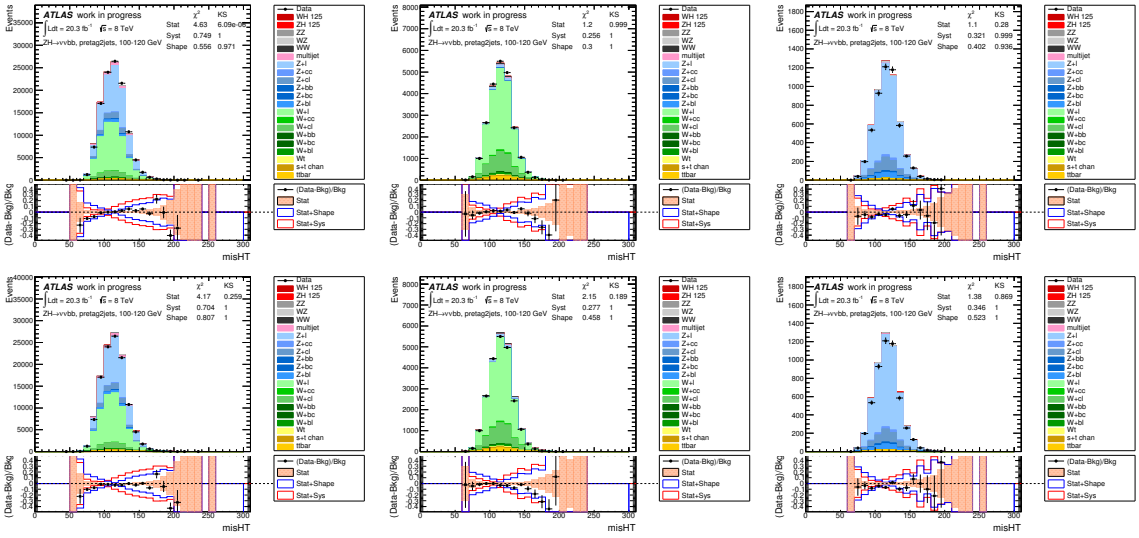

Figure 127: Pretag misH_T distributions for $100 < E_{\mathrm{T}}^{\mathrm{miss}} < 120$ GeV (Top) From left to right, 0-lepton, 1-lepton, 2-lepton with applying $\Delta\phi(j1, j2)$ correction for W+jets/Z+jets modeling. (Bottom) From left to right, 0-lepton, 1-lepton, 2-lepton without applying $\Delta\phi(j1, j2)$ correction for W+jets/Z+jets modeling.

D $E_{\mathrm{T}}^{\mathrm{miss}}$ trigger for 1 lepton events

For 1-lepton ($WH \to \ell\nu b\bar{b}$) analysis in muon channel, events triggered by $E_{\mathrm{T}}^{\mathrm{miss}}$ are used in addition to single lepton triggered events in order to recover the inefficiency of the muon trigger. In the EPS analysis $E_{\mathrm{T}}^{\mathrm{miss}}$ triggered events were also used when $p_{\mathrm{T}}^{W} > 160$ GeV. In this analysis, the application threshold is lowered to 120 GeV, thanks to well described $E_{\mathrm{T}}^{\mathrm{miss}}$ trigger properties derived in 0-lepton analysis.

D.1 $E_{\mathrm{T}}^{\mathrm{miss}}$ triggered muon events

At the level of on-line physics objects, $E_{\mathrm{T}}^{\mathrm{miss}}$ is calculated by using only calorimeter components, thus the muon momentum is not propagated to the $E_{\mathrm{T}}^{\mathrm{miss}}$ calculation. This is the reason why $E_{\mathrm{T}}^{\mathrm{miss}}$ triggers are helpful for this analysis.

In muon channel of 1-lepton analysis, the primary triggers are single muon triggers which are EF_mu24vhi_medium1 and EF_mu36_medium1. However, the plateaus of these trigger efficiencies are around 80%. This is because of the limited acceptance of L1 muon chambers in some region of the detector and also the inefficiency for the high p_{T} muons. In order to recover this inefficiency coming from muon trigger requirement, $E_{\mathrm{T}}^{\mathrm{miss}}$ triggers are introduced. They are a combination of EF_xe80_tclcw, EF_xe80T_tclcw_loose and EF_xe80_tclcw_loose. Details of the combination of $E_{\mathrm{T}}^{\mathrm{miss}}$ triggers are described in Appendix A.

In case of $p_{\mathrm{T}}^{W} > 120$ GeV, $E_{\mathrm{T}}^{\mathrm{miss}}$ triggers are used only when the single muon triggers mentioned above are not fired.

D.2 $E_{\mathrm{T}}^{\mathrm{miss}}$ trigger efficiency and scale factor

Trigger scale factor is provided by the 0 lepton analysis which is parametrized by $E_{\mathrm{T}}^{\mathrm{miss}}$. However to emulate this scale factor, $E_{\mathrm{T}}^{\mathrm{miss}}$ should be calculated without muon momentum in 1-lepton muon channel. This is because muons are not taken into account in the calculation of $E_{\mathrm{T}}^{\mathrm{miss}}$ at trigger level. Therefore, the data/MC agreement of $E_{\mathrm{T}}^{\mathrm{miss}}$ without muon contribution ($E_{\mathrm{T}}^{\mathrm{miss}}(\not{\mu})$) should be checked. Figures 128–130(131–133) show the distribution of $E_{\mathrm{T}}^{\mathrm{miss}}(\not{\mu})$ for 2 (3) jet bin.

D.3 QCD multi-jet background estimation

QCD multijet background is estimated from data with fitting of the muon p_{T}. The estimation method is the same as the nominal 1-lepton analysis except changing the trigger requirement for the templates from data. Details are described in Appendix R.

D.4 Sensitivity gain

Figures 134–136 (137–139) show the m_{jj} distribution for each p_{T}^{W} bin and b-tagging category in 2 (3) jet bin. Based on this distribution in each category, Poisson significance is calculated within the range of $100 < m_{jj} < 150$ GeV. The combined significance of the three 2 tag categories (loose, medium and tight) are shown in Table 83 for 2 and 3 jet bins with the final combined sensitivity of 2 and 3 jet bins. The sensitivity gain by $E_{\mathrm{T}}^{\mathrm{miss}}$ triggered events compared to single muon triggered events is 10.8%. The sensitivity gain compared to nominal 1-lepton analysis including electron channel is XX%(to be updated with the final fit).

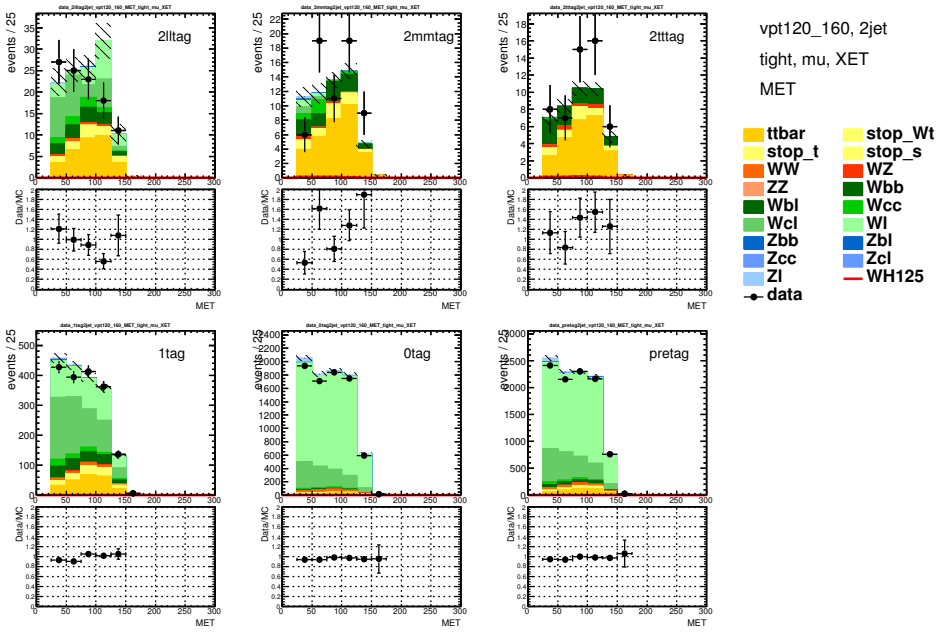

Figure 128: The distribution of $E_{\mathrm{T}}^{\mathrm{miss}}$ without muon contribution ($E_{\mathrm{T}}^{\mathrm{miss}}(\not{\mu})$) of $E_{\mathrm{T}}^{\mathrm{miss}}$ triggered events in 2 jet bin, $120 < p_{\mathrm{T}}^{W} < 160$ GeV. Each b-tagging category is shown in 2 loose tag (top left), 2 medium tag (top middle), 2 tight tag (top right), 1 tag (bottom left), 0 tag (bottom middle) and pre-tag (bottom right). Now plots are just $E_{\mathrm{T}}^{\mathrm{miss}}$(including muon), PLOTS TO BE UPDATED.

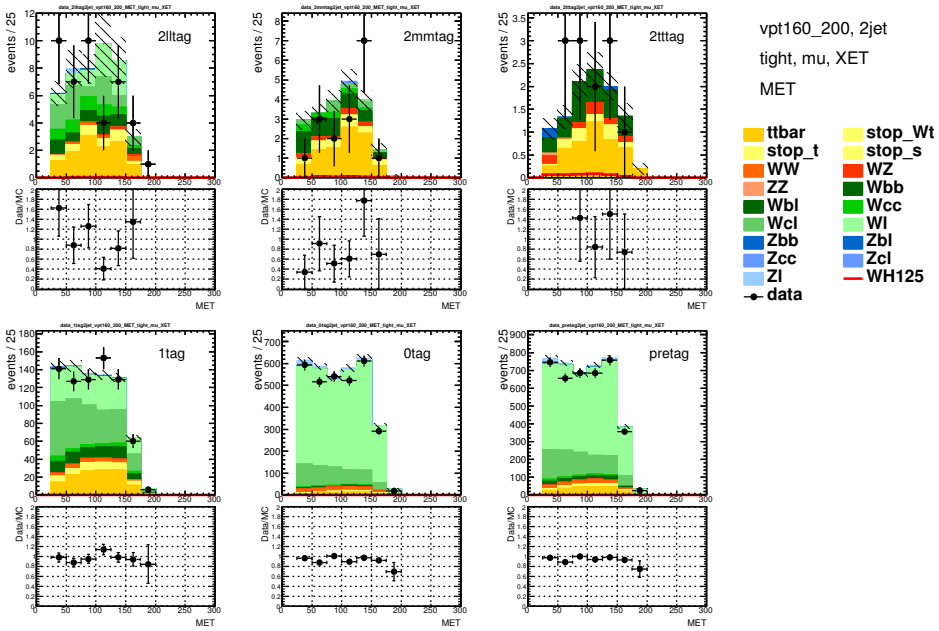

Figure 129: The distribution of $E_{\mathrm{T}}^{\mathrm{miss}}$ without muon contribution ($E_{\mathrm{T}}^{\mathrm{miss}}(\not{\mu})$) of $E_{\mathrm{T}}^{\mathrm{miss}}$ triggered events in 2 jet bin, $160 < p_{\mathrm{T}}^{W} < 200$ GeV. Each b-tagging category is shown in 2 loose tag (top left), 2 medium tag (top middle), 2 tight tag (top right), 1 tag (bottom left), 0 tag (bottom middle) and pre-tag (bottom right). Now plots are just $E_{\mathrm{T}}^{\mathrm{miss}}$(including muon), PLOTS TO BE UPDATED.

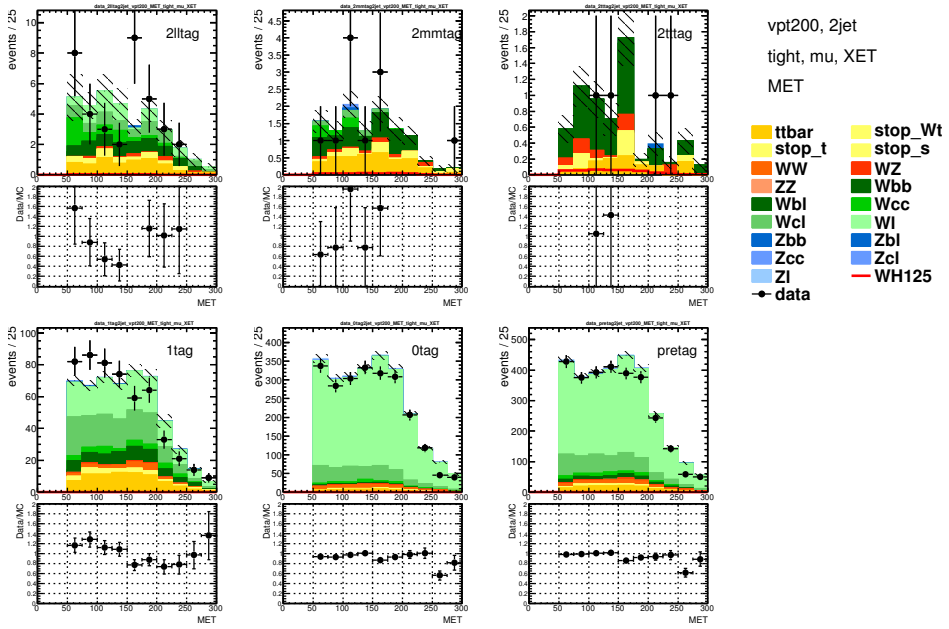

Figure 130: The distribution of $E_{\mathrm{T}}^{\mathrm{miss}}$ without muon contribution ($E_{\mathrm{T}}^{\mathrm{miss}}(\not\mu)$) of $E_{\mathrm{T}}^{\mathrm{miss}}$ triggered events in 2 jet bin, $p_{\mathrm{T}}^{W} > 200$ GeV. Each b-tagging category is shown in 2 loose tag (top left), 2 medium tag (top middle), 2 tight tag (top right), 1 tag (bottom left), 0 tag (bottom middle) and pre-tag (bottom right). Now plots are just $E_{\mathrm{T}}^{\mathrm{miss}}$(including muon), PLOTS TO BE UPDATED.

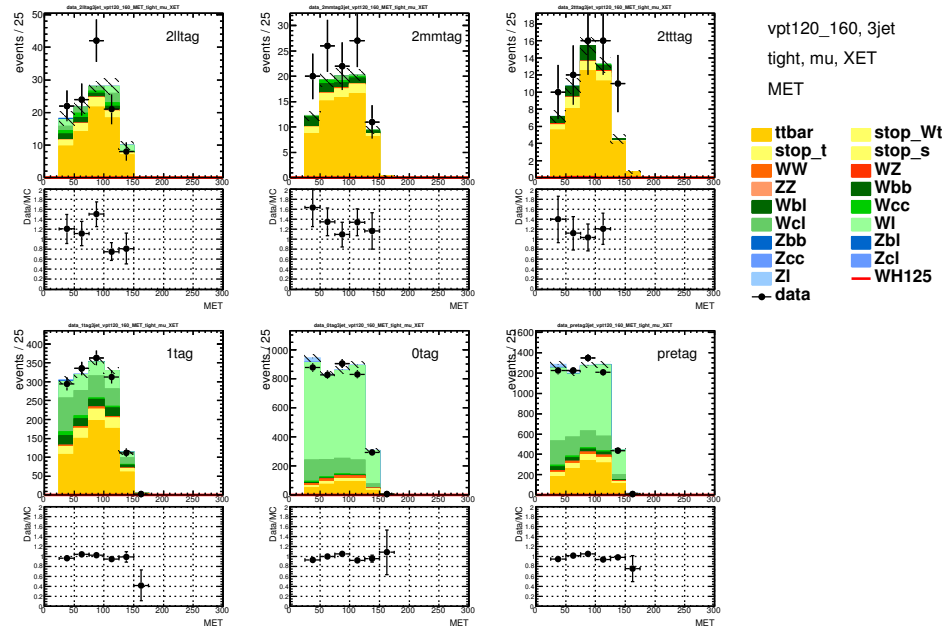

Figure 131: The distribution of $E_{\mathrm{T}}^{\mathrm{miss}}$ without muon contribution ($E_{\mathrm{T}}^{\mathrm{miss}}(\not\mu)$) of $E_{\mathrm{T}}^{\mathrm{miss}}$ triggered events in 3 jet bin, $120 < p_{\mathrm{T}}^{W} < 160$ GeV. Each b-tagging category is shown in 2 loose tag (top left), 2 medium tag (top middle), 2 tight tag (top right), 1 tag (bottom left), 0 tag (bottom middle) and pre-tag (bottom right). Now plots are just $E_{\mathrm{T}}^{\mathrm{miss}}$(including muon), PLOTS TO BE UPDATED.

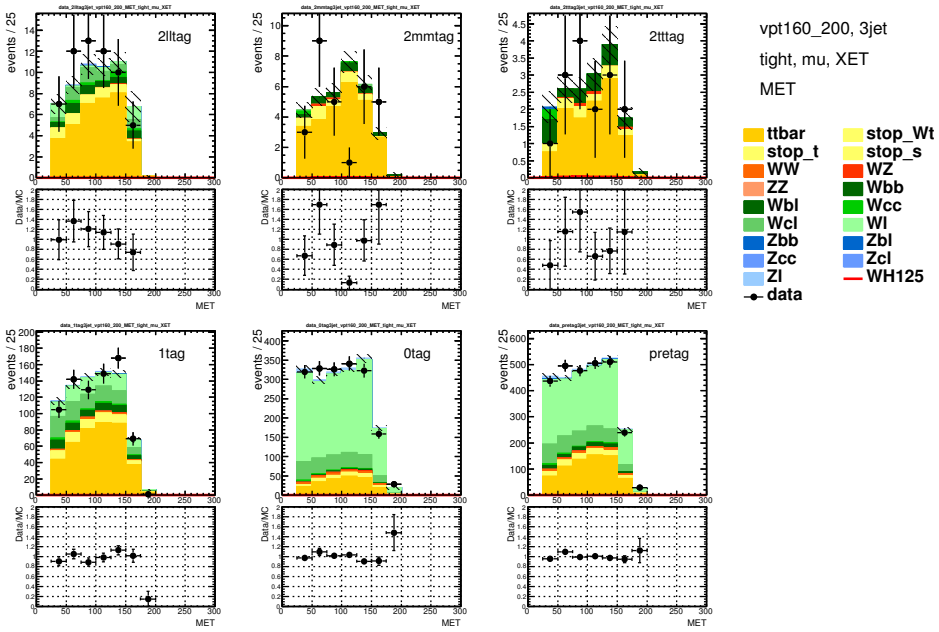

Figure 132: The distribution of $E_{\mathrm{T}}^{\mathrm{miss}}$ without muon contribution ($E_{\mathrm{T}}^{\mathrm{miss}}(\not\mu)$) of $E_{\mathrm{T}}^{\mathrm{miss}}$ triggered events in 3 jet bin, $160 < p_{\mathrm{T}}^{W} < 200$ GeV. Each b-tagging category is shown in 2 loose tag (top left), 2 medium tag (top middle), 2 tight tag (top right), 1 tag (bottom left), 0 tag (bottom middle) and pre-tag (bottom right). Now plots are just $E_{\mathrm{T}}^{\mathrm{miss}}$(including muon), PLOTS TO BE UPDATED.

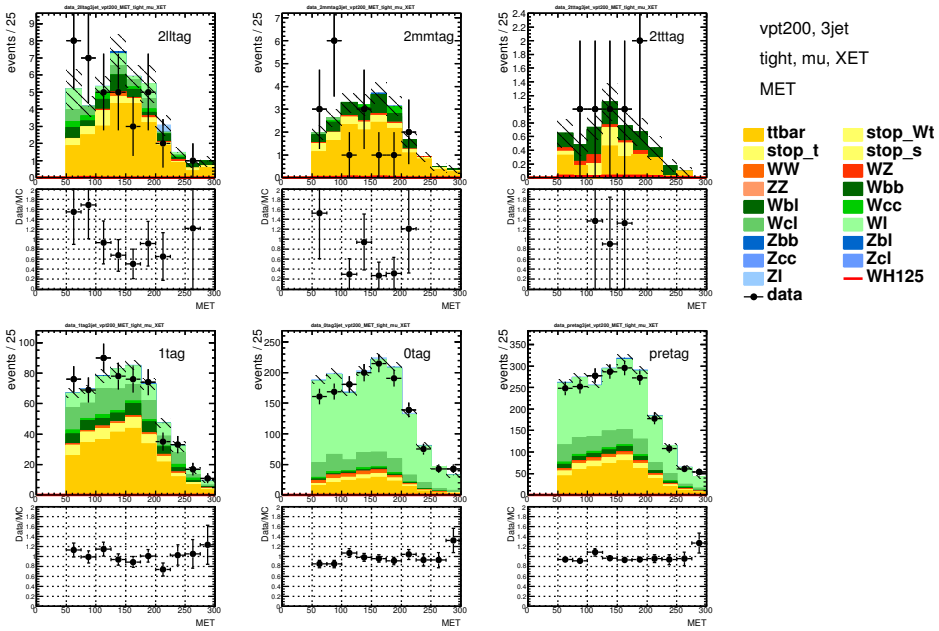

Figure 133: The distribution of $E_{\mathrm{T}}^{\mathrm{miss}}$ without muon contribution ($E_{\mathrm{T}}^{\mathrm{miss}}(\not\mu)$) of $E_{\mathrm{T}}^{\mathrm{miss}}$ triggered events in 3 jet bin, $p_{\mathrm{T}}^{W} > 200$ GeV. Each b-tagging category is shown in 2 loose tag (top left), 2 medium tag (top middle), 2 tight tag (top right), 1 tag (bottom left), 0 tag (bottom middle) and pre-tag (bottom right). Now plots are just $E_{\mathrm{T}}^{\mathrm{miss}}$(including muon), PLOTS TO BE UPDATED.

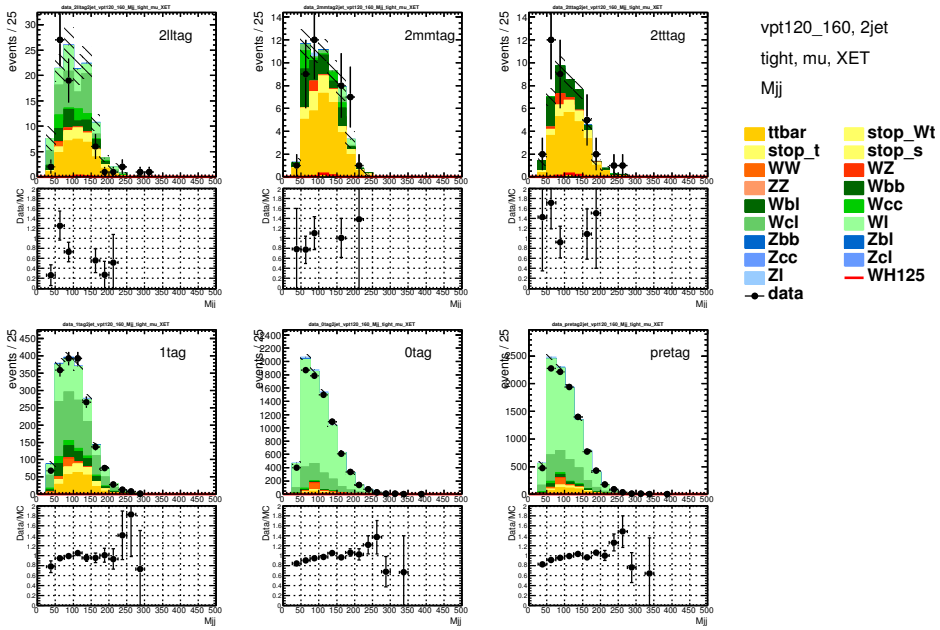

Figure 134: m_{jj} distributions of $E_{\mathrm{T}}^{\mathrm{miss}}$ triggered events in 2 jet bin, $120 < p_{\mathrm{T}}^{W} < 160$ GeV. Each b-tagging category is shown in 2 loose tag (top left), 2 medium tag (top middle), 2 tight tag (top right), 1 tag (bottom left), 0 tag (bottom middle) and pre-tag (bottom right). Data points are blinded in $100 < m_{jj} < 150$ GeV in 2 tag categories. PLOTS TO BE UPDATED.

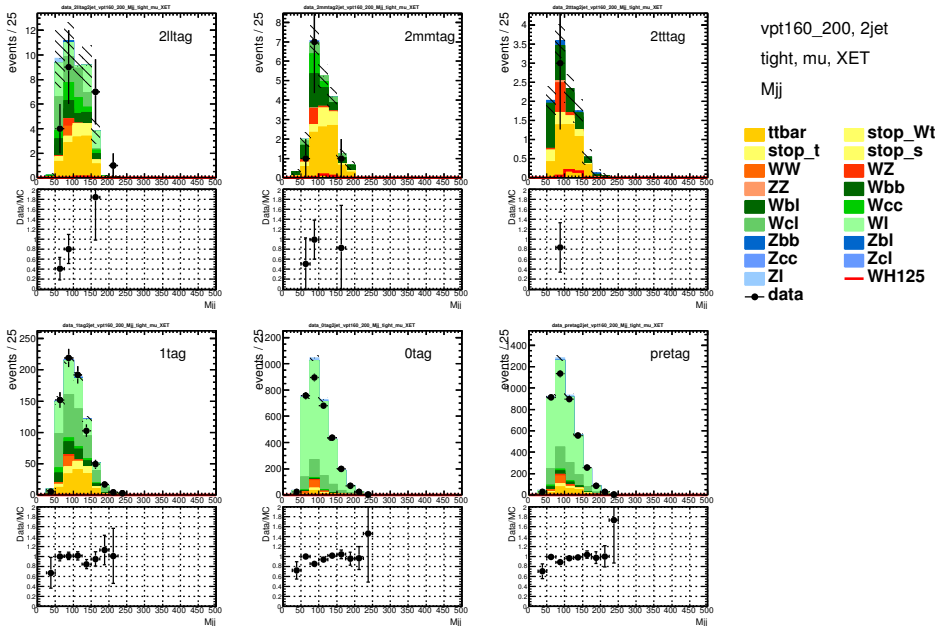

Figure 135: m_{jj} distributions of $E_{\mathrm{T}}^{\mathrm{miss}}$ triggered events in 2 jet bin, $160 < p_{\mathrm{T}}^{W} < 200$ GeV. Each b-tagging category is shown in 2 loose tag (top left), 2 medium tag (top middle), 2 tight tag (top right), 1 tag (bottom left), 0 tag (bottom middle) and pre-tag (bottom right). Data points are blinded in $100 < m_{jj} < 150$ GeV in 2 tag categories. PLOTS TO BE UPDATED.

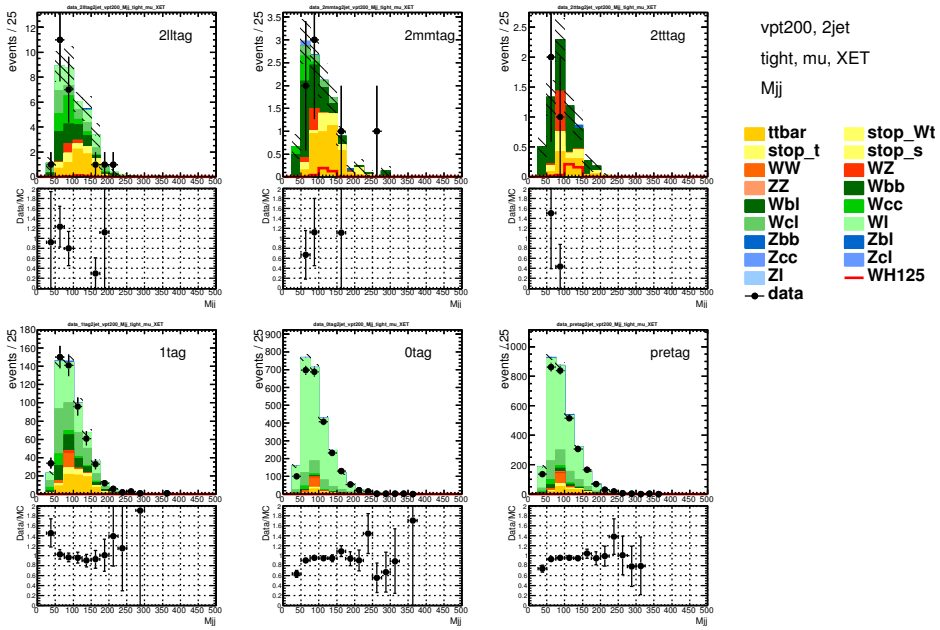

Figure 136: m_{jj} distributions of $E_{\mathrm{T}}^{\mathrm{miss}}$ triggered events in 2 jet bin, $p_{\mathrm{T}}^{W} > 200$ GeV. Each b-tagging category is shown in 2 loose tag (top left), 2 medium tag (top middle), 2 tight tag (top right), 1 tag (bottom left), 0 tag (bottom middle) and pre-tag (bottom right). Data points are blinded in $100 < m_{jj} < 150$ GeV in 2 tag categories. PLOTS TO BE UPDATED.

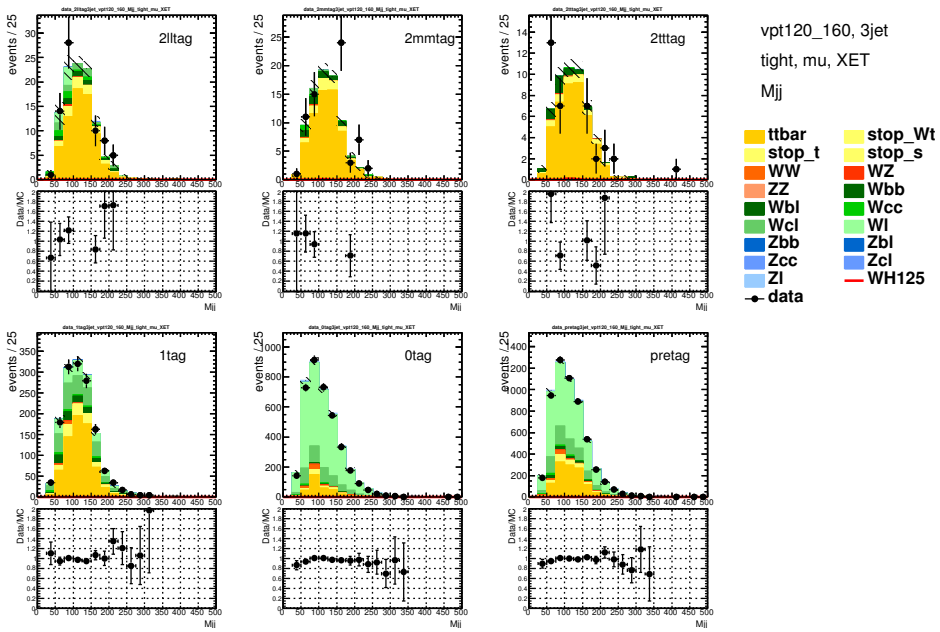

Figure 137: m_{jj} distributions of $E_{\mathrm{T}}^{\mathrm{miss}}$ triggered events in 3 jet bin, $120 < p_{\mathrm{T}}^{W} < 160$ GeV. Each b-tagging category is shown in 2 loose tag (top left), 2 medium tag (top middle), 2 tight tag (top right), 1 tag (bottom left), 0 tag (bottom middle) and pre-tag (bottom right). Data points are blinded in $100 < m_{jj} < 150$ GeV in 2 tag categories. PLOTS TO BE UPDATED.

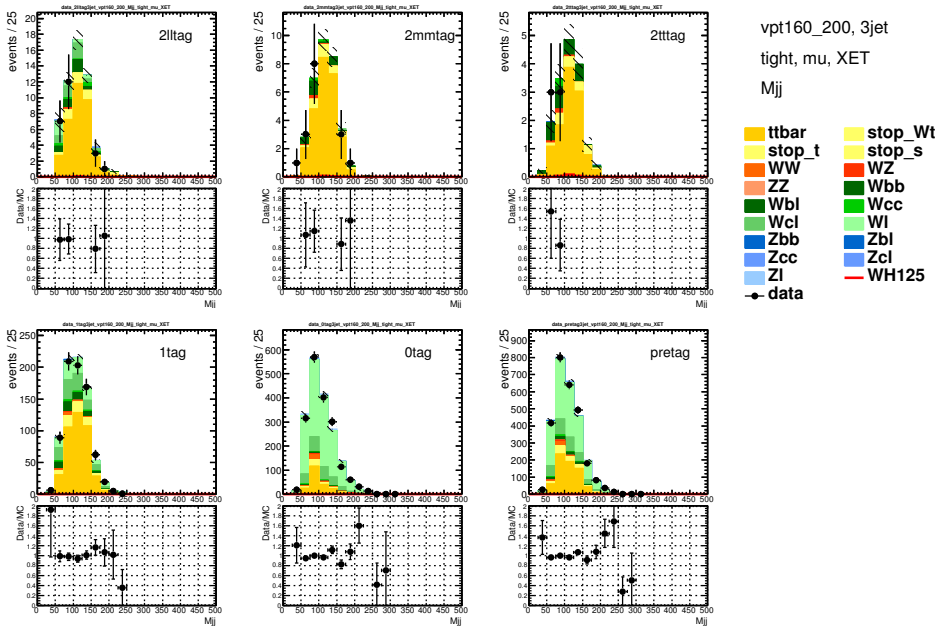

Figure 138: m_{jj} distributions of $E_{\mathrm{T}}^{\mathrm{miss}}$ triggered events in 3 jet bin, $160 < p_{\mathrm{T}}^{W} < 200$ GeV. Each b-tagging category is shown in 2 loose tag (top left), 2 medium tag (top middle), 2 tight tag (top right), 1 tag (bottom left), 0 tag (bottom middle) and pre-tag (bottom right). Data points are blinded in $100 < m_{jj} < 150$ GeV in 2 tag categories. PLOTS TO BE UPDATED.

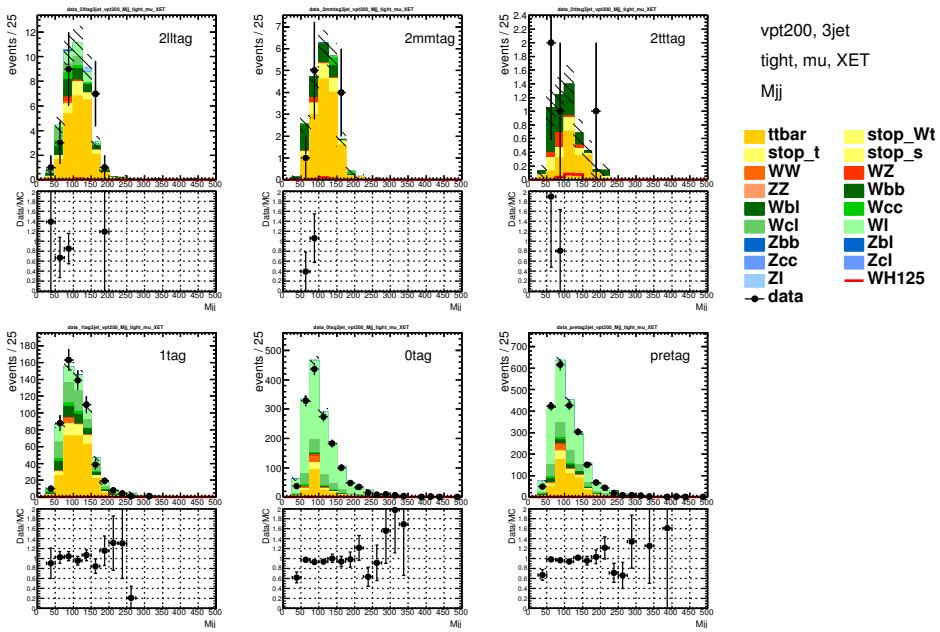

Figure 139: m_{jj} distributions of $E_{\mathrm{T}}^{\mathrm{miss}}$ triggered events in 3 jet bin, $p_{\mathrm{T}}^{W} > 200$ GeV. Each b-tagging category is shown in 2 loose tag (top left), 2 medium tag (top middle), 2 tight tag (top right), 1 tag (bottom left), 0 tag (bottom middle) and pre-tag (bottom right). Data points are blinded in $100 < m_{jj} < 150$ GeV in 2 tag categories. PLOTS TO BE UPDATED.

Table 83: Significance in 2 and 3 jet bins, and in the combination. NUMBERS TO BE UPDATED.

p_{T}^{W} GeV	all categories - muon channel
2 jet bin	
Single muon trigger	0.8256
$E_{\mathrm{T}}^{\mathrm{miss}}$ trigger	0.3943
3 jet bin	
Single muon trigger	0.2660
$E_{\mathrm{T}}^{\mathrm{miss}}$ trigger	0.1378
combination of 2 and 3 jet bins	
Single muon trigger	0.8674
$E_{\mathrm{T}}^{\mathrm{miss}}$ trigger	0.4157
Total	0.9619

E Electron Isolation

A Tag&Probe measurement of electron isolation efficiencies and derived scale factors is presented using $Z \to e^+e^-$ resonances in 2012 LHC data and `AF-II` *Sherpa Z+jets* Monte Carlo events. The measurement considers `VeryTightLH` electrons [17, 18] probing track and calorimeter isolation parameters as defined in Sections 3.2.1.3 (Equation 1) and 3.2.1.1 (Equation 2) respectively. Both parameter thresholds are set to 0.04 as previously defined for VH tight leptons. Furthermore, a variation of tag and probe quality requirements is applied to estimate systematic uncertainties of the method.

E.1 Tag and Probe Algorithm

Electrons may qualify to become a tag or probe candidate if the following criteria are fulfilled:

- a transverse energy $E_T > 20$ GeV,
- within a pseudorapidty range of $|\eta| < 2.47$ (`Si` tracking region),
- matched to a single lepton trigger (`EF_e24vhi_medium1` or `EF_e60_medium1`),
- truth matched to a Z boson incl. Bremsstrahlung and final state radiation in Monte Carlo events.

In addition, the tag selection excludes any electrons in the crack region ($1.37 < |\eta| < 1.52$), requires $E_T > 25$ GeV and uses 4 quality variations based on isolation:

1. no isolation requirement,
2. pass track isolation only,
3. pass calorimeter isolation only,
4. pass both track and calorimeter isolation.

The probe electron must be of opposite charge to the selected tag electron and form together an invariant di-electron mass close to the Z boson mass using 3 quality variations:

1. loose mass window of $|m_Z - m_{e^+e^-}| < 30$ GeV,
2. medium mass window of $|m_Z - m_{e^+e^-}| < 20$ GeV,
3. tight mass window of $|m_Z - m_{e^+e^-}| < 10$ GeV.

All possible permutations of tag&probe pairs in any given event are used for each of the 4×3 quality variations and finally contribute to the efficiency measurement, which is defined as

$$\varepsilon = \frac{N_{\text{probe + iso}}}{N_{\text{probe}}} \quad \text{per variation and event,} \tag{39}$$

where N_{probe} is the number of probes passing the basic selection criteria described above and $N_{\text{probe + iso}}$ is the number of probes that pass additionally the track and calorimeter isolation criteria. This is done for both data and Monte Carlo events in order to derive scale factors for each variation v. These are then combined using standard error propagation:

$$SF_{comb} = N_v^{-1} \sum SF_v, \qquad \sigma^{\text{stat}}_{\text{comb}} = N_v^{-1} \sum \sigma^{\text{stat}}_{SF_v}, \qquad \sigma^{\text{syst}}_{\text{comb}} = \sqrt{N_v^{-1} \sum (SF_v - \mu)^2}. \tag{40}$$

The measurement is done as a function of E_T and η, while other dependencies have also been studied, such as the dependence on jets and their multiplicity in the vicinity of the probing electron.

E.2 Results

The electron isolation efficiency measured in both 8TeVdata and Monte Carlo events using the above Tag&Probe method is shown in Fig. 140(a)–140(b) as a function of E_T and η. Generally the efficiency drops down to $\sim$ 73% at low E_T and central η and rises above 90% for all η for $E_T > 60$ GeV. The derived scale factors using these efficiencies are shown both as a function of E_T and η in Fig. 140(c) as well as inclusive in E_T in Fig. 140(d). This former nominal 2D scale factor map is used only in the 1-lepton analysis.

A similar measurement has been made for `VeryLooseLH` electrons probing track isolation only for the 2-lepton analysis. Since the resulting scale factors were $\sim$ 1, no isolation scale factors are applied in this analysis.

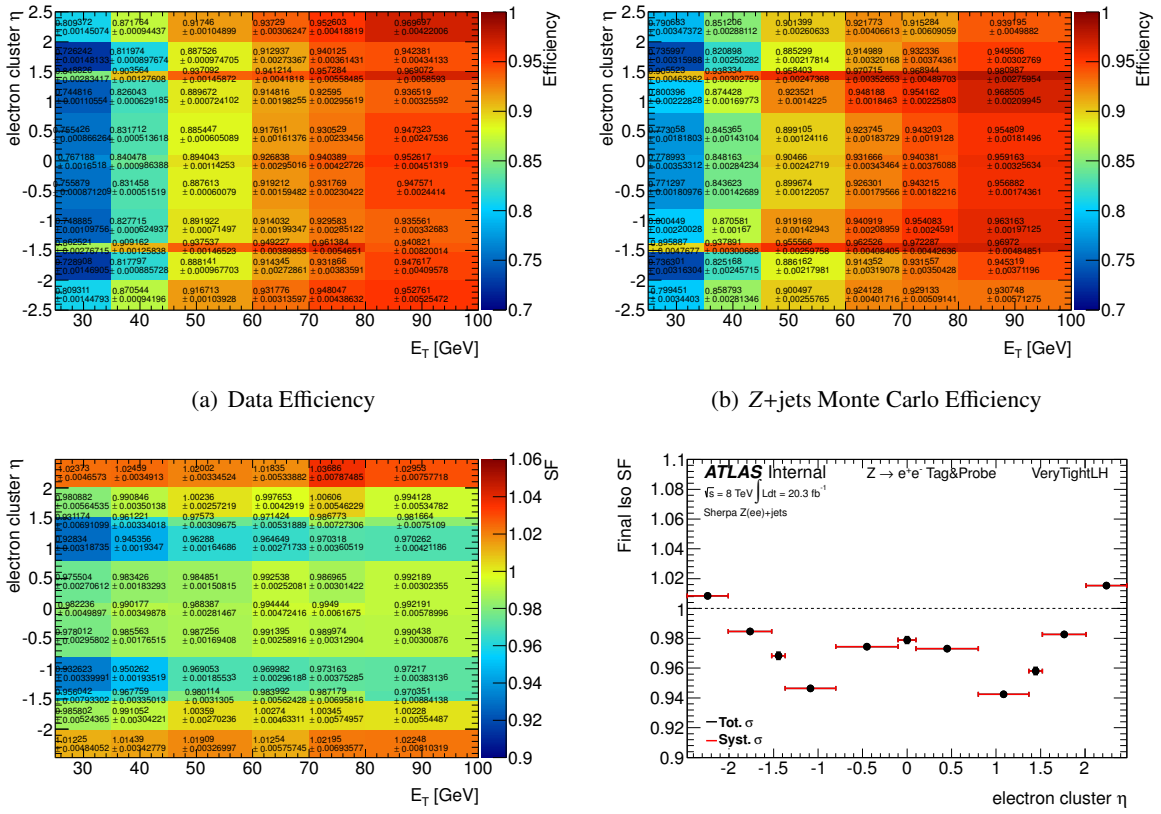

(a) Data Efficiency

(b) Z+jets Monte Carlo Efficiency

(c) Scale Factors

(d) Scale Factors inclusive in p_T

Figure 140: Electron isolation efficiencies and derived scale factors.

F Muon isolation

A Tag&Probe measurement of muon isolation efficiencies and derived scale factors is presented using $Z \to \mu^+\mu^-$ resonances in 2012 LHC data and `AF-II` *Sherpa Z+jets* Monte Carlo events. The measurement considers `Tight` muons probing track and calorimeter isolation thresholds and uses the same method as described in the previous section with only minor changes:

- the probe (tag) muon has a transverse momentum $p_{\mathrm{T}} > 15(20)$ GeV,
- within a pseudorapidty range of $|\eta| < 2.5$,
- matched to a single lepton trigger (`EF_mu24i_tight` or `EF_mu36_tight`),
- no Z boson truth matching.

F.1 Results

The muon isolation efficiency measured in both 8TeVdata and Monte Carlo events using the above Tag&Probe method is shown in Fig. 141(a)–141(b) as a function of p_{T} and η. Generally the efficiency decreases down to $\sim 73\%$ at low p_{T} and central η and rises above 90% for all η for $E_T > 50$ GeV. The derived scale factors using these efficiencies are shown both as a function of p_{T} and η in Fig. 141(c)as well as inclusive in p_{T} in Fig. 141(d). This former nominal 2D scale factor map is used in the 1-lepton analysis.

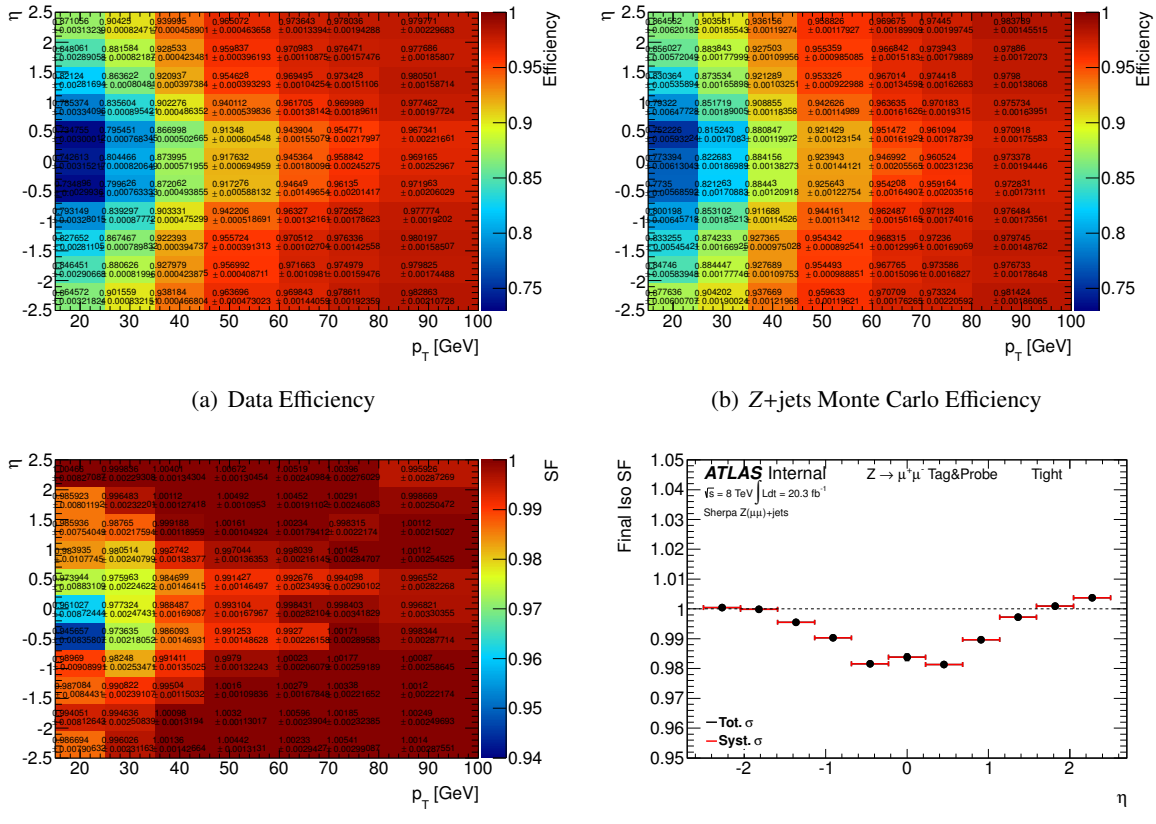

(a) Data Efficiency

(b) Z+jets Monte Carlo Efficiency

(c) Scale Factors

(d) Scale Factors inclusive in p_{T}

Figure 141: Muon isolation efficiencies and derived scale factors.

Further efficiency dependencies have been studied. The muon isolation efficiency as a function of the number of reconstructed vertices shown in Fig. 142(a) reveals a pile-up dependence; the efficiency drops down to $\sim$ 85% as the number of vertices increases. However, as Fig. 142(b) shows, if one does the probing for the track isolation parameter only, the efficiency of this cut remains stable. Thus the calorimeter isolation requirement causes this dependence.

The efficiency also depends on close-by jets and their multiplicity. The raw $\Delta R(\mu, \text{nearest jet})$ distribution in Fig. 142(c) is as expected similar to the electron results discussed in the previous section. Fig. 142(d) shows a significant decrease of the muon isolation efficiency to $\sim$ 60% as jets get closer to the probing muon.

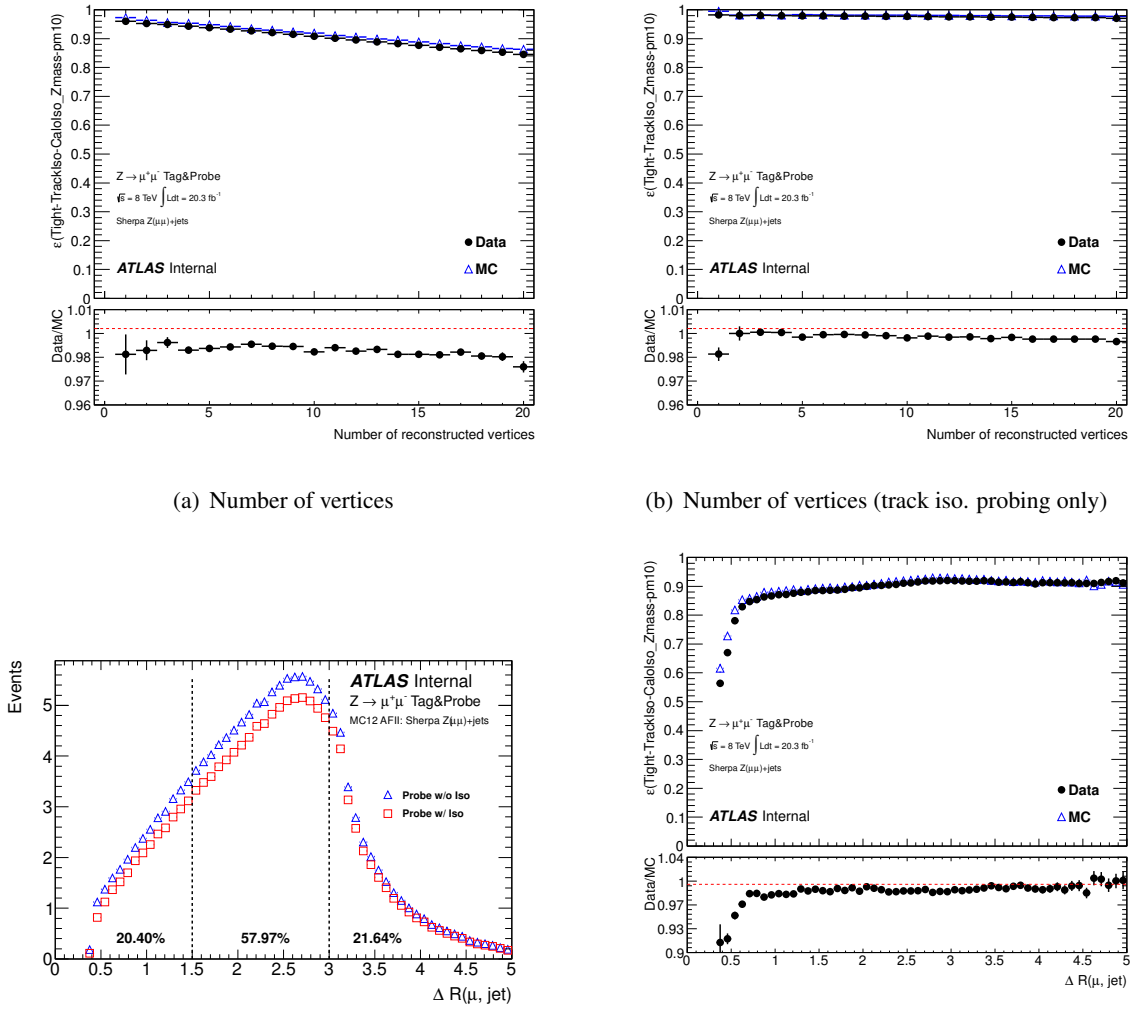

(a) Number of vertices

(b) Number of vertices (track iso. probing only)

(c) Raw ΔR distribution

(d) $\Delta R(\mu, \text{nearest jet})$

Figure 142: Muon isolation efficiencies as a function of the number of reconstructed vertices (a) and with track isolation probing only (b) as well as a function of close-by jets (c-d).

G Global sequential calibration

The Global Sequential Calibration (GSC) is a method dedicated to improve the resolution of the energy response of jets, and to reduce its flavor dependence. It has been introduced in Section 3.2.2 and is also discussed in Reference [23]. A note is in preparation by the JetETMiss group.

This Appendix describes the validation of the GSC method, in the specific case of its application to b-jets, in the context of VH(bb) analyses. Section G.1 describes the main common aspects of the validation analysis. The response results are described in Section G.2, and the comparisons between different Monte Carlo sets, from which one can derive systematic uncertainties, are shown in Section **??**.

G.1 GSC validation analysis

G.1.1 Monte Carlo samples

The impact of GSC on the jet response was evaluated with Monte Carlo simulations of inclusive QCD di-jet production, of $t\bar{t}$ production and with a sample of associated production of a leptonic W boson and a 125 GeV Higgs boson decaying to b-quark pairs. The references and version tags for the used MC samples are listed in Table 84. The WH and the inclusive QCD di-jet samples were generated with PYTHIA8, using two different PDF sets (CTEQ6L1 and CT10, respectively). Both use the same underlying event tuning, UA2. For details on the underlying event tunings see [36] and references therein.

Generator & Tune	Channel num.	tag
	di-jet JW[0-8]Z	
Pythia8 AU2CT10	14791[0-8]	e1126_s1469_s1470_r3542_r3549_p1328 e1126_a159_a171_r3549_p1328
	$t\bar{t}$	
PowhegPythia P2011C	117050	e1728_s1581_s1586_r3658_r3549_p1328 e1727_a188_a171_r3549_p1328
MadGraphPythia AUET2BCTEQ6L1	17483*	e1672_s1499_s1504_r3658_r3549_p1328
AlpGenAutoPythia_P2012	20102*	e2356_s1581_s1586_r3928_r4540_p1328
Sherpa_CT10	11780*	e1434_s1499_s1504_r3658_r3549_p1328
	$WH \to \ell\nu b\bar{b}$	
Pythia8 AU2CTEQ6L1	161805	e1812_a188_a171_r3549_p1328

Table 84: References and version tags for the different Monte Carlo samples used the GSC analysis.

G.1.2 Event and jet selection

The study was carried out with TopoEM, Anti-k_T [20] jets with $R = 0.4$, with the EM+JES calibration scheme. In the case of samples including leptons, these were ignored in the analysis. No pile-up reweighting corrections were applied, but the pile-up conditions in the Monte-Carlo were realistic, and were used in the calculation of the EM+JES Jet Area correction.

The following selection cuts were applied:

- Primary vertex selection, requiring that the first primary vertex contains at least three vertices;
- Truth jet isolation, requiring no additional truth jets in a cone of $R \times 2.5$;
- Isolation from sub-leading jet, requiring no additional reconstructed jets in a cone of $R \times 2.5$.

Truth p_T is defined for Monte Carlo jets by applying the same jet reconstruction algorithm, using the Monte Carlo particles as the jet constituents. Truth jets do not include muons or neutrinos.

In the case of the di-jet sample, a further cut was applied, by calculating the average truth p_T of the leading and sub-leading jets and defining a ratio of that average over to the leading jet p_T. The value of that ratio is required to be in the range $0.6 < \frac{p_T^{avg}(truth)}{p_T^{lead}(reco)} < 1.4$.

The jet flavor selection was carried out by using the standard hadron matching for the identification of b-jets as discussed in Section 3.2.2, and using a dedicated parton matching (based on the highest p_T truth parton within the jet cone) for the distinction between gluon and light-quark jets.

G.1.3 Calculation of energy scale and resolution

The jet response was calculated by matching each reconstructed jet to the closest truth jet that passed the isolation criteria within a radius of 0.3, and taking the ratio of reconstructed to truth p_T. The response distributions in several bins of eta and p_T were fit to a Gaussian function. In order to eliminate the sensitivity to tails, the fit was initially truncated to the $\pm 1.5 \times RMS$ region, and a second iteration done in the $\pm 1.5\sigma$ region, where σ is the width of the first Gaussian fit. For the highest p_T bins, where the response distribution is a very narrow Gaussian, a fixed window of 1 ± 0.4 is used for the fit.

The mean value (μ) of the second iteration Gaussian fit was taken as the jet energy scale, and the ratio σ/μ as the resolution.

Several alternative fitting schemes were tried, in order to obtain the best description of the central part of the response distribution, and the selected scheme proved to be robust, especially for the low p_T bins.

G.2 GSC performance

The following section details the GSC performance in comparison to the EM+JES calibration.

G.2.1 Energy scale of *b*-jets

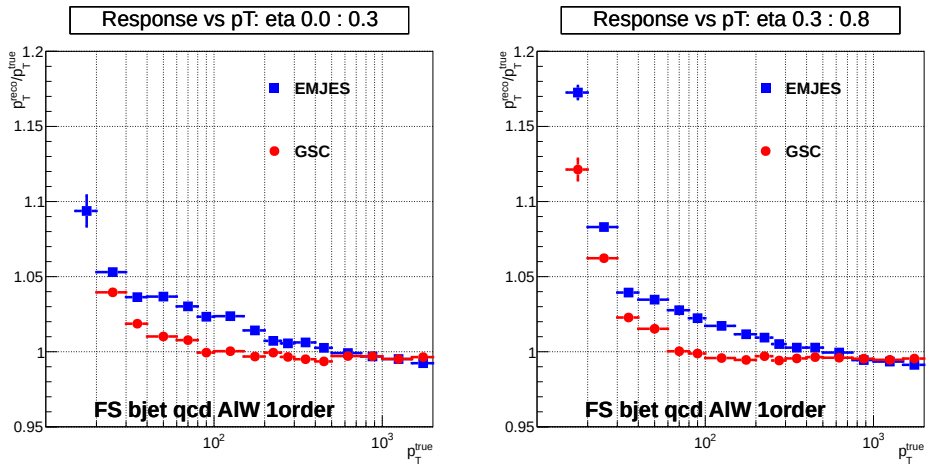

Figure 143: *b*-jet scale for the GSC versus EM+JES calibrations for jet in $0< \eta <0.3$ and $0.8< \eta <1.2$. More details are given in Section G.2.1.

Figure 143 shows the energy response as a function of the jet p_T, for b-jets from the QCD di-jet samples. GSC is compared with EM+JES. The response for b-jets is, in general, above 1, meaning that

the reconstructed p_T is overestimated with respect to the truth p_T. The reason for this is that both GSC and EM+JES calibrations were obtained for an inclusive QCD sample, dominated by gluon and light-quark jets, that have different response from b-jets. For p_T above 30 GeV, the EM+JES response scale is always better than 4%, while for lower p_T the differences with respect to the truth p_T may be up to 15-20%. One can see that GSC improves the response by few %, particularly for p_T below 200 GeV or so, that is the dominant range in this analysis. After GSC, the response is always better than 2% for p_T above 30 GeV, becoming better than 1% for p_T greater than 40-50 GeV.

G.2.2 Energy resolution for *b*-jets

Figure 144 shows the resolution for b-jets selected from the QCD di-jet MC samples as a function of the truth jet p_T. Two pseudorapidty bins are shown: $0< \eta <0.3$ and $0.8< \eta <1.2$ although the conclusions apply to all the p_T bins studied. GSC improves the jet resolution almost for all the p_T range, except for very low p_T jets (between 15 and 20-30 GeV), where it does not change it. For a 100 GeV jet, the typical improvement is of the order of 20%.

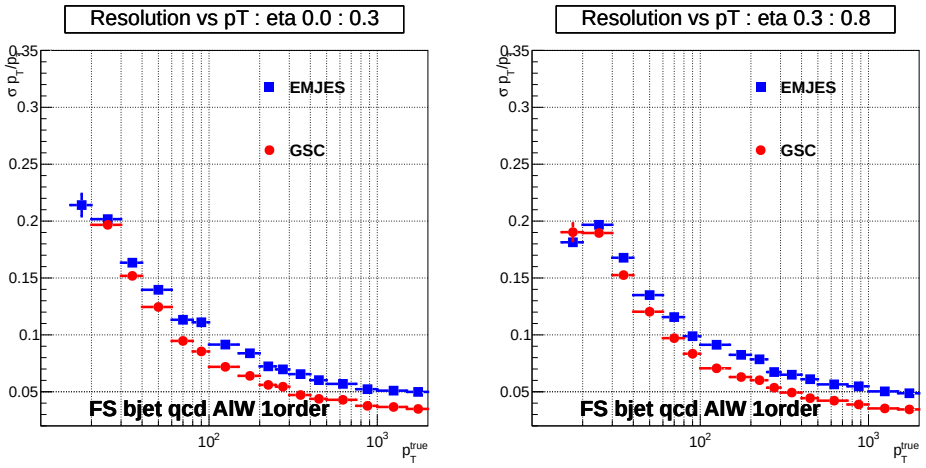

Figure 144: *b*-jet resolution for the GSC versus EM+JES calibrations for jet in $0< \eta <0.3$ and $0.8< \eta <1.2$. More details are given in Section G.2.2.

G.2.3 Closure tests for *b*-jets

The following shows the energy scale as a function of the four variables used in the GSC calibration. These variables are listed and defined in Table 4 with further details given in Section 3.2.2 including the track selection shown in Table 5.

- f_{tile0} - fraction of energy deposited in the first layer of the Tile calorimeter
- f_{em3} - fraction of energy deposited in the third layer of the EM calorimeter
- n_{trk} - track multiplicity
- W_{track} - p_T weighted average ΔR of tracks in the jet

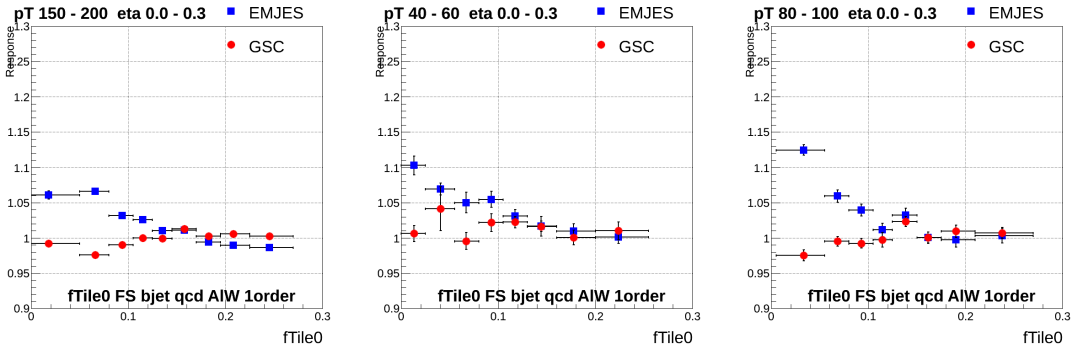

Figure 145: b-jet scale as a function of f_{tile0} for the GSC versus EM+JES calibrations

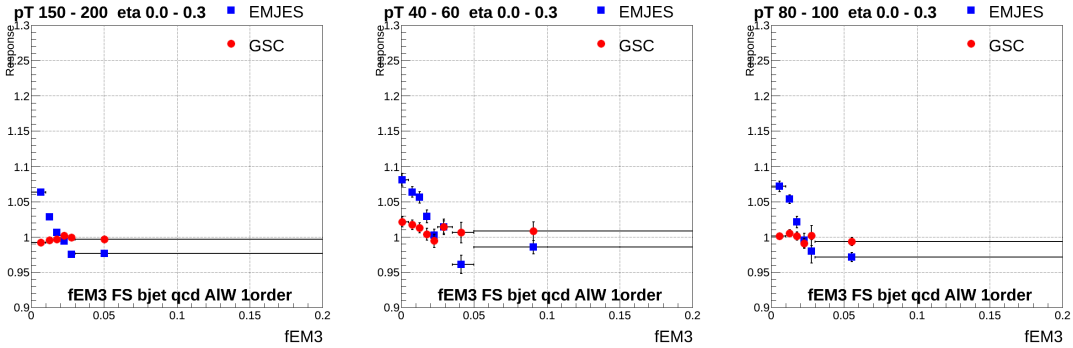

Figure 146: b-jet scale as a function of f_{em3} for the GSC versus EM+JES calibrations

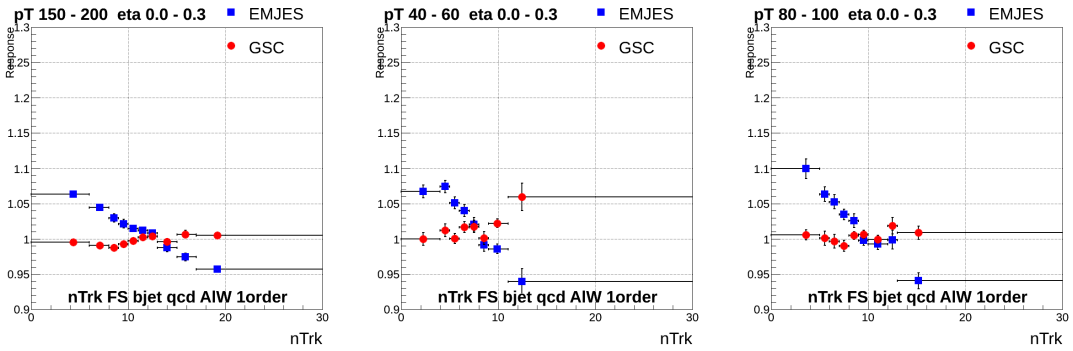

Figure 147: b-jet scale as a function of n_{trk} for the GSC versus EM+JES calibrations

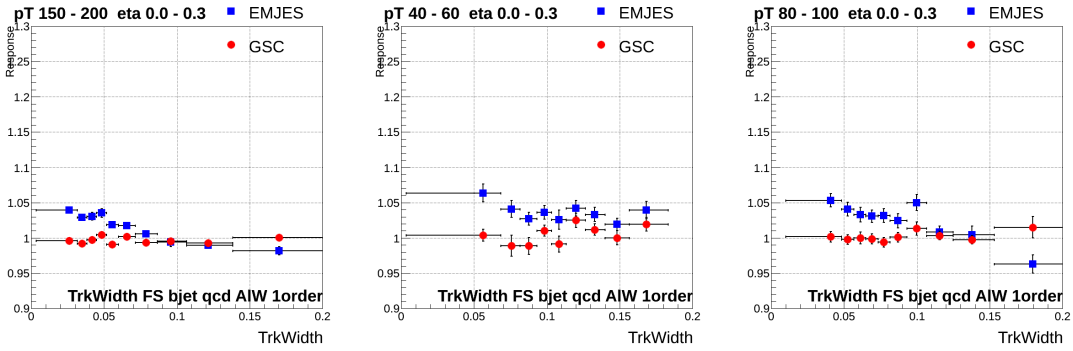

Figure 148: b-jet scale as a function of W_{track} for the GSC versus EM+JES calibrations

Since GSC does not correct the average response, the jet energy scale after the calibration is not necessarily at $p_T^{\text{reco}}/p_T^{\text{truth}} \sim 1$. For a given p_T bin, GSC corrects the scale as a function of the previous variables, flattening the response and therefore reducing the resolution.

The small non-closure observed in certain bins (normally smaller that 2% but that can reach up to 5%) is due to the fact that the calibrations were not derived for b-jets but for inclusive QCD jets.

H Muon-Jet Overlap Removal

The strategy adopted in [11] to solve the muon-jet overlap have been updated to increase the 2-lepton channel acceptance, while keeping under control any source of mis-identification in the other channels.

H.1 Characterization of the muons overlapping jets

In [11], all muons overlapping with a jet within $\Delta R < 0.4$ were removed. In the optimization of the 2-leptons channels, it was found that when accepting all muons with p_{T}> 20 GeV, overlapping with a jet, the signal acceptance in that channel can increase by 12% (Fig. 149). Even if muon overlapping jet can be generated in the semi-leptonic decays of heavy hadrons, the requirement p_{T}>20 GeV and the cut on $m_{\mu\mu}$ adopted by the 2-lepton analysis drastically reduce the muons produced in the semi-leptonic decays.

The same overlap removal have been tested in the 1-lepton channels. Here a strong selection like the dilepton invariant mass does not exist, and this overlap removal strategy will lead to a significant increase in muons from semi-leptonic bottom or charm decays, in particular when inverting the track isolation for the construction of the multijet template (see Figure 150). In the case of the prompt muons, a more detailed analysis of the muon-jet overlap showed that in the majority of the cases in which a prompt muon overlap a jet in signal events, the jets are electromagnetic showers probably caused by the electroweak final state radiation emitted by the muon or the jet is a caused by the muons showers when traversing the calorimeters (see Figure 151). So in summary, in the inclusive di-lepton channel, the muon-jet overlap is due to:

- prompt muons overlapping with showers from muon radiation in 66% of the cases,
- prompt muons overlapping with bottom flavored jets in 25% of the cases, and
- muons from semi-leptonic decays overlapping with bottom (or charm) flavored jets in 8% of the cases

not counting muons which are not prompt or due to semi-leptonic decays (e.g. τ, Kaon decays), and overlaps with pileup jets. Given the nature of the prompt muons in the first 2 items, the overlapping jets feature low multiplicities of the associated charged particle tracks.

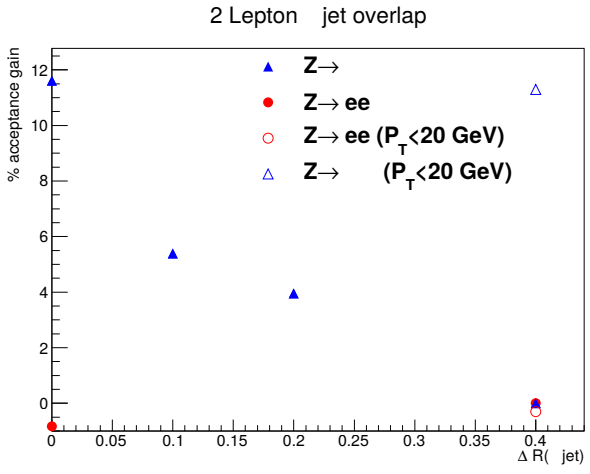

Figure 149: Acceptance gain when reducing the ΔR between muons and jets for which muons are removed.

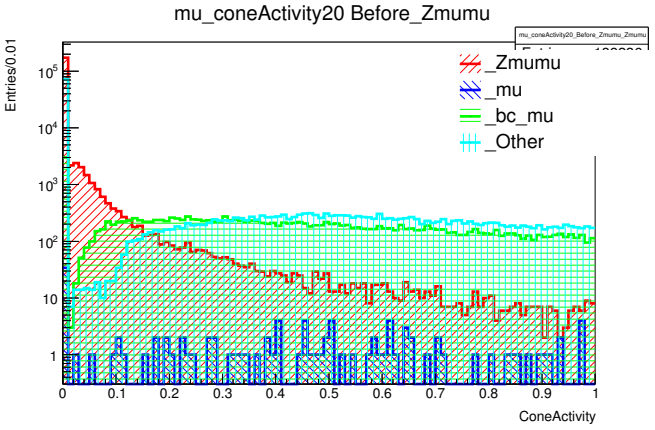

Figure 150: The scalar p_T sum of charged particle tracks around the muon inside a cone of $\Delta R < 0.2$ for prompt muons (_Zmumu) and muons from semi-leptonic decays (_bc_mu), and other non-truth matched muons.

(a) (b)

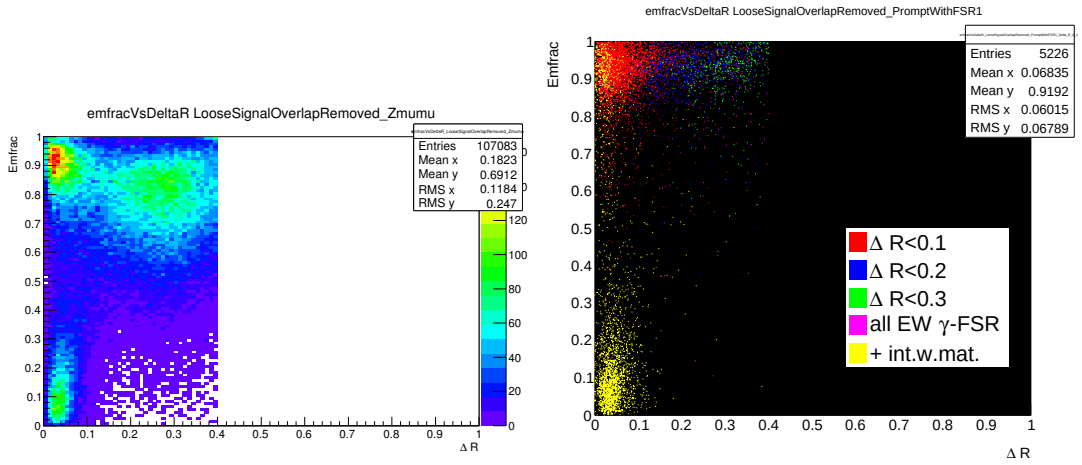

Figure 151: The fraction of the electromagnetic energy in a jet vs. the ΔR between the muon and the closest jet for all muons overlapping with jets (a) for prompt muons with FSR of total $p_T > 15$ GeV with the given cone (b).

H.2 Studies on the strategies to solve the muon-jet overlap

To get a better signal acceptance for the 2-lepton region, while keeping a proper identification of the objects for the 1-lepton analysis, the strategy for the muon-jet overlap removal for the 0-, 1- and 2-lepton channels are identical and

1. first perform the jet-electron overlap removal;

2. then jets which overlap with a muon with $\Delta R < 0.4$ and which feature a charged particle track multiplicity below or equal to 3 are removed where charged particle tracks must fulfill $p_T^{\text{track}} > 500$ MeV and are associated to the primary vertex of the hard interaction (he majority of the jets from muon radiation has a multiplicity of 1 but a sizable fraction has a multiplicity of 2 or larger - Figure 152. Jets with semi-leptonic b- or c- decays tend to have a multiplicity above 3, but there is already a significant fraction with a multiplicity of 2 or three);

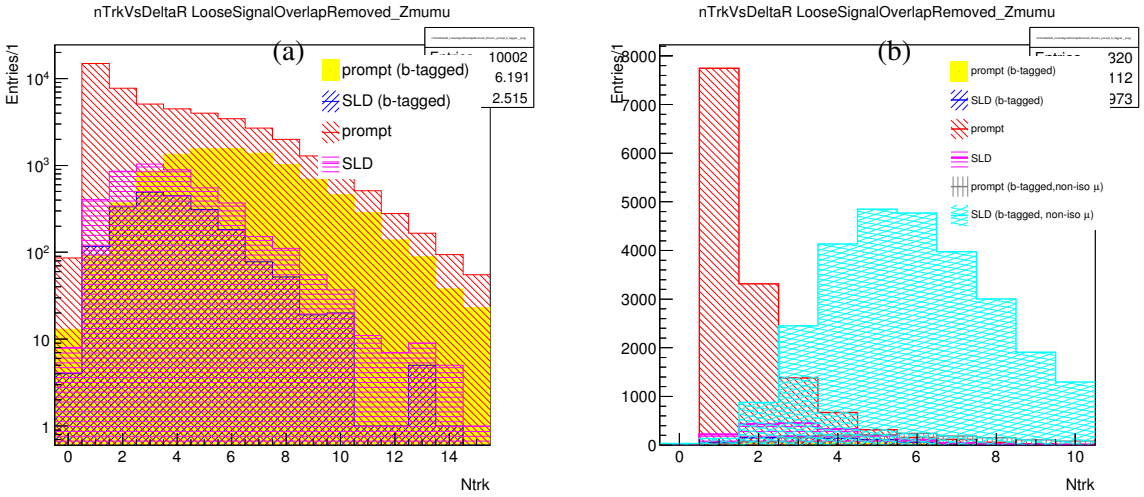

Isolated muons Muons with inverted track isolation.

Figure 152: Charged track multiplicity of jets overlapping with prompt muons or muons from semi-leptonic b or c-decays with $\Delta R < 0.4$ for all signal jets and b-tagged signal jets only.

3. finally all muons overlapping with the remaining jets are removed.

With this procedure, the final acceptance gain the 2-lepton channel amounts to $\sim 6\%$ and in the 1-lepton channel to 2%.

Different strategies have been proposed and studied:

- same as above but only remove jets with a charged track multiplicity below or equal to two
- remove jets with a charged particle track multiplicity below or equal to one, where charged particle tracks are considered only if $p_T^{\text{track}} > 1$ GeV and if they are associated to the primary vertex of the hard interaction. Moreover to remove jets from pileup, all jets for which the jet-vertex-fraction drops below 0.5, when the contribution of the muon is subtracted (see Figure 153), where the cut of 0.5 on the muon subtracted jet-vertex fraction is chosen to be identical to the criterion for for signal jets.

Of these strategies, the highest acceptance gain wrt. to removing all muons overlapping with jets is achieved when removing all jets with a track multiplicity below or equal to three (the used selection). Since the track multiplicity only considers track associated to the primary vertex, this also rejects pileup jets. An explicitly removal of pileup jets using the muon-subtracted-jet-vertex-fraction does not lead to an advantage. For reference also a multivariate technique was tried which exploited multiple variables to distinguish overlaps with jets from radiation, jets with semi-leptonic decays etc. . This multivariate technique could not improve substantially over the simple track multiplicity based criterion.

The acceptance can be further improved by trying to recover some the overlaps of prompt muons with b-jets, by accepting both, the muon and the jet, in case the muon p_T is larger than 30 GeV and the ΔR is larger than 0.25. While these requirements suppress muons from semi-leptonic decays, the constructed multi-jet templates show significant distortion wrt. to the templates determined after the original muon-jet overlap removal. Since, the b-tagging performance is not known in case of muons overlapping with b-jets and moreover it is difficult to estimate the contamination of multijet background for such events, the recovery of prompt muons overlapping with b-jets is not performed.

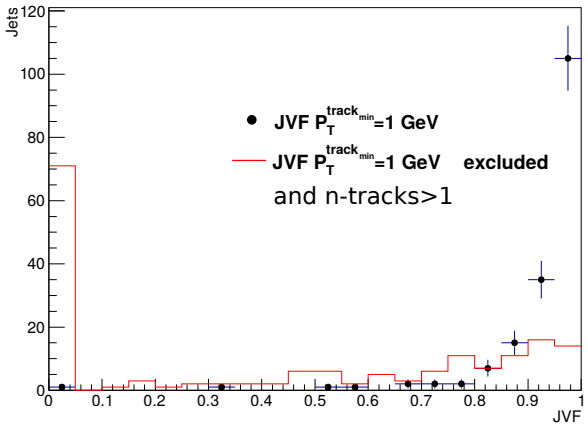

Figure 153: Jet vertex fraction after subtracting the contribution of the muon.

Sample	Signal Acceptance Increase (%)							
	ZH				WH			
Region	$p_T^V \leq 120$ GeV		$p_T^V > 120$ GeV		$p_T^V \leq 120$ GeV		$p_T^V > 120$ GeV	
	2-jet	3-jet	2-jet	3-jet	2-jet	3-jet	2-jet	3-jet
remove ≤2 track jets	3.7	3.3	5.7	5.8				
Remove ≤3 track jets	4.1	3.7	6.2	6.5	1.2	2.2	2.5	3.1
+ accept $p_T^\mu > 30$ GeV, $\Delta R > 0.25$	5.7	5.7	6.3	7.1				
remove ≤1 track jets, or no-μ-JVF< 0.5	3.4	3.9	3.7	6.0	1.3	1.6	1.2	2.4
accept all muons $p_T > 20$ GeV	2.7	15	0.2	13	0.4	5.1	0.0	4.8

Table 85: The signal acceptance increase of the 2 (ZH) and 1-lepton channel (WH) for different muon jet overlap removal strategies. The selected strategy is “Remove ≤3 track jets”.

I Signal modeling

Section 4 covers the systematics specific to the signal. Some investigations of the signal modeling concluded with null results - that is a systematic uncertainty was not needed. The studies yielding such a result were all introduced in Section 4.2.2 with the less interesting plots deferred to this appendix for interested parties.

Figure 154 shows the normalized p_{T}^{V} distribution of VH signal events for different PDF choices. No strong evidence for an additional shape uncertainty beyond what is already covered by the scale uncertainty (Section 4.2.2) is seen.

Figures 155 and 156 show results from the PDF uncertainty study cross-check outlined in Section 4.2.2. Here, the nominal Pythia 8.165 sample generated with CTEQ6L1 PDF was reweighted to each the full (central value and error) MSTW2008nlo68cl, CT10nlo, and NNPDF23_nlo_as_0120 PDF sets. For each event and each choice of PDF, a unique weight is applied according to equation 8. Because this procedure does not preserve normalization, the results are presented as a relative uncertainty. For this, the smallest envelope that spans the full range of PDF variations is used. The upper and lower uncertainty bounds in Figures 155 are calculated by dividing the maximum and minimum of this envelope by its central value. The results here are consistent with those obtained using the samples that had been regenerated with different central value PDFs.

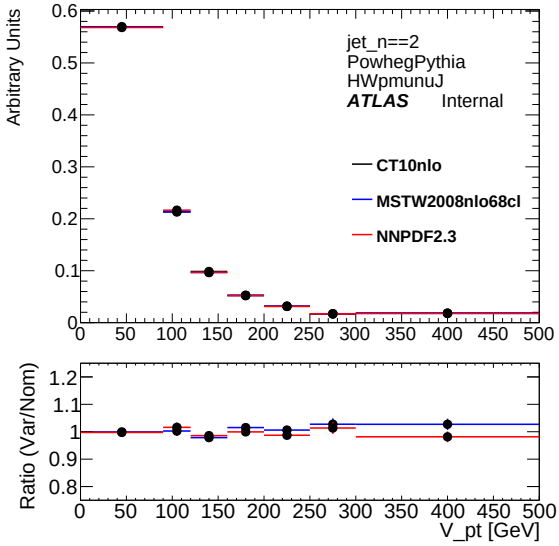

(a) WH 2-jet

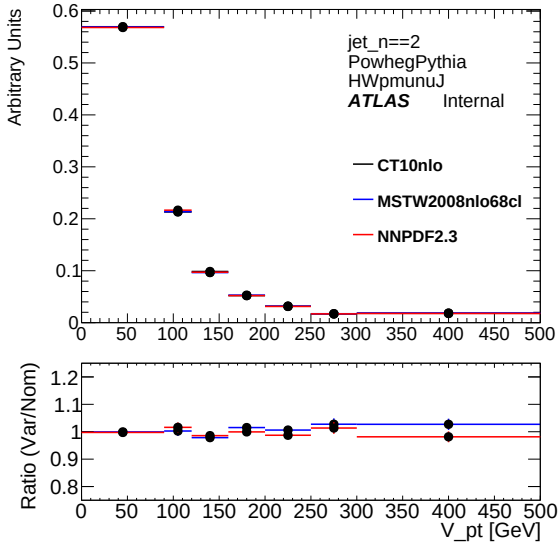

(b) WH 3-jet

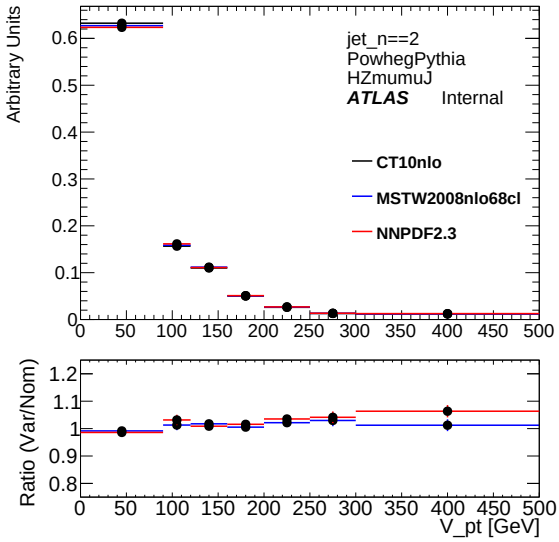

(c) $qq \to ZH$ 2-jet

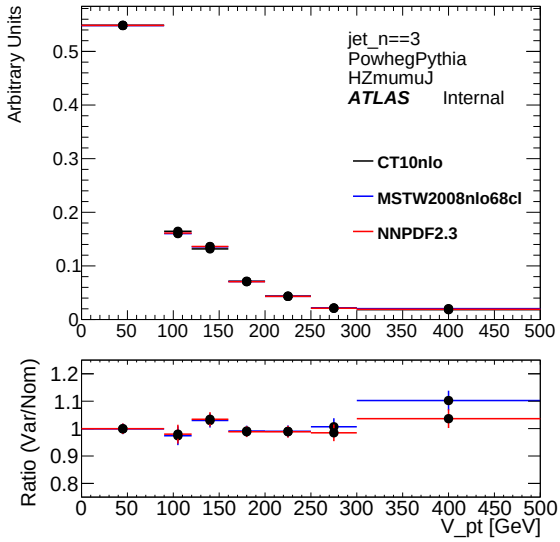

(d) $qq \to ZH$ 3-jet

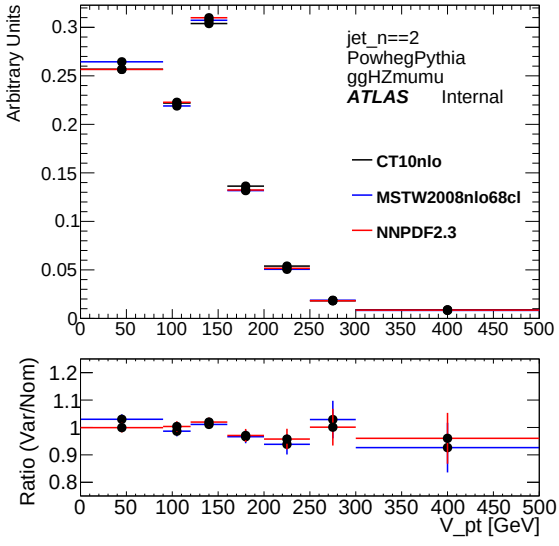

(e) $gg \to ZH$ 2-jet

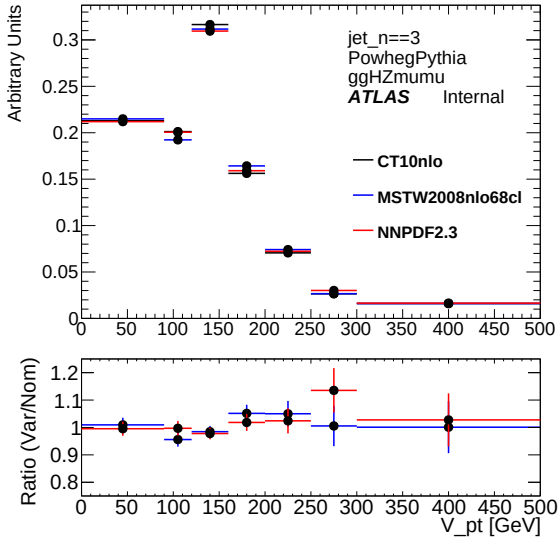

(f) $gg \to ZH$ 3-jet

Figure 154: Normalized p_{T}^{V} distributions after truth-level selection for WH, $qq \to ZH$, and $gg \to ZH$ PDF uncertainty studies on the 1^{st}, 2^{nd}, and 3^{rd} row respectively.

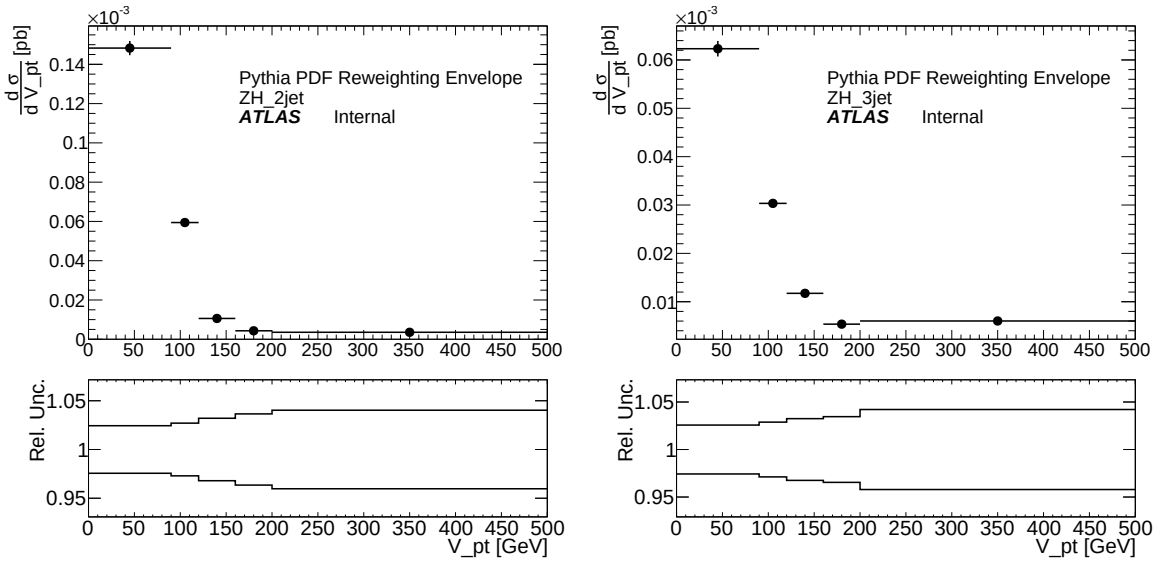

(a) 2-jet (b) 3-jet

Figure 155: PDF re-weighted p_{T}^{V}distribution for ZH events that pass a truth-level event selection.

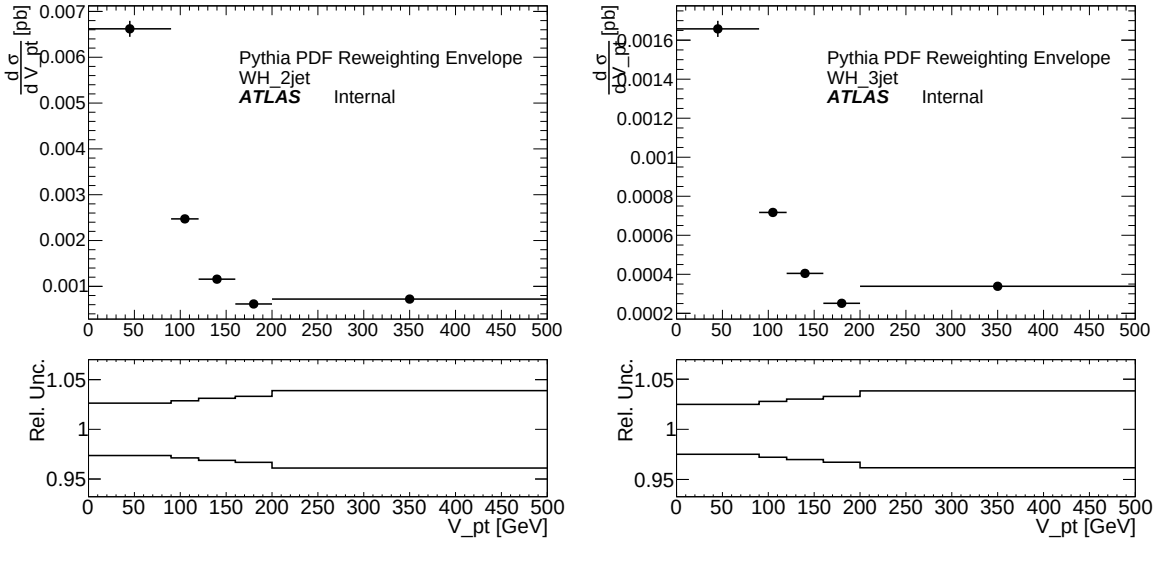

(a) 2-jet (b) 3-jet

Figure 156: PDF re-weighted p_{T}^{V}distribution for WH events that pass a truth-level event selection.

J Z+jet Modeling

This appendix summarize the studies done for the modeling of the Z+jets background.

J.1 Effect of Strict Jets Cuts

In Section 3.3.4, a mention of the fact that the jet cuts could be loosened for 2-lepton events was made. The main background in 2-lepton events is still Z+jets which is not characterized by forward jets like the top background in the 0 and 1-lepton analysis. Table 86 shows the total effect to the signal and the total background in 2 and 3-jet events above and below $p_{\mathrm{T}}^{Z} = 120$ GeV after removing

- forward jet veto
- veto of events with more than 3 signal jets
- veto of events with more than 2 b-tags

The changes in 2-jet events are solely from the removal of the forward jet veto. The change in the 3-jet event is minimally impacted by the 3^{rd} b-tag veto. This change in acceptance would increase the 2-lepton sensitivity 4% and the overall MVA sensitivity 1-2%. At the cost of added complexity and having the regions of phase space in each of the lepton selections further apart, these cuts were not released in the 2-lepton analysis. Clearly if the sensitivity was driven by the 2-lepton events or if this analysis was solely run on 2-lepton events the more relaxed set of cuts would have been used.

Sample	2-jet		3-jet	
	$p_{\mathrm{T}}^{Z} < 120$ GeV	$p_{\mathrm{T}}^{Z} > 120$ GeV	$p_{\mathrm{T}}^{Z} < 120$ GeV	$p_{\mathrm{T}}^{Z} > 120$ GeV
$qq \to Z(\to ll)H$	1.03	1.04	2.61	2.77
$gg \to Z(\to ll)H$	1.18	1.21	5.02	5.12
Background	1.12	1.13	3.82	3.82

Table 86: The default jet selection is to veto events with forward jets, use exactly 2 or 3 jet events (instead of 2 or 3+ jet events), and veto events with more than 2 b-tagged jets. This table shows the increase in 2 and 3-jet events above and below $p_{\mathrm{T}}^{Z} = 120$ GeV for the 2-lepton selection after releasing the above mentioned cuts. The smallest impact is from the veto on 3 or more b-tag events. The change in 2-jet events shows the impact from the release of the forward jet veto.

J.2 Determination of the data-driven corrections and systematics

In the in dilepton events, a relatively pure sample of Z+ jets can be obtained fairly well. Using the event selection for the MVA analysis given in table given in Table 12, with tighter dijet mass analysis $E_{\mathrm{T}}^{\mathrm{miss}}$ (< 60 GeV) and $m_{\ell\ell}$ (83-99 GeV) cuts, as well as only using the events with $m_{bb} < 100$ GeV or $m_{bb} > 150$ GeV in 2-tag events, a signal-depleted pure Z+jets sample is selected; These control regions have been used to derive data-driven corrections and systematics uncertainties. Tables 87 and 88 give a summary of the data-driven corrections and systematics for the Z+jets modelling.

The first table shows the fraction of events in the 2 and 3 jet categories, and the data/MC comparisons have been used to estimate the uncertainty on the 2/3 jets ratio for the Z+jets.

The second includes the correction and systematics on $\Delta\phi(jj)$ the correction and systematics on $p_{\mathrm{T}}^{V}$and the systematics on m_{bb}. The plots showning the distrubutions used to derived these corrections and systematics have been shown in Section 5.1.1.

p_{T}^{Z}	N Jet	data/MC
p_{T}^{Z}<120 GeV	2	1.018±0.002
	3	0.994±0.004
p_{T}^{Z}>120 GeV	2	1.016±0.005
	3	1.014±0.007

Table 87: Yield ratios for 2-lepton 0-tag events used to derive the 3/2 jet ratio systematic.

Variable	Function	Region	Parameter Value
$\Delta\phi(jj)$	$a(1+b\Delta\phi)$	p_{T}^{V} < 120 GeV	a=8.63343×10^{-1} b=8.62769×10^{-2}
		p_{T}^{V} > 120 GeV	a=9.33017×10^{-1} b=3.16033×10^{-2}
p_{T}^{V}	$a+b\log(p_{\mathrm{T}}^{V})$	all regions constant for p_{T}^{V} < 100 GeV	a=1.39975 b=-9.38026×10^{-2}
m_{bb}	$a(m_{bb}\times10^{-3}-b)$	all regions constant for m_{bb} > 300 GeV	a=5×10^{-4} b=100

Table 88: Functions and parameters used for Z+jets data-driven corrections and systematics. p_{T}^{V} and m_{bb} have units of MeV.

J.3 Comparison with other Monte Carlo samples

In addition to the SHERPA samples, other Monte Carlo samples have been studies, both to have a check of the corrections and systematics derived from the data, partially to complete the derivation of systematics uncertainties which cannot be derived from data. In particular, the systematics on the flavour fractions in Z+jets has been estimated by comaring different generators.

The natural generator to performace these comparisons is ALPGENḂoth ALPGEN and SHERPA are leading order multi leg generators, but they diffears in different aspects:

- The mass of the heavy quarks in the calculation: While SHERPA have been forced to have a massive heavy quarks, for the ALPGEN samples, a massless approach have been used.
- The parton density functions (CTEQ6L1 VS. CT10)
- The treatement of the matrix element and Parton shower matching.
- The parton shower model, where SHERPA used its internal implementation, while ALPGEN relies on Herwig.
- The hadronization model, where SHERPA used its internal implementation, while ALPGEN relies on Herwig.
- The underlying event model, where SHERPA used its internal implementation, while ALPGEN relies on Jimmy.

The list of samples used for these studies are listed the Table 89.

These samples have been used to estimate the relative havy flavor composition in Z+2 jets and Z+3 jets events. Tables 90 and 91 show the flavor composition uncertainty and the 3/2 jet ratio systematic for the heavy flavor events, determined from the comparison of the event yield in SHERPA and ALPGEN .

Process	Channel num.	tag	N_{events}
		Z samples, ALPGEN Jimmy, AUET2CTEQ6L1	
$Z \to ee$, Np0-5+	107650-5	e1571_s1499_s1504_r3658_r3549_p1328	6608782, 1335000, 404499, 110000, 30000, 10000
$Z \to \mu\mu$, Np0-5+	107660-5	e1571_s1499_s1504_r3658_r3549_p1328	6619489, 1334706, 404997, 110000, 30000, 10000
$Z \to \tau\tau$, Np0-5+	107670-5	e1571_s1499_s1504_r3658_r3549_p1328	6619683, 1334996, 404997, 110000,30000, 10000
$Z \to ee + cc$, Np0-3+	126414-7	e1601_s1499_s1504_r3658_r3549_p1328	604899, 259999, 109999, 40000
$Z \to \mu\mu + cc$, Np0-3+	126418-21	e1601_s1499_s1504_r3658_r3549_p1328	599397, 265000, 115000, 39999
$Z \to \tau\tau + cc$, Np0-3+	117706-9	e1601_s1499_s1504_r3658_r3549_p1328	599999, 264999, 115000, 39999
$Z \to ee + bb$, Np0-3+	109300-3	e1601_s1499_s1504_r3658_r3549_p1328	150000, 80000, 45000, 4999
$Z \to \mu\mu + bb$, Np0-3+	109305-8	e1601_s1499_s1504_r3658_r3549_p1328	149900, 80000, 45000, 5000
$Z \to \tau\tau + bb$, Np0-3+	109310-3	e1601_s1499_s1504_r3658_r3549_p1328	149900, 79999, 45000, 5000

Table 89: Monte Carlo samples and channel numbers and statistics used for Z+ jets systematics.

Jet Flavors	ALPGEN	SHERPA	difference (%)
bb	0.318	0.280	13.3
bl	0.394	0.357	10.3
cl	0.480	0.382	25.7

Table 90: Yield ratios for 2-lepton 2-tag events in ALPGEN and SHERPA used to derive the heavy-flavor fraction systematic.

p_{T}^{Z}	N Jet	ALPGEN	SHERPA	% difference
		bl/bb		
p_{T}^{Z}>0 GeV	2+3	0.207	0.225	-7.6
p_{T}^{Z}>120 GeV	2+3	0.241	0.238	1.4
p_{T}^{Z}>0 GeV	2	0.196	0.212	-7.4
p_{T}^{Z}>0 GeV	3	0.243	0.270	-9.9
		cc/bb		
p_{T}^{Z}>0 GeV	2+3	0.161	0.146	9.9
p_{T}^{Z}>120 GeV	2+3	0.110	0.133	-17.5
p_{T}^{Z}>0 GeV	2	0.155	0.144	-7.2
p_{T}^{Z}>0 GeV	3	0.178	0.151	17.7

Table 91: ALPGEN/SHERPA heavy-flavor jet multiplicity comparison in 2-lepton 2-tag events used to derive the 3/2 jet ratio systematic.

In addition to the determination of the systematics listed above, a consistency check for the important kinematic distribution entering in the analysis have been done.

Since the goal of this comparison, is a qualitative comparison of SHERPA and ALPGEN in this last one no corrections have been derived and applied. This means that some deviation are expected, expecially in the m_{bb} distributions. Figure 157 show the p_{T}^{V}correction derived for SHERPA and compared with the equivalent correction one could derive from ALPGENDespite the fact the Z p_{T}can depends on different aspects of the generator modeling, the p_{T}^{V}corrections are not that different.

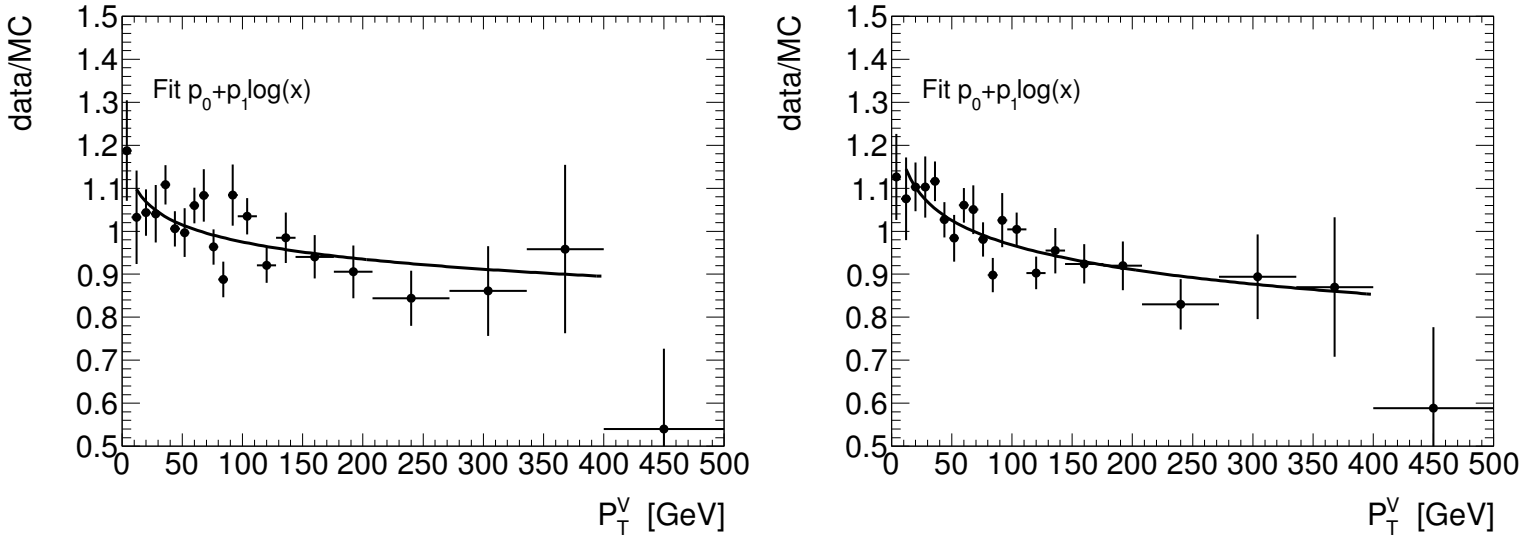

(a) 2-tag ALPGEN

(b) 2-tag SHERPA

Figure 157: A data-driven p_{T}^{Z} correction derived from data-MC ratios for Z+heavy events for ALPGEN motivated by the increase in discrepancy with increased number of b-tags.

Another important check done to validated the Z+jets modelling in SHERPA is to compare the data/MC agreement for the m_{bb}distrubution. Figure 158 shows the data/MC comparisons for ALPGEN and SHERPA in each the 0, 1, and inclusive 2-btag regions. It shows that the systematics uncertainties derived for SHERPA, and here used on ALPGEN, are consistent with the data/MC discrepancies.

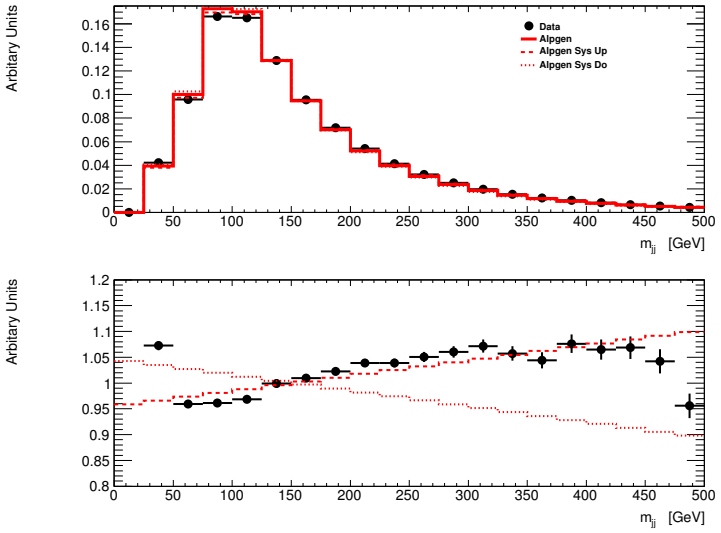

(a) 0-tag ALPGEN

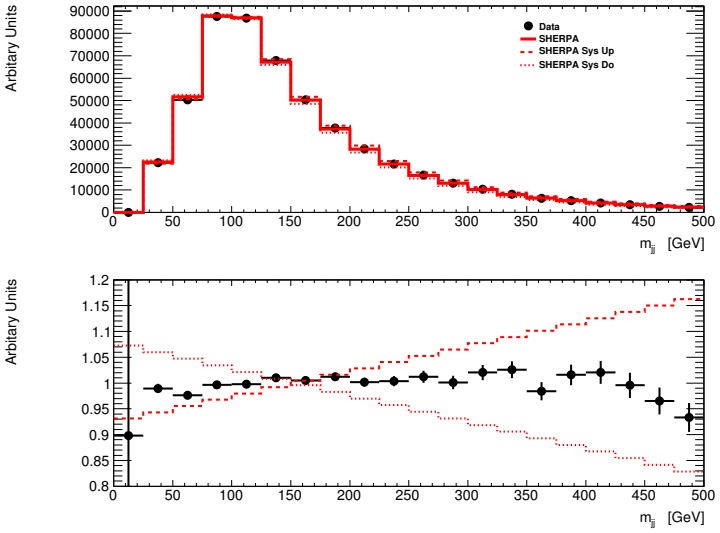

(b) 0-tag SHERPA

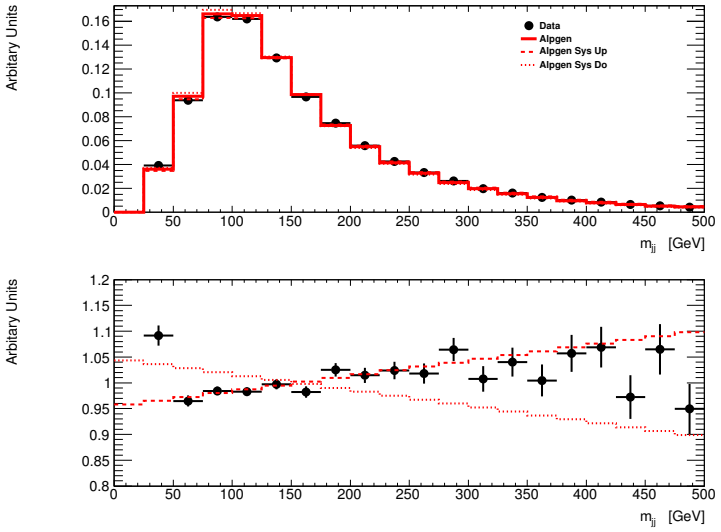

(c) 1-tag ALPGEN

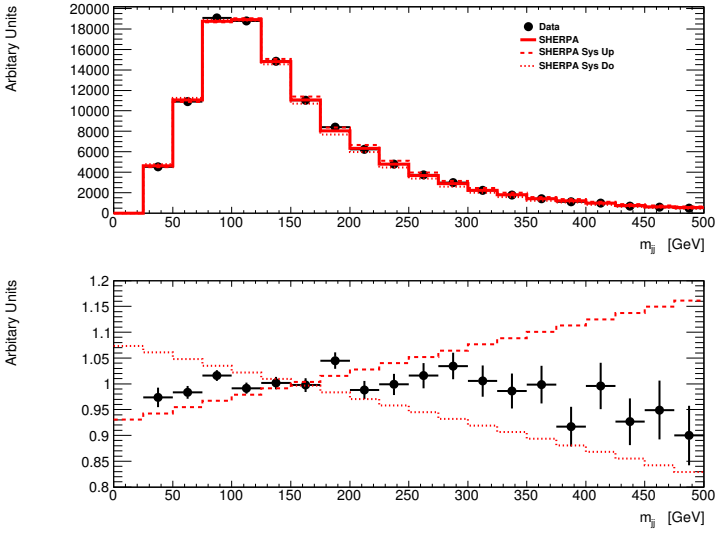

(d) 1-tag SHERPA

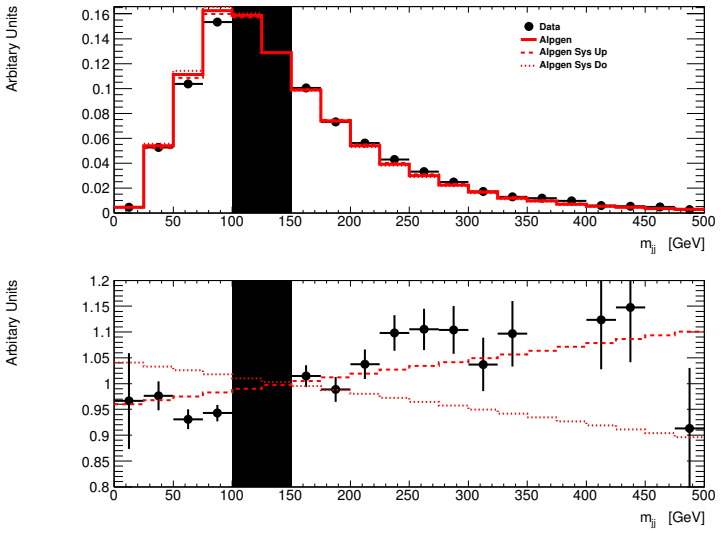

(e) 2-tag ALPGEN

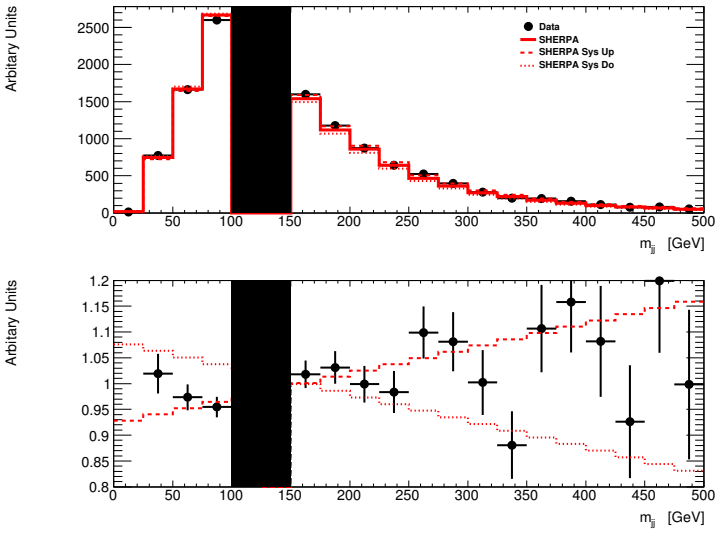

(f) 2-tag SHERPA

Figure 158: m_{jj} distribution in 2-lepton events from which a systematics uncertainty on the Monte Carlo modeling m_{bb} shape has been derived.

K W+jet Modeling

K.1 $\Delta\phi$Correction Derivation

Pervasive mismodeling is observed in regions dominated by W+light jets such as the 0-lepton 0 and 1-tag regions. Section 5.1.2.2 describes the data-driven reweighting used to correct the simulation. This appendix supplements the information given in said section with more details and more plots. Figure 159 and 160 show the level of disagreement $\Delta\phi(jet_1, jet_2)$ (simply $\Delta\phi$ from now on) and p_{T}^{W} out of the box. Ref [11] (Sections 4.2 and 4.3) motivate the stance that the issue is not driven by the multijet backgrond. In short, when harsh multijet-killing cuts are applied, the problem persists. Also the disagreement is seen in both the 1-lepton muon and electron channel which have different levels of multijet contamination. For EPS [11], an inclusive correction in p_{T}^{W} was derived. However, as shown in Figure 161 this over-corrects the high p_{T}^{W} $\Delta\phi$ distribution. Therefore, a correction below and above $p_{\mathrm{T}}^{W} = 120$ GeV is derived separately for 2 and 3-jets from the 0-tag region. A bin-by-bin correction was applied to yield the improvement in modeling summarized in Figure 162. A polynomial is fit to the correction as to not propagate the statistical fluctuations from the correction into the analysis as shown in Figure 163. The parameters of these polynomials are give in Table 92. From the information provided, it should be clear to the reader that the $\Delta\phi$ correction in effect migrates events from high p_{T}^{W} to low p_{T}^{W}. When doing an inclusive correction, this migration was done 'automaticly'. However, now with a separate correction at low and high p_{T}^{W} (the boarder is $p_{\mathrm{T}}^{W} = 120$ GeV), some of the migration has to be done 'by hand'. Scale factors were derived to this end by requiring the normalization of the simulation to agree with data. Table 93 holds the values of these scale factors.

Function	N-Jet	p_{T}^{W}	Parameter Value
$a + b\Delta\phi + c\Delta\phi^2 + d\Delta\phi^3$	2	$p_{\mathrm{T}}^{V} < 120$ GeV	a=0.842588 b=2.24706×10^{-2} c=4.87832×10^{-2} d=-1.00914×10^{-2}
		$p_{\mathrm{T}}^{V} > 120$ GeV	a=0.87972 b=8.59855×10^{-3} c=4.40779×10^{-2} d=-1.06175×10^{-2}
	3	$p_{\mathrm{T}}^{V} < 120$ GeV	a=0.872138 b=9.37018×10^{-3} c=-1.44165×10^{-2} d=1.06
$a + b\Delta\phi + c\Delta\phi^2 + d\Delta\phi^3 + e\Delta\phi^4$		$p_{\mathrm{T}}^{V} > 120$ GeV	a=0.978826 b=-0.169663 c=0.284077 d=0.0187571 e=0.98

Table 92: Functions and parameters used for W+jets data-driven $\Delta\phi$ corrections and systematics.

K.2 $\Delta\phi$Correction Usage

From the 1-lepton 0-tag plots shown above, it is clear a correction is needed for W+l and W+cl events. However it is not clear that the correction should be applied to W+hf. The agreement in the 1-tag was

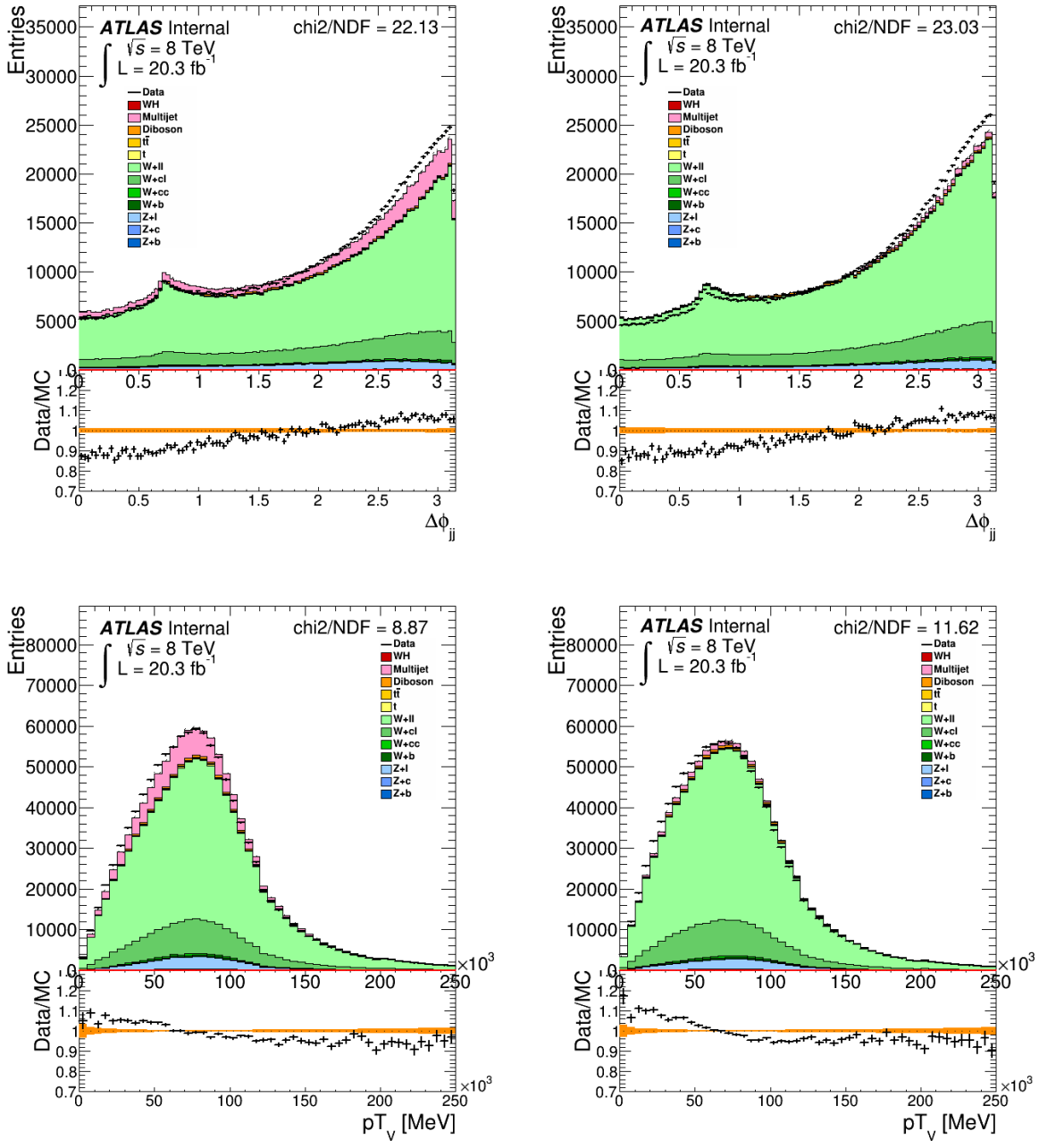

Figure 159: 1-lepton 2-jet 0-tag $\Delta\phi$ and p_{T}^{W} distributions before any corrections with electron (muon) events on the left (right).

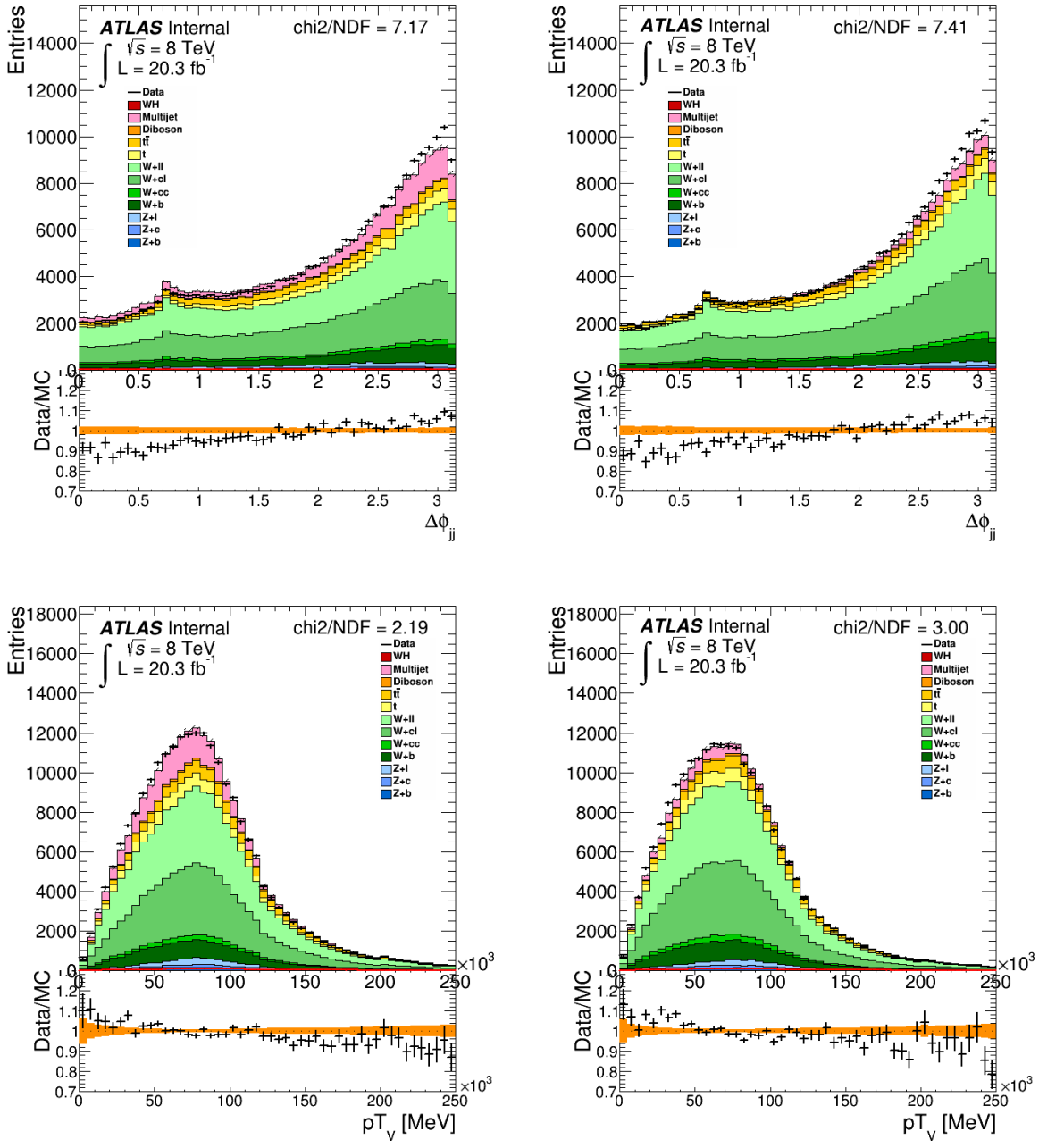

Figure 160: 1-lepton 2-jet 1-tag $\Delta\phi$ and p_{T}^{W} distributions before any corrections with electron (muon) events on the left (right).

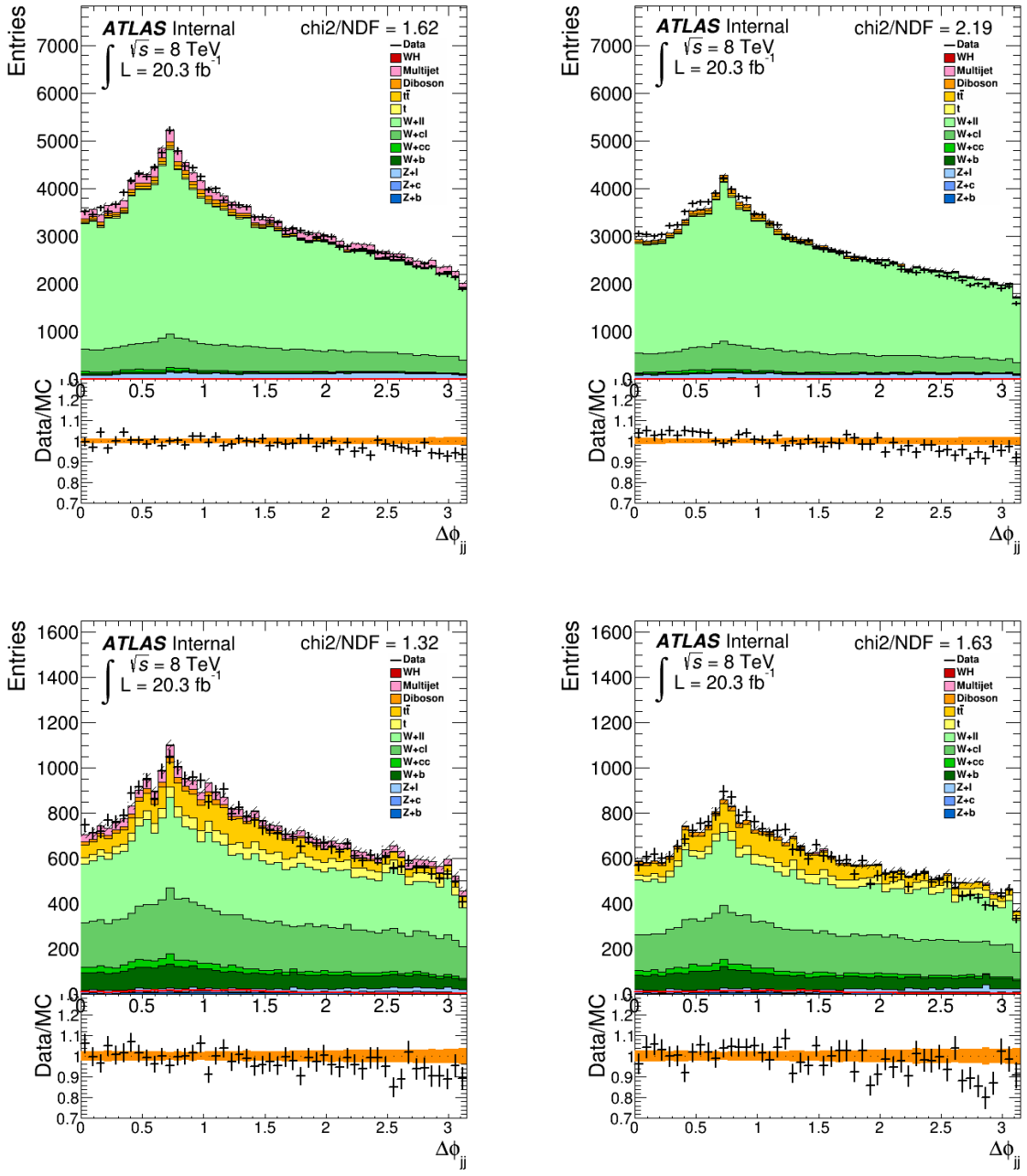

Figure 161: 1-lepton 2-jet 0 and 1-tag $\Delta\phi$ distributions using inclusive $\Delta\phi$ correction similiar to the one used for EPS. Notice the high p_{T}^{W} region is over corrected. Electron (Muon) events are shown on the left (right) with 0-tag on the top and 1-tag on the bottom.

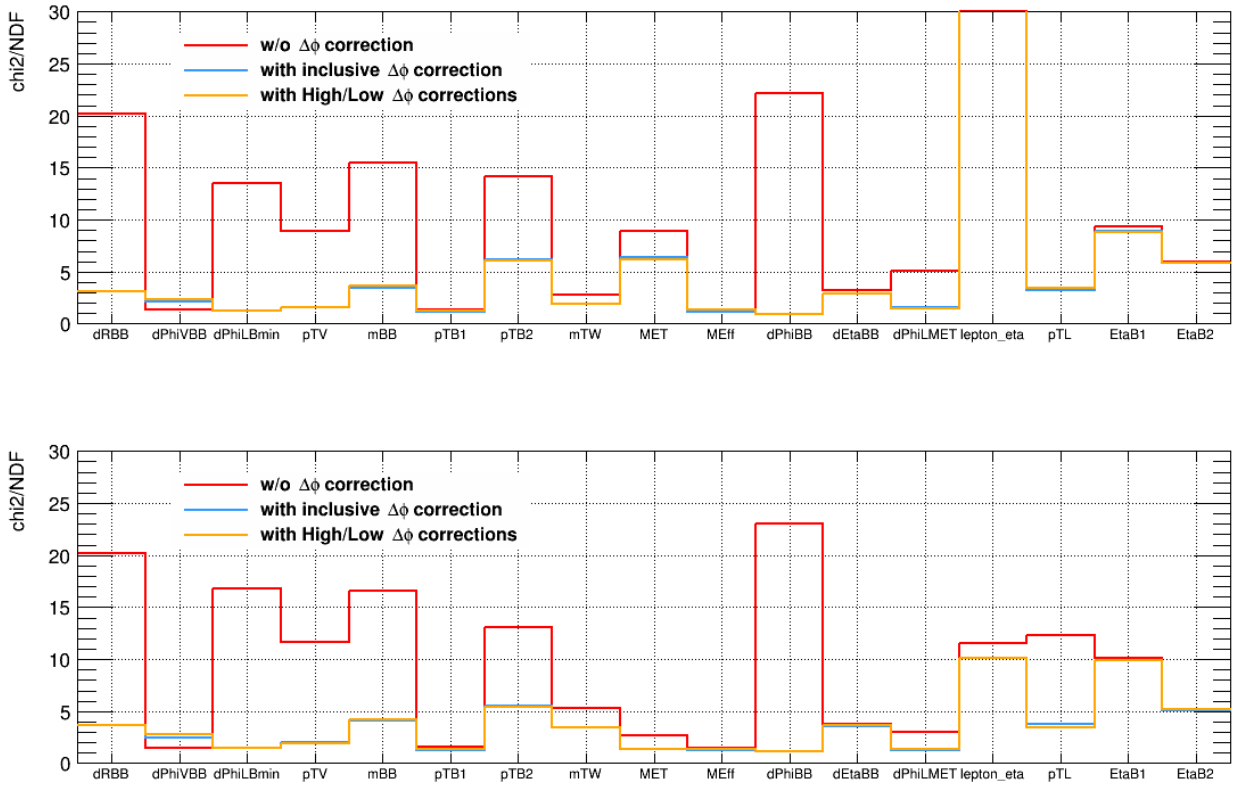

(a) 0-tag 2-jet

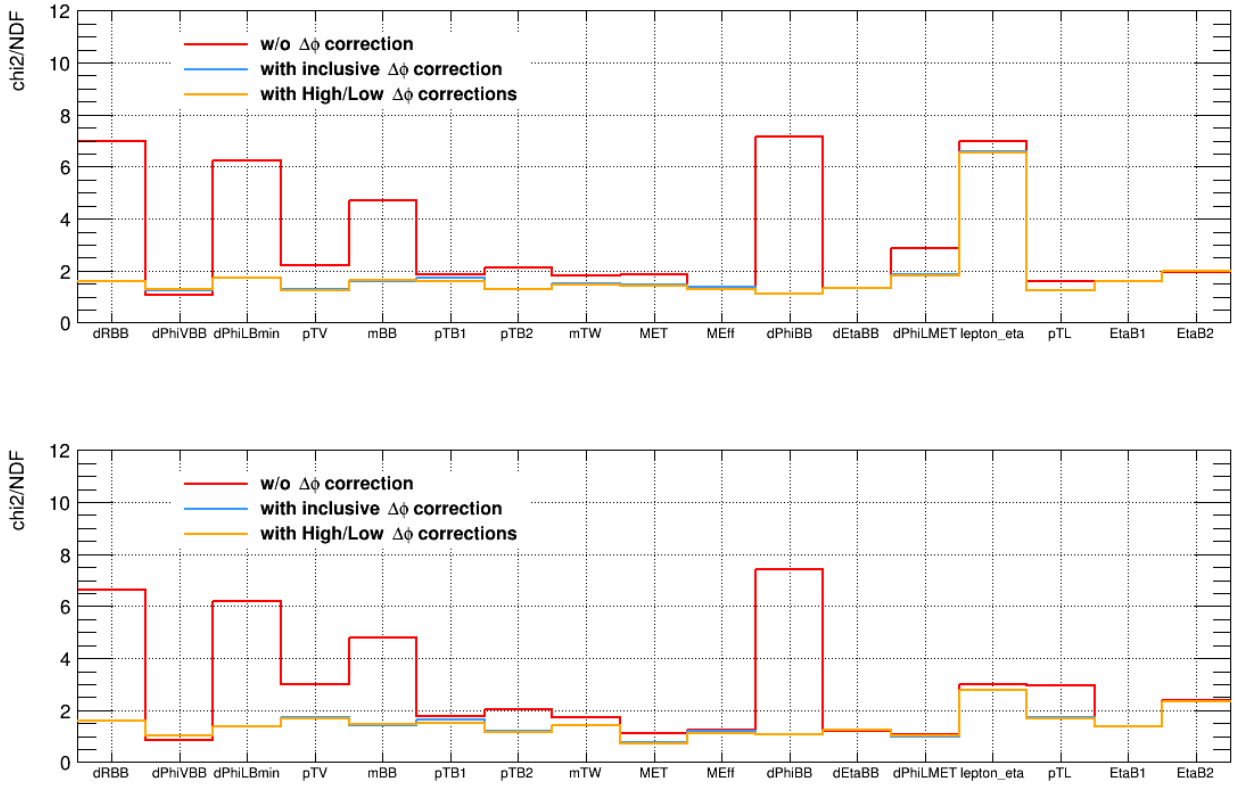

(b) 1-tag 2-jet

Figure 162: Improvements in the data/MC agreement (χ^2) of many kinematic variables in the 1-lepton 2-jet 0-tag and 1-tag events after various $\Delta\phi$ corrections derived from the 0-tag region. The electron channel is shown in top half of each plot and the muon channel in the bottom.

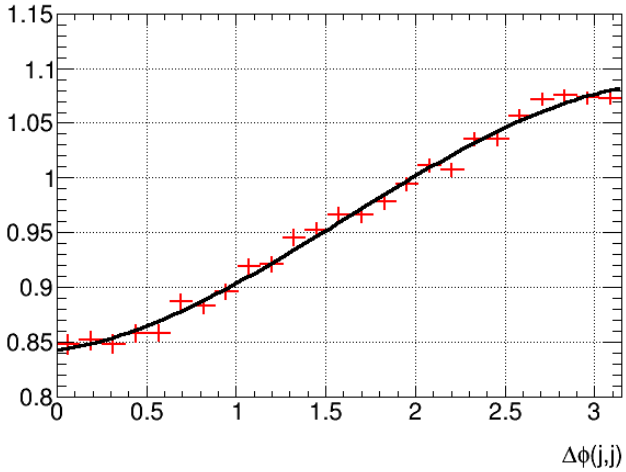

(a) 2-jet $p_{\mathrm{T}}^{W} < 120$ GeV

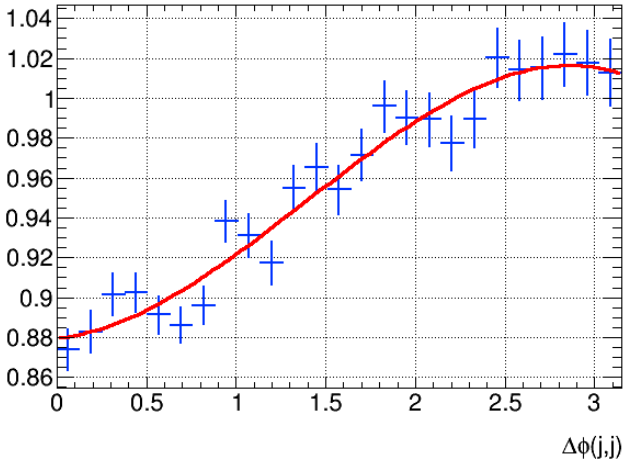

(b) 2-jet $p_{\mathrm{T}}^{W} > 120$ GeV

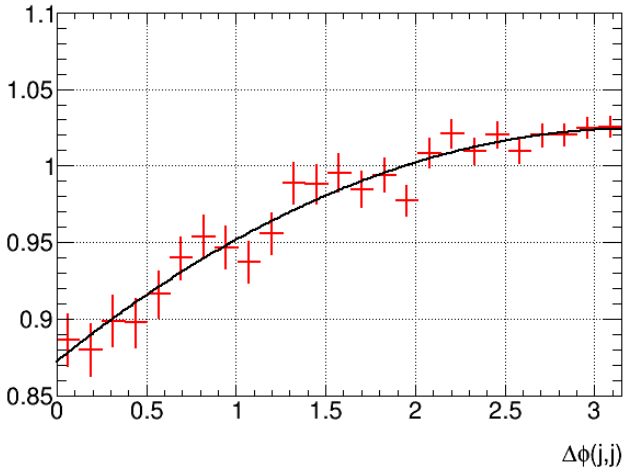

(c) 3-jet $p_{\mathrm{T}}^{W} < 120$ GeV

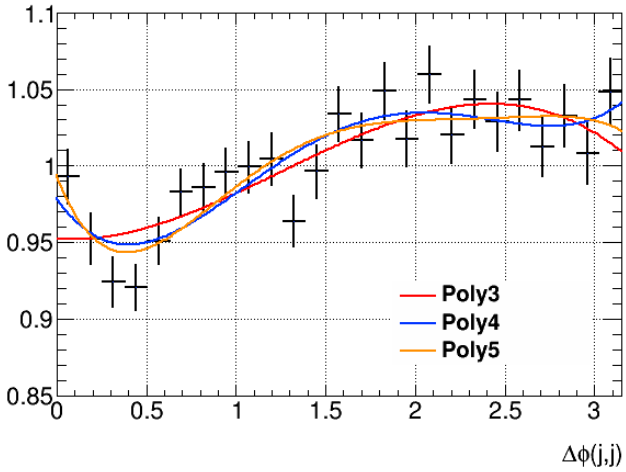

(d) 3-jet $p_{\mathrm{T}}^{W} > 120$ GeV

Figure 163: 1-lepton 2 and 3-jet $\Delta\phi$ corrections derived from the 0-tag region for $p_{\mathrm{T}}^{W} < 120$ GeV and $p_{\mathrm{T}}^{W} > 120$ GeV separately.

Region		Scale Factor (%)
2-jet	$p_{\mathrm{T}}^{W} > 120$ GeV	+7
	$p_{\mathrm{T}}^{W} < 120$ GeV	-5.6
3-jet	$p_{\mathrm{T}}^{W} > 120$ GeV	+5.8
	$p_{\mathrm{T}}^{W} < 120$ GeV	-2

Table 93: The normalization changes for the $\Delta\phi$ correction in each of the four regions is show. This is necessary in order to maintain overall agreement while events are migrated between high p_{T}^{W} and low p_{T}^{W}.

tested applying the corrections to all W+jet events and only to W+ll/cl as shown in Figure 164. Since no strong evidence is see for applying the correction to W+hf, one is not applied. For a systematic, half the correction is applied to W+ll/cl events and the full correction is used as a systematic for W+hf events. These are then decorrelated and so is the effect in 2 and 3-jet events.

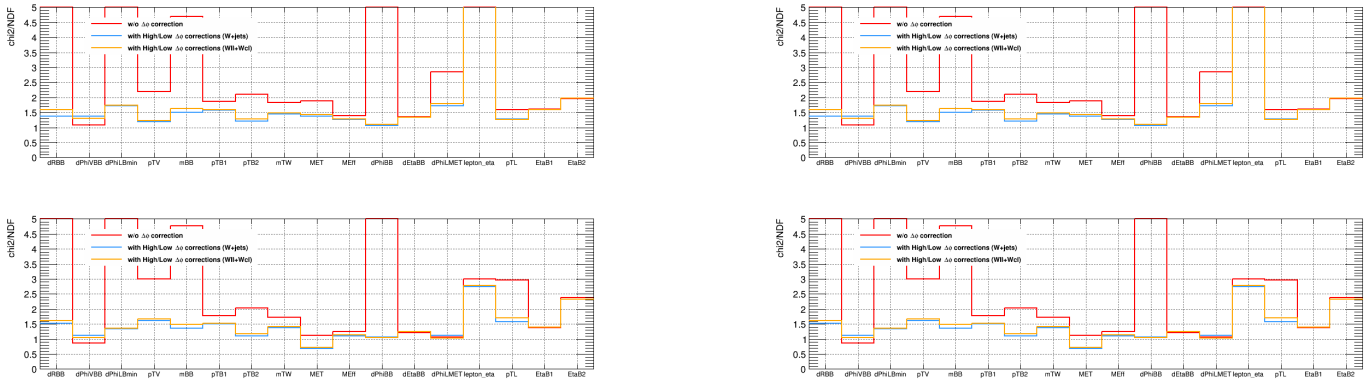

(a) 2-jet $p_{\mathrm{T}}^{W} < 120$ GeV

(b) 2-jet $p_{\mathrm{T}}^{W} > 120$ GeV

Figure 164: The improvement in modeling is shown aftering applying the bin-by-bin $\Delta\phi$ correction to either all W+jet events or just to W+ll/cl. The agreement is slightly better when only correcting the light jet contribution.

L W+Heavy-Flavor Modeling

The modeling of the process where a W-boson is produced in association with heavy flavor quarks is described in detail in this appendix. There is no pure region in the VH(bb) analysis where this process can be studied with data-driven techniques. Therefore, a Monte-Carlo study is performed to estimate uncertainties on the most relevant quantities.

The 1-lepton object and event dijet mass analysis selection is applied. The flavor labeling of the events is performed according to the flavor of hadrons with $p_T > 5$ GeV and their decay products in the contents of the signal jets.

This study is done in two approaches: a generator comparison of the main kinematic variables performed at truth-level, focusing on the $W + b(b)$ final state; and a generator comparison of the flavor composition at reconstruction-level, considering all W+jets final states (light, charm, bottom).

L.1 Monte-Carlo samples

The W+jets background is simulated with the Sherpa generator, where the matrix element is inclusive in the flavor of jets. Event filters are then applied to select the light, C and B-filtered samples, based on the flavor of hadrons with $p_T > 5$ GeV. This means that light matrix elements where the heavy flavor is coming from the parton shower can be present in the B-filtered sample.

The alternative Monte-Carlo samples available, however, produce heavy flavor quarks in the matrix element by definition. These samples are listed in Table 94, as well as the corresponding parton shower programs. For the purpose of this study, a dedicated $W + b\bar{b}$ Sherpa sample was privately produced (which will be referred to as Sherpa $W + b\bar{b}$ as opposed to the baseline Sherpa B-filter).

Given the available samples, the estimation of uncertainties related to the $W + b\bar{b}$ background can be parametrized into two different effects.

Firstly, the different predictions between Sherpa $W + b\bar{b}$ and the other generators are evaluated, and the full variations are considered to define the uncertainty. The specific choice of alternative generator will depend on the variable in question.

Secondly, the effect of having bottom quarks produced in the parton shower is studied by comparing the baseline Sherpa B-filter with the Sherpa $W + b\bar{b}$ sample. This comparison allows for the estimation of uncertainties related to the gluon splitting contribution in the parton shower, for which the rate is not well constrained from data at present. 50% of the observed variations are taken as the uncertainty in this case.

For the case of the flavor composition uncertainty estimation, the study is performed at reconstruction level. The Sherpa and Alpgen MC samples used are listed in Table 95. Given that the relative rates of bb, bc, bl, cc, cl and ll events need to be quantified, it is essential to use the full W+jets predictions in both Sherpa and Alpgen, i.e., heavy flavor produced both in the matrix element and in the parton shower. In the Alpgen case, this requires the use of the HFor tool to remove events in the heavy flavor samples where the bb/cc pair have $\Delta R < 0.4$, and avoid double counting of events. This tool is not available at the EVNT level at which the truth-level was performed, which motivated the reconstruction-level approach.

MC generator	Parton Shower	Comments
Sherpa	built-in	W+jets with B-filter
Sherpa	built-in	$W + b\bar{b}$
Alpgen	Herwig	$W + b\bar{b}$
Powheg	Pythia8	$W + b\bar{b}$
aMC@NLO	Herwig++	$W + b\bar{b}$

Table 94: MC samples used in the estimation of the modeling uncertainties. All samples were centrally-produced with the exception of aMC@NLO and Sherpa $W + b\bar{b}$.

MC generator	Parton Shower	Comments
Sherpa	built-in	W+jets with B-filter
Sherpa	built-in	W+jets with C-filter and B-veto
Sherpa	built-in	W+jets with C- and B-vetoes
Alpgen	Herwig	$W + b\bar{b}$+Np0-3 with HFor
Alpgen	Herwig	$W + c\bar{c}$+Np0-3 with HFor
Alpgen	Herwig	$W + c$+Np0-4 with HFor
Alpgen	Herwig	W+Np0-5

Table 95: MC samples used in the estimation of the flavor composition, at reconstruction-level.

L.1.1 aMC@NLO sample

The aMC@NLO sample was produced specifically for this study, and its details are described in this section. In the aMC@NLO implementation, the NLO QCD corrections to the $W + b\bar{b}$ process are computed and consistently matched to the HERWIG++ parton shower [69] according to the MC@NLO formalism [70]. One-loop corrections are obtained with MadLoop [71] and all other contributions to the parton-level NLO cross section are dealt with by MADFKS [72].

The aMC@NLO prediction is generated using the electroweak parameters listed in Table 96. The CT10 PDF [54] was used for the computation, which also sets the value of $\alpha_S(M_Z)$. The renormalization and factorization scales are based on the sum of the transverse masses of all final state particles and partons ($H_T/2$). The HERWIG++ parton shower uses CTEQ6L1 UE-EE-3 tune with CT10 ME pdf.

The jets are defined with the anti-k_T algorithm with $R = 0.4$ and required to have a $p_T > 7$ GeV. There is no minimum p_T cut on the leptons (electrons or muons) applied at generation level.

Table 96: List of electroweak physical parameters used in the generation of aMC@NLO events with the CT10 PDF set. Dimension quantities given in GeV.

Parameter	value
m_W	80.419
G_F	1.166390×10^{-5}
m_t	173
$\alpha_S^{(NLO)}(m_Z)$	0.11798
Γ_W	2.0476
m_Z	91.118

The effect of varying the factorization and renormalization scales on the jet multiplicity and $p_T(W)$ distributions can be seen on Figures 165 and 166.

L.2 Uncertainties considered in the fit

L.2.0.1 m_{jj}

The uncertainty on the dijet mass distribution is derived at truth-level, by considering only events where both leading and sub-leading jets are matched to a b-hadron. The dominant contribution to this uncertainty comes from the comparison of Alpgen to Sherpa $W+b\bar{b}$, and to this ratio a second order polynomial is fitted (see Figure 167, left). The full variation of this function is considered, symmetrized around 1. Due to the fact that W+bb/cc, W+bl/bc, W+cl, and W+l are all different physics processes, the m_{bb} systematic is decorrelated between the them. Since from the studies comparing different MC generators, no clear indication was found for correlation the dominant W+hf modeling in different p_{T}^V regions, to avoid introducing spurious propagations from low to high p_{T}^V, the W+bb/W+cc systematic is decorrelated in

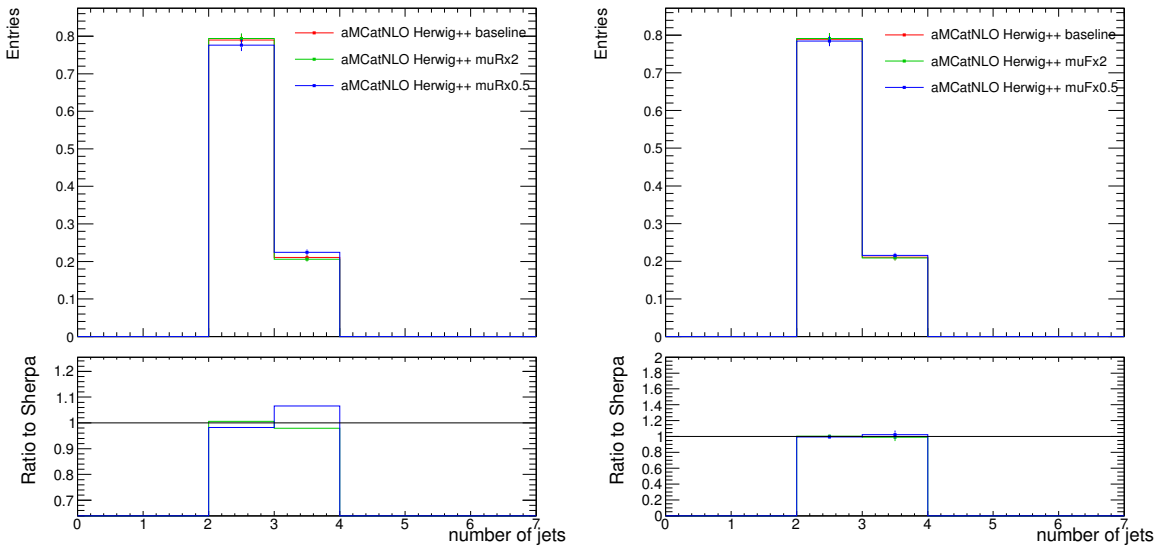

Figure 165: Distribution of number of signal jets in the baseline aMC@NLO sample and in the samples where the μ_R and μ_F parameters have been varied (independently). Normalized to same area.

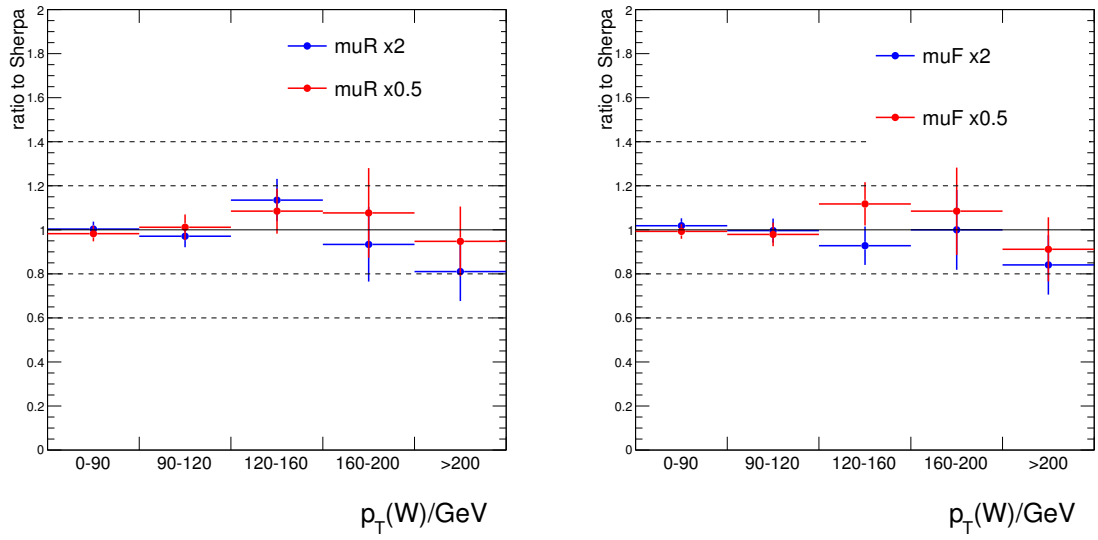

Figure 166: W-boson p_{T} distribution of 2-jet bb events at truth-level. The ratio is taken of each sample where the μ_R and μ_F parameters have been varied (independently) with respect to the baseline aMC@NLO sample. Normalized to same area.

the lower p_{T}^V bins ([0-90], [90-120], 120+ GeV). The other (smaller) contribution originates from the ratio of Sherpa $W + b\bar{b}$ to Sherpa B-filter, also fitted with a second-order polynomial and considering 50% of the up and down variation (see Figure 167, right). Both fit functions are shown in Figure 168. This later systematic is degenerate with the larger m_{bb} systematic described above. And since the above has been deorrelated and acts on exactly the same samples, this NP has been dropped.

The dependence of the $M_{b\bar{b}}$ shape with $p_T(W)$ was investigated and the ratios with respect to the baseline found to have the same trend (see Figure 169).

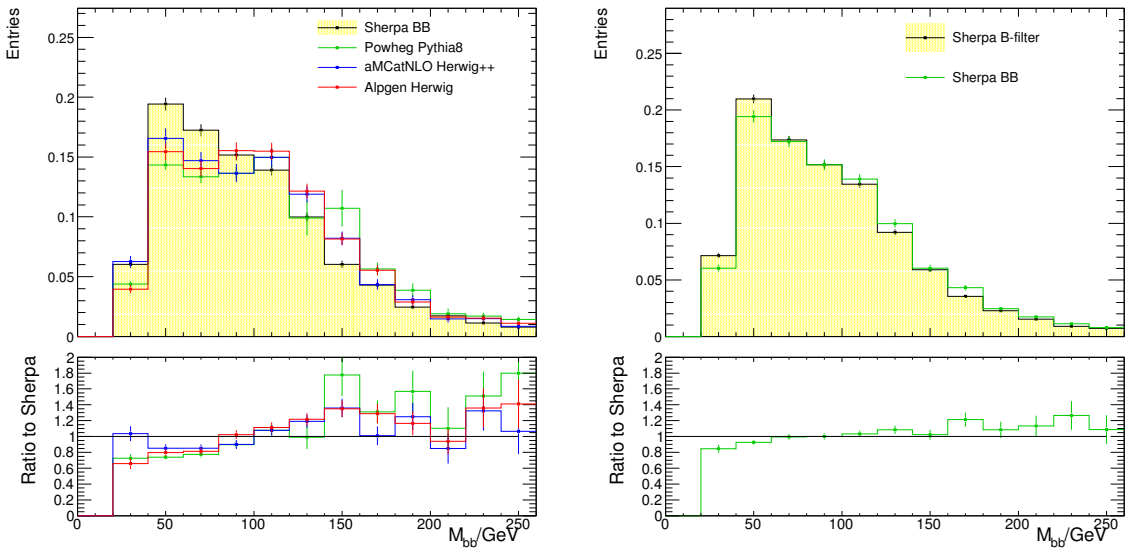

Figure 167: Invariant mass distribution of 2-jet bb events at truth-level as predicted by the available W+bb generators (left) and the Sherpa samples (right). Normalized to same area.

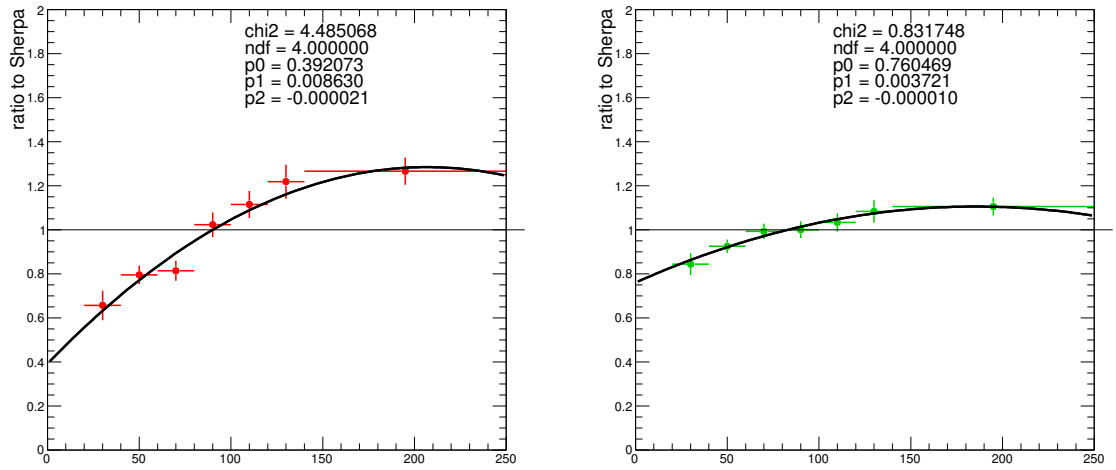

Figure 168: Fit functions to the ratio plots shown in Figure 167.

L.2.0.2 3- to 2-jet ratio

Figure 170 shows the number of events with 2 and 3 jets, for each sample, passing the full event selection at truth-level. The uncertainty on the normalization between the 3-jet and 2-jet region is derived from the relative difference in the ratios observed, with respect to the Sherpa prediction. It's clear from the plot that Powheg predicts a very discrepant 3-jet rate, when compared to the other generators and also to the effect of the scale variations seen on Figure 165. Powheg's prediction is therefore left out at the moment, while its behavior in the 3-jet bin is better understood.

A 10% uncertainty is derived for the 3- to 2-jet ratio from the aMC@NLOto SHERPA$W + b\bar{b}$ comparison. The effect from the Sherpa $W + b\bar{b}$ to Sherpa B-filter comparison is negligible.

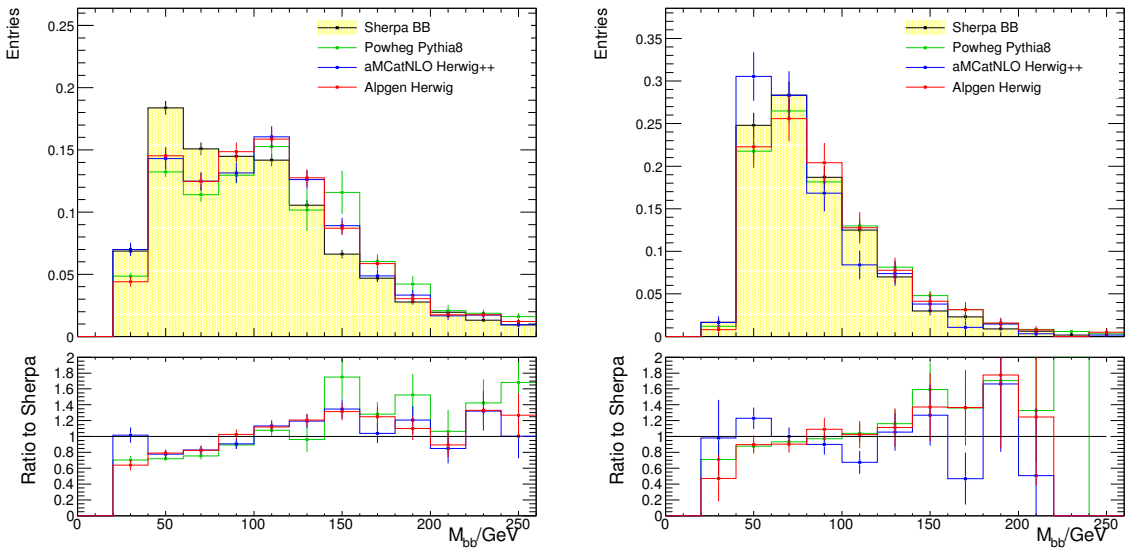

Figure 169: , for $p_T(W) < 120$ GeV (left) and $p_T(W) > 120$ GeV (right). Normalized to same area.

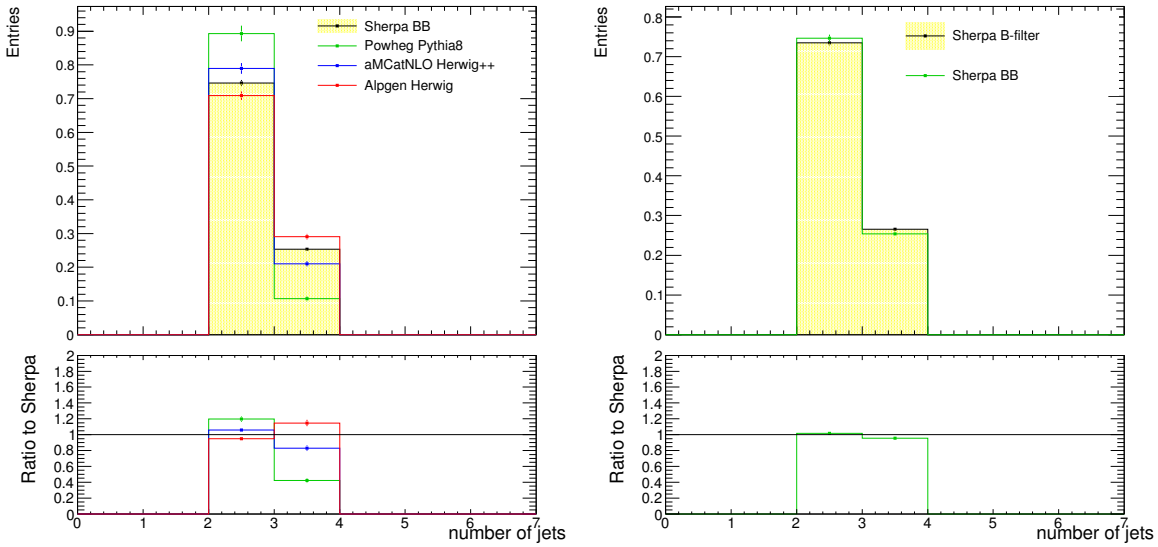

Figure 170: Distribution of the number of jets in bb events at truth-level. Comparison between generators (left) and between the different Sherpa samples (right). Normalized to same area.

L.2.0.3 p_{T}^{W}

The transverse momentum of the W is also compared at truth-level among the $W + b\bar{b}$ predictions. To define a shape uncertainty on this distribution, the aMC@NLO to SHERPA ratio is considered, and a function of the form $a + b\log(p_T)$ is fitted (see Figure 171). The p_{T}^{W} spectrum and ratios between the generator predictions are shown in Figure 23, on Section 5.1.2.3.

L.2.0.4 Flavor Composition

The uncertainty on the flavor composition is defined by comparing the fractions of bl, cc and bc events with respect to bb, using Sherpa and Alpgen generators, as described above. The comparison is done at

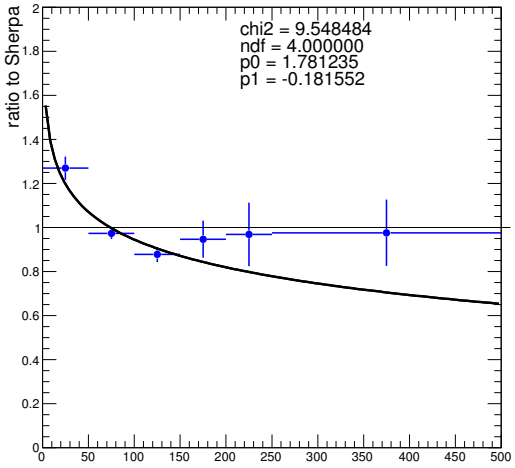

Figure 171: Fit function to the observed aMC@NLOto SHERPAratio in the p_{T}^{W}distribution, for 2-jet bb events at truth levee.

reconstruction level, without requiring the leading jets to be b-tagged, see Figure 172. The conservative estimate of 12% is taken for the bc/bb and cc/bb uncertainties, in accordance to what was derived also for Z+jets. For the specific bl/bb fraction in the W+jets case, a larger uncertainty of 35% was considered, given the discrepancy observed.

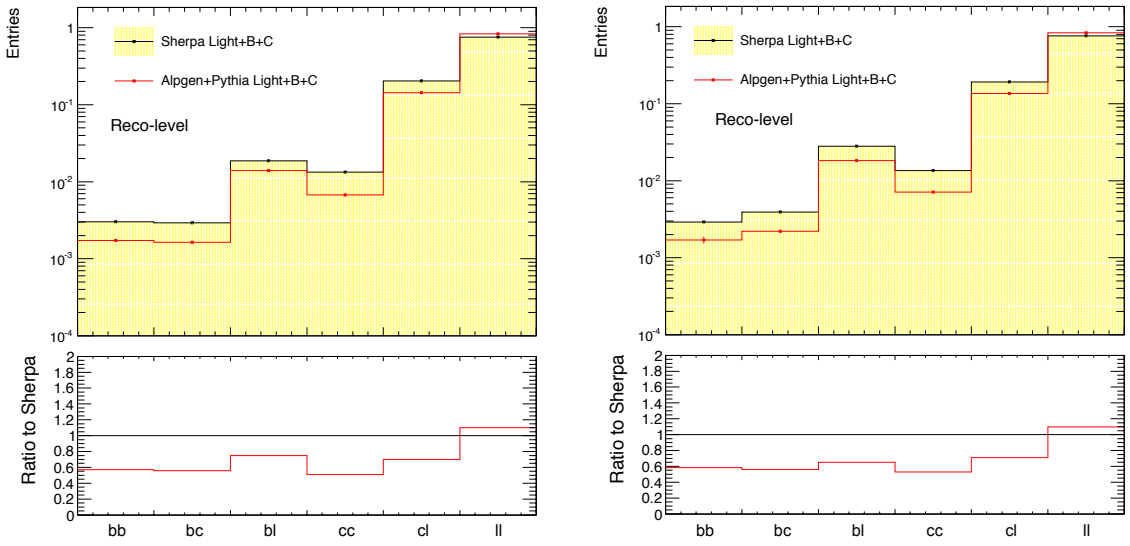

Figure 172: Fraction of events with each flavor label in the 2-jet (left) and 3-jet (right) pre-tag regions, for Alpgen and Sherpa W+jets. Reconstruction-level distribution. Normalized to same area.

L.3 *W*+Heavy-Flavor Modeling for MVA variables

The comparison between generators for the $W + b\bar{b}$ process was also performed with the MVA event selection, for the input variables that can be defined at truth-level. The following Figures 173-182 show

each distribution in the low and high $p_T(W)$, 2-jet and 3-jet regions, in events where the leading jets are matched to b-hadrons. The MV1c variables are not defined at truth level, however the difference between this variable in different MCs is already encapsulated in the MC-to-MC scale factors inttroduced in Section 3.3.4.3 and described in full detail in Appendix T.2.

The shape uncertainties derived with the dijet mass analysis selection, and applied to the $m_{b\bar{b}}$ and $p_T(W)$ distributions should in principle be designed to cover also the variations in the MVA output from any discrepancies in the input variables.

The 3- to 2-jet ratio in the low and high $p_T(W)$ MVA regions was cross-checked to be compatible with the one derived inclusively with the dijet mass analysis selection.

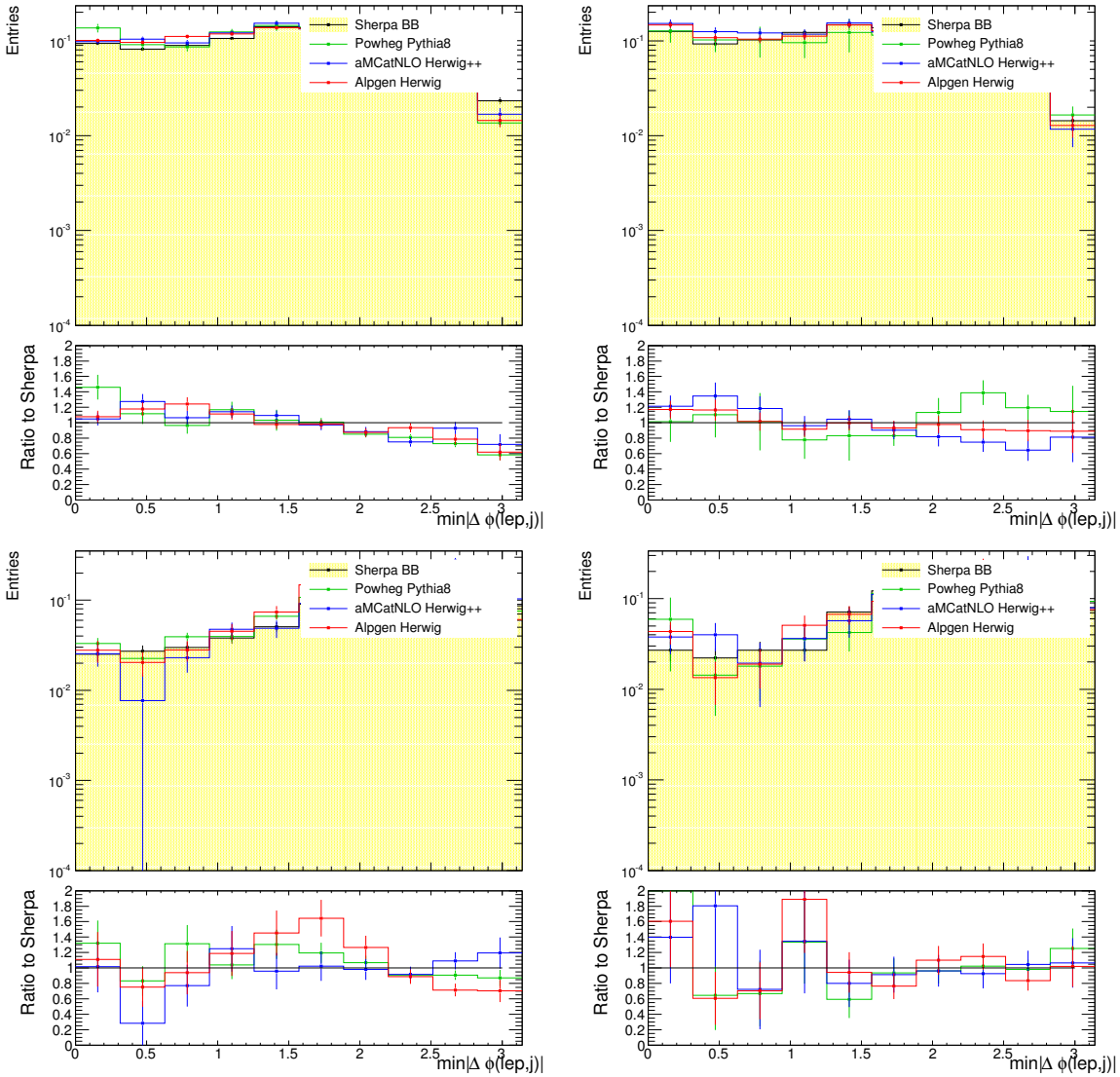

Figure 173: $\min|\Delta\phi(\ell, j)|$ variable in the low and high $p_T(W)$ regions, for the 2- and 3-jet cases. Events with leading jets matched to b-hadrons.

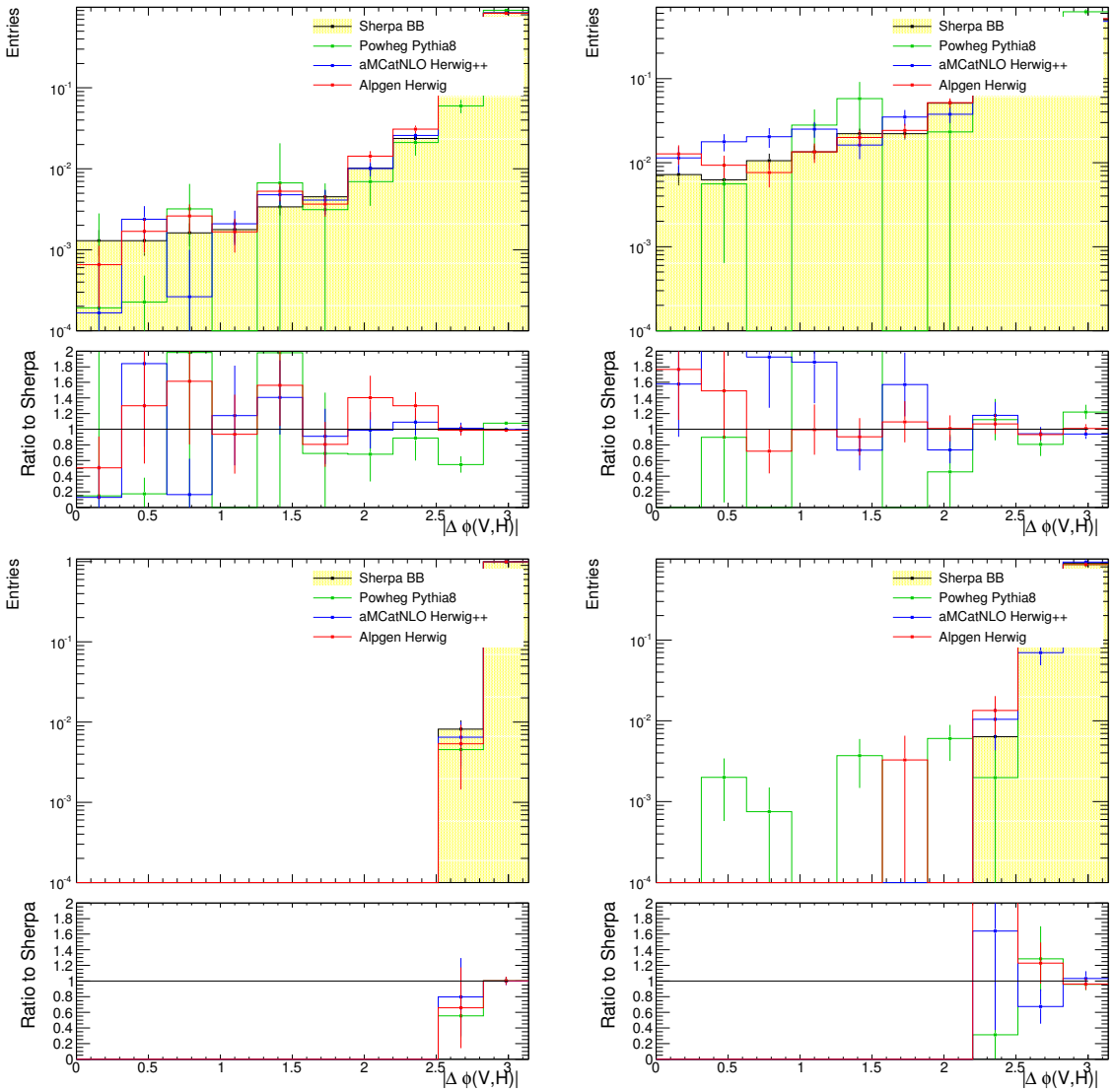

Figure 174: $|\Delta\phi(V,H)|$ variable in the low and high $p_T(W)$ regions, for the 2- and 3-jet cases. Events with leading jets matched to b-hadrons.

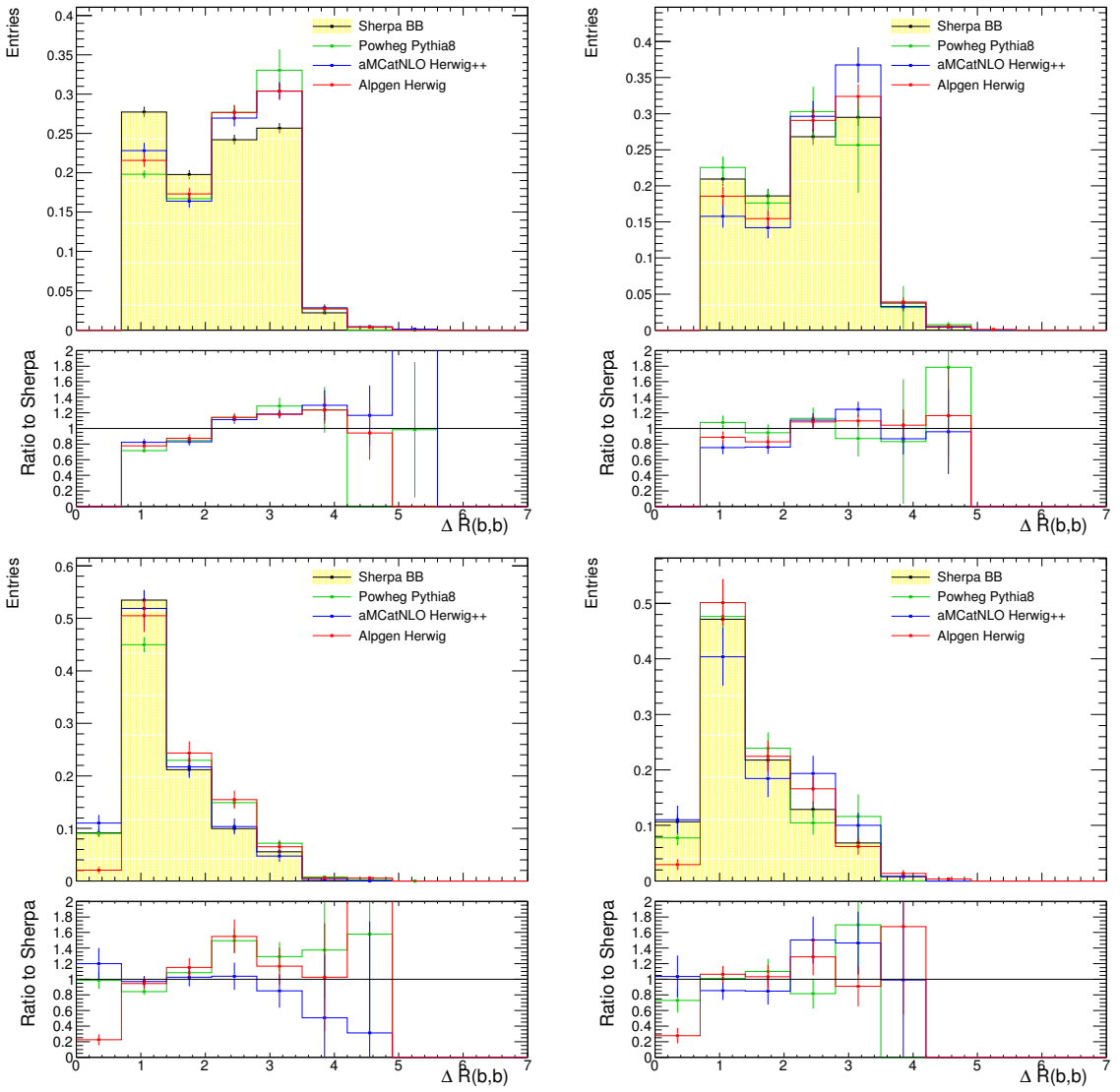

Figure 175: $\Delta R(b,b)$ variable in the low and high $p_T(W)$ regions, for the 2- and 3-jet cases. Events with leading jets matched to b-hadrons.

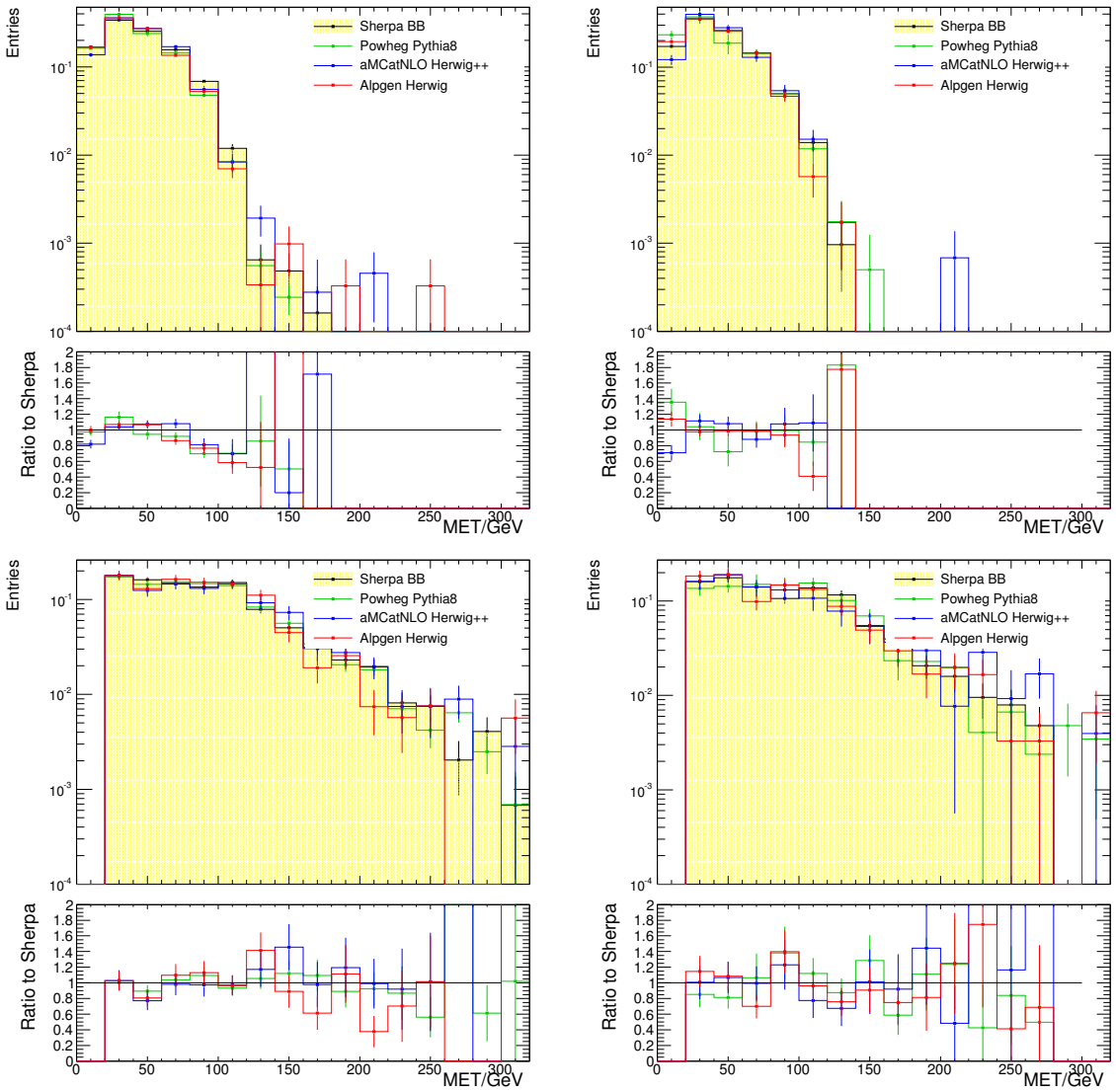

Figure 176: MET variable in the low and high $p_T(W)$ regions, for the 2- and 3-jet cases. Events with leading jets matched to b-hadrons.

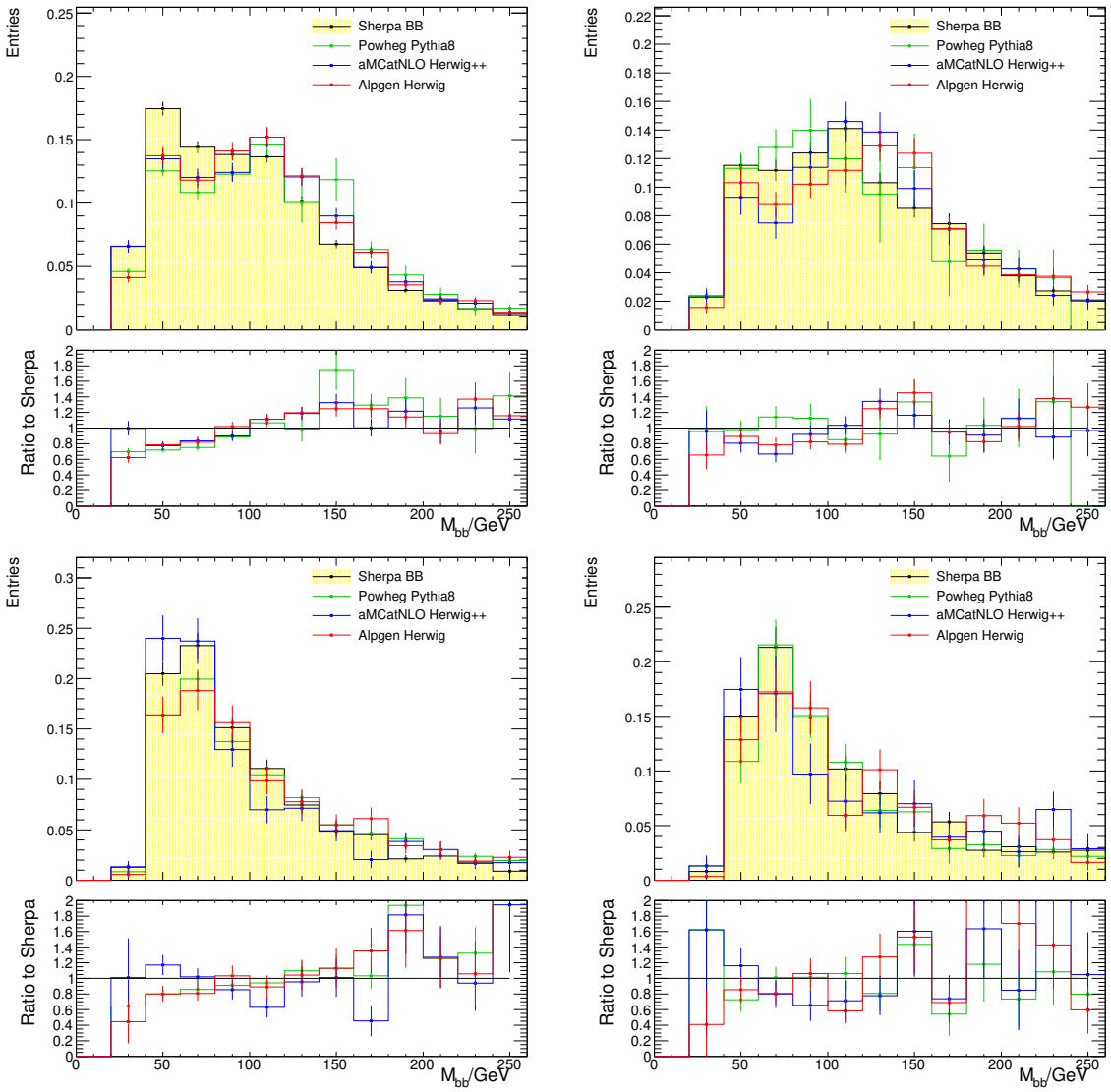

Figure 177: Dijet mass in the low and high $p_T(W)$ regions, for the 2- and 3-jet cases. Events with leading jets matched to b-hadrons.

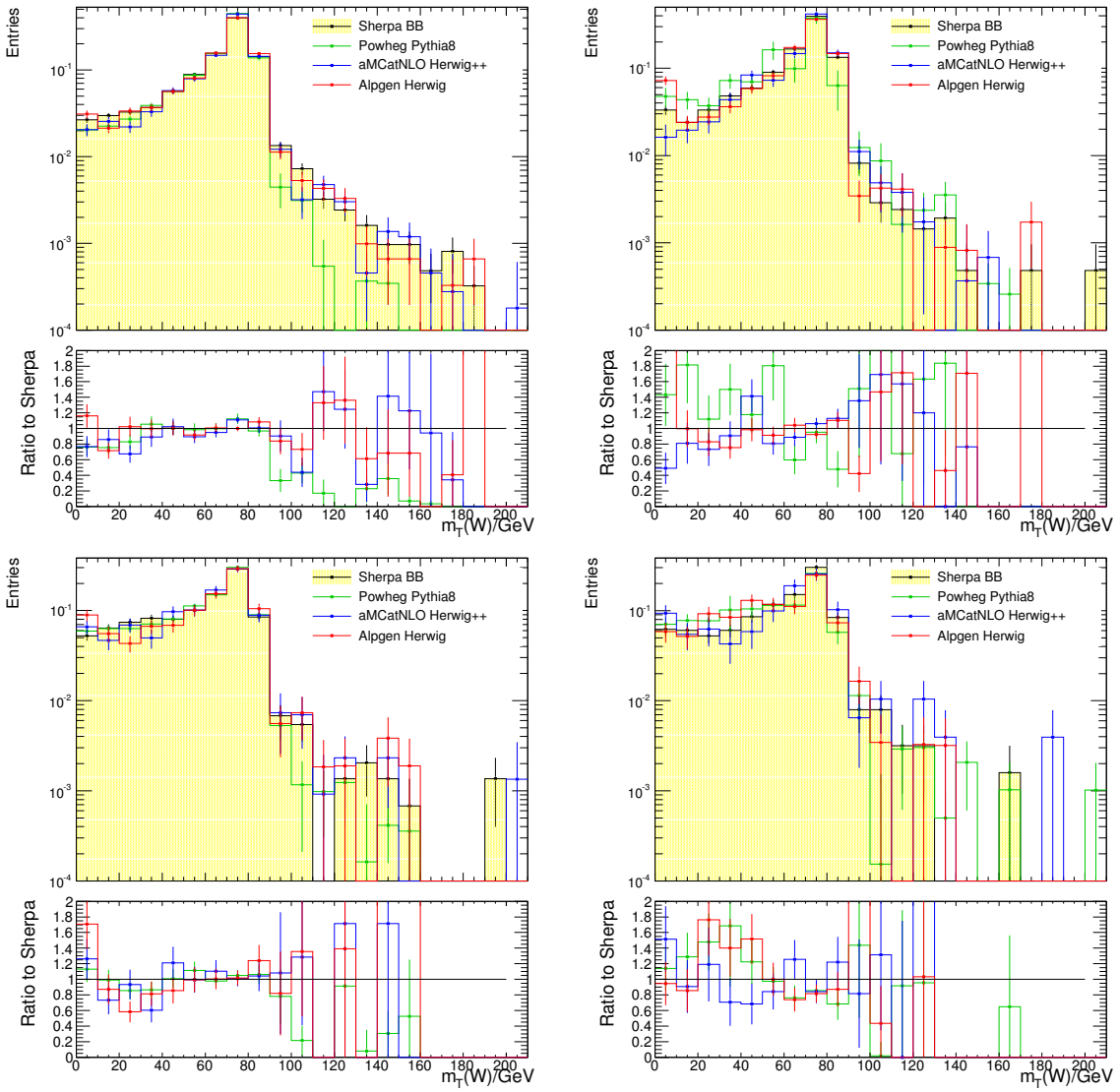

Figure 178: $M_T(W)$ in the low and high $p_T(W)$ regions, for the 2- and 3-jet cases. Events with leading jets matched to b-hadrons.

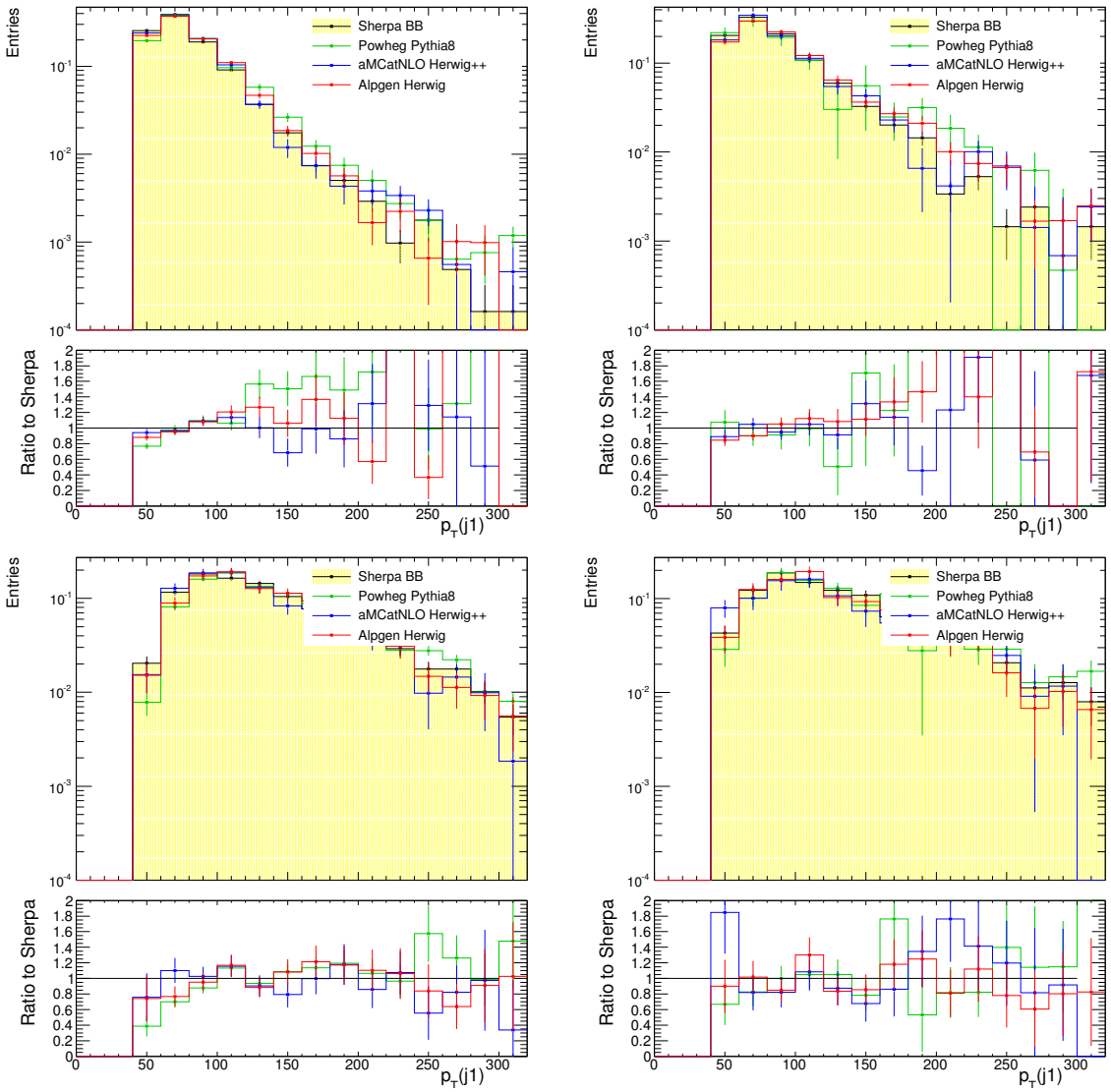

Figure 179: $p_T(j_1)$ in the low and high $p_T(W)$ regions, for the 2- and 3-jet cases. Events with leading jets matched to b-hadrons.

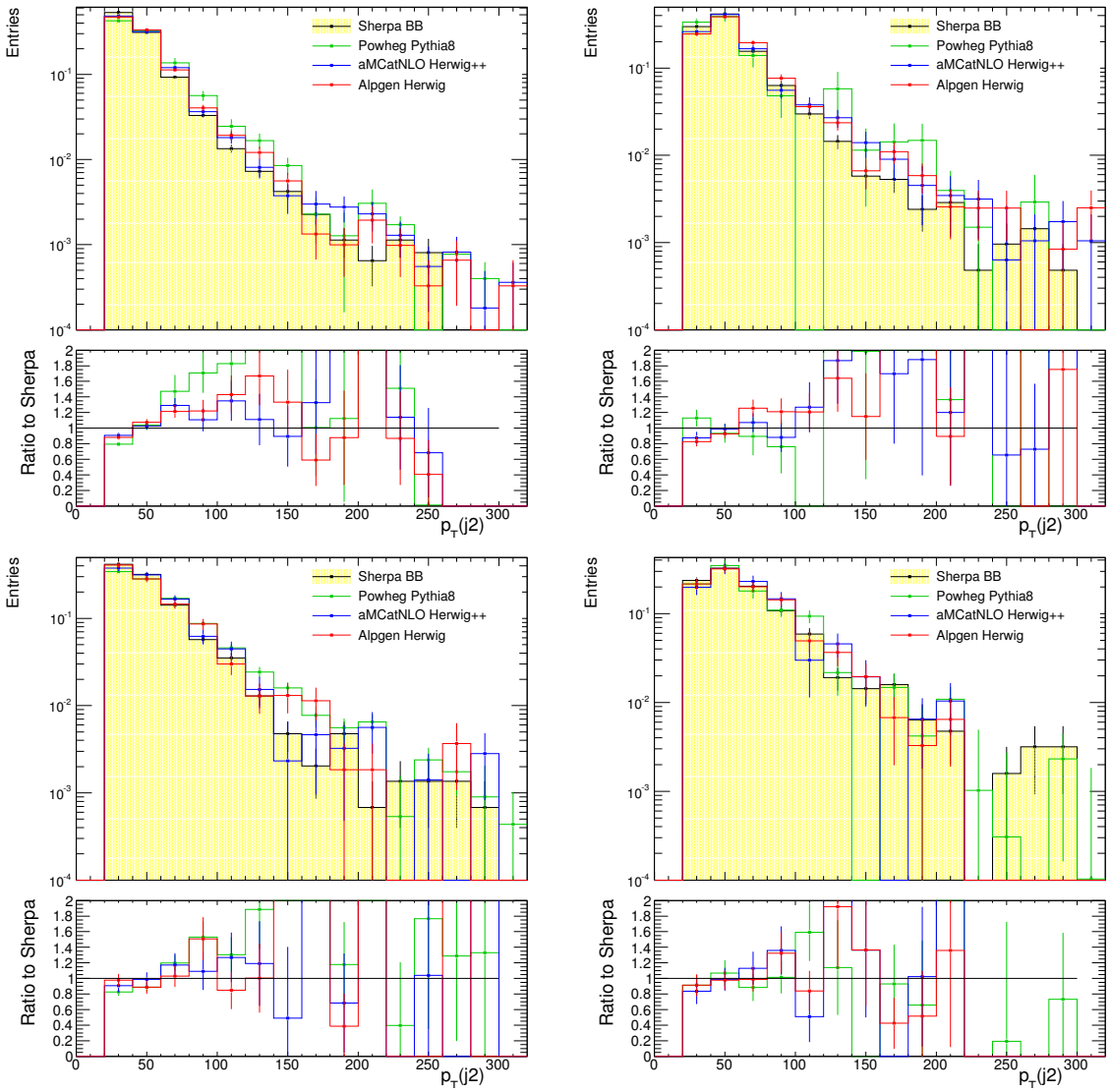

Figure 180: $p_T(j_2)$ in the low and high $p_T(W)$ regions, for the 2- and 3-jet cases. Events with leading jets matched to b-hadrons.

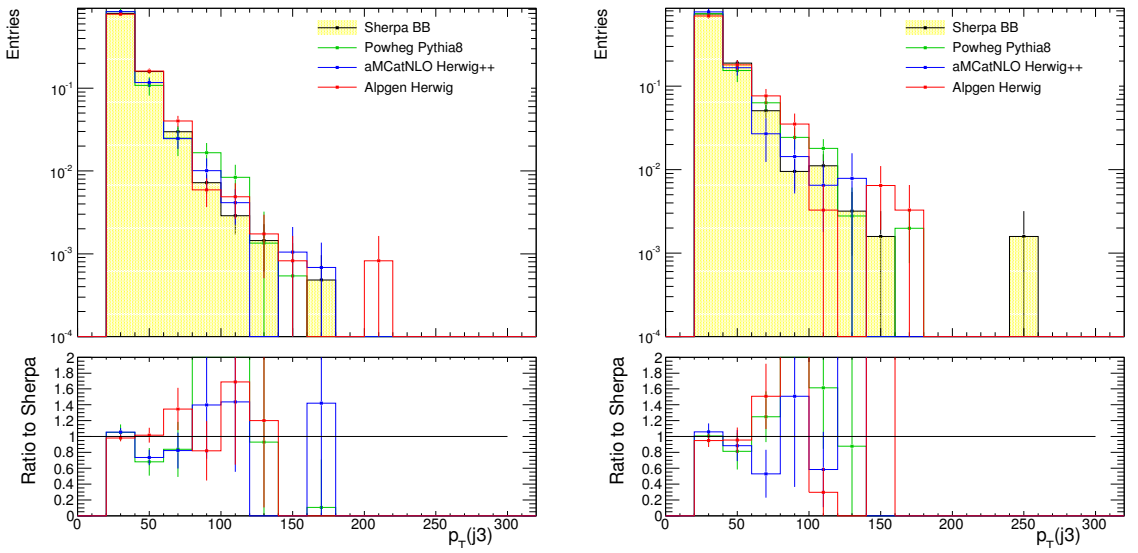

Figure 181: $p_T(j_3)$ in the low and high $p_T(W)$ 3-jet regions. Events with leading jets matched to b-hadrons.

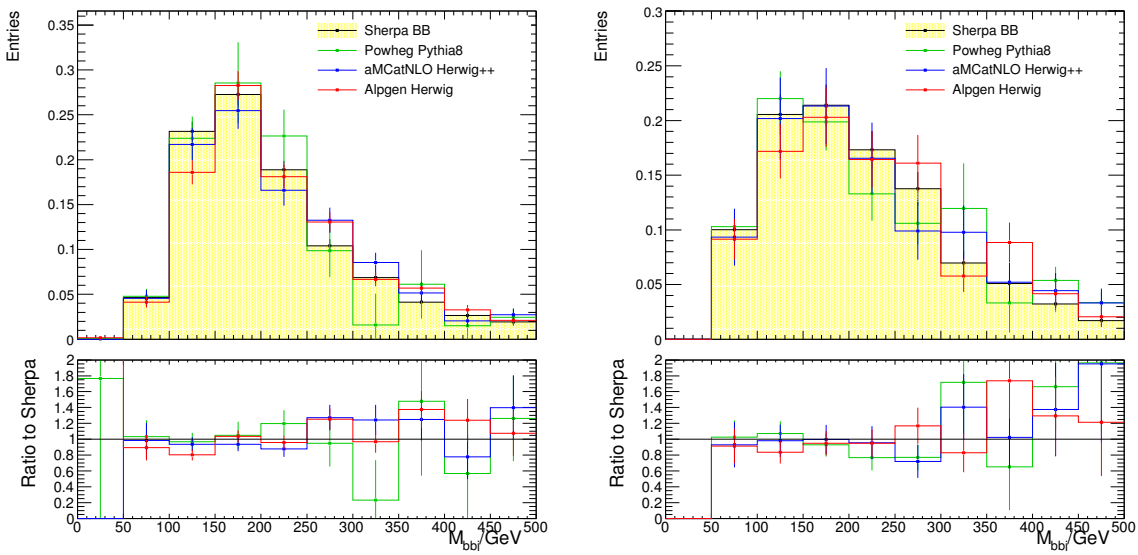

Figure 182: m_{bbj} in the low and high $p_T(W)$ 3-jet regions. Events with leading jets matched to b-hadrons.

M Single-top modeling

The study of the single-top modelling have been been done by comparing the agreement of different monte carlo generators in producing important distributions for the analysis while using the 1-lepton MVA-based selection. The Monte Carlo samples used for these studies are summarised in Table 97 and reproduced here. In this appendix, we show the comparisons for m_{bb}, $p_{\mathrm{T}}^{V}$and the leading and second leading jet $p_{\mathrm{T}}$for the s-channel production and the Wt production mechanisms, while for the t-channel, the appendix is completed with different additional variables.

Process	Channel num.	tag	N_{events}
		Single top, AcerMCPythia, P2011CCTEQ6L1	
$s-$ch.	110102	e2092_a188_a205_r4540_p1328	1199999
$Wt-$ch.	110103	e2092_a188_a205_r4540_p1328	998997
		Single top, PowhegHerwig, AUET2CT10	
Wt-ch	110144	e1743_s1581_s1586_r3658_r3549_p1328	998896
		Single top, PowhegPythia, P2011C, DS	
$Wt-$ch.	110142	e1743_s1581_s1586_r3658_r3549_p1328	994894
		Single top, aMcAtNloJimmy, AUET2CT10	
$t-$ch.	110095	e2240_a188_a205_r4540_p1328	996999
		Single top, McAtNloJimmy, AUET2CT10	
$s-$ch.	108343	e1525_a159_a171_r3549_p1328	999998
	108344	e1525_a159_a171_r3549_p1328	998000
	108345	e1525_a159_a171_r3549_p1328	999998
$Wt-$ch.	108346	e1525_a159_a171_r3549_p1328	4996492
		Single top AcerMCPythia, P2011CMorePSCTEQ6L1	
$t-$ch.	110105	e2092_a188_a205_r4540_p1328	2978000
$s-$ch.	110107	e2092_a188_a205_r4540_p1328	1199999
Wt-ch	110109	e2092_a188_a205_r4540_p1328	998999
		Single top AcerMCPythia, P2011CLessPSCTEQ6L1	
$t-$ch.	110106	e2092_a188_a205_r4540_p1328	2997999
$s-$ch.	110108	e2092_a188_a205_r4540_p1328	1198998
Wt-ch	110110	e2092_a188_a205_r4540_p1328	1000000

Table 97: Monte Carlo samples and channel numbers and statistics used for the single top and the $t\bar{t}$ systematics. More information is given in Section 5.2.2.

M.1 t-channel

For the single top t-channel, the baseline sample AcerMCPythia was compared to the aMcNLOJimmy sample. From this comparison, systematic uncertainties in normalization were extracted and found to be 52 and 25% for 2 b-tag 2 jet events at low and high p_{T}^{V}, respectively and 12 and -18% for 2 b-tag 3 jet events. The yield difference between the two samples comes primarily from the b-tagging procedure and jets p_{T}.

Figures 183 and 184 show the distrubutions for the t-channel single top variables in 1-lepton events for $p_{\mathrm{T}}^{W} < 120$ GeV with 2 b-tag and 2 jets.
Figures 185 and 186 show the distrubutions for the t-channel single top variables in 1-lepton events for $p_{\mathrm{T}}^{W} > 120$ GeV with 2 b-tag and 2 jets.
Figures 187 and 188 show the distrubutions for the t-channel single top variables in 1-lepton events for $p_{\mathrm{T}}^{W} < 120$ GeV with 2 b-tag and 3 jets.
Figures 189 and 190 show the distrubutions for the t-channel single top variables in 1-lepton events for $p_{\mathrm{T}}^{W} > 120$ GeV with 2 b-tag and 3 jets.

Several variables have different distribution shapes for the two Monte-Carlo generators. This mis-modelling is most of the time covered by the statistical uncertainties and no shape uncertainty was considered for the t-channel originating from this comparison.

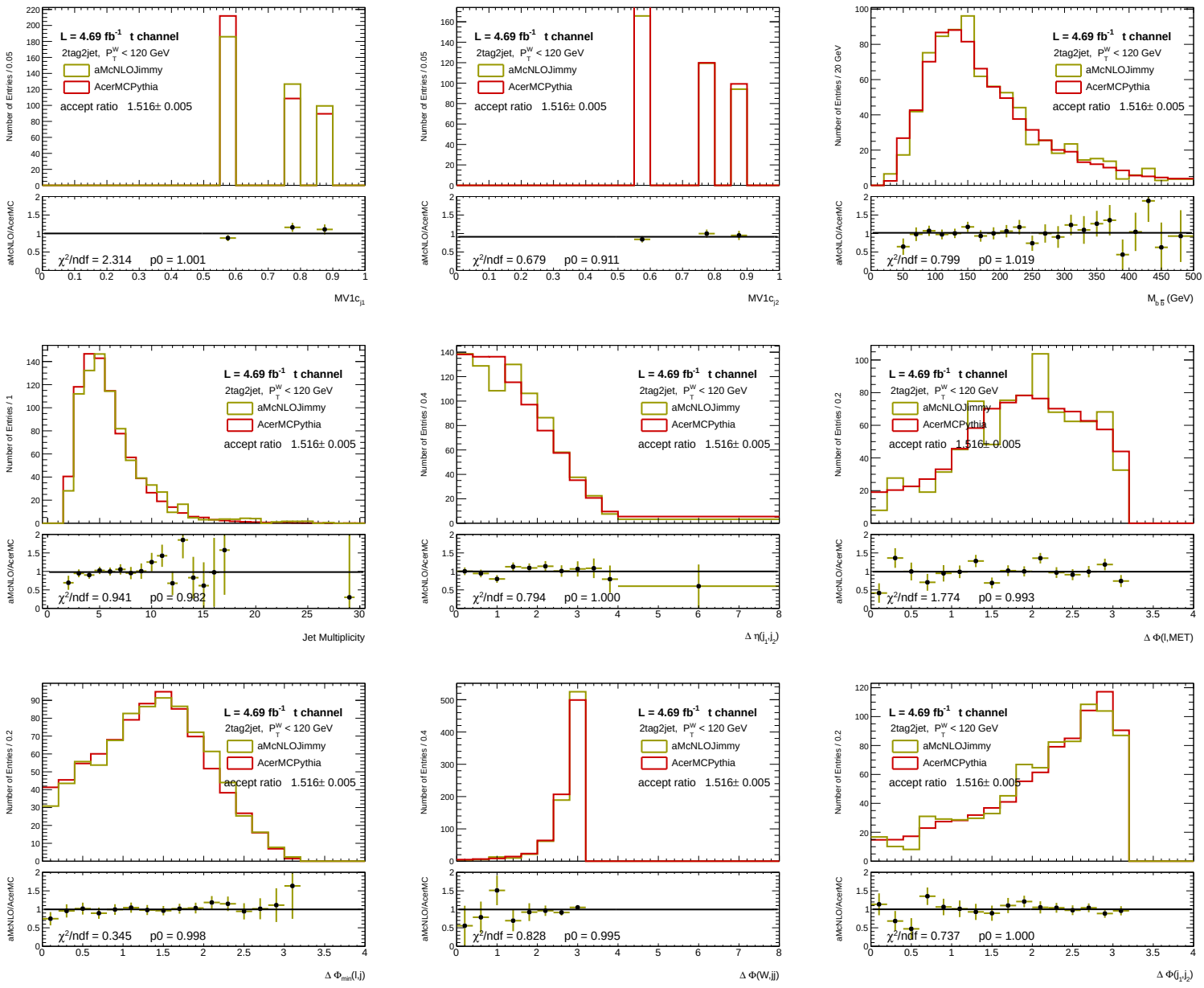

Figure 183: Distributions of t-channel single top variables used in 1-lepton events for $p_{\mathrm{T}}^{W} < 120$ GeV with 2 b-tag and 2 jets. From left to right: Row 1 - Pseudo-continuous MV1c distributions for leading then sub-leading jet and the m_{bb} of the same two jets. Row 2 - Number of jets, $\Delta\eta_{jj}$, $|\Delta\phi(\ell, E_{\mathrm{T}}^{\mathrm{miss}})|$; Row 3 - min$|\Delta\phi(\ell, jet)|$, $\Delta\phi(V,H)$, $\Delta\phi_{jj}$.

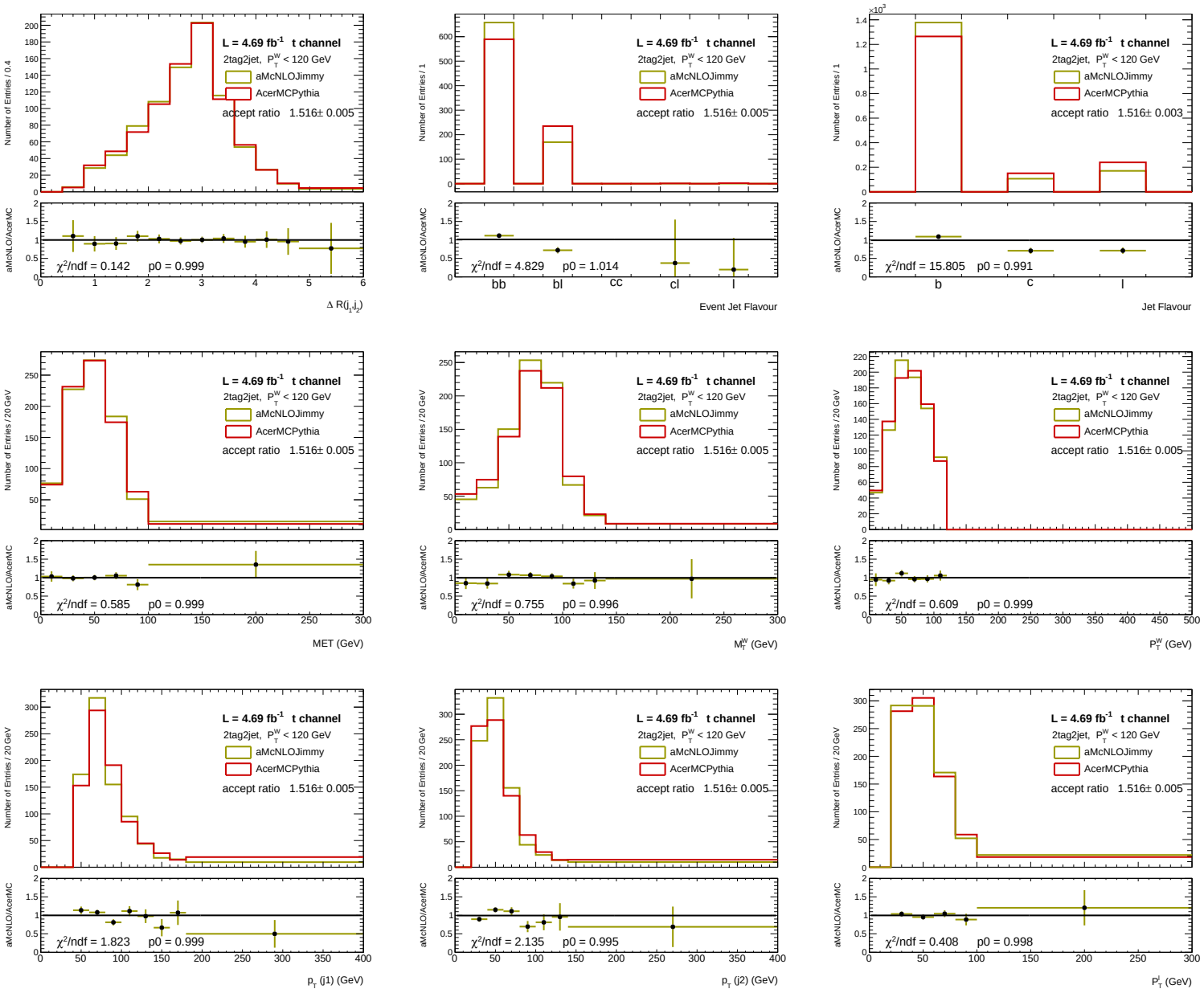

Figure 184: Distributions of t-channel single top variables used in 1-lepton events for $p_{\mathrm{T}}^{W} < 120$ GeV with 2 b-tag and 2 jets. From left to right: Row 1 - ΔR, Event flavour and jet flavour (using the truth information of the two leading jets in p_{T}). Row 2 - $E_{\mathrm{T}}^{\mathrm{miss}}$, m_{T}^{W} and p_{T}^{W}. Row 3 - Leading then sub-leading jet p_{T} and lepton p_{T} .

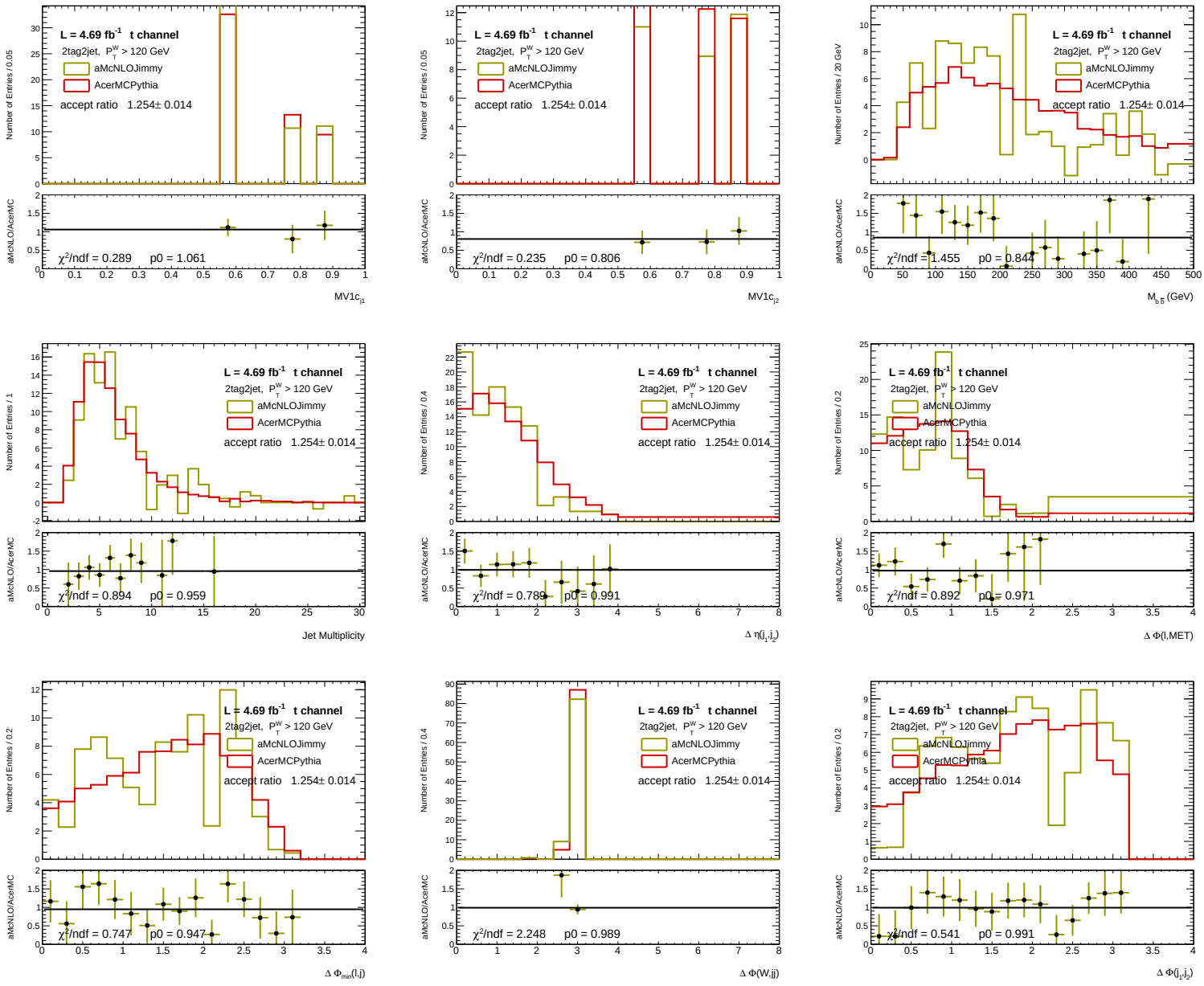

Figure 185: Distributions of t-channel single top variables used in 1-lepton events for $p_{\mathrm{T}}^{W} > 120$ GeV with 2 b-tag and 2 jets. From left to right: Row 1 - Pseudo-continuous MV1c distributions for leading then sub-leading jet and the m_{bb} of the same two jets. Row 2 - Number of jets, $\Delta\eta_{jj}$, $|\Delta\phi(\ell, E_{\mathrm{T}}^{\mathrm{miss}})|$; Row 3 - min$|\Delta\phi(\ell, jet)|$, $\Delta\phi(V,H)$, $\Delta\phi_{jj}$.

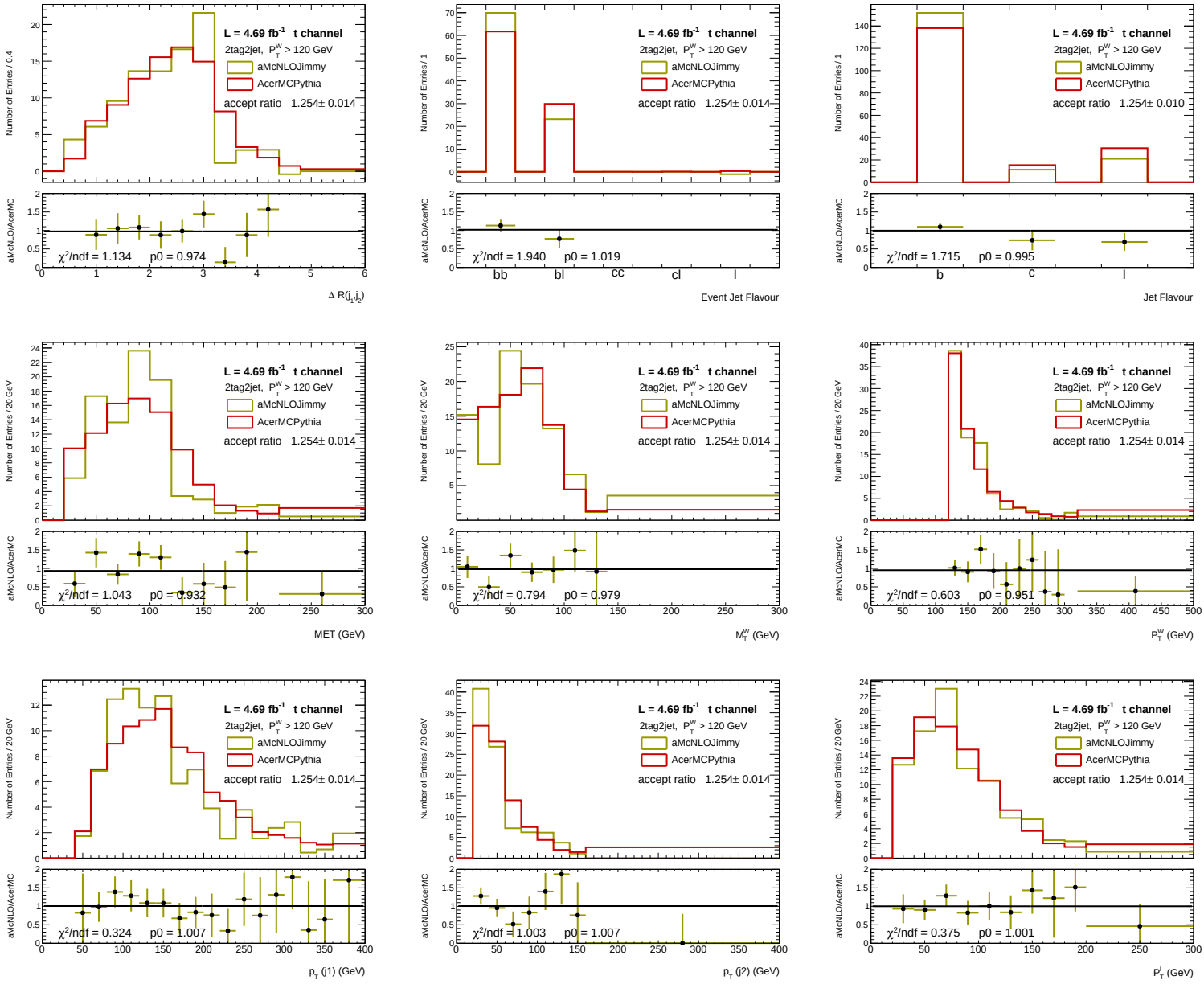

Figure 186: Distributions of t-channel single top variables used in 1-lepton events for $p_{\mathrm{T}}^{W} > 120$ GeV with 2 b-tag and 2 jets. From left to right: Row 1 - ΔR, Event flavour and jet flavour (using the truth information of the two leading jets in p_{T}). Row 2 - $E_{\mathrm{T}}^{\mathrm{miss}}$, m_{T}^{W} and p_{T}^{W}. Row 3 - Leading then sub-leading jet p_{T} and lepton p_{T}.

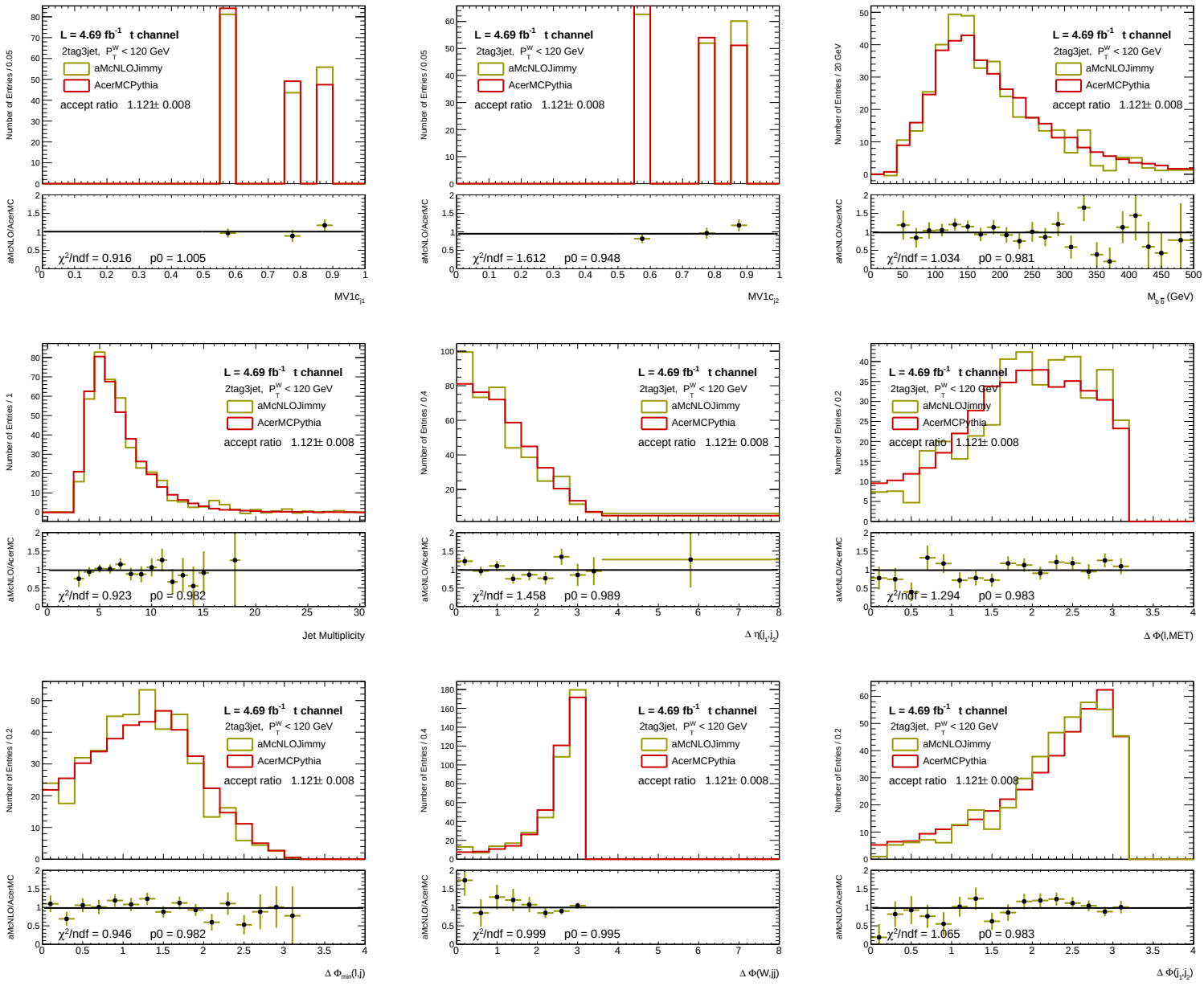

Figure 187: Distributions of t-channel single top variables used in 1-lepton events for $p_{\mathrm{T}}^{W} < 120$ GeV with 2 b-tag and 3 jets. From left to right: Row 1 - Pseudo-continuous MV1c distributions for leading then sub-leading jet and the m_{bb} of the same two jets. Row 2 - Number of jets, $\Delta\eta_{jj}$, $|\Delta\phi(\ell, E_{\mathrm{T}}^{\mathrm{miss}})|$; Row 3 - min$|\Delta\phi(\ell, jet)|$, $\Delta\phi(V,H)$, $\Delta\phi_{jj}$.

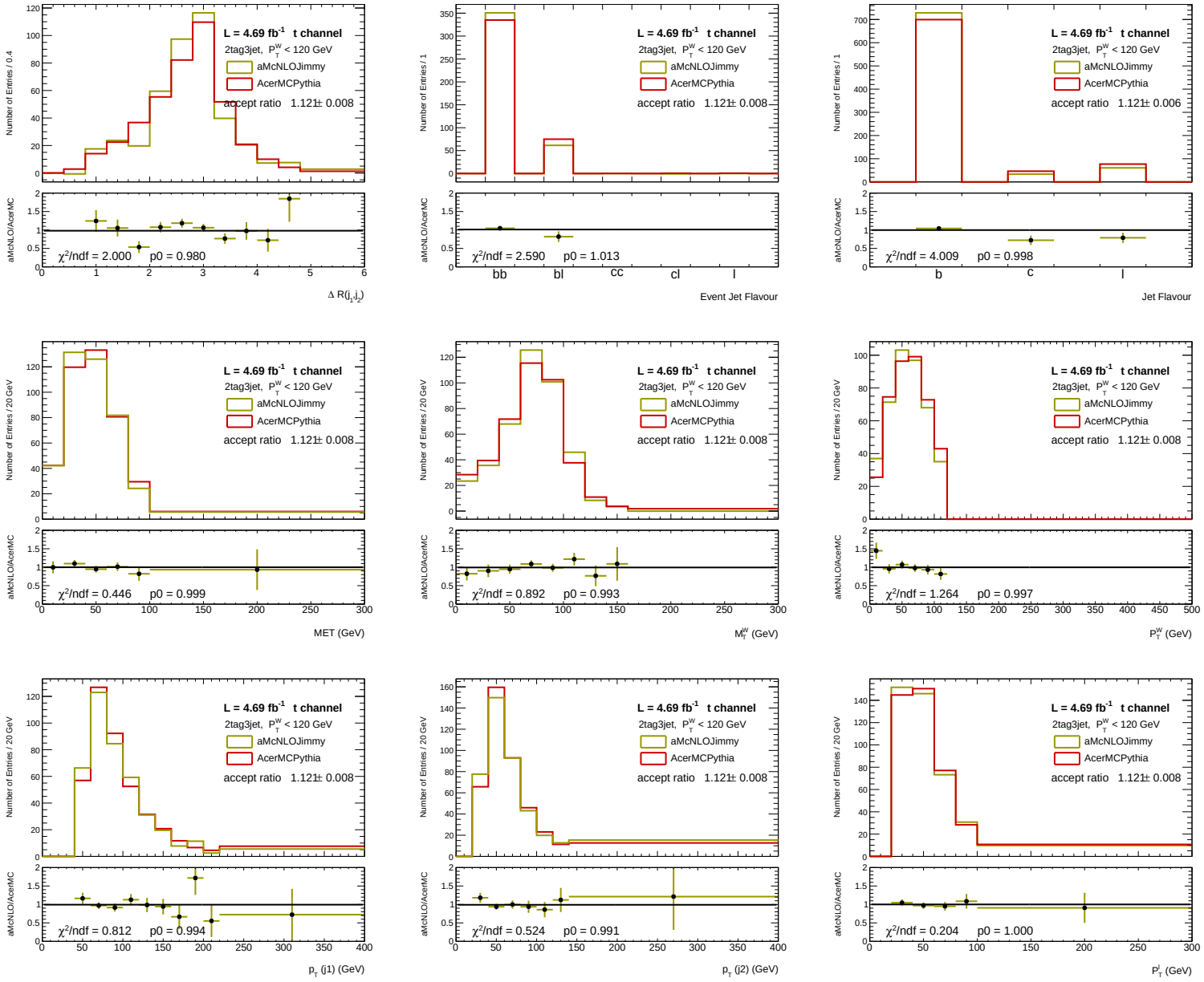

Figure 188: Distributions of t-channel single top variables used in 1-lepton events for $p_{\mathrm{T}}^{W} < 120$ GeV with 2 b-tag and 3 jets. From left to right: Row 1 - ΔR, Event flavour and jet flavour (using the truth information of the two leading jets in p_{T}). Row 2 - $E_{\mathrm{T}}^{\mathrm{miss}}$, m_{T}^{W} and p_{T}^{W}. Row 3 - Leading then sub-leading jet p_{T} and lepton p_{T}.

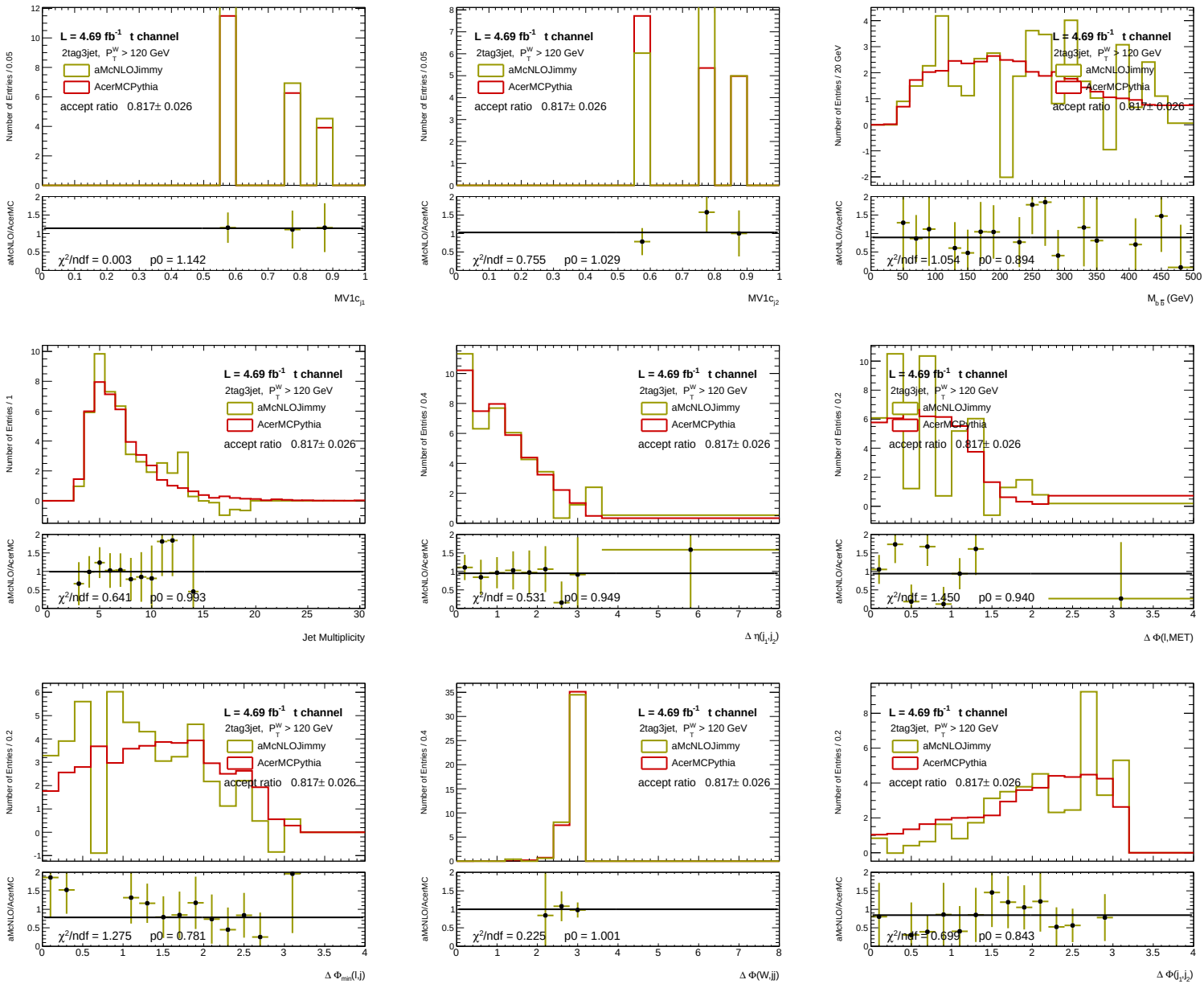

Figure 189: Distributions of t-channel single top variables used in 1-lepton events for $p_{\mathrm{T}}^{W} > 120$ GeV with 2 b-tag and 3 jets. From left to right: Row 1 - Pseudo-continuous MV1c distributions for leading then sub-leading jet and the m_{bb} of the same two jets. Row 2 - Number of jets, $\Delta\eta_{jj}$, $|\Delta\phi(\ell, E_{\mathrm{T}}^{\mathrm{miss}})|$; Row 3 - min$|\Delta\phi(\ell, jet)|$, $\Delta\phi(V,H)$, $\Delta\phi_{jj}$.

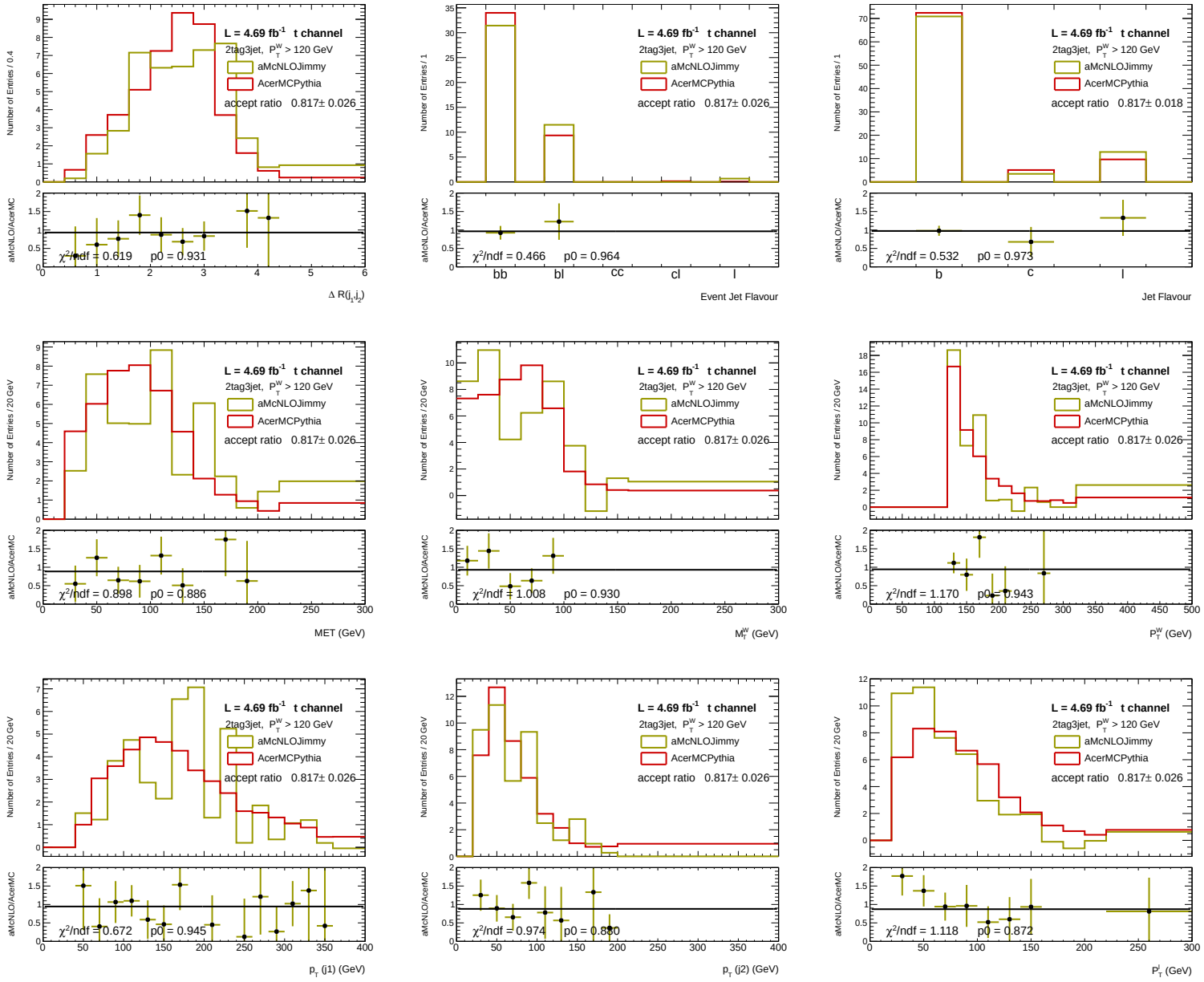

Figure 190: Distributions of t-channel single top variables used in 1-lepton events for $p_{\mathrm{T}}^{W} > 120$ GeV with 2 b-tag and 3 jets. From left to right: Row 1 - ΔR, Event flavour and jet flavour (using the truth information of the two leading jets in p_{T}). Row 2 - $E_{\mathrm{T}}^{\mathrm{miss}}$, m_{T}^{W} and p_{T}^{W}. Row 3 - Leading then sub-leading jet p_{T} and lepton p_{T}.

M.2 s-channel

For the single top s-channel, the baseline sample AcerMCPythia was compared to the McNLOJimmy and PowhegPythia samples. Systematic uncertainties in normalization were extracted from the yield difference observed between the baseline sample and the PowhegPythia sample. These systematics were found to be 13 and 22% for 2 b-tag 2 jet events at low and high p_{T}^{V}, respectively and 28 and 30% for 2 b-tag 3 jet events. The baseline yield differences to the McNLOJimmy sample was negligible with respect to the later ones. Furthermore, the parton shower effect, obtained by comparing the AcerMCPythia more PS and less PS dedicated samples, contributes with a normalization systematic uncertainty of 6 and 8% for 2 b-tag 2 jet events at low and high p_{T}^{V}, respectively and 4 and 4% for 2 b-tag 3 jet events.

Figure 191 shows the distrubutions for the s-channel single top variables in 1-lepton events for $p_{\mathrm{T}}^{W} < 120$ GeV with 2 b-tag and 2 jets.
Figure 192 shows the distrubutions for the s-channel single top variables in 1-lepton events for $p_{\mathrm{T}}^{W} > 120$ GeV with 2 b-tag and 2 jets.
Figure 193 shows the distrubutions for the s-channel single top variables in 1-lepton events for $p_{\mathrm{T}}^{W} < 120$ GeV with 2 b-tag and 3 jets.
Figure 194 shows the distrubutions for the s-channel single top variables in 1-lepton events for $p_{\mathrm{T}}^{W} > 120$ GeV with 2 b-tag and 3 jets.

The McNLOJimmy and PowhegPythia samples modelling for m_{bb}, $p_{\mathrm{T}}^{V}$and leading and second-leading jets $p_{\mathrm{T}}$is similar to the baseline sample for the selected events. The rare exceptions where mismodelling is observed have statistical uncertainty coverage. For the single top s-channel, no shape systematic uncertainty was considered.

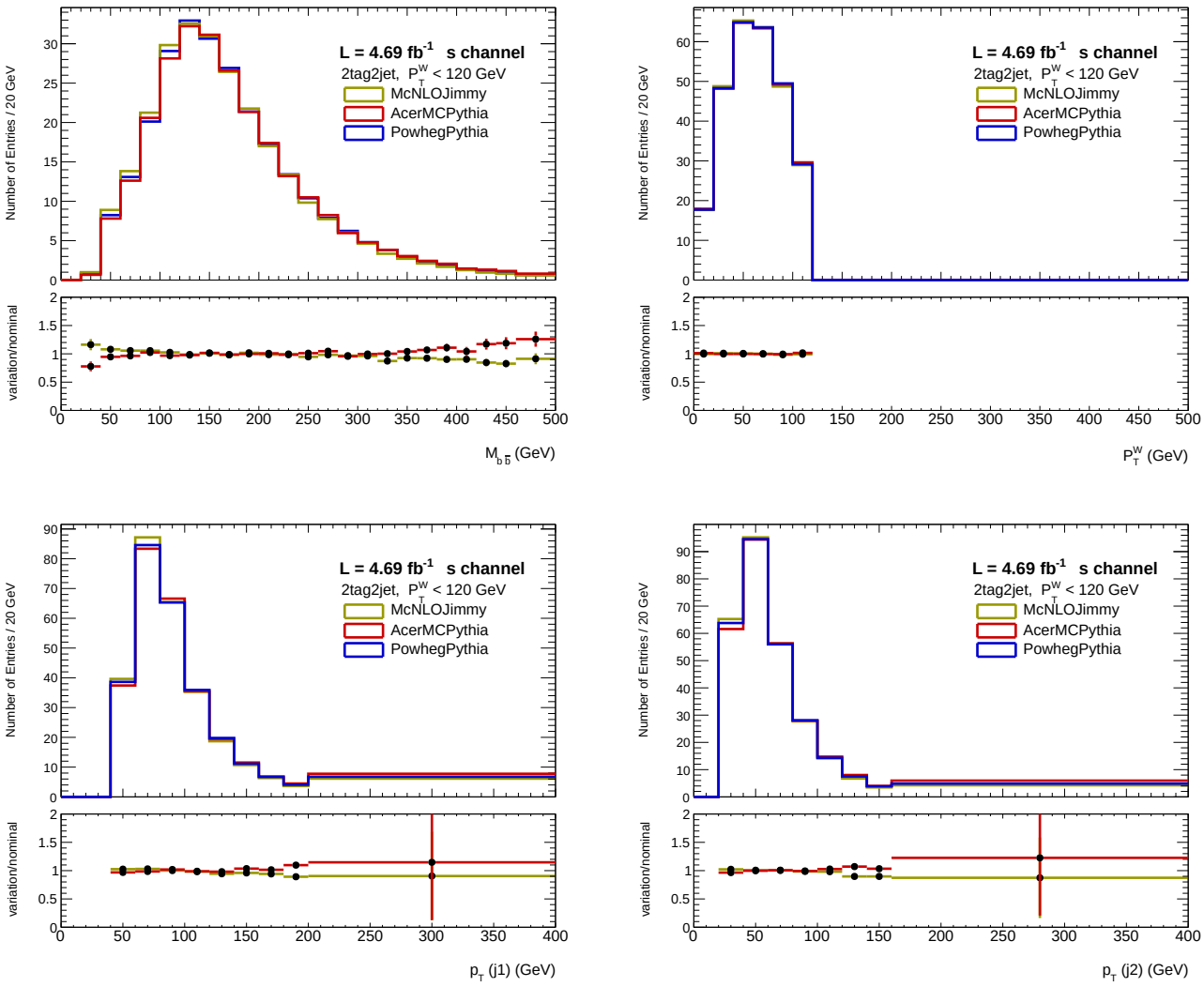

Figure 191: Distributions of s-channel single top variables used in 1-lepton events for $p_{\mathrm{T}}^{W} < 120$ GeV with 2 b-tag and 2 jets. From left to right: Row 1 - m_{bb} and p_{T}^{W}. Row 2 - leading then sub-leading jet p_{T}.

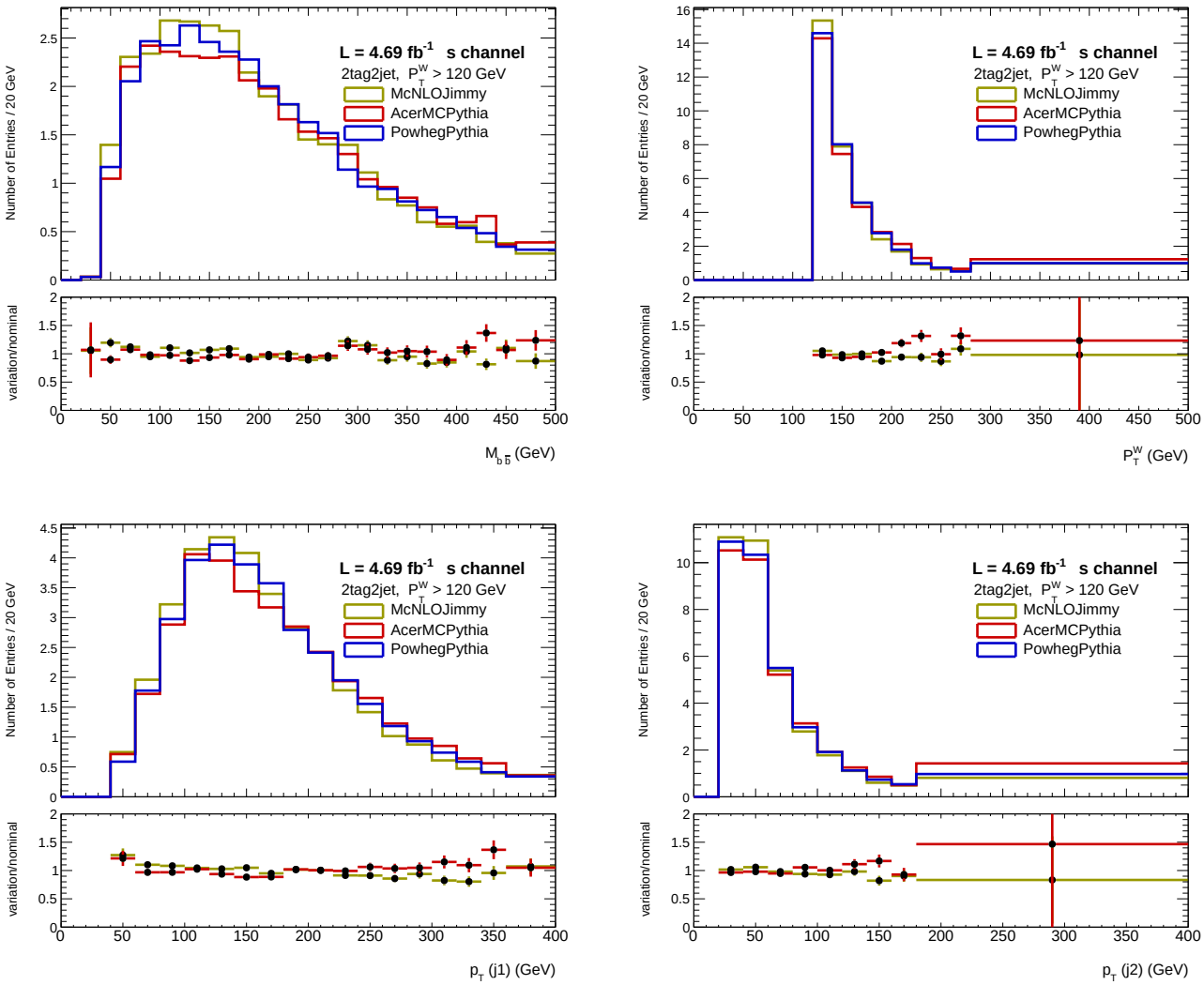

Figure 192: Distributions of s-channel single top variables used in 1-lepton events for $p_{\mathrm{T}}^{W} > 120$ GeV with 2 b-tag and 2 jets. From left to right: Row 1 - m_{bb} and p_{T}^{W}. Row 2 - leading then sub-leading jet p_{T}.

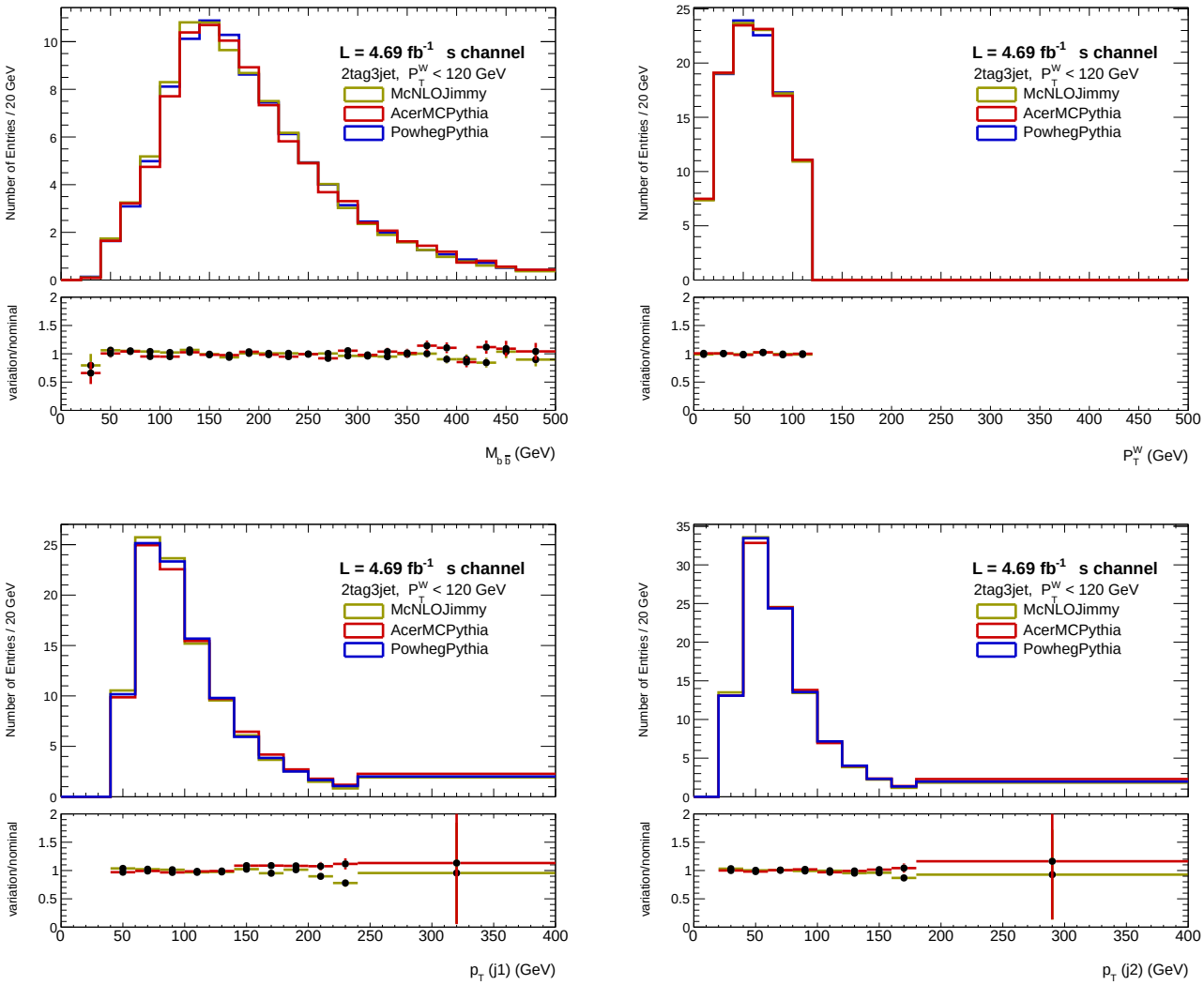

Figure 193: Distributions of s-channel single top variables used in 1-lepton events for $p_{\mathrm{T}}^{W} < 120$ GeV with 2 b-tag and 3 jets. From left to right: Row 1 - m_{bb} and p_{T}^{W}. Row 2 - leading then sub-leading jet p_{T}.

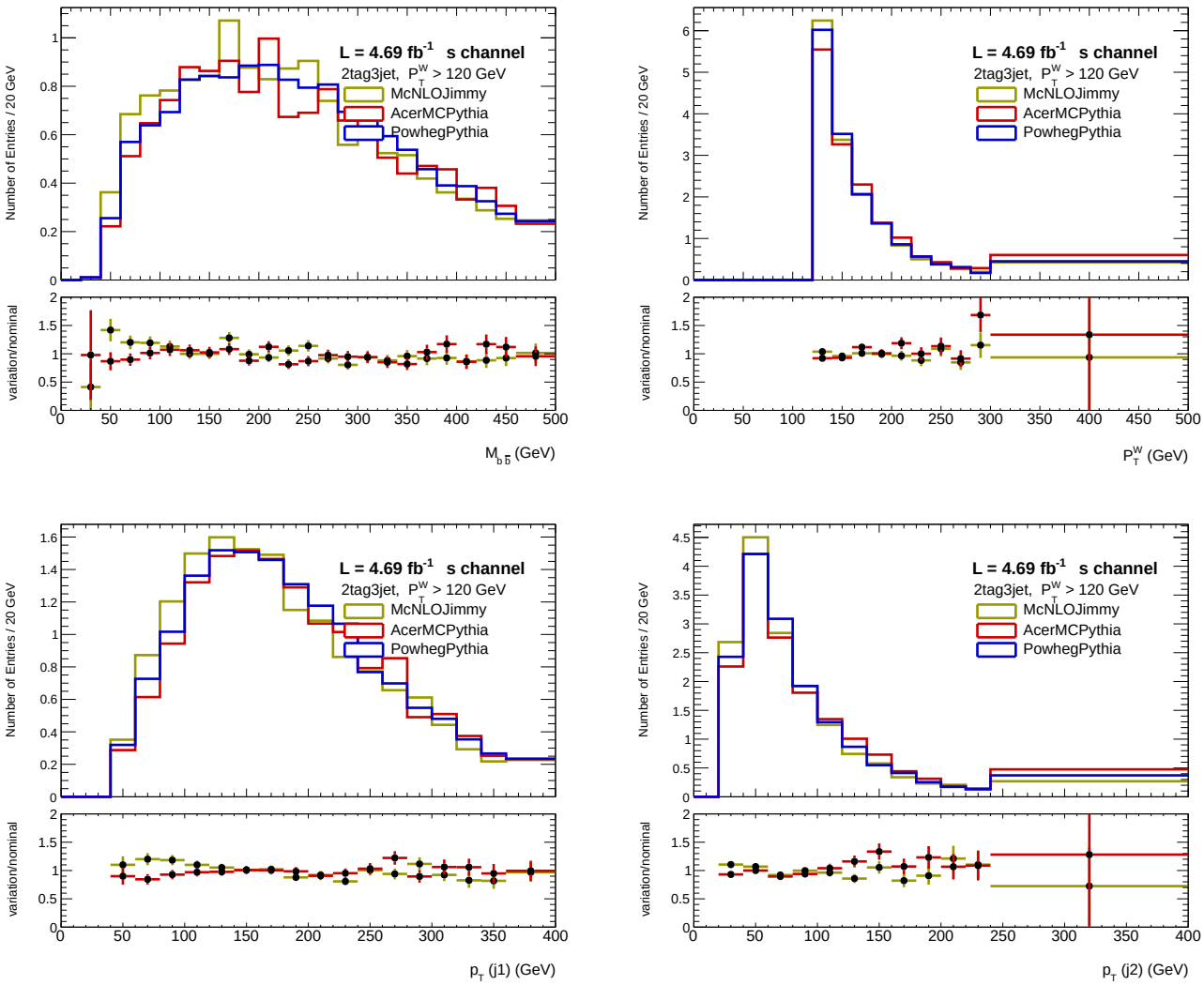

Figure 194: Distributions of s-channel single top variables used in 1-lepton events for $p_{\mathrm{T}}^{W} > 120$ GeV with 2 b-tag and 3 jets. From left to right: Row 1 - m_{bb} and p_{T}^{W}. Row 2 - leading then sub-leading jet p_{T}.

M.3 Wt

For the single top Wt-channel, the baseline sample AcerMCPythia was compared to several alternative samples -AcerMCPythia, McNLOJimmy and PowhegHerwig. The overlap between some of the single top Wt-channel production diagrams with $t\bar{t}$ events can be extracted in simulation either by diagram removal (DR) or diagram sustraction (DS). This ambiguity was exploited by comparing the DR baseline sample with the PowhegPythiaDS sample. Systematic uncertainties in normalization were extracted from the yield difference observed between the baseline sample and the AcerMCPythia sample. These systematics were found to be 1 and -2% for 2 b-tag 2 jet events at low and high p_{T}^{V}, respectively and 4 and -15% for 2 b-tag 3 jet events. Furthermore, the comparison to PowhegHerwig, contributes with a normalization systematic uncertainty of 5 and 3% for 2 b-tag 2 jet events at low and high p_{T}^{V}, respectively and 5 and -3% for 2 b-tag 3 jet events. The baseline yield differences to the McNLOJimmy and PowhegPythiaDS samples were negligible with respect to the later ones.

Figure 195 shows the distrubutions for the Wt-channel single top variables in 1-lepton events for $p_{\mathrm{T}}^{W} < 120$ GeV with 2 b-tag and 2 jets.
Figure 196 shows the distrubutions for the Wt-channel single top variables in 1-lepton events for $p_{\mathrm{T}}^{W} > 120$ GeV with 2 b-tag and 2 jets.
Figure 197 shows the distrubutions for the Wt-channel single top variables in 1-lepton events for $p_{\mathrm{T}}^{W} < 120$ GeV with 2 b-tag and 3 jets.
Figure 198 shows the distrubutions for the Wt-channel single top variables in 1-lepton events for $p_{\mathrm{T}}^{W} > 120$ GeV with 2 b-tag and 3 jets.

At 2 b-tags 2 jets low p_{T}^{V}a mismodelling is observed for the leadind and second-leading jets p_{T}distributions. A shape uncertainty on the leading jet $p_{\mathrm{T}}$was extracted from the comparison between the baseline and PowhegHerwig samples where the mismodelling is more prominent, covering the difference observed to the other alternative samples.

The same applies for m_{bb}at the 2 b-tags 2 jets high p_{T}^{V}, where a shape uncertainty was obtained from the comparison between the baseline sample and the AcerMCPythia sample. For the 2 b-tags 3 jets low p_{T}^{V}events, a shape uncertainty on the leading jet $p_{\mathrm{T}}$was extracted from the comparison between the baseline sample and the AcerMCPythia sample while for the high p_{T}^{V}events the shape uncertainty comes from the m_{bb}distribution. It was observed that this systematics could also cover the mismodelling observed in the remaining alternative samples. For the high p_{T}^{V}region, the shape uncertainty on $m_{bb}$is expected to vanish the mismodelling observed at the jets p_{T}, since these variables are highly correlated. All the systematic shape uncertainties mentioned were obtained through a linear fit of the alternative to baseline sample ratio.

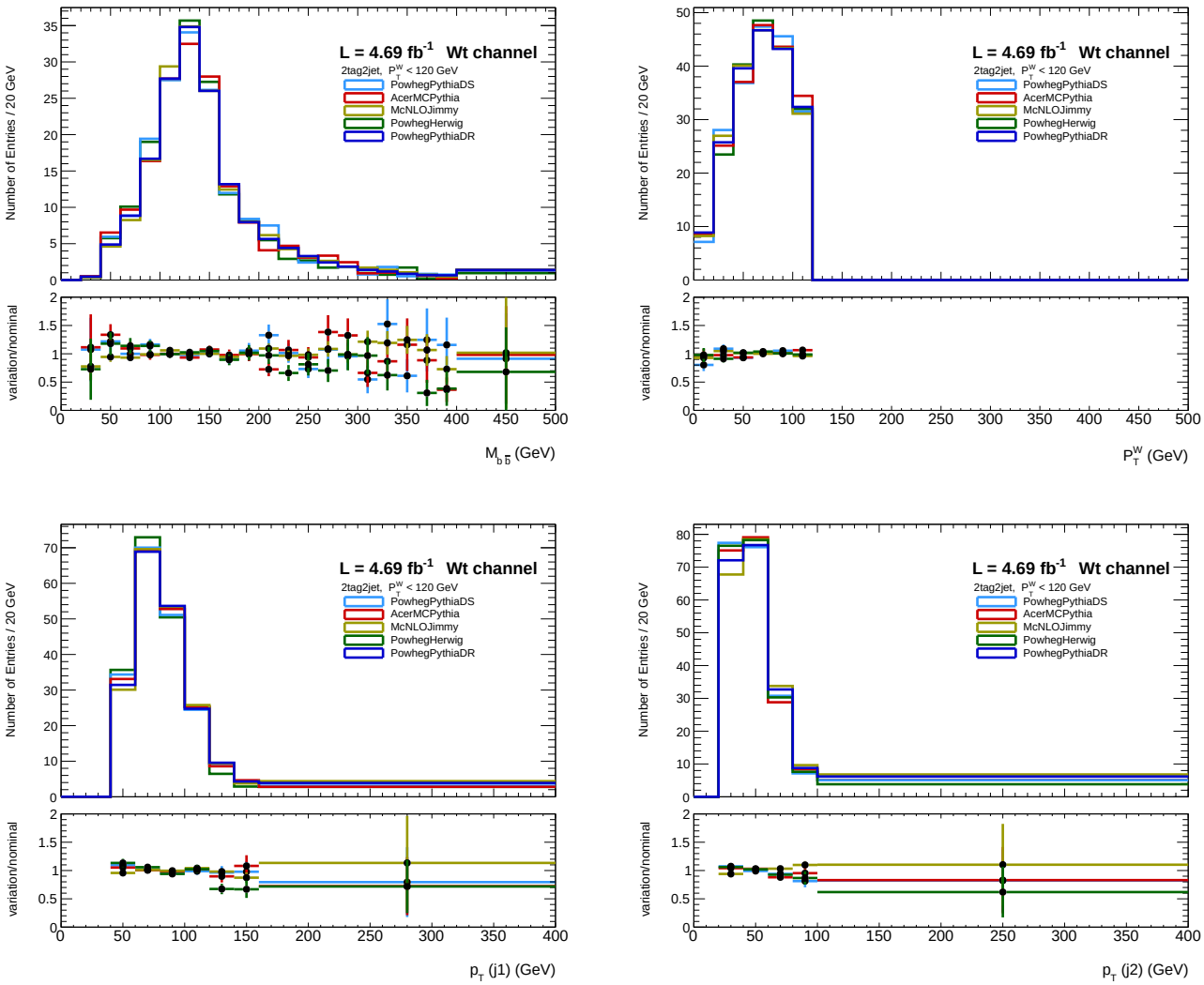

Figure 195: Distributions of Wt-channel single top variables used in 1-lepton events for $p_{\mathrm{T}}^{W} < 120$ GeV with 2 b-tag and 2 jets. From left to right: Row 1 - m_{bb} and p_{T}^{W}. Row 2 - leading then sub-leading jet p_{T}.

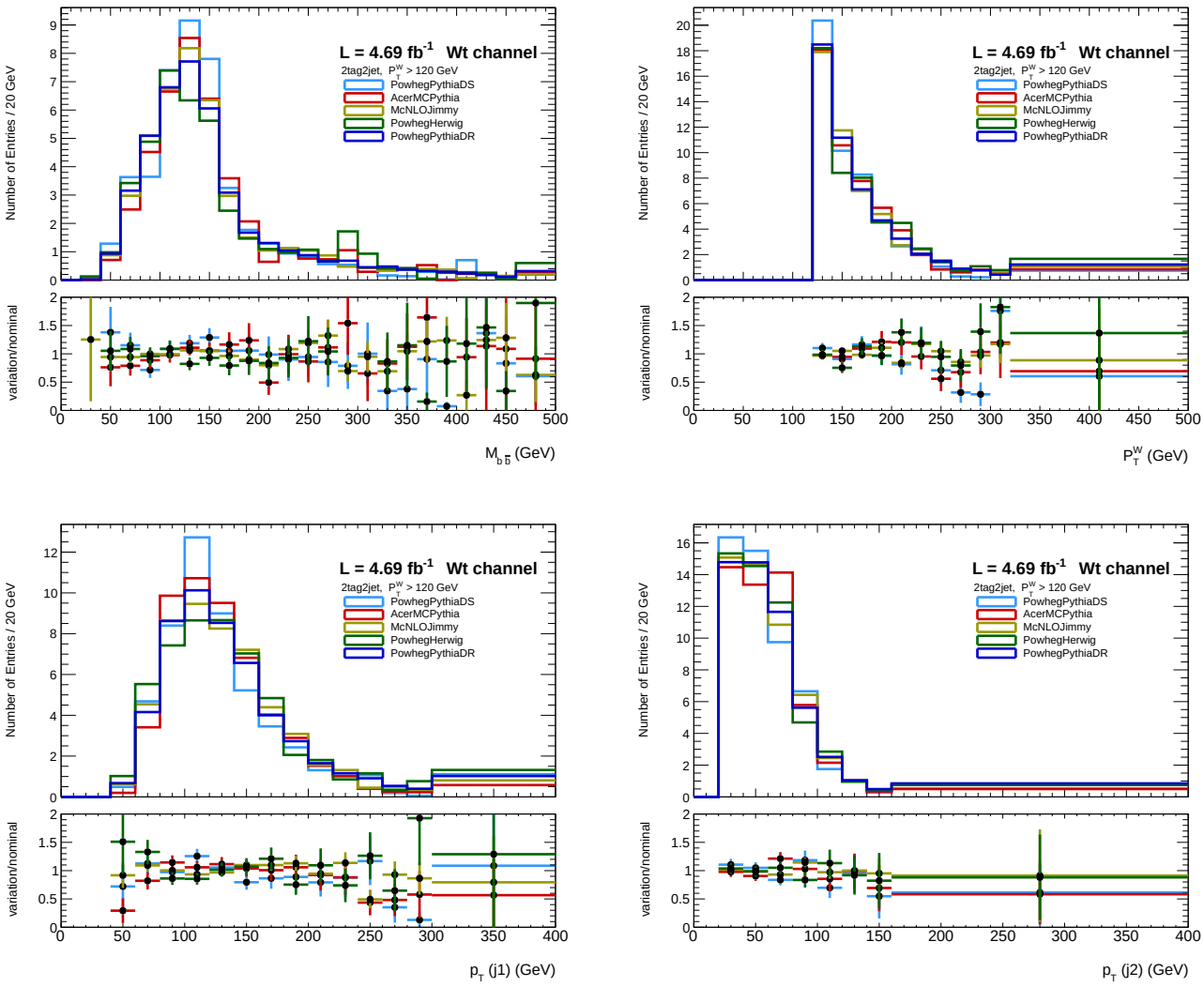

Figure 196: Distributions of Wt-channel single top variables used in 1-lepton events for $p_{\mathrm{T}}^{W} > 120$ GeV with 2 b-tag and 2 jets. From left to right: Row 1 - m_{bb} and p_{T}^{W}. Row 2 - leading then sub-leading jet p_{T}.

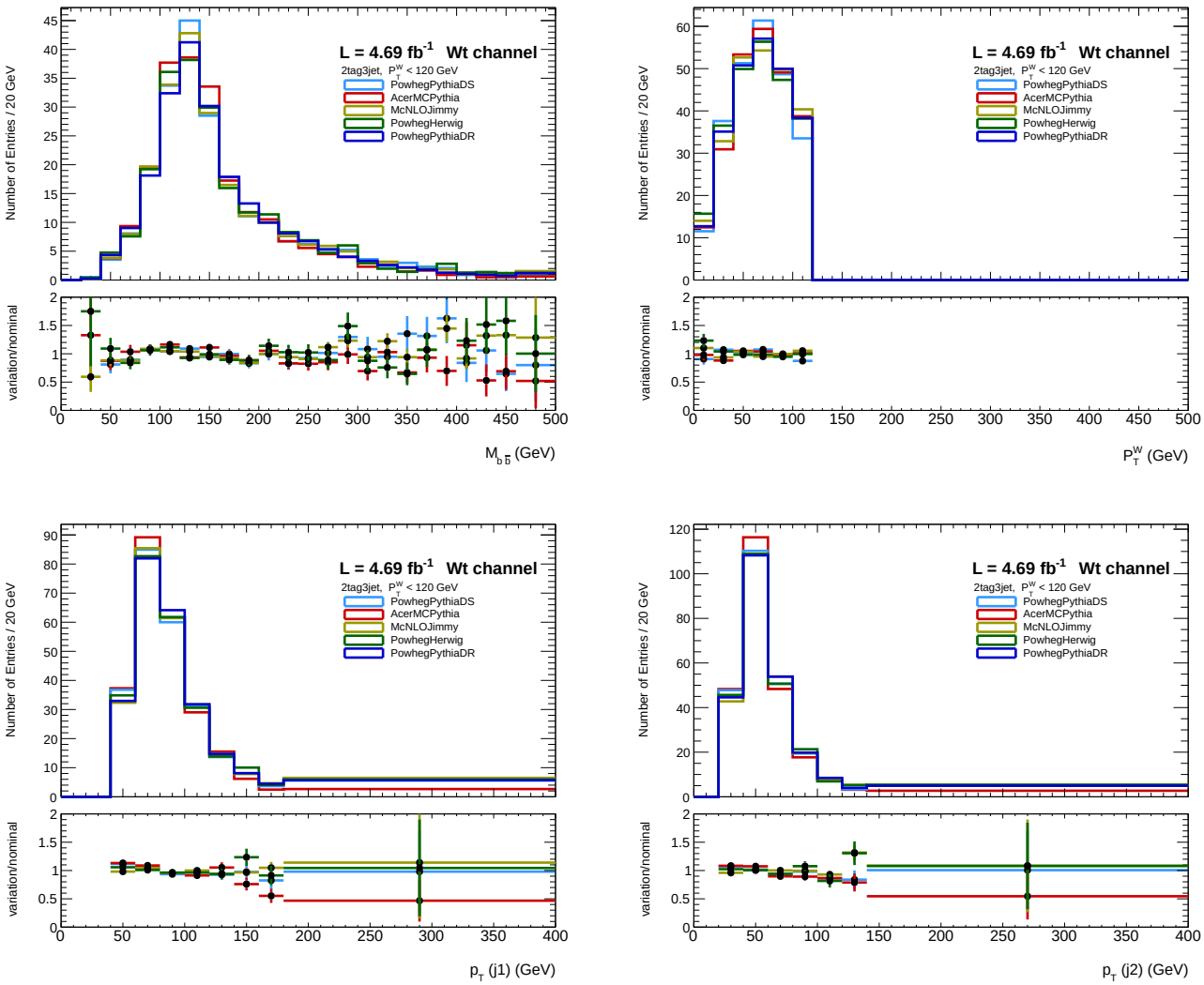

Figure 197: Distributions of Wt-channel single top variables used in 1-lepton events for $p_{\mathrm{T}}^{W} < 120$ GeV with 2 b-tag and 3 jets. From left to right: Row 1 - m_{bb} and p_{T}^{W}. Row 2 - leading then sub-leading jet p_{T}.

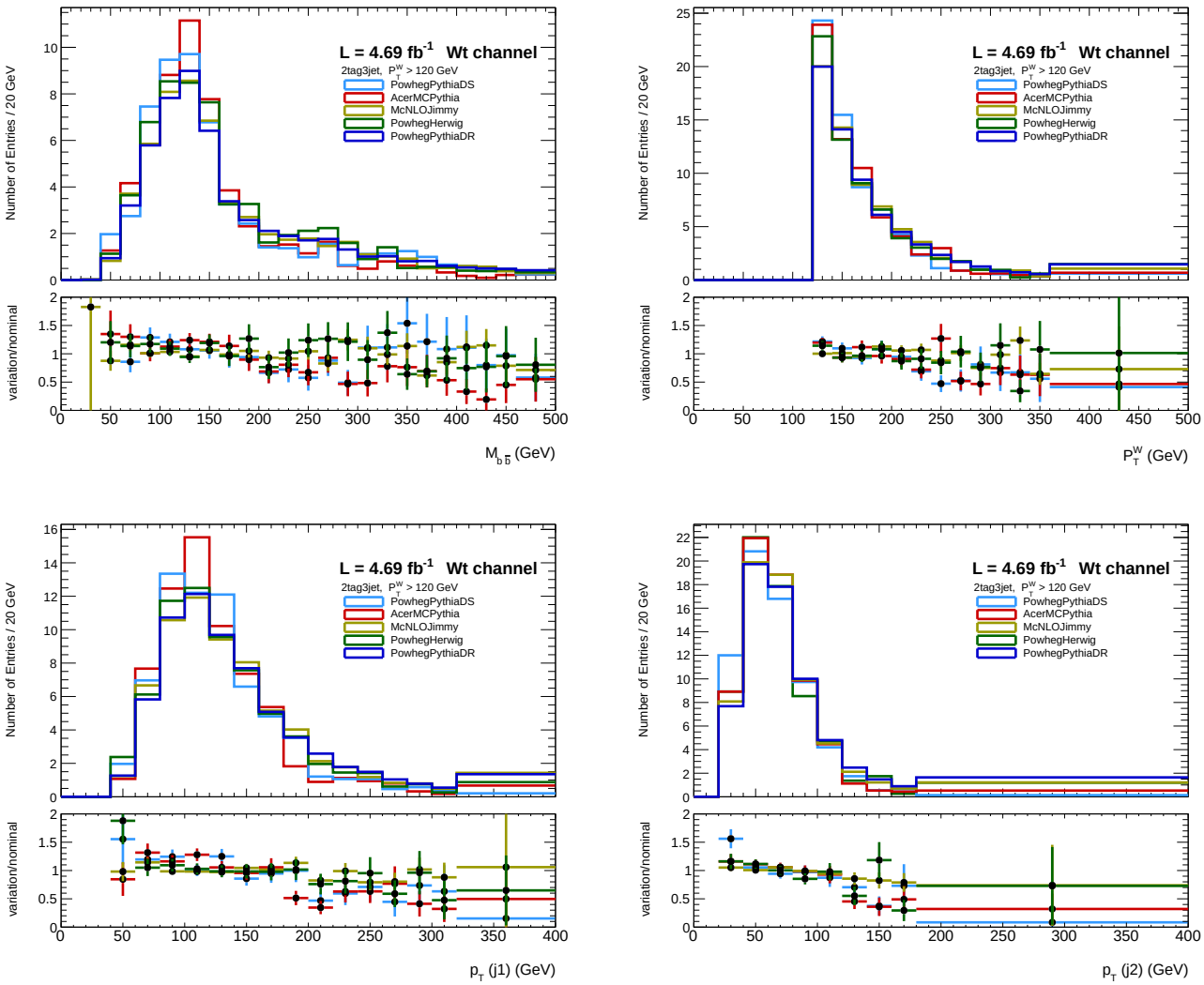

Figure 198: Distributions of Wt-channel single top variables used in 1-lepton events for $p_{\mathrm{T}}^{W} > 120$ GeV with 2 b-tag and 3 jets. From left to right: Row 1 - m_{bb} and p_{T}^{W}. Row 2 - leading then sub-leading jet p_{T}.

N $t\bar{t}$ modeling

Many generator comparison studies were performed to understand the *ttbar* modeling. The most important differences were used to derive a set of systematics which are given in more detail here. A large variety of generators and modifications of those generators are available. The list of generators considered is shown in Table 31 and the list of systematics used is described in Section 5.2.1.3 as well as summarized in Section 8.3. Comparisons and checks from where systematics were not derived are also described in the following along with explanations as to why these were not considered for the analysis. In practice, the Top group recommendations for comparisons was followed expect in the following cases were the comparison was not considered at all:

- *Compare samples with varied renormalization and factorization scales.* In this case only EvtGen files are available which adds some additional complication and reduces the comparability with the other tests which all use files with information on the reconstruction level. For a future analysis it would be useful to investigate the influence of the renormalization and factorization scale.
- *Compare to Sherpa with massive c/b quarks.* These samples have been shown to not model basic kinematic distributions such as lepton p_{T} and jet multiplicity. In addition these samples do not include tau final states and limited statistics are available.
- *Compare to $t\bar{t}$ without spin corrections.* This study should lead to no gain from since spin correlations are included in the Standard Model.
- *Compare to $t\bar{t}$ without modified branching ratios.* This study should lead to no gain since the assumptions for the modified BRs are unrealistic, e.g. BR($t \to b$)=0.5.
- *Compare to $t\bar{t}$ with top mass variations.* This study should lead to no gain since the top mass is sufficiently well known.
- *Compare FullSim to AFII for baseline PowHeg+Pythia.* FullSim has very limited statistics and this difference is already at the object level.

The 1-lepton MVA selection with 2 b-tags was used in the following and the derived systematics are applied to all channels in both the dijet mass and MVA analysis unless otherwise noted. The input variables to the BDT are compared between the generators. A ratio of the most discrepant variable is taken and used to reweight the events. After the reweighting, a ratio of the next most discrepant variables is used for another reweighting. This continues until all shape differences on the BDT are covered. Each ratio used as a reweighting is then taken as a separate systematics.

N.1 m_{bb} systematic

As m_{bb} is the most important variable in both versions of the analysis therefore a careful check is in order. For this a comparison was made between all considered generators for the regions which are relevant to the analysis — those are the region with 2 jets and 3 jets and in both cases exactly two b-tagged jets are required. These regions are again separated into a high and low p_{T}^{W} region (p_{T}^{W}¿120 GeVand p_{T}^{W}¡120 GeVrespectively). Plots of the comparisons for all regions are shown in Figure 199. From the ratios shown at the bottom of each plot, it was concluded that ALPGEN+PYTHIA (magenta) has the largest difference to the nominal. Also POWHEG+PYTHIA with the HERAPDF set (violet) shows significant deviation but those are dominated by statistical fluctuations due to the limited statistics available. Therefore ALPGEN+PYTHIA was used to derive a systematics uncertainty. The influence of the top p_{T} correction, which was applied to the nominal sample, was tested on ALPGEN+PYTHIA and shown in Figure 200. Details on the ALPGEN+PYTHIA top p_{T} reweighting are given in Appendix Section N.3. Since the top p_{T}

reweighting has a negligible effect on the m_{bb} shape in the range of $0 < m_{bb} < 200$ GeV for the 2-jet events and $0 < m_{bb} < 300$ GeV for the 3-jet events, the systematic uncertainty was derived in this range the full difference between ALPGEN+PYTHIA without the top p_{T} correction to POWHEG+PYTHIA with the top p_{T} correction. This difference for all regions is shown in Figure 201. Linear fits (Table **??**) were performed in the above mentioned m_{bb} ranges and used as systematic uncertainties.

The plots in Figure 201 as well as the fitted functions show that the slopes are opposite for the 2 and 3-jet region. Therefore a combined systematic uncertainty for the 2 and 3-jet region cannot be derived. Furthermore the systematic effect is significantly larger for $p_{\mathrm{T}}^{W} > 120$ GeV so four different fits are needed but the effect is correlated in all four regions in all channels.

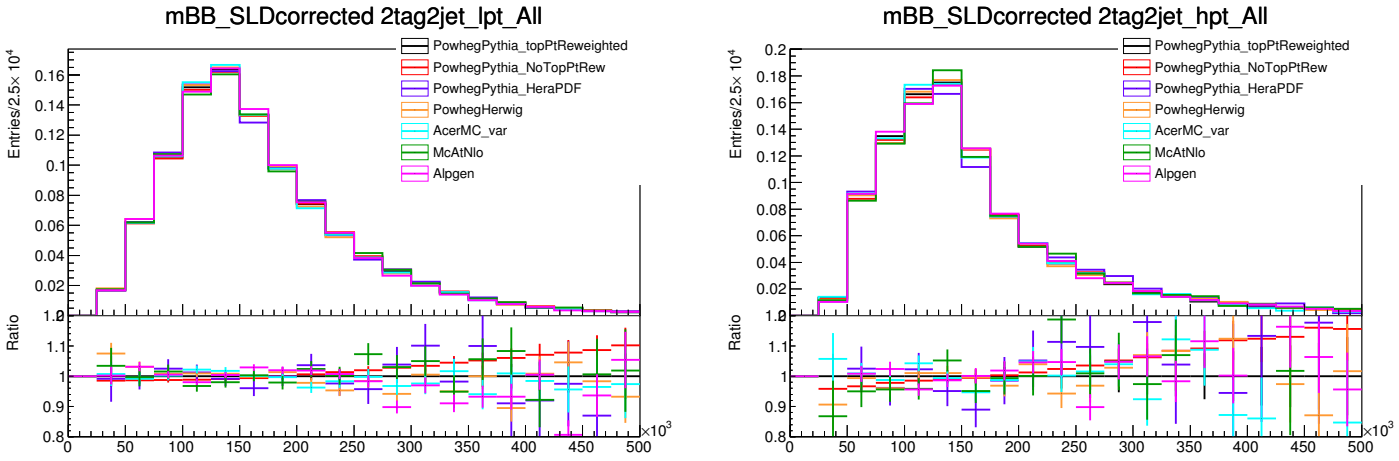

(a) 2-jet

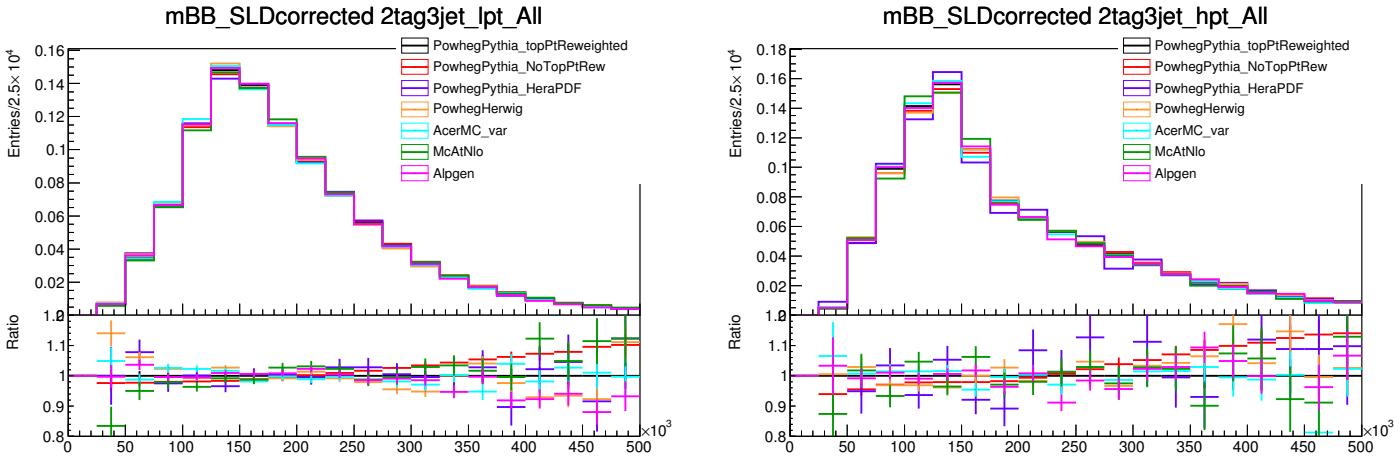

(b) 3-jet

Figure 199: 1-lepton 2 and 3-jet 2-tag MC comparisons for the $t\bar{t}$ m_{bb} systematic. The largest difference is between POWHEG+PYTHIA and ALPGEN+PYTHIA and is taken as the systematic uncertainty. $p_{\mathrm{T}}^{W} < 120$ GeV is shown on the left and $p_{\mathrm{T}}^{W} > 120$ GeV is shown on the right.

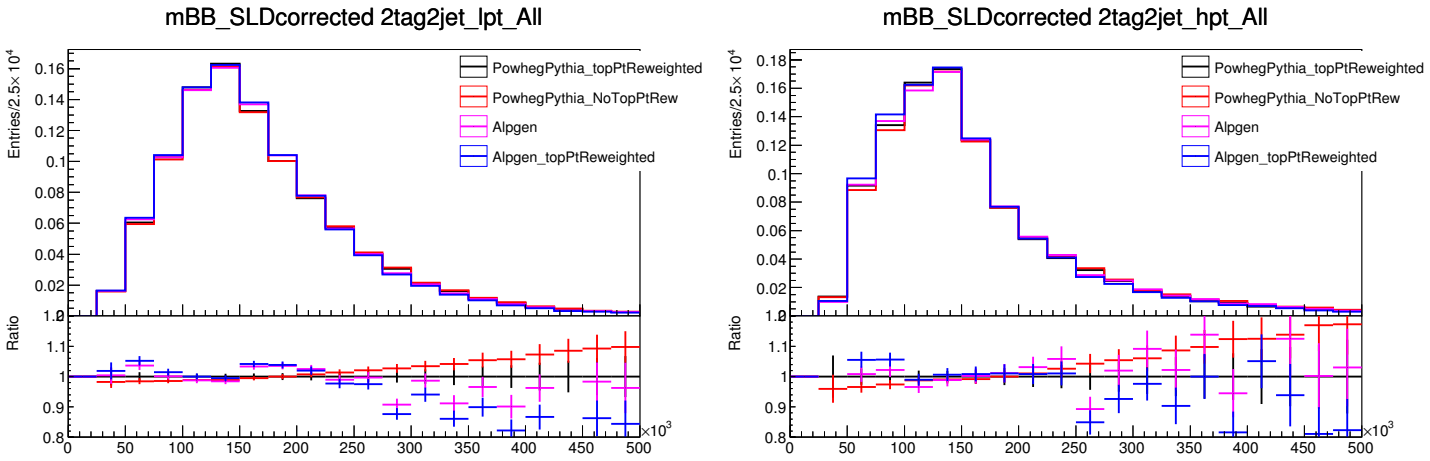

(a) 2-jet

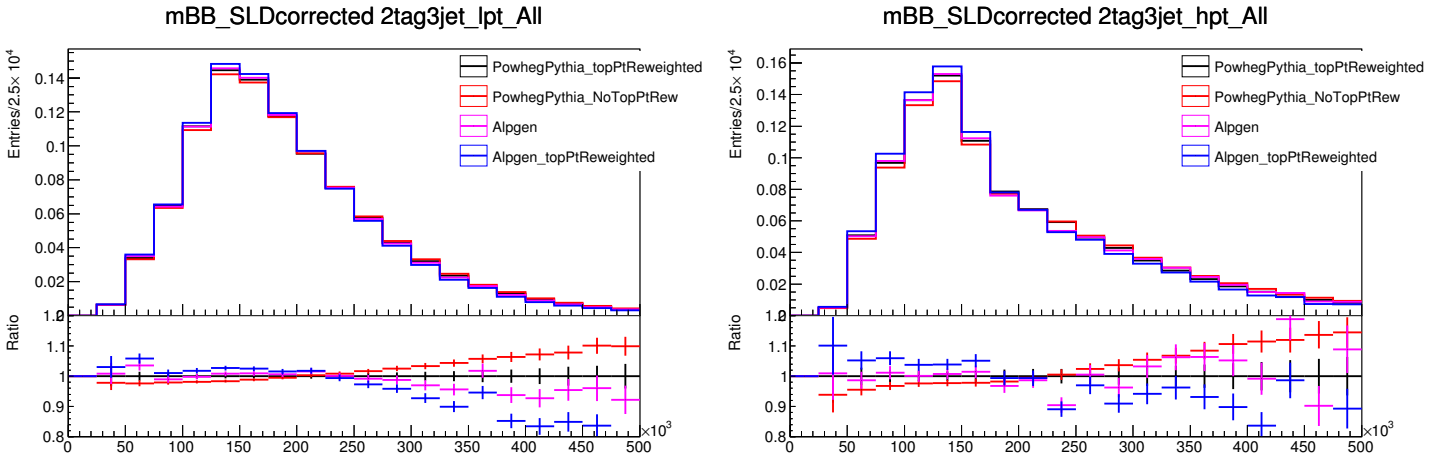

(b) 3-jet

Figure 200: 1-lepton 2 and 3-jet 2-tag MC comparisons for the $t\bar{t}$ m_{bb} systematic. ALPGEN+PYTHIA with and without the p_{T}^{top} correction is compared to POWHEG+PYTHIA with and without the same correction. $p_{\mathrm{T}}^{W} < 120$ GeV is shown on the left and $p_{\mathrm{T}}^{W} > 120$ GeV is shown on the right.

N.2 $E_{\mathrm{T}}^{\mathrm{miss}}$ systematic

After taking into account the coverage of the m_{bb} systematic described above, a systematic on the $E_{\mathrm{T}}^{\mathrm{miss}}$ shape was found to be necessary. Similar to m_{bb}, a comparison was made between all considered generators for the relevant analysis regions shown in Figure 202. From the ratio plots shown on the bottom of each plot it was concluded that ALPGEN+PYTHIA (magenta) again has the largest difference to the nominal and therefore was used to derive a systematics uncertainty. The influence of the top p_{T} correction, which was applied nominally in the analysis to POWHEG+PYTHIA, was tested on ALPGEN+PYTHIA and are shown in Figure 203. Since the top p_{T} reweighting has a small effect on ALPGEN+PYTHIA in the $E_{\mathrm{T}}^{\mathrm{miss}}$ distribution the full difference between ALPGEN+PYTHIA without the top p_{T} correction to POWHEG+PYTHIA with the correction was used. This difference for all regions is shown in Figure 201 (b) and (c). The (linear) fits for the 2 and 3-jet region agree amongst each other within the fitting errors so the regions were combined. After the combination (Figure 201a) the difference between ALPGEN+PYTHIA and POWHEG+PYTHIA

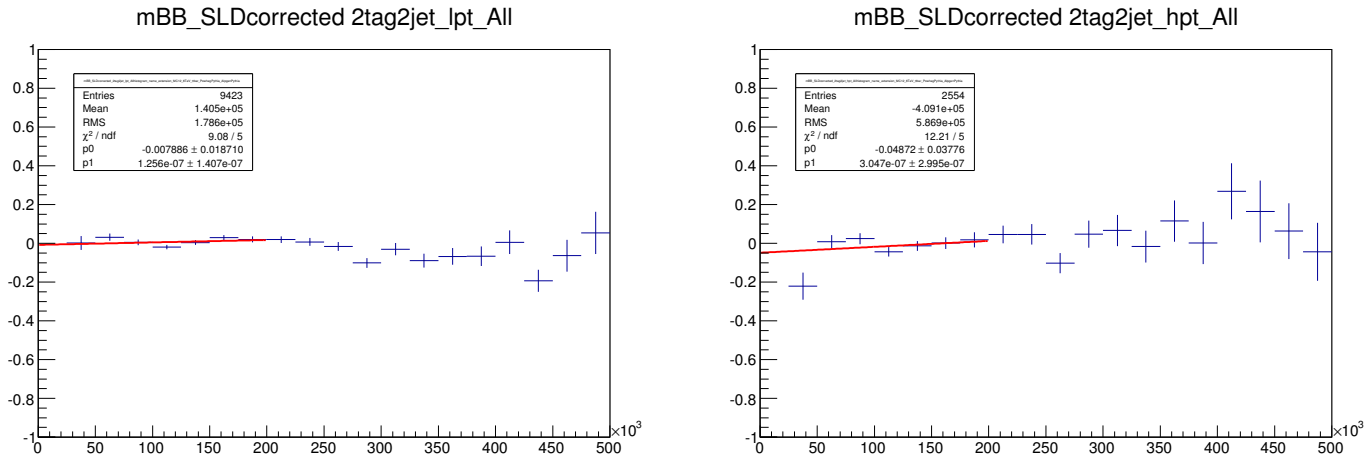

(a) 2-jet

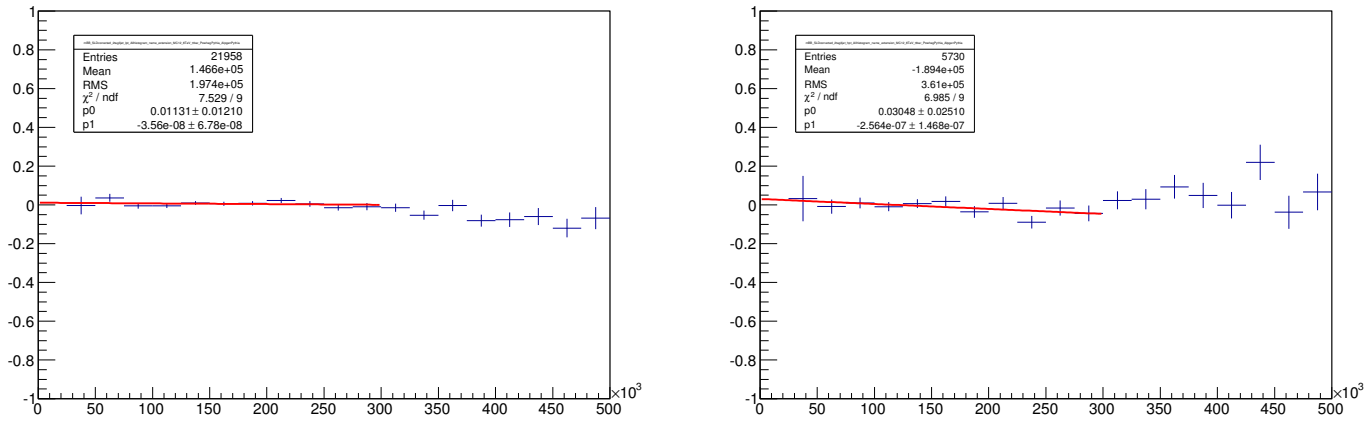

(b) 3-jet

Figure 201: 1-lepton 2 and 3-jet 2-tag m_{bb} systematic for $t\bar{t}$. The fit is made to the ratio of ALPGEN+PYTHIA without the p_{T}^{top} correction and POWHEG+PYTHIA with the p_{T}^{top} correction. $p_{\mathrm{T}}^{W} < 120$ GeV is shown on the left and $p_{\mathrm{T}}^{W} > 120$ GeV is shown on the right.

follows a second order polynomial which is different for the low and high p_{T}^{W}. Therefore the combination of the different p_{T}^{W} regions was not done. Table **??** contains the exact values of the polynomial fit to these points. This systematic is only applied to 1-lepton events since $E_{\mathrm{T}}^{\mathrm{miss}}$ itself if very different in each analysis. It is correlated in all 1-lepton regions. The functions are only valid up to 300 GeV. Above this value they are constant to maintain a reasonable size in the tail of the $E_{\mathrm{T}}^{\mathrm{miss}}$ distribution.

N.3 top p_{T} reweighting of ALPGEN+PYTHIA

As described in Section 5.2.1.2 it was found that the p_{T} of the top is modeled incorrectly in POWHEG+PYTHIA which lead to a correction based on comparisons with the ATLAS 7 TeVdata [59]. It can be assumed that similar mismodelings are also present in other generators. While deriving $t\bar{t}$ systematics a top p_{T} reweighting was applied to the generator which shows the largest difference to the nominal and from which the systematic uncertainties for m_{bb} and $E_{\mathrm{T}}^{\mathrm{miss}}$ were derived. This allows to see the effect of the

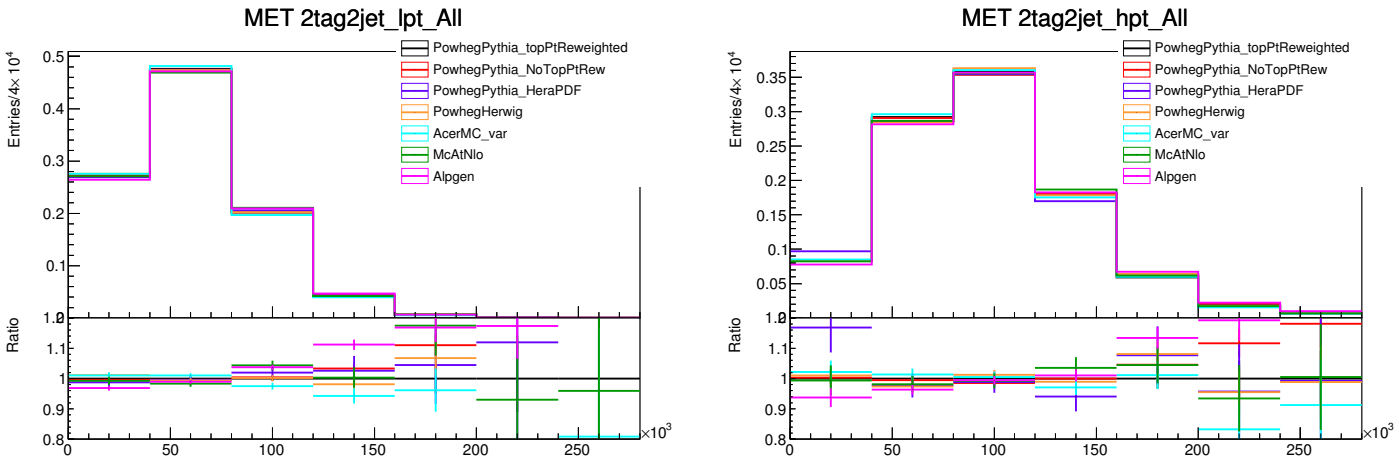

(a) 2-jet

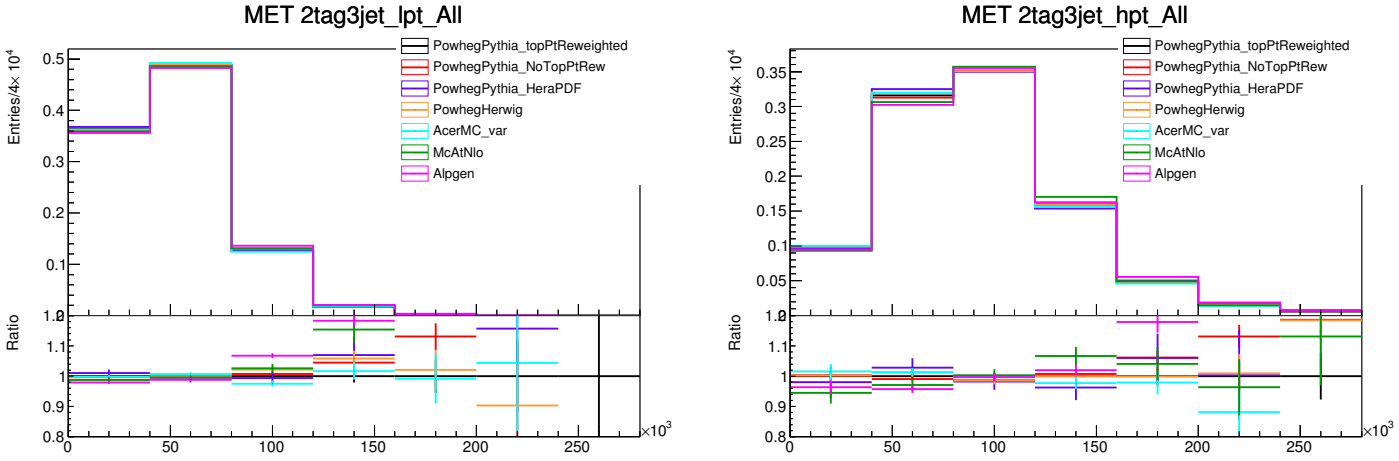

(b) 3-jet

Figure 202: 1-lepton 2 and 3-jet 2-tag MC comparisons for the $t\bar{t}$ $E_{\mathrm{T}}^{\mathrm{miss}}$ systematic. The largest difference is between PowHeg+Pythia and alpgen+Pythia and is taken as the systematic uncertainty. $p_{\mathrm{T}}^{W} < 120$ GeV is shown on the left and $p_{\mathrm{T}}^{W} > 120$ GeV is shown on the right.

top p_{T} reweighting on alpgen+Pythia. Since no official top p_{T} reweighting function is provided for alpgen+Pythia the function for PowHeg+Pythia was used. Before this was done, alpgen+Pythia was reweighted to PowHeg+Pythia according to the distributions of the average p_{T} of the two truth tops. This leads to a binned reweighting for the combination of the 2 and 3-jet region also combined in high and low p_{T}^{W}. The reweighting distribution is shown in Figure 205.

For future analyses at may be useful to redo this study with dedicated top p_{T} reweighting strategies for all $t\bar{t}$ generators.

N.4 The 2-to-3-jet and high-to-low-p_{T}^{W} uncertainties

The categorization of the analysis in terms of the number of jets and the p_{T}^{W} is dependent on the modeling of these properties in the different $t\bar{t}$ generators. The ratio of 3-to-2 jet production as well as low-to-high p_{T}^{W} production was checked for the generator dependence. Table 98 shows the ratio of these quantities for

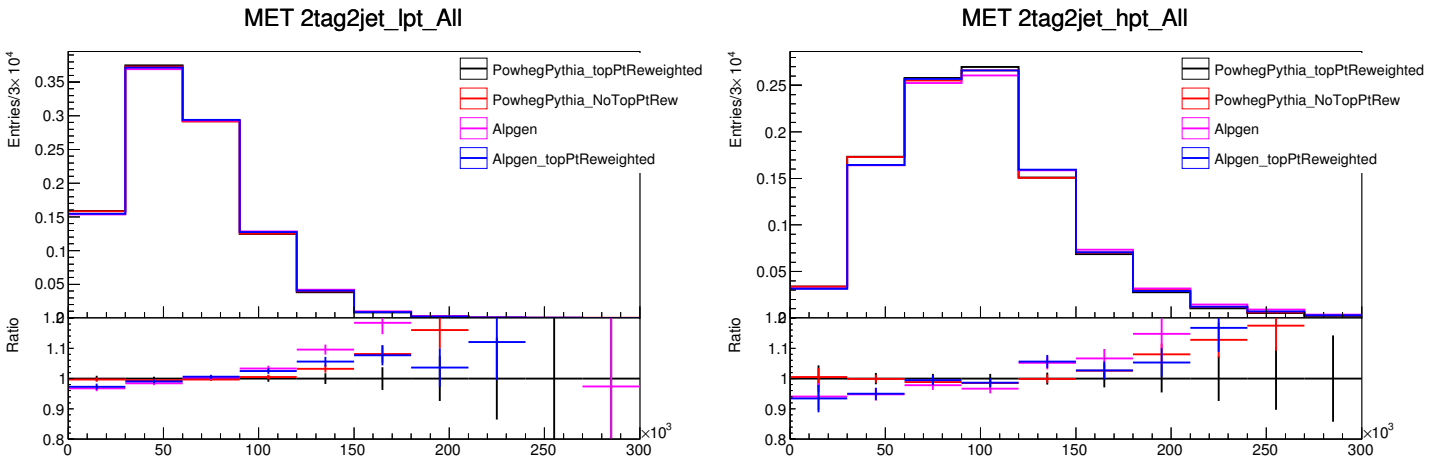

(a) 2-jet

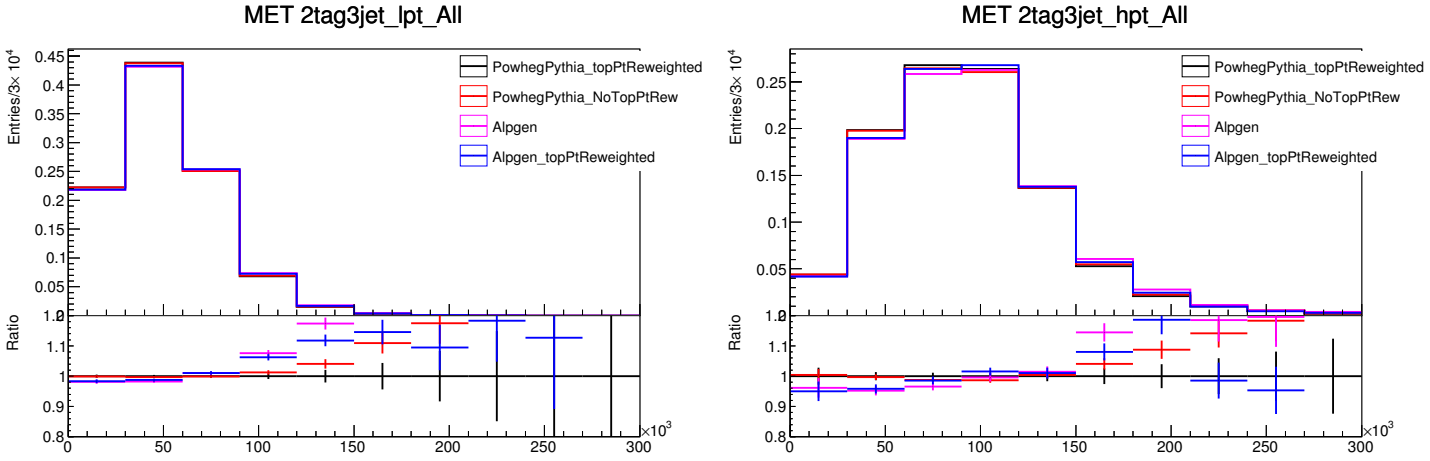

(b) 3-jet

Figure 203: 1-lepton 2 and 3-jet 2-tag MC comparisons for the $t\bar{t}$ $E_{\mathrm{T}}^{\mathrm{miss}}$ systematic. ALPGEN+PYTHIA with and without the p_{T}^{top} correction is compared to POWHEG+PYTHIA with and without the same correction. $p_{\mathrm{T}}^{W} < 120$ GeV is shown on the left and $p_{\mathrm{T}}^{W} > 120$ GeV is shown on the right.

the given generators. The uncertainty was derived from the largest difference which is ALPGEN+PYTHIAin both cases.

N.5 Flavor compositions of the $t\bar{t}$ generators

The flavor composition of the $t\bar{t}$ sample is not only important for the nominal sample which was used in the analysis but also for the generators which were used to derive the systematics uncertainties. Table 99 shows the flavor fractions of all considered generators amd the general agreement amongst the set. The fraction of *bc* events increases while the fraction of *bb* decreases from the low to high p_{T}^{W} region. The difference between the 2 and 3 jet region is non-significant for the *bb* and *bc* fraction and the *bl* fraction in the 3 jet region shows only a small decrease. The largest difference to the nominal in *bb* and *bc* comes from ALPGEN+PYTHIA. ALPGEN+PYTHIA predicts a larger fraction of *bb* and smaller fraction *bc* events than the other generators. The fraction of *bl* events agree quite well between the generators. Since there are

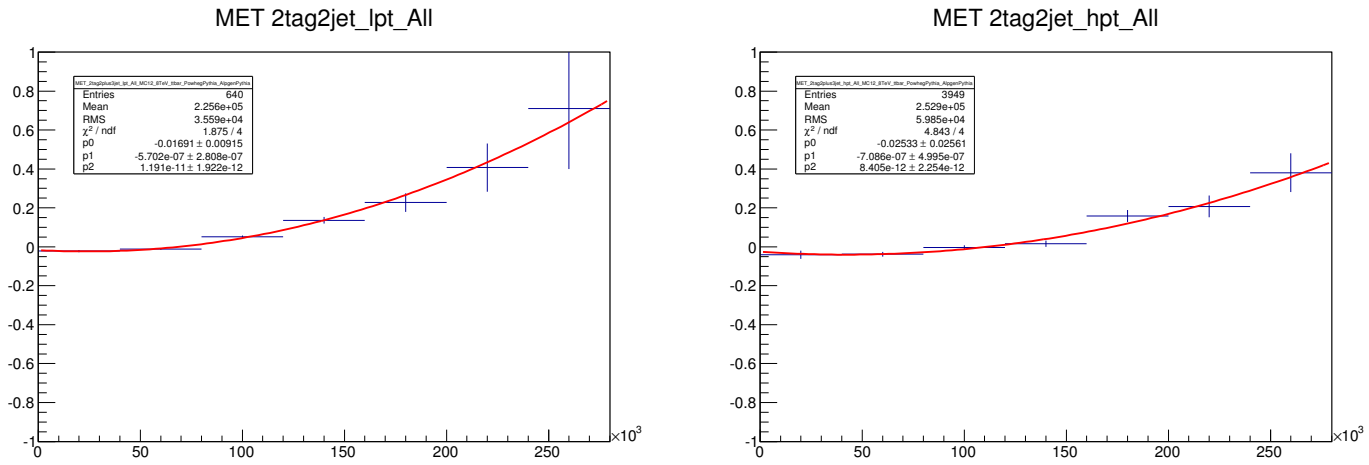

(a) 2 and 3 jet combined

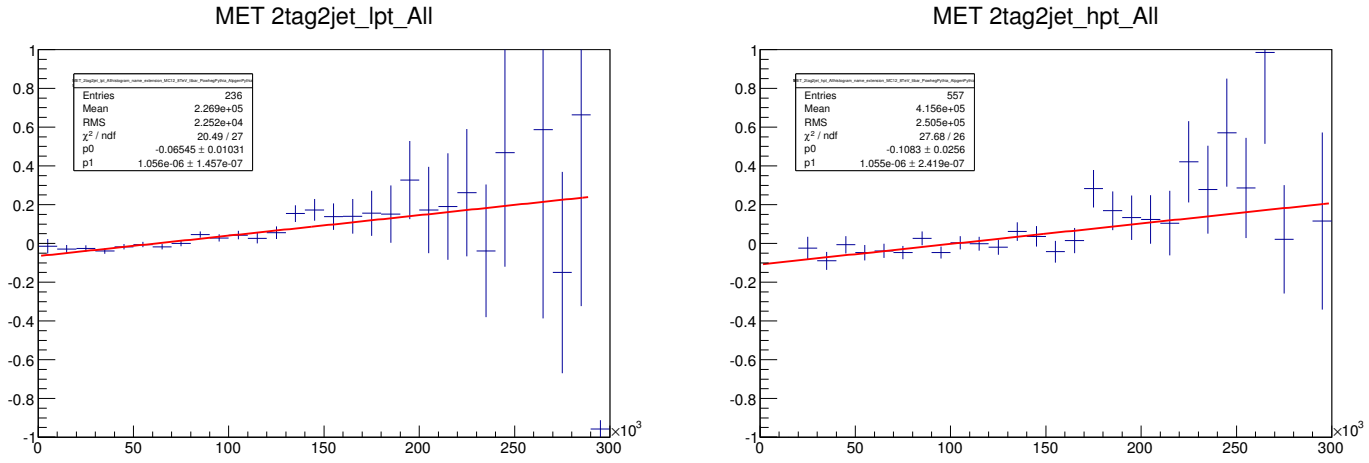

(b) 2 jet

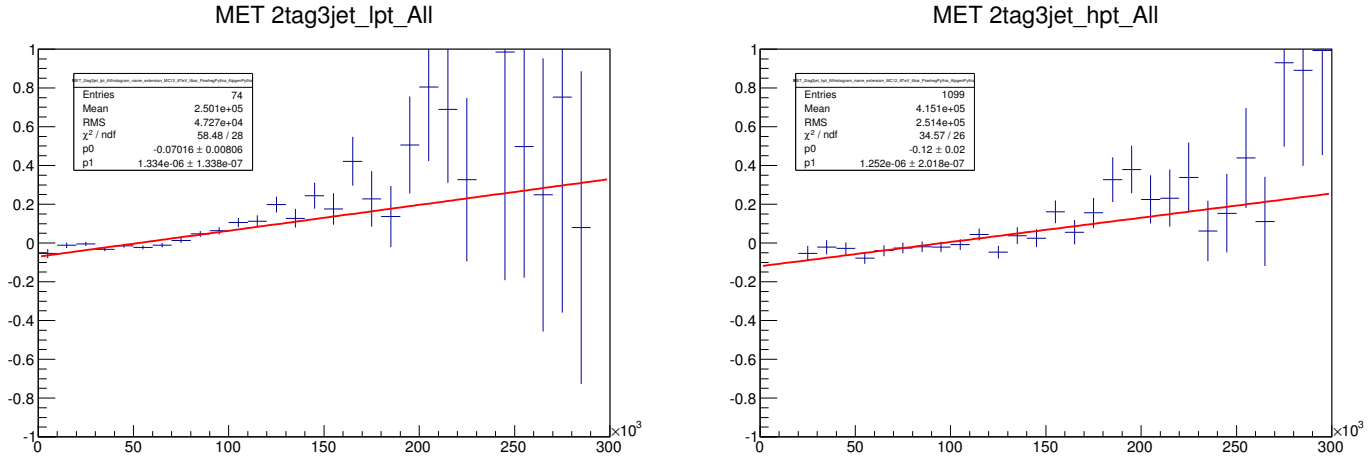

(c) 3 jet

Figure 204: 1-lepton $E_{\mathrm{T}}^{\mathrm{miss}}$ systematic for $t\bar{t}$ (a) 2+3-jet 2-tag which is used in the analysis, (b) only 2 jet 2-tag, (c) only 3 jet 2-tag . The fit is made to the ratio of ALPGEN+PYTHIA without the p_{T}^{top} correction and POWHEG+PYTHIAwith the p_{T}^{top} correction. $p_{\mathrm{T}}^{W} < 120$ GeV is shown on the left and $p_{\mathrm{T}}^{W} > 120$ GeV is shown on the right.

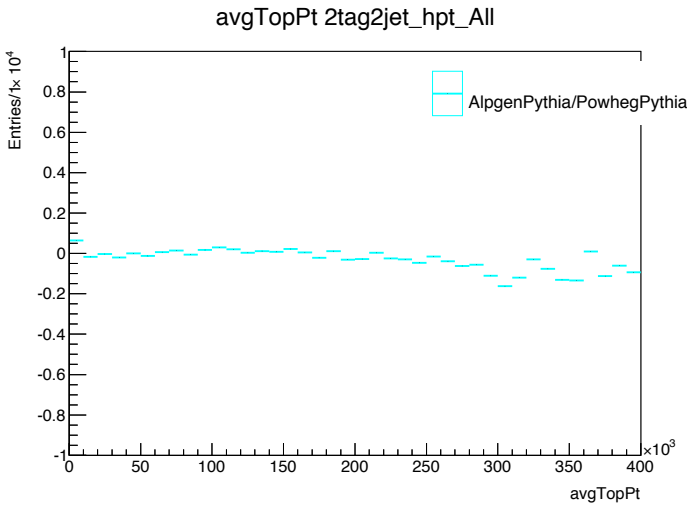

Figure 205: 1-lepton, 2+3 jet and low+high p_{T}^{W} distribution of the average top p_{T} of the two truth tops for the ratio between ALPGEN+PYTHIA and POWHEG+PYTHIA subtracted by 1. It was used to reweight ALPGEN+PYTHIA to apply the POWHEG+PYTHIA top p_{T} reweighting afterward.

Generator	3 jet/2 jet	ratio to POWHEG+PYTHIA	high p_{T}^{W} /low p_{T}^{W}	ratio to POWHEG+
PowhegPythia with top p_{T} reweighting	1.854	1.00	0.193	1.00
MC@NLO	1.872	1.01	0.207	1.07
PowhegHerwig	1.890	1.019	0.191	0.99
PowhegPythia with HERAPDF	1.841	0.99	0.197	1.02
AlpgenPythia	1.481	0.80	0.208	1.08

Table 98: $t\bar{t}$ 3-to-2-jet and high-to-lowp_{T}^{W} uncertainties. In both cases the uncertainty was derived from the largest difference to the nominal. This is ALPGEN+PYTHIA for the 3-to-2-jet uncertainty as well as for the high-to-lowp_{T}^{W} uncertainty.

significant differences in the fractions of bb and bc events between ALPGEN+PYTHIA and POWHEG+PYTHIAit was investigated if this leads to a difference in the shapes of kinematic variables. Figure 206 and 207 show the these shape comparisons for m_{bb} for bb, bc and bl events. Within the statistical fluctuations no significant difference between the shapes is observable. When the top p_{T} reweighting is applied to ALPGEN+PYTHIA these differences are even smaller.

N.6 Generator variations of the BDT input variables

For the determination of the shape systematics the spread between all considered $t\bar{t}$ generators for the different BDT input variables was investigated. As described in Sec 5.2.1.3 systematics have been assigned according to the generator differences in m_{bb} and $E_{\mathrm{T}}^{\mathrm{miss}}$. All other variables did not show significant differences between the generators or the differences were already covered by the systematics for top p_{T} m_{bb} and $E_{\mathrm{T}}^{\mathrm{miss}}$. Fig 208-212 show the generator differences for the remaining BDT input variables for the 1-lepton channel for the 2 and 3 jet region.

Generator	Jet Flavors	p_{T}^{W} GeV 0-120	>120
	2 jets, 2-tag		
PowhegPythia with top p_{T} reweighting	bb	79.8	67.3
	bc	11.5	20.4
	bl	8.5	11.6
MC@NLO	bb	81.9	68.5
	bc	9.8	19.5
	bl	8.1	11.5
PowhegHerwig	bb	80.6	67.6
	bc	11.1	19.9
	bl	8.1	11.9
PowhegPythia with HERAPDF	bb	79.7	70.0
	bc	11.6	18.9
	bl	8.6	10.7
AlpgenPythia	bb	84.4	74.8
	bc	6.7	12.7
	bl	8.8	11.9

	Jet Flavors	p_{T}^{W} GeV 0-120	>120
	3 jets, 2-tag		
PowhegPythia with top p_{T} reweighting	bb	81.1	66.0
	bc	12.5	23.0
	bl	6.3	10.4
MC@NLO	bb	82.1	67.3
	bc	11.5	21.8
	bl	6.3	10.2
PowhegHerwig	bb	81.8	66.3
	bc	11.8	21.9
	bl	6.3	11.1
PowhegPythia with HERAPDF	bb	81.5	65.7
	bc	12.3	22.9
	bl	6.1	10.8
AlpgenPythia	bb	83.6	70.5
	bc	9.6	17.8
	bl	6.7	11.0

Table 99: The fraction of jet flavor pairs in the 1-lepton analysis from events with two and three jets as a function of p_{T}^{W} for all $t\bar{t}$ generators which were considered for deriving the systematics.

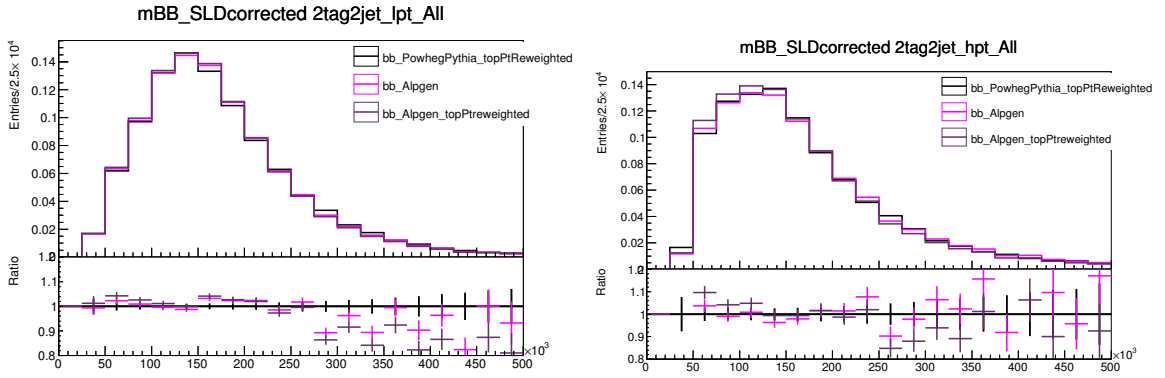

(a) *bb*, 2-jet

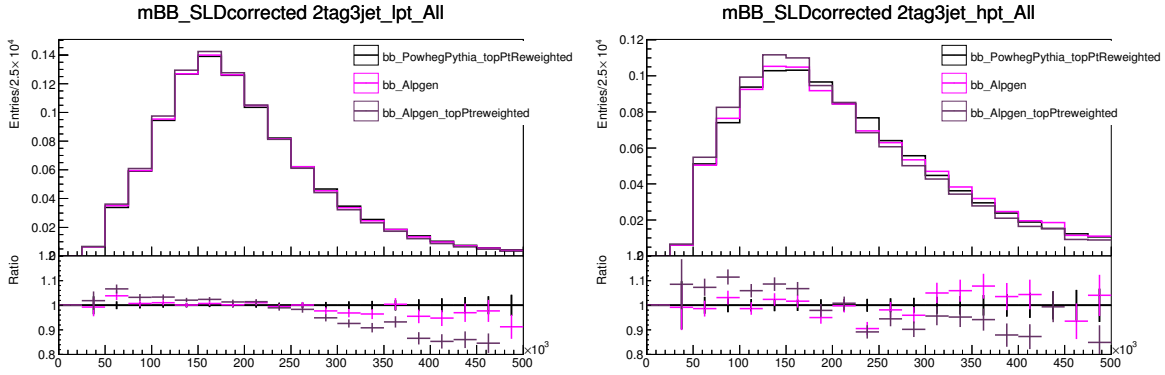

(b) *bb*, 3-jet

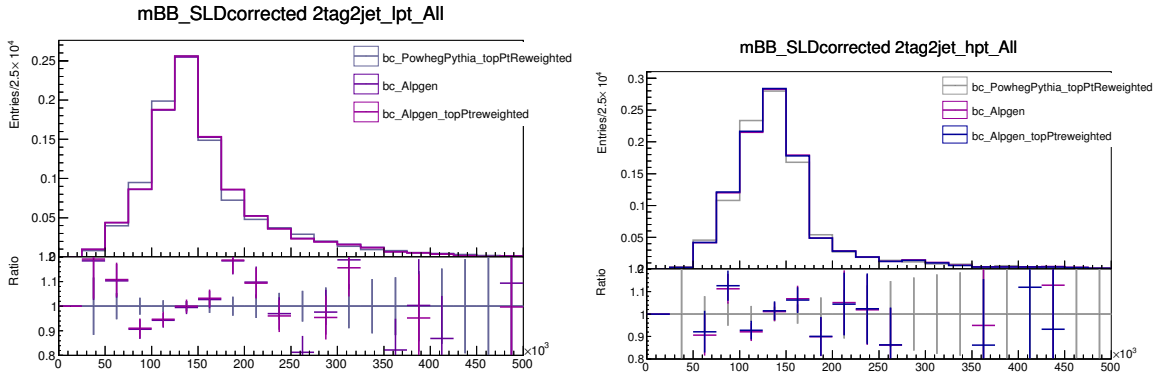

(c) *bc*, 2-jet

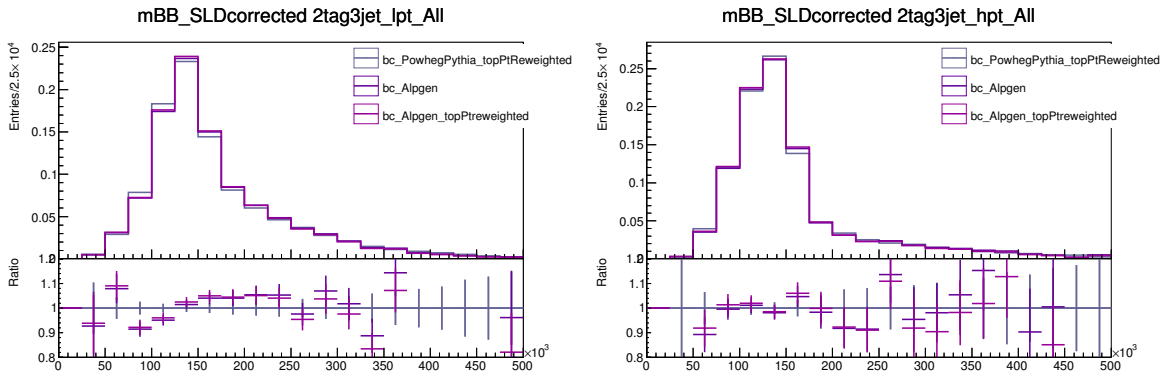

(d) *bc*, 3-jet

Figure 206: $t\bar{t}$ comparison of m_{bb} shapes between ALPGEN+PYTHIA with and without the top p_{T}reweighting and POWHEG+PYTHIA with the top p_{T} reweighting splitted into *bb* and *bc* events. No significant difference is observable.

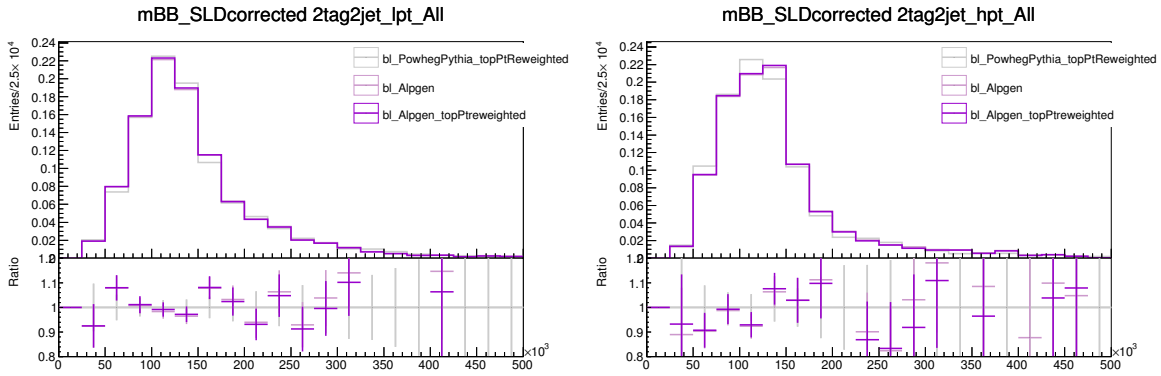

(a) *bl*, 2-jet

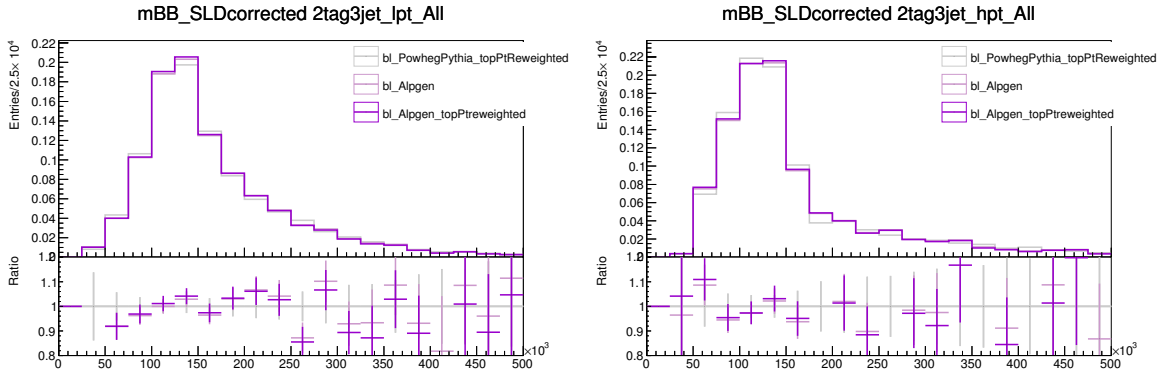

(b) *bl*, 3-jet

Figure 207: $t\bar{t}$ comparison of m_{bb} shapes between ALPGEN+PYTHIA with and without the top p_{T}reweighting and POWHEG+PYTHIA with the top p_{T} reweighting splitted for *bl* events. No significant difference is observable.

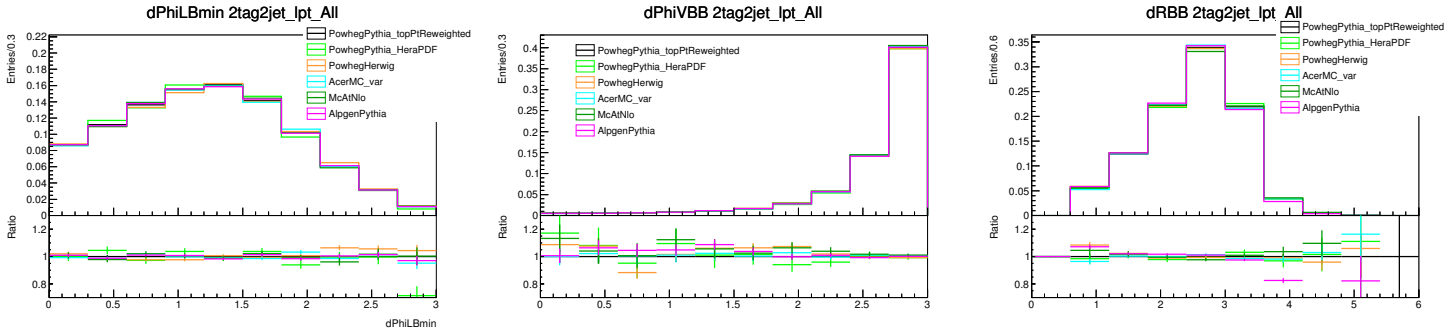

(a) from left to right: min. $\Delta\phi$(l,b), $\Delta\phi$(V,bb), ΔR(b,b)

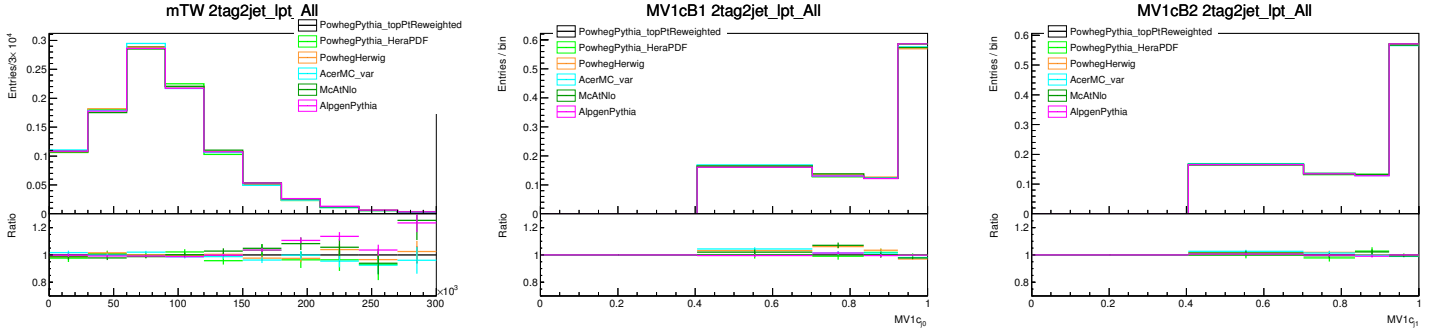

(b) from left to right: m_{T}^{W}, MV1c(b1), MV1c(b2)

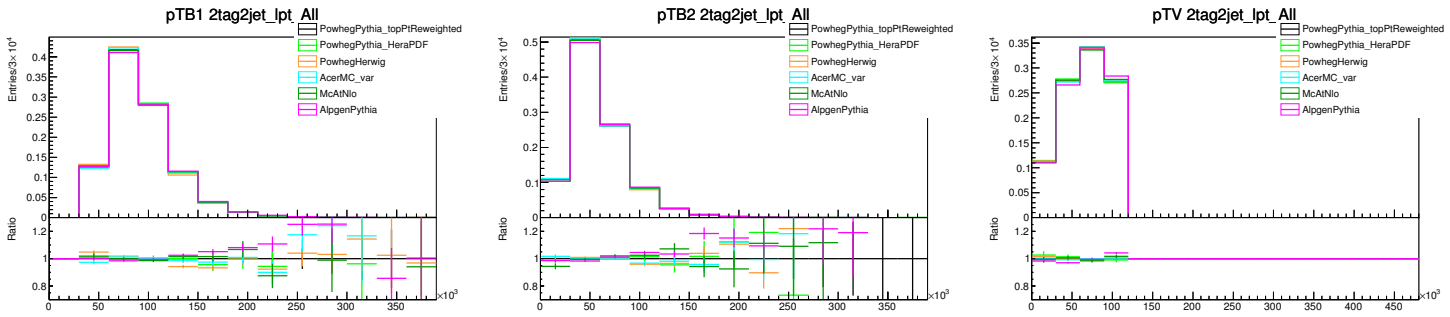

(c) from left to right: p_{T}(b1), p_{T}(b2), p_{T}^{W}

Figure 208: $t\bar{t}$ generator comparisons in the 2 jet region for low p_{T}^{W} for the BDT input variables (from left to right): min. $\Delta\phi$(l,b), $\Delta\phi$(V,bb), ΔR(b,b) (first row), m_{T}^{W}, MV1c(b1), MV1c(b2) (second row), p_{T}(b1), p_{T}(b2), p_{T}^{W} (third row); the effects were either already covered by the systematics or considered as negligible.

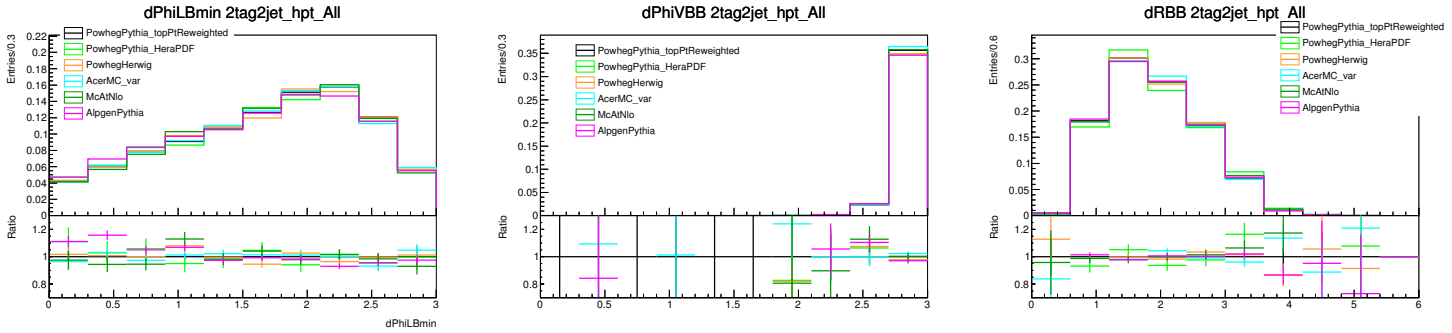

(a) from left to right: min. $\Delta\phi$(l,b), $\Delta\phi$(V,bb), ΔR(b,b)

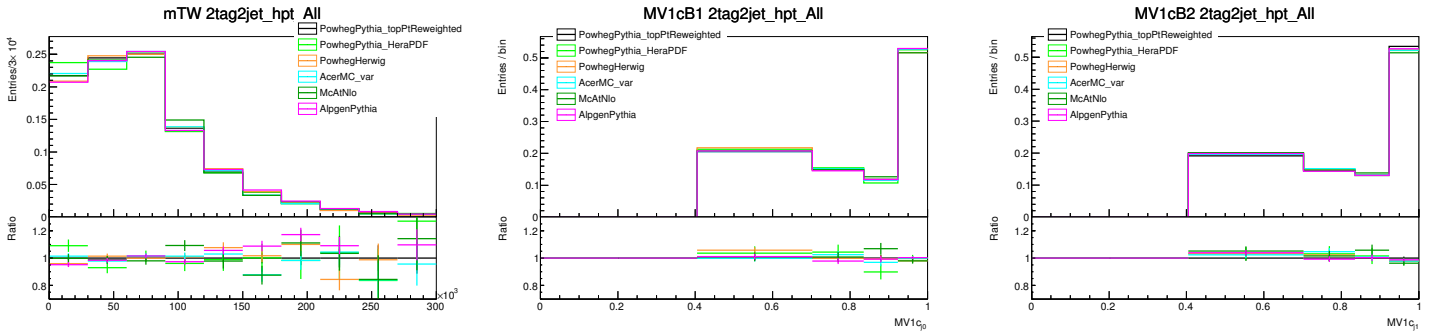

(b) from left to right: m_{T}^{W}, MV1c(b1), MV1c(b2)

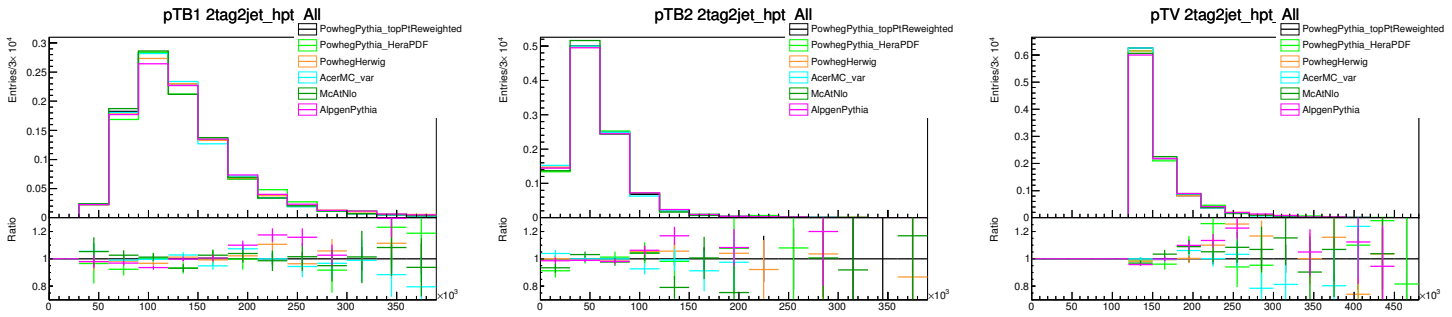

(c) from left to right: p_{T}(b1), p_{T}(b2), p_{T}^{W}

Figure 209: $t\bar{t}$ generator comparisons in the 2 jet region for high p_{T}^{W} for the BDT input variables; the effects were either already covered by the systematics or considered as negligible.

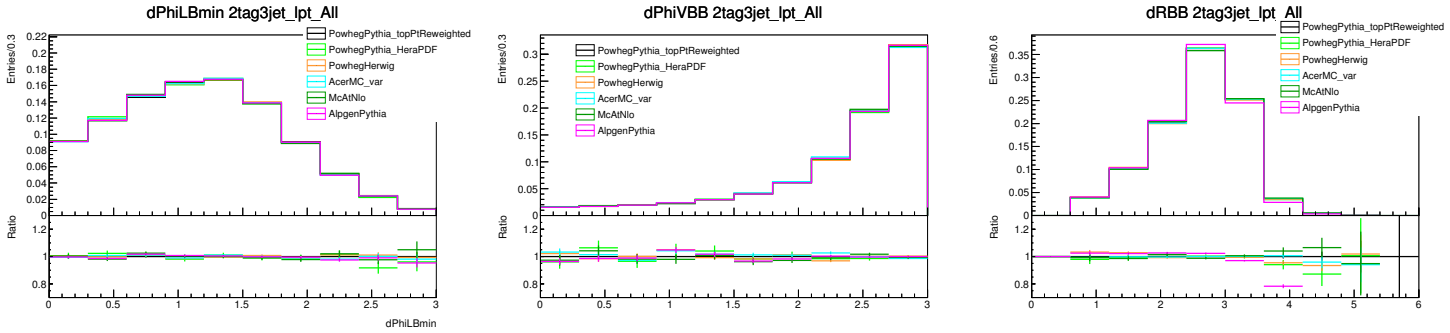

(a) from left to right: min. $\Delta\phi$(l,b), $\Delta\phi$(V,bb), ΔR(b,b)

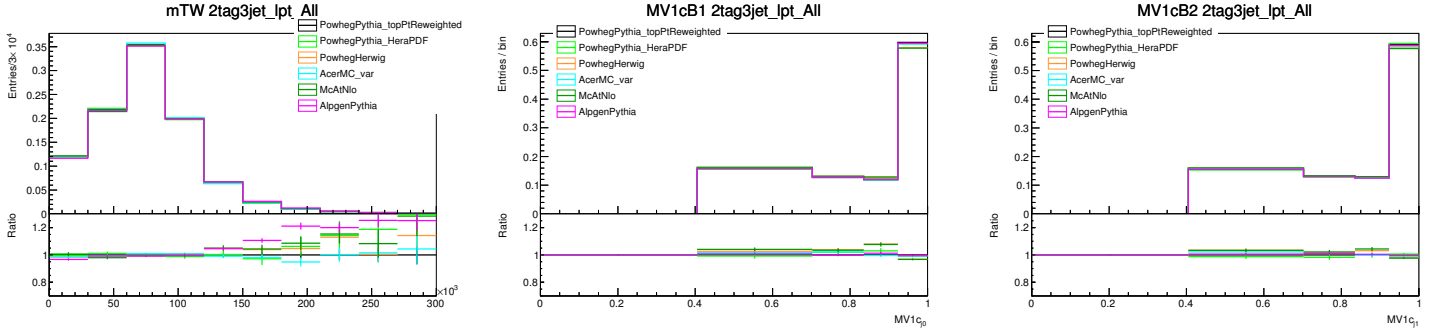

(b) from left to right: m_{T}^{W}, MV1c(b1), MV1c(b2)

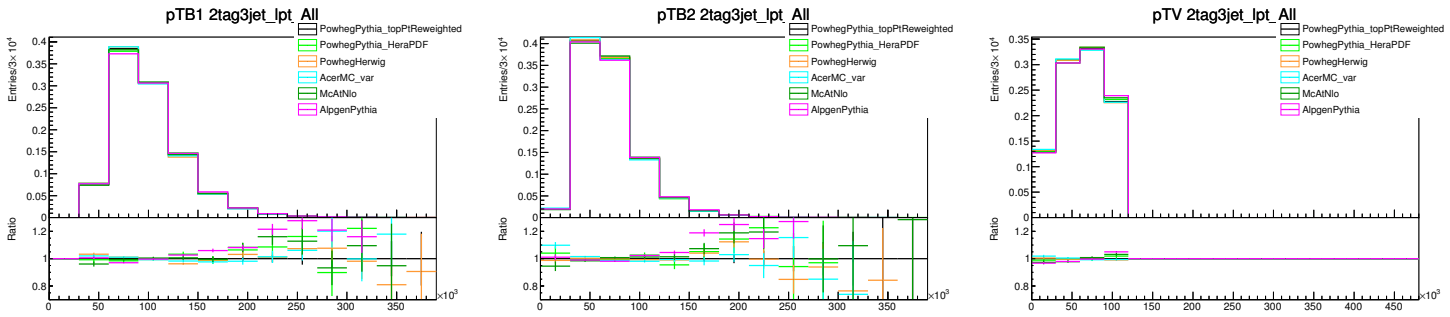

(c) from left to right: p_{T}(b1), p_{T}(b2), p_{T}^{W}

Figure 210: $t\bar{t}$ generator comparisons in the 3 jet region for low p_{T}^{W} for the BDT input variables (from left to right): min. $\Delta\phi$(l,b), $\Delta\phi$(V,bb), ΔR(b,b) (first row), m_{T}^{W}, MV1c(b1), MV1c(b2) (second row), p_{T}(b1), p_{T}(b2), p_{T}^{W} (third row); the effects were either already covered by the systematics or considered as negligible.

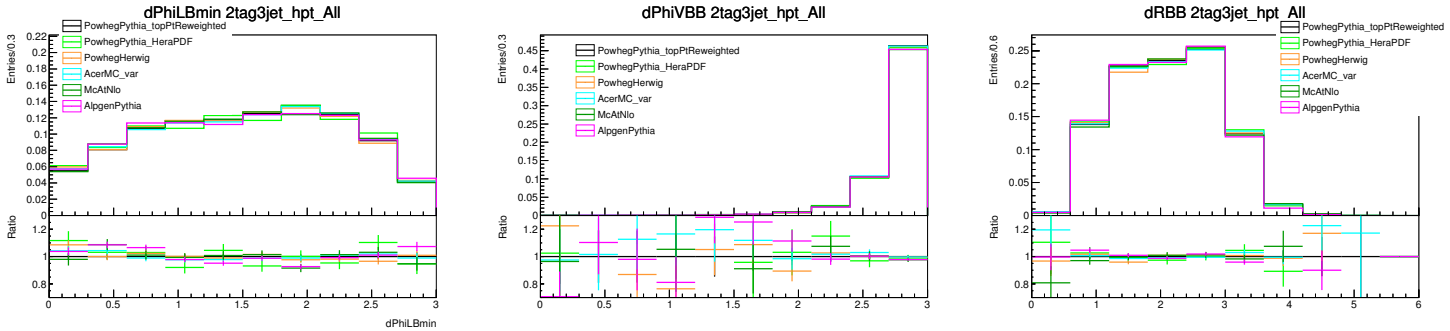

(a) from left to right: min. $\Delta\phi$(l,b), $\Delta\phi$(V,bb), ΔR(b,b)

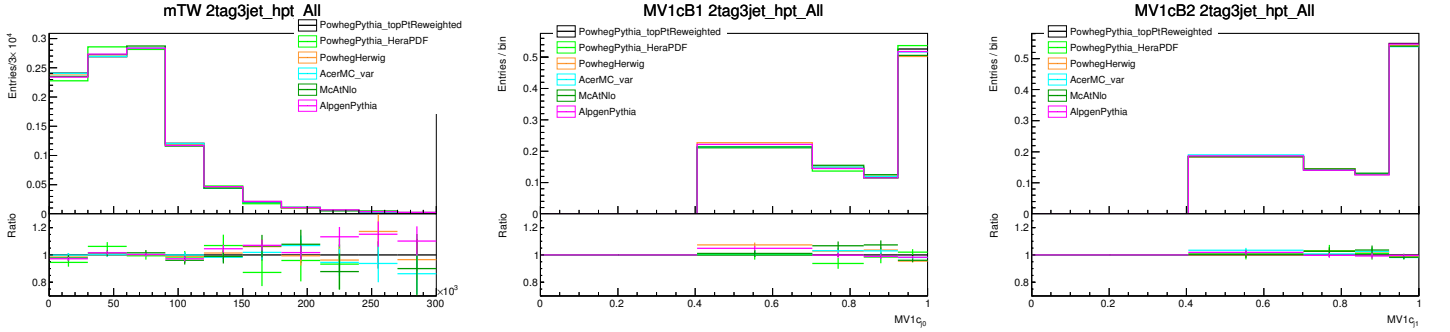

(b) from left to right: m_{T}^{W}, MV1c(b1), MV1c(b2)

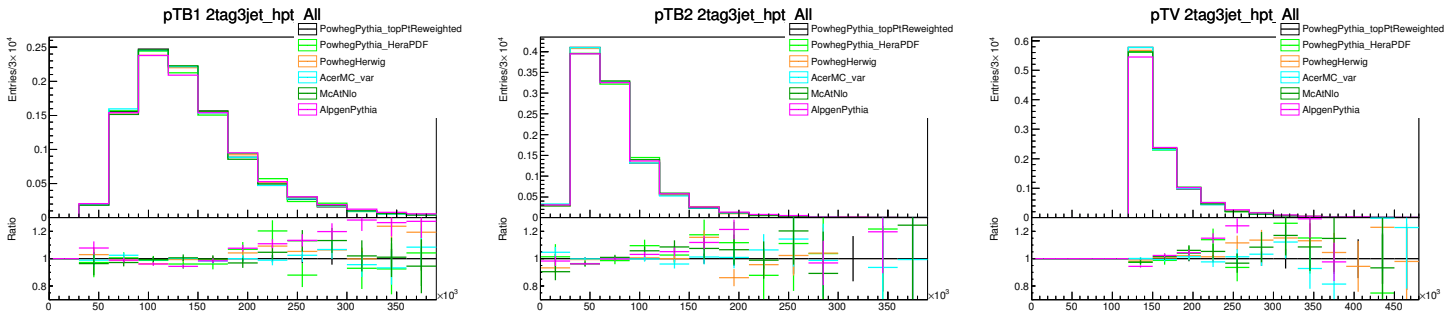

(c) from left to right: p_{T}(b1), p_{T}(b2), p_{T}^{W}

Figure 211: $t\bar{t}$ generator comparisons in the 3 jet region for high p_{T}^{W} for the BDT input variables (from left to right): min. $\Delta\phi$(l,b), $\Delta\phi$(V,bb), ΔR(b,b) (first row), m_{T}^{W}, MV1c(b1), MV1c(b2) (second row), p_{T}(b1), p_{T}(b2), p_{T}^{W}(third row); the effects were either already covered by the systematics or considered as negligible.

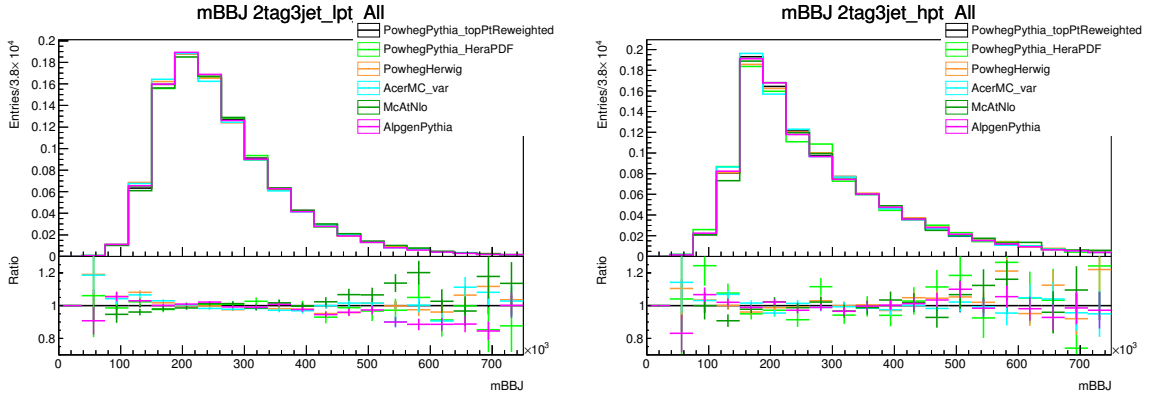

(a) m_{bbj}

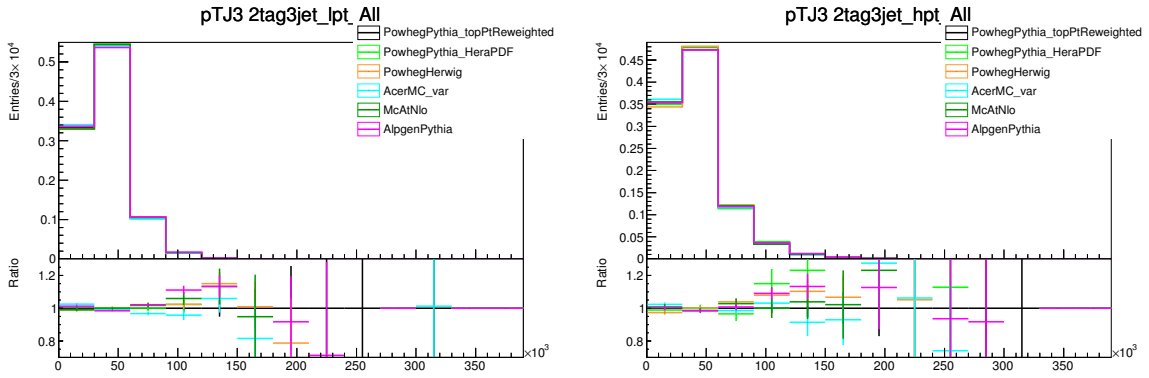

(b) p_{T}(j3)

Figure 212: $t\bar{t}$ generator comparisons for the additional BDT input variables for the 3 jet region in low and high p_{T}^{W} (bottom row); the effects were either already covered by the systematics or considered as negligible.

O Top Modeling from EPS

O.1 Top Composition

Table 100 shows the fraction of events which are from top-pair events with one and two leptonicly decaying W's and the flavor of the leading two jets in two and three jet events. This table was made using the EPS [11] selection with the MV1 tagger at the 70% operating point. One can see the increase in bc events at high p_{T}^{W} because of the ΔRcuts which motivates the change from the MV1 to the MV1c tagger discussed in Section 3.2.3. A more current top composition table is given in Section 5.2.1.1.

N $W \to \ell\nu$	Jet Flavors	p_{T}^{W} GeV					
		Inclusive	0-90	90-120	120-160	160-200	>200
	2 Jets						
1	bb	24.5	25.9	22.1	21.6	19.2	11.4
	bc	10.8	9.1	10.3	13.5	36.7	63.1
	bl	1.1	0.9	1.0	1.2	2.5	5.5
	!b	0.1	0.0	0.1	0.1	0.4	1.2
2	bb	61.2	61.7	64.5	61.0	37.0	10.7
	b!b	2.2	2.3	2.0	2.5	4.0	8.1
	3 Jets						
1	bb	51.4	55.7	46.6	35.8	20.2	9.2
	bc	16.6	13.6	16.8	27.6	53.0	74.1
	bl	1.6	1.3	1.6	2.4	6.7	6.8
	!b	0.1	0.1	0.1	0.3	0.8	1.6
2	bb	28.2	27.5	32.8	31.7	13.8	3.1
	b!b	2.0	1.9	2.0	2.2	5.5	5.0

Table 100: The fraction of jet flavor pairs in the 1-lepton EPS [11] analysis from events with one or two leptonicly decaying tops and two or three jets as a function of p_{T}^{W}. l includes τ jets.

P Diboson modeling

The modelling of the processes where a final state with two vector boson is produced is described in detail in this appendix. The diboson processes considered as background in this analysis are the following:

- $Z \to \nu\nu$ and $Z \to q\bar{q}$
- $Z \to ll$ and $Z \to q\bar{q}$
- $W \to l\nu$ and $Z \to q\bar{q}$
- $Z \to \nu\nu$ and $W \to q\bar{q}$
- $Z \to ll$ and $W \to q\bar{q}$
- WW (inclusive)

There is no pure region in the VH(bb) analysis where this process can be studied with data-driven techniques. Therefore, a Monte-Carlo study is performed to estimate uncertainties on the most relevant variables.
The diboson processes are modelled using the POWHEG MC generator, which provides a NLO prediction of this background, interfaced with the Pythia8 parton shower model. The Monte Carlo (MC) samples for the diboson processes are listed on Table 103 along with their cross-sections at $\sqrt{s} = 8$ TeV.

P.1 Cross section

The diboson MC samples are normalized to the cross-sections provided directly by the POWHEG generator. These cross-section have been validated by computing the NLO cross-sections for all the diboson processes considered using MCFM [*insert reference - here or in the previous diboson section*] with the setup outlined in Table 104. Note that some of the MCFM parameters may differ from the ones used in the POWHEG computation (e.g. energy scales), but the comparison still provides a fair cross-check.
The cross-section comparison between POWHEG and MCFM is shown in Table 101. The MCFM software does not provide an NLO calculation for the $Z \to \nu\nu$ and $Z \to q\bar{q}$, and the $Z \to ll$ and $Z \to q\bar{q}$ processes with quarks other than b-quarks, hence their contribution is computed separately by hand and added to the cross-section. The comparison shows larger discrepancies for these processes, but the agreement is overall good.
After the validation the cross-sections provided directly from the POWHEG generator are used to normalize the diboson samples.

***gg → VV* contribution** The contribution of gluon-gluon initiated VV processes is not included in the POWHEG prediction of the diboson background. We use the MCFM software (setup outlined in Table 104) to compute the relative contribution of these processes, which is used to correct the normalization of the POWHEG samples. Table 102 shows the relative contribution of $gg \to VV$ processes to the ZZ and WW backgrounds, which is added to the correspondent cross-sections from Table 101 to get the final normalization.

P.2 Modelling systematic uncertainties

The following sources of systematic uncertainties are considered to assess the modelling errors on the diboson background:

- Scale variations (higher order perturbative corrections)

- Parton density function (PDF) uncertainties
- α_S strong coupling constant uncertainties
- Parton shower (PS) and hadronization model uncertainties

For each of these errors we determined the effect on the shape and the normalization of the background. In the following paragraphs the details of the estimate of these systematic uncertainties is explained.

P.2.1 Stewart-Tackmann estimate of perturbative uncertainties on the diboson cross-section

The systematic uncertainties due to the perturbative nature of the cross-section are estimated through renormalization and factorization scale variation using the MCFM software. The dependence of the systematic errors with respect to p_T(V) is tested to assess their shape effect on the p_T(V) distributions. The analysis regions are defined requiring exactly 2 or 3 jets, so the uncertainties are estimated separatly in the 2-jet and 3-jet categories defined using the parton-level variables provided by the MCFM software as outlined in Table 105, and applying the Stewart-Tackmann method [*add reference*] to account for the effect of the jet veto in the definition of regions.

P.2.1.1 Scale variations

The variation of the diboson cross sections due to changing the factorization (μ_F) and renormalization (μ_R) scales of the process (Δ) is computed using the MCFM software. The nominal value of both the μ_R and μ_F is initially set to half the invariant mass of the four decay products from the VV bosons pair (dynamic mass m(3456)), and then varied down to $\frac{1}{4} \times m(3456)$ and up to m(3456), in a fully correlated way between μ_R and μ_F.

P.2.1.2 Shape dependence on p_T(V)

The effect of scale variations on the diboson cross sections shows a clear dependence with respect to the transverse momentum of the leptonically decaying V boson p_T(V), resulting in a larger error for higher values of p_T(V). To account for this dependence the perturbative uncertainties on σ_2 and $\sigma_{\geq 3}$ are derived separately in 5 p_T(V) bins, correspondent to the p_T(V) regions defined for the dijet mass analysis described in this note:

$$p_T(\mathrm{V}) \text{ bins} = [0, 90, 120, 160, 200, 500] \text{ (GeV)}$$

P.2.1.3 Symmetrization and smoothening

The upwards and downwards relative systematic variations obtained across the p_T(V) regions are symmetrized and smoothed in order to reduce the impact of statistical fluctuations due to the limited statistics of the MCFM generated samples, and avoid instabilities in the fit model.
The symmetrization is performed according to the following schema:

- symmetric up variation = 2× (up variation) / (up variation + down variation)
- symmetric down variation = 2× (down variation) / (up variation + down variation)

While the smoothening is done in order to obtain a final shape uncertainty which is a monotonically increasing function of p_T(V) across the chosen bins:

- if bin[i] > bin[i+1] ⇒ bin[i] = average(bin[i-1], bin[i+1])

These procedures are applied, in this order, on top of the systematic estimate for all the diboson processes, across the full p_T(V) range.

P.2.1.4 Uncertainties on the 2-jet and 3-jet cross-sections

MCFM does not provide the cross-section computation at orders higher than NLO, therefore the 3-jet bin corresponds necessarily to the inclusive 3-jet cross-section $\sigma_{\geq 3}$ for VV+1 jet, while the 2-jet bin corresponds to the exclusive 2-jet cross-section σ_2 for VV+0 jets.
The definition of the jet-bins used in the estimate of the systematics, shown in detail in Table 105, differs from the one used in the analysis: the categories are defined cutting on the kinematic of the parton-level objects provided by MCFM instead that on the reconstructed jets, always selecting the extra parton produced by the NLO calculation to discriminate between the 2-jet and the 3-jet bins. Note that the MCFM software is not interfaced with a parton shower algorithm, therefore the jet-bins are defined with truly parton-level quantities.
The calculation of the uncertainties in different jet bins relies on the assumption that the exclusive 2-jet cross section (σ_2) can be written as the difference between the 2-jet inclusive ($\sigma_{\geq 2}$) and the 3-jet inclusive ($\sigma_{\geq 3}$) cross sections: $\sigma_2 = \sigma_{\geq 2} - \sigma_{\geq 3}$, where the 2-jet inclusive term is defined as the 2-jet exclusive dropping the requirements on the extra NLO parton in MCFM. We can therefore write down the covariance matrix for the 2-jet exclusive and the 3-jet inclusive cross sections, assuming that $\sigma_{\geq 2}$ and $\sigma \geq 3$ are uncorrelated, as:

$$\mathrm{C}(\sigma_2, \sigma_{\geq 3}) = \begin{pmatrix} \Delta^2_{\geq 2} + \Delta^2_{\geq 3} & -\Delta^2_{\geq 3} \\ -\Delta^2_{\geq 3} & \Delta^2_{\geq 3} \end{pmatrix},$$

where $\Delta_{\geq 2}$ and $\Delta_{\geq 3}$ are the absolute uncertainties on the inclusive 2-jet cross-section ($\sigma_{\geq 2}$) and the inclusive 3-jet cross-section, obtained through scale variations and smoothed and symmetrized as explained in the previous paragraphs.
The covariance matrix C is decomposed in the sum of two matrices, which are then separately diagonalized to obtain a set of uncorrelated systematic variations on σ_2 and $\sigma_{\geq 3}$:

$$\mathrm{C}(\sigma_2, \sigma_{\geq 3}) = \begin{pmatrix} \Delta^2_{\geq 2} & 0 \\ 0 & 0 \end{pmatrix} + \begin{pmatrix} \Delta^2_{\geq 3} & -\Delta^2_{\geq 3} \\ -\Delta^2_{\geq 3} & \Delta^2_{\geq 3} \end{pmatrix} = \mathrm{C}_1 + \mathrm{C}_2.$$

The first term C_1 results in an absolute systematic error $\Delta_{\geq 2}$ on the 2jet-exclusive cross section σ_2 only (**SysVVJetScalePtST2**), while the second term C_2 has one singular eigenvector (hence no systematic variation) and one non-singular eigenvector which provides an anticorrelated $\Delta_{\geq 3}$ absolute systematic on σ_2 and $\sigma_{\geq 3}$ (**SysVVJetScalePtST1**).
This procedure is applied for each of the diboson processes, obtaining two orthogonal relative uncertainties on σ_2 and one relative systematic uncertainty on $\sigma_{\geq 3}$:

SysVVJetScalePtST1:

- relative uncertainty on $\sigma_2 = \dfrac{\Delta_{\geq 3}}{\sigma_2}$
- relative uncertainty on $\sigma_{\geq 3} = -\dfrac{\Delta_{\geq 3}}{\sigma_3}$

SysVVJetScalePtST2:

- relative uncertainty on $\sigma_2 = \dfrac{\Delta_{\geq 2}}{\sigma_2}$

Figure 213 and Figure 214 summarize the result of the full uncertainties computation for the 2-jet exclusive and 3-jet inclusive cross sections of the six diboson processes, showing the effect of the variation of σ_2 along the two eigenvectors and the change in $\sigma_{\geq 3}$ along the only non-singular eigenvector. The uncertainties are estimated in the different $p_T(\mathrm{V})$ bins, after applying the symmetrization and smoothening

procedures on $\Delta_{\geq 2}$ and $\Delta_{\geq 3}$. The shape dependence with respect to p_T(V) is clear for both the ortogonal variation **SysVVJetScalePtST1** and **SysVVJetScalePtST2**.

The resulting relative perturbative uncertainties on σ_2 and $\sigma_{\geq 3}$ for the six diboson processes, across the five p_T(V) regions are summarized in Table 106, Table 107 and Table 108. The tables show that the errors on the 2-jet exclusive cross sections go from 2-3% in the lowest p_T(V) bin, up to 15-30% in the latest p_T(V) bin; while for the 3-jet inclusive cross sections they range from 10% to 15%.

P.2.2 PDF and α_S uncertainties

In order to estimate the uncertainties on the diboson cross sections due to PDF and α_S we followed the latest prescription from PDF4LHC, using the MCFM softwer with the setup outlined in Table 104. As for the perturbative uncertainties these errors are computed separately in the five p_T(V) bins to test the shape dependence of the resulting systematics.

P.2.2.1 PDF uncertainties

The systematic variations of the cross section due to PDF errors is computed as follow (Hessian method):

- compute the up and down variations of the cross section for each of the eigenvector of the PDF set: X_i^{pm} are the plus and minus variation for the i-th eigenvector.
- compute the total upwards variation of the cross section as the quadrature sum of all the variations which result in an increase of the cross section:

$$\Delta X^{+}_{max} = \sqrt{\sum_{i=1}^{N} [max(X_i^{+} - X_0, X_i^{-} - X_0, 0)]^2},$$

  where X_0 is the nominal cross section.
- compute the total downwards variation of the cross section as the quadrature sum of all the variations which result in an decrease of the cross section:

$$\Delta X^{-}_{max} = \sqrt{\sum_{i=1}^{N} [max(X_0 - X_i^{+}, X_0 - X_i^{-}, 0)]^2}.$$

- repeat this procedure for two different PDF sets (CT10 and MSTW) and take the envelope of the two resulting uncertainties.

Since the CT10 and MSTW PDF sets are derived using different CL threshold for the eigenvector computation (CL=90% for CT10, CL=68% for MSTW), the CT10 variations are corrected with a simple rescaling to be consistent with the MSTW ones.
These uncertainties are computed for all six diboson processes, across the five p_T(V) bins, for the 2-jet exclusive and the 3-jet inclusive cross sections (defined as in Table 105). The resulting errors are shon in Figure 215 and 217 for the 2-jet exclusive cross section, respectively from the CT10 and MSTW PDF sets, for all the diboson processes, and in Figure 216 and Figure 218 for the 3-jet inclusive cross section. The relative variations do not show a significant dependence on the p_T(V), and are overall smaller than the perturbative uncertainties. The errors from the CT10 set are larger than the MSTW ones across the whole p_T(V) range.

P.2.2.2 α_S uncertainties

The cross section errors due to our knowledge of the strong coupling constant are derived as follow:

- consider two different central values for α_S: 0.117 and 0.119
- for each of the α_S central values calculate the cross section errors correspondent to a 90% CL variation of α_S: this is obtained by considering the cross section computation for $\alpha_S \pm 0.002$ for both the central values
- rescale the resulting error to 68% CL, for consistency with respect to the PDF uncertainties
- repeat for both the PDF sets considered (CT10 and MSTW)

Following this schema we obtain four variations of the cross section, for two α_S central values and two PDF sets. The uncertainties are computed in the different p_T(V) bins, and are shown in Figure 219 and Figure 221 for the 2-jet exclusive cross section of the six diboson processes, for CT10 and MSTW respectively, and in Figure 220 and Figure 222 for the 3-jet inclusive cross section. While it is possible to observe a dependence with respect to p_T(V), the size of this systematic variation is rather smaller than the PDF and the perturbative errors. It can be noted that the two α_S central values produce a very similar variation of the cross sections.

P.2.2.3 PDF and α_S combination

The uncertainties from our knowledge of PDF and α_S are combined taking the quadrature sum of the two separately for the two PDF sets considered, for both the α_S central values, resulting in four relative variation of the cross section: $\Delta^{0.117}_{CT10}$, $\Delta^{0.119}_{CT10}$, $\Delta^{0.117}_{MSTW}$ and $\Delta^{0.119}_{MSTW}$, according to the formula:

$$\Delta^{\alpha_S^j}_{PDF_i} = \sqrt{\Delta^2_{PDF_i} + \Delta^2_{\alpha_S^j - PDF_i}}$$

where i = CT10, MSTW and j = 0.117, 0.119.
The final systematic uncertainty on the cross section is derived taking the envelop of these four uncertainties. Figure 223 and Figure 223 show these envelops for the 2-jet exclusive and the 3-jet inclusive cross section respectively, for the six diboson processes. It is worth noting that since the α_S uncertainties are much smaller than the PDF ones, when taking the quadrature sum of the two the shape dependence coming from the α_S variations does not appear anymore, therefore these systematic uncertainties are taken as a variation of the normalization only, neglecting the shape dependence with respect to p_T(V). For the same reason the difference between the uncertainties for the two different α_S central values is completely negligible (and thus it is not shown in the plots).

These systematics are estimated for all the six diboson processes, in the 2-jet exclusive and the 3-jet inclusive cases. Both the PDF and the α_S uncertainties do not depend on the decay of the vector bosons, but only on the V bosons pair considered, therefore the uncertainties are grouped for the three different VV pairs. The final normalization systematic variations obtained are shown in Table 109.

P.2.3 Parton shower and hadronization model

The last set of systematics uncertainties is derived comparing different models of parton shower and hadronization: in detail we considered a comparison between POWHEG+Pythia8, the nominal MC generator used to model the diboson background in this analysis, and the Herwig LO+LL MC prediction.

The estimate the systematic uncertainties we compared the distribution of the invariant mass of the jets pair (m_{jj}), which is considered most sensitive to PS and hadronization effects, between the two generators. Since the Herwig generator does not provide a separate computation of the diboson cross sections for different decay modes, the uncertainties are derived separately for the three VV pairs (ZZ, WW, WZ), combining together the different final states.

The comparison is done applying the full event selection for the 0-lepton channel except the b-tagging requirement, outlined in Section [*add reference*] as pre-tag selection, for the WZ and WW processes, while for the ZZ processes the b-tagging requirement is applied for the two leading jets (corresponding to the inclusive MV1c operating point of 80%). Since we are mainly interested to differences in the shapes of the m_{jj} distribution, the comparison is done normalizing the prediction from the two MC generator to unit area, neglecting discrepancies in the normalization which may be due to the different matrix element computation. The uncertainties obtained from this estimate are then applied consistently in all the three decay channels: 0-lepton, 1-lepton, 2-lepton.

Figure 225, 226, and 227 shows the POWHEG+Pythia8 versus Herwig comparison for the WZ, ZZ and WW diboson process: to reduce the impact of statistical fluctuations the ratio between the two predictions is fitted with a function that best describe the variations. This fitting function is the same for the ZZ and WZ processes:

$$f(x) = p_0 + p_1 \frac{1}{1 + e^{-p_2(x-p_3)}},$$

while a simple linear function is found better describe the variations for WW processes. The fits are performed between 30 GeV and 300 GeV for the WZ processes, between 30 GeV and 500 GeV for the WW and ZZ processes.

The resulting systematic uncertainties range from about 10% to 20% in the ZZ case, from 10% to 40-50% in the WZ, and up to about 20% for the WW processes. These systematic uncertainties affect only the shape of the m_{jj} distribution and they don't have any effects on the normalization of the diboson processes.

	σ_{MCFM}[pb]	σ_{POWHEG}[pb]
$Z \to \nu\nu\, Z \to q\bar{q}$	2.202	1.964
$Z \to ll\, Z \to q\bar{q}$	1.259	1.145
$W \to l\nu\, Z \to q\bar{q}$	4.658	4.870
$Z \to \nu\nu\, W \to q\bar{q}$	2.663	2.777
$Z \to ll\, W \to q\bar{q}$	1.611	1.594
WW (inclusive)	52.173	51.022

Table 101: Comparison between diboson cross-sections provided by POWHEG and computed with MCFM.

$gg \to WW$	2.65%
$gg \to Z_{ee}Z_{b\bar{b}}$	5.43%
$gg \to Z_{\nu\nu}Z_{b\bar{b}}$	5.97%

Table 102: Relative contribution of $gg \to VV$ processes to WW and ZZ backgrounds.

Process	Generator	Cross-Section ($\sqrt{s}$ = 8 TeV) [pb]
$Z \to \nu\nu\, Z \to q\bar{q}$	POWHEG+PYTHIA8	2.081
$Z \to ll\, Z \to q\bar{q}$		1.207
$W \to l\nu\, Z \to q\bar{q}$		4.870
$Z \to \nu\nu\, W \to q\bar{q}$		2.777
$Z \to ll\, W \to q\bar{q}$		1.594
WW		52.4

Table 103: Monte Carlo generator used for the modelling of the diboson processes and correspondent cross-sections.

MCFM parameter	Value
hmass	126d0
scale:QCD scale choice	+0.5
facscale:QCD fac_scale choice	+0.5
dynamicscale	m(3456)
itmx1, itmx2	10
ncall1, ncall2	500000
LHAPDF group	CT10nlo.LHgrid

Table 104: Main settings for the MCFM software used to compute the cross-sections for the diboson processes.

2-jet inclusive bin	$p_T(\text{j1}) > 20$ GeV $\wedge$ $\lvert\eta(\text{j1})\rvert < 2.5$
	$p_T(\text{j2}) > 20$ GeV $\wedge$ $\lvert\eta(\text{j2})\rvert < 2.5$
2-jet exclusive bin	$p_T(\text{j1}) > 20$ GeV $\wedge$ $\lvert\eta(\text{j1})\rvert < 2.5$
	$p_T(\text{j2}) > 20$ GeV $\wedge$ $\lvert\eta(\text{j2})\rvert < 2.5$
	$p_T(\text{j3}) < 20$ GeV
3-jet inclusive bin	$p_T(\text{j1}) > 20$ GeV $\wedge$ $\lvert\eta(\text{j1})\rvert < 2.5$
	$p_T(\text{j2}) > 20$ GeV $\wedge$ $\lvert\eta(\text{j2})\rvert < 2.5$
	$p_T(\text{j3}) > 20$ GeV $\wedge$ $\lvert\eta(\text{j3})\rvert > 2.5$

Table 105: Parton-level jet-bins definition applied on the output of the MCFM simulation. The j1 and j2 objects are the two jets originated by the hadronically decaying V boson, while j3 is the extra parton produce by the NLO calculation.

p_T^V bins [GeV]	0-90	90-120	120-160	160-200	> 200
$Z \to \nu\nu\, Z \to q\bar{q}$	0.03	0.05	0.07	0.10	0.14
$Z \to ll\, Z \to q\bar{q}$	0.03	0.05	0.07	0.10	0.13
$W \to l\nu\, Z \to q\bar{q}$	0.03	0.08	0.12	0.19	0.28
$Z \to \nu\nu\, W \to q\bar{q}$	0.03	0.07	0.12	0.18	0.28
$Z \to ll\, W \to q\bar{q}$	0.03	0.08	0.13	0.19	0.29
WW	0.03	0.06	0.09	0.13	0.19

Table 106: Perturbative systematics on σ_2 from the C_1 term of the covariance matrix across the different p_T^V bins.

p_T^V bins [GeV]	0-90	90-120	120-160	160-200	> 200
$Z \to \nu\nu\, Z \to q\bar{q}$	0.02	0.04	0.05	0.07	0.11
$Z \to ll\, Z \to q\bar{q}$	0.02	0.04	0.06	0.08	0.11
$W \to l\nu\, Z \to q\bar{q}$	0.03	0.06	0.10	0.14	0.22
$Z \to \nu\nu\, W \to q\bar{q}$	0.02	0.05	0.08	0.12	0.20
$Z \to ll\, W \to q\bar{q}$	0.02	0.06	0.09	0.13	0.21
WW	0.02	0.04	0.06	0.09	0.13

Table 107: Perturbative systematics on σ_2 from the C_2 term of the covariance matrix across the different p_T^V bins.

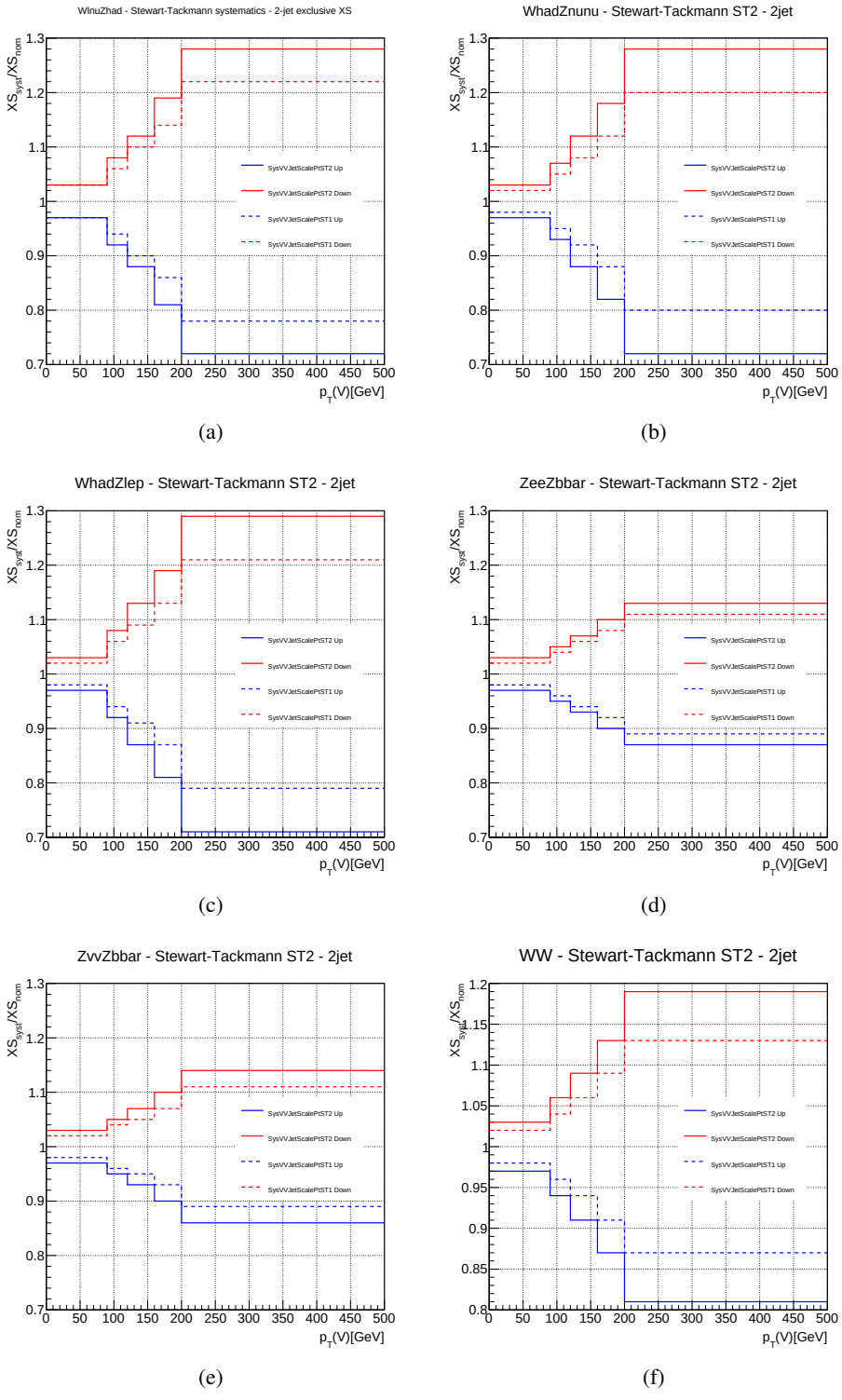

Figure 213: Perturbative systematics on σ_2 for the six diboson processes obtained applying scale variations according to the Stewart-Tackmann method. The solid line corresponds to the errors derived from the C_1 term and the dotted line from the C_2 term of the covariance matrix C.

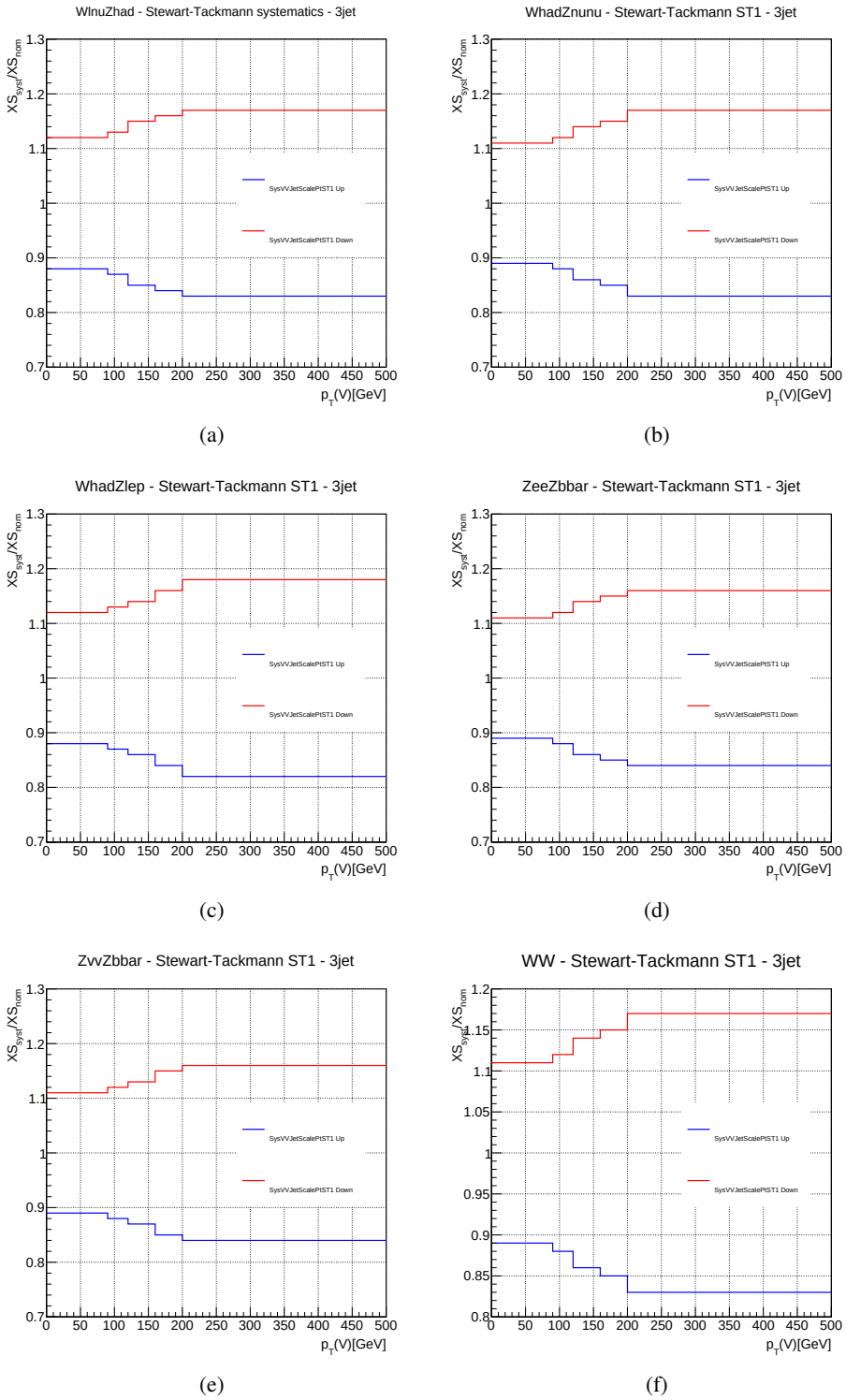

Figure 214: Perturbative systematics on $\sigma_{\geq 3}$ for the six diboson processes obtained applying scale variations according to the Stewart-Tackmann method. The solid line corresponds to the errors derived from the C_2 term of the covariance matrix C, while the C_1 term of the matrix does not provide any contribution to the 3-jet errors.

p_T^V bins [GeV]	0-90	90-120	120-160	160-200	> 200
$Z \to \nu\nu\, Z \to q\bar{q}$	-0.11	-0.12	-0.13	-0.15	-0.16
$Z \to ll\, Z \to q\bar{q}$	-0.10	-0.12	-0.14	-0.15	-0.16
$W \to l\nu\, Z \to q\bar{q}$	-0.12	-0.13	-0.15	-0.16	-0.17
$Z \to \nu\nu\, W \to q\bar{q}$	-0.11	-0.12	-0.14	-0.15	-0.17
$Z \to ll\, W \to q\bar{q}$	-0.12	-0.13	-0.14	-0.16	-0.18
WW	-0.11	-0.12	-0.14	-0.15	-0.17

Table 108: Perturbative systematics on $\sigma_{\geq 3}$ from the C_2 term of the covariance matrix across the different p_T^V bins.

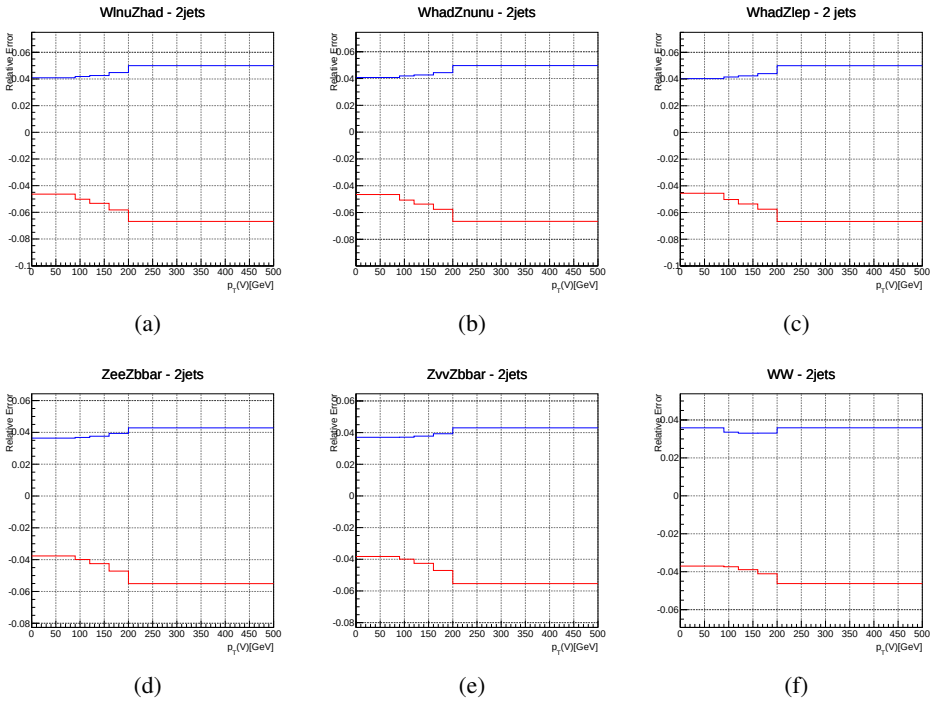

(a) (b) (c)

(d) (e) (f)

Figure 215: Systematic uncertainties due to PDF errors on the 2-jet exclusive cross section for the six diboson processes, computed from the CT10 PDF set, across the five p_T(V) bins.

Process	PDF+α_S (2-jet)	PDF+α_S (3-jet)
ZZ	0.03	0.03
WZ	0.04	0.02
WW	0.03	0.02

Table 109: PDF+α_S systematic uncertainties for ZZ, WZ and WW processes, in the 2-jet and 3-jet categories.

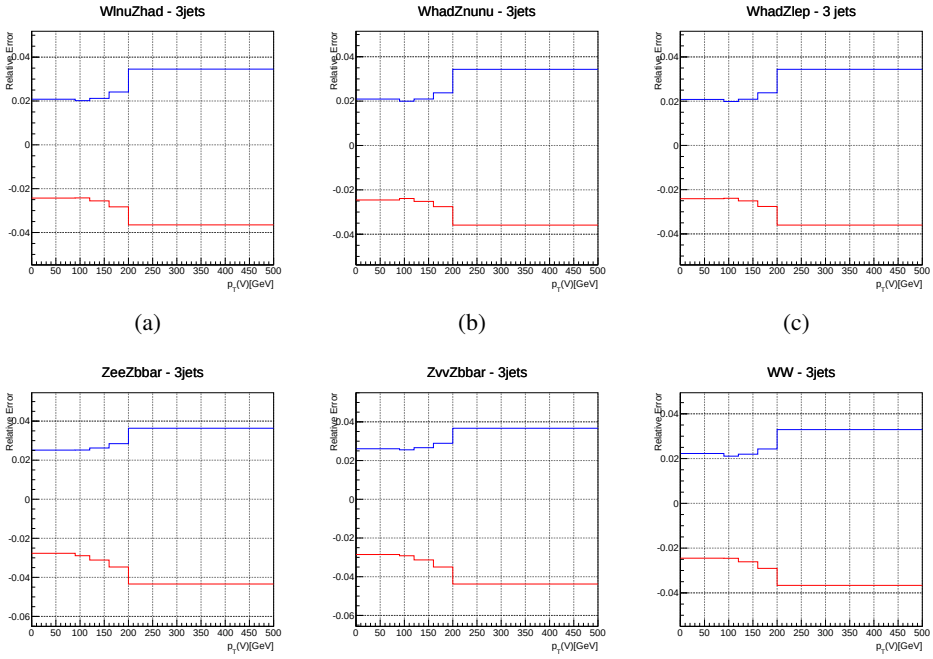

(a) (b) (c)

(d) (e) (f)

Figure 216: Systematic uncertainties due to PDF errors on the 3-jet inclusive cross section for the six diboson processes, computed from the CT10 PDF set, across the five p_T(V) bins.

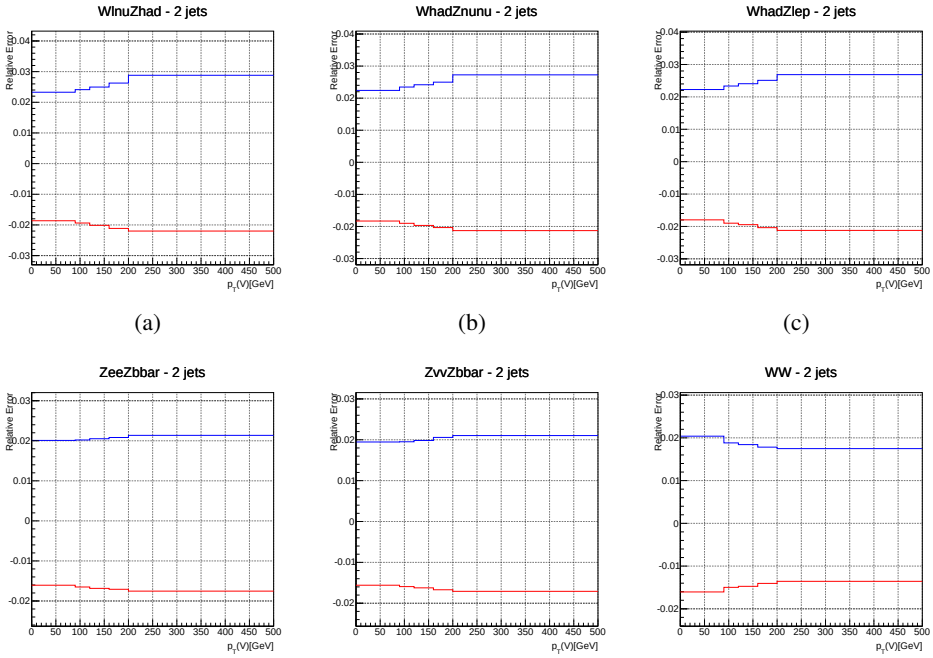

(a) (b) (c)

(d) (e) (f)

Figure 217: Systematic uncertainties due to PDF errors on the 2-jet exclusive cross section for the six diboson processes, computed from the MSTW PDF set, across the five p_T(V) bins.

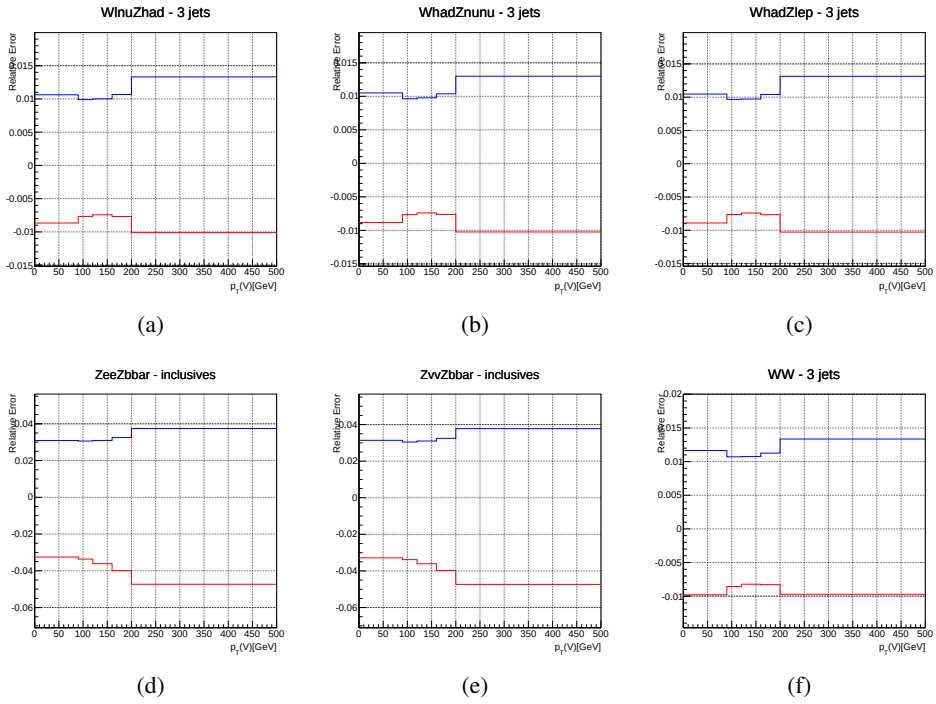

(a) (b) (c)

(d) (e) (f)

Figure 218: Systematic uncertainties due to PDF errors on the 3-jet inclusive cross section for the six diboson processes, computed from the MSTW PDF set, across the five p_T(V) bins.

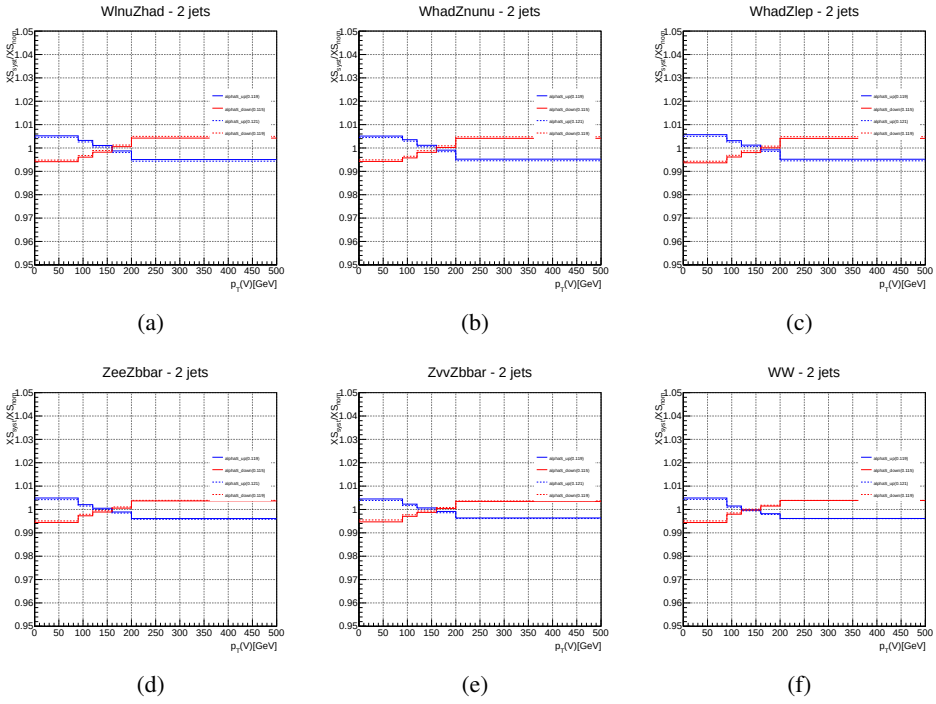

(a) (b) (c)

(d) (e) (f)

Figure 219: Systematic uncertainties from α_S on the 2-jet exclusive cross section for the six diboson processes, computed from the CT10 PDF set, across the five p_T(V) bins. The solid line corresponds to the variation of the central value $\alpha_S = 0.117$, while the dotted line corresponds to the variation of $\alpha_S = 0.119$.

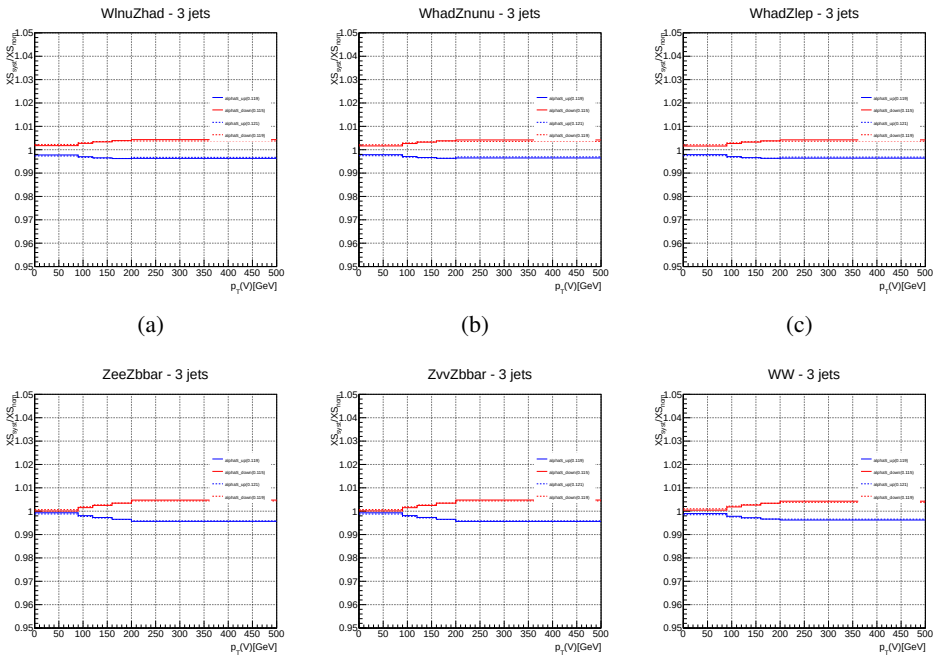

(a) (b) (c)

(d) (e) (f)

Figure 220: Systematic uncertainties from α_S on the 3-jet inclusive cross section for the six diboson processes, computed from the CT10 PDF set, across the five p_T(V) bins. The solid line corresponds to the variation of the central value $\alpha_S = 0.117$, while the dotted line corresponds to the variation of $\alpha_S = 0.119$.

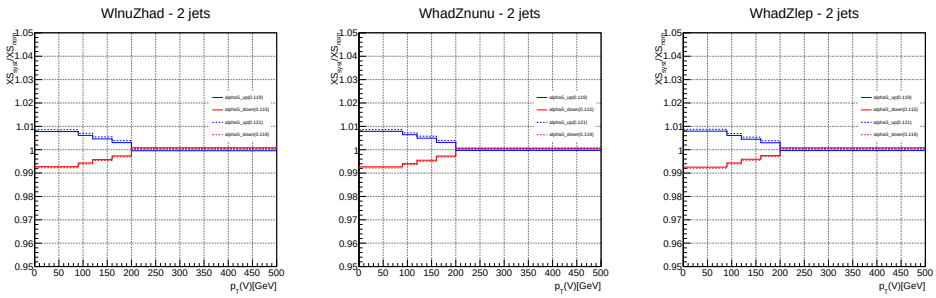

(a) (b) (c)

(d) (e) (f)

Figure 221: Systematic uncertainties from α_S on the 2-jet exclusive cross section for the six diboson processes, computed from the MSTW PDF set, across the five p_T(V) bins. The solid line corresponds to the variation of the central value $\alpha_S = 0.117$, while the dotted line corresponds to the variation of $\alpha_S = 0.119$.

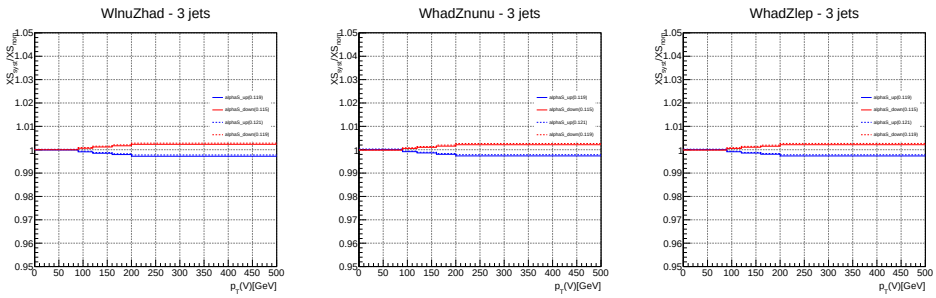

(a) (b) (c)

(d) (e) (f)

Figure 222: Systematic uncertainties from α_S on the 3-jet inclusive cross section for the six diboson processes, computed from the MSTW PDF set, across the five p_T(V) bins. The solid line corresponds to the variation of the central value $\alpha_S = 0.117$, while the dotted line corresponds to the variation of $\alpha_S = 0.119$.

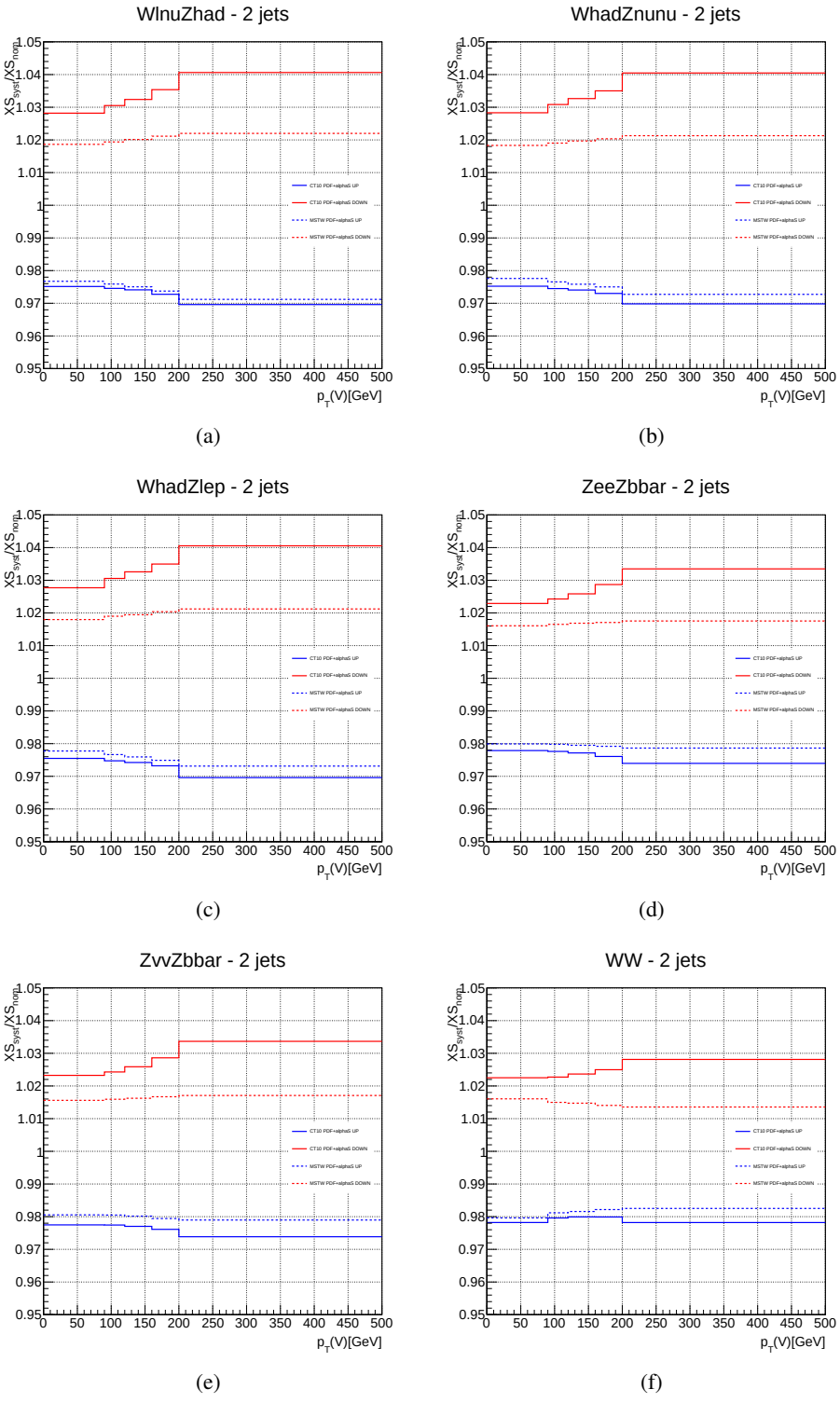

Figure 223: Envelope of the systematic uncertainties from PDF+α_S on the 2-jet exclusive cross section for the six diboson processes. The solid line corresponds to the variations from the CT10 PDF set, while the dotted line from the MSTW PDF set.

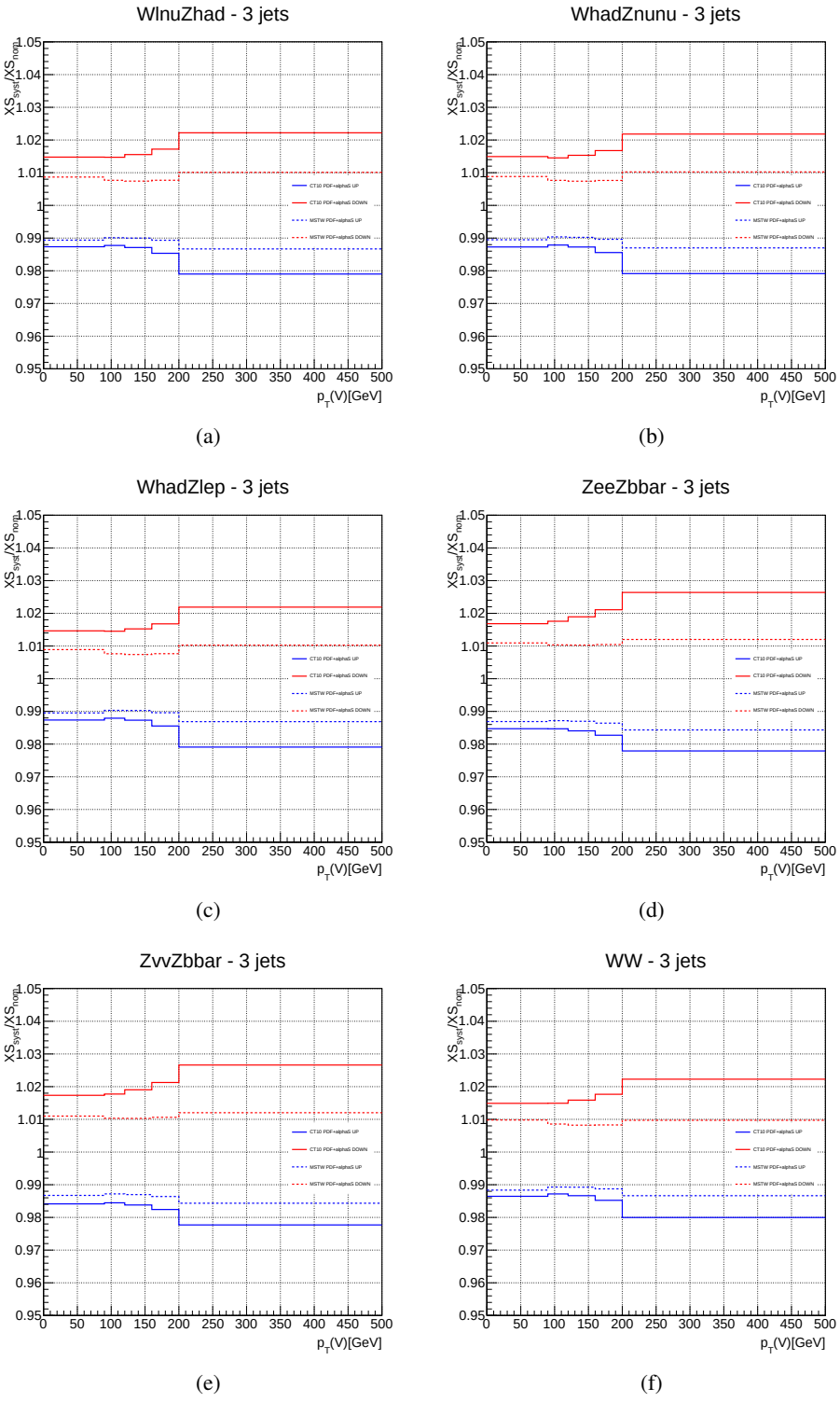

Figure 224: Envelope of the systematic uncertainties from PDF+α_S on the 3-jet inclusive cross section for the six diboson processes. The solid line corresponds to the variations from the CT10 PDF set, while the dotted line from the MSTW PDF set.

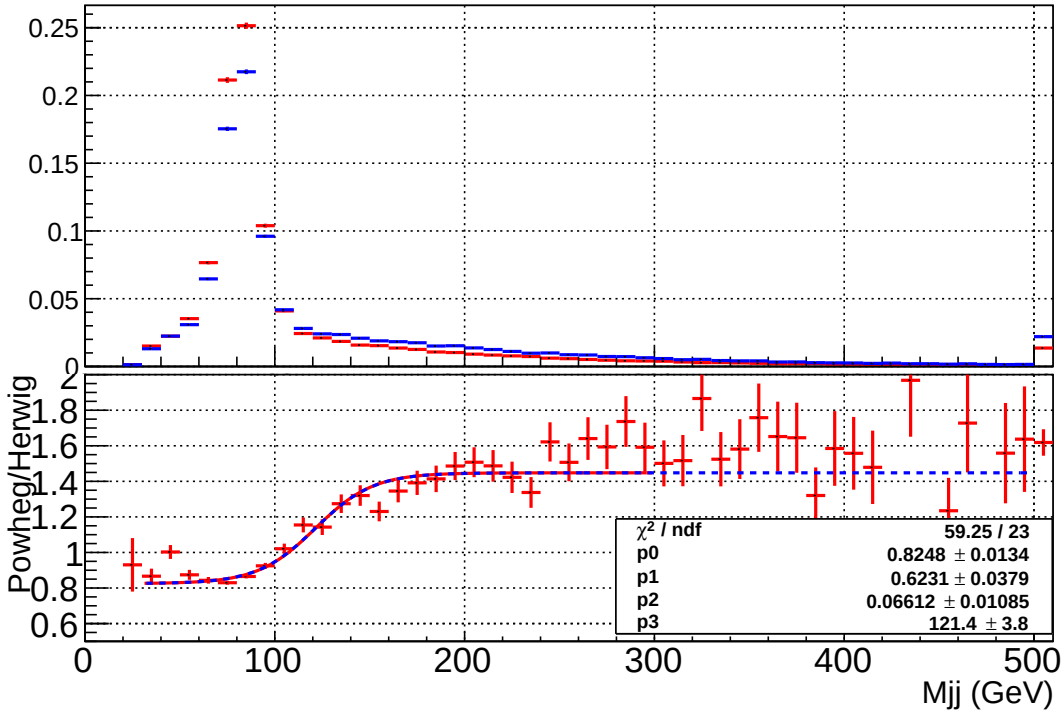

Figure 225: POWHEG+Pythia8 versus Herwig comparison for the WZ diboson processes applying the 0-lepton selection in the 2-tag inclusive (LL+MM+TT) category: the systematic uncertainties from the PS/hadronization model is estimated taking the fit of the ratio of the different MC predictions.

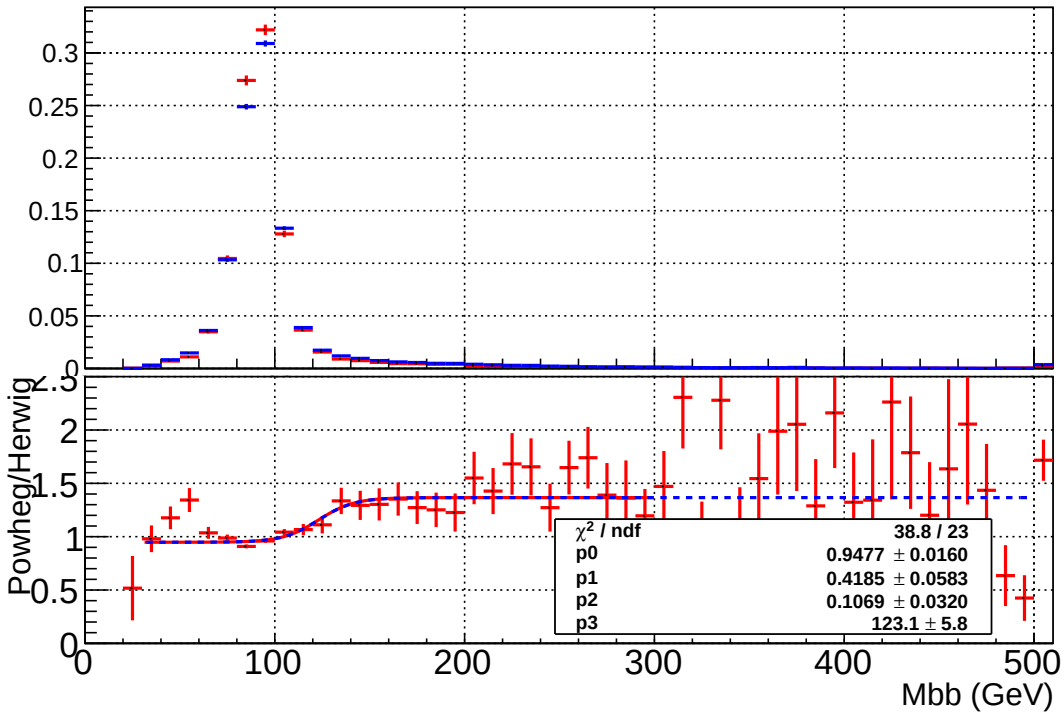

Figure 226: POWHEG+Pythia8 versus Herwig comparison for the ZZ diboson processes applying the 0-lepton selection in the pre-tag category: the systematic uncertainties from the PS/hadronization model is estimated taking the fit of the ratio of the different MC predictions.

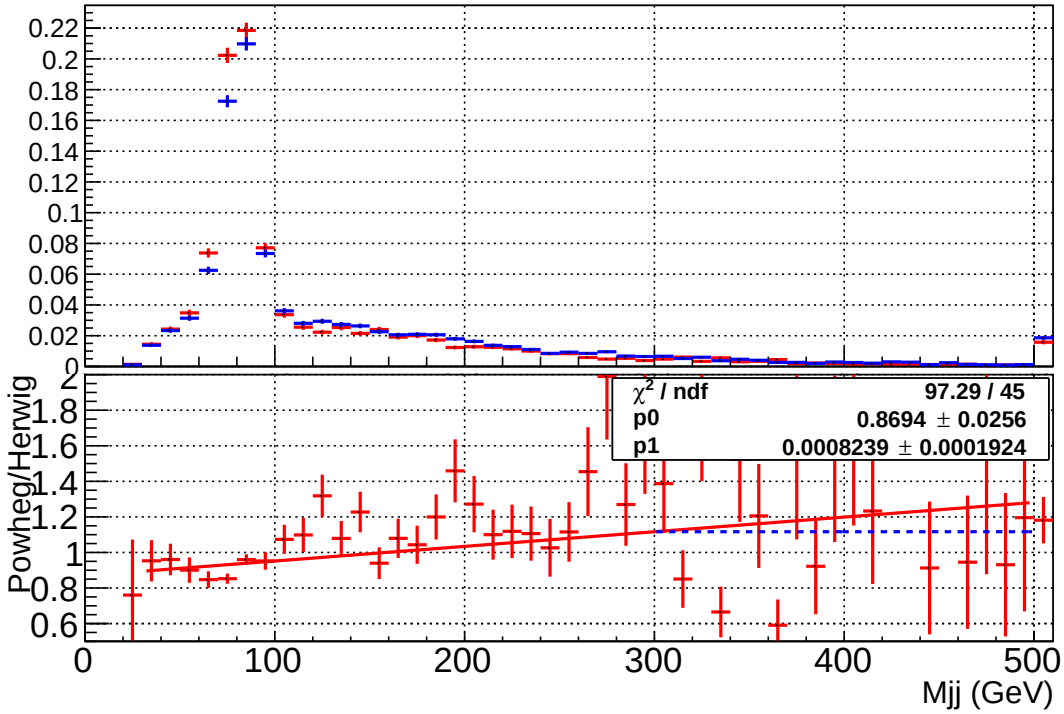

Figure 227: POWHEG+Pythia8 versus Herwig comparison for the WW diboson processes applying the 0-lepton selection in the pre-tag category: the systematic uncertainties from the PS/hadronization model is estimated taking the fit of the ratio of the different MC predictions.

Q Multi-jet background for 0-lepton analysis

The following is a free-standing description of the current rendering of the $ZH \to \nu\bar{\nu}b\bar{b}$ multijet background estimate, an evaluation of the systematic uncertainties, and recent cross-checks.

The procedure based on the method documented in Section 4.3 of Reference [73] and Section 4.1.1 of Reference [11] contains information pertaining to the previous result. Between EPS and now, no major changes to this method were introduced.

Q.1 Introduction: ABCD

Multijet events with considerable $E_{\mathrm{T}}^{\mathrm{miss}}$(i.e. > 120 GeV) do not occur very often since substantial fluctuations in calorimeter jet energy measurements are the root cause. However, due to the extremely large multijet production cross section compared to that of the Higgs, such events are a considerable background in the $ZH \to \nu\bar{\nu}b\bar{b}$ search. To simulate large-$E_{\mathrm{T}}^{\mathrm{miss}}$ multijet events one would need a considerable amount of MC and the appropriate computing resources. This is not a practical approach, therefore a data-driven estimate is performed using the 'ABCD' method.

Two kinematic variables,

1. $\Delta\phi(E_{\mathrm{T}}^{\mathrm{miss}}, p_{\mathrm{T}}^{\mathrm{miss}})$: azimuthal separation between $E_{\mathrm{T}}^{\mathrm{miss}}$ and $p_{\mathrm{T}}^{\mathrm{miss}}$ (both described in Section 3.2.4)
2. $min|\Delta\phi(E_{\mathrm{T}}^{\mathrm{miss}}, jet)|$: minimum azimuthal separation between $E_{\mathrm{T}}^{\mathrm{miss}}$ and any signal jet,

in which the multijet background has a markedly different distribution from the EW backgrounds and the Higgs signal have been chosen and are show in Figure 228.

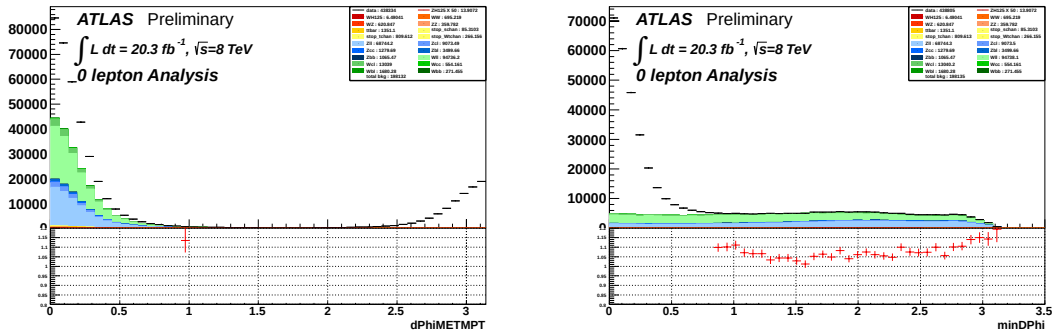

(a) $\Delta\phi(E_{\mathrm{T}}^{\mathrm{miss}}, p_{\mathrm{T}}^{\mathrm{miss}})$ (b) $min|\Delta\phi(E_{\mathrm{T}}^{\mathrm{miss}}, jet)|$

Figure 228: $\Delta\phi(E_{\mathrm{T}}^{\mathrm{miss}}, p_{\mathrm{T}}^{\mathrm{miss}})$ and $min|\Delta\phi(E_{\mathrm{T}}^{\mathrm{miss}}, jet)|$ distribution

Figure 229 shows the two-dimensional plane defining four regions A, B, C, and D where A/C is $\Delta\phi(E_{\mathrm{T}}^{\mathrm{miss}}, p_{\mathrm{T}}^{\mathrm{miss}}) > \pi/2$. The prediction for multijet events in the signal region (region A) is given by

$$N_{QCD}(A) = \frac{N(B)}{N(D)} \times N(C), \tag{41}$$

where $N(B)$, $N(C)$ and $N(D)$ represent the data yield minus the contributions from the EW backgrounds (described in Section 5) in regions B, C and D, respectively, after all event selection cuts (described in Section 3.4) are applied except $\Delta\phi(E_{\mathrm{T}}^{\mathrm{miss}}, p_{\mathrm{T}}^{\mathrm{miss}})$ and $min|\Delta\phi(E_{\mathrm{T}}^{\mathrm{miss}}, jet)|$ cuts themselves.

In order to use the ABCD method, these two variables should be at most weakly correlated for multijet events. This was checked by showing the $min|\Delta\phi(E_{\mathrm{T}}^{\mathrm{miss}}, jet)|$ shape with $\Delta\phi(E_{\mathrm{T}}^{\mathrm{miss}}, p_{\mathrm{T}}^{\mathrm{miss}})$ on either side of $\pi/2$ is similar as demonstrated in Figure 230.

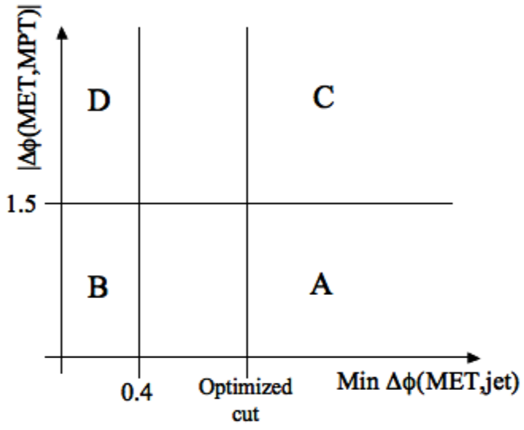

Figure 229: Two-dimensional kinematic plane for estimating QCD multi-jet background in the 0-lepton signal region (region A). $dphi(E_{\mathrm{T}}^{\mathrm{miss}}, p_{\mathrm{T}}^{\mathrm{miss}}) > \pi/2$ defines region A/C.

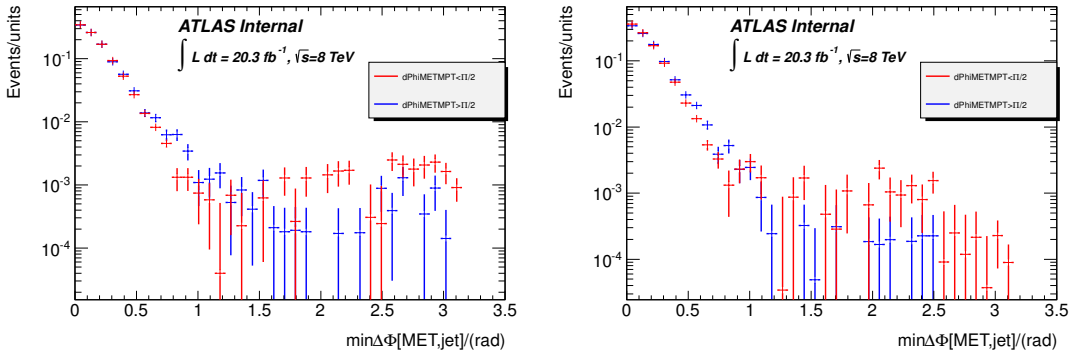

(a) (b)

Figure 230: $min|\Delta\phi(E_{\mathrm{T}}^{\mathrm{miss}}, jet)|$ distribution of multijet background in $\Delta\phi(E_{\mathrm{T}}^{\mathrm{miss}}, p_{\mathrm{T}}^{\mathrm{miss}}) < \pi/2$ in red (region A/B) and in $\Delta\phi(E_{\mathrm{T}}^{\mathrm{miss}}, p_{\mathrm{T}}^{\mathrm{miss}}) > \pi/2$ in blue (region C/D) obtained from the data, after subtracting away contribution from EW processes estimated from simulation. The results shown are before b-tagging, and for events in $90 < E_{\mathrm{T}}^{\mathrm{miss}} < 120$ GeV for two (three) jet events on the left (right).

A/C definition	N(B)	N(D)	N(C)	$N(A)_{pred}$	$N(A)_{obs}$
0.4< $min\|\Delta\phi(E_{\mathrm{T}}^{\mathrm{miss}}, jet)\|$ <0.9	267267 ± 586	155094 ± 396	19537.6 ± 147.4	33668.3 ± 278.1	27976.3 ± 346.7
0.9< $min\|\Delta\phi(E_{\mathrm{T}}^{\mathrm{miss}}, jet)\|$ <1.5			3659.7 ± 73.3	6306.5 ± 128.2	3987.5 ± 348.2

Table 110: A closure test comparing the predicted number of multijet events from Equation 42 to the observed calculated from data minus MC in different slices of $min|\Delta\phi(E_{\mathrm{T}}^{\mathrm{miss}}, jet)|$. The results shown are before b-tagging, and for events in $90 < E_{\mathrm{T}}^{\mathrm{miss}} < 120$ GeV.

The population of data events in regions B, C and D are too small after all selection cuts to produce a robust estimate. To increase the data statistics, the b-tagging requirements were lifted from B, C, and D and the ΔR cuts of the dijet mass analysis were also removed from regions B and D. Then the shape obtained in region C is multiplied by the b-tagging rate R_B (R_D) measured in region B (D). The b-tagging rate is defined as the probability that an event passes the two b-tagged jet requirement outlined in Section 3.3.4 after satisfying all other event selection requirements. Equation 41 is then rewritten as

$$N_{QCD}(A) = \frac{N(B)}{N(D)} \times N(C) \times R. \tag{42}$$

where R can be either R_B or R_D.

Q.2 Cross Checks

Several cross checks have been done. Looking closer at Figure 230 one might notice that the red points ($\Delta\phi(E_{\mathrm{T}}^{\mathrm{miss}}, p_{\mathrm{T}}^{\mathrm{miss}}) < \pi/2$ region A/B) above $min|\Delta\phi(E_{\mathrm{T}}^{\mathrm{miss}}, jet)| = \pi/2$ are systematically much higher than the blue ($\Delta\phi(E_{\mathrm{T}}^{\mathrm{miss}}, p_{\mathrm{T}}^{\mathrm{miss}}) > \pi/2$ region C/D). Recall, the histograms in Figure 230 are obtained from data minus MC and Figure 228 shows that the difference between MC and data is very small in the region $min|\Delta\phi(E_{\mathrm{T}}^{\mathrm{miss}}, jet)| > \pi/2$ and therefore highly sensitive to the MC prediction. For example, increasing the MC prediction 5% brings N(C) and N(A) into agreement in Figure 230. To show this, and to prove that the number of events in C is representative of the number of events in A (within a factor equal to the ratio of N(B)/N(D)), a closer test comparing the predicted number of multijet events in different $min|\Delta\phi(E_{\mathrm{T}}^{\mathrm{miss}}, jet)|$ regions

- 0.4< $min|\Delta\phi(E_{\mathrm{T}}^{\mathrm{miss}}, jet)|$ <0.9,
- 0.9< $min|\Delta\phi(E_{\mathrm{T}}^{\mathrm{miss}}, jet)|$ <1.5

was performed and shown in Table 110. For $0.4 < min|\Delta\phi(E_{\mathrm{T}}^{\mathrm{miss}}, jet)| < 0.9$ the predicted number of multijet events is not sensitive to the number of MC events and agrees to a 20 % accuracy with the observed value. Stepping closer to the signal region, $0.9 < min|\Delta\phi(E_{\mathrm{T}}^{\mathrm{miss}}, jet)| < 1.5$, where the multijet prediction is more sensitive to the MC normalization, the estimated multijet yield is larger than the observed but within the systematics described below. This suggests that the method is sound but the regions used are very sensitive to the predicted EW yield. This has been taken into consideration when the systematic uncertainty described below was chosen.

To further build confidence that the $min|\Delta\phi(E_{\mathrm{T}}^{\mathrm{miss}}, jet)|$ variable and the $\Delta\phi(E_{\mathrm{T}}^{\mathrm{miss}}, p_{\mathrm{T}}^{\mathrm{miss}})$ are sufficiently de-correlated the Pythia8 QCD samples (Pythia8_AU2CT10_jetjet_JZxW, with $x = 2 - 7$) are employed. Figure 231 shows the shape of $min|\Delta\phi(E_{\mathrm{T}}^{\mathrm{miss}}, jet)|$ is very similar above and below $\phi(E_{\mathrm{T}}^{\mathrm{miss}}, p_{\mathrm{T}}^{\mathrm{miss}}) = \pi/2$.

Another cross check was done to explore the difference in the tagging rate in regions B and D. The tagging rate in region D rather than region B is used to estimate the multijet contamination in region A. Region D is more representative of A since B is enhanced in heavy flavor jets. Figure 232

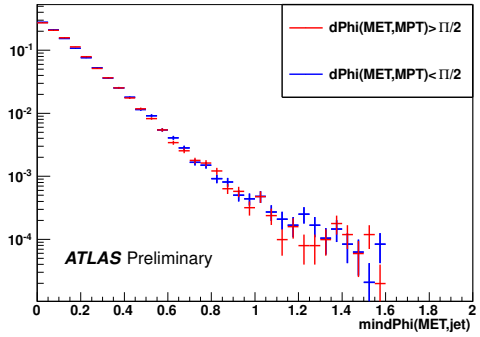

Figure 231: The $min|\Delta\phi(E_{\mathrm{T}}^{\mathrm{miss}}, jet)|$ variable is shown to have the same shape above and below $\phi(E_{\mathrm{T}}^{\mathrm{miss}}, p_{\mathrm{T}}^{\mathrm{miss}}) = \pi/2$ which supports that the two variables are not correlated. These plots were made using Pythia8 QCD samples (Pythia8_AU2CT10_jetjet_JZxW, with $x = 2 - 7$).

$min\|\Delta\phi(E_{\mathrm{T}}^{\mathrm{miss}}, jet)\|$	0-0.4	0.5-1.0	1.0-1.5
R_B	0.090	0.046	0.018
R_D	0.036	0.022	0.016

Table 111: Event b-tagging rate for different slices of $min|\Delta\phi(E_{\mathrm{T}}^{\mathrm{miss}}, jet)|$.

provides a visual aid for the following discussion. In region B, both the $E_{\mathrm{T}}^{\mathrm{miss}}$ and $p_{\mathrm{T}}^{\mathrm{miss}}$ point in a similar azimuthal direction as well as the $E_{\mathrm{T}}^{\mathrm{miss}}$ and some jet. This can be a signature of semi-leptonic b-quark decay. While in region D, the $E_{\mathrm{T}}^{\mathrm{miss}}$ and $p_{\mathrm{T}}^{\mathrm{miss}}$ are pointing in the opposite azimuthal direction, which is more indicative of a calorimeter or an inner-detector mis-measurement. Therefore, with the $min|\Delta\phi(E_{\mathrm{T}}^{\mathrm{miss}}, jet)|$ increasing, the b-tagging rate will decrease. Table 111 shows the tagging rate in different $min|\Delta\phi(E_{\mathrm{T}}^{\mathrm{miss}}, jet)|$ ranges. Again, Pythia8 QCD samples (Pythia8_AU2CT10_jetjet_JZxW, with $x = 2 - 7$) are used to further validate the above claim. Figure 233 shows the truth label of a jet with the smallest azimuthal separation from the $E_{\mathrm{T}}^{\mathrm{miss}}$. Region B has the largest fraction of b-jets and even though region D is closer to A, it still has a larger b-jet contribution. This also indicates that the multijet background is somehow overestimated when using R_B or R_D.

Please see Reference [11] for previously performed cross-checks.

Q.3 Final Product

As can be seen from Tables 112 and 113, both version of this analysis have very small multijet contamination. Based on the closure test (Table 110) and the b-tagging rate in region D , the multijet events for $E_{\mathrm{T}}^{\mathrm{miss}} > 120$ GeV background is estimated to be well under 2% in most regions as shown in Tables 112 113 with respect to the electroweak background. These estimates are inserted into each search categories using the same dijet mass and BDT template shown in Figure 234.

In the fits, a gaussian priors on the multijet normalization is used, with an error of ±100% on its normalization. This systematic uncertainty has been evaluated to cover the different effects described in this These priors correlate LL, MM, TT categories for the different p_{T}^{V} regions (with the exception of the region with 100< p_{T}^{V} <120 GeV), while it takes non correlated regions with different number of jets and different number of tagged jets (i.e. 1-tag VS. 2-tag).

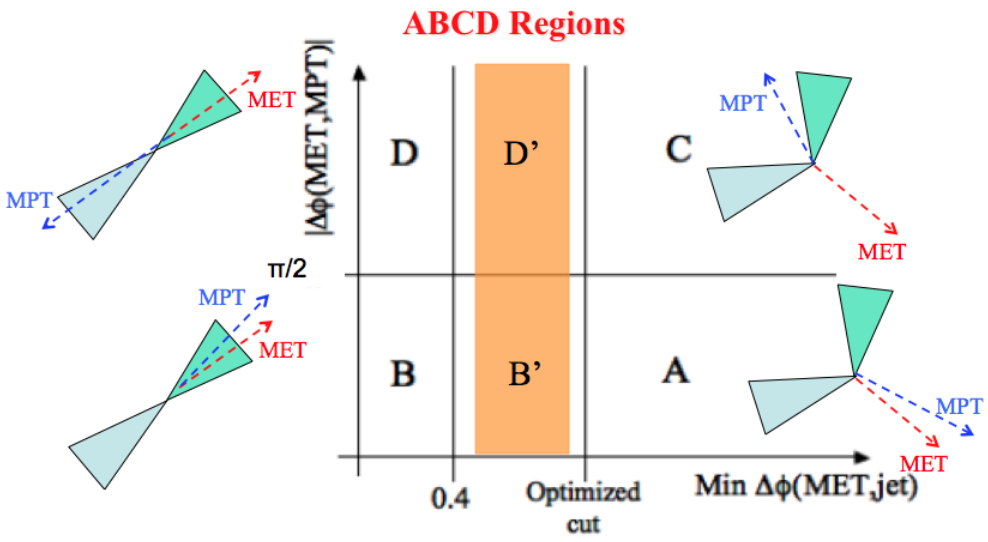

Figure 232: Sketch of jets, $E_{\mathrm{T}}^{\mathrm{miss}}$, and $p_{\mathrm{T}}^{\mathrm{miss}}$in the regions used for the 0-lepton multijet estimate.

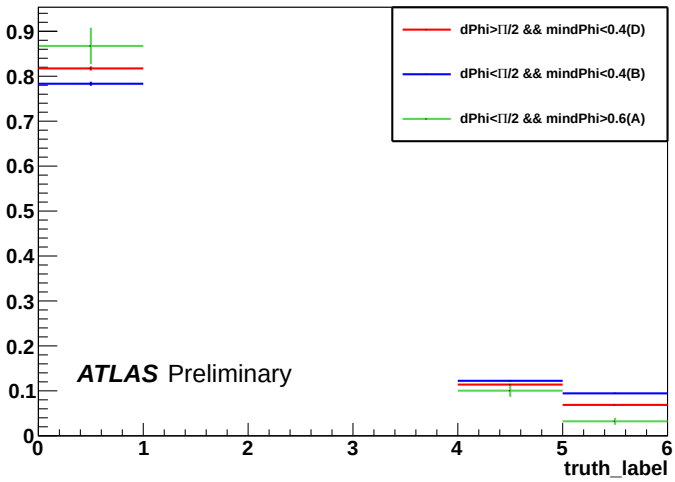

Figure 233: Truth label of the jet closest to the $E_{\mathrm{T}}^{\mathrm{miss}}$ in ϕ showing the enhancement of b-jets in region B and that both R_B and R_D will overestimate the tagging rate in region A. This plot was made using Pythia dijet Monte Carlo simulation.

N_{jet}	p_T^Z (GeV)	b-tag Region	MJ Events (with R_D)	EW Background	MJ/EW (%)
2	120-160	LL	12.08	800.16	1.51
		MM	5.77	410.94	1.41
		TT	2.42	284.01	0.85
	160-200	LL	1.48	255.93	0.58
		MM	0.61	118.95	0.52
		TT	0.26	76.95	0.34
	>200	LL	0.98	119.95	0.49
		MM	0.40	81.37	0.49
		TT	0.10	49.21	0.20
3	120-160	LL	2.88	221.29	1.30
		MM	1.56	141.37	1.11
		TT	0.74	100.08	0.74
	160-200	LL	0.71	92.29	0.76
		MM	0.24	49.89	0.47
		TT	0.18	30.40	0.39
	>200	LL	0.37	86.35	0.43
		MM	0.17	35.14	0.48
		TT	0.06	19.25	0.32

Table 112: Result for estimate of multijet events in the signal region of the 0-lepton dijet mass analysis.

N_{jet}	MJ Events (with R_D)	EW Background	MJ/EW (%)
2	15.58	1653.65	0.94
3	3.49	697.88	0.50

Table 113: Result for estimate of multijet events in the signal region of the 0-lepton MVA analysis.

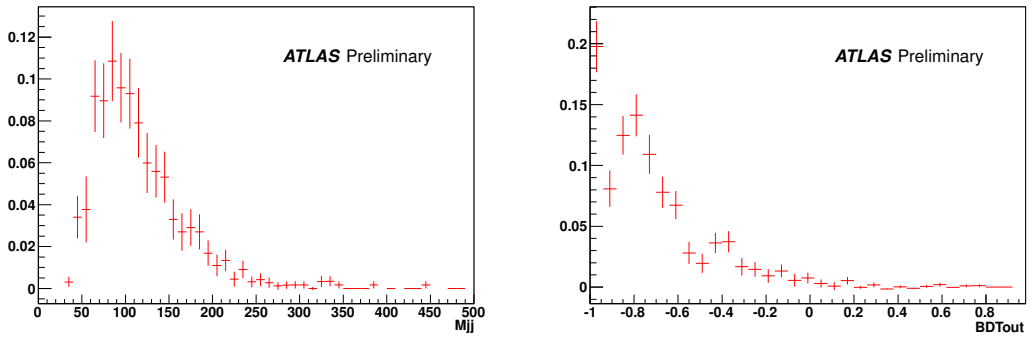

Figure 234: Shape used for the MJ in the 0-lepton analysis for the di-jet mass and BDT on the left and right respectively. For each the same shape is used in all search regions.

R Multijet background for 1-lepton analysis

Multijet events mimicking the $WH \rightarrow \ell\nu b\bar{b}$ signal topology is a major background of the 1-lepton analysis. As with most backgrounds of this type, the efficiency is small but the production rate is so large that the background cannot be ignored easily nor can enough MC be produced to simulate the processes. For these reasons, the multijet background is estimated directly from data. The following outlines the procedure used to estimate this background, an optimization to reduce its contribution, and modeling checks performed in order to ascertain the systematic uncertainty.

R.1 Template Overview

Data events are used to estimate the contribution of multijet events which satisfy the 1-lepton selection. A multijet model region or template region is defined from which data events are taken and the electroweak contribution is subtracted to obtain the multijet template. The multijet model region is defined as Medium VH leptons with the modification of $0.05(0.07) < iso_{track} < 0.50$ in the $e(\mu)$ channel, $iso_{calo} < 0.07$ in both and the quality of MediumPP [19] in the e channel on top of the *VeryLoose* LH criteria. After overlap removal, the iso_{track} range is modified for nominal and systematic evaluations as described below. All event level cuts are applied. The following describes the studies used to arrive at the above definition which is a modification of the EPS choice. The template is then fit in the signal region to obtain the expected multijet yield.

R.2 Multijet Rejection

For EPS [11] the multijet background was reduced with requiring $E_{\mathrm{T}}^{\mathrm{miss}} > 20$ GeV for $p_{\mathrm{T}}^{W} < 200$ GeV and $E_{\mathrm{T}}^{\mathrm{miss}} > 50$ GeV above. Also for $p_{\mathrm{T}}^{W} < 160$ GeV an $m_{\mathrm{T}}^{W} > 40$ GeV cut was employed. The signal efficiency for the multijet rejection cuts was 65% for $p_{\mathrm{T}}^{W} < 120$ GeV (using the MVA selection i.e. no $\Delta R(bb)$ cuts). An optimization was done using the events in the multijet template region and the signal MC. To avoid over-tuning of cuts and to get a realistic estimate of cut efficiencies, a closure test was performed. In the signal region, the Monte Carlo predictions for the EW backgrounds are subtracted to the data to get another estimate of the multijet templates. The overall S/B is at the per-mill level and the multijet yield is much larger than the expected Higgs yield before the application of dedicated anti-MJ cuts so this procedure should be relatively safe. As in the signal region multijet is not the dominant background, the EW background subtraction can affect significantly the multijet estimation through normalization and systematics issues. In conclusion, both multijet templates (from the QCD control region and from the signal region) have their own bias, but the use of both of them gave a handle on the robustness of the proposed cuts since at the time of this optimization, the modeling of the analysis was not stable.

Lepton variables were considered such as properties of jet overlapping the electrons, impact parameters, and isolations. A $|d_0$ significance$| < 3$ cut was entertained for a time but was then shown to provide no additional rejection after all other cuts are applied. The MV1 output of the jet overlapping an electron is interesting but requires a dedicated calibration since MV1 is not calibrated for electrons. The iso_{calo} was tightened for the signal region leptons to 0.04 from (0.07) since this rejected between 25 and 35% of multijet events with 95% signal efficiency which increased with p_{T}^{W}.

Several event level cuts were explored including two-dimensional cuts on m_{T}^{W} and $E_{\mathrm{T}}^{\mathrm{miss}}$, STVF $E_{\mathrm{T}}^{\mathrm{miss}}$, and $p_{\mathrm{T}}^{\mathrm{miss}}$, but a cut of $M_{eff} > 180$ GeV for $p_{\mathrm{T}}^{W} < 120$ GeV with the m_{T}^{W} and $E_{\mathrm{T}}^{\mathrm{miss}}$ cuts in the same region removed was chosen in the end. Figure 235 shows an MVA output for the multijet and signal, left and right respectively, for the EPS (optimized) cuts in blue (red). Two different trainings were used but one can clearly see that the change in cuts resulted in a large increase in the signal and no considerable increase of the multijet component in the sensitive region of the MVA output. This optimization study

called for a $E_{\mathrm{T}}^{\mathrm{miss}}$cut of 20 GeV for the high p_{T}^{W}region ($p_{\mathrm{T}}^{W} > 120$ GeV). Therefore in the dijet analysis with $120 < p_{\mathrm{T}}^{W} < 200$ GeV the $E_{\mathrm{T}}^{\mathrm{miss}}$cut was reduced to 20 GeV (from 25 GeV [11]). Above p_{T}^{W} of 200 GeV a reduction of the $E_{\mathrm{T}}^{\mathrm{miss}}$cut from 50 GeVdecreases the expected dijet mass sensitivity so the EPS value was maintained. The success of dropping the m_{T}^{W} cut for $p_{\mathrm{T}}^{W} < 120$ GeV prompted a test to abandon it in the region $120 < p_{\mathrm{T}}^{W} < 160$ GeV in the dijet mass analysis which subsequently showed an increase in both the signal and background yield by more than 50% and no large increase in the multijet component was observed as shown in Figure 236. In total these changes increased the expected statistical sensitivity of the 2-jet region in the 1-lepton analysis 5 (8)% in the MVA (dijet) analysis. Note the upper bound of m_{T}^{W} which was present for EPS has been maintained in the dijet mass analysis.

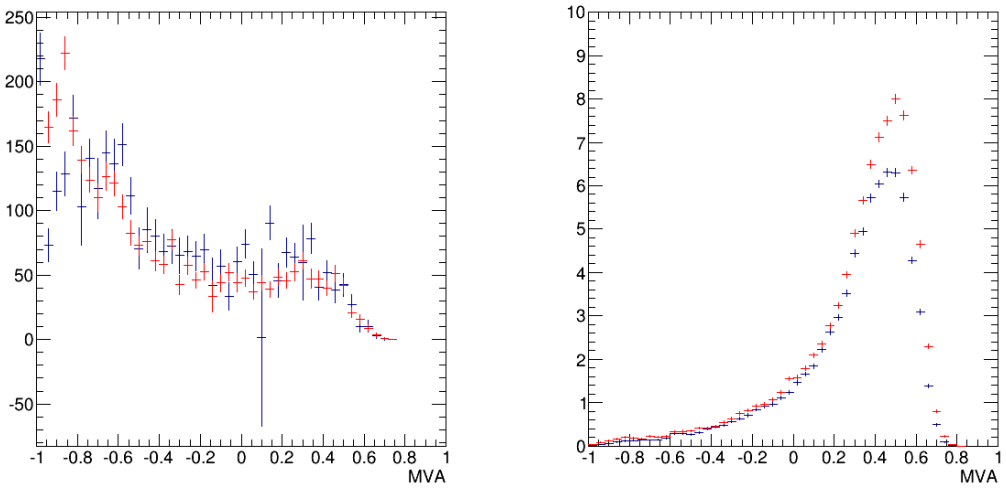

Figure 235: This figure shows an MVA output for the multijet and signal on the left and right respectively for the EPS (optimized) cuts in blue (red) discussed in Section 3.4. Two different trainings were used but one can clearly see that the change in cuts resulted in a large increase in the signal and no considerable increase of the multijet component in the sensitive region of the MVA output. The difference yields a 17% increase in the MVA analysis sensitivity.

R.3 Multijet Template Region

Multijet events are taken from an orthogonal region in data refered to as the multijet template region. This region is contructed to be orthogonal to the signal region by selecting leptons with inverted track isolation criteria and vetoing any event with multiple leptons (counting both the normal leptons and the leptons used to obtain the multijet template described here). The low end of the iso_{track} range was moved from 0.04 (EPS) to 0.05 (0.07) in the electron (muon) channel in order to reduce the electroweak contamination. The upper range was extended to 0.50 to increase statistics. In the muon channel channel the full range is used and statistically half the range is used for the up and down systematics ($0.07 < iso_{track} < 0.095$ and $0.095 < iso_{track} < 0.50$ respectively) (`SysMJMuTrkIso`). In the electron channel $0.05 < iso_{track} < 0.12$ is used for the nominal template (roughtly 1/2 the statistics) and the upper range $0.12 < iso_{track} < 0.50$ is used for a systematic variation which is symmetrized (`SysMJElTrkIso`). Reguardless of the range used to select the leptons, the full range, $0.05(0.07) < iso_{track} < 0.50$ in electron (muon) events, is used for the objects in overlap removal. Afterwards, the range is modified for the desired selection. As stated above, the iso_{calo} cut was tightened to 0.04 from 0.07 but this was not done for the multijet template to increase the available statistics. It has been shown that this change in the range also changed the electroweak contamination which has a different effect on the template compared to the

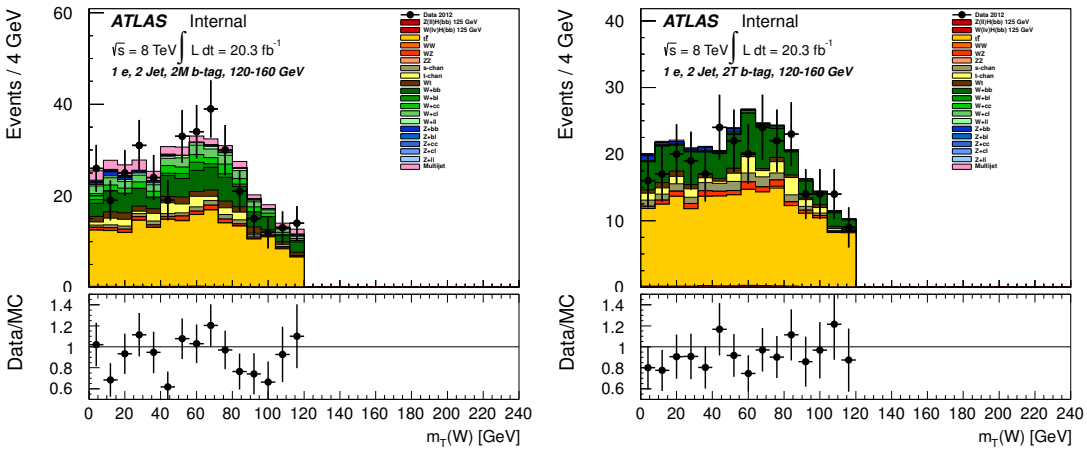

Figure 236: This figure shows the m_{T}^{W} distribution in the for $120 < p_{\mathrm{T}}^{W} < 160$ in the electron channel of the dijet mass analysis after requiring two exclusive medium and tight tags on the left and right respectively. For $m_{\mathrm{T}}^{W} < 40$ GeV, which was excluded previously [11], the agreement is acceptable and the multijet contribution is not significantly more then above 40 GeV. Removing this cut increases the signal and background in this p_{T}^{W} range by 50%.

iso_{track} change in the electon channel only. A reduced upper limit of 0.04, matching the signal region is used for a systematic variation in the electron channel with the effect symmetrized (`SysMJElCaloIso`). In terms of object quality, other choices were explored besides using MediumPP in the electron channel. VeryTight LH and Tight LH cuts both reduce the available template statistics and while looking very similar amongst themselves do differ somewhat from the MediumPP template. The Medium LH cut produced a template very similar to the MediumPP template. In light of this information, the choice from EPS MediumPP was preserved. An inversion of iso_{calo} was explored for the nominal template and for a systematic but was not used since many variables, including m_{T}^{W} were adversely affected. The m_{T}^{W} template seemed to suffer from a very large contamination from electroweak events.

R.4 Multijet Normalization

The above template method does not determine the normalization. A fit to data is performed using the $E_{\mathrm{T}}^{\mathrm{miss}}$ distribution. This fit is performed separately for muon and electron events, 2 and 3 jet events, and 1 and 2 b-tag events. The 2 b-tag region is fit inclusively, that is 2L, 2M, and 2T events are all fit with one multijet scale factor. Due to the small contribution of multijet events to the 2T region, this helps stabilize the normalization estimate. Since the multijet normalization is coupled to the electroweak background normalization, a scale factor for the electroweak background is also used. Also, a set of scale factors from the profile likelihood, determined from the ratio of the post-fit yield to the pre-fit yield, are also used to have the electroweak background as close to our best guess as possible. The $E_{\mathrm{T}}^{\mathrm{miss}}$ variable was found to be the most stable interms of template variations. Other variables such as m_{T}^{W} and lepton p_{T} were considered.

The normalization uncertainity (`SysMJMuNorm` and `SysMJElNorm`) is derived from two sources added in quadrature. One is the statistical error of the multijet scale factor. The normalization fit is performed inclusively in 2-tag events, but the statistical error is take from the exclusive fits. That is the normalization in each 2L, 2M, and 2T events separtely. Even though the inclusive fit is used to determine the normalization, the statistical error of exclusive fits are used for the systematic to reflect our imperfect knowledge of the heavy-flavor contribution to the multijet template. The second, is the difference in the

multijet yield when the EW scale factors are used compared to when they are not used.

R.5 Template Statistics: Using 1 b-tag events for the 2 b-tag regions

The templates have decent statistics but after 2-tags and in the high p_{T}^{W} region, the events dry up. It has been shown that the kinematics of 1-tag match quite well the kinematic of 2 b-tag events in the muon channel (Figures 237-240) and in 2L tag electron events. The 2T tag events are considerably different from the 1-tag kinematics in the electron channel. The muon channel multijet is predominantly from heavy flavor jet decays, while the electron channel is a mixture of heavy flavor jet decays and light jets or photons faking electrons therefore the difference in relationship between 1 and 2 b-tag events based on the lepton flavor is not unexpected. A procedure was developed which, given the rank (leading or sub-leading) of the un-tagged jet and the MV1c value of the tagged jet, a MV1c value is generated for the un-tagged jet promoting this event into the 2-tag region. Said procedure reproduces exactly (by construction) the 2D distribution of the MV1c of the two leading jets and is performed separately on the muon and electron channel. Afterwards, in the electron + 2-jet events only, the 1-tag events used in the 2L, 2M, and 2T tagged template are each kinematicly reweighted to match the distribution of the 'real' 2-tag template. The reweighting is performed sequentially on $\Delta R(bb)$ and p_{T}^{W} using the ratio of 1-tag over 2-tag events. The TH1 smooth function is used five times on the ratio such that the statistical fluctuations of the limited 2-tag events are not encapsulated in the reweighting. 'Real' 2-tag events are not discarded and represent roughly 10% of the events used for the final 2-tag multijet templates. The variables used for the reweighting and the dijet invariant mass as well as the BDT itself (in the MVA selection) are shown in Figures 241 to 245 for 2L, 2M, and 2T events respectively along with several important kinematic variables in Figures 247 to 251 for the same regions. One half of the reweight is used as a systematic variation (`SysMJDR` and `SysMJPtV`). In the muon channel and in 3-jet events, such a reweighting is not applied.

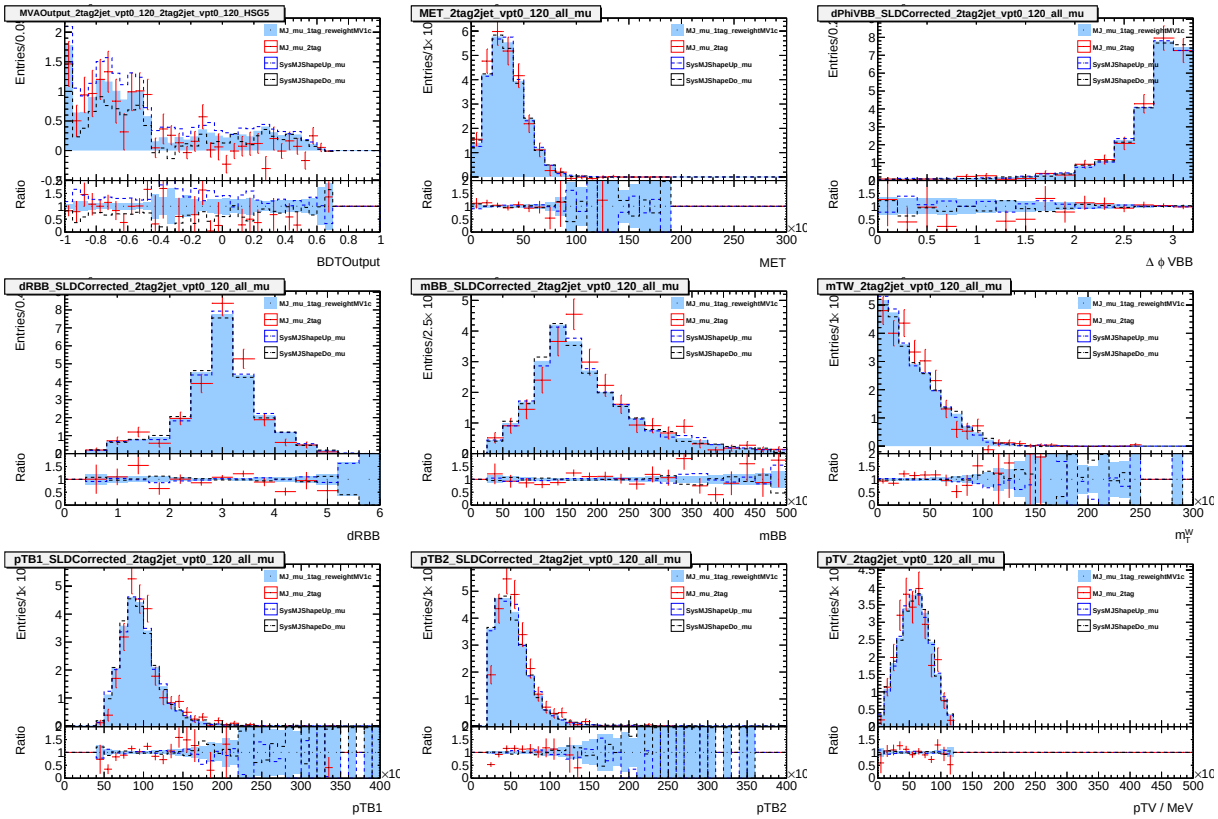

Figure 237: A comparison of 1-tag and 2-tag multijet events in the muon 2-jet channel with $p_{\mathrm{T}}^{W} < 120$ GeV. The red histogram is 2-tag events, the blue solid histogram is the 1-tag events spoofed into the 2-tag region and the dashed histograms show the effect from the iso_{track} systematics

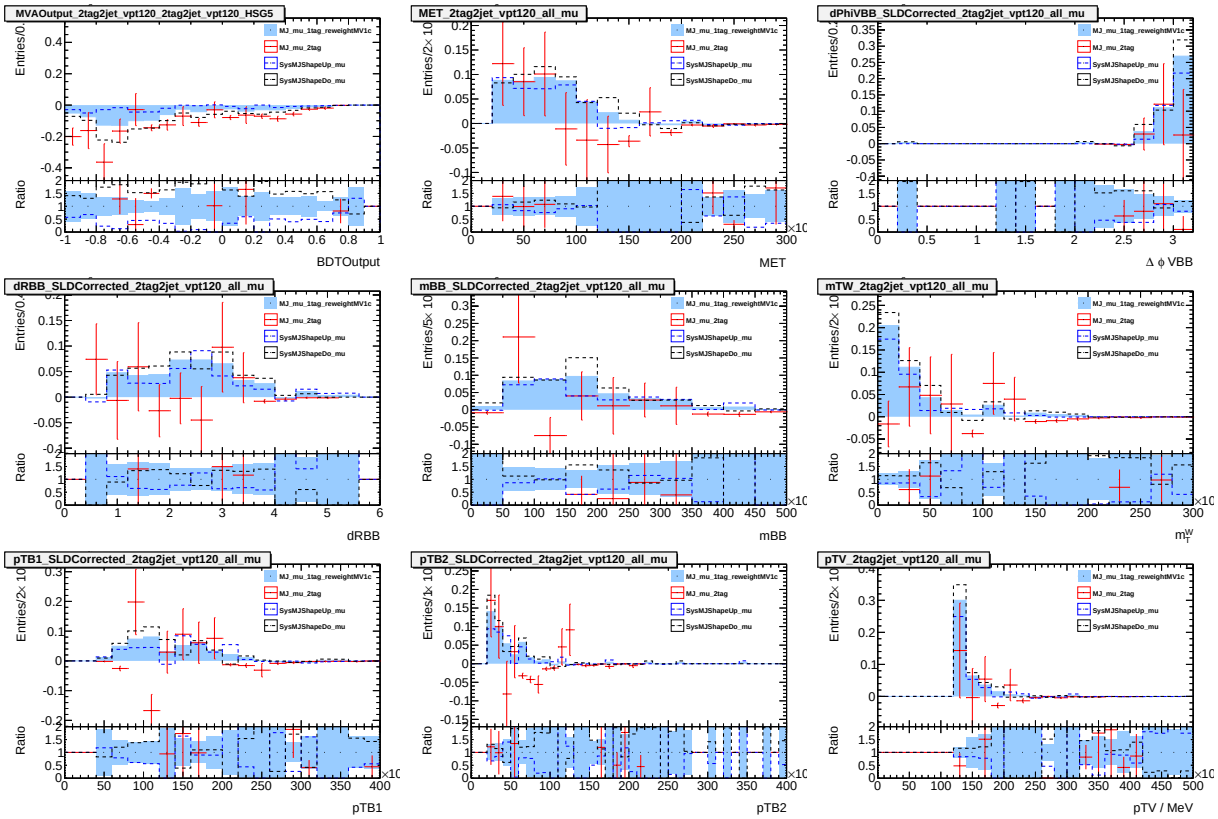

Figure 238: A comparison of 1-tag and 2-tag multijet events in the muon 2-jet channel with $p_{\mathrm{T}}^{W} > 120$ GeV. The red histogram is 2-tag events, the blue solid histogram is the 1-tag events spoofed into the 2-tag region and the dashed histograms show the effect from the iso_{track} systematics

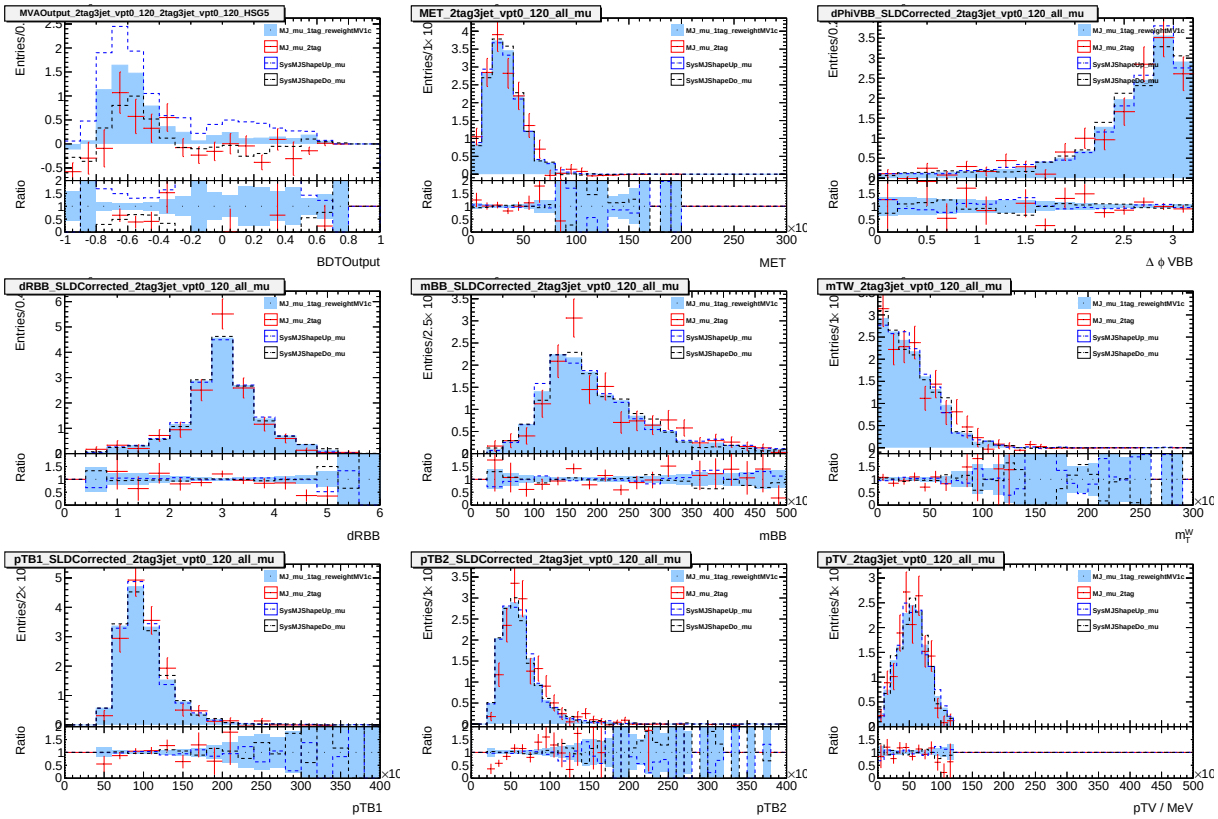

Figure 239: A comparison of 1-tag and 2-tag multijet events in the muon 3-jet channel with $p_{\mathrm{T}}^{W} < 120$ GeV. The red histogram is 2-tag events, the blue solid histogram is the 1-tag events spoofed into the 2-tag region and the dashed histograms show the effect from the iso_{track} systematics

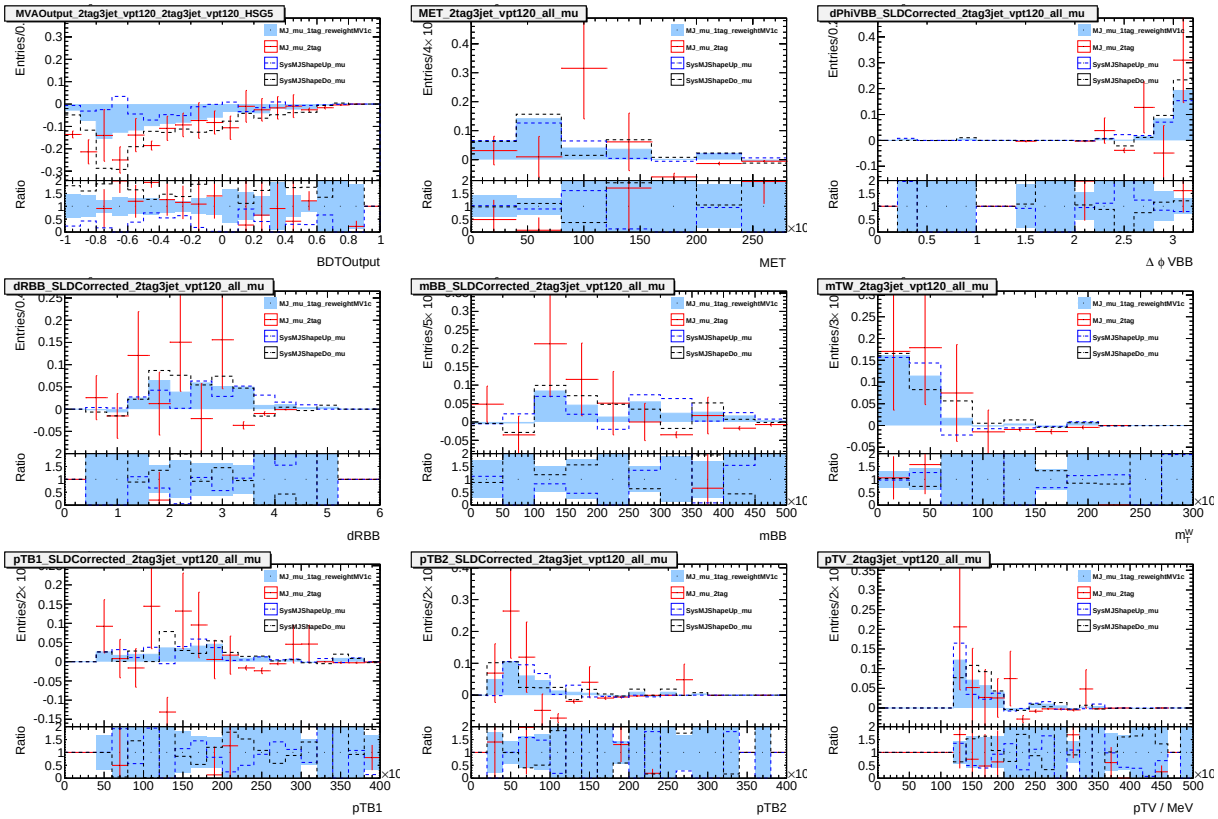

Figure 240: A comparison of 1-tag and 2-tag multijet events in the muon 3-jet channel with $p_{\mathrm{T}}^{W} > 120$ GeV. The red histogram is 2-tag events, the blue solid histogram is the 1-tag events spoofed into the 2-tag region and the dashed histograms show the effect from the iso_{track} systematics

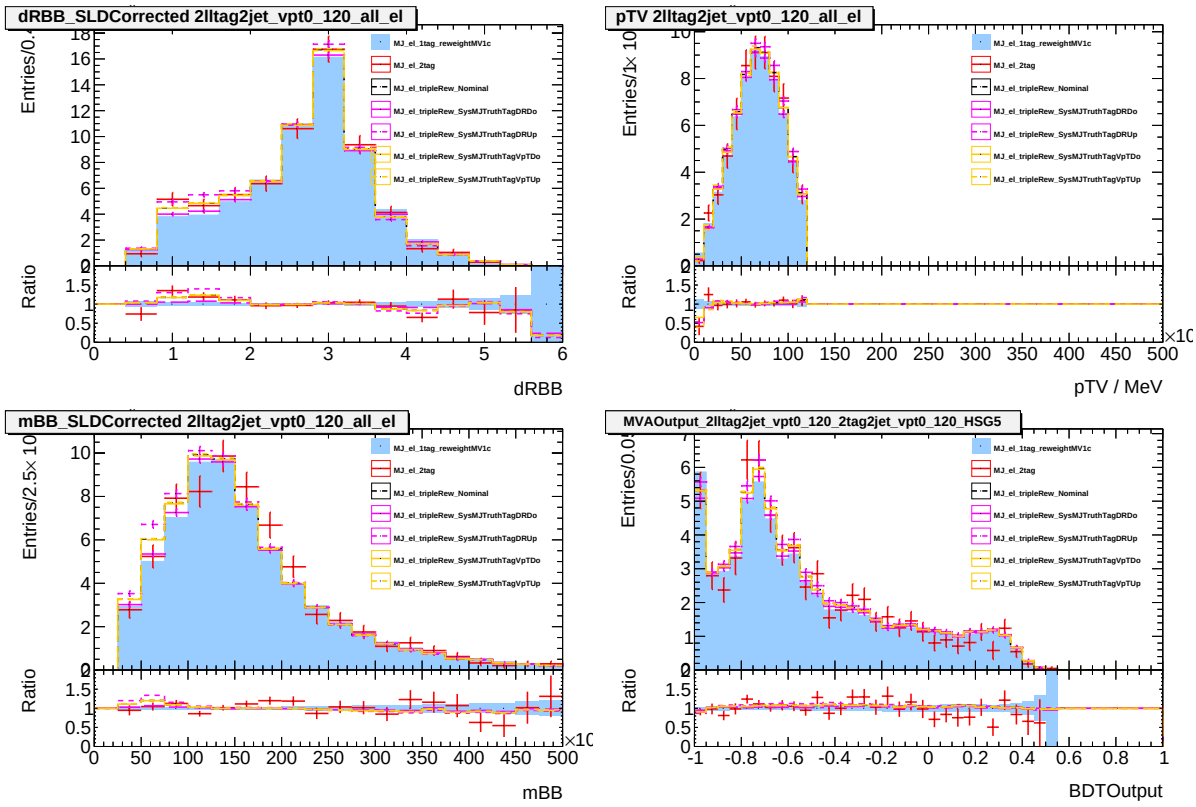

Figure 241: The top two figures show the variables on which the reweighting was derived and the bottom two show the dijet mass and the BDT for 2L tag $p_{\mathrm{T}}^{W} < 120$ GeV electron events. The red histogram is 2-tag events, the blue solid histogram is the 1-tag events spoofed into the 2-tag region and the black distribution shows the reweighted 1-tag events. The purple and yellow histograms are centered around the black and show the systematic from 1/2 of each reweighting - $\Delta R(bb)$ and p_{T}^{W} respectively. The ratio are taken wrt the blue histogram.

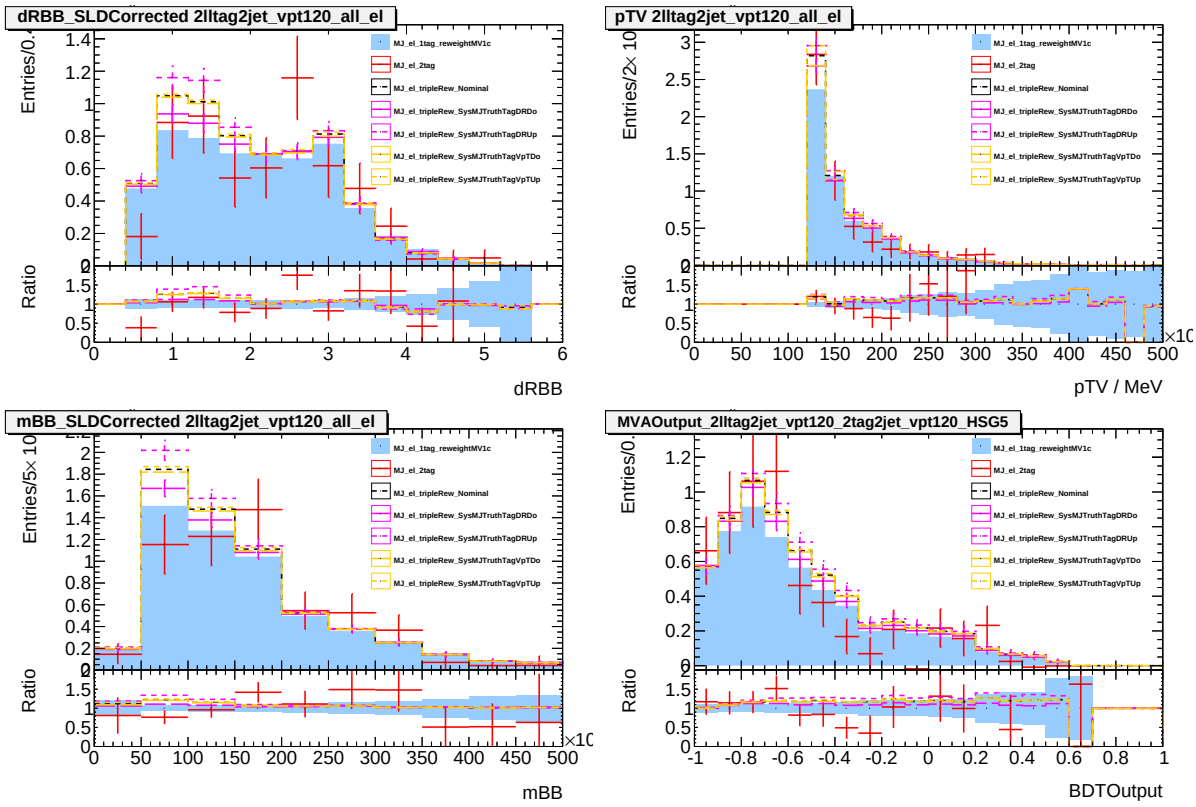

Figure 242: The top two figures show the variables on which the reweighting was derived and the bottom two show the dijet mass and the BDT for 2L tag $p_{\mathrm{T}}^{W} > 120$ GeV electron events. The red histogram is 2-tag events, the blue solid histogram is the 1-tag events spoofed into the 2-tag region and the black distribution shows the reweighted 1-tag events. The purple and yellow histograms are centered around the black and show the systematic from 1/2 of each reweighting - $\Delta R(bb)$ and p_{T}^{W} respectively. The ratio are taken wrt the blue histogram.

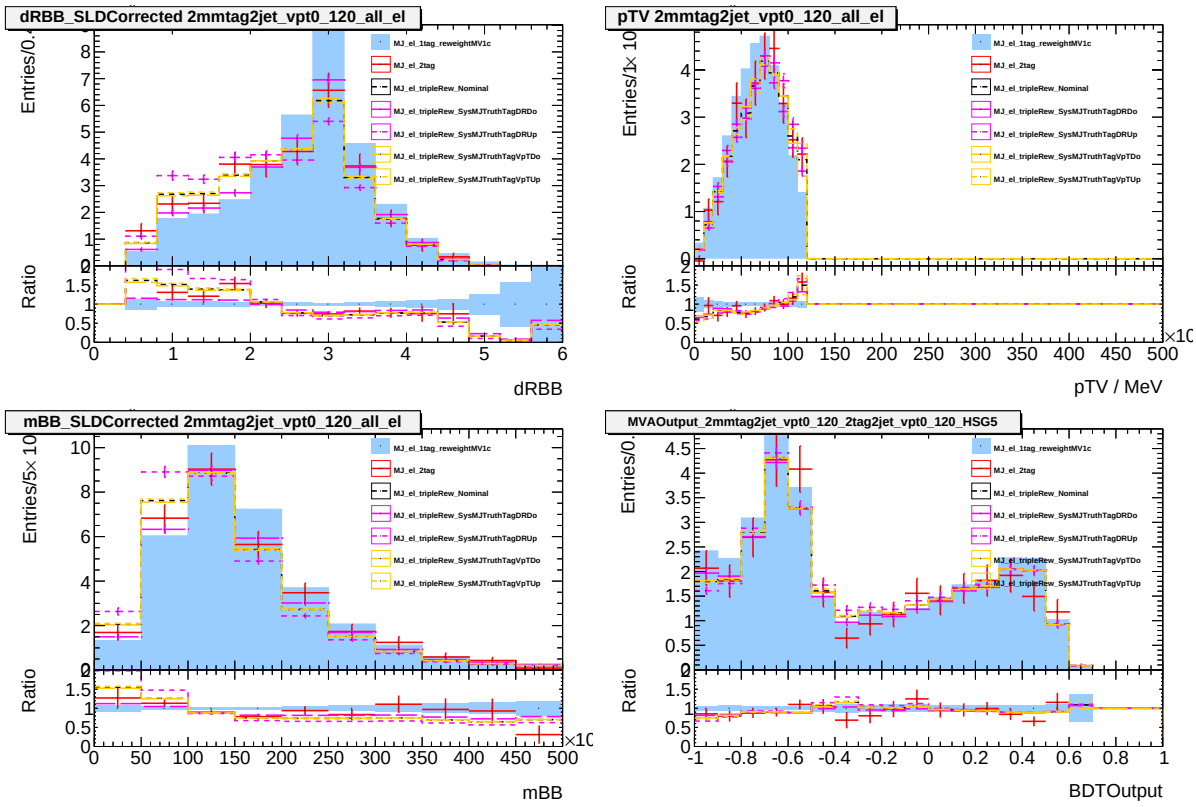

Figure 243: The top two figures show the variables on which the reweighting was derived and the bottom two show the dijet mass and the BDT for 2M tag $p_{\mathrm{T}}^{W} < 120$ GeV electron events. The red histogram is 2-tag events, the blue solid histogram is the 1-tag events spoofed into the 2-tag region and the black distribution shows the reweighted 1-tag events. The purple and yellow histograms are centered around the black and show the systematic from 1/2 of each reweighting - $\Delta R(bb)$ and p_{T}^{W} respectively. The ratio are taken wrt the blue histogram.

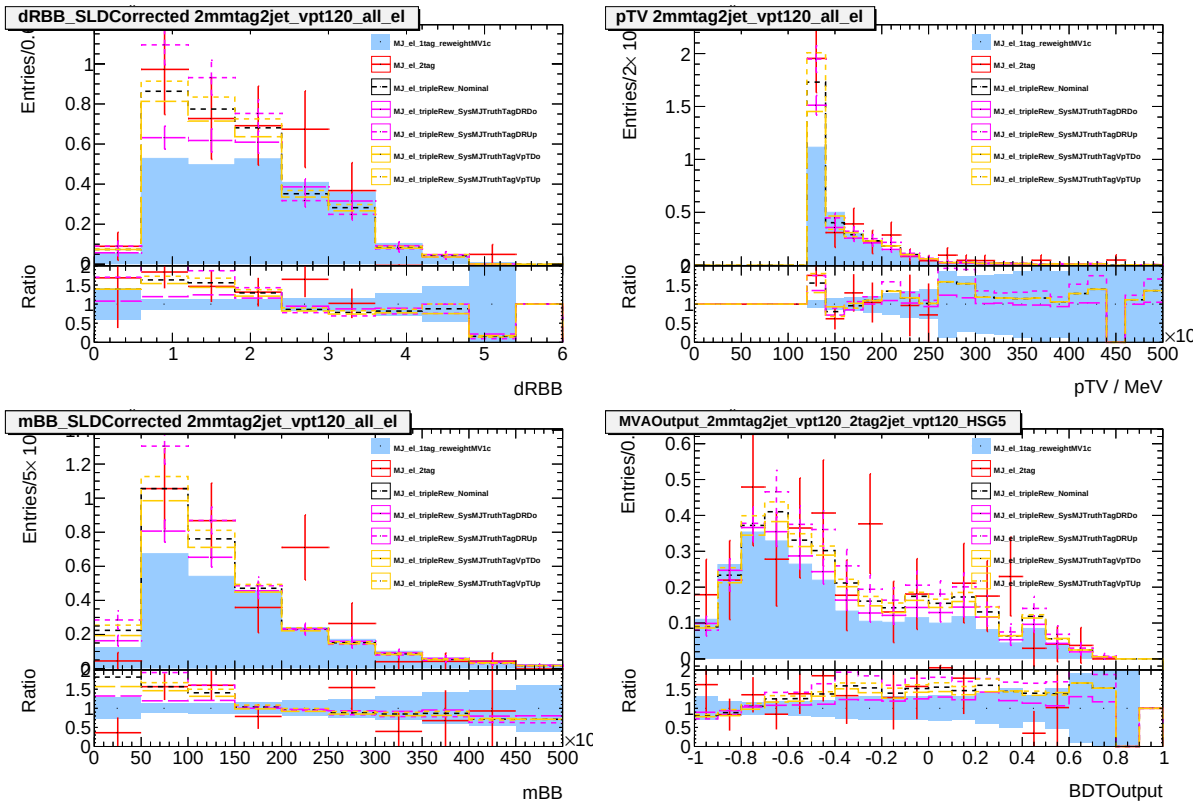

Figure 244: The top two figures show the variables on which the reweighting was derived and the bottom two show the dijet mass and the BDT for 2M tag $p_{\mathrm{T}}^{W} > 120$ GeV electron events. The red histogram is 2-tag events, the blue solid histogram is the 1-tag events spoofed into the 2-tag region and the black distribution shows the reweighted 1-tag events. The purple and yellow histograms are centered around the black and show the systematic from 1/2 of each reweighting - $\Delta R(bb)$ and p_{T}^{W} respectively. The ratio are taken wrt the blue histogram.

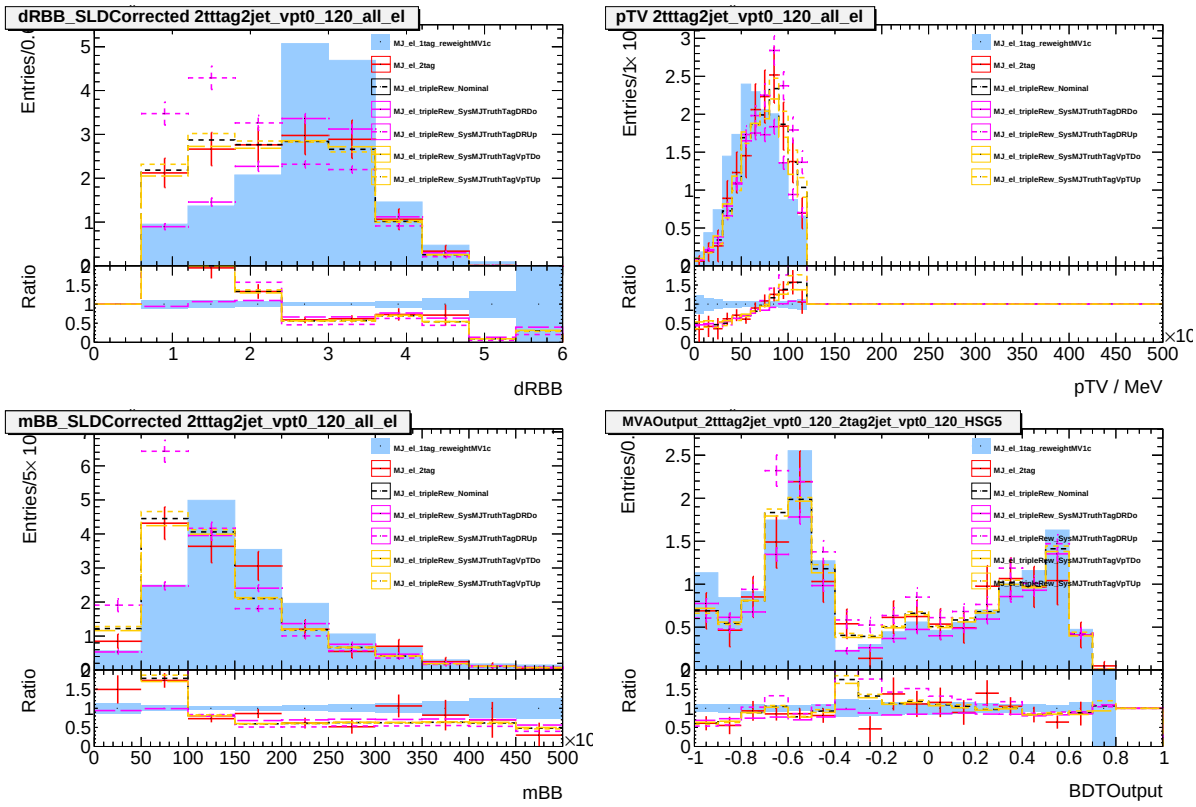

Figure 245: The top two figures show the variables on which the reweighting was derived and the bottom two show the dijet mass and the BDT for 2T tag $p_{\mathrm{T}}^{W} < 120$ GeV electron events. The red histogram is 2-tag events, the blue solid histogram is the 1-tag events spoofed into the 2-tag region and the black distribution shows the reweighted 1-tag events. The purple and yellow histograms are centered around the black and show the systematic from 1/2 of each reweighting - $\Delta R(bb)$ and p_{T}^{W} respectively. The ratio are taken wrt the blue histogram.

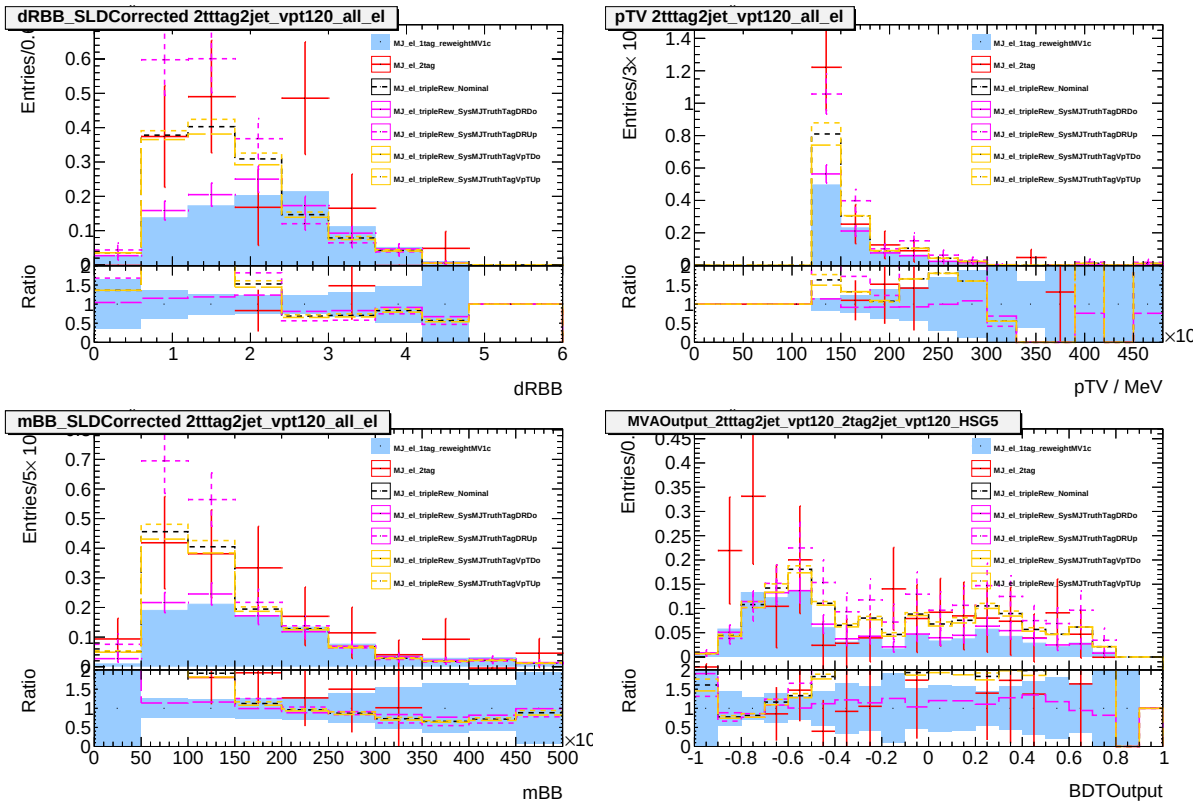

Figure 246: The top two figures show the variables on which the reweighting was derived and the bottom two show the dijet mass and the BDT for 2T tag $p_{\mathrm{T}}^{W} > 120$ GeV electron events. The red histogram is 2-tag events, the blue solid histogram is the 1-tag events spoofed into the 2-tag region and the black distribution shows the reweighted 1-tag events. The purple and yellow histograms are centered around the black and show the systematic from 1/2 of each reweighting - $\Delta R(bb)$ and p_{T}^{W} respectively. The ratio are taken wrt the blue histogram.

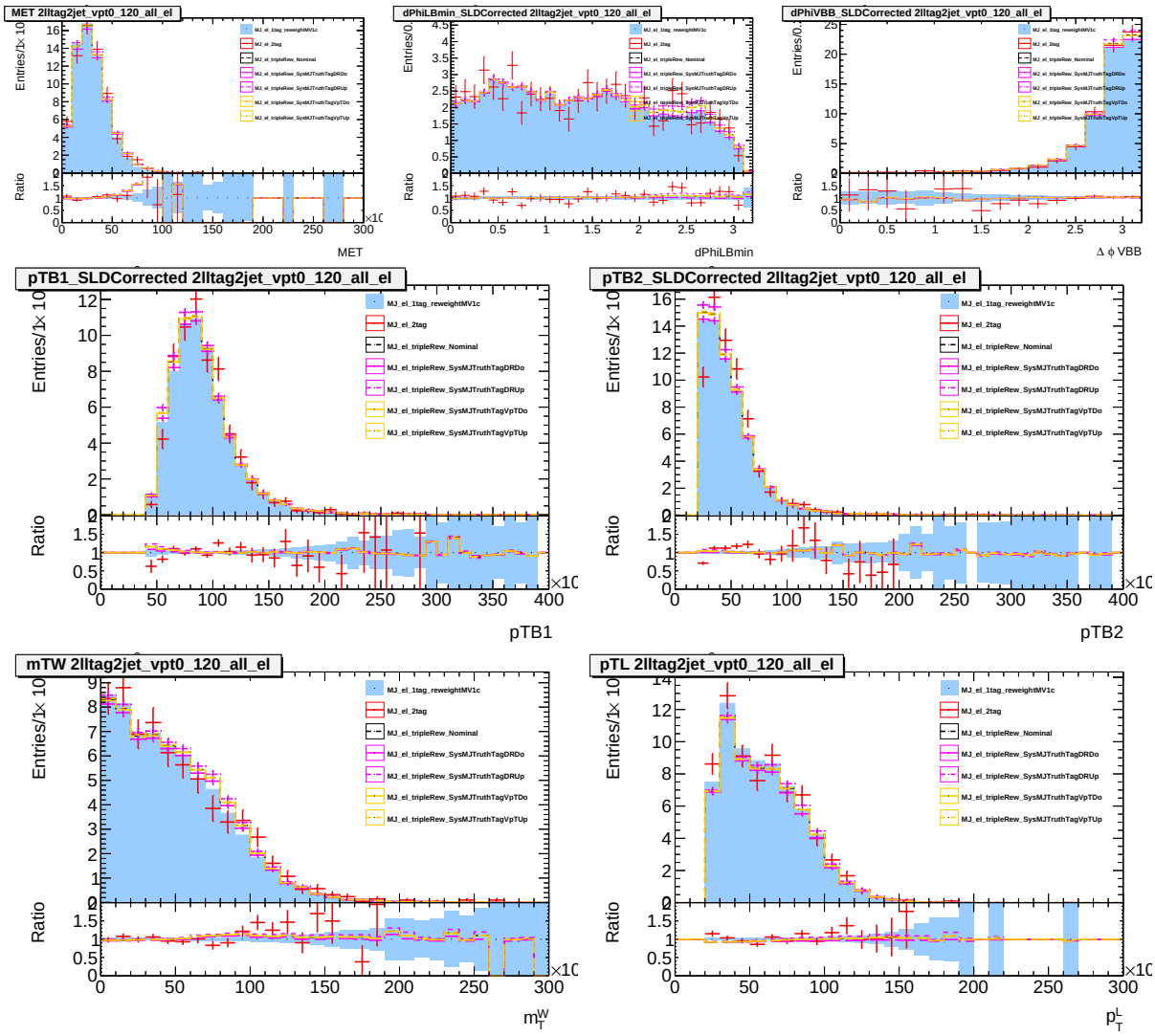

Figure 247: In 2L tag $p_{\mathrm{T}}^{W} < 120$ GeV electron events, the top three variables are $E_{\mathrm{T}}^{\mathrm{miss}}$, $\Delta\phi(l,b)$, and $\Delta\phi(V,B)$, the middle two show the p_{T} of the leading two jets and the bottom two are m_{T}^{W} and lepton p_{T}. The red histogram is 2-tag events, the blue solid histogram is the 1-tag events spoofed into the 2-tag region and the black distribution shows the reweighted 1-tag events. The purple and yellow histograms are centered around the black and show the systematic from 1/2 of each reweighting - $\Delta R(bb)$ and p_{T}^{W} respectively. The ratio are taken wrt the blue histogram.

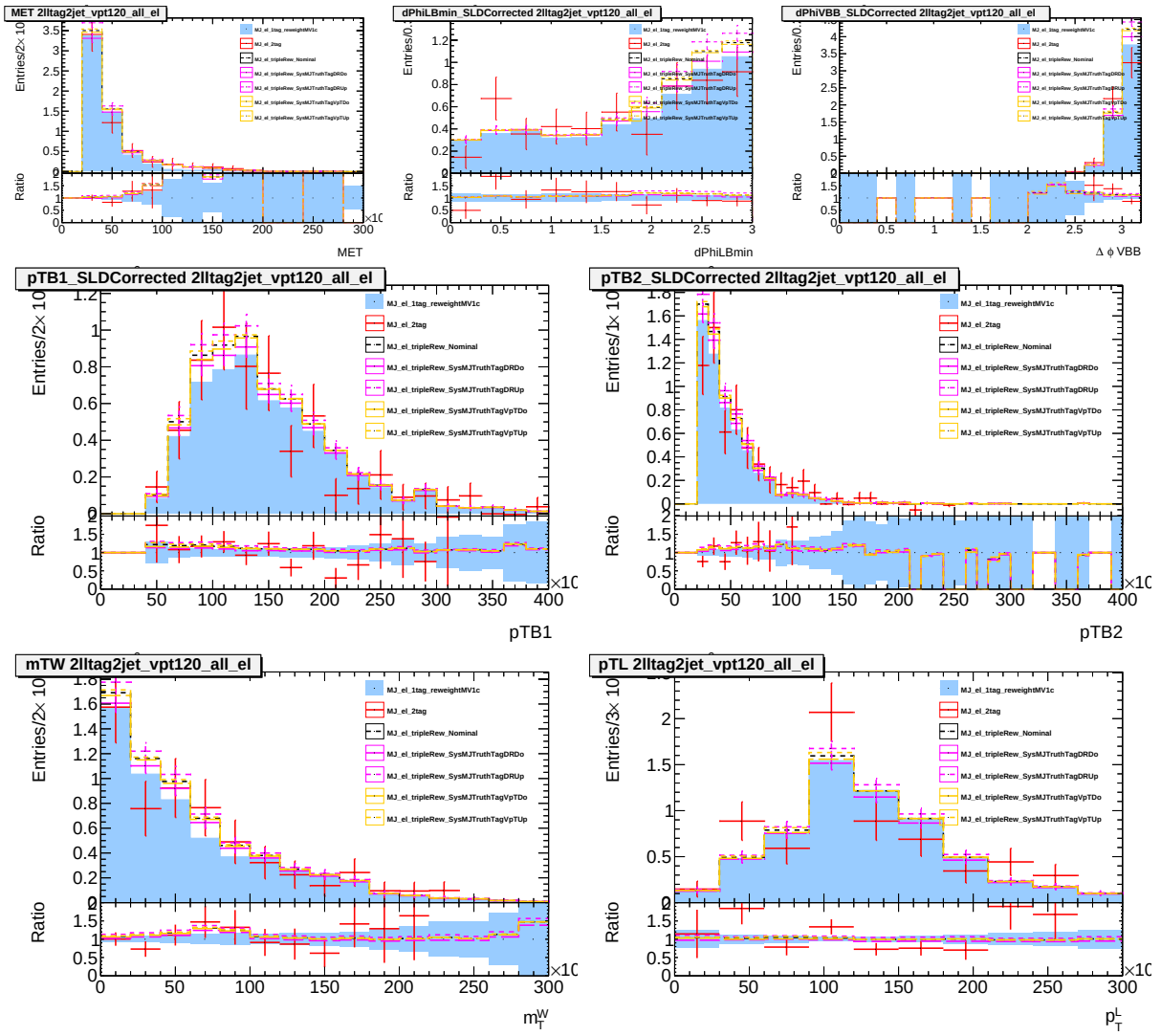

Figure 248: In 2L tag $p_{\mathrm{T}}^{W} > 120$ GeV electron events, the top three variables are $E_{\mathrm{T}}^{\mathrm{miss}}$, $\Delta\phi(l,b)$, and $\Delta\phi(V,B)$, the middle two show the p_{T} of the leading two jets and the bottom two are m_{T}^{W} and lepton p_{T}. The red histogram is 2-tag events, the blue solid histogram is the 1-tag events spoofed into the 2-tag region and the black distribution shows the reweighted 1-tag events. The purple and yellow histograms are centered around the black and show the systematic from 1/2 of each reweighting - $\Delta R(bb)$ and p_{T}^{W} respectively. The ratio are taken wrt the blue histogram.

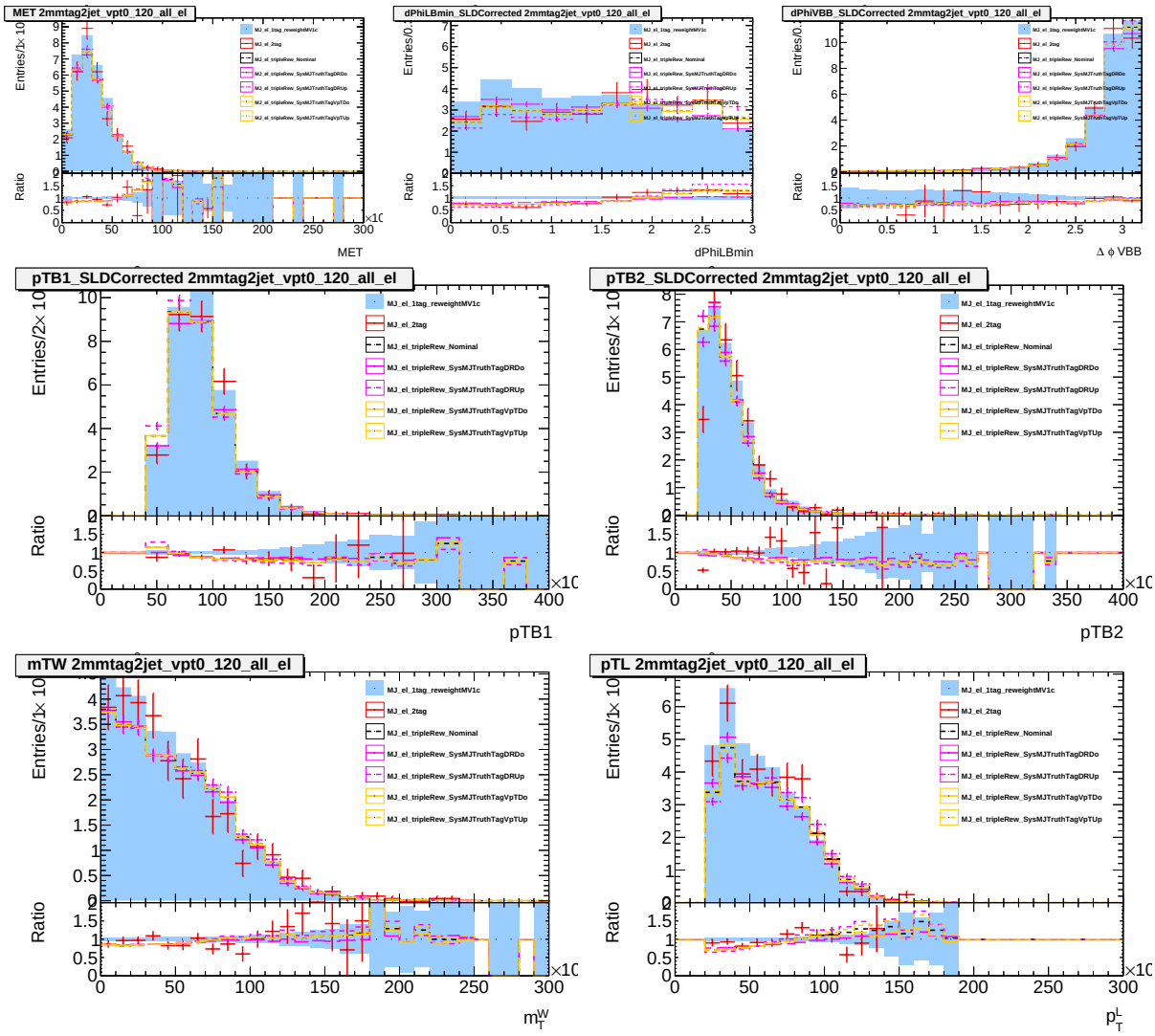

Figure 249: In 2M tag $p_{\mathrm{T}}^{W} < 120$ GeV electron events, the top three variables are $E_{\mathrm{T}}^{\mathrm{miss}}$, $\Delta\phi(l,b)$, and $\Delta\phi(V,B)$, the middle two show the p_{T} of the leading two jets and the bottom two are m_{T}^{W} and lepton p_{T}. The red histogram is 2-tag events, the blue solid histogram is the 1-tag events spoofed into the 2-tag region and the black distribution shows the reweighted 1-tag events. The purple and yellow histograms are centered around the black and show the systematic from 1/2 of each reweighting - $\Delta R(bb)$ and p_{T}^{W} respectively. The ratio are taken wrt the blue histogram.

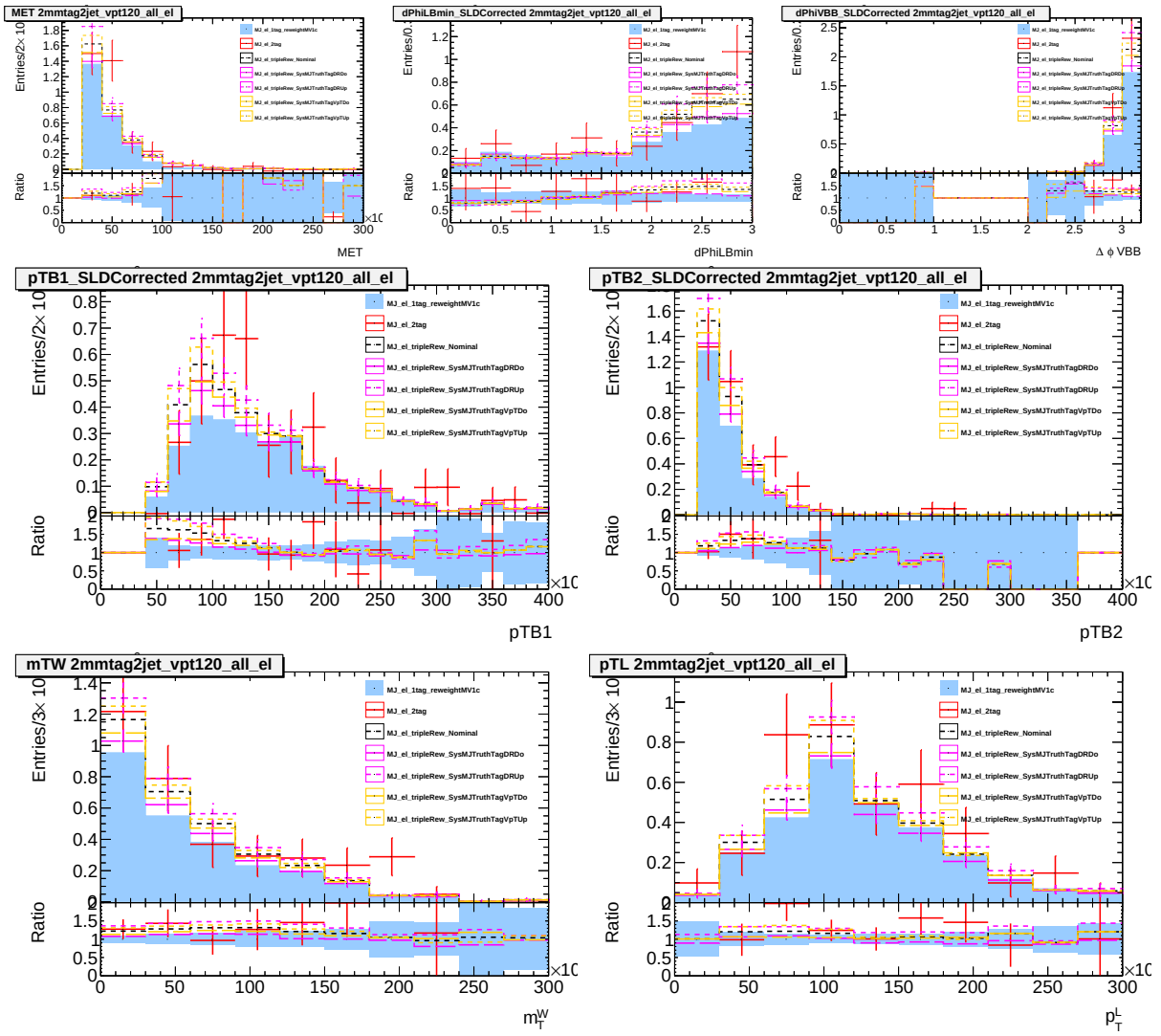

Figure 250: In 2M tag $p_{\mathrm{T}}^{W} > 120$ GeV electron events, the top three variables are $E_{\mathrm{T}}^{\mathrm{miss}}$, $\Delta\phi(l,b)$, and $\Delta\phi(V,B)$, the middle two show the p_{T} of the leading two jets and the bottom two are m_{T}^{W} and lepton p_{T}. The red histogram is 2-tag events, the blue solid histogram is the 1-tag events spoofed into the 2-tag region and the black distribution shows the reweighted 1-tag events. The purple and yellow histograms are centered around the black and show the systematic from 1/2 of each reweighting - $\Delta R(bb)$ and p_{T}^{W} respectively. The ratio are taken wrt the blue histogram.

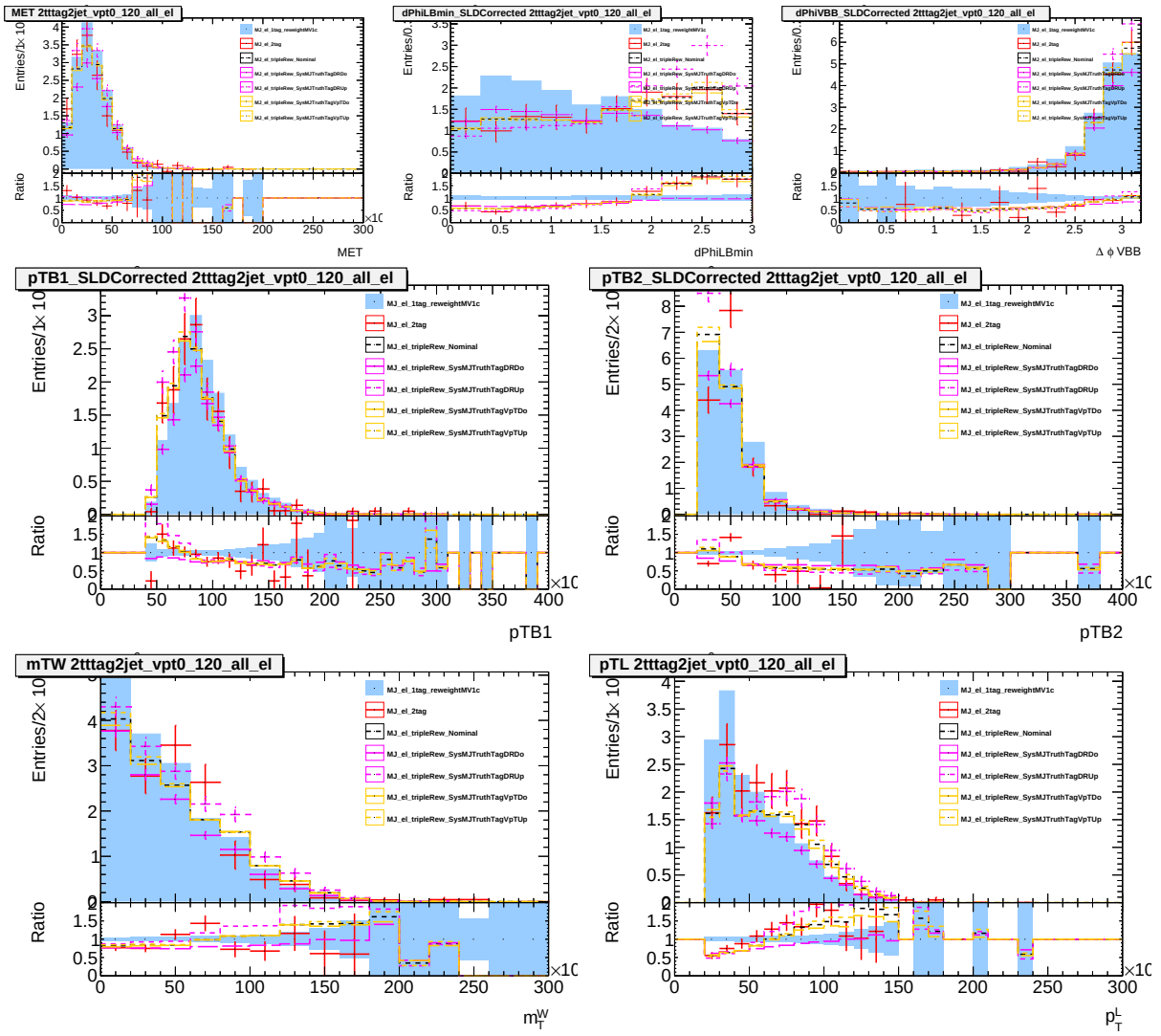

Figure 251: In 2T tag $p_{\mathrm{T}}^{W} < 120$ GeV electron events, the top three variables are $E_{\mathrm{T}}^{\mathrm{miss}}$, $\Delta\phi(l,b)$, and $\Delta\phi(V,B)$, the middle two show the p_{T} of the leading two jets and the bottom two are m_{T}^{W} and lepton p_{T}. The red histogram is 2-tag events, the blue solid histogram is the 1-tag events spoofed into the 2-tag region and the black distribution shows the reweighted 1-tag events. The purple and yellow histograms are centered around the black and show the systematic from 1/2 of each reweighting - $\Delta R(bb)$ and p_{T}^{W} respectively. The ratio are taken wrt the blue histogram.

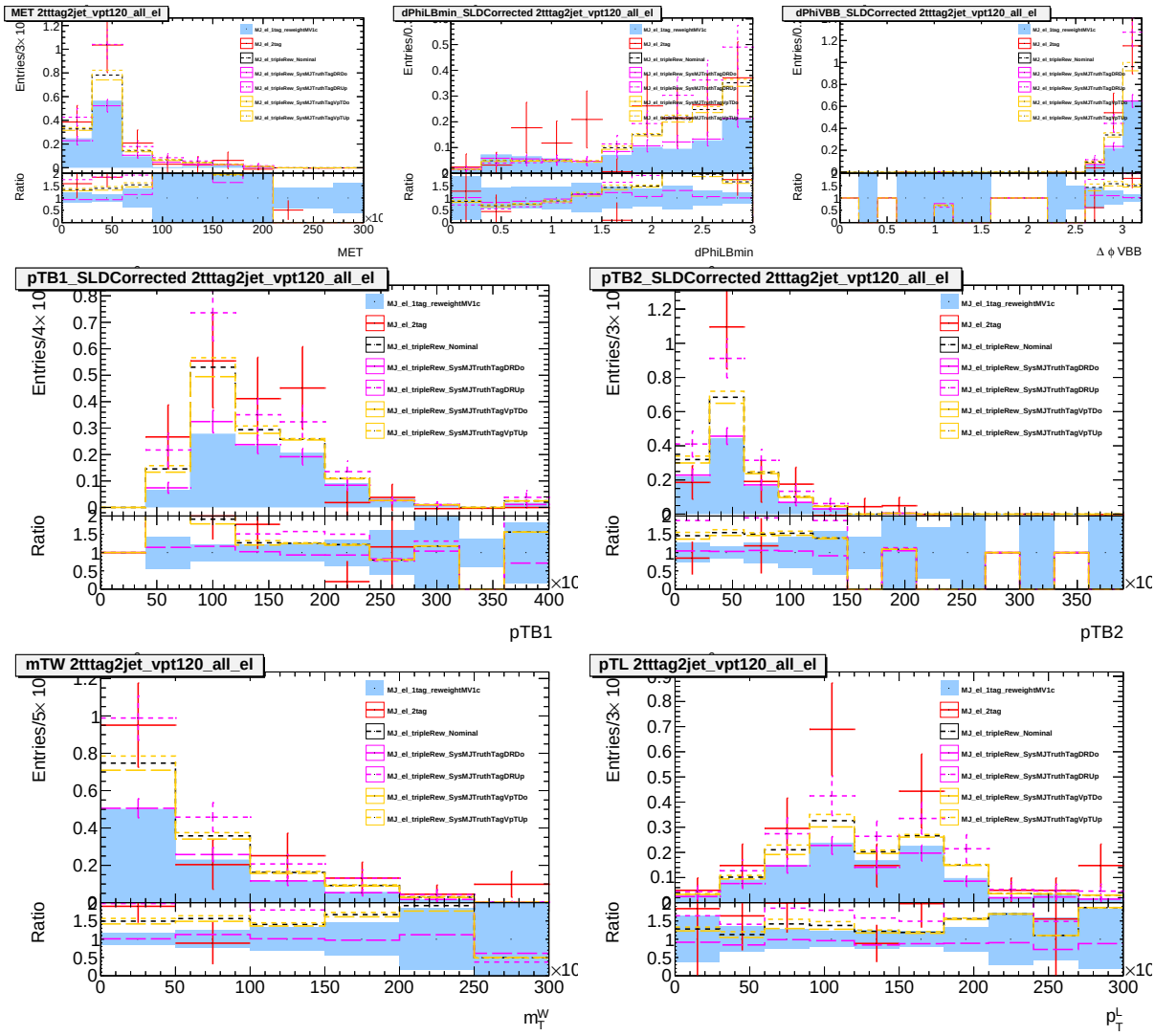

Figure 252: In 2T tag $p_{\mathrm{T}}^{W} > 120$ GeV electron events, the top three variables are $E_{\mathrm{T}}^{\mathrm{miss}}$, $\Delta\phi(l,b)$, and $\Delta\phi(V,B)$, the middle two show the p_{T} of the leading two jets and the bottom two are m_{T}^{W} and lepton p_{T}. The red histogram is 2-tag events, the blue solid histogram is the 1-tag events spoofed into the 2-tag region and the black distribution shows the reweighted 1-tag events. The purple and yellow histograms are centered around the black and show the systematic from 1/2 of each reweighting - $\Delta R(bb)$ and p_{T}^{W} respectively. The ratio are taken wrt the blue histogram.

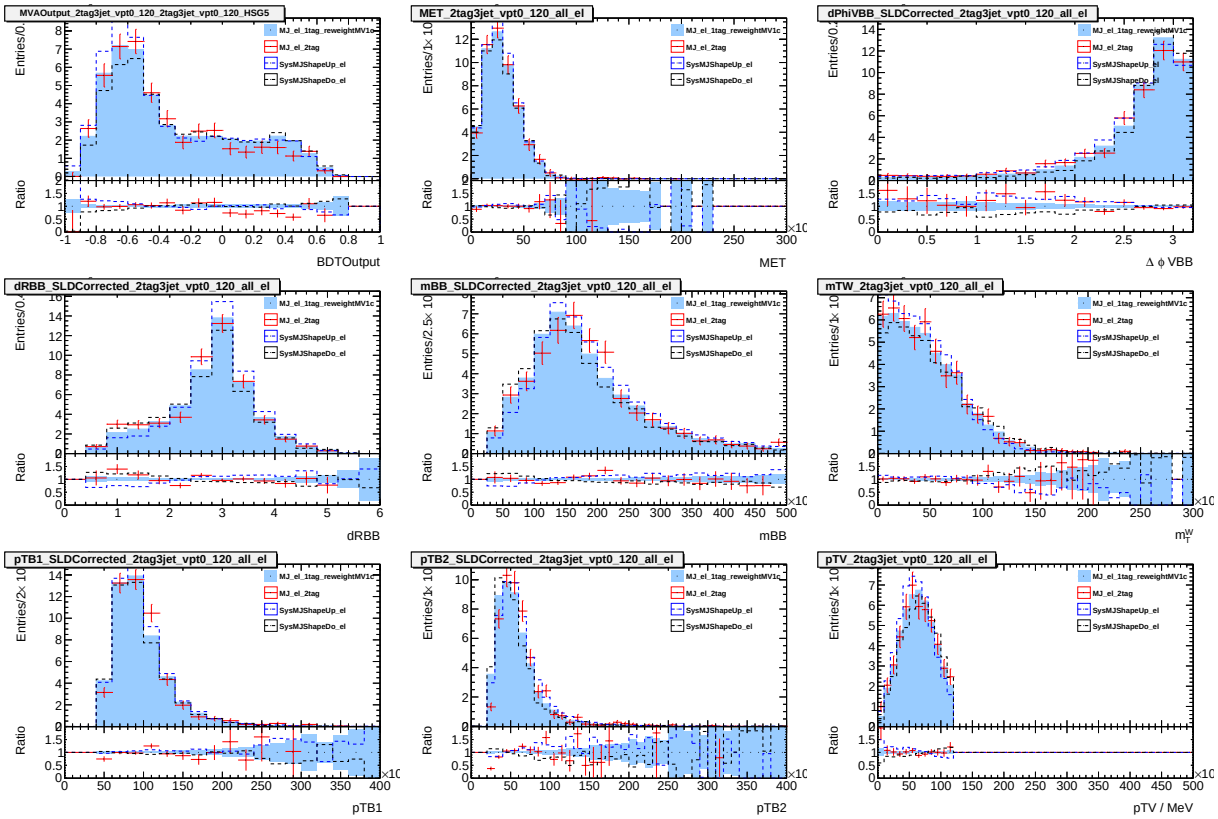

Figure 253: A comparison of 1-tag and 2-tag multijet events in the electron 3-jet channel with $ptW > 120$ GeV. The red histogram is 2-tag events, the blue solid histogram is the 1-tag events spoofed into the 2-tag region and the dashed histograms show the effect from the iso_{track} systematics

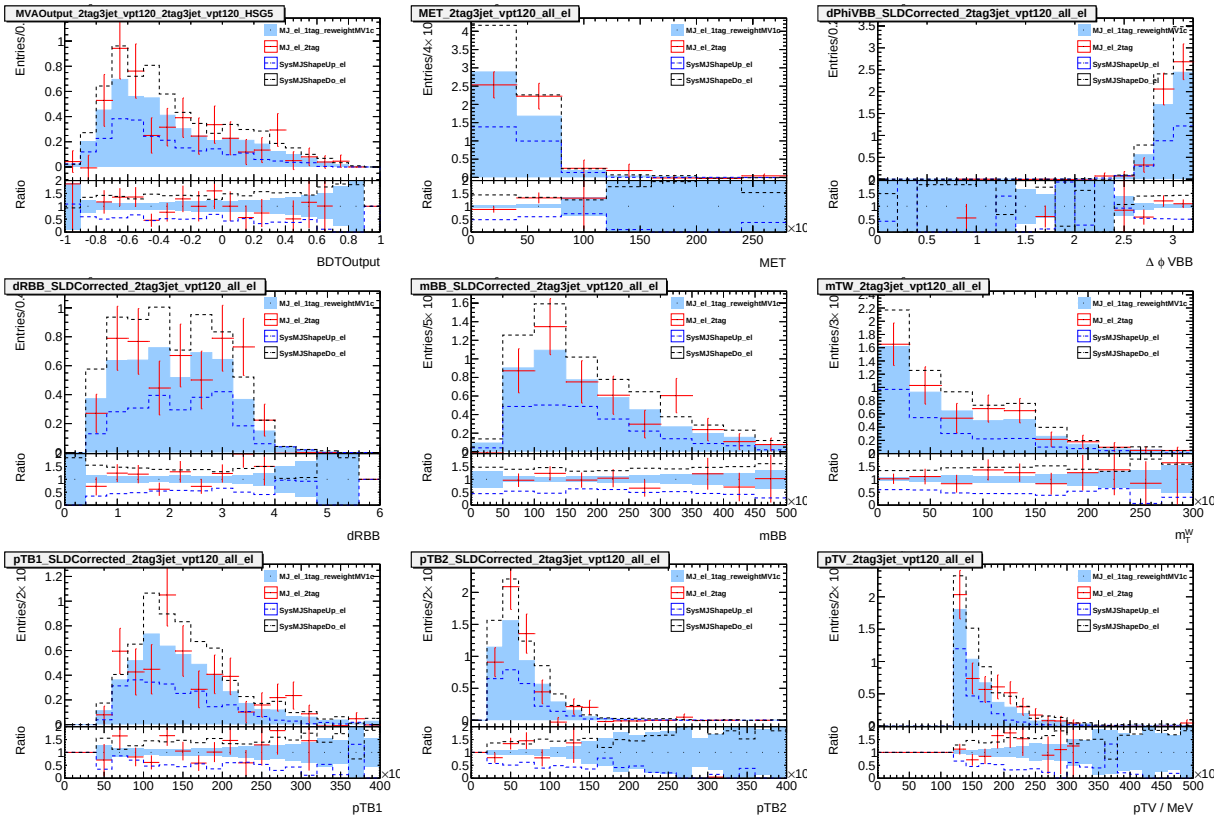

Figure 254: A comparison of 1-tag and 2-tag multijet events in the electron 3-jet channel with $ptW > 120$ GeV. The red histogram is 2-tag events, the blue solid histogram is the 1-tag events spoofed into the 2-tag region and the dashed histograms show the effect from the iso_{track} systematics

S Multi-jet background for 2-lepton analysis

Multijet events in which two jets are mistakenly identified as leptons form a background if the two misidentified leptons have an invariant mass compatible with the Z boson mass. Photon conversions also contribute in the case of electrons. In addition to fake leptons, true leptons from the semi-leptonic decay of heavy flavor hadrons may also contribute.

The multijet background in the electron channel is estimated from data. The shape of the background is obtained from a sample dominated by multijet events and then subsequently normalized to the signal selection. A data sample dominated by multijet events is obtained by reversing the track isolation cut of the two electrons. The remaining analysis selections are applied and the resulting data histograms are used as templates to describe the shape of the multijet background in the various distributions.

Although the templates describe the shape of the multijet background, they must be normalized to take into account the difference in efficiency between the two electron selections. The normalization is estimated by fitting the di-electron invariant mass distribution after applying the nominal selection up to the requirement of $\geq$ 2 jets. The fit is performed over the range $40 < m_{ee} < 150GeV$ using three components:

- The multijet template derived from data using an inverted iso_{track} cut ($iso_{track} > 0.1$)
- The $Z \rightarrow ee$ background distribution from the Monte Carlo simulation using the nominal electron selection.
- The sum of the all other background distributions from the Monte Carlo simulation using the nominal electron selection.

Only the normalizations of the multijet template and $Z \rightarrow ee$ background are allowed to vary (the other backgrounds are fixed). The fit is performed for each 0, 1, and 2-tag samples. For the 2-tag sample the $m_e e$ sidebands are dominated by $t\bar{t}$ events so the resulting scale factor is very uncertain (since the $t\bar{t}$ background is not floated but it is known to have a non-unity scale factor in the combined likelihood fit). For the 0, 1 and 2 tag samples the resulting multijet scale factor is 2.36 ± 0.02 (stat.), 1.89 ± 0.04 (stat.) and 2.22 ± 0.20 (stat.) respectively. The results of the fits are shown in figure 255. Due to the smaller backgrounds in the 0 tag, the 0-tag scale factor is used for the 1 and 2-tag samples alike with a 100% uncertainity applied (`MJ_L0`).

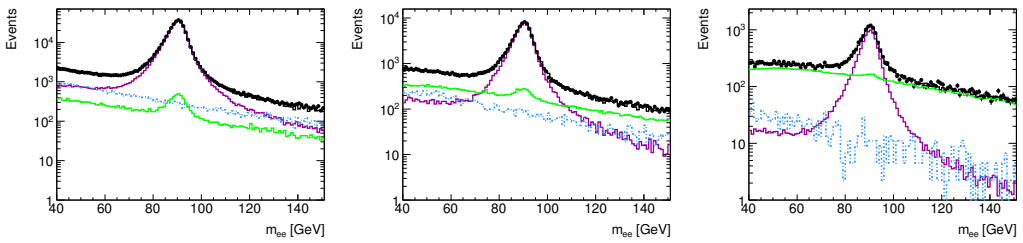

(a) 0-tag (b) 1-tag (c) 2-tag

Figure 255: The di-electron invariant mass distribution for (a) 0-tag, (b) 1-tag and (c) 2-tag. The background expectations have been scaled by the results of the fits. The purple distribution is Z+jets, the green is the other non-multijet backgrounds, and the blue histogram is the multijet background.

The statistics of the 2 tag sample are rather poor, so in order to produce a more accurate shape in the 2 tag distributions we use a method similar to the truth tagging method used for the Monte Carlo

(Section 3.3.4.1). Each event in the multijet template is used to form the 2 tag template with an additional event weight assigned as the fraction of 2 tag events in the multijet sample. Since the binned MV1c values of the two jets are used in the analysis, values are randomly assigned, based on the fraction of observed events in with each MV1c combination. This is shown in figure 256 where the sum of the MV1c values of the two jets is plotted, which (since the MV1c values are binned) displays each combination. The plot represents a closure test and displays the large improvement in statistical precision using the truth tagging method.

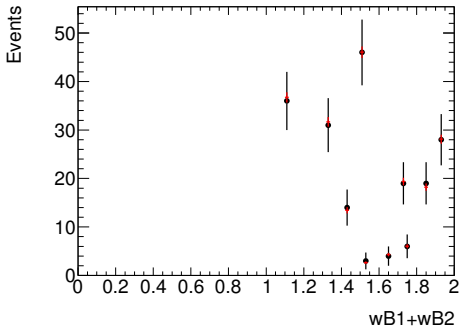

Figure 256: Distribution of the sum of the MV1c values of the two tagged jets in the 2 tag multijet template (black points). Also shown is the distribution of the multijet template using the truth tagging method (red points).

The multijet background in the muon channel was investigated by comparing the data and Monte Carlo in the $m_{\mu\mu}$ sidebands and found to be negligible. The 0-tag distribution for the electron and muon channel are compared in Figure 257.

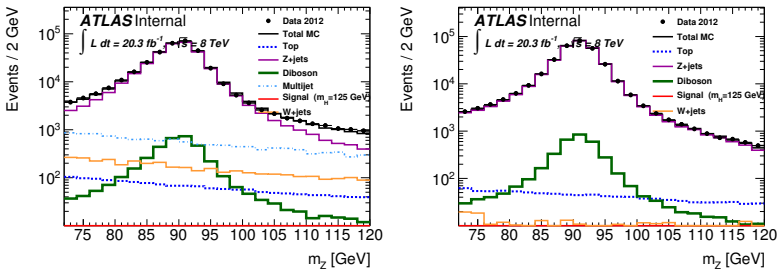

(a) electron (b) muon

Figure 257: The di-electron (di-muon) invariant mass distribution in a (b) showing the level of multijet contamination. The muon channel shows no evidence for a significant multijet contribution which the electron channel does. The distributions are made with the 2-lepton MVA selection with 2 or more jets requiring 0 b-tags.

T *b*-tagging Related Studies

This appendix discussed the efficiecny maps derived for the truth tagging procedure described in Section 3.3.4.1, the closure test of the truth tagging procedure, and additional scale factors derived to take into consideration the different intrinsic tagging efficiency in various generators.

T.1 Custom *b*-tagging Efficiency Maps

The truth tagging procedure described in Section 3.3.4.1 relies on the knowing the tagging efficiencies in MC. In preparation for EPS [11], a sample dependence was seen in the MC efficiency [74] so custom efficiency maps are needed so that a sample-dependent bias is not introduced.

One map for each of the operating points listed in Table 7 (including !Loose) has been derived for different main backgrounds, $t\bar{t}$, W+jets, and Z+jets, detailed in Section 5. A minimal selection consisting of the the cleaning cuts described in Section 3.3.1 and at least one jet with $p_{\mathrm{T}} > 15$ GeV and $|\eta| < 2.7$. The JVF cut and flavor labeling scheme described in Section are both used. When truth tagging is performed on processes such as single-top and diboson, which is not often, the $t\bar{t}$ derived efficiency map is used.

The maps are 2-dimensional histograms with dimensions of jet p_{T} and η. Very fine binning in both dimensions leaves some bins unpopulated. After extensive studies it was decided to use coarser binning instead of a smoothing algorithm due to the fewer implicit assumptions. The final bin width in η was 0.2 for b-jets in the $t\bar{t}$ sample and 0.3 in all others. In the case of τ efficiency maps an $|\eta|$ symmetrization was needed in order to compensate for the low statistics. For the jet p_{T}, and original binning of

$$0, 10, 15, 17.5, 20, 22.5, 25, 27.5, 30, 35, 40, 45, 50, 55, 60, 65, 70, 75,$$

$$80, 85, 90, 95, 100, 105, 110, 115, 120, 130, 140, 150, 160, 170, 180, 190,$$

$$200, 225, 250, 275, 300(325, 350, 400, 450, 500, 550, 600)$$

was chosen such that at low p_{T}, where the efficiency is steeply falling and many jets are available to improve the accuracy of the map. However a rebin factor of 2 (3) was necessary for all flavor (τ) maps. Jets with $p_{\mathrm{T}} > 300$ GeV are gathered into one bin and assigned the efficiency from the penultimate bin (the one just below 300 GeV). b-jet efficiency maps are shown in Figure 258, c-jets in Figure 259, *light*-jets in Figure 260, and *tau*-jets in Figure 261. Table 7 details the operating points including the corresponding MV1c value.

The tag weight distribution in a given jet p_{T} and η bin follows a multinomial distribution and using the total yield such the parameters of such a distribution are obtained. A new set of efficiency maps can be created by sampling said multinomial distribution. The difference between the result with the varied efficiency map and the nominal efficiency map can be used to estimate the systematics impact introduced by the statistical fluctuation of the efficiency maps.

Figure 262 shows the efficiency as a function jet η with the tag weight in the 80% efficiency bin for both the nominal map and the varied map, between which the difference is less than 1%. Figure 263 shows a comparison of the m_{jj} distribution of $Z+cc$ sample after truth tagging in the the 0-lepton channel with the nominal and varied map. The difference negligible.

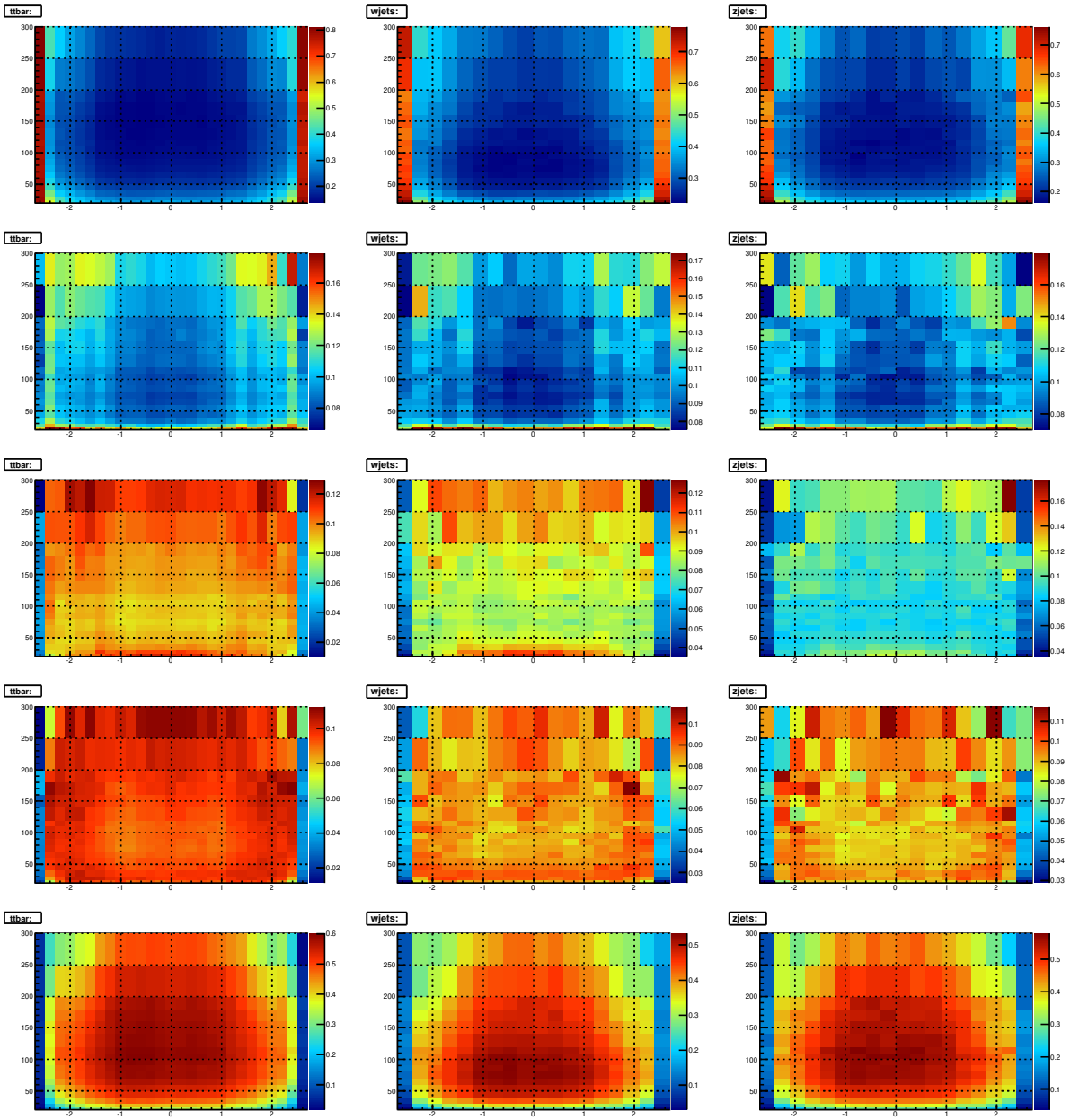

Figure 258: *b*-jet efficiency maps for >80% OP MV1c< 0.4050 (row 1), 80% OP 0.4050<MV1c<0.7028 (row 2), 70% OP 0.7028<MV1c<0.8353 (row 3), 60% 0.8353<MV1c<0.9237 (row 4), and 50% OP MV1c > 0.9237 (row 5) with $t\bar{t}$, Z+jets, and W+jets shown from left to right. Table 7 details the operating points (OP) including the corresponding MV1c value.

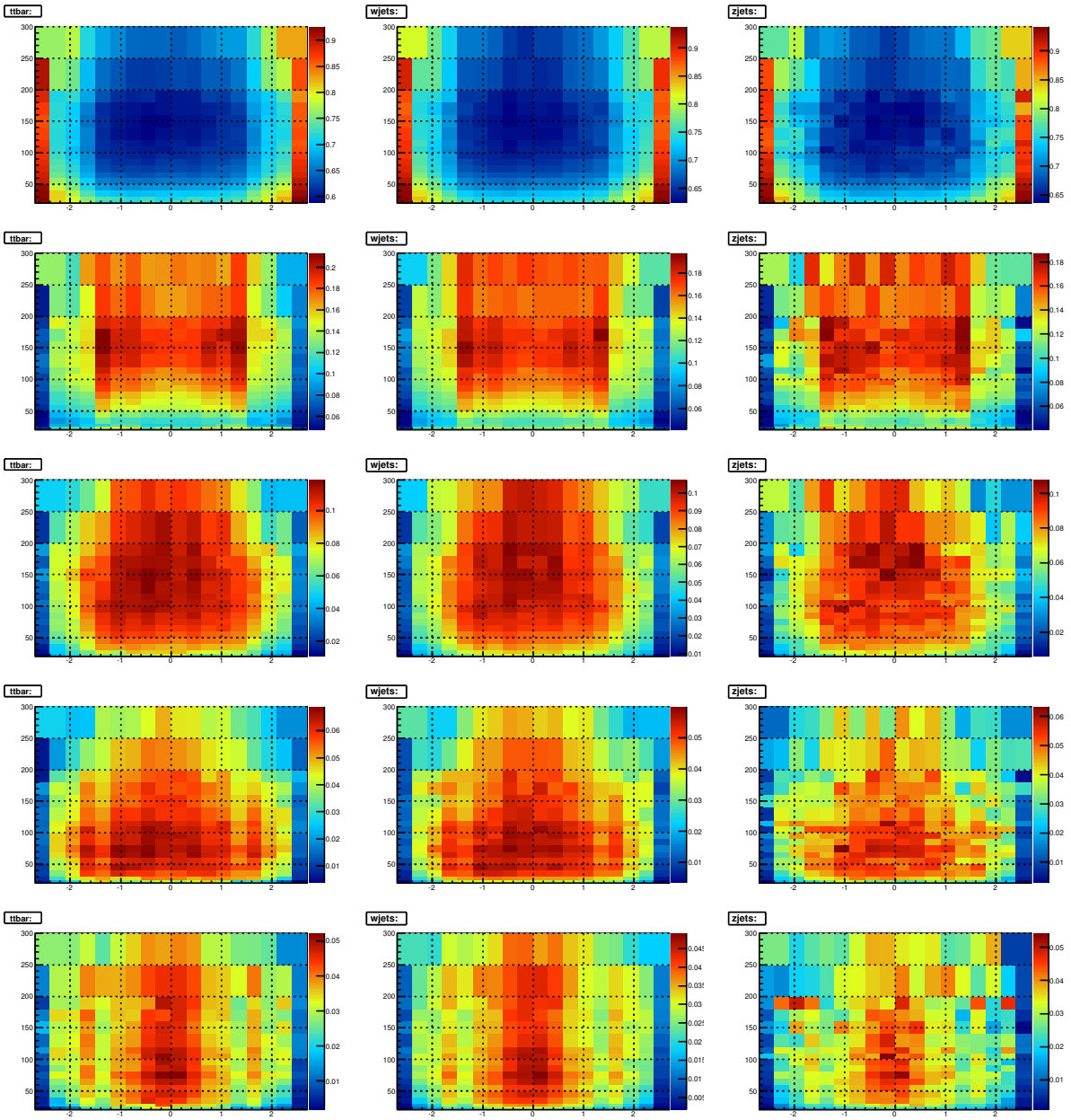

Figure 259: c-jet efficiency maps for >80% OP MV1c< 0.4050 (row 1), 80% OP 0.4050<MV1c<0.7028 (row 2), 70% OP 0.7028<MV1c<0.8353 (row 3), 60% 0.8353<MV1c<0.9237 (row 4), and 50% OP MV1c > 0.9237 (row 5) with $t\bar{t}$, Z+jets, and W+jets shown from left to right. Table 7 details the operating points (OP) including the corresponding MV1c value.

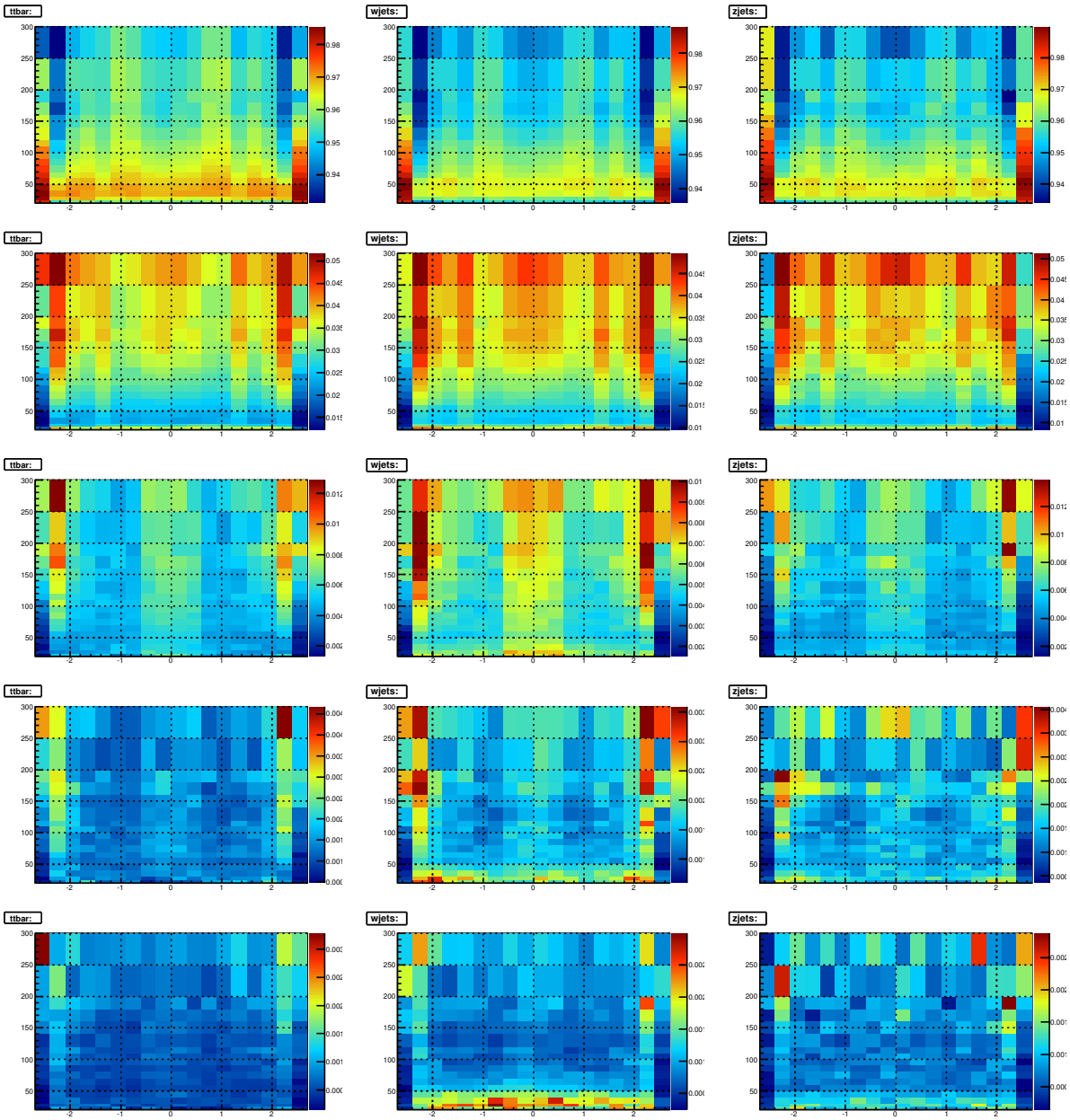

Figure 260: *light*-jet efficiency maps for >80% OP MV1c< 0.4050 (row 1), 80% OP 0.4050<MV1c<0.7028 (row 2), 70% OP 0.7028<MV1c<0.8353 (row 3), 60% 0.8353<MV1c<0.9237 (row 4), and 50% OP MV1c > 0.9237 (row 5) with $t\bar{t}$, Z+jets, and W+jets shown from left to right. Table 7 details the operating points (OP) including the corresponding MV1c value.

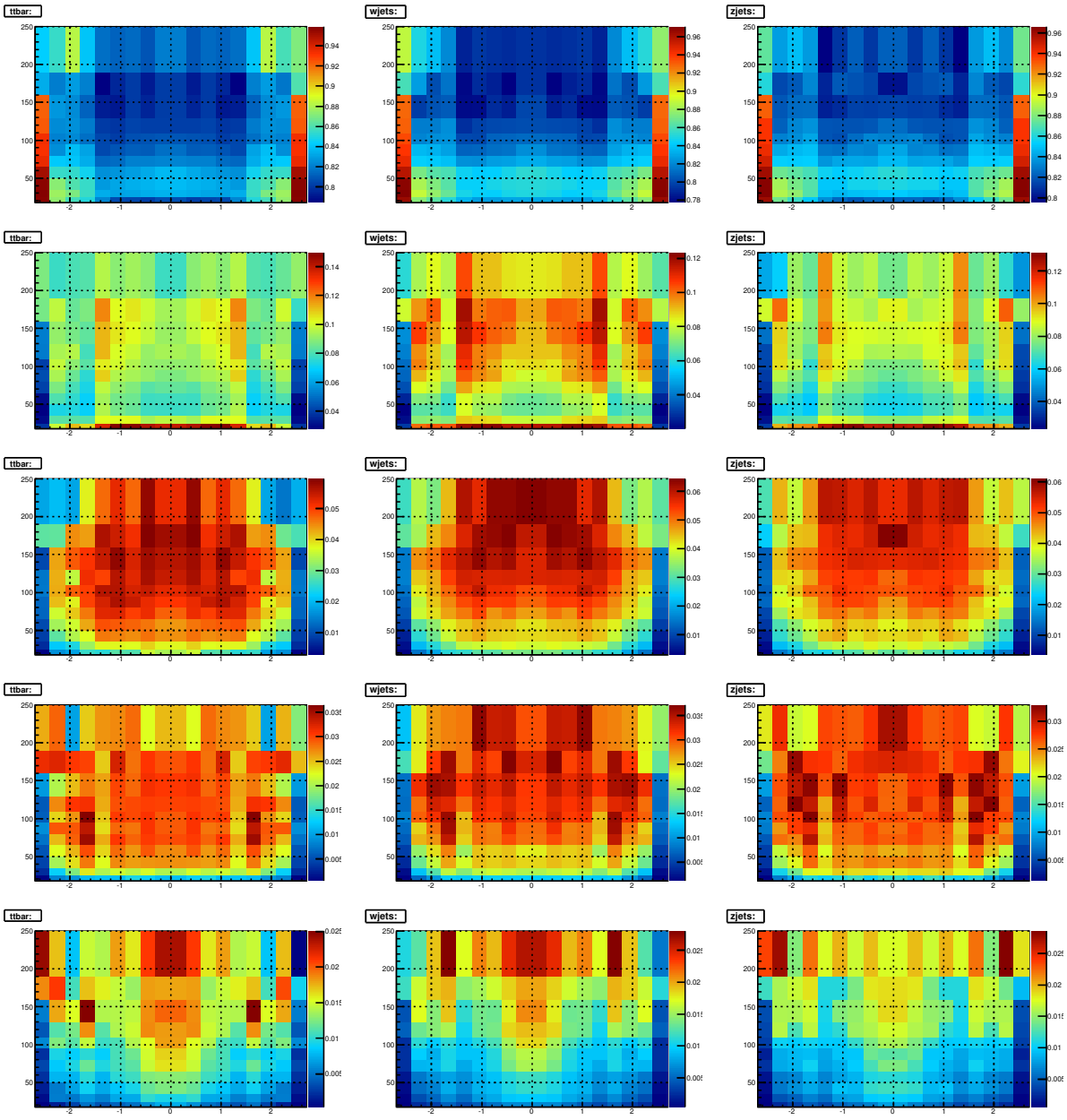

Figure 261: τ-jet efficiency maps for >80% OP MV1c< 0.4050 (row 1), 80% OP 0.4050<MV1c<0.7028 (row 2), 70% OP 0.7028<MV1c<0.8353 (row 3), 60% 0.8353<MV1c<0.9237 (row 4), and 50% OP MV1c > 0.9237 (row 5) with $t\bar{t}$, Z+jets, and W+jets shown from left to right. Table 7 details the operating points (OP) including the corresponding MV1c value.

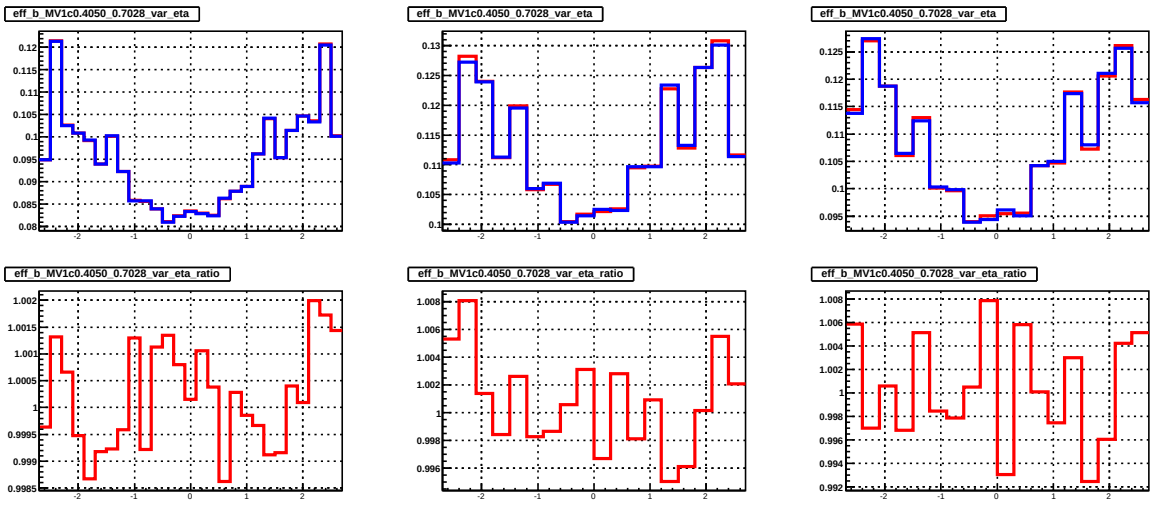

Figure 262: The top plots are the efficiency as function of jet η, while bottom is the ratio between the varied(Red) and the nominal(Blue). The left for $t\bar{t}$, the middle for Z jets, and the right for W jets.

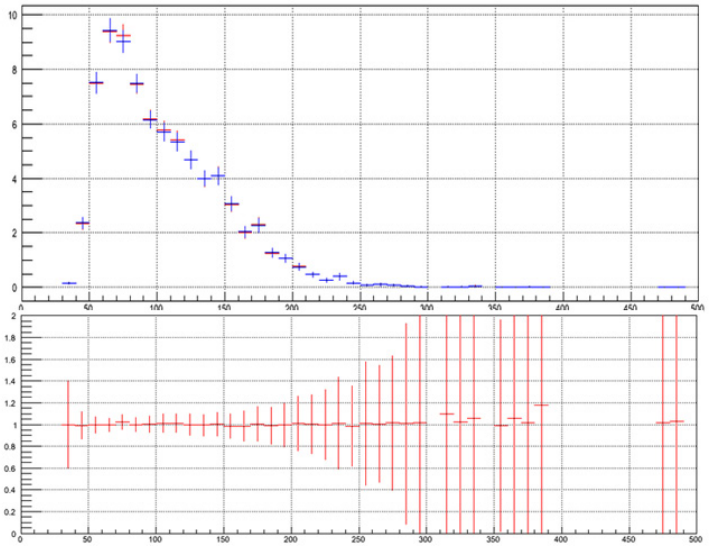

Figure 263: The m_{jj} distribution of Zcc at ll-tag region with truth tagging in the 0-lepton channel. The red is from the varied efficiency map, while the blue is from the nominal efficiency map. The bottom plot is the ratio.

T.2 *b*-tagging generator dependence scale factor

As demonstrated in EPS [11], and is widely known, the flavor tagging efficiency is generator dependent due to the different parton shower, hadronization models, and hadron branching ratios. The efficiency scale factors provided by the flavor tagging group which correct to the efficiecny in data, $SF = \epsilon_{data}/\epsilon_{MC}$, are with respect to PYTHIA6. An analysis such as this using several generators (PYTHIA6, PYTHIA8 and SHERPA), each with a different tagging efficiecny, ϵ'_{MC}, must take these differences into consideration. To this end, MC-to-MC scale factors, $SF_{MC-to-MC} = \epsilon_{MC}/\epsilon'_{MC}$ have been derived using the following $t\bar{t}$ samples:

- mc12_8TeV.117050.PowhegPythia_P2011C_ttbar.merge.NTUP_SMWZ.e1728_s1581_s1586_r3658_r3549_p1328
- mc12_8TeV.18138X.Sherpa_CT10_TTbarX.merge.NTUP_SMWZ.e20_s1581_s1586_r4485_r4540_p1328 (X∈0-9)
- mc12_8TeV.110898.Pythia8_AU2MSTW2008LO_EWttbar.merge.NTUP_TOP.e2512_s1499_s1504_r3658_r3549_p1400

Figures 264 to 268 show the b-tagging efficiency as a function of jet p_{T} in the 5 MV1c operating points for *b* and *c*-jets in $t\bar{t}$ events for the above samples. The ratio to PYTHIA6 is shown and this is the value used for the MC-to-MC scale factors for *b* and *c* jets.

Modeling of heavy flavor hadrons is the main difference between the generators. Even though long-lived light hardrons iė K_s and Λ can differ in a similar way, it has been shown to be a small effect. This, plus the fact that the light jet component is relatviely small in the most sensitive regions, MC-to-MC scale factors have not been applied to light jets.

Half of the correction has been assigned as the systematic uncertainty which is for each generator and for *b* and *c* jets separately (`BTagBSherpa`, `BTagBPythia8`, `BTagCSherpa`, `BTagCPythia8`).

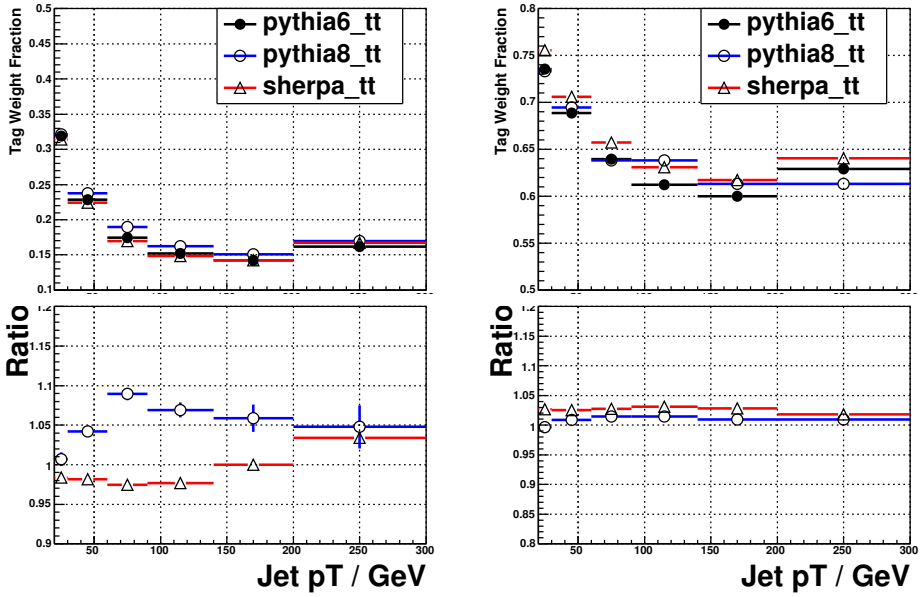

Figure 264: *b*-jet (left) and *c*-jet (right) tagging efficiency for the jets between the 100% OP and 80% OP (0.0<MV1c< 0.4050) in $t\bar{t}$ events produced by PYTHIA6 (Black), PYTHIA8 (Blue) and SHERPA (Red). The ratio is the MC-to-MC scale factor.

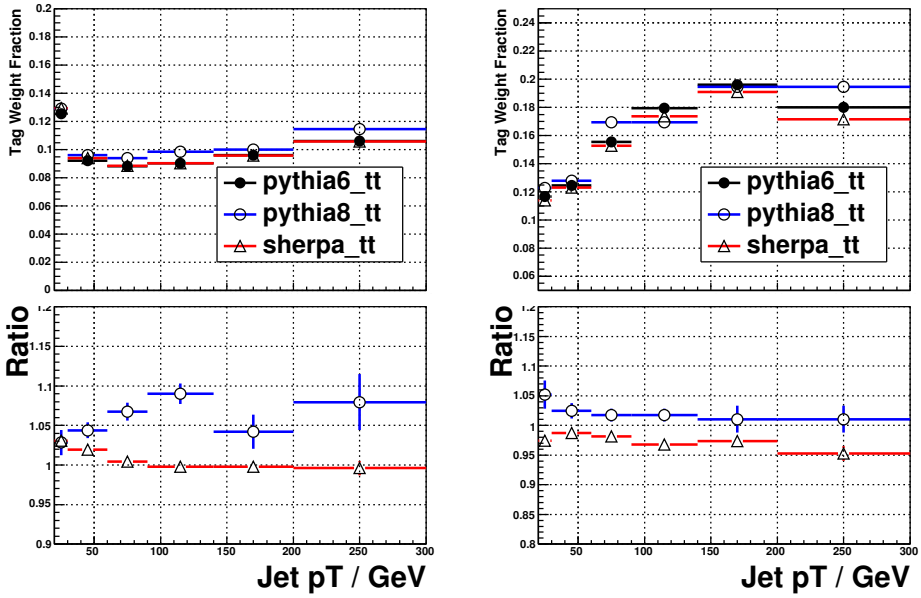

Figure 265: *b*-jet (left) and *c*-jet (right) tagging efficiency for the jets between the 80% OP and 70% OP (0.4050<MV1c<0.7028) in $t\bar{t}$ events produced by PYTHIA6 (Black), PYTHIA8 (Blue) and SHERPA (Red). The ratio is the MC-to-MC scale factor.

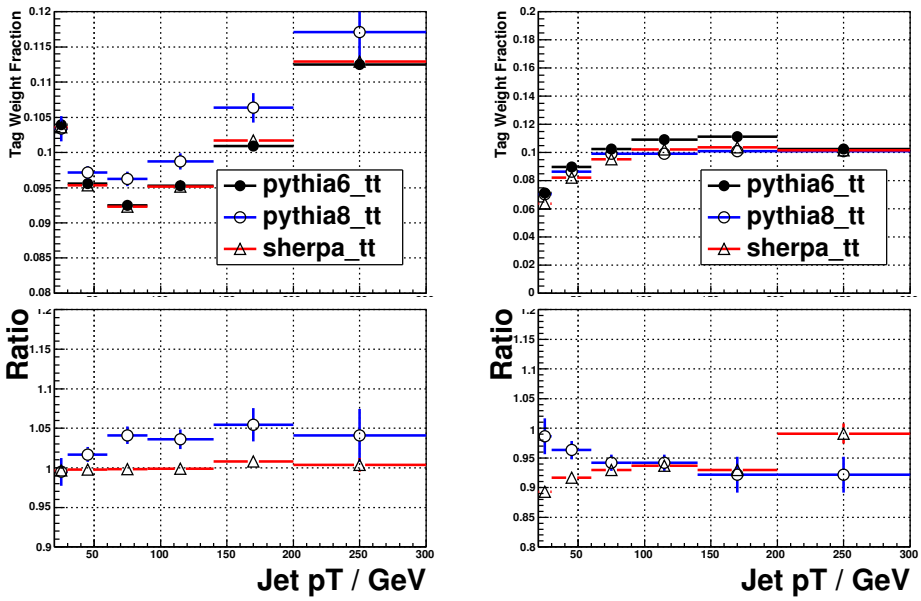

Figure 266: *b*-jet (left) and *c*-jet (right) tagging efficiency for the jets between the 70% OP and 60% OP (0.7028<MV1c<0.8353) in $t\bar{t}$ events produced by PYTHIA6 (Black), PYTHIA8 (Blue) and SHERPA (Red). The ratio is the MC-to-MC scale factor.

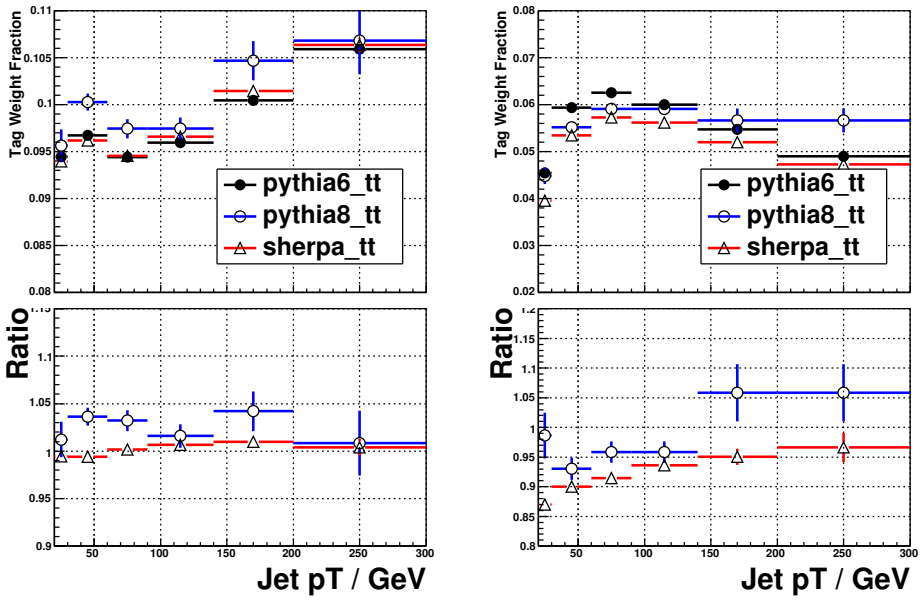

Figure 267: *b*-jet (left) and *c*-jet (right) tagging efficiency for the jets between the 60% OP and 50% OP (0.8353<MV1c<0.9237) in $t\bar{t}$ events produced by PYTHIA6 (Black), PYTHIA8 (Blue) and SHERPA (Red). The ratio is the MC-to-MC scale factor.

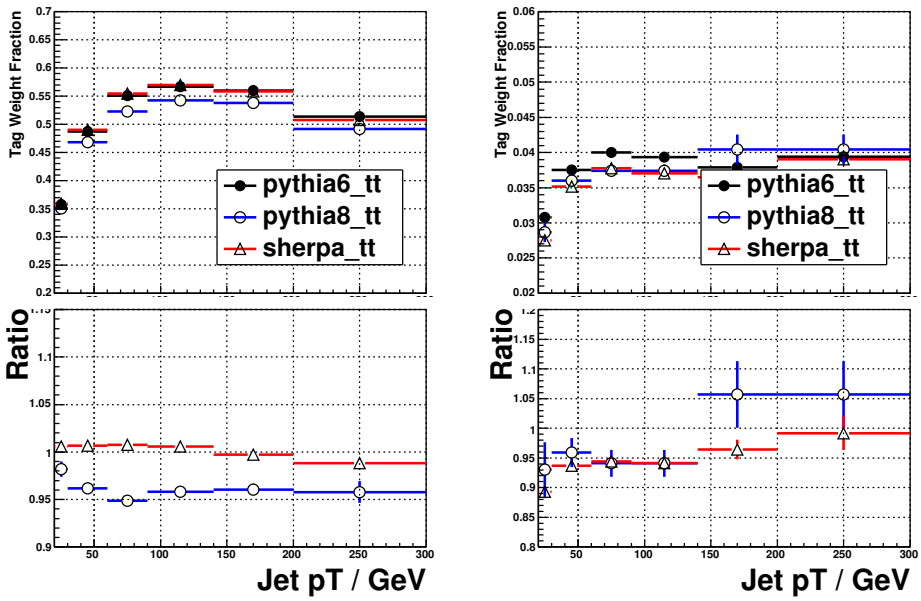

Figure 268: *b*-jet (left) and *c*-jet (right) tagging efficiency for the jets above the 50% OP (0.9237<MV1c<1.0) in $t\bar{t}$ events produced by PYTHIA6 (Black), PYTHIA8 (Blue) and SHERPA (Red). The ratio is the MC-to-MC scale factor.

T.3 truth *b*-tagging efficiency maps closure test

In order to gain statistics, truth tagging has been applied to events in which neither of the leading two jets is truth matched to a b hadron, as described in Section 3.3.4.1, using the efficiency map as shown in Appendix T.1. After applying the truth tagging procedure, the predicted yield and kinematics of each sample should be consistent with prediction using the direct tagging procedure (simply cutting on the MV1c value itself). The most basic variable which showed a systematic difference in the truth and direct tag predictions was $\Delta R(jet_1, jet_2)$ shown in Figures 269-272 for V+ll, V+cl, V+cc, and WW events passing the 0-lepton MVA selection with 2 b-tags. Within the available statistics only the V+cc processes lack agreement between the two approaches. Tagging efficiency dependence on variables other than jet p_{T} and η are not directly parameterized in the efficiency maps and therefore need to be accounted for in another way. Since both W+cc and Z+cc both show consistent behavior in 2 and 3-jet events (Figure 273), the four samples have been combined in order to derive a correction (Figure 274) with the maximum available statistics. The correction is given by:

$$0.9509 + 0.418 \times ln(\Delta R) - 0.3697 \times ln^2(\Delta R) \tag{43}$$

defined only for $\Delta R < 2.7$. After the correction, agreement between the truth tagging and direct tagging procedures is restored as demonstrated in Figure 275. Half the correction has been assigned as the systematic uncertainty (`BTagTruthTagDR`).

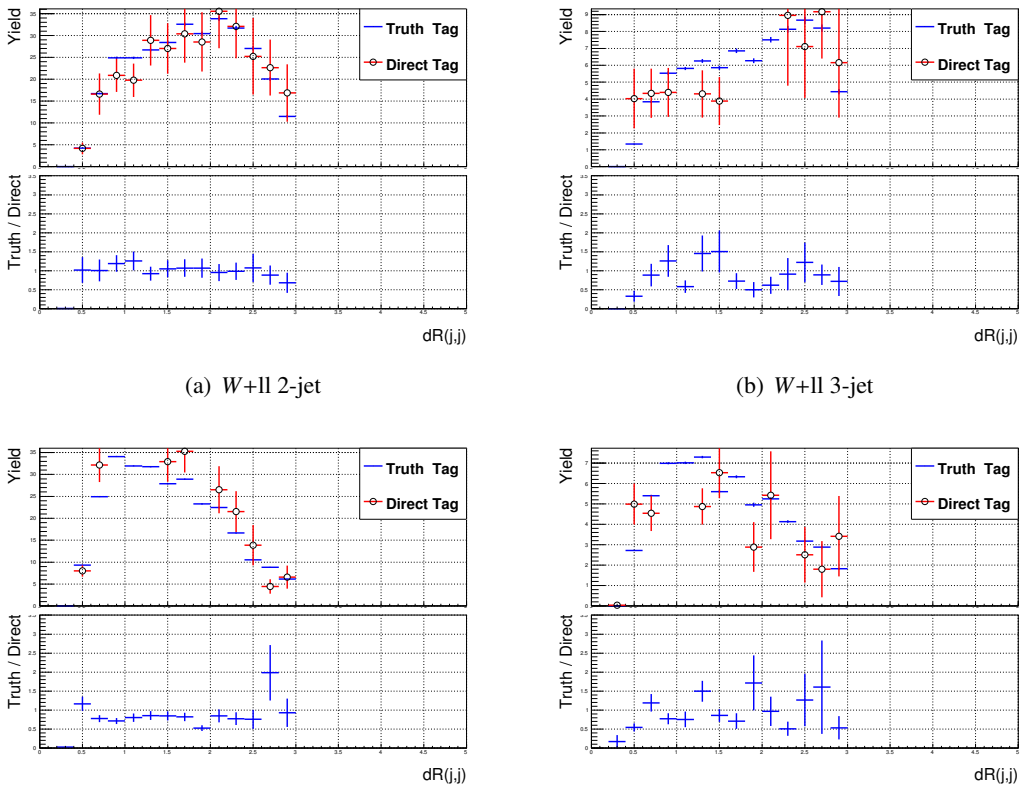

(a) W+ll 2-jet (b) W+ll 3-jet

(c) Z+ll 2-jet (d) Z+ll 3-jet

Figure 269: Comparison between truth tagging and direct tagging for V+ll events using the 0-lepton MVA selection and requiring 2 b-tags.

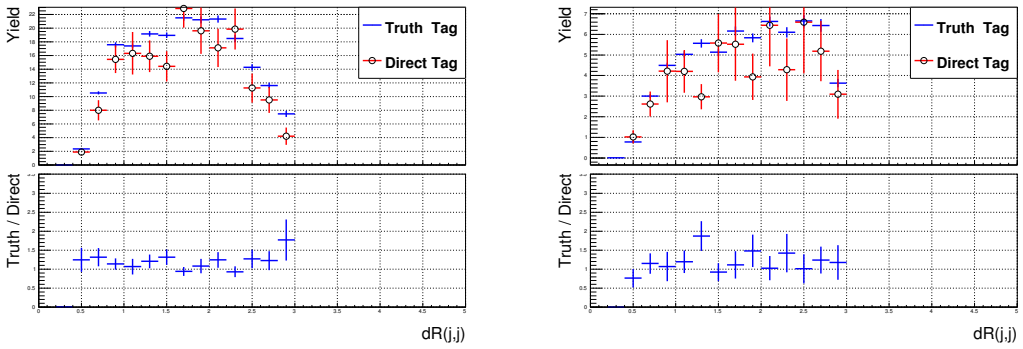

(a) W+cl 2-jet (b) W+cl 3-jet

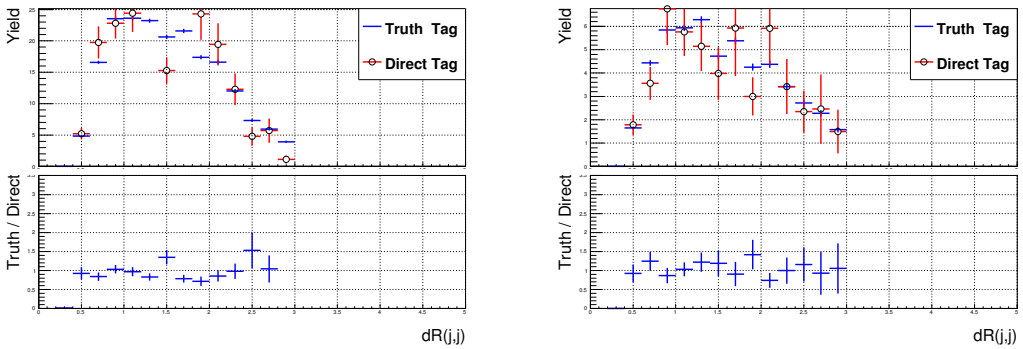

(c) Z+cl 2-jet (d) Z+cl 3-jet

Figure 270: Comparison between truth tagging and direct tagging for V+cl events using the 0-lepton MVA selection and requiring 2 b-tags.

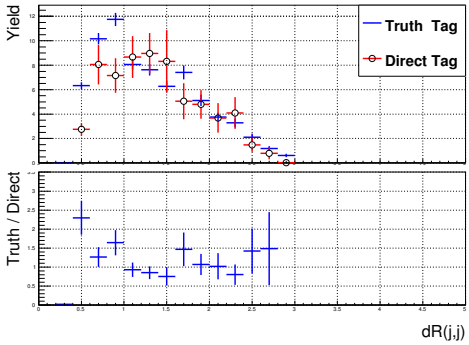

(a) W+cc 2-jet

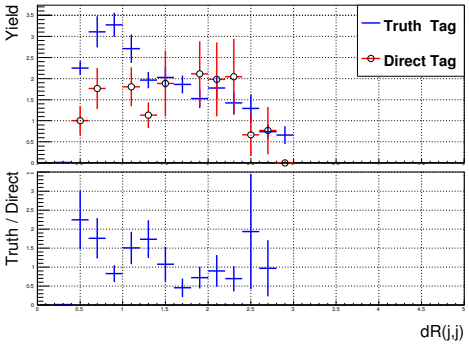

(b) W+cc 3-jet

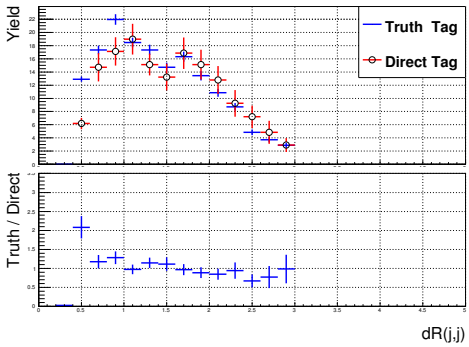

(c) Z+cc 2-jet

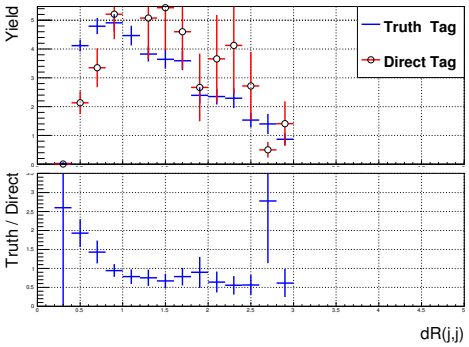

(d) Z+cc 3-jet

Figure 271: Comparison between truth tagging and direct tagging for V+cc events using the 0-lepton MVA selection and requiring 2 b-tags.

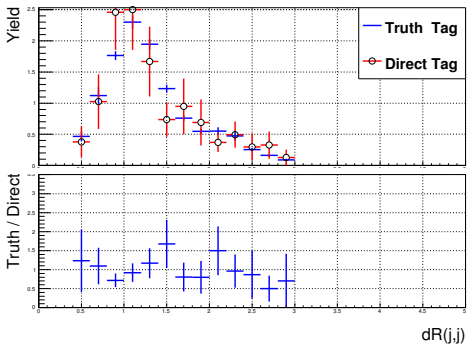

(a) WW 2-jet

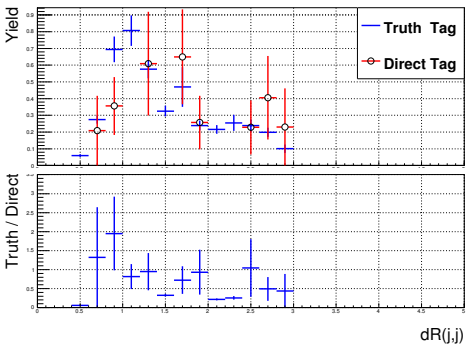

(b) WW 3-jet

Figure 272: Comparison between truth tagging and direct tagging for WW events using the 0-lepton MVA selection and requiring 2 b-tags.

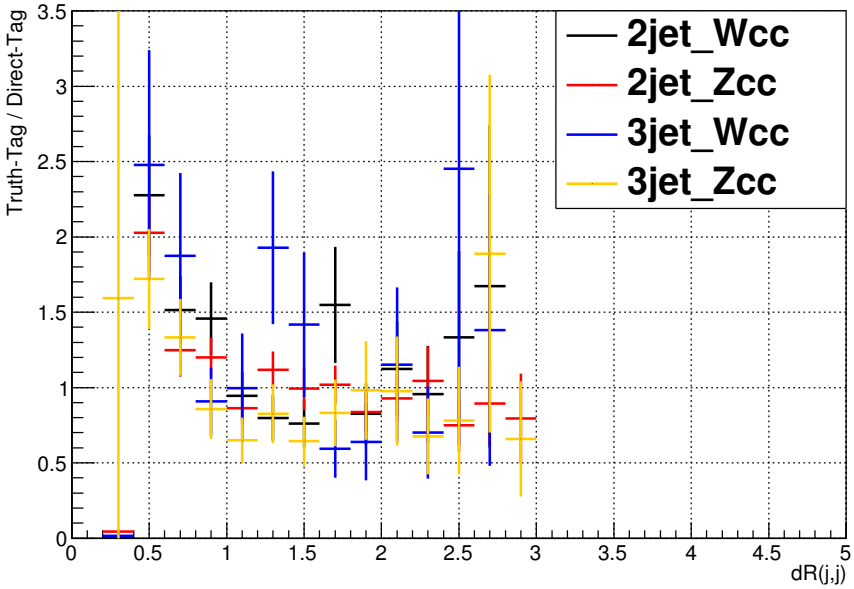

Figure 273: The ratios of truth to direct tagging for W+cc and Z+cc in 2 and 3-jet events using the 0-lepton MVA selection. The four ratios are consistent within the available statistics.

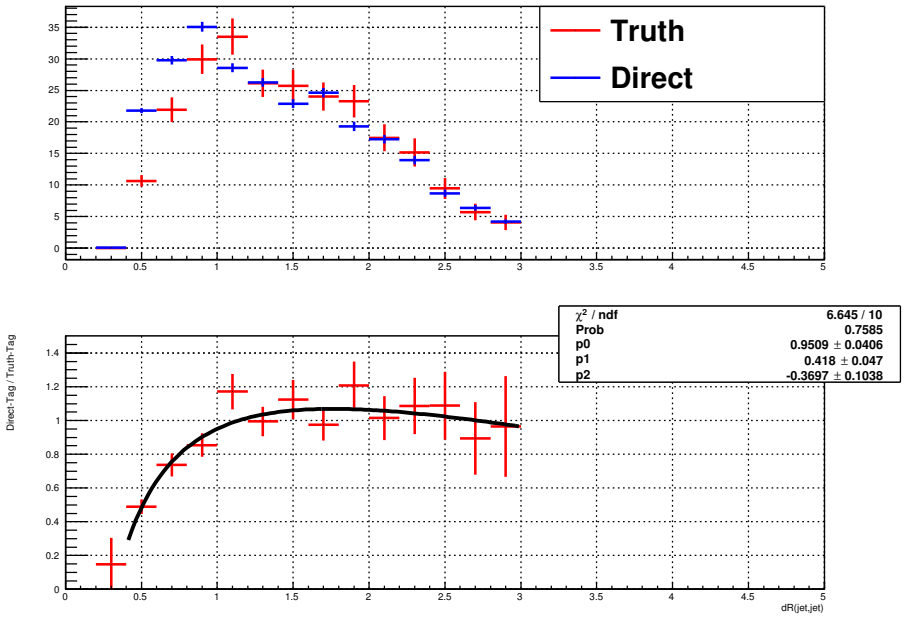

Figure 274: The truth tagging ΔR correction is derived from the ratio truth to directed tagged events using W+cc and Z+cc in 2 and 3-jet events (top). The correction itself is obtained from a fit to the ratio (bottom): $0.9509 + 0.418 \times \ln(\Delta R) - 0.3697 \times \ln^2(\Delta R)$.

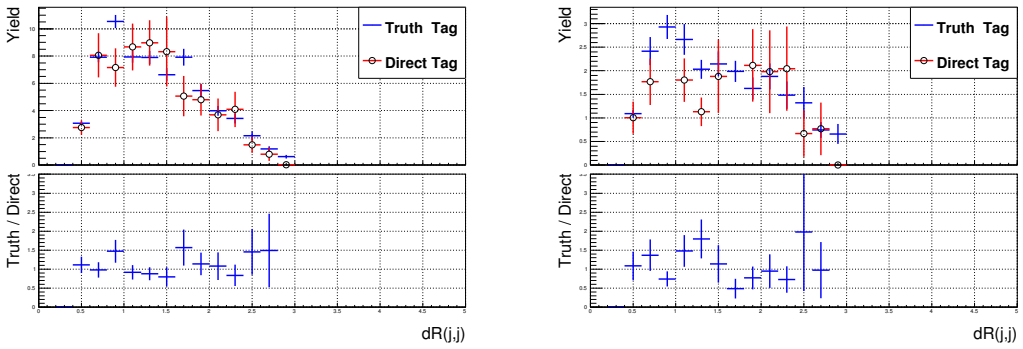

(a) W+cc 2-jet

(b) W+cc 3-jet

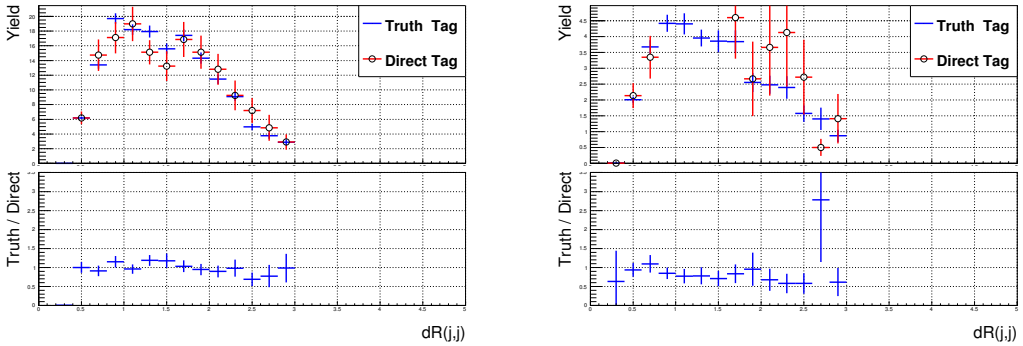

(c) Z+cc 2-jet

(d) Z+cc 3-jet

Figure 275: Comparison between truth tagging and direct tagging for after the dR correction for the samples on which the correction is derived.

U Event-level Kinematic Likelihood Fit

Final state radiation and reconstruction effects may decrease the $H \to b\bar{b}$ resonance resolution significantly while comparably decreasing the probability of observing the decay over the background. One powerful technique to improve the resonance resolution and to possibly increase the sensitivity of this search is to utilize an event-level Kinematic Likelihood Fit (KF), which exploits the full kinematic potential of any event topology within the uncertainty of its reconstructed signatures.

The $ZH \to \ell\ell b\bar{b}$ analysis has the beneficial feature that the expected signal event topology is fully reconstructed and balanced in the transverse plane. At the Monte Carlo truth level, the $E_{\mathrm{T}}^{\mathrm{miss}}$ should only arise from the inherent transverse momentum of the colliding partons and semi-leptonic b-decays. The former determines the resolution to which the transverse energy of any given event can be balanced. Therefore, one can adjust the energies of the reconstructed particles in order to force the event into a balanced configuration within the event and object resolutions. Effectively, since leptons in general have a much better resolution than jets, the jet energies are balanced against the ~static leptons. This can be achieved by maximizing an event-level likelihood built from the expected signal topology without considering the Higgs mass.

The other event topologies, such as$WH \to \ell\nu b\bar{b}$, are left for future versions of the analysis.

U.1 Likelihood Model

A model has been constructed in which the reconstructed $\ell\ell b\bar{b}$ system is constrained to be balanced in the transverse plane. The baseline version of this model is intended for events containing 2 b-tagged jets, which can be extended for events with additional jets yielding more contributions from hard final or initial state radiation.

The inputs for this model are comprised by 12 fit parameters,

- energies of 2 electrons or inverse transverse momenta of 2 muons and the energies of 2 jets,
- pseudorapidty and azimuthal angles of the 2 leptons and 2 jets,
- transverse momentum of the $\ell\ell b\bar{b}$ system,
- reconstructed dilepton mass $m_{\ell\ell}$,

and 3 constraints for the variation of these parameters,

- the $m_{\ell\ell}$ is constrained to follow a Breit-Wigner (BW) distribution around a pole mass and width of the Z boson,
- the $\sum P_{x,y}^{\ell\ell b\bar{b}}$ is constraint to be zero with a width of $\sim$ 9 GeV obtained from ZH Monte Carlo events,
- assume parameters to follow Gaussian distributions (except for the jets, for which dedicated asymmetric transfer functions are derived).

Given the fit parameters and constraints defined above, the probability density function is defined as

$$\begin{aligned}\mathscr{L} &= \prod_i f(y_i^{obs}, y_i^{pred}) \\ &= G\left(\Omega_\ell^n; \Omega_\ell^0, \sigma_\Omega\right) L^j\left(P_T^n; P_T^0, \eta_j^0\right) L^j_{truth}\left(P_T^n; \eta_j^0\right) \\ &\quad \prod_{i=j} G\left(\phi_i^n; \phi_i^0, \sigma_\phi\right) \\ &\quad \prod_{i=x,y} G\left(\sum p_i^n; \sum P_i, \sigma_{\sum p_i}\right) \\ &\quad \mathcal{B}(m^n_{\ell\ell}; M_Z, \Gamma_Z),\end{aligned}$$

where the energy E of electrons or $1/p_{\mathrm{T}}$ of muons are denoted by $\Omega = \{E, 1/p_{\mathrm{T}}\}$ respectively, the L^j corresponds to a p_{T} and *eta*-dependent jet response likelihood (the 'transfer functions' for jets), the G indicates Gaussian terms and $\mathcal{B}$ a Z boson Breit-Wigner function. The likelihood also integrates the $p_{\mathrm{T}}^{\mathrm{reco}}$ correction L^j_{truth} (introduced in Sec. X) by adding a prior for the underlying $p_{\mathrm{T}}^{\mathrm{true}}$ spectrum of the jets according to what is found after signal event selection cuts in $ZH \to \ell\ell b\bar{b}$ Monte Carlo events.

Building a test statistics and dropping all constant terms we obtain

$$\begin{aligned}-2\ln(\mathscr{L}) = &\sum_{i=j}\left(\frac{\left(\phi_i^n - \phi_i^0\right)^2}{\sigma_\phi^2}\right) + \frac{\left(\Omega_\ell^n - \Omega_\ell^0\right)^2}{\sigma_\Omega^2} - 2\ln\left(L^j\right) - 2\ln\left(L^j_{truth}\right) \\ &+ \sum_{i=x,y}\frac{\left(\sum p_i^n - \sum P_i\right)^2}{\sigma^2_{\sum p_i}} + 2\ln\left((m^2_{\ell\ell} - M_Z^2)^2 + M_Z^2\Gamma_Z^2\right)\end{aligned}$$

where M_Z and Γ_Z are the Z boson mass and width respectively. Finally this statistics is used to minimize and balance the reconstructed $\ell\ell b\bar{b}$ system on an event-by-event basis.

U.2 Resolutions

This method relies on having the resolutions of objects in hand. The standard CP provided resolutions were used for electrons [75] [76] and muons [64] [77] Jet resolutions were derived from the signal sample in 5 p_{T} bins ($< 40, 40-60, 60-80, 80-100, > 100\ GeV$ separately for η above and below 1.2 and for jets with and without a reconstructed muon. The balance of the system is constrained to 9 GeV from MC studies. The studies were redone after a series of bug-fixes to the underling framework. The updated width is shown in Figure 276 is 11 GeV. The dependence of the choice of system balance constraint on the final width is discussed in the following section.

U.3 Results

A kinematic likelihood fit with the above model has been used to balance the $ZH \to \ell\ell b\bar{b}$ system in ZH Monte Carlo events for a Higgs mass hypothesis of $m_H = 125$ GeV. As shown in Fig. 277, the fit achieves an improvement of the dijet invariant mass resolution of $\approx 21.64\%$. In parentheses, the sigma over the mean is given. As expected the fit moves the peak closer to the true Higgs mass.

The kinematic fit uses features of the signal event to improve the signal invariant mass reconstruction. In that process, the invariant mass distribution of the backgrounds is expected to change. For this reason it is important to verify that the fit does not increase the background rates in the region of the peak. Results for Z+jets Monte Carlo events have shown that the shape of the m_{bb} distribution changes in such a way that events migrate from ≈ 100 GeV to higher $m_{b\bar{b}}$. This leads to an improvement in sensitivity

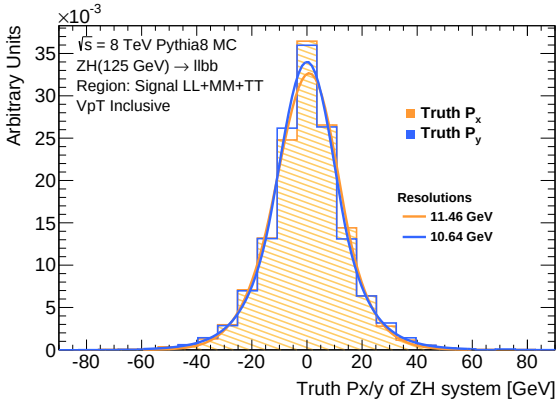

Figure 276: Dijet invariant mass before and after applying a kinematic likelihood fit in ZH m_H = 125 GeV signal Monte Carlo events showing a $\sim$ 22% resolution improvement.

of $\approx$ 4%, when estimating it using $S/\sqrt{B}$ in an $m_{b\bar{b}}$ window between 80 GeV and 150 GeV. This is smaller than what was expected by looking at the resolution improvement in the signal sample, but still significant. Given that Z+jets is the predominant background for this channel, this is evidence that the kinematic fit improves the performance of the analysis as desired.

The dependence of the resolution improvement in shown in Figure 278. For a balance resolution of 4 GeV the improvement is minimal. A more constrained system results in a resolution degredation. This could be due to the fact that the imbalance can be caused by low p_{T} objects which are not reconstructed and are not properly recovered in this method. Above 4 GeV the resolution improves plateauing above 12 GeV. The choice of 9 GeV is therefore not completely optimal but the analysis was too mature to make a change. The expected improvement is stable around the chosen operating point.

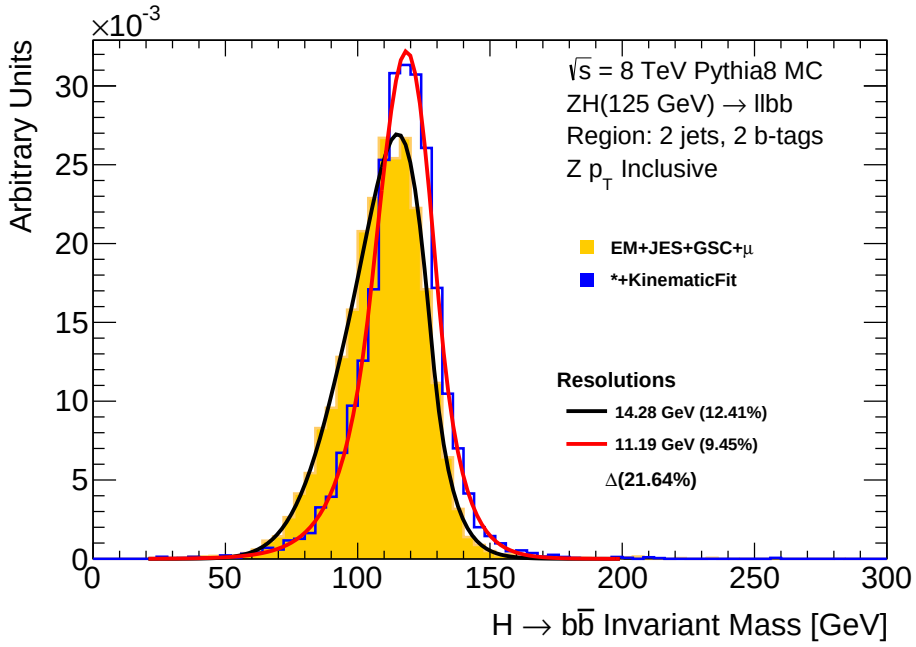

Figure 277: Dijet invariant mass before and after applying a kinematic likelihood fit in ZH m_H = 125 GeV signal Monte Carlo events showing a $\sim$ 19% resolution improvement.

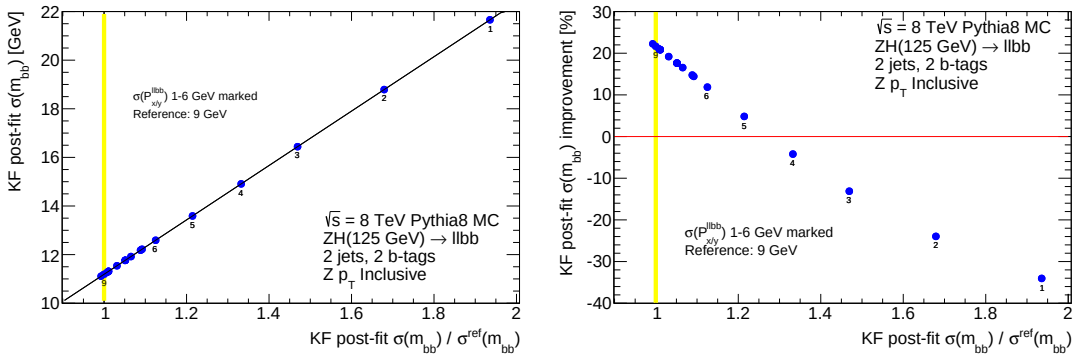

Figure 278: The postfit dijet mass resolution shown as a function of the resolution of the system balance is shown on the left while the right shows the improvement with respect to the prefit resolution. The resolution here is obtained from the width of a Bukin fit.

V Dijet Mass (m_{jj}) Distributions: Zero Lepton

This appendix contains m_{jj} distributions of the dijet mass analysis selection outlined in Section 3.3 for the the 0-Lepton analysis. Note: the 3-jet region for $p_{\mathrm{T}}^{Z} < 120$ GeV is shown in the plots, but it is not used in the analysis. In particular, in this region we expect to have a non negligible contribution of multi-jet, which is not properly shown in the plot. These plots are done by applying the latest scale factors, obtained for the 2 jet region and the 3 jet region separately, by comparing the event yield before and after the MVA combined fit. They are summarized in Table 114. Explicitly stated, the theoretical expectation

Sample	2-jets	3-jets
Zl	1.03 ± 0.05	0.98 ± 0.06
Zcl	0.89 ± 0.11	0.99 ± 0.12
Zcc	1.13 ± 0.13	1.12 ± 0.13
Zbl	1.10 ± 0.05	0.95 ± 0.05
Zbc	1.10 ± 0.11	1.09 ± 0.12
Zbb	1.12 ± 0.06	1.13 ± 0.07
Wl	1.00 ± 0.06	0.92 ± 0.06
Wcl	1.14 ± 0.07	1.07 ± 0.07
Wcc	0.75 ± 0.16	0.73 ± 0.16
Wbl	0.63 ± 0.15	0.64 ± 0.15
Wbc	0.81 ± 0.16	0.81 ± 0.16
Wbb	0.82 ± 0.16	0.86 ± 0.17
Wt	1.06 ± 0.09	1.05 ± 0.11
single top t-ch.	1.34 ± 0.27	1.08 ± 0.08
single top s-ch.	1.07 ± 0.11	1.04 ± 0.10
0 l $t\bar{t}$	1.36 ± 0.13	1.12 ± 0.10
1 l $t\bar{t}$	1.16 ± 0.07	1.00 ± 0.03
2 l $t\bar{t}$	1.01 ± 0.04	1.11 ± 0.05
WW	1.01 ± 0.05	1.01 ± 0.05
ZZ	1.03 ± 0.04	1.02 ± 0.05
WZ	1.01 ± 0.04	1.01 ± 0.03
0 l Multijet	0.97 ± 0.78	1.13 ± 0.93
1 μ Multijet	0.94 ± 0.13	1.11 ± 0.25
1 e Multijet	0.98 ± 0.07	1.00 ± 0.07
2 l Multijet	0.73 ± 0.47	0.73 ± 0.47

Table 114: Normalization scale factors obtained by comparing the event yield for the different backgrounds before and after the 0+1+2-lepton MVA fit. The normalization scal factors are give for 2-jet events and 3-jet events

for each background is used for the given luminosity. All the plots in this section are done with the status-of-art analysis. Figure 279 shows events with one b-tag and two jets.
Figure 280 shows events with one b-tag and three jets.
Figure 281 shows events with two exclusive loose b-tags and two jets.
Figure 282 shows events with two exclusive loose b-tags and three jets.
Figure 283 shows events with two exclusive medium b-tags and two jets.
Figure 284 shows events with two exclusive medium b-tags and three jets.
Figure 285 shows events with two exclusive tight b-tags and two jets.

Figure 286 shows events with two exclusive tight b-tags and three jets.

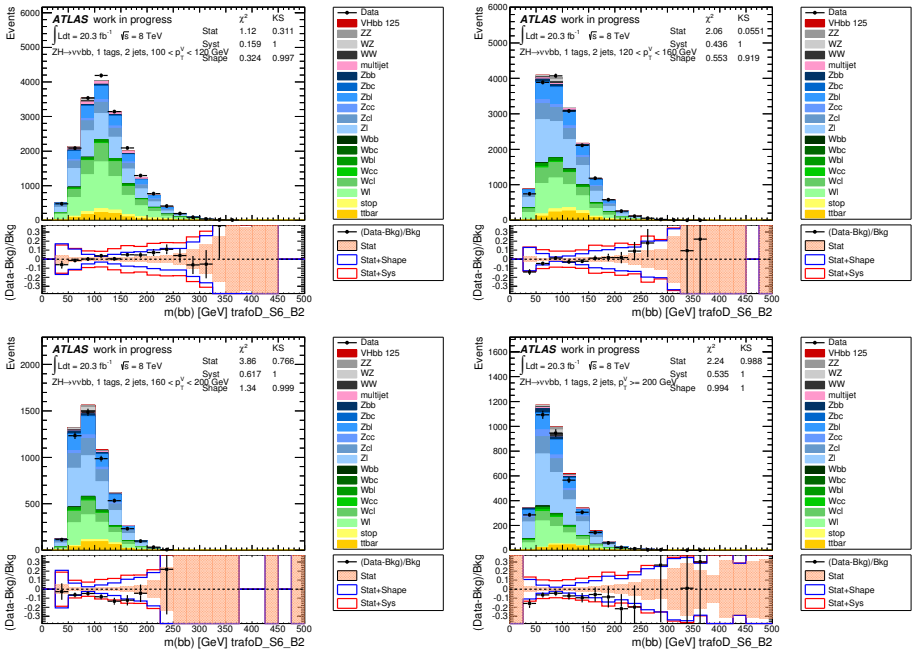

Figure 279: m_{jj} in 0-lepton events in the dijet mass analysis with 1 b-tag and 2 jets. From left to right: Row 1 - $100 < p_{\mathrm{T}}^{Z} < 120$ GeV and $120 < p_{\mathrm{T}}^{Z} < 160$ GeV. Row 2 - $160 < p_{\mathrm{T}}^{Z} < 200$ GeV and $p_{\mathrm{T}}^{Z} > 200$ GeV. Section 6.1 details the selection criteria.

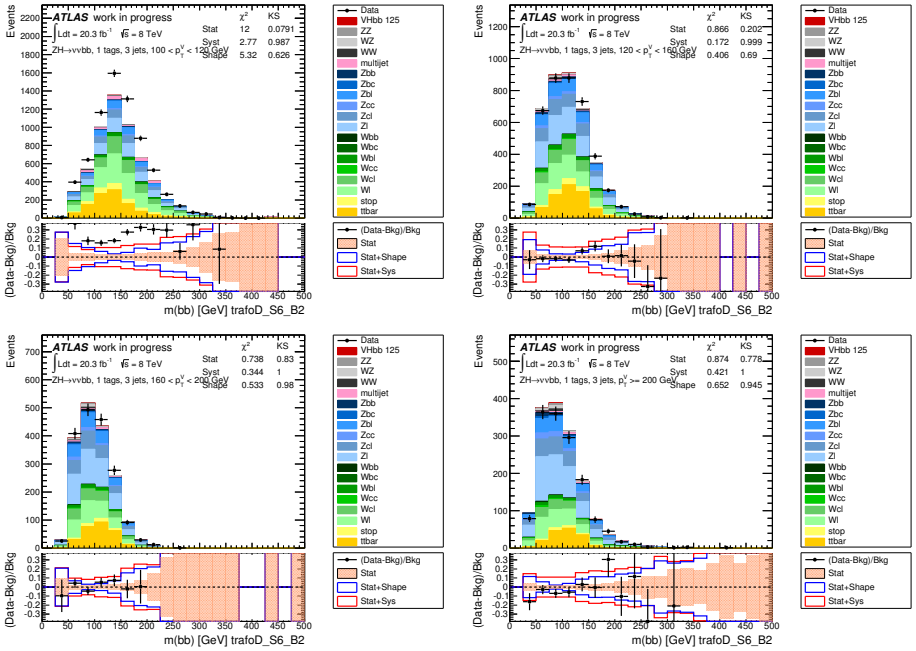

Figure 280: m_{jj} in 0-lepton events in the dijet mass analysis with 1 b-tag and 3 jets. From left to right: Row 1 - $100 < p_{\mathrm{T}}^{Z} < 120$ GeV and $120 < p_{\mathrm{T}}^{Z} < 160$ GeV. Row 2 - $160 < p_{\mathrm{T}}^{Z} < 200$ GeV and $p_{\mathrm{T}}^{Z} > 200$ GeV. Section 6.1 details the selection criteria.

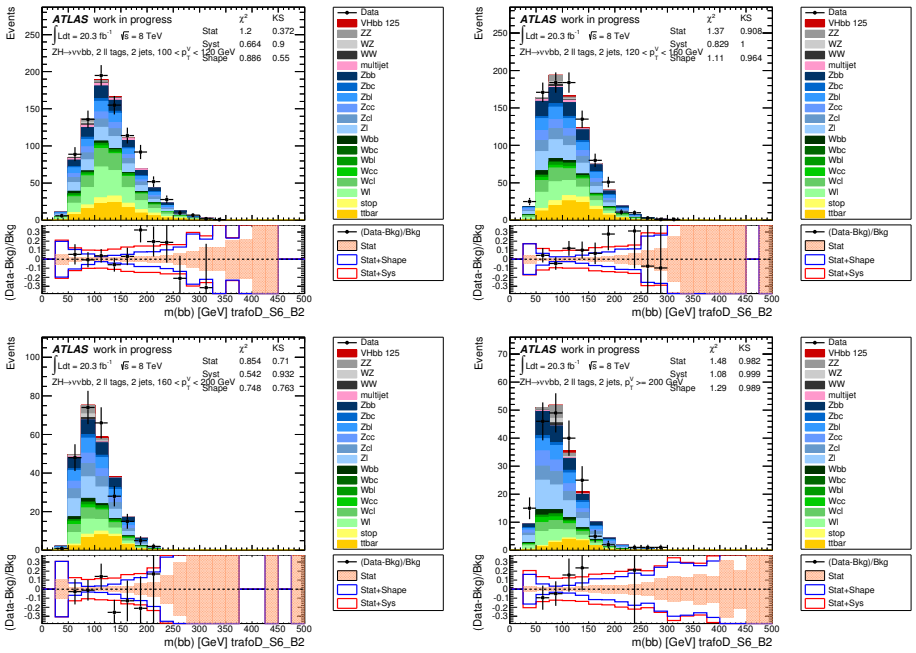

Figure 281: m_{jj} in 0-lepton events in the dijet mass analysis with 2L exclusive b-tags and 2 jets. From left to right: Row 1 - $100 < p_{\mathrm{T}}^{Z} < 120$ GeV and $120 < p_{\mathrm{T}}^{Z} < 160$ GeV. Row 2 - $160 < p_{\mathrm{T}}^{Z} < 200$ GeV and $p_{\mathrm{T}}^{Z} > 200$ GeV. Section 6.1 details the selection criteria.

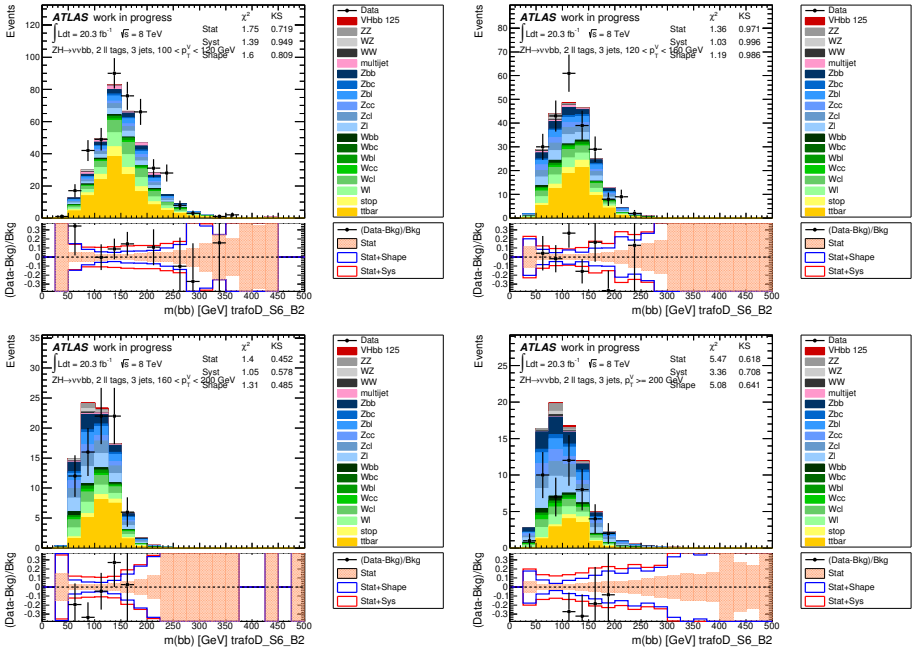

Figure 282: m_{jj} in 0-lepton events in the dijet mass analysis with 2L exclusive b-tags and 3 jets. From left to right: Row 1 - $100 < p_{\mathrm{T}}^{Z} < 120$ GeV and $120 < p_{\mathrm{T}}^{Z} < 160$ GeV. Row 2 - $160 < p_{\mathrm{T}}^{Z} < 200$ GeV and $p_{\mathrm{T}}^{Z} > 200$ GeV. Section 6.1 details the selection criteria.

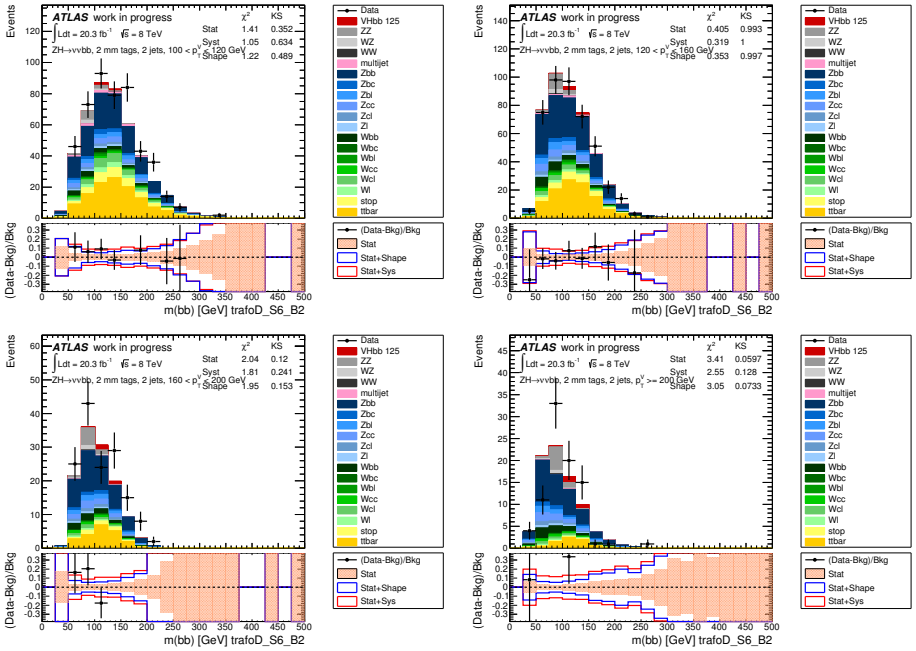

Figure 283: m_{jj} in 0-lepton events in the dijet mass analysis with 2M exclusive b-tags and 2 jets. From left to right: Row 1 - $100 < p_{\mathrm{T}}^{Z} < 120$ GeV and $120 < p_{\mathrm{T}}^{Z} < 160$ GeV. Row 2 - $160 < p_{\mathrm{T}}^{Z} < 200$ GeV and $p_{\mathrm{T}}^{Z} > 200$ GeV. Section 6.1 details the selection criteria.

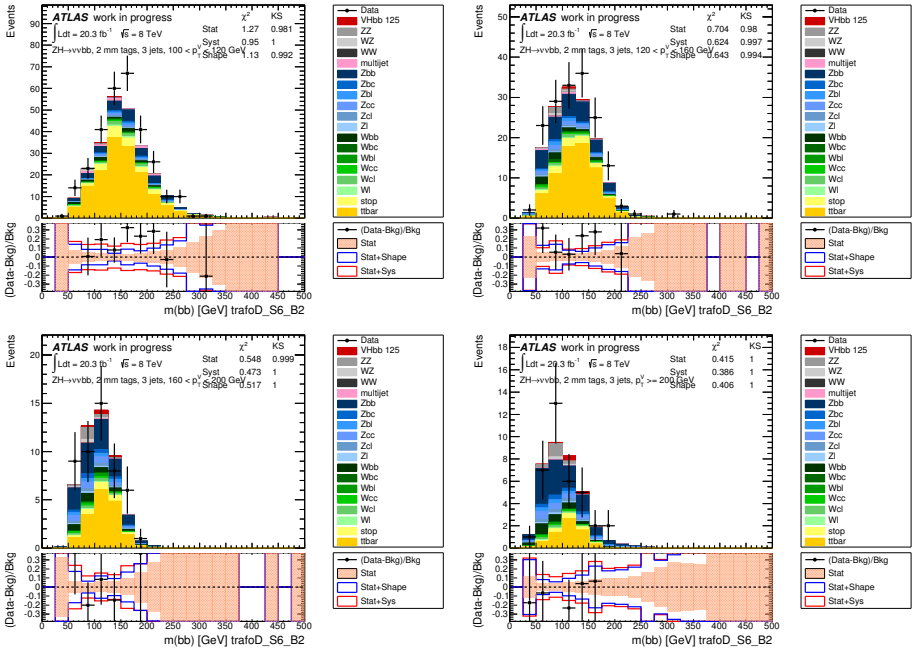

Figure 284: m_{jj} in 0-lepton events in the dijet mass analysis with 2M exclusive b-tags and 3 jets. From left to right: Row 1 - $100 < p_{\mathrm{T}}^{Z} < 120$ GeV and $120 < p_{\mathrm{T}}^{Z} < 160$ GeV. Row 2 - $160 < p_{\mathrm{T}}^{Z} < 200$ GeV and $p_{\mathrm{T}}^{Z} > 200$ GeV. Section 6.1 details the selection criteria.

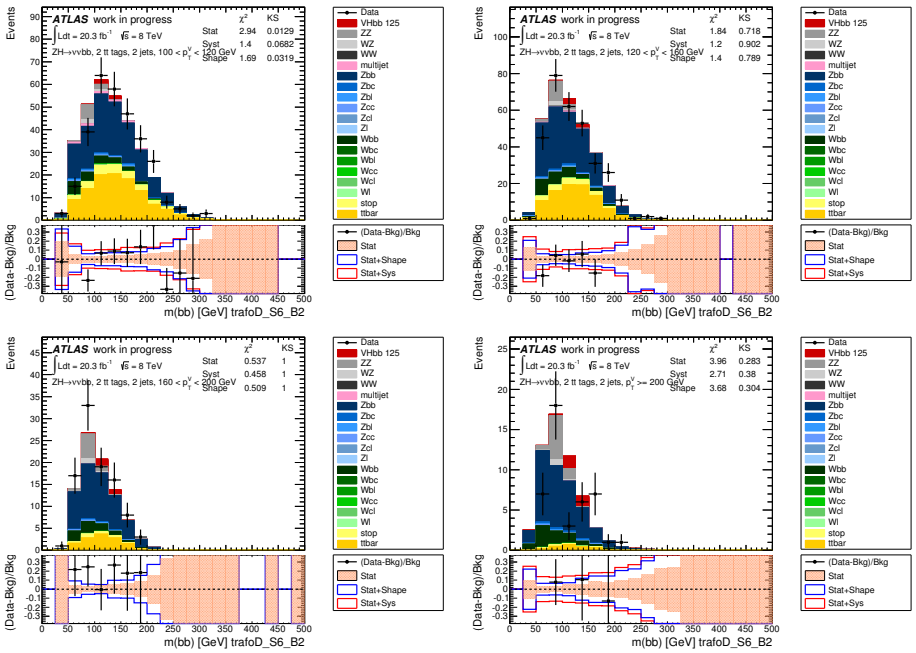

Figure 285: m_{jj} in 0-lepton events in the dijet mass analysis with 2T exclusive b-tags and 2 jets. From left to right: Row 1 - $100 < p_{\mathrm{T}}^{Z} < 120$ GeV and $120 < p_{\mathrm{T}}^{Z} < 160$ GeV. Row 2 - $160 < p_{\mathrm{T}}^{Z} < 200$ GeV and $p_{\mathrm{T}}^{Z} > 200$ GeV. Section 6.1 details the selection criteria.

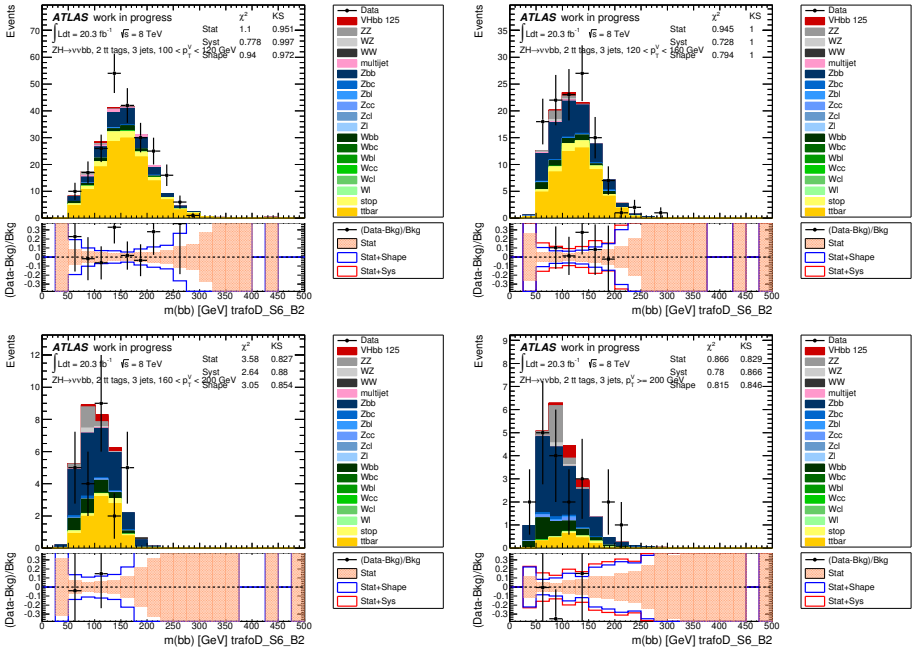

Figure 286: m_{jj} in 0-lepton events in the dijet mass analysis with 2T exclusive b-tags and 3 jets. From left to right: Row 1 - $100 < p_{\mathrm{T}}^{Z} < 120$ GeV and $120 < p_{\mathrm{T}}^{Z} < 160$ GeV. Row 2 - $160 < p_{\mathrm{T}}^{Z} < 200$ GeV and $p_{\mathrm{T}}^{Z} > 200$ GeV. Section 6.1 details the selection criteria.

W Dijet Mass (m_{jj}) Distributions: One Lepton

This appendix contains m_{jj} distributions of the dijet mass analysis selection outlined in Section 3.3 for the the 1-Lepton analysis. These plots are done by applying the latest scale factors, obtained for the 2 jet region and the 3 jet region separately, by comparing the event yield before and after the MVA combined fit. They are summarized in Table 114. Explicitly stated, the theoretical expectation for each background is used for the given luminosity. All the plots in this section are done with the status-of-art analysis.
Figure 287 shows events with one b-tag and two jets.
Figure 288 shows events with one b-tag and three jets.
Figure 289 shows events with two exclusive loose b-tags and two jets.
Figure 290 shows events with two exclusive loose b-tags and three jets.
Figure 291 shows events with two exclusive medium b-tags and two jets.
Figure 292 shows events with two exclusive medium b-tags and three jets.
Figure 293 shows events with two exclusive tight b-tags and two jets.
Figure 294 shows events with two exclusive tight b-tags and three jets.

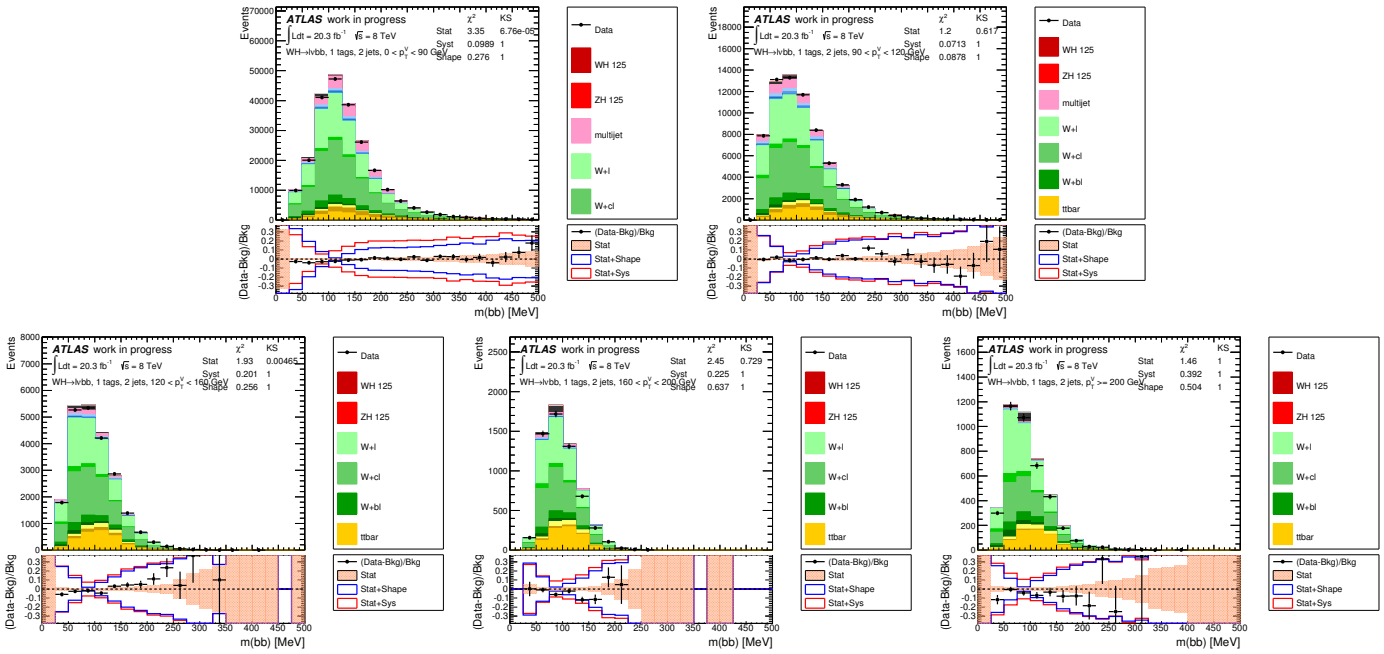

Figure 287: m_{jj} in 1-lepton events in the dijet mass analysis with 1 b-tag and 2 jets. From left to right: Row 1 - inclusive in p_{T}^{W}, $p_{\mathrm{T}}^{W} < 90$ GeV, and $90 < p_{\mathrm{T}}^{W} < 120$ GeV. Row 2 - $120 < p_{\mathrm{T}}^{W} < 160$ GeV, $160 < p_{\mathrm{T}}^{W} < 200$ GeV, and $p_{\mathrm{T}}^{W} > 200$ GeV. Section 6.1 details the selection criteria.

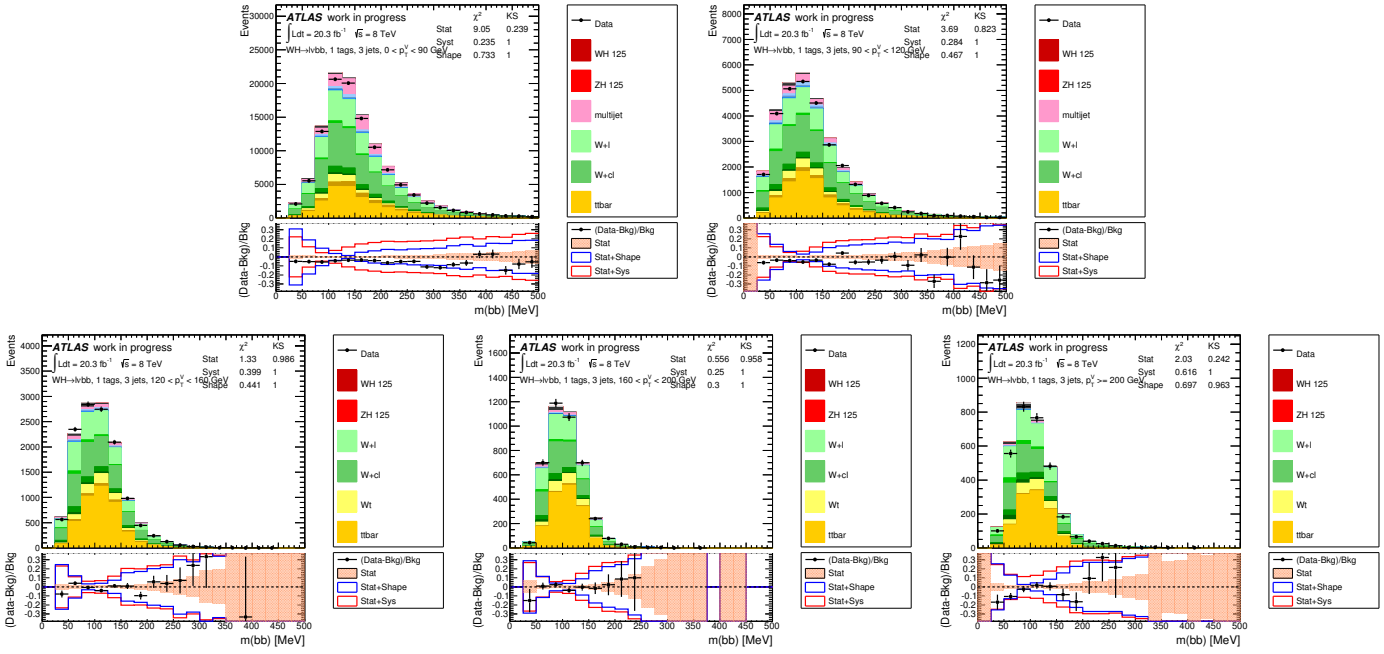

Figure 288: m_{jj} in 1-lepton events in the dijet mass analysis with 1 b-tag and 3 jets. From left to right: Row 1 - inclusive in p_{T}^{W}, $p_{\mathrm{T}}^{W} < 90$ GeV, and $90 < p_{\mathrm{T}}^{W} < 120$ GeV. Row 2 - $120 < p_{\mathrm{T}}^{W} < 160$ GeV, $160 < p_{\mathrm{T}}^{W} < 200$ GeV, and $p_{\mathrm{T}}^{W} > 200$ GeV. Section 6.1 details the selection criteria.

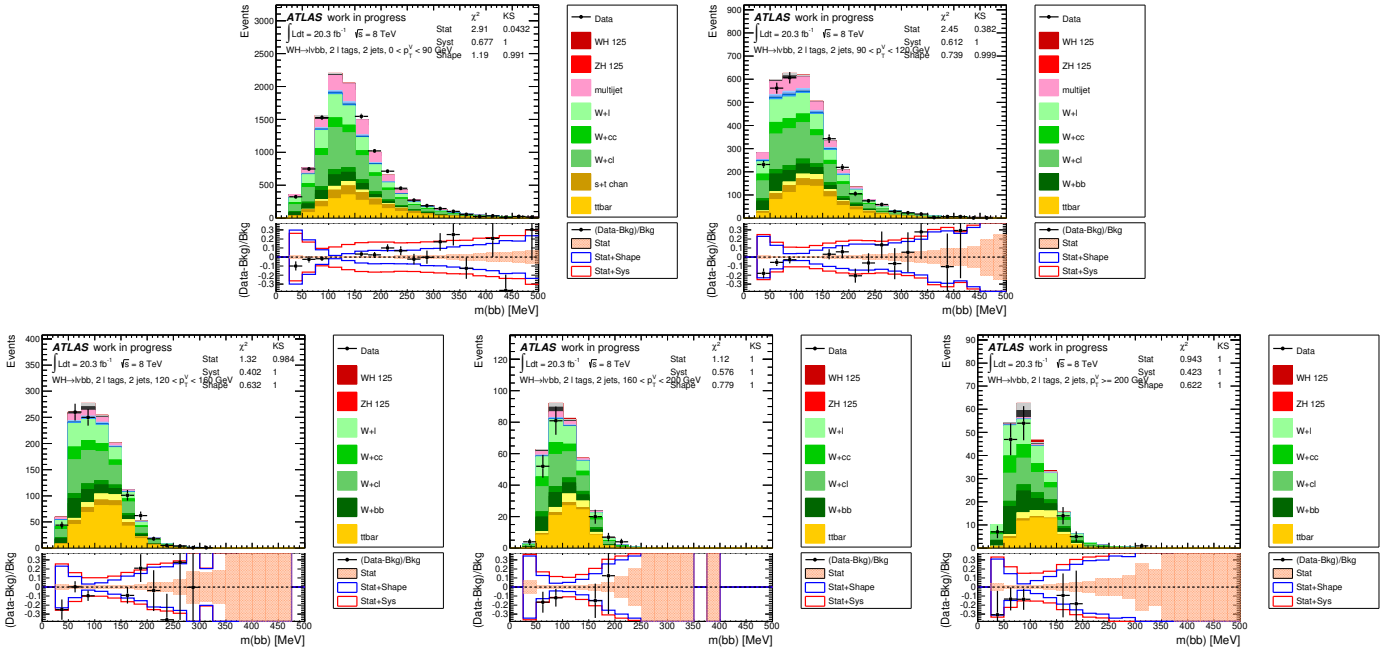

Figure 289: m_{jj} in 1-lepton events in the dijet mass analysis with 2L exclusive b-tags and 2 jets. From left to right: Row 1 - inclusive in p_{T}^{W}, $p_{\mathrm{T}}^{W} < 90$ GeV, and $90 < p_{\mathrm{T}}^{W} < 120$ GeV. Row 2 - $120 < p_{\mathrm{T}}^{W} < 160$ GeV, $160 < p_{\mathrm{T}}^{W} < 200$ GeV, and $p_{\mathrm{T}}^{W} > 200$ GeV. Section 6.1 details the selection criteria.

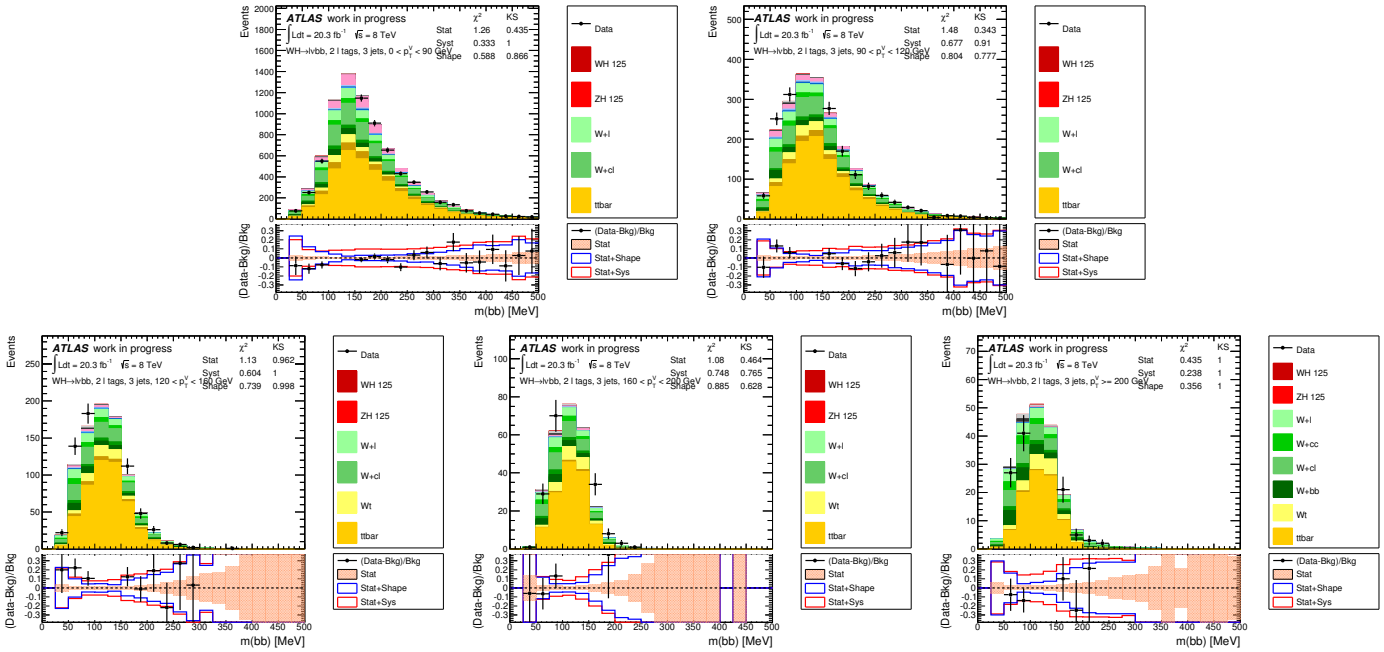

Figure 290: m_{jj} in 1-lepton events in the dijet mass analysis with 2L exclusive b-tags and 3 jets. From left to right: Row 1 - inclusive in p_{T}^{W}, $p_{\mathrm{T}}^{W} < 90$ GeV, and $90 < p_{\mathrm{T}}^{W} < 120$ GeV. Row 2 - $120 < p_{\mathrm{T}}^{W} < 160$ GeV, $160 < p_{\mathrm{T}}^{W} < 200$ GeV, and $p_{\mathrm{T}}^{W} > 200$ GeV. Section 6.1 details the selection criteria.

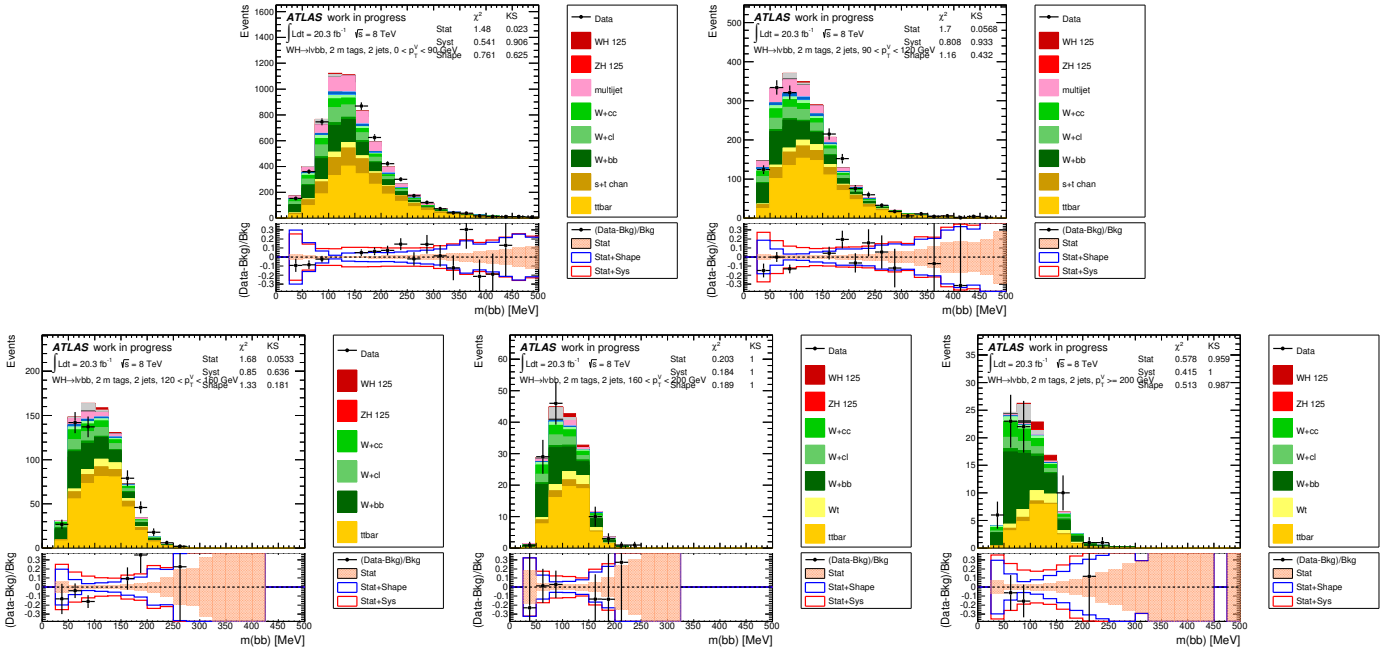

Figure 291: m_{jj} in 1-lepton events in the dijet mass analysis with 2M exclusive b-tags and 2 jets. From left to right: Row 1 - inclusive in p_{T}^{W}, $p_{\mathrm{T}}^{W} < 90$ GeV, and $90 < p_{\mathrm{T}}^{W} < 120$ GeV. Row 2 - $120 < p_{\mathrm{T}}^{W} < 160$ GeV, $160 < p_{\mathrm{T}}^{W} < 200$ GeV, and $p_{\mathrm{T}}^{W} > 200$ GeV. Section 6.1 details the selection criteria.

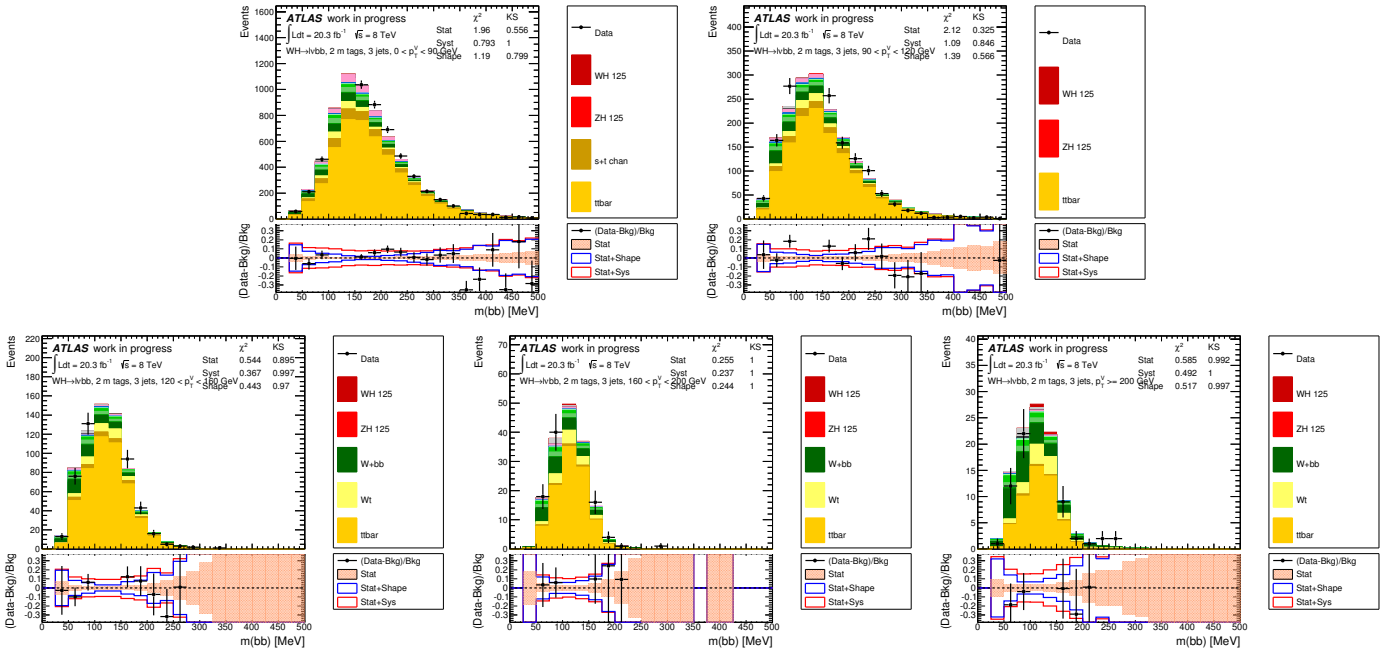

Figure 292: m_{jj} in 1-lepton events in the dijet mass analysis with 2M exclusive b-tags and 3 jets. From left to right: Row 1 - inclusive in p_{T}^{W}, $p_{\mathrm{T}}^{W} < 90$ GeV, and $90 < p_{\mathrm{T}}^{W} < 120$ GeV. Row 2 - $120 < p_{\mathrm{T}}^{W} < 160$ GeV, $160 < p_{\mathrm{T}}^{W} < 200$ GeV, and $p_{\mathrm{T}}^{W} > 200$ GeV. Section 6.1 details the selection criteria.

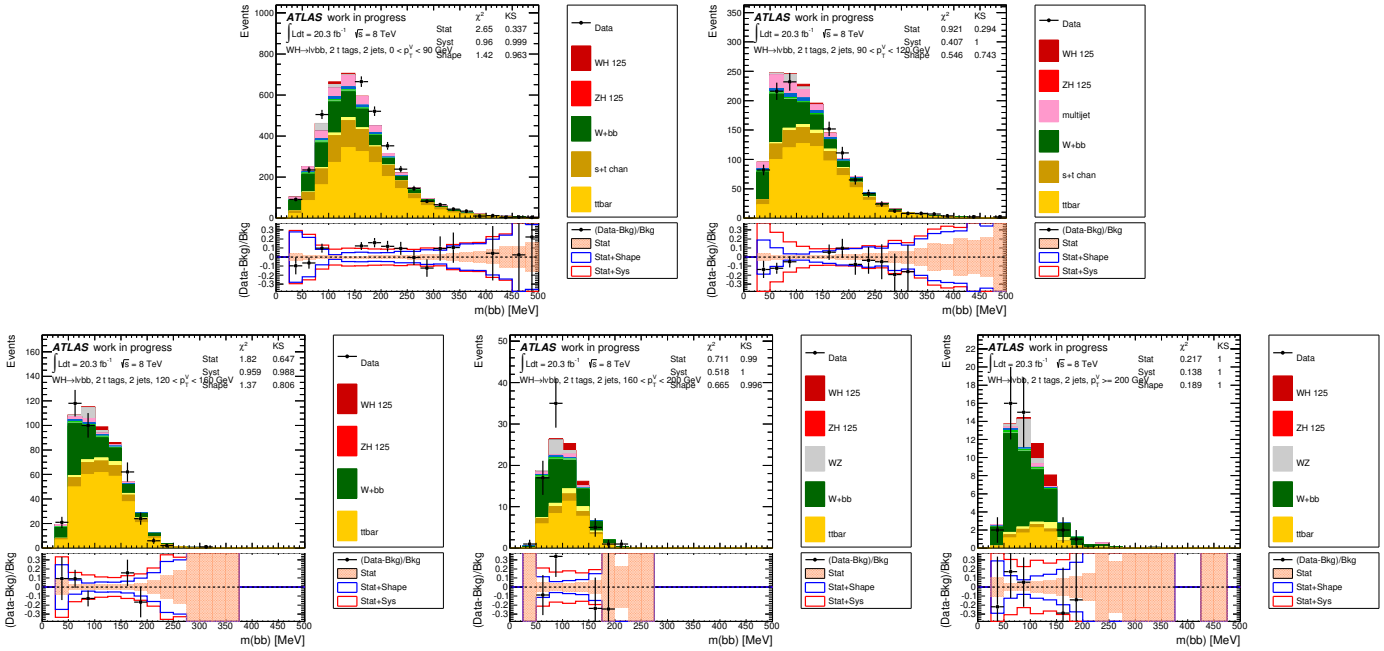

Figure 293: m_{jj} in 1-lepton events in the dijet mass analysis with 2T exclusive b-tags and 2 jets. From left to right: Row 1 - inclusive in p_{T}^{W}, $p_{\mathrm{T}}^{W} < 90$ GeV, and $90 < p_{\mathrm{T}}^{W} < 120$ GeV. Row 2 - $120 < p_{\mathrm{T}}^{W} < 160$ GeV, $160 < p_{\mathrm{T}}^{W} < 200$ GeV, and $p_{\mathrm{T}}^{W} > 200$ GeV. Section 6.1 details the selection criteria.

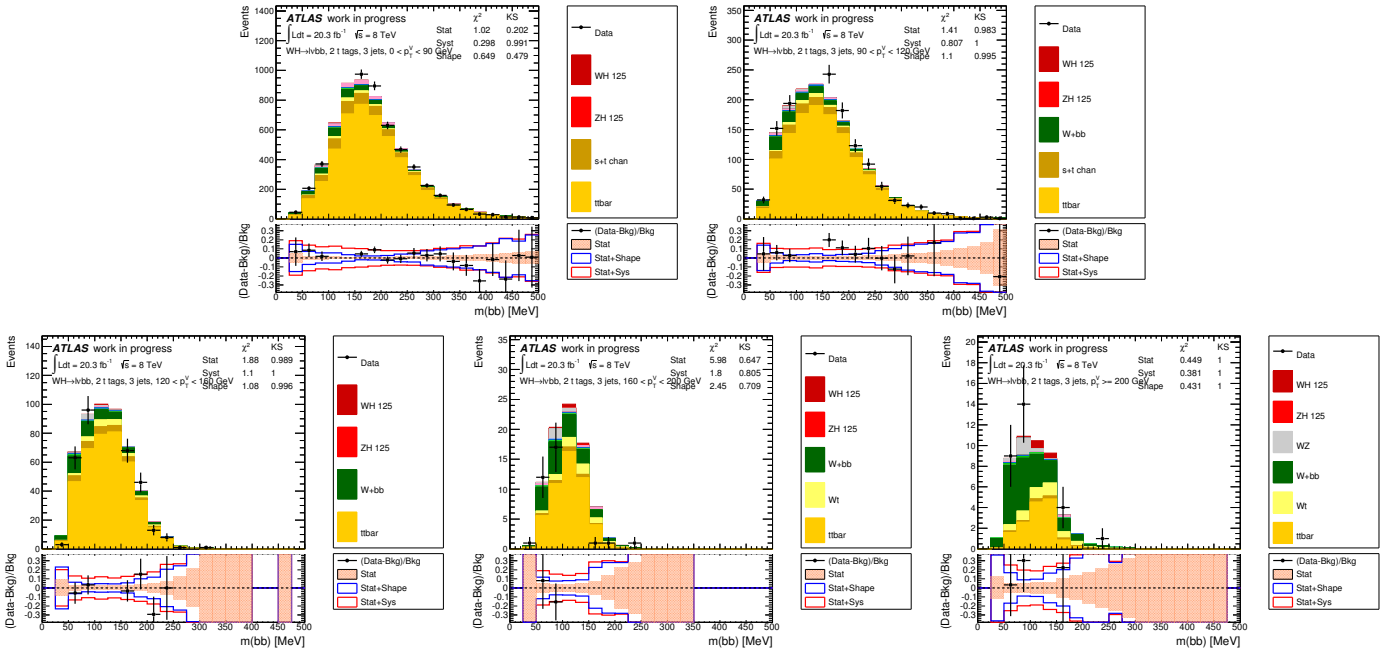

Figure 294: m_{jj} in 1-lepton events in the dijet mass analysis with 2T exclusive b-tags and 3 jets. From left to right: Row 1 - inclusive in p_{T}^{W}, $p_{\mathrm{T}}^{W} < 90$ GeV, and $90 < p_{\mathrm{T}}^{W} < 120$ GeV. Row 2 - $120 < p_{\mathrm{T}}^{W} < 160$ GeV, $160 < p_{\mathrm{T}}^{W} < 200$ GeV, and $p_{\mathrm{T}}^{W} > 200$ GeV. Section 6.1 details the selection criteria.

X Dijet Mass (m_{jj}) Distributions: Two Lepton

This appendix contains m_{jj} distributions of the dijet mass analysis selection outlined in Section 3.3 for the the 2-lepton analysis. These plots are done by applying the latest scale factors, obtained for the 2 jet region and the 3 jet region separately, by comparing the event yield before and after the MVA combined fit. They are summarized in Table 114. Explicitly stated, the theoretical expectation for each background is used for the given luminosity. All the plots in this section are done with the status-of-art analysis.
Figure 295 shows events with one b-tag and two jets.
Figure 296 shows events with one b-tag and three jets.
Figure 297 shows events with two exclusive loose b-tags and two jets.
Figure 298 shows events with two exclusive loose b-tags and three jets.
Figure 299 shows events with two exclusive medium b-tags and two jets.
Figure 300 shows events with two exclusive medium b-tags and three jets.
Figure 301 shows events with two exclusive tight b-tags and two jets.
Figure 302 shows events with two exclusive tight b-tags and three jets.

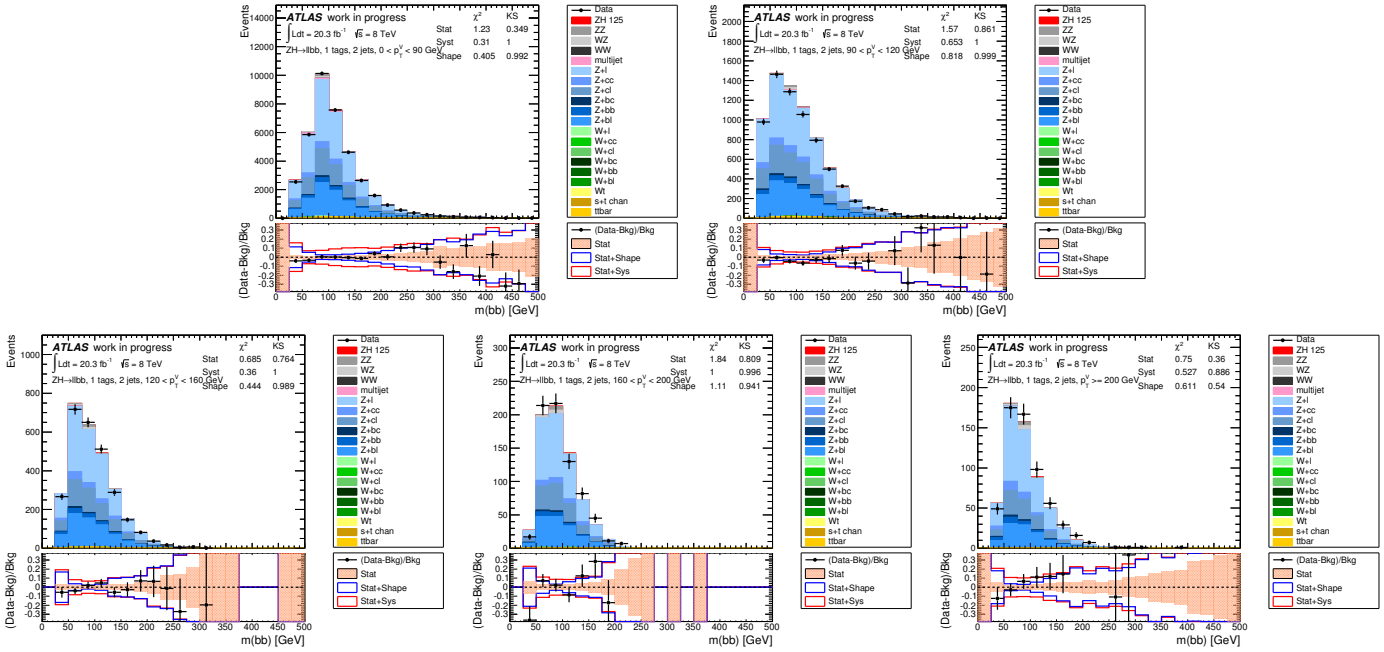

Figure 295: m_{jj} in 2-lepton events in the dijet mass analysis with 1 b-tag and 2 jets. From left to right: Row 1 - $p_{\mathrm{T}}^{Z} < 90$ GeV, and $90 < p_{\mathrm{T}}^{Z} < 120$ GeV. Row 2 - $120 < p_{\mathrm{T}}^{Z} < 160$ GeV, $160 < p_{\mathrm{T}}^{Z} < 200$ GeV, and $p_{\mathrm{T}}^{Z} > 200$ GeV. Section 6.1 details the selection criteria.

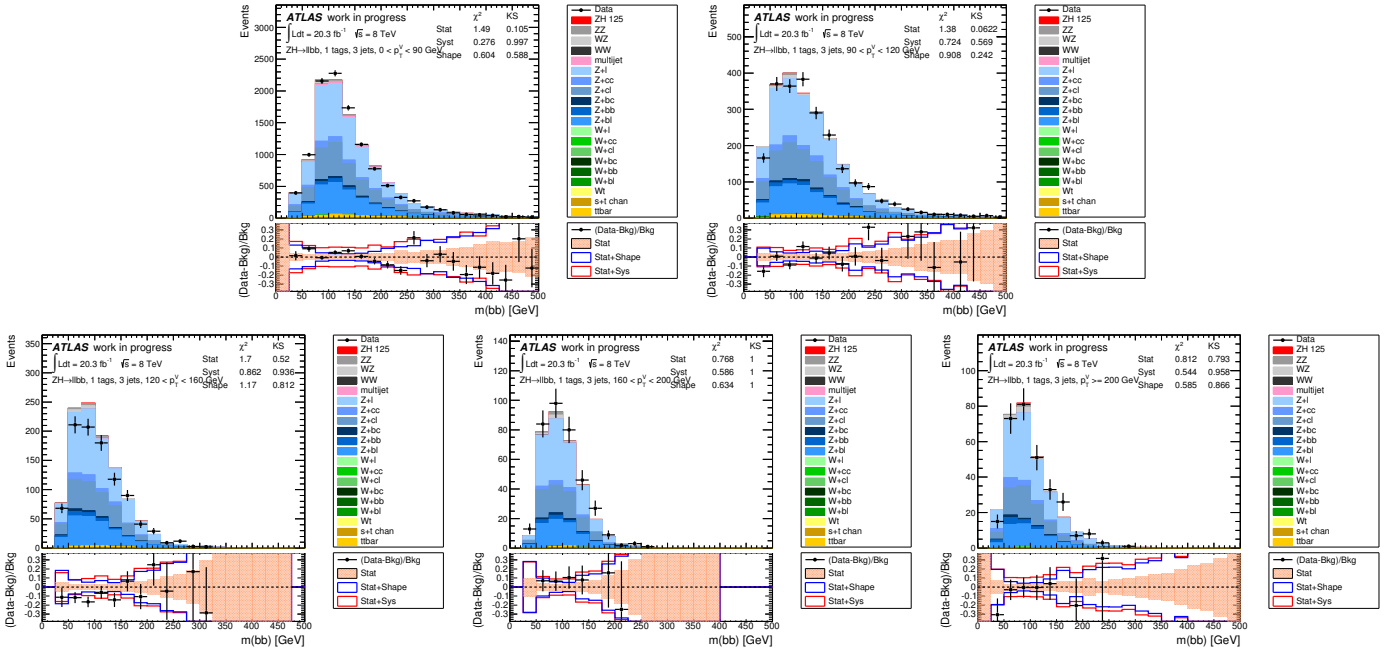

Figure 296: m_{jj} in 2-lepton events in the dijet mass analysis with 1 b-tag and 3 jets. From left to right: Row 1 - $p_{\mathrm{T}}^{Z} < 90$ GeV, and $90 < p_{\mathrm{T}}^{Z} < 120$ GeV. Row 2 - $120 < p_{\mathrm{T}}^{Z} < 160$ GeV, $160 < p_{\mathrm{T}}^{Z} < 200$ GeV, and $p_{\mathrm{T}}^{Z} > 200$ GeV. Section 6.1 details the selection criteria.

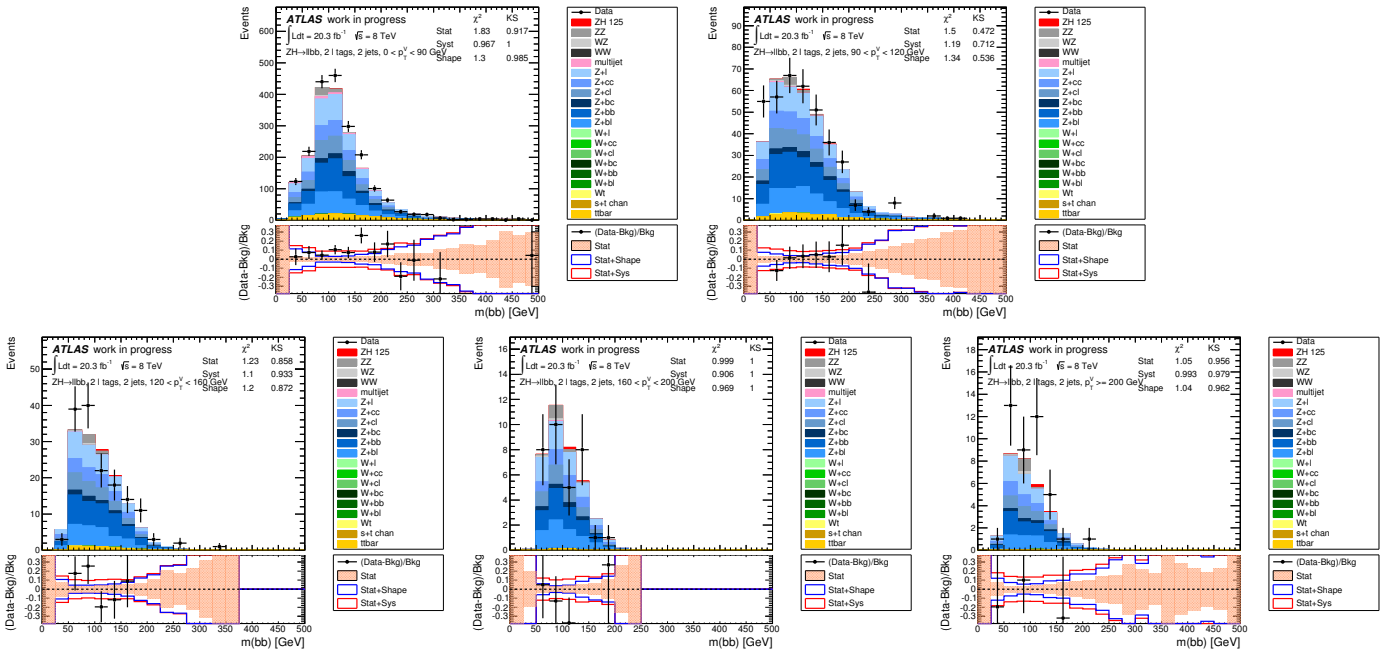

Figure 297: m_{jj} in 2-lepton events in the dijet mass analysis with 2L exclusive b-tags and 2 jets. From left to right: Row 1 - $p_{\mathrm{T}}^{Z} < 90$ GeV, and $90 < p_{\mathrm{T}}^{Z} < 120$ GeV. Row 2 - $120 < p_{\mathrm{T}}^{Z} < 160$ GeV, $160 < p_{\mathrm{T}}^{Z} < 200$ GeV, and $p_{\mathrm{T}}^{Z} > 200$ GeV. Section 6.1 details the selection criteria.

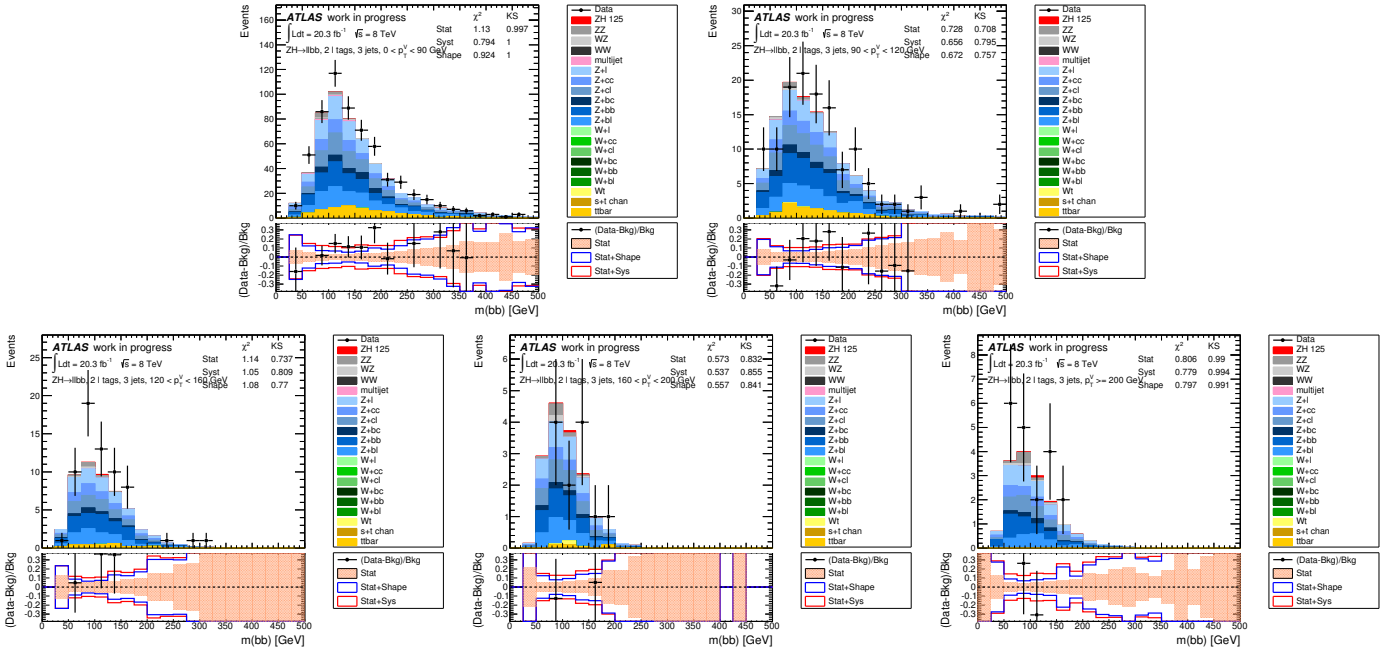

Figure 298: m_{jj} in 2-lepton events in the dijet mass analysis with 2L exclusive b-tags and 3 jets. From left to right: Row 1 - $p_{\mathrm{T}}^{Z} < 90$ GeV, and $90 < p_{\mathrm{T}}^{Z} < 120$ GeV. Row 2 - $120 < p_{\mathrm{T}}^{Z} < 160$ GeV, $160 < p_{\mathrm{T}}^{Z} < 200$ GeV, and $p_{\mathrm{T}}^{Z} > 200$ GeV. Section 6.1 details the selection criteria.

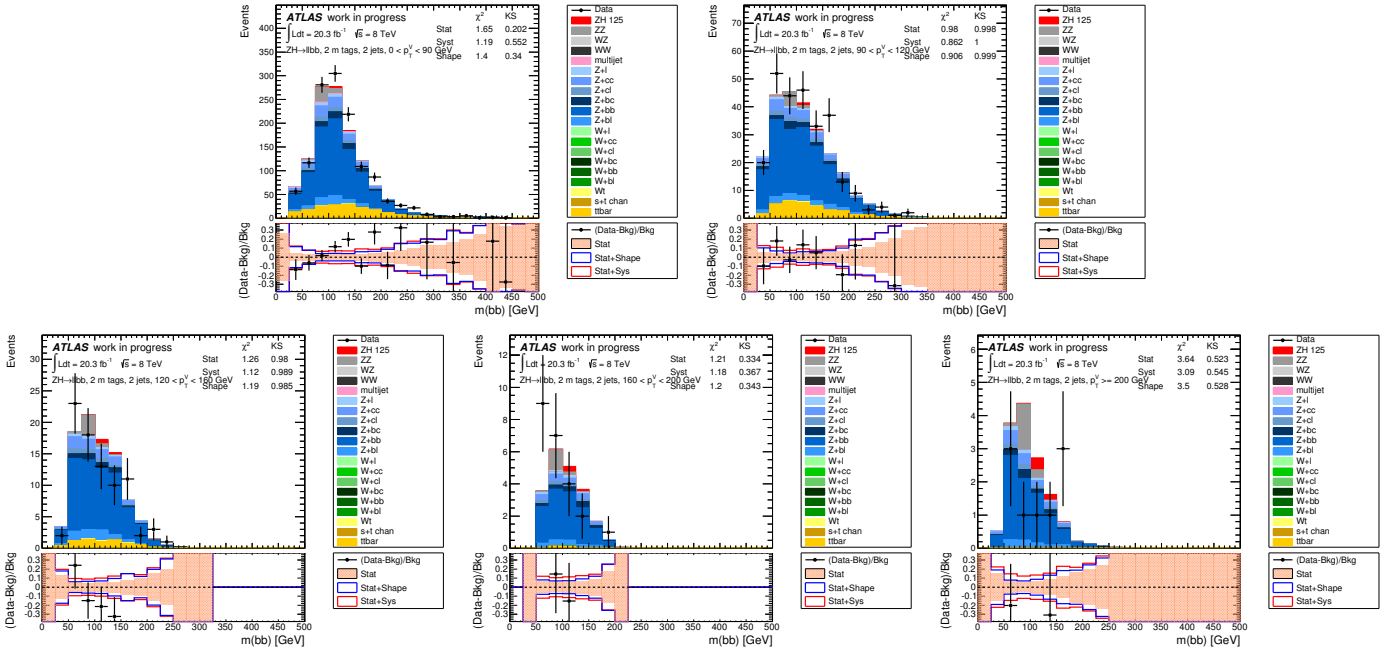

Figure 299: m_{jj} in 2-lepton events in the dijet mass analysis with 2M exclusive b-tags and 2 jets. From left to right: Row 1 - $p_{\mathrm{T}}^{Z} < 90$ GeV, and $90 < p_{\mathrm{T}}^{Z} < 120$ GeV. Row 2 - $120 < p_{\mathrm{T}}^{Z} < 160$ GeV, $160 < p_{\mathrm{T}}^{Z} < 200$ GeV, and $p_{\mathrm{T}}^{Z} > 200$ GeV. Section 6.1 details the selection criteria.

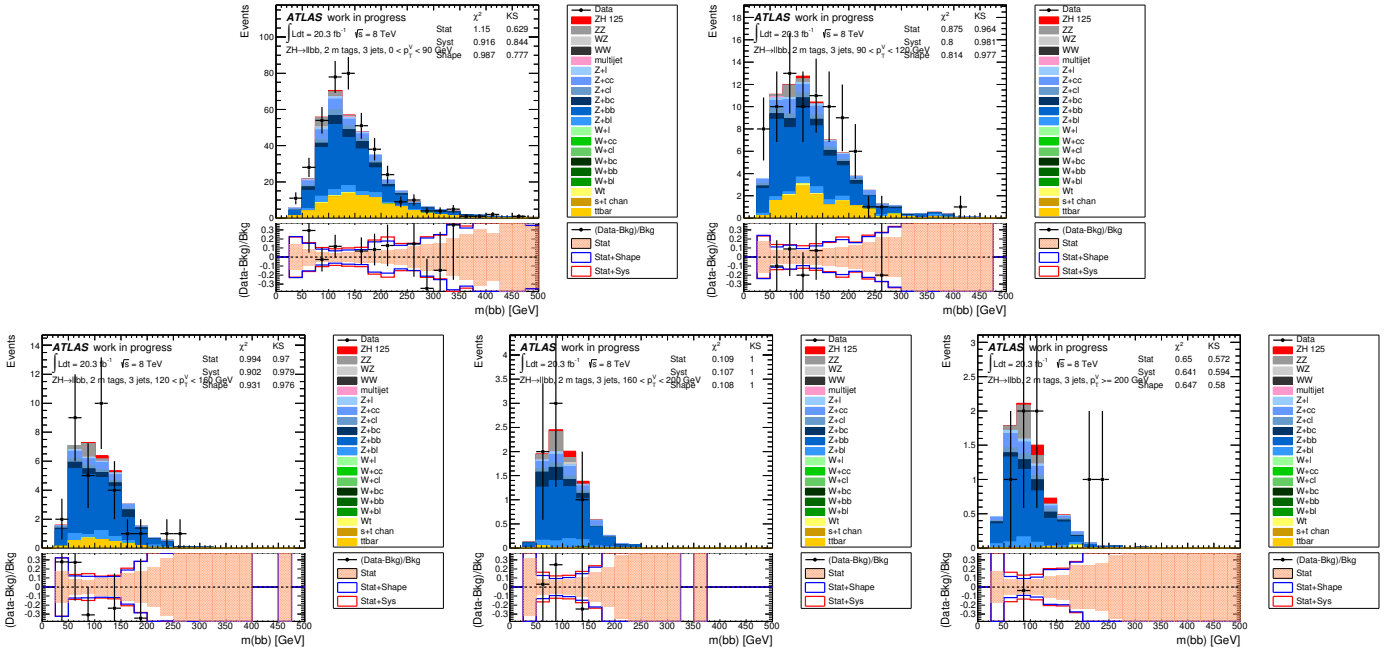

Figure 300: m_{jj} in 2-lepton events in the dijet mass analysis with 2M exclusive b-tags and 3 jets. From left to right: Row 1 - $p_{\mathrm{T}}^{Z} < 90$ GeV, and $90 < p_{\mathrm{T}}^{Z} < 120$ GeV. Row 2 - $120 < p_{\mathrm{T}}^{Z} < 160$ GeV, $160 < p_{\mathrm{T}}^{Z} < 200$ GeV, and $p_{\mathrm{T}}^{Z} > 200$ GeV. Section 6.1 details the selection criteria.

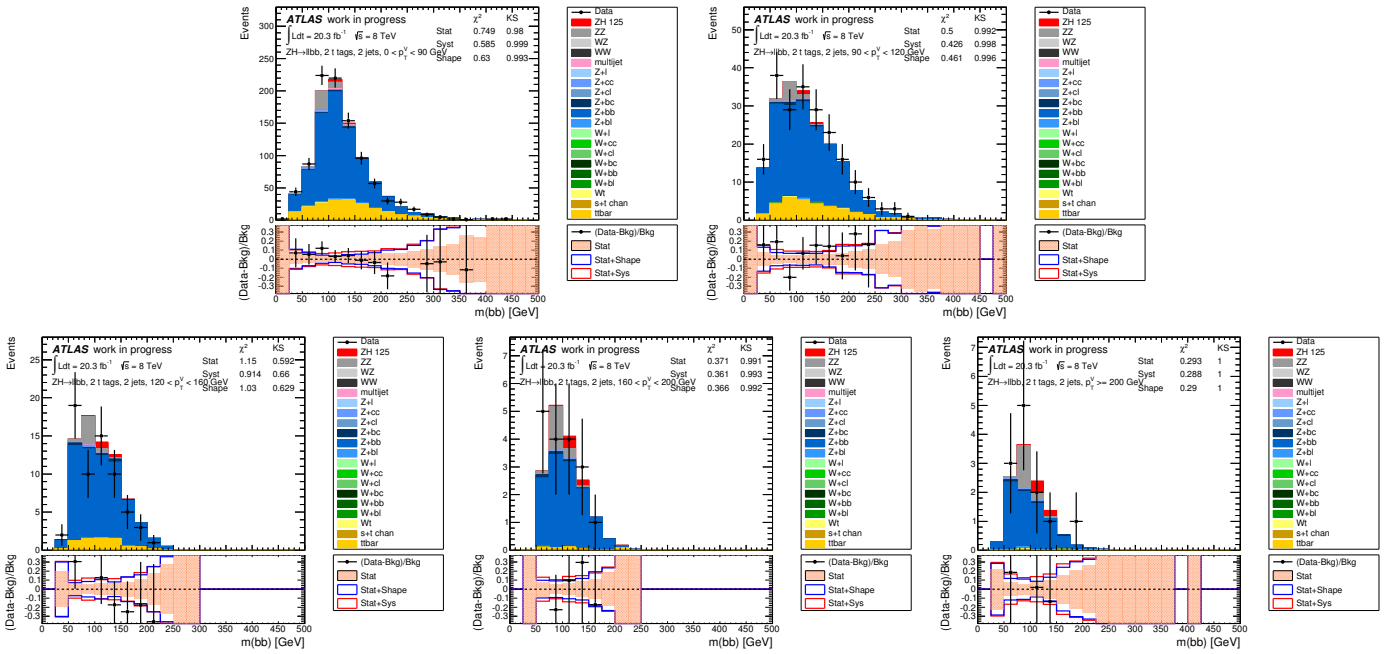

Figure 301: m_{jj} in 2-lepton events in the dijet mass analysis with 2T exclusive b-tags and 2 jets. From left to right: Row 1 - $p_{\mathrm{T}}^{Z} < 90$ GeV, and $90 < p_{\mathrm{T}}^{Z} < 120$ GeV. Row 2 - $120 < p_{\mathrm{T}}^{Z} < 160$ GeV, $160 < p_{\mathrm{T}}^{Z} < 200$ GeV, and $p_{\mathrm{T}}^{Z} > 200$ GeV. Section 6.1 details the selection criteria.

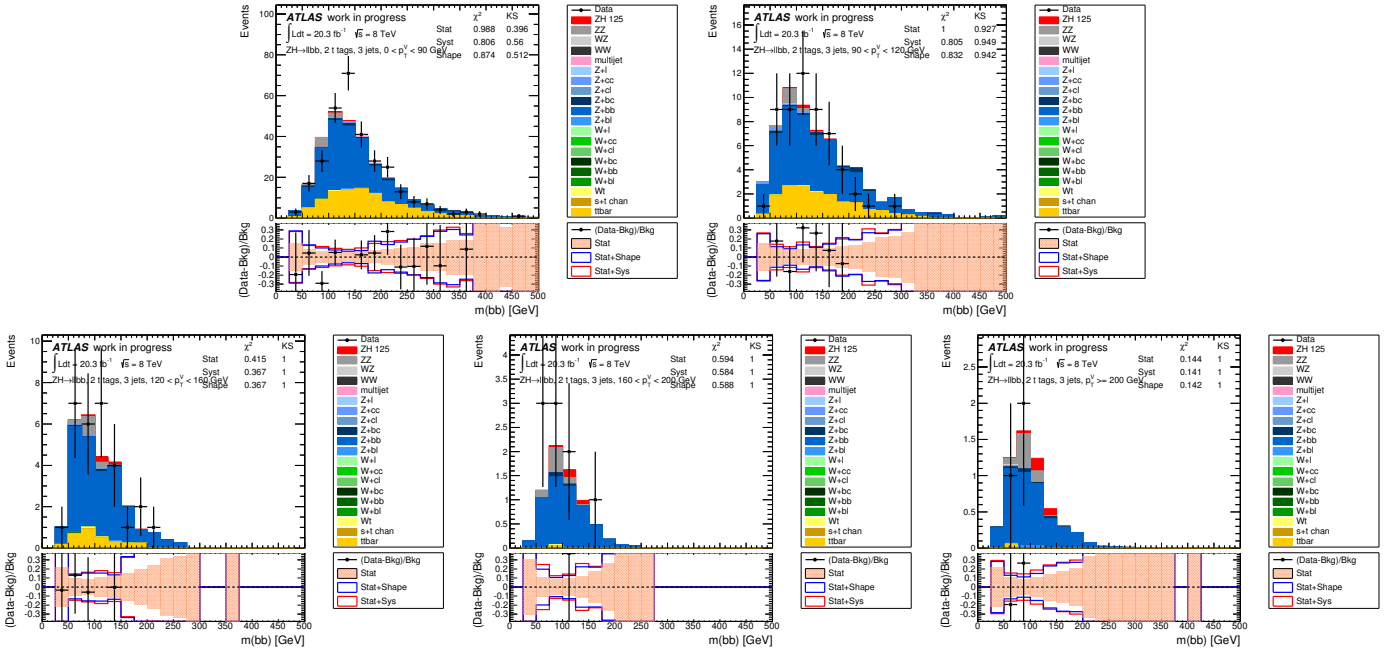

Figure 302: m_{jj} in 2-lepton events in the dijet mass analysis with 2T exclusive b-tags and 3 jets. From left to right: Row 1 - $p_{\mathrm{T}}^{Z} < 90$ GeV, and $90 < p_{\mathrm{T}}^{Z} < 120$ GeV. Row 2 - $120 < p_{\mathrm{T}}^{Z} < 160$ GeV, $160 < p_{\mathrm{T}}^{Z} < 200$ GeV, and $p_{\mathrm{T}}^{Z} > 200$ GeV. Section 6.1 details the selection criteria.

Y MVA Input Variable Distributions: Zero Lepton

This appendix contains distributions of the BDT input variables defined in Section 6 in the 0-lepton analysis. Note the the 0-lepton selection only included events with $p_{\mathrm{T}}^{Z} > 120$ GeV in the MVA analysis. These plots are done by applying the latest scale factors, obtained for the 2-jet region and the 3-jet region separately, by comparing the event yield before and after the MVA combined fit. They are summarized in Table 114. Explicitly stated, the theoretical expectation for each background is used for the given luminosity. All the plots in this section are done with the status-of-art analysis.

Figure 303 shows one b-tag two jet events prefit and Figure 304 postfit.
Figure 305 shows two loose b-tag two jet events prefit and Figure 306 postfit.
Figure 307 shows two medium or two tight b-tag two jet events prefit and Figure 308 postfit.
Figure 309 shows one b-tag three jet events prefit and Figure 310 postfit.
Figure 311 shows two loose b-tag three jet events prefit and Figure 312 postfit.
Figure 313 shows two medium or two tight b-tag two jet events prefit and Figure 314 postfit.

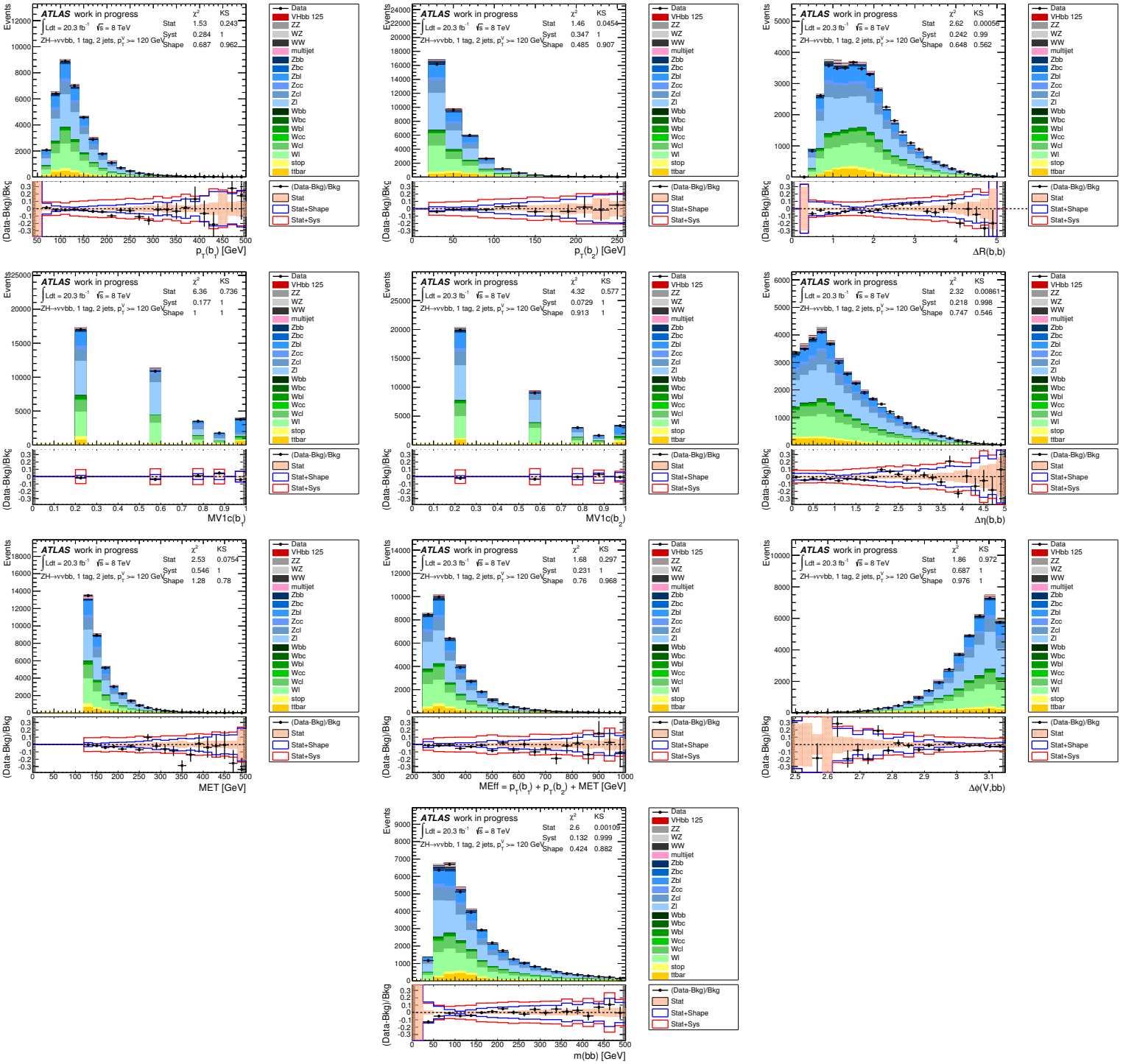

Figure 303: Distributions of MVA training variables used in 0-lepton events ($p_{\mathrm{T}}^{Z} > 120$ GeV) with 1 b-tag and 2 jets. From left to right: Row 1 - leading then sub-leading jet p_{T} and ΔR of the same jets. Row 2 - pseudo-continuous MV1c distributions for leading then sub-leading jet and the $\Delta\eta$ of the same jets. Row 3 - $E_{\mathrm{T}}^{\mathrm{miss}}$, H_{T}, and $\Delta\phi(V,H)$. Row 4 - m_{jj}. Section 6.1 details the definition of each variable.

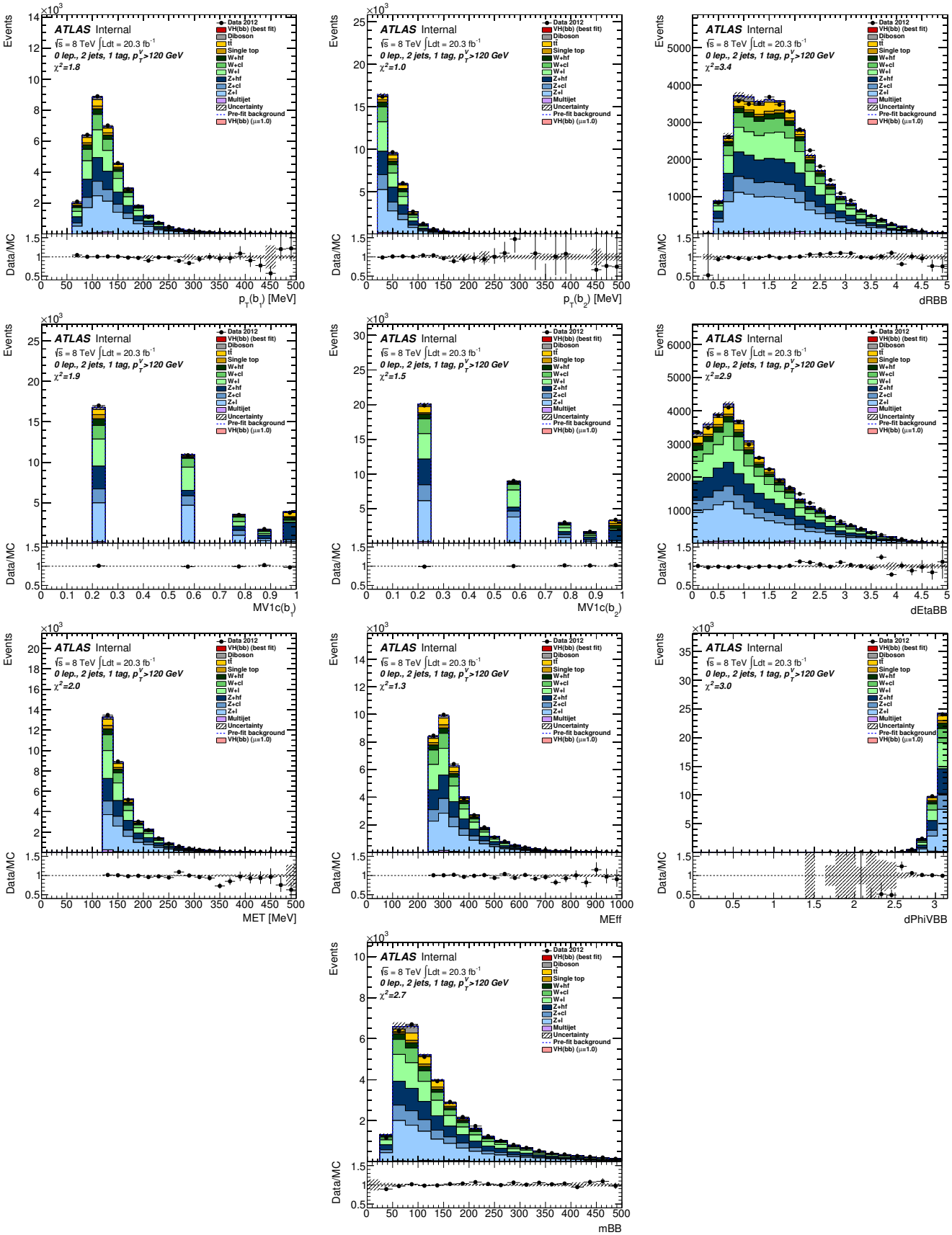

Figure 304: Distributions of MVA training variables used in 0-lepton events ($p_{\mathrm{T}}^{Z} > 120$ GeV) with 1 b-tag and 2 jets after the combined 0+1+2 lepton MVA fit. From left to right: Row 1 - leading then sub-leading jet p_{T} and ΔR of the same jets. Row 2 - pseudo-continuous MV1c distributions for leading then sub-leading jet and the $\Delta\eta$ of the same jets. Row 3 - $E_{\mathrm{T}}^{\mathrm{miss}}$, H_{T}, and $\Delta\phi(V,H)$. Row 4 - m_{jj}. Section 6.1 details the definition of each variable.

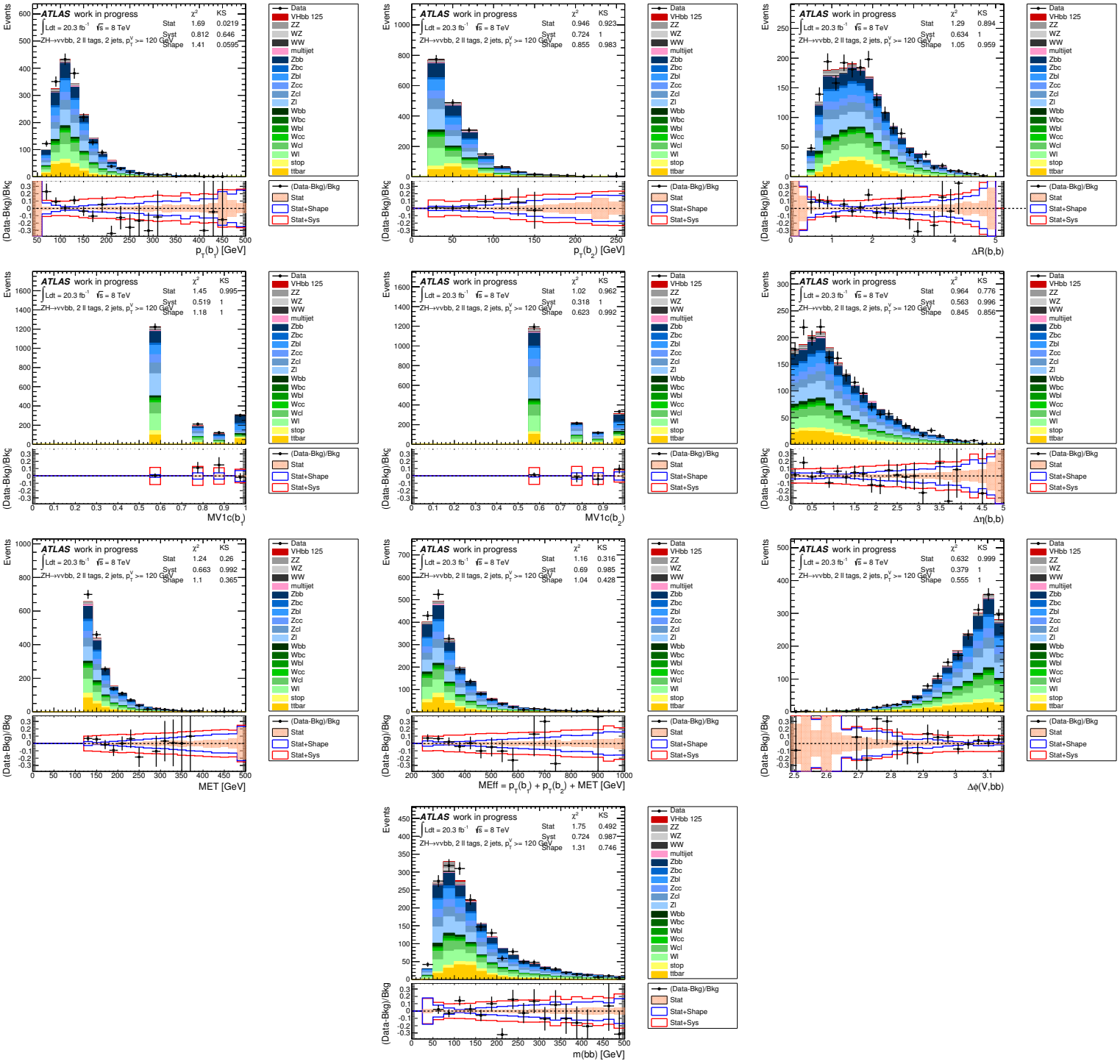

Figure 305: Distributions of MVA training variables used in 0-lepton events ($p_{\mathrm{T}}^{Z} > 120$ GeV) with 2 loose b-tags and 2 jets. From left to right: Row 1 - leading then sub-leading jet p_{T} and ΔR of the same jets. Row 2 - pseudo-continuous MV1c distributions for leading then sub-leading jet and the $\Delta\eta$ of the same jets. Row 3 - $E_{\mathrm{T}}^{\mathrm{miss}}$, H_{T}, and $\Delta\phi(V,H)$. Row 4 - m_{jj}. Section 6.1 details the definition of each variable.

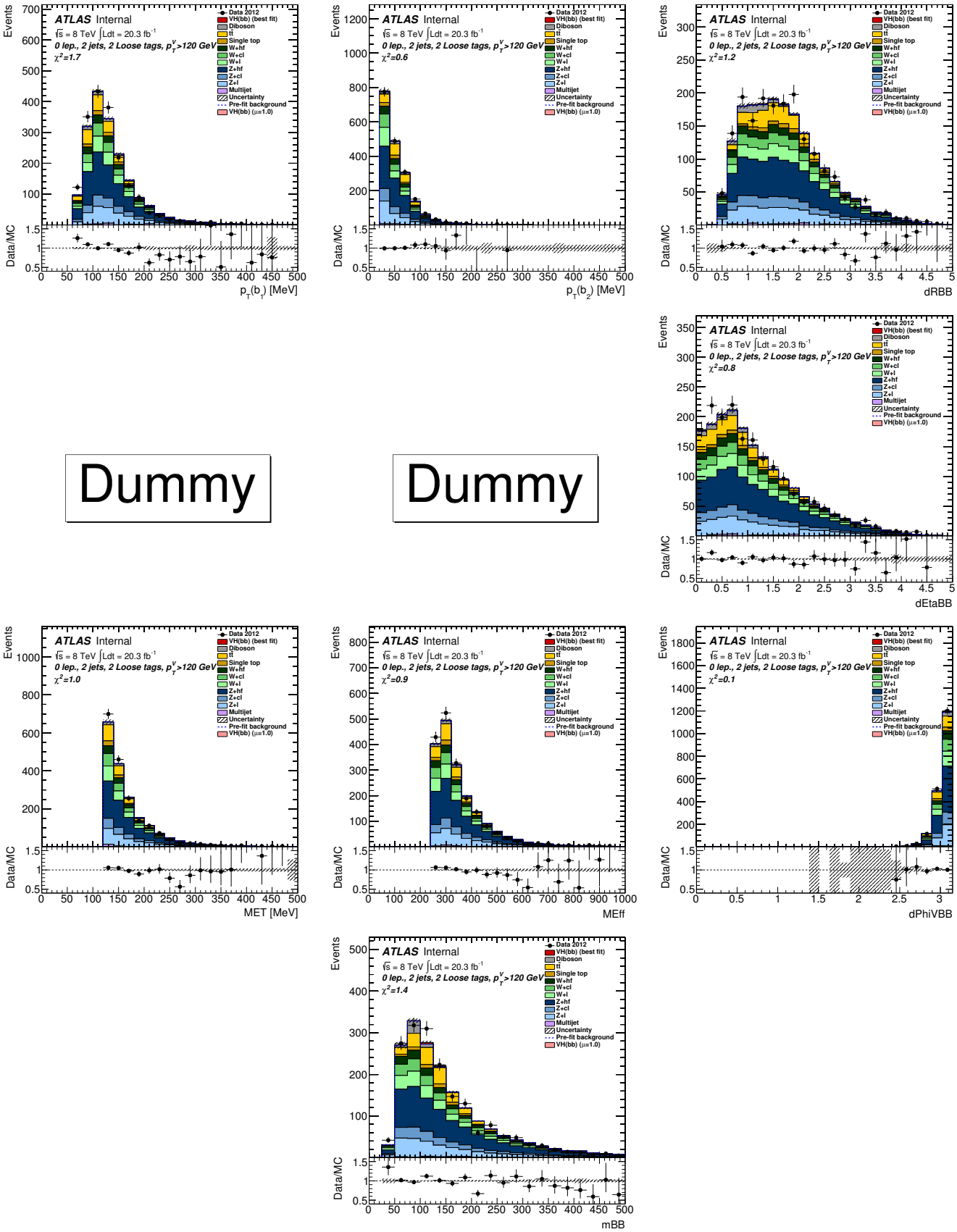

Figure 306: Distributions of MVA training variables used in 0-lepton events ($p_{\mathrm{T}}^{Z} > 120$ GeV) with 2 loose b-tags and 2 jets after the combined 0+1+2 lepton MVA fit. From left to right: Row 1 - leading then sub-leading jet p_{T} and ΔR of the same jets. Row 2 - pseudo-continuous MV1c distributions for leading then sub-leading jet and the $\Delta\eta$ of the same jets. Row 3 - $E_{\mathrm{T}}^{\mathrm{miss}}$, H_{T}, and $\Delta\phi(V,H)$. Row 4 - m_{jj}. Section 6.1 details the definition of each variable.

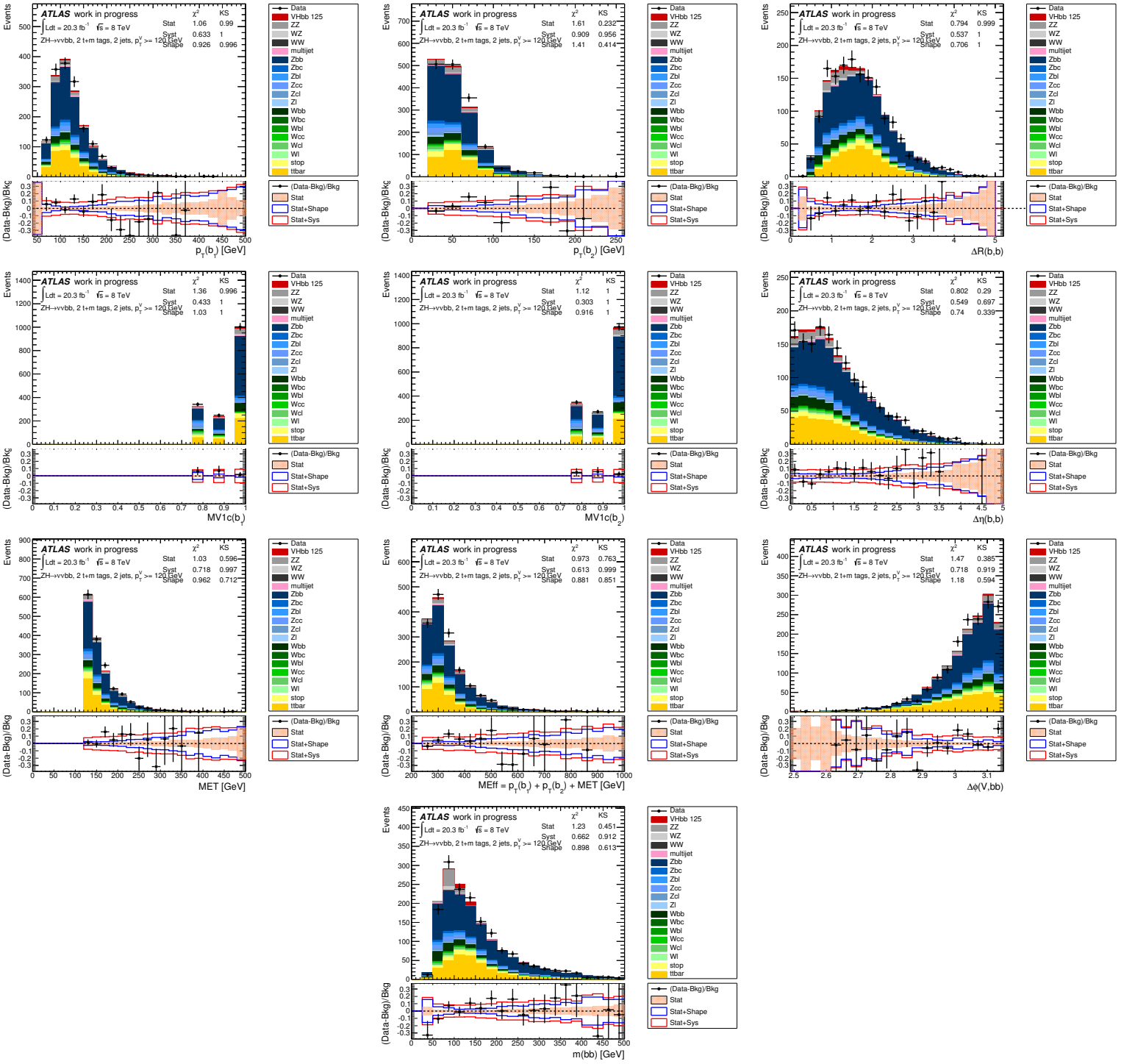

Figure 307: Distributions of MVA training variables used in 0-lepton events ($p_{\mathrm{T}}^{Z} > 120$ GeV) with 2 MM+TT b-tags and 2 jets. From left to right: Row 1 - leading then sub-leading jet p_{T} and ΔR of the same jets. Row 2 - pseudo-continuous MV1c distributions for leading then sub-leading jet and the $\Delta\eta$ of the same jets. Row 3 - $E_{\mathrm{T}}^{\mathrm{miss}}$, H_{T}, and $\Delta\phi(V,H)$. Row 4 - m_{jj}. Section 6.1 details the definition of each variable.

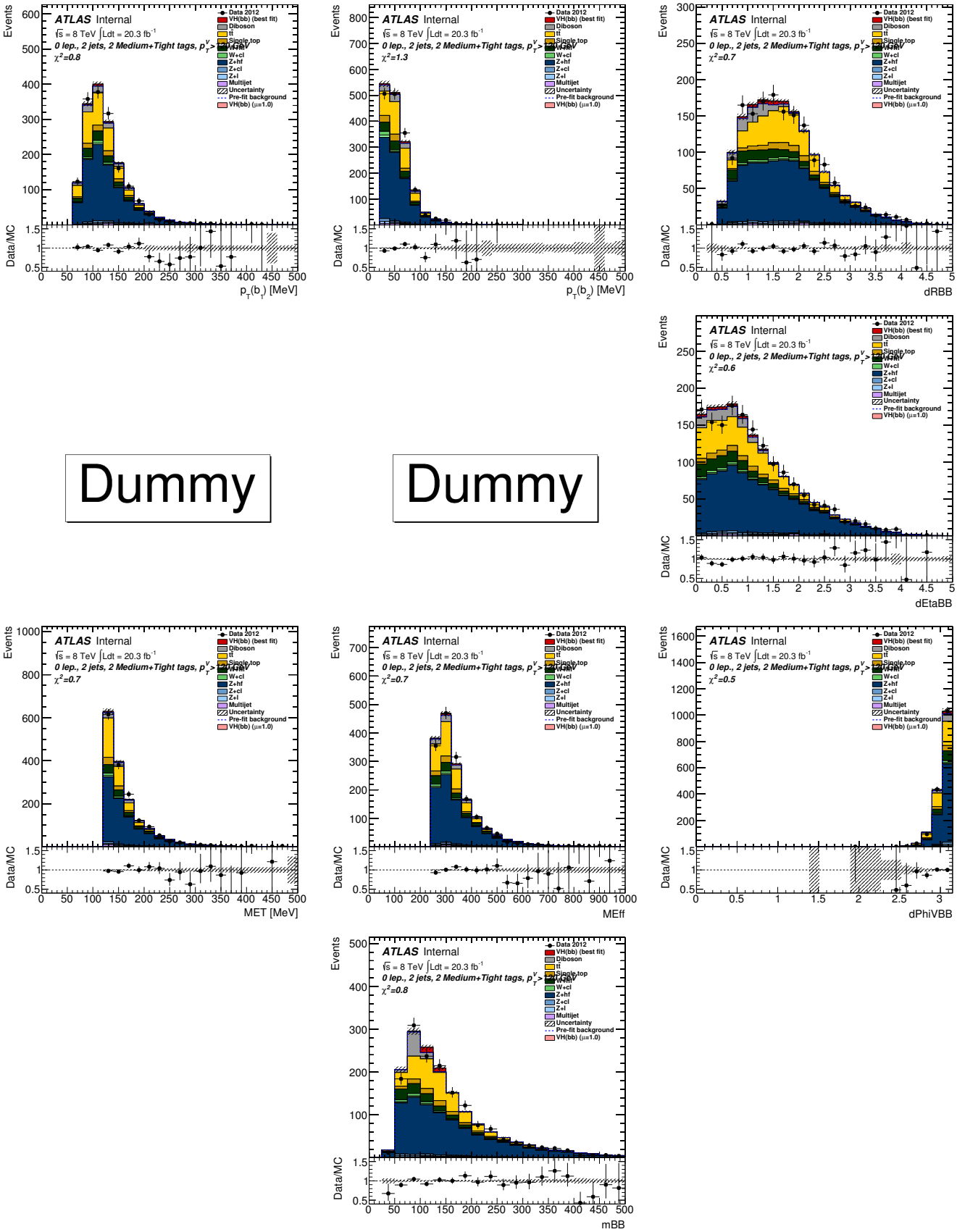

Figure 308: Distributions of MVA training variables used in 0-lepton events ($p_{\mathrm{T}}^{Z} > 120$ GeV) with 2 MM+TT b-tags and 2 jets after the combined 0+1+2 lepton MVA fit. From left to right: Row 1 - leading then sub-leading jet p_{T} and ΔR of the same jets. Row 2 - pseudo-continuous MV1c distributions for leading then sub-leading jet and the $\Delta\eta$ of the same jets. Row 3 - $E_{\mathrm{T}}^{\mathrm{miss}}$, H_{T}, and $\Delta\phi(V,H)$. Row 4 - m_{jj}. Section 6.1 details the definition of each variable.

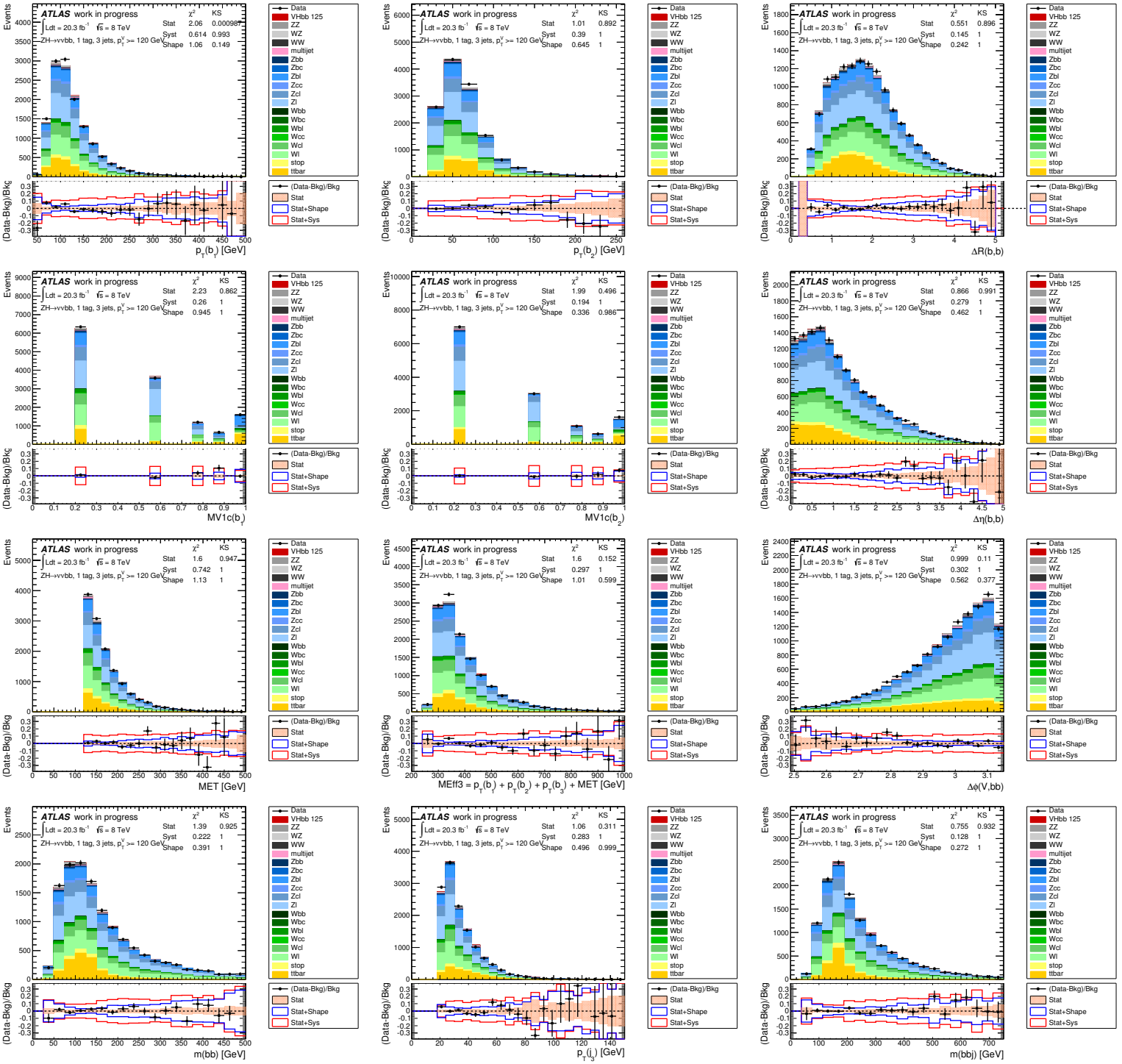

Figure 309: Distributions of MVA training variables used in 0-lepton events ($p_{\mathrm{T}}^{Z} > 120$ GeV) with 1 b-tag and 3 jets. From left to right: Row 1 - leading then sub-leading jet p_{T} and ΔR of the same jets. Row 2 - pseudo-continuous MV1c distributions for leading then sub-leading jet and the $\Delta\eta$ of the same jets. Row 3 - $E_{\mathrm{T}}^{\mathrm{miss}}$, H_{T}, and $\Delta\phi(V,H)$. Row 4 - m_{jj}, the 3^{rd} jet p_{T}, and the tri-jet mass (m_{jjj}). Section 6.1 details the definition of each variable.

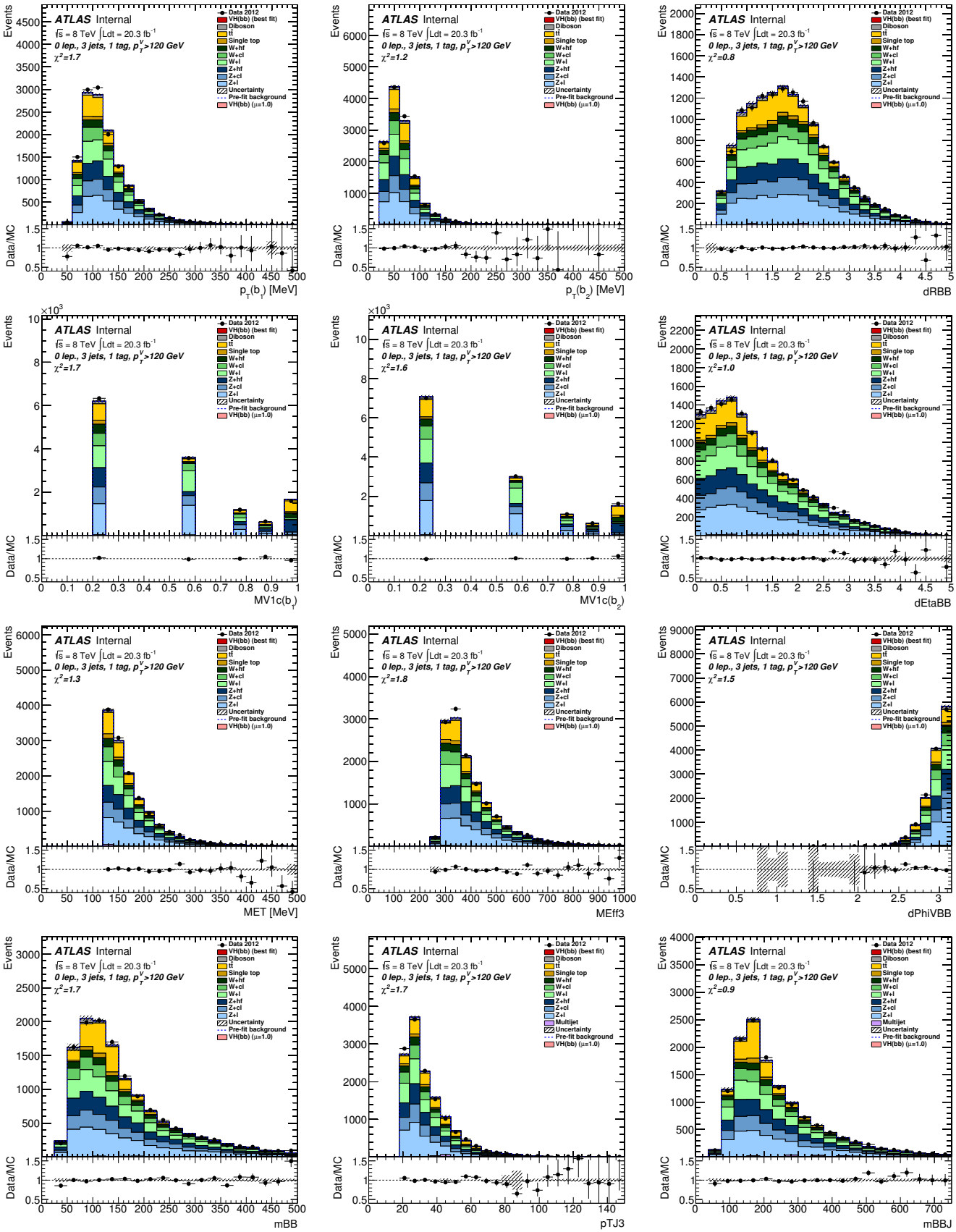

Figure 310: Distributions of MVA training variables used in 0-lepton events ($p_{\mathrm{T}}^{Z} > 120$ GeV) with 1 b-tag and 3 jets after the combined 0+1+2 lepton MVA fit. From left to right: Row 1 - leading then sub-leading jet p_{T} and ΔR of the same jets. Row 2 - pseudo-continuous MV1c distributions for leading then sub-leading jet and the $\Delta\eta$ of the same jets. Row 3 - $E_{\mathrm{T}}^{\mathrm{miss}}$, H_{T}, and $\Delta\phi(V,H)$. Row 4 - m_{jj}, the 3^{rd} jet p_{T}, and the tri-jet mass (m_{jjj}). Section 6.1 details the definition of each variable.

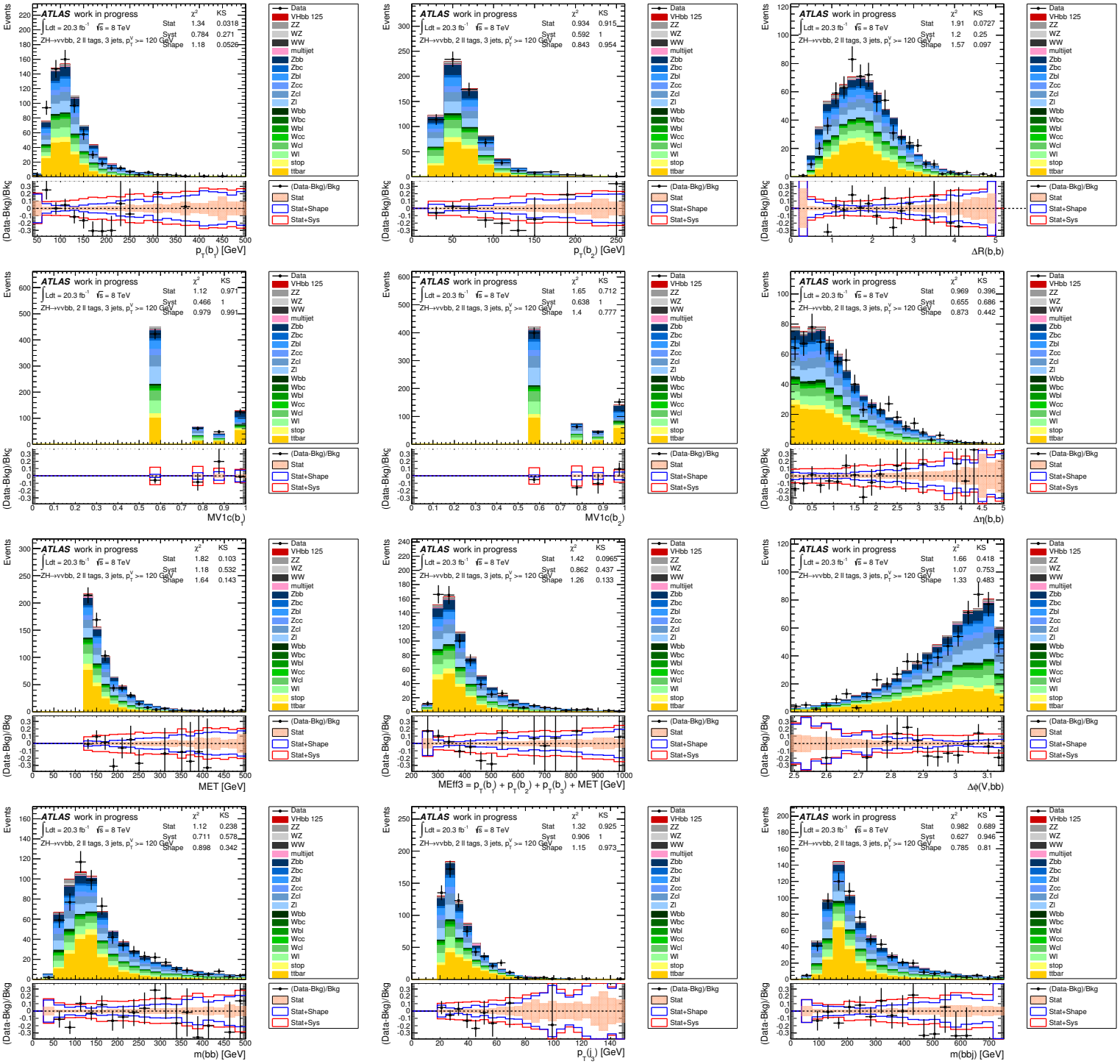

Figure 311: Distributions of MVA training variables used in 0-lepton events ($p_{\mathrm{T}}^{Z} > 120$ GeV) with 2 loose b-tags and 3 jets. From left to right: Row 1 - leading then sub-leading jet p_{T} and ΔR of the same jets. Row 2 - pseudo-continuous MV1c distributions for leading then sub-leading jet and the $\Delta\eta$ of the same jets. Row 3 - $E_{\mathrm{T}}^{\mathrm{miss}}$, H_{T}, and $\Delta\phi(V,H)$. Row 4 - m_{jj}, the 3^{rd} jet p_{T}, and the tri-jet mass (m_{jjj}). Section 6.1 details the definition of each variable.

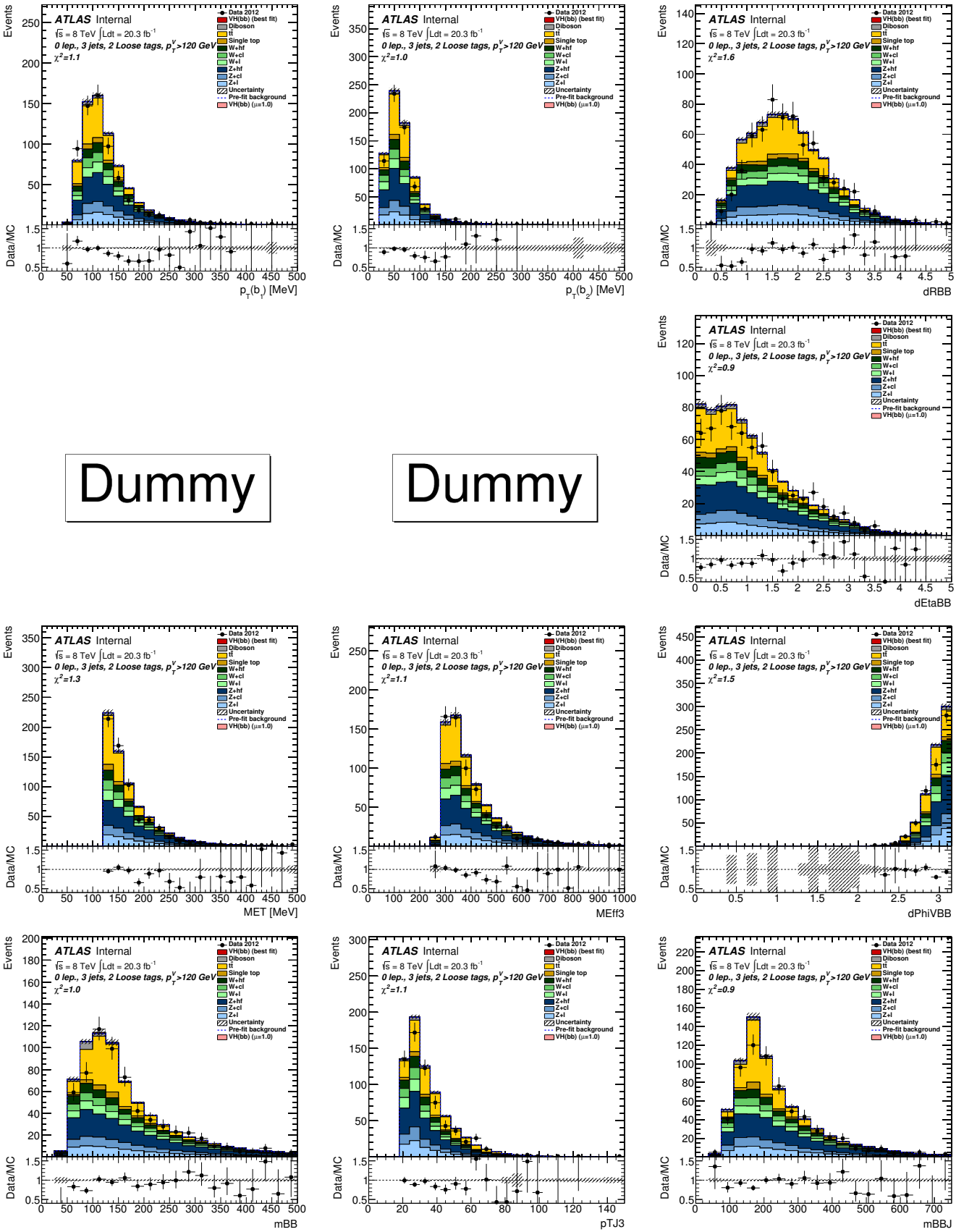

Figure 312: Distributions of MVA training variables used in 0-lepton events ($p_{\mathrm{T}}^{Z} > 120$ GeV) with 2 loose b-tags and 3 jets after the combined 0+1+2 lepton MVA fit. From left to right: Row 1 - leading then sub-leading jet p_{T} and ΔR of the same jets. Row 2 - pseudo-continuous MV1c distributions for leading then sub-leading jet and the $\Delta\eta$ of the same jets. Row 3 - $E_{\mathrm{T}}^{\mathrm{miss}}$, H_{T}, and $\Delta\phi(V,H)$. Row 4 - m_{jj}, the 3^{rd} jet p_{T}, and the tri-jet mass (m_{jjj}). Section 6.1 details the definition of each variable.

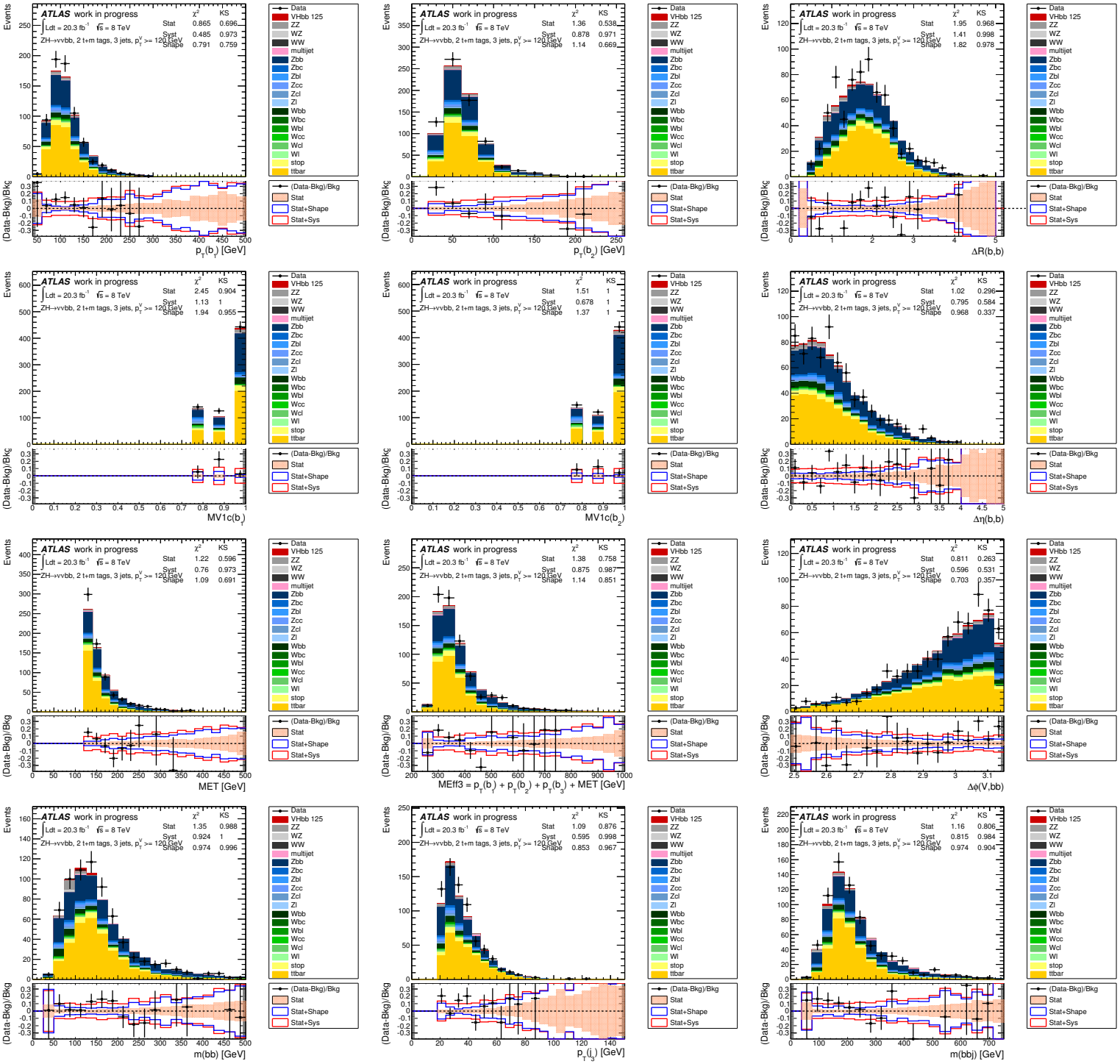

Figure 313: Distributions of MVA training variables used in 0-lepton events ($p_{\mathrm{T}}^{Z} > 120$ GeV) with 2 MM+TT b-tags and 3 jets. From left to right: Row 1 - leading then sub-leading jet p_{T} and ΔR of the same jets. Row 2 - pseudo-continuous MV1c distributions for leading then sub-leading jet and the $\Delta\eta$ of the same jets. Row 3 - $E_{\mathrm{T}}^{\mathrm{miss}}$, H_{T}, and $\Delta\phi(V,H)$. Row 4 - m_{jj}, the 3^{rd} jet p_{T}, and the tri-jet mass (m_{jjj}). Section 6.1 details the definition of each variable.

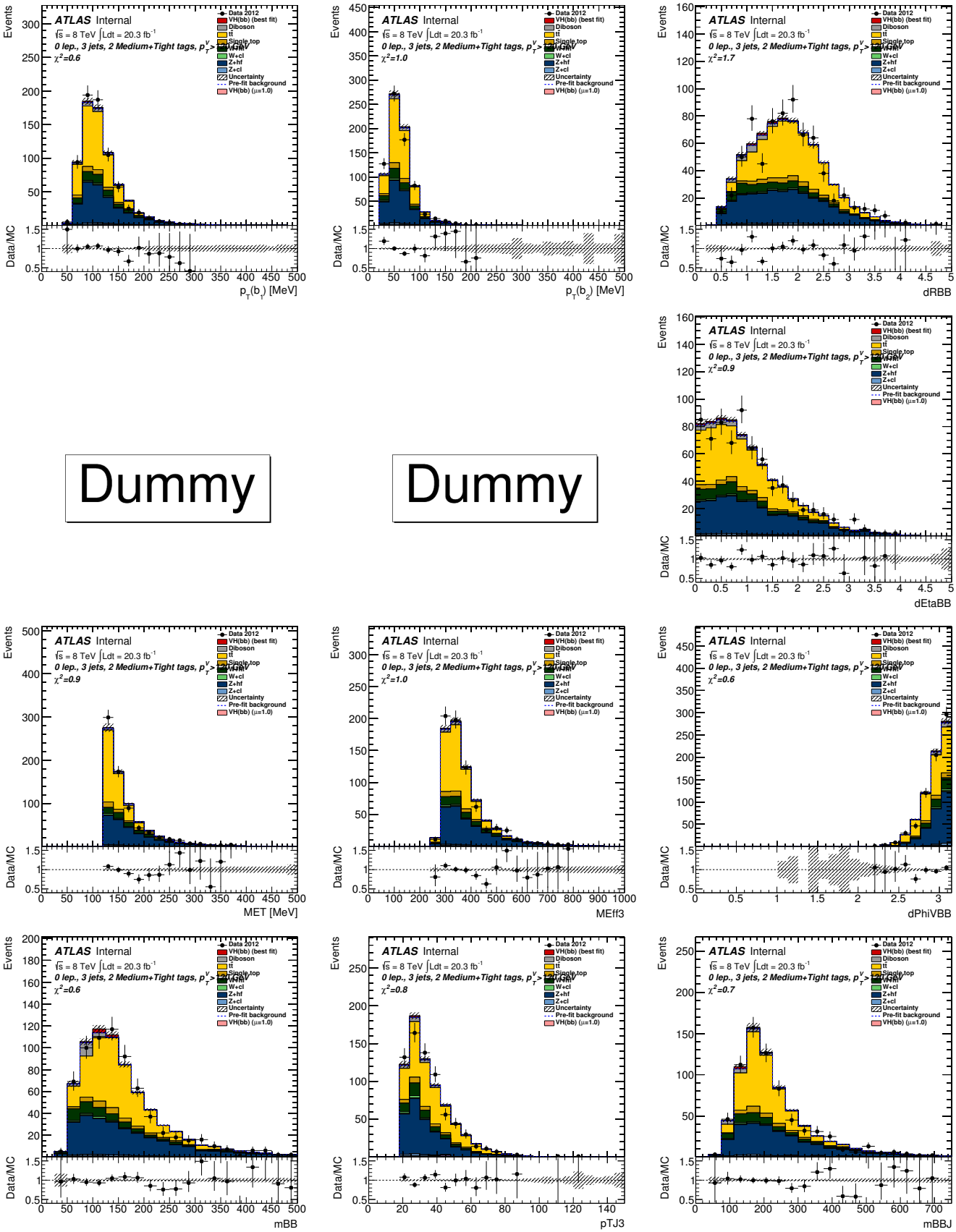

Dummy

Dummy

Figure 314: Distributions of MVA training variables used in 0-lepton events ($p_{\mathrm{T}}^{Z} > 120$ GeV) with 2 MM+TT b-tags and 3 jets after the combined 0+1+2 lepton MVA fit. From left to right: Row 1 - leading then sub-leading jet p_{T} and ΔR of the same jets. Row 2 - pseudo-continuous MV1c distributions for leading then sub-leading jet and the $\Delta\eta$ of the same jets. Row 3 - $E_{\mathrm{T}}^{\mathrm{miss}}$, H_{T}, and $\Delta\phi(V,H)$. Row 4 - m_{jj}, the 3^{rd} jet p_{T}, and the tri-jet mass (m_{jjj}). Section 6.1 details the definition of each variable.

Z MVA Input Variable Distributions: One Lepton

This appendix contains distributions of the BDT input variables defined in Section 6 in the 1-lepton analysis for low and high p_{T}^{W} regions ($p_{\mathrm{T}}^{W} < 120$ GeV and $p_{\mathrm{T}}^{W} > 120$ GeV respectively). The electron and muon events have been combined. These plots are done by applying the latest scale factors, obtained for the 2-jet region and the 3-jet region separately, by comparing the event yield before and after the MVA combined fit. They are summarized in Table 114. Explicitly stated, the theoretical expectation for each background is used for the given luminosity. All the plots in this section are done with the status-of-art analysis.

Figure 315 shows one b-tag two jet events with $p_{\mathrm{T}}^{W} < 120$ GeV prefit and Figure 316 postfit.
Figure 317 shows one b-tag two jet events with $p_{\mathrm{T}}^{W} > 120$ GeV prefit and Figure 318 postfit.
Figure 319 shows LL b-tag two jet events with $p_{\mathrm{T}}^{W} < 120$ GeV prefit and Figure 320 postfit.
Figure 321 shows LL b-tag two jet events with $p_{\mathrm{T}}^{W} > 120$ GeV prefit and Figure 322 postfit.
Figure 323 shows MM b-tag two jet events with $p_{\mathrm{T}}^{W} < 120$ GeV prefit and Figure 324 postfit.
Figure 325 shows MM b-tag two jet events with $p_{\mathrm{T}}^{W} > 120$ GeV prefit and Figure 326 postfit.
Figure 327 shows TT b-tag two jet events with $p_{\mathrm{T}}^{W} < 120$ GeV prefit and Figure 328 postfit.
Figure 329 shows TT b-tag two jet events with $p_{\mathrm{T}}^{W} > 120$ GeV prefit and Figure 330 postfit.
Figure 331 shows one b-tag three jet events with $p_{\mathrm{T}}^{W} < 120$ GeV prefit and Figure 332 postfit.
Figure 333 shows one b-tag three jet events with $p_{\mathrm{T}}^{W} > 120$ GeV prefit and Figure 334 postfit.
Figure 335 shows LL b-tag three jet events with $p_{\mathrm{T}}^{W} < 120$ GeV prefit and Figure 336 postfit.
Figure 337 shows LL b-tag three jet events with $p_{\mathrm{T}}^{W} > 120$ GeV prefit and Figure 338 postfit.
Figure 339 shows MM b-tag three jet events with $p_{\mathrm{T}}^{W} < 120$ GeV prefit and Figure 340 postfit.
Figure 341 shows MM b-tag three jet events with $p_{\mathrm{T}}^{W} > 120$ GeV prefit and Figure 342 postfit.
Figure 343 shows TT b-tag three jet events with $p_{\mathrm{T}}^{W} < 120$ GeV prefit and Figure 344 postfit.
Figure 345 shows TT b-tag three jet events with $p_{\mathrm{T}}^{W} > 120$ GeV prefit and Figure 346 postfit.

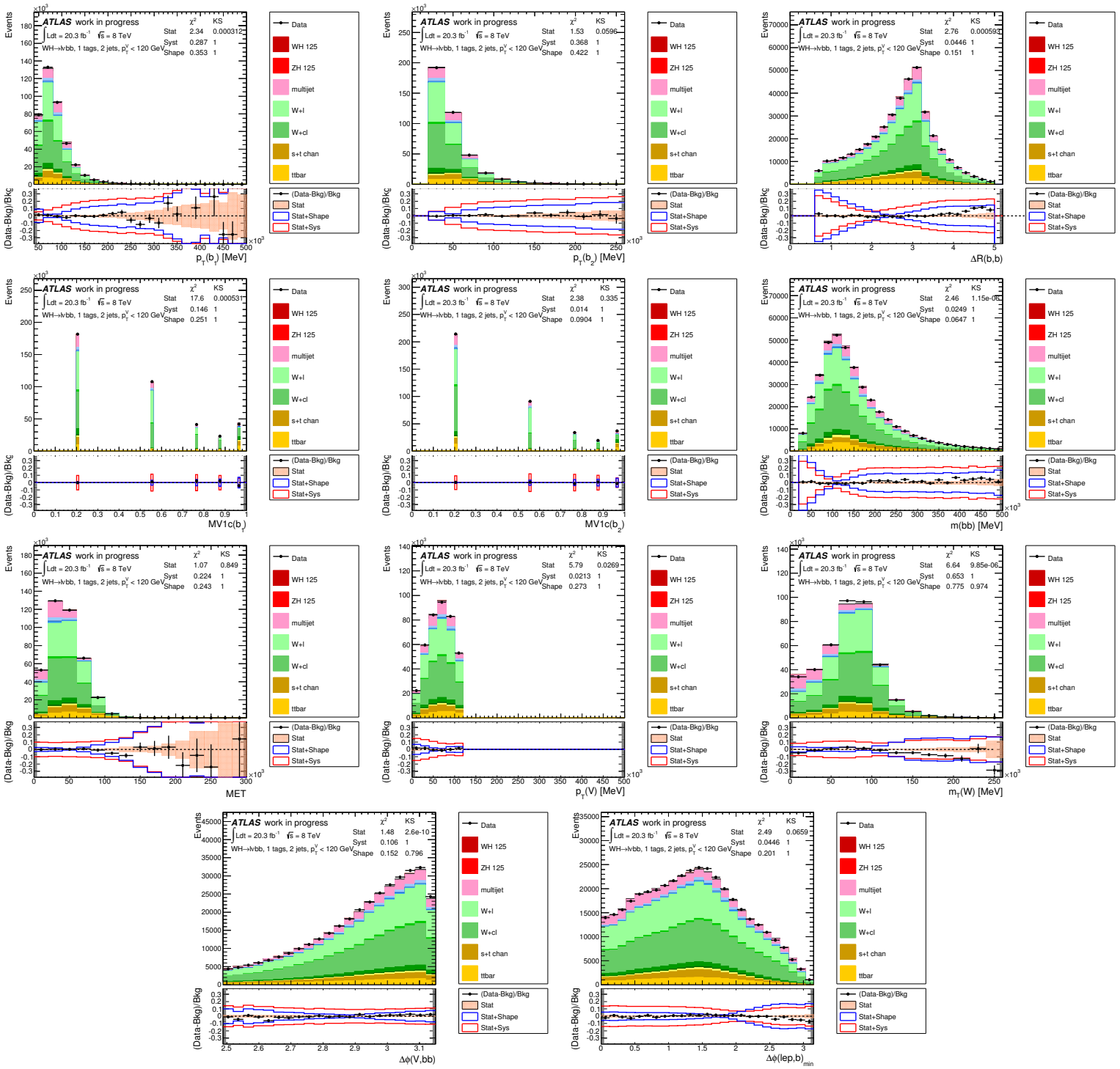

Figure 315: Distributions of MVA training variables used in 1-lepton events for $p_{\mathrm{T}}^{W} < 120$ GeV with 1 b-tag and 2 jets. From left to right: Row 1 - leading then sub-leading jet p_{T} and ΔR of the same two jets. Row 2 - pseudo-continuous MV1c distributions for leading then sub-leading jet and the m_{jj} of the same two jets. Row 3 - $E_{\mathrm{T}}^{\mathrm{miss}}$, p_{T}^{W}, and m_{T}^{W}. Row 4 - $\Delta\phi(V,H)$ and min$|\Delta\phi(\ell, jet)|$. Section 6.1 details the definition of each variable.

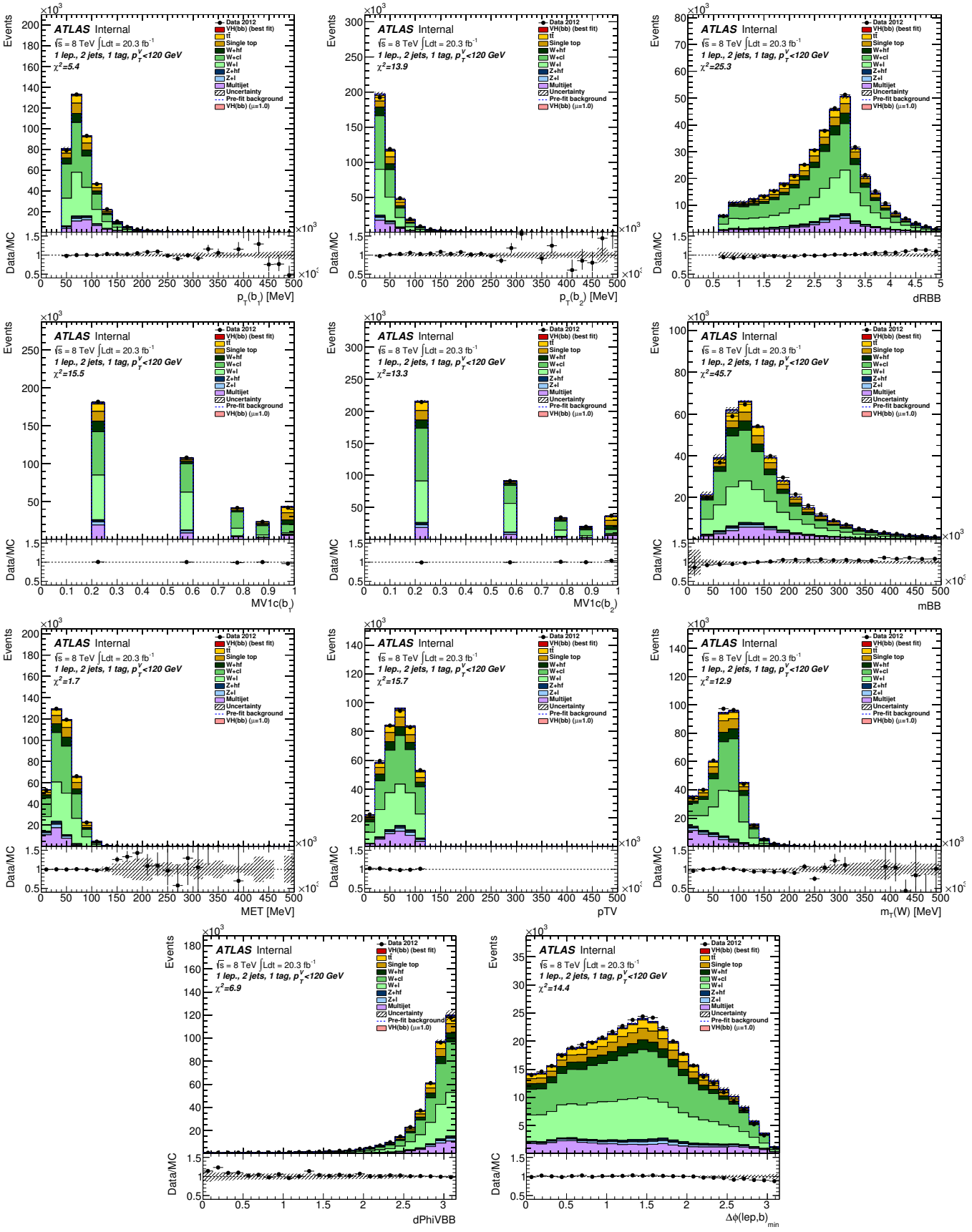

Figure 316: Distributions of MVA training variables used in 1-lepton events for $p_{\mathrm{T}}^{W} < 120$ GeV with 1 b-tag and 2 jets after the combined 0+1+2 lepton MVA fit. From left to right: Row 1 - leading then sub-leading jet p_{T} and ΔR of the same two jets. Row 2 - pseudo-continuous MV1c distributions for leading then sub-leading jet and the m_{jj} of the same two jets. Row 3 - $E_{\mathrm{T}}^{\mathrm{miss}}$, p_{T}^{W}, and m_{T}^{W}. Row 4 - $\Delta\phi(V,H)$ and $\min|\Delta\phi(\ell, jet)|$. Section 6.1 details the definition of each variable.

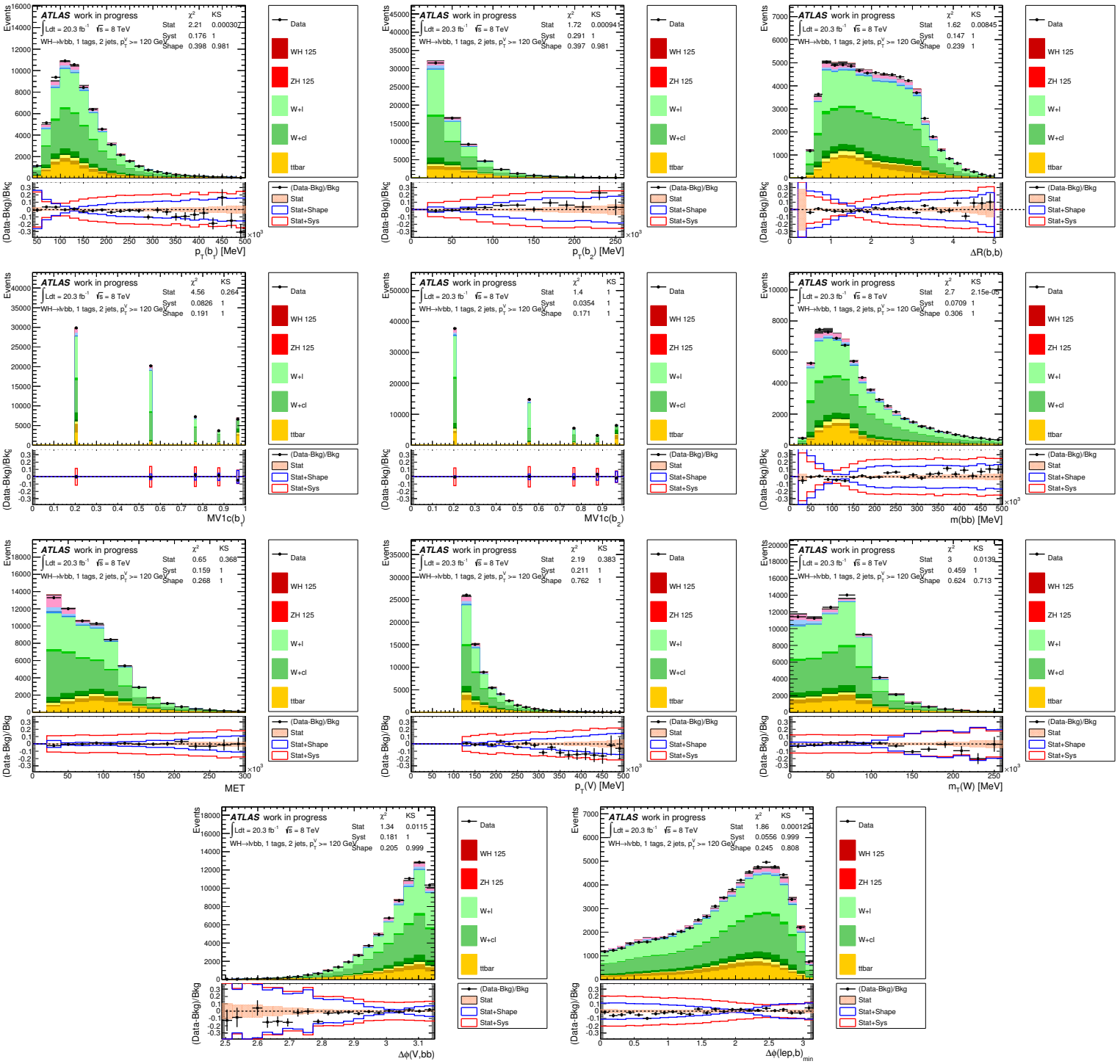

Figure 317: Distributions of MVA training variables used in 1-lepton events for $p_{\mathrm{T}}^{W} > 120$ GeV with 1 b-tag and 2 jets. From left to right: Row 1 - leading then sub-leading jet p_{T} and ΔR of the same two jets. Row 2 - pseudo-continuous MV1c distributions for leading then sub-leading jet and the m_{jj} of the same two jets. Row 3 - $E_{\mathrm{T}}^{\mathrm{miss}}$, p_{T}^{W}, and m_{T}^{W}. Row 4 - $\Delta\phi(V,H)$ and $\min|\Delta\phi(\ell, jet)|$. Section 6.1 details the definition of each variable.

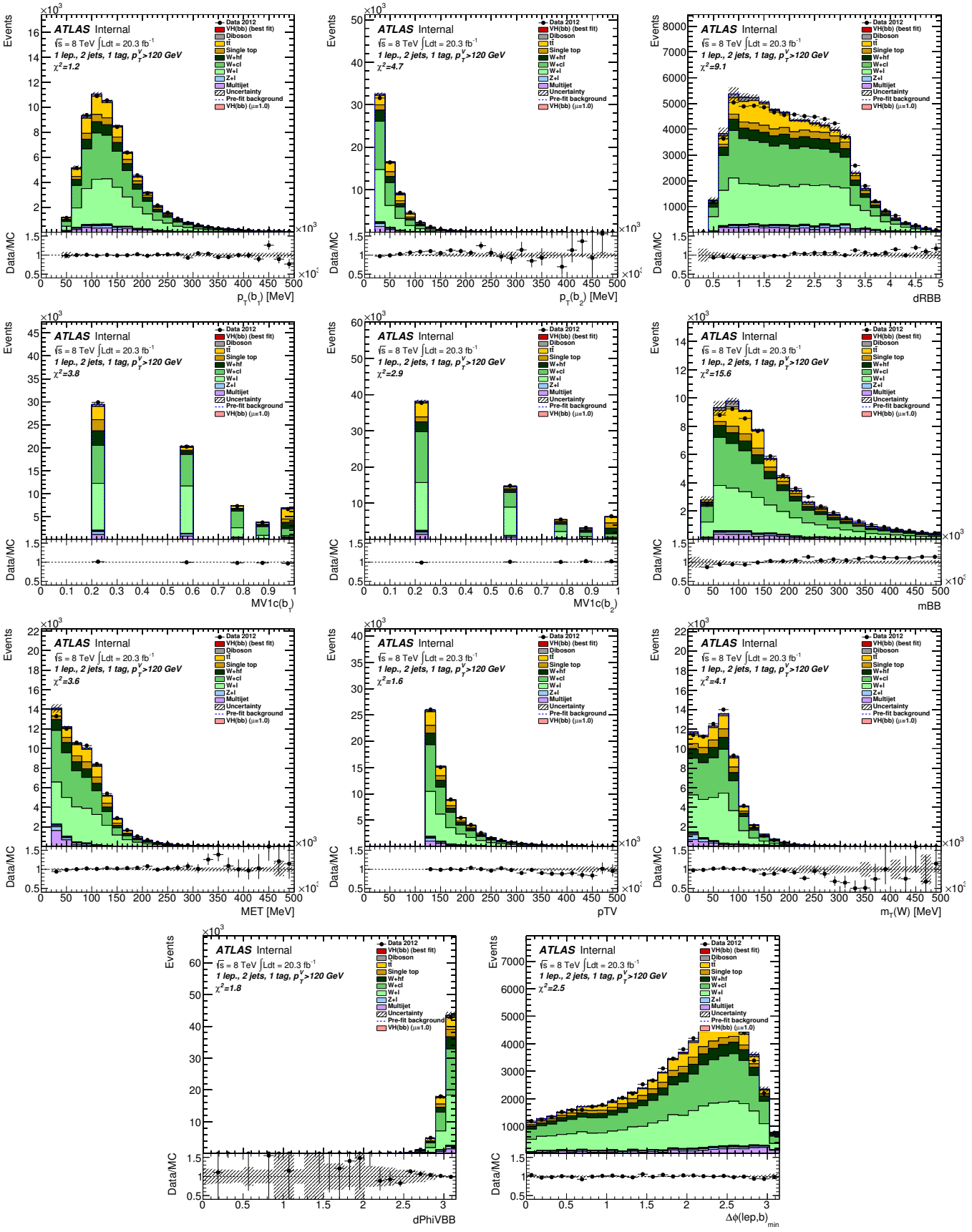

Figure 318: Distributions of MVA training variables used in 1-lepton events for $p_{\mathrm{T}}^{W} > 120$ GeV with 1 b-tag and 2 jets after the combined 0+1+2 lepton MVA fit. From left to right: Row 1 - leading then sub-leading jet p_{T} and ΔR of the same two jets. Row 2 - pseudo-continuous MV1c distributions for leading then sub-leading jet and the m_{jj} of the same two jets. Row 3 - $E_{\mathrm{T}}^{\mathrm{miss}}$, p_{T}^{W}, and m_{T}^{W}. Row 4 - $\Delta\phi(V, H)$ and $\min|\Delta\phi(\ell, jet)|$. Section 6.1 details the definition of each variable.

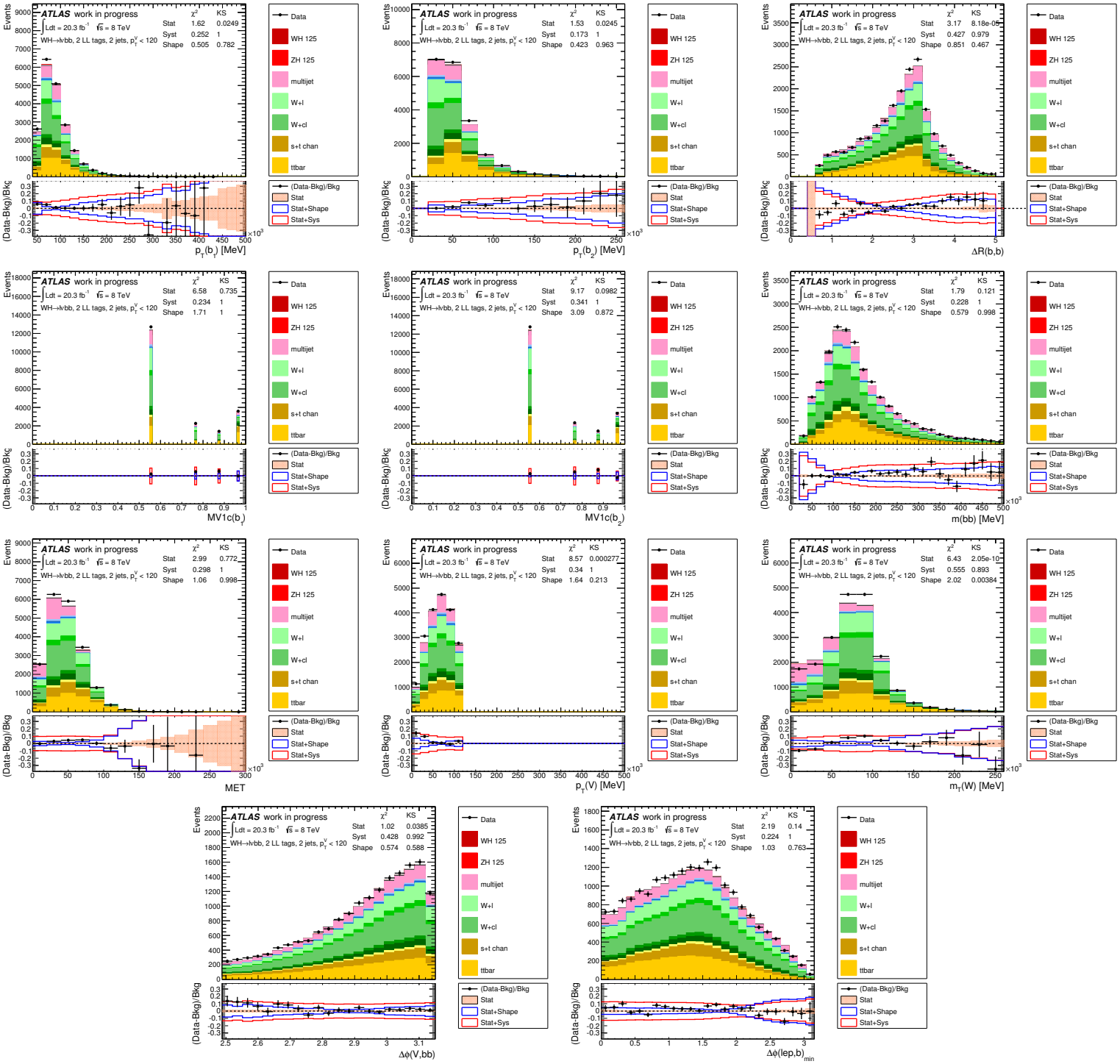

Figure 319: Distributions of MVA training variables used in 1-lepton events for $p_{\mathrm{T}}^{W} < 120$ GeV with 2 LL b-tags and 2 jets. From left to right: Row 1 - leading then sub-leading jet p_{T} and ΔR of the same two jets. Row 2 - pseudo-continuous MV1c distributions for leading then sub-leading jet and the m_{jj} of the same two jets. Row 3 - $E_{\mathrm{T}}^{\mathrm{miss}}$, p_{T}^{W}, and m_{T}^{W}. Row 4 - $\Delta\phi(V,H)$ and $\min|\Delta\phi(\ell, jet)|$. Section 6.1 details the definition of each variable.

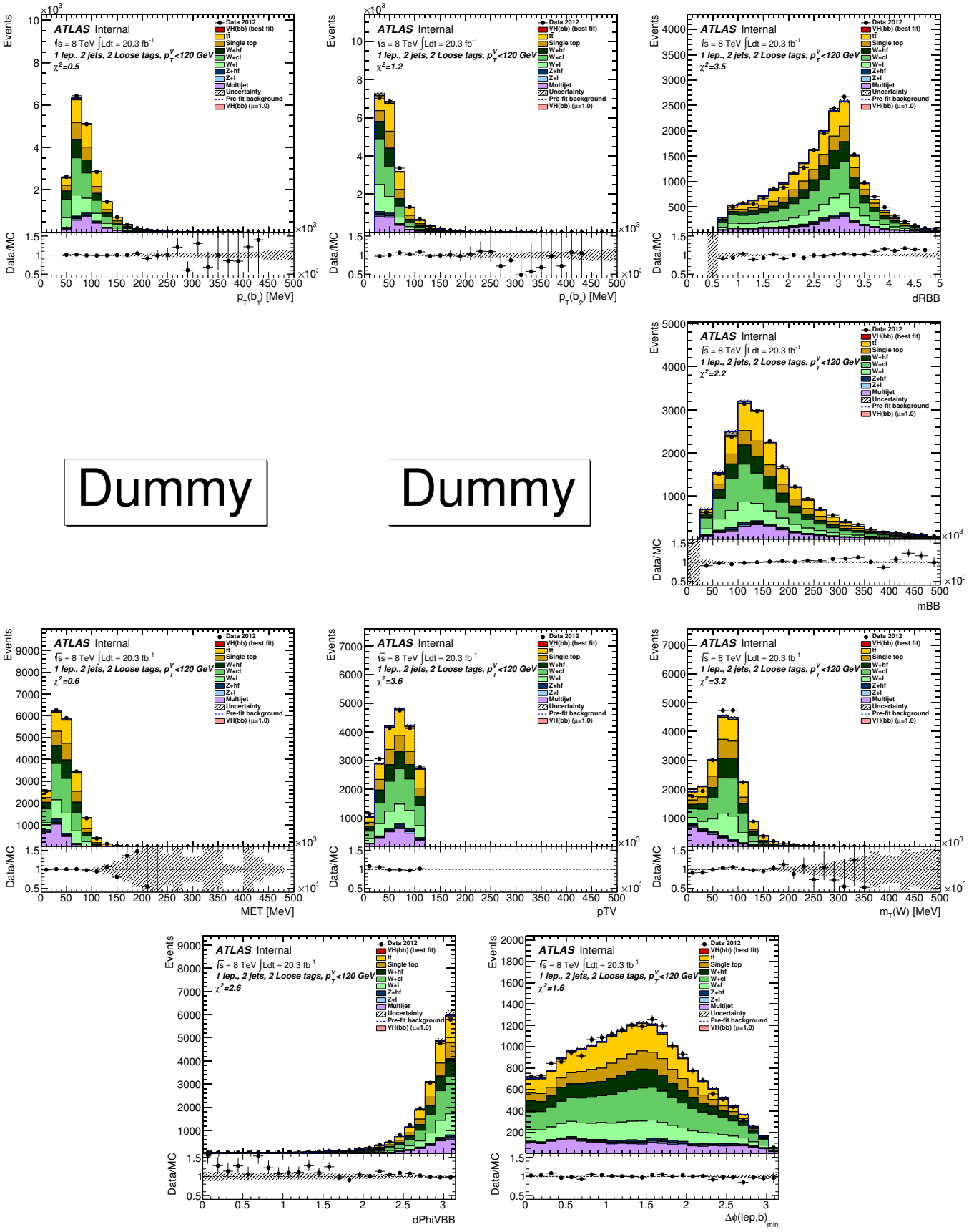

Figure 320: Distributions of MVA training variables used in 1-lepton events for $p_{\mathrm{T}}^{W} < 120$ GeV with 2 LL b-tags and 2 jets after the combined 0+1+2 lepton MVA fit. From left to right: Row 1 - leading then sub-leading jet p_{T} and ΔR of the same two jets. Row 2 - pseudo-continuous MV1c distributions for leading then sub-leading jet and the m_{jj} of the same two jets. Row 3 - $E_{\mathrm{T}}^{\mathrm{miss}}$, p_{T}^{W}, and m_{T}^{W}. Row 4 - $\Delta\phi(V,H)$ and $\min|\Delta\phi(\ell, jet)|$. Section 6.1 details the definition of each variable.

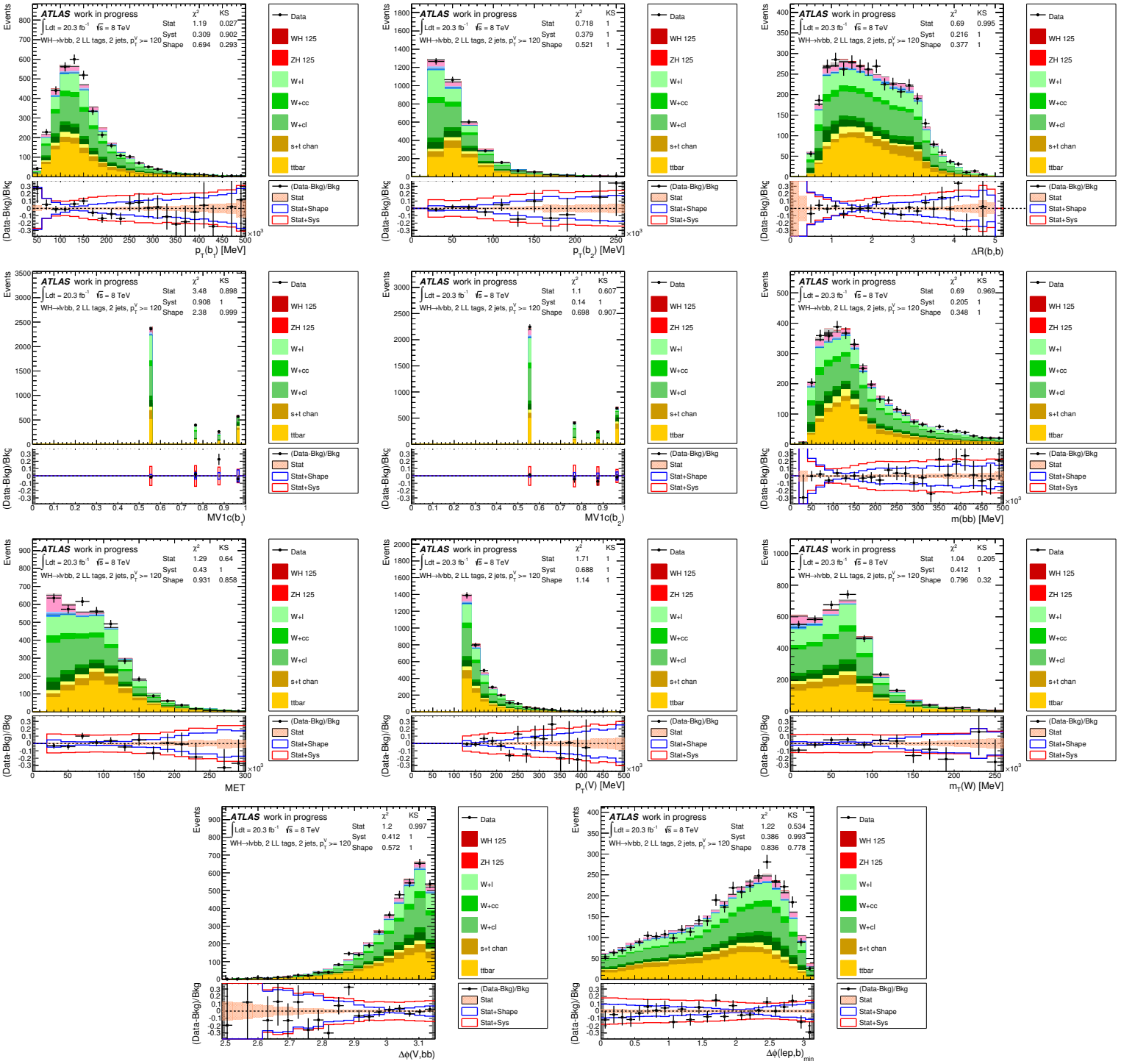

Figure 321: Distributions of MVA training variables used in 1-lepton events for $p_{\mathrm{T}}^{W} > 120$ GeV with 2 LL b-tags and 2 jets. From left to right: Row 1 - leading then sub-leading jet p_{T} and ΔR of the same two jets. Row 2 - pseudo-continuous MV1c distributions for leading then sub-leading jet and the m_{jj} of the same two jets. Row 3 - $E_{\mathrm{T}}^{\mathrm{miss}}$, p_{T}^{W}, and m_{T}^{W}. Row 4 - $\Delta\phi(V,H)$ and $\min|\Delta\phi(\ell, jet)|$. Section 6.1 details the definition of each variable.

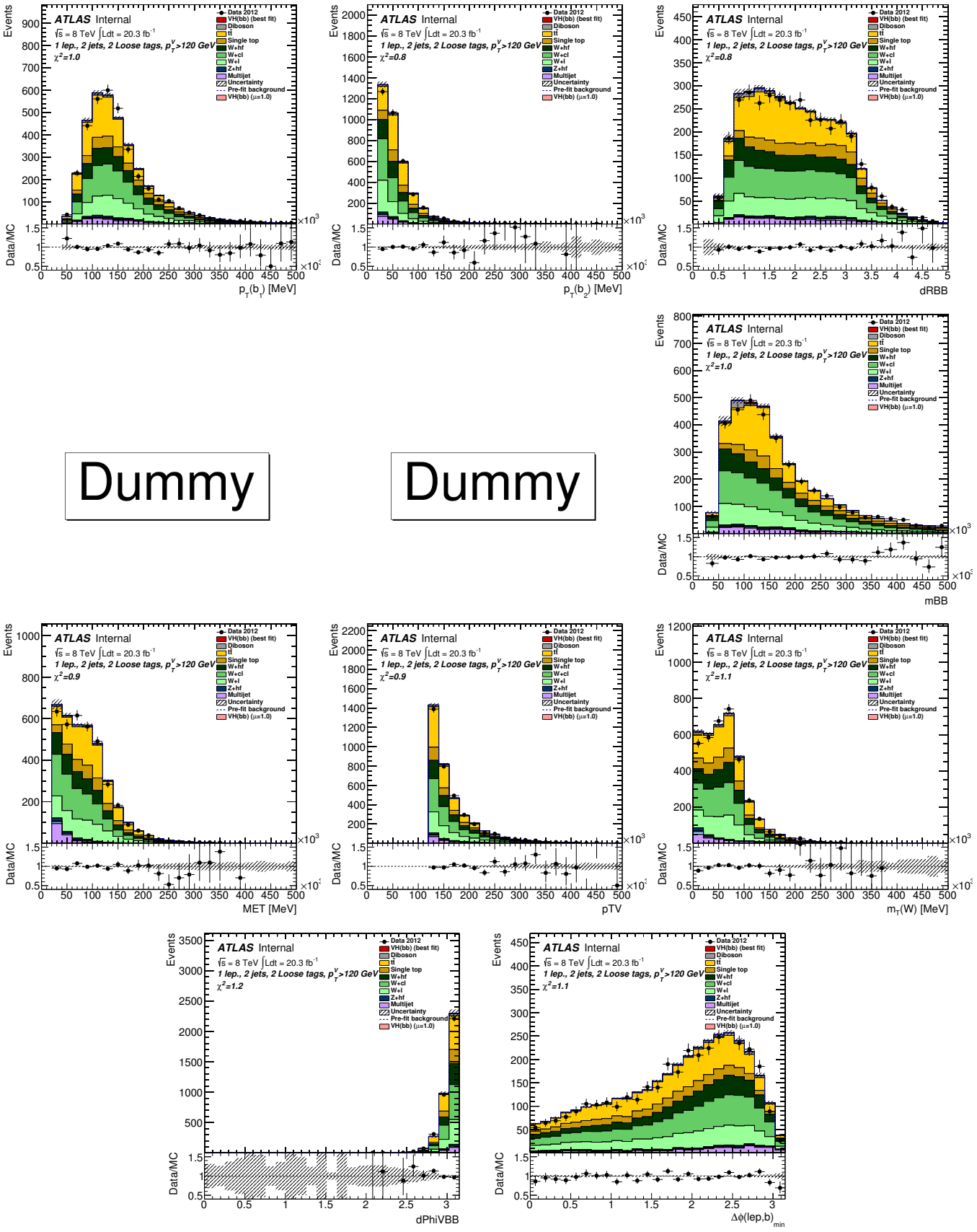

Figure 322: Distributions of MVA training variables used in 1-lepton events for $p_{\mathrm{T}}^{W} > 120$ GeV with 2 LL b-tags and 2 jets after the combined 0+1+2 lepton MVA fit. From left to right: Row 1 - leading then sub-leading jet p_{T} and ΔR of the same two jets. Row 2 - pseudo-continuous MV1c distributions for leading then sub-leading jet and the m_{jj} of the same two jets. Row 3 - $E_{\mathrm{T}}^{\mathrm{miss}}$, p_{T}^{W}, and m_{T}^{W}. Row 4 - $\Delta\phi(V,H)$ and $\min|\Delta\phi(\ell, jet)|$. Section 6.1 details the definition of each variable.

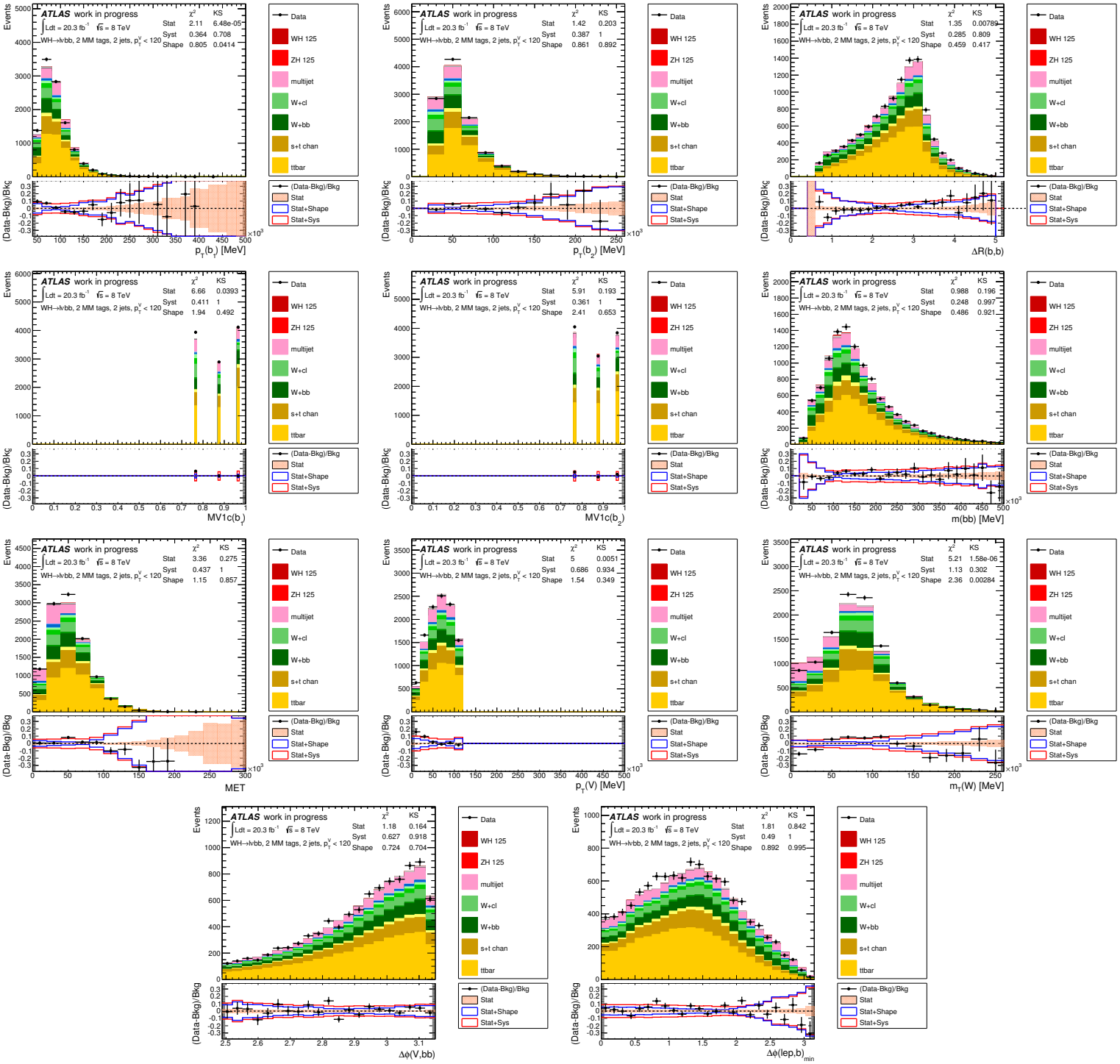

Figure 323: Distributions of MVA training variables used in 1-lepton events for $p_{\mathrm{T}}^{W} < 120$ GeV with 2 MM b-tags and 2 jets. From left to right: Row 1 - leading then sub-leading jet p_{T} and ΔR of the same two jets. Row 2 - pseudo-continuous MV1c distributions for leading then sub-leading jet and the m_{jj} of the same two jets. Row 3 - $E_{\mathrm{T}}^{\mathrm{miss}}$, p_{T}^{W}, and m_{T}^{W}. Row 4 - $\Delta\phi(V,H)$ and min$|\Delta\phi(\ell, jet)|$. Section 6.1 details the definition of each variable.

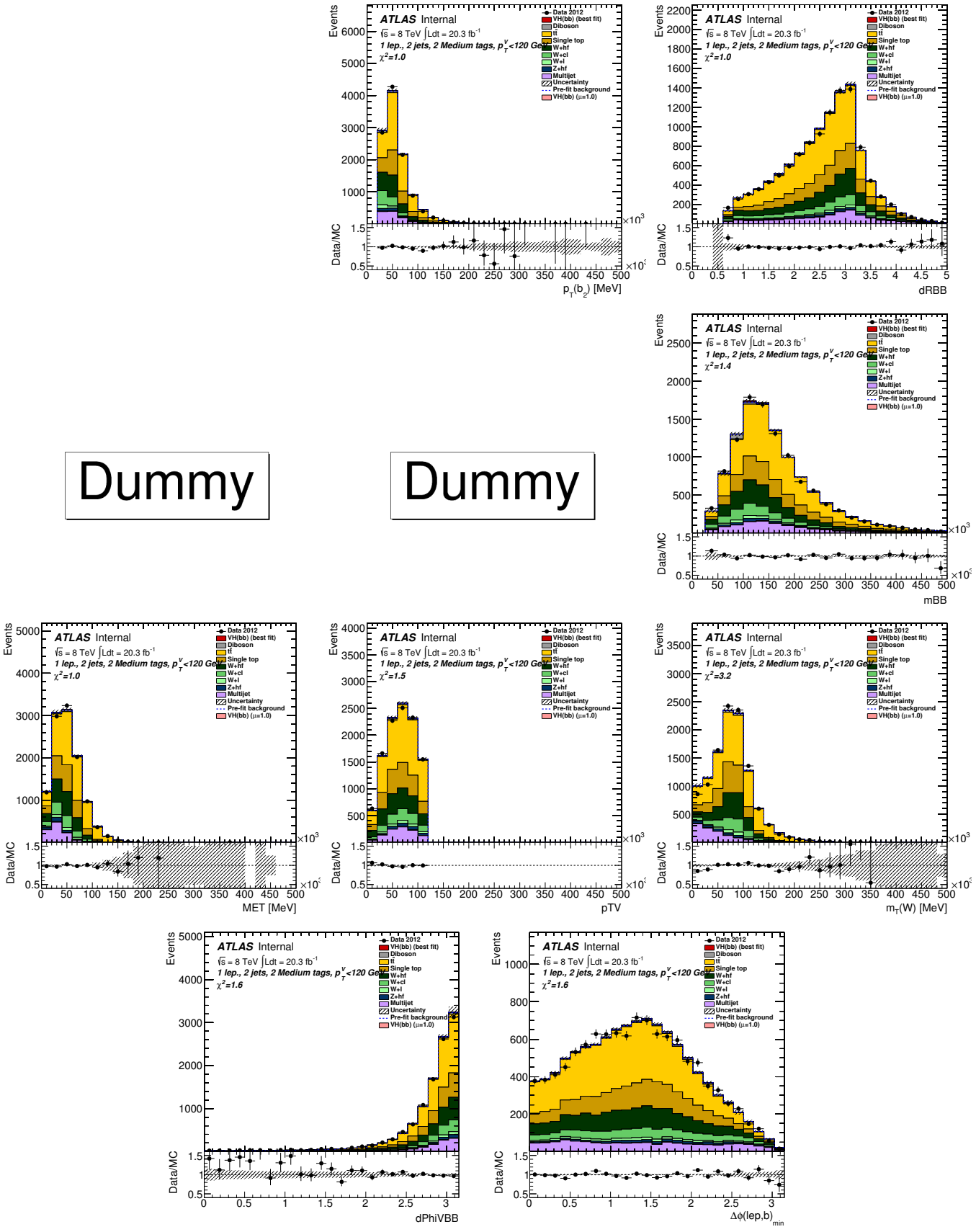

Figure 324: Distributions of MVA training variables used in 1-lepton events for $p_{\mathrm{T}}^{W} < 120$ GeV with 2 MM b-tags and 2 jets after the combined 0+1+2 lepton MVA fit. From left to right: Row 1 - leading then sub-leading jet p_{T} and ΔR of the same two jets. Row 2 - pseudo-continuous MV1c distributions for leading then sub-leading jet and the m_{jj} of the same two jets. Row 3 - $E_{\mathrm{T}}^{\mathrm{miss}}$, p_{T}^{W}, and m_{T}^{W}. Row 4 - $\Delta\phi(V,H)$ and $\min|\Delta\phi(\ell, jet)|$. Section 6.1 details the definition of each variable.

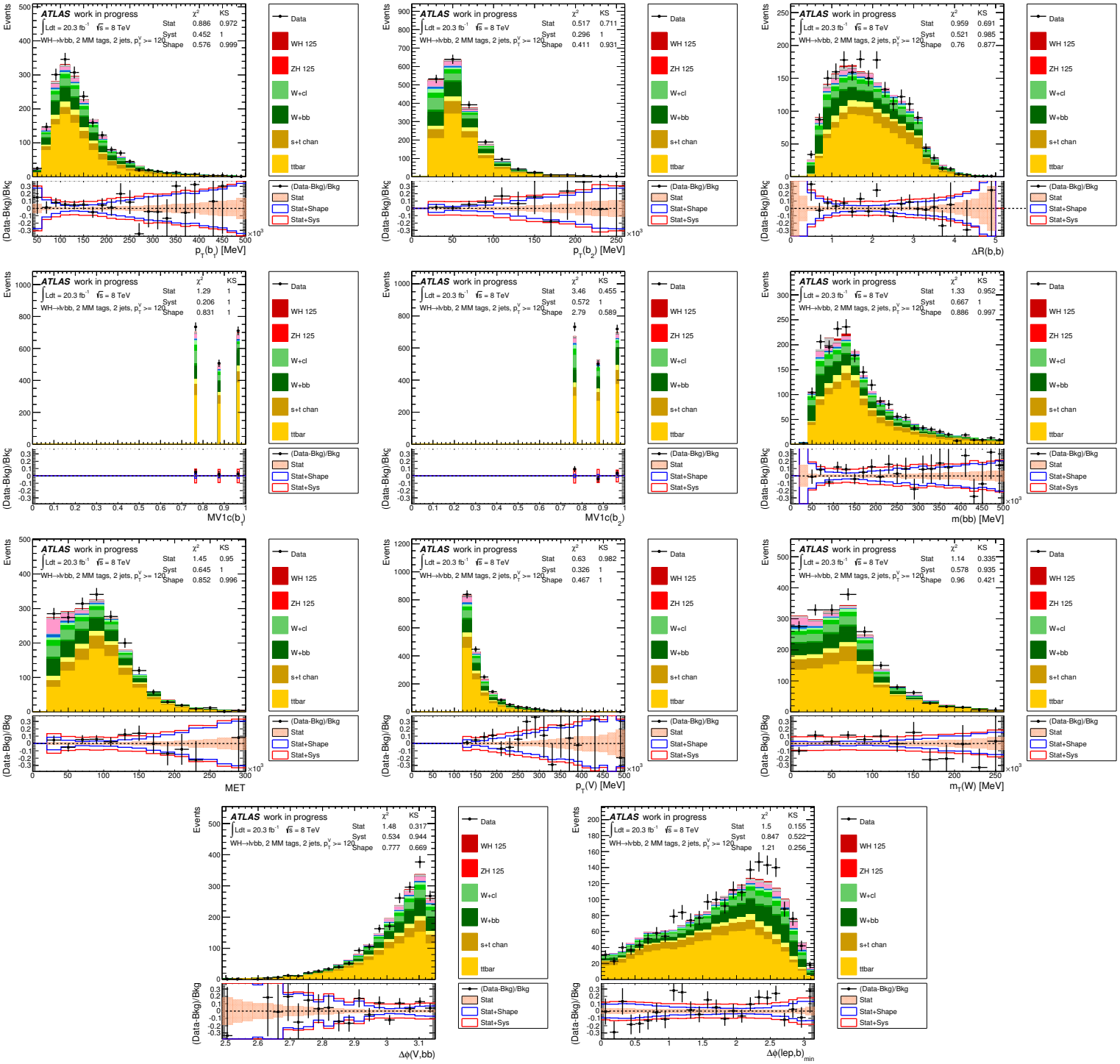

Figure 325: Distributions of MVA training variables used in 1-lepton events for $p_{\mathrm{T}}^{W} > 120$ GeV with 2 MM b-tags and 2 jets. From left to right: Row 1 - leading then sub-leading jet p_{T} and ΔR of the same two jets. Row 2 - pseudo-continuous MV1c distributions for leading then sub-leading jet and the m_{jj} of the same two jets. Row 3 - $E_{\mathrm{T}}^{\mathrm{miss}}$, p_{T}^{W}, and m_{T}^{W}. Row 4 - $\Delta\phi(V,H)$ and min$|\Delta\phi(\ell, jet)|$. Section 6.1 details the definition of each variable.

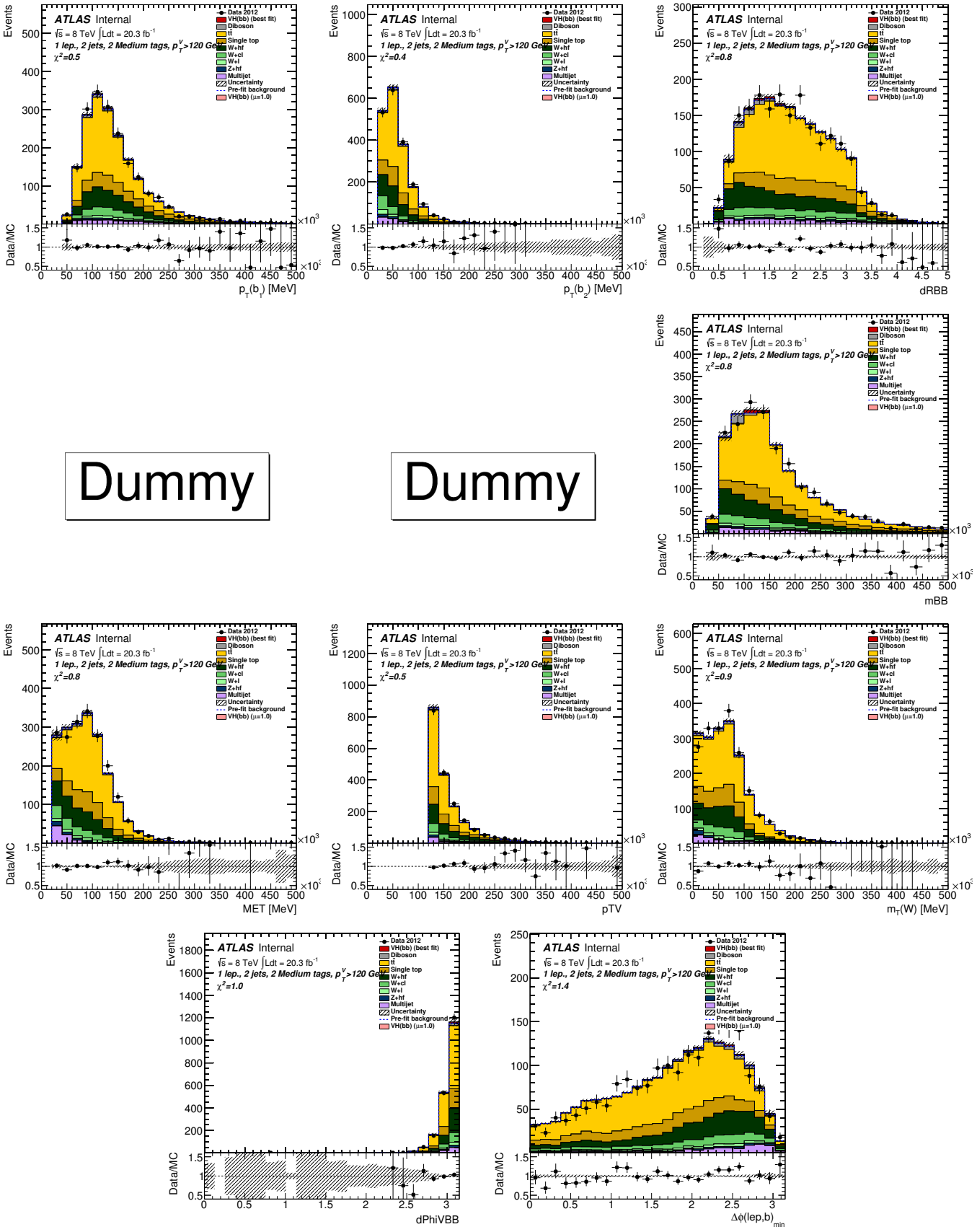

Figure 326: Distributions of MVA training variables used in 1-lepton events for $p_{\mathrm{T}}^{W} > 120$ GeV with 2 MM b-tags and 2 jets after the combined 0+1+2 lepton MVA fit. From left to right: Row 1 - leading then sub-leading jet p_{T} and ΔR of the same two jets. Row 2 - pseudo-continuous MV1c distributions for leading then sub-leading jet and the m_{jj} of the same two jets. Row 3 - $E_{\mathrm{T}}^{\mathrm{miss}}$, p_{T}^{W}, and m_{T}^{W}. Row 4 - $\Delta\phi(V,H)$ and $\min|\Delta\phi(\ell, jet)|$. Section 6.1 details the definition of each variable.

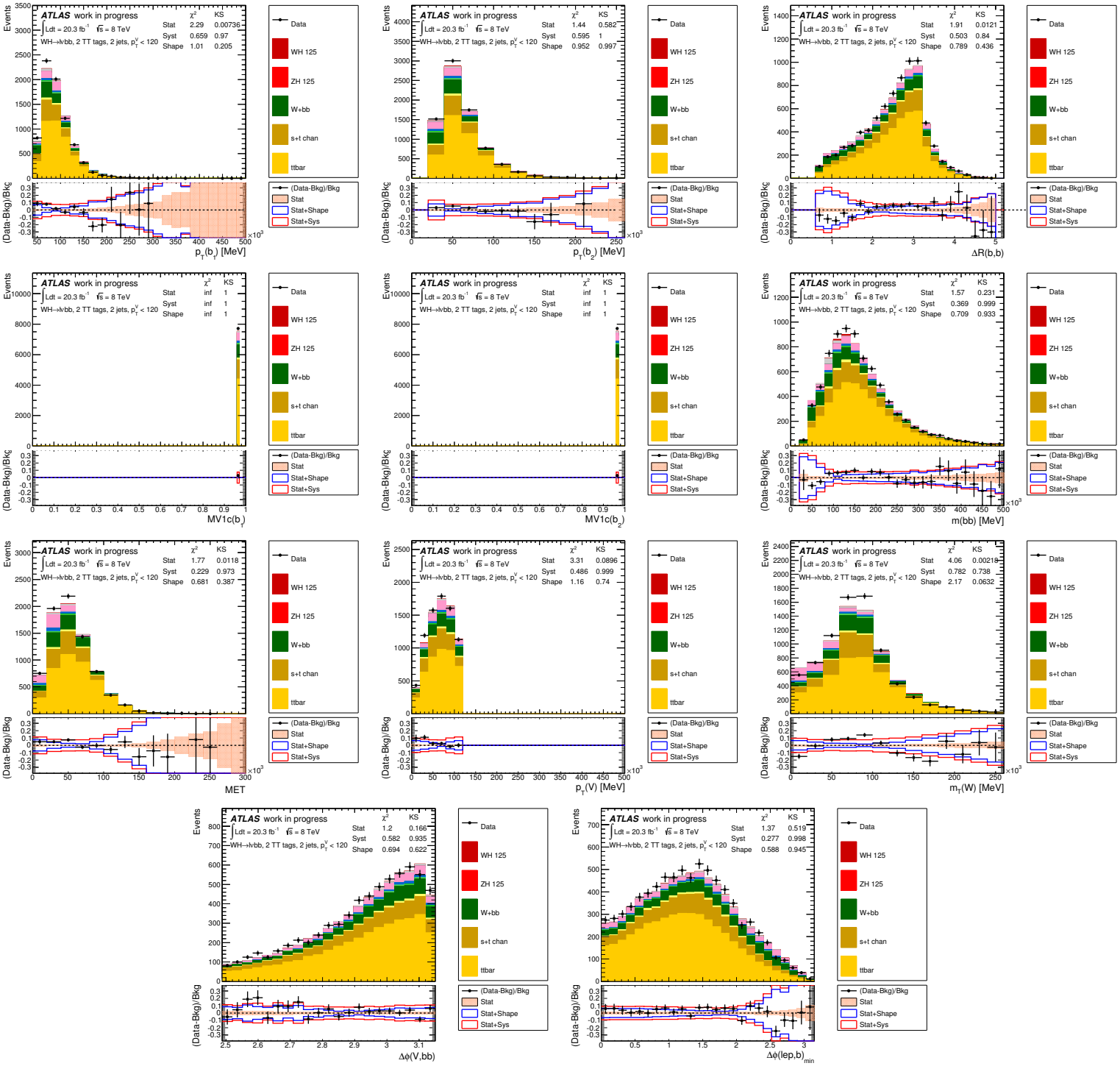

Figure 327: Distributions of MVA training variables used in 1-lepton events for $p_{\mathrm{T}}^{W} < 120$ GeV with 2 TT b-tags and 2 jets. From left to right: Row 1 - leading then sub-leading jet p_{T} and ΔR of the same two jets. Row 2 - pseudo-continuous MV1c distributions for leading then sub-leading jet and the m_{jj} of the same two jets. Row 3 - $E_{\mathrm{T}}^{\mathrm{miss}}$, p_{T}^{W}, and m_{T}^{W}. Row 4 - $\Delta\phi(V,H)$ and $\min|\Delta\phi(\ell, jet)|$. Section 6.1 details the definition of each variable.

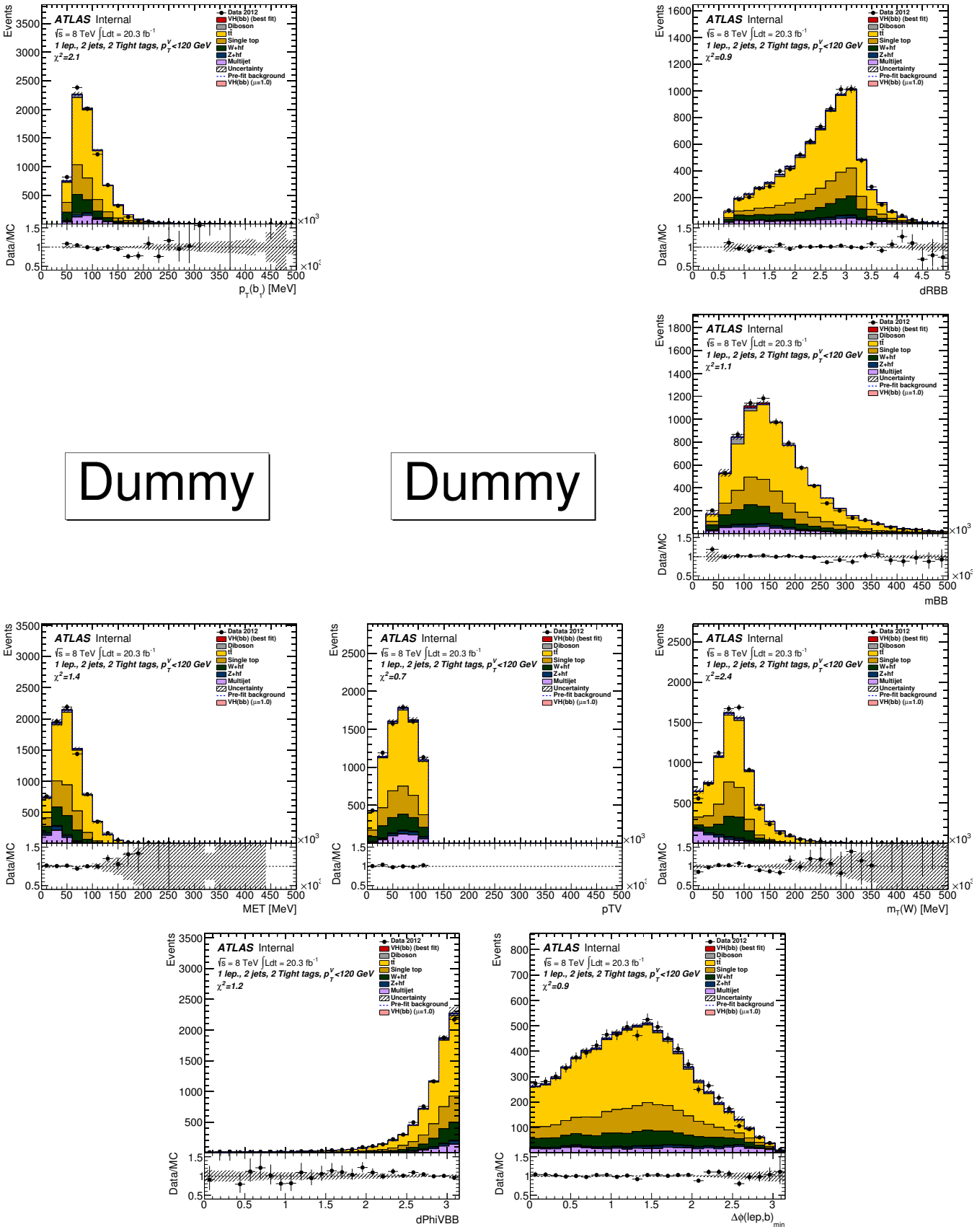

Figure 328: Distributions of MVA training variables used in 1-lepton events for $p_{\mathrm{T}}^{W} < 120$ GeV with 2 TT b-tags and 2 jets after the combined 0+1+2 lepton MVA fit. From left to right: Row 1 - leading then sub-leading jet p_{T} and ΔR of the same two jets. Row 2 - pseudo-continuous MV1c distributions for leading then sub-leading jet and the m_{jj} of the same two jets. Row 3 - $E_{\mathrm{T}}^{\mathrm{miss}}$, p_{T}^{W}, and m_{T}^{W}. Row 4 - $\Delta\phi(V,H)$ and min$|\Delta\phi(\ell, jet)|$. Section 6.1 details the definition of each variable.

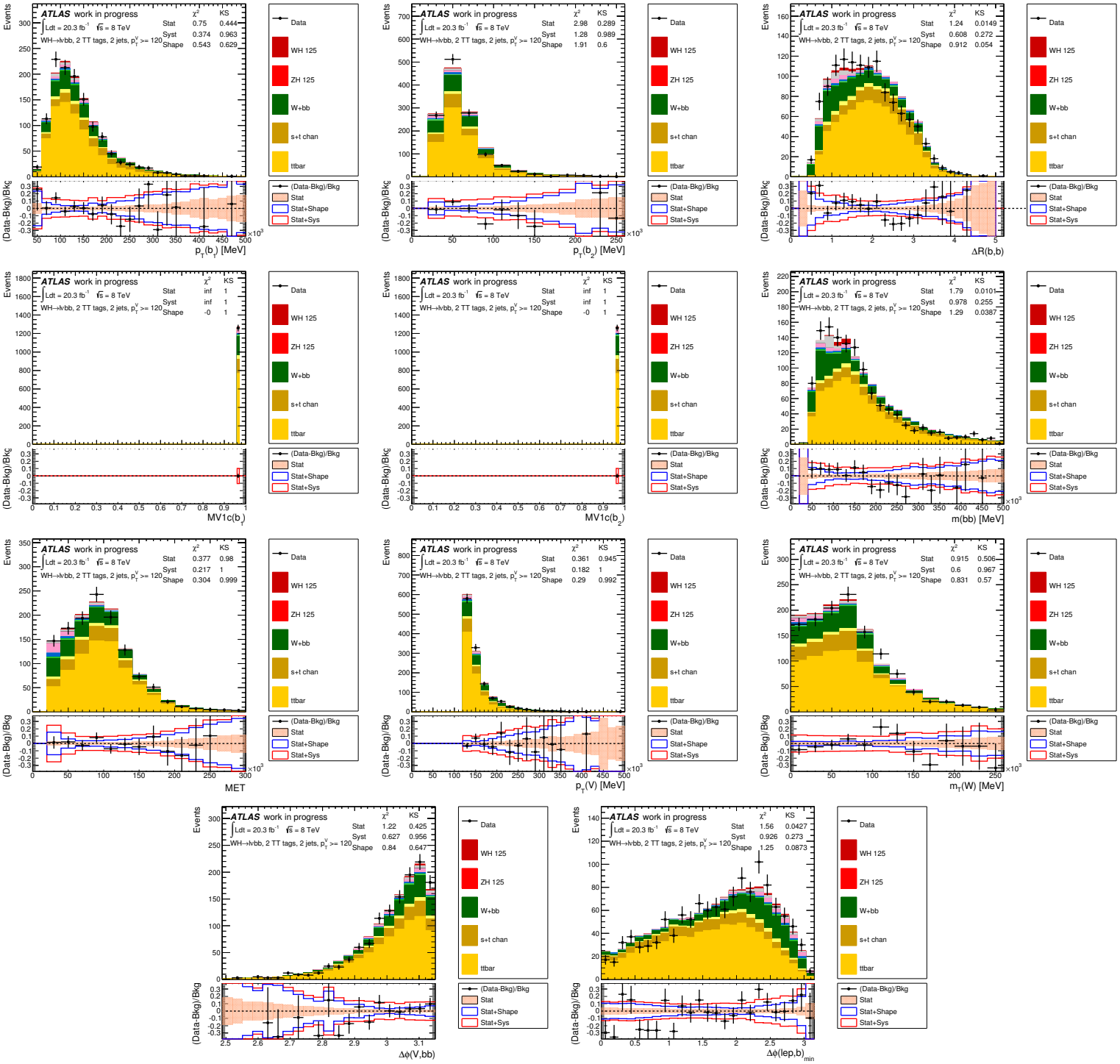

Figure 329: Distributions of MVA training variables used in 1-lepton events for $p_{\mathrm{T}}^{W} > 120$ GeV with 2 TT b-tags and 2 jets. From left to right: Row 1 - leading then sub-leading jet p_{T} and ΔR of the same two jets. Row 2 - pseudo-continuous MV1c distributions for leading then sub-leading jet and the m_{jj} of the same two jets. Row 3 - $E_{\mathrm{T}}^{\mathrm{miss}}$, p_{T}^{W}, and m_{T}^{W}. Row 4 - $\Delta\phi(V,H)$ and min$|\Delta\phi(\ell, jet)|$. Section 6.1 details the definition of each variable.

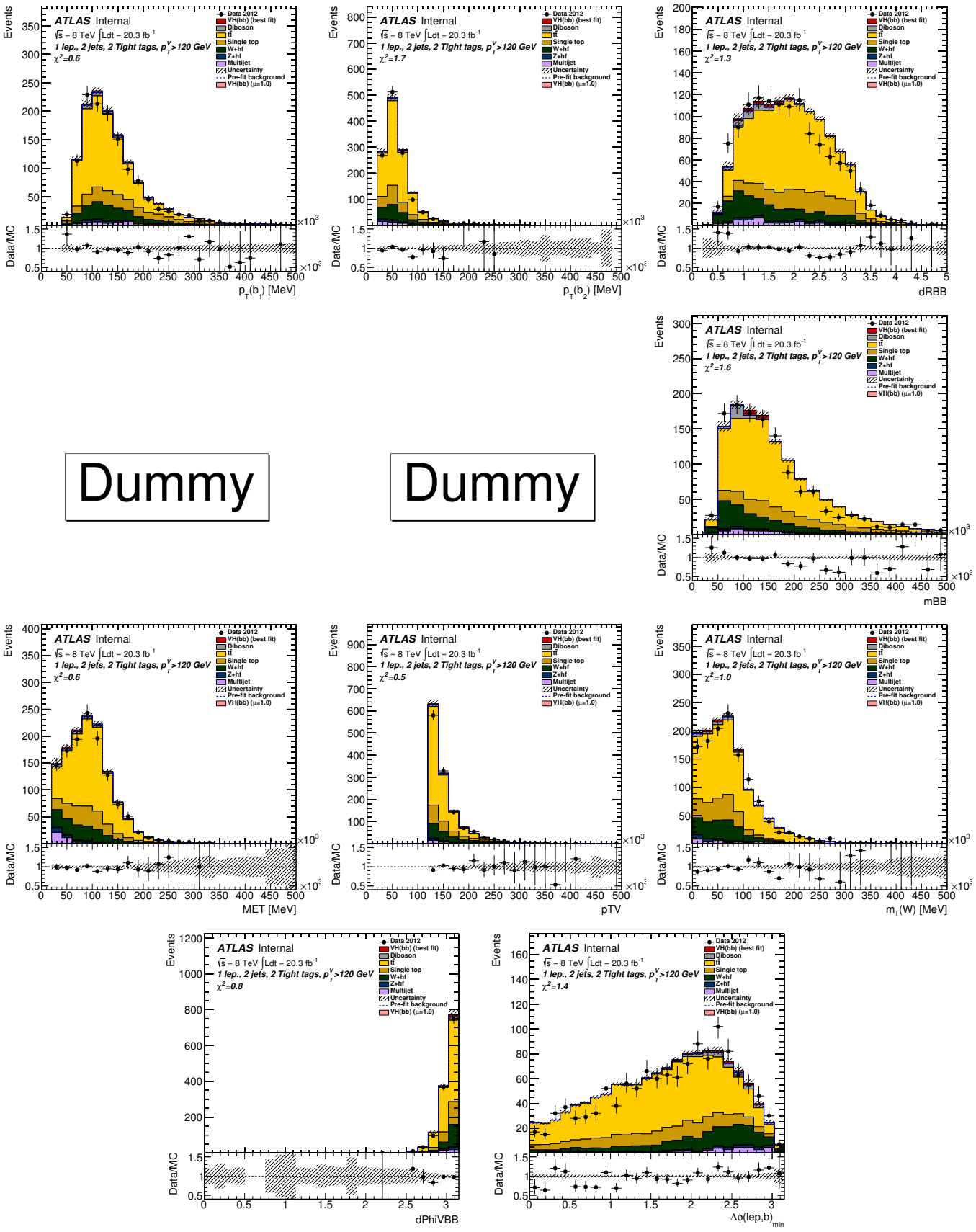

Figure 330: Distributions of MVA training variables used in 1-lepton events for $p_{\mathrm{T}}^{W} > 120$ GeV with 2 TT b-tags and 2 jets after the combined 0+1+2 lepton MVA fit. From left to right: Row 1 - leading then sub-leading jet p_{T} and ΔR of the same two jets. Row 2 - pseudo-continuous MV1c distributions for leading then sub-leading jet and the m_{jj} of the same two jets. Row 3 - $E_{\mathrm{T}}^{\mathrm{miss}}$, p_{T}^{W}, and m_{T}^{W}. Row 4 - $\Delta\phi(V,H)$ and $\min|\Delta\phi(\ell, jet)|$. Section 6.1 details the definition of each variable.

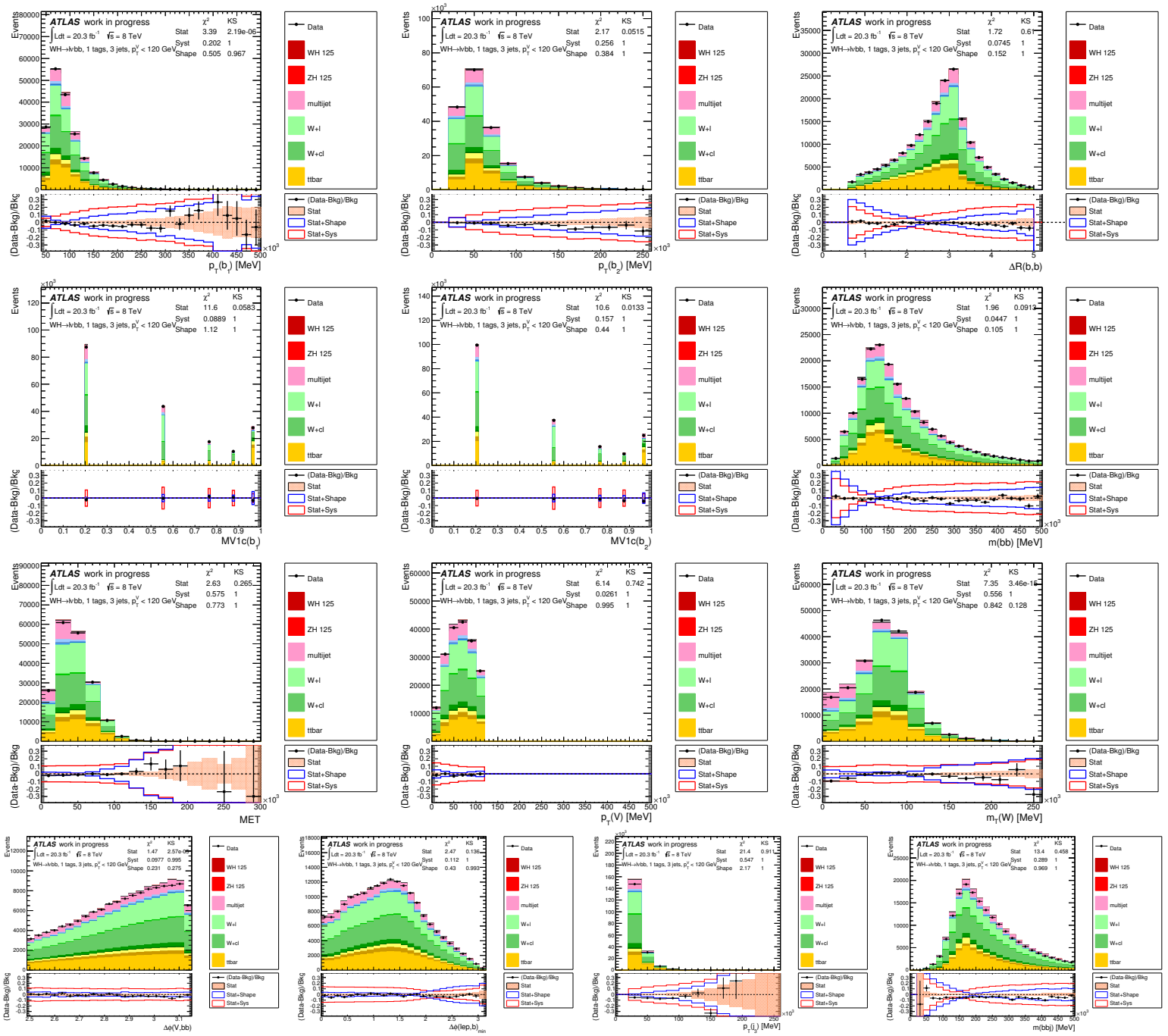

Figure 331: Distributions of MVA training variables used in 1-lepton events for $p_{\mathrm{T}}^{W} < 120$ GeV with 1 b-tag and 3 jets. From left to right: Row 1 - leading then sub-leading jet p_{T} and ΔR of the same two jets. Row 2 - pseudo-continuous MV1c distributions for leading then sub-leading jet and the m_{jj} of the same two jets. Row 3 - $E_{\mathrm{T}}^{\mathrm{miss}}$, p_{T}^{W}, and m_{T}^{W}. Row 4 - $\Delta\phi(V,H)$, $\min|\Delta\phi(\ell, jet)|$, the 3^{rd} jet p_{T}, and the tri-jet mass (m_{jjj}). Section 6.1 details the definition of each variable.

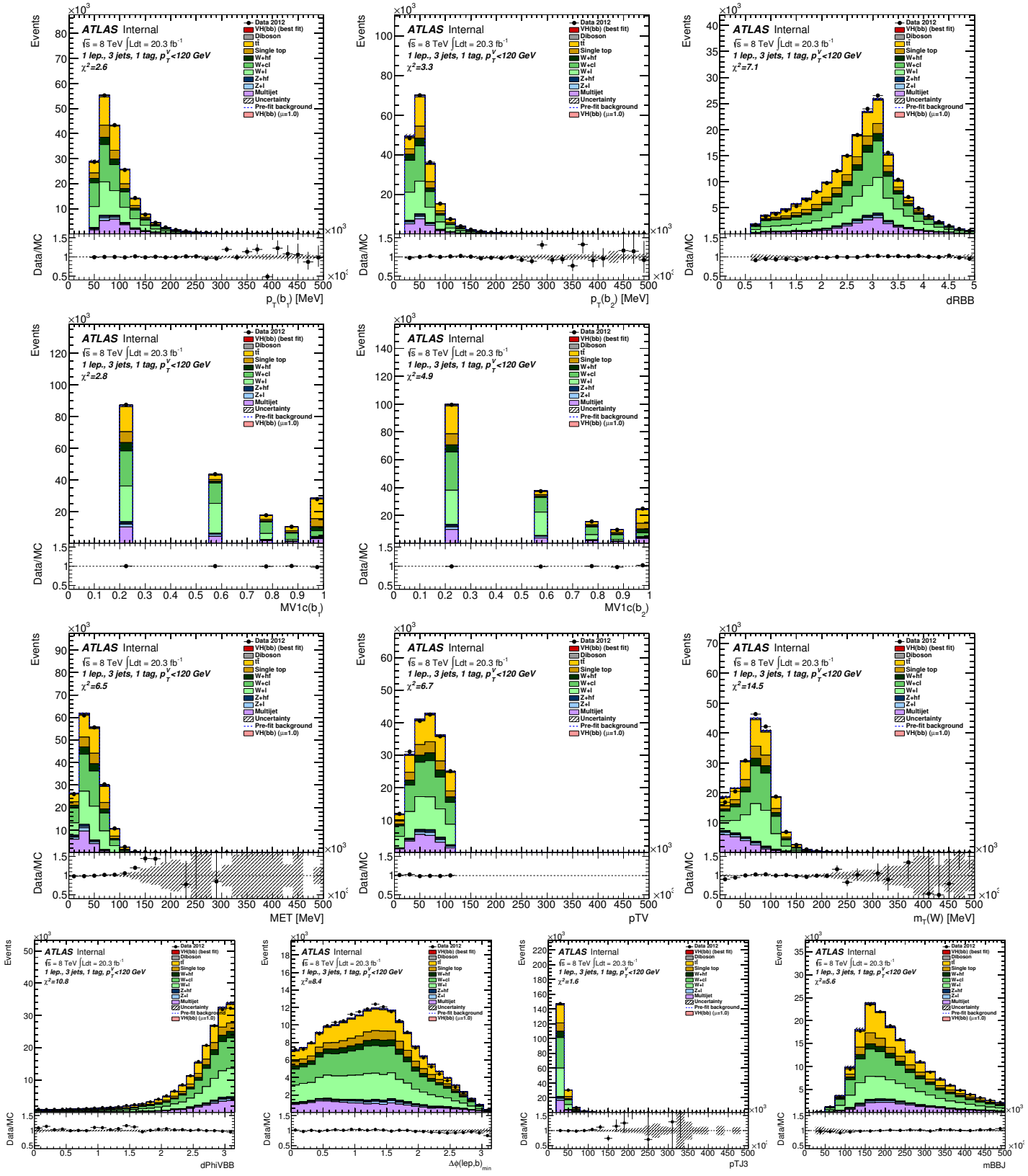

Figure 332: Distributions of MVA training variables used in 1-lepton events for $p_{\mathrm{T}}^{W} < 120$ GeV with 1 b-tag and 3 jets after the combined 0+1+2 lepton MVA fit. From left to right: Row 1 - leading then sub-leading jet p_{T} and ΔR of the same two jets. Row 2 - pseudo-continuous MV1c distributions for leading then sub-leading jet and the m_{jj} of the same two jets. Row 3 - $E_{\mathrm{T}}^{\mathrm{miss}}$, p_{T}^{W}, and m_{T}^{W}. Row 4 - $\Delta\phi(V,H)$, min$|\Delta\phi(\ell, jet)|$, the 3^{rd} jet p_{T}, and the tri-jet mass (m_{jjj}). Section 6.1 details the definition of each variable.

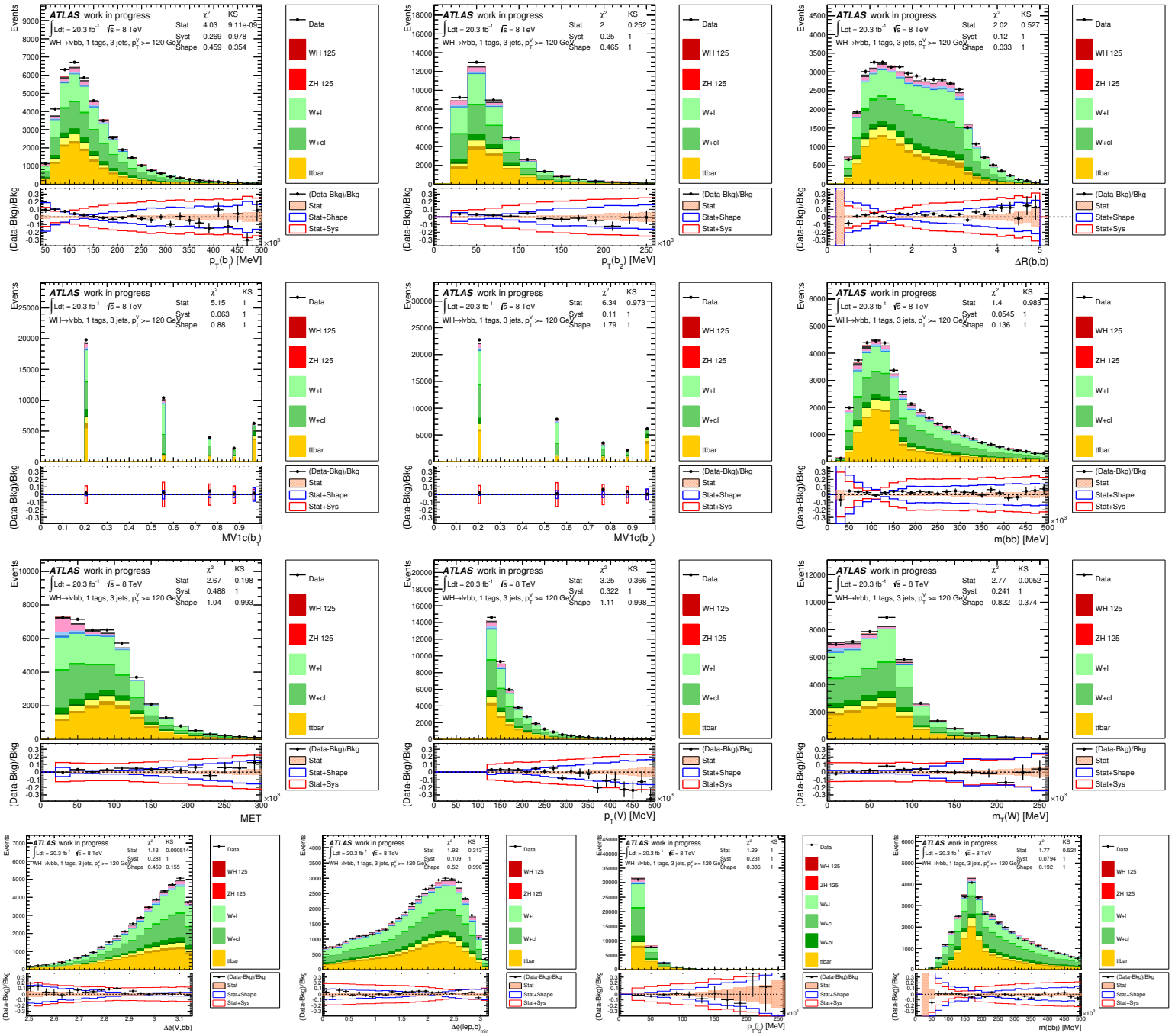

Figure 333: Distributions of MVA training variables used in 1-lepton events for $p_{\mathrm{T}}^{W} > 120$ GeV with 1 b-tag and 3 jets. From left to right: Row 1 - leading then sub-leading jet p_{T} and ΔR of the same two jets. Row 2 - pseudo-continuous MV1c distributions for leading then sub-leading jet and the m_{jj} of the same two jets. Row 3 - $E_{\mathrm{T}}^{\mathrm{miss}}$, p_{T}^{W}, and m_{T}^{W}. Row 4 - $\Delta\phi(V,H)$, $\min|\Delta\phi(\ell, jet)|$, the 3^{rd} jet p_{T}, and the tri-jet mass (m_{jjj}). Section 6.1 details the definition of each variable.

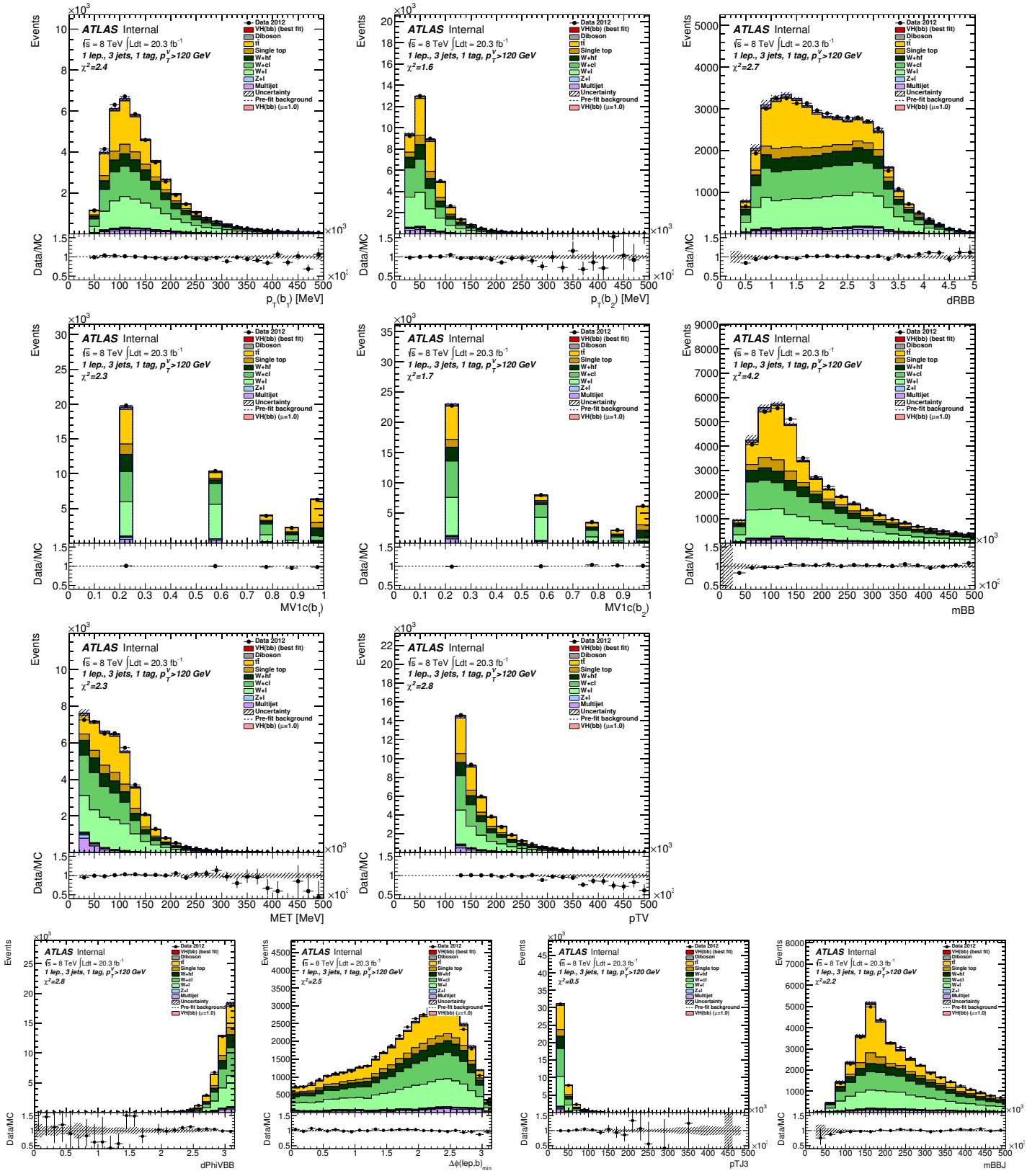

Figure 334: Distributions of MVA training variables used in 1-lepton events for $p_{\mathrm{T}}^{W} > 120$ GeV with 1 b-tag and 3 jets after the combined 0+1+2 lepton MVA fit. From left to right: Row 1 - leading then sub-leading jet p_{T} and ΔR of the same two jets. Row 2 - pseudo-continuous MV1c distributions for leading then sub-leading jet and the m_{jj} of the same two jets. Row 3 - $E_{\mathrm{T}}^{\mathrm{miss}}$, p_{T}^{W}, and m_{T}^{W}. Row 4 - $\Delta\phi(V,H)$, min$|\Delta\phi(\ell, jet)|$, the 3^{rd} jet p_{T}, and the tri-jet mass (m_{jjj}). Section 6.1 details the definition of each variable.

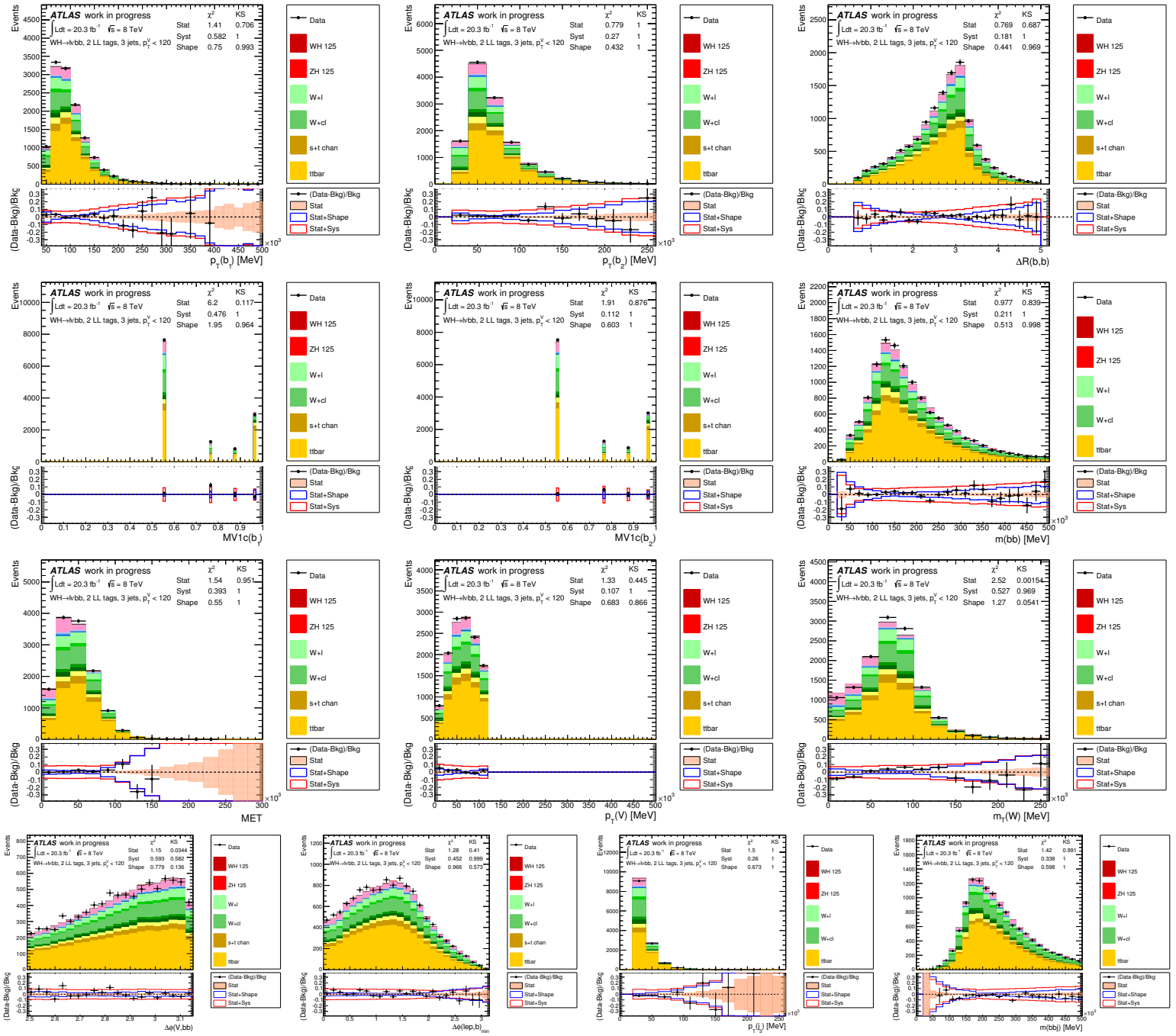

Figure 335: Distributions of MVA training variables used in 1-lepton events for $p_{\mathrm{T}}^{W} < 120$ GeV with 2 LL b-tags and 3 jets. From left to right: Row 1 - leading then sub-leading jet p_{T} and ΔR of the same two jets. Row 2 - pseudo-continuous MV1c distributions for leading then sub-leading jet and the m_{jj} of the same two jets. Row 3 - $E_{\mathrm{T}}^{\mathrm{miss}}$, p_{T}^{W}, and m_{T}^{W}. Row 4 - $\Delta\phi(V,H)$, $\min|\Delta\phi(\ell, jet)|$, the 3^{rd} jet p_{T}, and the tri-jet mass (m_{jjj}). Section 6.1 details the definition of each variable.

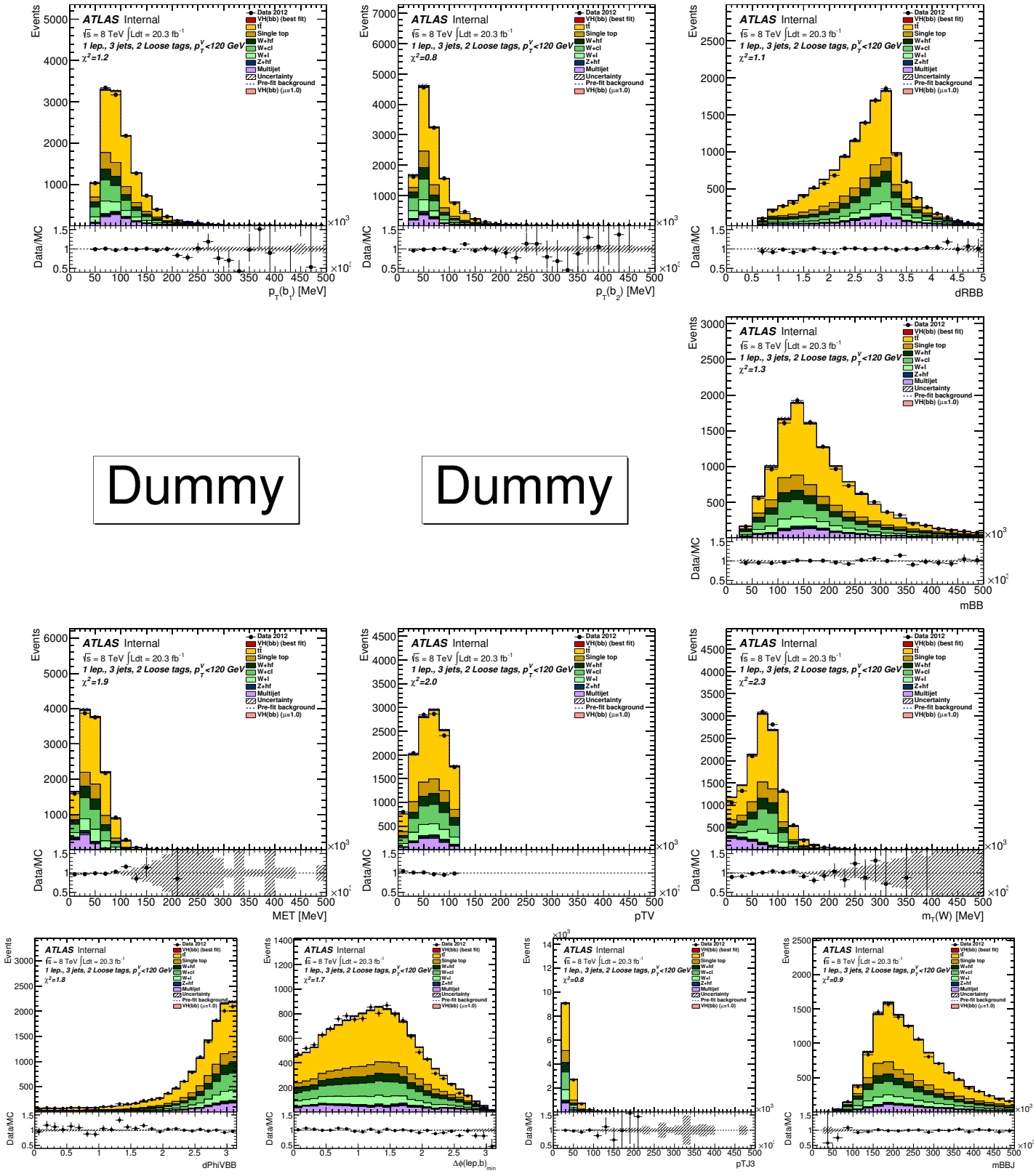

Figure 336: Distributions of MVA training variables used in 1-lepton events for $p_{\mathrm{T}}^{W} < 120$ GeV with 2 LL b-tags and 3 jets after the combined 0+1+2 lepton MVA fit. From left to right: Row 1 - leading then sub-leading jet p_{T} and ΔR of the same two jets. Row 2 - pseudo-continuous MV1c distributions for leading then sub-leading jet and the m_{jj} of the same two jets. Row 3 - $E_{\mathrm{T}}^{\mathrm{miss}}$, p_{T}^{W}, and m_{T}^{W}. Row 4 - $\Delta\phi(V,H)$, min$|\Delta\phi(\ell, jet)|$, the 3^{rd} jet p_{T}, and the tri-jet mass (m_{jjj}). Section 6.1 details the definition of each variable.

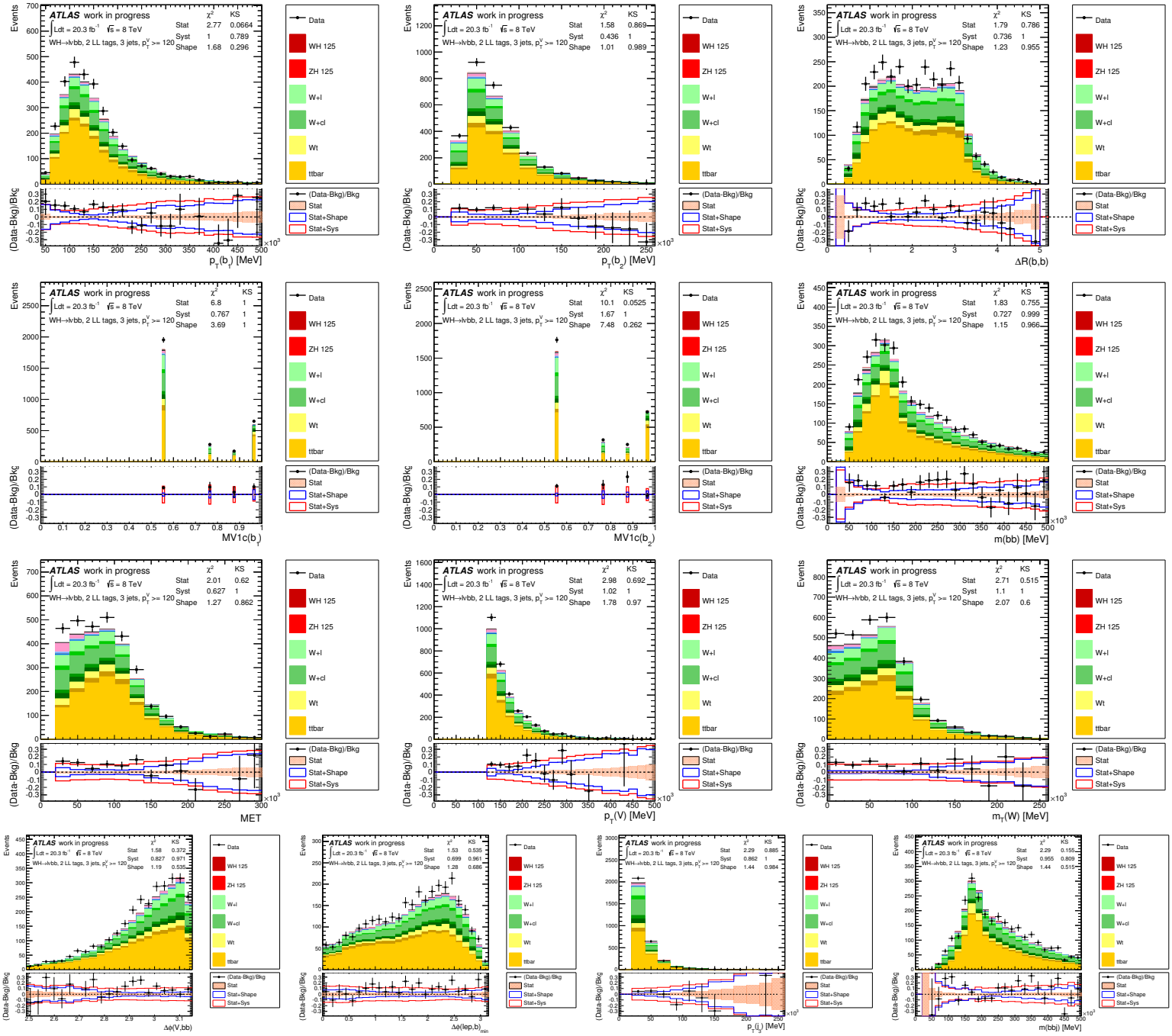

Figure 337: Distributions of MVA training variables used in 1-lepton events for $p_{\mathrm{T}}^{W} > 120$ GeV with 2 LL b-tags and 3 jets. From left to right: Row 1 - leading then sub-leading jet p_{T} and ΔR of the same two jets. Row 2 - pseudo-continuous MV1c distributions for leading then sub-leading jet and the m_{jj} of the same two jets. Row 3 - $E_{\mathrm{T}}^{\mathrm{miss}}$, p_{T}^{W}, and m_{T}^{W}. Row 4 - $\Delta\phi(V,H)$, $\min|\Delta\phi(\ell, jet)|$, the 3^{rd} jet p_{T}, and the tri-jet mass (m_{jjj}). Section 6.1 details the definition of each variable.

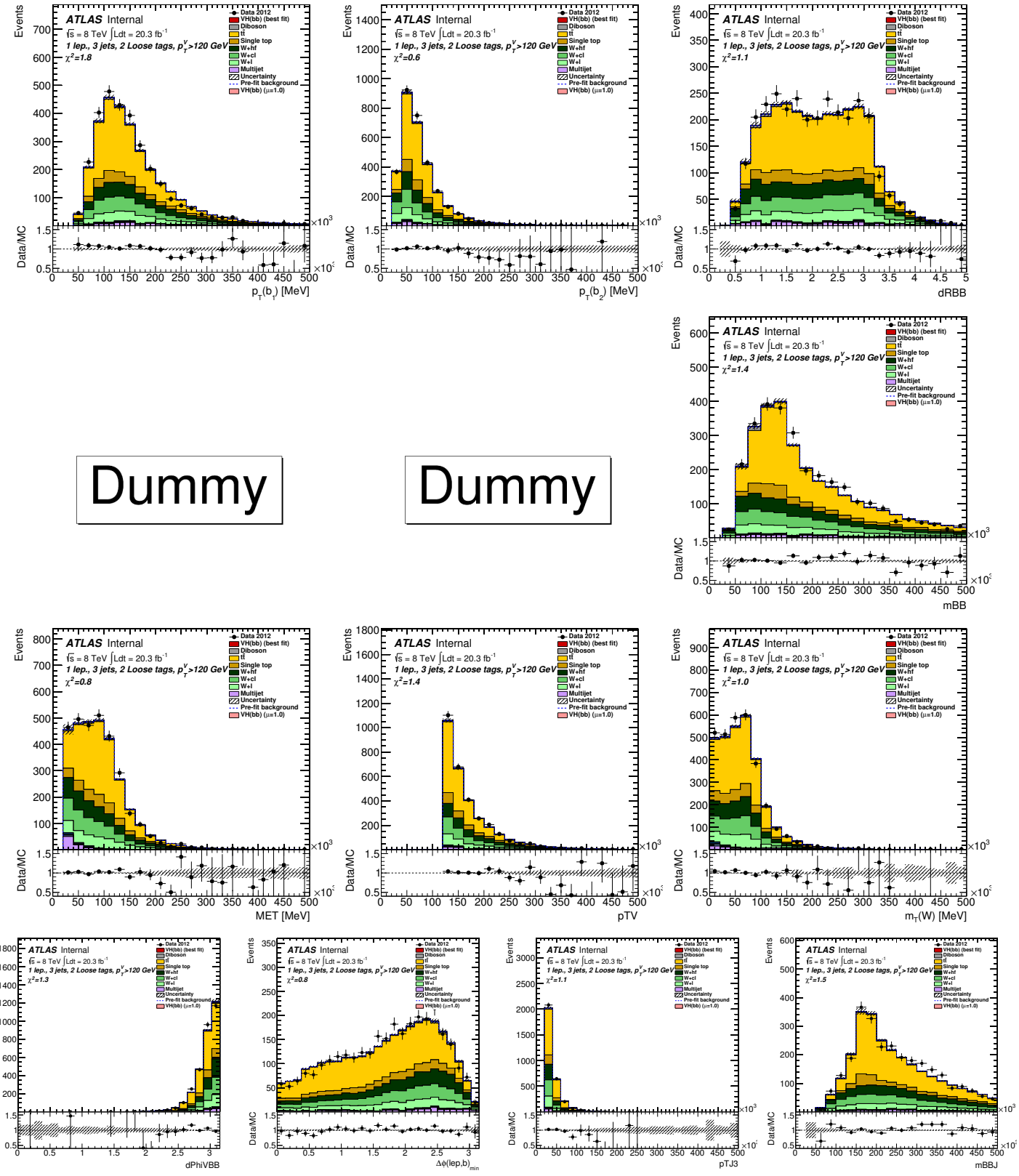

Figure 338: Distributions of MVA training variables used in 1-lepton events for $p_{\mathrm{T}}^{W} > 120$ GeV with 2 LL b-tags and 3 jets after the combined 0+1+2 lepton MVA fit. From left to right: Row 1 - leading then sub-leading jet p_{T} and ΔR of the same two jets. Row 2 - pseudo-continuous MV1c distributions for leading then sub-leading jet and the m_{jj} of the same two jets. Row 3 - $E_{\mathrm{T}}^{\mathrm{miss}}$, p_{T}^{W}, and m_{T}^{W}. Row 4 - $\Delta\phi(V,H)$, min$|\Delta\phi(\ell, jet)|$, the 3^{rd} jet p_{T}, and the tri-jet mass (m_{jjj}). Section 6.1 details the definition of each variable.

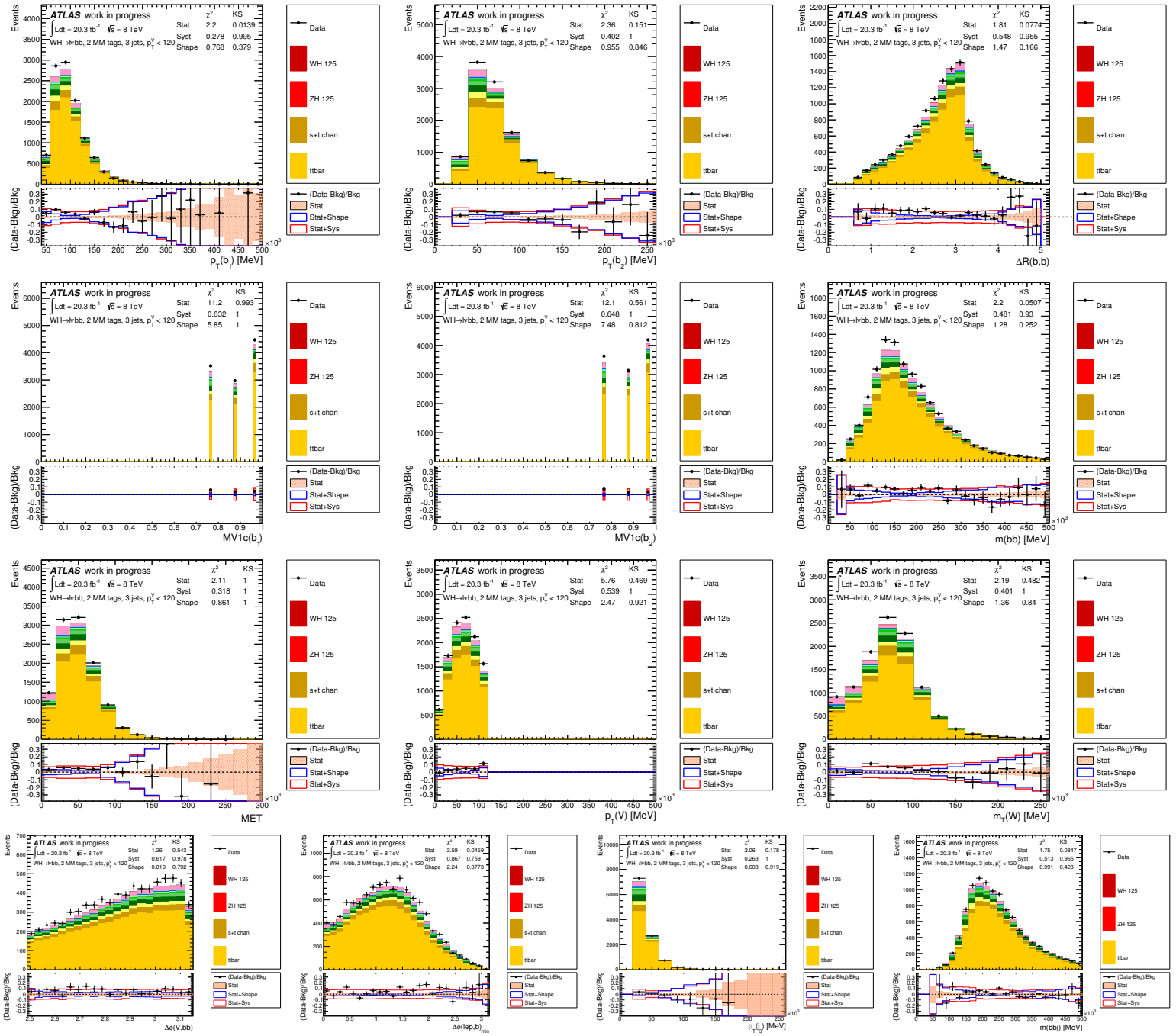

Figure 339: Distributions of MVA training variables used in 1-lepton events for $p_{\mathrm{T}}^{W} < 120$ GeV with 2 MM b-tags and 3 jets. From left to right: Row 1 - leading then sub-leading jet p_{T} and ΔR of the same two jets. Row 2 - pseudo-continuous MV1c distributions for leading then sub-leading jet and the m_{jj} of the same two jets. Row 3 - $E_{\mathrm{T}}^{\mathrm{miss}}$, p_{T}^{W}, and m_{T}^{W}. Row 4 - $\Delta\phi(V,H)$, min$|\Delta\phi(\ell, jet)|$, the 3^{rd} jet p_{T}, and the tri-jet mass (m_{jjj}). Section 6.1 details the definition of each variable.

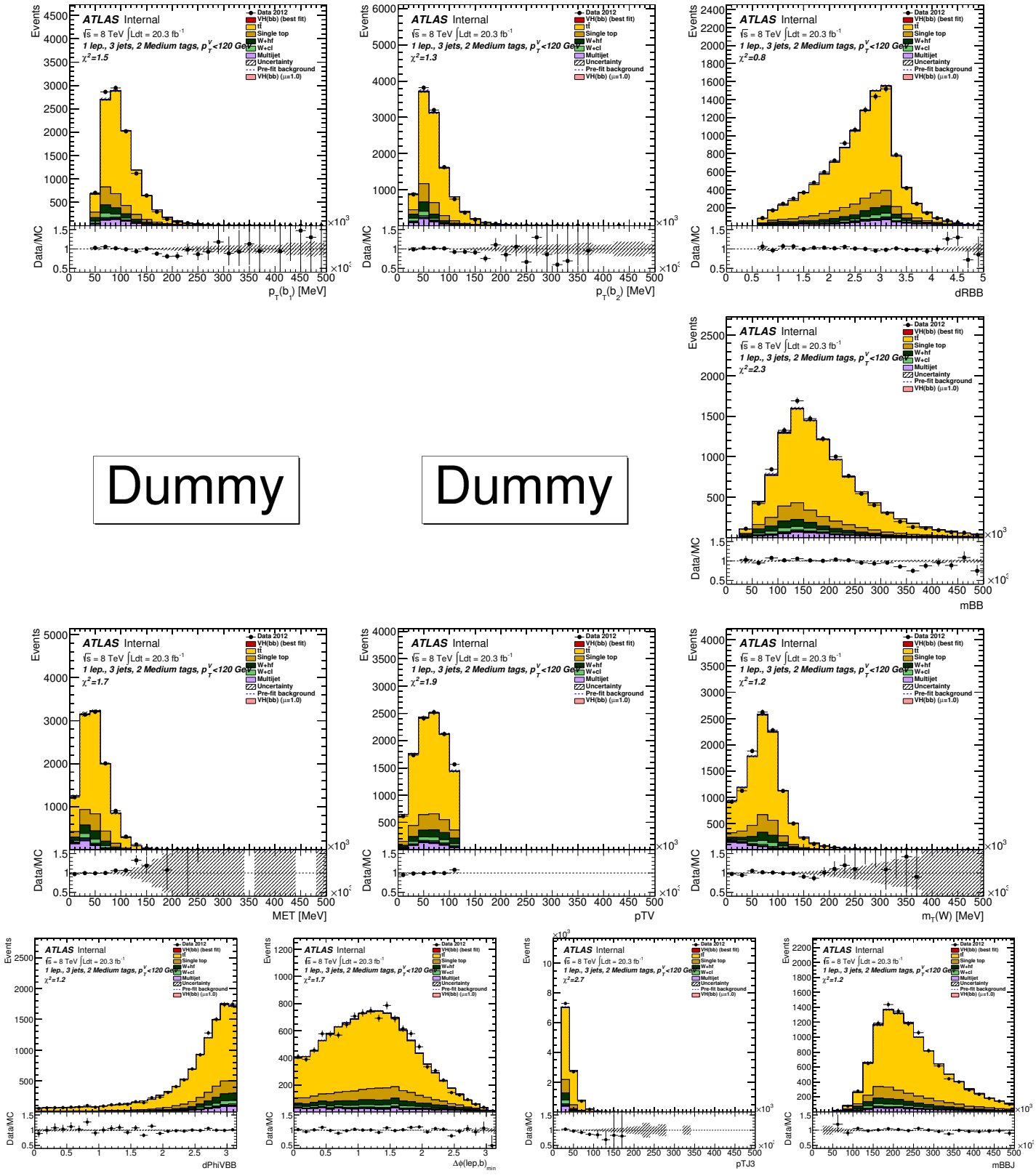

Figure 340: Distributions of MVA training variables used in 1-lepton events for $p_{\mathrm{T}}^{W} < 120$ GeV with 2 MM b-tags and 3 jets after the combined 0+1+2 lepton MVA fit. From left to right: Row 1 - leading then sub-leading jet p_{T} and ΔR of the same two jets. Row 2 - pseudo-continuous MV1c distributions for leading then sub-leading jet and the m_{jj} of the same two jets. Row 3 - $E_{\mathrm{T}}^{\mathrm{miss}}$, p_{T}^{W}, and m_{T}^{W}. Row 4 - $\Delta\phi(V,H)$, min$|\Delta\phi(\ell, jet)|$, the 3^{rd} jet p_{T}, and the tri-jet mass (m_{jjj}). Section 6.1 details the definition of each variable.

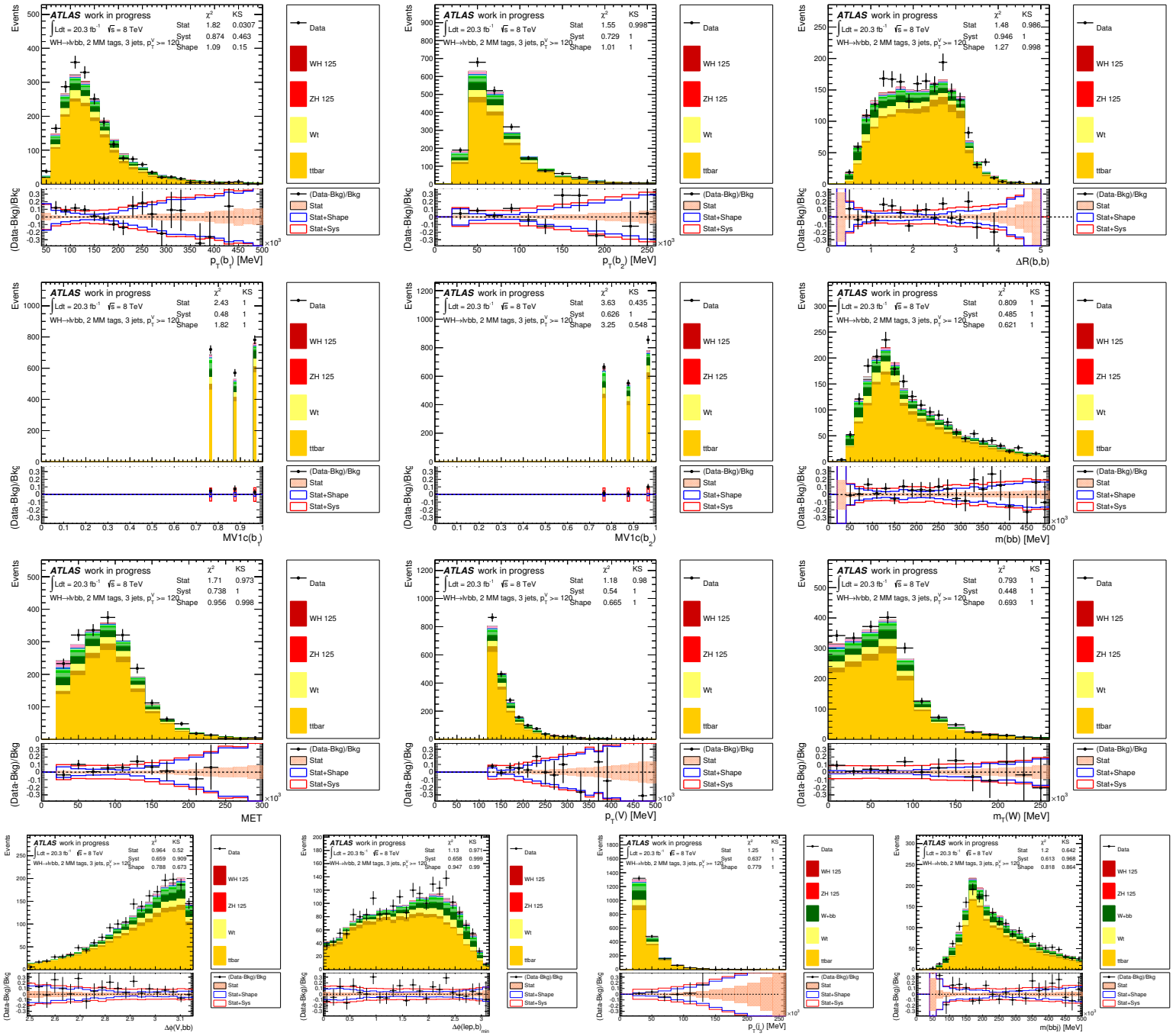

Figure 341: Distributions of MVA training variables used in 1-lepton events for $p_{\mathrm{T}}^{W} > 120$ GeV with 2 MM b-tags and 3 jets. From left to right: Row 1 - leading then sub-leading jet p_{T} and ΔR of the same two jets. Row 2 - pseudo-continuous MV1c distributions for leading then sub-leading jet and the m_{jj} of the same two jets. Row 3 - $E_{\mathrm{T}}^{\mathrm{miss}}$, p_{T}^{W}, and m_{T}^{W}. Row 4 - $\Delta\phi(V,H)$, $\min|\Delta\phi(\ell, jet)|$, the 3^{rd} jet p_{T}, and the tri-jet mass (m_{jjj}). Section 6.1 details the definition of each variable.

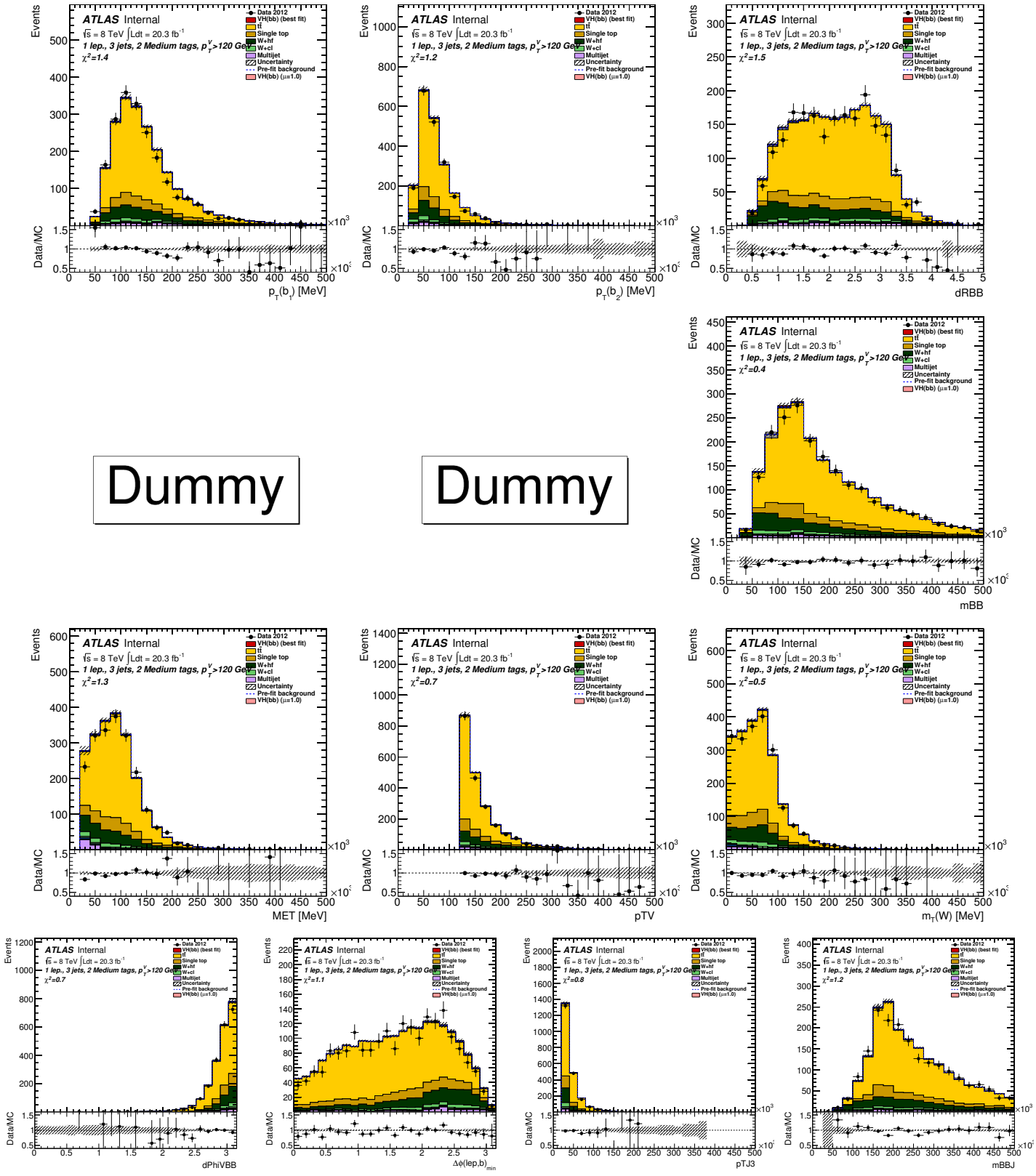

Figure 342: Distributions of MVA training variables used in 1-lepton events for $p_{\mathrm{T}}^{W} > 120$ GeV with 2 MM b-tags and 3 jets after the combined 0+1+2 lepton MVA fit. From left to right: Row 1 - leading then sub-leading jet p_{T} and ΔR of the same two jets. Row 2 - pseudo-continuous MV1c distributions for leading then sub-leading jet and the m_{jj} of the same two jets. Row 3 - $E_{\mathrm{T}}^{\mathrm{miss}}$, p_{T}^{W}, and m_{T}^{W}. Row 4 - $\Delta\phi(V,H)$, min$|\Delta\phi(\ell, jet)|$, the 3^{rd} jet p_{T}, and the tri-jet mass (m_{jjj}). Section 6.1 details the definition of each variable.

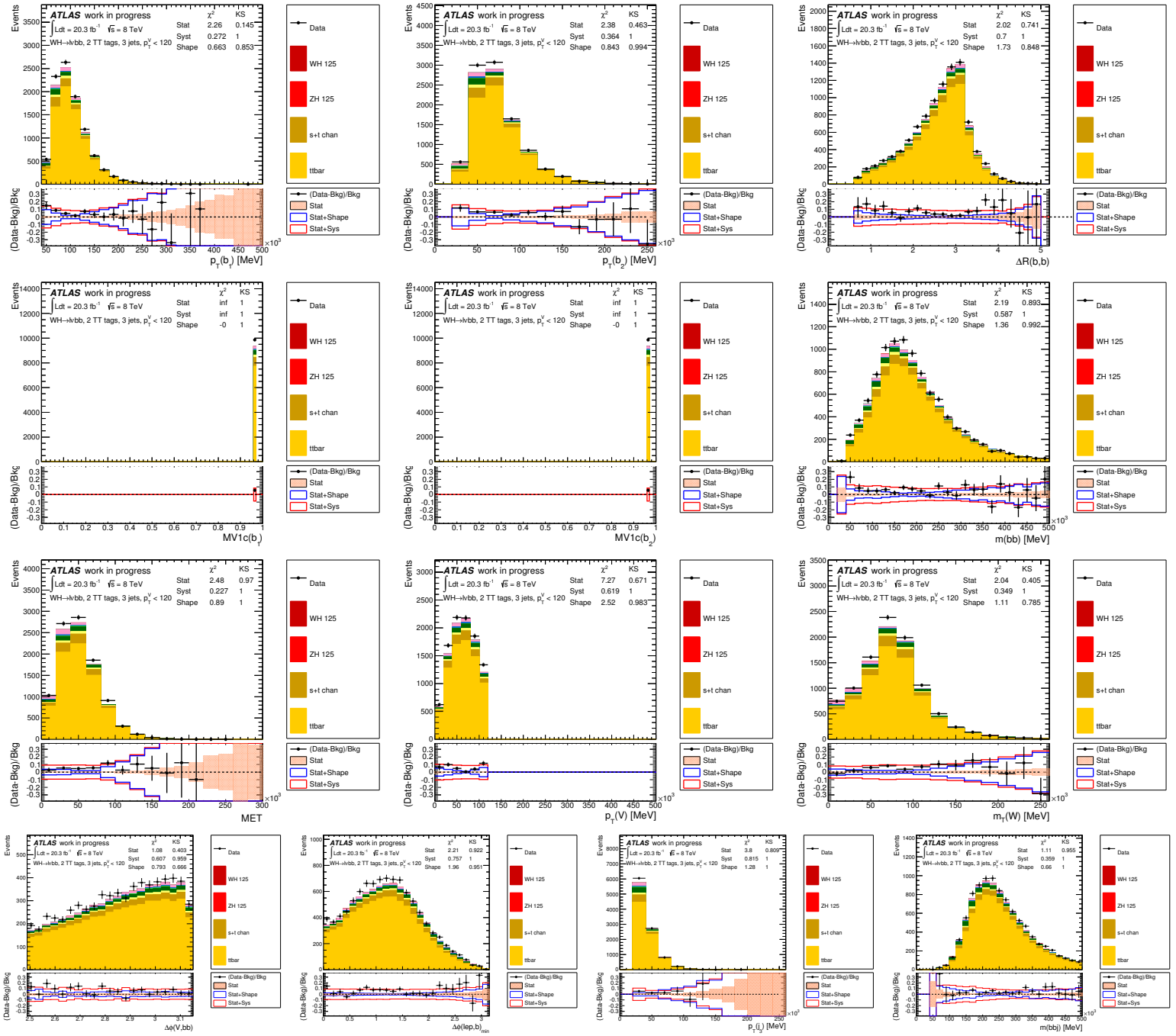

Figure 343: Distributions of MVA training variables used in 1-lepton events for $p_{\mathrm{T}}^{W} < 120$ GeV with 2 TT b-tags and 3 jets. From left to right: Row 1 - leading then sub-leading jet p_{T} and ΔR of the same two jets. Row 2 - pseudo-continuous MV1c distributions for leading then sub-leading jet and the m_{jj} of the same two jets. Row 3 - $E_{\mathrm{T}}^{\mathrm{miss}}$, p_{T}^{W}, and m_{T}^{W}. Row 4 - $\Delta\phi(V,H)$, min$|\Delta\phi(\ell, jet)|$, the 3^{rd} jet p_{T}, and the tri-jet mass (m_{jjj}). Section 6.1 details the definition of each variable.

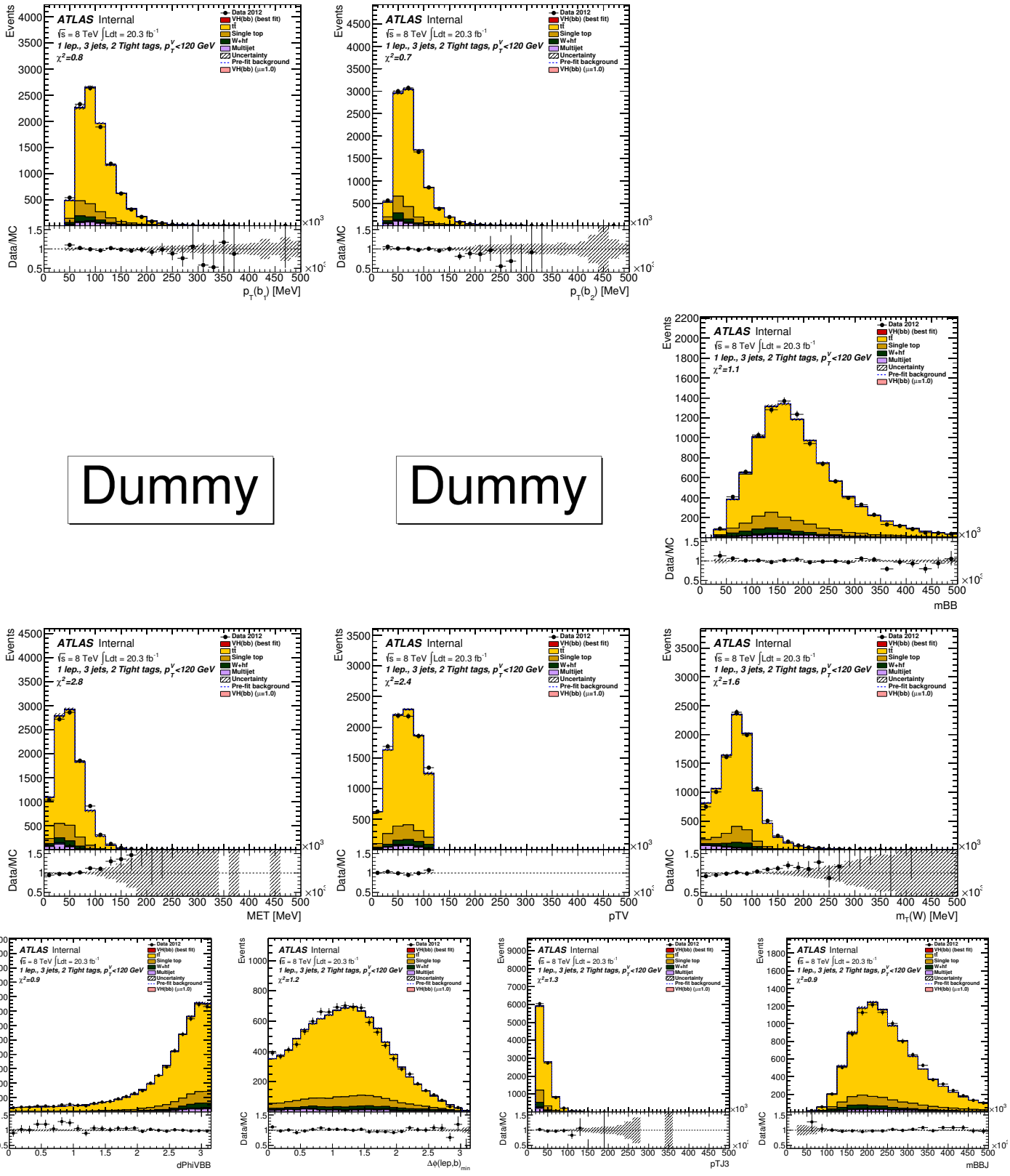

Figure 344: Distributions of MVA training variables used in 1-lepton events for $p_{\mathrm{T}}^{W} < 120$ GeV with 2 TT b-tags and 3 jets after the combined 0+1+2 lepton MVA fit. From left to right: Row 1 - leading then sub-leading jet p_{T} and ΔR of the same two jets. Row 2 - pseudo-continuous MV1c distributions for leading then sub-leading jet and the m_{jj} of the same two jets. Row 3 - $E_{\mathrm{T}}^{\mathrm{miss}}$, p_{T}^{W}, and m_{T}^{W}. Row 4 - $\Delta\phi(V,H)$, min$|\Delta\phi(\ell, jet)|$, the 3^{rd} jet p_{T}, and the tri-jet mass (m_{jjj}). Section 6.1 details the definition of each variable.

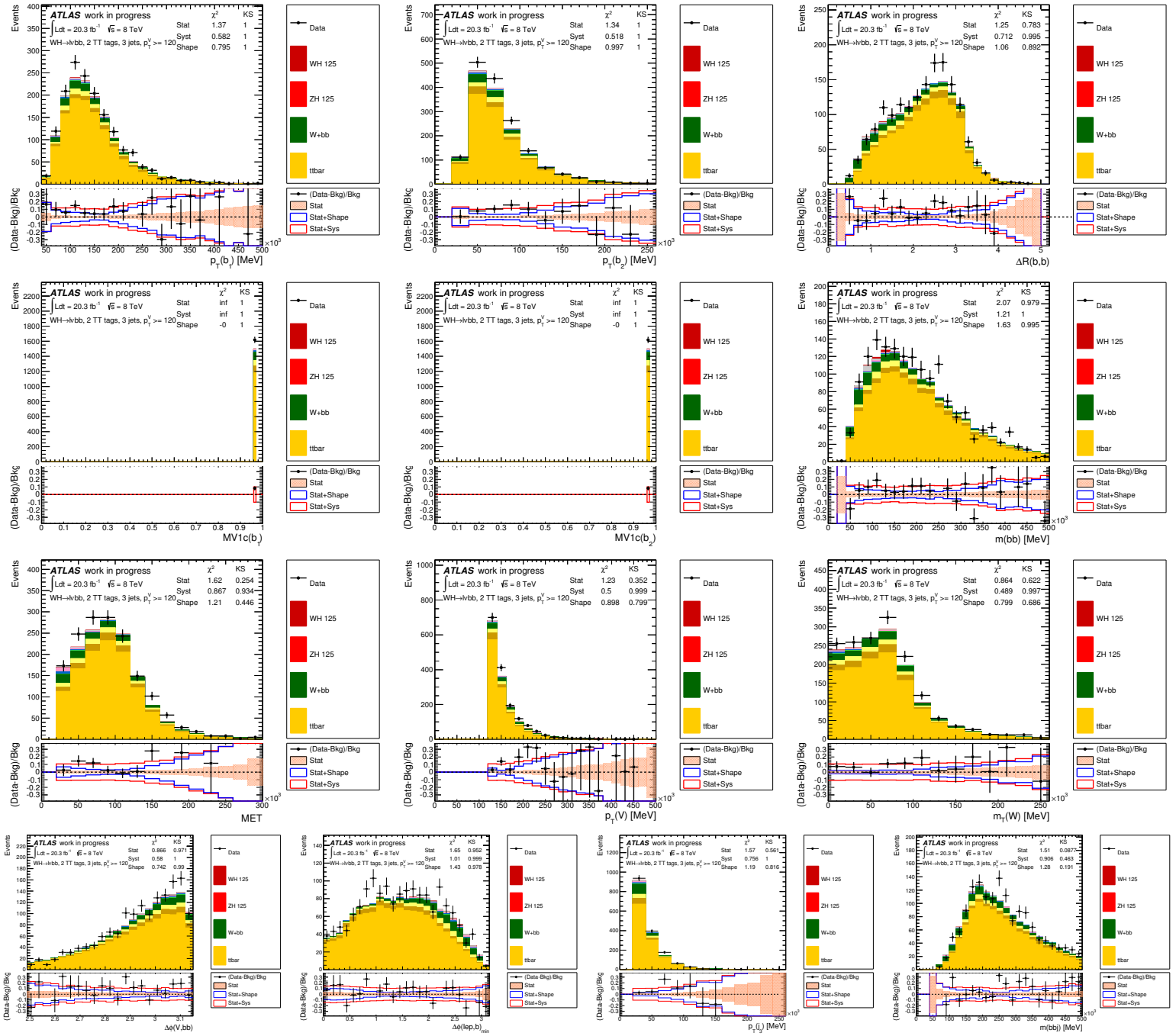

Figure 345: Distributions of MVA training variables used in 1-lepton events for $p_{\mathrm{T}}^{W} > 120$ GeV with 2 TT b-tags and 3 jets. From left to right: Row 1 - leading then sub-leading jet p_{T} and ΔR of the same two jets. Row 2 - pseudo-continuous MV1c distributions for leading then sub-leading jet and the m_{jj} of the same two jets. Row 3 - $E_{\mathrm{T}}^{\mathrm{miss}}$, p_{T}^{W}, and m_{T}^{W}. Row 4 - $\Delta\phi(V,H)$, $\min|\Delta\phi(\ell, jet)|$, the 3^{rd} jet p_{T}, and the tri-jet mass (m_{jjj}). Section 6.1 details the definition of each variable.

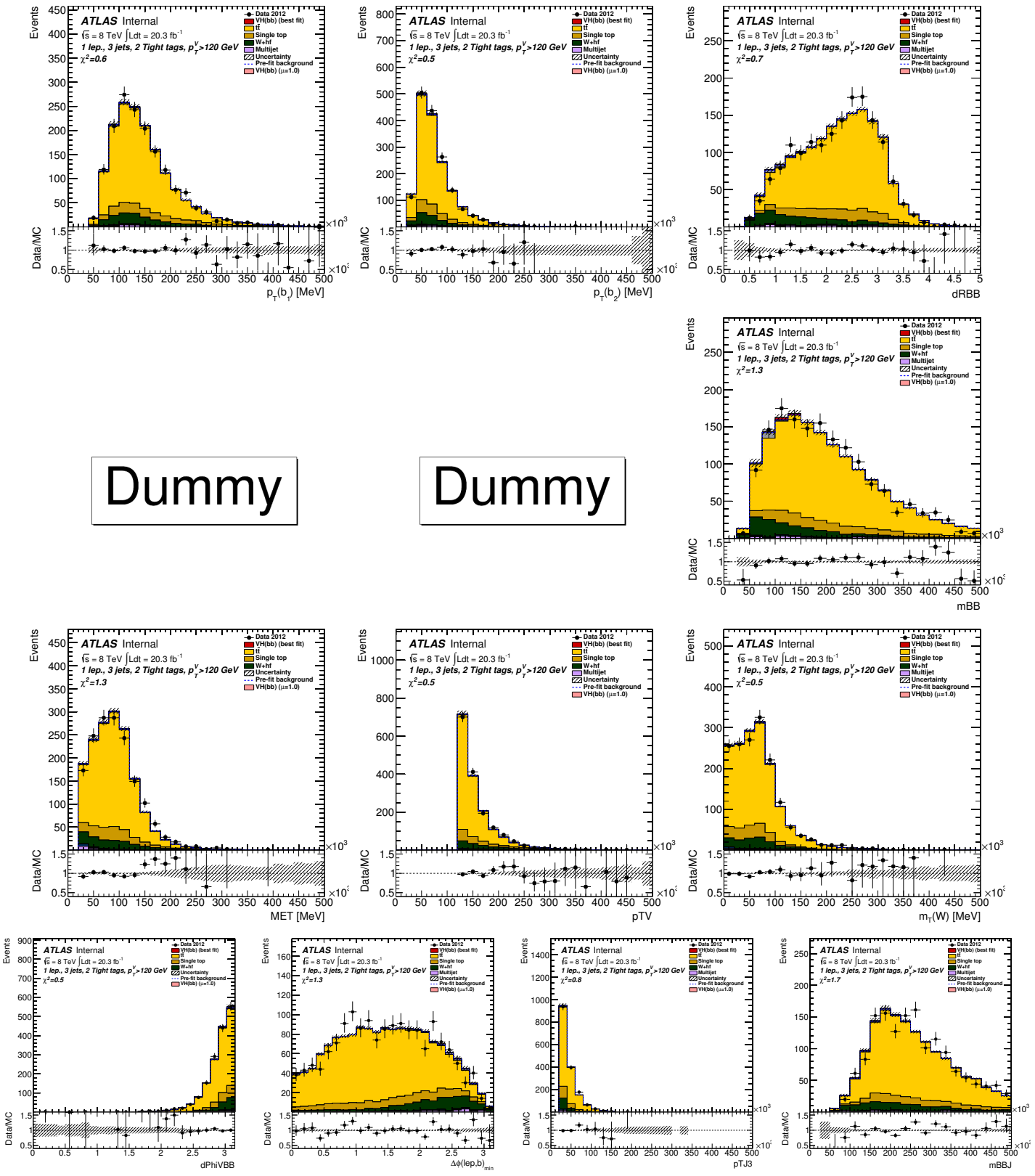

Figure 346: Distributions of MVA training variables used in 1-lepton events for $p_{\mathrm{T}}^{W} > 120$ GeV with 2 TT b-tags and 3 jets after the combined 0+1+2 lepton MVA fit. From left to right: Row 1 - leading then sub-leading jet p_{T} and ΔR of the same two jets. Row 2 - pseudo-continuous MV1c distributions for leading then sub-leading jet and the m_{jj} of the same two jets. Row 3 - $E_{\mathrm{T}}^{\mathrm{miss}}$, p_{T}^{W}, and m_{T}^{W}. Row 4 - $\Delta\phi(V, H)$, min$|\Delta\phi(\ell, jet)|$, the 3^{rd} jet p_{T}, and the tri-jet mass (m_{jjj}). Section 6.1 details the definition of each variable.

AA MVA Input Variable Distributions: Two Lepton

This appendix contains distributions of the BDT input variables defined in Section 6 in the 2-lepton analysis for low and high p_{T}^{Z} regions ($p_{\mathrm{T}}^{Z} < 120$ GeV and $p_{\mathrm{T}}^{Z} > 120$ GeV respectively). The electron and muon events have been combined. These plots are done by applying the latest scale factors, obtained for the 2 jet region and the 3-jet region separately, by comparing the event yield before and after the MVA combined fit. They are summarized in Table 114. Explicitly stated, the theoretical expectation for each background is used for the given luminosity. All the plots in this section are done with the status-of-art analysis.

Figure 347 shows one b-tag two jet events with $p_{\mathrm{T}}^{Z} < 120$ GeV prefit and Figure 348 postfit.
Figure 349 shows one b-tag two jet events with $p_{\mathrm{T}}^{Z} > 120$ GeV prefit and Figure 350 postfit.
Figure 351 shows LL b-tag two jet events with $p_{\mathrm{T}}^{Z} < 120$ GeV prefit and Figure 352 postfit.
Figure 353 shows LL b-tag two jet events with $p_{\mathrm{T}}^{Z} > 120$ GeV prefit and Figure 354 postfit.
Figure 355 shows MM+TT b-tag two jet events with $p_{\mathrm{T}}^{Z} < 120$ GeV prefit and Figure 356 postfit.
Figure 357 shows MM+TT b-tag two jet events with $p_{\mathrm{T}}^{Z} > 120$ GeV prefit and Figure 358 postfit.
Figure 359 shows one b-tag three jet events with $p_{\mathrm{T}}^{Z} < 120$ GeV prefit and Figure 360 postfit.
Figure 361 shows one b-tag three jet events with $p_{\mathrm{T}}^{Z} > 120$ GeV prefit and Figure 362 postfit.
Figure 363 shows LL b-tag three jet events with $p_{\mathrm{T}}^{Z} < 120$ GeV prefit and Figure 364 postfit.
Figure 365 shows LL b-tag three jet events with $p_{\mathrm{T}}^{Z} > 120$ GeV prefit and Figure 366 postfit.
Figure 367 shows MMTT b-tag three jet events with $p_{\mathrm{T}}^{Z} < 120$ GeV prefit and Figure 368 postfit.
Figure 369 shows MMTT b-tag three jet events with $p_{\mathrm{T}}^{Z} > 120$ GeV prefit and Figure 370 postfit.

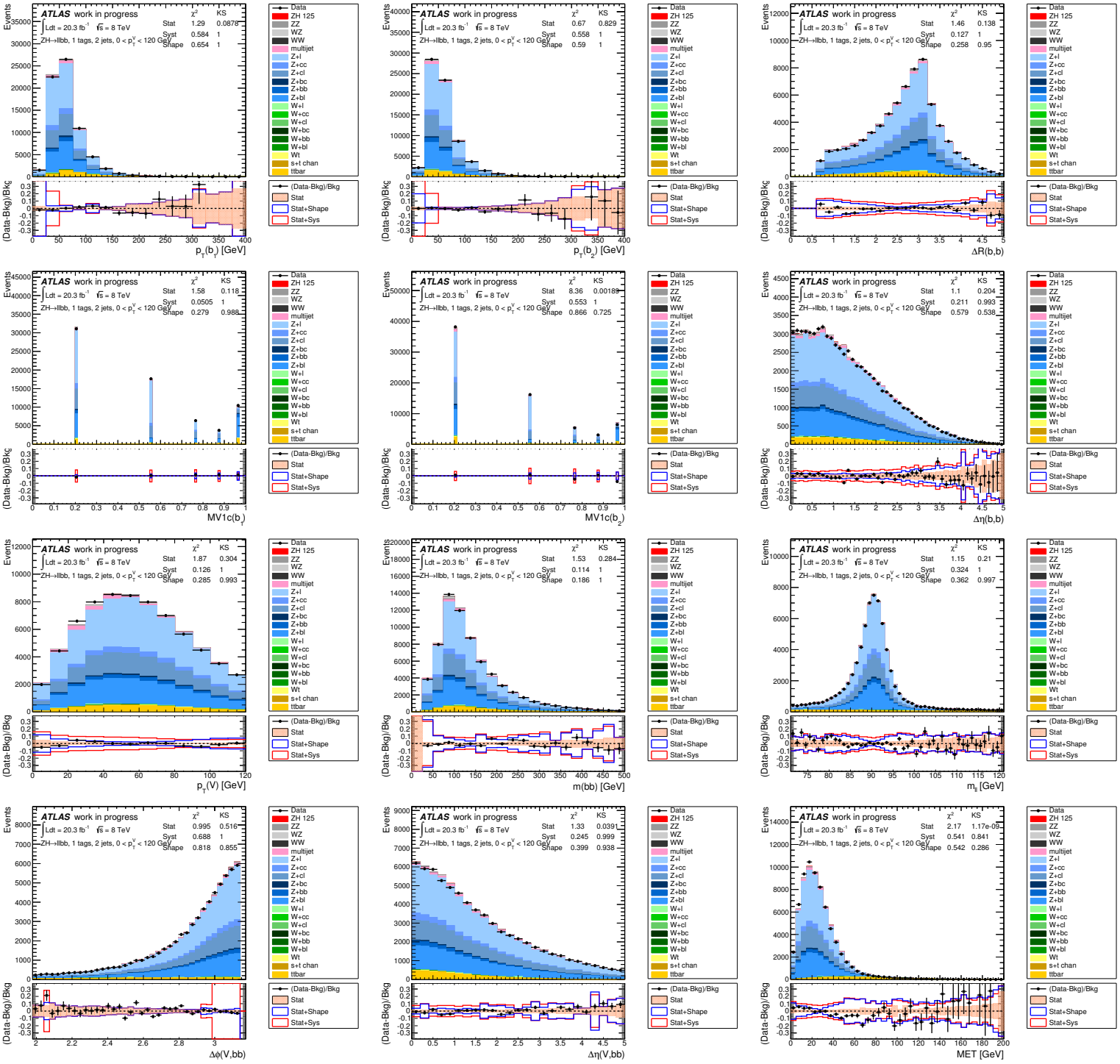

Figure 347: Distributions of MVA training variables used in 2-lepton events for $p_{\mathrm{T}}^{Z} < 120$ GeV with 1 b-tag and 2-jets. From left to right: Row 1 - leading then sub-leading jet p_{T} and ΔR of the same two jets. Row 2 - pseudo-continuous MV1c distributions for leading then sub-leading jet and the $\Delta\eta$ of the same two jets. Row 3 - p_{T}^{Z}, m_{jj}, and $m_{\ell\ell}$. Row 4 - $\Delta\phi(V,H)$, $\Delta\eta(V,H)$, and $E_{\mathrm{T}}^{\mathrm{miss}}$. Section 6.1 details the definition of each variable.

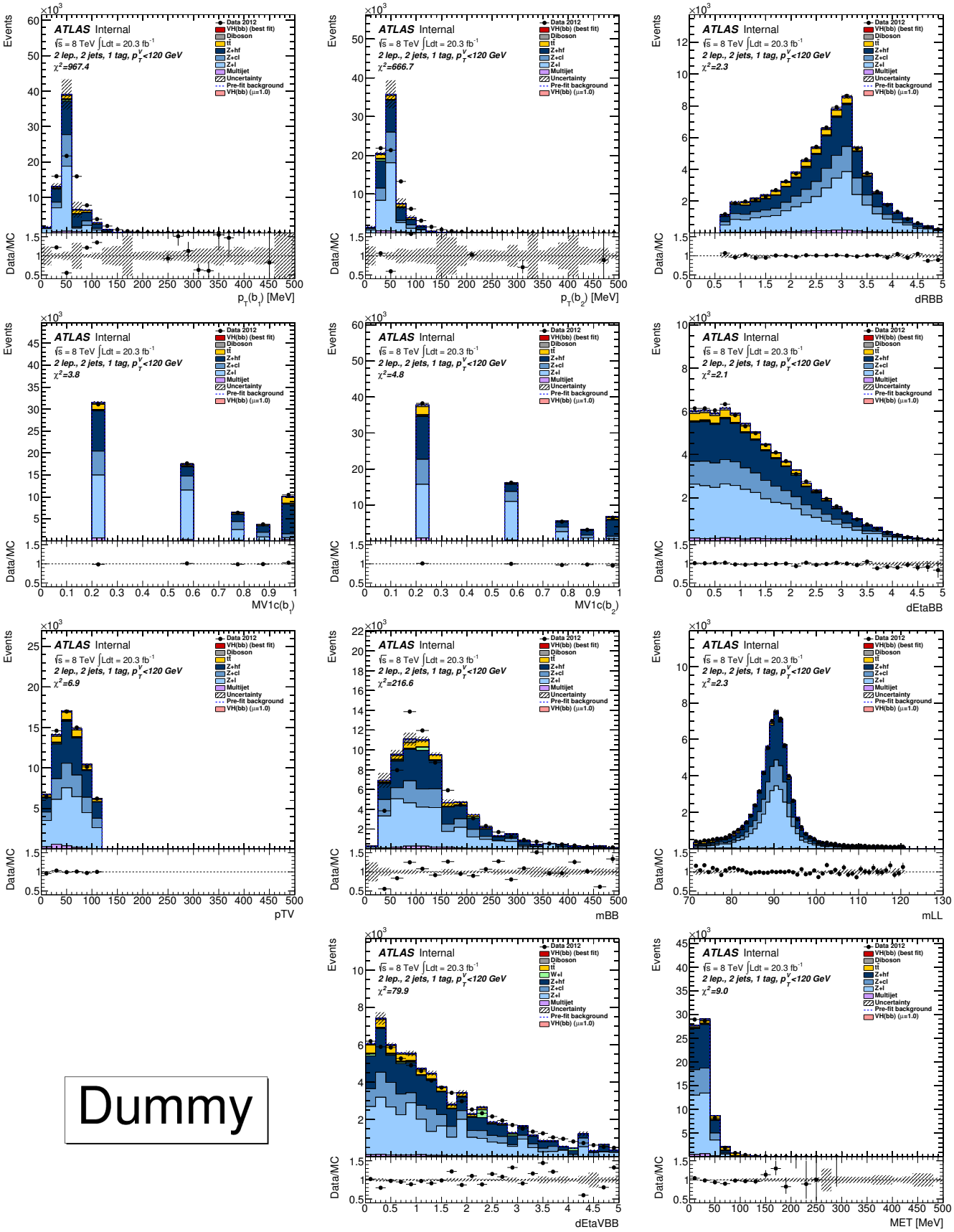

Dummy

Figure 348: Distributions of MVA training variables used in 2-lepton events for $p_{\mathrm{T}}^{Z} < 120$ GeV with 1 b-tag and 2-jets after the combined 0+1+2 lepton MVA fit. From left to right: Row 1 - leading then sub-leading jet p_{T} and ΔR of the same two jets. Row 2 - pseudo-continuous MV1c distributions for leading then sub-leading jet and the $\Delta\eta$ of the same two jets. Row 3 - p_{T}^{Z}, m_{jj}, and $m_{\ell\ell}$. Row 4 - $\Delta\phi(V,H)$, $\Delta\eta(V,H)$, and $E_{\mathrm{T}}^{\mathrm{miss}}$. Section 6.1 details the definition of each variable.

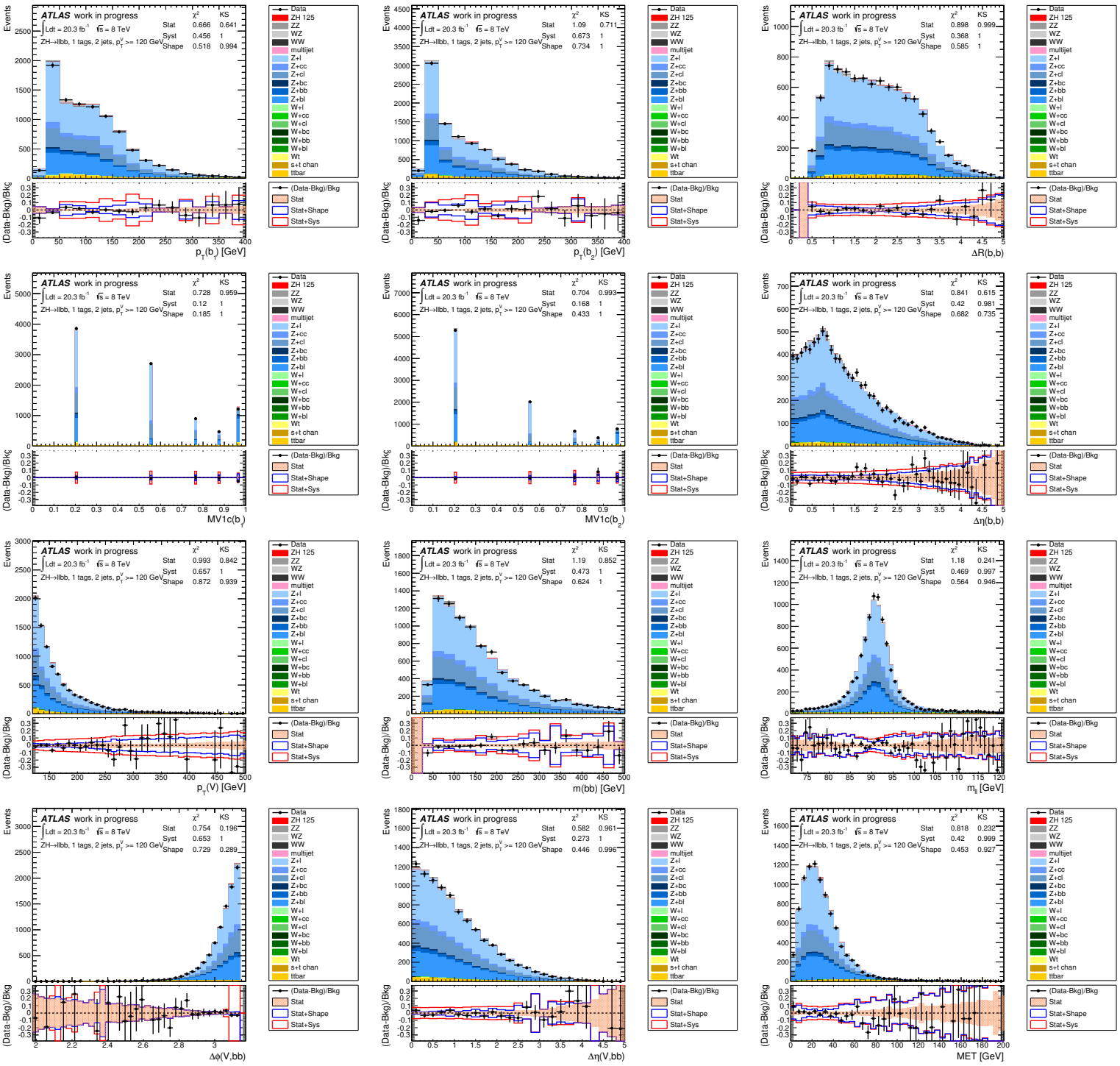

Figure 349: Distributions of MVA training variables used in 2-lepton events for $p_{\mathrm{T}}^{Z} > 120$ GeV with 1 b-tag and 2-jets. From left to right: Row 1 - leading then sub-leading jet p_{T} and ΔR of the same two jets. Row 2 - pseudo-continuous MV1c distributions for leading then sub-leading jet and the $\Delta\eta$ of the same two jets. Row 3 - p_{T}^{Z}, m_{jj}, and $m_{\ell\ell}$. Row 4 - $\Delta\phi(V,H)$, $\Delta\eta(V,H)$, and $E_{\mathrm{T}}^{\mathrm{miss}}$. Section 6.1 details the definition of each variable.

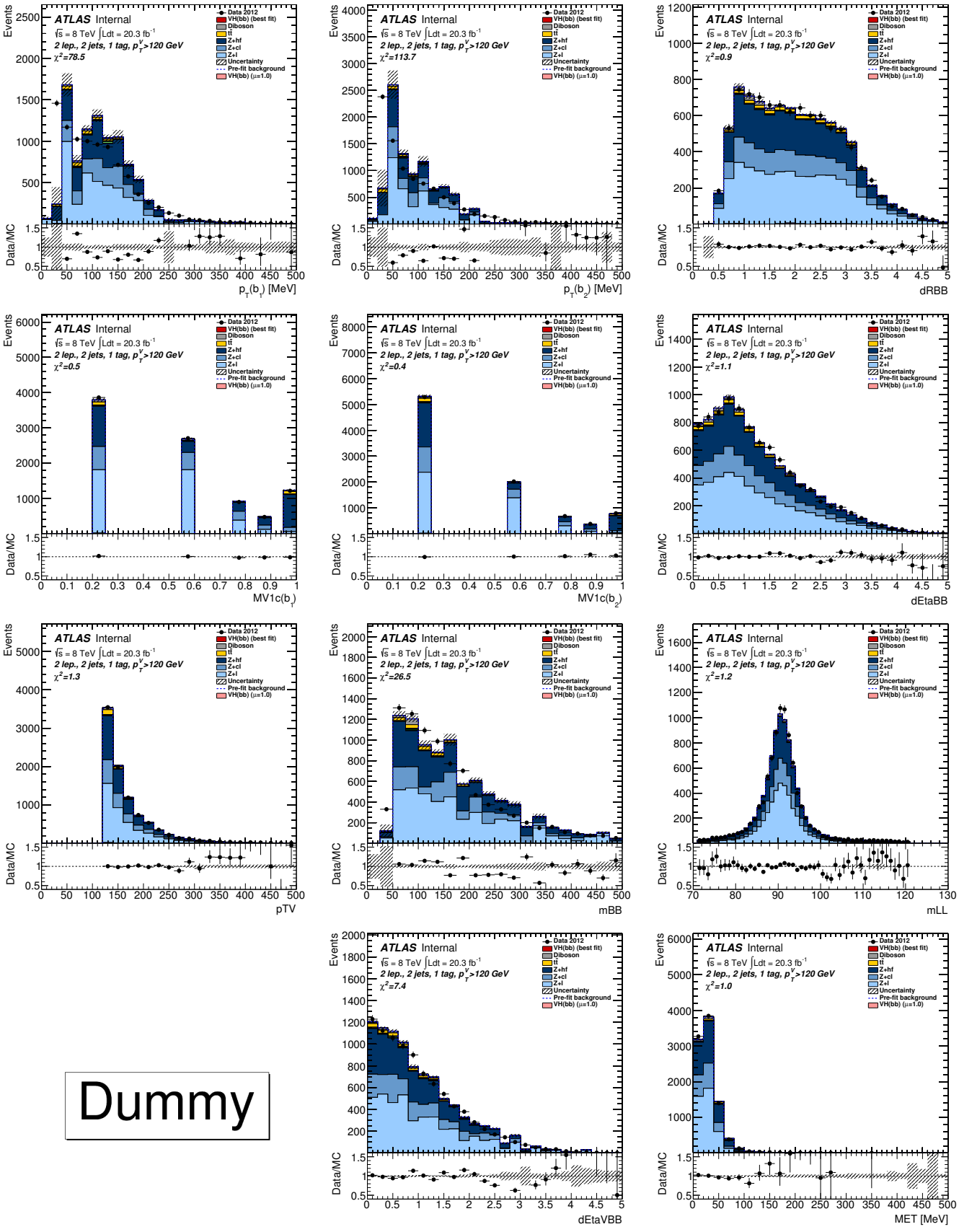

Dummy

Figure 350: Distributions of MVA training variables used in 2-lepton events for $p_{\mathrm{T}}^{Z} > 120$ GeV with 1 b-tag and 2-jets after the combined 0+1+2 lepton MVA fit. From left to right: Row 1 - leading then sub-leading jet p_{T} and ΔR of the same two jets. Row 2 - pseudo-continuous MV1c distributions for leading then sub-leading jet and the $\Delta\eta$ of the same two jets. Row 3 - p_{T}^{Z}, m_{jj}, and $m_{\ell\ell}$. Row 4 - $\Delta\phi(V,H)$, $\Delta\eta(V,H)$, and $E_{\mathrm{T}}^{\mathrm{miss}}$. Section 6.1 details the definition of each variable.

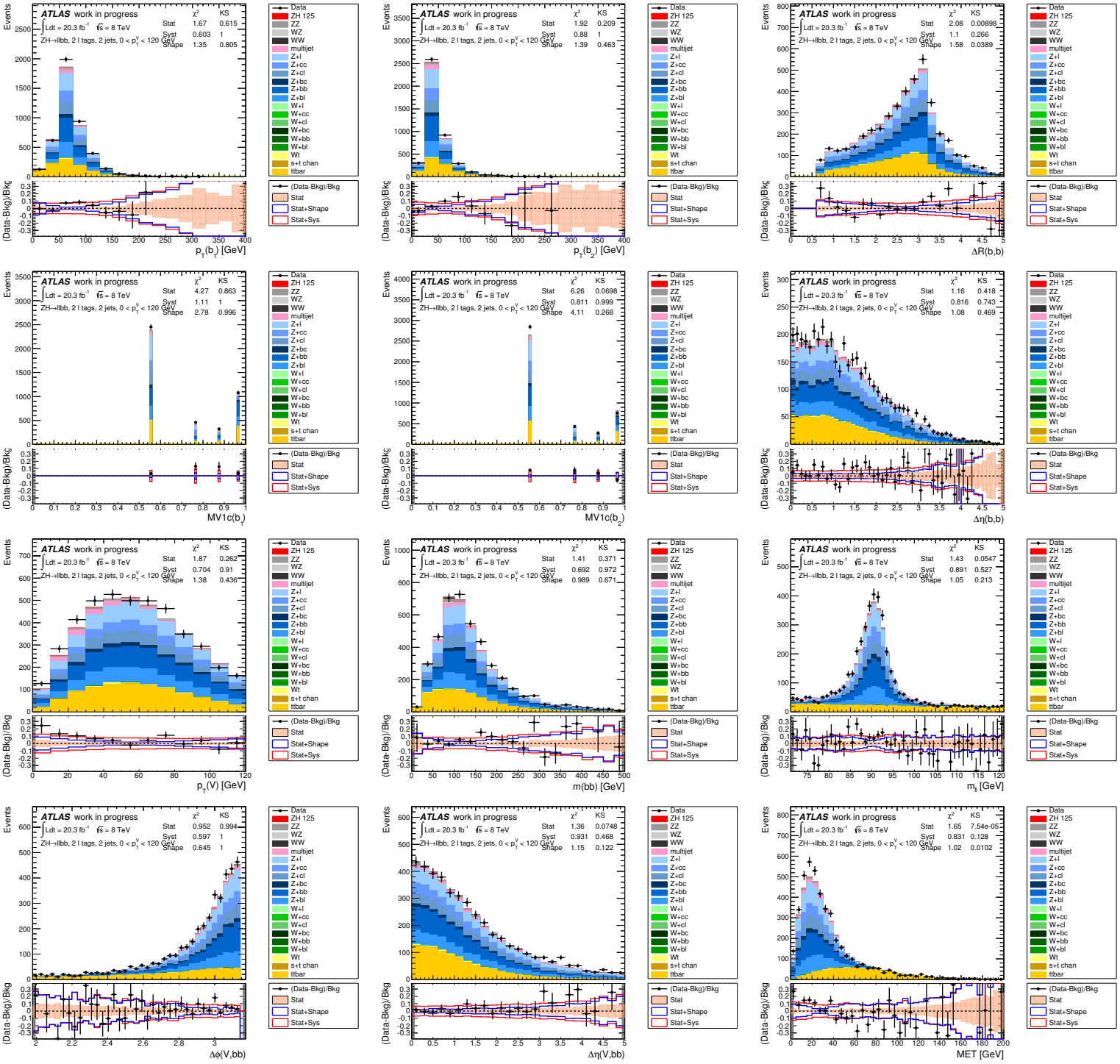

Figure 351: Distributions of MVA training variables used in 2-lepton events for $p_{\mathrm{T}}^{Z} < 120$ GeV with 2 LL b-tags and 2-jets. From left to right: Row 1 - leading then sub-leading jet p_{T} and ΔR of the same two jets. Row 2 - pseudo-continuous MV1c distributions for leading then sub-leading jet and the $\Delta\eta$ of the same two jets. Row 3 - p_{T}^{Z}, m_{jj}, and $m_{\ell\ell}$. Row 4 - $\Delta\phi(V,H)$, $\Delta\eta(V,H)$, and $E_{\mathrm{T}}^{\mathrm{miss}}$. Section 6.1 details the definition of each variable.

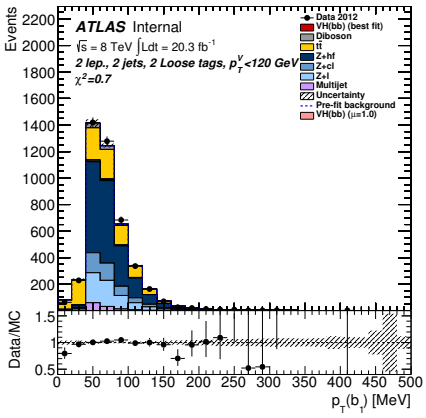

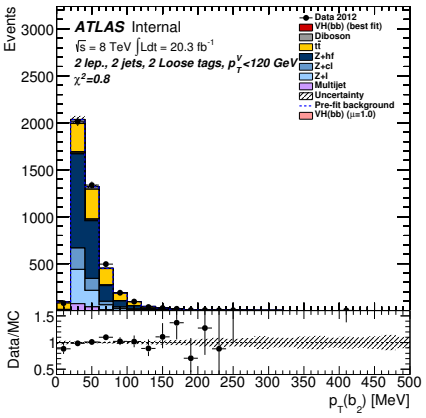

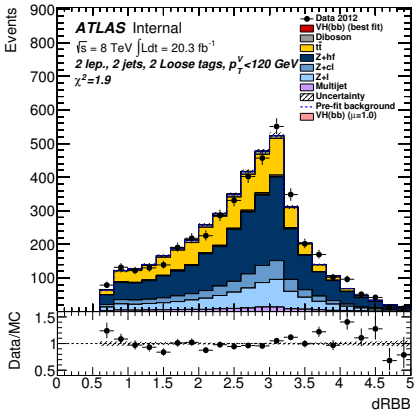

Dummy

Dummy

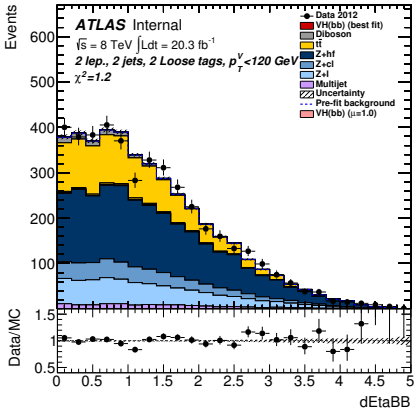

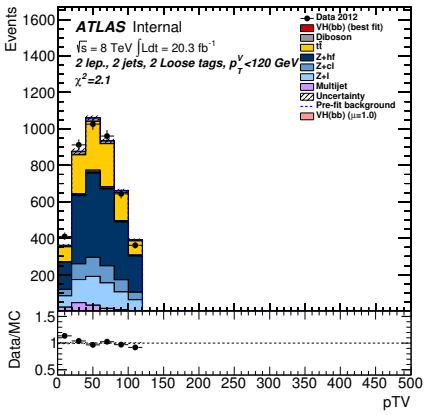

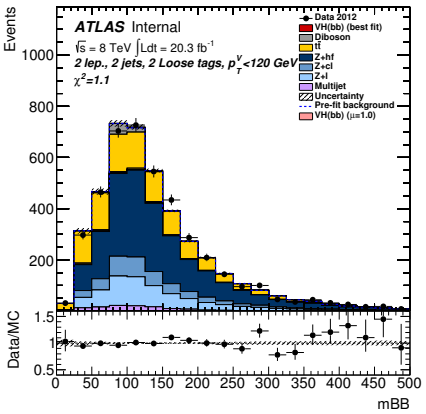

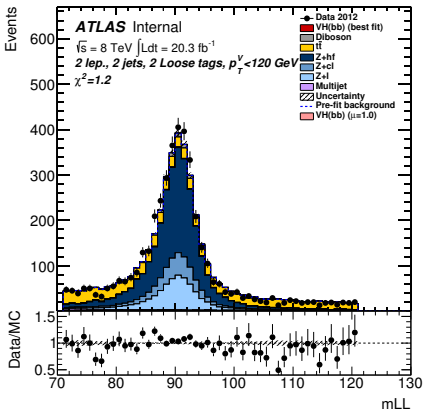

Dummy

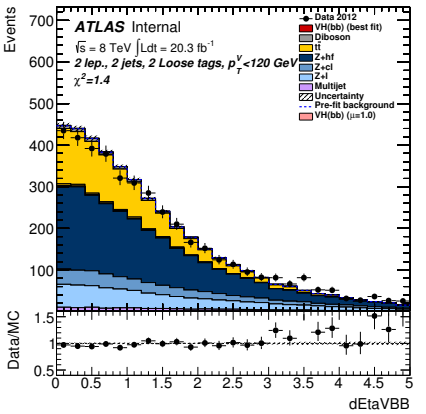

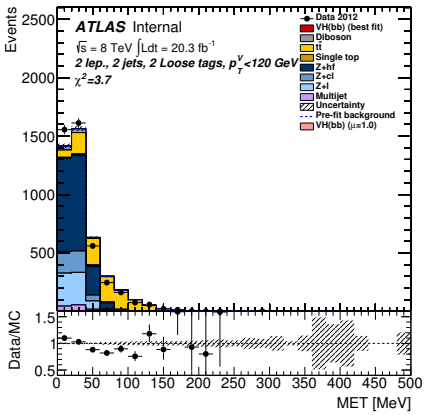

Figure 352: Distributions of MVA training variables used in 2-lepton events for $p_{\mathrm{T}}^{Z} < 120$ GeV with 2 LL b-tags and 2-jets after the combined 0+1+2 lepton MVA fit. From left to right: Row 1 - leading then sub-leading jet p_{T} and ΔR of the same two jets. Row 2 - pseudo-continuous MV1c distributions for leading then sub-leading jet and the $\Delta\eta$ of the same two jets. Row 3 - p_{T}^{Z}, m_{jj}, and $m_{\ell\ell}$. Row 4 - $\Delta\phi(V,H)$, $\Delta\eta(V,H)$, and $E_{\mathrm{T}}^{\mathrm{miss}}$. Section 6.1 details the definition of each variable.

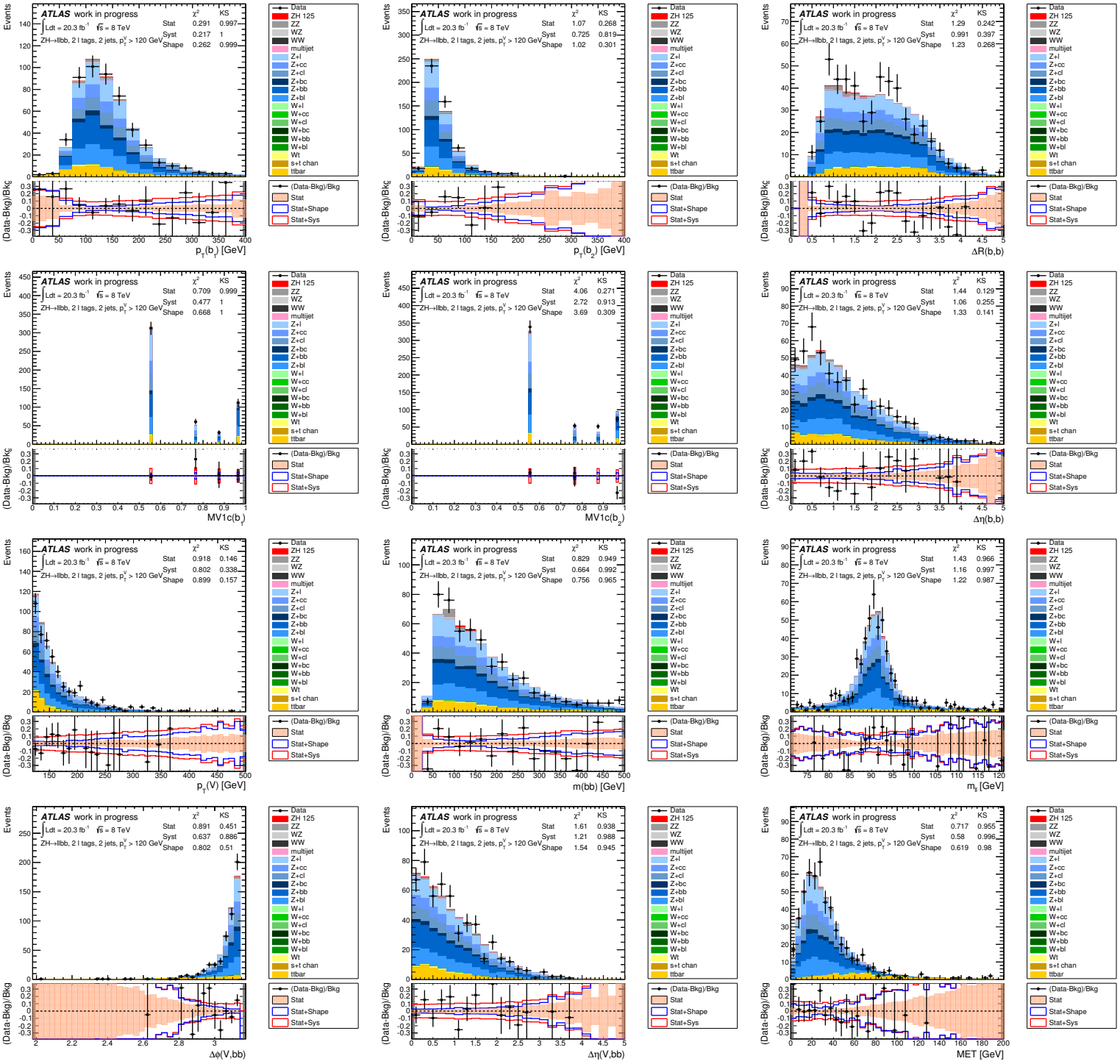

Figure 353: Distributions of MVA training variables used in 2-lepton events for $p_{\mathrm{T}}^{Z} > 120$ GeV with 2 LL b-tags and 2-jets. From left to right: Row 1 - leading then sub-leading jet p_{T} and ΔR of the same two jets. Row 2 - pseudo-continuous MV1c distributions for leading then sub-leading jet and the $\Delta\eta$ of the same two jets. Row 3 - p_{T}^{Z}, m_{jj}, and $m_{\ell\ell}$. Row 4 - $\Delta\phi(V,H)$, $\Delta\eta(V,H)$, and $E_{\mathrm{T}}^{\mathrm{miss}}$. Section 6.1 details the definition of each variable.

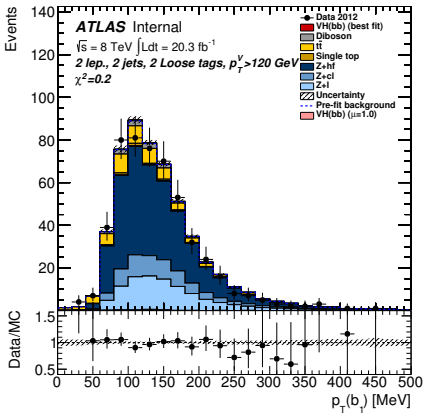

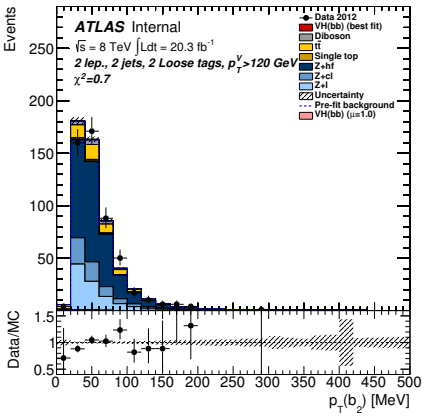

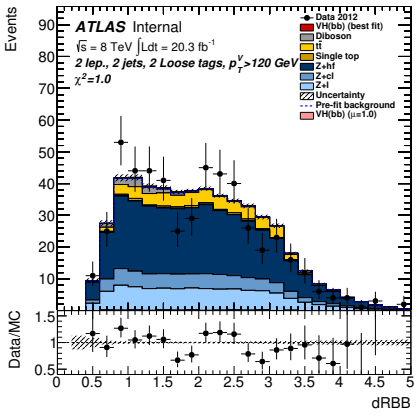

Dummy

Dummy

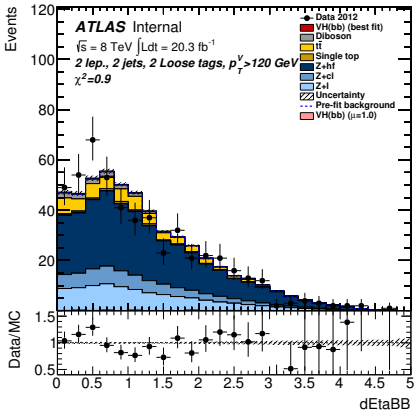

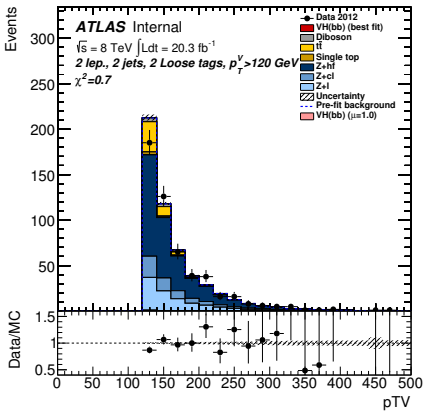

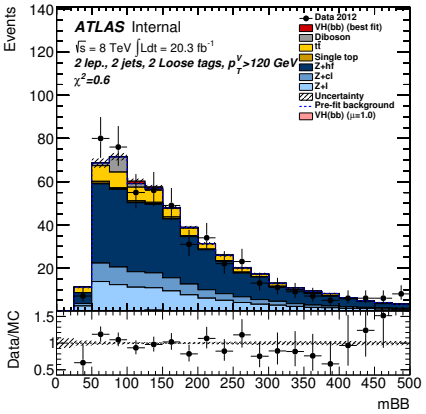

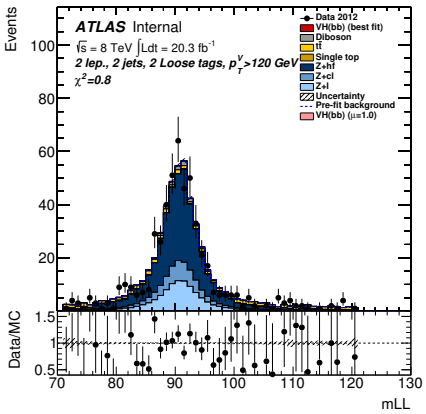

Dummy

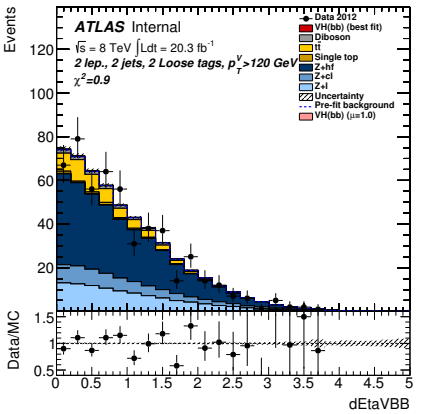

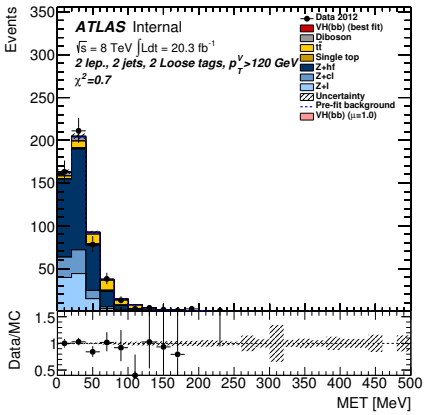

Figure 354: Distributions of MVA training variables used in 2-lepton events for $p_{\mathrm{T}}^{Z} > 120$ GeV with 2 LL b-tags and 2-jets after the combined 0+1+2 lepton MVA fit. From left to right: Row 1 - leading then sub-leading jet p_{T} and ΔR of the same two jets. Row 2 - pseudo-continuous MV1c distributions for leading then sub-leading jet and the $\Delta\eta$ of the same two jets. Row 3 - p_{T}^{Z}, m_{jj}, and $m_{\ell\ell}$. Row 4 - $\Delta\phi(V,H)$, $\Delta\eta(V,H)$, and $E_{\mathrm{T}}^{\mathrm{miss}}$. Section 6.1 details the definition of each variable.

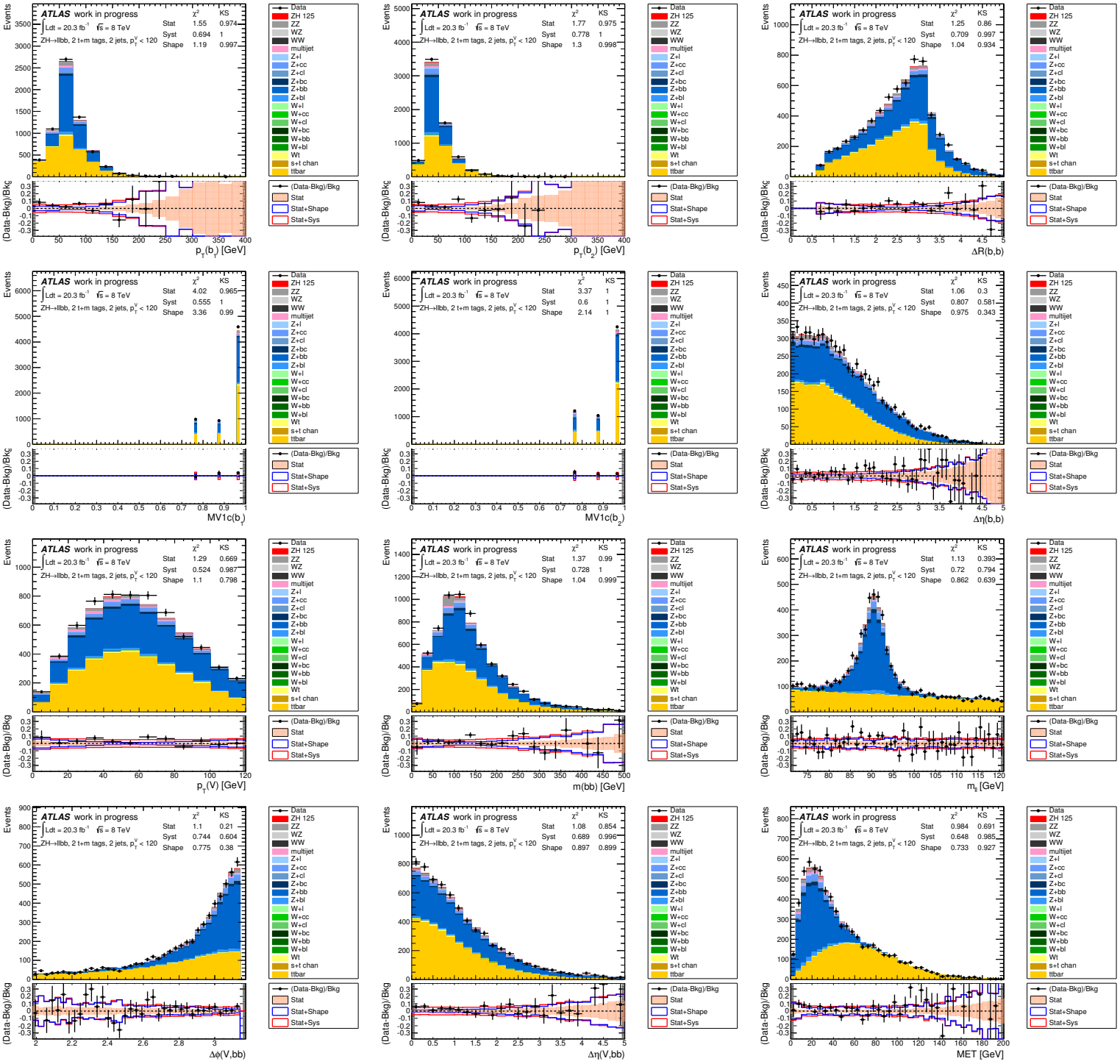

Figure 355: Distributions of MVA training variables used in 2-lepton events for $p_{\mathrm{T}}^{Z} < 120$ GeV with 2 MM+TT b-tags and 2-jets. From left to right: Row 1 - leading then sub-leading jet p_{T} and ΔR of the same two jets. Row 2 - pseudo-continuous MV1c distributions for leading then sub-leading jet and the $\Delta\eta$ of the same two jets. Row 3 - p_{T}^{Z}, m_{jj}, and $m_{\ell\ell}$. Row 4 - $\Delta\phi(V,H)$, $\Delta\eta(V,H)$, and $E_{\mathrm{T}}^{\mathrm{miss}}$. Section 6.1 details the definition of each variable.

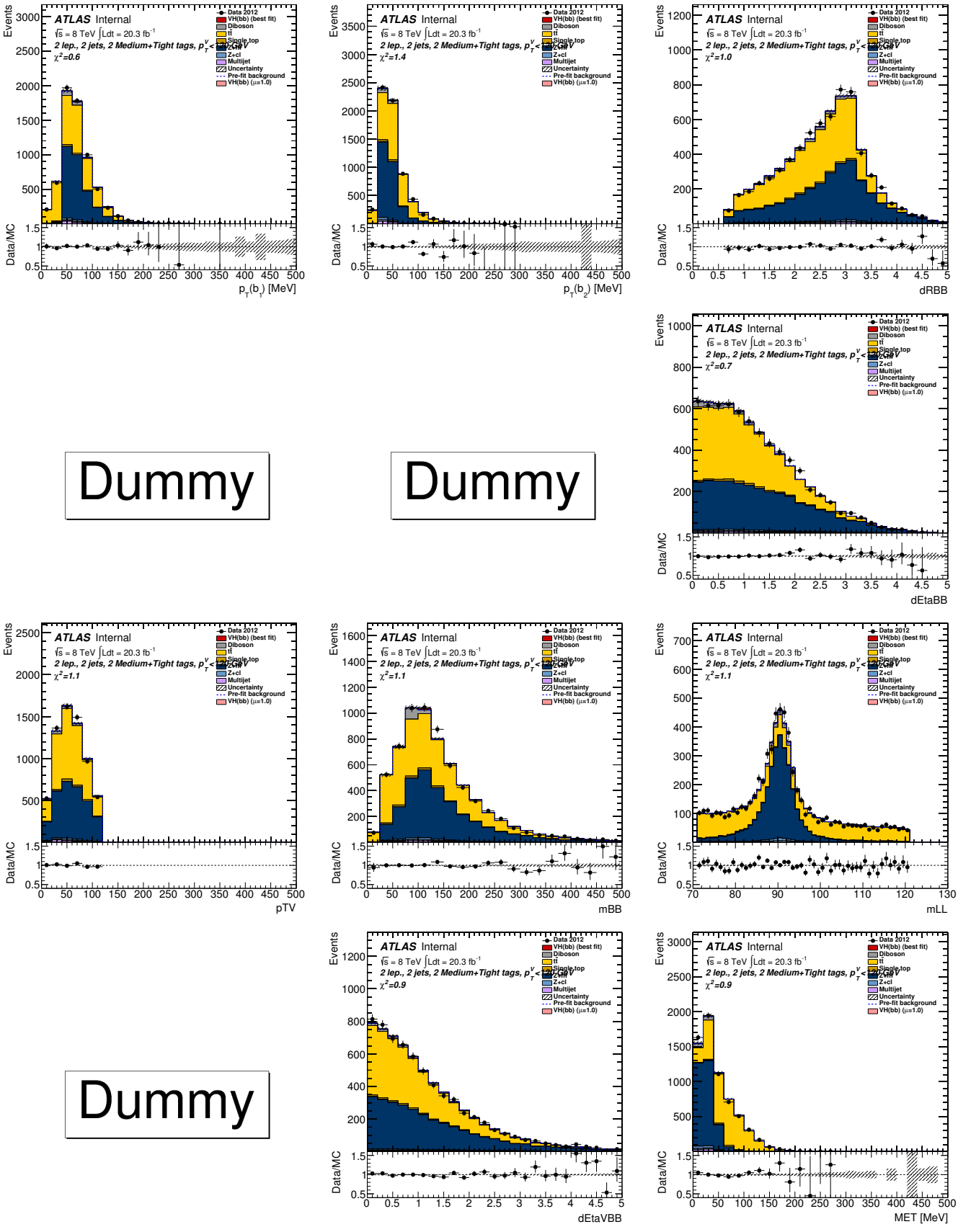

Figure 356: Distributions of MVA training variables used in 2-lepton events for $p_{\mathrm{T}}^{Z} < 120$ GeV with 2 MM+TT b-tags and 2-jets after the combined 0+1+2 lepton MVA fit. From left to right: Row 1 - leading then sub-leading jet p_{T} and ΔR of the same two jets. Row 2 - pseudo-continuous MV1c distributions for leading then sub-leading jet and the $\Delta\eta$ of the same two jets. Row 3 - p_{T}^{Z}, m_{jj}, and $m_{\ell\ell}$. Row 4 - $\Delta\phi(V,H)$, $\Delta\eta(V,H)$, and $E_{\mathrm{T}}^{\mathrm{miss}}$. Section 6.1 details the definition of each variable.

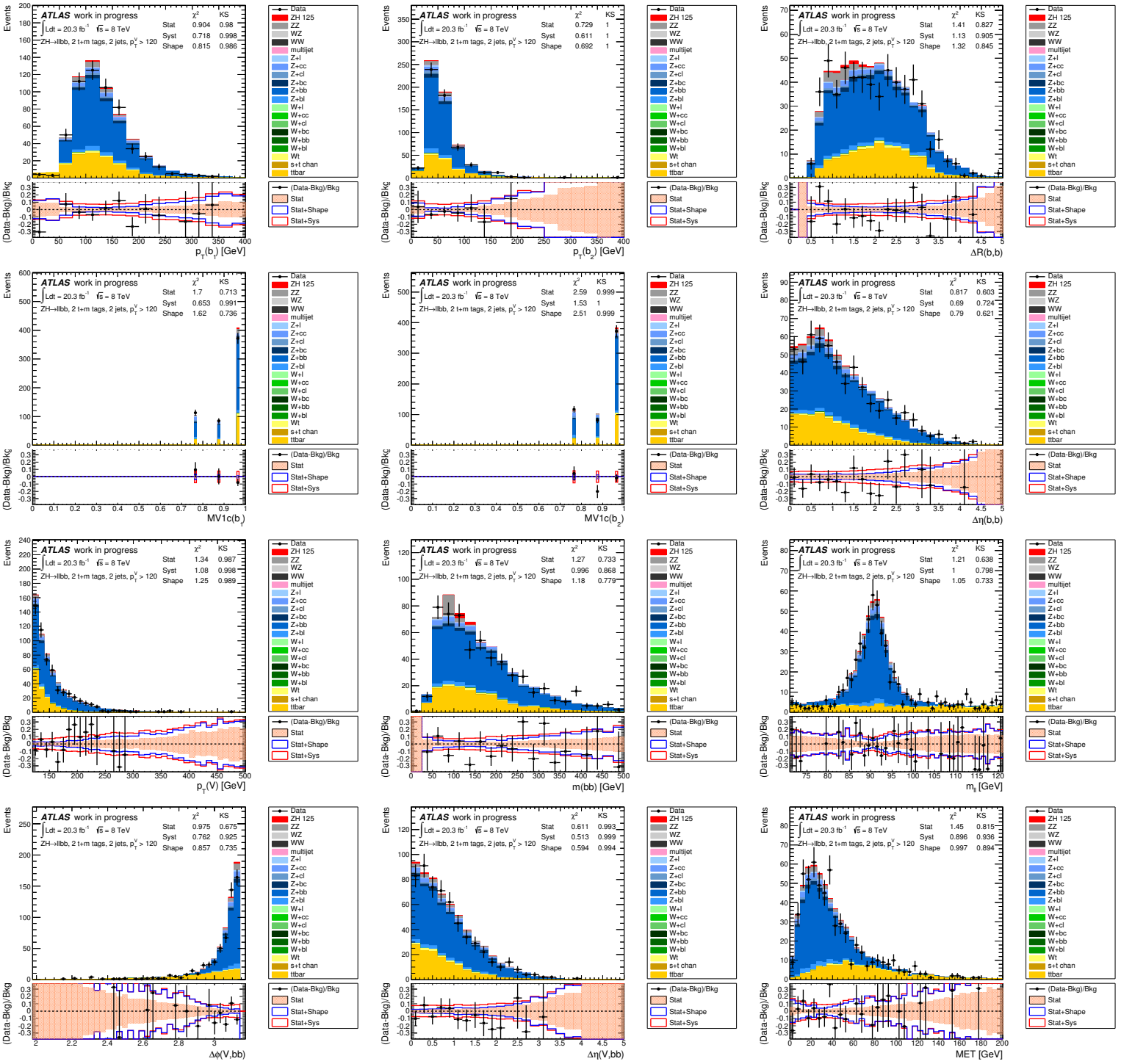

Figure 357: Distributions of MVA training variables used in 2-lepton events for $p_{\mathrm{T}}^{Z} > 120$ GeV with 2 MM+TT b-tags and 2-jets. From left to right: Row 1 - leading then sub-leading jet p_{T} and ΔR of the same two jets. Row 2 - pseudo-continuous MV1c distributions for leading then sub-leading jet and the $\Delta\eta$ of the same two jets. Row 3 - p_{T}^{Z}, m_{jj}, and $m_{\ell\ell}$. Row 4 - $\Delta\phi(V,H)$, $\Delta\eta(V,H)$, and $E_{\mathrm{T}}^{\mathrm{miss}}$. Section 6.1 details the definition of each variable.

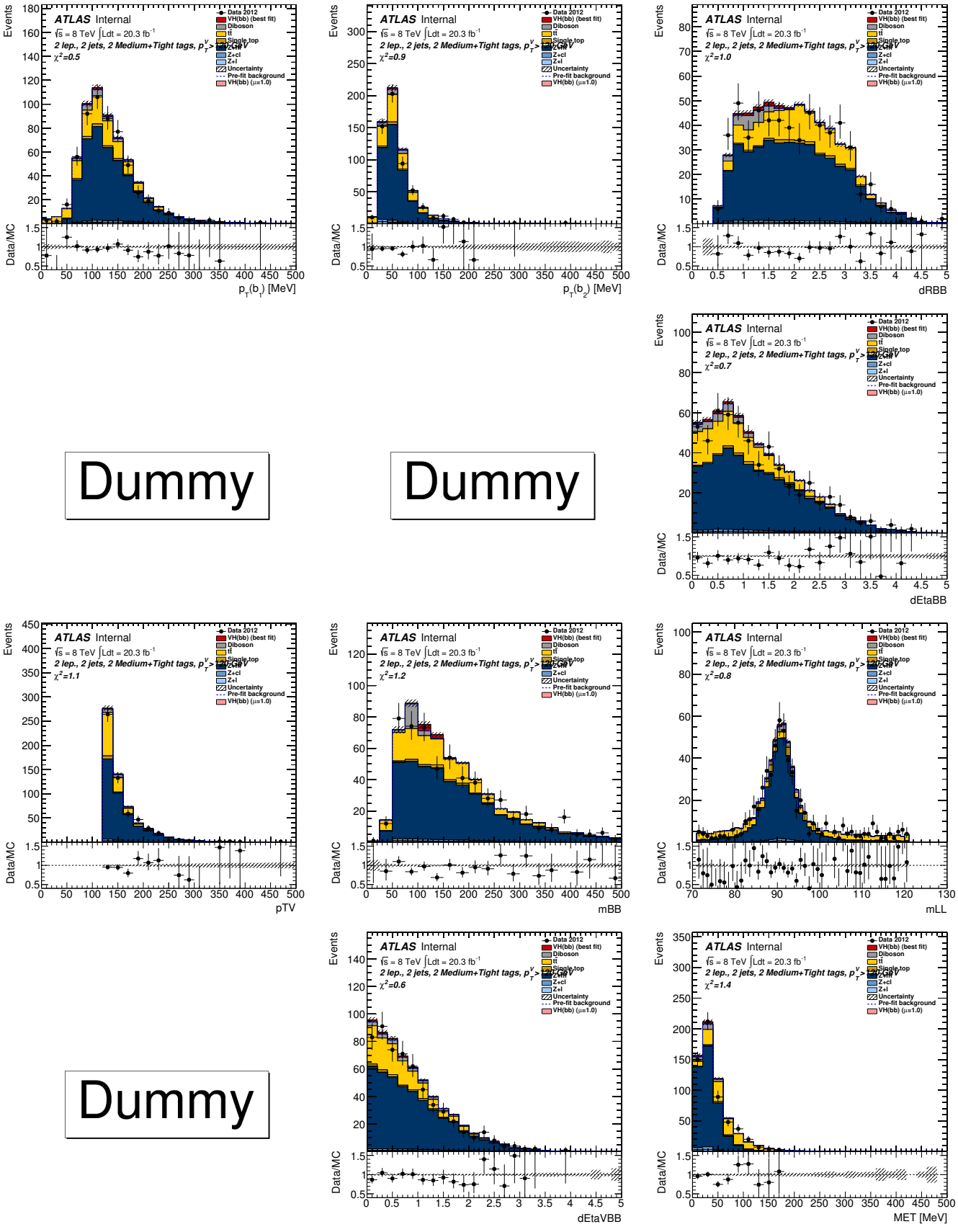

Figure 358: Distributions of MVA training variables used in 2-lepton events for $p_{\mathrm{T}}^{Z} > 120$ GeV with 2 MM+TT b-tags and 2-jets after the combined 0+1+2 lepton MVA fit. From left to right: Row 1 - leading then sub-leading jet p_{T} and ΔR of the same two jets. Row 2 - pseudo-continuous MV1c distributions for leading then sub-leading jet and the $\Delta\eta$ of the same two jets. Row 3 - p_{T}^{Z}, m_{jj}, and $m_{\ell\ell}$. Row 4 - $\Delta\phi(V,H)$, $\Delta\eta(V,H)$, and $E_{\mathrm{T}}^{\mathrm{miss}}$. Section 6.1 details the definition of each variable.

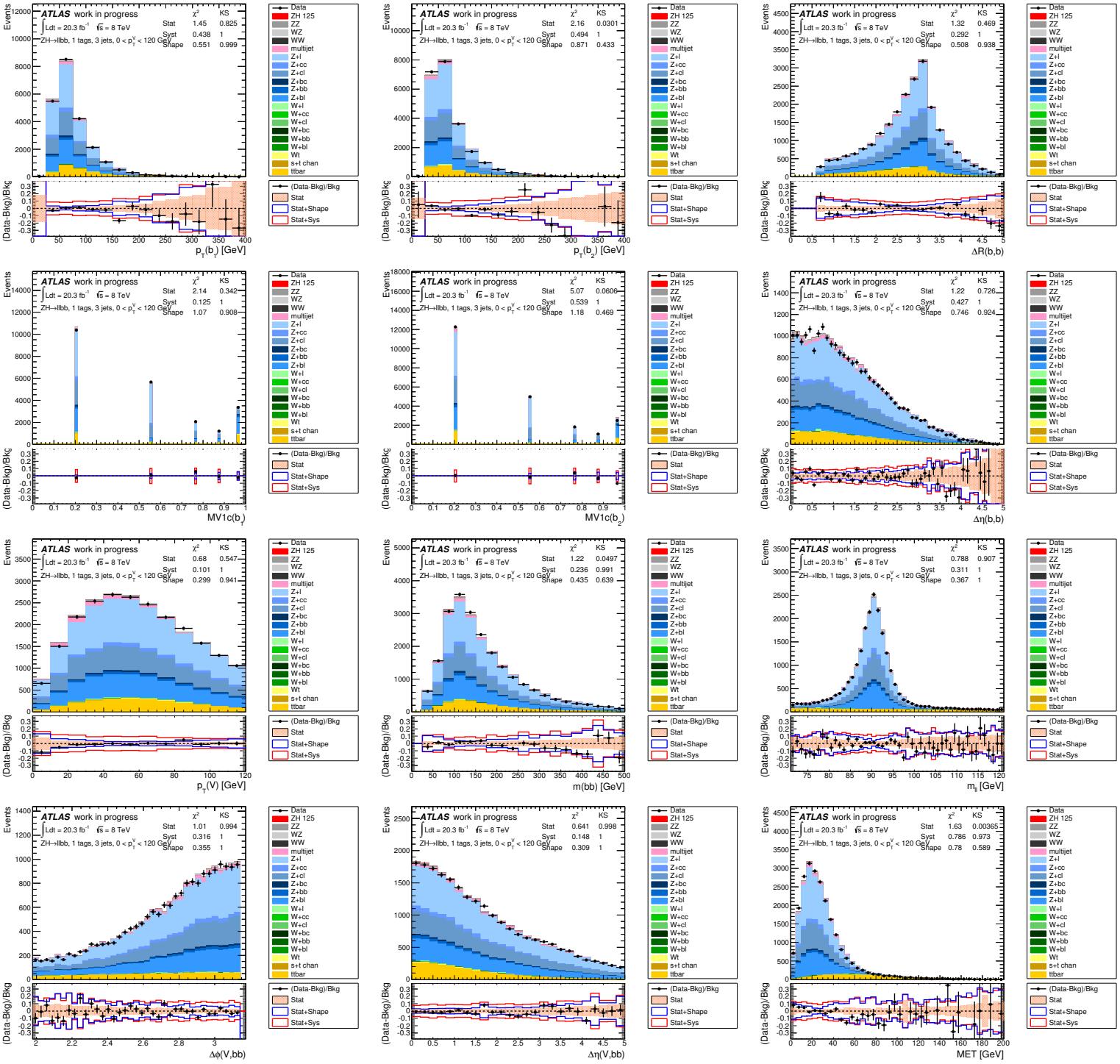

Figure 359: Distributions of MVA training variables used in 2-lepton events for $p_{\mathrm{T}}^{Z} < 120$ GeV with 1 b-tag and 3 jets. From left to right: Row 1 - leading then sub-leading jet p_{T} and ΔR of the same two jets. Row 2 - pseudo-continuous MV1c distributions for leading then sub-leading jet and the $\Delta\eta$ of the same two jets. Row 3 - p_{T}^{Z}, m_{jj}, and $m_{\ell\ell}$. Row 4 - $\Delta\phi(V,H)$, $\Delta\eta(V,H)$, and $E_{\mathrm{T}}^{\mathrm{miss}}$. Section 6.1 details the definition of each variable.

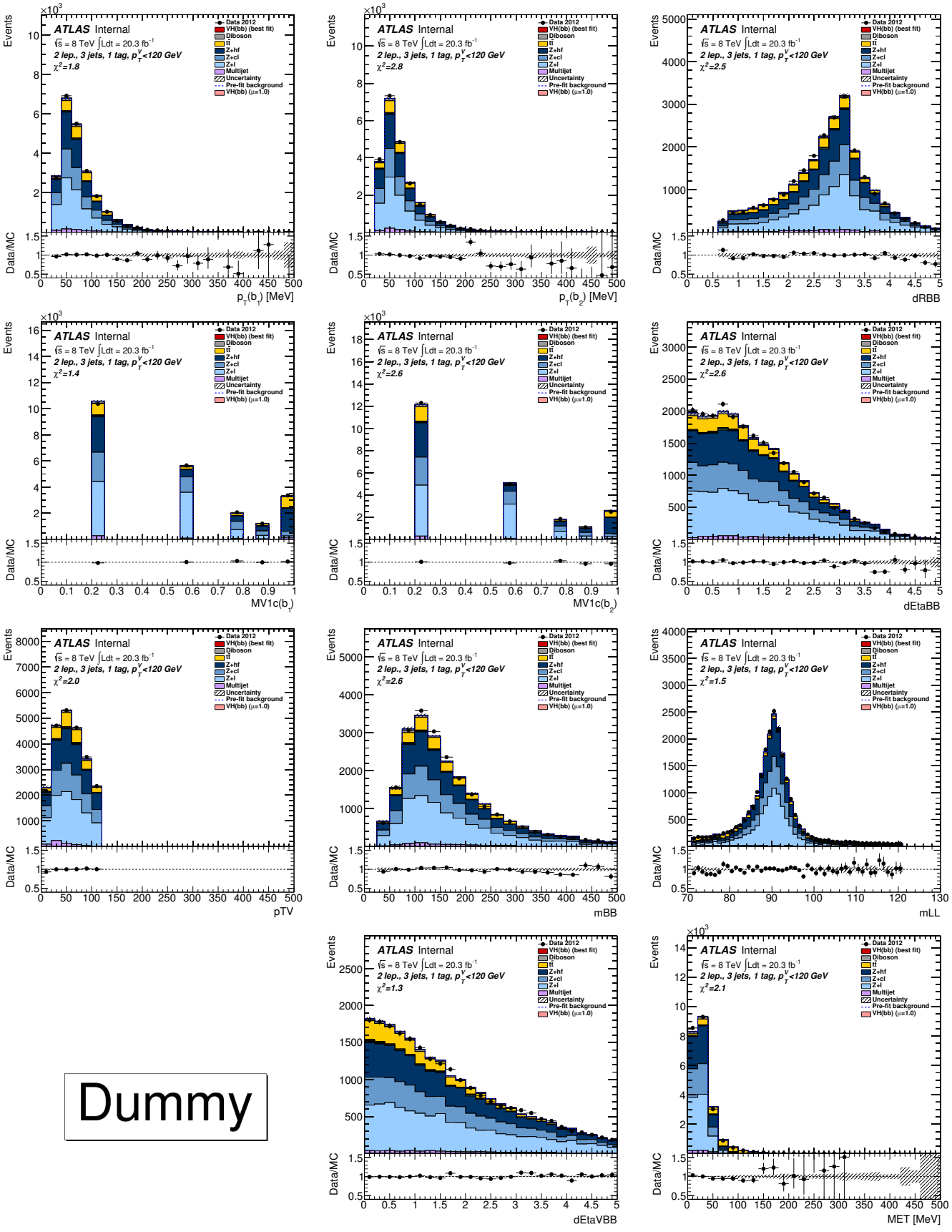

Dummy

Figure 360: Distributions of MVA training variables used in 2-lepton events for $p_{\mathrm{T}}^{Z} < 120$ GeV with 1 b-tag and 3-jets after the combined 0+1+2 lepton MVA fit. From left to right: Row 1 - leading then sub-leading jet p_{T} and ΔR of the same two jets. Row 2 - pseudo-continuous MV1c distributions for leading then sub-leading jet and the $\Delta\eta$ of the same two jets. Row 3 - p_{T}^{Z}, m_{jj}, and $m_{\ell\ell}$. Row 4 - $\Delta\phi(V,H)$, $\Delta\eta(V,H)$, and $E_{\mathrm{T}}^{\mathrm{miss}}$. Section 6.1 details the definition of each variable.

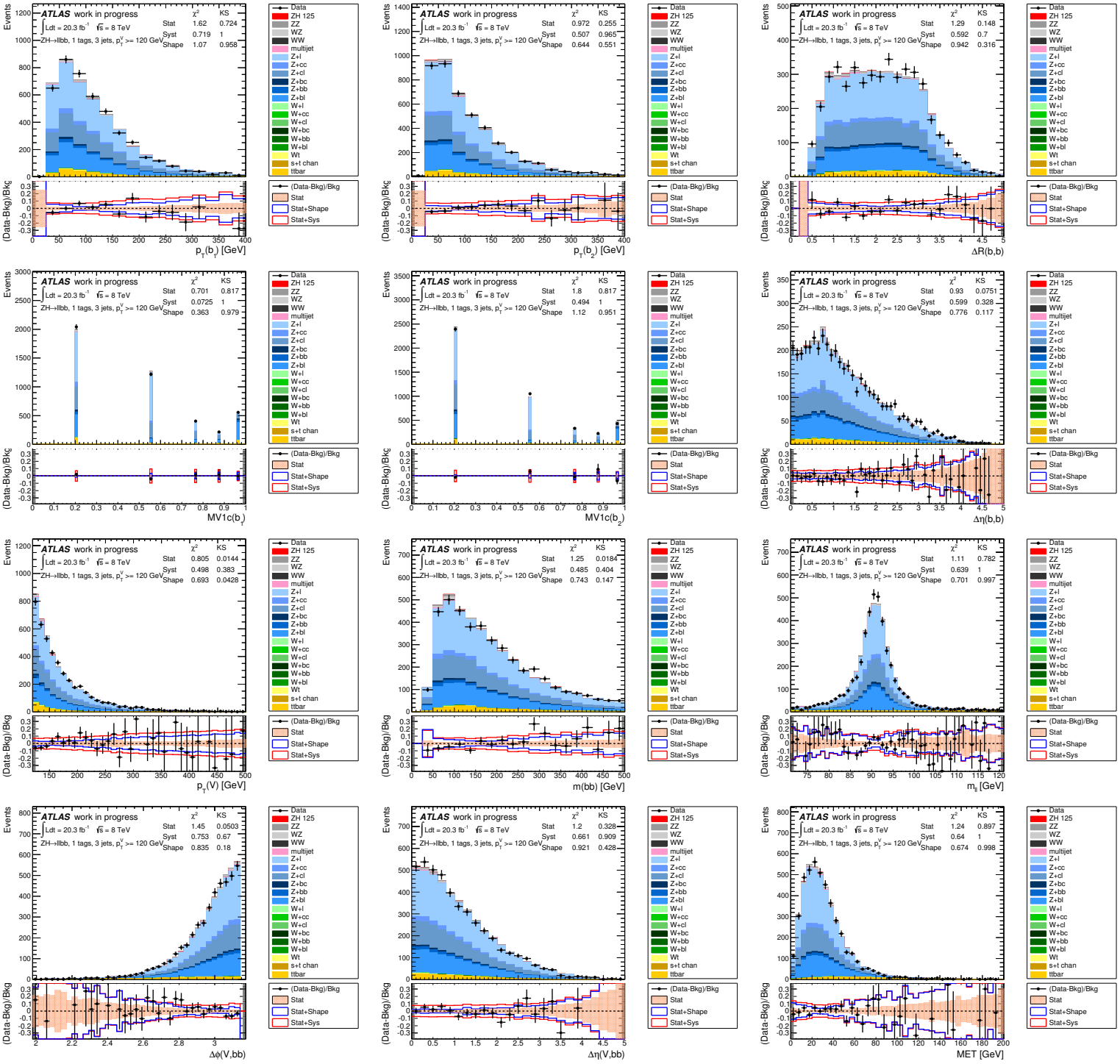

Figure 361: Distributions of MVA training variables used in 2-lepton events for $p_{\mathrm{T}}^{Z} > 120$ GeV with 1 b-tag and 3 jets. From left to right: Row 1 - leading then sub-leading jet p_{T} and ΔR of the same two jets. Row 2 - pseudo-continuous MV1c distributions for leading then sub-leading jet and the $\Delta\eta$ of the same two jets. Row 3 - p_{T}^{Z}, m_{jj}, and $m_{\ell\ell}$. Row 4 - $\Delta\phi(V,H)$, $\Delta\eta(V,H)$, and $E_{\mathrm{T}}^{\mathrm{miss}}$. Section 6.1 details the definition of each variable.

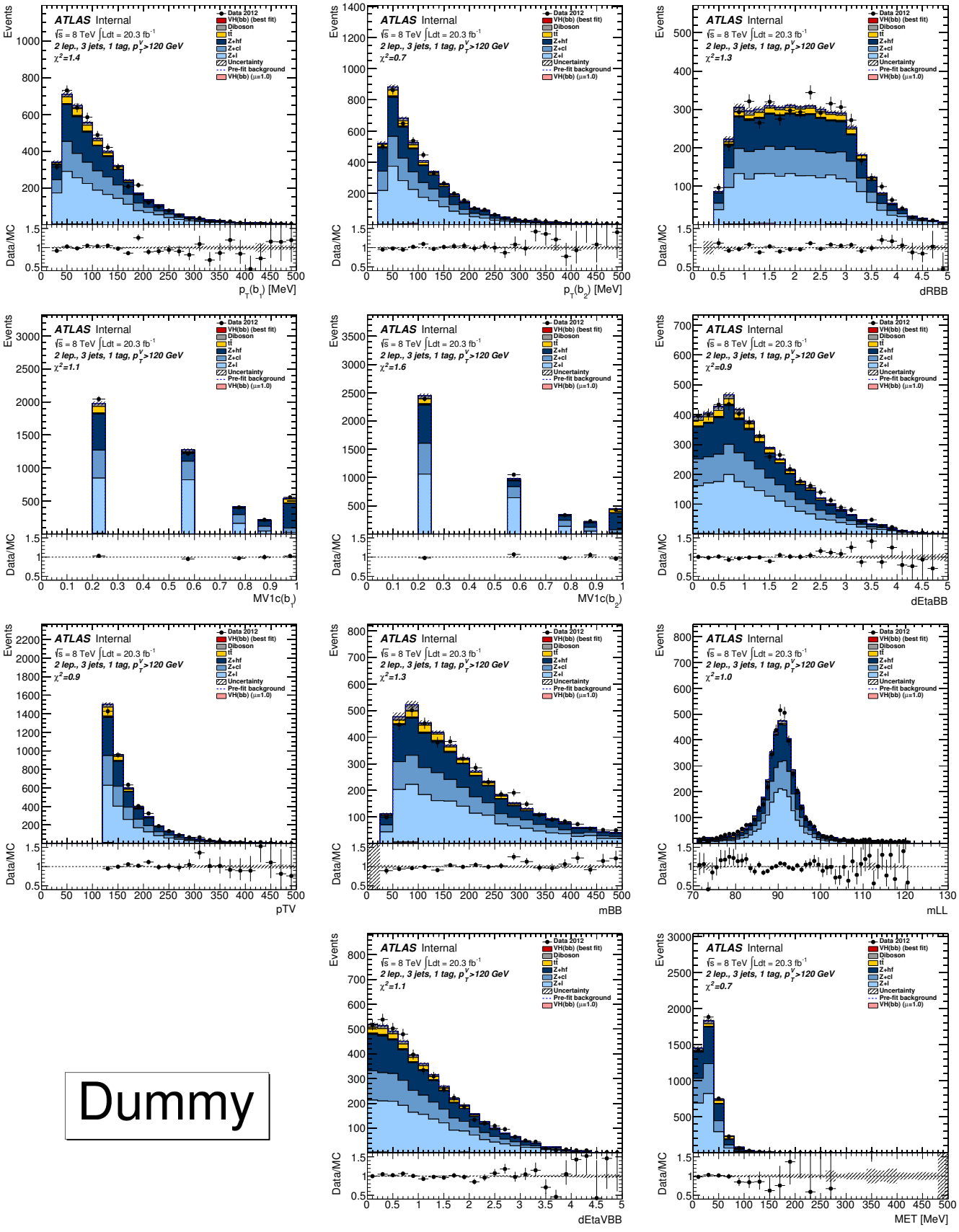

Dummy

Figure 362: Distributions of MVA training variables used in 2-lepton events for $p_{\mathrm{T}}^{Z} > 120$ GeV with 1 b-tag and 3-jets after the combined 0+1+2 lepton MVA fit. From left to right: Row 1 - leading then sub-leading jet p_{T} and ΔR of the same two jets. Row 2 - pseudo-continuous MV1c distributions for leading then sub-leading jet and the $\Delta\eta$ of the same two jets. Row 3 - p_{T}^{Z}, m_{jj}, and $m_{\ell\ell}$. Row 4 - $\Delta\phi(V,H)$, $\Delta\eta(V,H)$, and $E_{\mathrm{T}}^{\mathrm{miss}}$. Section 6.1 details the definition of each variable.

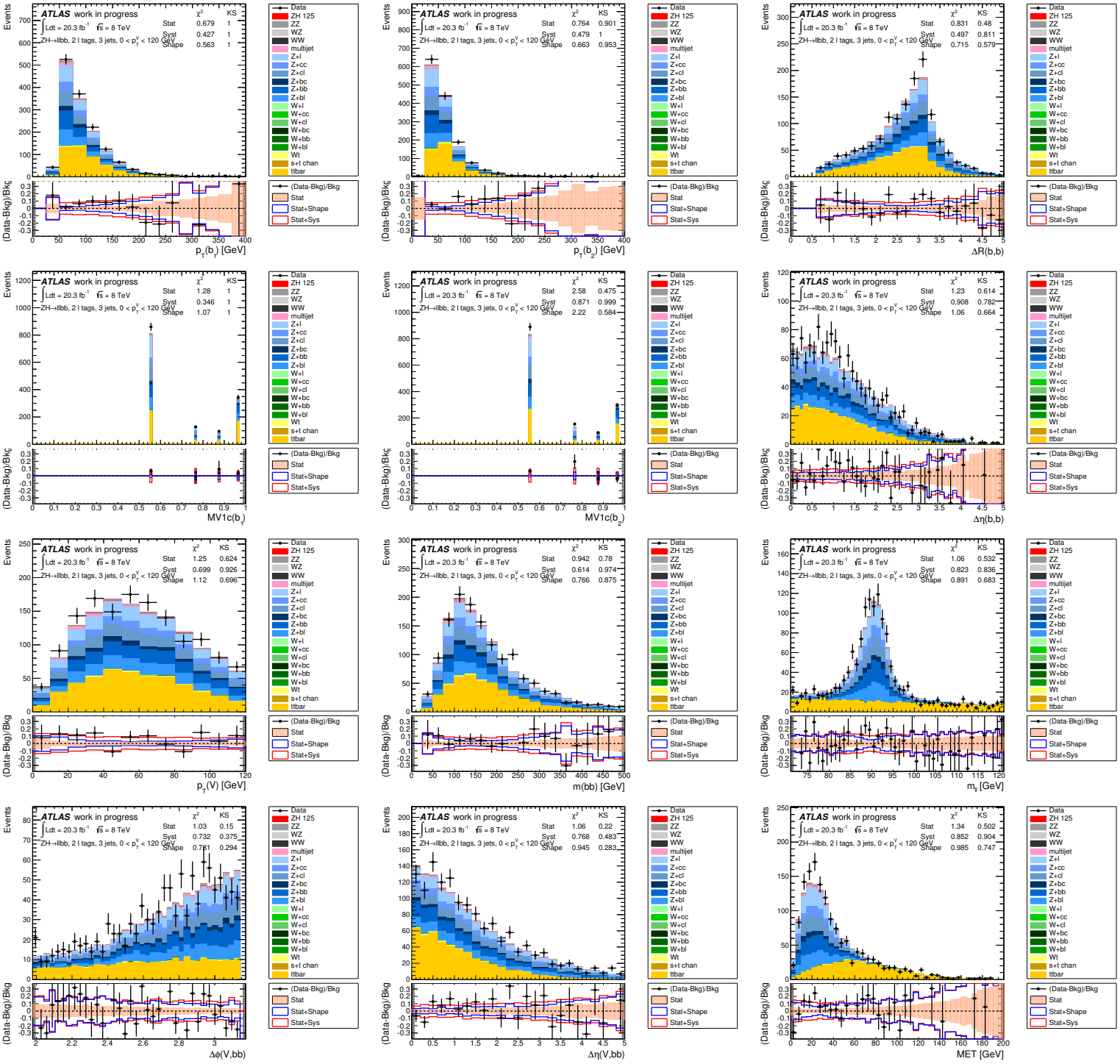

Figure 363: Distributions of MVA training variables used in 2-lepton events for $p_{\mathrm{T}}^{Z} < 120$ GeV with 2 LL b-tags and 3 jets. From left to right: Row 1 - leading then sub-leading jet p_{T} and ΔR of the same two jets. Row 2 - pseudo-continuous MV1c distributions for leading then sub-leading jet and the $\Delta\eta$ of the same two jets. Row 3 - p_{T}^{Z}, m_{jj}, and $m_{\ell\ell}$. Row 4 - $\Delta\phi(V,H)$, $\Delta\eta(V,H)$, and $E_{\mathrm{T}}^{\mathrm{miss}}$. Section 6.1 details the definition of each variable.

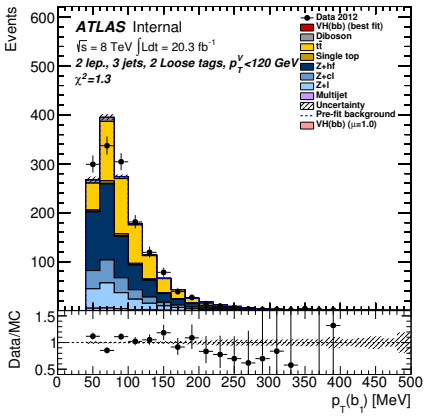

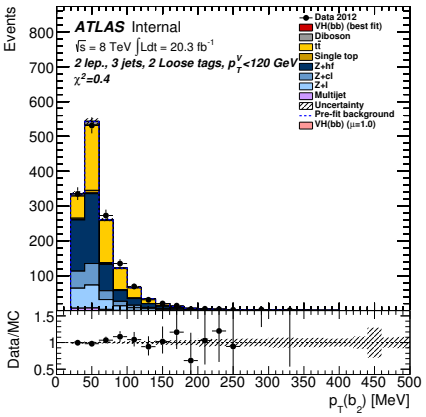

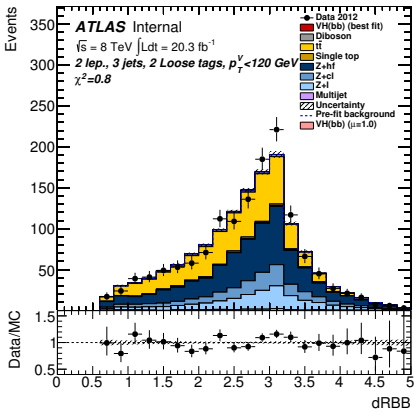

Dummy

Dummy

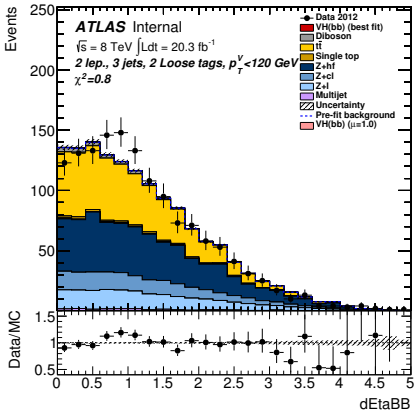

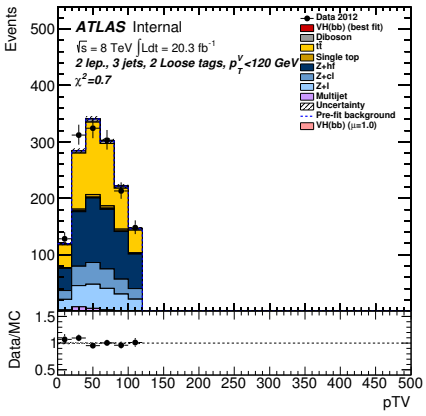

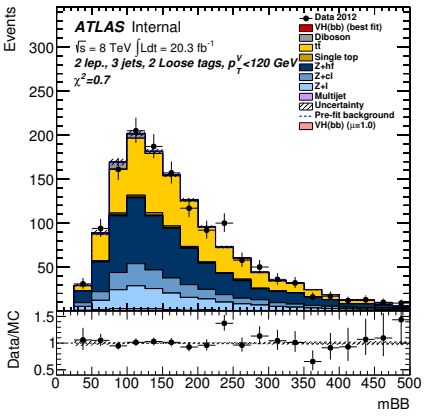

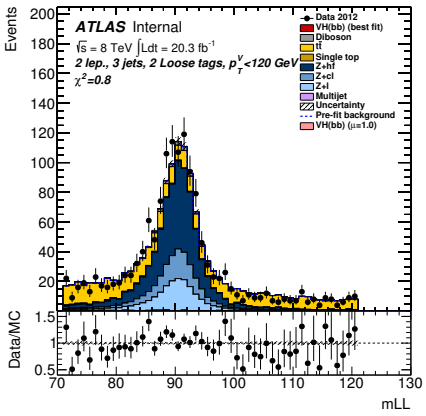

Dummy

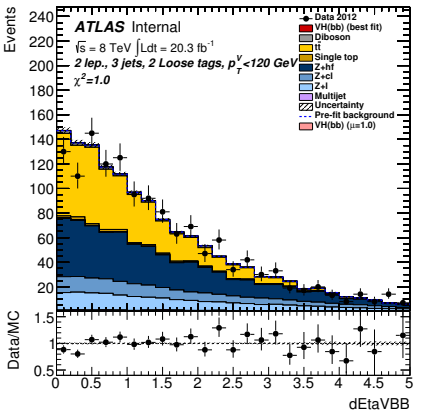

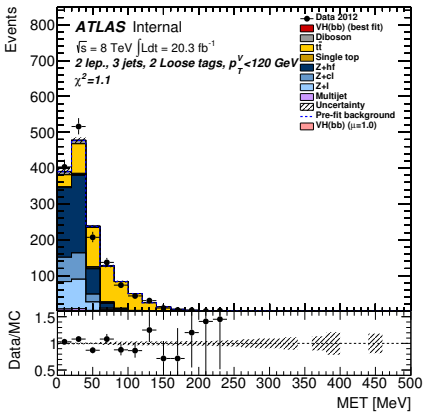

Figure 364: Distributions of MVA training variables used in 2-lepton events for $p_{\mathrm{T}}^{Z} < 120$ GeV with 2 LL b-tags and 3-jets after the combined 0+1+2 lepton MVA fit. From left to right: Row 1 - leading then sub-leading jet p_{T} and ΔR of the same two jets. Row 2 - pseudo-continuous MV1c distributions for leading then sub-leading jet and the $\Delta\eta$ of the same two jets. Row 3 - p_{T}^{Z}, m_{jj}, and $m_{\ell\ell}$. Row 4 - $\Delta\phi(V,H)$, $\Delta\eta(V,H)$, and $E_{\mathrm{T}}^{\mathrm{miss}}$. Section 6.1 details the definition of each variable.

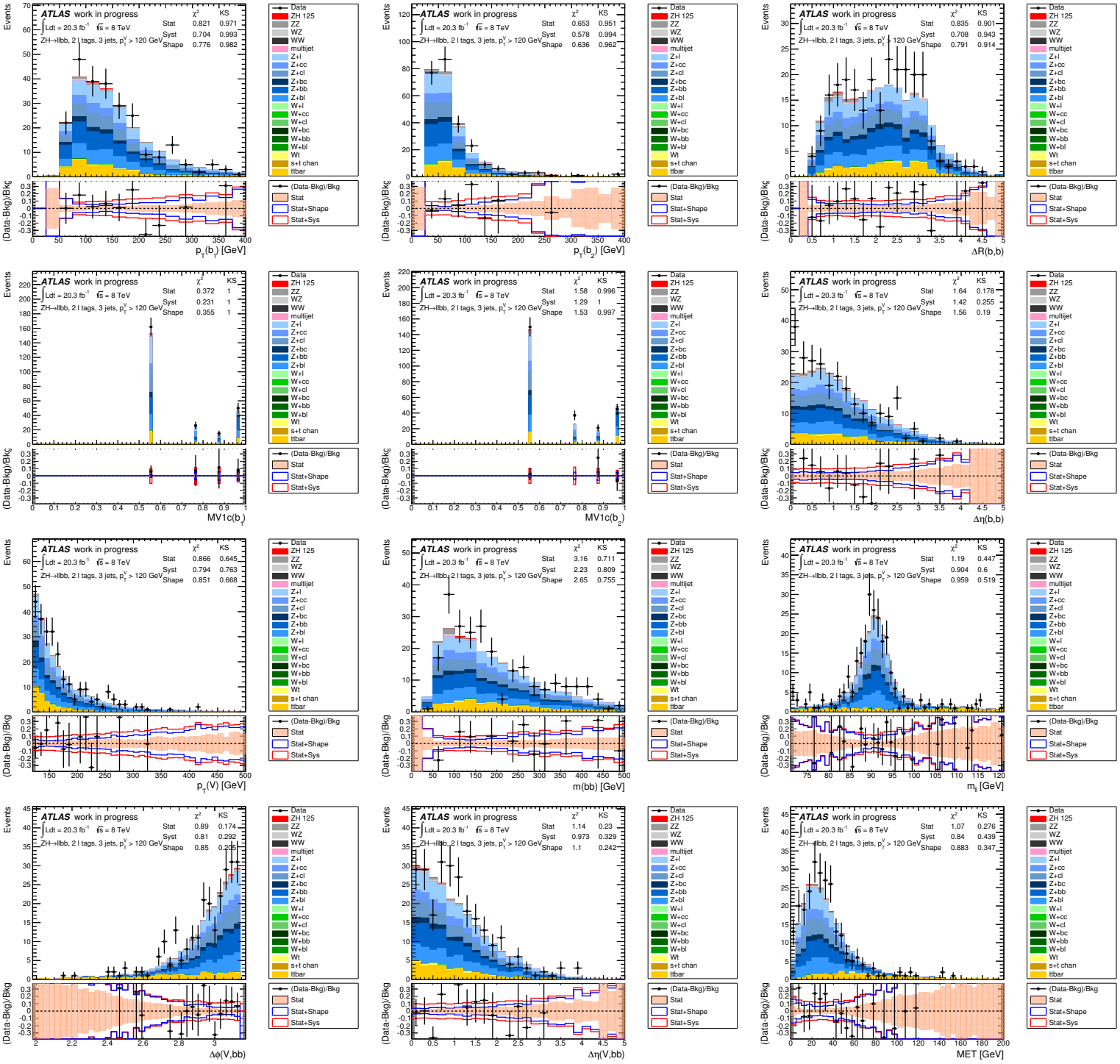

Figure 365: Distributions of MVA training variables used in 2-lepton events for $p_{\mathrm{T}}^{Z} > 120$ GeV with 2 LL b-tags and 3 jets. From left to right: Row 1 - leading then sub-leading jet p_{T} and ΔR of the same two jets. Row 2 - pseudo-continuous MV1c distributions for leading then sub-leading jet and the $\Delta\eta$ of the same two jets. Row 3 - p_{T}^{Z}, m_{jj}, and $m_{\ell\ell}$. Row 4 - $\Delta\phi(V,H)$, $\Delta\eta(V,H)$, and $E_{\mathrm{T}}^{\mathrm{miss}}$. Section 6.1 details the definition of each variable.

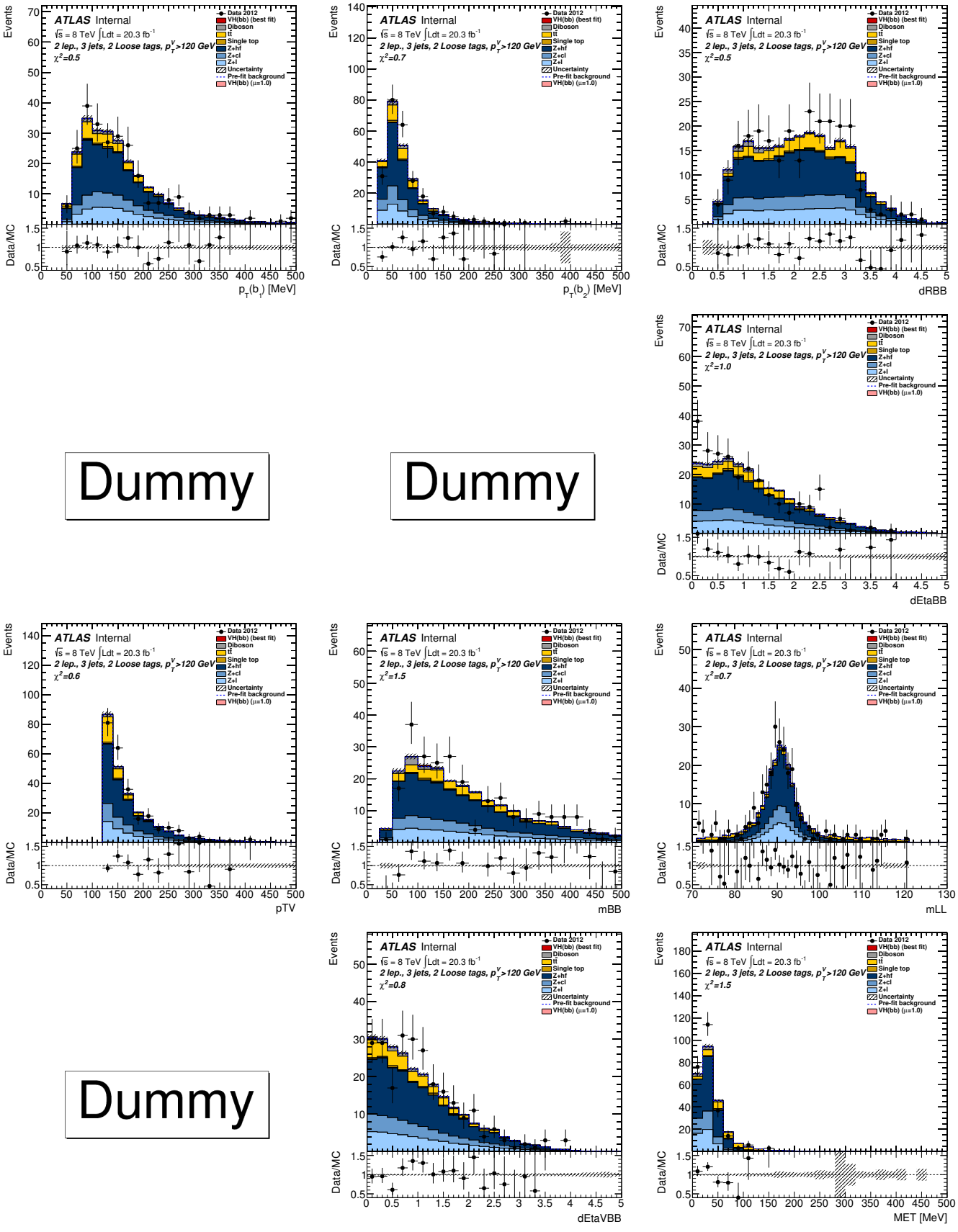

Figure 366: Distributions of MVA training variables used in 2-lepton events for $p_{\mathrm{T}}^{Z} > 120$ GeV with 2 LL b-tags and 3-jets after the combined 0+1+2 lepton MVA fit. From left to right: Row 1 - leading then sub-leading jet p_{T} and ΔR of the same two jets. Row 2 - pseudo-continuous MV1c distributions for leading then sub-leading jet and the $\Delta\eta$ of the same two jets. Row 3 - p_{T}^{Z}, m_{jj}, and $m_{\ell\ell}$. Row 4 - $\Delta\phi(V,H)$, $\Delta\eta(V,H)$, and $E_{\mathrm{T}}^{\mathrm{miss}}$. Section 6.1 details the definition of each variable.

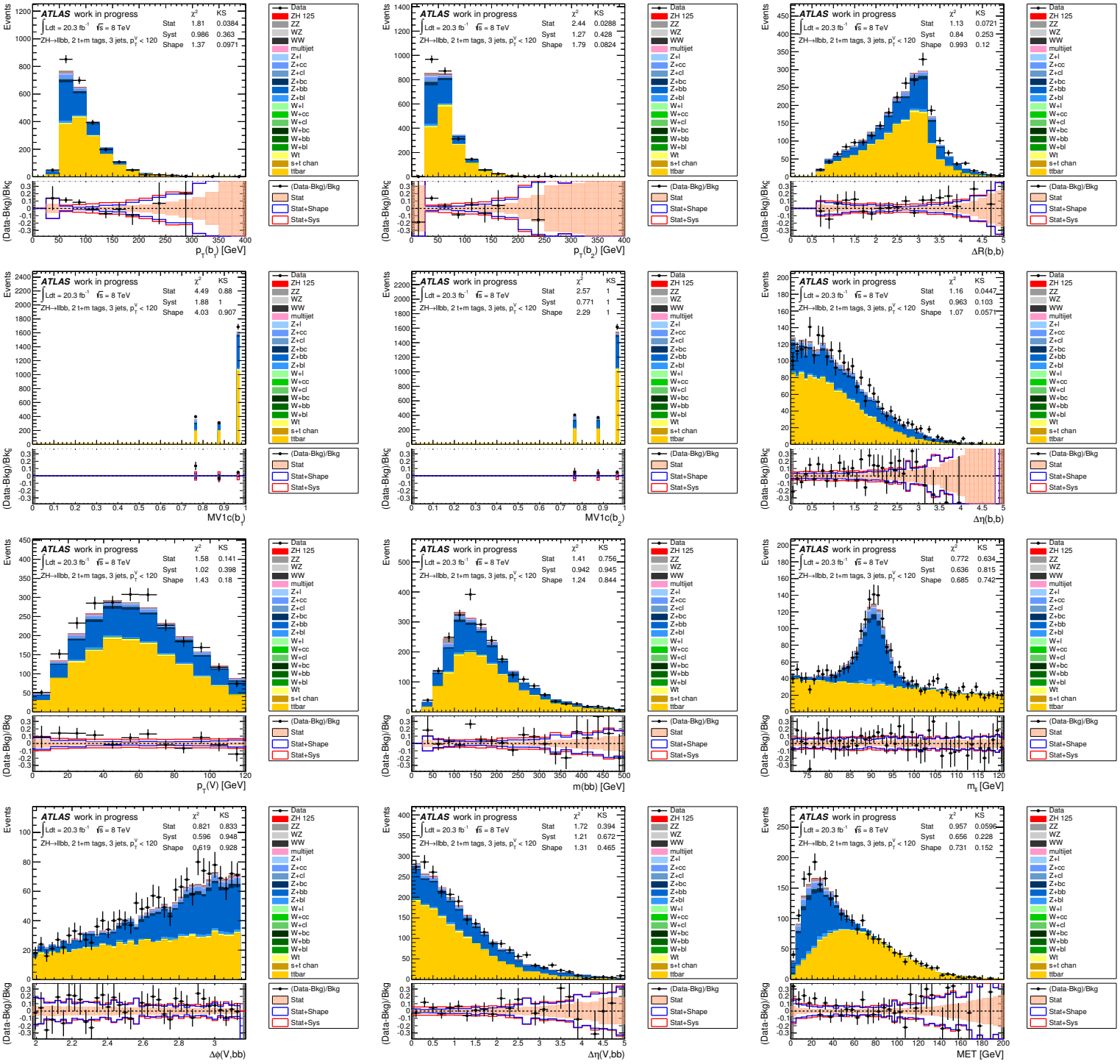

Figure 367: Distributions of MVA training variables used in 2-lepton events for $p_{\mathrm{T}}^{Z} < 120$ GeV with 2 MM+TT b-tags and 3 jets. From left to right: Row 1 - leading then sub-leading jet p_{T} and ΔR of the same two jets. Row 2 - pseudo-continuous MV1c distributions for leading then sub-leading jet and the $\Delta\eta$ of the same two jets. Row 3 - p_{T}^{Z}, m_{jj}, and $m_{\ell\ell}$. Row 4 - $\Delta\phi(V,H)$, $\Delta\eta(V,H)$, and $E_{\mathrm{T}}^{\mathrm{miss}}$. Section 6.1 details the definition of each variable.

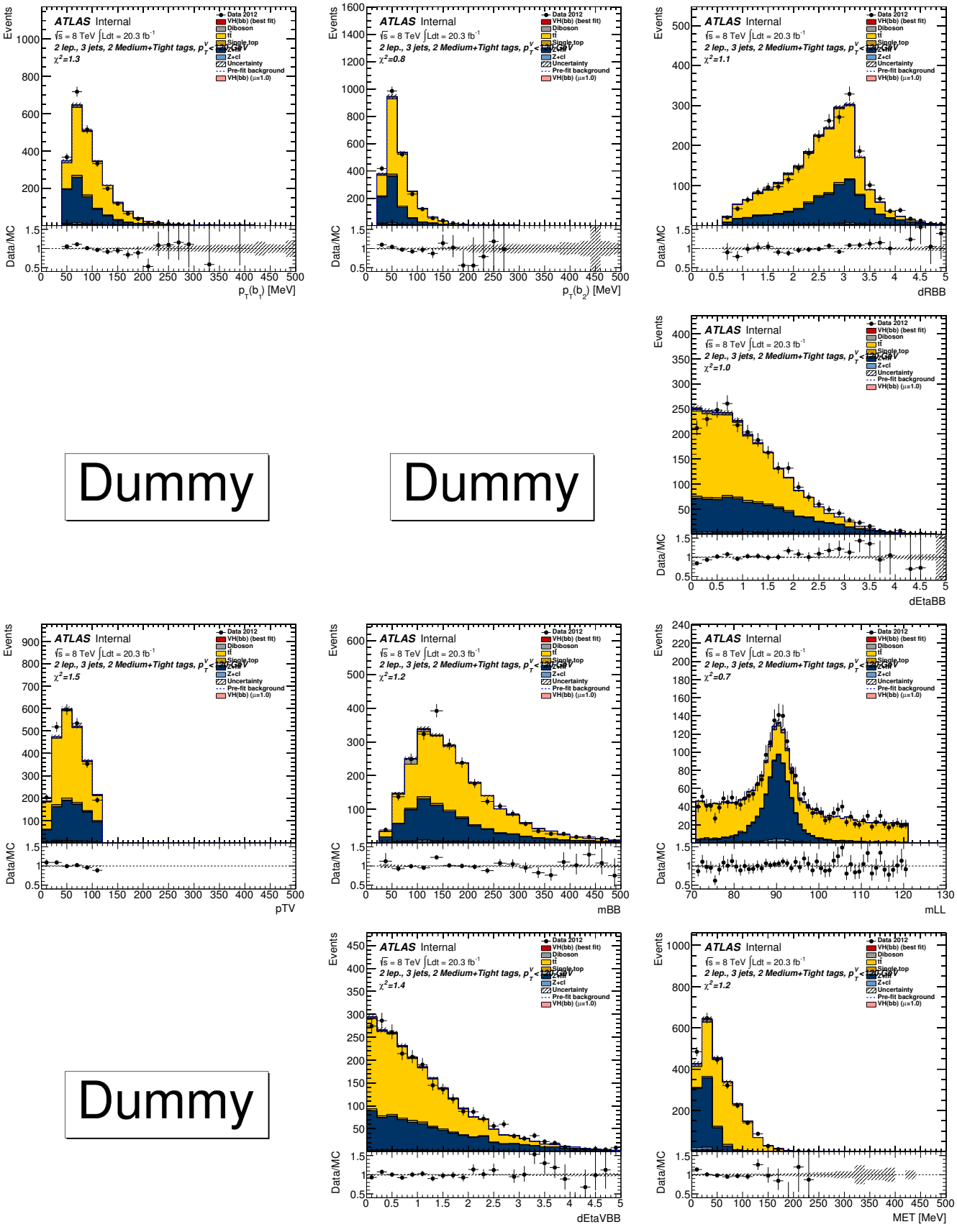

Figure 368: Distributions of MVA training variables used in 2-lepton events for $p_{\mathrm{T}}^{Z} < 120$ GeV with 2 MM+TT b-tags and 3-jets after the combined 0+1+2 lepton MVA fit. From left to right: Row 1 - leading then sub-leading jet p_{T} and ΔR of the same two jets. Row 2 - pseudo-continuous MV1c distributions for leading then sub-leading jet and the $\Delta\eta$ of the same two jets. Row 3 - p_{T}^{Z}, m_{jj}, and $m_{\ell\ell}$. Row 4 - $\Delta\phi(V,H)$, $\Delta\eta(V,H)$, and $E_{\mathrm{T}}^{\mathrm{miss}}$. Section 6.1 details the definition of each variable.

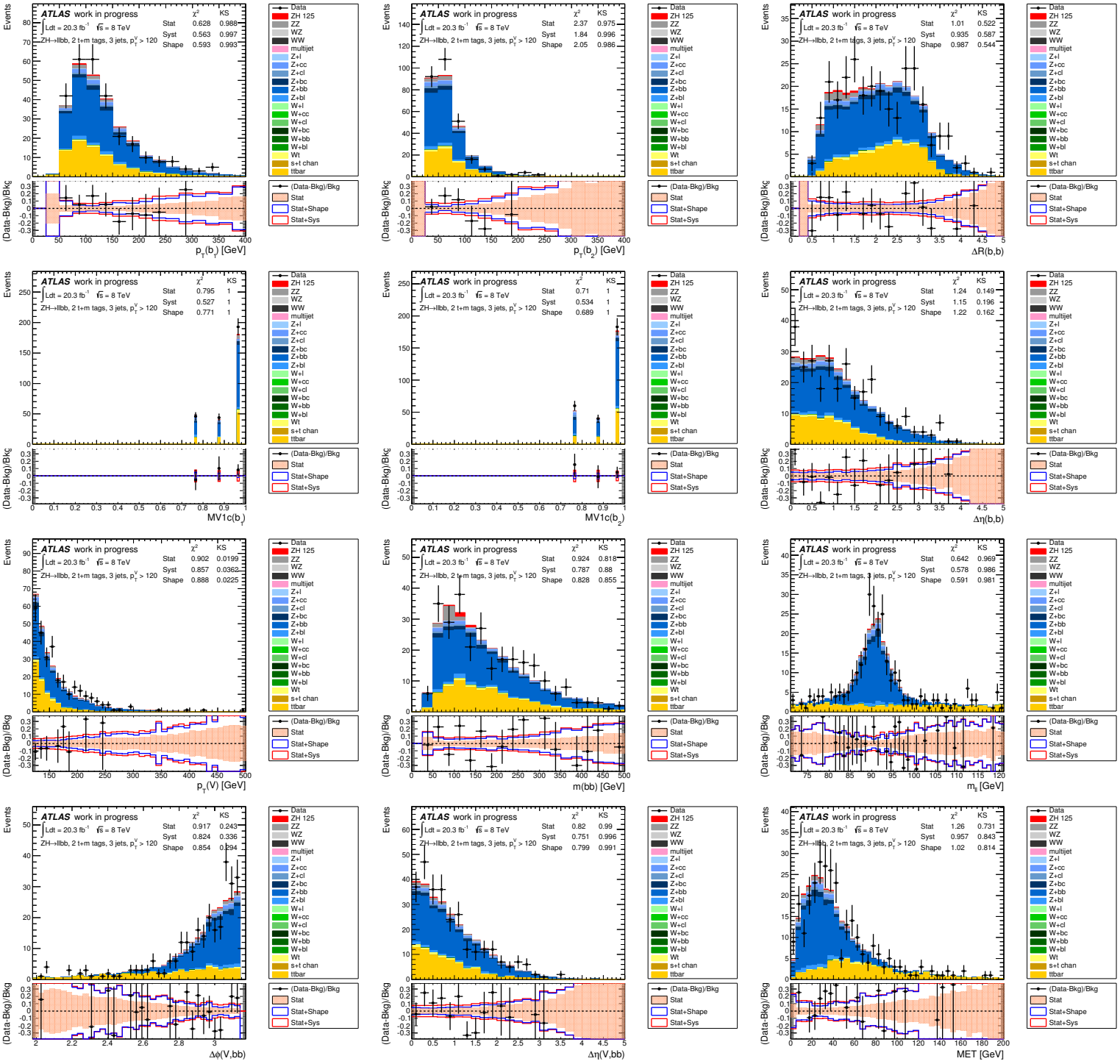

Figure 369: Distributions of MVA training variables used in 2-lepton events for $p_{\mathrm{T}}^{Z} > 120$ GeV with 2 MM+TT b-tags and 3 jets. From left to right: Row 1 - leading then sub-leading jet p_{T} and ΔR of the same two jets. Row 2 - pseudo-continuous MV1c distributions for leading then sub-leading jet and the $\Delta\eta$ of the same two jets. Row 3 - p_{T}^{Z}, m_{jj}, and $m_{\ell\ell}$. Row 4 - $\Delta\phi(V,H)$, $\Delta\eta(V,H)$, and $E_{\mathrm{T}}^{\mathrm{miss}}$. Section 6.1 details the definition of each variable.

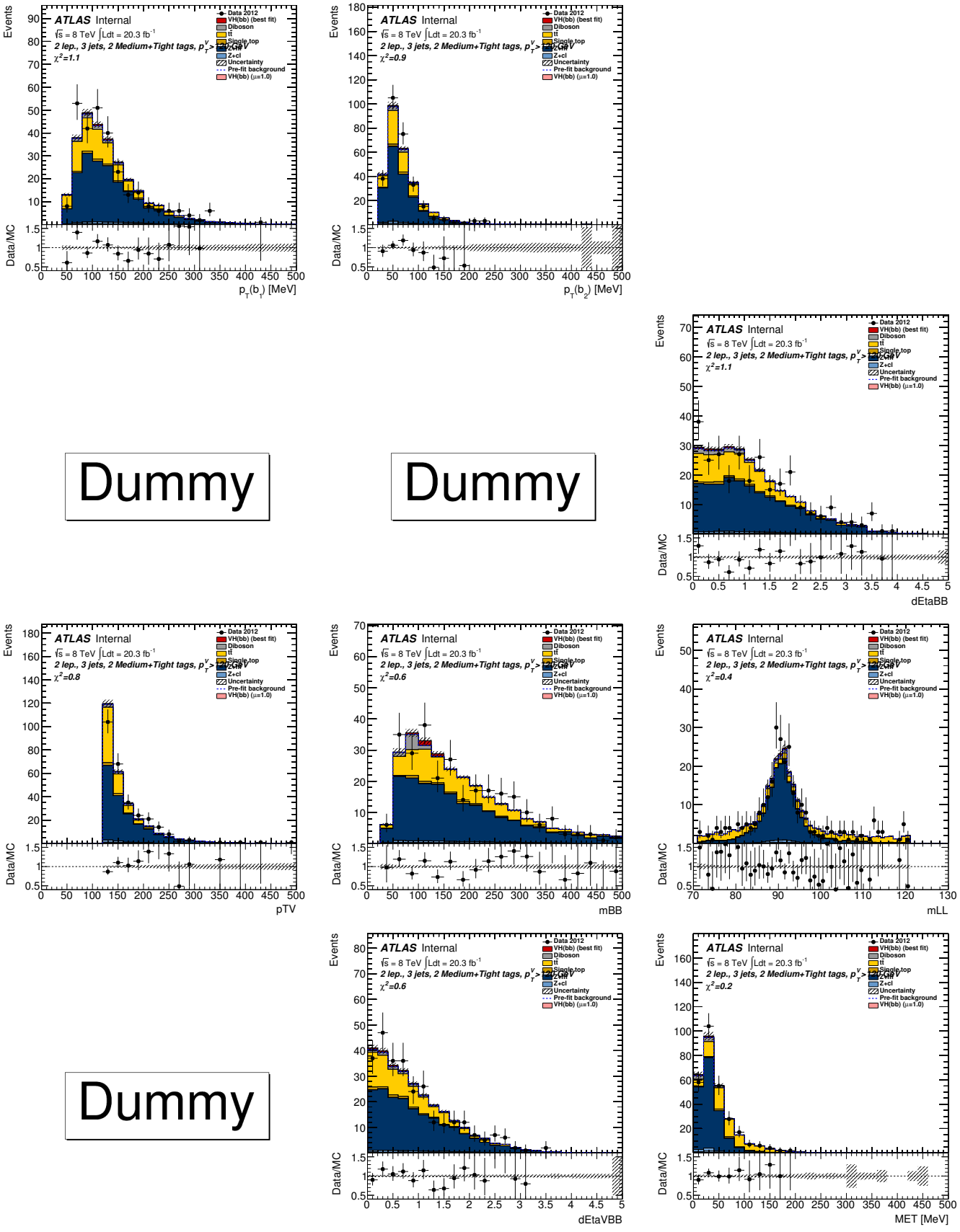

Figure 370: Distributions of MVA training variables used in 2-lepton events for $p_{\mathrm{T}}^{Z} > 120$ GeV with 2 MM+TT b-tags and 3-jets after the combined 0+1+2 lepton MVA fit. From left to right: Row 1 - leading then sub-leading jet p_{T} and ΔR of the same two jets. Row 2 - pseudo-continuous MV1c distributions for leading then sub-leading jet and the $\Delta\eta$ of the same two jets. Row 3 - p_{T}^{Z}, m_{jj}, and $m_{\ell\ell}$. Row 4 - $\Delta\phi(V,H)$, $\Delta\eta(V,H)$, and $E_{\mathrm{T}}^{\mathrm{miss}}$. Section 6.1 details the definition of each variable.

AB MVA Training Diagnostics

This section contains diagnostic plots for the mva training. The layout is identical in the following pages. The input variables shown first with the signal in red and background in blue both normalized to the same integral. This is followed by the background (signal) correlation matrix on the left (right). Finally an overtraining check is shown with the corresponding KS test values. As noted in Section 6.2.3 the total statistics are divided into sample A and B for training and evaluation. Only diagnostic plots from sample A are shown to conserve space. No large differences have been seen between the two sets.
Figures 371 to 372 are for the 0-lepton $m_H = 125$ GeV training.
Figures 373 to 374 are for the 1-lepton $m_H = 125$ GeV training.
Figures 377 to 378 are for the 2-lepton $m_H = 125$ GeV training.

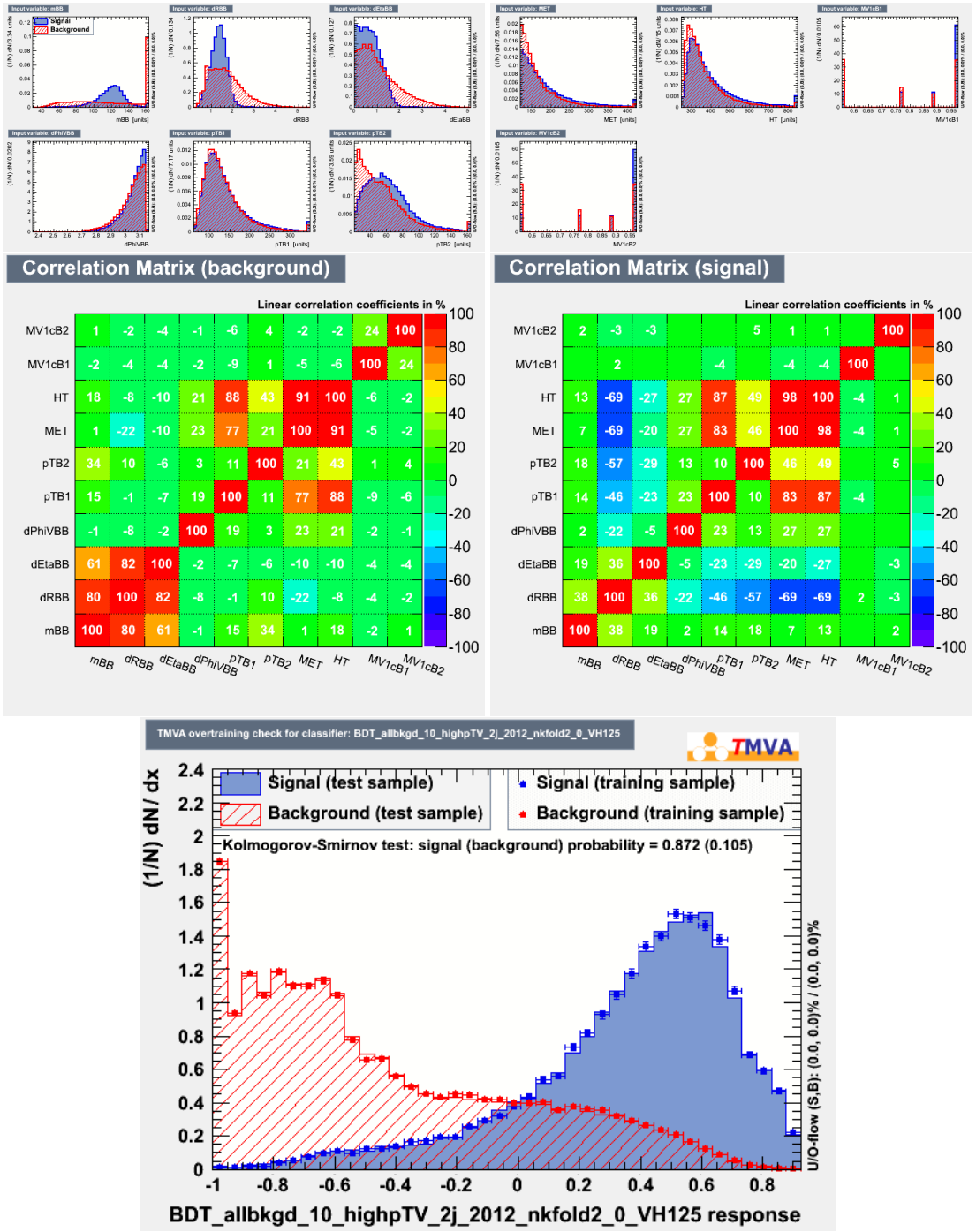

Figure 371: Zero Lepton analysis, 2 jets final state p_{T}^{V}> 120 GeV. Training variables distributions and correlations for the sum of the backgrounds and for the signal in sample A. The overtraining have been evaluated in the plot on the bottom.

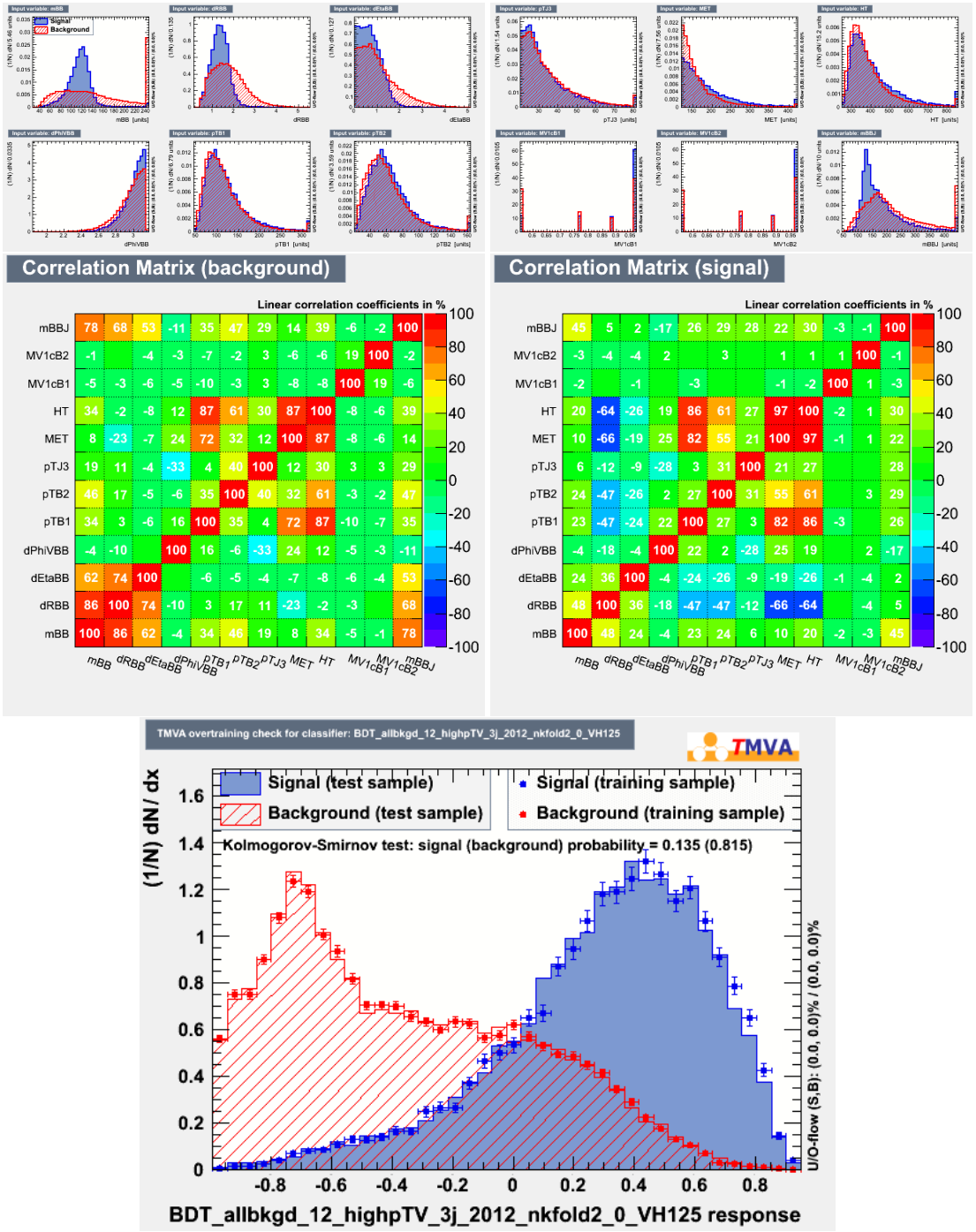

Figure 372: Zero Lepton analysis, 3 jets final state p_{T}^{V}> 120 GeV. Training variables distributions and correlations for the sum of the backgrounds and for the signal in sample A. The overtraining have been evaluated in the plot on the bottom.

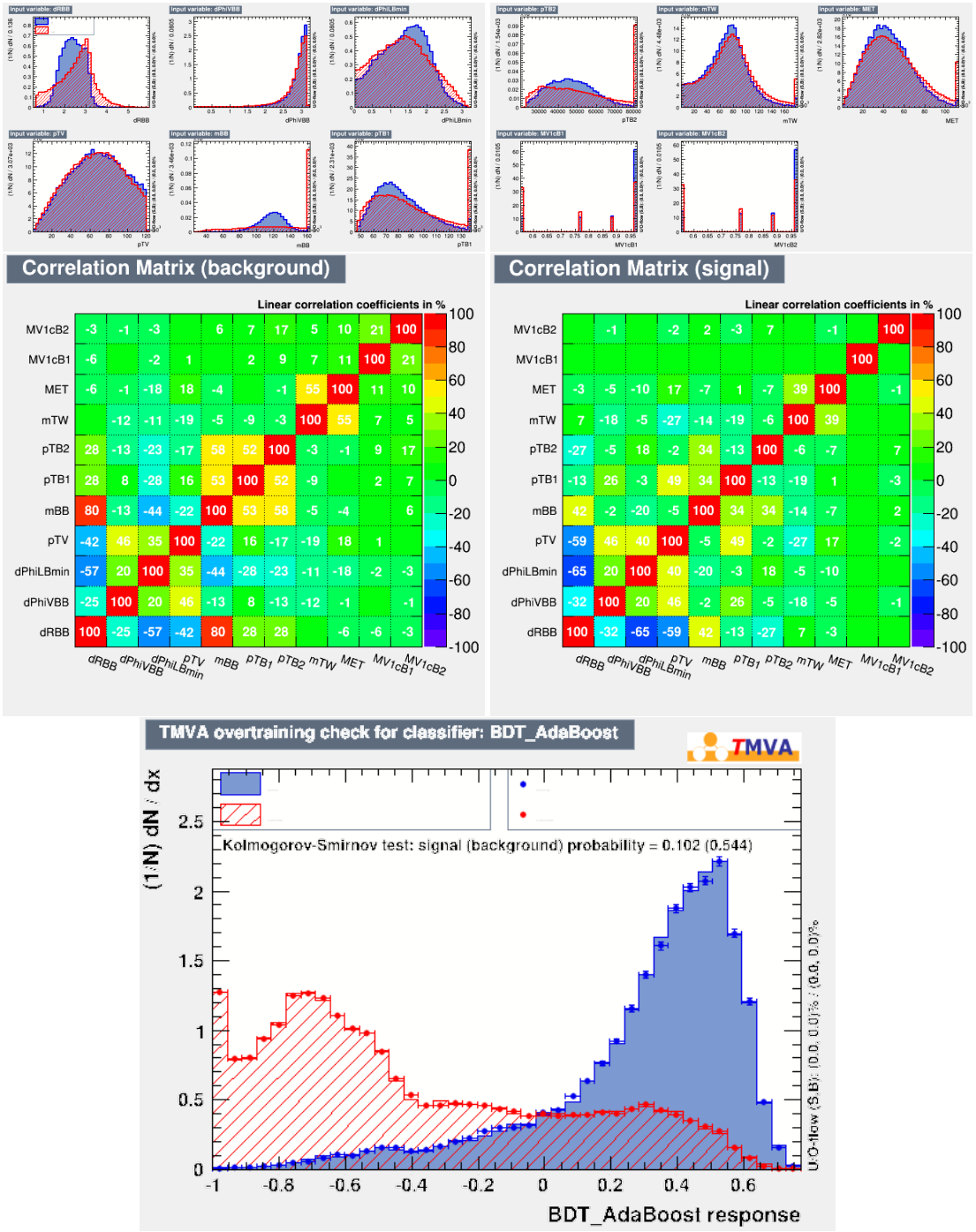

Figure 373: One Lepton analysis, 2 jets final state p_{T}^{V}< 120 GeV. Training variables distributions and correlations for the sum of the backgrounds and for the signal in sample A. The overtraining have been evaluated in the plot on the bottom.

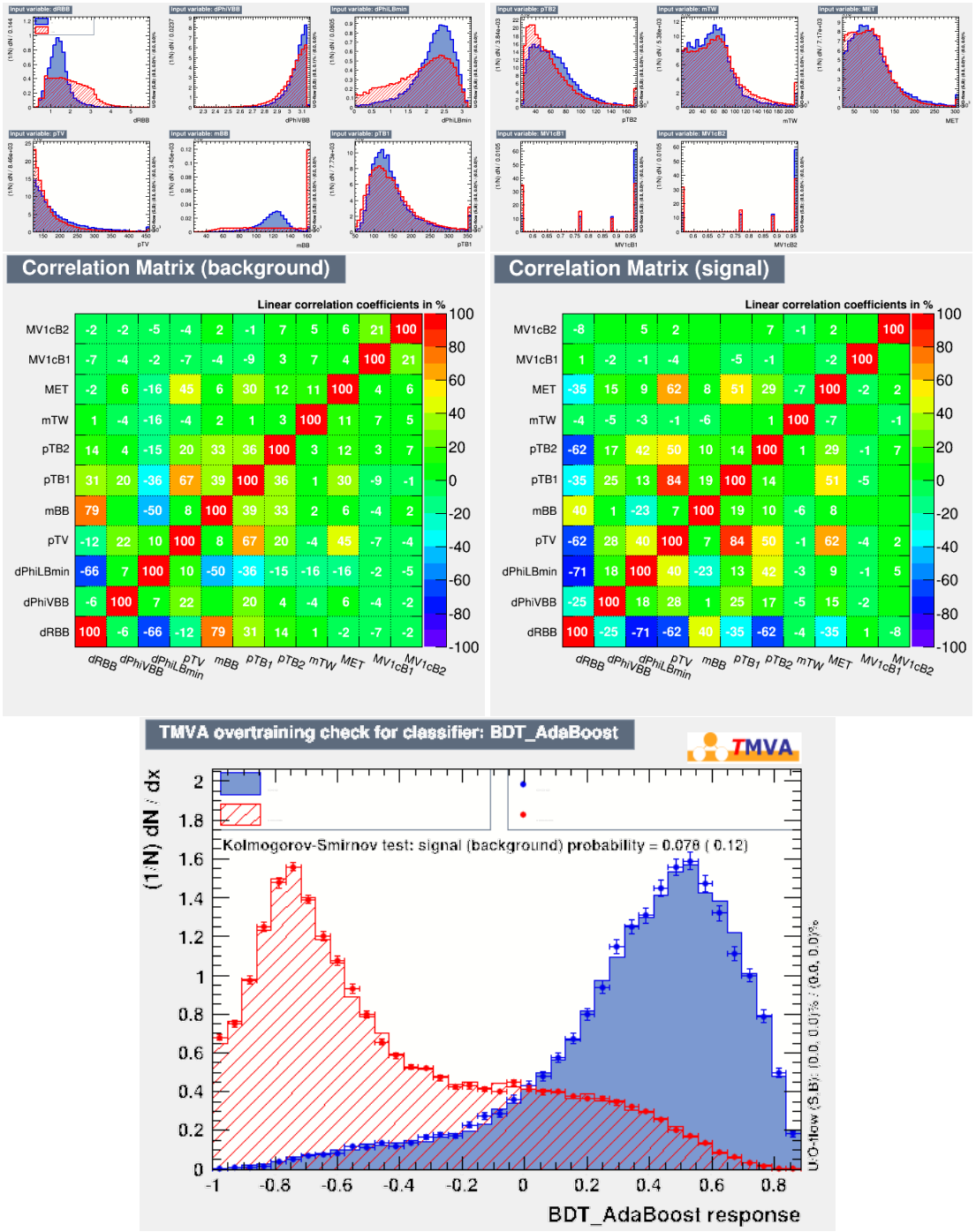

Figure 374: One Lepton analysis, 2 jets final state p_{T}^{V}> 120 GeV. Training variables distributions and correlations for the sum of the backgrounds and for the signal in sample A. The overtraining have been evaluated in the plot on the bottom.

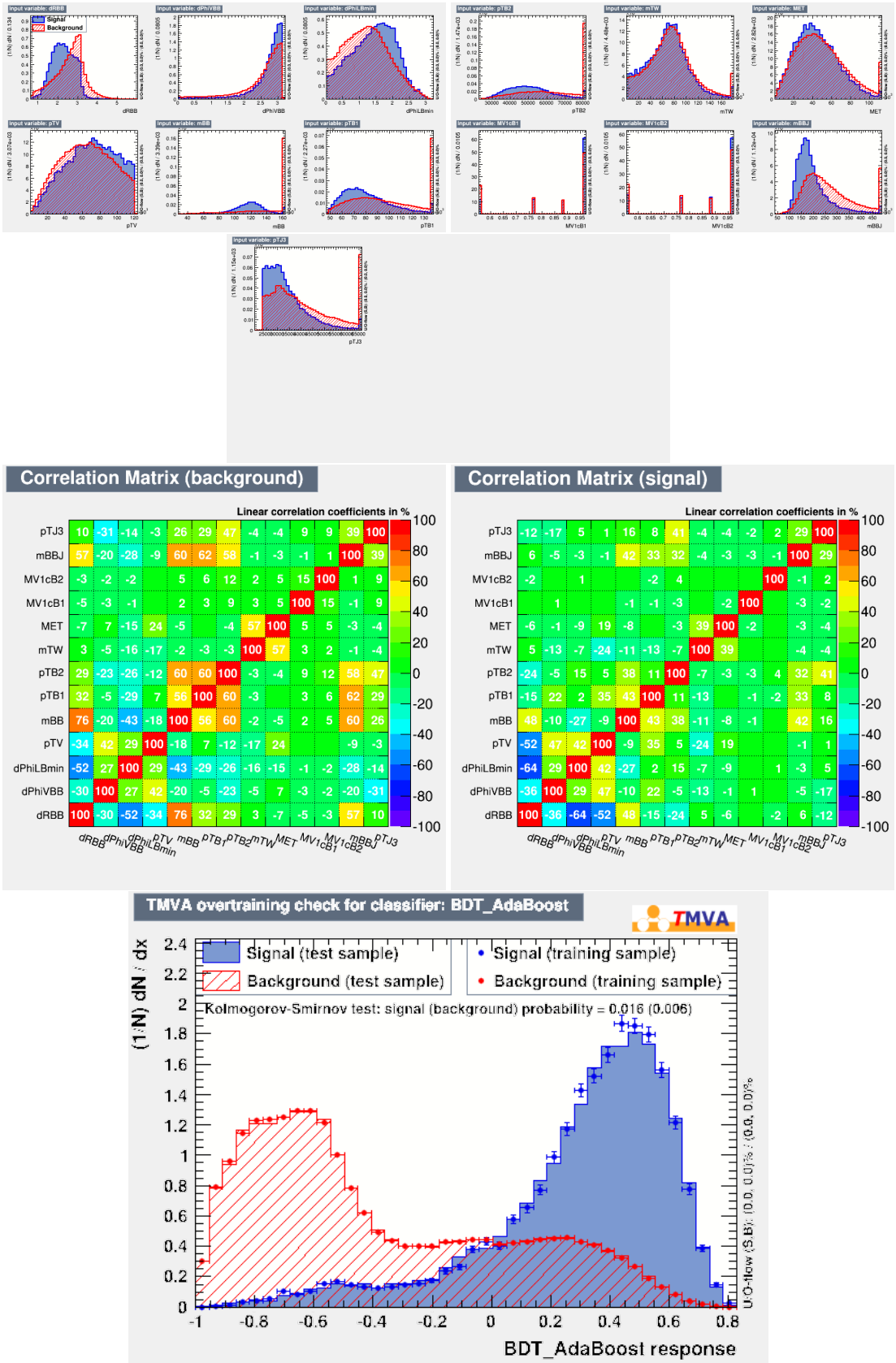

Figure 375: One Lepton analysis, 3 jets final state p_{T}^{V}< 120 GeV. Training variables distributions and correlations for the sum of the backgrounds and for the signal in sample A. The overtraining have been evaluated in the plot on the bottom.

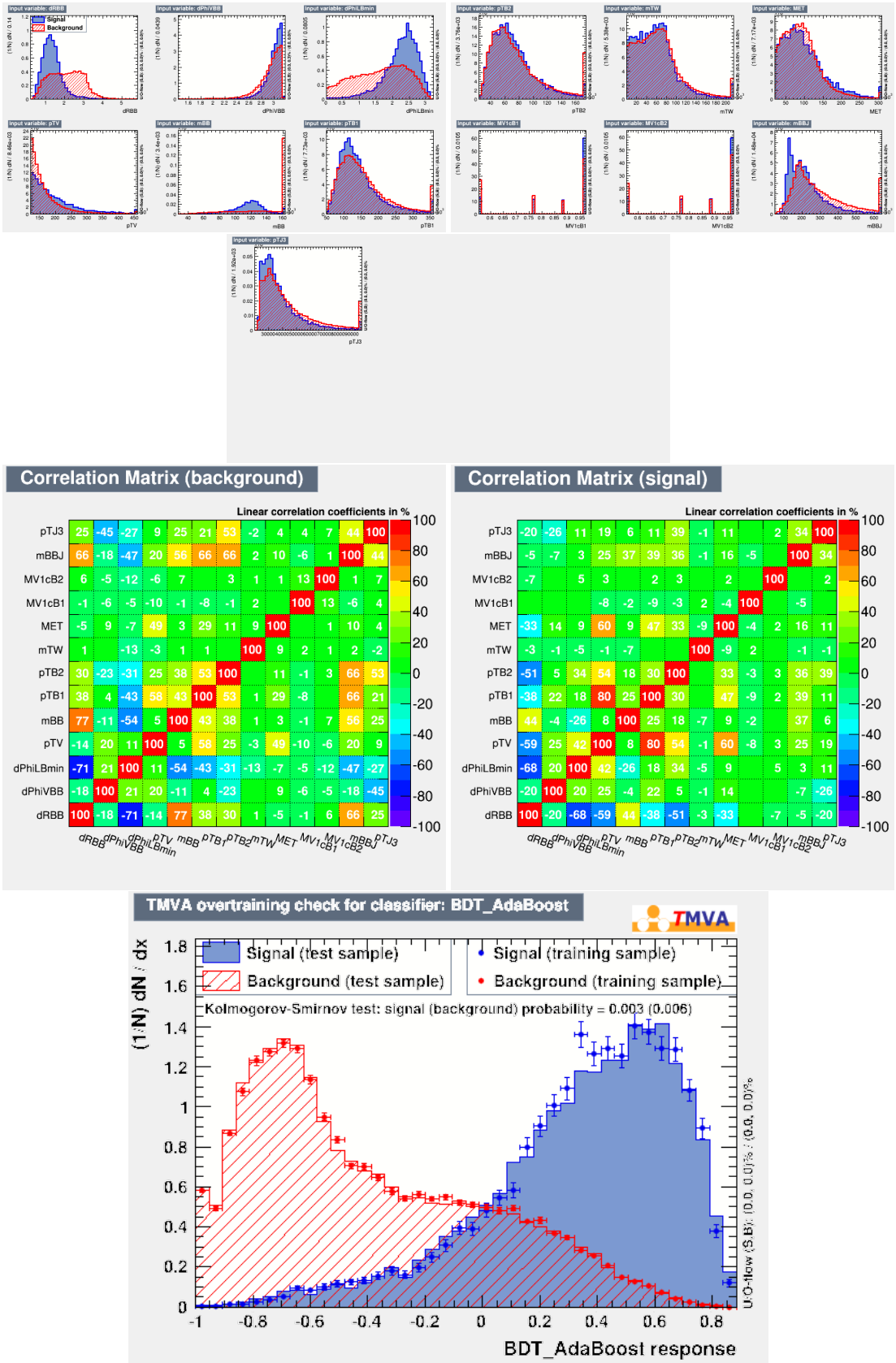

Figure 376: One Lepton analysis, 3 jets final state p_{T}^{V}> 120 GeV. Training variables distributions and correlations for the sum of the backgrounds and for the signal in sample A. The overtraining have been evaluated in the plot on the bottom.

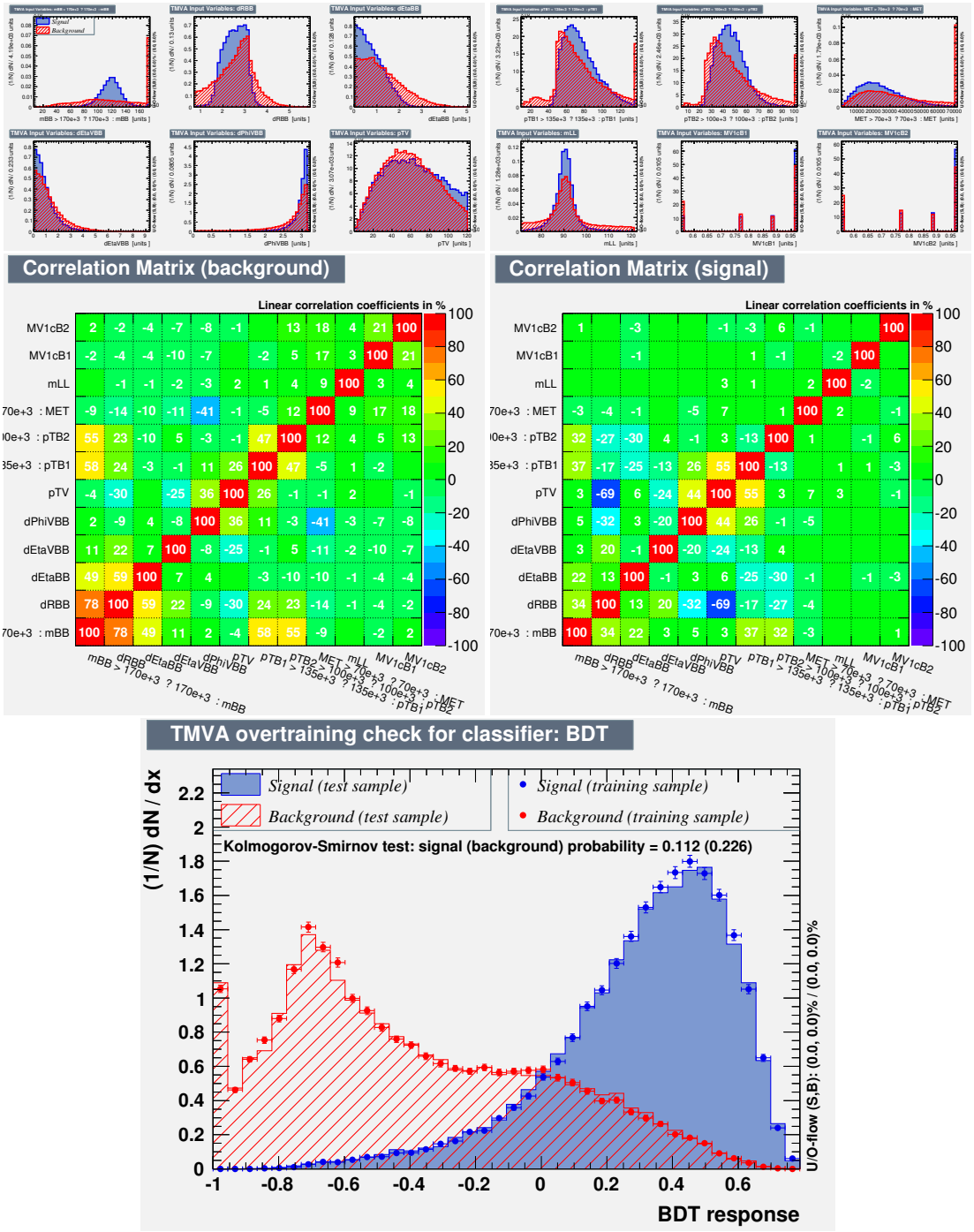

Figure 377: Two Leptons analysis, 2 jets final state p_{T}^{V}< 120 GeV. Training variables distributions and correlations for the sum of the backgrounds and for the signal in sample A. The overtraining have been evaluated in the plot on the bottom.

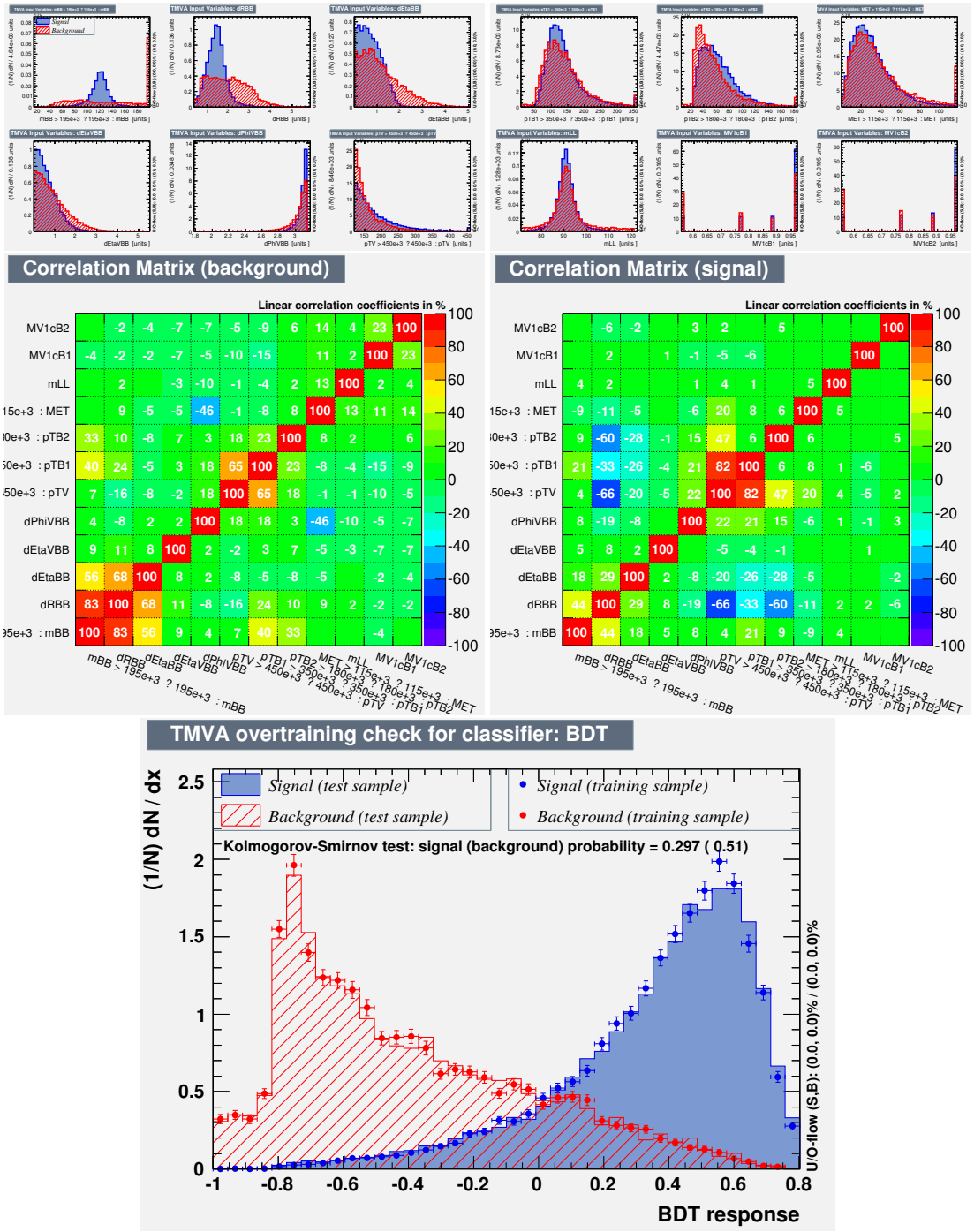

Figure 378: Two Lepton analysis, 2 jets final state p_{T}^{V}> 120 GeV. Training variables distributions and correlations for the sum of the backgrounds and for the signal in sample A. The overtraining have been evaluated in the plot on the bottom.

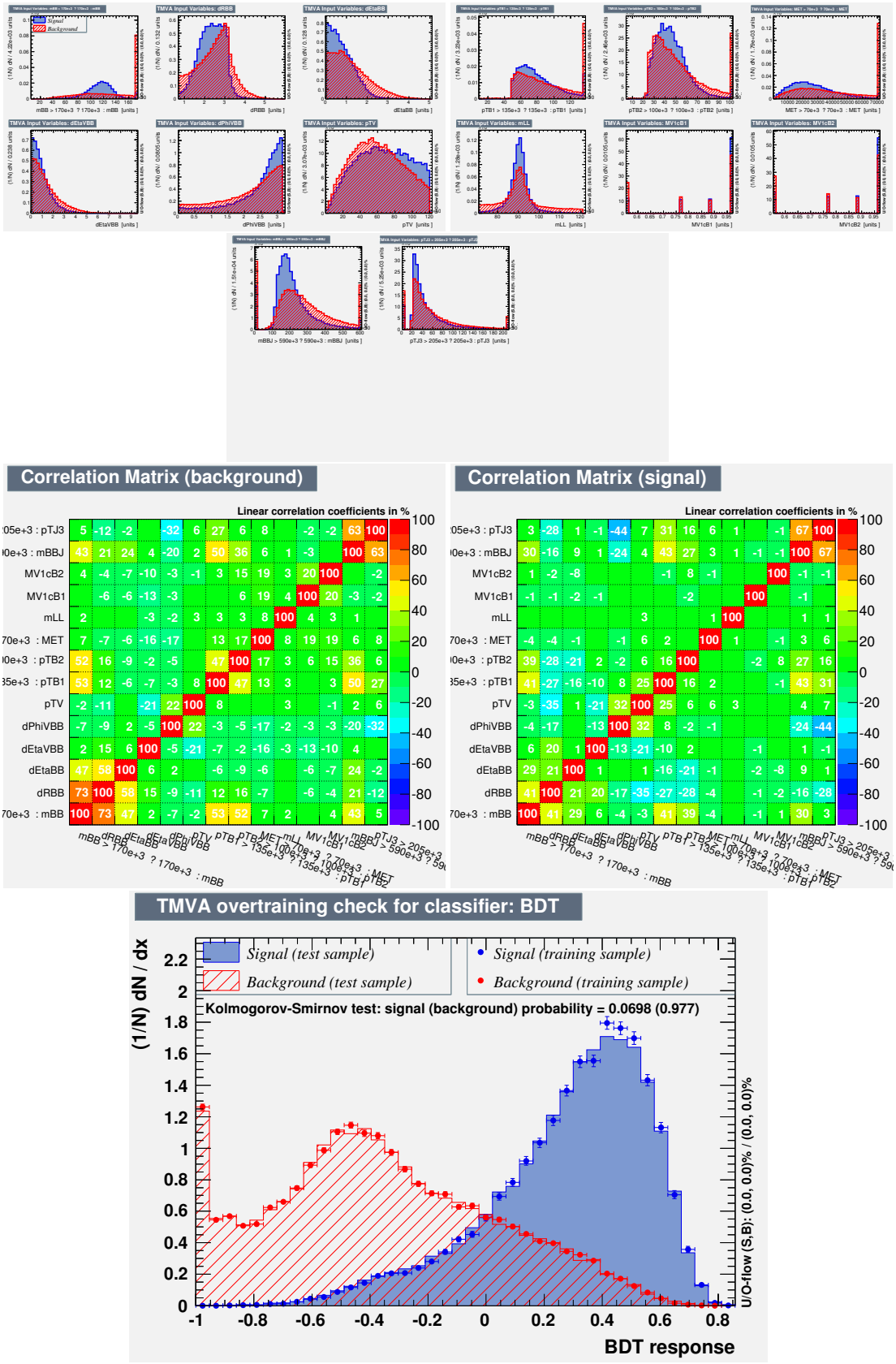

Figure 379: Two Leptons analysis, 3 jets final state p_{T}^{V}< 120 GeV. Training variables distributions and correlations for the sum of the backgrounds and for the signal in sample A. The overtraining have been evaluated in the plot on the bottom.

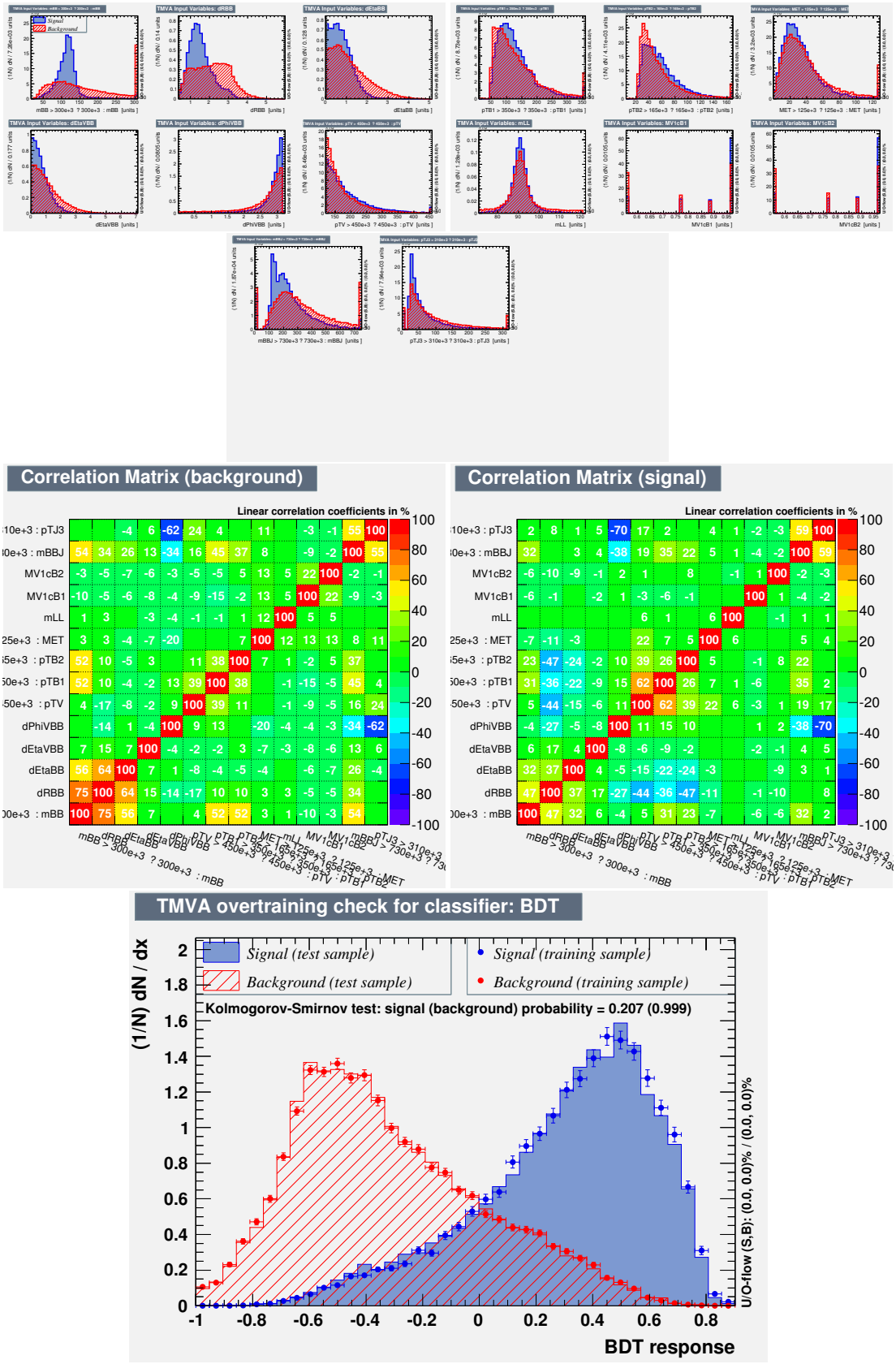

Figure 380: Two Leptons analysis, 3 jets final state p_{T}^{V}> 120 GeV. Training variables distributions and correlations for the sum of the backgrounds and for the signal in sample A. The overtraining have been evaluated in the plot on the bottom.

AC MVA optimization and the transformation D

As described in Section 8.4, the transformation D have been optimize for the MVA analisis, and this appendix contains the dexcription of the these studies. This can be useful as reference for future studies, and in to read some of the plots in the note, in case they result to be done with this transformation.

For the MVA analysis, a first study defined the working point (z_s, z_b)=(6,6) as a good starting point for additional optimizations. From this working point, the values for z_s and z_b have been redefined for each of the the multi-variate analysis region following the formula:

$$z_s = f_{tags} \times f_{jets} \times f_{p_{\mathrm{T}}^V} \times f_{leptons} \times \zeta_s \tag{44}$$

$$z_b = f_{tags} \times f_{jets} \times f_{p_{\mathrm{T}}^V} \times f_{leptons} \times \zeta_b \tag{45}$$

where each term have been optimized in a sequence. By keeping all the other f parameters equal to 1, $\zeta_s = \zeta_b = 6$, and fixing the total number of bins, the impact of the fraction of bins in the different tagging categories (LL VS. MM+TT for 0 and 2 leptons, LL VS. MM VS. TT for 1 lepton) have been studied by changing the parameter f_{tags}. Once the best working point for the parameter f_{tags} was obtained, the optimization strategy moved to the fraction of bins in the 2-jet category versus 3-jet category (f_{jets}), then to the fraction of bins in the low p_{T}^V versus the high p_{T}^V region ($f_{p_{\mathrm{T}}^V}$), and finally to the fraction of bins in the 3 lepton categories ($f_{leptons}$). In each step of the sequence, the optimized value of the parameters studies in the previous steps have been used. For each step, the expected limit as a function of the parameter of interest is shown in Figures 381. Finally, the optimal values for the 2 parameters ζ_s, ζ_b have been reevaluated to be $\zeta_s = 6$ and $\zeta_b = 4$. The complete list of parameters can be found in Table 115. This output transform reduced the number of bins by almost 60% with a degradation of less than 1% in the final significance.

As an example, one of the MVA distributions, before and after the transform can be seen in Figure 382 The MVA output distributions are all contained in Appendix AD showing both the original shape with a reduced number of bins and the transformed output.

Parameter	Description	N leptons	Tag	N Jets	p_{T}^V region	value
f_{tags}	fractions in the different tagging regions	0,2	LL	2,3	low and high p_{T}^V	0.6
			MM+TT			1.4
		1	LL			0.2
			MM			0.9
			TT			0.9
f_{jets}	fractions in the different jet categories	0,1,2	LL,MM,TT	2	low and high p_{T}^V	0.8
				3		1.2
$f_{p_{\mathrm{T}}^V}$	fractions in low and high p_{T}^V	1,2	LL,MM,TT	2,3	low p_{T}^V	0.6
					high p_{T}^V	1.4
$f_{leptons}$	fractions in the different lepton categories	0	LL,MM,TT	2,3	low and high p_{T}^V	0.9
		1				1.2
		2				0.9
$\zeta_s = 6$	weight for the signal	0,1,2	LL,MM,TT	2,3	low and high p_{T}^V	6
$\zeta_b = 4$	weight for the background	0,1,2	LL,MM,TT	2,3	low and high p_{T}^V	4

Table 115: Binning optimization for the cut based analysis

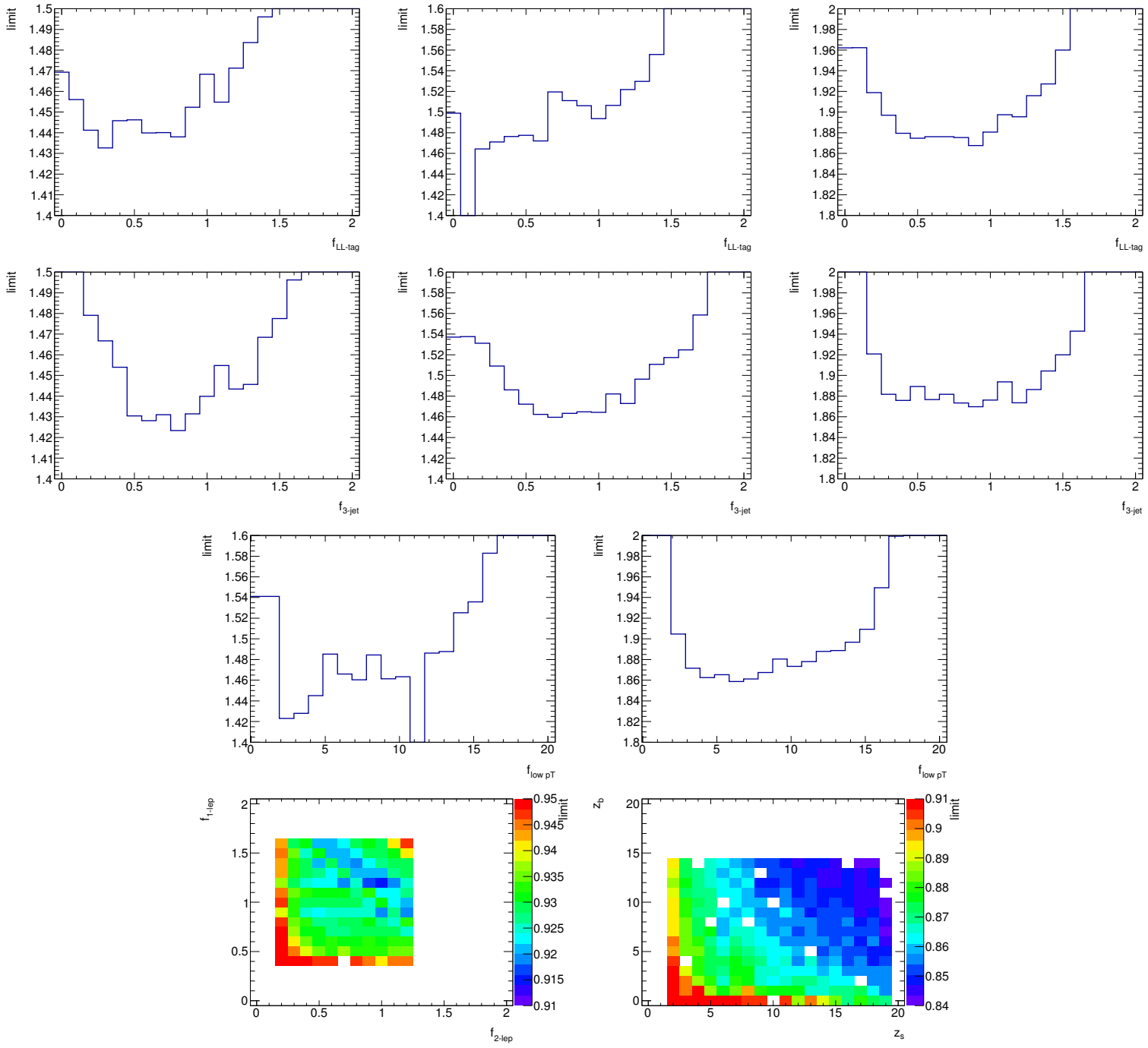

Figure 381: Dependence of the expected limit as a function of the f parameters.From the left to the right: Row 1 - Expected limit dependence on f_{tags} for 0,1 and 2 leptons. Row 2 - Expected limit dependence on f_{jets} for 0,1 and 2 leptons. Row 3 - Expected limit dependence on $f_{p_{\mathrm{T}}^V}$ for 1 and 2 leptons. Row 4 - 2D Expected limit dependence on the fraction of bins in 1 lepton and 2 leptons, and 2D Expected limit dependence on ζ_s, ζ_b.

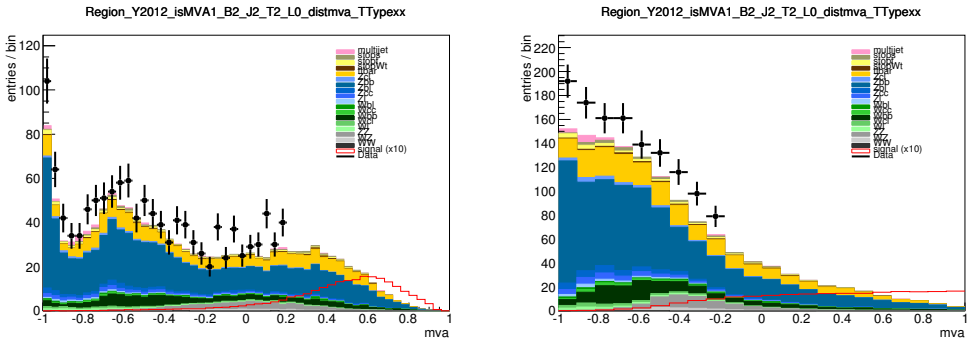

Figure 382: Example of the effect of the binning transform on the MVAoutput for one of the signal regions. Left: before the binning transform; Right: After the binning Transform.

AD MVA Distributions

This appendix contains the MVA distributions for low and high p_{T}^{V} regions ($p_{\mathrm{T}}^{V} < 120$ GeV and $p_{\mathrm{T}}^{V} > 120$ GeV respectively) for the $m_H = 125$ GeV training. When leptons are selected, the electron and muon events have been combined. The MVA configuration is detailed in Section 6 and the input variable distributions are show in Appendix Y, Z, and AA for the 0, 1, and 2 lepton selections respectively. The binning strategy discussed in Section 8.4 has not been applied in these plots. Note the the 0-lepton selection only included events with $p_{\mathrm{T}}^{Z} > 120$ GeV in the MVA analysis. These plots are done by applying the latest scale factors, obtained for the 2 jet region and the 3 jet region separately, by comparing the event yield before and after the MVA combined fit. They are summarized in Table 114. Explicitly stated, the theoretical expectation for each background is used for the given luminosity. All the plots in this section are done with the status-of-art analysis.

Zero Lepton BDT distributions are shown in Figures 383, 384 before the transformation discussed in Section 8.4. One Lepton low p_{T}^{W} ($p_{\mathrm{T}}^{W} < 120$ GeV) BDT distributions are shown in Figures 385, 386 before the transformation discussed in Section 8.4. One Lepton high p_{T}^{W} ($p_{\mathrm{T}}^{W} > 120$ GeV) BDT distributions are shown in Figures 387 388 before the transformation discussed in Section 8.4. Two Lepton low p_{T}^{Z} ($p_{\mathrm{T}}^{Z} < 120$ GeV) BDT distributions are shown in Figures 389, 390 before the transformation discussed in Section 8.4. Two Lepton high p_{T}^{Z} ($p_{\mathrm{T}}^{Z} > 120$ GeV) BDT distributions are shown in Figures 391, 392 before the transformation discussed in Section 8.4.

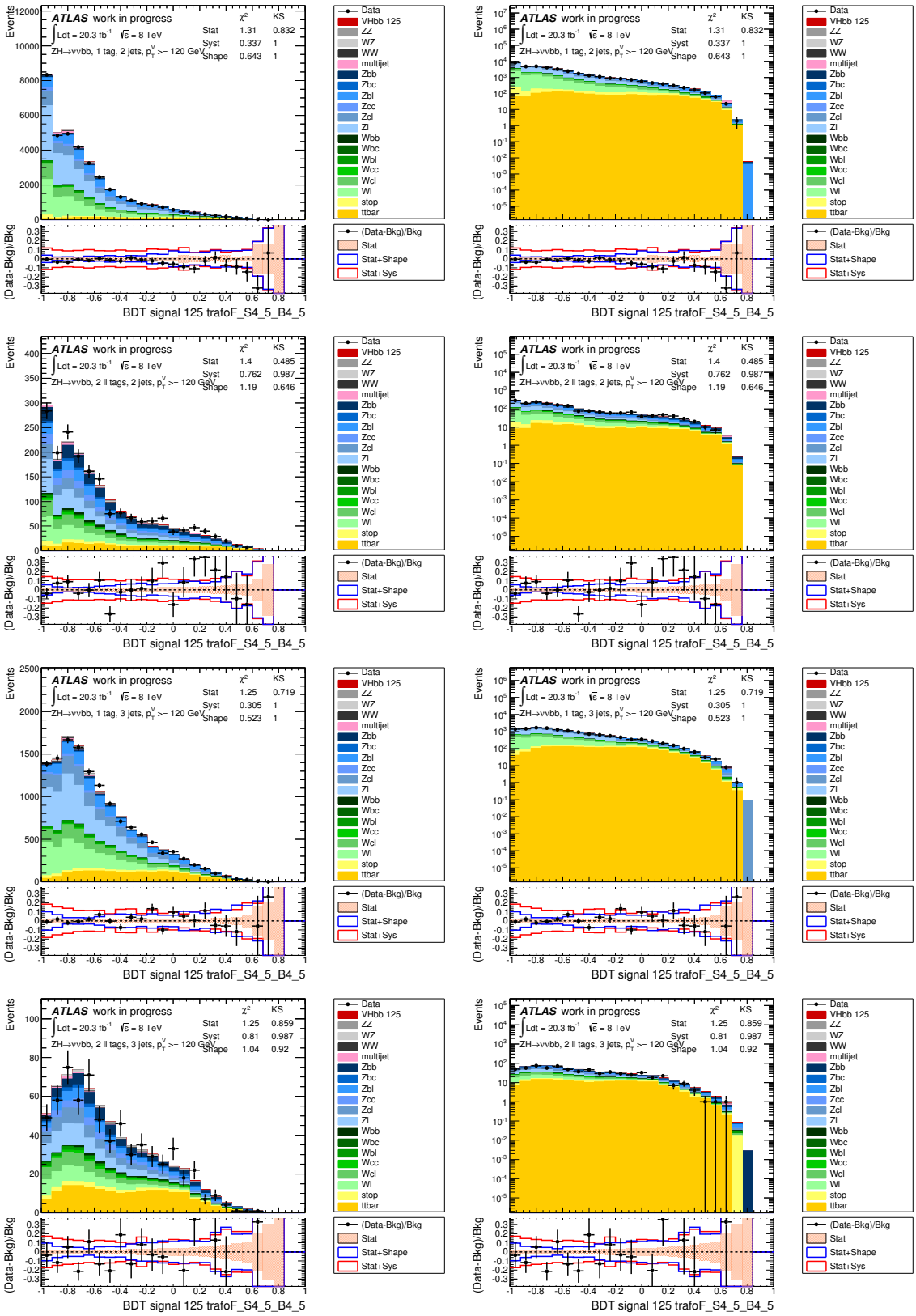

Figure 383: MVA distribution in 0-lepton events ($p_{\mathrm{T}}^{Z} > 120$ GeV). Each row contains the same plot with the left (right) in linear (log) scale. From top to bottom: Row 1 - 1 b-tag 2 jet events. Row 2 - 2 loose b-tags 2 jet events. Row 3 - 1 b-tag 3 jet events. Row 4 - 2 loose b-tags 3 jet events. Section 6 details the MVA configuration.

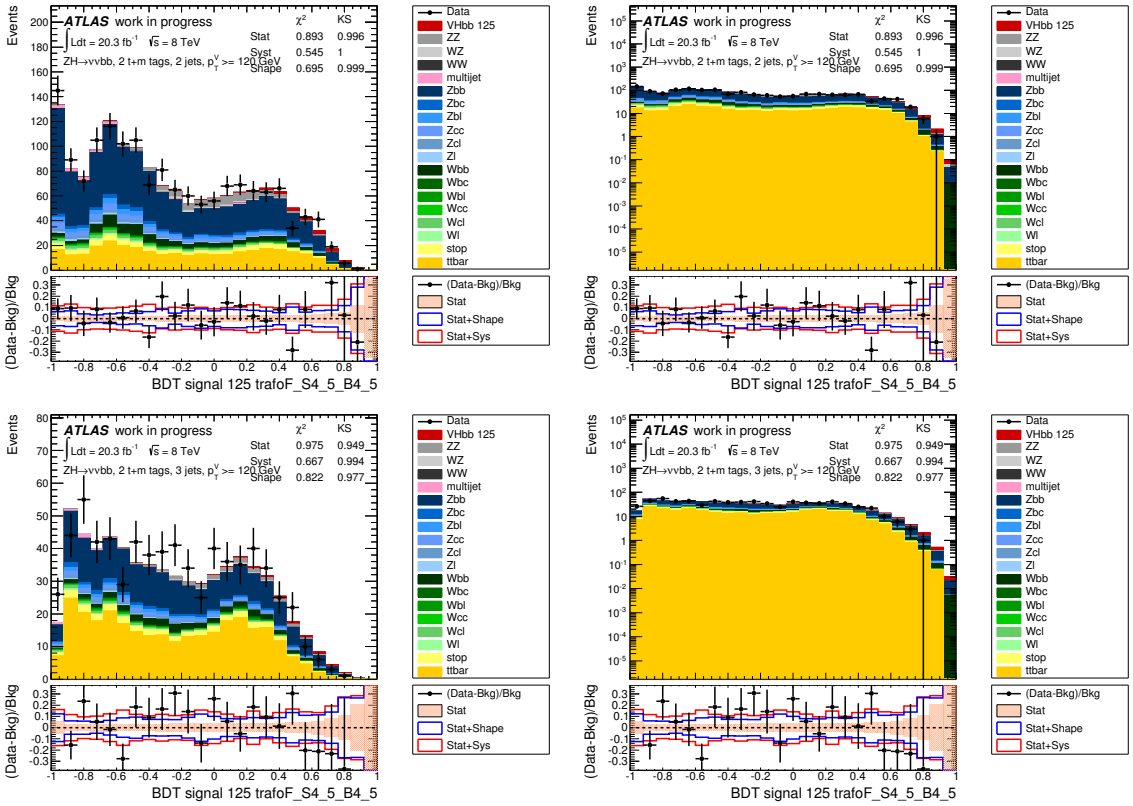

Figure 384: MVA distribution in 0-lepton events ($p_{\mathrm{T}}^{Z} > 120$ GeV). Each row contains the same plot with the left (right) in linear (log) scale. From top to bottom: Row 1 - 2 MM+TT b-tag 2 jet events. Row 2 - 2 MM+TT b-tag 3 jet events. Section 6 details the MVA configuration.

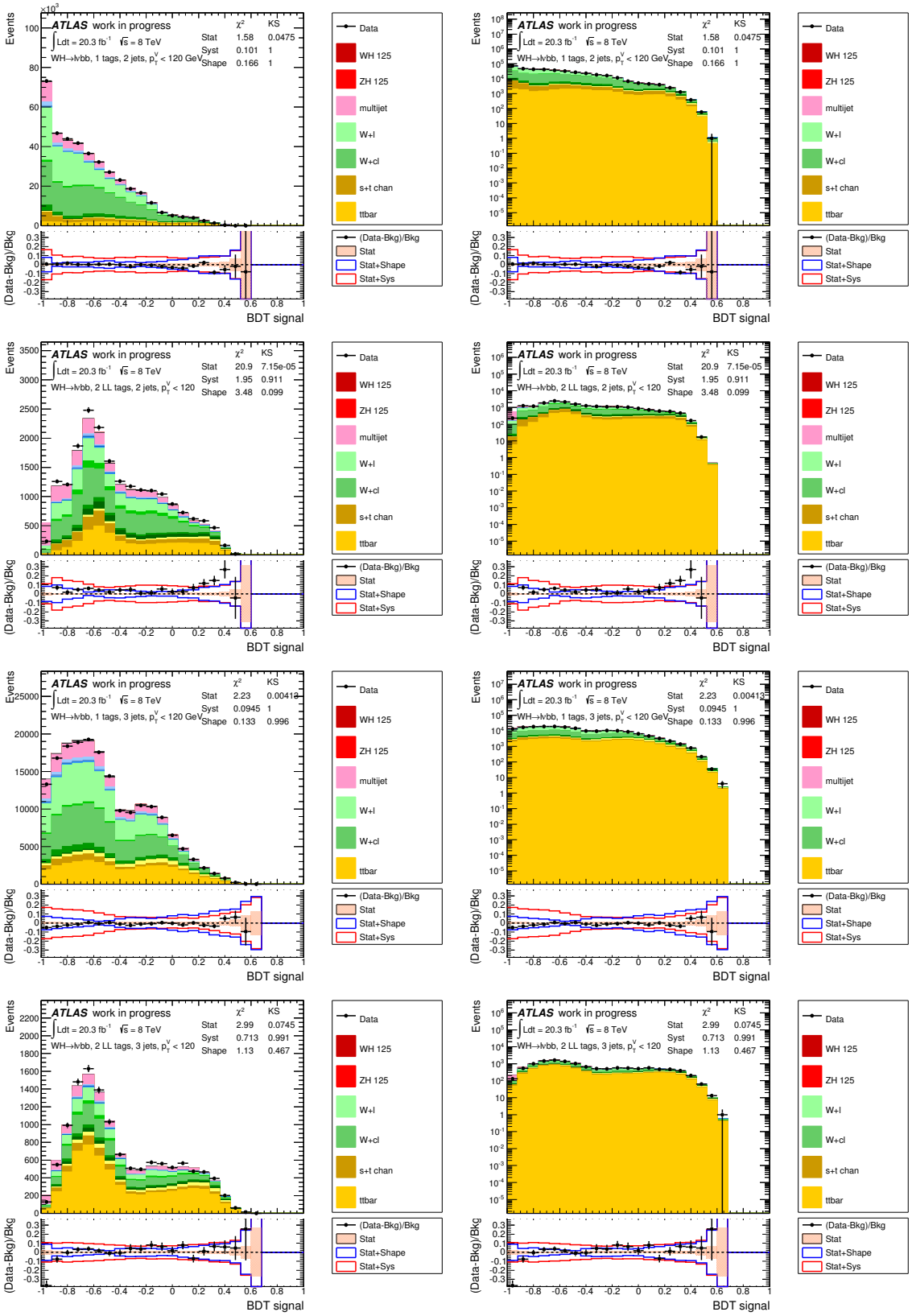

Figure 385: MVA distribution in 1-lepton events with $p_{\mathrm{T}}^{W} < 120$ GeV. Each row contains the same plot with the left (right) in linear (log) scale. From top to bottom: Row 1 - 1 b-tag 2 jet events. Row 2 - 2 LL b-tags 2 jet events. Row 3 - 1 b-tag 3 jet events. Row 4 - 2 LL b-tags 3 jet events. Section 6 details the MVA configuration.

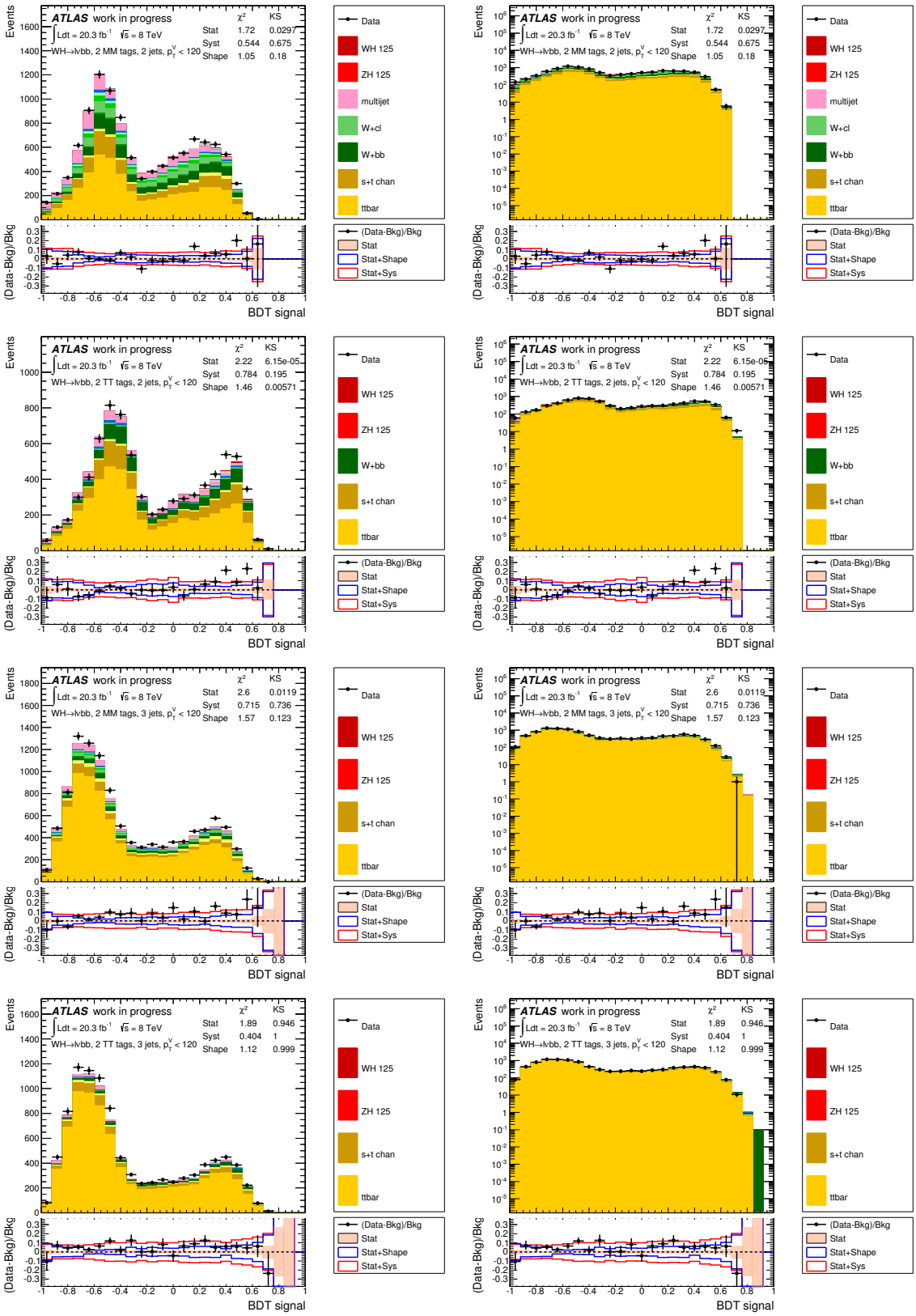

Figure 386: MVA distribution in 1-lepton events with $p_{\mathrm{T}}^{W} < 120$ GeV. Each row contains the same plot with the left (right) in linear (log) scale. From top to bottom: Row 1 - 2 MM *b*-tag 2 jet events. Row 2 - 2 TT *b*-tags 2 jet events. Row 3 - 2 MM *b*-tag 3 jet events. Row 4 - 2 TT *b*-tags 3 jet events. Section 6 details the MVA configuration.

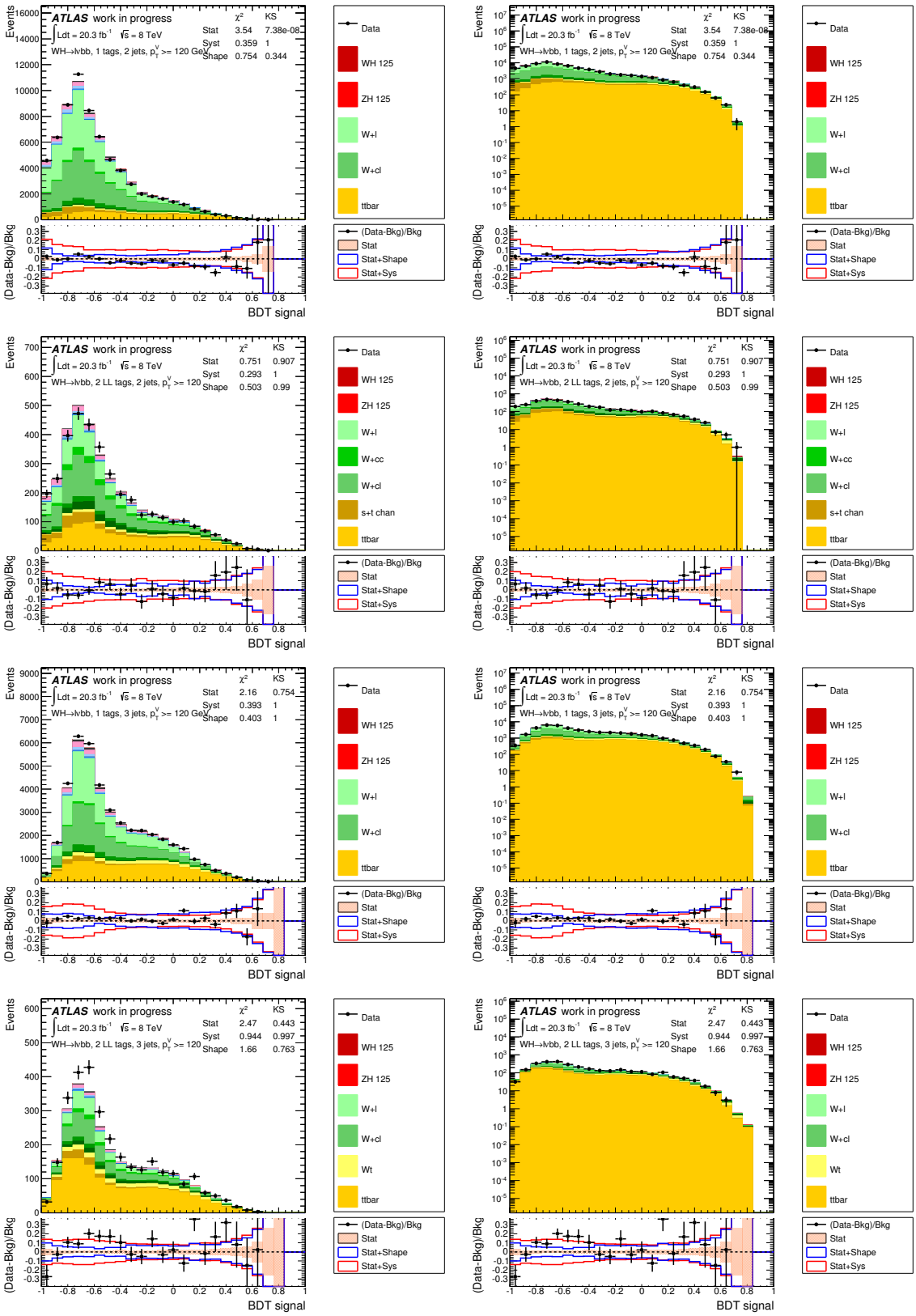

Figure 387: MVA distribution in 1-lepton events with $p_{\mathrm{T}}^{W} > 120$ GeV. Each row contains the same plot with the left (right) in linear (log) scale. From top to bottom: Row 1 - 1 b-tag 2 jet events. Row 2 - 2 LL b-tags 2 jet events. Row 3 - 1 b-tag 3 jet events. Row 4 - 2 LL b-tags 3 jet events. Section 6 details the MVA configuration.

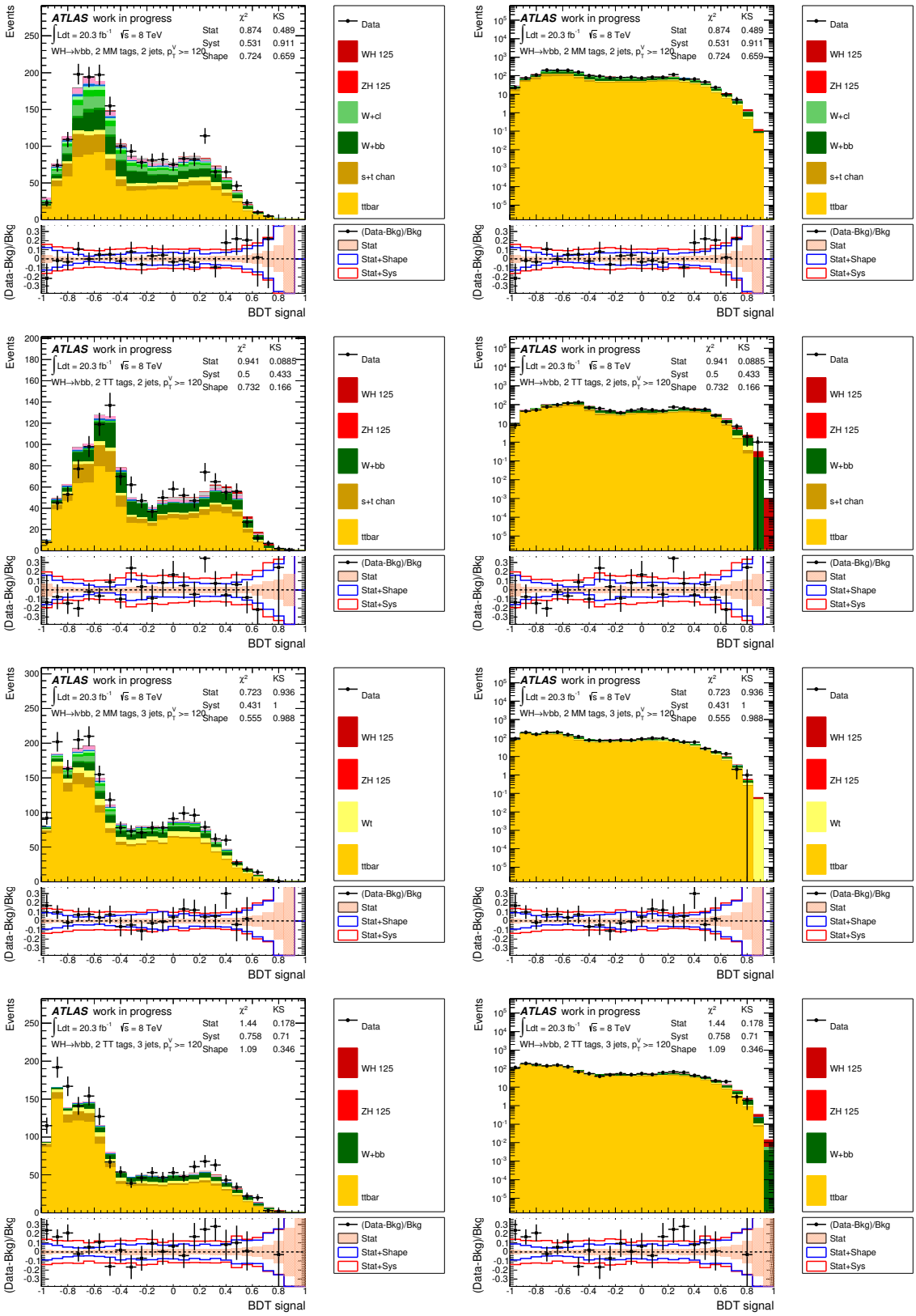

Figure 388: MVA distribution in 1-lepton events with $p_{\mathrm{T}}^{W} > 120$ GeV. Each row contains the same plot with the left (right) in linear (log) scale. From top to bottom: Row 1 - 2MM b-tag 2 jet events. Row 2 - 2 TT b-tags 2 jet events. Row 3 - 2 MM b-tag 3 jet events. Row 4 - 2 TT b-tags 3 jet events. Section 6 details the MVA configuration.

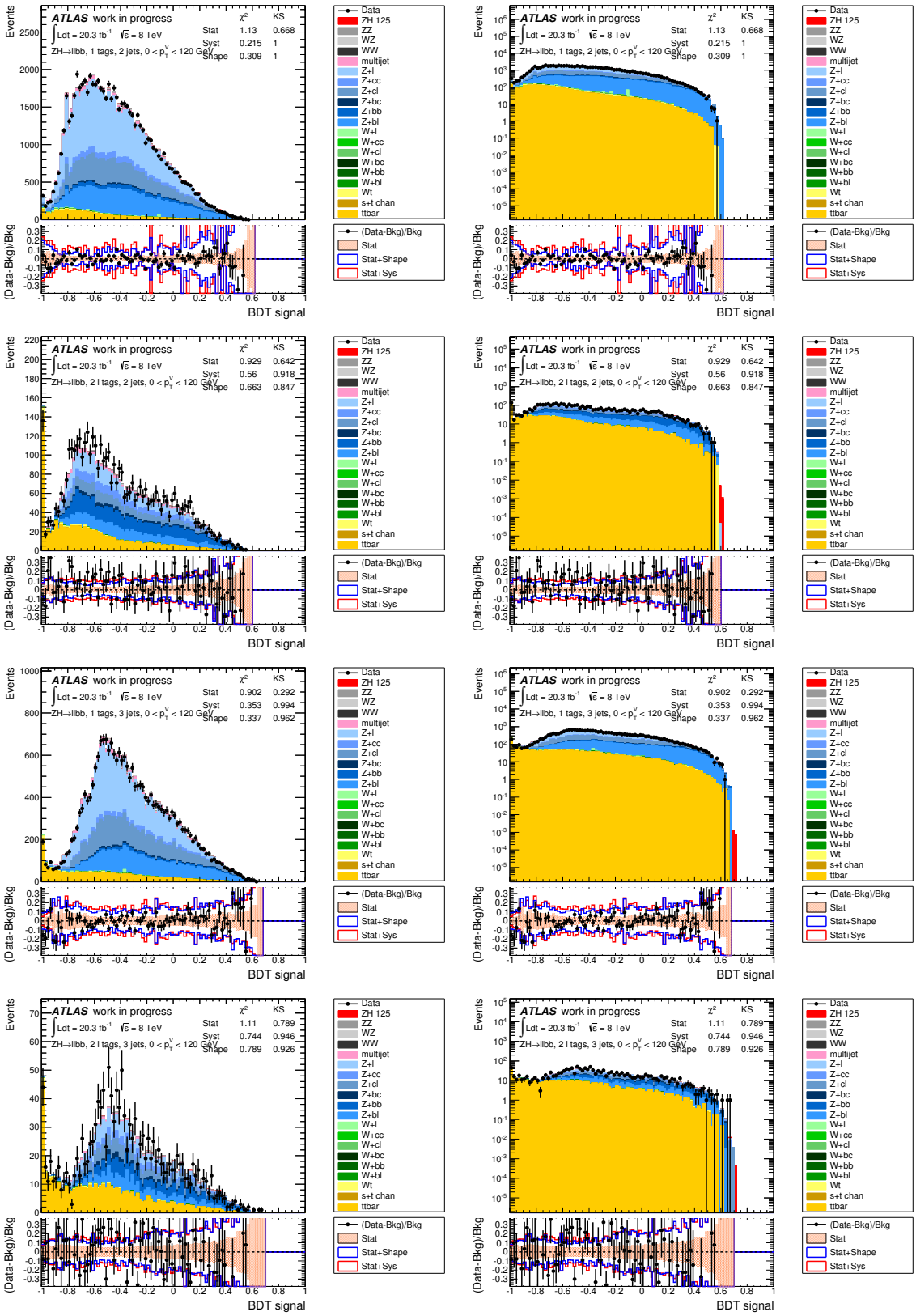

Figure 389: MVA distribution in 2-lepton events with $p_{\mathrm{T}}^{W} < 120$ GeV. Each row contains the same plot with the left (right) in linear (log) scale. From top to bottom: Row 1 - 1 b-tag 2 jet events. Row 2 - 2 LL b-tags 2 jet events. Row 3 - 1 b-tag 3 jet events. Row 4 - 2 LL b-tags 3 jet events. Section 6 details the MVA configuration.

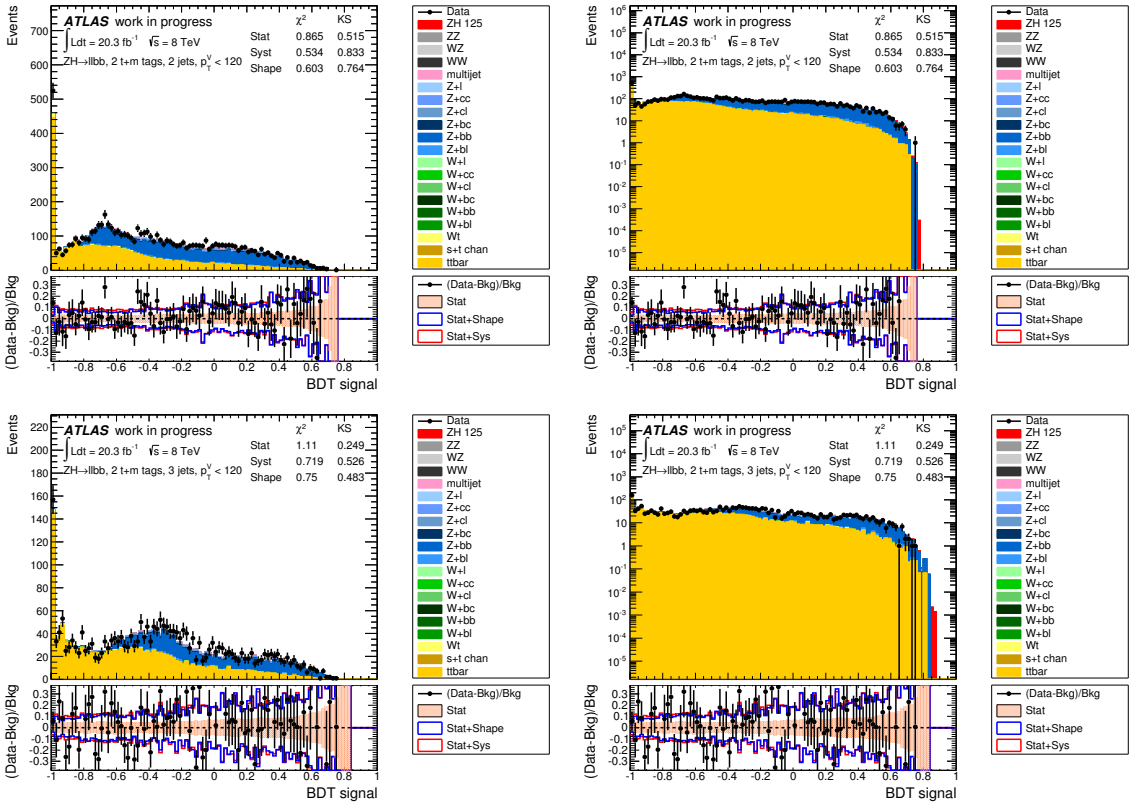

Figure 390: MVA distribution in 2-lepton events with $p_{\mathrm{T}}^{W} < 120$ GeV. Each row contains the same plot with the left (right) in linear (log) scale. From top to bottom: Row 1 - 2 MM+TT b-tag 2 jet events. Row 2 - 2 MM+TT b-tag 3 jet events. Section 6 details the MVA configuration.

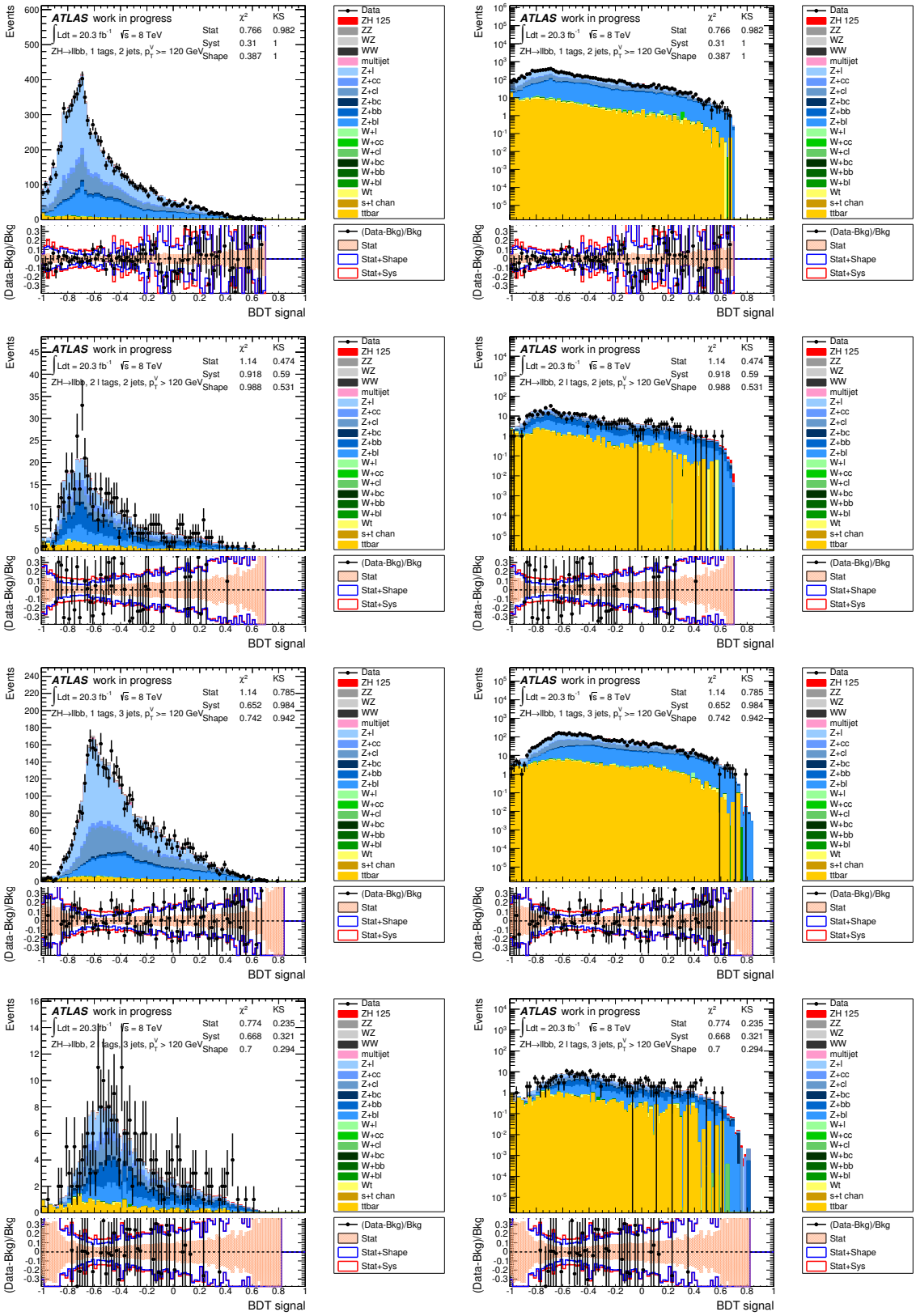

Figure 391: MVA distribution in 2-lepton events with $p_{\mathrm{T}}^{W} > 120$ GeV. Each row contains the same plot with the left (right) in linear (log) scale. From top to bottom: Row 1 - 1 b-tag 2 jet events. Row 2 - 2 LL b-tags 2 jet events. Row 3 - 1 b-tag 3 jet events. Row 4 - 2 LL b-tags 3 jet events. Section 6 details the MVA configuration.

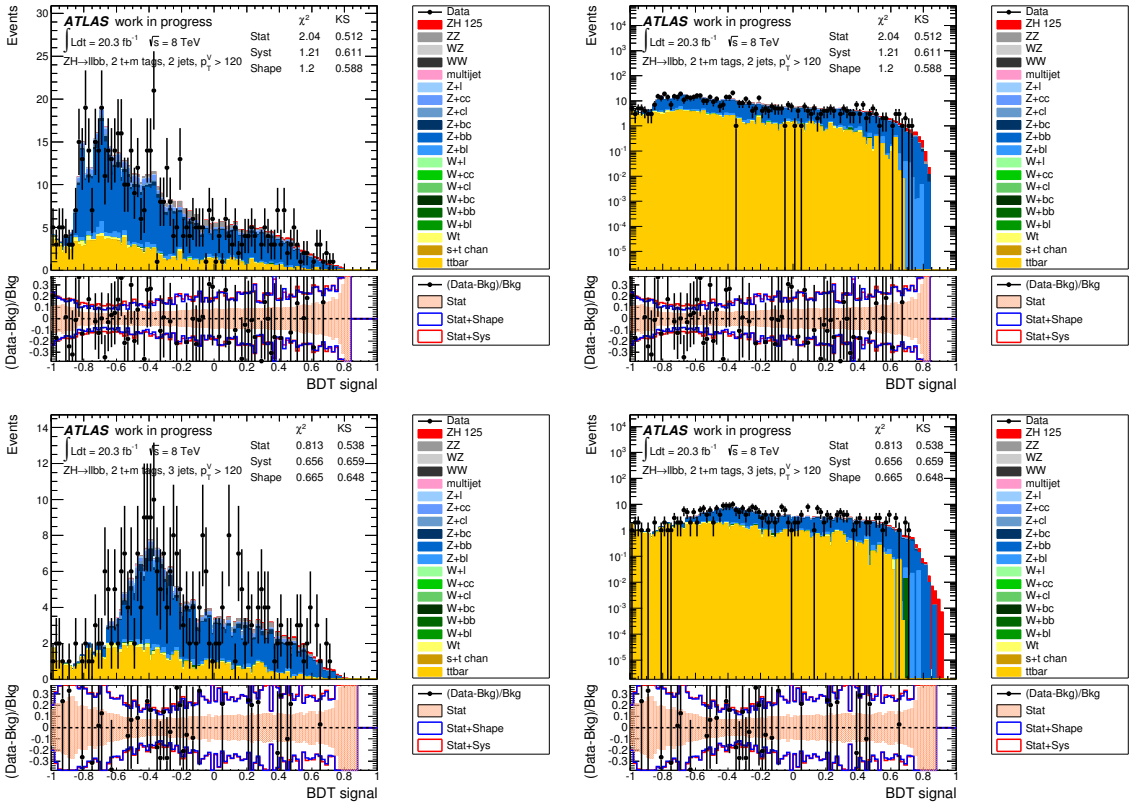

Figure 392: MVA distribution in 2-lepton events with $p_{\mathrm{T}}^{W} > 120$ GeV. Each row contains the same plot with the left (right) in linear (log) scale. From top to bottom: Row 1 - 2 MM+TT b-tag 2 jet events. Row 2 - 2 MM+TT b-tag 3 jet events. Section 6 details the MVA configuration.

AE Correlations between MVA Variables: Zero Lepton

This appendix contains correlations between input and output variables of the BDT, defined in Section 6 in the 0-lepton analysis. Note that the 0-lepton selection only included events with $p_{\mathrm{T}}^{Z} > 120$ GeV in the MVA analysis. These plots are done by applying the latest scale factors, obtained for the 2 jet region and the 3 jet region separately, by comparing the event yield before and after the MVA combined fit. They are summarized in Table 114. Explicitly stated, the theoretical expectation for each background is used for the given luminosity. All the plots in this section are done with the status-of-art analysis.

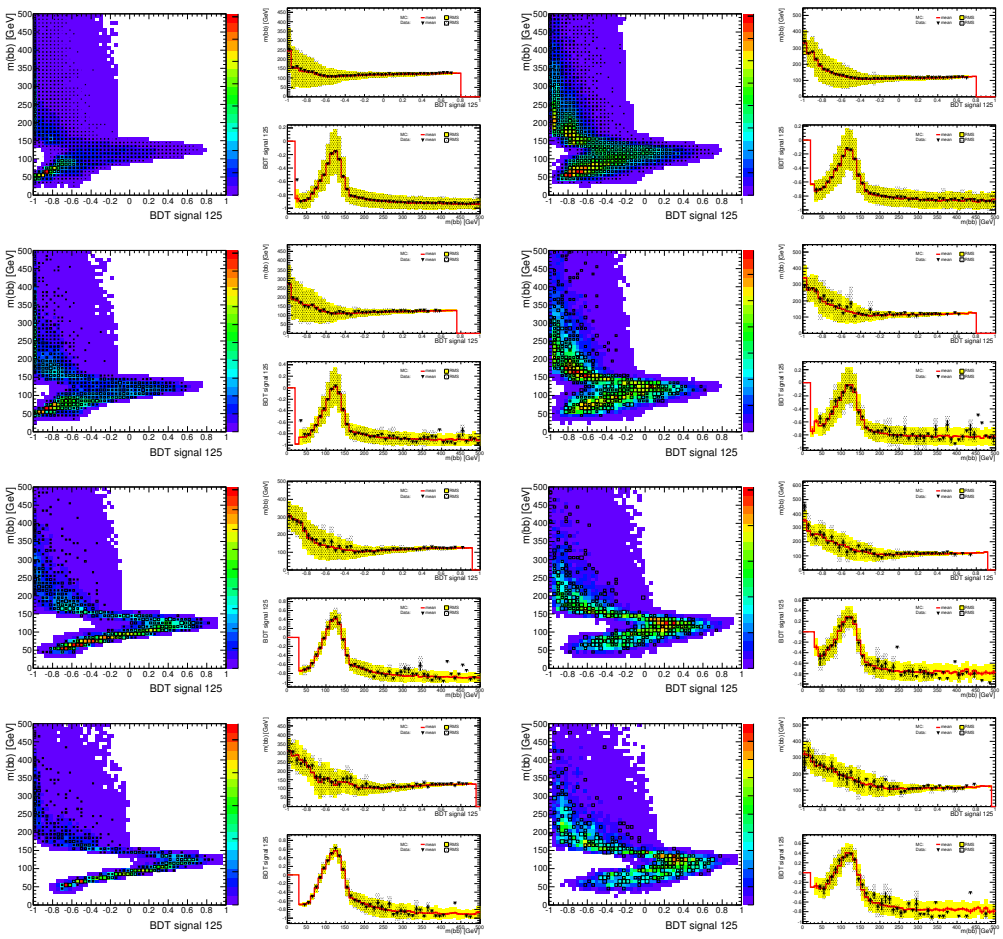

Figure 393: Correlation between BDTinput and output variables used in 0-lepton events ($p_{\mathrm{T}}^{Z} > 120$ GeV) Row 1 - Left: 1 tag 2 jets Right: 1 tag 3 jets; Row 2 - Left: 2 LL tag 2 jets Right: 2 LL tag 3 jets; Row 3 - Left: 2 MM tag 2 jets Right: 2 MM tag 3 jets; Row 4 - Left: 2 TT tag 2 jets Right: 2 TT tag 3 jets. Section 6.1 details the definition of each variable.

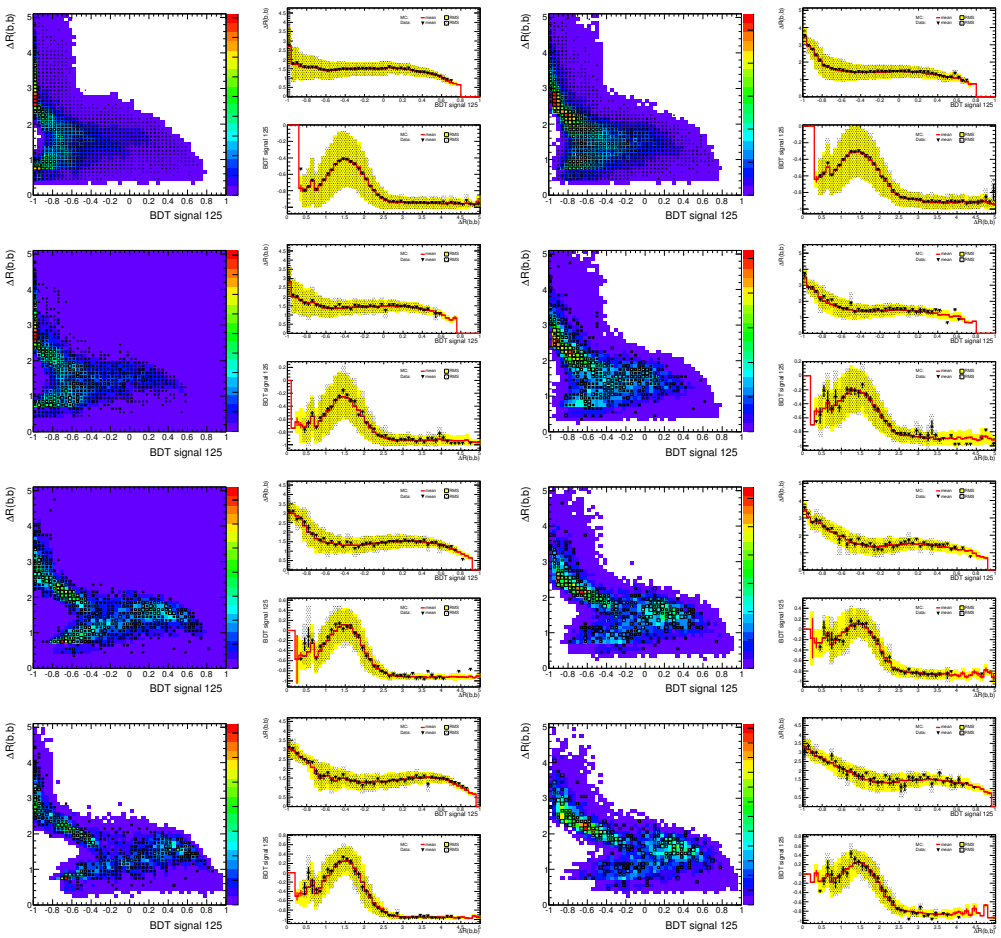

Figure 394: Correlation between BDTinput and output variables used in 0-lepton events ($p_{\mathrm{T}}^{Z} > 120$ GeV) Row 1 - Left: 1 tag 2 jets Right: 1 tag 3 jets; Row 2 - Left: 2 LL tag 2 jets Right: 2 LL tag 3 jets; Row 3 - Left: 2 MM tag 2 jets Right: 2 MM tag 3 jets; Row 4 - Left: 2 TT tag 2 jets Right: 2 TT tag 3 jets. Section 6.1 details the definition of each variable.

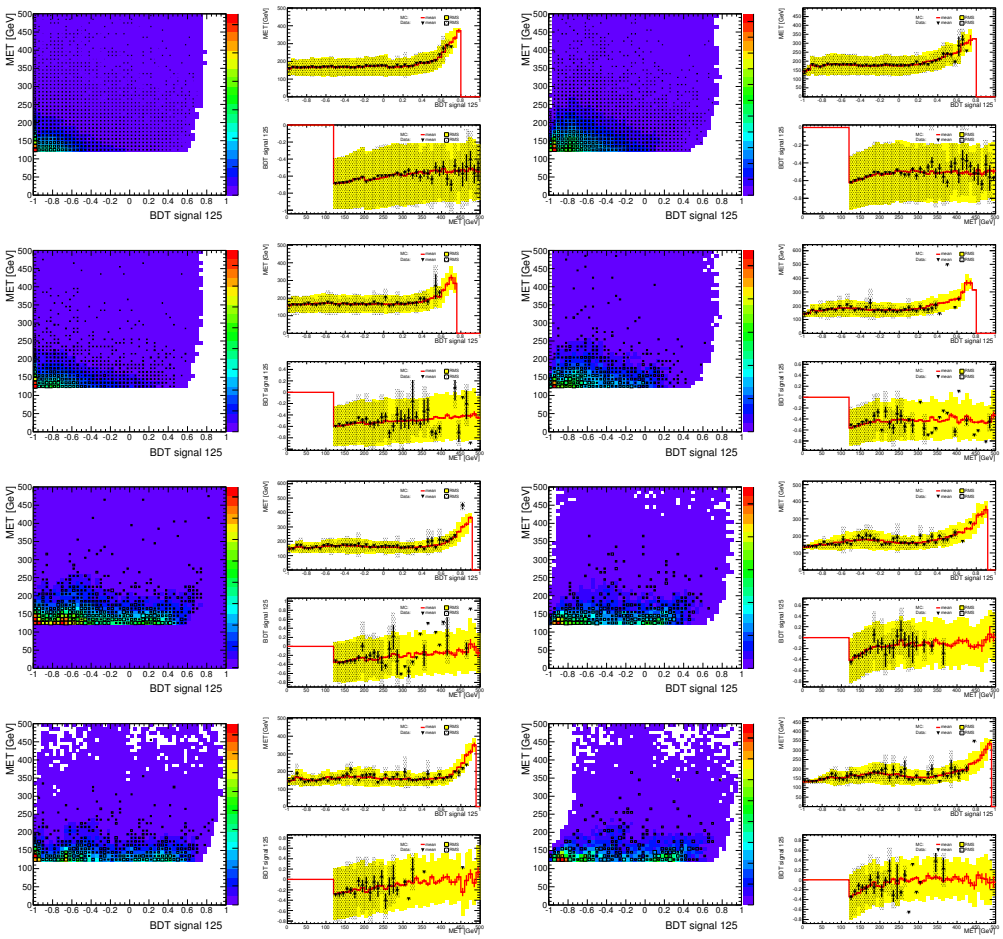

Figure 395: Correlation between BDTinput and output variables used in 0-lepton events ($p_{\mathrm{T}}^{Z} > 120$ GeV) Row 1 - Left: 1 tag 2 jets Right: 1 tag 3 jets; Row 2 - Left: 2 LL tag 2 jets Right: 2 LL tag 3 jets; Row 3 - Left: 2 MM tag 2 jets Right: 2 MM tag 3 jets; Row 4 - Left: 2 TT tag 2 jets Right: 2 TT tag 3 jets. Section 6.1 details the definition of each variable.

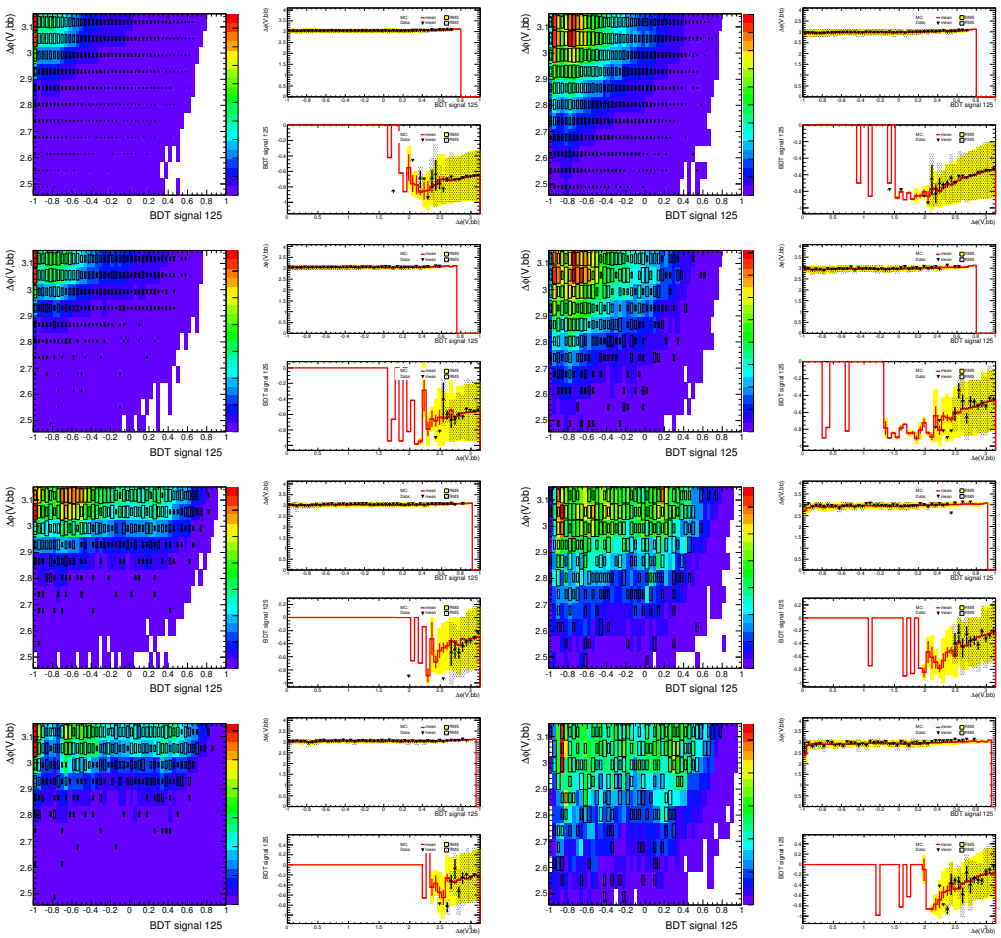

Figure 396: Correlation between BDTinput and output variables used in 0-lepton events ($p_{\mathrm{T}}^{Z} > 120$ GeV) Row 1 - Left: 1 tag 2 jets Right: 1 tag 3 jets; Row 2 - Left: 2 LL tag 2 jets Right: 2 LL tag 3 jets; Row 3 - Left: 2 MM tag 2 jets Right: 2 MM tag 3 jets; Row 4 - Left: 2 TT tag 2 jets Right: 2 TT tag 3 jets. Section 6.1 details the definition of each variable.

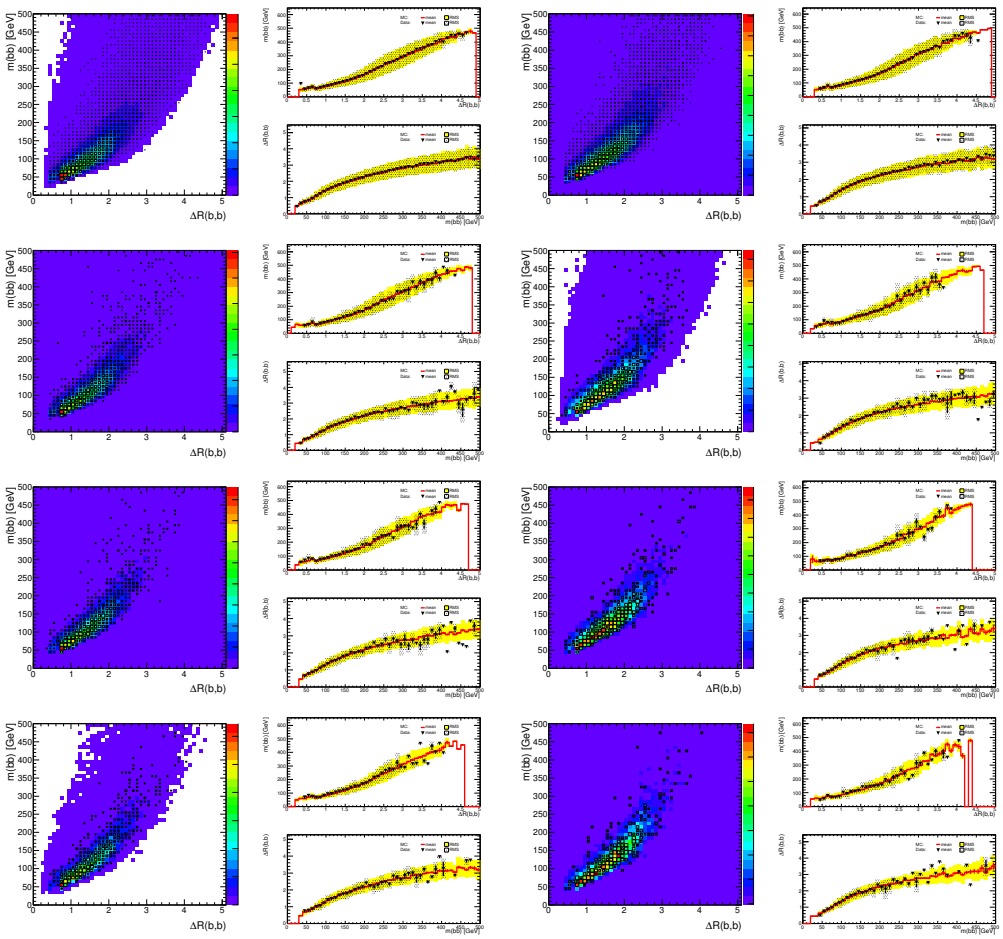

Figure 397: Correlation between BDTinput and output variables used in 0-lepton events ($p_{\mathrm{T}}^{Z} > 120$ GeV) Row 1 - Left: 1 tag 2 jets Right: 1 tag 3 jets; Row 2 - Left: 2 LL tag 2 jets Right: 2 LL tag 3 jets; Row 3 - Left: 2 MM tag 2 jets Right: 2 MM tag 3 jets; Row 4 - Left: 2 TT tag 2 jets Right: 2 TT tag 3 jets. Section 6.1 details the definition of each variable.

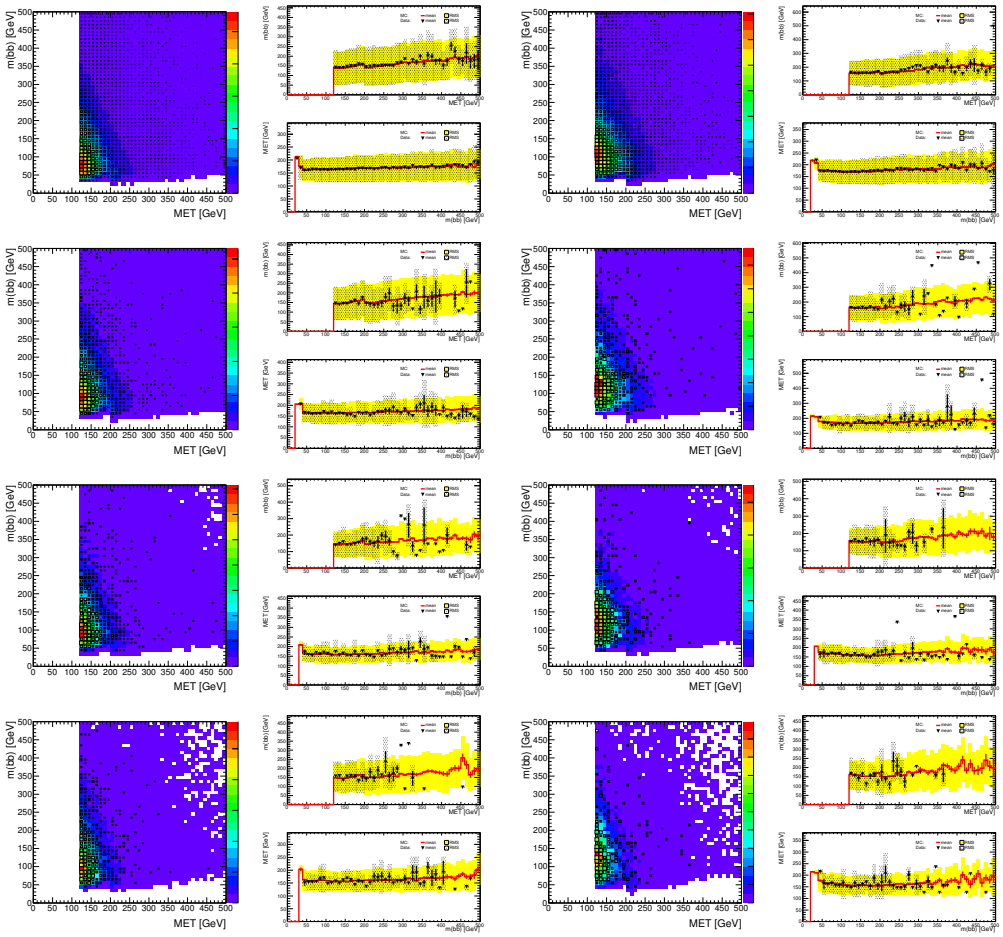

Figure 398: Correlation between BDTinput and output variables used in 0-lepton events ($p_{\mathrm{T}}^{Z} > 120$ GeV) Row 1 - Left: 1 tag 2 jets Right: 1 tag 3 jets; Row 2 - Left: 2 LL tag 2 jets Right: 2 LL tag 3 jets; Row 3 - Left: 2 MM tag 2 jets Right: 2 MM tag 3 jets; Row 4 - Left: 2 TT tag 2 jets Right: 2 TT tag 3 jets. Section 6.1 details the definition of each variable.

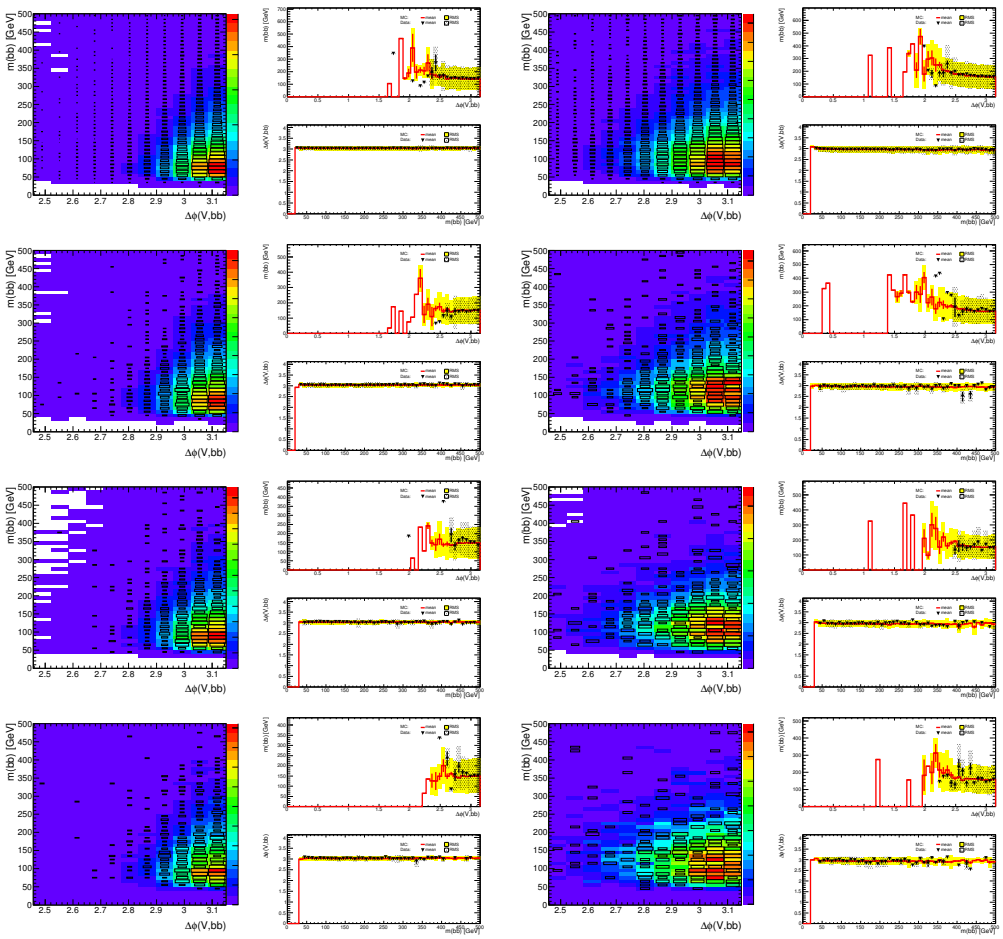

Figure 399: Correlation between BDTinput and output variables used in 0-lepton events ($p_{\mathrm{T}}^{Z} > 120$ GeV) Row 1 - Left: 1 tag 2 jets Right: 1 tag 3 jets; Row 2 - Left: 2 LL tag 2 jets Right: 2 LL tag 3 jets; Row 3 - Left: 2 MM tag 2 jets Right: 2 MM tag 3 jets; Row 4 - Left: 2 TT tag 2 jets Right: 2 TT tag 3 jets. Section 6.1 details the definition of each variable.

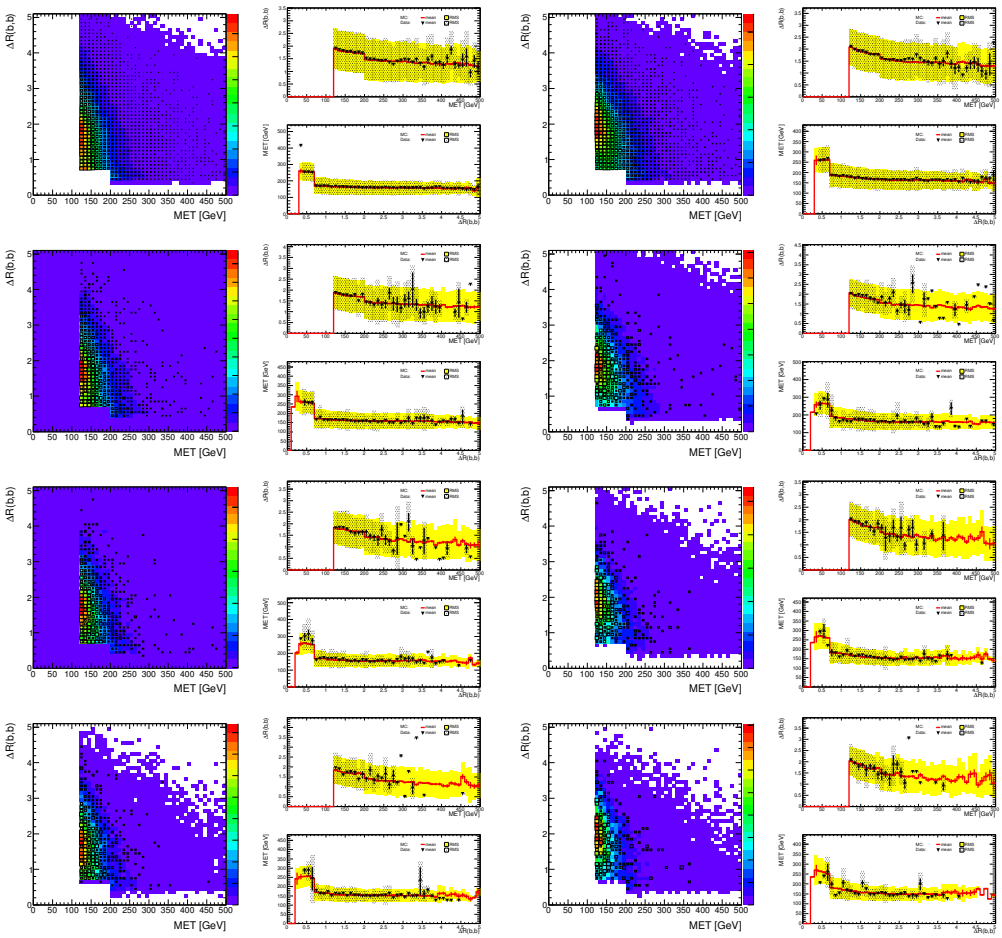

Figure 400: Correlation between BDTinput and output variables used in 0-lepton events ($p_{\mathrm{T}}^{Z} > 120$ GeV) Row 1 - Left: 1 tag 2 jets Right: 1 tag 3 jets; Row 2 - Left: 2 LL tag 2 jets Right: 2 LL tag 3 jets; Row 3 - Left: 2 MM tag 2 jets Right: 2 MM tag 3 jets; Row 4 - Left: 2 TT tag 2 jets Right: 2 TT tag 3 jets. Section 6.1 details the definition of each variable.

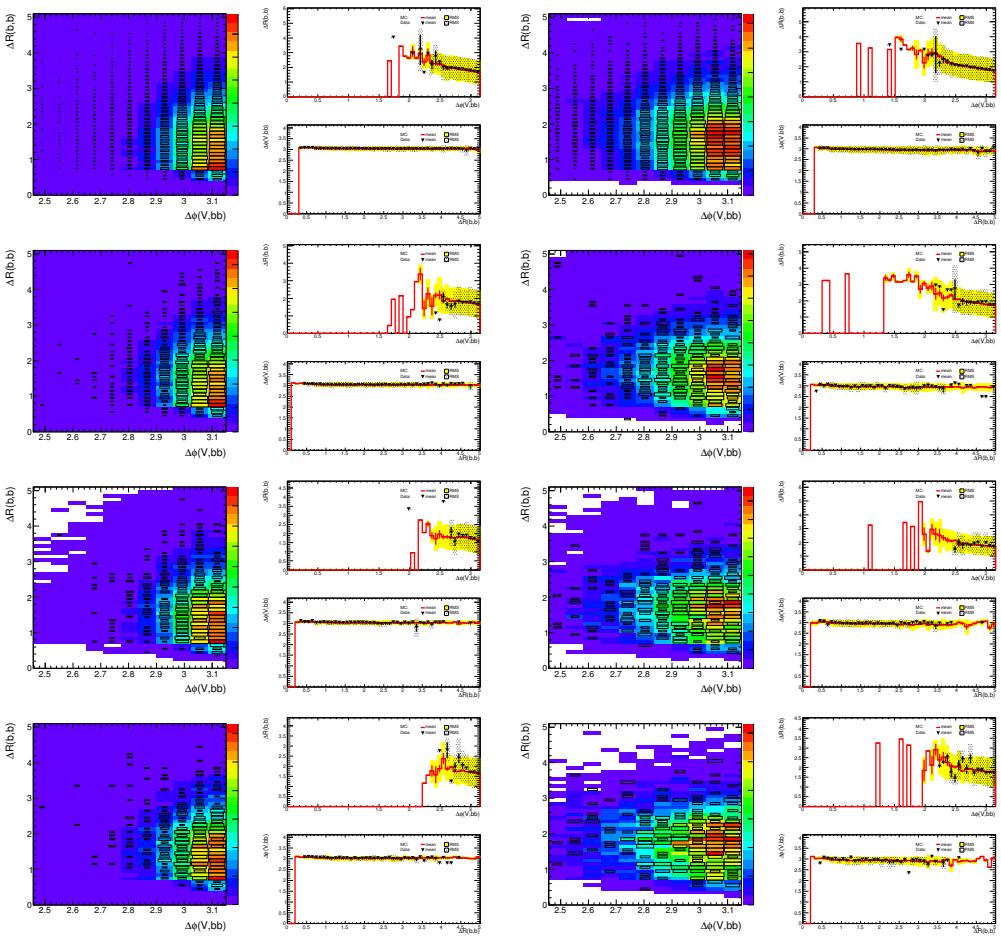

Figure 401: Correlation between BDTinput and output variables used in 0-lepton events ($p_{\mathrm{T}}^{Z} > 120$ GeV) Row 1 - Left: 1 tag 2 jets Right: 1 tag 3 jets; Row 2 - Left: 2 LL tag 2 jets Right: 2 LL tag 3 jets; Row 3 - Left: 2 MM tag 2 jets Right: 2 MM tag 3 jets; Row 4 - Left: 2 TT tag 2 jets Right: 2 TT tag 3 jets. Section 6.1 details the definition of each variable.

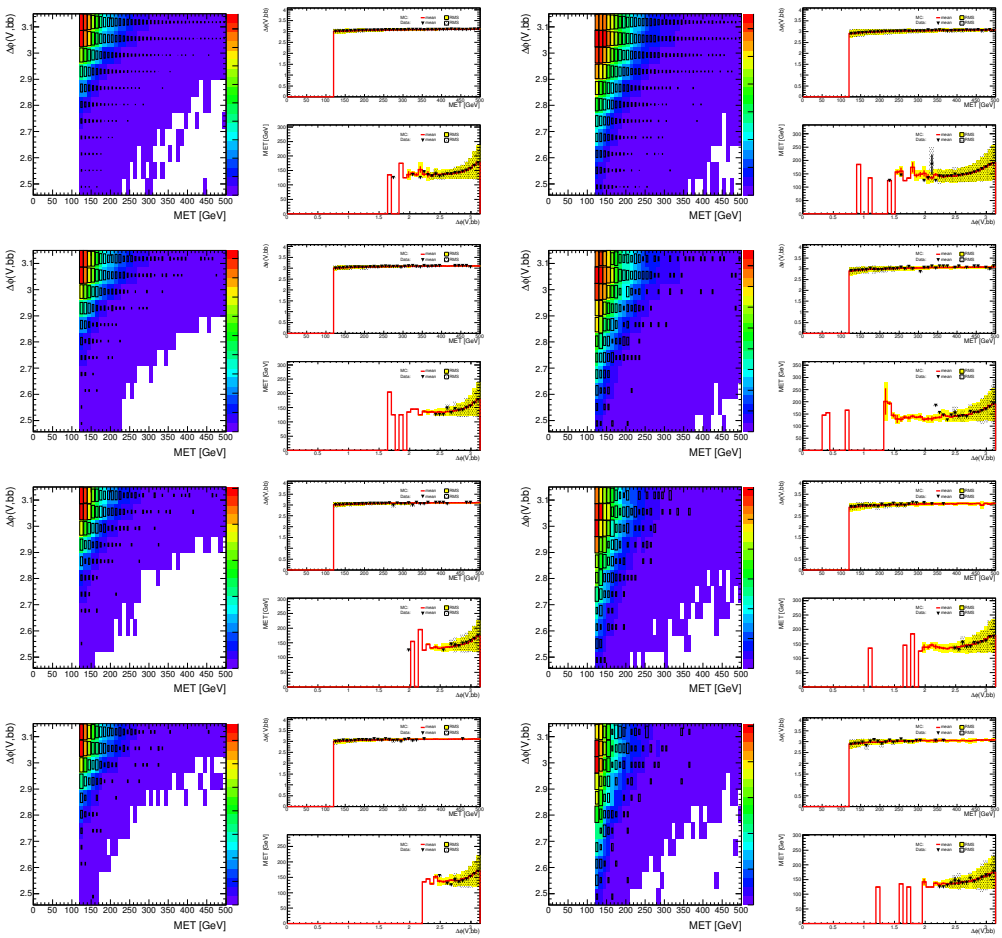

Figure 402: Correlation between BDTinput and output variables used in 0-lepton events ($p_{\mathrm{T}}^{Z} > 120$ GeV) Row 1 - Left: 1 tag 2 jets Right: 1 tag 3 jets; Row 2 - Left: 2 LL tag 2 jets Right: 2 LL tag 3 jets; Row 3 - Left: 2 MM tag 2 jets Right: 2 MM tag 3 jets; Row 4 - Left: 2 TT tag 2 jets Right: 2 TT tag 3 jets. Section 6.1 details the definition of each variable.

AF Correlations between MVA Variables: One Lepton

This appendix contains correlations between input and output variables of the BDT, defined in Section 6 in the 1-lepton analysis. These plots are done by applying the latest scale factors, obtained for the 2 jet region and the 3 jet region separately, by comparing the event yield before and after the MVA combined fit. They are summarized in Table 114. Explicitly stated, the theoretical expectation for each background is used for the given luminosity. All the plots in this section are done with the status-of-art analysis.

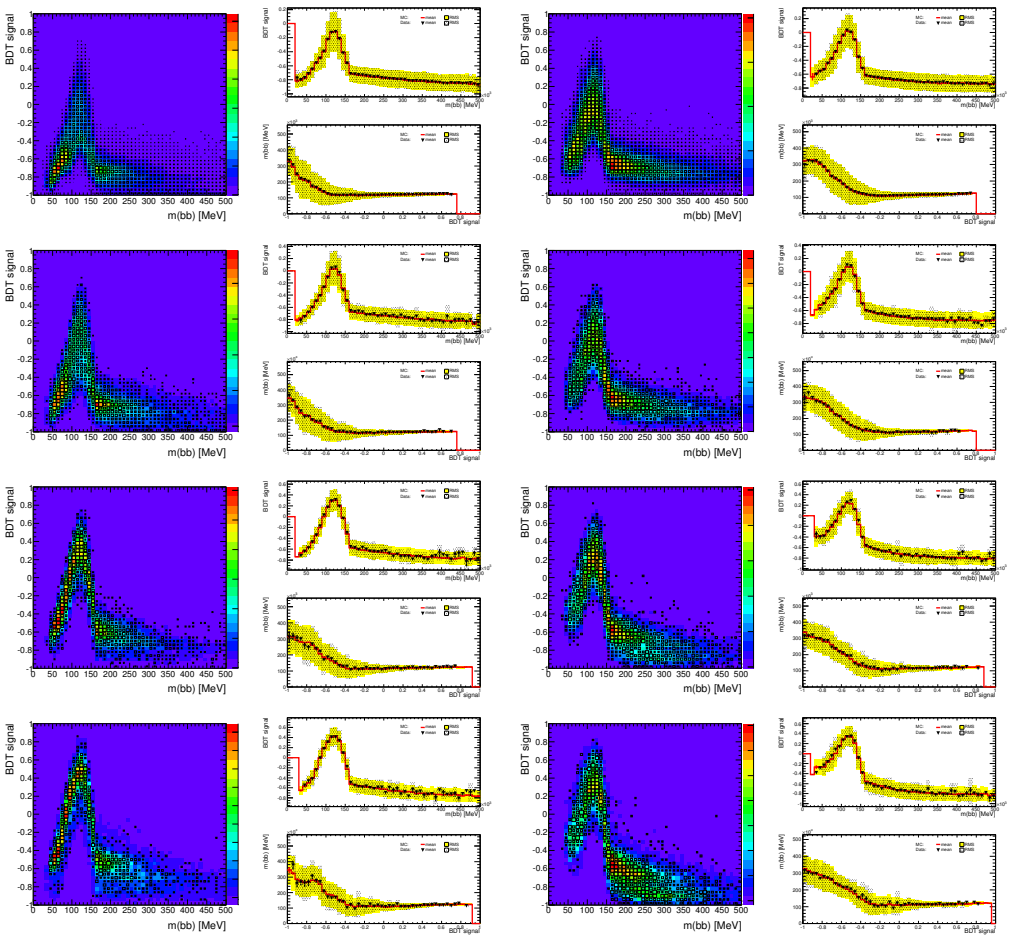

Figure 403: Correlation between BDTinput and output variables used in 0-lepton events ($p_{\mathrm{T}}^{W} > 120$ GeV) Row 1 - Left: 1 tag 2 jets Right: 1 tag 3 jets; Row 2 - Left: 2 LL tag 2 jets Right: 2 LL tag 3 jets; Row 3 - Left: 2 MM tag 2 jets Right: 2 MM tag 3 jets; Row 4 - Left: 2 TT tag 2 jets Right: 2 TT tag 3 jets. Section 6.1 details the definition of each variable.

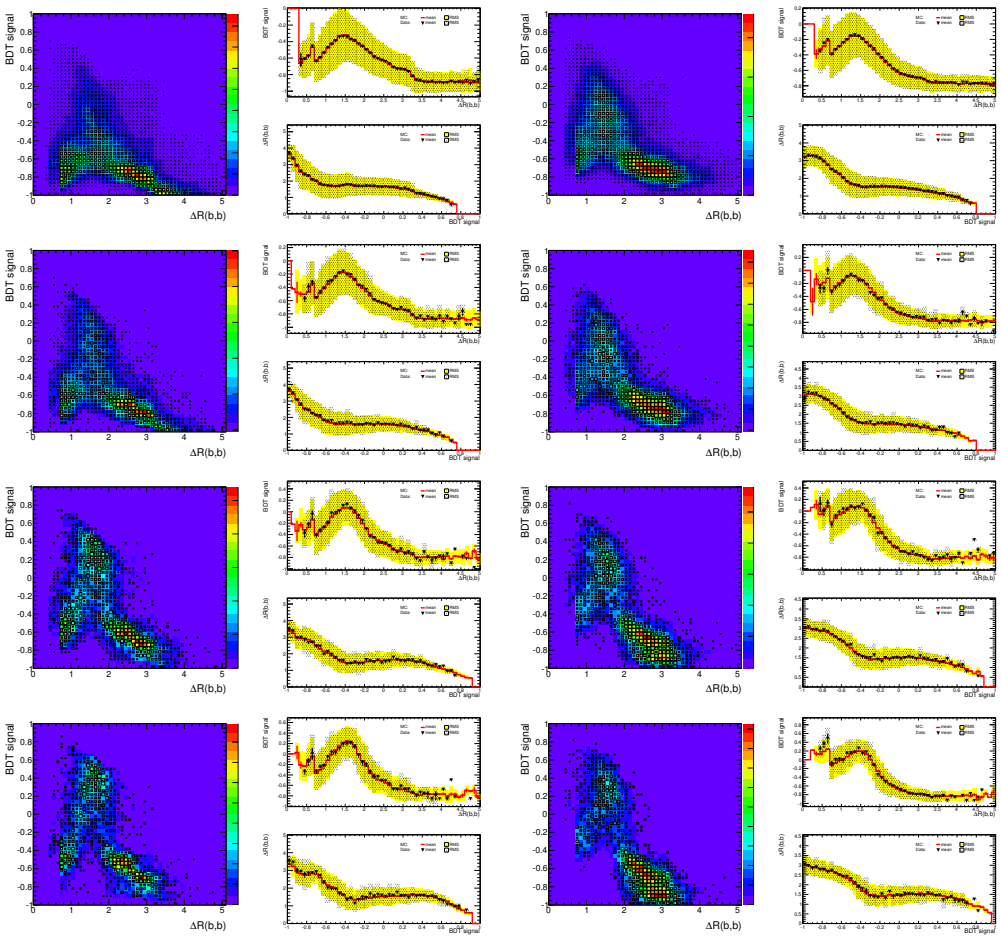

Figure 404: Correlation between BDTinput and output variables used in 0-lepton events ($p_{\mathrm{T}}^{W} > 120$ GeV) Row 1 - Left: 1 tag 2 jets Right: 1 tag 3 jets; Row 2 - Left: 2 LL tag 2 jets Right: 2 LL tag 3 jets; Row 3 - Left: 2 MM tag 2 jets Right: 2 MM tag 3 jets; Row 4 - Left: 2 TT tag 2 jets Right: 2 TT tag 3 jets. Section 6.1 details the definition of each variable.

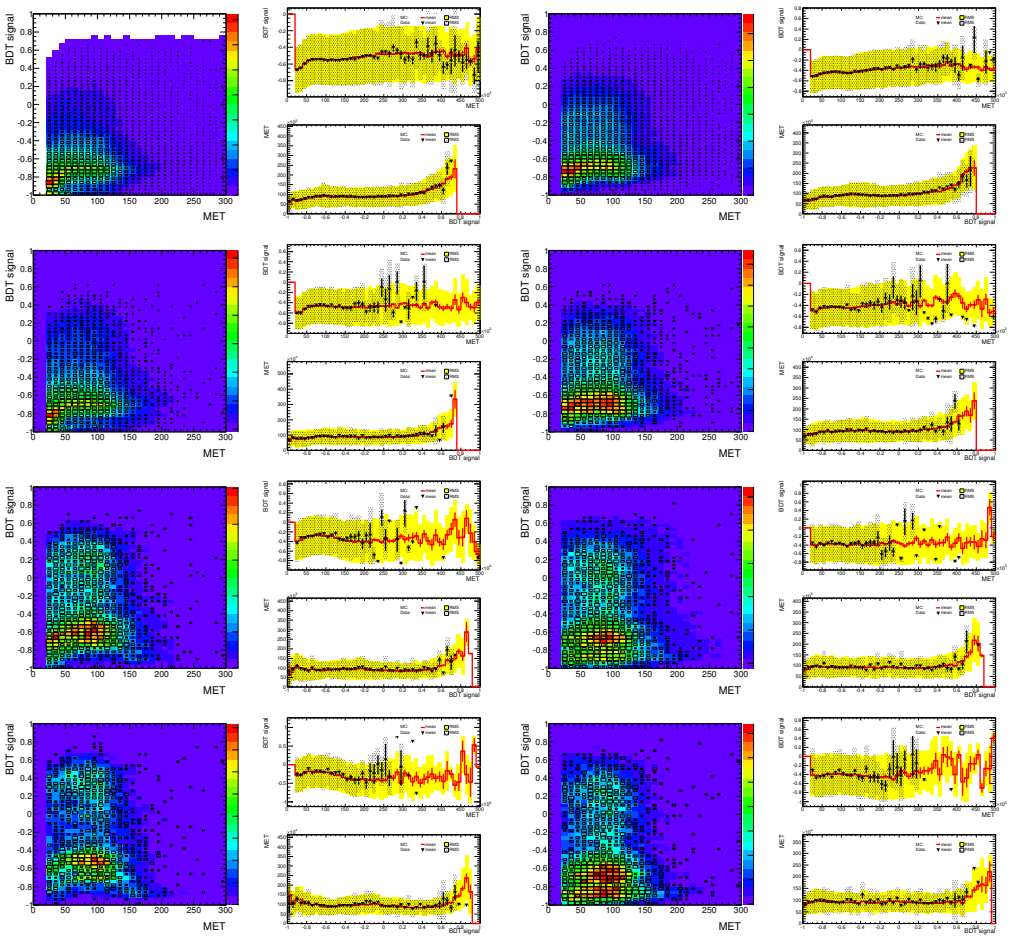

Figure 405: Correlation between BDTinput and output variables used in 0-lepton events ($p_{\mathrm{T}}^{W} > 120$ GeV) Row 1 - Left: 1 tag 2 jets Right: 1 tag 3 jets; Row 2 - Left: 2 LL tag 2 jets Right: 2 LL tag 3 jets; Row 3 - Left: 2 MM tag 2 jets Right: 2 MM tag 3 jets; Row 4 - Left: 2 TT tag 2 jets Right: 2 TT tag 3 jets. Section 6.1 details the definition of each variable.

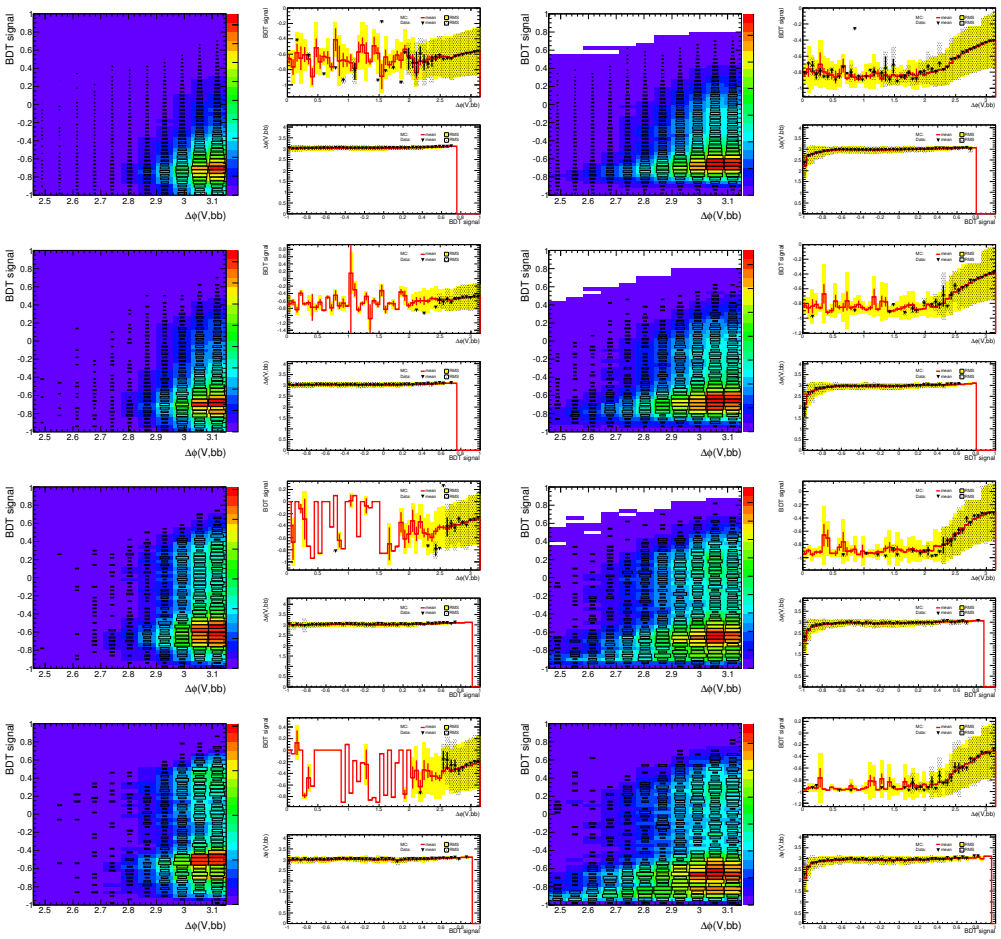

Figure 406: Correlation between BDTinput and output variables used in 0-lepton events ($p_{\mathrm{T}}^{W} > 120$ GeV) Row 1 - Left: 1 tag 2 jets Right: 1 tag 3 jets; Row 2 - Left: 2 LL tag 2 jets Right: 2 LL tag 3 jets; Row 3 - Left: 2 MM tag 2 jets Right: 2 MM tag 3 jets; Row 4 - Left: 2 TT tag 2 jets Right: 2 TT tag 3 jets. Section 6.1 details the definition of each variable.

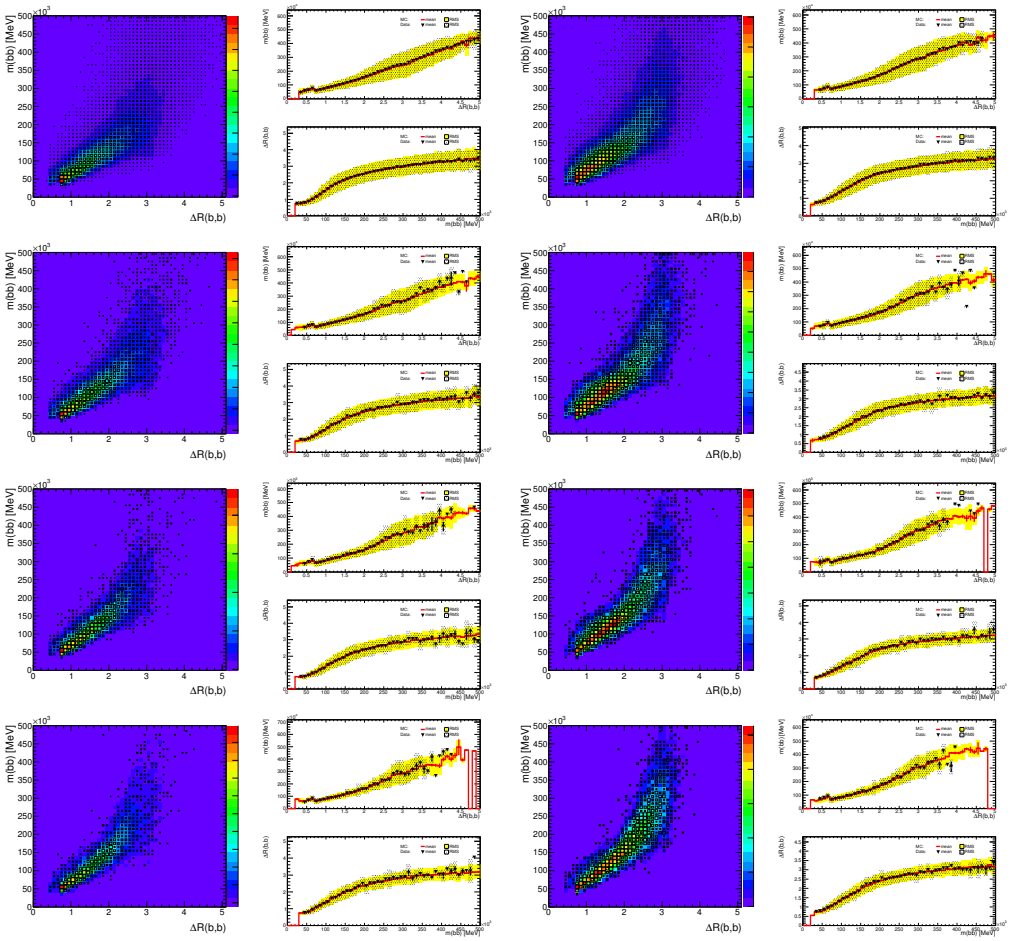

Figure 407: Correlation between BDTinput and output variables used in 0-lepton events ($p_{\mathrm{T}}^{W} > 120$ GeV) Row 1 - Left: 1 tag 2 jets Right: 1 tag 3 jets; Row 2 - Left: 2 LL tag 2 jets Right: 2 LL tag 3 jets; Row 3 - Left: 2 MM tag 2 jets Right: 2 MM tag 3 jets; Row 4 - Left: 2 TT tag 2 jets Right: 2 TT tag 3 jets. Section 6.1 details the definition of each variable.

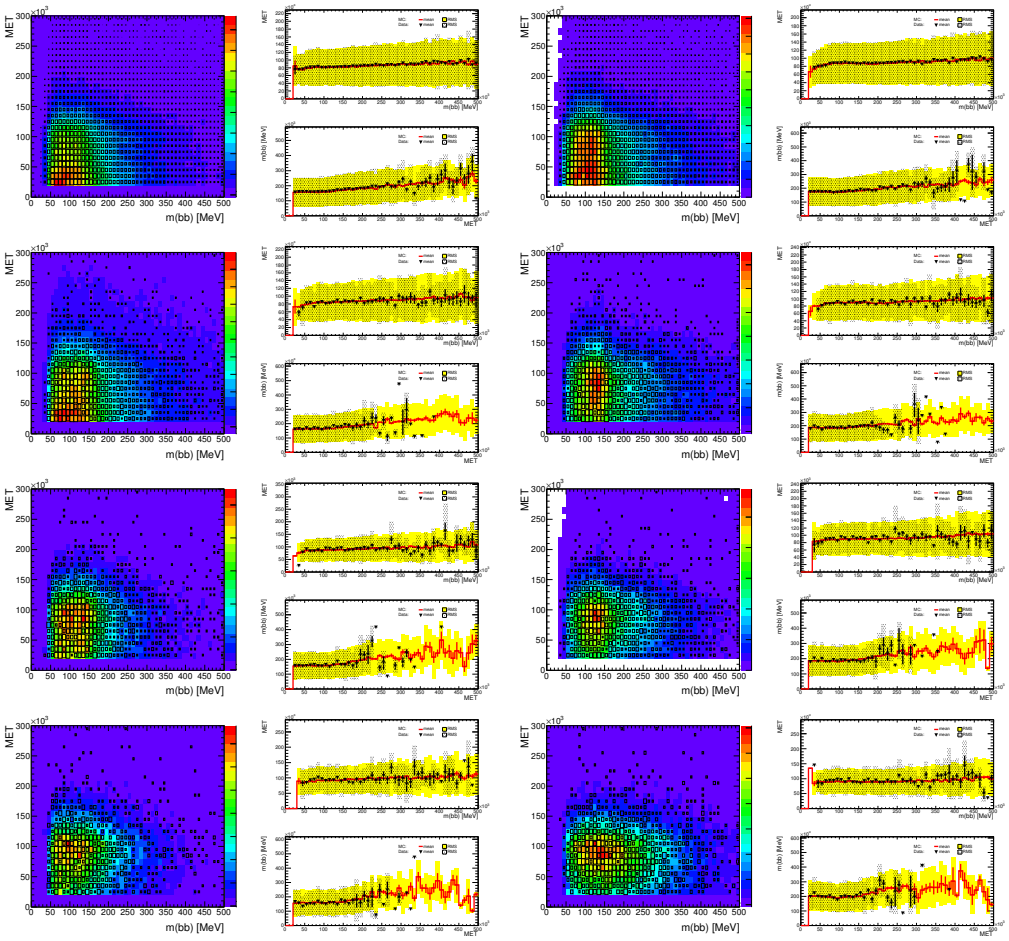

Figure 408: Correlation between BDTinput and output variables used in 0-lepton events ($p_{\mathrm{T}}^{W} > 120$ GeV) Row 1 - Left: 1 tag 2 jets Right: 1 tag 3 jets; Row 2 - Left: 2 LL tag 2 jets Right: 2 LL tag 3 jets; Row 3 - Left: 2 MM tag 2 jets Right: 2 MM tag 3 jets; Row 4 - Left: 2 TT tag 2 jets Right: 2 TT tag 3 jets. Section 6.1 details the definition of each variable.

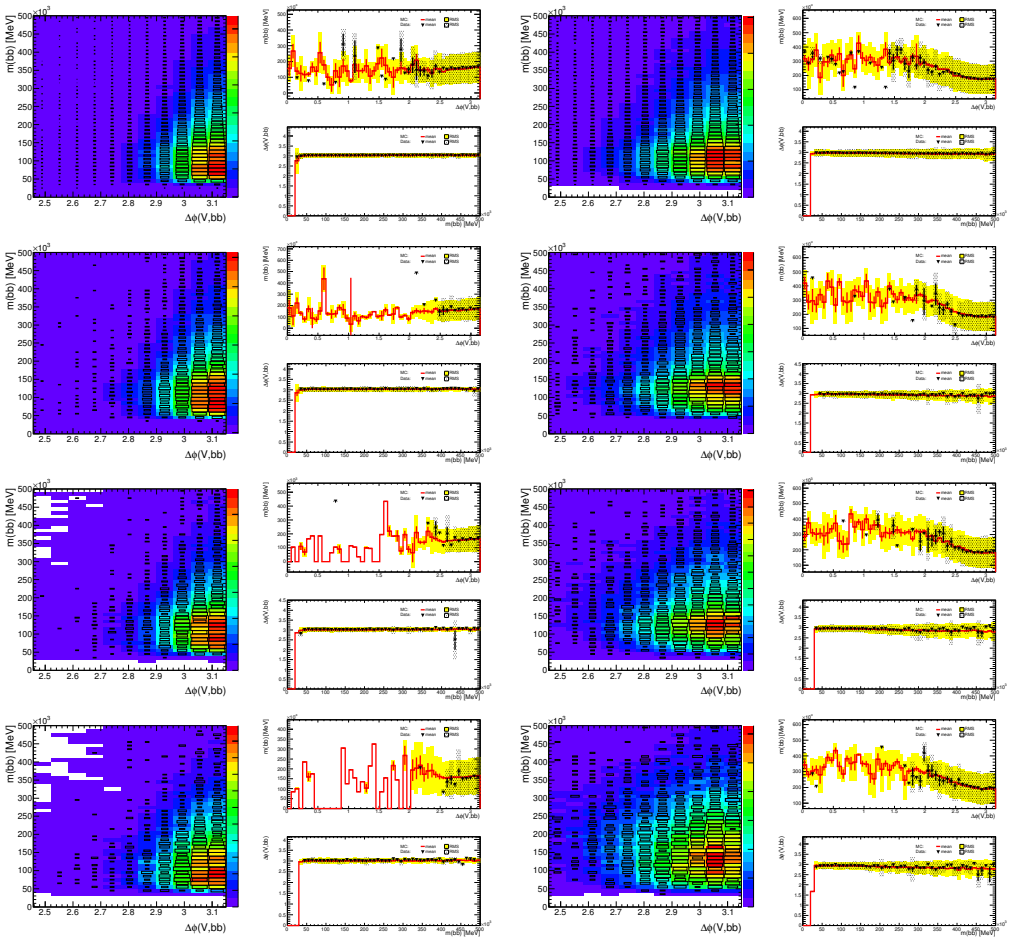

Figure 409: Correlation between BDTinput and output variables used in 0-lepton events ($p_{\mathrm{T}}^{W} > 120$ GeV) Row 1 - Left: 1 tag 2 jets Right: 1 tag 3 jets; Row 2 - Left: 2 LL tag 2 jets Right: 2 LL tag 3 jets; Row 3 - Left: 2 MM tag 2 jets Right: 2 MM tag 3 jets; Row 4 - Left: 2 TT tag 2 jets Right: 2 TT tag 3 jets. Section 6.1 details the definition of each variable.

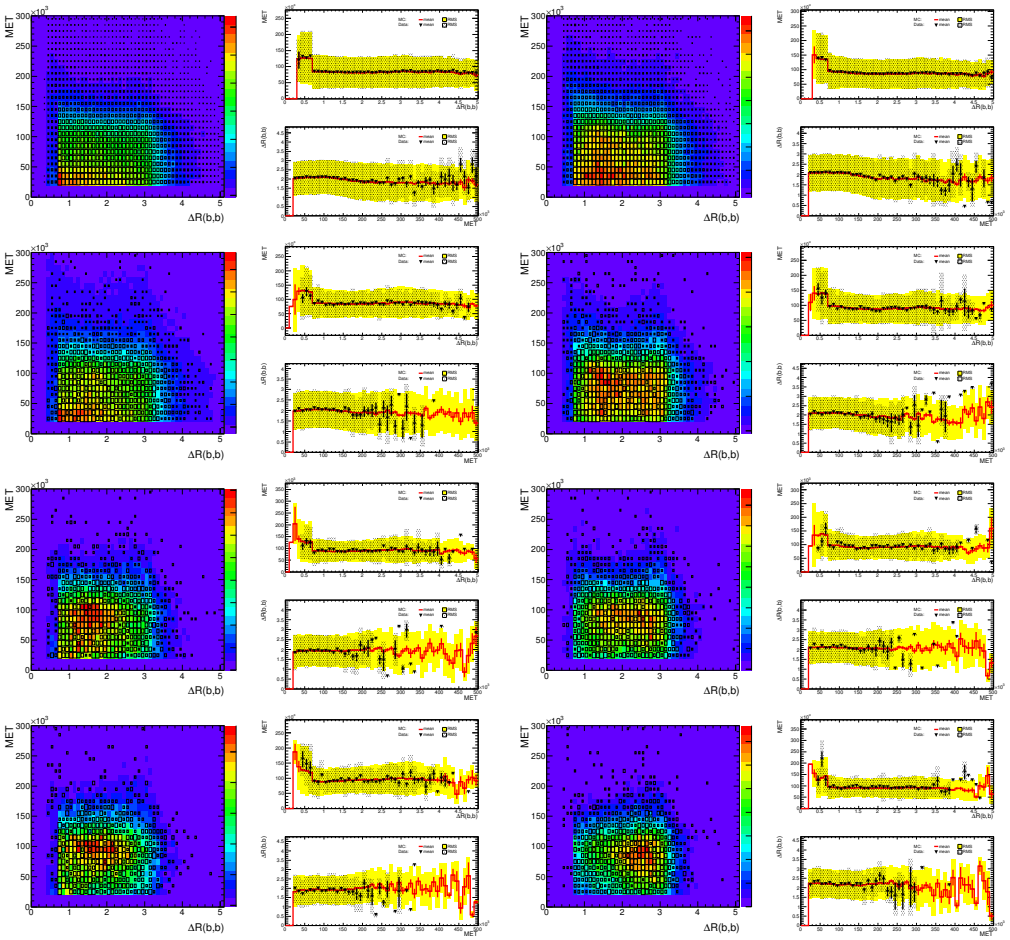

Figure 410: Correlation between BDTinput and output variables used in 0-lepton events ($p_{\mathrm{T}}^{W} > 120$ GeV) Row 1 - Left: 1 tag 2 jets Right: 1 tag 3 jets; Row 2 - Left: 2 LL tag 2 jets Right: 2 LL tag 3 jets; Row 3 - Left: 2 MM tag 2 jets Right: 2 MM tag 3 jets; Row 4 - Left: 2 TT tag 2 jets Right: 2 TT tag 3 jets. Section 6.1 details the definition of each variable.

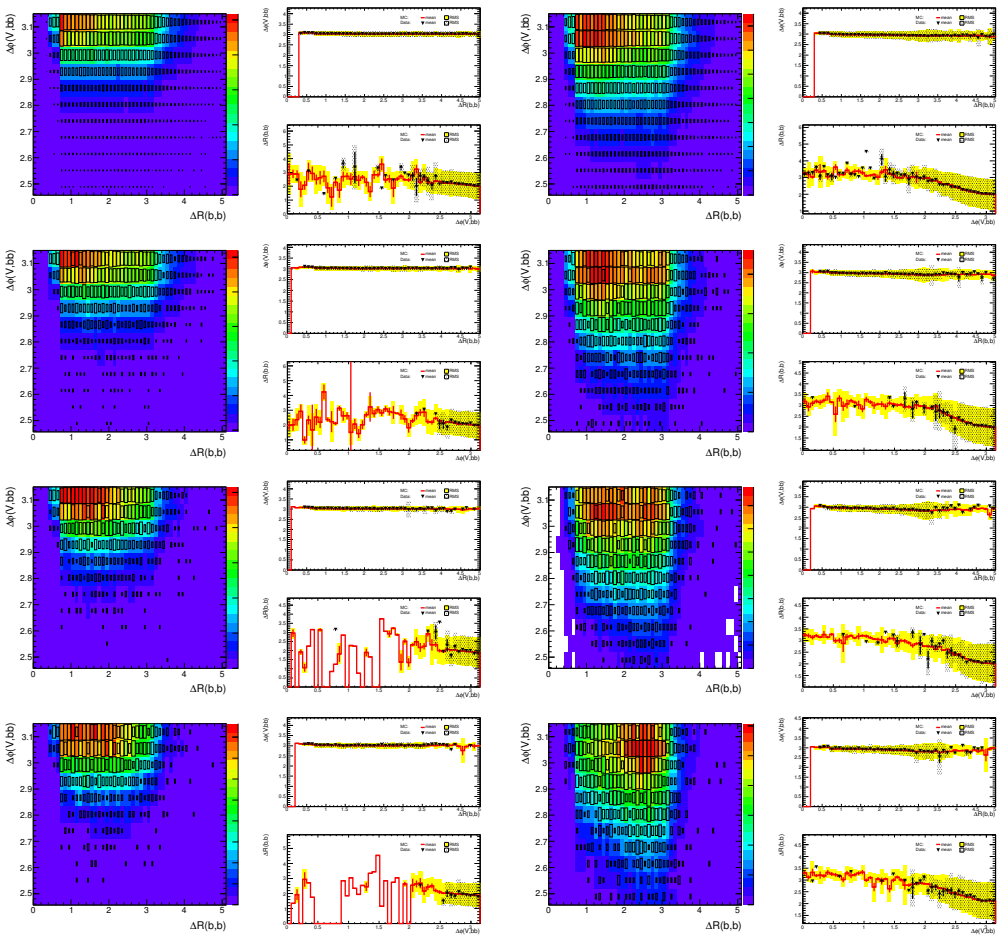

Figure 411: Correlation between BDTinput and output variables used in 0-lepton events ($p_{\mathrm{T}}^{W} > 120$ GeV) Row 1 - Left: 1 tag 2 jets Right: 1 tag 3 jets; Row 2 - Left: 2 LL tag 2 jets Right: 2 LL tag 3 jets; Row 3 - Left: 2 MM tag 2 jets Right: 2 MM tag 3 jets; Row 4 - Left: 2 TT tag 2 jets Right: 2 TT tag 3 jets. Section 6.1 details the definition of each variable.

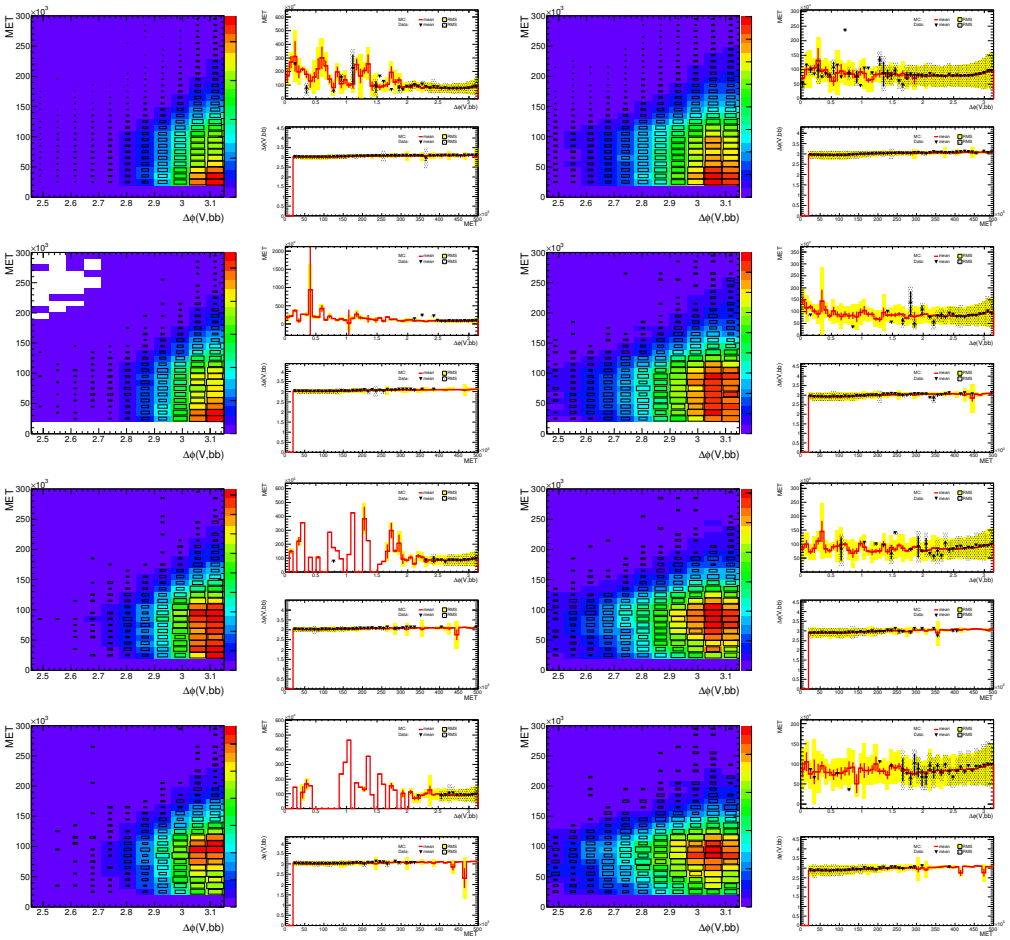

Figure 412: Correlation between BDTinput and output variables used in 0-lepton events ($p_{\mathrm{T}}^{W} > 120$ GeV) Row 1 - Left: 1 tag 2 jets Right: 1 tag 3 jets; Row 2 - Left: 2 LL tag 2 jets Right: 2 LL tag 3 jets; Row 3 - Left: 2 MM tag 2 jets Right: 2 MM tag 3 jets; Row 4 - Left: 2 TT tag 2 jets Right: 2 TT tag 3 jets. Section 6.1 details the definition of each variable.

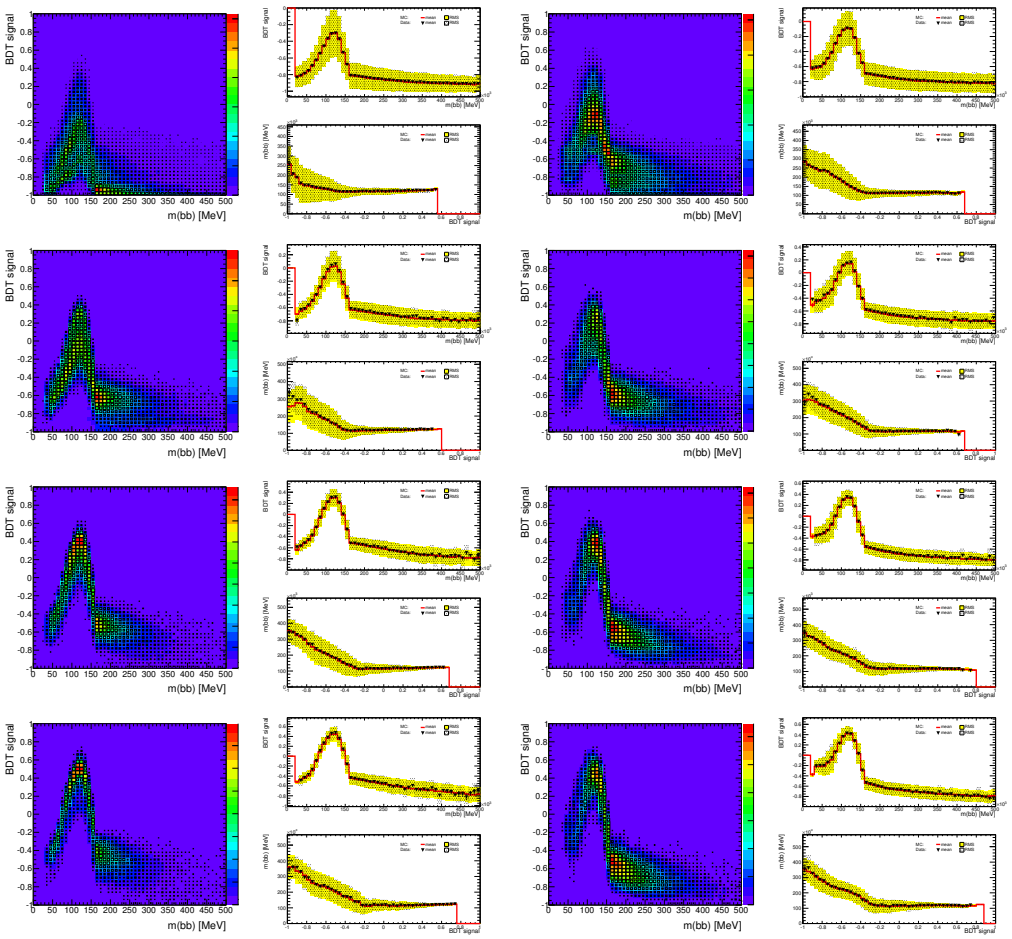

Figure 413: Correlation between BDTinput and output variables used in 0-lepton events ($p_{\mathrm{T}}^{W} < 120$ GeV) Row 1 - Left: 1 tag 2 jets Right: 1 tag 3 jets; Row 2 - Left: 2 LL tag 2 jets Right: 2 LL tag 3 jets; Row 3 - Left: 2 MM tag 2 jets Right: 2 MM tag 3 jets; Row 4 - Left: 2 TT tag 2 jets Right: 2 TT tag 3 jets. Section 6.1 details the definition of each variable.

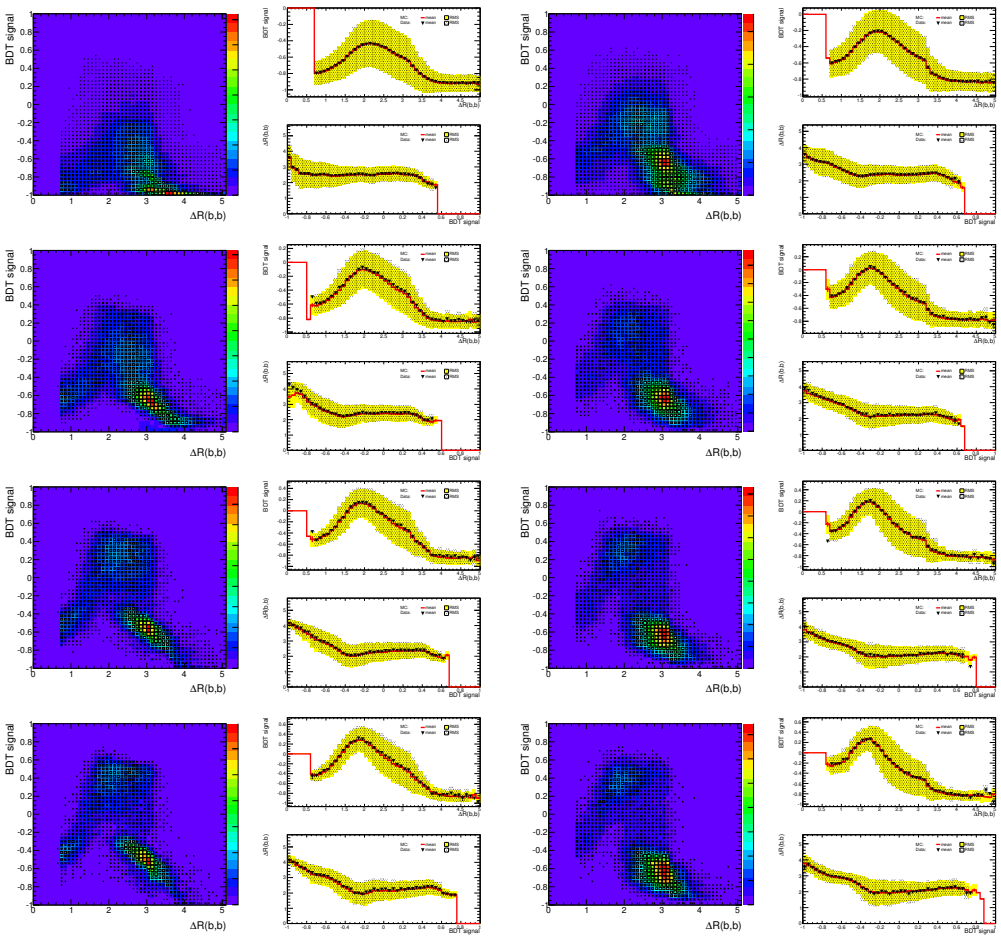

Figure 414: Correlation between BDTinput and output variables used in 0-lepton events ($p_{\mathrm{T}}^{W} < 120$ GeV) Row 1 - Left: 1 tag 2 jets Right: 1 tag 3 jets; Row 2 - Left: 2 LL tag 2 jets Right: 2 LL tag 3 jets; Row 3 - Left: 2 MM tag 2 jets Right: 2 MM tag 3 jets; Row 4 - Left: 2 TT tag 2 jets Right: 2 TT tag 3 jets. Section 6.1 details the definition of each variable.

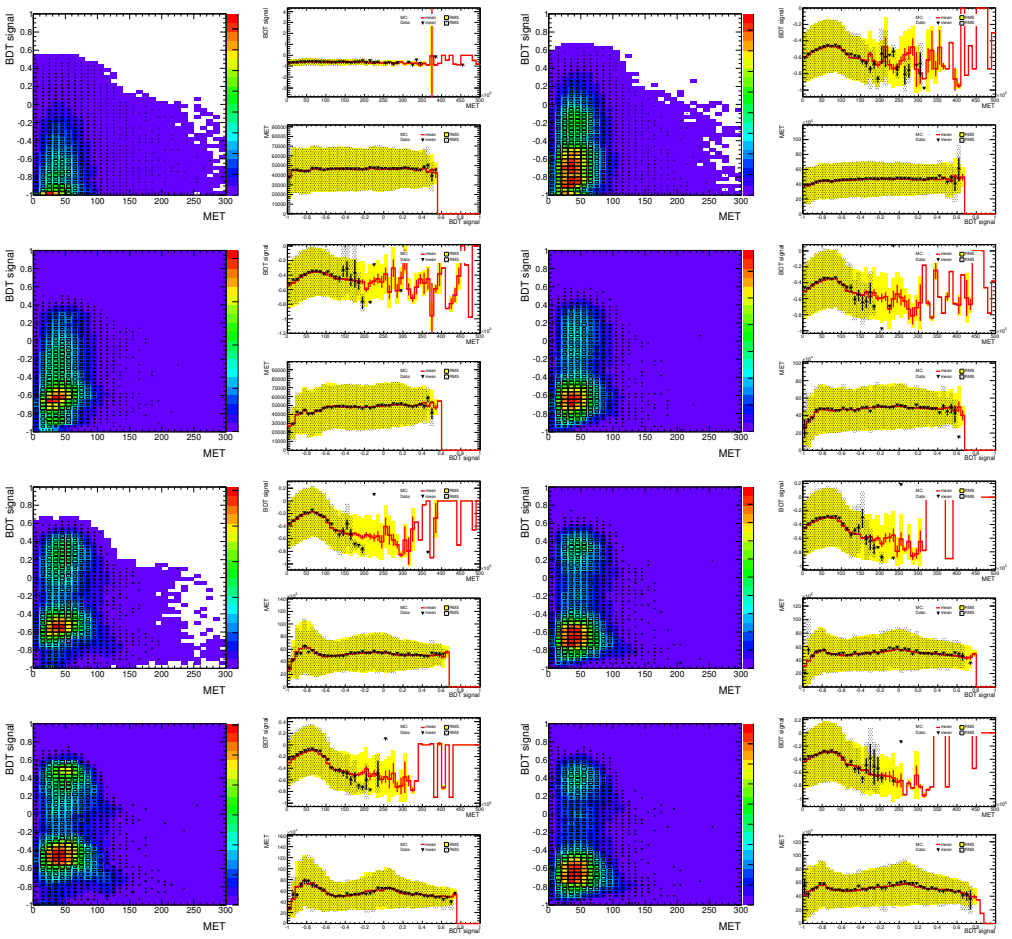

Figure 415: Correlation between BDTinput and output variables used in 0-lepton events ($p_{\mathrm{T}}^{W} < 120$ GeV) Row 1 - Left: 1 tag 2 jets Right: 1 tag 3 jets; Row 2 - Left: 2 LL tag 2 jets Right: 2 LL tag 3 jets; Row 3 - Left: 2 MM tag 2 jets Right: 2 MM tag 3 jets; Row 4 - Left: 2 TT tag 2 jets Right: 2 TT tag 3 jets. Section 6.1 details the definition of each variable.

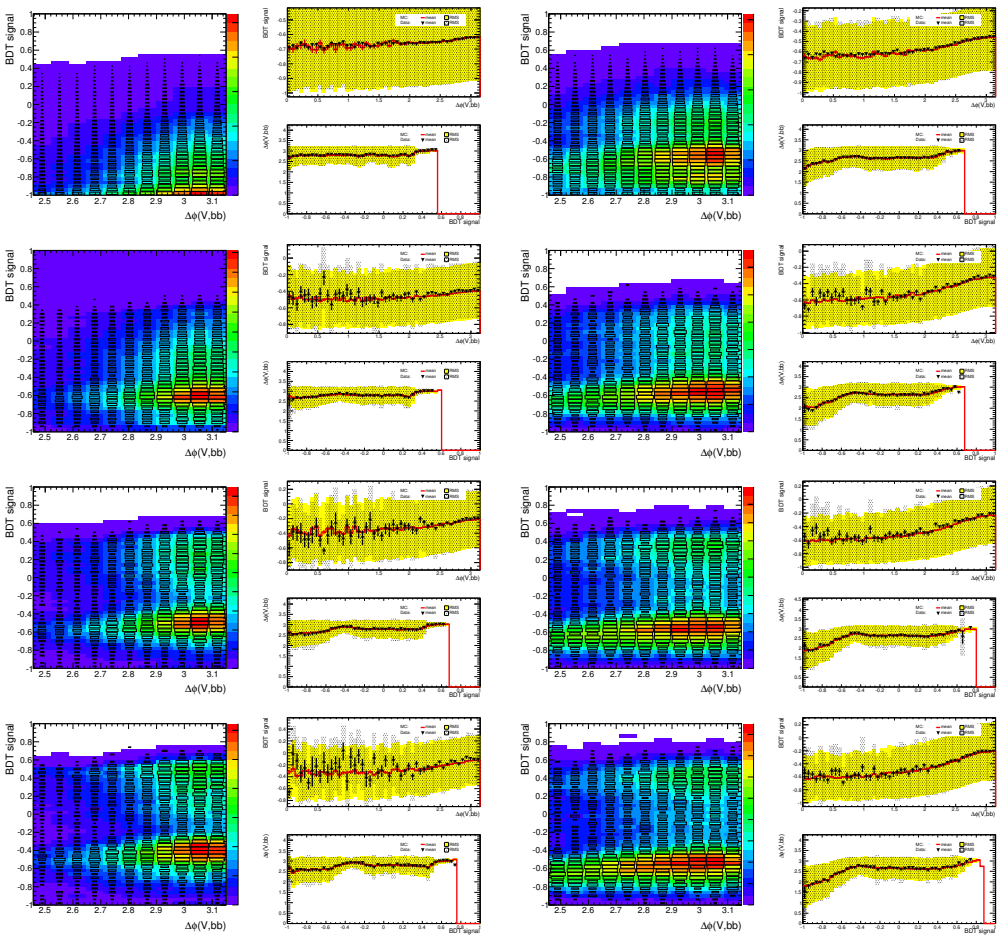

Figure 416: Correlation between BDTinput and output variables used in 0-lepton events ($p_{\mathrm{T}}^{W} < 120$ GeV) Row 1 - Left: 1 tag 2 jets Right: 1 tag 3 jets; Row 2 - Left: 2 LL tag 2 jets Right: 2 LL tag 3 jets; Row 3 - Left: 2 MM tag 2 jets Right: 2 MM tag 3 jets; Row 4 - Left: 2 TT tag 2 jets Right: 2 TT tag 3 jets. Section 6.1 details the definition of each variable.

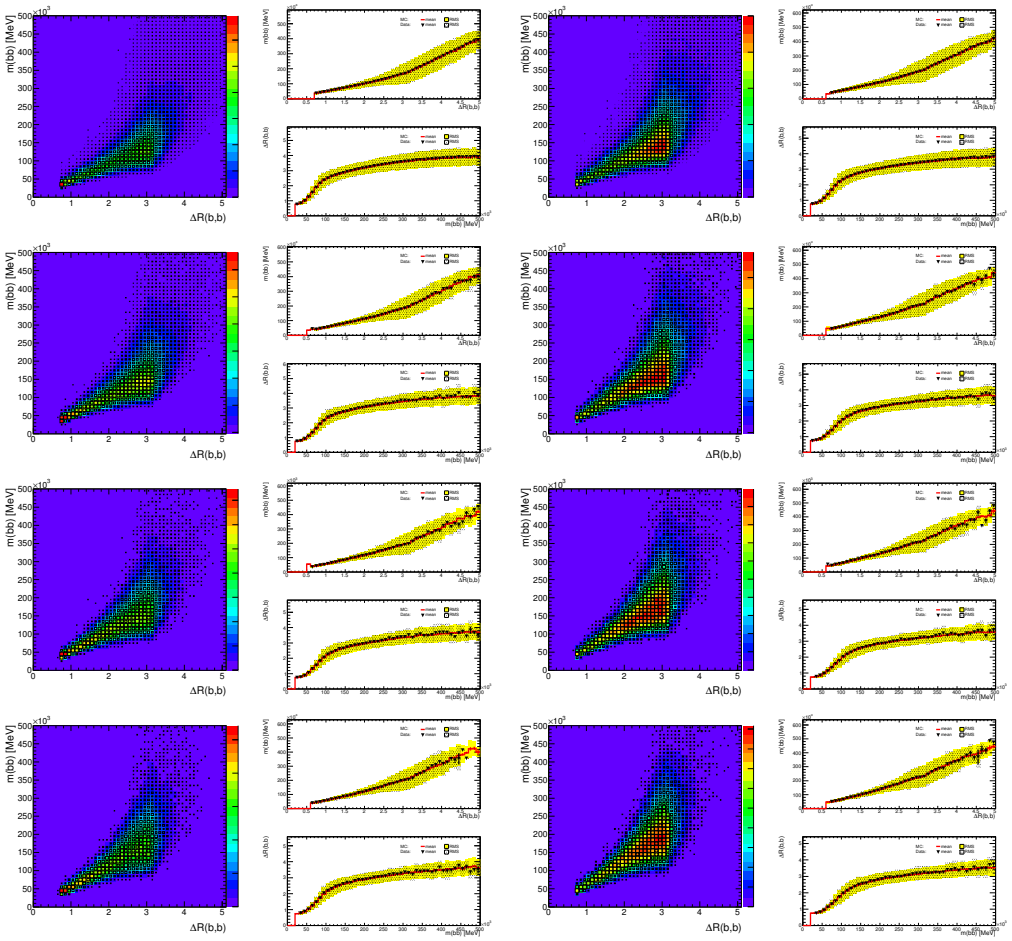

Figure 417: Correlation between BDTinput and output variables used in 0-lepton events ($p_{\mathrm{T}}^{W} < 120$ GeV) Row 1 - Left: 1 tag 2 jets Right: 1 tag 3 jets; Row 2 - Left: 2 LL tag 2 jets Right: 2 LL tag 3 jets; Row 3 - Left: 2 MM tag 2 jets Right: 2 MM tag 3 jets; Row 4 - Left: 2 TT tag 2 jets Right: 2 TT tag 3 jets. Section 6.1 details the definition of each variable.

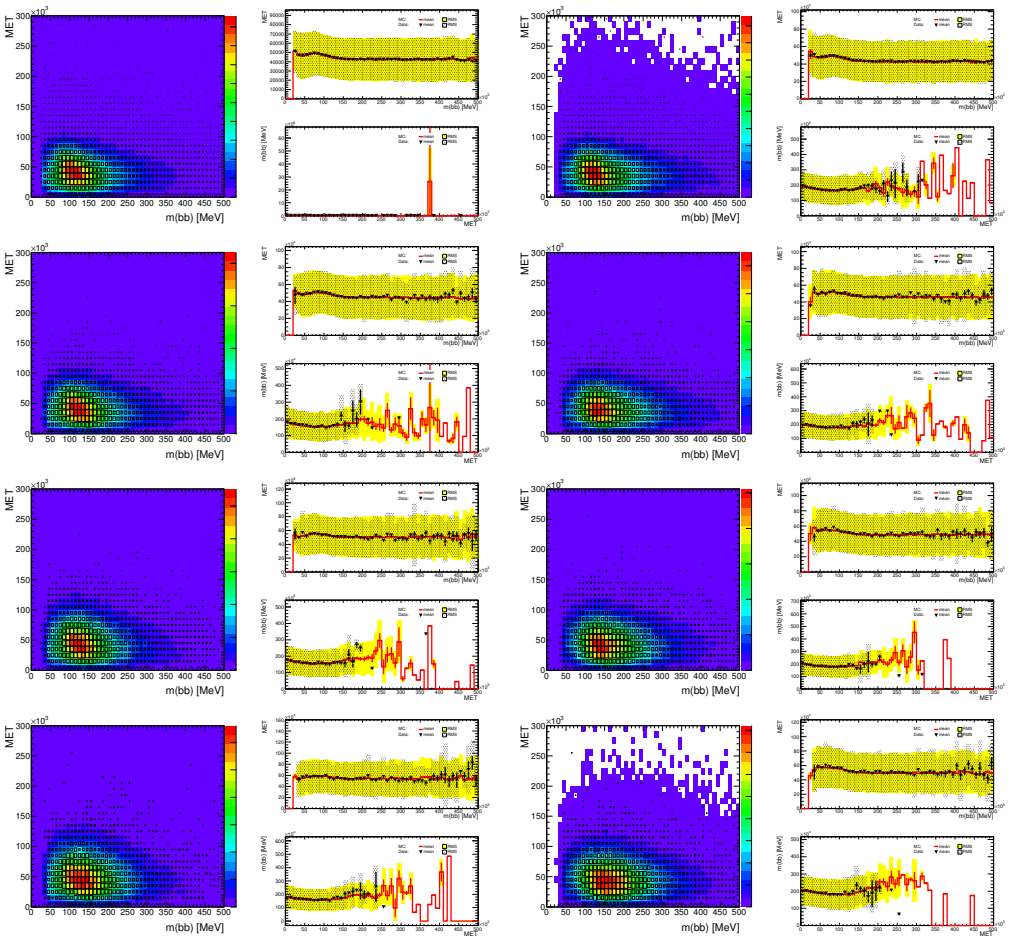

Figure 418: Correlation between BDTinput and output variables used in 0-lepton events ($p_{\mathrm{T}}^{W} < 120$ GeV) Row 1 - Left: 1 tag 2 jets Right: 1 tag 3 jets; Row 2 - Left: 2 LL tag 2 jets Right: 2 LL tag 3 jets; Row 3 - Left: 2 MM tag 2 jets Right: 2 MM tag 3 jets; Row 4 - Left: 2 TT tag 2 jets Right: 2 TT tag 3 jets. Section 6.1 details the definition of each variable.

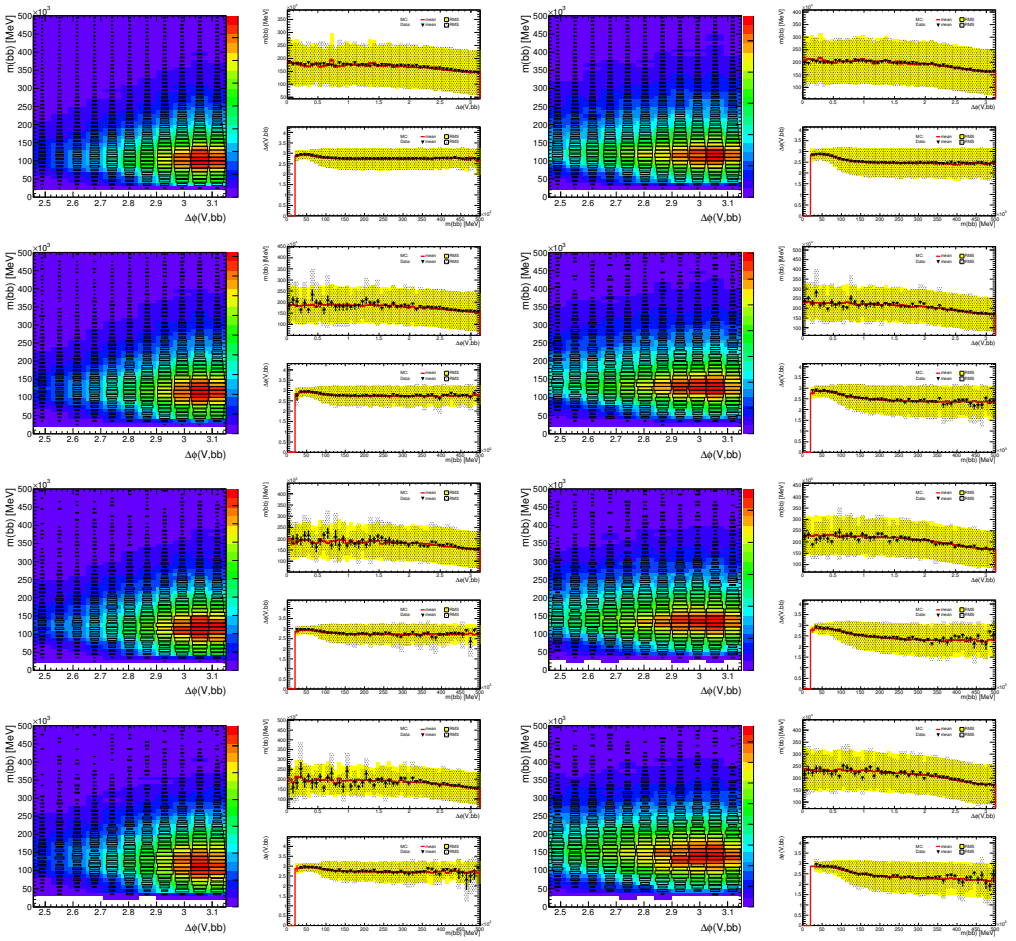

Figure 419: Correlation between BDTinput and output variables used in 0-lepton events ($p_{\mathrm{T}}^{W} < 120$ GeV) Row 1 - Left: 1 tag 2 jets Right: 1 tag 3 jets; Row 2 - Left: 2 LL tag 2 jets Right: 2 LL tag 3 jets; Row 3 - Left: 2 MM tag 2 jets Right: 2 MM tag 3 jets; Row 4 - Left: 2 TT tag 2 jets Right: 2 TT tag 3 jets. Section 6.1 details the definition of each variable.

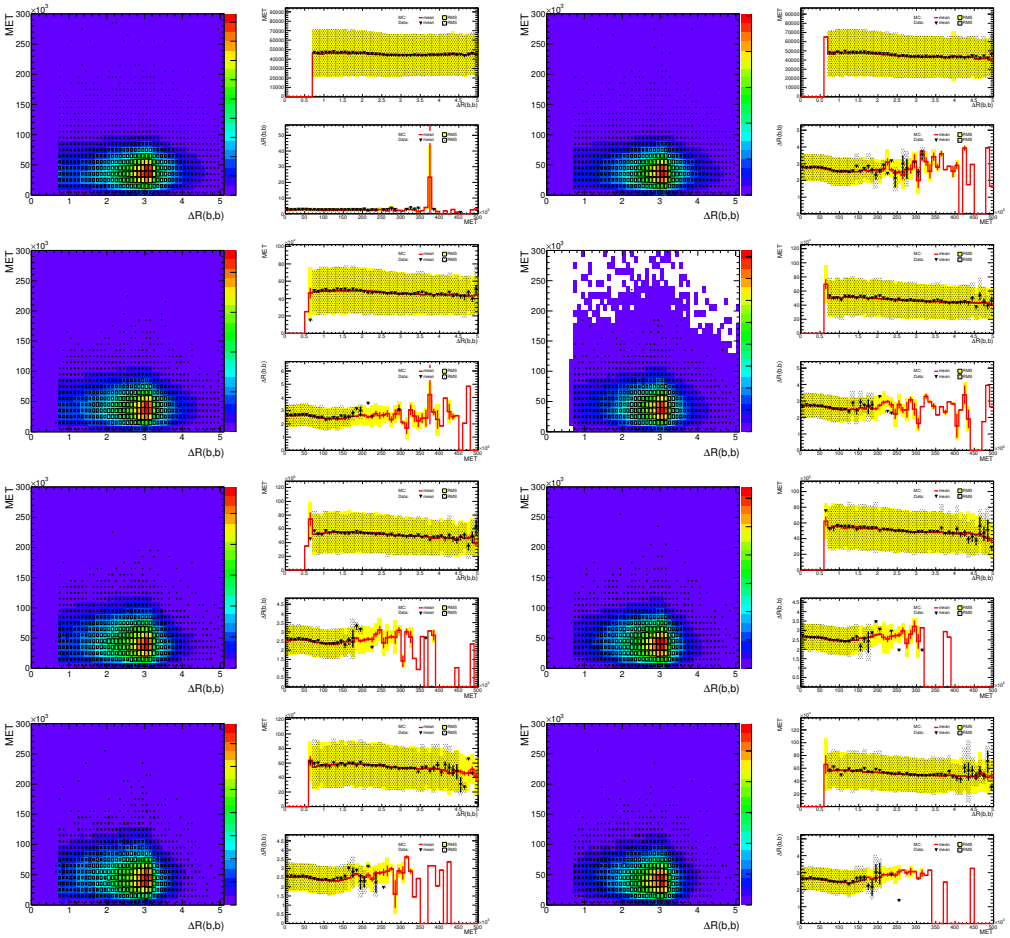

Figure 420: Correlation between BDTinput and output variables used in 0-lepton events ($p_{\mathrm{T}}^{W} < 120$ GeV) Row 1 - Left: 1 tag 2 jets Right: 1 tag 3 jets; Row 2 - Left: 2 LL tag 2 jets Right: 2 LL tag 3 jets; Row 3 - Left: 2 MM tag 2 jets Right: 2 MM tag 3 jets; Row 4 - Left: 2 TT tag 2 jets Right: 2 TT tag 3 jets. Section 6.1 details the definition of each variable.

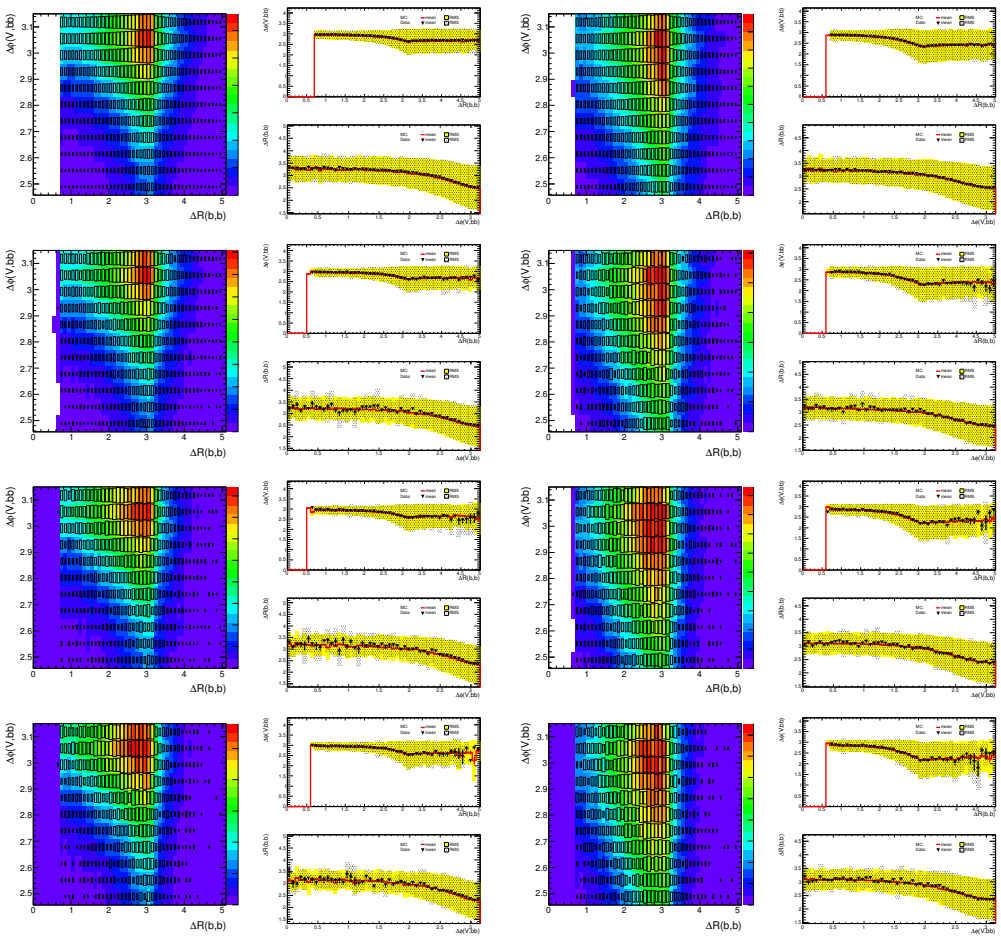

Figure 421: Correlation between BDTinput and output variables used in 0-lepton events ($p_{\mathrm{T}}^{W} < 120$ GeV) Row 1 - Left: 1 tag 2 jets Right: 1 tag 3 jets; Row 2 - Left: 2 LL tag 2 jets Right: 2 LL tag 3 jets; Row 3 - Left: 2 MM tag 2 jets Right: 2 MM tag 3 jets; Row 4 - Left: 2 TT tag 2 jets Right: 2 TT tag 3 jets. Section 6.1 details the definition of each variable.

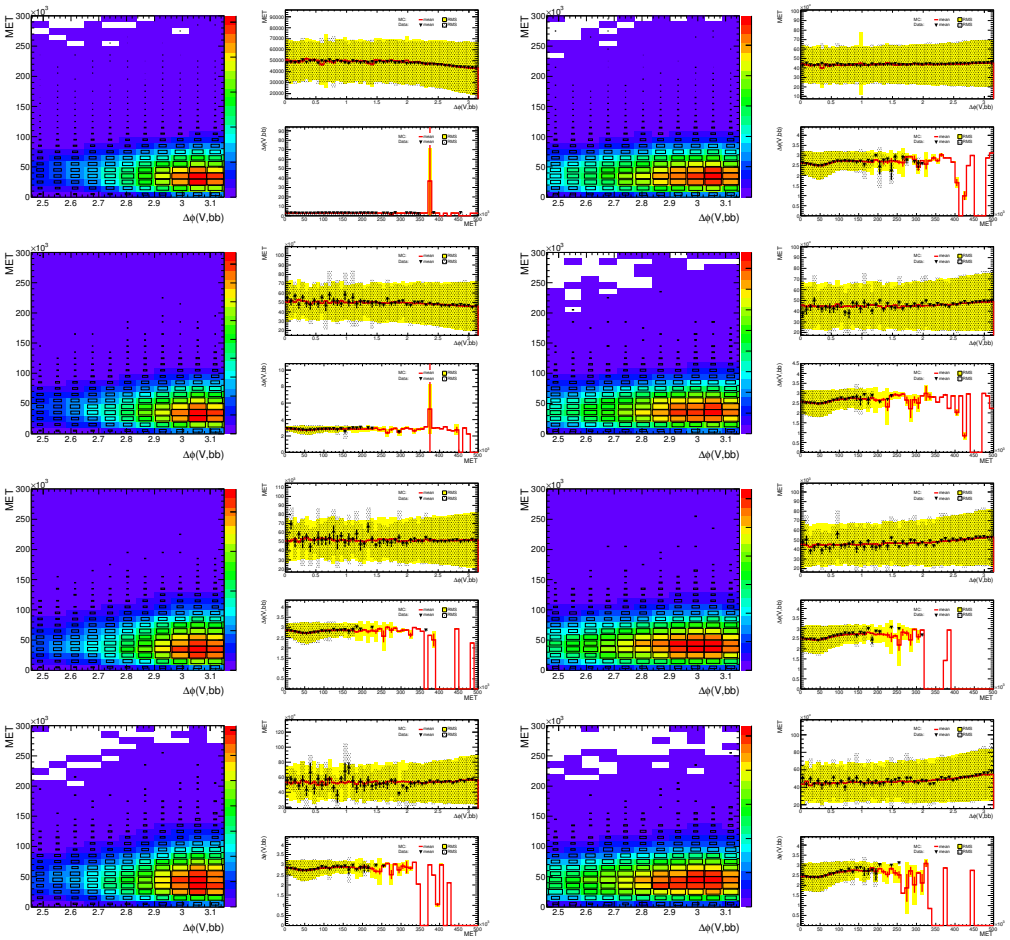

Figure 422: Correlation between BDTinput and output variables used in 0-lepton events ($p_{\mathrm{T}}^{W} < 120$ GeV) Row 1 - Left: 1 tag 2 jets Right: 1 tag 3 jets; Row 2 - Left: 2 LL tag 2 jets Right: 2 LL tag 3 jets; Row 3 - Left: 2 MM tag 2 jets Right: 2 MM tag 3 jets; Row 4 - Left: 2 TT tag 2 jets Right: 2 TT tag 3 jets. Section 6.1 details the definition of each variable.

AG Correlations between MVA Variables: Two Lepton

This appendix contains correlations between input and output variables of the BDT, defined in Section 6 in the 2-lepton analysis. These plots are done by applying the latest scale factors, obtained for the 2 jet region and the 3 jet region separately, by comparing the event yield before and after the MVA combined fit. They are summarized in Table 114. Explicitly stated, the theoretical expectation for each background is used for the given luminosity. All the plots in this section are done with the status-of-art analysis. Part of the plots in this appendix will be added in a future version of the note.

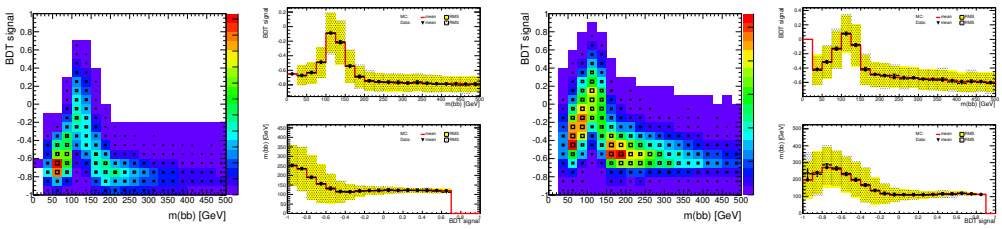

Figure 423: Correlation between mva and mBB variables used in 2-lepton MVAanalysis ($p_{\mathrm{T}}^{Z} > 120$ GeV) Row 1 - Left: 1 tag 2 jets Right: 1 tag 3 jets; Row 2 - Left: 2 LL tag 2 jets Right: 2 LL tag 3 jets; Row 3 - Left: 2 MM tag 2 jets Right: 2 MM tag 3 jets; Row 4 - Left: 2 TT tag 2 jets Right: 2 TT tag 3 jets. Section 6.1 details the definition of each variable.

Figure 424: Correlation between mva and dRBB variables used in 2-lepton MVAanalysis ($p_{\mathrm{T}}^{Z} > 120$ GeV) Row 1 - Left: 1 tag 2 jets Right: 1 tag 3 jets; Row 2 - Left: 2 LL tag 2 jets Right: 2 LL tag 3 jets; Row 3 - Left: 2 MM tag 2 jets Right: 2 MM tag 3 jets; Row 4 - Left: 2 TT tag 2 jets Right: 2 TT tag 3 jets. Section 6.1 details the definition of each variable.

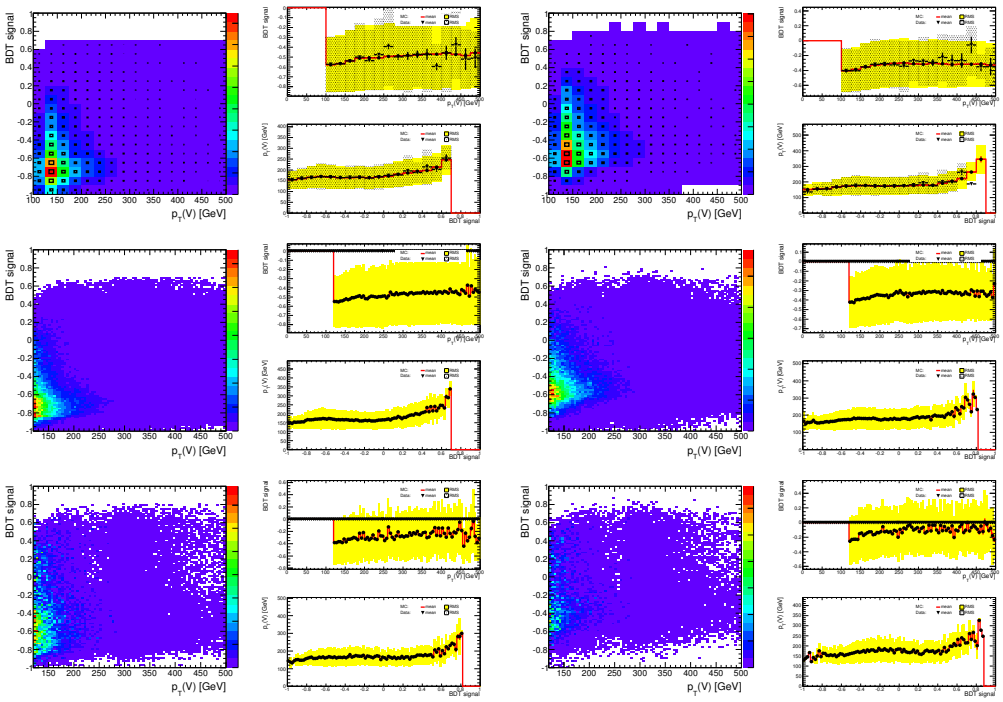

Figure 425: Correlation between mva and pTV variables used in 2-lepton MVAanalysis ($p_{\mathrm{T}}^{Z} > 120$ GeV) Row 1 - Left: 1 tag 2 jets Right: 1 tag 3 jets; Row 2 - Left: 2 LL tag 2 jets Right: 2 LL tag 3 jets; Row 3 - Left: 2 MM tag 2 jets Right: 2 MM tag 3 jets; Row 4 - Left: 2 TT tag 2 jets Right: 2 TT tag 3 jets. Section 6.1 details the definition of each variable.

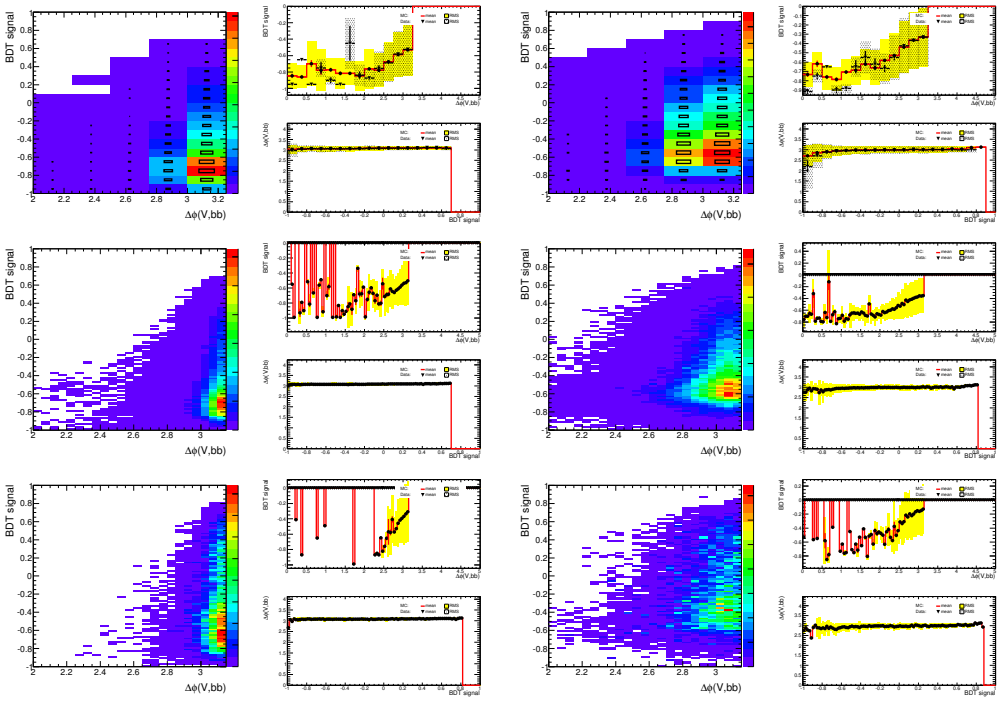

Figure 426: Correlation between mva and dPhiVBB variables used in 2-lepton MVAanalysis ($p_{\mathrm{T}}^{Z} > 120$ GeV) Row 1 - Left: 1 tag 2 jets Right: 1 tag 3 jets; Row 2 - Left: 2 LL tag 2 jets Right: 2 LL tag 3 jets; Row 3 - Left: 2 MM tag 2 jets Right: 2 MM tag 3 jets; Row 4 - Left: 2 TT tag 2 jets Right: 2 TT tag 3 jets. Section 6.1 details the definition of each variable.

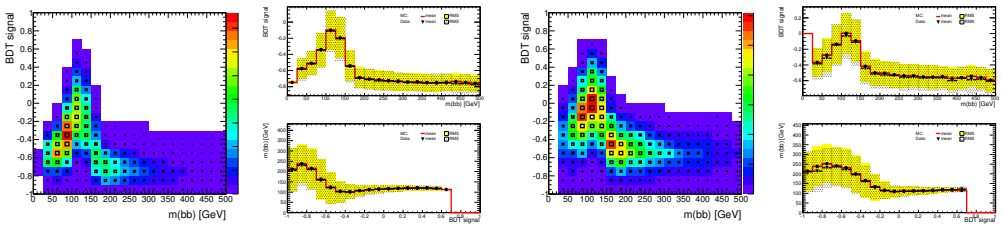

Figure 427: Correlation between mva and mBB variables used in 2-lepton MVAanalysis ($p_{\mathrm{T}}^{Z} < 120$ GeV) Row 1 - Left: 1 tag 2 jets Right: 1 tag 3 jets; Row 2 - Left: 2 LL tag 2 jets Right: 2 LL tag 3 jets; Row 3 - Left: 2 MM+TT tag 2 jets Right: 2 MM+TT tag 3 jets; Section 6.1 details the definition of each variable.

Figure 428: Correlation between mva and dRBB variables used in 2-lepton MVAanalysis ($p_{\mathrm{T}}^{Z} < 120$ GeV) Row 1 - Left: 1 tag 2 jets Right: 1 tag 3 jets; Row 2 - Left: 2 LL tag 2 jets Right: 2 LL tag 3 jets; Row 3 - Left: 2 MM+TT tag 2 jets Right: 2 MM+TT tag 3 jets; Section 6.1 details the definition of each variable.

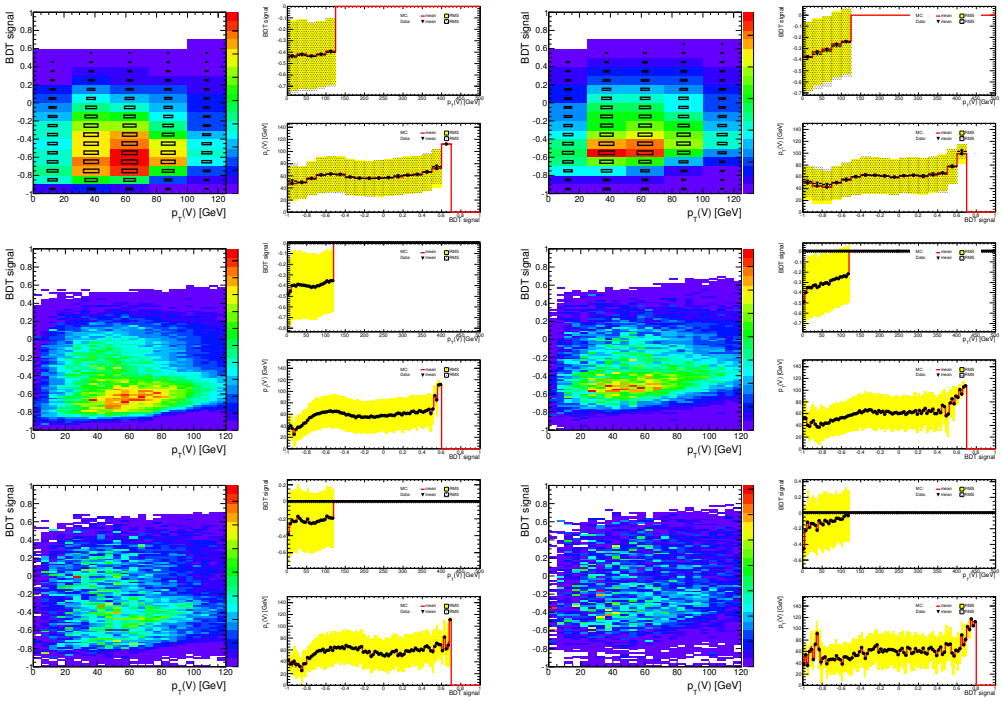

Figure 429: Correlation between mva and pTV variables used in 2-lepton MVAanalysis ($p_{\mathrm{T}}^{Z} < 120$ GeV) Row 1 - Left: 1 tag 2 jets Right: 1 tag 3 jets; Row 2 - Left: 2 LL tag 2 jets Right: 2 LL tag 3 jets; Row 3 - Left: 2 MM+TT tag 2 jets Right: 2 MM+TT tag 3 jets; Section 6.1 details the definition of each variable.

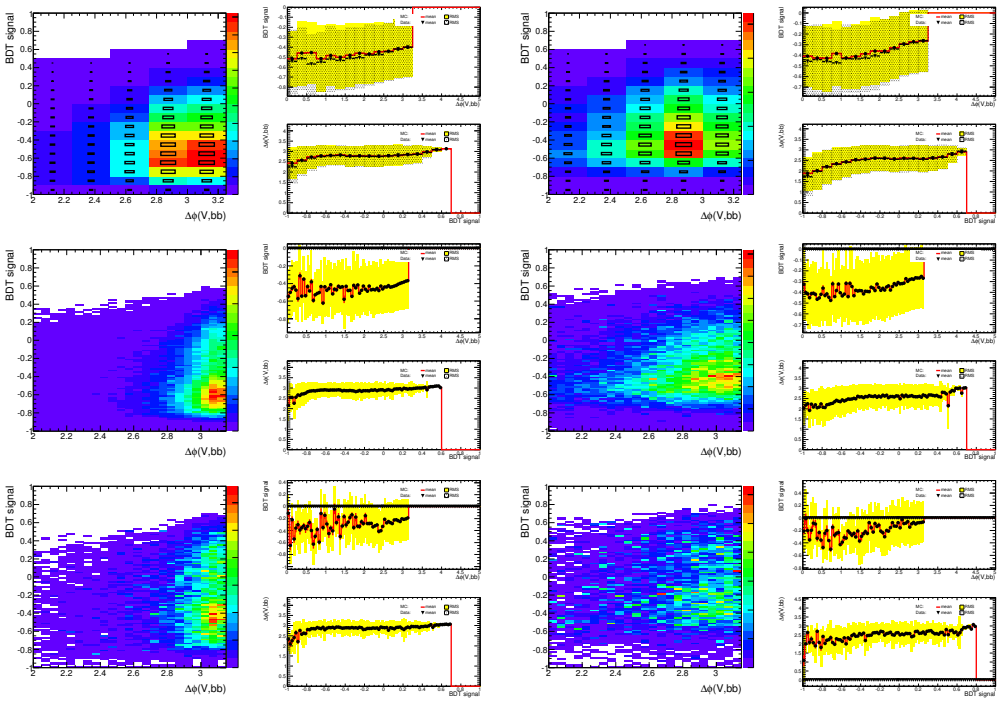

Figure 430: Correlation between mva and dPhiVBB variables used in 2-lepton MVAanalysis ($p_{\mathrm{T}}^{Z} < 120$ GeV) Row 1 - Left: 1 tag 2 jets Right: 1 tag 3 jets; Row 2 - Left: 2 LL tag 2 jets Right: 2 LL tag 3 jets; Row 3 - Left: 2 MM+TT tag 2 jets Right: 2 MM+TT tag 3 jets; Section 6.1 details the definition of each variable.

AH Pulls for the Individual Channels

Fits to the nominal Asimov are shown in red and the data pulls in black. Each fit is performed in the individual channels alone. The $e - \mu$ control sample is included in the 2-lepton fit.

AH.1 Dijet Mass Analysis

??

AH.1.1 0-lepton

The pull plots for 0-lepton are shown in Figure. 431-435.

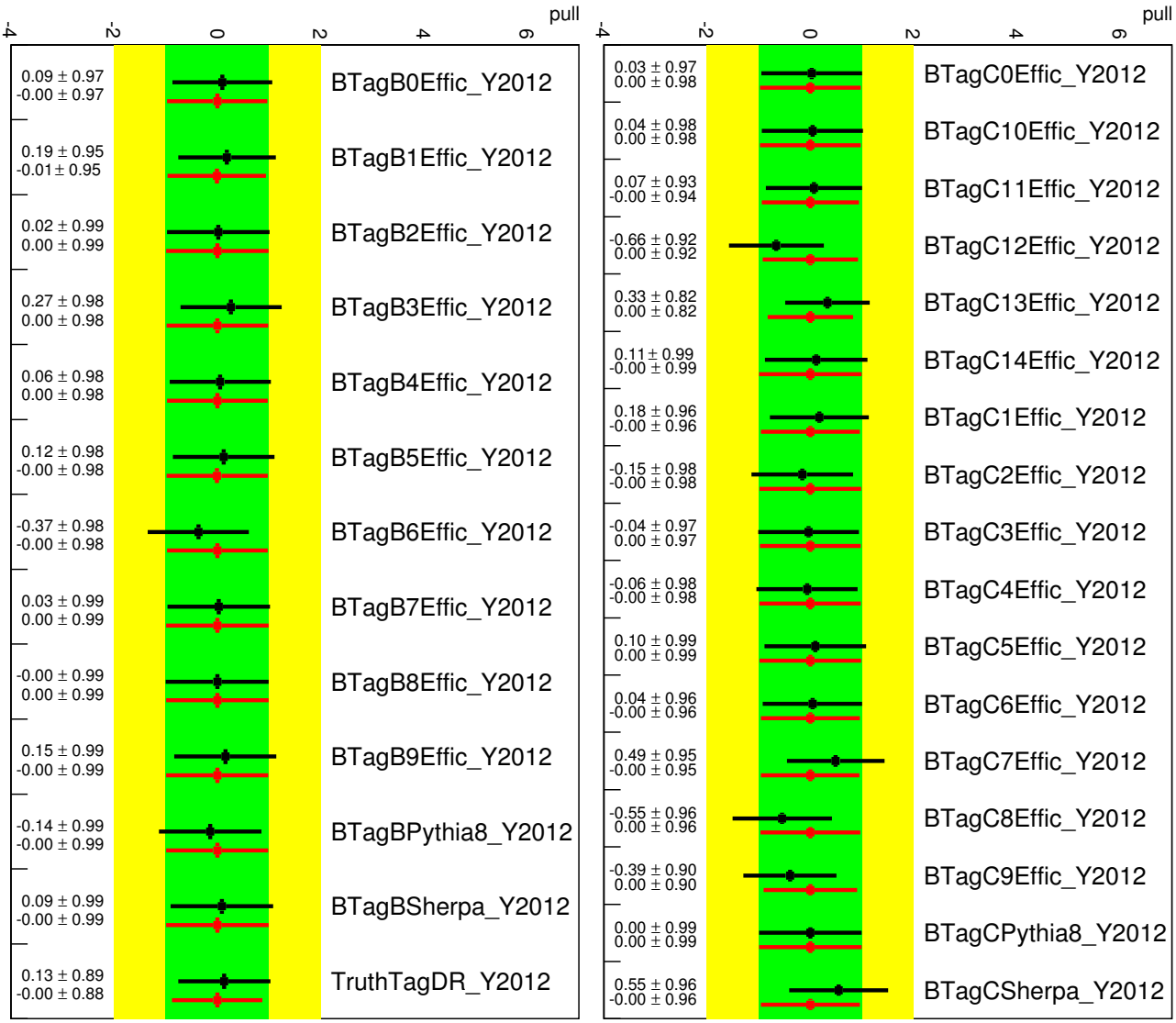

Figure 431: Pull plots for 0-lepton channel: b- and c-jet tagging.

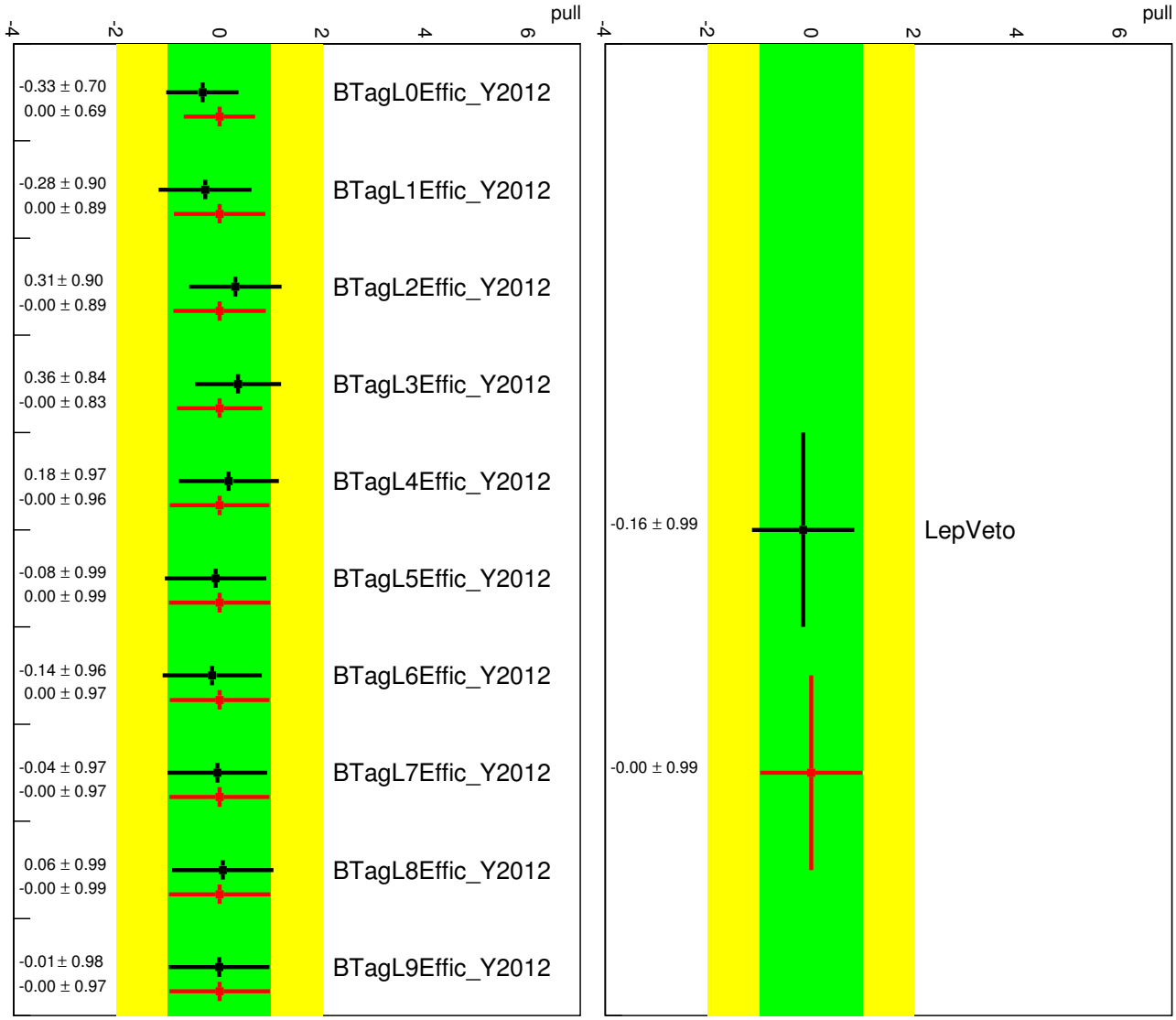

Figure 432: Pull plots for 0-lepton channel: light-jet tagging and leptons.

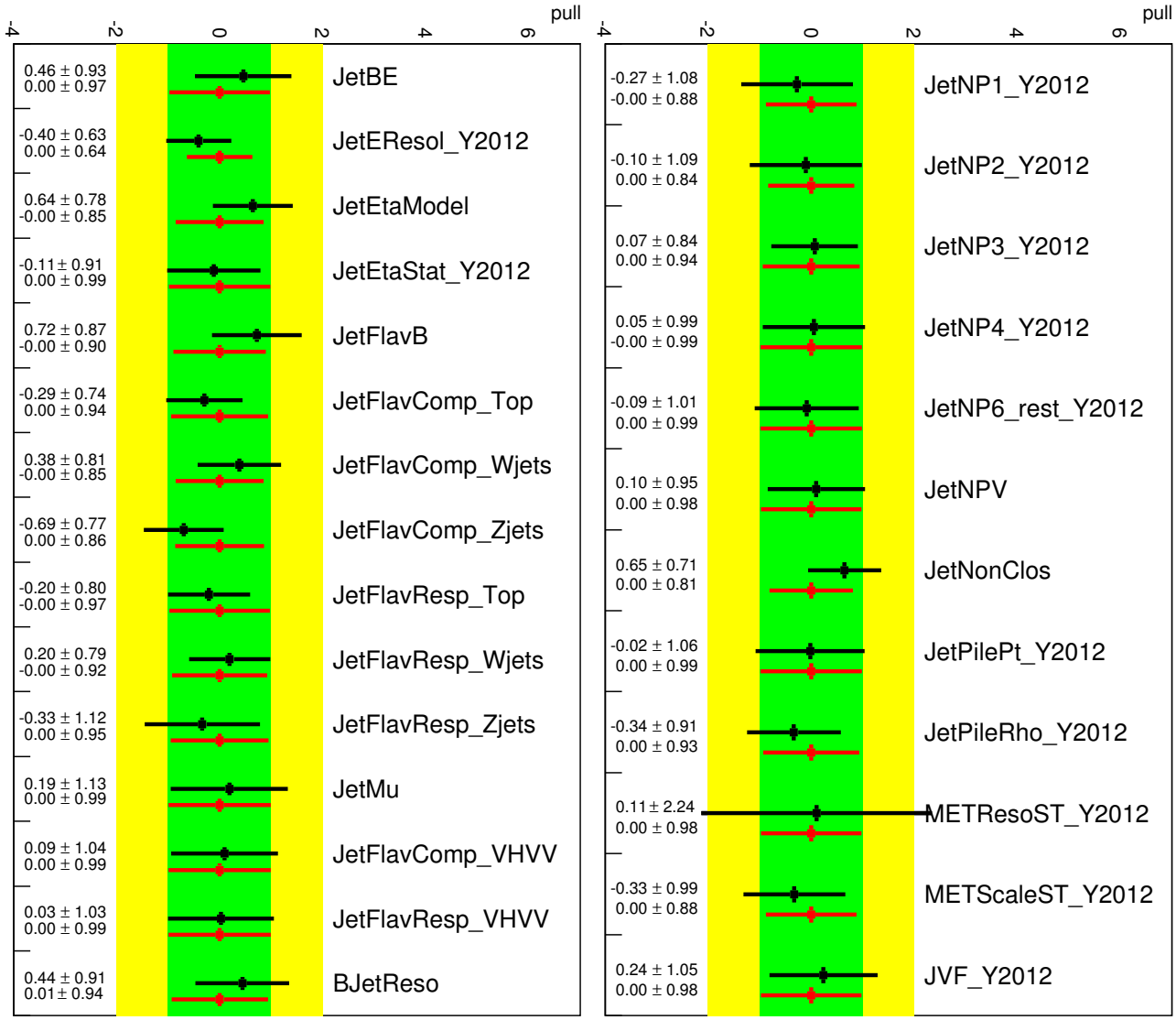

Figure 433: Pull plots for 0-lepton channel: Jet NPs.

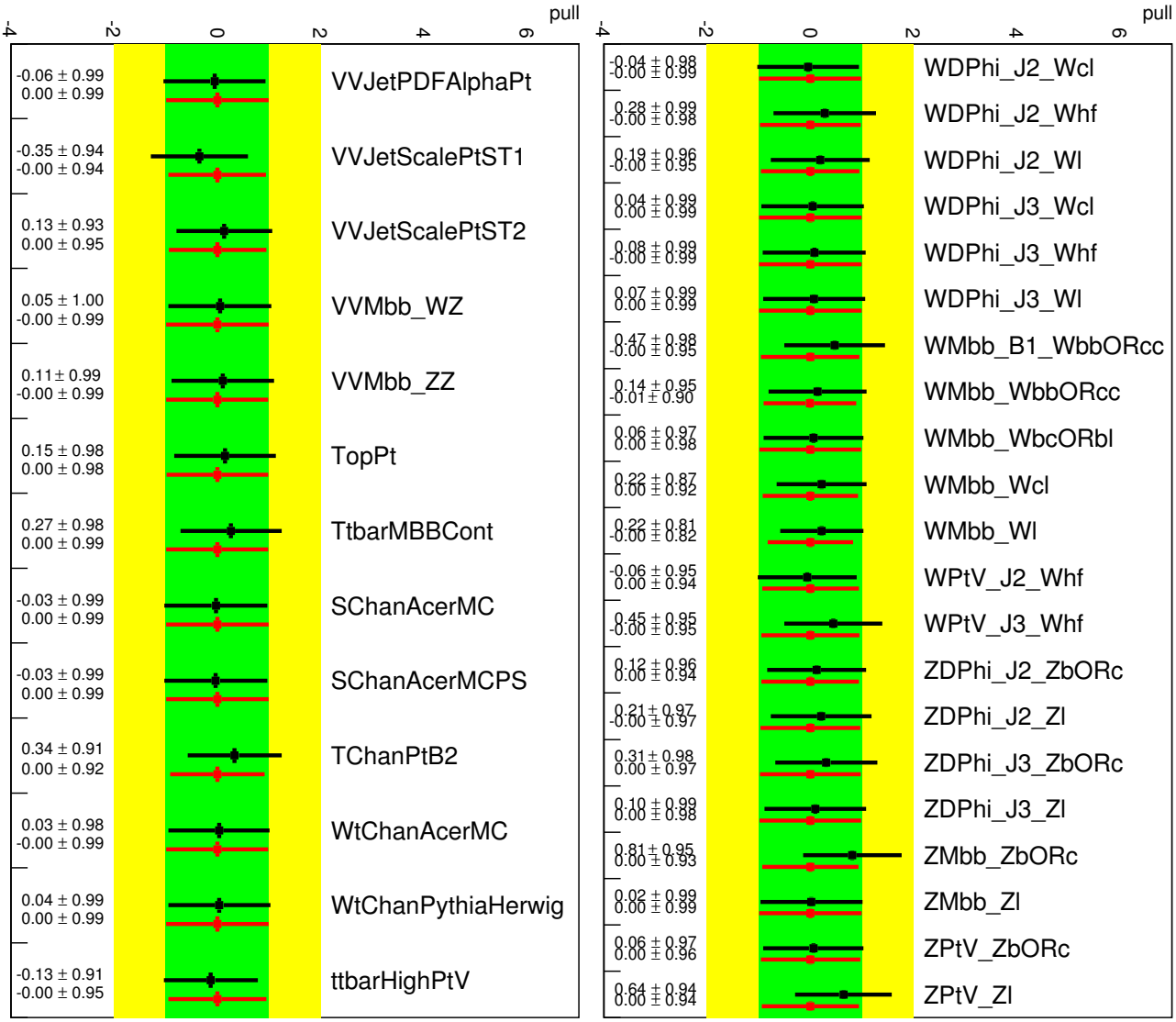

Figure 434: Pull plots for 0-lepton channel: Diboson and Top related uncertainties.

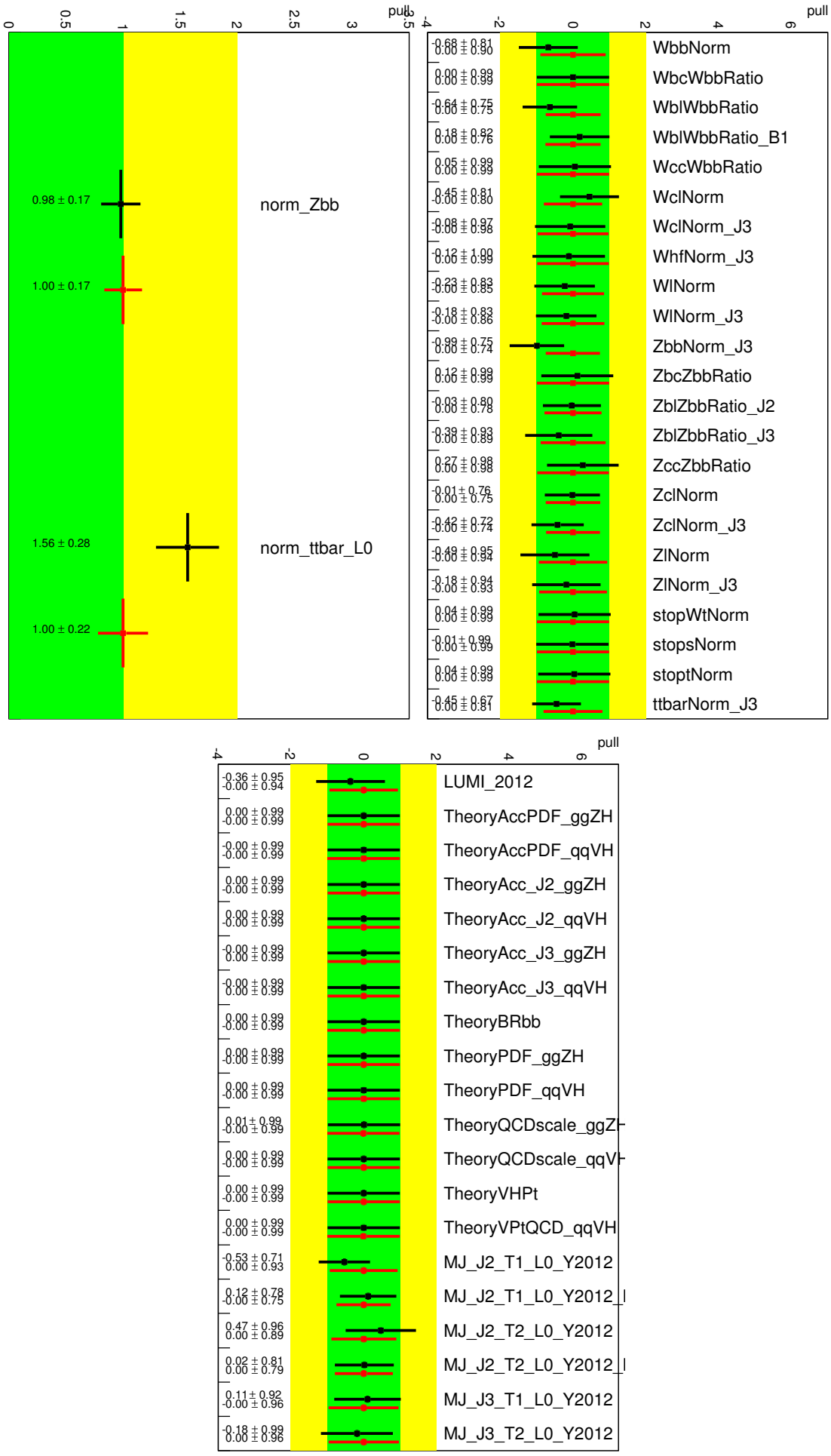

Figure 435: Pull plots for 0-lepton channel: Normalization and residual uncertainties.

AH.1.2 Pre-fit and Post-Fit for the m_{jj} shape analysis in the 0-lepton fit

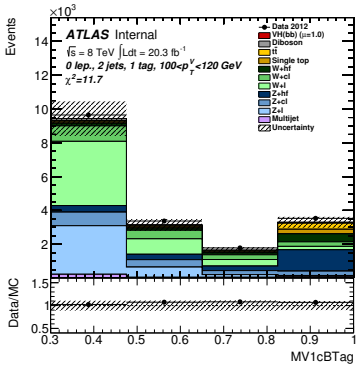

(a) $p_{\mathrm{T}}^{V} < 120$ GeV, 2 jets, 1-tag

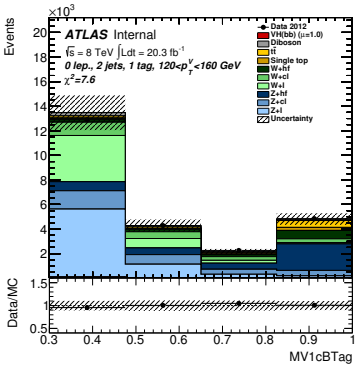

(b) $p_{\mathrm{T}}^{V} > 120$ GeV, 2 jets, 1-tag

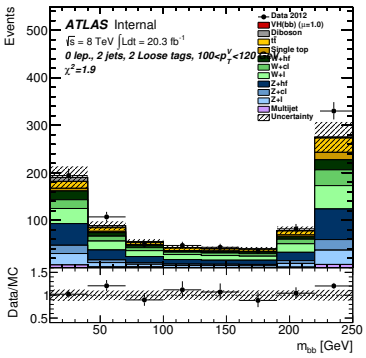

(c) $100 < p_{\mathrm{T}}^{V} < 120$ GeV, 2 jets, LL

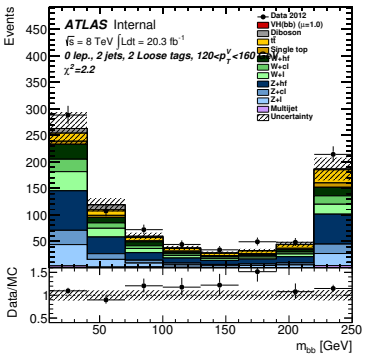

(d) $120 < p_{\mathrm{T}}^{V} < 160$ GeV, 2 jets, LL

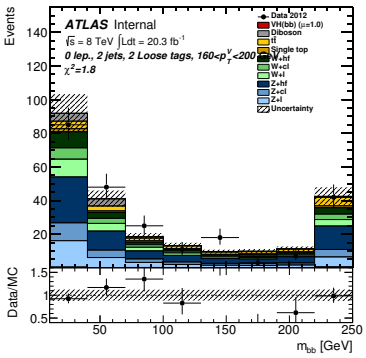

(e) $160 < p_{\mathrm{T}}^{V} < 200$ GeV, 2 jets, LL

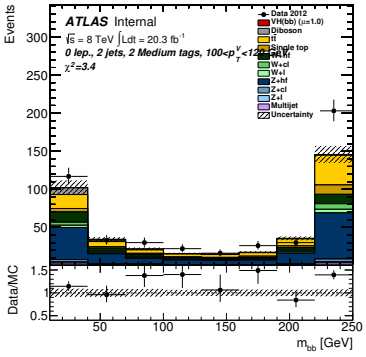

(f) $100 < p_{\mathrm{T}}^{V} < 120$ GeV, 2 jets, MM

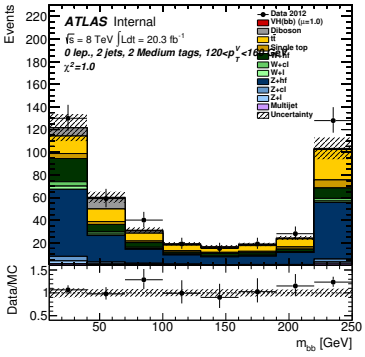

(g) $120 < p_{\mathrm{T}}^{V} < 160$ GeV, 2 jets, MM

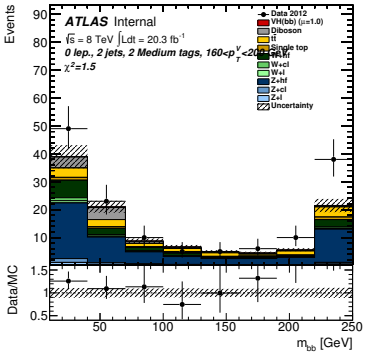

(h) $160 < p_{\mathrm{T}}^{V} < 200$ GeV, 2 jets, MM

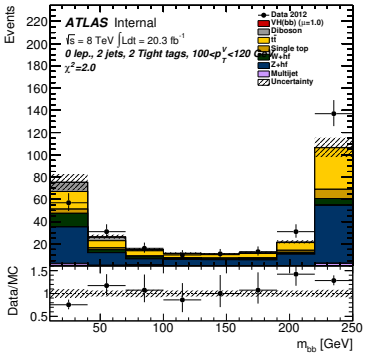

(i) $100 < p_{\mathrm{T}}^{V} < 120$ GeV, 2 jets, TT

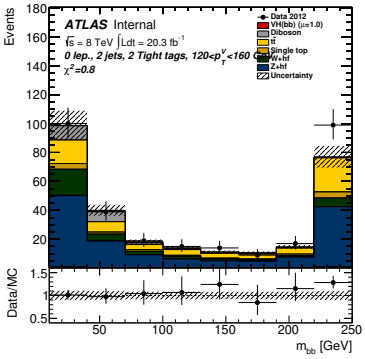

(j) $120 < p_{\mathrm{T}}^{V} < 160$ GeV, 2 jets, TT

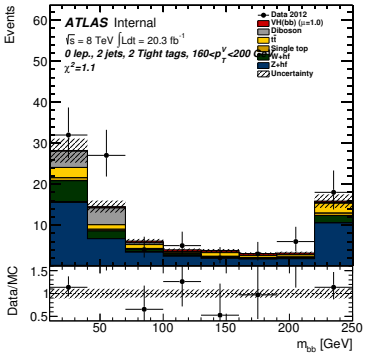

(k) $160 < p_{\mathrm{T}}^{V} < 200$ GeV, 2 jets, TT

Figure 436: Pre-fit plots for m_{jj} distribution in 0-lepton events in the 1-tag (where mv1c is used in the fit) *LL*, *MM* and *TT* tag categories for the 2-jets events in the 0-lepton fit. Plots are shown for $100 < p_{\mathrm{T}}^{V} < 120$ GeV, $120 < p_{\mathrm{T}}^{V} < 160$ GeVand $160 < p_{\mathrm{T}}^{V} < 200$ GeV.

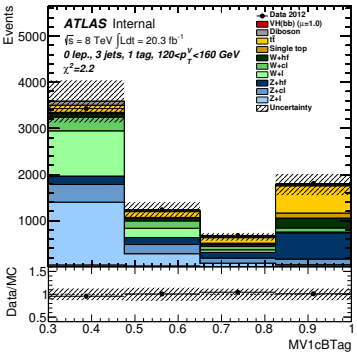

(a) $p_{\mathrm{T}}^{V} > 120$ GeV, 3 jets, 1-tag

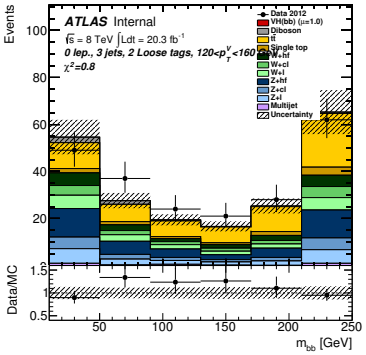

(b) $120 < p_{\mathrm{T}}^{V} < 160$ GeV, 3 jets, LL

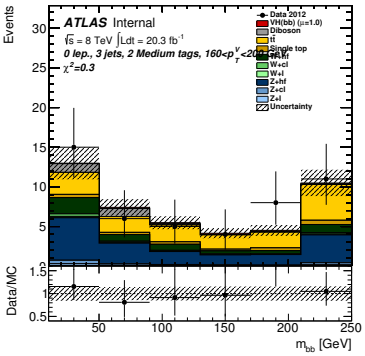

(c) $160 < p_{\mathrm{T}}^{V} < 200$ GeV, 3 jets, LL

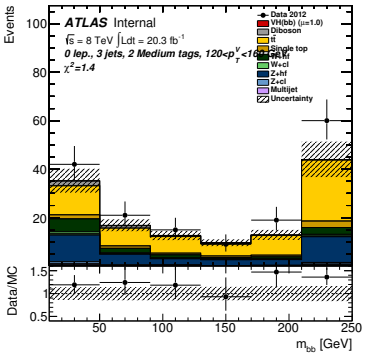

(d) $120 < p_{\mathrm{T}}^{V} < 160$ GeV, 3 jets, MM

(e) $160 < p_{\mathrm{T}}^{V} < 200$ GeV, 3 jets, MM

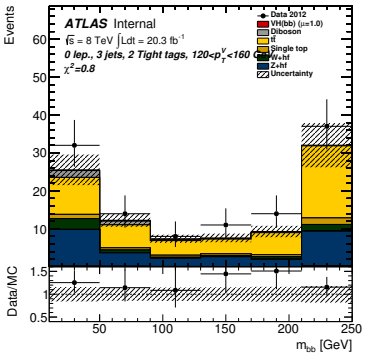

(f) $120 < p_{\mathrm{T}}^{V} < 160$ GeV, 3 jets, TT

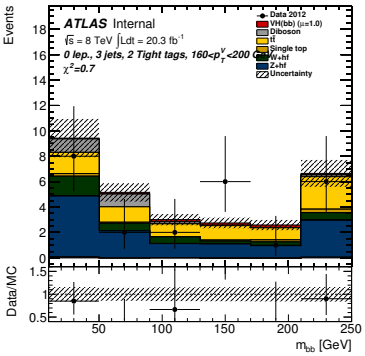

(g) $160 < p_{\mathrm{T}}^{V} < 200$ GeV, 3 jets, TT

Figure 437: Pre-fit plots for m_{jj} distribution in 0-lepton events in the 1-tag (where mv1c is used in the fit) *LL*, *MM* and *TT* tag categories for the 3-jets events in the 0-lepton fit. Plots are shown for $120 < p_{\mathrm{T}}^{V} < 160$ GeVand $160 < p_{\mathrm{T}}^{V} < 200$ GeV.

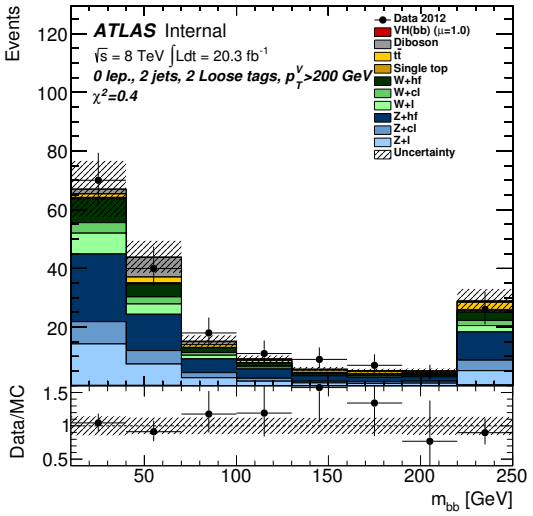

(a) p_{T}^{V} > 200 GeV, 2 jets, LL

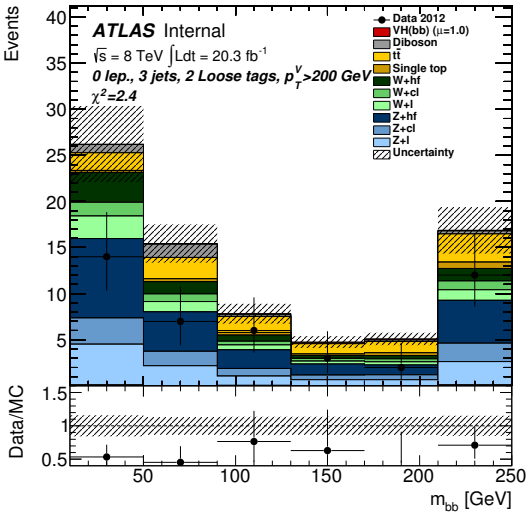

(b) p_{T}^{V} > 200 GeV, 3 jets, LL

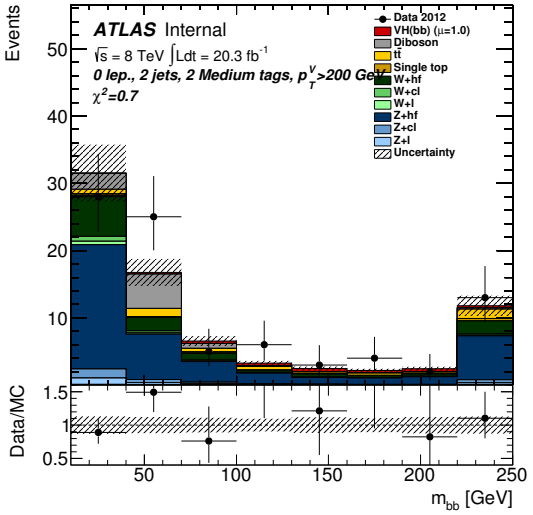

(c) p_{T}^{V} > 200 GeV, 2 jets, MM

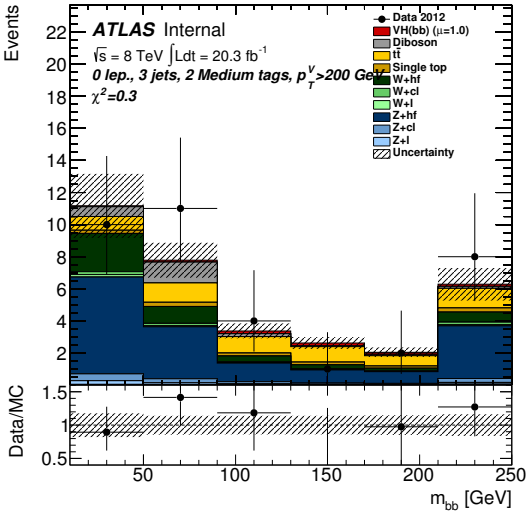

(d) p_{T}^{V} > 200 GeV, 3 jets, MM

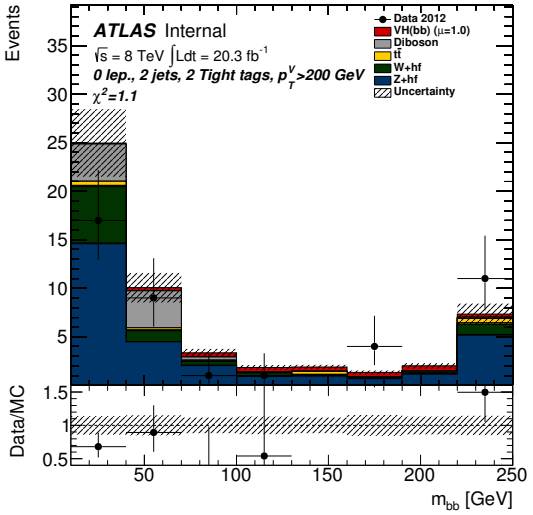

(e) p_{T}^{V} > 200 GeV, 2 jets, TT

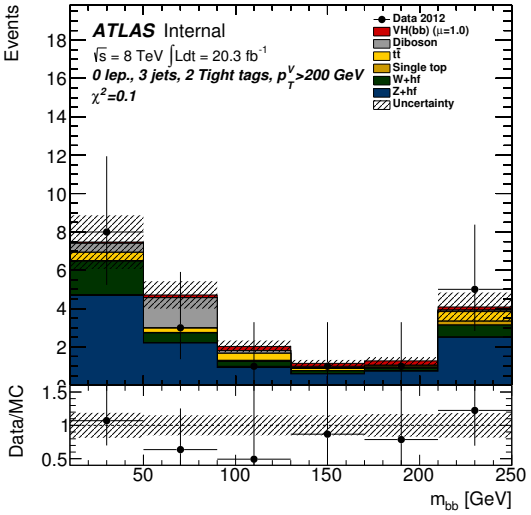

(f) p_{T}^{V} > 200 GeV, 3 jets, TT

Figure 438: Pre-fit plots for m_{jj} distribution in 0-lepton events in the LL, MM and TT tag categories for the 2-jets and the 3-jets events in the 0-lepton fit. Plots are shown for $p_{\mathrm{T}}^{V} > 200$ GeV.

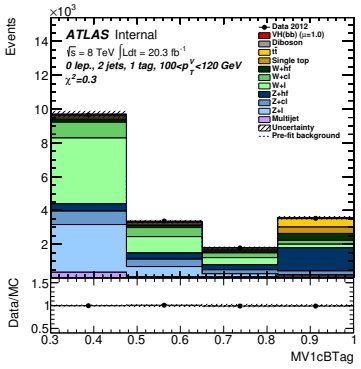

(a) $p_{\mathrm{T}}^{V} < 120$ GeV, 2 jets, 1-tag

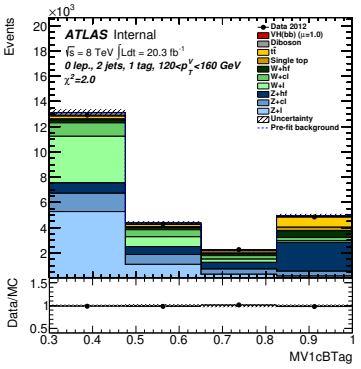

(b) $p_{\mathrm{T}}^{V} > 120$ GeV, 2 jets, 1-tag

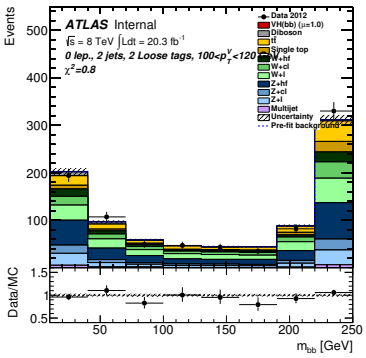

(c) $100 < p_{\mathrm{T}}^{V} < 120$ GeV, 2 jets, LL

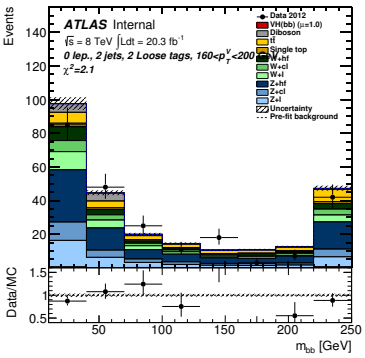

(d) $120 < p_{\mathrm{T}}^{V} < 160$ GeV, 2 jets, LL (e) $160 < p_{\mathrm{T}}^{V} < 200$ GeV, 2 jets, LL

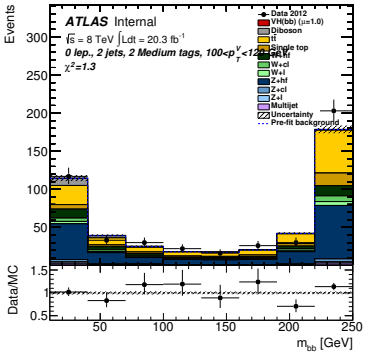

(f) $100 < p_{\mathrm{T}}^{V} < 120$ GeV, 2 jets, MM

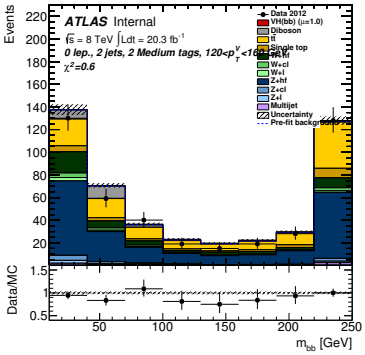

(g) $120 < p_{\mathrm{T}}^{V} < 160$ GeV, 2 jets, MM

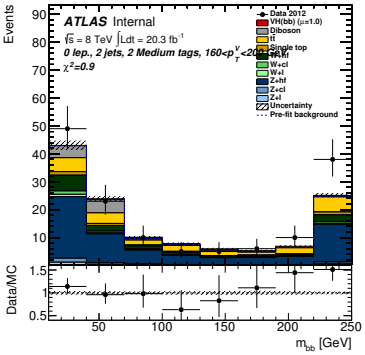

(h) $160 < p_{\mathrm{T}}^{V} < 200$ GeV, 2 jets, MM

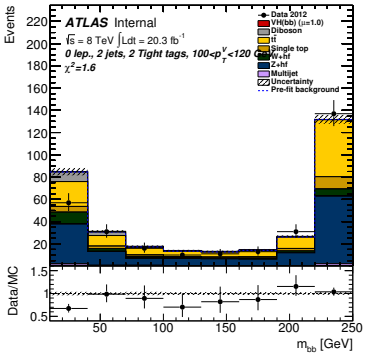

(i) $100 < p_{\mathrm{T}}^{V} < 120$ GeV, 2 jets, TT

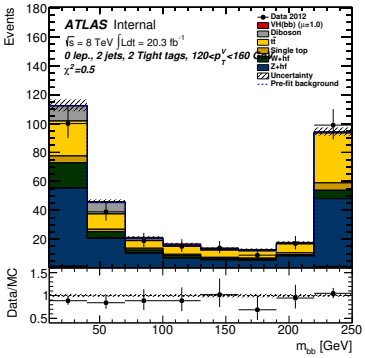

(j) $120 < p_{\mathrm{T}}^{V} < 160$ GeV, 2 jets, TT

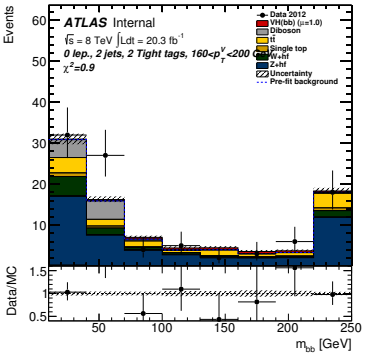

(k) $160 < p_{\mathrm{T}}^{V} < 200$ GeV, 2 jets, TT

Figure 439: Post-fit plots for m_{jj} distribution in 0-lepton events in the 1-tag (where mv1c is used in the fit) *LL*, *MM* and *TT* tag categories for the 2-jets events in the 0-lepton fit. Plots are shown for $100 < p_{\mathrm{T}}^{V} < 120$ GeV, $120 < p_{\mathrm{T}}^{V} < 160$ GeVand $160 < p_{\mathrm{T}}^{V} < 200$ GeV. The pre-fit background expectation is indicated by the dashed blue line.

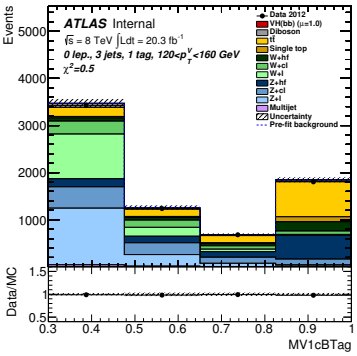

(a) $p_{\mathrm{T}}^{V} > 120$ GeV, 3 jets, 1-tag

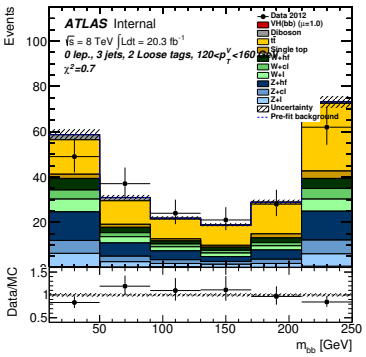

(b) $120 < p_{\mathrm{T}}^{V} < 160$ GeV, 3 jets, LL

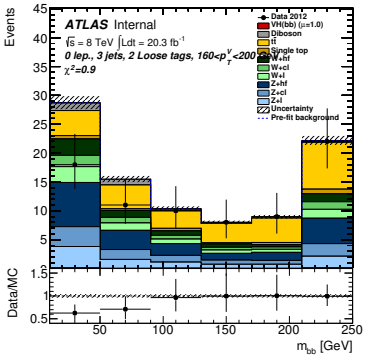

(c) $160 < p_{\mathrm{T}}^{V} < 200$ GeV, 3 jets, LL

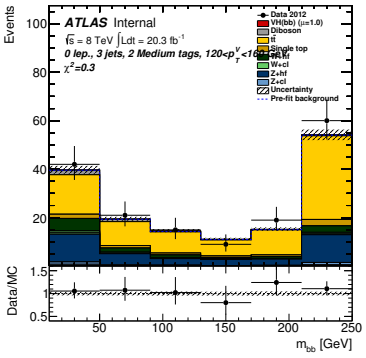

(d) $120 < p_{\mathrm{T}}^{V} < 160$ GeV, 3 jets, MM

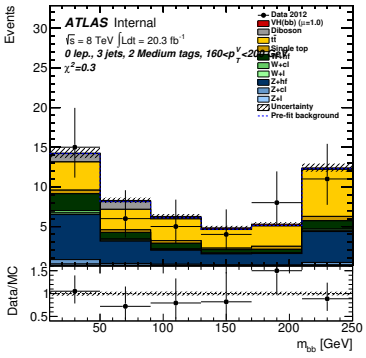

(e) $160 < p_{\mathrm{T}}^{V} < 200$ GeV, 3 jets, MM

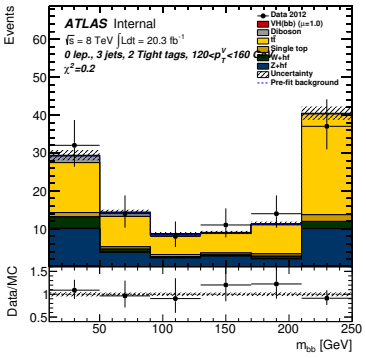

(f) $120 < p_{\mathrm{T}}^{V} < 160$ GeV, 3 jets, TT

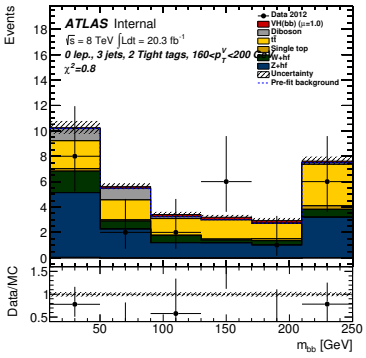

(g) $160 < p_{\mathrm{T}}^{V} < 200$ GeV, 3 jets, TT

Figure 440: Post-fit plots for m_{jj} distribution in 0-lepton events in the 1-tag (where mv1c is used in the fit) *LL*, *MM* and *TT* tag categories for the 3-jets events in the 0-lepton fit. Plots are shown for $120 < p_{\mathrm{T}}^{V} < 160$ GeVand $160 < p_{\mathrm{T}}^{V} < 200$ GeV. The pre-fit background expectation is indicated by the dashed blue line.

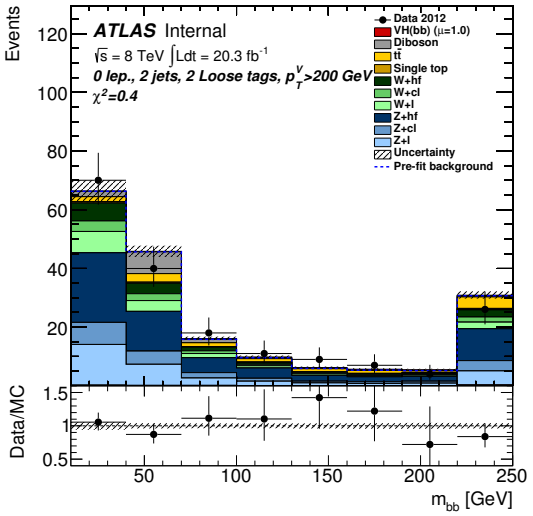

(a) $p_{\mathrm{T}}^{V} > 200$ GeV, 2 jets, LL

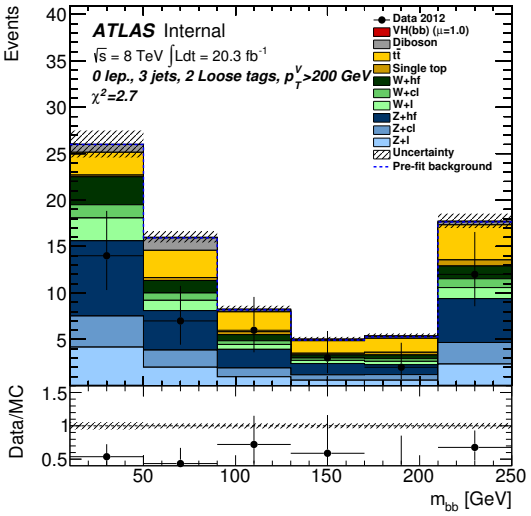

(b) $p_{\mathrm{T}}^{V} > 200$ GeV, 3 jets, LL

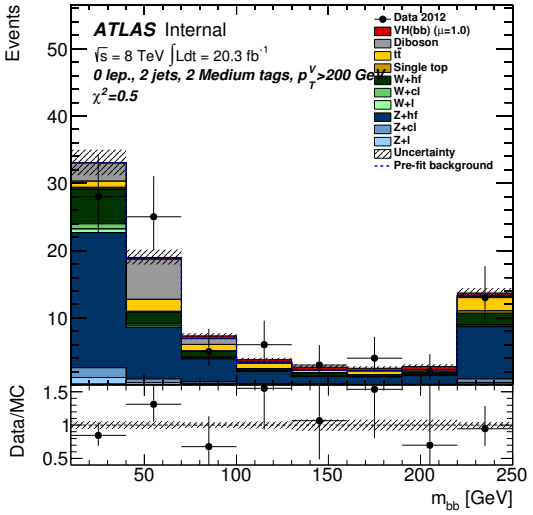

(c) $p_{\mathrm{T}}^{V} > 200$ GeV, 2 jets, MM

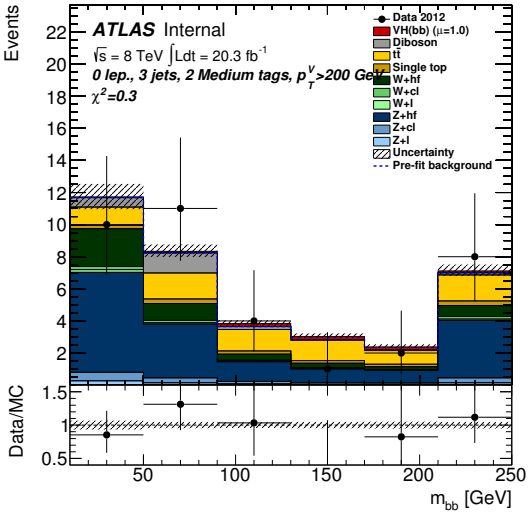

(d) $p_{\mathrm{T}}^{V} > 200$ GeV, 3 jets, MM

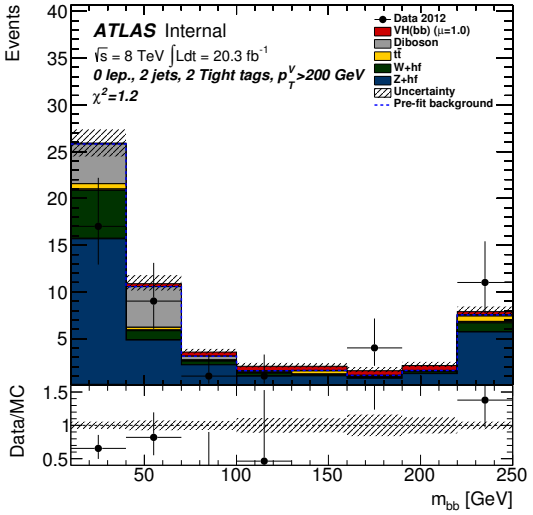

(e) $p_{\mathrm{T}}^{V} > 200$ GeV, 2 jets, TT

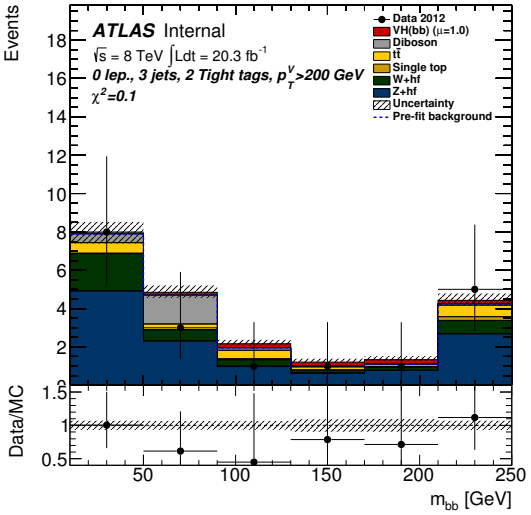

(f) $p_{\mathrm{T}}^{V} > 200$ GeV, 3 jets, TT

Figure 441: Post-fit plots for m_{jj} distribution in 0-lepton events in the LL, MM and TT tag categories for the 2-jets and the 3-jets events in the 0-lepton fit. Plots are shown for $p_{\mathrm{T}}^{V} > 200$ GeV. The pre-fit background expectation is indicated by the dashed blue line.

AH.1.3 1-lepton

The pull plots for 1-lepton are shown in Figure. 442-446.

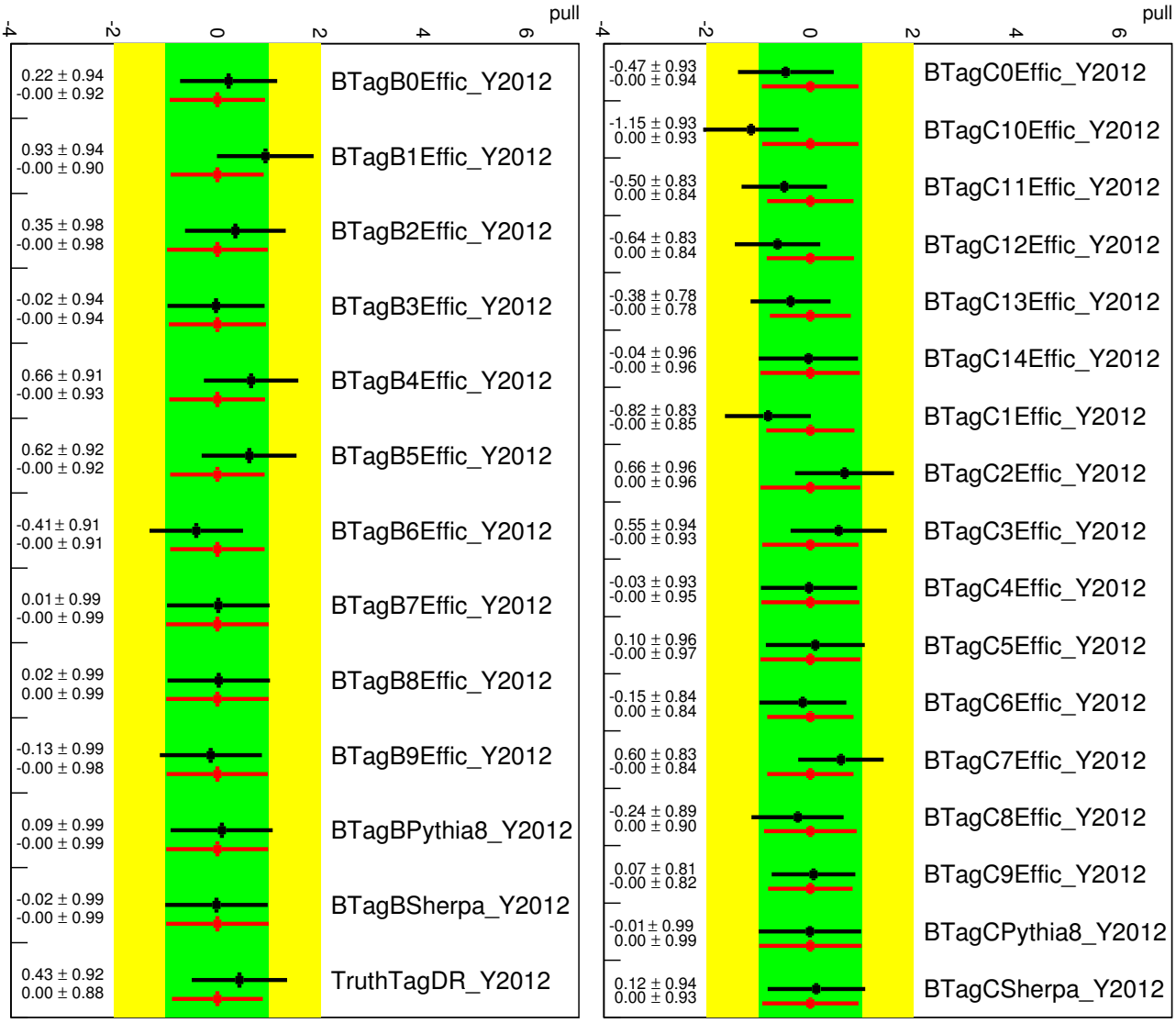

Figure 442: Pull plots for 1-lepton channel: *b*- and *c*-jet tagging.

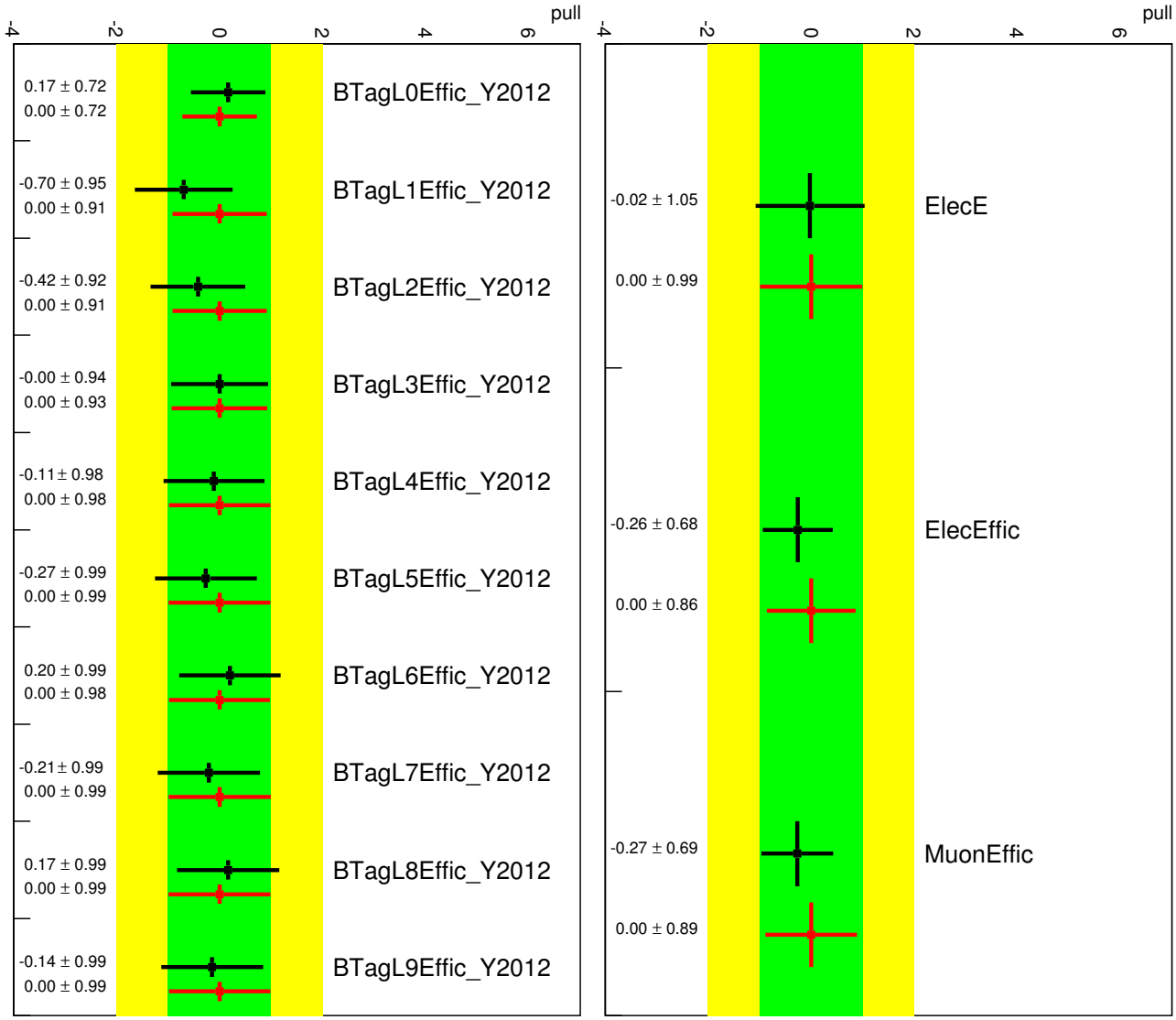

Figure 443: Pull plots for 1-lepton channel: light-jet tagging and leptons.

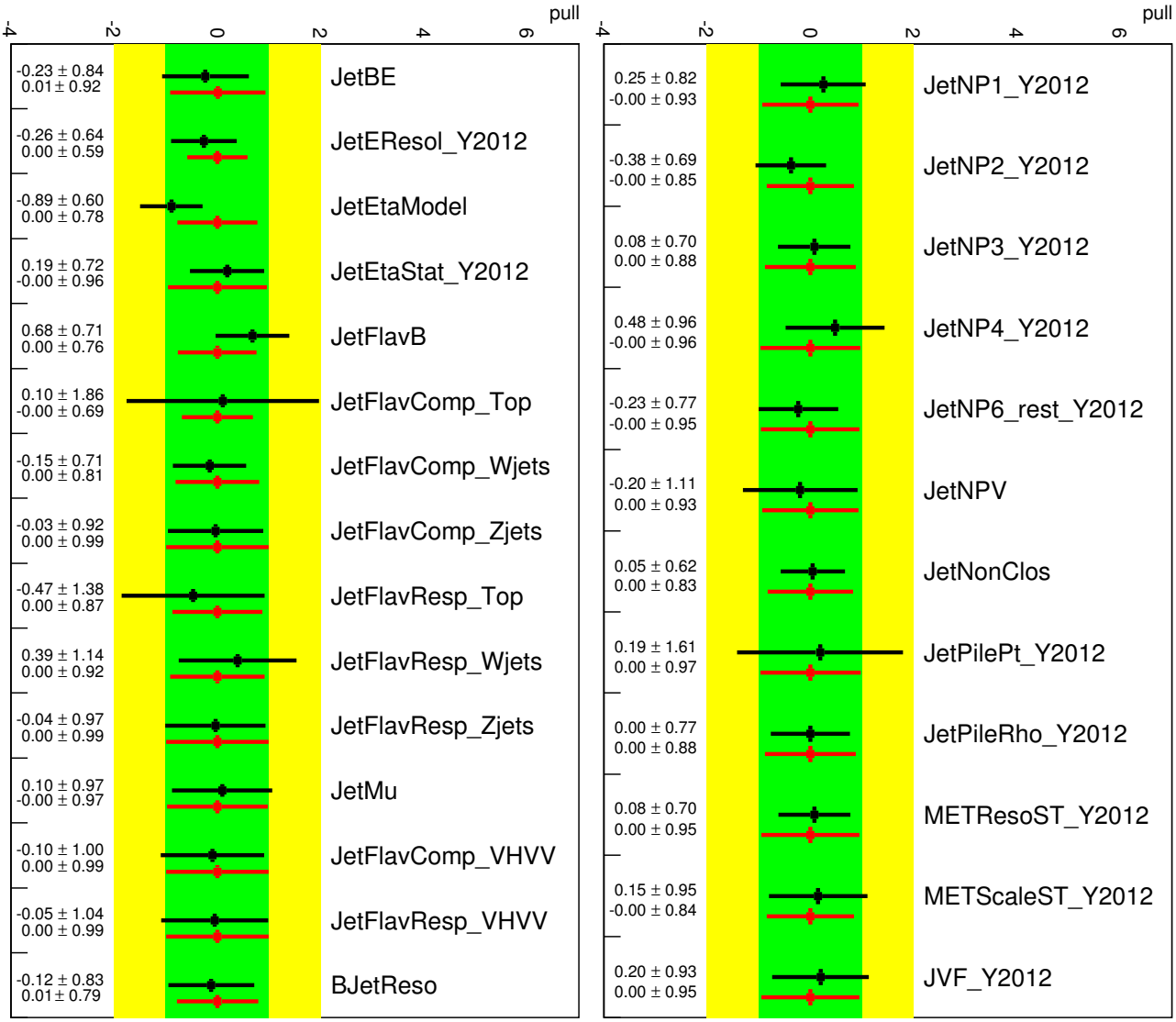

Figure 444: Pull plots for 1-lepton channel: Jet NPs.

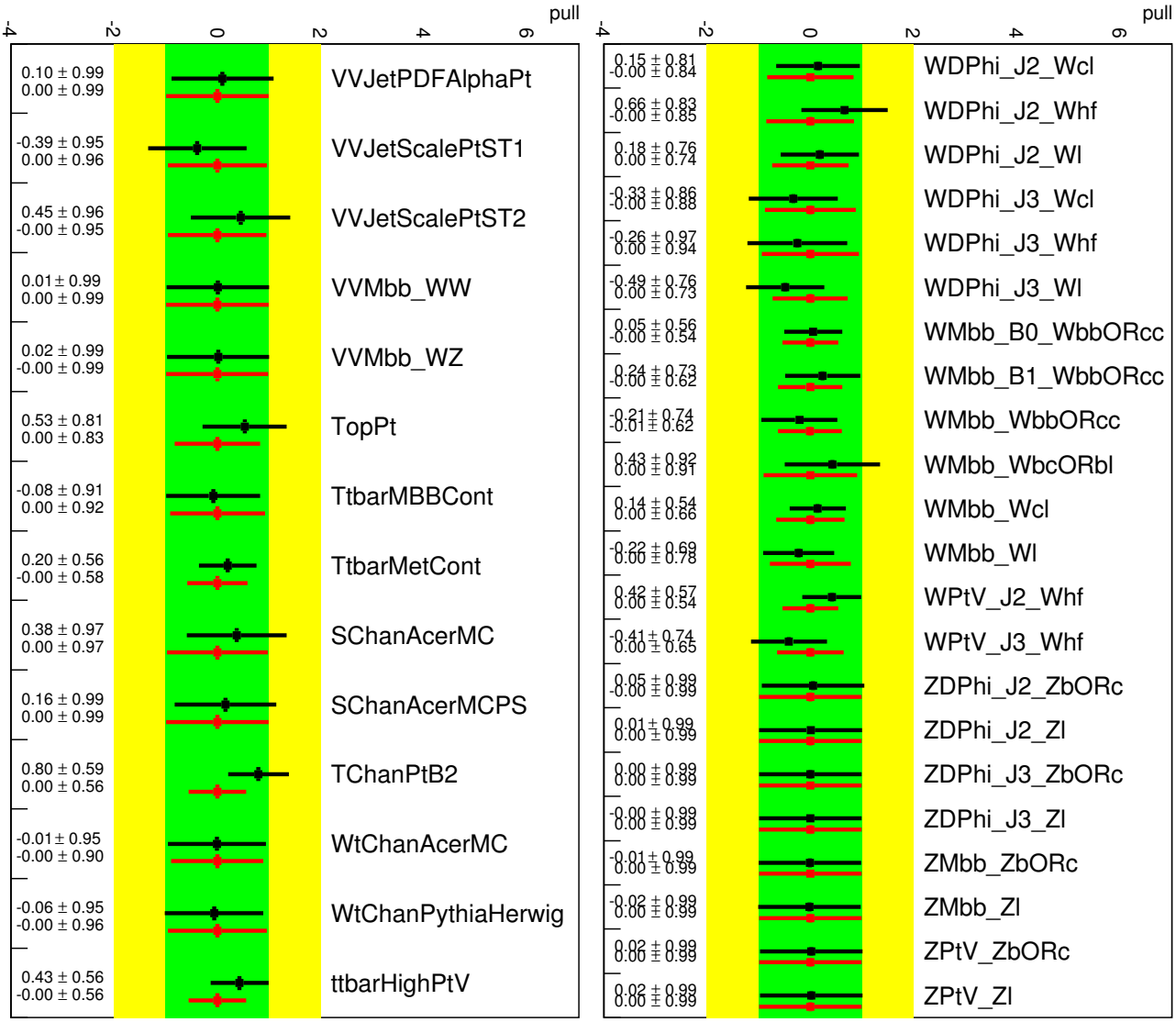

Figure 445: Pull plots for 1-lepton channel: Diboson and Top related uncertainties.

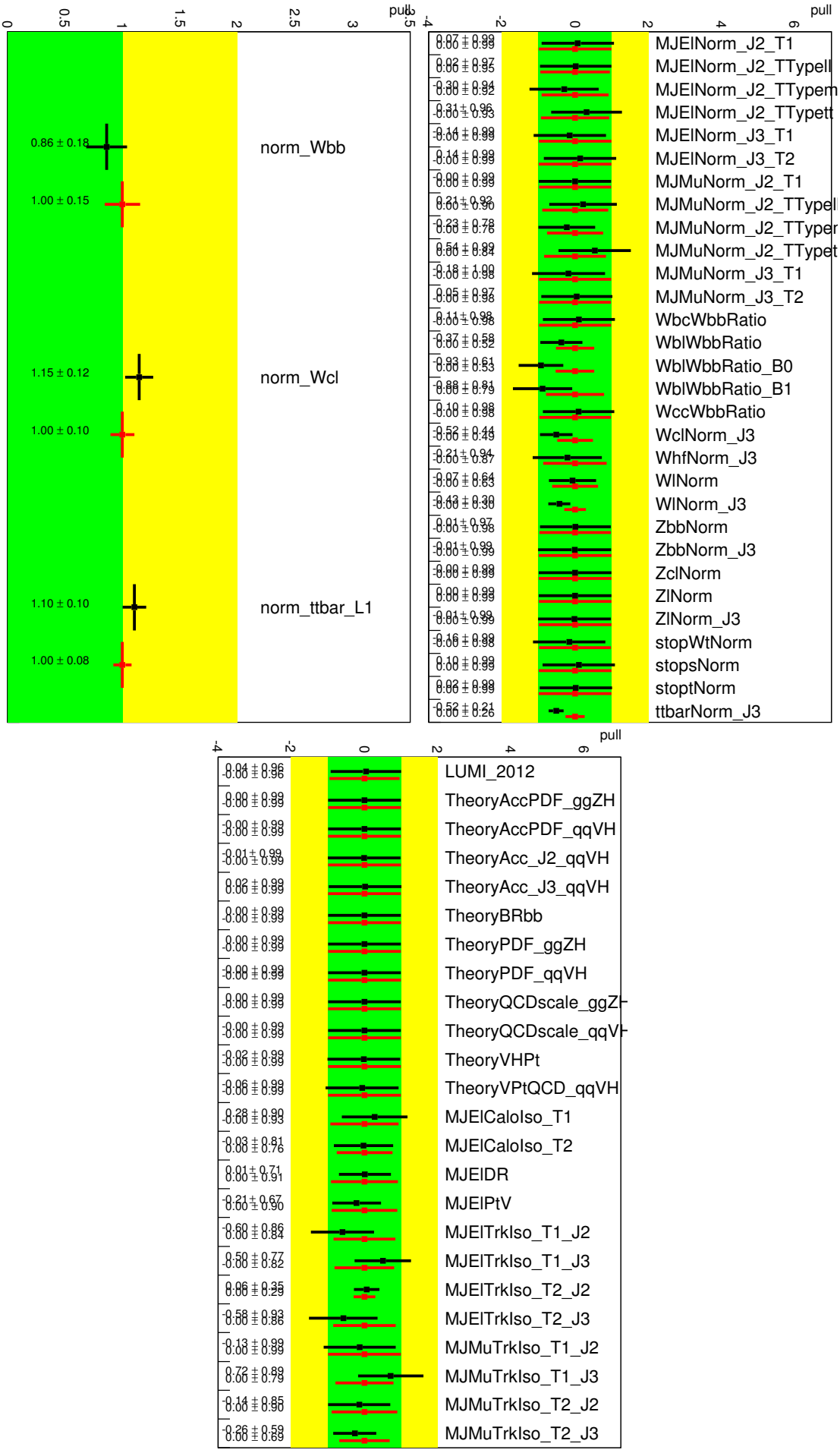

Figure 446: Pull plots for 1-lepton channel: Normalization and residual uncertainties.

AH.1.4 Pre-fit and Post-Fit for the m_{jj} shape analysis in the 1-lepton fit

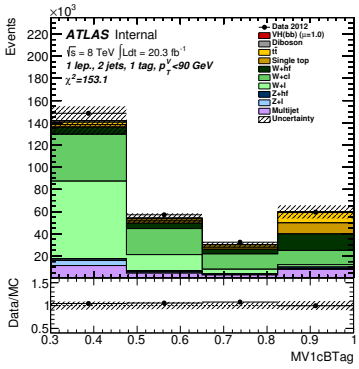

(a) $p_{\mathrm{T}}^{V} < 120$ GeV, 2 jets, 1-tag

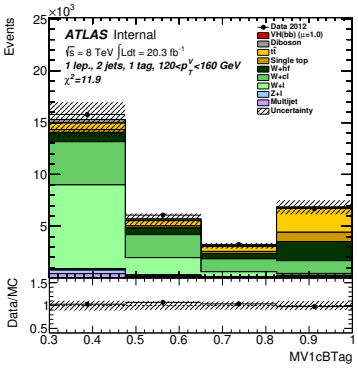

(b) $p_{\mathrm{T}}^{V} > 120$ GeV, 2 jets, 1-tag

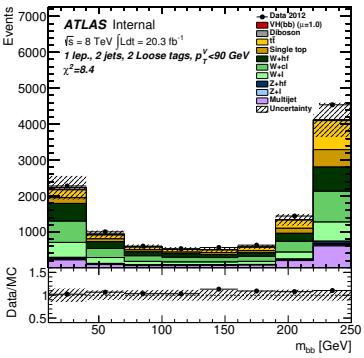

(c) $p_{\mathrm{T}}^{V} < 90$ GeV, 2 jets, LL

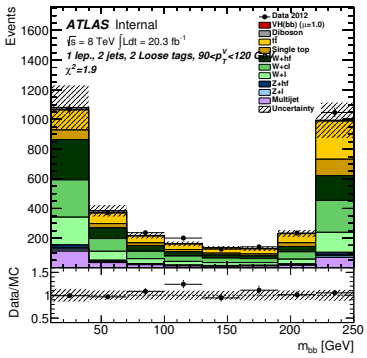

(d) $90 < p_{\mathrm{T}}^{V} < 120$ GeV, 2 jets, LL

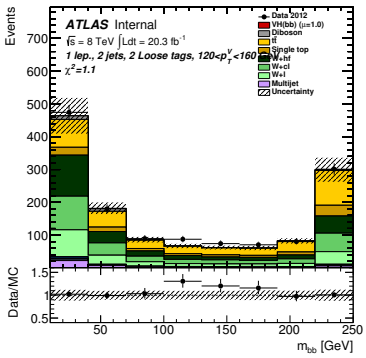

(e) $120 < p_{\mathrm{T}}^{V} < 160$ GeV, 2 jets, LL

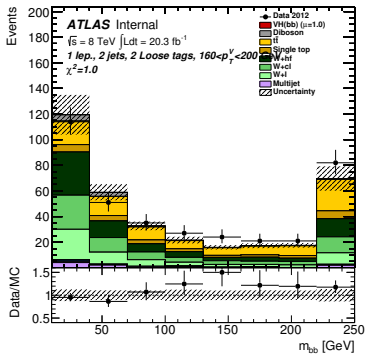

(f) $160 < p_{\mathrm{T}}^{V} < 200$ GeV, 2 jets, LL

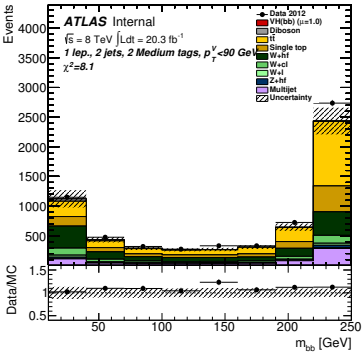

(g) $p_{\mathrm{T}}^{V} < 90$ GeV, 2 jets, MM

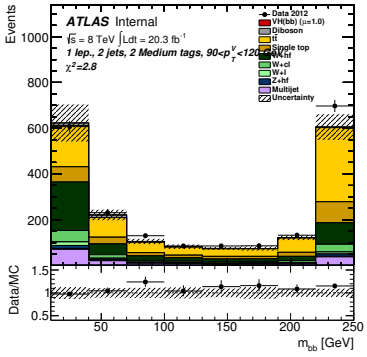

(h) $90 < p_{\mathrm{T}}^{V} < 120$ GeV, 2 jets, MM

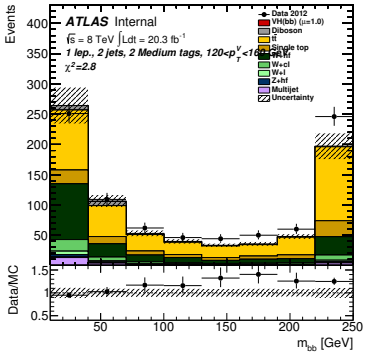

(i) $120 < p_{\mathrm{T}}^{V} < 160$ GeV, 2 jets, MM

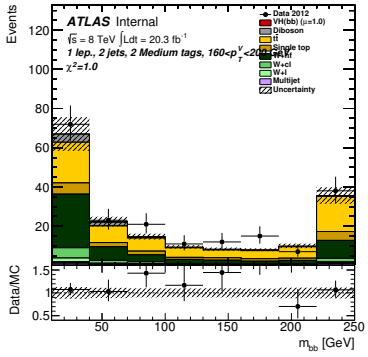

(j) $160 < p_{\mathrm{T}}^{V} < 200$ GeV, 2 jets, MM

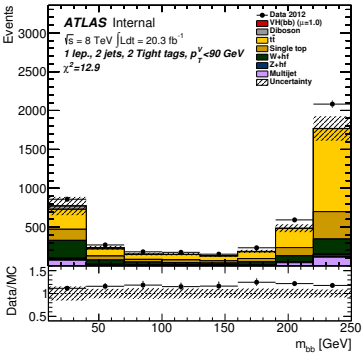

(k) $p_{\mathrm{T}}^{V} < 90$ GeV, 2 jets, TT

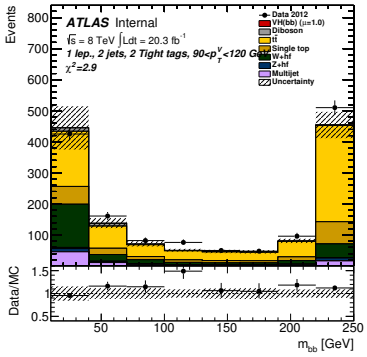

(l) $90 < p_{\mathrm{T}}^{V} < 120$ GeV, 2 jets, TT

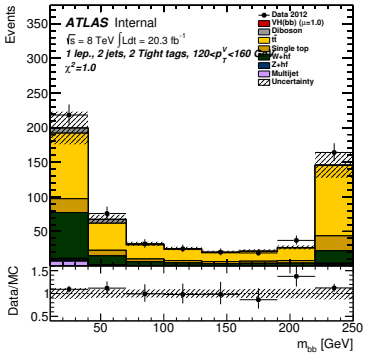

(m) $120 < p_{\mathrm{T}}^{V} < 160$ GeV, 2 jets, TT

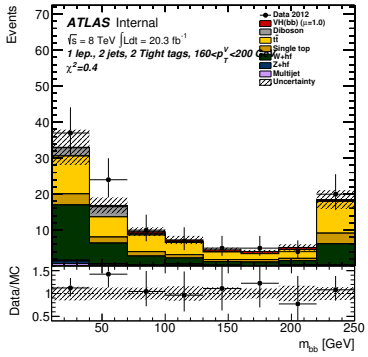

(n) $160 < p_{\mathrm{T}}^{V} < 200$ GeV, 2 jets, TT

Figure 447: Pre-fit plots for m_{jj} distribution in 1-lepton events in the 1-tag (where mv1c is used in the fit) *LL*, *MM* and *TT* tag categories for the 2-jets events in the 1-lepton fit. Plots are shown for $p_{\mathrm{T}}^{V} < 90$ GeV, $90 < p_{\mathrm{T}}^{V} < 120$ GeV, $120 < p_{\mathrm{T}}^{V} < 160$ GeVand $160 < p_{\mathrm{T}}^{V} < 200$ GeV. The pre-fit background expectation is indicated by the dashed blue line.

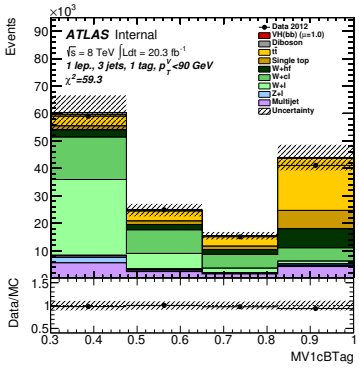

(a) $p_{\mathrm{T}}^{V} < 120$ GeV, 3 jets, 1-tag

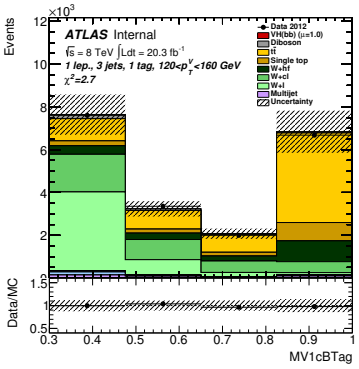

(b) $p_{\mathrm{T}}^{V} > 120$ GeV, 3 jets, 1-tag

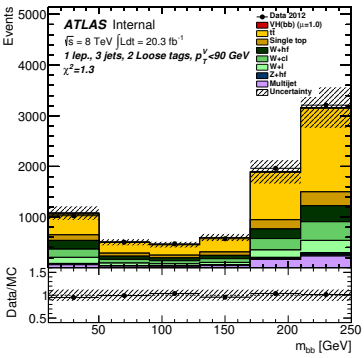

(c) $p_{\mathrm{T}}^{V} < 90$ GeV, 3 jets, LL

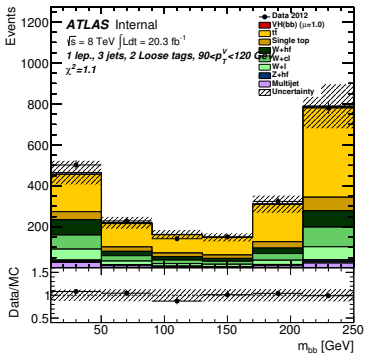

(d) $90 < p_{\mathrm{T}}^{V} < 120$ GeV, 3 jets, LL

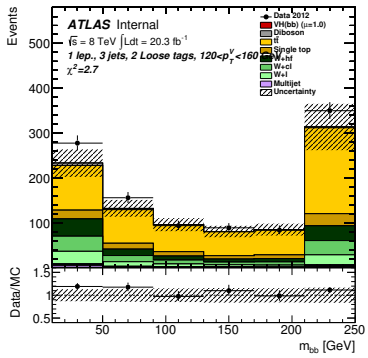

(e) $120 < p_{\mathrm{T}}^{V} < 160$ GeV, 3 jets, LL

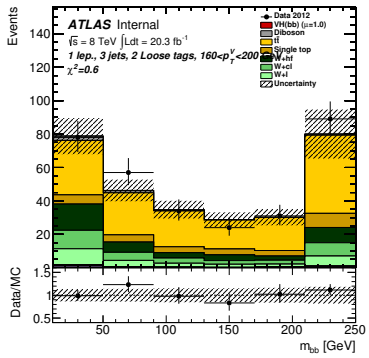

(f) $160 < p_{\mathrm{T}}^{V} < 200$ GeV, 3 jets, LL

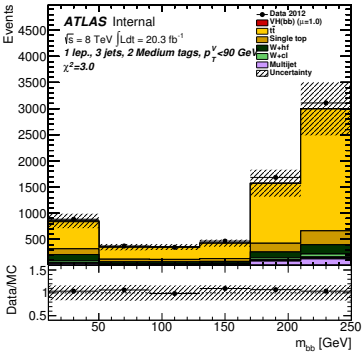

(g) $p_{\mathrm{T}}^{V} < 90$ GeV, 3 jets, MM

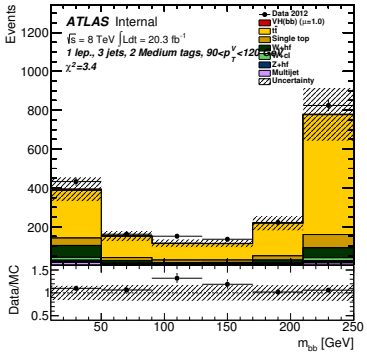

(h) $90 < p_{\mathrm{T}}^{V} < 120$ GeV, 3 jets, MM

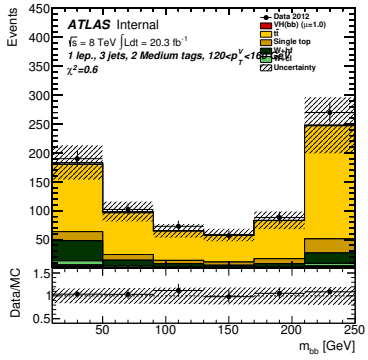

(i) $120 < p_{\mathrm{T}}^{V} < 160$ GeV, 3 jets, MM

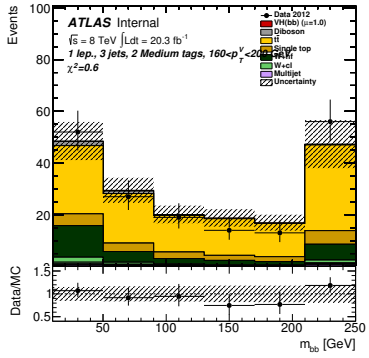

(j) $160 < p_{\mathrm{T}}^{V} < 200$ GeV, 3 jets, MM

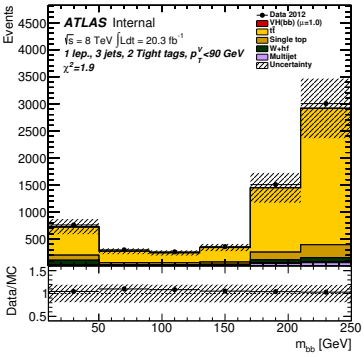

(k) $p_{\mathrm{T}}^{V} < 90$ GeV, 3 jets, TT

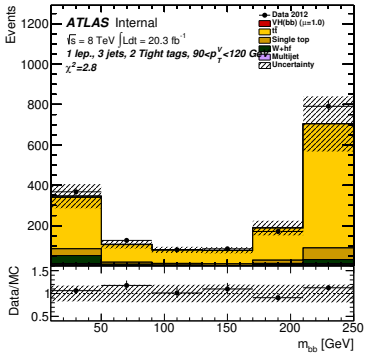

(l) $90 < p_{\mathrm{T}}^{V} < 120$ GeV, 3 jets, TT

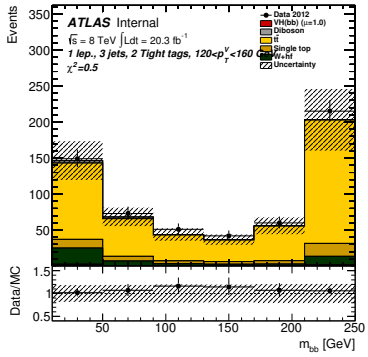

(m) $120 < p_{\mathrm{T}}^{V} < 160$ GeV, 3 jets, TT

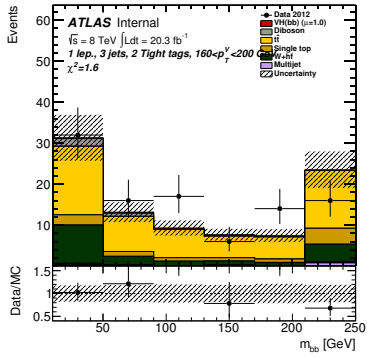

(n) $160 < p_{\mathrm{T}}^{V} < 200$ GeV, 3 jets, TT

Figure 448: Pre-fit plots for m_{jj} distribution in 1-lepton events in the 1-tag (where mv1c is used in the fit) *LL*, *MM* and *TT* tag categories for the 3-jets events in the 1-lepton fit. Plots are shown for $p_{\mathrm{T}}^{V} < 90$ GeV, $90 < p_{\mathrm{T}}^{V} < 120$ GeV, $120 < p_{\mathrm{T}}^{V} < 160$ GeVand $160 < p_{\mathrm{T}}^{V} < 200$ GeV. The pre-fit background expectation is indicated by the dashed blue line.

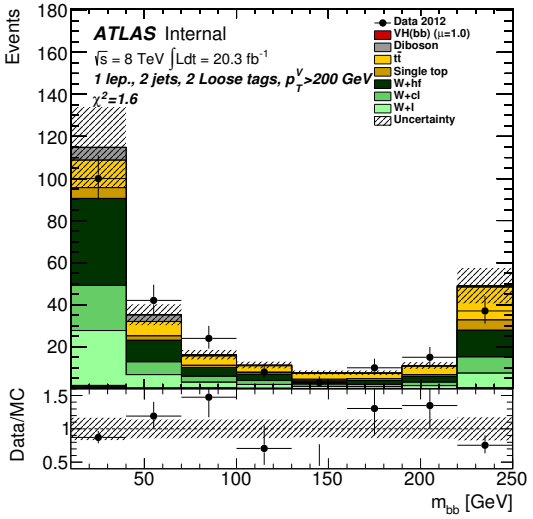

(a) $p_{\mathrm{T}}^{V} > 200$ GeV, 2 jets, LL

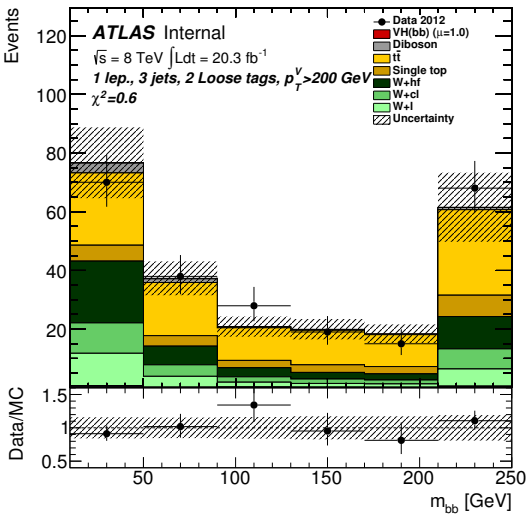

(b) $p_{\mathrm{T}}^{V} > 200$ GeV, 3 jets, LL

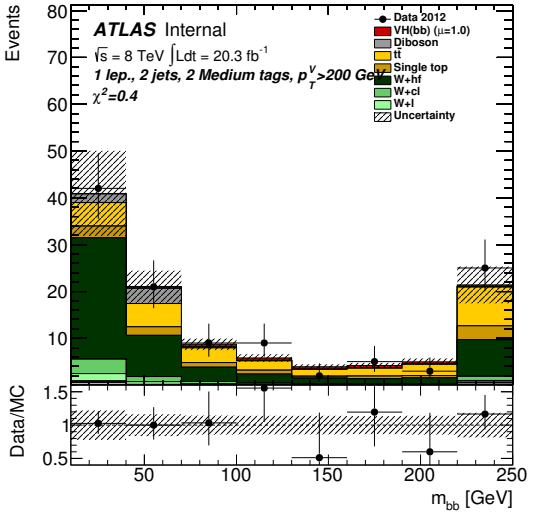

(c) $p_{\mathrm{T}}^{V} > 200$ GeV, 2 jets, MM

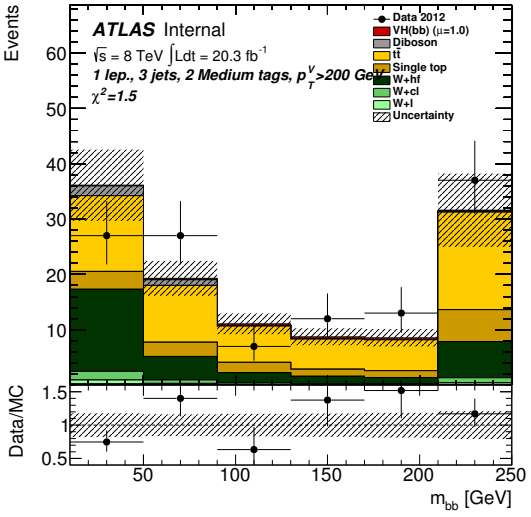

(d) $p_{\mathrm{T}}^{V} > 200$ GeV, 3 jets, MM

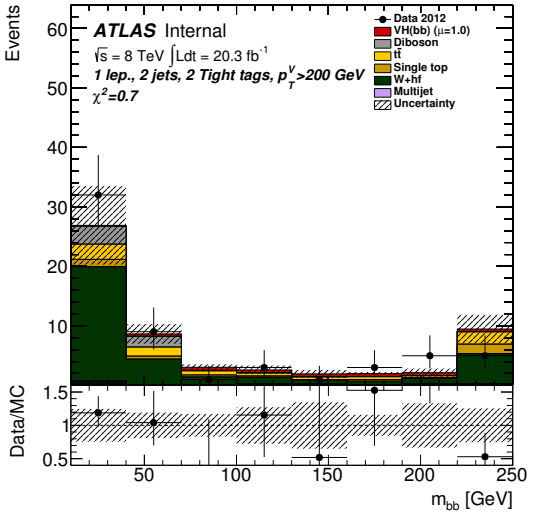

(e) $p_{\mathrm{T}}^{V} > 200$ GeV, 2 jets, TT

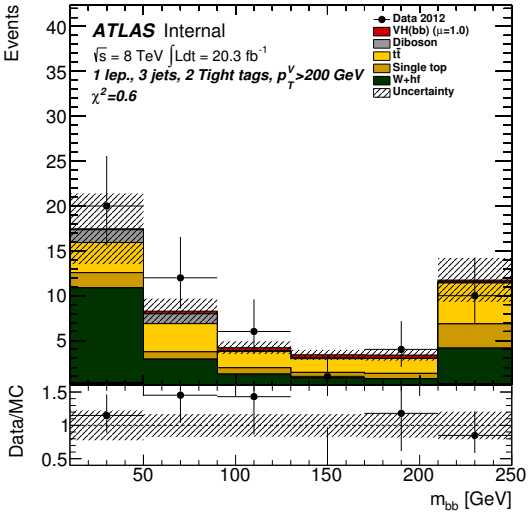

(f) $p_{\mathrm{T}}^{V} > 200$ GeV, 3 jets, TT

Figure 449: Pre-fit plots for m_{jj} distribution in 1-lepton events in the LL, MM and TT tag categories for the 2-jets and the 3-jets events in the 1-lepton fit. Plots are shown for $p_{\mathrm{T}}^{V} > 200$ GeV. The pre-fit background expectation is indicated by the dashed blue line.

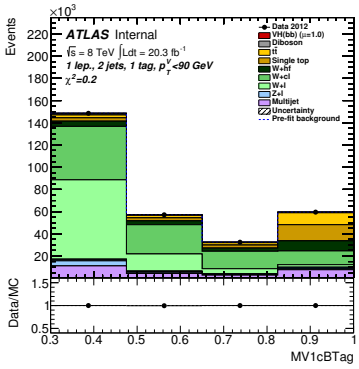

(a) $p_{\mathrm{T}}^{V} < 120$ GeV, 2 jets, 1-tag

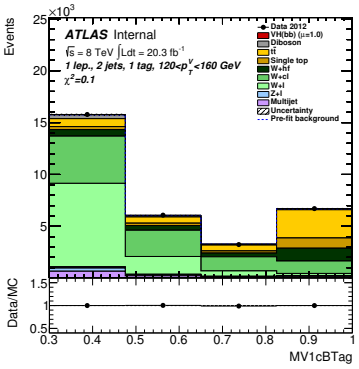

(b) $p_{\mathrm{T}}^{V} > 120$ GeV, 2 jets, 1-tag

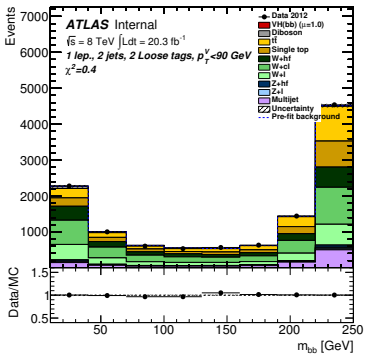

(c) $p_{\mathrm{T}}^{V} < 90$ GeV, 2 jets, LL

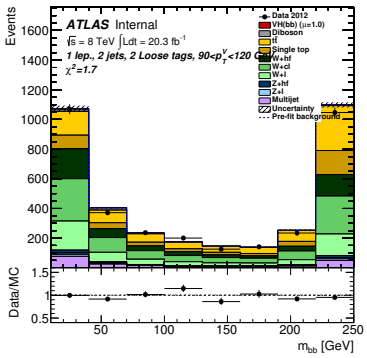

(d) $90 < p_{\mathrm{T}}^{V} < 120$ GeV, 2 jets, LL

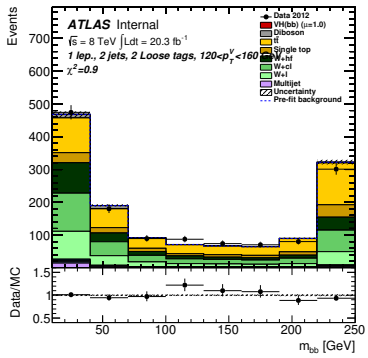

(e) $120 < p_{\mathrm{T}}^{V} < 160$ GeV, 2 jets, LL

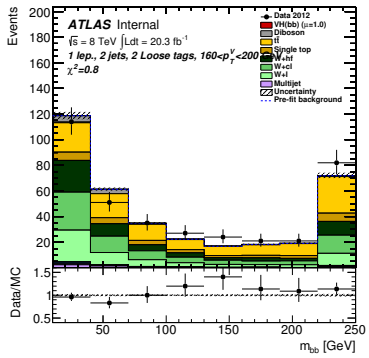

(f) $160 < p_{\mathrm{T}}^{V} < 200$ GeV, 2 jets, LL

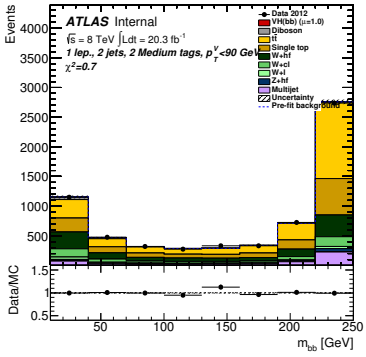

(g) $p_{\mathrm{T}}^{V} < 90$ GeV, 2 jets, MM

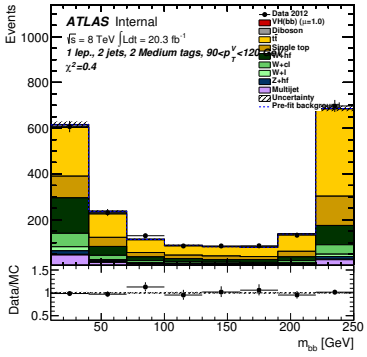

(h) $90 < p_{\mathrm{T}}^{V} < 120$ GeV, 2 jets, MM

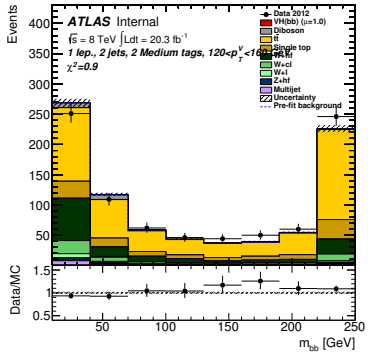

(i) $120 < p_{\mathrm{T}}^{V} < 160$ GeV, 2 jets, MM

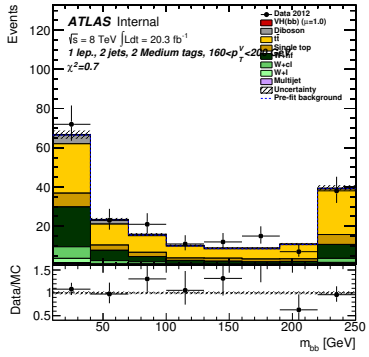

(j) $160 < p_{\mathrm{T}}^{V} < 200$ GeV, 2 jets, MM

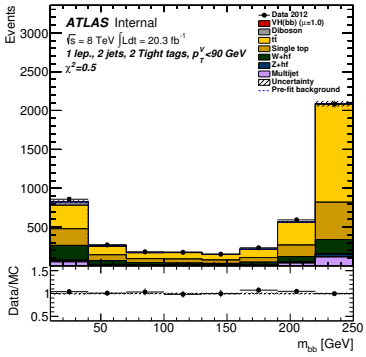

(k) $p_{\mathrm{T}}^{V} < 90$ GeV, 2 jets, TT

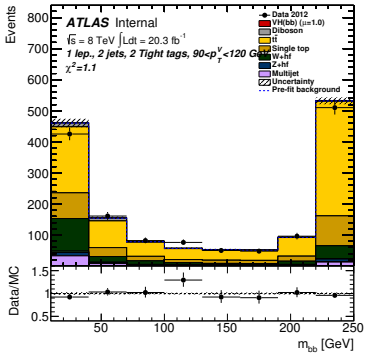

(l) $90 < p_{\mathrm{T}}^{V} < 120$ GeV, 2 jets, TT

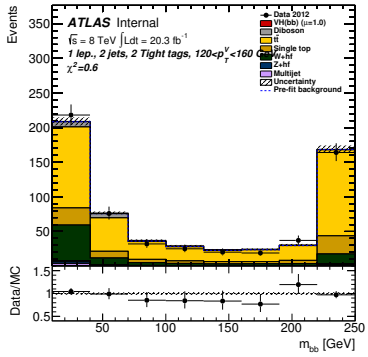

(m) $120 < p_{\mathrm{T}}^{V} < 160$ GeV, 2 jets, TT

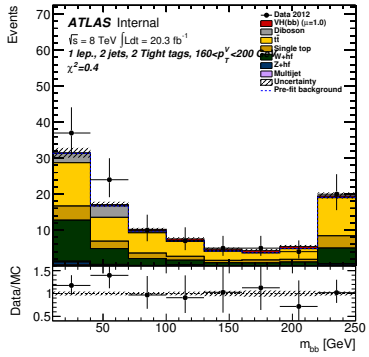

(n) $160 < p_{\mathrm{T}}^{V} < 200$ GeV, 2 jets, TT

Figure 450: Post-fit plots for m_{jj} distribution in 1-lepton events in the 1-tag (where mv1c is used in the fit) *LL*, *MM* and *TT* tag categories for the 2-jets events in the 1-lepton fit. Plots are shown for $p_{\mathrm{T}}^{V} < 90$ GeV, $90 < p_{\mathrm{T}}^{V} < 120$ GeV, $120 < p_{\mathrm{T}}^{V} < 160$ GeVand $160 < p_{\mathrm{T}}^{V} < 200$ GeV. The pre-fit background expectation is indicated by the dashed blue line.

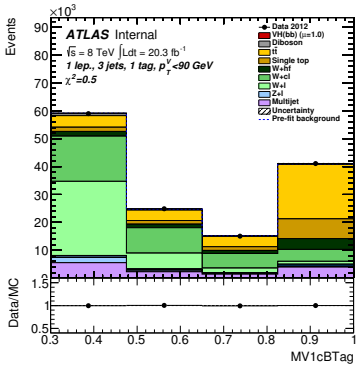

(a) $p_{\mathrm{T}}^{V} < 120$ GeV, 3 jets, 1-tag

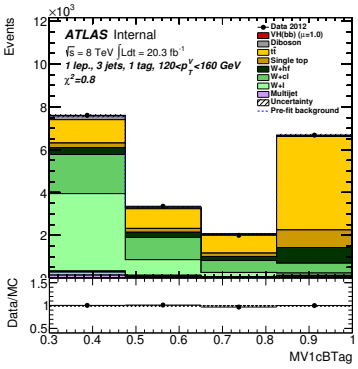

(b) $p_{\mathrm{T}}^{V} > 120$ GeV, 3 jets, 1-tag

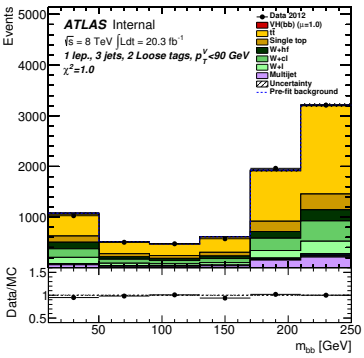

(c) $p_{\mathrm{T}}^{V} < 90$ GeV, 3 jets, LL

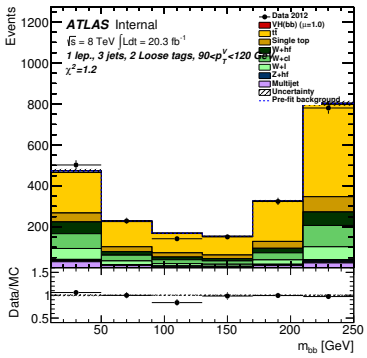

(d) $90 < p_{\mathrm{T}}^{V} < 120$ GeV, 3 jets, LL

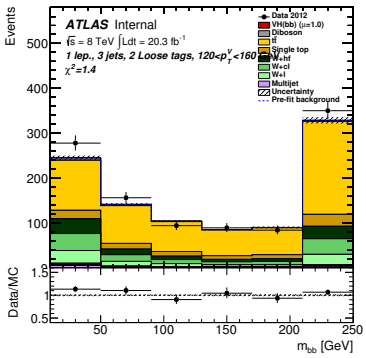

(e) $120 < p_{\mathrm{T}}^{V} < 160$ GeV, 3 jets, LL

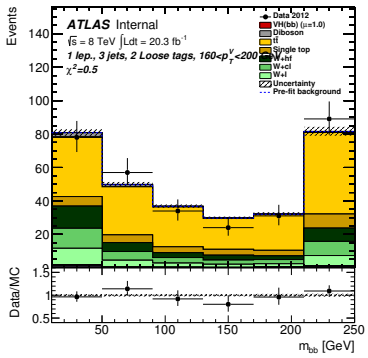

(f) $160 < p_{\mathrm{T}}^{V} < 200$ GeV, 3 jets, LL

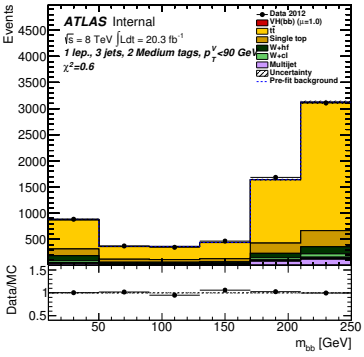

(g) $p_{\mathrm{T}}^{V} < 90$ GeV, 3 jets, MM

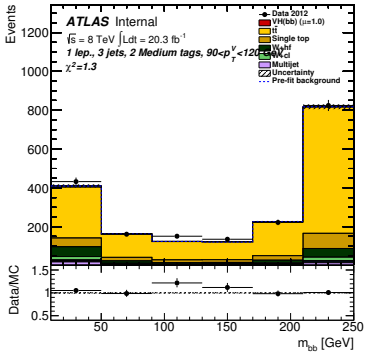

(h) $90 < p_{\mathrm{T}}^{V} < 120$ GeV, 3 jets, MM

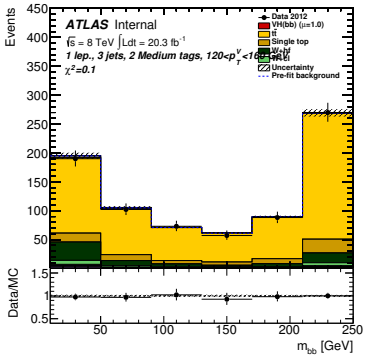

(i) $120 < p_{\mathrm{T}}^{V} < 160$ GeV, 3 jets, MM

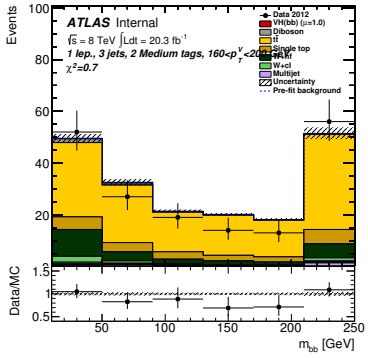

(j) $160 < p_{\mathrm{T}}^{V} < 200$ GeV, 3 jets, MM

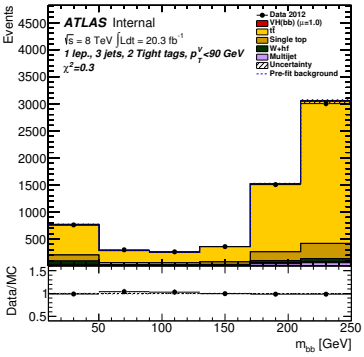

(k) $p_{\mathrm{T}}^{V} < 90$ GeV, 3 jets, TT

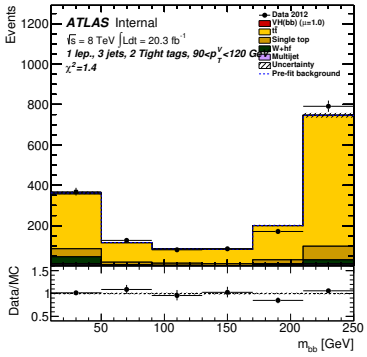

(l) $90 < p_{\mathrm{T}}^{V} < 120$ GeV, 3 jets, TT

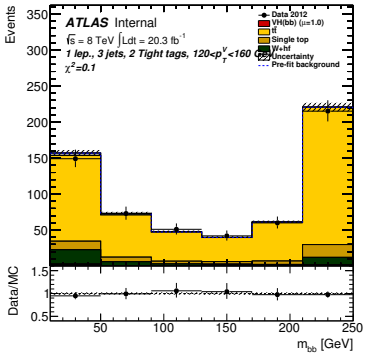

(m) $120 < p_{\mathrm{T}}^{V} < 160$ GeV, 3 jets, TT

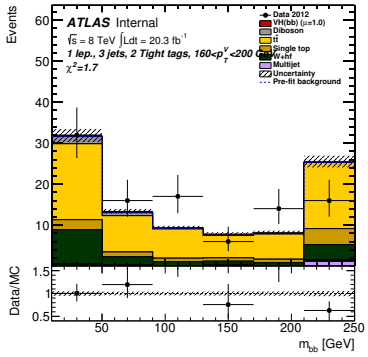

(n) $160 < p_{\mathrm{T}}^{V} < 200$ GeV, 3 jets, TT

Figure 451: Post-fit plots for m_{jj} distribution in 1-lepton events in the 1-tag (where mv1c is used in the fit) *LL*, *MM* and *TT* tag categories for the 3-jets events in the 1-lepton fit. Plots are shown for $p_{\mathrm{T}}^{V} < 90$ GeV, $90 < p_{\mathrm{T}}^{V} < 120$ GeV, $120 < p_{\mathrm{T}}^{V} < 160$ GeVand $160 < p_{\mathrm{T}}^{V} < 200$ GeV. The pre-fit background expectation is indicated by the dashed blue line.

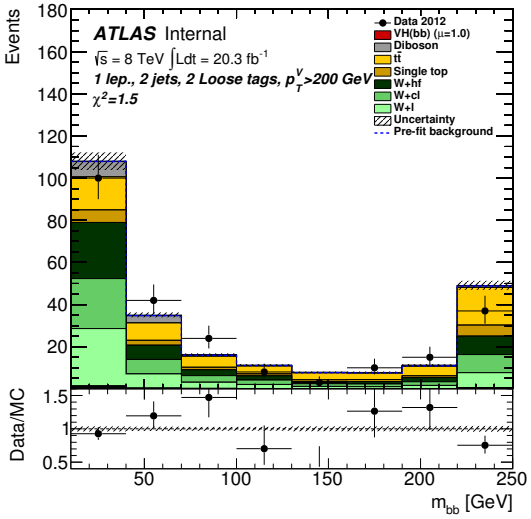

(a) $p_{\mathrm{T}}^{V} > 200$ GeV, 2 jets, LL

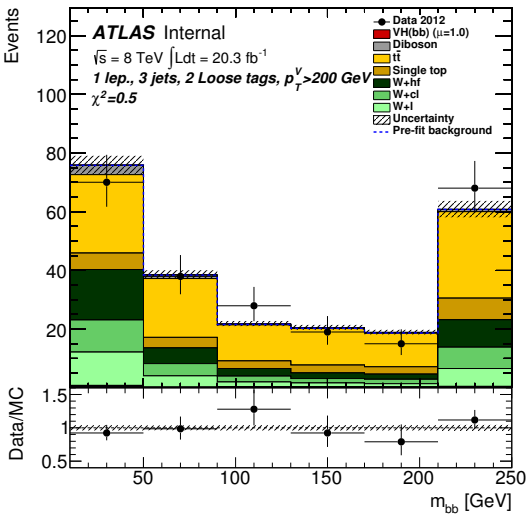

(b) $p_{\mathrm{T}}^{V} > 200$ GeV, 3 jets, LL

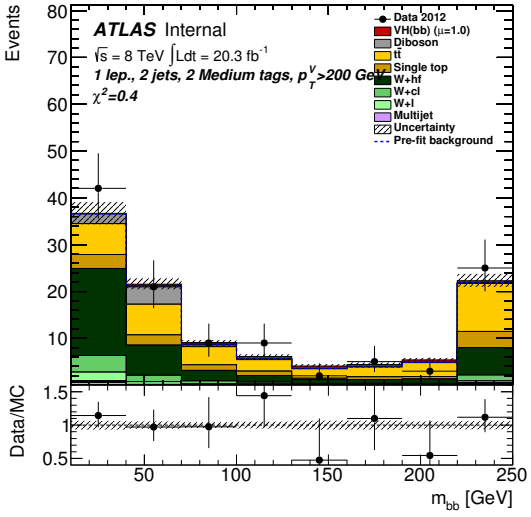

(c) $p_{\mathrm{T}}^{V} > 200$ GeV, 2 jets, MM

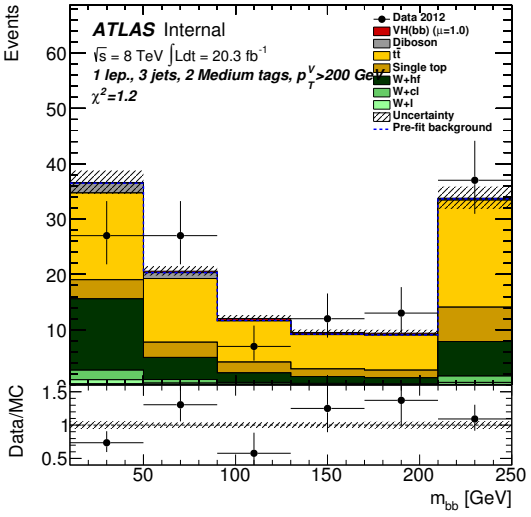

(d) $p_{\mathrm{T}}^{V} > 200$ GeV, 3 jets, MM

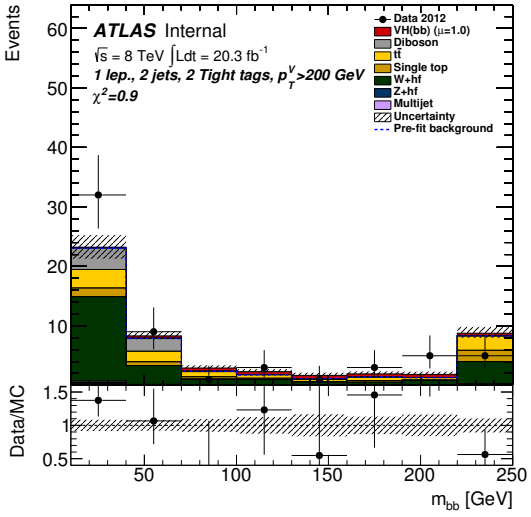

(e) $p_{\mathrm{T}}^{V} > 200$ GeV, 2 jets, TT

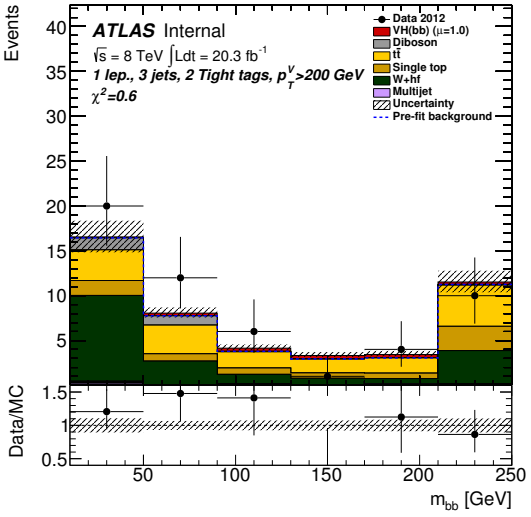

(f) $p_{\mathrm{T}}^{V} > 200$ GeV, 3 jets, TT

Figure 452: Post-fit plots for m_{jj} distribution in 1-lepton events in the LL, MM and TT tag categories for the 2-jets and the 3-jets events in the 1-lepton fit. Plots are shown for $p_{\mathrm{T}}^{V} > 200$ GeV. The pre-fit background expectation is indicated by the dashed blue line.

AH.1.5 2-lepton

The pull plots for 2-lepton are shown in Figure. 453-457.

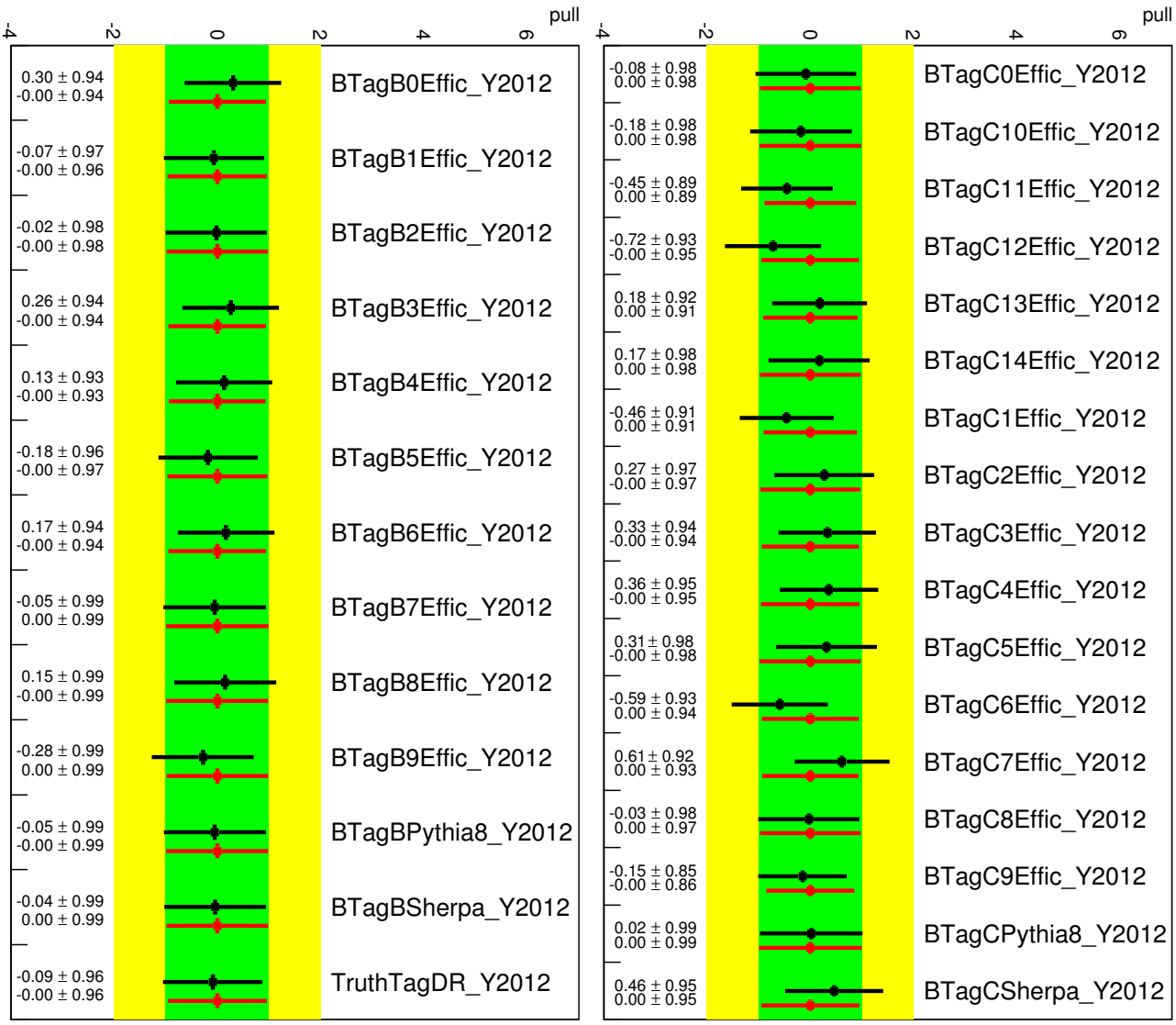

Figure 453: Pull plots for 2-lepton channel: *b*- and *c*-jet tagging.

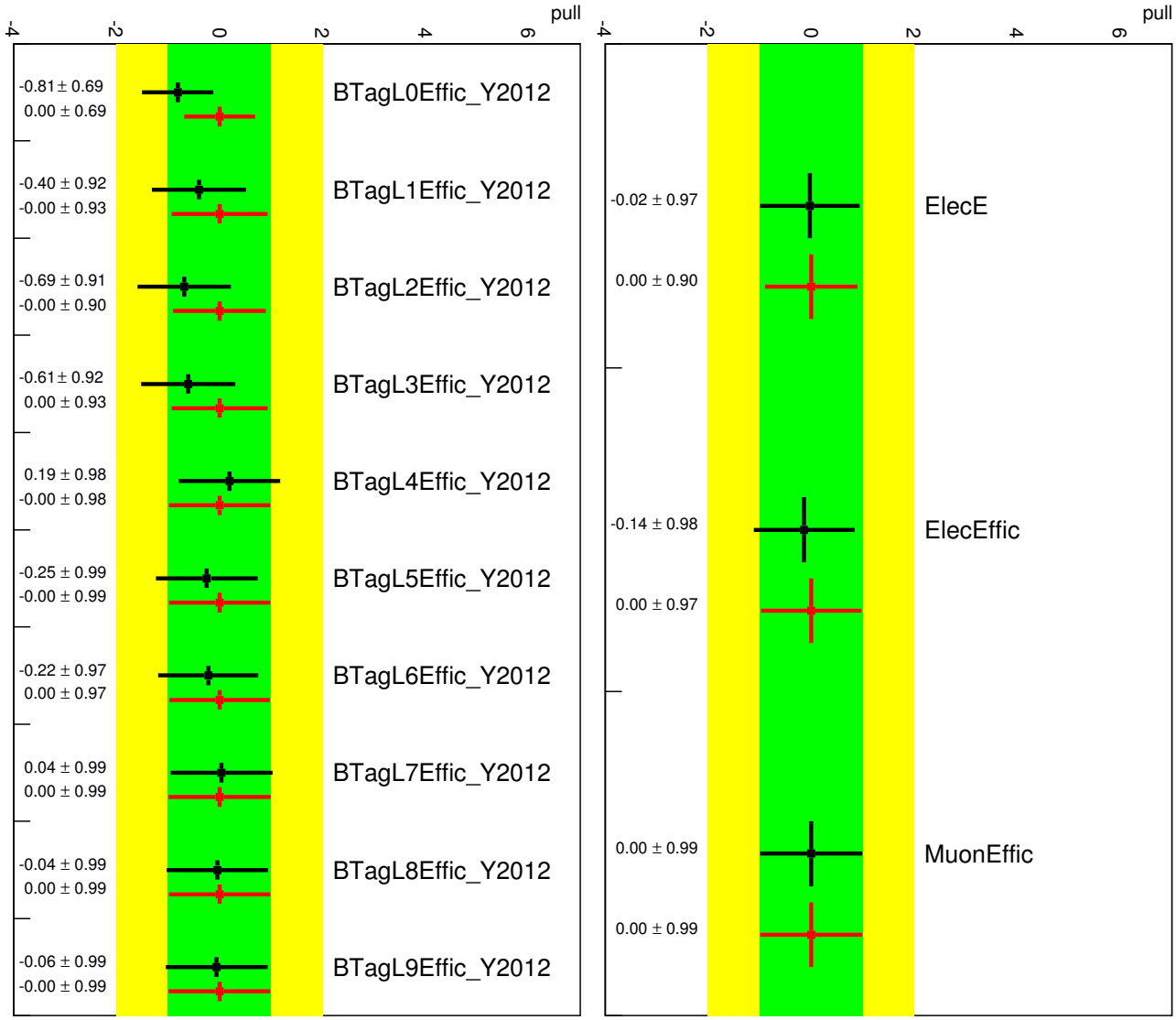

Figure 454: Pull plots for 2-lepton channel: light-jet tagging and leptons.

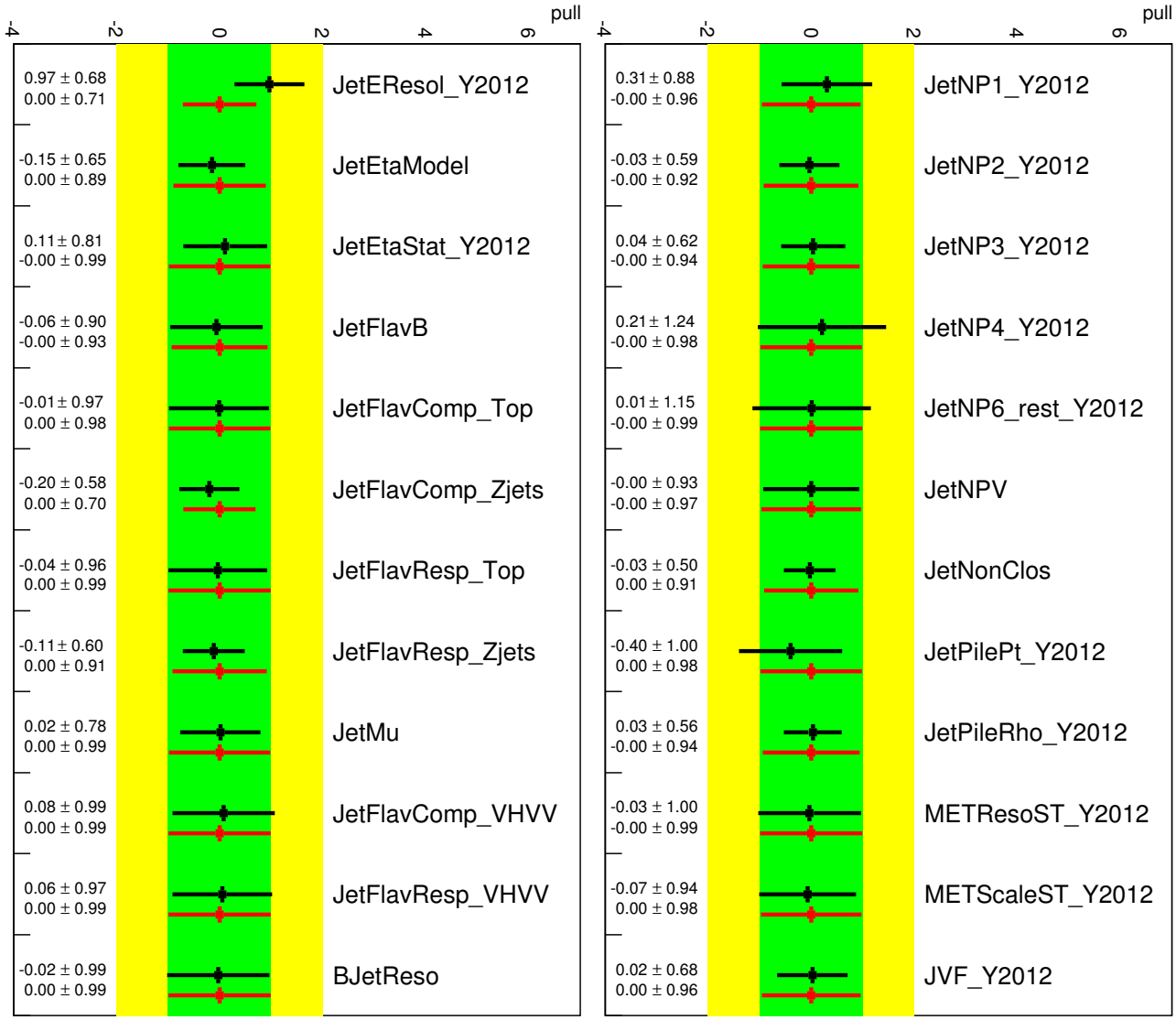

Figure 455: Pull plots for 2-lepton channel: Jet NPs.

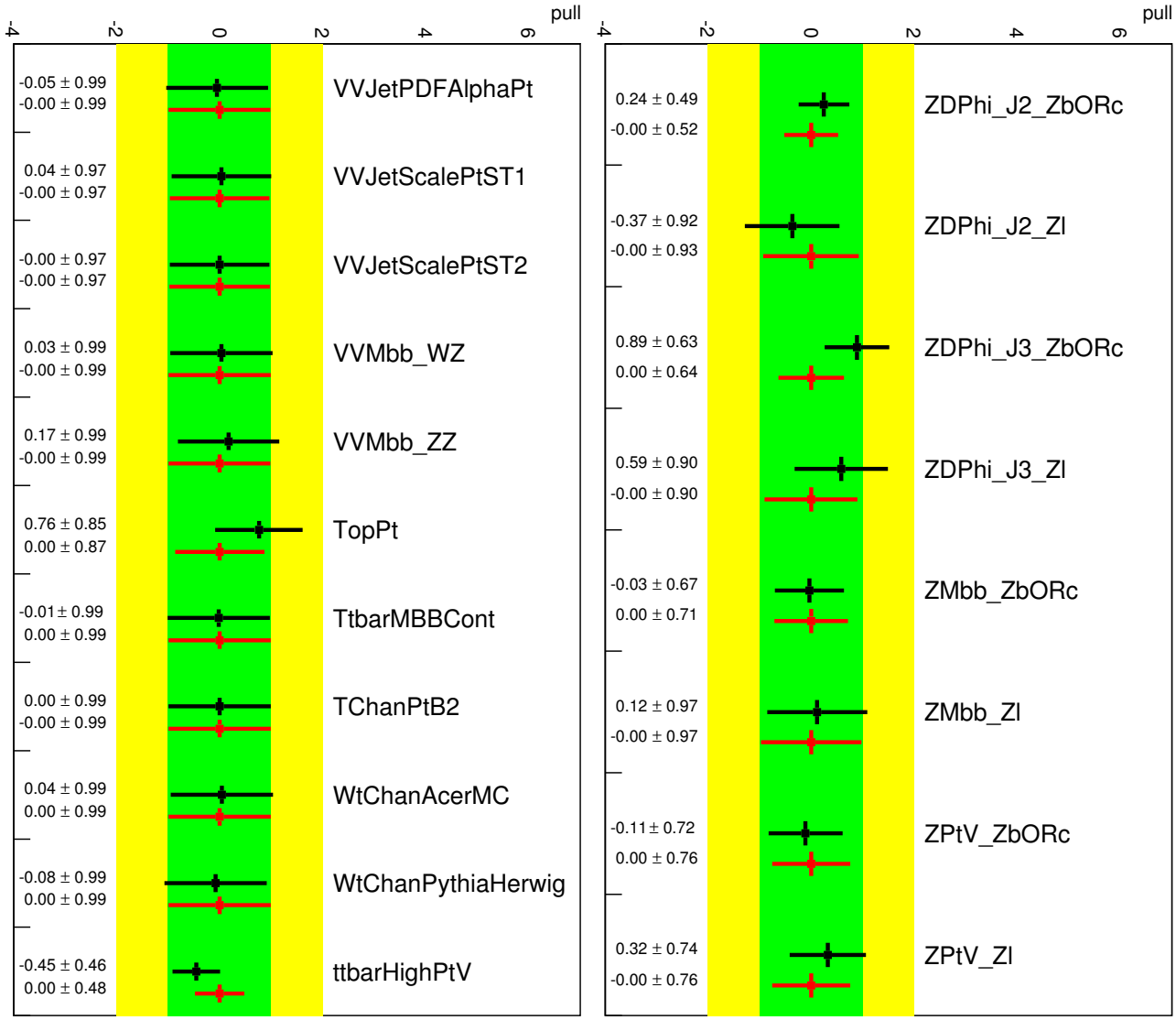

Figure 456: Pull plots for 2-lepton channel: Diboson and Top related uncertainties.

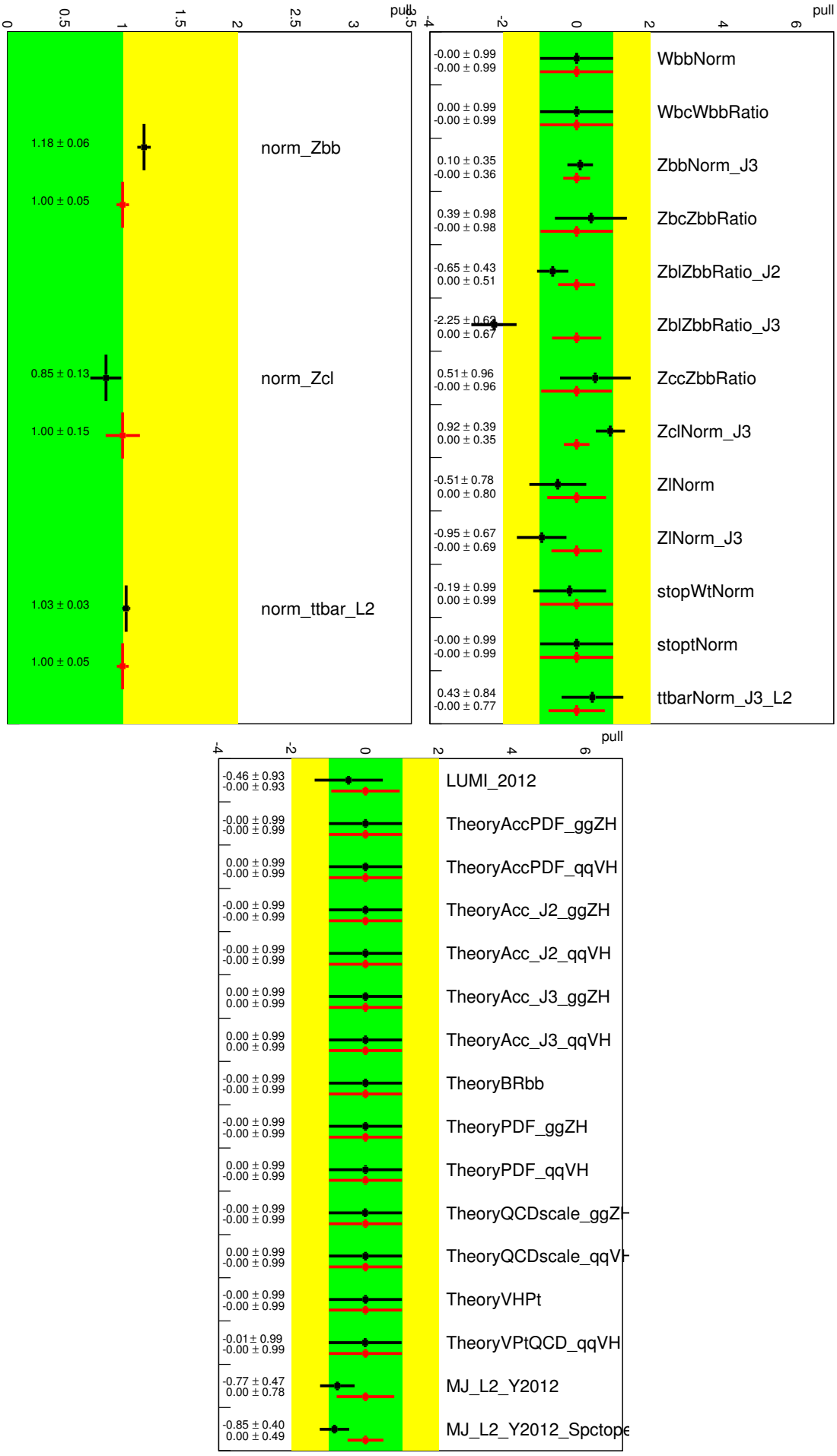

Figure 457: Pull plots for 2-lepton channel: Normalization and residual uncertainties.

AH.1.6 Pre-fit and Post-Fit for the m_{jj} shape analysis in the 2-lepton fit

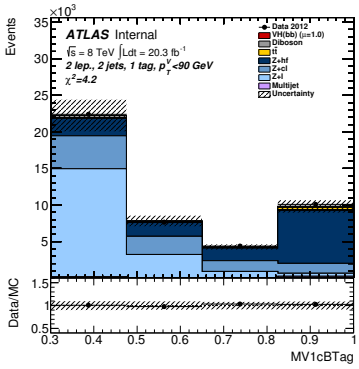

(a) $p_{\mathrm{T}}^{V} < 120$ GeV, 2 jets, 1-tag

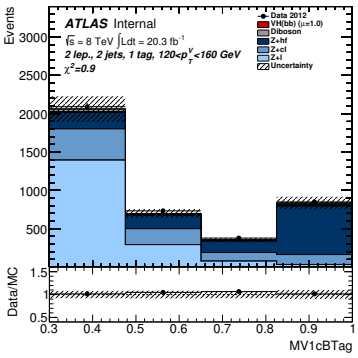

(b) $p_{\mathrm{T}}^{V} > 120$ GeV, 2 jets, 1-tag

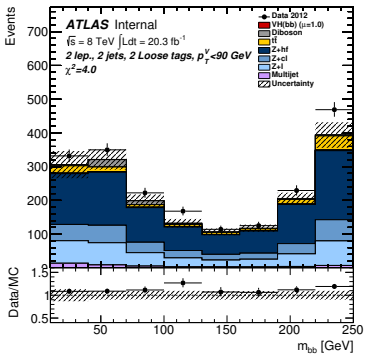

(c) $p_{\mathrm{T}}^{V} < 90$ GeV, 2 jets, LL

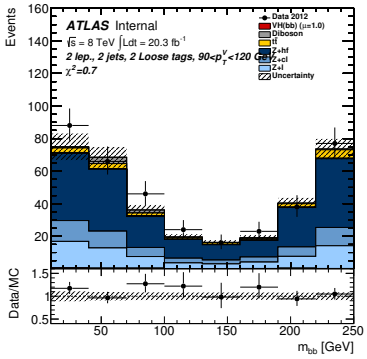

(d) $90 < p_{\mathrm{T}}^{V} < 120$ GeV, 2 jets, LL

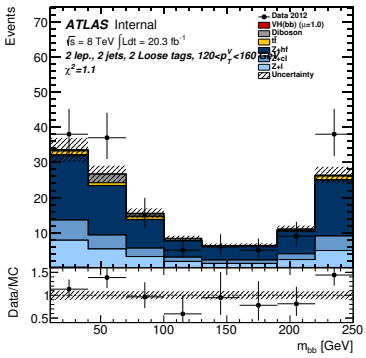

(e) $120 < p_{\mathrm{T}}^{V} < 160$ GeV, 2 jets, LL

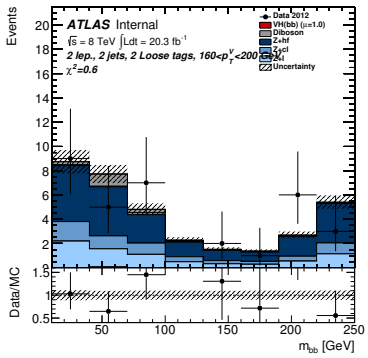

(f) $160 < p_{\mathrm{T}}^{V} < 200$ GeV, 2 jets, LL

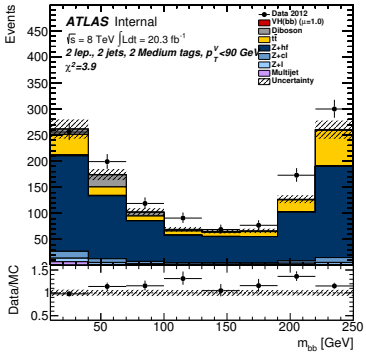

(g) $p_{\mathrm{T}}^{V} < 90$ GeV, 2 jets, MM

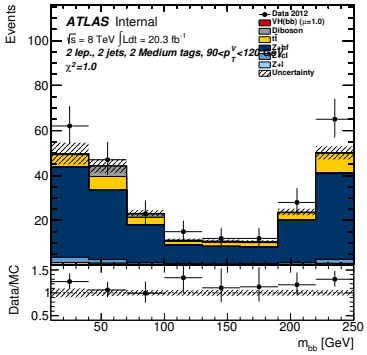

(h) $90 < p_{\mathrm{T}}^{V} < 120$ GeV, 2 jets, MM

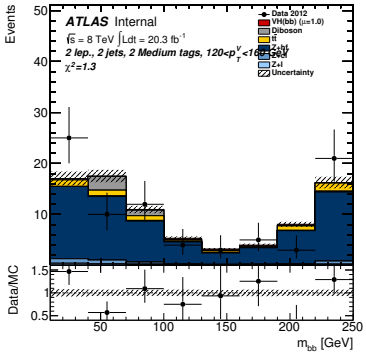

(i) $120 < p_{\mathrm{T}}^{V} < 160$ GeV, 2 jets, MM

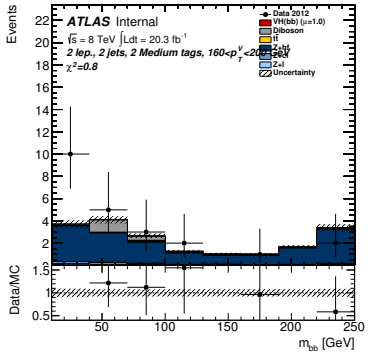

(j) $160 < p_{\mathrm{T}}^{V} < 200$ GeV, 2 jets, MM

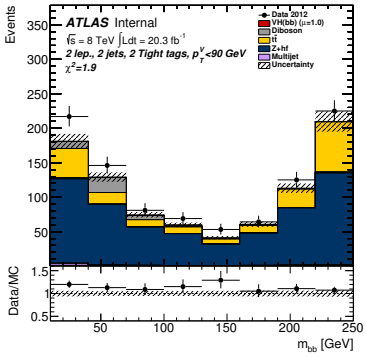

(k) $p_{\mathrm{T}}^{V} < 90$ GeV, 2 jets, TT

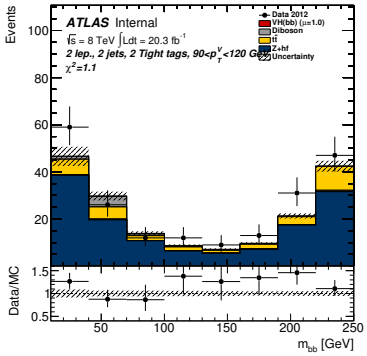

(l) $90 < p_{\mathrm{T}}^{V} < 120$ GeV, 2 jets, TT

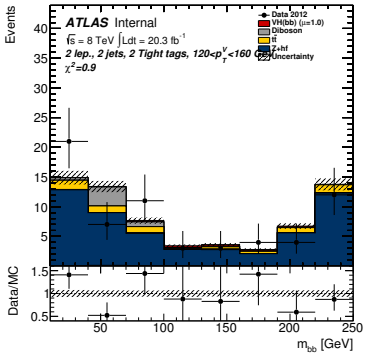

(m) $120 < p_{\mathrm{T}}^{V} < 160$ GeV, 2 jets, TT

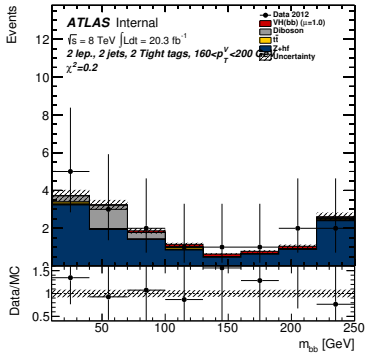

(n) $160 < p_{\mathrm{T}}^{V} < 200$ GeV, 2 jets, TT

Figure 458: Pre-fit plots for m_{jj} distribution in 2-lepton events in the 1-tag (where mv1c is used in the fit) *LL*, *MM* and *TT* tag categories for the 2-jets events in the 2-lepton fit. Plots are shown for $p_{\mathrm{T}}^{V} < 90$ GeV, $90 < p_{\mathrm{T}}^{V} < 120$ GeV, $120 < p_{\mathrm{T}}^{V} < 160$ GeVand $160 < p_{\mathrm{T}}^{V} < 200$ GeV. The pre-fit background expectation is indicated by the dashed blue line.

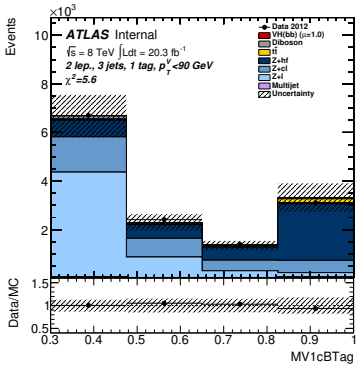

(a) $p_{\mathrm{T}}^{V} < 120$ GeV, 3 jets, 1-tag

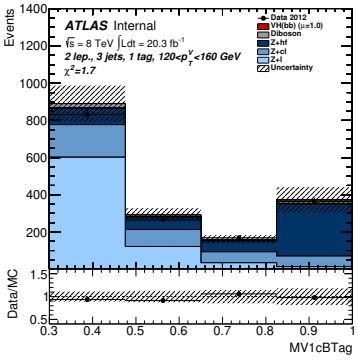

(b) $p_{\mathrm{T}}^{V} > 120$ GeV, 3 jets, 1-tag

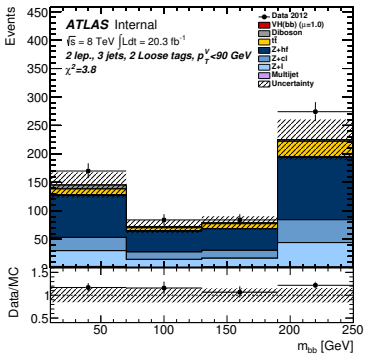

(c) $p_{\mathrm{T}}^{V} < 90$ GeV, 3 jets, LL

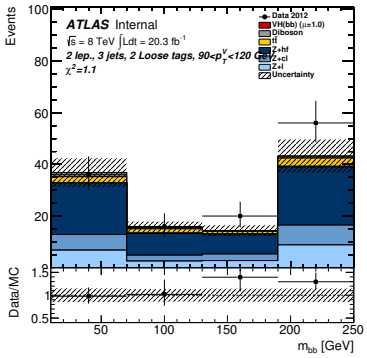

(d) $90 < p_{\mathrm{T}}^{V} < 120$ GeV, 3 jets, LL

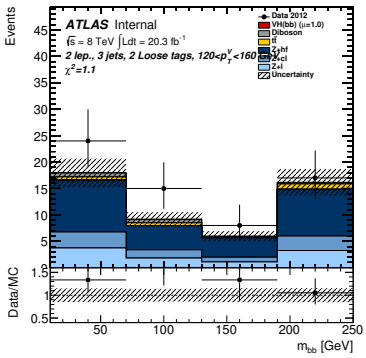

(e) $120 < p_{\mathrm{T}}^{V} < 160$ GeV, 3 jets, LL

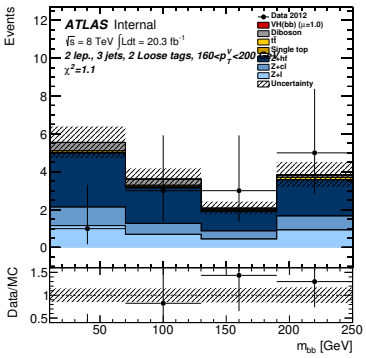

(f) $160 < p_{\mathrm{T}}^{V} < 200$ GeV, 3 jets, LL

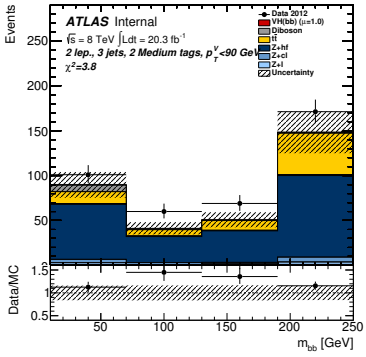

(g) $p_{\mathrm{T}}^{V} < 90$ GeV, 3 jets, MM

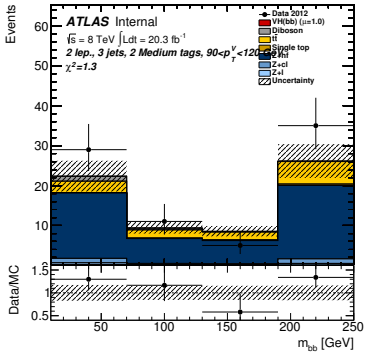

(h) $90 < p_{\mathrm{T}}^{V} < 120$ GeV, 3 jets, MM

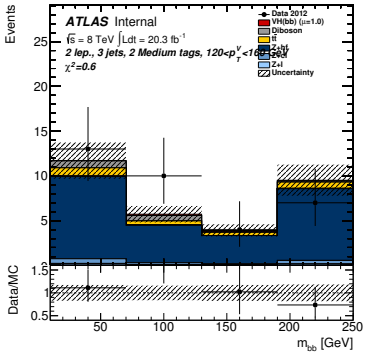

(i) $120 < p_{\mathrm{T}}^{V} < 160$ GeV, 3 jets, MM

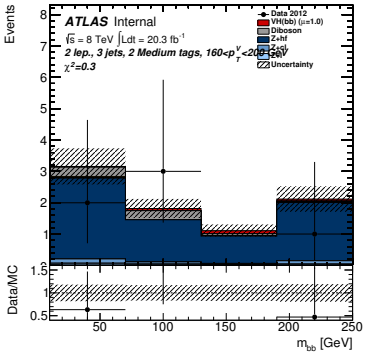

(j) $160 < p_{\mathrm{T}}^{V} < 200$ GeV, 3 jets, MM

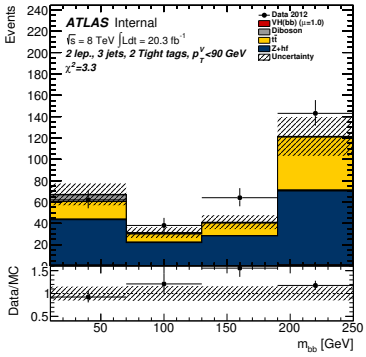

(k) $p_{\mathrm{T}}^{V} < 90$ GeV, 3 jets, TT

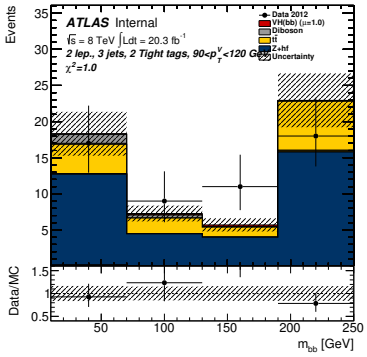

(l) $90 < p_{\mathrm{T}}^{V} < 120$ GeV, 3 jets, TT

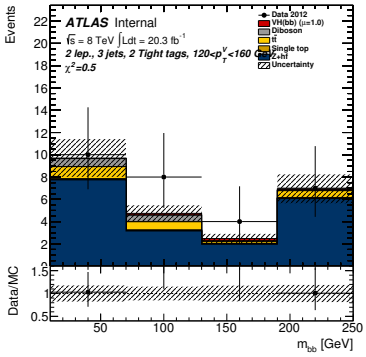

(m) $120 < p_{\mathrm{T}}^{V} < 160$ GeV, 3 jets, TT

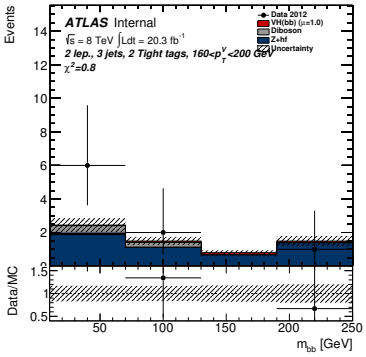

(n) $160 < p_{\mathrm{T}}^{V} < 200$ GeV, 3 jets, TT

Figure 459: Pre-fit plots for m_{jj} distribution in 2-lepton events in the 1-tag (where mv1c is used in the fit) *LL*, *MM* and *TT* tag categories for the 3-jets events in the 2-lepton fit. Plots are shown for $p_{\mathrm{T}}^{V} < 90$ GeV, $90 < p_{\mathrm{T}}^{V} < 120$ GeV, $120 < p_{\mathrm{T}}^{V} < 160$ GeVand $160 < p_{\mathrm{T}}^{V} < 200$ GeV. The pre-fit background expectation is indicated by the dashed blue line.

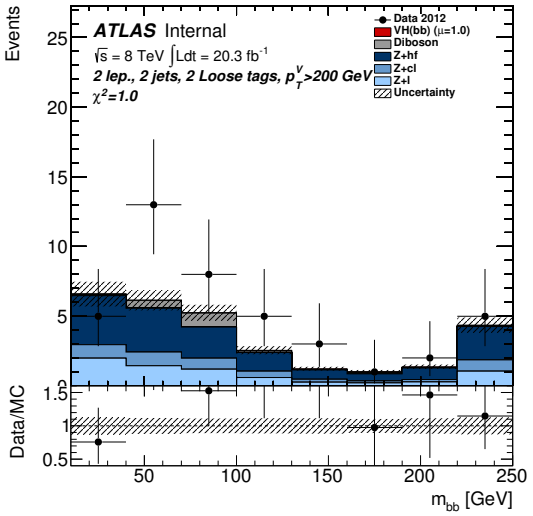

(a) $p_{\mathrm{T}}^{V} > 200$ GeV, 2 jets, LL

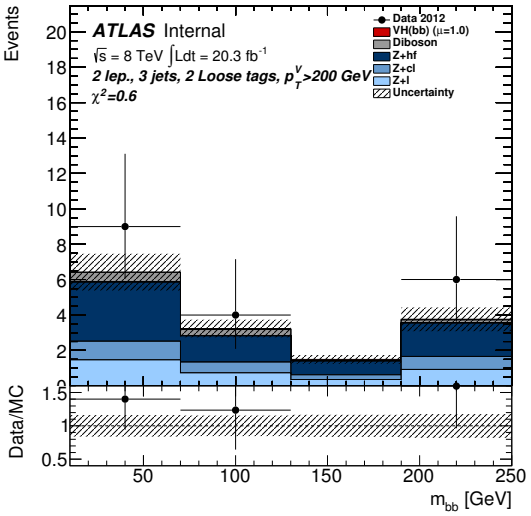

(b) $p_{\mathrm{T}}^{V} > 200$ GeV, 3 jets, LL

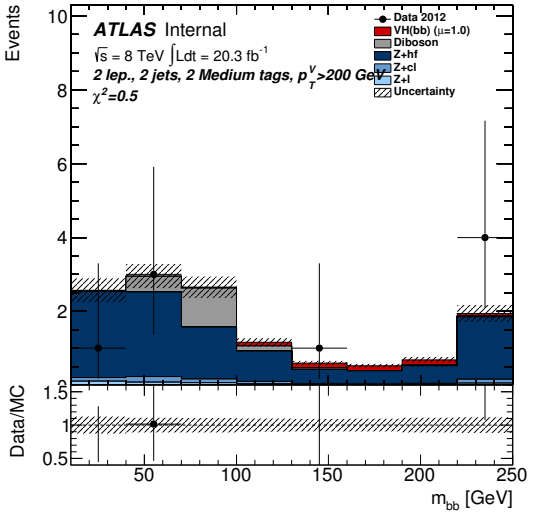

(c) $p_{\mathrm{T}}^{V} > 200$ GeV, 2 jets, MM

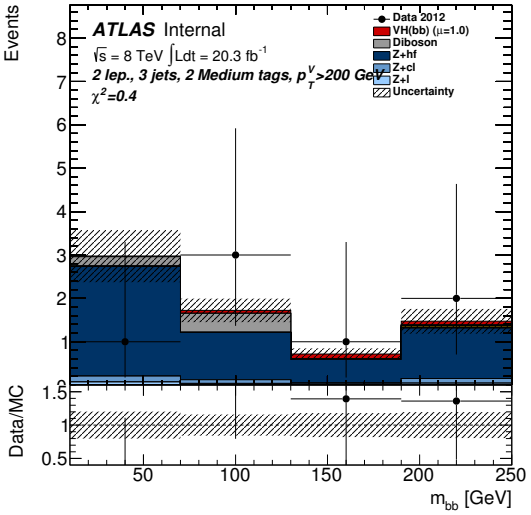

(d) $p_{\mathrm{T}}^{V} > 200$ GeV, 3 jets, MM

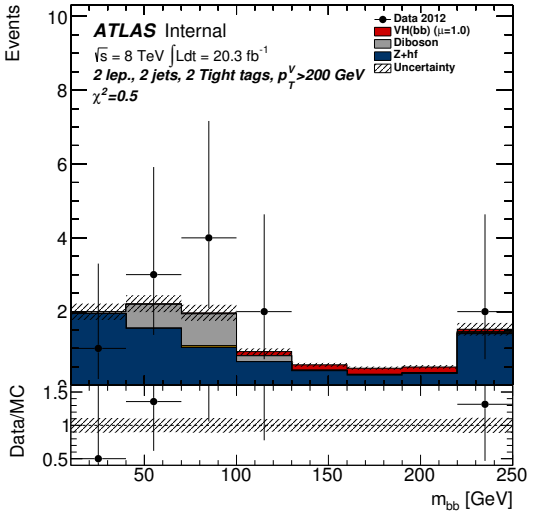

(e) $p_{\mathrm{T}}^{V} > 200$ GeV, 2 jets, TT

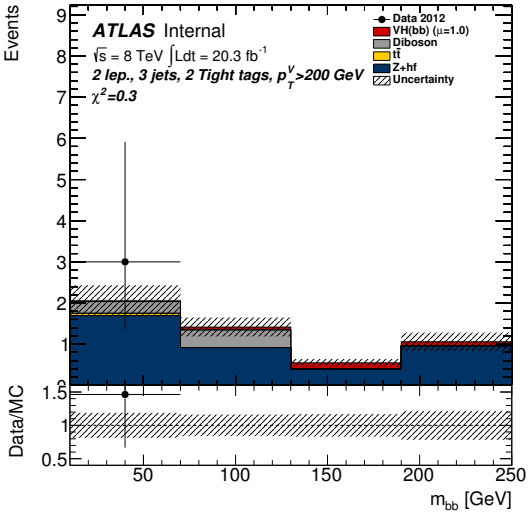

(f) $p_{\mathrm{T}}^{V} > 200$ GeV, 3 jets, TT

Figure 460: Pre-fit plots for m_{jj} distribution in 2-lepton events in the LL, MM and TT tag categories for the 2-jets and the 3-jets events in the 2-lepton fit. Plots are shown for $p_{\mathrm{T}}^{V} > 200$ GeV. The pre-fit background expectation is indicated by the dashed blue line.

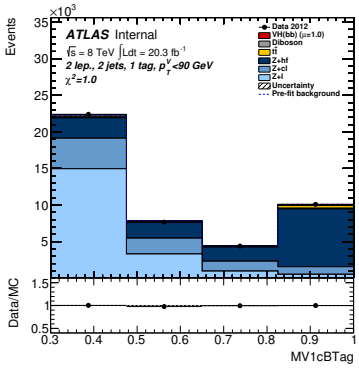

(a) $p_{\mathrm{T}}^{V} < 120$ GeV, 2 jets, 1-tag

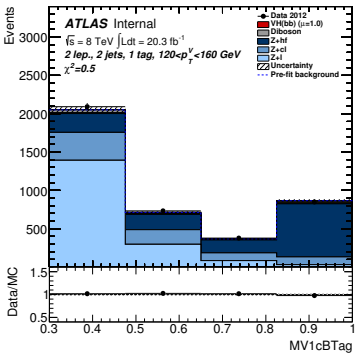

(b) $p_{\mathrm{T}}^{V} > 120$ GeV, 2 jets, 1-tag

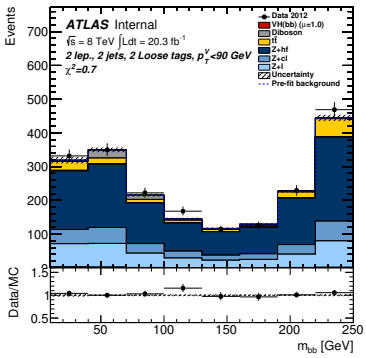

(c) $p_{\mathrm{T}}^{V} < 90$ GeV, 2 jets, LL

(d) $90 < p_{\mathrm{T}}^{V} < 120$ GeV, 2 jets, LL

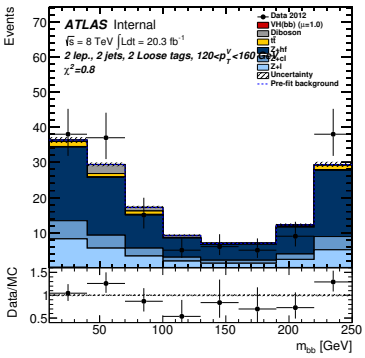

(e) $120 < p_{\mathrm{T}}^{V} < 160$ GeV, 2 jets, LL

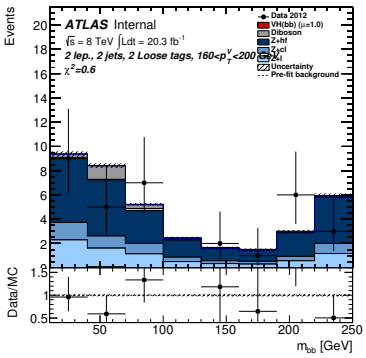

(f) $160 < p_{\mathrm{T}}^{V} < 200$ GeV, 2 jets, LL

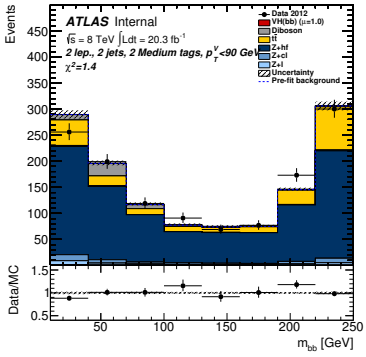

(g) $p_{\mathrm{T}}^{V} < 90$ GeV, 2 jets, MM

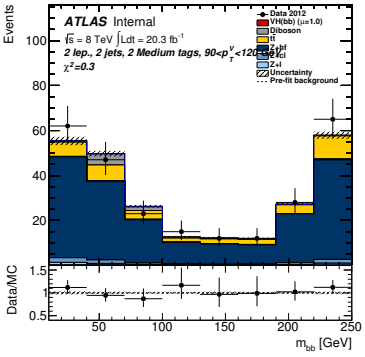

(h) $90 < p_{\mathrm{T}}^{V} < 120$ GeV, 2 jets, MM

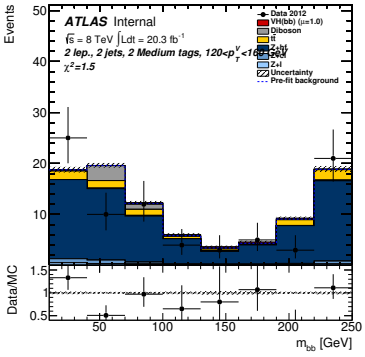

(i) $120 < p_{\mathrm{T}}^{V} < 160$ GeV, 2 jets, MM

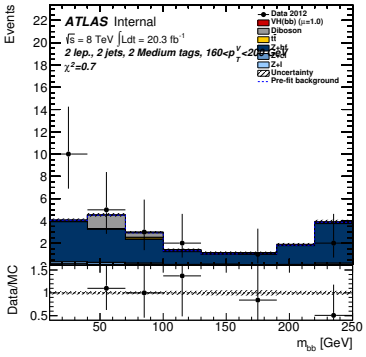

(j) $160 < p_{\mathrm{T}}^{V} < 200$ GeV, 2 jets, MM

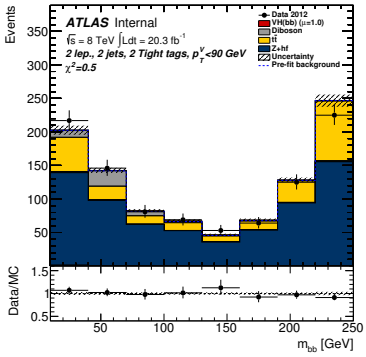

(k) $p_{\mathrm{T}}^{V} < 90$ GeV, 2 jets, TT

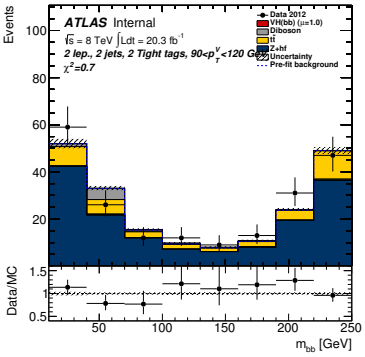

(l) $90 < p_{\mathrm{T}}^{V} < 120$ GeV, 2 jets, TT

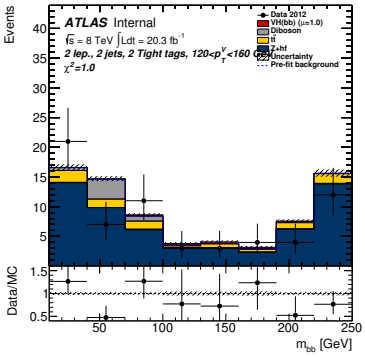

(m) $120 < p_{\mathrm{T}}^{V} < 160$ GeV, 2 jets, TT

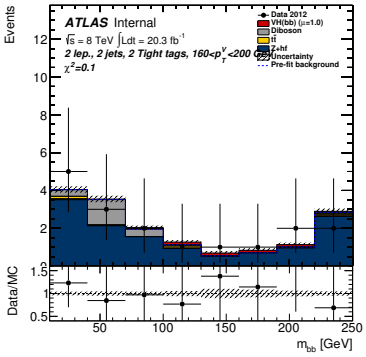

(n) $160 < p_{\mathrm{T}}^{V} < 200$ GeV, 2 jets, TT

Figure 461: Post-fit plots for m_{jj} distribution in 2-lepton events in the 1-tag (where mv1c is used in the fit) *LL*, *MM* and *TT* tag categories for the 2-jets events in the 2-lepton fit. Plots are shown for $p_{\mathrm{T}}^{V} < 90$ GeV, $90 < p_{\mathrm{T}}^{V} < 120$ GeV, $120 < p_{\mathrm{T}}^{V} < 160$ GeVand $160 < p_{\mathrm{T}}^{V} < 200$ GeV. The pre-fit background expectation is indicated by the dashed blue line.

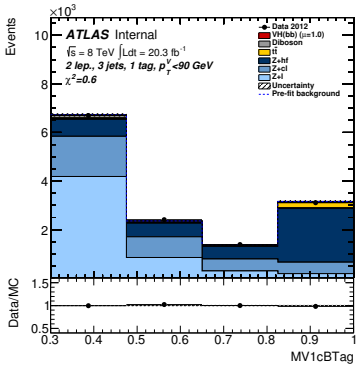

(a) $p_{\mathrm{T}}^{V} < 120$ GeV, 3 jets, 1-tag

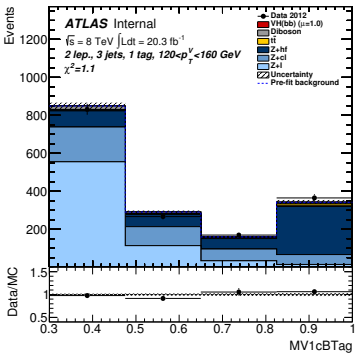

(b) $p_{\mathrm{T}}^{V} > 120$ GeV, 3 jets, 1-tag

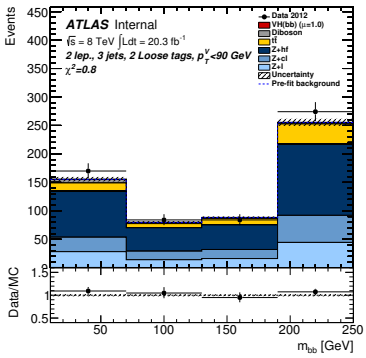

(c) $p_{\mathrm{T}}^{V} < 90$ GeV, 3 jets, LL

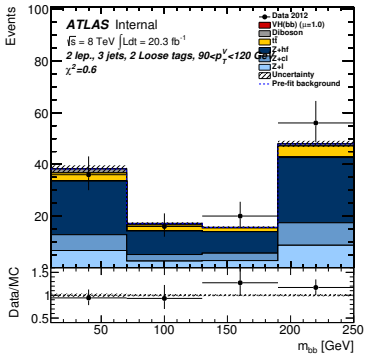

(d) $90 < p_{\mathrm{T}}^{V} < 120$ GeV, 3 jets, LL

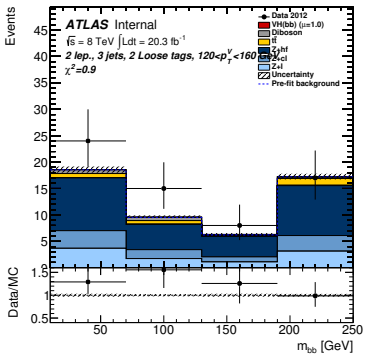

(e) $120 < p_{\mathrm{T}}^{V} < 160$ GeV, 3 jets, LL

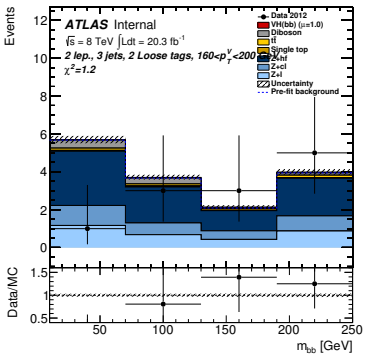

(f) $160 < p_{\mathrm{T}}^{V} < 200$ GeV, 3 jets, LL

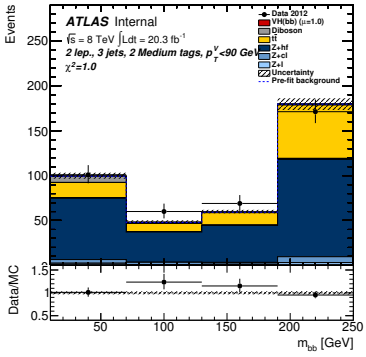

(g) $p_{\mathrm{T}}^{V} < 90$ GeV, 3 jets, MM

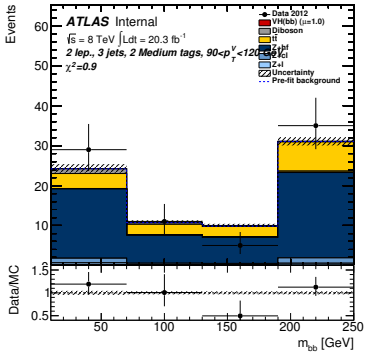

(h) $90 < p_{\mathrm{T}}^{V} < 120$ GeV, 3 jets, MM

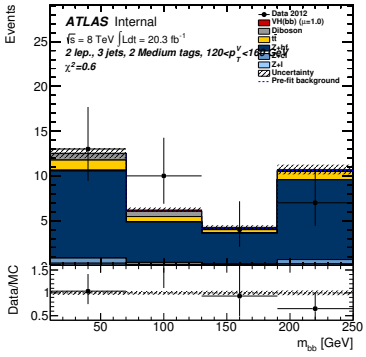

(i) $120 < p_{\mathrm{T}}^{V} < 160$ GeV, 3 jets, MM

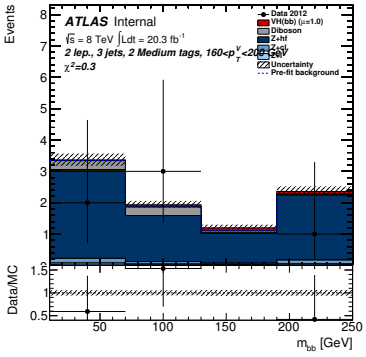

(j) $160 < p_{\mathrm{T}}^{V} < 200$ GeV, 3 jets, MM

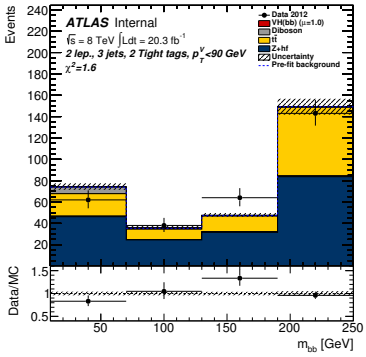

(k) $p_{\mathrm{T}}^{V} < 90$ GeV, 3 jets, TT

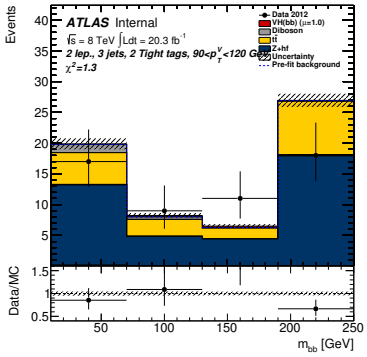

(l) $90 < p_{\mathrm{T}}^{V} < 120$ GeV, 3 jets, TT

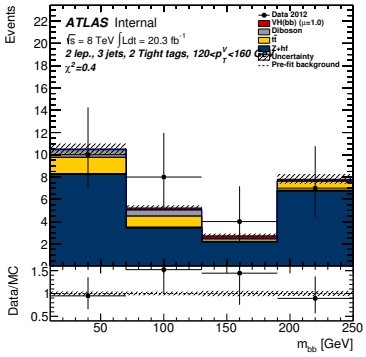

(m) $120 < p_{\mathrm{T}}^{V} < 160$ GeV, 3 jets, TT

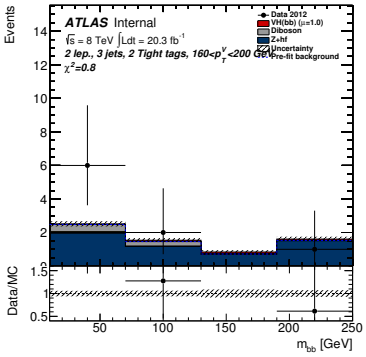

(n) $160 < p_{\mathrm{T}}^{V} < 200$ GeV, 3 jets, TT

Figure 462: Post-fit plots for m_{jj} distribution in 2-lepton events in the 1-tag (where mv1c is used in the fit) *LL*, *MM* and *TT* tag categories for the 3-jets events in the 2-lepton fit. Plots are shown for $p_{\mathrm{T}}^{V} < 90$ GeV, $90 < p_{\mathrm{T}}^{V} < 120$ GeV, $120 < p_{\mathrm{T}}^{V} < 160$ GeVand $160 < p_{\mathrm{T}}^{V} < 200$ GeV. The pre-fit background expectation is indicated by the dashed blue line.

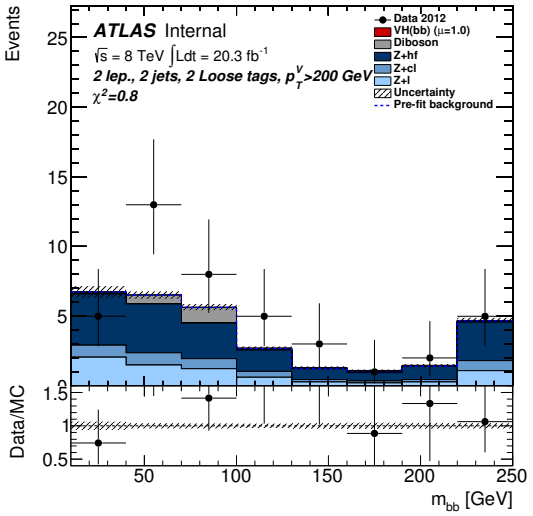

(a) $p_{\mathrm{T}}^{V} > 200$ GeV, 2 jets, LL

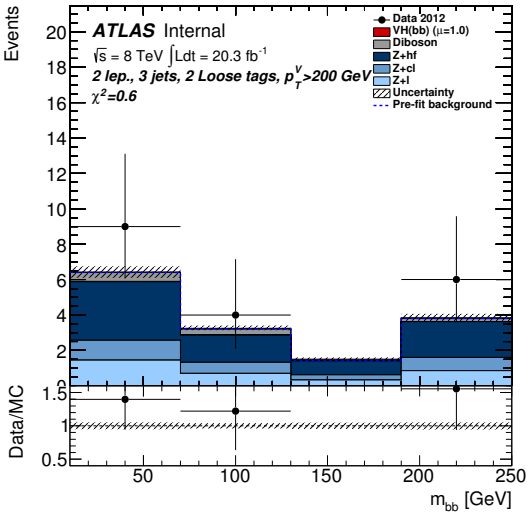

(b) $p_{\mathrm{T}}^{V} > 200$ GeV, 3 jets, LL

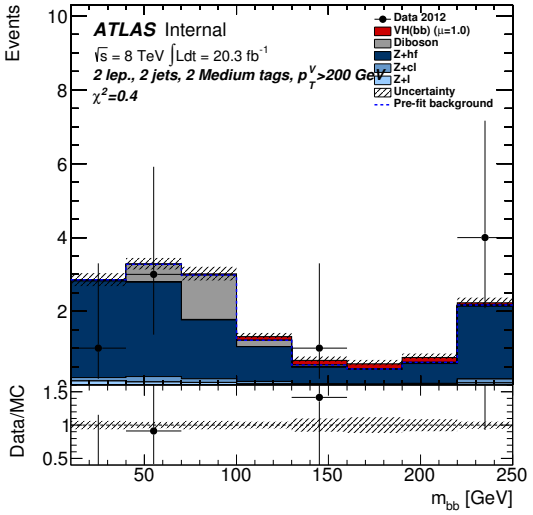

(c) $p_{\mathrm{T}}^{V} > 200$ GeV, 2 jets, MM

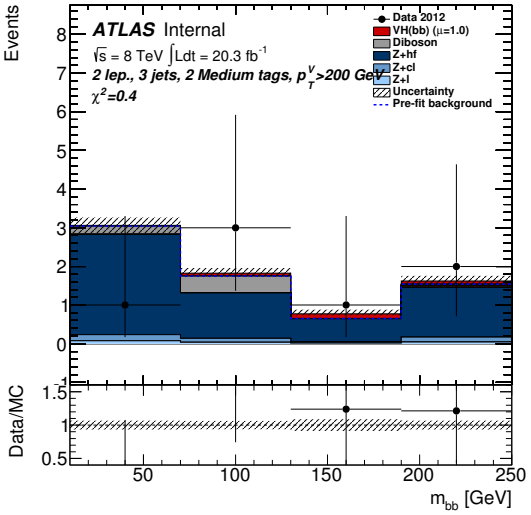

(d) $p_{\mathrm{T}}^{V} > 200$ GeV, 3 jets, MM

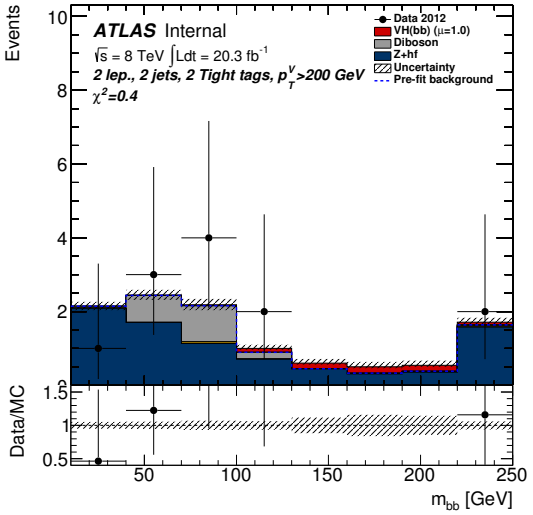

(e) $p_{\mathrm{T}}^{V} > 200$ GeV, 2 jets, TT

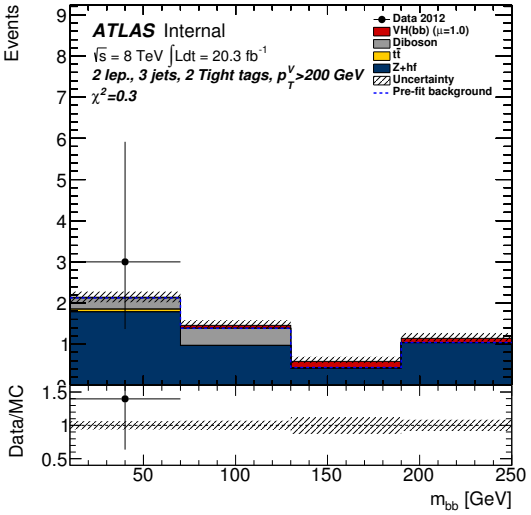

(f) $p_{\mathrm{T}}^{V} > 200$ GeV, 3 jets, TT

Figure 463: Post-fit plots for m_{jj} distribution in 2-lepton events in the LL, MM and TT tag categories for the 2-jets and the 3-jets events in the 2-lepton fit. Plots are shown for $p_{\mathrm{T}}^{V} > 200$ GeV. The pre-fit background expectation is indicated by the dashed blue line.

AH.2 MVA

??

AH.2.1 0-lepton pull plots

The pull plots for 0-lepton are shown in Figure. 464-468.

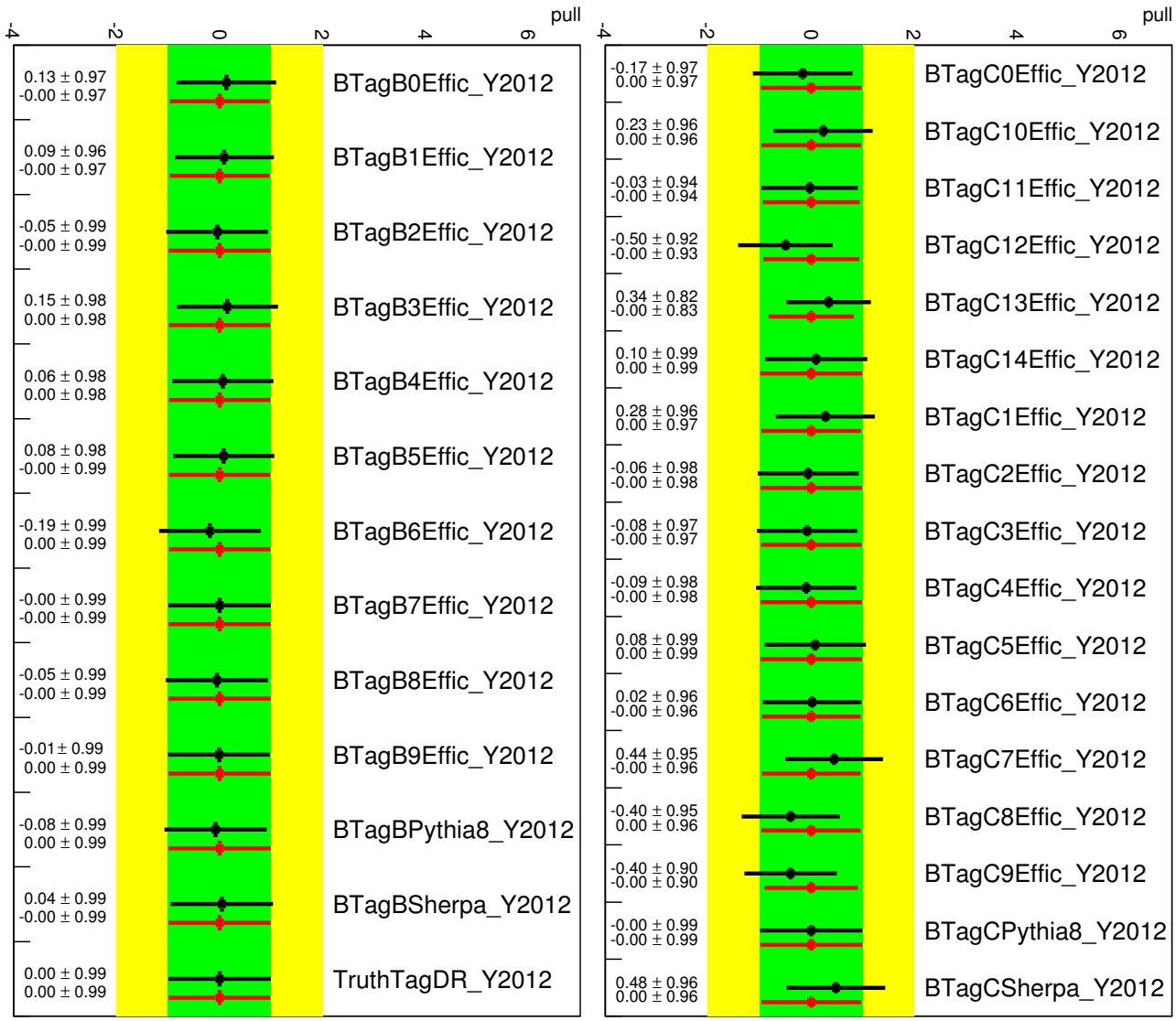

Figure 464: Pull plots for 0-lepton channel: *b*- and *c*-jet tagging.

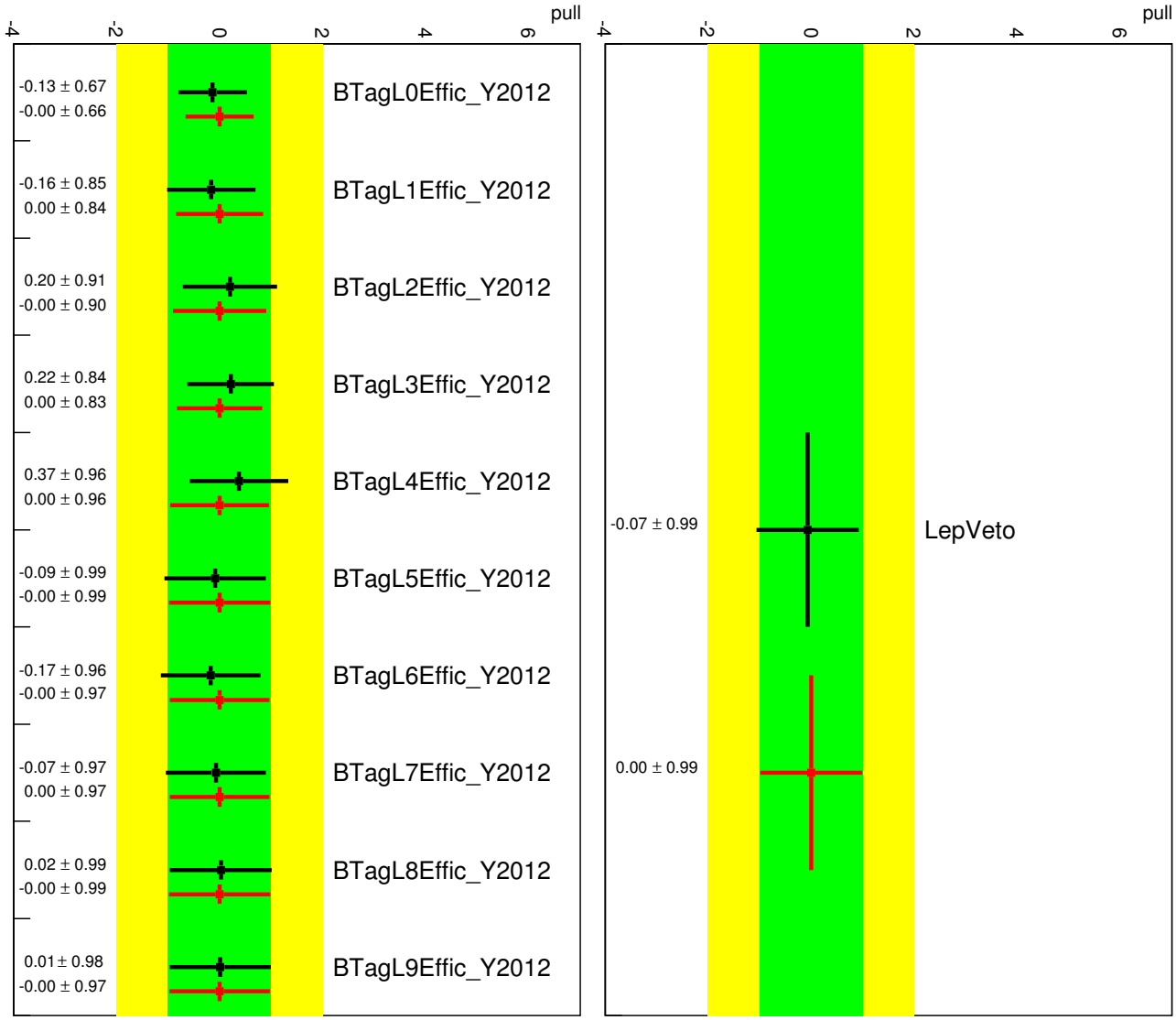

Figure 465: Pull plots for 0-lepton channel: light-jet tagging and leptons.

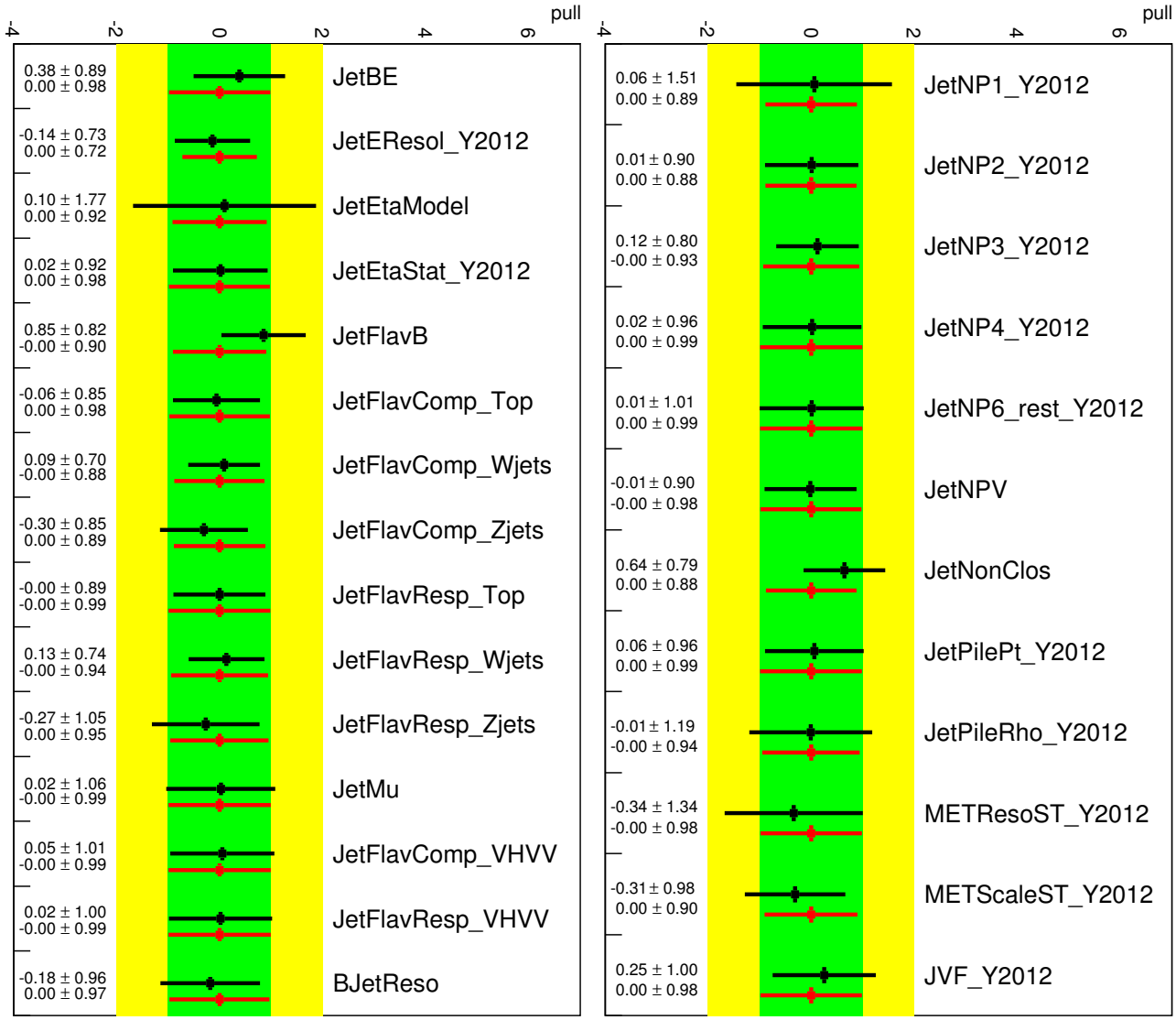

Figure 466: Pull plots for 0-lepton channel: Jet NPs.

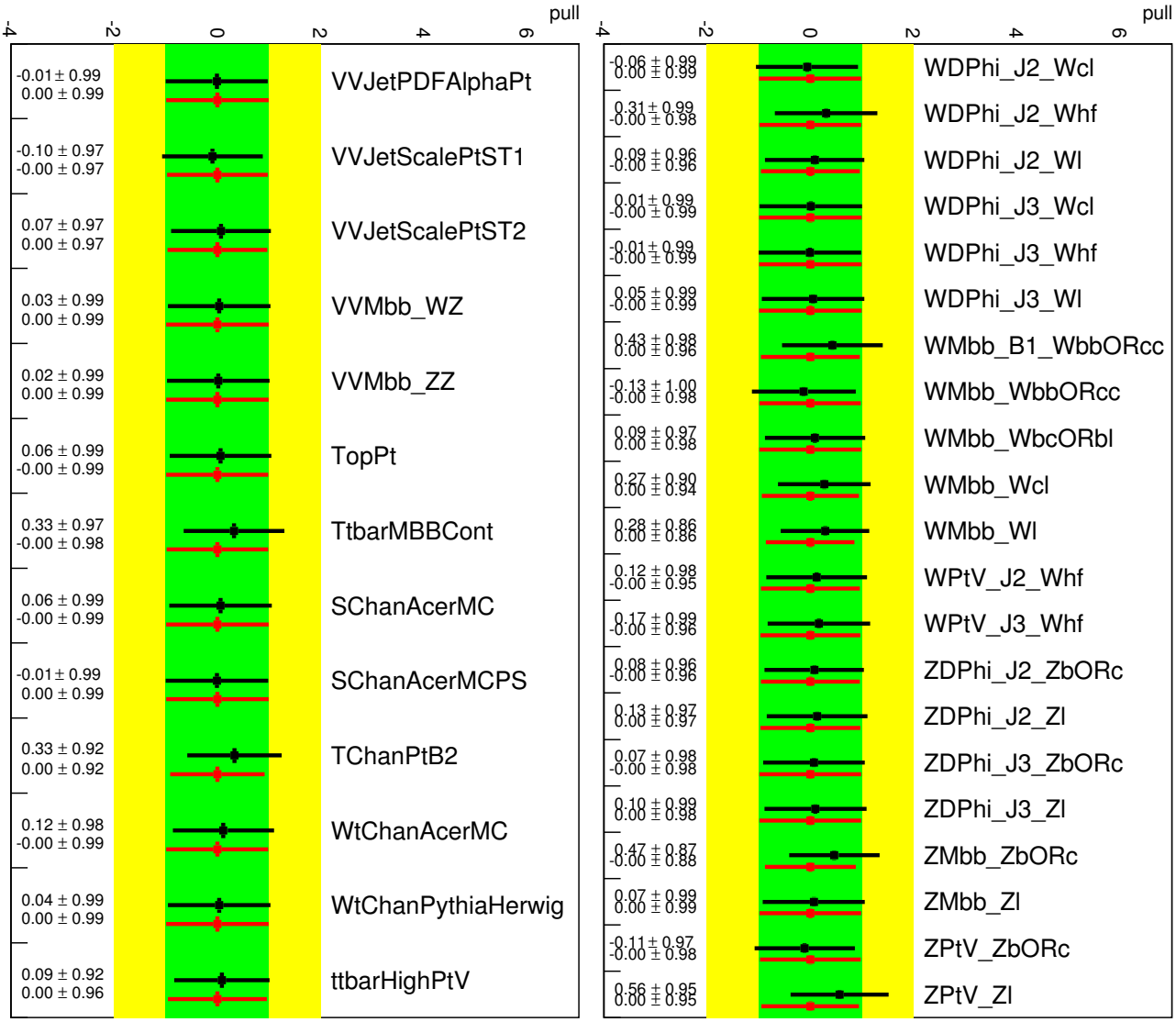

Figure 467: Pull plots for 0-lepton channel: Diboson/Top and W/Z related uncertainties.

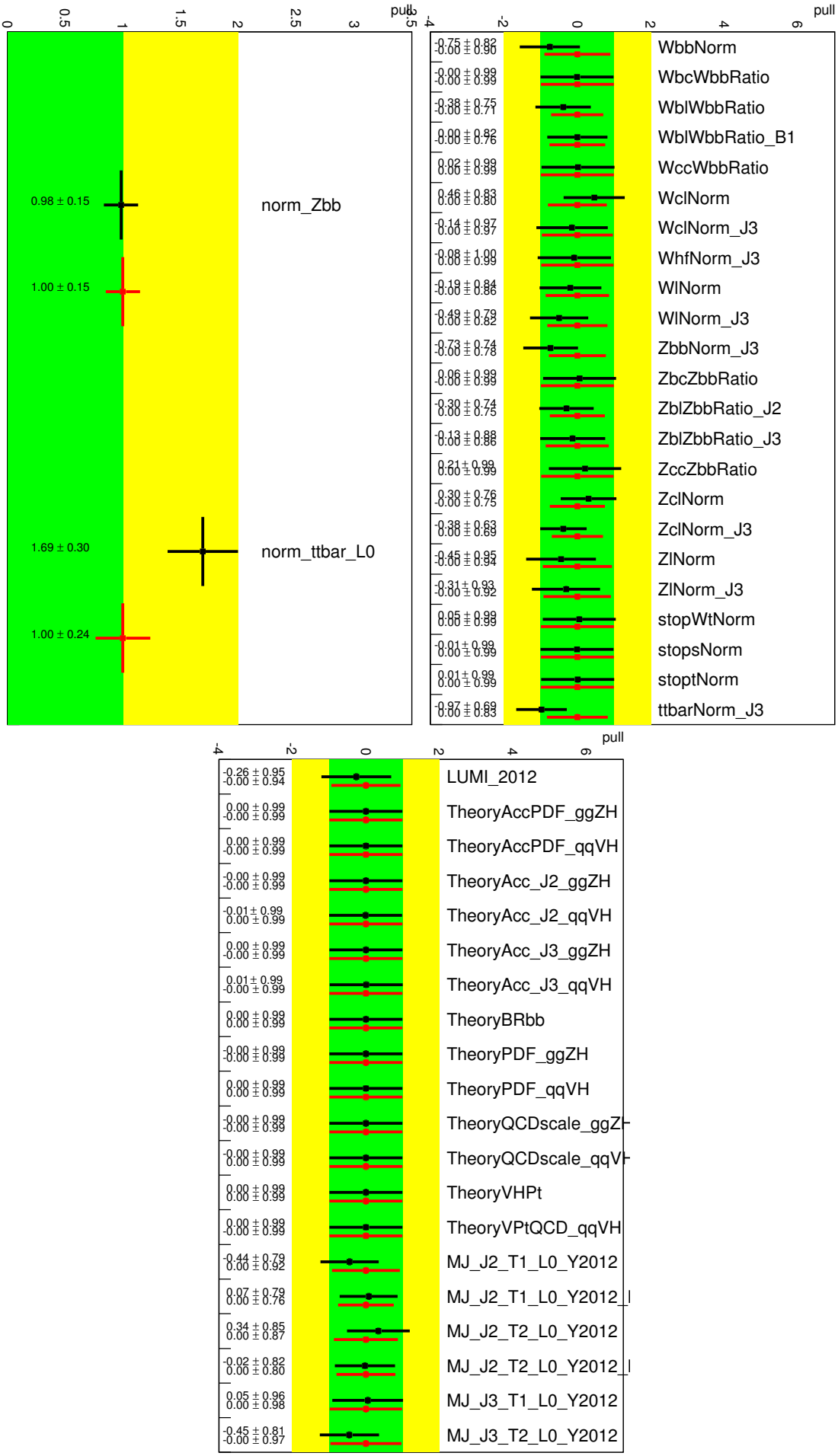

Figure 468: Pull plots for 0-lepton channel: Other model and normalization uncertainties.

AH.2.2 Pre-fit and Post-Fit for the MVA analysis in the 0-lepton fit

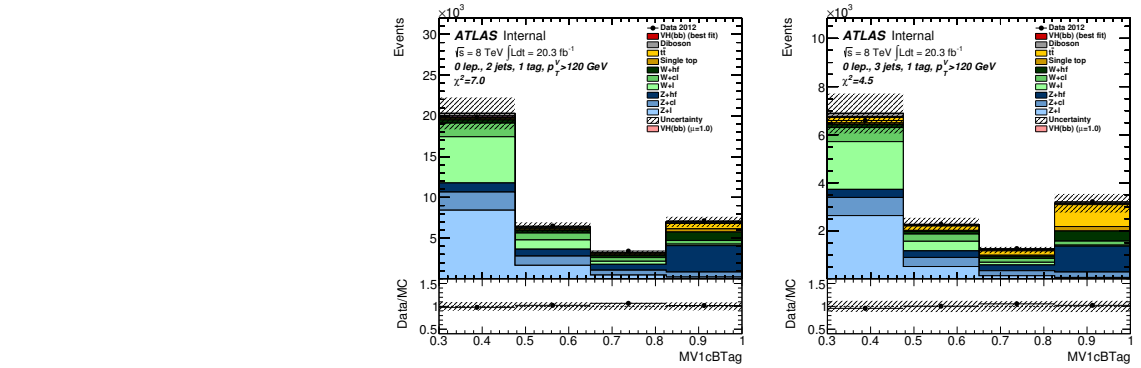

(a) $p_{\mathrm{T}}^{V} < 120$ GeV, 2 jets, 1-tag (b) $p_{\mathrm{T}}^{V} > 120$ GeV, 2 jets, 1-tag (c) $p_{\mathrm{T}}^{V} > 120$ GeV, 3 jets, 1-tag

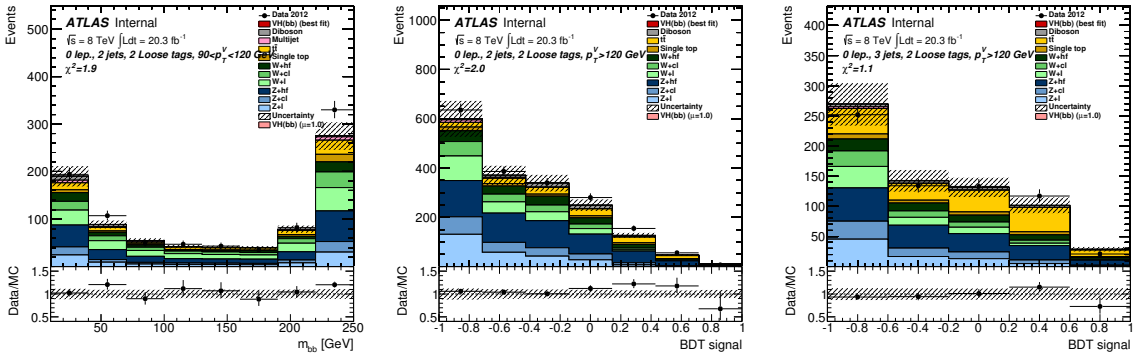

(d) $p_{\mathrm{T}}^{V} < 120$ GeV, 2 jets, LL (e) $p_{\mathrm{T}}^{V} > 120$ GeV, 2 jets, LL (f) $p_{\mathrm{T}}^{V} > 120$ GeV, 3 jets, LL

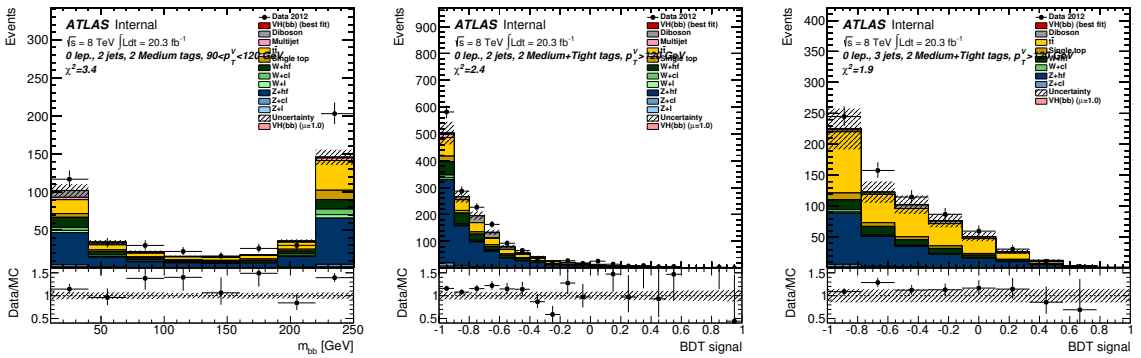

(g) $p_{\mathrm{T}}^{V} < 120$ GeV, 2 jets, MM+TT (h) $p_{\mathrm{T}}^{V} > 120$ GeV, 2 jets, MM+TT (i) $p_{\mathrm{T}}^{V} > 120$ GeV, 3 jets, MM+TT

Figure 469: Pre-fit plots for MVA distribution in 0-lepton events with 1 b-tag (MV1c is fit here), LL and $MM + TT$ b-tags in the 0 lepton fit.

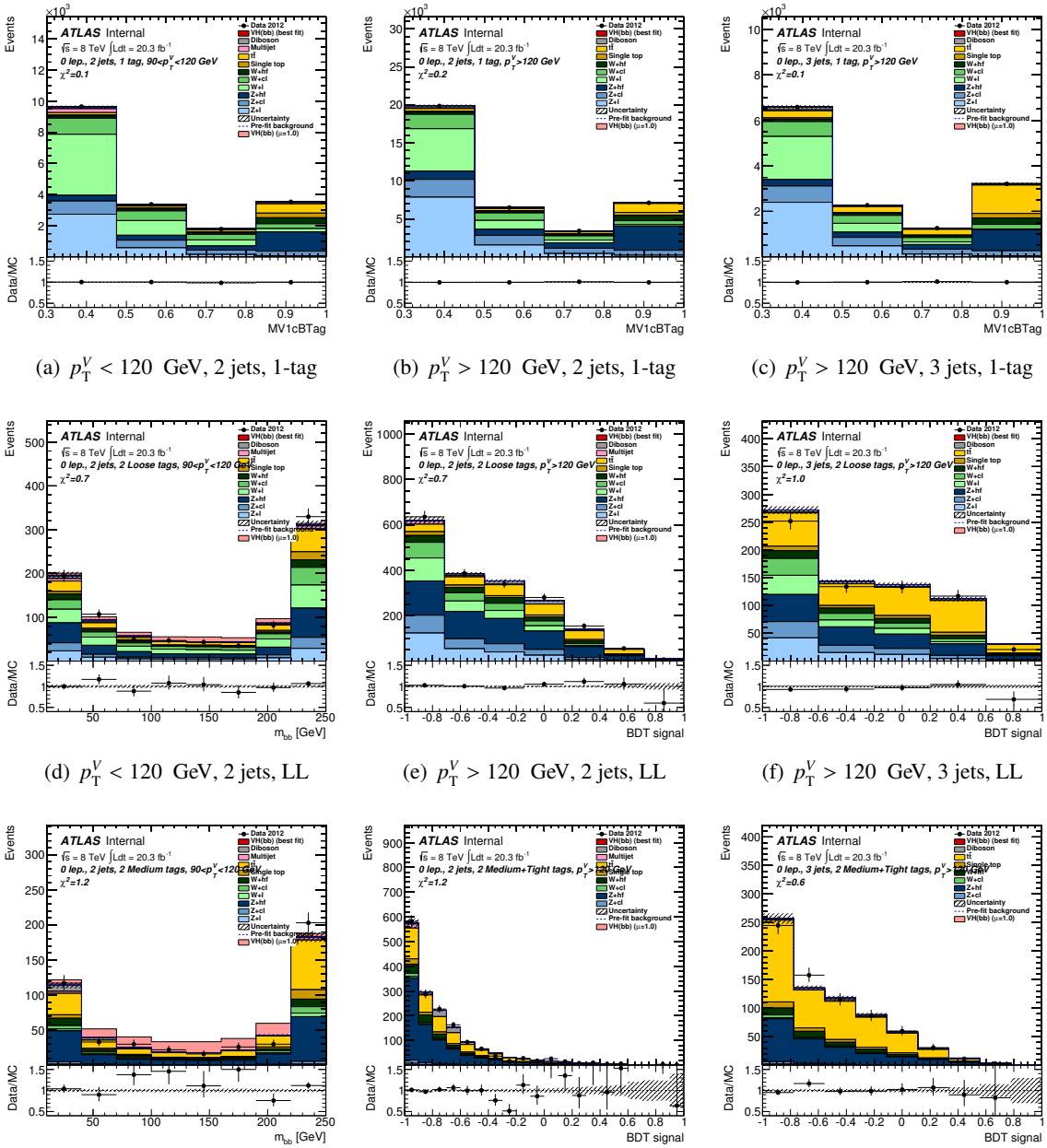

(a) $p_{\mathrm{T}}^{V} < 120$ GeV, 2 jets, 1-tag (b) $p_{\mathrm{T}}^{V} > 120$ GeV, 2 jets, 1-tag (c) $p_{\mathrm{T}}^{V} > 120$ GeV, 3 jets, 1-tag

(d) $p_{\mathrm{T}}^{V} < 120$ GeV, 2 jets, LL (e) $p_{\mathrm{T}}^{V} > 120$ GeV, 2 jets, LL (f) $p_{\mathrm{T}}^{V} > 120$ GeV, 3 jets, LL

(g) $p_{\mathrm{T}}^{V} < 120$ GeV, 2 jets, MM+TT (h) $p_{\mathrm{T}}^{V} > 120$ GeV, 2 jets, MM+TT (i) $p_{\mathrm{T}}^{V} > 120$ GeV, 3 jets, MM+TT

Figure 470: Post-fit plots for MVA distribution in 0-lepton events with 1 b-tag (MV1c is fit here), *LL* and $MM + TT$ b-tags in the 0 lepton fit. The pre-fit background expectation is indicated by the dashed blue line.

AH.2.3 1-lepton pull plots

The pull plots for 1-lepton are shown in Figure. 471-475.

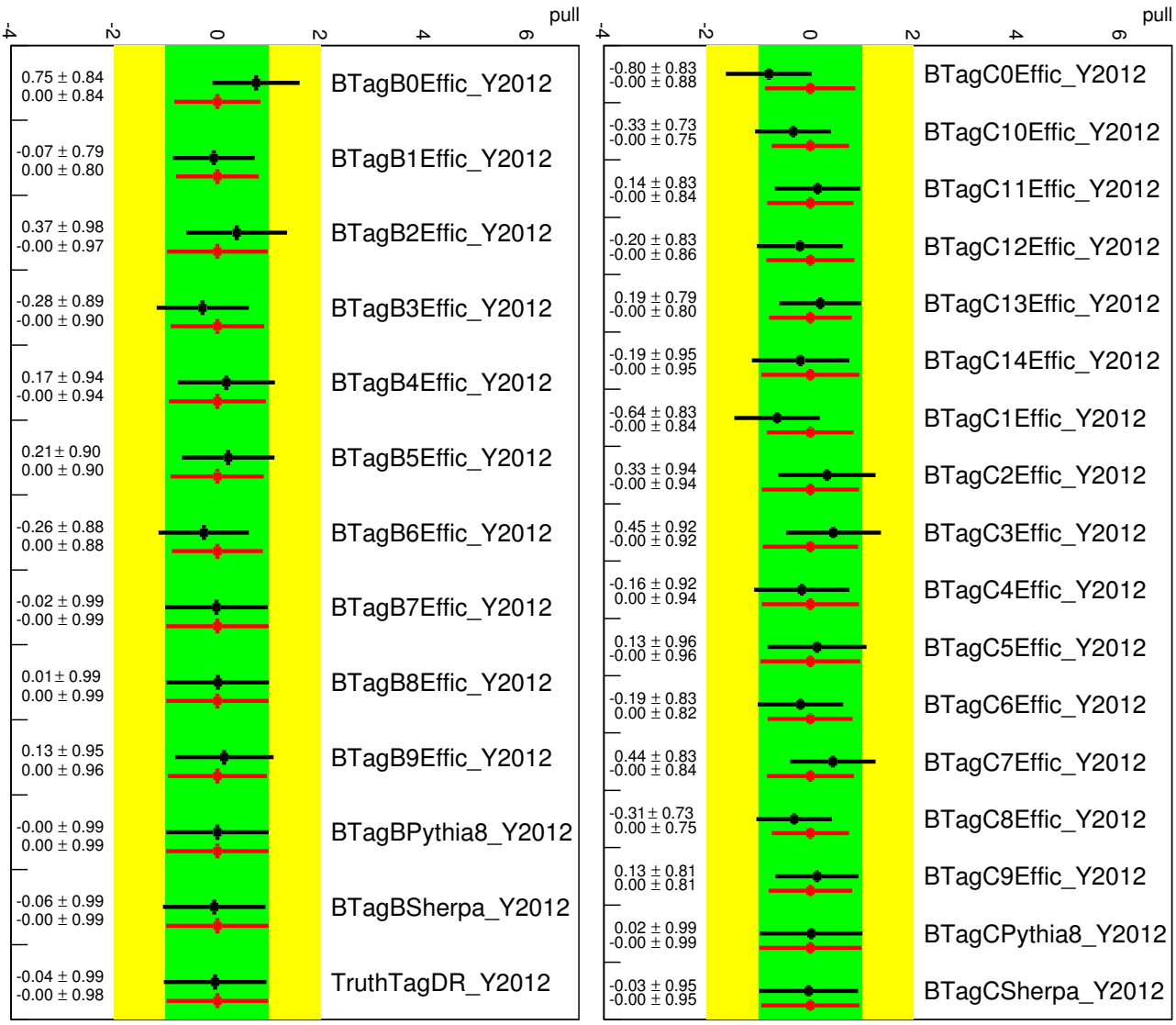

Figure 471: Pull plots for 1-lepton channel: *b*- and *c*-jet tagging.

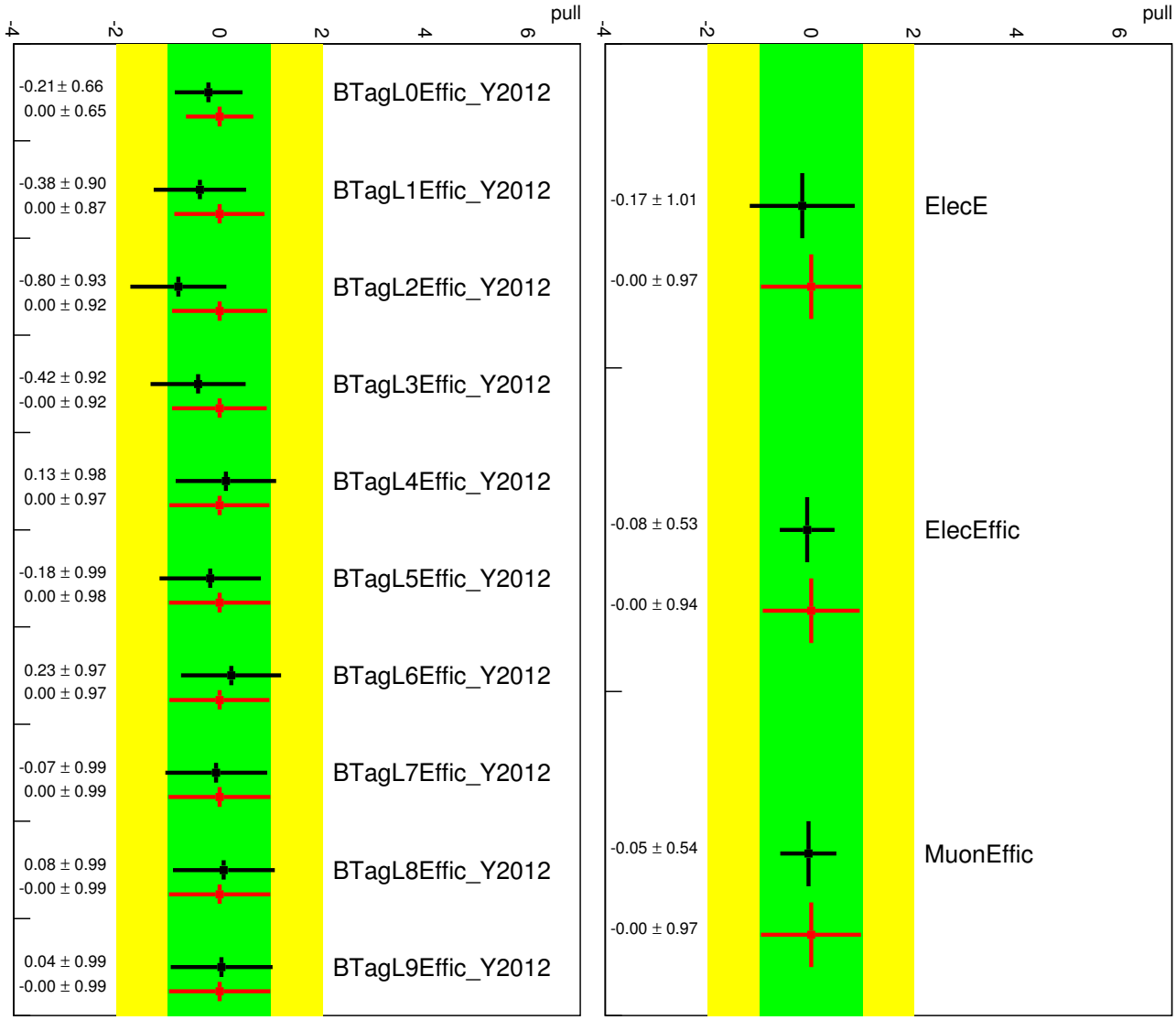

Figure 472: Pull plots for 1-lepton channel: light-jet tagging and leptons.

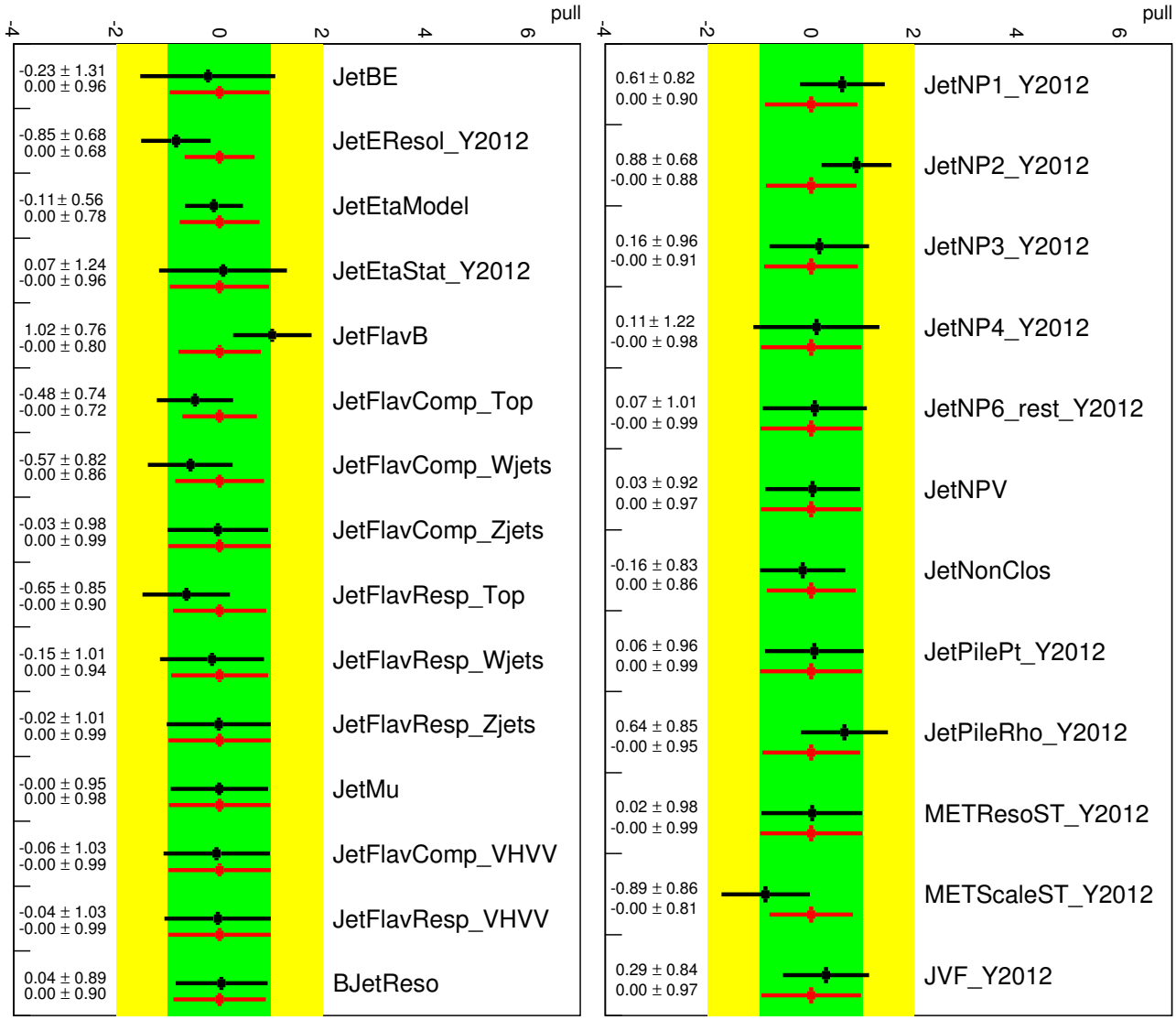

Figure 473: Pull plots for 1-lepton channel: Jet NPs.

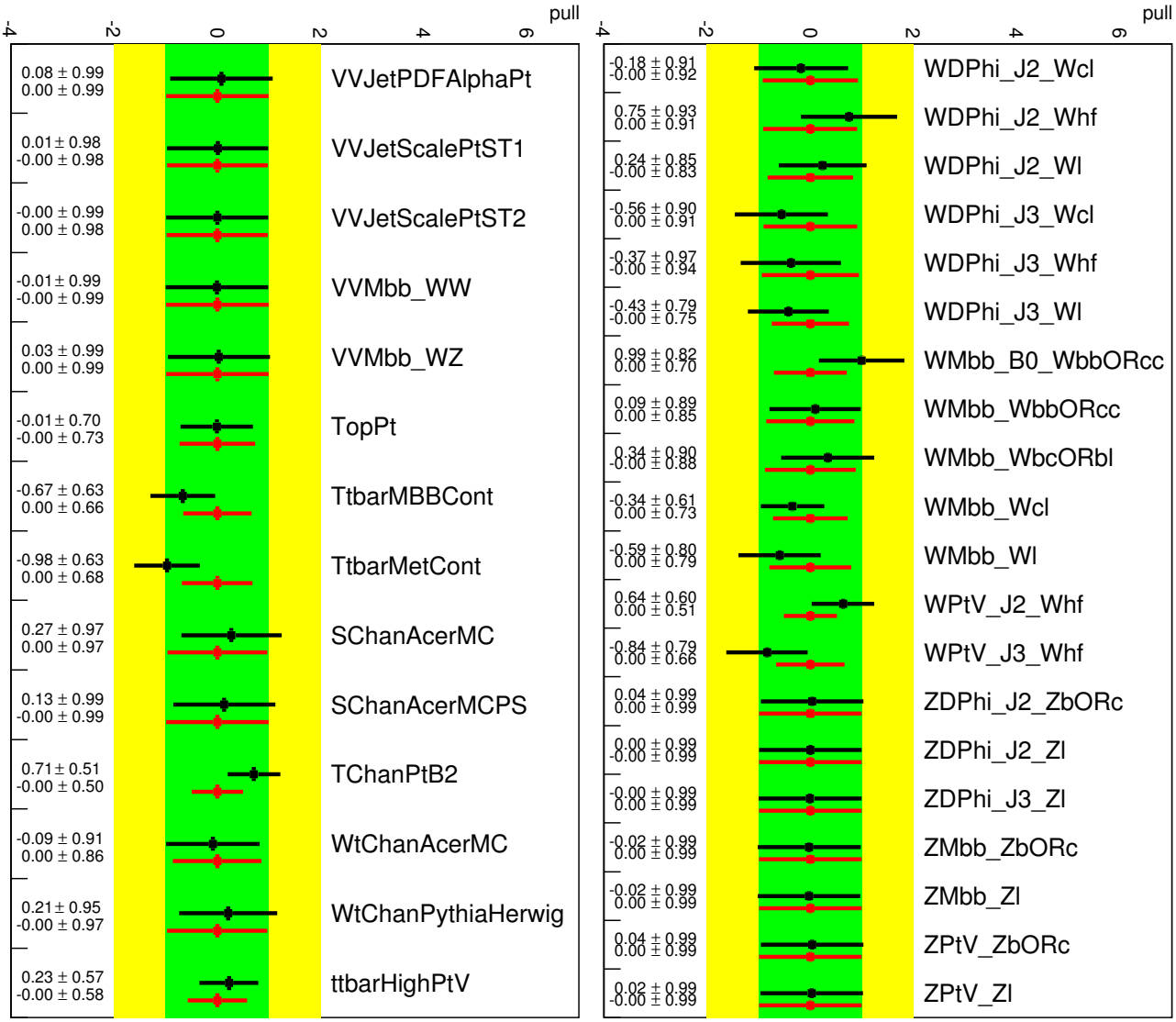

Figure 474: Pull plots for 1-lepton channel: Diboson/Top and W/Z related uncertainties.

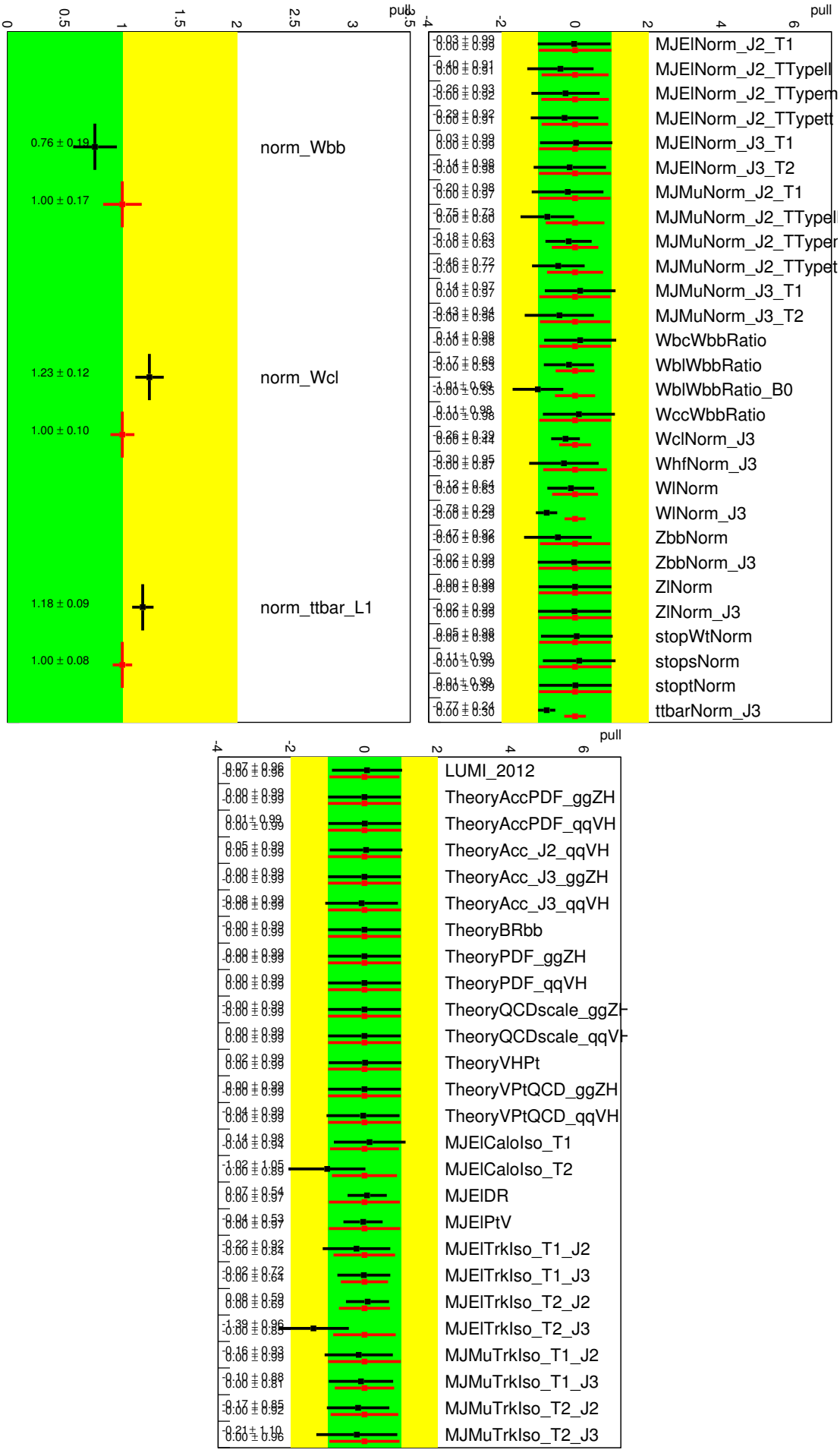

Figure 475: Pull plots for 1-lepton channel: Other model and normalization uncertainties.

AH.2.4 Pre-fit and Post-Fit for the MVA analysis in the 1-lepton fit

For the moment, the prefit plots are in the section.

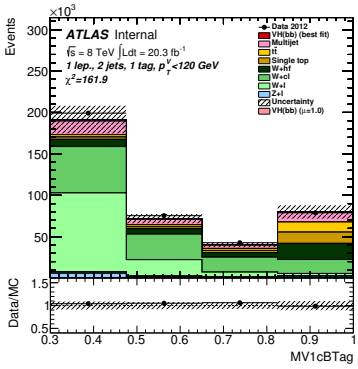

(a) $p_{\mathrm{T}}^{V} < 120$ GeV, 2 jets, 1-tag

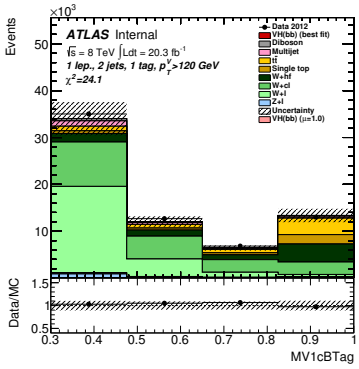

(b) $p_{\mathrm{T}}^{V} > 120$ GeV, 2 jets, 1-tag

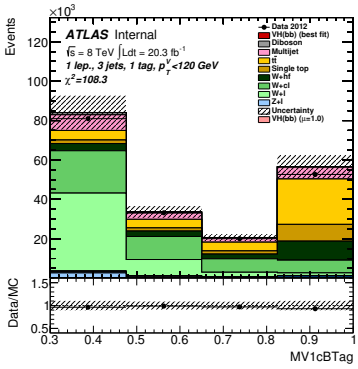

(c) $p_{\mathrm{T}}^{V} < 120$ GeV, 3 jets, 1-tag

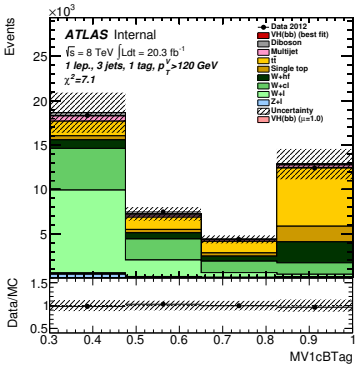

(d) $p_{\mathrm{T}}^{V} > 120$ GeV, 3 jets, 1-tag

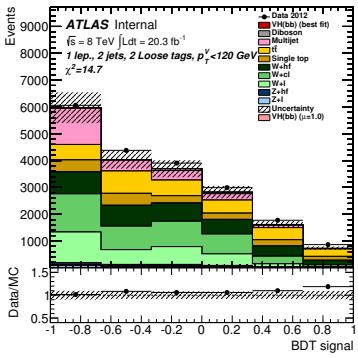

(e) $p_{\mathrm{T}}^{V} < 120$ GeV, 2 jets, LL

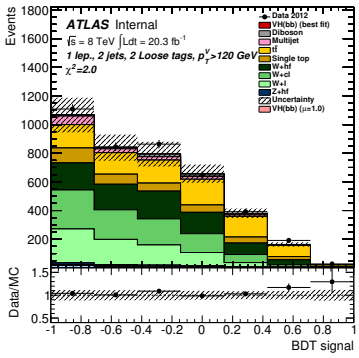

(f) $p_{\mathrm{T}}^{V} > 120$ GeV, 2 jets, LL

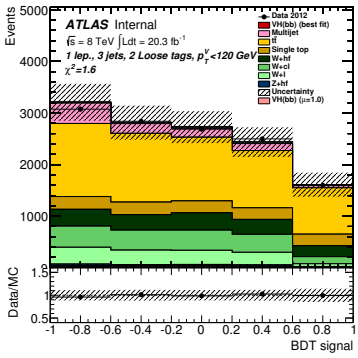

(g) $p_{\mathrm{T}}^{V} < 120$ GeV, 3 jets, LL

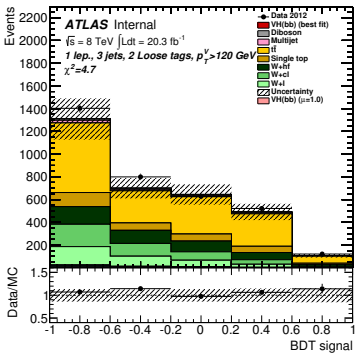

(h) $p_{\mathrm{T}}^{V} > 120$ GeV, 3 jets, LL

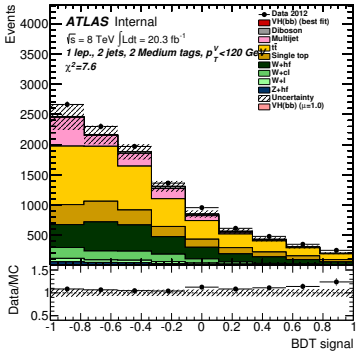

(i) $p_{\mathrm{T}}^{V} < 120$ GeV 2 jets, MM

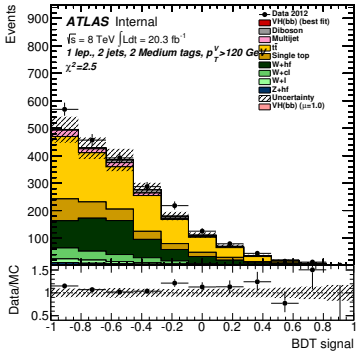

(j) $p_{\mathrm{T}}^{V} > 120$ GeV 2 jets, MM

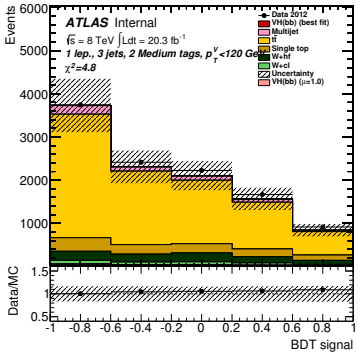

(k) $p_{\mathrm{T}}^{V} < 120$ GeV, 3 jets, MM

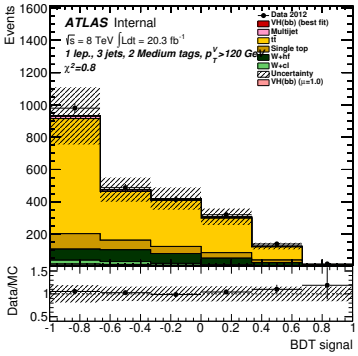

(l) $p_{\mathrm{T}}^{V} > 120$ GeV, 3 jets, MM

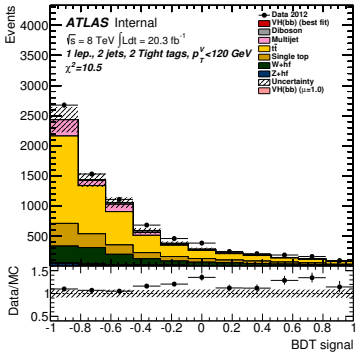

(m) $p_{\mathrm{T}}^{V} < 120$ GeV 2 jets, TT

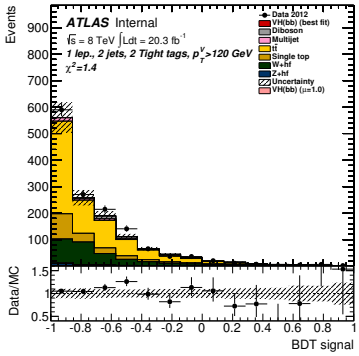

(n) $p_{\mathrm{T}}^{V} > 120$ GeV 2 jets, TT

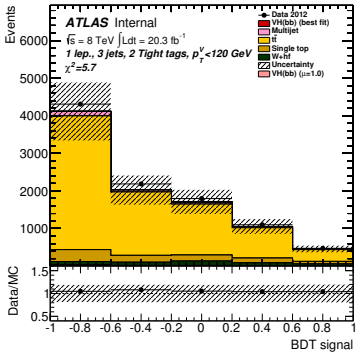

(o) $p_{\mathrm{T}}^{V} < 120$ GeV, 3 jets, TT

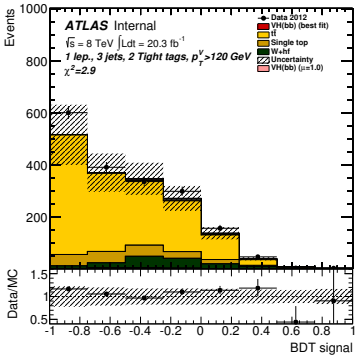

(p) $p_{\mathrm{T}}^{V} > 120$ GeV, 3 jets, TT

Figure 476: Pre-fit plots for MVA distribution in 1-lepton 2-jet and 3-jets , $p_{\mathrm{T}}^{V} < 120$ GeV (left) and $p_{\mathrm{T}}^{V} > 120$ GeV (right) events with 1 b-tag (MV1c is fit here), *LL*, *MM* and *TT* b-tags in the 1 lepton fit.

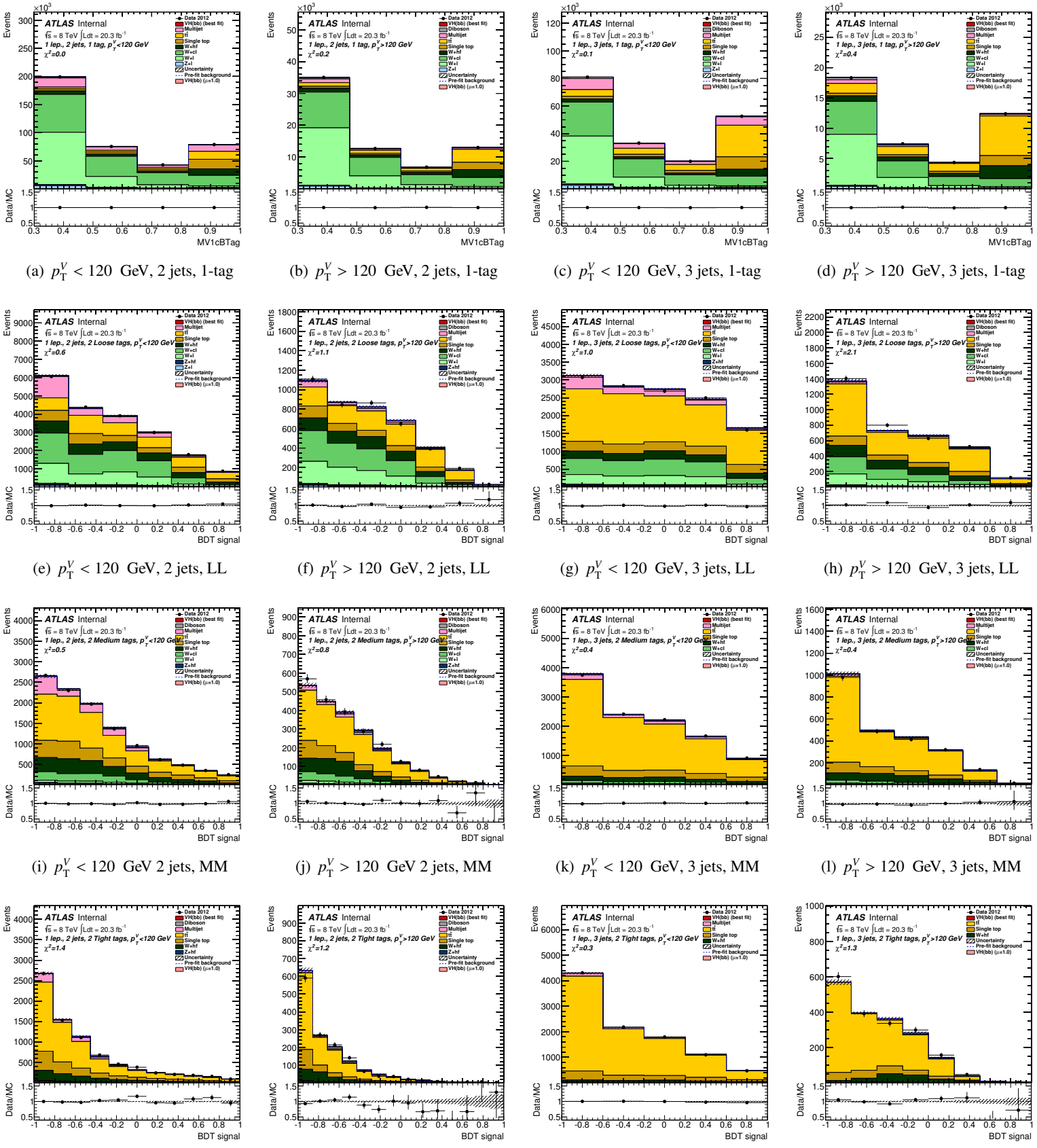

(a) $p_{\mathrm{T}}^{V} < 120$ GeV, 2 jets, 1-tag (b) $p_{\mathrm{T}}^{V} > 120$ GeV, 2 jets, 1-tag (c) $p_{\mathrm{T}}^{V} < 120$ GeV, 3 jets, 1-tag (d) $p_{\mathrm{T}}^{V} > 120$ GeV, 3 jets, 1-tag

(e) $p_{\mathrm{T}}^{V} < 120$ GeV, 2 jets, LL (f) $p_{\mathrm{T}}^{V} > 120$ GeV, 2 jets, LL (g) $p_{\mathrm{T}}^{V} < 120$ GeV, 3 jets, LL (h) $p_{\mathrm{T}}^{V} > 120$ GeV, 3 jets, LL

(i) $p_{\mathrm{T}}^{V} < 120$ GeV 2 jets, MM (j) $p_{\mathrm{T}}^{V} > 120$ GeV 2 jets, MM (k) $p_{\mathrm{T}}^{V} < 120$ GeV, 3 jets, MM (l) $p_{\mathrm{T}}^{V} > 120$ GeV, 3 jets, MM

(m) $p_{\mathrm{T}}^{V} < 120$ GeV 2 jets, TT (n) $p_{\mathrm{T}}^{V} > 120$ GeV 2 jets, TT (o) $p_{\mathrm{T}}^{V} < 120$ GeV, 3 jets, TT (p) $p_{\mathrm{T}}^{V} > 120$ GeV, 3 jets, TT

Figure 477: Post-fit plots for MVA distribution in 1-lepton 2-jet and 3-jets , $p_{\mathrm{T}}^{V} < 120$ GeV (left) and $p_{\mathrm{T}}^{V} > 120$ GeV (right) events with 1 b-tag (MV1c is fit here), *LL*, *MM* and *TT* b-tags in the 1 lepton fit.

AH.2.5 2-lepton pull plots

The pull plots for 2-lepton are shown in Figure. 478-482.

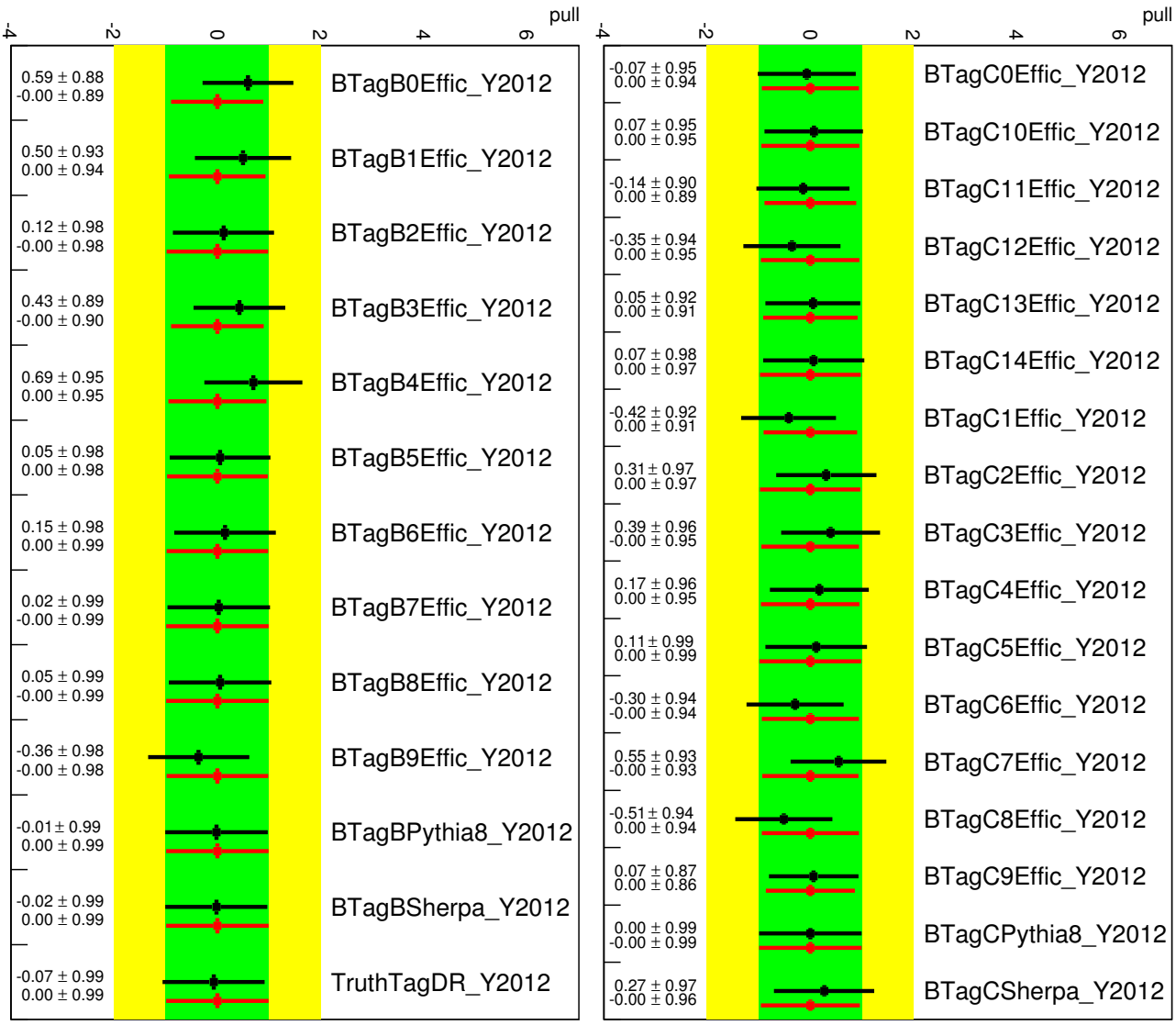

Figure 478: Pull plots for 2-lepton channel: *b*- and *c*-jet tagging.

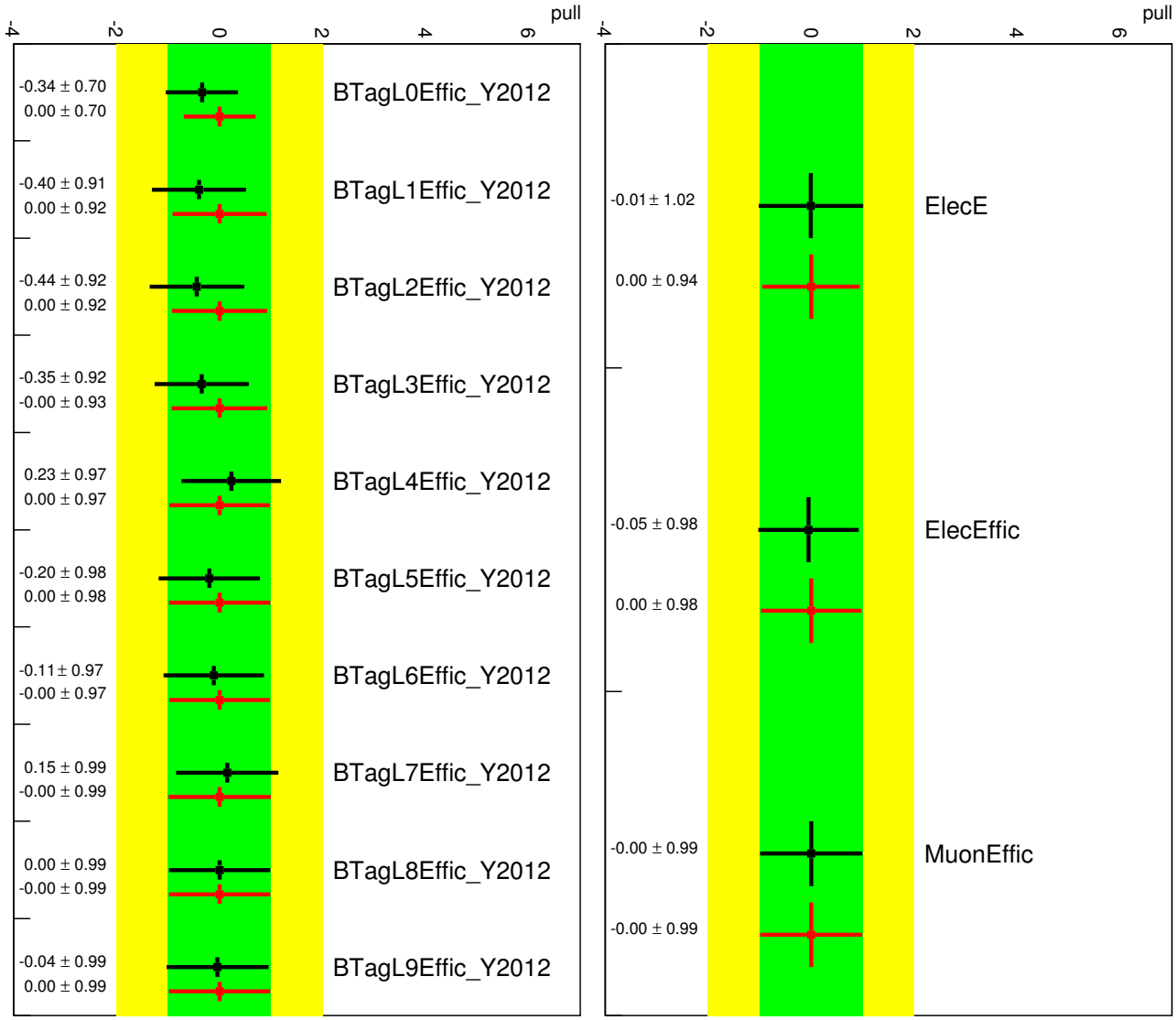

Figure 479: Pull plots for 2-lepton channel: light-jet tagging and leptons.

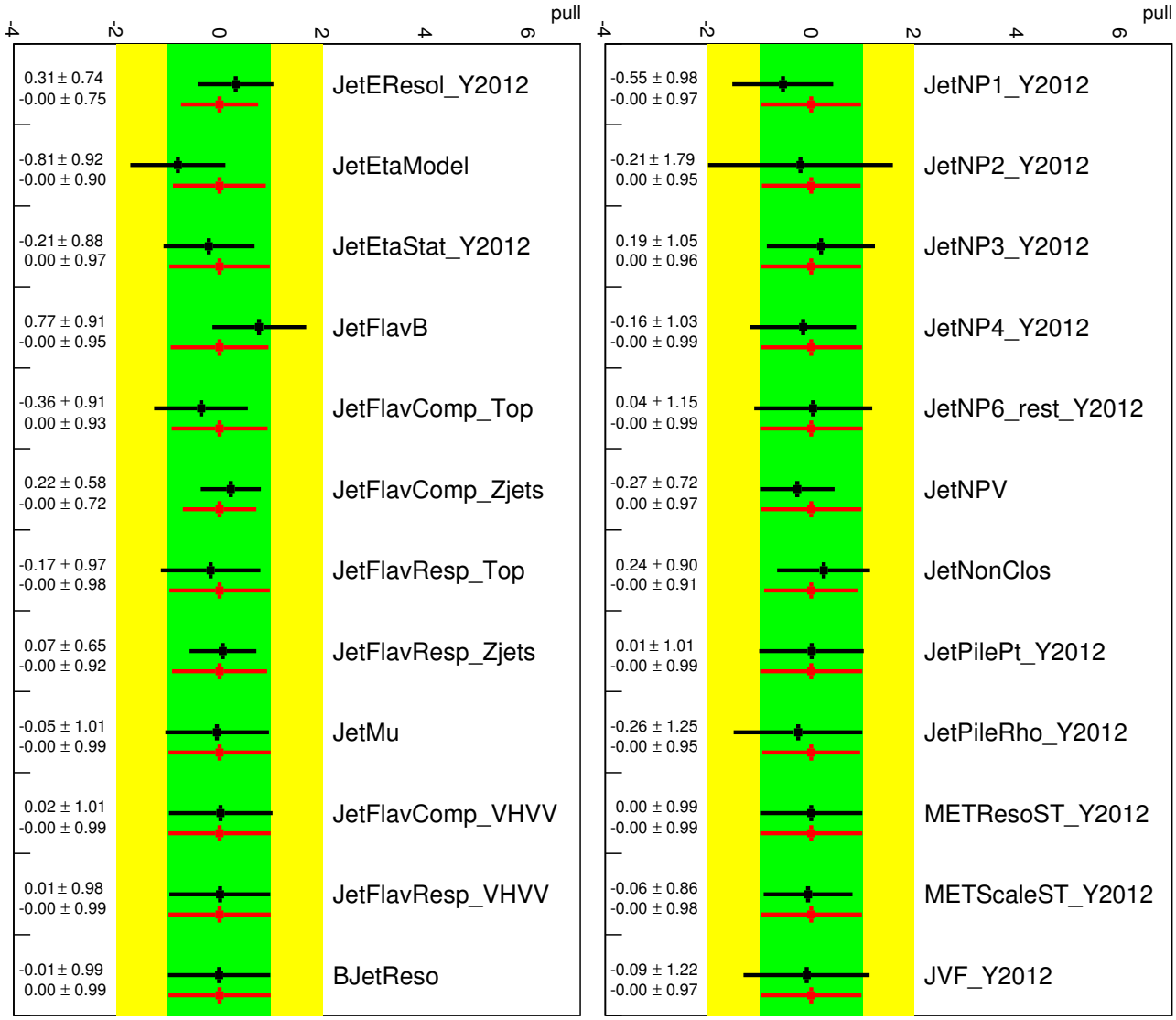

Figure 480: Pull plots for 2-lepton channel: Jet NPs.

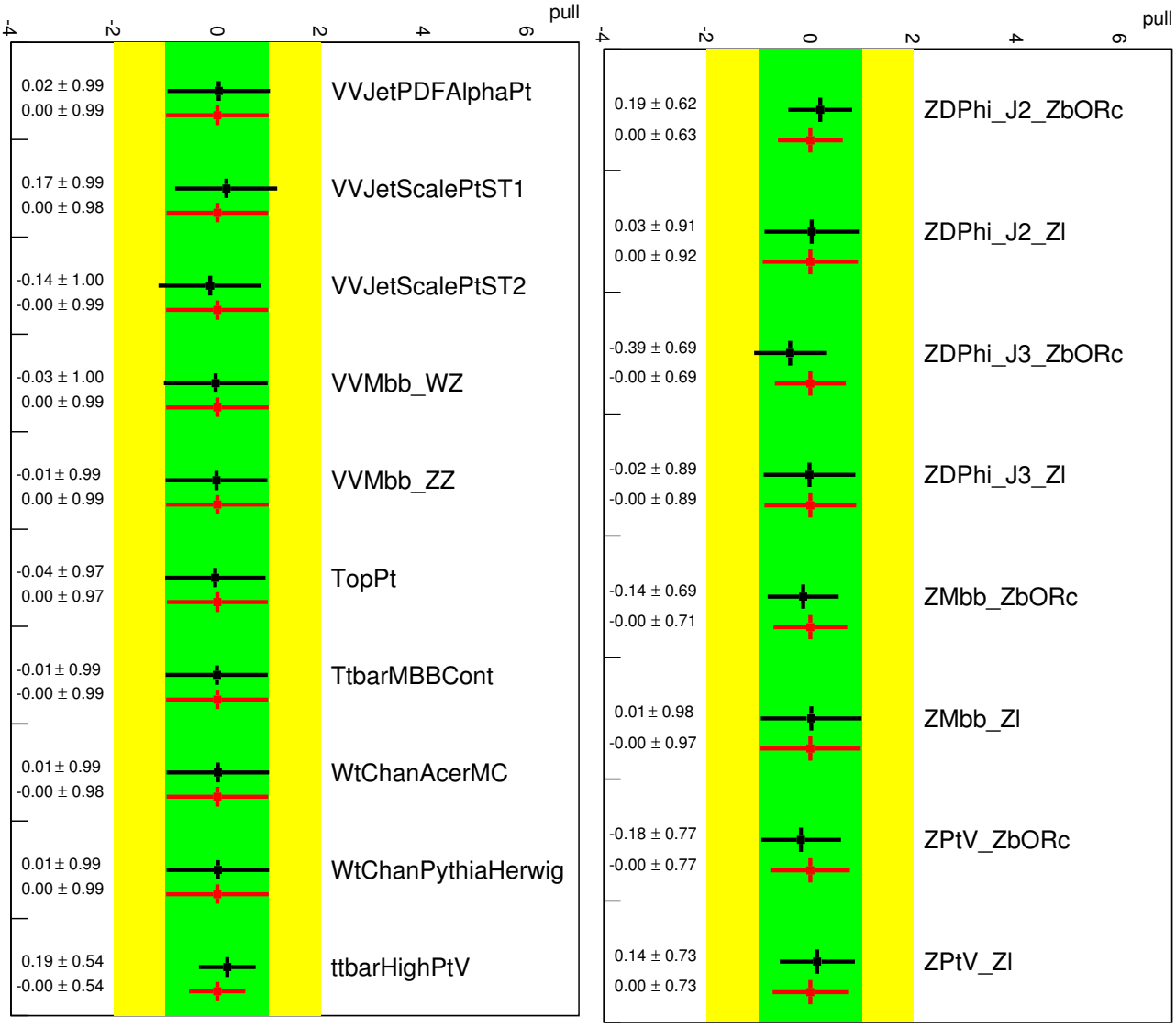

Figure 481: Pull plots for 2-lepton channel: Diboson/Top and W/Z related uncertainties.

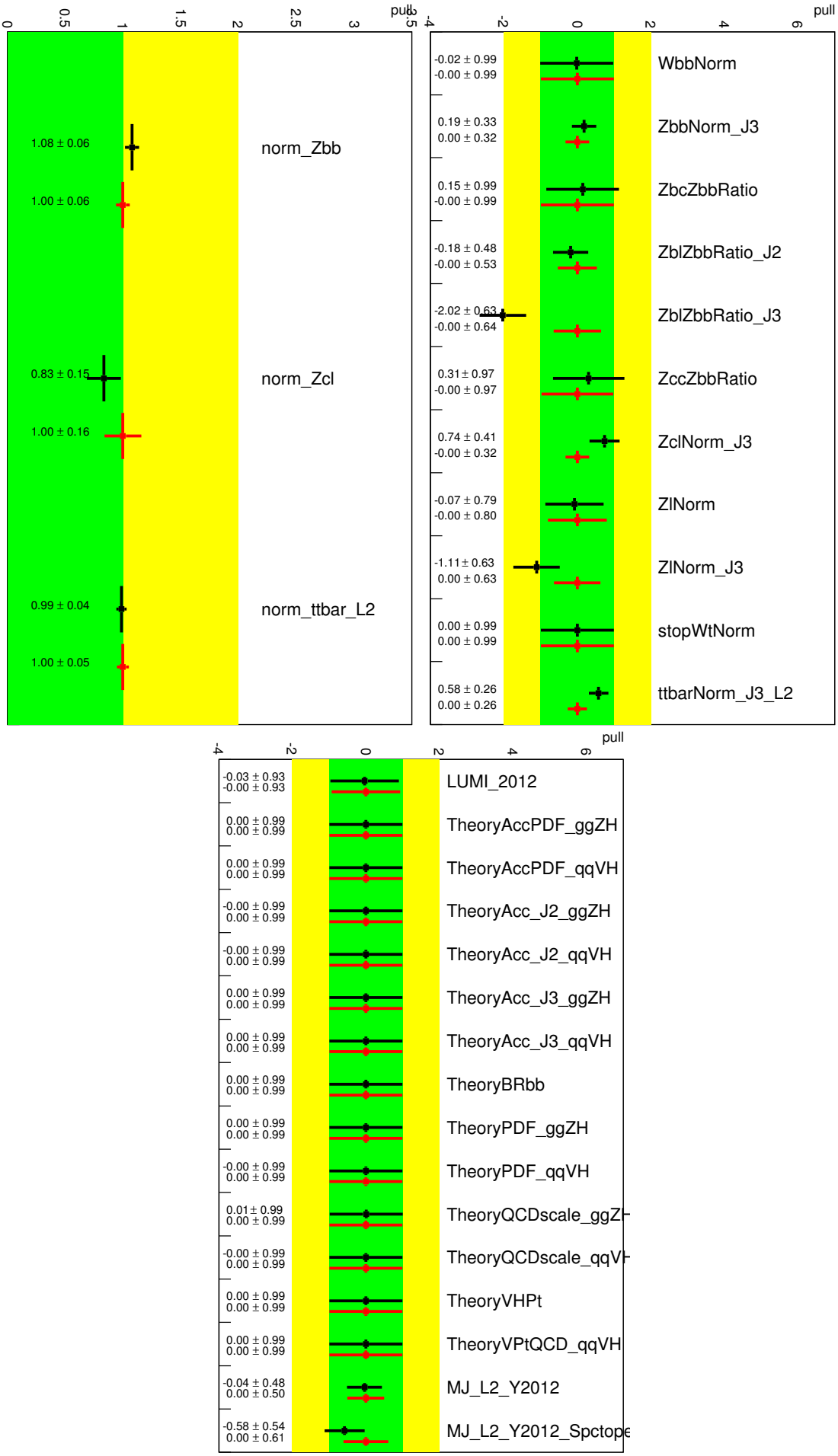

Figure 482: Pull plots for 2-lepton channel: Other model and normalization uncertainties.

AH.2.6 Pre-fit and Post-Fit for the MVA analysis in the 2-lepton fit

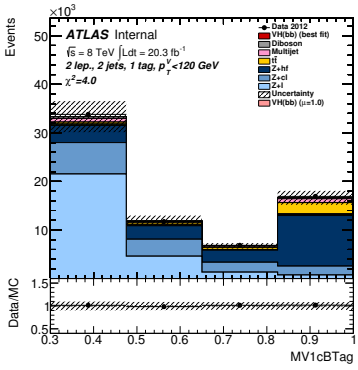

(a) $p_{\mathrm{T}}^{V} < 120$ GeV, 2 jets, 1-tag

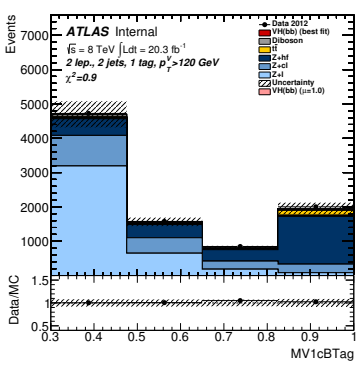

(b) $p_{\mathrm{T}}^{V} > 120$ GeV, 2 jets, 1-tag

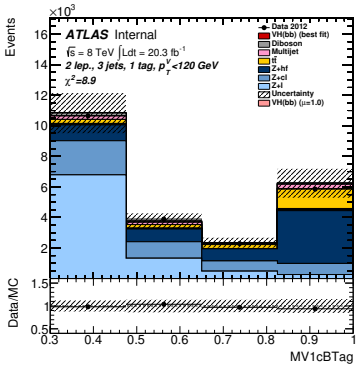

(c) $p_{\mathrm{T}}^{V} < 120$ GeV, 3 jets, 1-tag

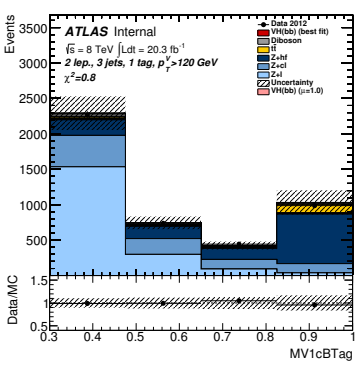

(d) $p_{\mathrm{T}}^{V} > 120$ GeV, 3 jets, 1-tag

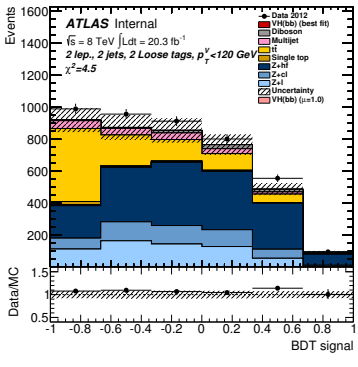

(e) $p_{\mathrm{T}}^{V} < 120$ GeV, 2 jets, LL

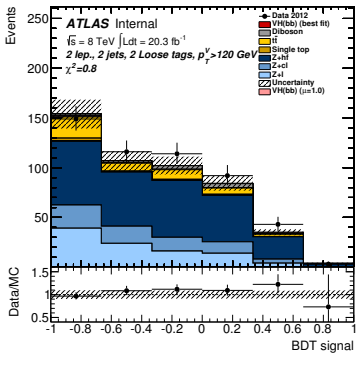

(f) $p_{\mathrm{T}}^{V} > 120$ GeV, 2 jets, LL

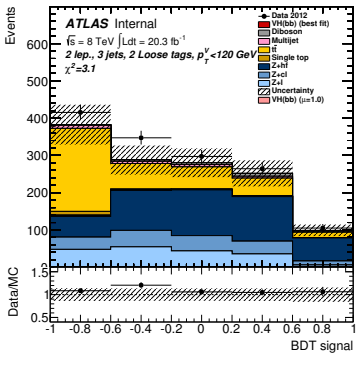

(g) $p_{\mathrm{T}}^{V} < 120$ GeV, 3 jets, LL

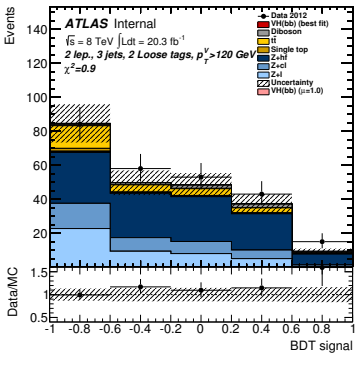

(h) $p_{\mathrm{T}}^{V} > 120$ GeV, 3 jets, LL

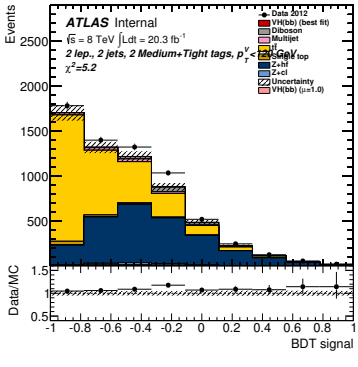

(i) $p_{\mathrm{T}}^{V} < 120$ GeV 2 jets, MM+TT

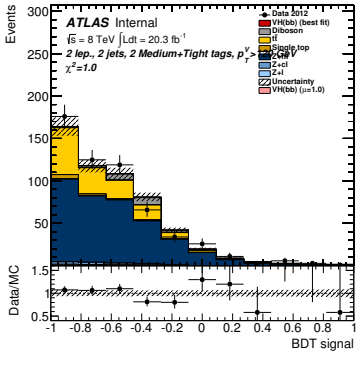

(j) $p_{\mathrm{T}}^{V} > 120$ GeV 2 jets, MM+TT

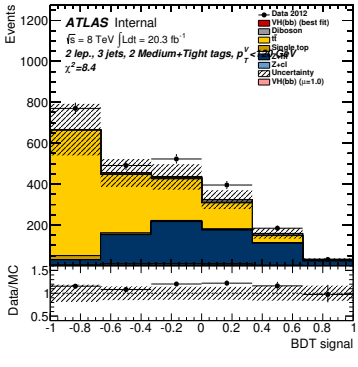

(k) $p_{\mathrm{T}}^{V} < 120$ GeV, 3 jets, MM+TT

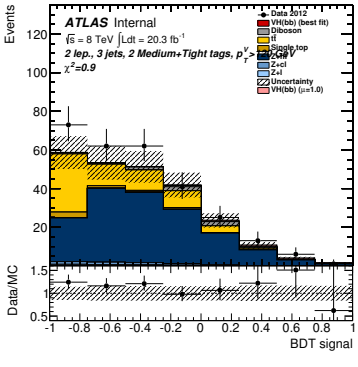

(l) $p_{\mathrm{T}}^{V} > 120$ GeV, 3 jets, MM+TT

Figure 483: Pre-fit plots for MVA distribution in 2-lepton 2-jet and 3-jets , $p_{\mathrm{T}}^{V} < 120$ GeV (left) and $p_{\mathrm{T}}^{V} > 120$ GeV (right) events with 1 b-tag (MV1c is fit here), LL and $MM+TT$ b-tags in the 2 lepton fit.

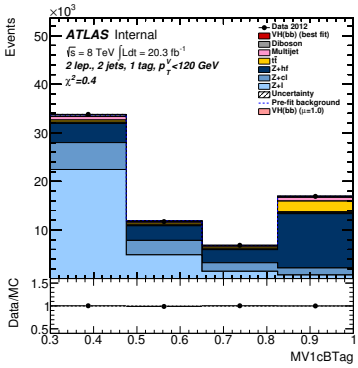

(a) $p_{\mathrm{T}}^{V} < 120$ GeV, 2 jets, 1-tag

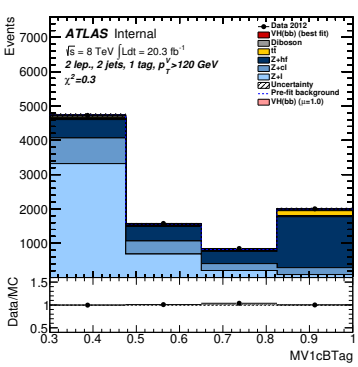

(b) $p_{\mathrm{T}}^{V} > 120$ GeV, 2 jets, 1-tag

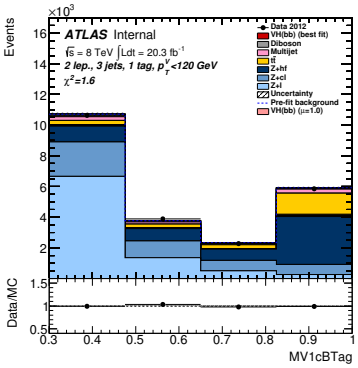

(c) $p_{\mathrm{T}}^{V} < 120$ GeV, 3 jets, 1-tag

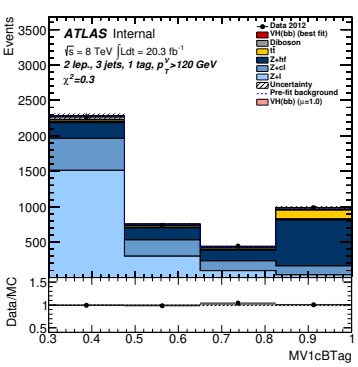

(d) $p_{\mathrm{T}}^{V} > 120$ GeV, 3 jets, 1-tag

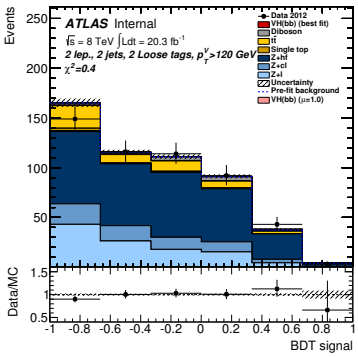

(f) $p_{\mathrm{T}}^{V} > 120$ GeV, 2 jets, LL

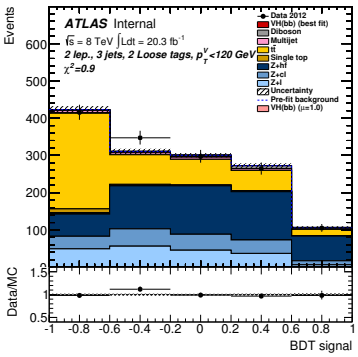

(g) $p_{\mathrm{T}}^{V} < 120$ GeV, 3 jets, LL

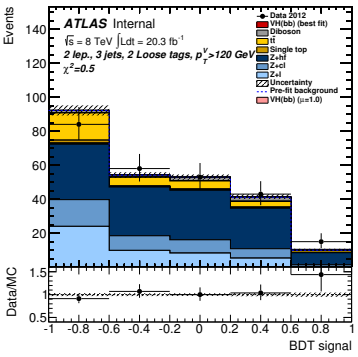

(h) $p_{\mathrm{T}}^{V} > 120$ GeV, 3 jets, LL

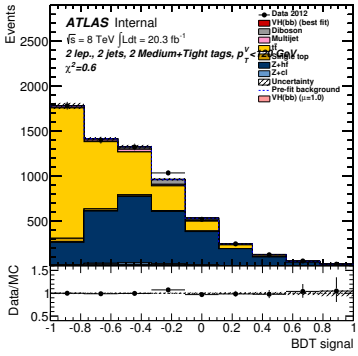

(i) $p_{\mathrm{T}}^{V} < 120$ GeV 2 jets, MM+TT

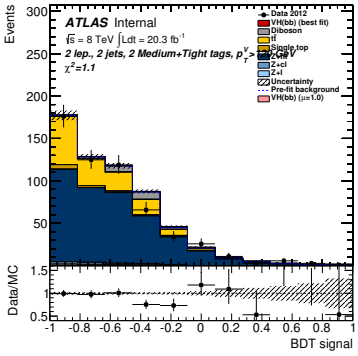

(j) $p_{\mathrm{T}}^{V} > 120$ GeV 2 jets, MM+TT

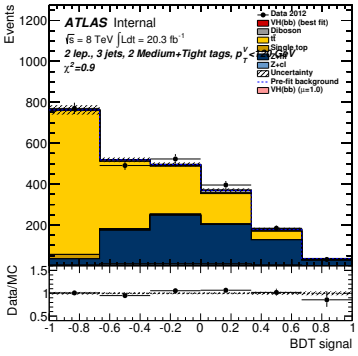

(k) $p_{\mathrm{T}}^{V} < 120$ GeV, 3 jets, MM+TT

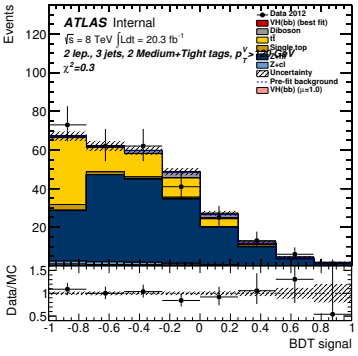

(l) $p_{\mathrm{T}}^{V} > 120$ GeV, 3 jets, MM+TT

Figure 484: Post-fit plots for MVA distribution in 2-lepton 2-jet and 3-jets , $p_{\mathrm{T}}^{V} < 120$ GeV (left) and $p_{\mathrm{T}}^{V} > 120$ GeV (right) events with 1 b-tag (MV1c is fit here), LL and $MM + TT$ b-tags in the 2 lepton fit. The pre-fit background expectation is indicated by the dashed blue line.

AH.3 Dijet Mass versus MVA

?? The following shows a comparison of the dijet mass pulls (red) to the MVA pulls (black) in each channel.

AH.3.1 0-lepton pull plots

The pull plot comparison for 0-lepton are shown in Figure. 485-489.

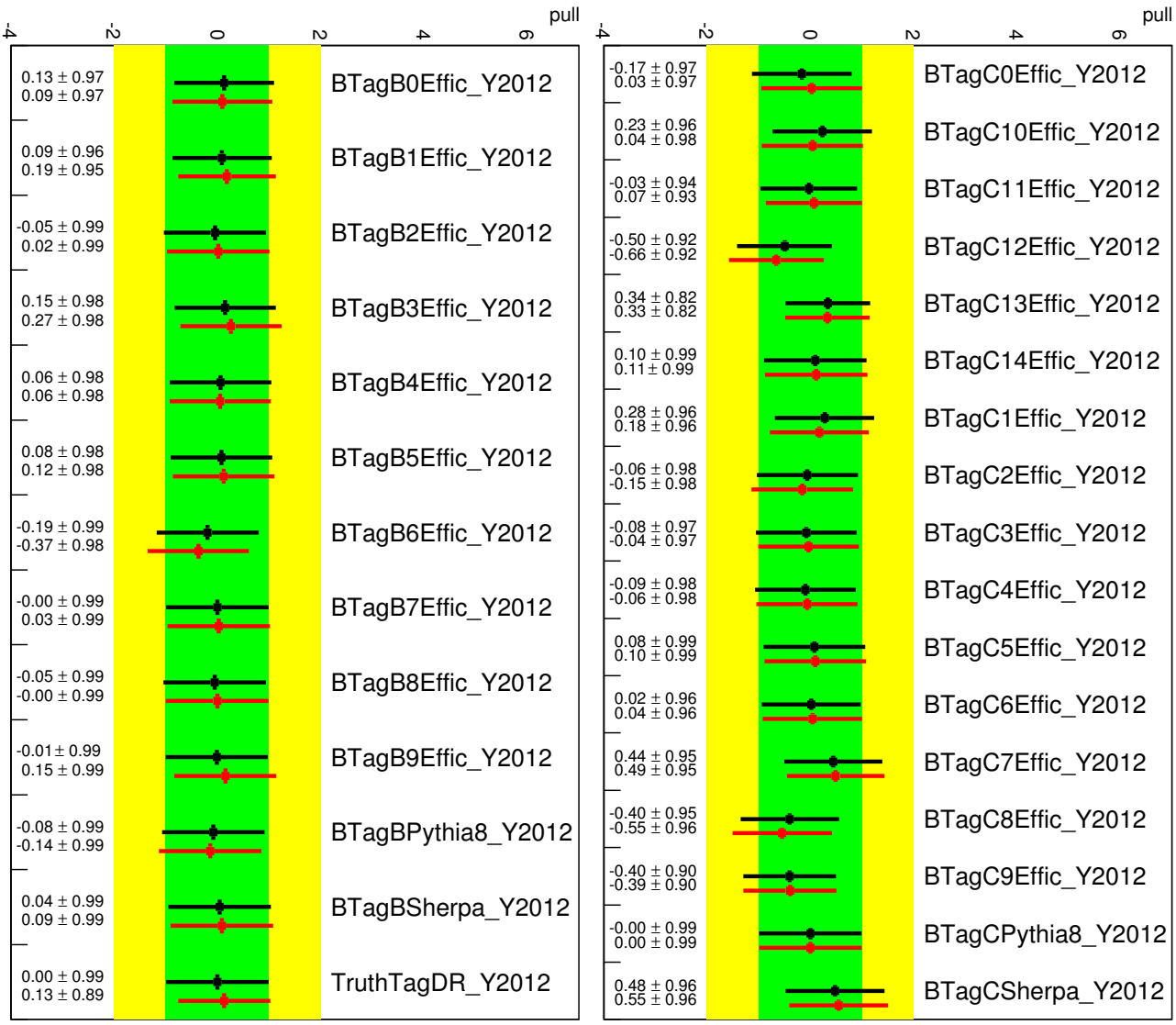

Figure 485: Pull plots for 0-lepton channel: *b*- and *c*-jet tagging.

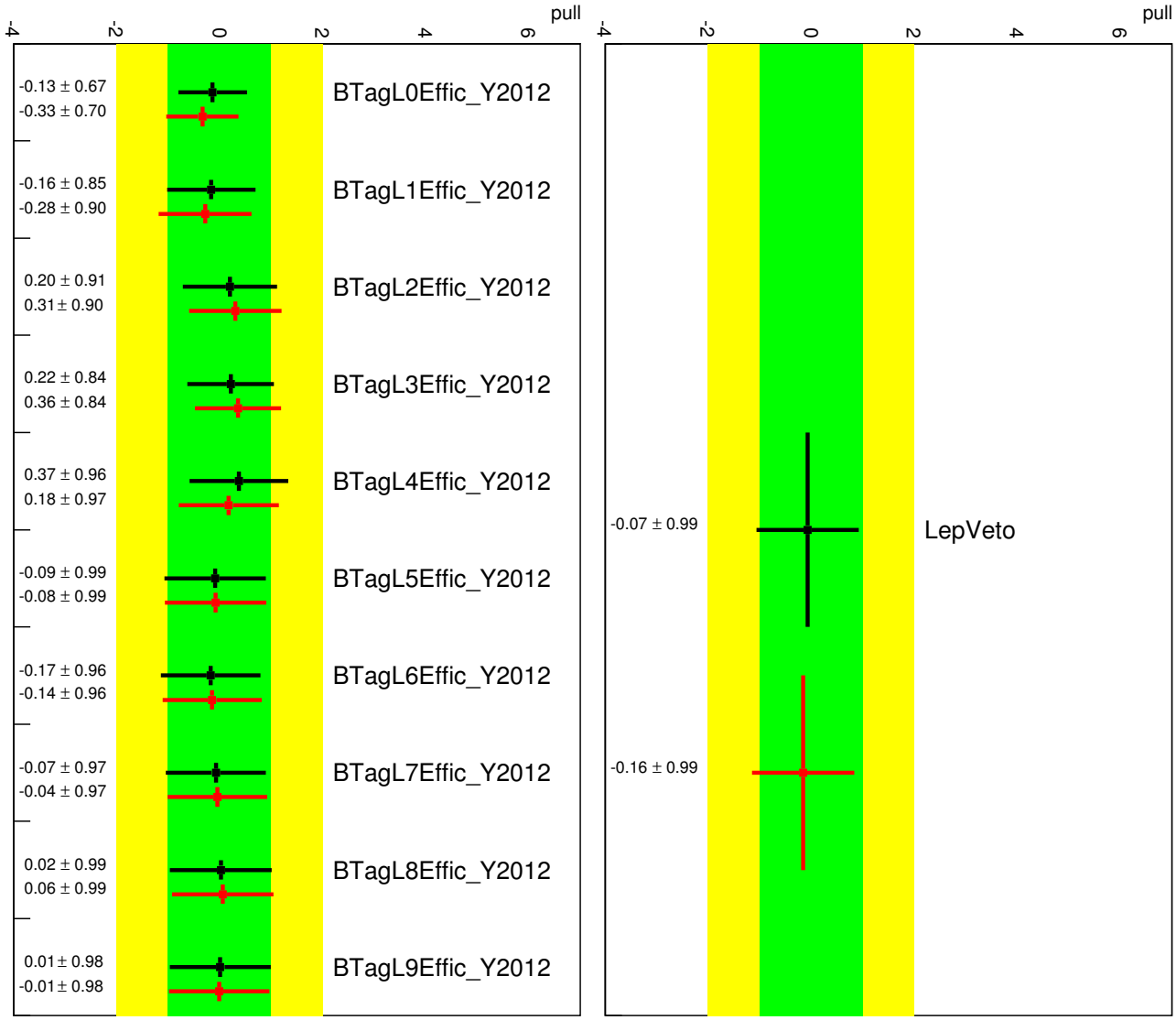

Figure 486: Pull plots for 0-lepton channel: light-jet tagging and leptons.

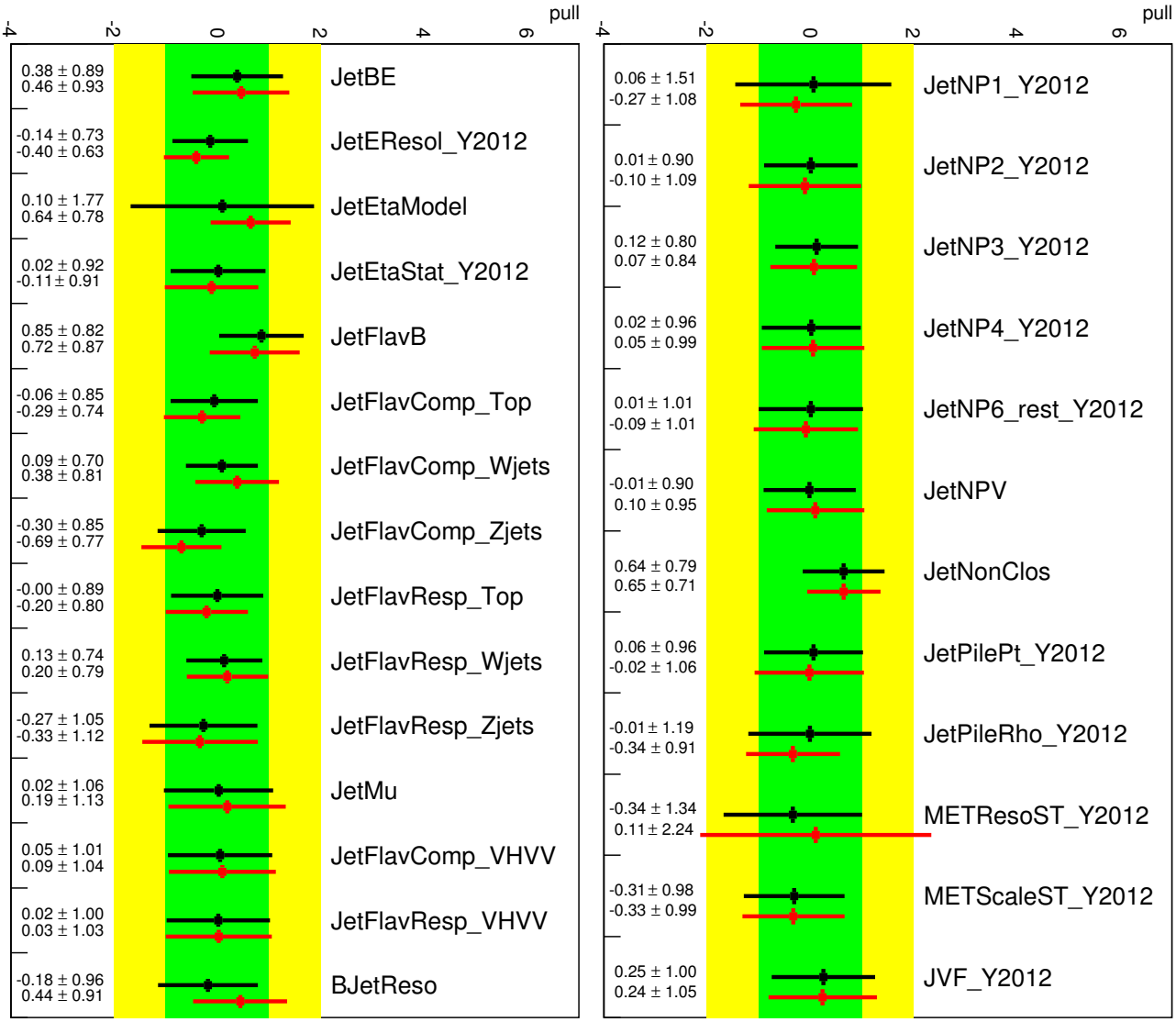

Figure 487: Pull plots for 0-lepton channel: Jet NPs.

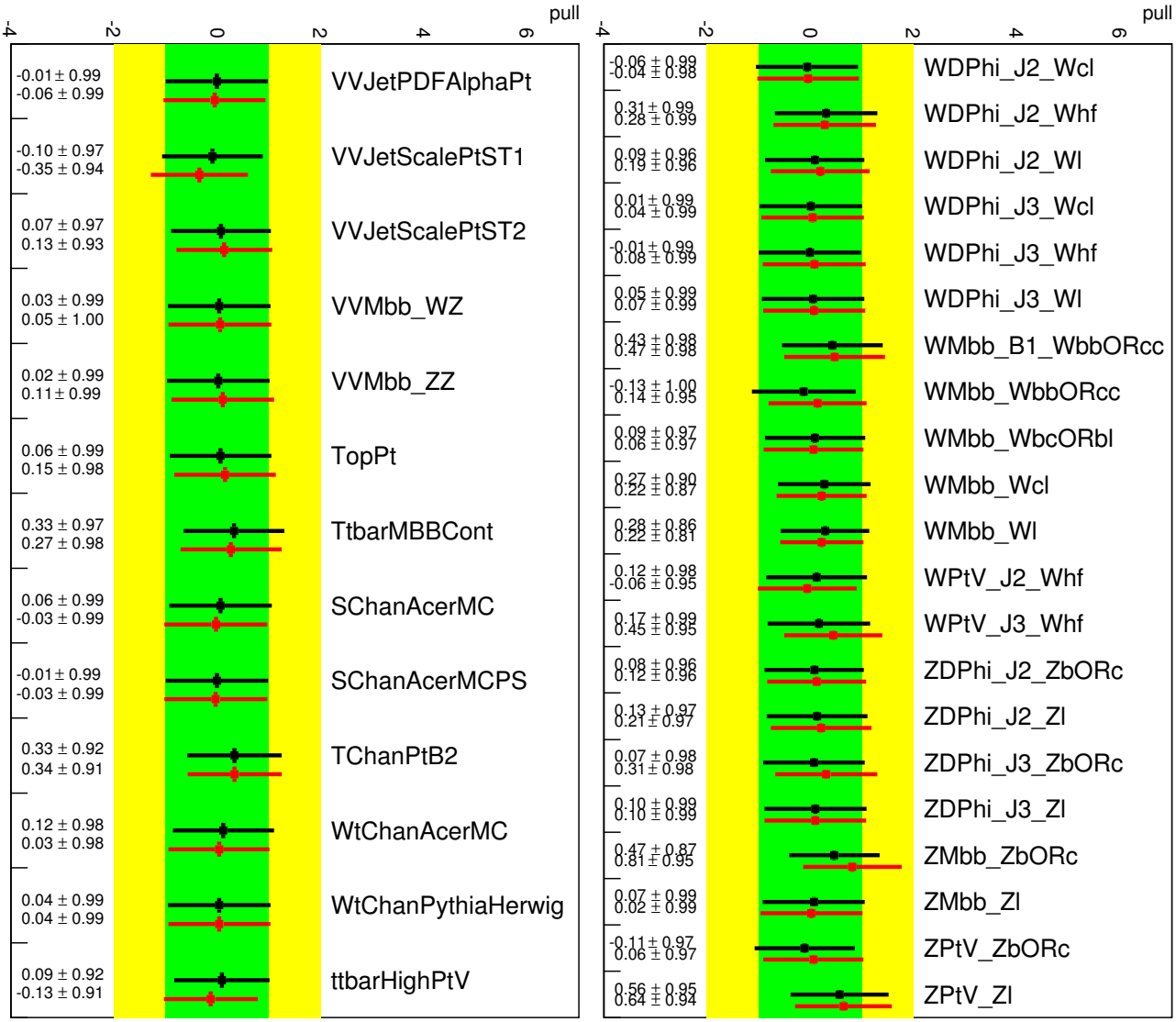

Figure 488: Pull plots for 0-lepton channel: Diboson/Top and W/Z related uncertainties.

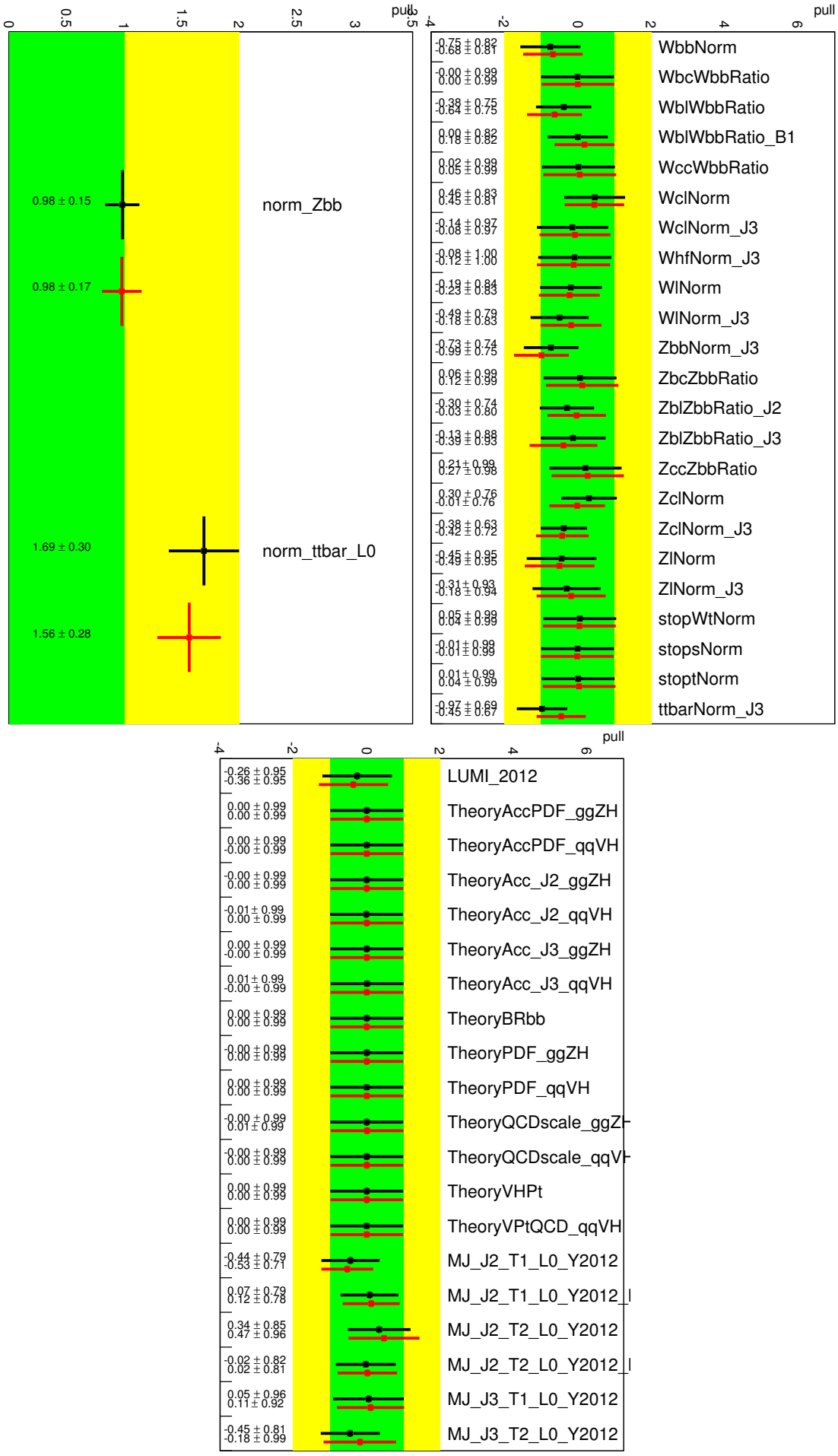

Figure 489: Pull plots for 0-lepton channel: Other model and normalization uncertainties.

AH.3.2 1-lepton pull plots

The pull plots for 1-lepton are shown in Figure. 490-494.

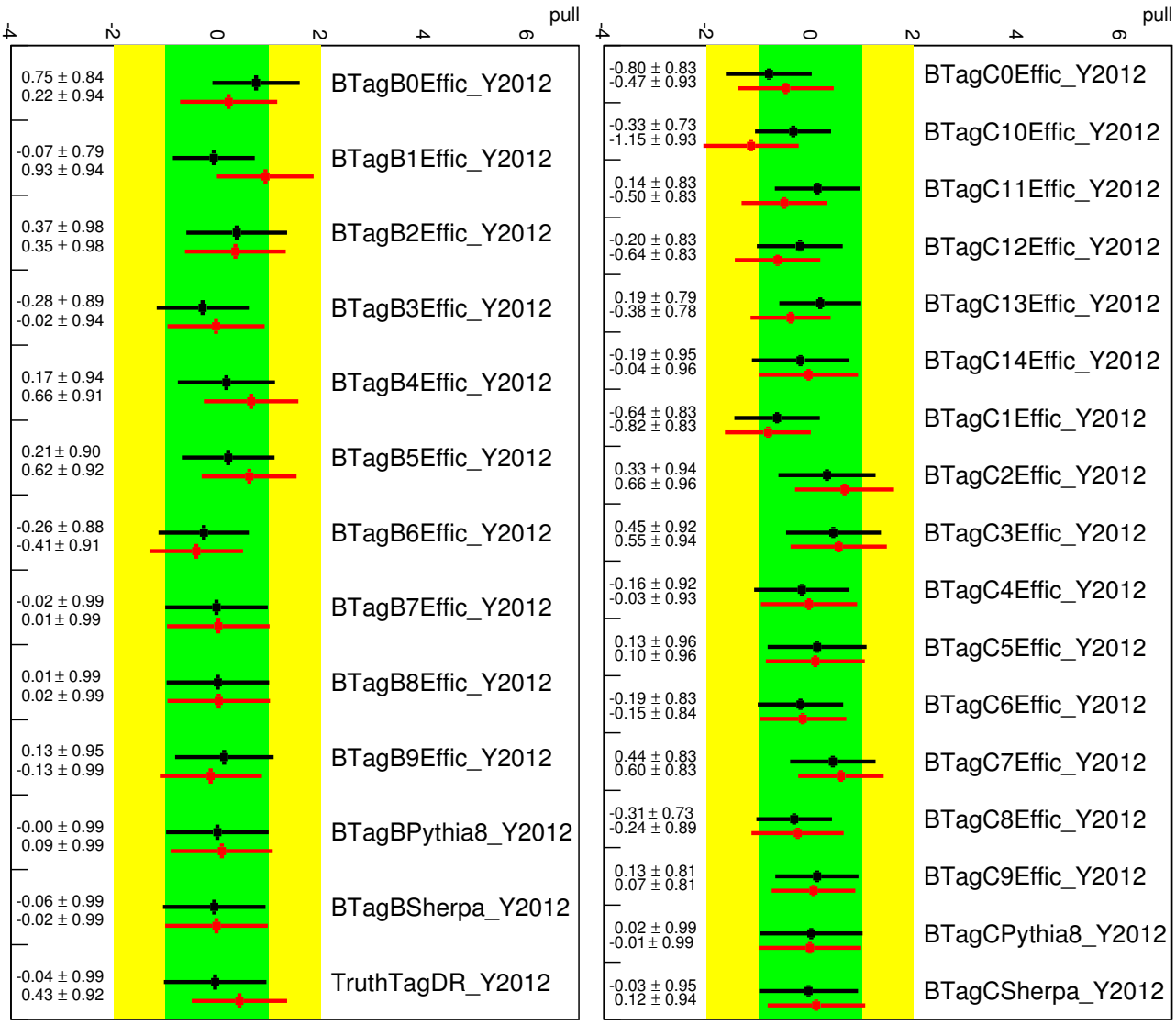

Figure 490: Pull plots for 1-lepton channel: *b*- and *c*-jet tagging.

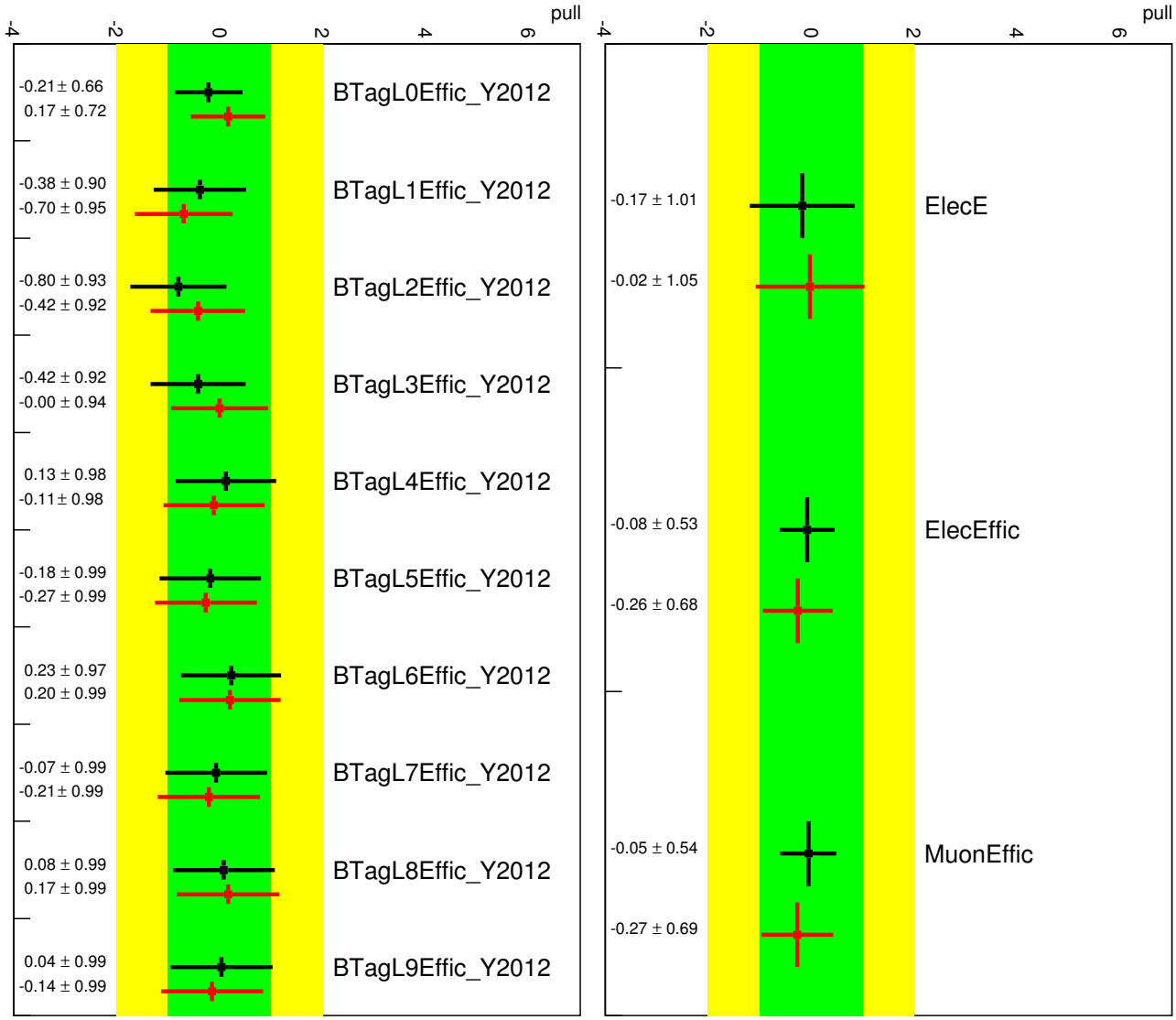

Figure 491: Pull plots for 1-lepton channel: light-jet tagging and leptons.

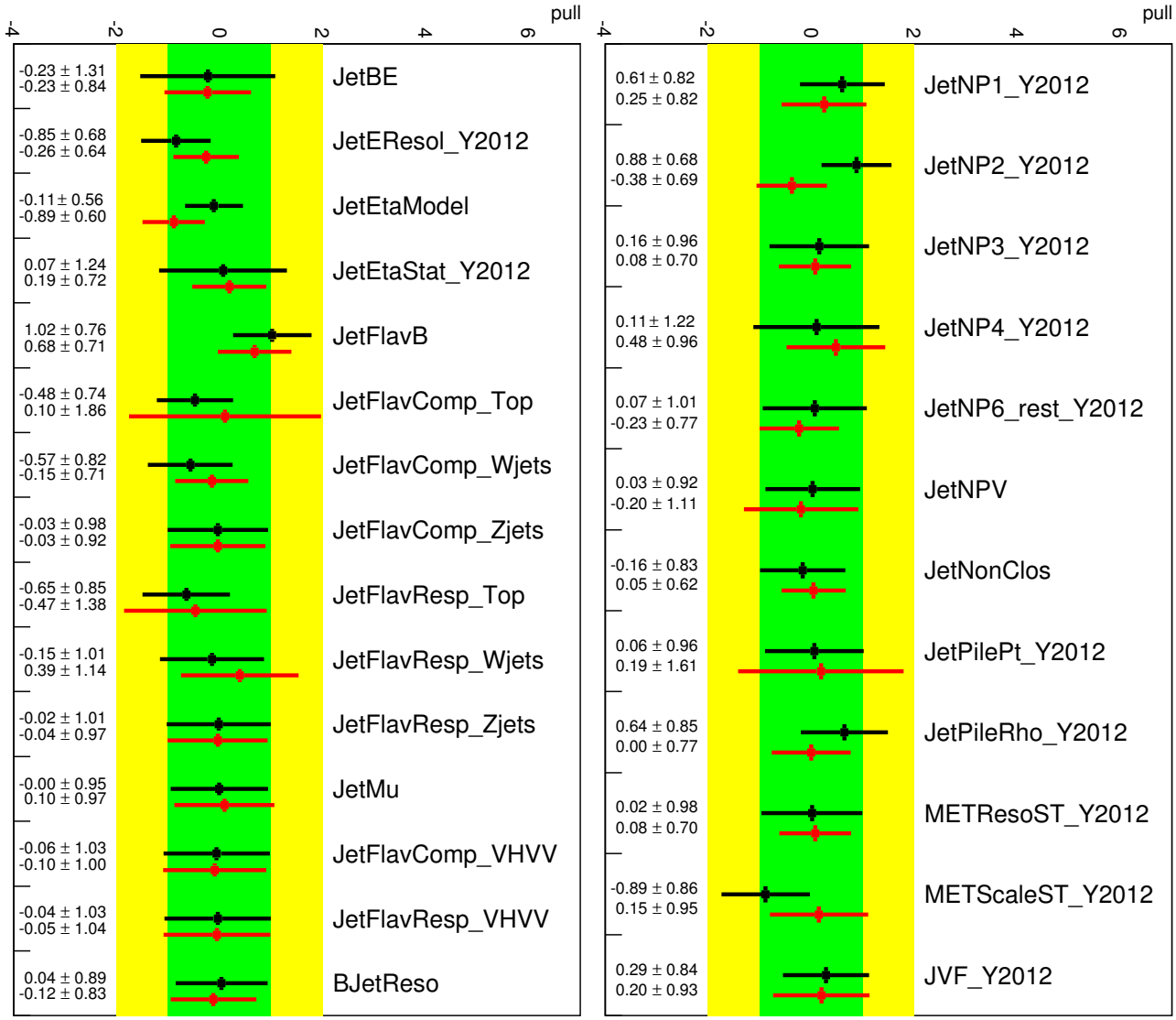

Figure 492: Pull plots for 1-lepton channel: Jet NPs.

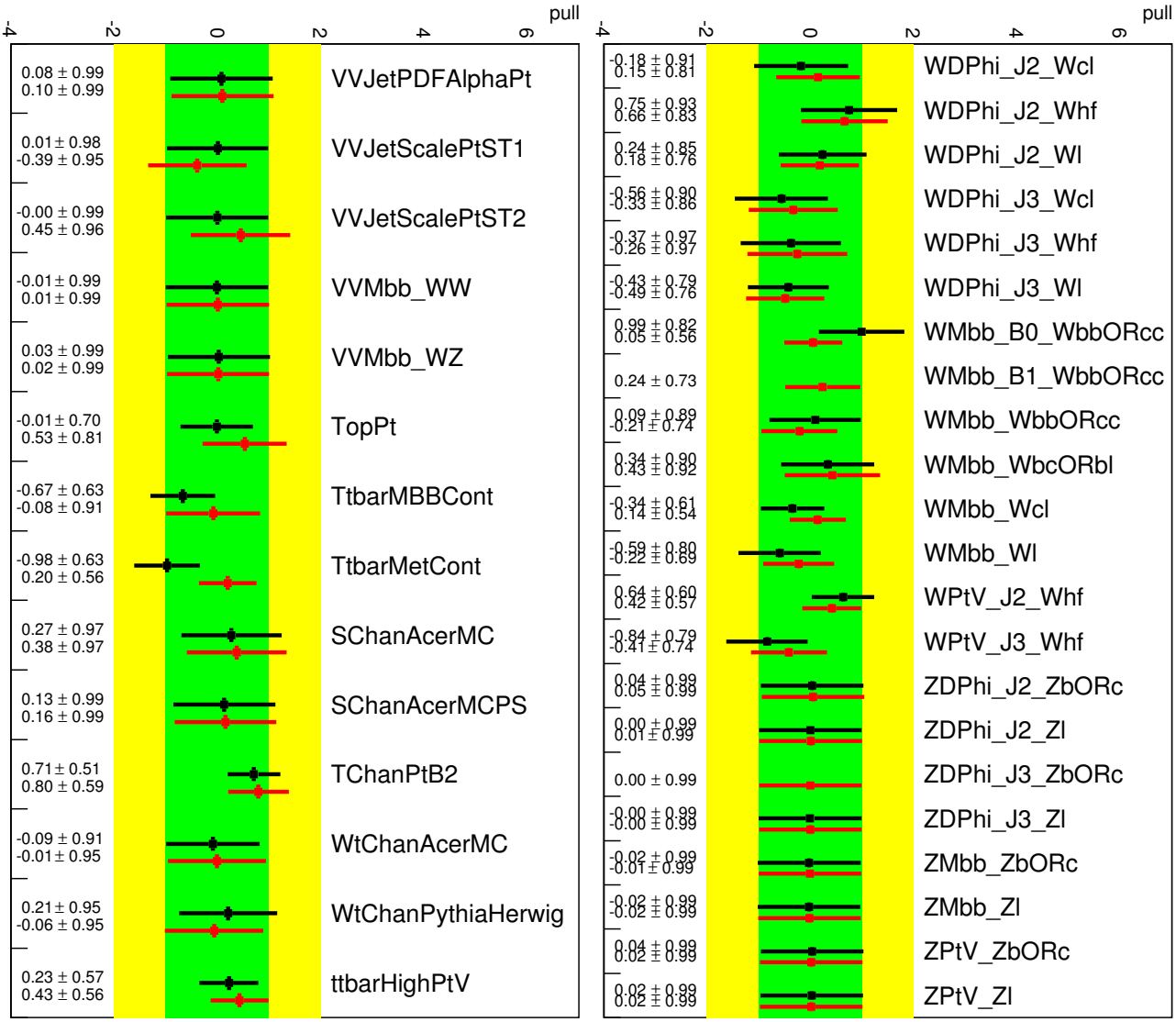

Figure 493: Pull plots for 1-lepton channel: Diboson/Top and W/Z related uncertainties.

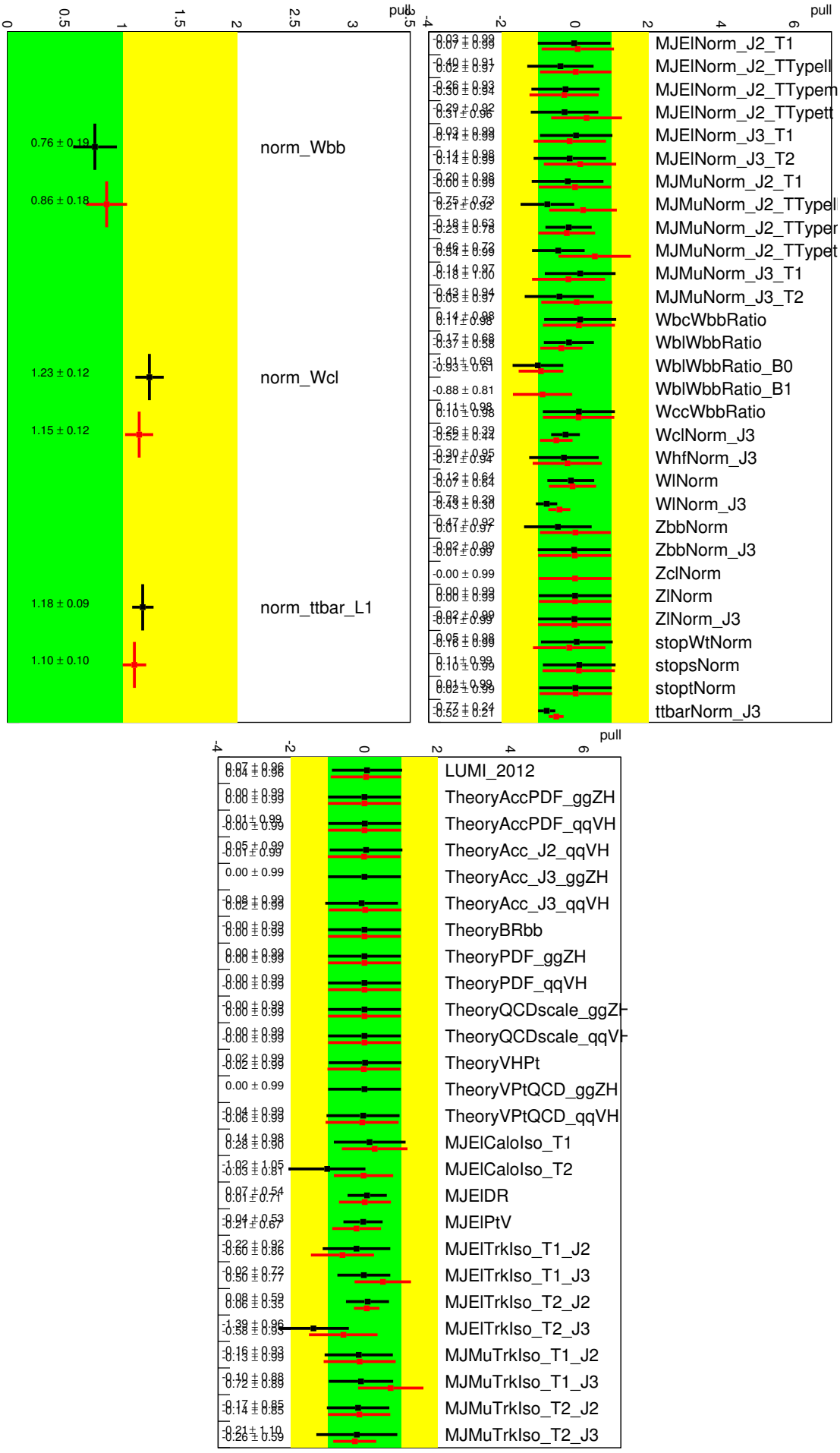

Figure 494: Pull plots for 1-lepton channel: Other model and normalization uncertainties.

AH.3.3 2-lepton pull plots

The pull plots for 2-lepton are shown in Figure. 495-499.

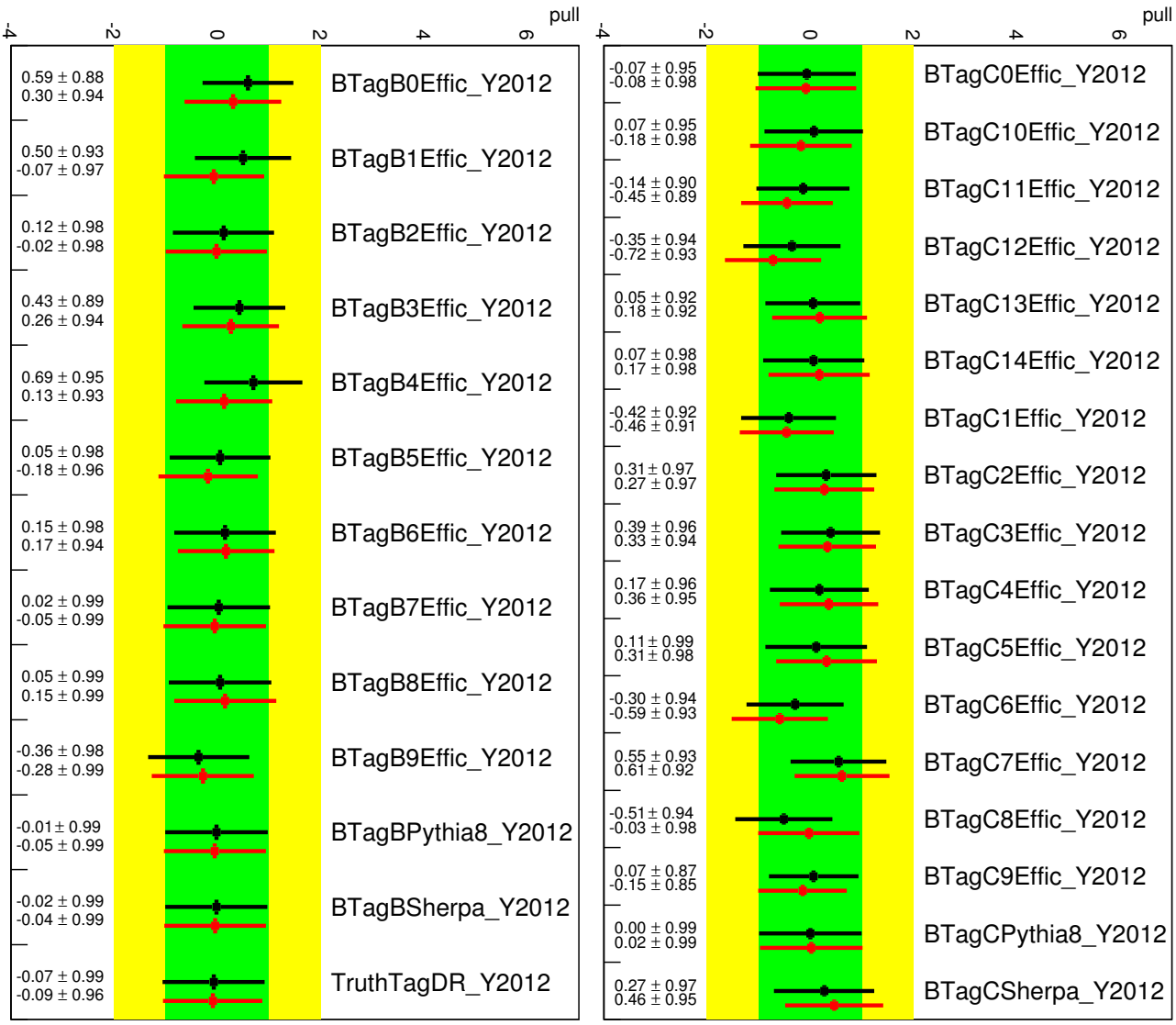

Figure 495: Pull plots for 2-lepton channel: *b*- and *c*-jet tagging.

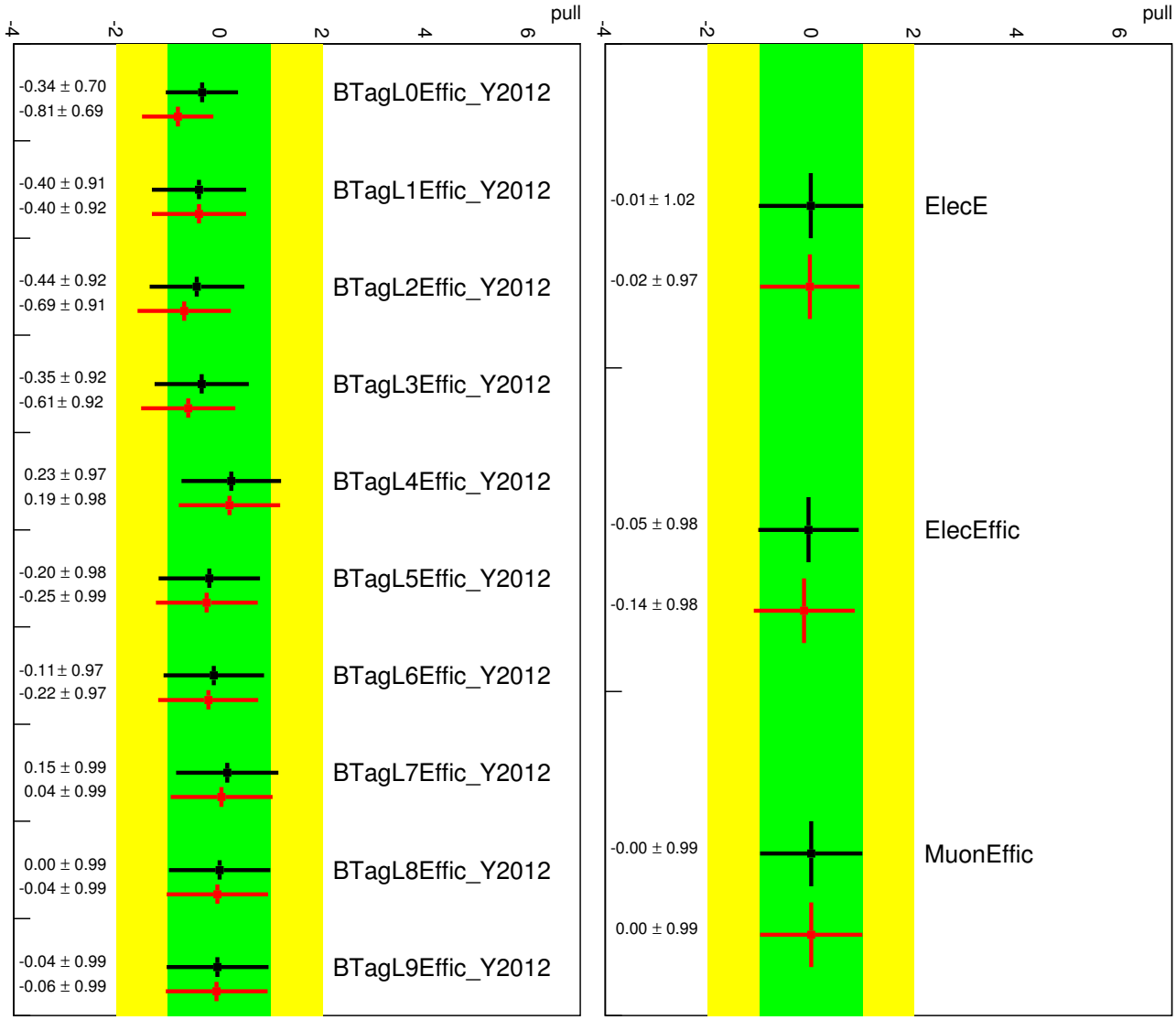

Figure 496: Pull plots for 2-lepton channel: light-jet tagging and leptons.

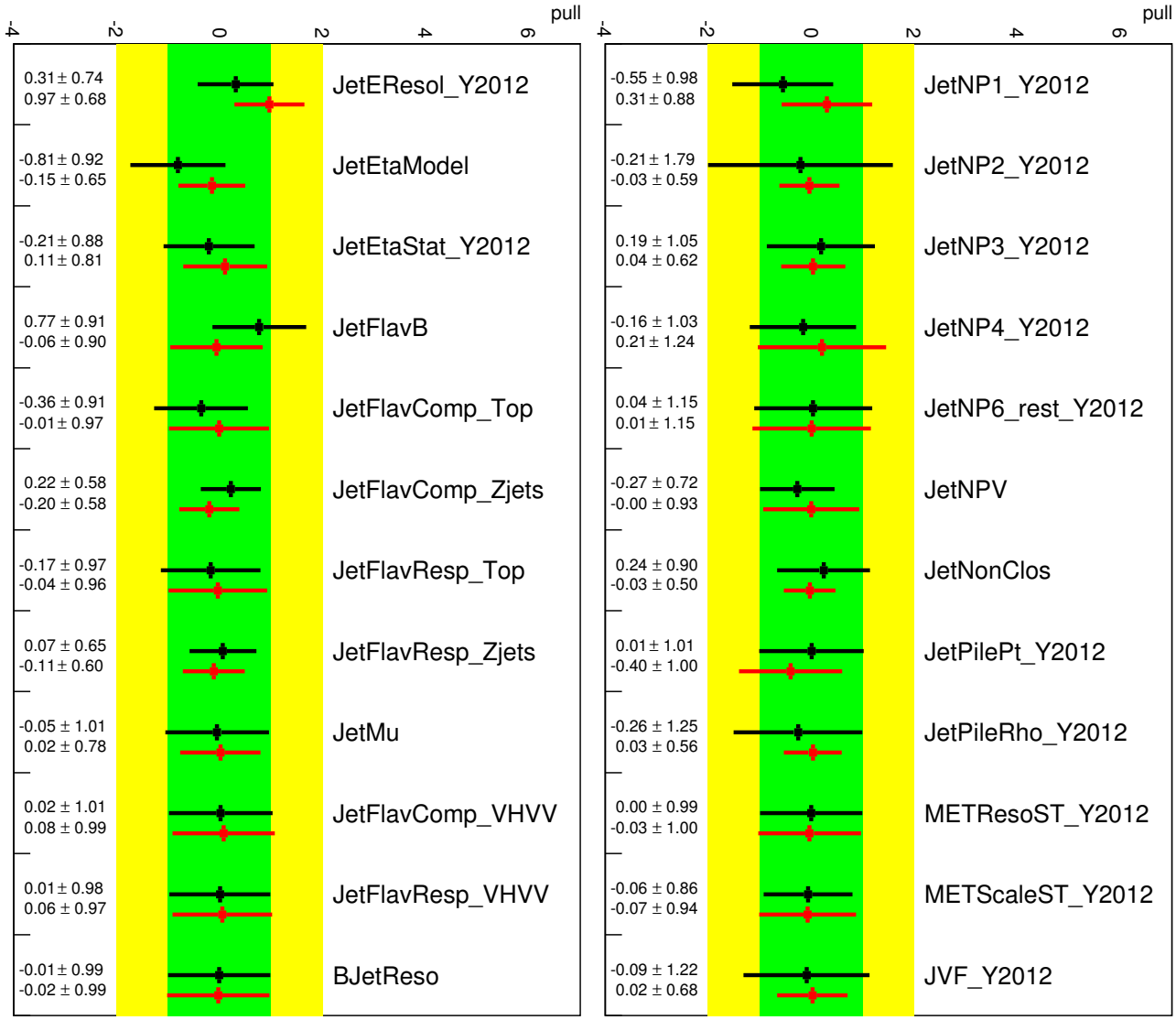

Figure 497: Pull plots for 2-lepton channel: Jet NPs.

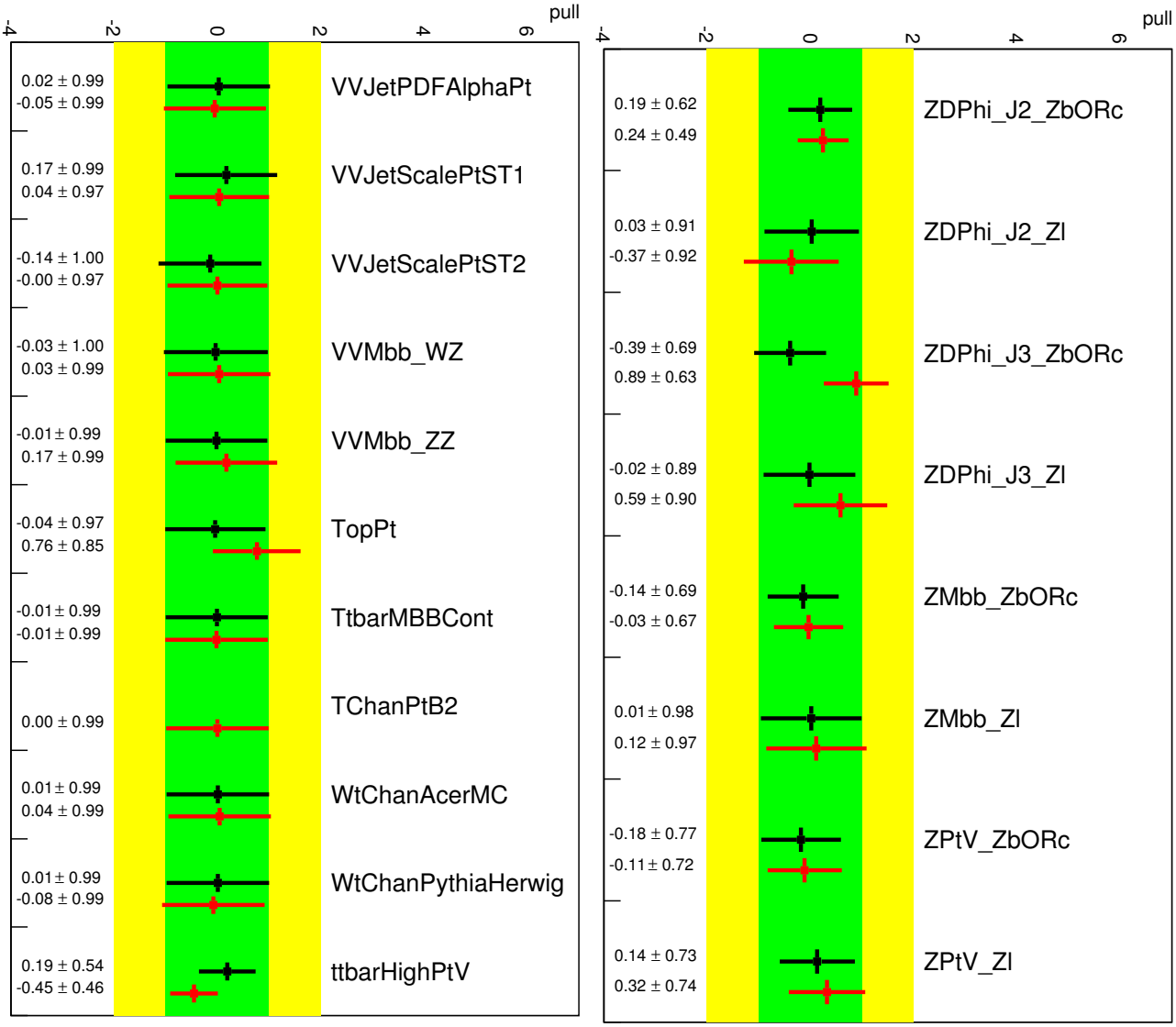

Figure 498: Pull plots for 2-lepton channel: Diboson/Top and W/Z related uncertainties.

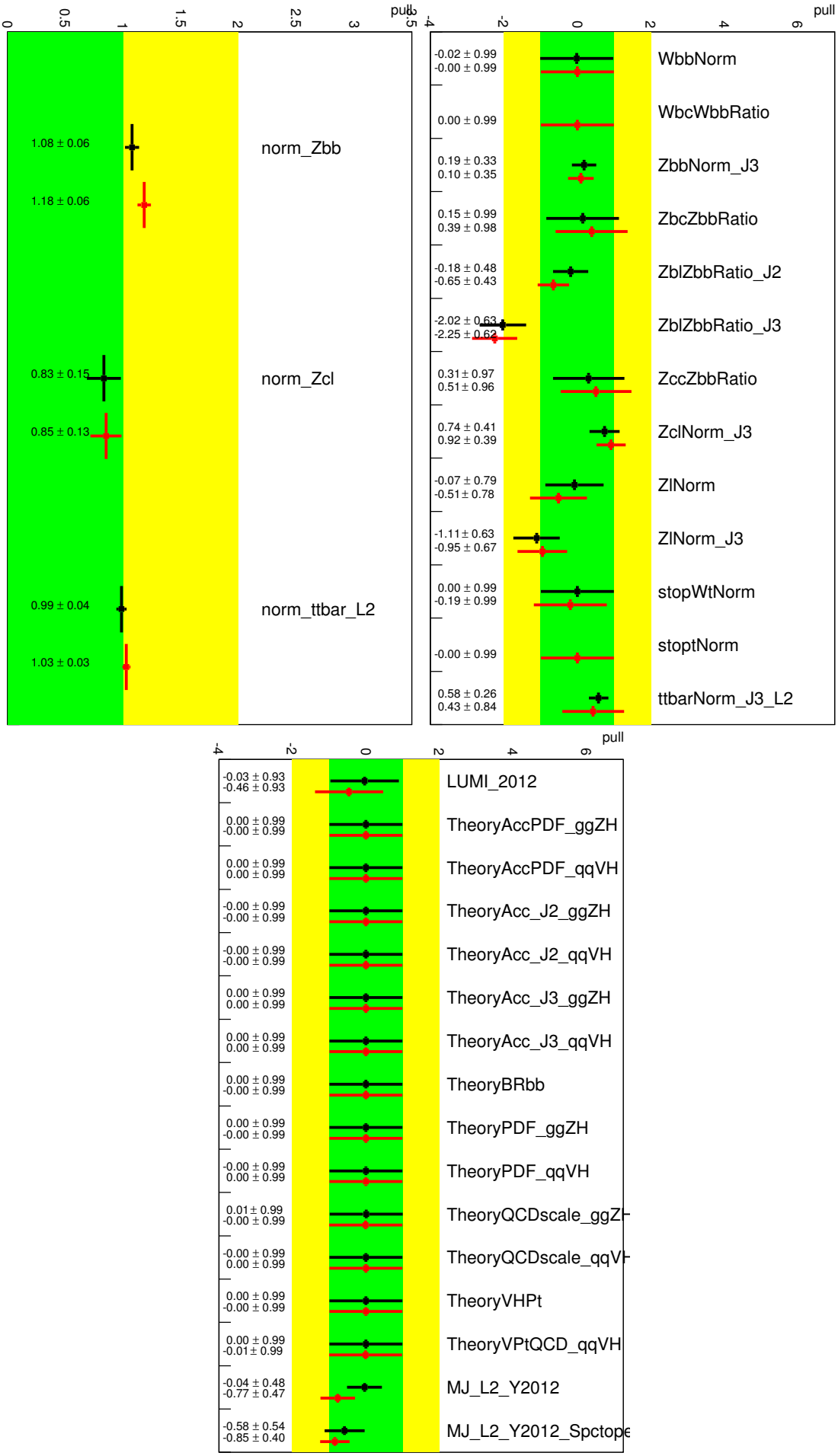

Figure 499: Pull plots for 2-lepton channel: Other model and normalization uncertainties.

AI Postfit p_{T}^{V} Spectrums

The following contains the postfit p_{T}^{V} spectrums for the dijet mass analysis AI.1 and the MVA analysis AI.2 where the error is the full post-unconditional-fit error including the constraints on all nusicance parameters from the respective fits.

AI.1 Dijet Mass p_{T}^{V}

The p_{T}^{V} binning reflects the bins used in the profile likelihood in the 2-tag distributions. For the 1-tag the bins shown are $p_{\mathrm{T}}^{V} < 90$ GeV, $90 < p_{\mathrm{T}}^{V} < 120$ GeV, and $p_{\mathrm{T}}^{V} > 120$ GeV while in the profile likelihood $p_{\mathrm{T}}^{V} < 120$ GeV and $p_{\mathrm{T}}^{V} > 120$ GeV are used (with the MV1c distribution).

Figure 500 shows the p_{T}^{V} distribution in 0-lepton 1 and 2-tag inclusive regions for 2 and 3-jets and Figure 501 shows the 3 2-tag regions. Figure 502 and 503 show the same for 1-lepton and Figure 504 and 505 shows the 2-lepton channel.

AI.2 MVA p_{T}^{V}

The p_{T}^{V} binning reflects the bins used in the profile likelihood.

Figure 506 shows the p_{T}^{V} distribution in 0-lepton 1 and 2-tag inclusive regions for 2 and 3-jets and Figure 507 shows the 3 2-tag regions. Figure 508 and 509 show the same for 1-lepton and Figure 510 and 511 shows the 2-lepton channel.

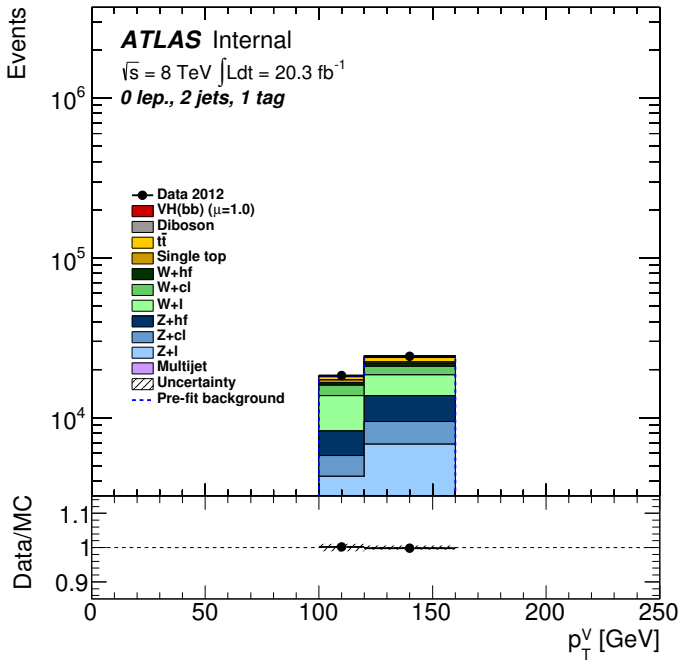

(a) 2-jet 1-tag

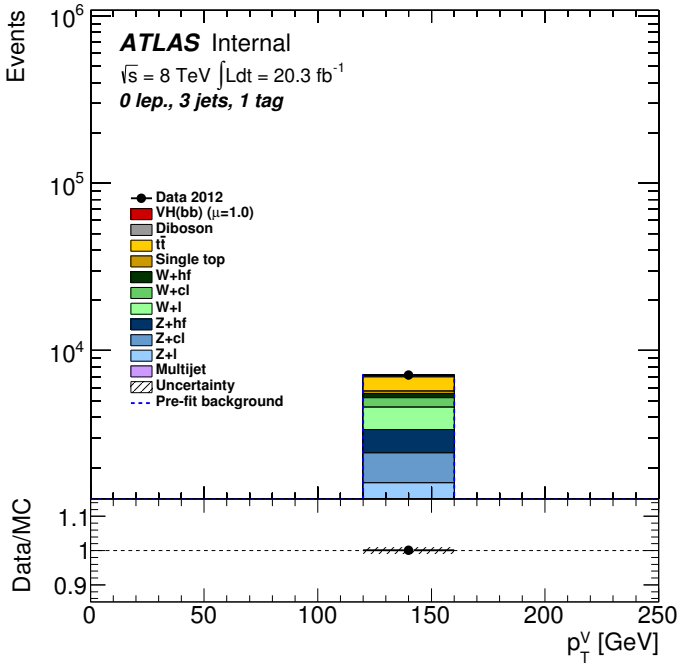

(b) 3-jet 1-tag

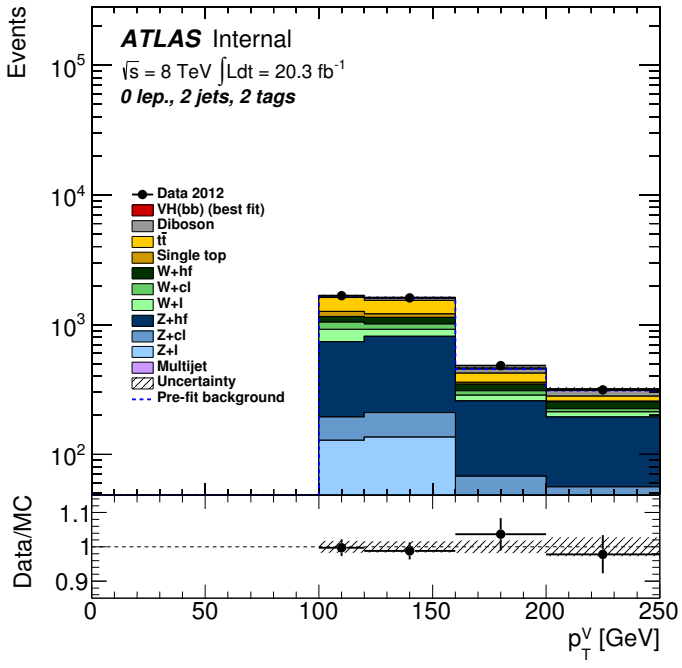

(c) 2-jet 2-tag

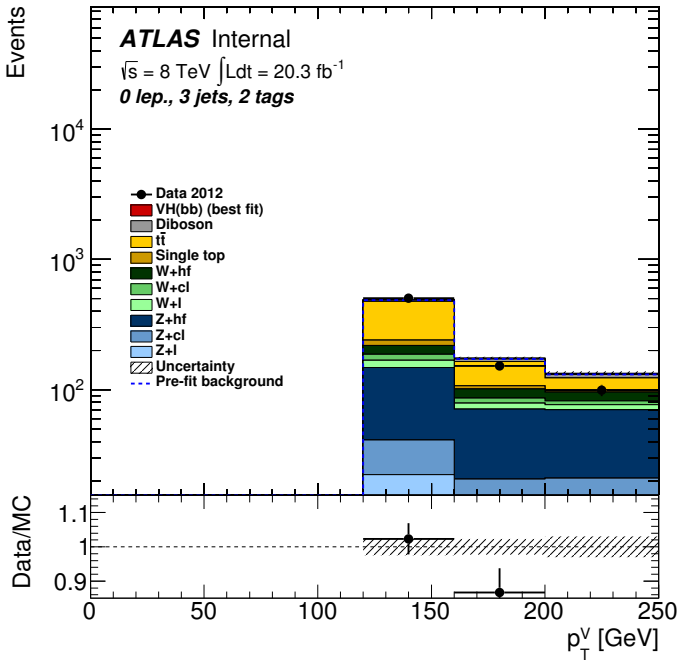

(d) 3-jet 2-tag

Figure 500: p_{T}^{V} distribution in the 0-lepton dijet mass analysis using the postfit NPs for the corresponding 0+1+2 lepton unconditional fit. The 2 and 3-jet regions are shown in the 1-tag and inclusive 2-tag regions. In the 1-tag plot, the bin from 120 − 160 GeV contains events with $p_{\mathrm{T}}^{V} > 120$ GeV.

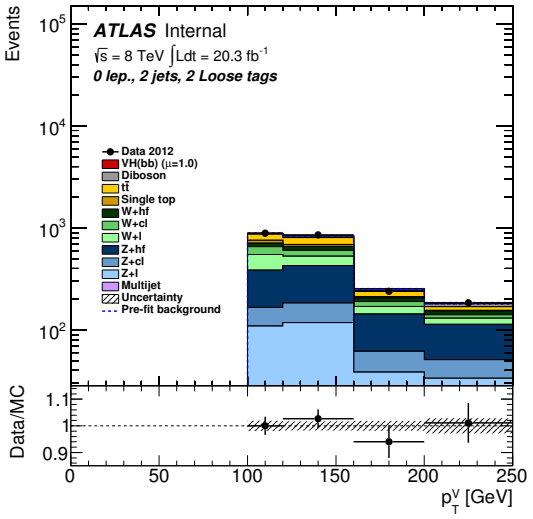

(a) 2-jet LL-tag

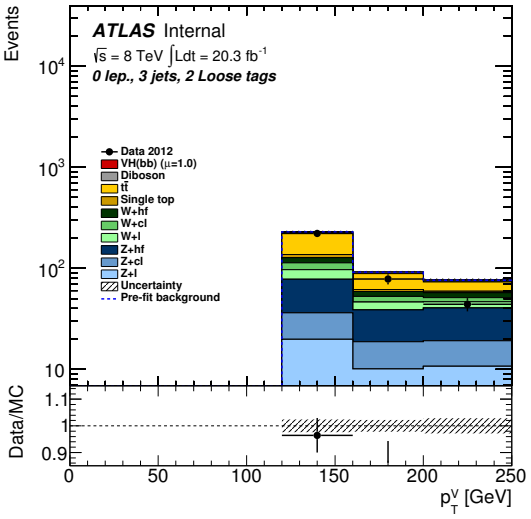

(b) 3-jet LL-tag

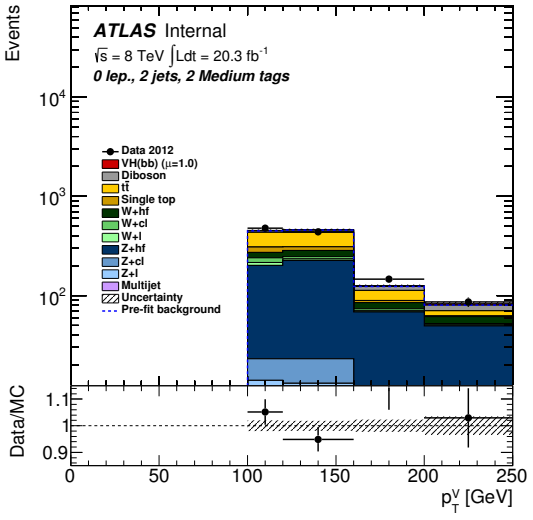

(c) 2-jet MM-tag

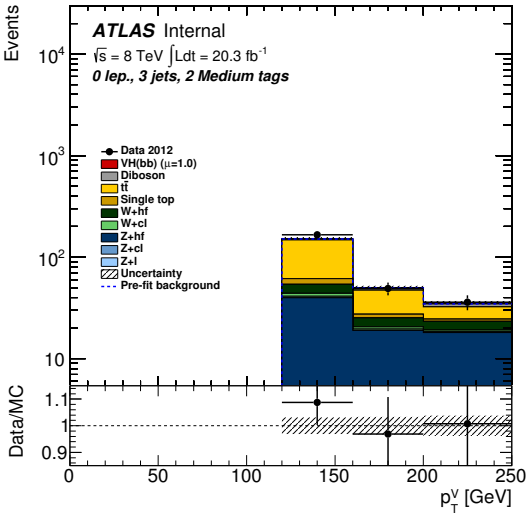

(d) 3-jet MM-tag

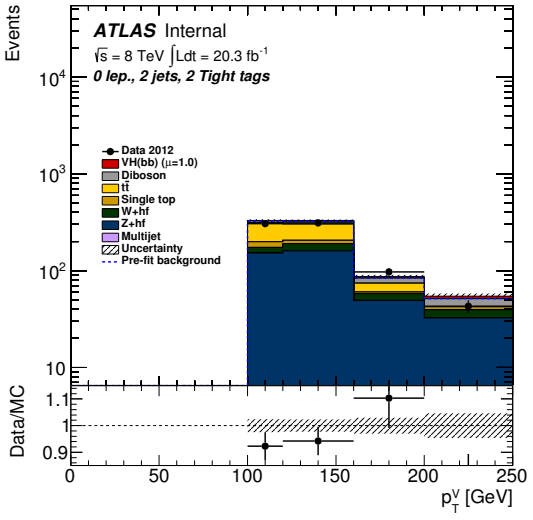

(e) 2-jet TT-tag

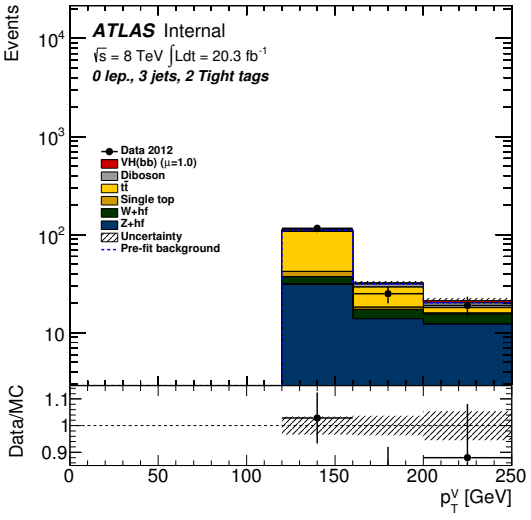

(f) 3-jet TT-tag

Figure 501: p_{T}^{V} distribution in the 0-lepton dijet mass analysis using the postfit NPs for the corresponding 0+1+2 lepton unconditional fit. The 2 and 3-jet regions are shown in the three 2-tag regions.

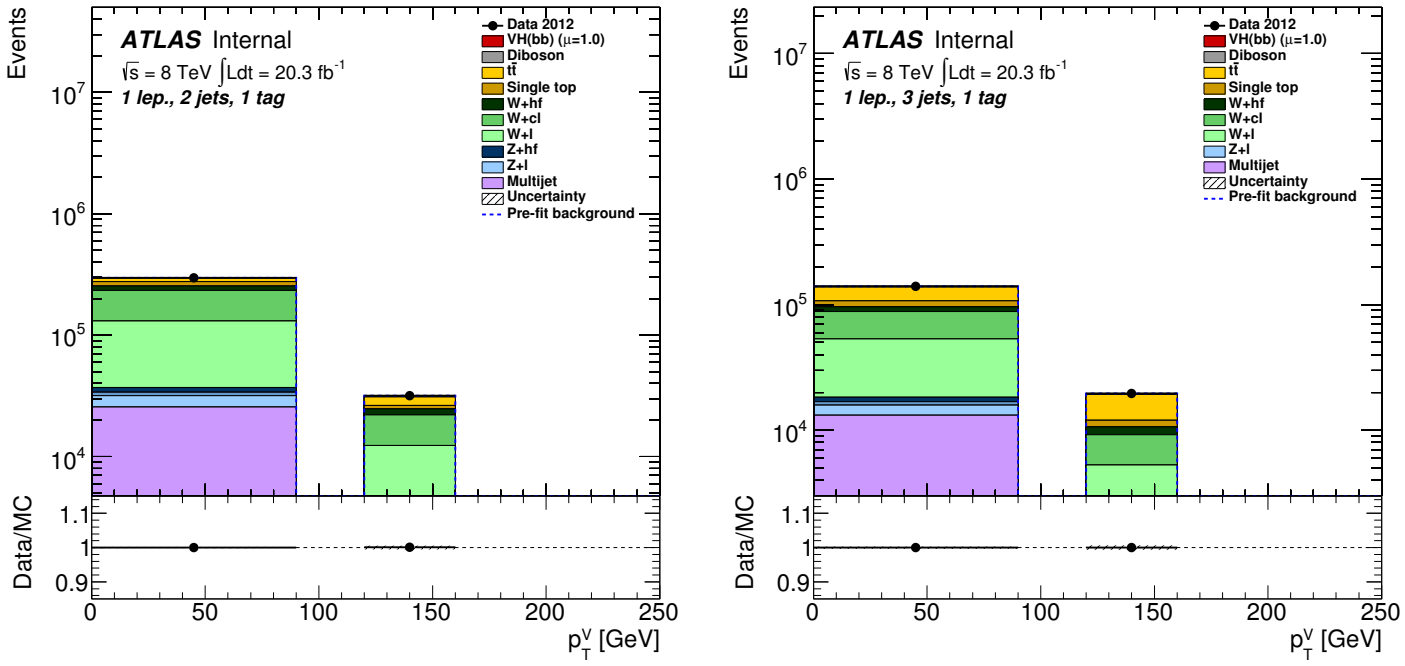

(a) 2-jet 1-tag

(b) 3-jet 1-tag

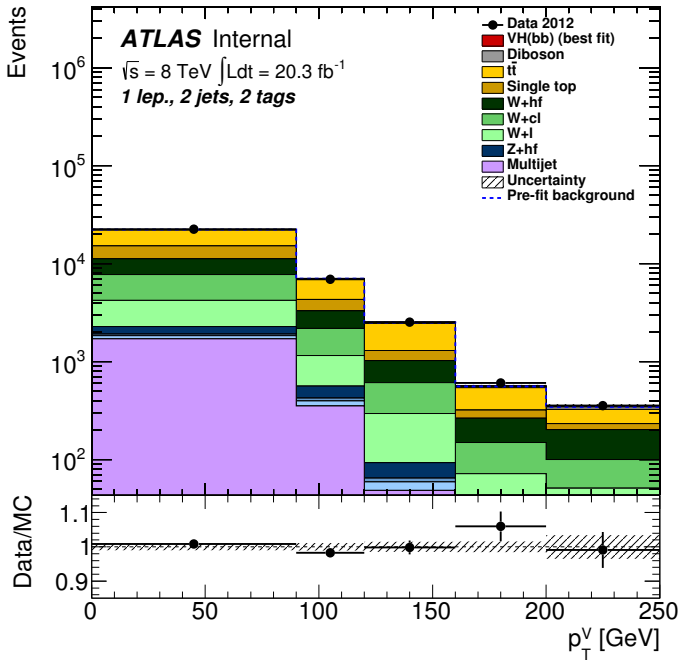

(c) 2-jet 2-tag

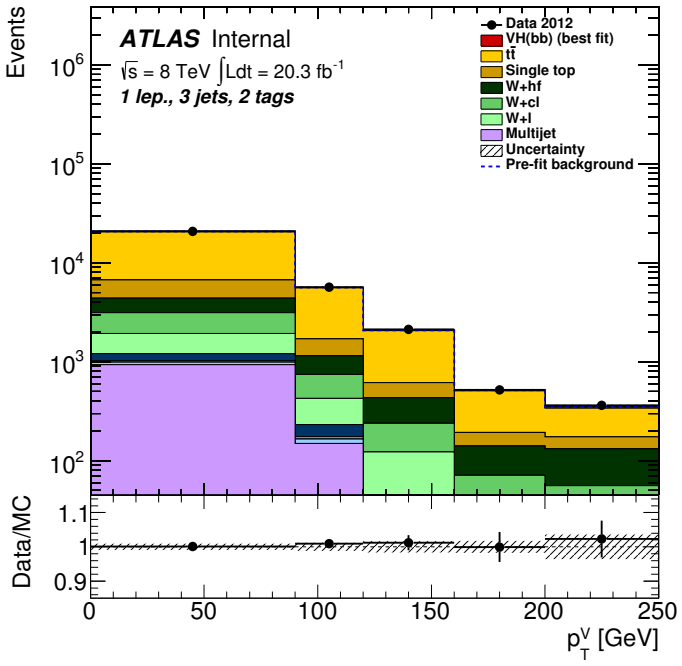

(d) 3-jet 2-tag

Figure 502: p_{T}^{V} distribution in the 1-lepton dijet mass analysis using the postfit NPs for the corresponding 0+1+2 lepton unconditional fit. The 2 and 3-jet regions are shown in the 1-tag and inclusive 2-tag regions. In the 1-tag plot, the bin from 120 − 160 GeV contains events with $p_{\mathrm{T}}^{V} > 120$ GeV.

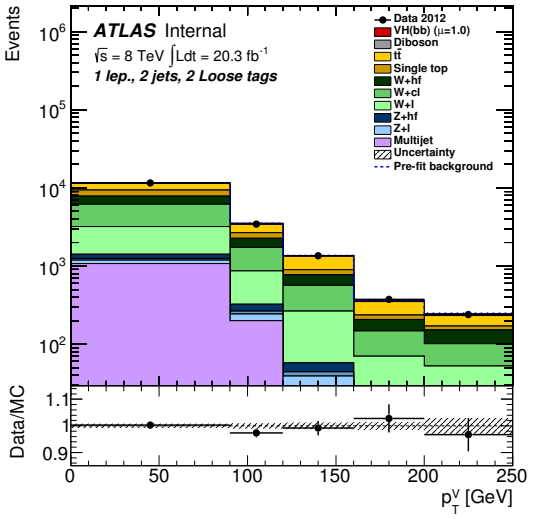

(a) 2-jet LL-tag

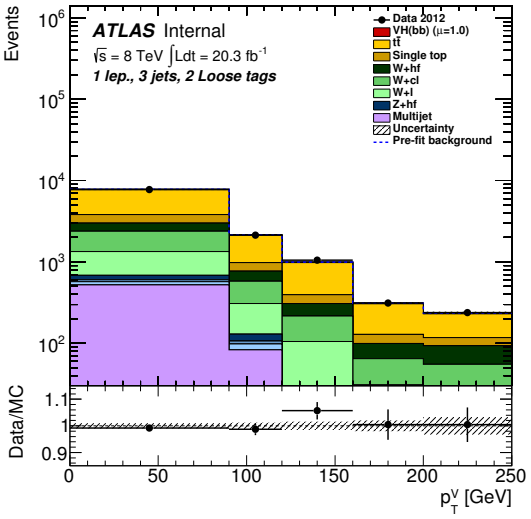

(b) 3-jet LL-tag

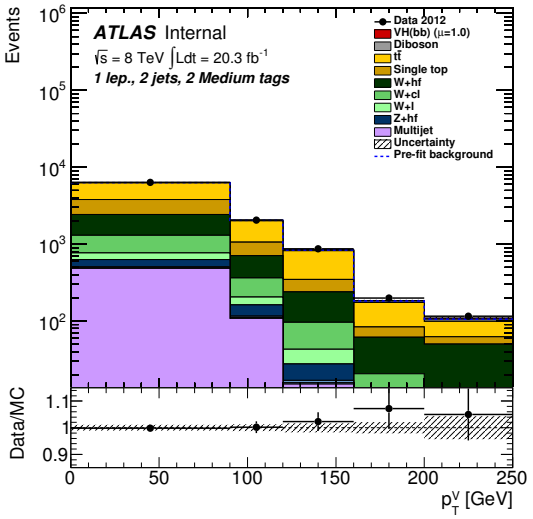

(c) 2-jet MM-tag

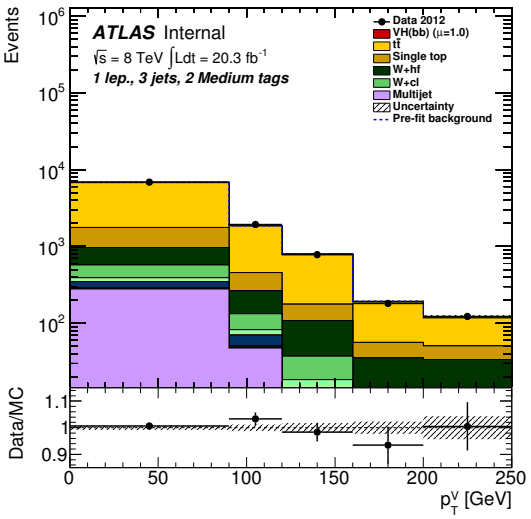

(d) 3-jet MM-tag

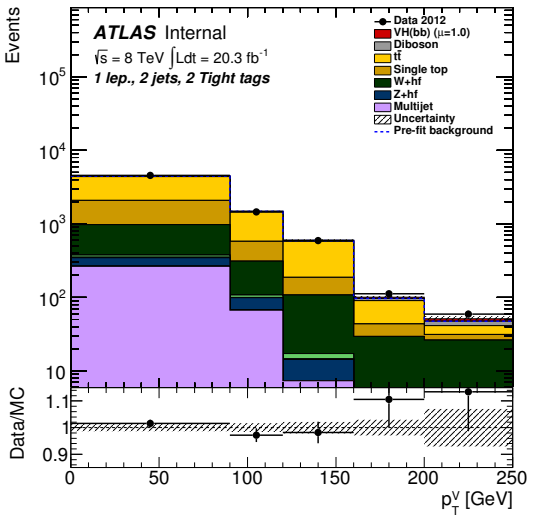

(e) 2-jet TT-tag

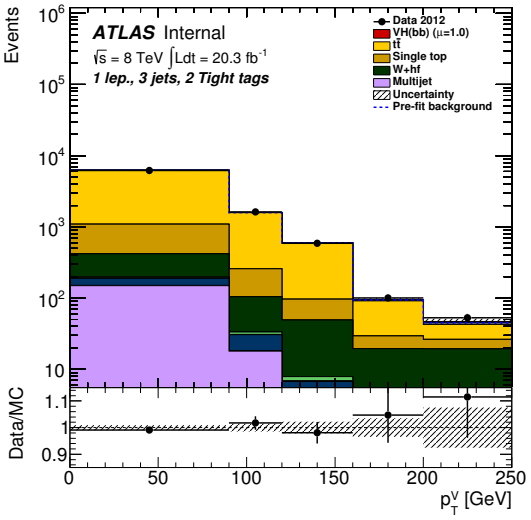

(f) 3-jet TT-tag

Figure 503: p_{T}^{V} distribution in the 1-lepton dijet mass analysis using the postfit NPs for the corresponding 0+1+2 lepton unconditional fit. The 2 and 3-jet regions are shown in the three 2-tag regions.

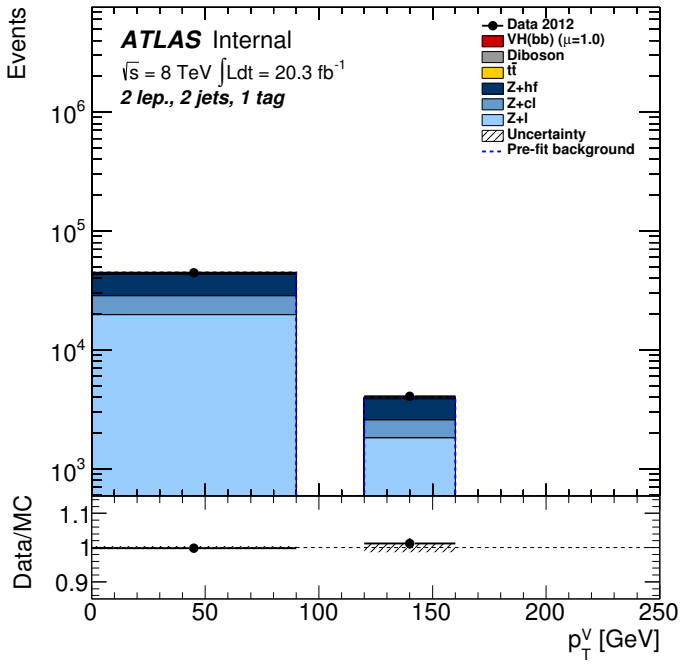

(a) 2-jet 1-tag

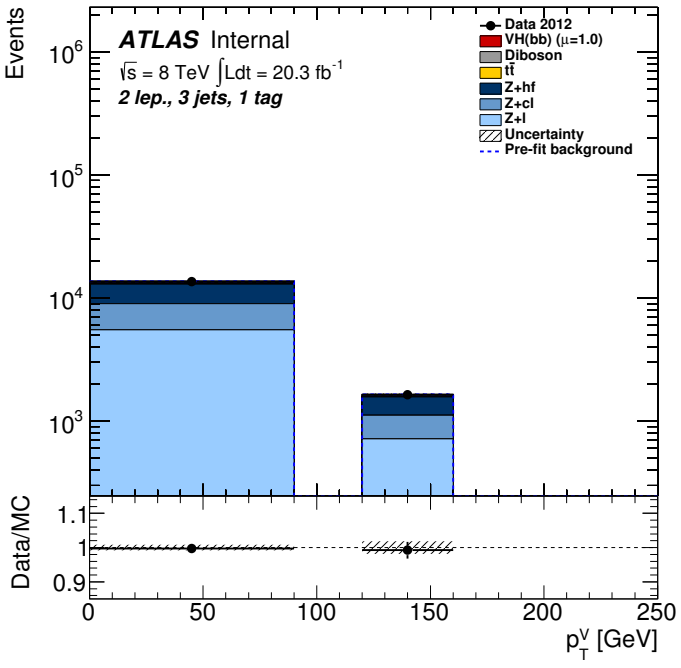

(b) 3-jet 1-tag

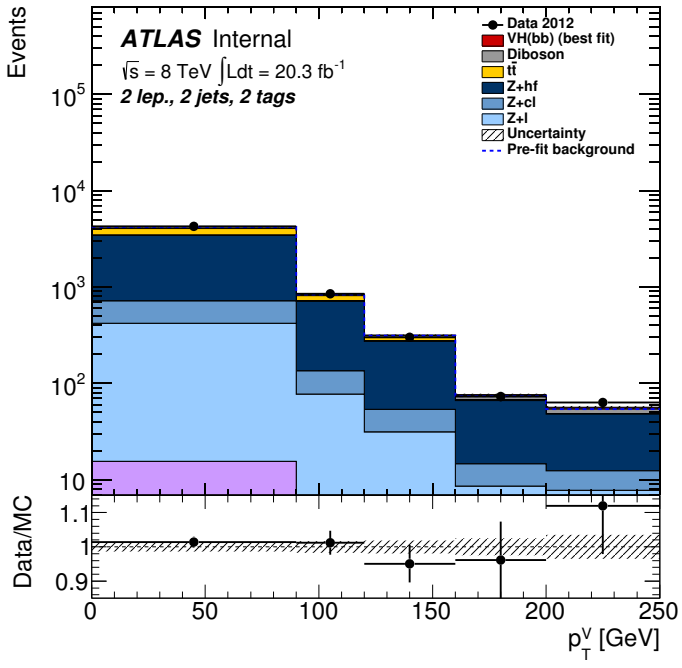

(c) 2-jet 2-tag

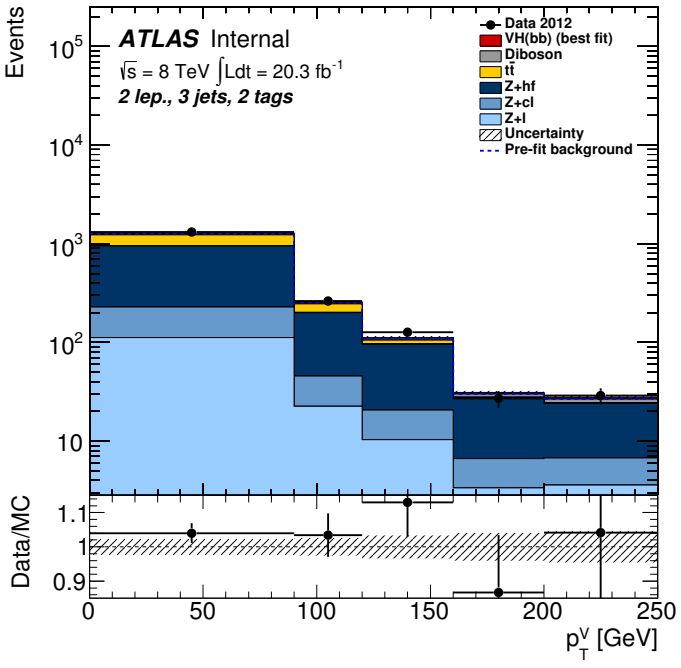

(d) 3-jet 2-tag

Figure 504: p_{T}^{V} distribution in the 2-lepton dijet mass analysis using the postfit NPs for the corresponding 0+1+2 lepton unconditional fit. The 2 and 3-jet regions are shown in the 1-tag and inclusive 2-tag regions. In the 1-tag plot, the bin from 120 − 160 GeV contains events with $p_{\mathrm{T}}^{V} > 120$ GeV.

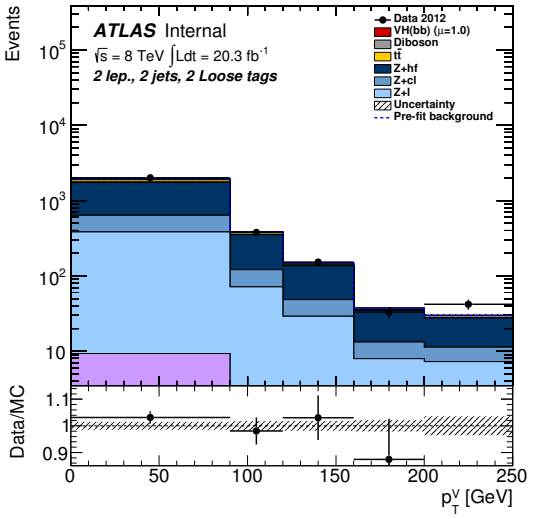

(a) 2-jet LL-tag

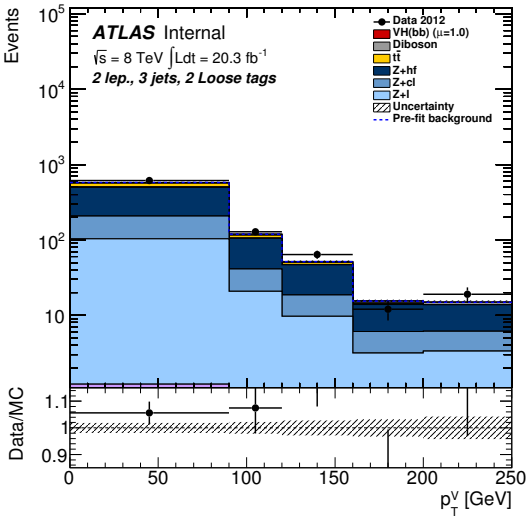

(b) 3-jet LL-tag

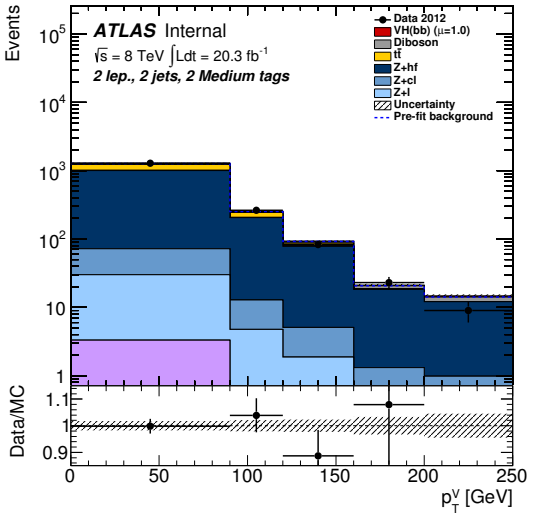

(c) 2-jet MM-tag

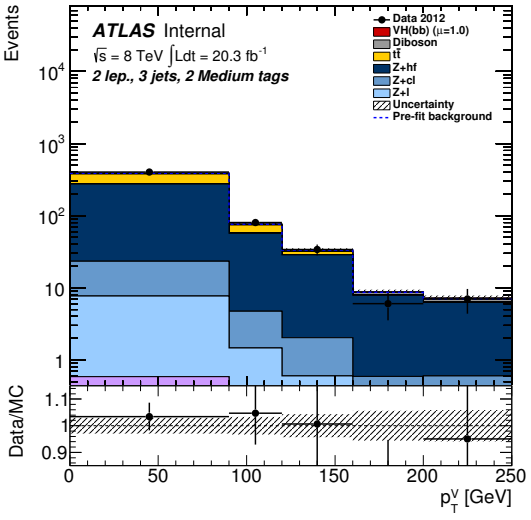

(d) 3-jet MM-tag

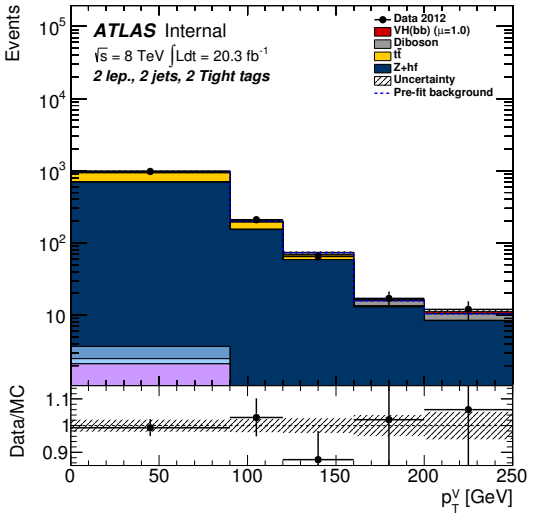

(e) 2-jet TT-tag

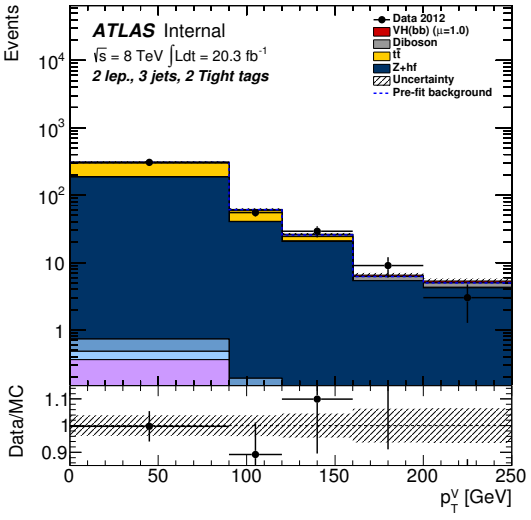

(f) 3-jet TT-tag

Figure 505: p_{T}^{V} distribution in the 2-lepton dijet mass analysis using the postfit NPs for the corresponding 0+1+2 lepton unconditional fit. The 2 and 3-jet regions are shown in the three 2-tag regions.

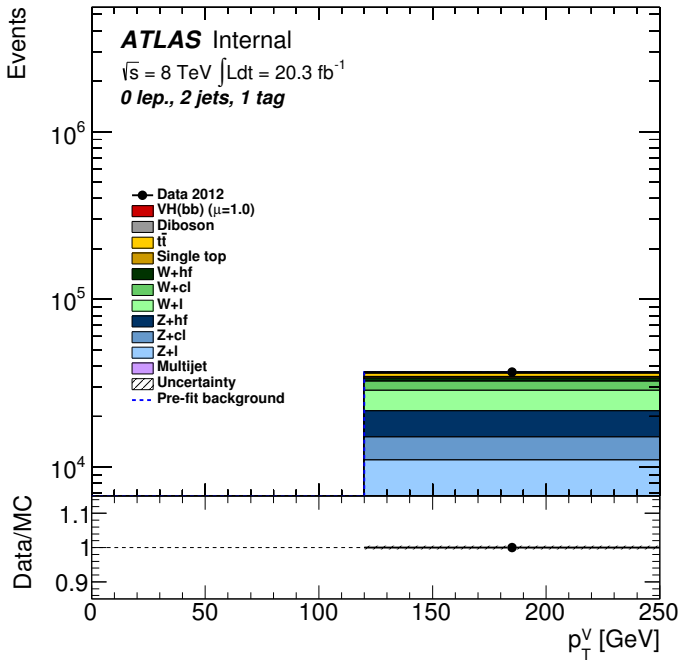

(a) 2-jet 1-tag

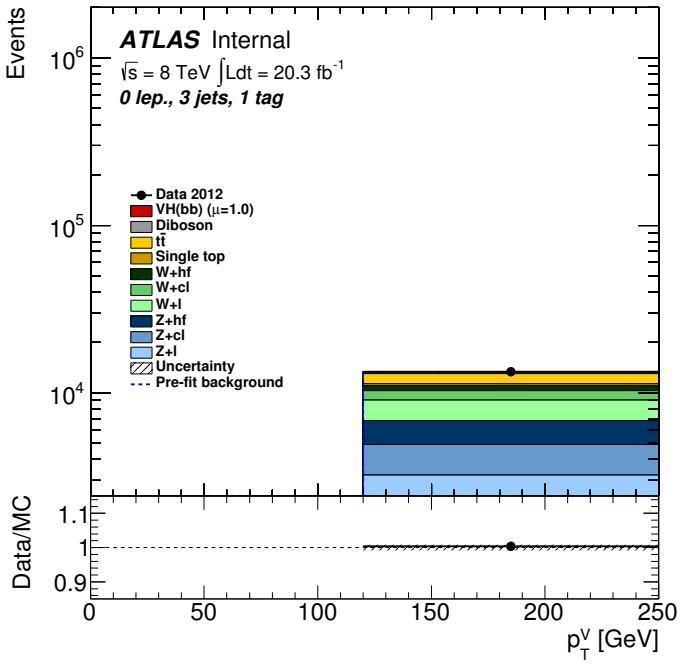

(b) 3-jet 1-tag

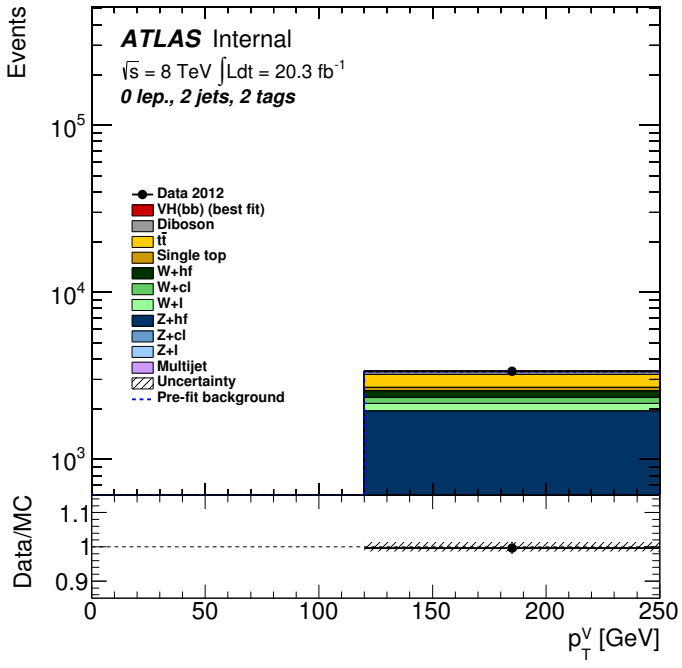

(c) 2-jet 2-tag

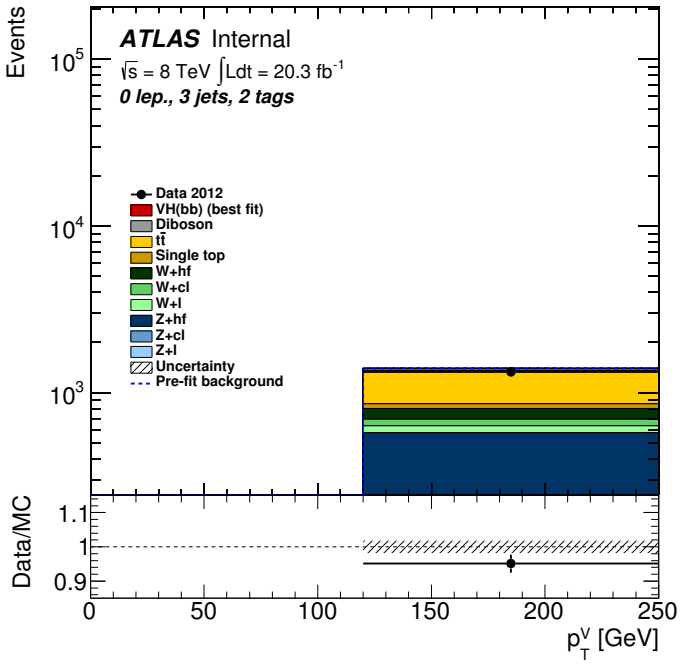

(d) 3-jet 2-tag

Figure 506: p_{T}^{V} distribution in the 0-lepton MVA analysis using the postfit NPs for the corresponding 0+1+2 lepton unconditional fit. The 2 and 3-jet regions are shown in the 1-tag and inclusive 2-tag regions. In the 1-tag plot, the bin from 120 – 160 GeV contains events with $p_{\mathrm{T}}^{V} > 120$ GeV.

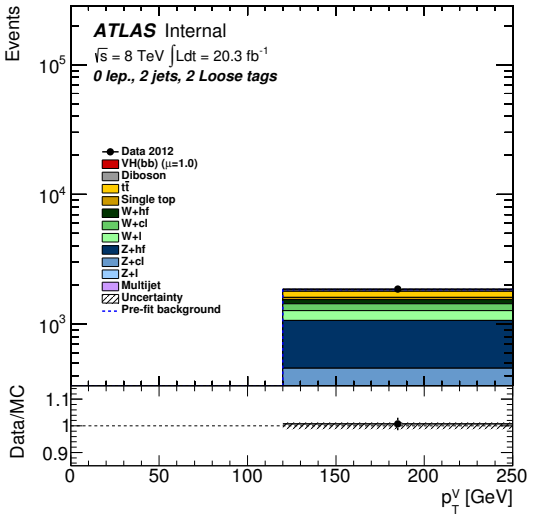

(a) 2-jet LL-tag

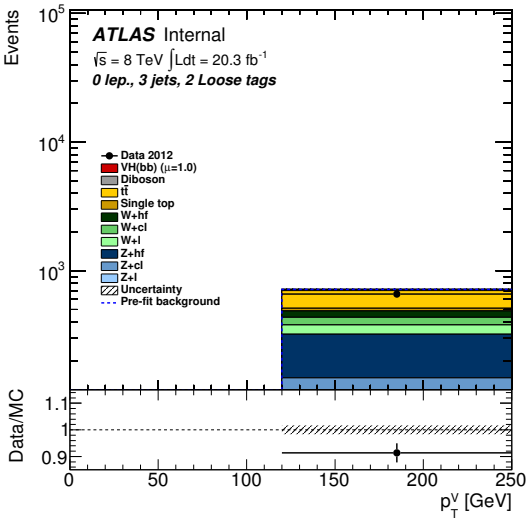

(b) 3-jet LL-tag

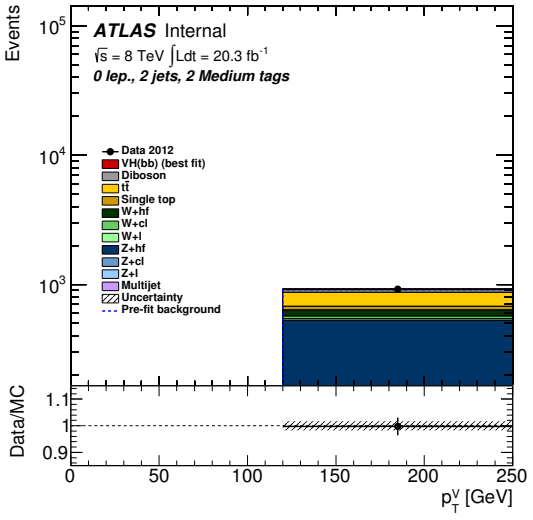

(c) 2-jet MM-tag

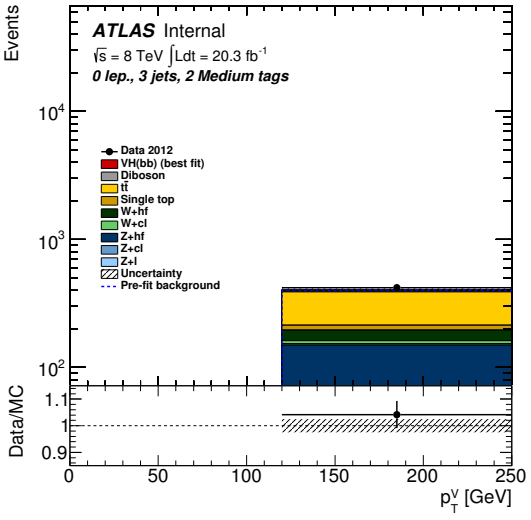

(d) 3-jet MM-tag

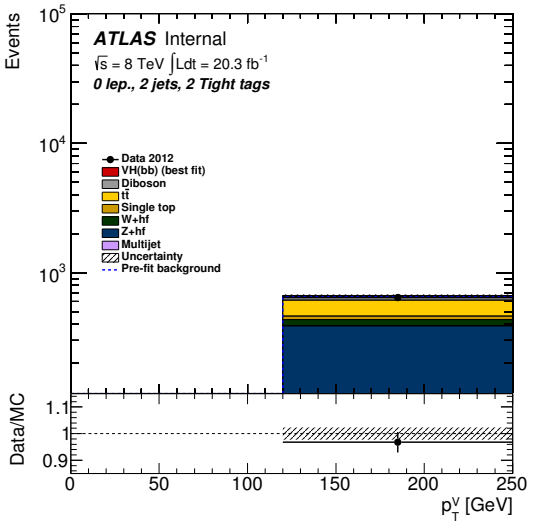

(e) 2-jet TT-tag

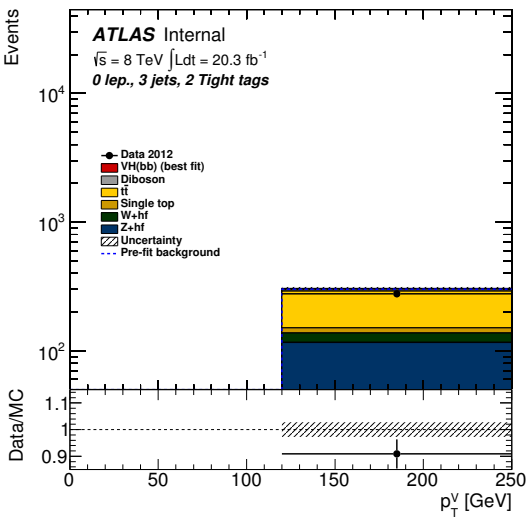

(f) 3-jet TT-tag

Figure 507: p_{T}^{V} distribution in the 0-lepton MVA analysis using the postfit NPs for the corresponding 0+1+2 lepton unconditional fit. The 2 and 3-jet regions are shown in the three 2-tag regions.

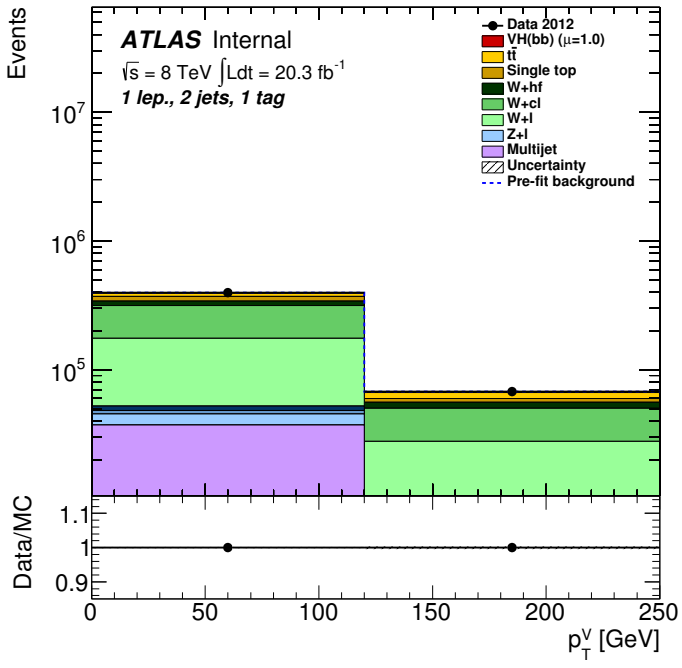

(a) 2-jet 1-tag

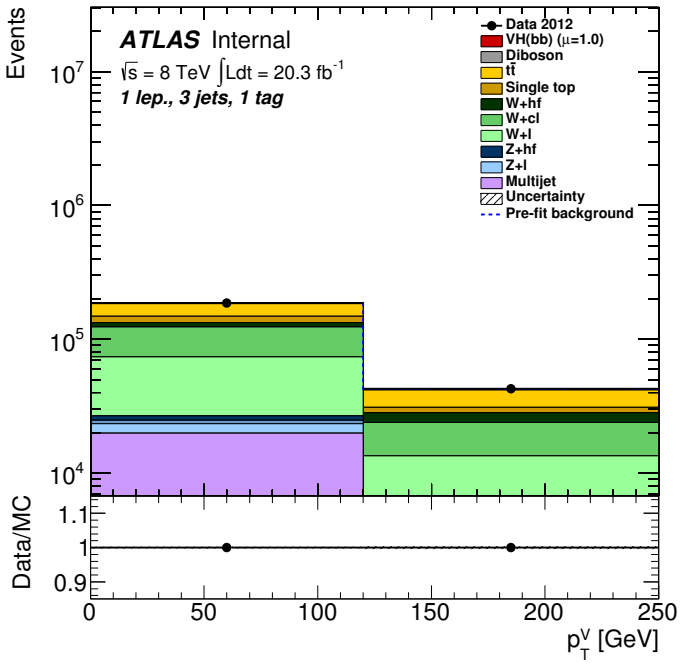

(b) 3-jet 1-tag

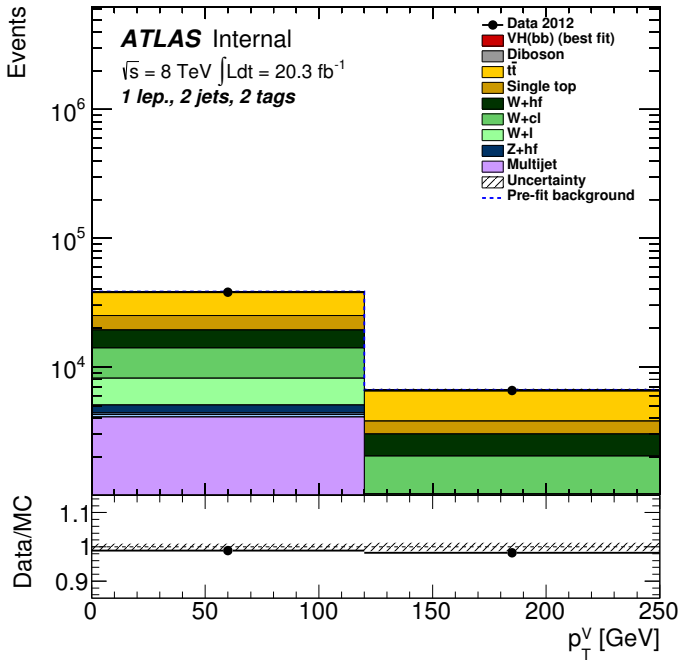

(c) 2-jet 2-tag

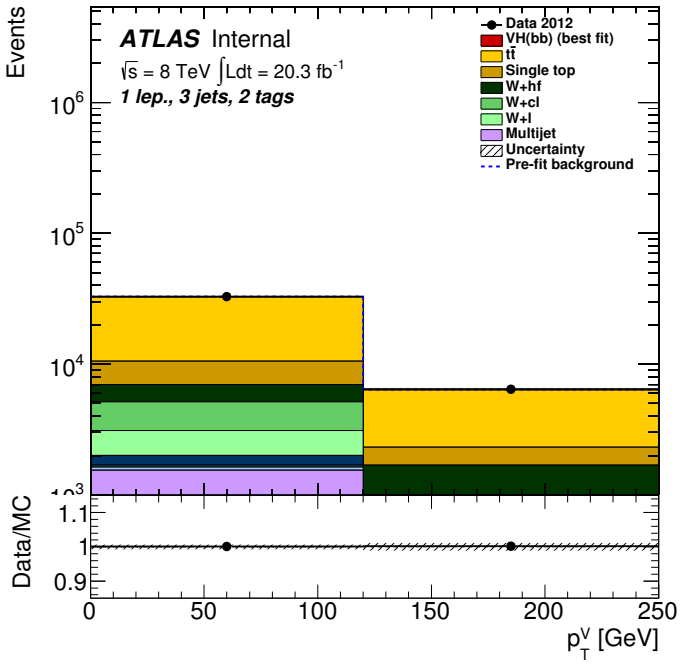

(d) 3-jet 2-tag

Figure 508: p_{T}^{V} distribution in the 1-lepton MVA analysis using the postfit NPs for the corresponding 0+1+2 lepton unconditional fit. The 2 and 3-jet regions are shown in the 1-tag and inclusive 2-tag regions. In the 1-tag plot, the bin from 120 – 160 GeV contains events with $p_{\mathrm{T}}^{V} > 120$ GeV.

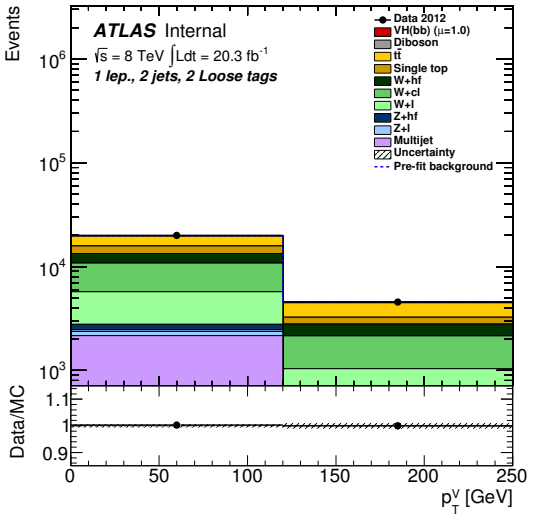

(a) 2-jet LL-tag

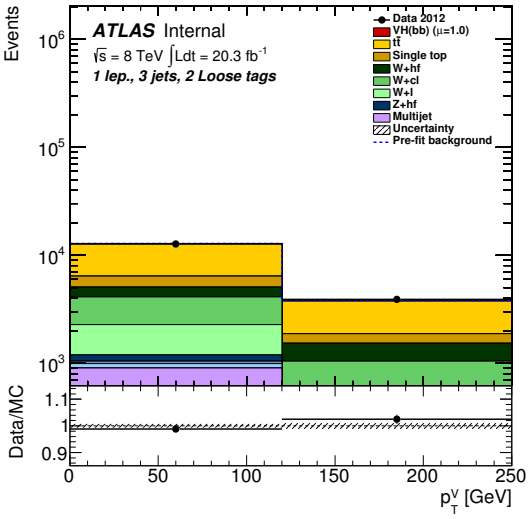

(b) 3-jet LL-tag

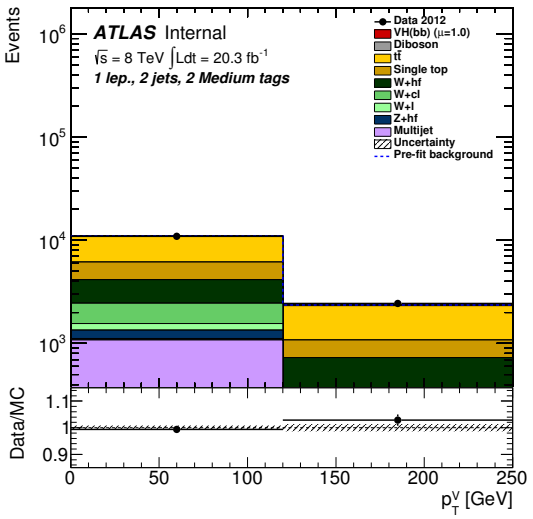

(c) 2-jet MM-tag

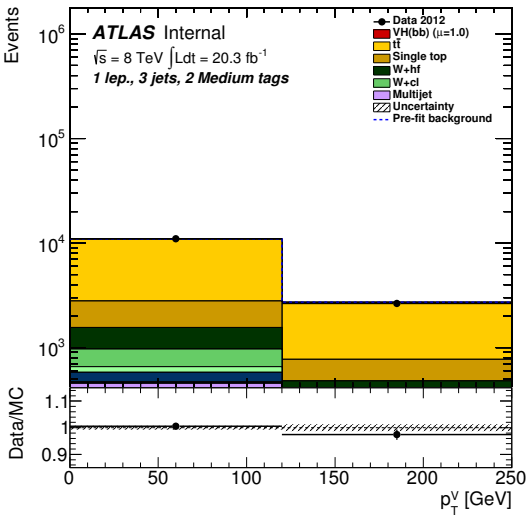

(d) 3-jet MM-tag

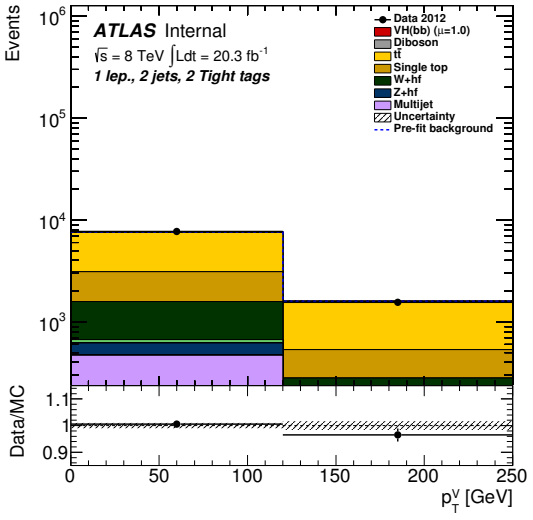

(e) 2-jet TT-tag

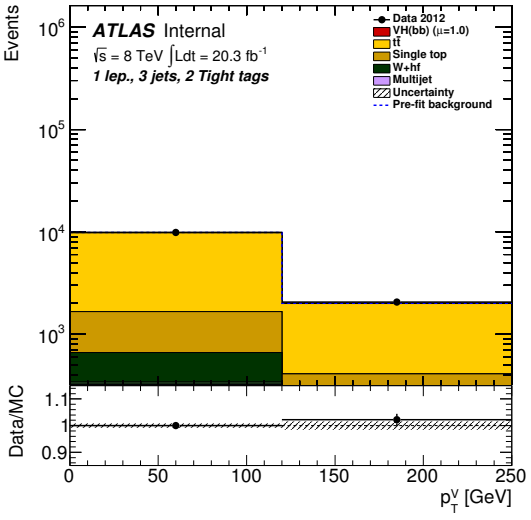

(f) 3-jet TT-tag

Figure 509: p_{T}^{V} distribution in the 1-lepton MVA analysis using the postfit NPs for the corresponding 0+1+2 lepton unconditional fit. The 2 and 3-jet regions are shown in the three 2-tag regions.

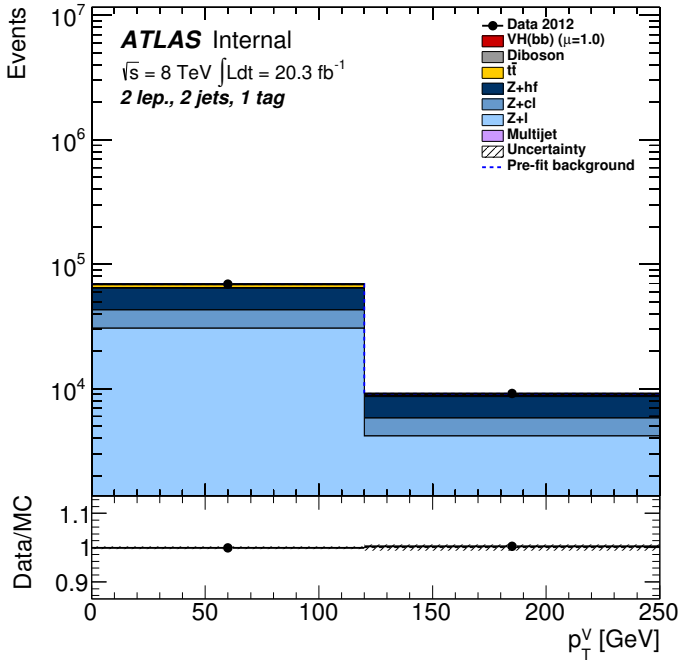

(a) 2-jet 1-tag

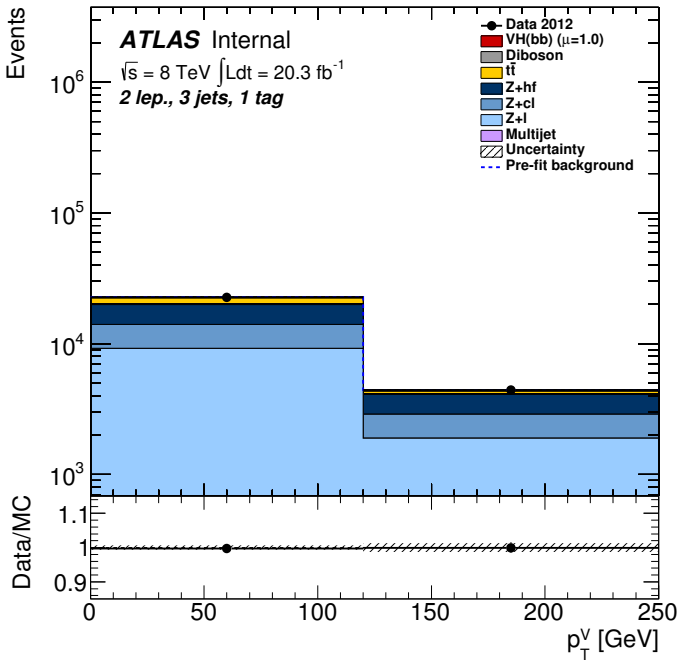

(b) 3-jet 1-tag

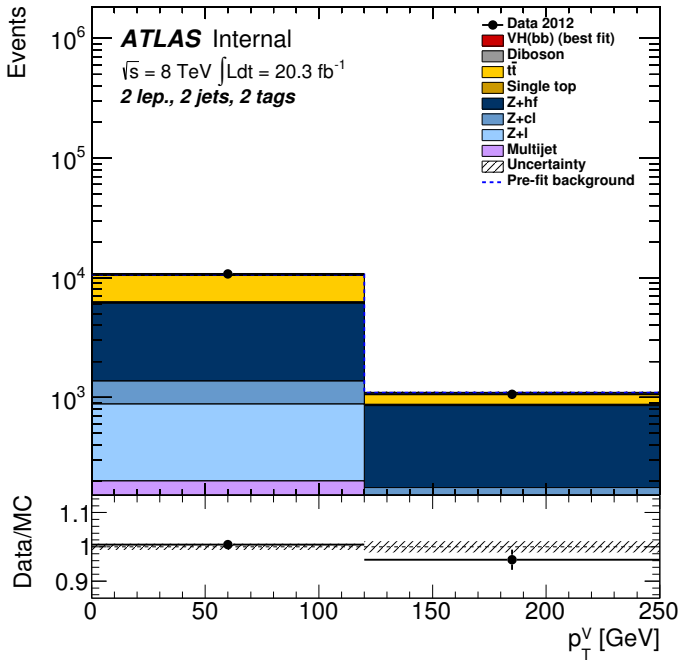

(c) 2-jet 2-tag

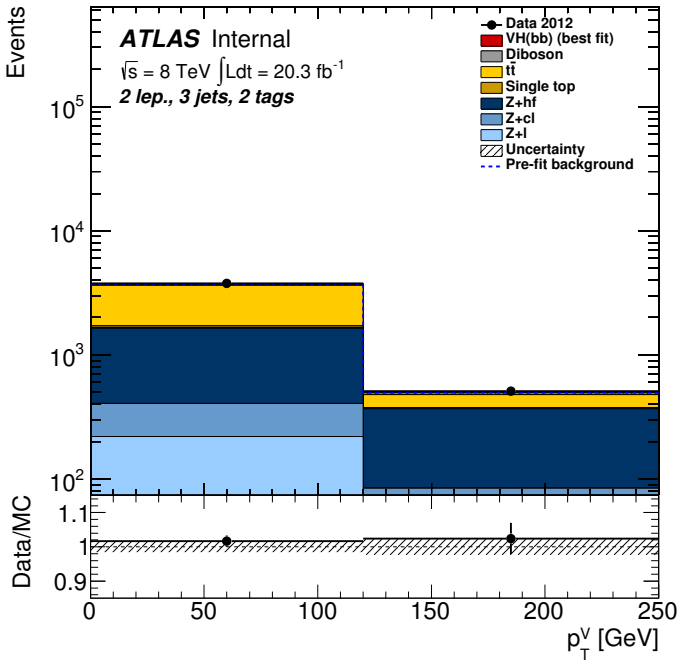

(d) 3-jet 2-tag

Figure 510: p_{T}^{V} distribution in the 2-lepton MVA analysis using the postfit NPs for the corresponding 0+1+2 lepton unconditional fit. The 2 and 3-jet regions are shown in the 1-tag and inclusive 2-tag regions. In the 1-tag plot, the bin from 120 – 160 GeV contains events with $p_{\mathrm{T}}^{V} > 120$ GeV.

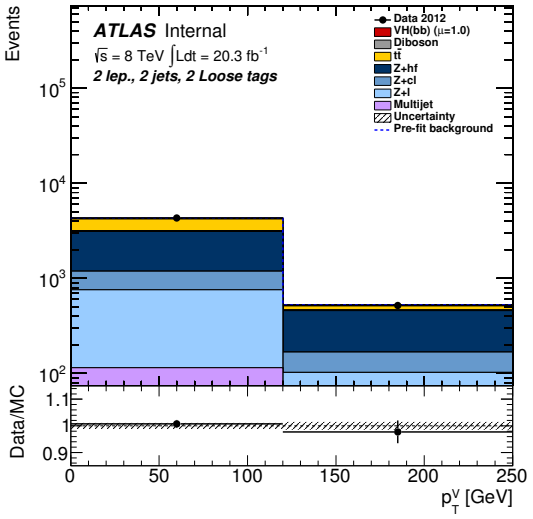

(a) 2-jet LL-tag

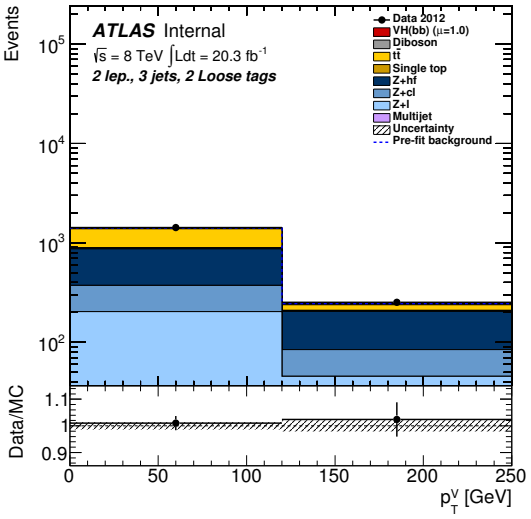

(b) 3-jet LL-tag

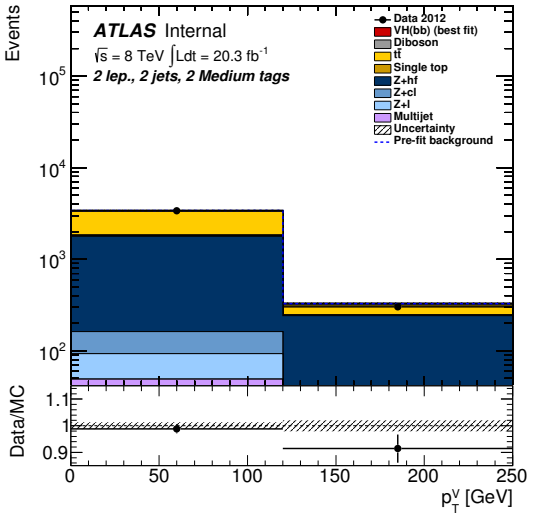

(c) 2-jet MM-tag

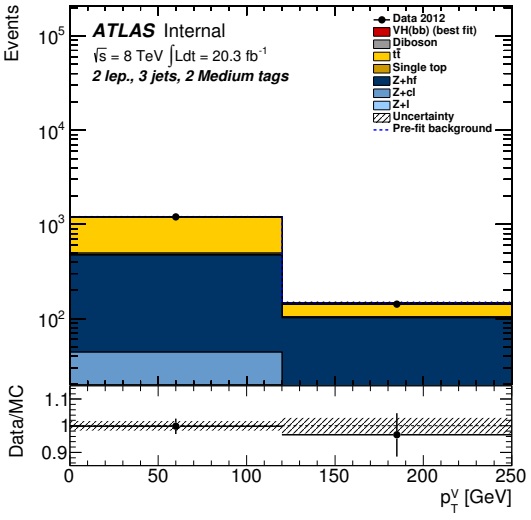

(d) 3-jet MM-tag

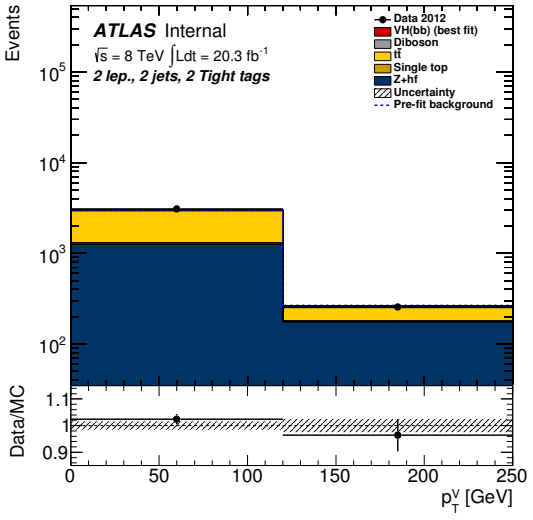

(e) 2-jet TT-tag

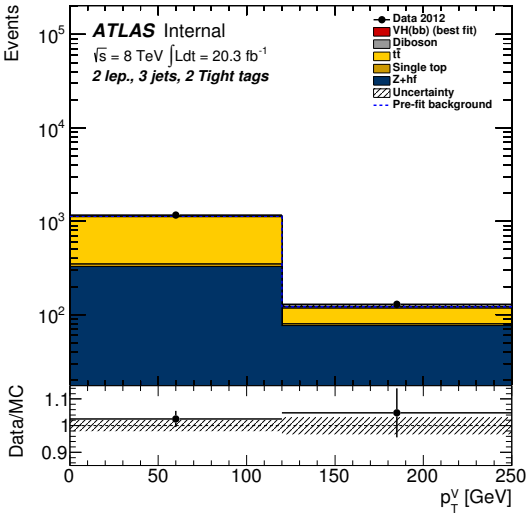

(f) 3-jet TT-tag

Figure 511: p_{T}^{V} distribution in the 2-lepton MVA analysis using the postfit NPs for the corresponding 0+1+2 lepton unconditional fit. The 2 and 3-jet regions are shown in the three 2-tag regions.

AJ Yield Tables

AJ.1 Dijet Mass Analysis: Prefit

Sample	1-tag	
	$100 < p_{\mathrm{T}}^{V} < 120\ GeV$	$p_{\mathrm{T}}^{V} > 120\ GeV$
	2-jet	
VH	7.9 ± 0.7	19.3 ± 2.0
VV	233.5 ± 6.5	547.1 ± 15.3
$t\bar{t}$	596.6 ± 53.3	968.7 ± 98.9
s-top	443.2 ± 155.8	421.3 ± 59.4
W+l	5290.0 ± 844.1	4880.9 ± 834.8
W+cl	1975.9 ± 184.1	2212.7 ± 223.6
W+hf	883.2 ± 246.4	1334.8 ± 394.4
Z+l	3709.6 ± 498.0	7026.1 ± 969.7
Z+cl	1741.4 ± 206.8	3105.1 ± 310.8
Z+hf	2236.6 ± 242.3	3942.1 ± 457.2
MJ	410.6 ± 400.4	244.4 ± 238.3
Total	17528.5 ± 1477.1	24702.6 ± 2001.1
Data	18343.0 ± 135.4	24289.0 ± 155.8
	3-jet	
VH	–	5.8 ± 0.7
VV	–	167.1 ± 4.7
$t\bar{t}$	–	985.9 ± 214.2
s-top	–	184.1 ± 22.2
W+l	–	1251.5 ± 268.0
W+cl	–	617.0 ± 109.9
W+hf	–	398.5 ± 118.6
Z+l	–	1722.5 ± 296.8
Z+cl	–	823.6 ± 248.6
Z+hf	–	1019.4 ± 236.9
MJ	–	71.7 ± 69.9
Total	–	7247.1 ± 772.8
Data	–	7148.0 ± 84.5

Table 116: Table of prefit yields for 0-lepton 2 and 3-jet 1-tag events in the dijet mass selection. The uncertainties are from the full prefit nusicance parameters (NPs) except the floating normalizations under the assumption that each NP is independent (uncorrelated).

Sample	2L-tag			
	$100 < p_{\mathrm{T}}^{V} < 120\ GeV$	$120 < p_{\mathrm{T}}^{V} < 160\ GeV$	$160 < p_{\mathrm{T}}^{V} < 200\ GeV$	$p_{\mathrm{T}}^{V} > 200\ GeV$
	2-jet			
VH	2.2 ± 0.2	3.1 ± 0.3	1.6 ± 0.2	1.8 ± 0.2
VV	16.8 ± 0.9	23.0 ± 1.6	10.5 ± 1.5	10.2 ± 2.1
$t\bar{t}$	78.2 ± 7.4	77.6 ± 9.8	19.8 ± 2.4	9.6 ± 1.4
s-top	34.4 ± 10.3	26.4 ± 3.8	5.6 ± 0.7	1.9 ± 0.2
W+l	159.0 ± 32.5	97.1 ± 22.1	25.5 ± 5.7	16.1 ± 3.8
W+cl	93.9 ± 11.8	66.2 ± 9.1	17.6 ± 2.4	10.0 ± 1.4
W+hf	64.4 ± 12.1	74.6 ± 15.3	22.4 ± 5.8	19.0 ± 6.4
Z+l	89.1 ± 18.3	102.6 ± 21.1	36.8 ± 7.7	33.1 ± 7.3
Z+cl	63.8 ± 8.5	73.6 ± 10.0	26.4 ± 3.6	20.4 ± 3.0
Z+hf	187.7 ± 15.8	214.3 ± 22.9	70.6 ± 7.9	57.5 ± 7.8
MJ	18.9 ± 18.4	11.4 ± 11.1	1.4 ± 1.3	0.9 ± 0.8
Total	808.4 ± 77.6	769.8 ± 74.9	238.2 ± 25.3	180.6 ± 21.2
Data	887.0 ± 29.8	856.0 ± 29.3	239.0 ± 15.5	185.0 ± 13.6
	3-jet			
VH	–	0.7 ± 0.1	0.5 ± 0.1	0.6 ± 0.1
VV	–	5.0 ± 0.4	2.9 ± 0.4	3.1 ± 0.6
$t\bar{t}$	–	65.1 ± 14.5	21.4 ± 4.8	11.3 ± 2.7
s-top	–	10.0 ± 1.4	2.6 ± 0.5	2.0 ± 0.3
W+l	–	18.9 ± 5.1	7.3 ± 1.8	5.9 ± 1.5
W+cl	–	14.8 ± 3.2	6.0 ± 1.1	4.3 ± 0.7
W+hf	–	17.5 ± 4.1	7.3 ± 1.9	7.3 ± 2.6
Z+l	–	19.4 ± 4.6	10.3 ± 2.2	11.4 ± 2.6
Z+cl	–	15.7 ± 4.9	8.1 ± 2.5	8.2 ± 2.5
Z+hf	–	39.2 ± 8.8	19.6 ± 4.7	21.8 ± 5.3
MJ	–	2.7 ± 2.6	0.6 ± 0.6	0.3 ± 0.3
Total	–	209.0 ± 24.9	86.5 ± 10.4	76.2 ± 10.2
Data	–	221.0 ± 14.9	78.0 ± 8.8	44.0 ± 6.6

Table 117: Table of prefit yields for 0-lepton 2 and 3-jet 2L-tag events in the dijet mass selection. The uncertainties are from the full prefit nusicance parameters (NPs) except the floating normalizations under the assumption that each NP is independent (uncorrelated).

Sample	2M-tag			
	$100 < p_{\mathrm{T}}^{V} < 120\ GeV$	$120 < p_{\mathrm{T}}^{V} < 160\ GeV$	$160 < p_{\mathrm{T}}^{V} < 200\ GeV$	$p_{\mathrm{T}}^{V} > 200\ GeV$
	2-jet			
VH	3.5 ± 0.3	5.0 ± 0.5	2.6 ± 0.3	2.7 ± 0.3
VV	13.9 ± 1.5	20.7 ± 2.6	9.5 ± 1.6	8.6 ± 1.8
$t\bar{t}$	90.1 ± 7.8	81.6 ± 9.0	15.5 ± 2.1	5.3 ± 0.7
s-top	27.2 ± 6.2	20.7 ± 3.2	3.8 ± 0.5	1.0 ± 0.1
W+l	13.2 ± 3.0	7.2 ± 2.0	1.7 ± 0.5	1.0 ± 0.3
W+cl	20.9 ± 2.9	11.7 ± 1.9	2.8 ± 0.4	1.5 ± 0.3
W+hf	39.1 ± 7.0	48.6 ± 9.0	14.7 ± 3.6	12.4 ± 4.0
Z+l	5.2 ± 1.5	5.8 ± 1.7	2.0 ± 0.6	1.8 ± 0.5
Z+cl	9.9 ± 1.8	10.8 ± 1.8	3.5 ± 0.7	2.8 ± 0.5
Z+hf	155.9 ± 10.3	177.7 ± 15.6	55.3 ± 5.7	39.4 ± 4.8
MJ	9.0 ± 8.8	5.4 ± 5.3	0.6 ± 0.6	0.4 ± 0.4
Total	387.9 ± 25.7	395.2 ± 29.0	112.2 ± 9.9	77.0 ± 8.0
Data	477.0 ± 21.8	438.0 ± 20.9	146.0 ± 12.1	86.0 ± 9.3
	3-jet			
VH	–	1.0 ± 0.1	0.8 ± 0.1	0.8 ± 0.1
VV	–	3.6 ± 0.5	2.5 ± 0.5	2.3 ± 0.4
$t\bar{t}$	–	64.8 ± 14.9	15.2 ± 3.6	5.9 ± 1.4
s-top	–	7.2 ± 1.0	2.1 ± 0.4	1.2 ± 0.3
W+l	–	1.2 ± 0.4	0.5 ± 0.2	0.4 ± 0.1
W+cl	–	2.6 ± 0.6	0.9 ± 0.2	0.6 ± 0.1
W+hf	–	12.7 ± 3.4	5.4 ± 1.4	4.8 ± 1.6
Z+l	–	1.1 ± 0.3	0.6 ± 0.2	0.6 ± 0.2
Z+cl	–	2.3 ± 0.8	1.2 ± 0.4	1.2 ± 0.4
Z+hf	–	33.4 ± 7.7	15.7 ± 3.7	15.3 ± 3.6
MJ	–	1.4 ± 1.4	0.2 ± 0.2	0.2 ± 0.2
Total	–	131.4 ± 18.6	45.0 ± 6.5	33.3 ± 4.8
Data	–	166.0 ± 12.9	49.0 ± 7.0	36.0 ± 6.0

Table 118: Table of prefit yields for 0-lepton 2 and 3-jet 2M-tag events in the dijet mass selection. The uncertainties are from the full prefit nusicance parameters (NPs) except the floating normalizations under the assumption that each NP is independent (uncorrelated).

Sample	2T-tag			
	$100 < p_{\mathrm{T}}^{V} < 120\ GeV$	$120 < p_{\mathrm{T}}^{V} < 160\ GeV$	$160 < p_{\mathrm{T}}^{V} < 200\ GeV$	$p_{\mathrm{T}}^{V} > 200\ GeV$
	2-jet			
VH	4.0 ± 0.4	5.8 ± 0.6	3.1 ± 0.4	3.1 ± 0.4
VV	12.4 ± 1.6	19.1 ± 2.6	9.0 ± 1.5	8.3 ± 1.8
$t\bar{t}$	81.4 ± 9.3	65.9 ± 8.6	9.2 ± 1.4	1.6 ± 0.4
s-top	18.8 ± 4.1	13.5 ± 2.3	2.3 ± 0.4	0.4 ± 0.1
W+l	0.2 ± 0.0	0.1 ± 0.0	0.0 ± 0.0	0.0 ± 0.0
W+cl	0.9 ± 0.1	0.5 ± 0.0	0.2 ± 0.0	0.1 ± 0.0
W+hf	26.2 ± 3.8	35.8 ± 6.9	10.9 ± 2.6	9.3 ± 2.9
Z+l	0.1 ± 0.0	0.1 ± 0.0	0.0 ± 0.0	0.0 ± 0.0
Z+cl	0.3 ± 0.0	0.4 ± 0.0	0.1 ± 0.0	0.1 ± 0.0
Z+hf	129.2 ± 9.1	141.3 ± 12.3	43.7 ± 4.1	29.8 ± 3.6
MJ	6.5 ± 6.3	2.4 ± 2.3	0.3 ± 0.2	0.1 ± 0.1
Total	279.9 ± 18.4	284.9 ± 22.9	78.7 ± 6.6	52.8 ± 6.1
Data	306.0 ± 17.5	312.0 ± 17.7	97.0 ± 9.8	43.0 ± 6.6
	3-jet			
VH	–	1.3 ± 0.2	0.9 ± 0.1	1.0 ± 0.1
VV	–	3.1 ± 0.5	2.4 ± 0.4	2.4 ± 0.4
$t\bar{t}$	–	48.4 ± 11.6	8.5 ± 2.1	1.8 ± 0.5
s-top	–	5.0 ± 0.9	0.8 ± 0.2	0.3 ± 0.1
W+l	–	0.0 ± 0.0	0.0 ± 0.0	0.0 ± 0.0
W+cl	–	0.1 ± 0.0	0.0 ± 0.0	0.0 ± 0.0
W+hf	–	6.6 ± 1.3	3.7 ± 0.9	3.5 ± 1.2
Z+l	–	0.0 ± 0.0	0.0 ± 0.0	0.0 ± 0.0
Z+cl	–	0.1 ± 0.0	0.0 ± 0.0	0.0 ± 0.0
Z+hf	–	28.9 ± 6.5	13.0 ± 3.0	11.6 ± 2.7
MJ	–	0.7 ± 0.7	0.1 ± 0.1	0.1 ± 0.1
Total	–	94.1 ± 14.6	29.6 ± 4.3	20.7 ± 3.3
Data	–	116.0 ± 10.8	25.0 ± 5.0	19.0 ± 4.4

Table 119: Table of prefit yields for 0-lepton 2 and 3-jet 2T-tag events in the dijet mass selection. The uncertainties are from the full prefit nusicance parameters (NPs) except the floating normalizations under the assumption that each NP is independent (uncorrelated).

Sample	1-tag	
	$p_{\mathrm{T}}^{V} < 120\ GeV$	$p_{\mathrm{T}}^{V} > 120\ GeV$
	2-jet	
VH	65.6 ± 5.0	19.6 ± 1.8
VV	3157.5 ± 88.4	649.9 ± 85.1
$t\bar{t}$	15159.5 ± 1385.1	3919.5 ± 355.8
s-top	16117.6 ± 5815.3	1543.2 ± 180.8
W+l	90688.6 ± 13716.3	10421.4 ± 1701.0
W+cl	92424.0 ± 7674.2	8865.1 ± 971.1
W+hf	30302.8 ± 6946.6	3920.3 ± 1092.2
Z+l	6142.9 ± 724.5	455.4 ± 67.1
Z+cl	2449.0 ± 0.2	151.2 ± 0.0
Z+hf	2962.2 ± 0.3	181.2 ± 0.0
MJ_e	19940.7 ± 1455.9	779.2 ± 378.7
MJ_μ	6547.5 ± 785.7	29.3
Total	285957.7 ± 21043.5	30935.2 ± 2740.4
Data	297618.0 ± 545.5	31777.0 ± 178.3
	3-jet	
VH	25.2 ± 2.1	9.1 ± 0.9
VV	1696.5 ± 47.5	356.4 ± 48.7
$t\bar{t}$	30222.6 ± 6312.2	6917.2 ± 1491.0
s-top	10635.8 ± 877.4	1433.0 ± 209.5
W+l	35828.7 ± 6717.9	4672.3 ± 924.0
W+cl	33883.6 ± 4838.1	3749.5 ± 604.8
W+hf	13295.2 ± 3610.8	1915.7 ± 570.5
Z+l	2690.4 ± 372.2	188.8 ± 5.3
Z+cl	1173.5 ± 0.1	79.0 ± 0.0
Z+hf	1385.1 ± 0.1	88.5 ± 0.0
MJ_e	9241.8 ± 653.9	355.9 ± 135.9
MJ_μ	4449.4 ± 2243.3	23.0
Total	144527.8 ± 12058.7	19788.4 ± 2152.3
Data	140060.0 ± 374.2	19649.0 ± 140.2

Table 120: Table of prefit yields for 1-lepton 2 and 3-jet 1-tag events in the dijet mass selection. The uncertainties are from the full prefit nusicance parameters (NPs) except the floating normalizations under the assumption that each NP is independent (uncorrelated).

Sample	2L-tag				
	$p_{\mathrm{T}}^{V} < 90\ GeV$	$90 < p_{\mathrm{T}}^{V} < 120\ GeV$	$120 < p_{\mathrm{T}}^{V} < 160\ GeV$	$160 < p_{\mathrm{T}}^{V} < 200\ GeV$	$p_{\mathrm{T}}^{V} > 200\ GeV$
	2-jet				
VH	13.8 ± 1.3	5.1 ± 0.5	3.7 ± 0.4	1.8 ± 0.2	2.1 ± 0.3
VV	125.3 ± 3.5	44.0 ± 1.2	25.0 ± 0.7	9.6 ± 2.0	10.2 ± 3.0
$t\bar{t}$	1680.8 ± 175.5	672.6 ± 60.7	361.4 ± 37.5	94.6 ± 10.0	52.3 ± 7.9
s-top	1080.4 ± 342.4	286.4 ± 82.3	106.6 ± 14.0	26.9 ± 2.8	16.6 ± 1.8
W+l	1653.8 ± 353.7	508.2 ± 110.5	196.1 ± 44.0	56.0 ± 13.0	47.2 ± 11.3
W+cl	2546.9 ± 313.7	748.5 ± 98.9	263.1 ± 37.9	68.5 ± 10.0	43.7 ± 6.7
W+hf	1982.2 ± 310.4	654.6 ± 99.2	269.6 ± 54.7	80.1 ± 20.5	77.7 ± 27.0
Z+l	112.1 ± 20.4	43.3 ± 7.6	10.3 ± 0.3	1.7 ± 0.0	0.7 ± 0.0
Z+cl	70.3 ± 0.0	25.5 ± 0.0	5.8 ± 0.0	1.0 ± 0.0	0.4 ± 0.0
Z+hf	155.6 ± 0.0	55.5 ± 0.0	12.7 ± 0.0	2.4 ± 0.0	1.0 ± 0.0
MJ$_e$	945.2 ± 790.5	241.5 ± 210.1	42.3 ± 39.6	9.7 ± 9.3	1.2 ± 1.5
MJ$_\mu$	434.5 ± 121.6	46.2 ± 12.9	3.9 ± 0.0	1.0	–
Total	10800.7 ± 1204.3	3331.5 ± 349.1	1300.7 ± 127.1	353.2 ± 38.4	253.2 ± 37.1
Data	11597.0 ± 107.7	3426.0 ± 58.5	1355.0 ± 36.8	375.0 ± 19.4	239.0 ± 15.5
	3-jet				
VH	3.9 ± 0.4	1.6 ± 0.2	1.3 ± 0.1	0.7 ± 0.1	1.0 ± 0.2
VV	58.0 ± 1.6	19.9 ± 0.6	11.5 ± 0.3	5.2 ± 0.1	5.7 ± 1.2
$t\bar{t}$	3691.9 ± 810.6	1092.5 ± 235.7	533.4 ± 119.7	162.9 ± 36.4	105.7 ± 26.8
s-top	743.0 ± 68.5	193.4 ± 18.0	85.4 ± 12.3	28.7 ± 4.9	23.9 ± 4.0
W+l	652.5 ± 159.3	176.0 ± 43.0	75.6 ± 18.9	24.9 ± 6.4	24.8 ± 6.5
W+cl	963.9 ± 161.9	255.9 ± 44.7	101.3 ± 18.9	31.4 ± 5.8	25.7 ± 4.7
W+hf	860.1 ± 181.3	232.3 ± 44.6	108.8 ± 25.3	40.2 ± 11.4	45.9 ± 16.5
Z+l	49.7 ± 1.4	15.0 ± 0.4	3.7 ± 0.1	0.8 ± 0.0	0.5 ± 0.0
Z+cl	35.3 ± 0.0	10.0 ± 0.0	2.5 ± 0.0	0.5 ± 0.0	0.3 ± 0.0
Z+hf	77.8 ± 0.0	21.8 ± 0.0	6.8 ± 0.0	1.2 ± 0.0	0.7 ± 0.0
MJ$_e$	313.2 ± 34.8	63.6 ± 12.2	11.5 ± 4.5	2.3 ± 0.0	0.7 ± 0.2
MJ$_\mu$	246.3 ± 169.2	13.9 ± 5.3	–	–	–
Total	7695.7 ± 920.6	2095.9 ± 263.8	941.9 ± 135.0	298.9 ± 43.8	234.8 ± 36.9
Data	7746.0 ± 88.0	2128.0 ± 46.1	1051.0 ± 32.4	313.0 ± 17.7	238.0 ± 15.4

Table 121: Table of prefit yields for 1-lepton 2 and 3-jet 2L-tag events in the dijet mass selection. The uncertainties are from the full prefit nusicance parameters (NPs) except the floating normalizations under the assumption that each NP is independent (uncorrelated).

Sample	2M-tag				
	$p_T^V < 90\ GeV$	$90 < p_T^V < 120\ GeV$	$120 < p_T^V < 160\ GeV$	$160 < p_T^V < 200\ GeV$	$p_T^V > 200\ GeV$
	2-jet				
VH	21.7 ± 1.8	7.9 ± 0.7	5.9 ± 0.5	2.9 ± 0.3	3.3 ± 0.4
VV	78.2 ± 6.2	27.5 ± 2.7	16.6 ± 2.4	6.6 ± 1.5	5.7 ± 1.7
$t\bar{t}$	2057.2 ± 204.6	800.7 ± 73.7	387.1 ± 40.6	72.4 ± 8.4	29.1 ± 4.4
s-top	975.5 ± 271.6	253.0 ± 66.2	88.8 ± 12.1	19.1 ± 2.2	10.5 ± 1.4
W+l	120.3 ± 34.9	37.0 ± 10.7	13.4 ± 4.0	3.6 ± 1.1	3.0 ± 0.9
W+cl	443.6 ± 73.3	131.3 ± 22.0	44.8 ± 7.7	11.0 ± 2.0	6.5 ± 1.1
W+hf	1298.7 ± 154.8	433.3 ± 53.4	183.0 ± 33.2	54.1 ± 12.9	51.0 ± 16.8
Z+l	8.4 ± 0.2	3.3 ± 0.1	0.7 ± 0.0	0.1 ± 0.0	0.0 ± 0.0
Z+cl	13.5 ± 0.0	5.0 ± 0.0	1.2 ± 0.0	0.1 ± 0.0	0.0 ± 0.0
Z+hf	111.8 ± 4.6	40.8 ± 2.7	9.8 ± 0.4	1.5 ± 0.1	0.7 ± 0.0
MJ_e	399.3 ± 338.2	148.0 ± 134.9	25.6 ± 26.0	4.0 ± 4.2	1.1 ± 0.1
MJ_μ	241.4 ± 101.4	17.6 ± 7.4	–	–	–
Total	5769.6 ± 550.4	1905.2 ± 189.2	776.9 ± 69.3	175.5 ± 18.4	110.9 ± 18.7
Data	6344.0 ± 79.6	2053.0 ± 45.3	868.0 ± 29.5	199.0 ± 14.1	116.0 ± 10.8
	3-jet				
VH	5.8 ± 0.6	2.6 ± 0.2	2.1 ± 0.2	1.3 ± 0.1	1.5 ± 0.2
VV	26.5 ± 0.7	10.1 ± 0.3	6.3 ± 0.2	3.0 ± 0.5	3.2 ± 0.5
$t\bar{t}$	4746.3 ± 1052.6	1310.8 ± 285.4	547.4 ± 125.6	119.9 ± 27.3	59.1 ± 15.0
s-top	698.2 ± 68.9	170.1 ± 16.7	70.0 ± 9.1	19.5 ± 3.1	16.0 ± 2.7
W+l	44.2 ± 1.2	12.1 ± 0.3	5.1 ± 0.1	1.5 ± 0.0	1.4 ± 0.5
W+cl	159.4 ± 32.7	42.9 ± 9.3	17.0 ± 3.6	4.8 ± 1.0	3.6 ± 0.8
W+hf	515.6 ± 85.3	154.7 ± 22.8	77.1 ± 15.2	27.6 ± 7.1	30.0 ± 10.2
Z+l	3.2 ± 0.1	1.1 ± 0.0	0.3 ± 0.0	0.1 ± 0.0	0.0 ± 0.0
Z+cl	6.3 ± 0.0	1.9 ± 0.0	0.4 ± 0.0	0.1 ± 0.0	0.0 ± 0.0
Z+hf	56.1 ± 0.0	18.5 ± 0.0	5.0 ± 0.0	1.2 ± 0.0	0.5 ± 0.0
MJ_e	160.3 ± 18.8	32.1 ± 7.5	5.8 ± 3.0	2.1 ± 1.7	–
MJ_μ	127.4 ± 17.8	12.0	–	–	–
Total	6549.2 ± 1072.3	1768.8 ± 291.3	736.5 ± 129.2	181.0 ± 29.6	115.4 ± 19.7
Data	6863.0 ± 82.8	1925.0 ± 43.9	780.0 ± 27.9	181.0 ± 13.5	123.0 ± 11.1

Table 122: Table of prefit yields for 1-lepton 2 and 3-jet 2M-tag events in the dijet mass selection. The uncertainties are from the full prefit nusicance parameters (NPs) except the floating normalizations under the assumption that each NP is independent (uncorrelated).

Sample	2T-tag				
	$p_T^V < 90\ GeV$	$90 < p_T^V < 120\ GeV$	$120 < p_T^V < 160\ GeV$	$160 < p_T^V < 200\ GeV$	$p_T^V > 200\ GeV$
	2-jet				
VH	24.3 ± 2.3	8.9 ± 0.8	6.8 ± 0.6	3.6 ± 0.4	3.7 ± 0.5
VV	61.2 ± 6.4	22.6 ± 2.6	13.8 ± 2.3	5.8 ± 1.5	5.0 ± 1.7
$t\bar{t}$	1942.6 ± 196.4	731.6 ± 65.9	316.5 ± 36.1	39.2 ± 4.9	8.5 ± 1.3
s-top	794.4 ± 215.6	192.6 ± 51.6	66.1 ± 10.4	11.7 ± 1.8	4.3 ± 0.7
W+l	3.8 ± 0.1	1.0 ± 0.0	0.3 ± 0.0	0.1 ± 0.0	0.1 ± 0.0
W+cl	22.6 ± 4.7	6.8 ± 1.2	2.1 ± 0.5	0.5 ± 0.2	0.4 ± 0.1
W+hf	678.8 ± 70.0	248.8 ± 27.4	117.2 ± 20.8	34.4 ± 8.2	33.2 ± 10.8
Z+l	0.2 ± 0.0	0.1 ± 0.0	0.0 ± 0.0	0.0 ± 0.0	0.0 ± 0.0
Z+cl	0.8 ± 0.0	0.2 ± 0.0	0.1 ± 0.0	0.0 ± 0.0	–
Z+hf	72.4 ± 4.4	28.2 ± 2.5	6.2 ± 0.9	1.5 ± 0.3	0.5 ± 0.1
MJ_e	195.3 ± 173.8	83.9 ± 95.0	11.5 ± 16.0	1.9 ± 3.9	1.1 ± 2.0
MJ_μ	100.5 ± 60.3	9.3 ± 5.7	–	–	–
Total	3896.7 ± 377.1	1334.0 ± 141.4	540.5 ± 53.3	98.9 ± 12.4	56.7 ± 11.8
Data	4560.0 ± 67.5	1448.0 ± 38.1	591.0 ± 24.3	112.0 ± 10.6	59.0 ± 7.7
	3-jet				
VH	6.8 ± 0.7	2.9 ± 0.3	2.4 ± 0.3	1.5 ± 0.2	1.8 ± 0.3
VV	16.5 ± 0.5	7.2 ± 0.2	5.8 ± 0.2	2.8 ± 0.5	2.7 ± 0.5
$t\bar{t}$	4874.0 ± 1095.3	1247.2 ± 275.6	443.2 ± 105.1	57.0 ± 14.9	16.1 ± 4.2
s-top	581.9 ± 64.6	133.0 ± 15.8	48.8 ± 7.5	10.0 ± 1.8	7.1 ± 1.2
W+l	1.2 ± 0.0	0.4 ± 0.0	0.1 ± 0.0	0.0 ± 0.0	0.0 ± 0.0
W+cl	7.9 ± 0.0	2.3 ± 0.0	0.9 ± 0.0	0.2 ± 0.0	0.1 ± 0.0
W+hf	274.3 ± 38.1	84.2 ± 12.1	46.9 ± 8.6	18.6 ± 4.6	20.0 ± 6.8
Z+l	0.0 ± 0.0	0.0 ± 0.0	0.0 ± 0.0	0.0 ± 0.0	0.0 ± 0.0
Z+cl	0.2 ± 0.0	0.1 ± 0.0	0.0 ± 0.0	0.0 ± 0.0	0.0 ± 0.0
Z+hf	36.9 ± 0.0	11.7 ± 0.0	3.7 ± 0.0	0.9 ± 0.2	0.3 ± 0.1
MJ_e	85.8 ± 6.2	15.7 ± 4.6	2.3 ± 1.0	0.7 ± 0.9	0.3 ± 0.4
MJ_μ	66.1 ± 9.3	–	–	0.6 ± 0.1	–
Total	5951.8 ± 1112.8	1504.7 ± 281.1	554.3 ± 108.6	92.4 ± 16.6	48.4 ± 8.8
Data	6196.0 ± 78.7	1624.0 ± 40.3	590.0 ± 24.3	101.0 ± 10.0	53.0 ± 7.3

Table 123: Table of prefit yields for 1-lepton 2 and 3-jet 2T-tag events in the dijet mass selection. The uncertainties are from the full prefit nusicance parameters (NPs) except the floating normalizations under the assumption that each NP is independent (uncorrelated).

Sample	1-tag	
	$p_T^V < 120\ GeV$	$p_T^V > 120\ GeV$
	2-jet	
VH	16.3 ± 1.2	4.5 ± 0.5
VV	614.4 ± 17.2	83.7 ± 14.5
$t\bar{t}$	493.0 ± 23.5	23.5 ± 0.0
s-top	53.6 ± 1.5	3.8 ± 0.1
W+l	69.8 ± 2.0	1.1 ± 0.0
W+cl	37.5 ± 0.0	2.9 ± 0.0
W+hf	20.3 ± 0.0	2.2 ± 0.0
Z+l	19153.6 ± 2437.4	1796.9 ± 208.6
Z+cl	9818.8 ± 810.9	854.4 ± 69.0
Z+hf	13260.2 ± 1310.8	1172.5 ± 126.5
MJ	606.5 ± 591.4	4.7 ± 4.6
Total	44144.1 ± 3561.5	3950.2 ± 284.9
Data	44551.0 ± 211.1	4052.0 ± 63.7
	3-jet	
VH	5.7 ± 0.6	2.1 ± 0.3
VV	252.0 ± 21.0	47.2 ± 7.5
$t\bar{t}$	279.2 ± 57.0	14.8 ± 3.0
s-top	19.0 ± 0.5	1.9 ± 0.1
W+l	7.7 ± 0.2	0.9 ± 0.0
W+cl	11.6 ± 0.0	1.4 ± 0.0
W+hf	9.4 ± 0.0	0.9 ± 0.0
Z+l	5602.5 ± 852.3	769.0 ± 99.2
Z+cl	3157.5 ± 875.6	381.5 ± 104.3
Z+hf	4107.3 ± 948.7	491.8 ± 112.4
MJ	172.3 ± 168.0	2.4 ± 2.3
Total	13624.1 ± 1771.5	1713.8 ± 192.3
Data	13595.0 ± 116.6	1631.0 ± 40.4

Table 124: Table of prefit yields for 2-lepton 2 and 3-jet 1-tag events in the dijet mass selection. The uncertainties are from the full prefit nusicance parameters (NPs) except the floating normalizations under the assumption that each NP is independent (uncorrelated).

Sample	2L-tag				
	$p_T^V < 90\ GeV$	$90 < p_T^V < 120\ GeV$	$120 < p_T^V < 160\ GeV$	$160 < p_T^V < 200\ GeV$	$p_T^V > 200\ GeV$
	2-jet				
VH	3.6 ± 0.3	1.0 ± 0.1	0.7 ± 0.1	0.3 ± 0.0	0.4 ± 0.0
VV	46.2 ± 3.8	7.8 ± 0.6	4.7 ± 0.4	1.8 ± 0.3	1.7 ± 0.4
$t\bar{t}$	117.5 ± 7.6	18.6 ± 1.2	4.4 ± 0.5	0.3 ± 0.1	0.0 ± 0.0
s-top	4.8 ± 0.1	0.9 ± 0.0	0.5 ± 0.0	0.0 ± 0.0	0.1 ± 0.0
W+l	0.6 ± 0.0	0.1 ± 0.0	0.0 ± 0.0	0.0 ± 0.0	0.0 ± 0.0
W+cl	0.9 ± 0.0	0.2 ± 0.0	0.0 ± 0.0	0.0 ± 0.0	0.0 ± 0.0
W+hf	2.4 ± 0.0	0.4 ± 0.0	0.1 ± 0.0	0.0 ± 0.0	0.0 ± 0.0
Z+l	352.1 ± 69.6	67.3 ± 12.5	27.6 ± 5.2	7.6 ± 1.5	7.0 ± 1.5
Z+cl	280.4 ± 38.0	54.0 ± 6.0	20.9 ± 2.4	5.8 ± 0.7	4.5 ± 0.6
Z+hf	926.5 ± 80.3	195.9 ± 16.9	75.1 ± 7.1	18.7 ± 1.9	14.7 ± 1.9
MJ	45.9 ± 44.7	2.4 ± 2.3	0.4	0.1	–
Total	1780.8 ± 165.9	348.6 ± 29.3	134.4 ± 12.1	34.6 ± 3.5	28.5 ± 3.3
Data	2009.0 ± 44.8	378.0 ± 19.4	153.0 ± 12.4	33.0 ± 5.7	42.0 ± 6.5
	3-jet				
VH	0.9 ± 0.1	0.3 ± 0.0	0.3 ± 0.0	0.2 ± 0.0	0.2 ± 0.0
VV	12.4 ± 1.3	2.9 ± 0.4	1.7 ± 0.3	0.9 ± 0.2	1.1 ± 0.2
$t\bar{t}$	52.0 ± 10.8	8.2 ± 1.7	2.2 ± 0.5	0.3 ± 0.1	–
s-top	1.8 ± 0.1	0.5 ± 0.0	0.1 ± 0.0	0.2 ± 0.1	–
W+l	0.2 ± 0.0	0.0 ± 0.0	0.0 ± 0.0	0.0 ± 0.0	0.0 ± 0.0
W+cl	0.4 ± 0.0	0.0 ± 0.0	0.0 ± 0.0	0.0 ± 0.0	0.0 ± 0.0
W+hf	0.3 ± 0.0	0.0 ± 0.0	0.0 ± 0.0	0.0 ± 0.0	0.0 ± 0.0
Z+l	100.0 ± 21.2	20.9 ± 4.2	9.9 ± 1.9	3.2 ± 0.7	3.5 ± 0.8
Z+cl	90.1 ± 26.7	18.5 ± 5.3	8.2 ± 2.4	2.7 ± 0.8	2.6 ± 0.8
Z+hf	257.1 ± 58.7	58.5 ± 12.6	26.8 ± 5.9	7.7 ± 1.7	7.5 ± 1.8
MJ	6.0 ± 5.8	0.1	0.1 ± 0.1	–	–
Total	521.3 ± 79.4	110.1 ± 15.8	49.3 ± 7.3	15.1 ± 2.3	14.9 ± 2.4
Data	612.0 ± 24.7	128.0 ± 11.3	64.0 ± 8.0	12.0 ± 3.5	19.0 ± 4.4

Table 125: Table of prefit yields for 2-lepton 2 and 3-jet 2L-tag events in the dijet mass selection. The uncertainties are from the full prefit nusicance parameters (NPs) except the floating normalizations under the assumption that each NP is independent (uncorrelated).

Sample	2M-tag				
	$p_T^V < 90\ GeV$	$90 < p_T^V < 120\ GeV$	$120 < p_T^V < 160\ GeV$	$160 < p_T^V < 200\ GeV$	$p_T^V > 200\ GeV$
	2-jet				
VH	5.8 ± 0.5	1.6 ± 0.1	1.2 ± 0.1	0.6 ± 0.1	0.6 ± 0.1
VV	46.2 ± 4.0	7.6 ± 0.7	4.5 ± 0.5	1.8 ± 0.3	1.7 ± 0.3
$t\bar{t}$	179.9 ± 11.8	31.2 ± 2.0	6.7 ± 0.6	0.3 ± 0.1	0.0 ± 0.0
s-top	5.7 ± 0.2	1.5 ± 0.2	0.4 ± 0.1	0.0 ± 0.0	–
W+l	0.0 ± 0.0	0.0 ± 0.0	0.0 ± 0.0	0.0 ± 0.0	0.0 ± 0.0
W+cl	0.2 ± 0.0	0.0 ± 0.0	0.0 ± 0.0	0.0 ± 0.0	0.0 ± 0.0
W+hf	0.7 ± 0.0	0.1 ± 0.0	0.0 ± 0.0	–	0.0 ± 0.0
Z+l	23.3 ± 6.4	4.1 ± 1.1	1.6 ± 0.4	0.4 ± 0.1	0.4 ± 0.1
Z+cl	46.4 ± 8.0	8.6 ± 1.3	3.3 ± 0.5	0.9 ± 0.1	0.6 ± 0.1
Z+hf	803.1 ± 51.0	168.6 ± 11.9	64.4 ± 4.8	15.0 ± 1.3	9.8 ± 1.1
MJ	16.3 ± 15.9	0.4 ± 0.4	0.1	–	–
Total	1127.6 ± 63.0	223.7 ± 14.1	82.4 ± 5.5	19.0 ± 1.5	13.1 ± 1.4
Data	1284.0 ± 35.8	264.0 ± 16.2	83.0 ± 9.1	23.0 ± 4.8	9.0 ± 3.0
	3-jet				
VH	1.4 ± 0.2	0.5 ± 0.1	0.4 ± 0.1	0.3 ± 0.0	0.3 ± 0.0
VV	9.7 ± 1.4	1.8 ± 0.3	1.5 ± 0.2	0.7 ± 0.2	0.7 ± 0.1
$t\bar{t}$	77.4 ± 15.8	12.4 ± 2.6	2.5 ± 0.6	0.1 ± 0.0	0.0 ± 0.0
s-top	2.5 ± 0.1	0.7 ± 0.1	0.1 ± 0.0	–	0.0 ± 0.0
W+l	0.0 ± 0.0	0.0 ± 0.0	0.0 ± 0.0	0.0 ± 0.0	0.0 ± 0.0
W+cl	0.1 ± 0.0	0.0 ± 0.0	0.0 ± 0.0	0.0 ± 0.0	0.0 ± 0.0
W+hf	0.2 ± 0.0	0.0 ± 0.0	0.0 ± 0.0	0.0 ± 0.0	0.0 ± 0.0
Z+l	6.4 ± 1.8	1.2 ± 0.3	0.6 ± 0.2	0.2 ± 0.0	0.2 ± 0.1
Z+cl	13.2 ± 4.1	3.0 ± 0.9	1.3 ± 0.4	0.4 ± 0.1	0.4 ± 0.1
Z+hf	216.2 ± 47.7	46.7 ± 9.9	24.5 ± 5.2	6.7 ± 1.4	5.3 ± 1.2
MJ	2.9 ± 2.8	0.1	–	–	–
Total	330.0 ± 51.8	66.5 ± 10.6	30.9 ± 5.3	8.2 ± 1.5	6.9 ± 1.3
Data	401.0 ± 20.0	80.0 ± 8.9	34.0 ± 5.8	6.0 ± 2.4	7.0 ± 2.6

Table 126: Table of prefit yields for 2-lepton 2 and 3-jet 2M-tag events in the dijet mass selection. The uncertainties are from the full prefit nusicance parameters (NPs) except the floating normalizations under the assumption that each NP is independent (uncorrelated).

Sample	2T-tag $p_T^V < 90\ GeV$	$90 < p_T^V < 120\ GeV$	$120 < p_T^V < 160\ GeV$	$160 < p_T^V < 200\ GeV$	$p_T^V > 200\ GeV$
	2-jet				
VH	6.6 ± 0.6	1.8 ± 0.2	1.5 ± 0.2	0.7 ± 0.1	0.7 ± 0.1
VV	42.1 ± 4.1	6.9 ± 0.7	4.7 ± 0.6	2.1 ± 0.3	1.8 ± 0.3
$t\bar{t}$	196.6 ± 12.9	32.3 ± 1.5	7.1 ± 0.7	0.3 ± 0.0	–
s-top	4.7 ± 0.1	1.3 ± 0.2	0.2 ± 0.0	0.1 ± 0.0	0.1 ± 0.0
W+l	0.0 ± 0.0	–	–	–	–
W+hf	0.7 ± 0.0	0.3 ± 0.0	0.0 ± 0.0	0.0 ± 0.0	–
Z+l	0.4 ± 0.0	0.1 ± 0.0	0.0 ± 0.0	0.0 ± 0.0	0.0 ± 0.0
Z+cl	1.4 ± 0.0	0.2 ± 0.0	0.1 ± 0.0	0.0 ± 0.0	0.0 ± 0.0
Z+hf	606.2 ± 37.8	136.3 ± 8.9	52.6 ± 4.0	11.8 ± 1.0	7.5 ± 0.8
MJ	10.4 ± 10.1	0.2 ± 0.2	0.1 ± 0.1	–	–
Total	869.0 ± 44.0	179.4 ± 9.7	66.3 ± 4.5	15.1 ± 1.1	10.1 ± 1.0
Data	980.0 ± 31.3	209.0 ± 14.5	65.0 ± 8.1	17.0 ± 4.1	12.0 ± 3.5
	3-jet				
VH	1.6 ± 0.2	0.6 ± 0.1	0.5 ± 0.1	0.3 ± 0.0	0.3 ± 0.0
VV	7.9 ± 1.3	2.0 ± 0.3	1.4 ± 0.2	0.8 ± 0.1	0.7 ± 0.1
$t\bar{t}$	85.6 ± 17.7	14.4 ± 3.0	2.7 ± 0.7	0.0 ± 0.0	0.0 ± 0.0
s-top	1.9 ± 0.1	0.3 ± 0.0	0.3 ± 0.1	0.0 ± 0.0	–
W+l	0.0 ± 0.0	–	–	–	–
W+hf	0.1 ± 0.0	–	0.0 ± 0.0	0.0 ± 0.0	–
Z+l	0.1 ± 0.0	0.0 ± 0.0	0.0 ± 0.0	0.0 ± 0.0	0.0 ± 0.0
Z+cl	0.3 ± 0.0	0.1 ± 0.0	0.1 ± 0.0	0.0 ± 0.0	0.0 ± 0.0
Z+hf	161.8 ± 33.6	36.8 ± 7.9	18.9 ± 4.0	5.0 ± 1.1	3.9 ± 0.9
MJ	1.8 ± 1.7	0.1	–	–	–
Total	261.1 ± 38.6	54.2 ± 8.6	23.9 ± 4.1	6.2 ± 1.1	5.1 ± 0.9
Data	307.0 ± 17.5	55.0 ± 7.4	29.0 ± 5.4	9.0 ± 3.0	3.0 ± 1.7

Table 127: Table of prefit yields for 2-lepton 2 and 3-jet 2T-tag events in the dijet mass selection. The uncertainties are from the full prefit nusicance parameters (NPs) except the floating normalizations under the assumption that each NP is independent (uncorrelated).

AJ.2 Dijet Mass Analysis: Postfit

Sample	1-tag	
	$100 < p_{\mathrm{T}}^{V} < 120\ GeV$	$p_{\mathrm{T}}^{V} > 120\ GeV$
	2-jet	
VH	9.8 ± 4.3	23.4 ± 10.3
VV	233.4 ± 5.9	547.0 ± 13.8
$t\bar{t}$	829.0 ± 68.6	1387.1 ± 115.5
s-top	631.3 ± 78.9	487.6 ± 28.6
W+l	5472.5 ± 281.5	4836.6 ± 280.2
W+cl	2214.7 ± 154.0	2426.3 ± 179.9
W+hf	648.3 ± 145.2	901.6 ± 153.1
Z+l	3700.9 ± 164.0	6724.3 ± 300.6
Z+cl	1482.6 ± 187.6	2635.3 ± 322.1
Z+hf	2465.5 ± 91.6	4266.9 ± 163.3
MJ	611.4 ± 398.3	99.5 ± 151.3
Total	18299.4 ± 202.1	24335.6 ± 148.3
Data	18343.0 ± 135.4	24289.0 ± 155.8
$\frac{\text{Sim}-\text{Data}}{\sigma}$	-0.18	0.22
	3-jet	
VH	–	7.0 ± 3.1
VV	–	167.1 ± 4.2
$t\bar{t}$	–	1247.9 ± 86.6
s-top	–	183.5 ± 19.2
W+l	–	1209.7 ± 74.9
W+cl	–	639.5 ± 51.9
W+hf	–	306.7 ± 60.5
Z+l	–	1543.0 ± 84.2
Z+cl	–	827.9 ± 94.2
Z+hf	–	931.8 ± 54.5
MJ	–	77.9 ± 64.3
Total	–	7142.2 ± 72.6
Data	–	7148.0 ± 84.5
$\frac{\text{Sim}-\text{Data}}{\sigma}$	–	-0.05

Table 128: Table of post unconditional fit yields for 0-lepton 2 and 3-jet 1-tag events in the dijet mass selection. The uncertainties are the full postfit errors including all nusicance parameters with priors, floating normalizations, and the correlations deduced from the data. The difference in the data and the postfit simulation is compared to σ which is obtained from the sum in simulation as the sum in quadrature of the postfit and Poissonian error.

Sample	2L-tag			
	$100 < p_{\mathrm{T}}^{V} < 120\ GeV$	$120 < p_{\mathrm{T}}^{V} < 160\ GeV$	$160 < p_{\mathrm{T}}^{V} < 200\ GeV$	$p_{\mathrm{T}}^{V} > 200\ GeV$
	2-jet			
VH	2.8 ± 1.2	4.0 ± 1.7	2.1 ± 0.9	2.3 ± 1.0
VV	17.7 ± 0.8	24.4 ± 1.3	11.7 ± 1.4	11.4 ± 1.8
$t\bar{t}$	111.7 ± 9.1	115.6 ± 9.4	28.3 ± 2.4	13.7 ± 1.4
s-top	47.3 ± 5.2	30.2 ± 1.9	6.0 ± 0.4	2.0 ± 0.1
W+l	163.9 ± 12.4	99.2 ± 8.5	26.3 ± 2.5	16.8 ± 1.7
W+cl	106.9 ± 7.5	75.3 ± 5.1	20.0 ± 1.4	11.1 ± 0.9
W+hf	50.7 ± 8.7	57.4 ± 8.5	16.4 ± 2.4	12.6 ± 2.1
Z+l	91.9 ± 7.5	104.1 ± 8.3	36.9 ± 3.0	32.5 ± 2.8
Z+cl	57.1 ± 6.3	65.3 ± 7.2	23.2 ± 2.5	17.5 ± 2.0
Z+hf	219.8 ± 9.7	244.6 ± 11.3	81.6 ± 3.9	62.0 ± 4.4
MJ	17.1 ± 14.4	13.9 ± 10.5	1.7 ± 1.3	1.1 ± 0.8
Total	886.9 ± 17.2	833.9 ± 14.1	254.2 ± 4.7	183.0 ± 5.2
Data	887.0 ± 29.8	856.0 ± 29.3	239.0 ± 15.5	185.0 ± 13.6
$\frac{\text{Sim}-\text{Data}}{\sigma}$	-0.0	-0.69	0.91	-0.14
	3-jet			
VH	–	0.8 ± 0.4	0.6 ± 0.3	0.7 ± 0.3
VV	–	5.0 ± 0.3	2.9 ± 0.4	2.9 ± 0.5
$t\bar{t}$	–	86.7 ± 6.0	27.2 ± 2.1	14.1 ± 1.3
s-top	–	9.9 ± 1.1	2.7 ± 0.4	1.9 ± 0.3
W+l	–	18.9 ± 1.8	7.4 ± 0.7	6.0 ± 0.6
W+cl	–	16.1 ± 1.2	6.4 ± 0.5	4.6 ± 0.4
W+hf	–	14.1 ± 2.5	6.1 ± 1.1	6.0 ± 1.3
Z+l	–	18.3 ± 1.6	9.7 ± 0.8	10.5 ± 1.0
Z+cl	–	16.5 ± 1.7	8.6 ± 0.9	8.4 ± 0.9
Z+hf	–	41.4 ± 2.8	20.0 ± 1.4	21.3 ± 1.7
MJ	–	1.4 ± 2.0	0.3 ± 0.5	0.2 ± 0.2
Total	–	229.1 ± 5.4	92.0 ± 2.0	76.8 ± 2.2
Data	–	221.0 ± 14.9	78.0 ± 8.8	44.0 ± 6.6
$\frac{\text{Sim}-\text{Data}}{\sigma}$	–	0.51	1.43	3.63

Table 129: Table of post unconditional fit yields for 0-lepton 2 and 3-jet 2L-tag events in the dijet mass selection. The uncertainties are the full postfit errors including all nusicance parameters with priors, floating normalizations, and the correlations deduced from the data. The difference in the data and the postfit simulation is compared to σ which is obtained from the sum in simulation as the sum in quadrature of the postfit and Poissonian error.

Sample	2M-tag			
	$100 < p_{\mathrm{T}}^{V} < 120\ GeV$	$120 < p_{\mathrm{T}}^{V} < 160\ GeV$	$160 < p_{\mathrm{T}}^{V} < 200\ GeV$	$p_{\mathrm{T}}^{V} > 200\ GeV$
	2-jet			
VH	4.5 ± 1.9	6.4 ± 2.7	3.4 ± 1.4	3.5 ± 1.5
VV	15.0 ± 1.1	22.6 ± 2.2	10.5 ± 1.3	10.1 ± 1.6
$t\bar{t}$	126.6 ± 10.2	123.5 ± 9.2	23.2 ± 1.9	7.8 ± 0.8
s-top	35.7 ± 3.6	24.8 ± 2.5	4.5 ± 0.5	1.0 ± 0.1
W+l	14.9 ± 1.7	7.8 ± 1.1	2.0 ± 0.3	1.1 ± 0.2
W+cl	24.3 ± 1.7	13.8 ± 0.9	3.4 ± 0.2	1.9 ± 0.2
W+hf	32.1 ± 5.3	37.8 ± 5.6	11.3 ± 1.7	8.9 ± 1.4
Z+l	5.8 ± 0.9	6.4 ± 0.9	2.2 ± 0.3	1.9 ± 0.3
Z+cl	9.0 ± 0.8	10.0 ± 0.9	3.2 ± 0.3	2.7 ± 0.3
Z+hf	177.5 ± 7.9	201.9 ± 8.6	62.0 ± 2.8	44.2 ± 2.5
MJ	8.2 ± 6.8	6.6 ± 5.0	0.7 ± 0.5	0.4 ± 0.3
Total	453.6 ± 9.3	461.6 ± 8.7	126.4 ± 2.9	83.5 ± 2.9
Data	477.0 ± 21.8	438.0 ± 20.9	146.0 ± 12.1	86.0 ± 9.3
$\frac{\text{Sim}-\text{Data}}{\sigma}$	-1.01	1.02	-1.69	-0.26
	3-jet			
VH	–	1.4 ± 0.6	1.0 ± 0.4	1.1 ± 0.5
VV	–	3.5 ± 0.4	2.4 ± 0.4	2.2 ± 0.4
$t\bar{t}$	–	86.3 ± 5.6	19.7 ± 1.5	7.9 ± 0.7
s-top	–	7.4 ± 0.8	2.2 ± 0.3	1.3 ± 0.2
W+l	–	1.4 ± 0.2	0.6 ± 0.1	0.4 ± 0.1
W+cl	–	2.8 ± 0.2	1.0 ± 0.1	0.7 ± 0.1
W+hf	–	10.1 ± 2.0	4.7 ± 0.9	4.2 ± 0.9
Z+l	–	1.3 ± 0.2	0.6 ± 0.1	0.6 ± 0.1
Z+cl	–	2.4 ± 0.2	1.3 ± 0.1	1.3 ± 0.1
Z+hf	–	35.3 ± 2.6	17.0 ± 1.3	16.1 ± 1.3
MJ	–	0.8 ± 1.1	0.1 ± 0.2	0.1 ± 0.1
Total	–	152.6 ± 4.8	50.6 ± 1.7	35.7 ± 1.4
Data	–	166.0 ± 12.9	49.0 ± 7.0	36.0 ± 6.0
$\frac{\text{Sim}-\text{Data}}{\sigma}$	–	-1.01	0.21	-0.04

Table 130: Table of post unconditional fit yields for 0-lepton 2 and 3-jet 2M-tag events in the dijet mass selection. The uncertainties are the full postfit errors including all nusicance parameters with priors, floating normalizations, and the correlations deduced from the data. The difference in the data and the postfit simulation is compared to σ which is obtained from the sum in simulation as the sum in quadrature of the postfit and Poissonian error.

Sample	2T-tag			
	$100 < p_{\mathrm{T}}^{V} < 120\ GeV$	$120 < p_{\mathrm{T}}^{V} < 160\ GeV$	$160 < p_{\mathrm{T}}^{V} < 200\ GeV$	$p_{\mathrm{T}}^{V} > 200\ GeV$
	2-jet			
VH	5.1 ± 2.1	7.4 ± 3.1	3.9 ± 1.7	3.9 ± 1.7
VV	13.1 ± 1.2	20.8 ± 2.2	9.9 ± 1.3	9.3 ± 1.6
$t\bar{t}$	114.6 ± 9.1	96.8 ± 7.3	13.8 ± 1.2	2.2 ± 0.3
s-top	24.9 ± 2.6	16.2 ± 2.2	2.6 ± 0.3	0.5 ± 0.1
W+l	0.2 ± 0.0	0.1 ± 0.0	0.0 ± 0.0	0.0 ± 0.0
W+cl	1.0 ± 0.1	0.5 ± 0.0	0.2 ± 0.0	0.1 ± 0.0
W+hf	20.9 ± 3.4	28.9 ± 4.8	8.4 ± 1.3	6.9 ± 1.2
Z+l	0.1 ± 0.0	0.1 ± 0.0	0.0 ± 0.0	0.0 ± 0.0
Z+cl	0.3 ± 0.0	0.3 ± 0.0	0.1 ± 0.0	0.1 ± 0.0
Z+hf	145.6 ± 6.6	157.1 ± 7.5	48.7 ± 2.3	32.2 ± 1.9
MJ	5.9 ± 4.9	2.9 ± 2.2	0.3 ± 0.2	0.1 ± 0.1
Total	331.6 ± 8.1	331.1 ± 7.7	88.0 ± 2.6	55.5 ± 2.6
Data	306.0 ± 17.5	312.0 ± 17.7	97.0 ± 9.8	43.0 ± 6.6
$\frac{\text{Sim}-\text{Data}}{\sigma}$	1.29	0.97	-0.93	1.58
	3-jet			
VH	–	1.6 ± 0.7	1.1 ± 0.5	1.3 ± 0.6
VV	–	3.0 ± 0.4	2.2 ± 0.3	2.2 ± 0.4
$t\bar{t}$	–	65.7 ± 4.1	11.0 ± 0.9	2.2 ± 0.3
s-top	–	5.2 ± 0.7	0.9 ± 0.1	0.3 ± 0.1
W+l	–	0.0 ± 0.0	0.0 ± 0.0	0.0 ± 0.0
W+cl	–	0.1 ± 0.0	0.0 ± 0.0	0.0 ± 0.0
W+hf	–	5.9 ± 1.1	3.4 ± 0.6	3.2 ± 0.7
Z+l	–	0.0 ± 0.0	0.0 ± 0.0	0.0 ± 0.0
Z+cl	–	0.1 ± 0.0	0.0 ± 0.0	0.0 ± 0.0
Z+hf	–	30.8 ± 2.4	13.9 ± 1.1	12.2 ± 1.0
MJ	–	0.4 ± 0.5	0.1 ± 0.1	0.0 ± 0.0
Total	–	112.8 ± 3.8	32.6 ± 1.2	21.6 ± 1.2
Data	–	116.0 ± 10.8	25.0 ± 5.0	19.0 ± 4.4
$\frac{\text{Sim}-\text{Data}}{\sigma}$	–	-0.29	1.3	0.54

Table 131: Table of post unconditional fit yields for 0-lepton 2 and 3-jet 2T-tag events in the dijet mass selection. The uncertainties are the full postfit errors including all nusicance parameters with priors, floating normalizations, and the correlations deduced from the data. The difference in the data and the postfit simulation is compared to σ which is obtained from the sum in simulation as the sum in quadrature of the postfit and Poissonian error.

Sample	1-tag $p_T^V < 120\ GeV$	1-tag $p_T^V > 120\ GeV$
	2-jet	
VH	81.4 ± 35.6	23.9 ± 10.5
VV	3156.9 ± 79.9	693.3 ± 74.4
$t\bar{t}$	17626.7 ± 1032.7	4641.9 ± 279.3
s-top	23120.3 ± 2993.2	1716.2 ± 111.8
W+l	93688.2 ± 5581.4	10485.9 ± 640.4
W+cl	102819.8 ± 6418.5	9640.4 ± 679.1
W+hf	20000.3 ± 4073.5	2666.6 ± 428.6
Z+l	6207.6 ± 258.5	430.5 ± 24.9
Z+cl	2128.2 ± 261.5	131.4 ± 16.1
Z+hf	3165.5 ± 167.0	193.6 ± 10.2
MJ_e	19140.2 ± 1117.5	1098.3 ± 354.4
MJ_μ	6471.4 ± 776.9	29.3
Total	297606.5 ± 573.5	31751.3 ± 178.9
Data	297618.0 ± 545.5	31777.0 ± 178.3
$\frac{\text{Sim}-\text{Data}}{\sigma}$	-0.01	-0.1
	3-jet	
VH	32.0 ± 14.1	11.2 ± 5.0
VV	1696.2 ± 42.9	341.5 ± 40.5
$t\bar{t}$	31046.4 ± 979.5	7234.5 ± 318.0
s-top	11353.1 ± 688.5	1386.7 ± 175.8
W+l	34891.0 ± 2023.0	4646.3 ± 277.2
W+cl	34853.5 ± 2360.9	3894.6 ± 304.0
W+hf	7863.3 ± 1556.7	1471.7 ± 285.0
Z+l	2632.5 ± 144.0	188.7 ± 4.8
Z+cl	1019.7 ± 125.3	68.7 ± 8.4
Z+hf	1480.1 ± 78.1	94.6 ± 5.0
MJ_e	9499.0 ± 553.4	279.4 ± 96.6
MJ_μ	3719.2 ± 1157.5	23.0
Total	140086.1 ± 461.9	19641.0 ± 131.4
Data	140060.0 ± 374.2	19649.0 ± 140.2
$\frac{\text{Sim}-\text{Data}}{\sigma}$	0.04	-0.04

Table 132: Table of post unconditional fit yields for 1-lepton 2 and 3-jet 1-tag events in the dijet mass selection. The uncertainties are the full postfit errors including all nusicance parameters with priors, floating normalizations, and the correlations deduced from the data. The difference in the data and the postfit simulation is compared to σ which is obtained from the sum in simulation as the sum in quadrature of the postfit and Poissonian error.

Sample	2L-tag				
	$p_T^V < 90\ GeV$	$90 < p_T^V < 120\ GeV$	$120 < p_T^V < 160\ GeV$	$160 < p_T^V < 200\ GeV$	$p_T^V > 200\ GeV$
	2-jet				
VH	18.0 ± 7.8	6.8 ± 2.9	4.9 ± 2.1	2.3 ± 1.0	2.7 ± 1.2
VV	125.3 ± 3.2	44.0 ± 1.1	25.0 ± 0.6	10.8 ± 1.8	12.3 ± 2.8
$t\bar{t}$	2027.9 ± 116.5	803.4 ± 45.5	442.2 ± 24.5	115.6 ± 6.8	61.7 ± 5.5
s-top	1569.1 ± 183.6	403.8 ± 44.9	126.3 ± 9.1	29.5 ± 2.0	18.2 ± 1.4
W+l	1771.3 ± 166.9	539.9 ± 50.3	205.9 ± 19.5	58.6 ± 5.7	49.5 ± 5.0
W+cl	2999.4 ± 168.3	868.6 ± 52.5	301.4 ± 18.8	76.9 ± 4.9	48.8 ± 3.7
W+hf	1635.5 ± 332.4	529.1 ± 87.9	203.2 ± 30.7	59.5 ± 8.8	51.1 ± 8.5
Z+l	117.1 ± 8.5	43.6 ± 3.1	10.3 ± 0.3	1.7 ± 0.0	0.7 ± 0.0
Z+cl	61.1 ± 7.5	22.2 ± 2.7	5.1 ± 0.6	0.9 ± 0.1	0.4 ± 0.0
Z+hf	166.3 ± 8.8	59.3 ± 3.1	13.6 ± 0.7	2.6 ± 0.1	1.1 ± 0.1
MJ_e	613.8 ± 256.7	150.9 ± 67.9	24.8 ± 13.5	5.4 ± 3.2	0.7 ± 0.6
MJ_μ	456.6 ± 114.3	48.6 ± 12.2	4.0 ± 0.0	1.0	–
Total	11561.2 ± 98.0	3520.0 ± 37.4	1366.7 ± 17.6	364.8 ± 5.5	247.2 ± 7.4
Data	11597.0 ± 107.7	3426.0 ± 58.5	1355.0 ± 36.8	375.0 ± 19.4	239.0 ± 15.5
$\frac{\text{Sim}-\text{Data}}{\sigma}$	-0.25	1.34	0.29	-0.51	0.47
	3-jet				
VH	5.2 ± 2.3	2.2 ± 0.9	1.7 ± 0.7	1.0 ± 0.4	1.3 ± 0.6
VV	57.9 ± 1.5	19.9 ± 0.5	11.5 ± 0.3	5.2 ± 0.1	5.5 ± 0.9
$t\bar{t}$	3918.0 ± 103.4	1152.6 ± 30.6	587.3 ± 21.5	177.0 ± 8.3	112.4 ± 9.5
s-top	832.7 ± 47.3	213.8 ± 13.4	85.4 ± 10.1	29.2 ± 4.1	24.3 ± 3.5
W+l	657.6 ± 61.8	178.0 ± 16.4	78.5 ± 7.3	25.8 ± 2.5	25.7 ± 2.6
W+cl	1037.7 ± 63.6	272.9 ± 16.4	111.0 ± 7.6	34.0 ± 2.4	27.2 ± 2.2
W+hf	615.0 ± 122.4	187.3 ± 31.9	92.3 ± 16.0	34.5 ± 6.5	38.2 ± 8.5
Z+l	49.7 ± 1.3	15.0 ± 0.4	3.7 ± 0.1	0.8 ± 0.0	0.5 ± 0.0
Z+cl	30.7 ± 3.8	8.7 ± 1.1	2.2 ± 0.3	0.5 ± 0.1	0.2 ± 0.0
Z+hf	83.1 ± 4.4	23.3 ± 1.2	7.3 ± 0.4	1.3 ± 0.1	0.8 ± 0.0
MJ_e	298.3 ± 31.9	69.5 ± 12.1	13.7 ± 4.6	2.3 ± 0.1	0.8 ± 0.3
MJ_μ	223.4 ± 90.0	13.2 ± 2.9	–	–	–
Total	7809.3 ± 79.0	2156.4 ± 26.6	994.6 ± 15.2	311.5 ± 6.3	237.0 ± 7.9
Data	7746.0 ± 88.0	2128.0 ± 46.1	1051.0 ± 32.4	313.0 ± 17.7	238.0 ± 15.4
$\frac{\text{Sim}-\text{Data}}{\sigma}$	0.53	0.53	-1.61	-0.08	-0.06

Table 133: Table of post unconditional fit yields for 1-lepton 2 and 3-jet 2L-tag events in the dijet mass selection. The uncertainties are the full postfit errors including all nusicance parameters with priors, floating normalizations, and the correlations deduced from the data. The difference in the data and the postfit simulation is compared to σ which is obtained from the sum in simulation as the sum in quadrature of the postfit and Poissonian error.

Sample	2M-tag $p_T^V < 90\ GeV$	$90 < p_T^V < 120\ GeV$	$120 < p_T^V < 160\ GeV$	$160 < p_T^V < 200\ GeV$	$p_T^V > 200\ GeV$
	2-jet				
VH	28.5 ± 12.3	10.3 ± 4.4	7.6 ± 3.3	3.7 ± 1.6	4.3 ± 1.9
VV	82.1 ± 4.6	29.8 ± 2.3	18.4 ± 2.1	7.2 ± 1.3	6.9 ± 1.6
$t\bar{t}$	2436.0 ± 130.6	949.3 ± 49.9	475.5 ± 24.3	91.2 ± 5.2	36.8 ± 3.3
s-top	1385.3 ± 151.0	348.9 ± 36.4	107.9 ± 8.9	22.1 ± 1.7	12.2 ± 1.0
W+l	141.5 ± 22.2	42.8 ± 6.8	15.3 ± 2.4	4.1 ± 0.6	3.4 ± 0.5
W+cl	534.8 ± 36.4	158.2 ± 11.4	53.6 ± 4.0	12.4 ± 0.9	7.9 ± 0.7
W+hf	1117.8 ± 229.4	347.9 ± 56.7	142.5 ± 21.4	40.9 ± 6.0	37.2 ± 5.8
Z+l	8.4 ± 0.2	3.3 ± 0.1	0.7 ± 0.0	0.1 ± 0.0	0.0 ± 0.0
Z+cl	11.8 ± 1.4	4.3 ± 0.5	1.0 ± 0.1	0.1 ± 0.0	0.0 ± 0.0
Z+hf	123.5 ± 6.0	46.3 ± 2.3	10.7 ± 0.6	1.6 ± 0.1	0.7 ± 0.0
MJ_e	258.1 ± 119.4	91.6 ± 44.5	15.1 ± 8.6	2.2 ± 1.6	1.1 ± 0.0
MJ_μ	227.9 ± 77.2	16.6 ± 5.6	–	–	–
Total	6355.6 ± 69.7	2049.3 ± 26.2	848.5 ± 14.5	185.7 ± 4.0	110.5 ± 4.7
Data	6344.0 ± 79.6	2053.0 ± 45.3	868.0 ± 29.5	199.0 ± 14.1	116.0 ± 10.8
$\frac{\text{Sim}-\text{Data}}{\sigma}$	0.11	-0.07	-0.6	-0.94	-0.47
	3-jet				
VH	7.5 ± 3.3	3.3 ± 1.5	2.7 ± 1.2	1.7 ± 0.7	2.0 ± 0.9
VV	26.5 ± 0.7	10.1 ± 0.3	6.3 ± 0.2	2.8 ± 0.4	3.2 ± 0.4
$t\bar{t}$	5017.4 ± 91.7	1392.0 ± 28.7	606.7 ± 19.3	132.9 ± 5.6	66.5 ± 5.8
s-top	802.1 ± 49.5	193.3 ± 12.4	69.5 ± 7.7	21.0 ± 3.0	17.1 ± 2.5
W+l	44.2 ± 1.1	12.1 ± 0.3	5.1 ± 0.1	1.5 ± 0.0	1.6 ± 0.3
W+cl	181.1 ± 13.0	50.5 ± 3.7	18.9 ± 1.5	5.6 ± 0.6	4.3 ± 0.5
W+hf	393.5 ± 78.9	131.4 ± 22.5	70.5 ± 12.0	23.8 ± 4.4	27.1 ± 5.8
Z+l	3.2 ± 0.1	1.1 ± 0.0	0.3 ± 0.0	0.1 ± 0.0	0.0 ± 0.0
Z+cl	5.5 ± 0.7	1.6 ± 0.2	0.3 ± 0.0	0.1 ± 0.0	0.0 ± 0.0
Z+hf	59.9 ± 3.2	19.8 ± 1.0	5.4 ± 0.3	1.2 ± 0.1	0.5 ± 0.0
MJ_e	152.0 ± 17.2	35.7 ± 7.4	7.3 ± 3.1	3.0 ± 2.1	–
MJ_μ	126.7 ± 17.5	12.0	–	–	–
Total	6819.7 ± 55.0	1862.8 ± 23.3	793.0 ± 14.1	193.6 ± 4.5	122.4 ± 5.3
Data	6863.0 ± 82.8	1925.0 ± 43.9	780.0 ± 27.9	181.0 ± 13.5	123.0 ± 11.1
$\frac{\text{Sim}-\text{Data}}{\sigma}$	-0.44	-1.27	0.41	0.87	-0.05

Table 134: Table of post unconditional fit yields for 1-lepton 2 and 3-jet 2M-tag events in the dijet mass selection. The uncertainties are the full postfit errors including all nusicance parameters with priors, floating normalizations, and the correlations deduced from the data. The difference in the data and the postfit simulation is compared to σ which is obtained from the sum in simulation as the sum in quadrature of the postfit and Poissonian error.

Sample	2T-tag				
	$p_T^V < 90\ GeV$	$90 < p_T^V < 120\ GeV$	$120 < p_T^V < 160\ GeV$	$160 < p_T^V < 200\ GeV$	$p_T^V > 200\ GeV$
	2-jet				
VH	31.2 ± 13.4	11.4 ± 4.9	8.7 ± 3.7	4.6 ± 2.0	4.7 ± 2.0
VV	64.6 ± 4.7	24.3 ± 2.3	15.3 ± 2.1	6.7 ± 1.3	6.0 ± 1.6
$t\bar{t}$	2300.7 ± 121.9	874.8 ± 45.0	389.9 ± 19.2	46.6 ± 2.7	10.1 ± 1.0
s-top	1117.4 ± 123.3	268.4 ± 28.9	80.3 ± 8.1	14.1 ± 1.3	5.0 ± 0.5
W+l	3.8 ± 0.1	1.0 ± 0.0	0.3 ± 0.0	0.1 ± 0.0	0.1 ± 0.0
W+cl	26.7 ± 4.3	8.2 ± 1.0	2.6 ± 0.3	0.6 ± 0.2	0.4 ± 0.1
W+hf	597.3 ± 129.0	203.1 ± 34.2	90.3 ± 14.4	25.9 ± 4.0	24.6 ± 4.1
Z+l	0.2 ± 0.0	0.1 ± 0.0	0.0 ± 0.0	0.0 ± 0.0	0.0 ± 0.0
Z+cl	0.7 ± 0.1	0.1 ± 0.0	0.0 ± 0.0	0.0 ± 0.0	–
Z+hf	81.5 ± 4.3	31.5 ± 1.6	7.0 ± 0.5	1.7 ± 0.2	0.5 ± 0.0
MJ_e	132.5 ± 66.7	55.3 ± 30.7	7.3 ± 4.9	1.0 ± 1.0	0.7 ± 0.5
MJ_μ	131.5 ± 67.4	11.9 ± 6.1	–	–	–
Total	4488.1 ± 62.3	1490.1 ± 25.1	601.8 ± 12.9	101.3 ± 3.0	52.0 ± 3.7
Data	4560.0 ± 67.5	1448.0 ± 38.1	591.0 ± 24.3	112.0 ± 10.6	59.0 ± 7.7
$\frac{\text{Sim}-\text{Data}}{\sigma}$	-0.79	0.92	0.39	-1.02	-0.86
	3-jet				
VH	8.8 ± 3.8	3.8 ± 1.6	3.1 ± 1.3	1.9 ± 0.8	2.3 ± 1.0
VV	16.5 ± 0.4	7.2 ± 0.2	5.8 ± 0.1	2.7 ± 0.4	2.6 ± 0.4
$t\bar{t}$	5135.0 ± 88.5	1326.4 ± 26.8	495.9 ± 16.0	62.3 ± 3.2	16.2 ± 1.8
s-top	675.4 ± 43.1	154.1 ± 10.3	47.4 ± 5.4	10.0 ± 1.4	7.0 ± 1.0
W+l	1.2 ± 0.0	0.4 ± 0.0	0.1 ± 0.0	0.0 ± 0.0	0.0 ± 0.0
W+cl	8.8 ± 0.7	2.5 ± 0.2	1.0 ± 0.1	0.3 ± 0.0	0.2 ± 0.0
W+hf	218.5 ± 45.7	71.4 ± 12.6	41.4 ± 7.3	16.7 ± 3.2	18.4 ± 4.0
Z+l	0.0 ± 0.0	0.0 ± 0.0	0.0 ± 0.0	0.0 ± 0.0	0.0 ± 0.0
Z+cl	0.2 ± 0.0	0.1 ± 0.0	0.0 ± 0.0	0.0 ± 0.0	0.0 ± 0.0
Z+hf	39.5 ± 2.1	12.5 ± 0.7	3.9 ± 0.2	0.9 ± 0.1	0.4 ± 0.1
MJ_e	84.1 ± 5.9	18.0 ± 4.6	2.8 ± 1.2	1.1 ± 1.3	0.5 ± 0.6
MJ_μ	65.8 ± 9.1	–	–	0.6 ± 0.1	–
Total	6253.8 ± 60.1	1596.5 ± 23.6	601.5 ± 13.4	96.4 ± 3.3	47.5 ± 3.6
Data	6196.0 ± 78.7	1624.0 ± 40.3	590.0 ± 24.3	101.0 ± 10.0	53.0 ± 7.3
$\frac{\text{Sim}-\text{Data}}{\sigma}$	0.58	-0.59	0.41	-0.44	-0.7

Table 135: Table of post unconditional fit yields for 1-lepton 2 and 3-jet 2T-tag events in the dijet mass selection. The uncertainties are the full postfit errors including all nusicance parameters with priors, floating normalizations, and the correlations deduced from the data. The difference in the data and the postfit simulation is compared to σ which is obtained from the sum in simulation as the sum in quadrature of the postfit and Poissonian error.

Sample	1-tag	
	$p_{\mathrm{T}}^{V} < 120\ GeV$	$p_{\mathrm{T}}^{V} > 120\ GeV$
	2-jet	
VH	20.2 ± 8.8	5.5 ± 2.4
VV	614.3 ± 15.5	91.7 ± 12.8
$t\bar{t}$	586.7 ± 93.9	27.4 ± 4.3
s-top	53.6 ± 1.4	3.8 ± 0.1
W+l	69.8 ± 1.8	1.1 ± 0.0
W+cl	41.8 ± 3.5	3.3 ± 0.3
W+hf	17.1 ± 3.3	1.8 ± 0.4
Z+l	19631.8 ± 905.7	1810.1 ± 85.4
Z+cl	8728.5 ± 1021.2	752.4 ± 90.4
Z+hf	14740.3 ± 478.6	1306.4 ± 45.0
MJ	123.4 ± 263.3	1.0 ± 2.0
Total	44627.6 ± 209.0	4004.5 ± 55.4
Data	44551.0 ± 211.1	4052.0 ± 63.7
$\frac{\text{Sim}-\text{Data}}{\sigma}$	0.26	-0.56
	3-jet	
VH	7.0 ± 3.1	2.6 ± 1.1
VV	247.0 ± 18.2	45.0 ± 6.5
$t\bar{t}$	345.3 ± 62.6	18.4 ± 3.3
s-top	19.0 ± 0.5	1.9 ± 0.0
W+l	7.7 ± 0.2	0.9 ± 0.0
W+cl	13.0 ± 1.1	1.5 ± 0.1
W+hf	7.9 ± 1.5	0.8 ± 0.1
Z+l	5484.0 ± 307.9	716.0 ± 38.8
Z+cl	3462.6 ± 367.4	396.5 ± 43.4
Z+hf	3998.9 ± 195.7	459.6 ± 24.2
MJ	35.0 ± 74.8	0.5 ± 1.0
Total	13627.4 ± 112.0	1643.6 ± 30.5
Data	13595.0 ± 116.6	1631.0 ± 40.4
$\frac{\text{Sim}-\text{Data}}{\sigma}$	0.2	0.25

Table 136: Table of post unconditional fit yields for 2-lepton 2 and 3-jet 1-tag events in the dijet mass selection. The uncertainties are the full postfit errors including all nusicance parameters with priors, floating normalizations, and the correlations deduced from the data. The difference in the data and the postfit simulation is compared to σ which is obtained from the sum in simulation as the sum in quadrature of the postfit and Poissonian error.

Sample	2L-tag				
	$p_T^V < 90\ GeV$	$90 < p_T^V < 120\ GeV$	$120 < p_T^V < 160\ GeV$	$160 < p_T^V < 200\ GeV$	$p_T^V > 200\ GeV$
	2-jet				
VH	4.7 ± 2.0	1.3 ± 0.6	0.9 ± 0.4	0.4 ± 0.2	0.5 ± 0.2
VV	49.8 ± 2.8	8.4 ± 0.5	5.0 ± 0.4	2.0 ± 0.2	2.0 ± 0.3
$t\bar{t}$	145.7 ± 23.2	22.6 ± 3.6	5.6 ± 0.9	0.3 ± 0.1	0.1 ± 0.0
s-top	4.8 ± 0.1	0.9 ± 0.0	0.5 ± 0.0	0.0 ± 0.0	0.1 ± 0.0
W+l	0.6 ± 0.0	0.1 ± 0.0	0.0 ± 0.0	0.0 ± 0.0	0.0 ± 0.0
W+cl	1.0 ± 0.1	0.2 ± 0.0	0.1 ± 0.0	0.0 ± 0.0	0.0 ± 0.0
W+hf	2.0 ± 0.4	0.4 ± 0.1	0.1 ± 0.0	0.0 ± 0.0	0.0 ± 0.0
Z+l	373.7 ± 31.4	71.0 ± 5.9	28.8 ± 2.4	7.9 ± 0.7	7.3 ± 0.7
Z+cl	256.7 ± 27.0	49.4 ± 5.3	19.2 ± 2.1	5.3 ± 0.6	4.1 ± 0.5
Z+hf	1099.2 ± 47.9	230.6 ± 9.7	87.9 ± 3.6	21.6 ± 0.9	16.3 ± 1.0
MJ	9.3 ± 19.9	0.5 ± 1.0	0.4	0.1	–
Total	1947.4 ± 28.9	385.3 ± 6.9	148.5 ± 2.7	37.7 ± 0.8	30.3 ± 1.1
Data	2009.0 ± 44.8	378.0 ± 19.4	153.0 ± 12.4	33.0 ± 5.7	42.0 ± 6.5
$\frac{\text{Sim}-\text{Data}}{\sigma}$	-1.17	0.35	-0.36	0.76	-2.08
	3-jet				
VH	1.2 ± 0.5	0.4 ± 0.2	0.4 ± 0.2	0.2 ± 0.1	0.2 ± 0.1
VV	12.3 ± 1.0	3.0 ± 0.4	1.7 ± 0.2	0.9 ± 0.1	1.1 ± 0.2
$t\bar{t}$	66.7 ± 12.1	10.8 ± 2.0	2.9 ± 0.5	0.4 ± 0.1	–
s-top	1.8 ± 0.0	0.5 ± 0.0	0.1 ± 0.0	0.2 ± 0.0	–
W+l	0.2 ± 0.0	0.0 ± 0.0	0.0 ± 0.0	0.0 ± 0.0	0.0 ± 0.0
W+cl	0.5 ± 0.0	0.0 ± 0.0	0.0 ± 0.0	0.0 ± 0.0	0.0 ± 0.0
W+hf	0.3 ± 0.1	0.0 ± 0.0	0.0 ± 0.0	0.0 ± 0.0	0.0 ± 0.0
Z+l	101.8 ± 9.2	20.6 ± 1.8	9.6 ± 0.8	3.1 ± 0.3	3.4 ± 0.3
Z+cl	104.0 ± 10.2	20.1 ± 2.0	8.9 ± 0.9	2.9 ± 0.3	2.8 ± 0.3
Z+hf	289.4 ± 18.6	63.4 ± 3.8	28.1 ± 1.8	7.8 ± 0.5	7.6 ± 0.6
MJ	1.2 ± 2.6	0.1	0.0 ± 0.0	–	–
Total	579.5 ± 10.9	119.2 ± 2.6	51.9 ± 1.5	15.6 ± 0.5	15.1 ± 0.6
Data	612.0 ± 24.7	128.0 ± 11.3	64.0 ± 8.0	12.0 ± 3.5	19.0 ± 4.4
$\frac{\text{Sim}-\text{Data}}{\sigma}$	-1.23	-0.79	-1.65	0.89	-0.99

Table 137: Table of post unconditional fit yields for 2-lepton 2 and 3-jet 2L-tag events in the dijet mass selection. The uncertainties are the full postfit errors including all nusicance parameters with priors, floating normalizations, and the correlations deduced from the data. The difference in the data and the postfit simulation is compared to σ which is obtained from the sum in simulation as the sum in quadrature of the postfit and Poissonian error.

Sample	2M-tag				
	$p_T^V < 90\ GeV$	$90 < p_T^V < 120\ GeV$	$120 < p_T^V < 160\ GeV$	$160 < p_T^V < 200\ GeV$	$p_T^V > 200\ GeV$
	2-jet				
VH	7.5 ± 3.2	2.0 ± 0.9	1.6 ± 0.7	0.7 ± 0.3	0.8 ± 0.3
VV	48.6 ± 2.7	8.1 ± 0.5	4.9 ± 0.4	2.0 ± 0.2	2.0 ± 0.3
$t\bar{t}$	220.4 ± 34.4	37.5 ± 5.9	8.6 ± 1.4	0.3 ± 0.1	0.0 ± 0.0
s-top	5.7 ± 0.1	1.5 ± 0.1	0.4 ± 0.0	0.0 ± 0.0	–
W+l	0.0 ± 0.0	0.0 ± 0.0	0.0 ± 0.0	0.0 ± 0.0	0.0 ± 0.0
W+cl	0.2 ± 0.0	0.0 ± 0.0	0.0 ± 0.0	0.0 ± 0.0	0.0 ± 0.0
W+hf	0.6 ± 0.1	0.1 ± 0.0	0.0 ± 0.0	–	0.0 ± 0.0
Z+l	26.7 ± 4.0	4.7 ± 0.7	1.8 ± 0.3	0.5 ± 0.1	0.4 ± 0.1
Z+cl	42.1 ± 3.6	8.0 ± 0.7	3.2 ± 0.3	0.8 ± 0.1	0.6 ± 0.1
Z+hf	931.2 ± 40.5	192.1 ± 8.0	72.9 ± 3.0	17.0 ± 0.8	11.1 ± 0.6
MJ	3.3 ± 7.1	0.1 ± 0.2	0.1	–	–
Total	1286.4 ± 22.7	254.1 ± 5.5	93.6 ± 2.2	21.3 ± 0.7	14.9 ± 0.7
Data	1284.0 ± 35.8	264.0 ± 16.2	83.0 ± 9.1	23.0 ± 4.8	9.0 ± 3.0
$\frac{\text{Sim}-\text{Data}}{\sigma}$	0.06	-0.59	1.07	-0.36	1.5
	3-jet				
VH	1.9 ± 0.8	0.6 ± 0.3	0.6 ± 0.2	0.3 ± 0.1	0.4 ± 0.2
VV	9.4 ± 1.0	1.8 ± 0.2	1.5 ± 0.2	0.7 ± 0.1	0.7 ± 0.1
$t\bar{t}$	99.2 ± 17.8	16.3 ± 3.0	3.1 ± 0.6	0.1 ± 0.0	0.0 ± 0.0
s-top	2.5 ± 0.1	0.7 ± 0.1	0.1 ± 0.0	–	0.0 ± 0.0
W+l	0.0 ± 0.0	0.0 ± 0.0	0.0 ± 0.0	0.0 ± 0.0	0.0 ± 0.0
W+cl	0.1 ± 0.0	0.0 ± 0.0	0.0 ± 0.0	0.0 ± 0.0	0.0 ± 0.0
W+hf	0.1 ± 0.0	0.0 ± 0.0	0.0 ± 0.0	0.0 ± 0.0	0.0 ± 0.0
Z+l	7.1 ± 1.1	1.3 ± 0.2	0.6 ± 0.1	0.2 ± 0.0	0.2 ± 0.0
Z+cl	15.6 ± 1.4	3.3 ± 0.3	1.4 ± 0.1	0.4 ± 0.0	0.4 ± 0.0
Z+hf	251.1 ± 18.8	52.2 ± 3.6	26.5 ± 1.8	7.3 ± 0.5	5.6 ± 0.4
MJ	0.6 ± 1.3	0.1	–	–	–
Total	387.7 ± 11.4	76.4 ± 2.5	33.8 ± 1.5	8.9 ± 0.5	7.4 ± 0.4
Data	401.0 ± 20.0	80.0 ± 8.9	34.0 ± 5.8	6.0 ± 2.4	7.0 ± 2.6
$\frac{\text{Sim}-\text{Data}}{\sigma}$	-0.59	-0.39	-0.04	0.96	0.13

Table 138: Table of post unconditional fit yields for 2-lepton 2 and 3-jet 2M-tag events in the dijet mass selection. The uncertainties are the full postfit errors including all nusicance parameters with priors, floating normalizations, and the correlations deduced from the data. The difference in the data and the postfit simulation is compared to σ which is obtained from the sum in simulation as the sum in quadrature of the postfit and Poissonian error.

Sample	2T-tag				
	$p_T^V < 90\ GeV$	$90 < p_T^V < 120\ GeV$	$120 < p_T^V < 160\ GeV$	$160 < p_T^V < 200\ GeV$	$p_T^V > 200\ GeV$
	2-jet				
VH	8.4 ± 3.6	2.2 ± 1.0	1.8 ± 0.8	0.9 ± 0.4	0.9 ± 0.4
VV	44.2 ± 3.0	7.3 ± 0.6	5.0 ± 0.5	2.3 ± 0.3	2.0 ± 0.3
$t\bar{t}$	238.7 ± 37.0	38.9 ± 6.1	8.9 ± 1.5	0.4 ± 0.1	–
s-top	4.7 ± 0.1	1.3 ± 0.1	0.2 ± 0.0	0.1 ± 0.0	0.1 ± 0.0
W+l	0.0 ± 0.0	–	–	–	–
W+hf	0.6 ± 0.1	0.3 ± 0.1	0.0 ± 0.0	0.0 ± 0.0	–
Z+l	0.4 ± 0.0	0.1 ± 0.0	0.0 ± 0.0	0.0 ± 0.0	0.0 ± 0.0
Z+cl	1.2 ± 0.1	0.2 ± 0.0	0.1 ± 0.0	0.0 ± 0.0	0.0 ± 0.0
Z+hf	687.7 ± 33.3	152.4 ± 7.2	58.4 ± 2.7	12.9 ± 0.6	8.3 ± 0.5
MJ	2.1 ± 4.5	0.0 ± 0.1	0.0 ± 0.1	–	–
Total	988.0 ± 22.2	202.8 ± 5.1	74.5 ± 2.0	16.6 ± 0.7	11.3 ± 0.6
Data	980.0 ± 31.3	209.0 ± 14.5	65.0 ± 8.1	17.0 ± 4.1	12.0 ± 3.5
$\frac{\text{Sim}-\text{Data}}{\sigma}$	0.21	-0.41	1.07	-0.09	-0.2
	3-jet				
VH	2.1 ± 0.9	0.7 ± 0.3	0.7 ± 0.3	0.4 ± 0.2	0.4 ± 0.2
VV	7.8 ± 0.9	1.9 ± 0.2	1.4 ± 0.2	0.8 ± 0.1	0.7 ± 0.1
$t\bar{t}$	109.9 ± 19.6	18.4 ± 3.3	3.5 ± 0.7	0.0 ± 0.0	0.1 ± 0.0
s-top	1.9 ± 0.0	0.3 ± 0.0	0.2 ± 0.0	0.0 ± 0.0	–
W+l	0.0 ± 0.0	–	–	–	–
W+hf	0.1 ± 0.0	–	0.0 ± 0.0	0.0 ± 0.0	–
Z+l	0.1 ± 0.0	0.0 ± 0.0	0.0 ± 0.0	0.0 ± 0.0	0.0 ± 0.0
Z+cl	0.2 ± 0.0	0.1 ± 0.0	0.1 ± 0.0	0.0 ± 0.0	0.0 ± 0.0
Z+hf	185.3 ± 14.9	40.1 ± 3.0	20.5 ± 1.5	5.3 ± 0.4	4.2 ± 0.3
MJ	0.4 ± 0.8	0.1	–	–	–
Total	307.9 ± 11.9	61.7 ± 2.4	26.4 ± 1.2	6.6 ± 0.4	5.4 ± 0.4
Data	307.0 ± 17.5	55.0 ± 7.4	29.0 ± 5.4	9.0 ± 3.0	3.0 ± 1.7
$\frac{\text{Sim}-\text{Data}}{\sigma}$	0.04	0.81	-0.5	-0.93	1.03

Table 139: Table of post unconditional fit yields for 2-lepton 2 and 3-jet 2T-tag events in the dijet mass selection. The uncertainties are the full postfit errors including all nusicance parameters with priors, floating normalizations, and the correlations deduced from the data. The difference in the data and the postfit simulation is compared to σ which is obtained from the sum in simulation as the sum in quadrature of the postfit and Poissonian error.

AJ.3 Dijet Mass Analysis: Postfit over Prefit

Sample	1-tag	
	$100 < p_{\mathrm{T}}^{V} < 120\ GeV$	$p_{\mathrm{T}}^{V} > 120\ GeV$
	2-jet	
VH	1.24	1.21
VV	1.0	1.0
$t\bar{t}$	1.39	1.43
s-top	1.42	1.16
W+l	1.03	0.99
W+cl	1.12	1.1
W+hf	0.73	0.68
Z+l	1.0	0.96
Z+cl	0.85	0.85
Z+hf	1.1	1.08
MJ	1.49	0.41
Total	1.04	0.99
	3-jet	
VH	–	1.22
VV	–	1.0
$t\bar{t}$	–	1.27
s-top	–	1.0
W+l	–	0.97
W+cl	–	1.04
W+hf	–	0.77
Z+l	–	0.9
Z+cl	–	1.01
Z+hf	–	0.91
MJ	–	1.09
Total	–	0.99

Table 140: Table of post unconditional fit over prefit yields for 0-lepton 2 and 3-jet 1-tag events in the dijet mass selection.

Sample	2L-tag			
	$100 < p_{\mathrm{T}}^{V} < 120\ GeV$	$120 < p_{\mathrm{T}}^{V} < 160\ GeV$	$160 < p_{\mathrm{T}}^{V} < 200\ GeV$	$p_{\mathrm{T}}^{V} > 200\ GeV$
	2-jet			
VH	1.3	1.3	1.29	1.29
VV	1.05	1.06	1.12	1.12
$t\bar{t}$	1.43	1.49	1.42	1.42
s-top	1.37	1.15	1.09	1.03
W+l	1.03	1.02	1.03	1.04
W+cl	1.14	1.14	1.13	1.1
W+hf	0.79	0.77	0.73	0.67
Z+l	1.03	1.01	1.0	0.98
Z+cl	0.89	0.89	0.88	0.86
Z+hf	1.17	1.14	1.16	1.08
MJ	0.91	1.22	1.22	1.22
Total	1.1	1.08	1.07	1.01
	3-jet			
VH	–	1.28	1.28	1.3
VV	–	0.99	1.0	0.95
$t\bar{t}$	–	1.33	1.27	1.25
s-top	–	0.99	1.04	0.99
W+l	–	1.0	1.02	1.02
W+cl	–	1.09	1.07	1.07
W+hf	–	0.81	0.84	0.82
Z+l	–	0.94	0.95	0.92
Z+cl	–	1.05	1.06	1.02
Z+hf	–	1.06	1.02	0.98
MJ	–	0.53	0.53	0.53
Total	–	1.1	1.06	1.01

Table 141: Table of post unconditional fit over prefit yields for 0-lepton 2 and 3-jet 2L-tag events in the dijet mass selection.

Sample	2M-tag			
	$100 < p_{\mathrm{T}}^{V} < 120\ GeV$	$120 < p_{\mathrm{T}}^{V} < 160\ GeV$	$160 < p_{\mathrm{T}}^{V} < 200\ GeV$	$p_{\mathrm{T}}^{V} > 200\ GeV$
	2-jet			
VH	1.28	1.28	1.28	1.3
VV	1.07	1.09	1.11	1.17
$t\bar{t}$	1.41	1.51	1.5	1.48
s-top	1.32	1.2	1.2	1.06
W+l	1.13	1.09	1.13	1.08
W+cl	1.16	1.18	1.19	1.21
W+hf	0.82	0.78	0.77	0.72
Z+l	1.12	1.1	1.09	1.05
Z+cl	0.91	0.93	0.9	0.93
Z+hf	1.14	1.14	1.12	1.12
MJ	0.91	1.22	1.22	1.22
Total	1.17	1.17	1.13	1.09
	3-jet			
VH	–	1.29	1.29	1.28
VV	–	0.97	0.98	0.97
$t\bar{t}$	–	1.33	1.3	1.33
s-top	–	1.03	1.05	1.06
W+l	–	1.12	1.1	1.11
W+cl	–	1.05	1.09	1.14
W+hf	–	0.8	0.86	0.86
Z+l	–	1.14	1.01	1.0
Z+cl	–	1.06	1.1	1.08
Z+hf	–	1.06	1.08	1.05
MJ	–	0.53	0.53	0.53
Total	–	1.16	1.12	1.07

Table 142: Table of post unconditional fit over prefit yields for 0-lepton 2 and 3-jet 2M-tag events in the dijet mass selection.

Sample	2T-tag			
	$100 < p_{\mathrm{T}}^{V} < 120\ GeV$	$120 < p_{\mathrm{T}}^{V} < 160\ GeV$	$160 < p_{\mathrm{T}}^{V} < 200\ GeV$	$p_{\mathrm{T}}^{V} > 200\ GeV$
	2-jet			
VH	1.27	1.27	1.27	1.28
VV	1.06	1.09	1.11	1.13
$t\bar{t}$	1.41	1.47	1.5	1.37
s-top	1.32	1.2	1.13	1.16
W+l	1.0	1.0	1.0	1.0
W+cl	1.21	1.12	1.16	1.12
W+hf	0.8	0.8	0.77	0.74
Z+l	1.0	1.0	1.0	1.0
Z+cl	0.87	0.87	0.87	0.87
Z+hf	1.13	1.11	1.11	1.08
MJ	0.91	1.22	1.22	1.22
Total	1.18	1.16	1.12	1.05
	3-jet			
VH	–	1.27	1.28	1.27
VV	–	0.98	0.92	0.95
$t\bar{t}$	–	1.36	1.29	1.22
s-top	–	1.04	1.04	1.0
W+l	–	1.0	1.0	1.0
W+cl	–	1.12	1.12	1.12
W+hf	–	0.89	0.9	0.92
Z+l	–	1.0	1.0	1.0
Z+cl	–	0.87	0.74	0.87
Z+hf	–	1.06	1.07	1.06
MJ	–	0.53	0.53	0.53
Total	–	1.2	1.1	1.04

Table 143: Table of post unconditional fit over prefit yields for 0-lepton 2 and 3-jet 2T-tag events in the dijet mass selection.

Sample	1-tag	
	$p_{\mathrm{T}}^{V} < 120\ GeV$	$p_{\mathrm{T}}^{V} > 120\ GeV$
	2-jet	
VH	1.24	1.22
VV	1.0	1.07
$t\bar{t}$	1.16	1.18
s-top	1.43	1.11
W+l	1.03	1.01
W+cl	1.11	1.09
W+hf	0.66	0.68
Z+l	1.01	0.95
Z+cl	0.87	0.87
Z+hf	1.07	1.07
MJ_e	0.96	1.41
MJ_μ	0.99	1.0
Total	1.04	1.03
	3-jet	
VH	1.27	1.24
VV	1.0	0.96
$t\bar{t}$	1.03	1.05
s-top	1.07	0.97
W+l	0.97	0.99
W+cl	1.03	1.04
W+hf	0.59	0.77
Z+l	0.98	1.0
Z+cl	0.87	0.87
Z+hf	1.07	1.07
MJ_e	1.03	0.79
MJ_μ	0.84	1.0
Total	0.97	0.99

Table 144: Table of post unconditional fit over prefit yields for 1-lepton 2 and 3-jet 1-tag events in the dijet mass selection.

Sample	2L-tag				
	$p_{\mathrm{T}}^{V} < 90\ GeV$	$90 < p_{\mathrm{T}}^{V} < 120\ GeV$	$120 < p_{\mathrm{T}}^{V} < 160\ GeV$	$160 < p_{\mathrm{T}}^{V} < 200\ GeV$	$p_{\mathrm{T}}^{V} > 200\ GeV$
	2-jet				
VH	1.31	1.32	1.31	1.28	1.31
VV	1.0	1.0	1.0	1.12	1.2
$t\bar{t}$	1.21	1.19	1.22	1.22	1.18
s-top	1.45	1.41	1.18	1.1	1.1
W+l	1.07	1.06	1.05	1.05	1.05
W+cl	1.18	1.16	1.15	1.12	1.12
W+hf	0.83	0.81	0.75	0.74	0.66
Z+l	1.04	1.01	1.0	1.0	1.0
Z+cl	0.87	0.87	0.87	0.87	0.87
Z+hf	1.07	1.07	1.07	1.07	1.07
MJ_{e}	0.65	0.62	0.59	0.56	0.55
MJ_{μ}	1.05	1.05	1.01	1.0	–
Total	1.07	1.06	1.05	1.03	0.98
	3-jet				
VH	1.32	1.34	1.3	1.35	1.28
VV	1.0	1.0	1.0	1.0	0.96
$t\bar{t}$	1.06	1.05	1.1	1.09	1.06
s-top	1.12	1.11	1.0	1.02	1.02
W+l	1.01	1.01	1.04	1.04	1.04
W+cl	1.08	1.07	1.1	1.08	1.06
W+hf	0.72	0.81	0.85	0.86	0.83
Z+l	1.0	1.0	1.0	1.0	1.0
Z+cl	0.87	0.87	0.87	0.87	0.87
Z+hf	1.07	1.07	1.07	1.07	1.07
MJ_{e}	0.95	1.09	1.19	1.0	1.16
MJ_{μ}	0.91	0.95	–	–	–
Total	1.01	1.03	1.06	1.04	1.01

Table 145: Table of post unconditional fit over prefit yields for 1-lepton 2 and 3-jet 2L-tag events in the dijet mass selection.

Sample	2M-tag				
	$p_{\mathrm{T}}^{V} < 90\ GeV$	$90 < p_{\mathrm{T}}^{V} < 120\ GeV$	$120 < p_{\mathrm{T}}^{V} < 160\ GeV$	$160 < p_{\mathrm{T}}^{V} < 200\ GeV$	$p_{\mathrm{T}}^{V} > 200\ GeV$
	2-jet				
VH	1.31	1.31	1.29	1.28	1.32
VV	1.05	1.08	1.11	1.09	1.2
$t\bar{t}$	1.18	1.19	1.23	1.26	1.26
s-top	1.42	1.38	1.21	1.16	1.17
W+l	1.18	1.16	1.14	1.14	1.15
W+cl	1.21	1.2	1.2	1.14	1.22
W+hf	0.86	0.8	0.78	0.75	0.73
Z+l	1.0	1.0	1.0	1.0	1.0
Z+cl	0.87	0.87	0.87	0.87	0.87
Z+hf	1.11	1.14	1.1	1.05	1.07
MJ_{e}	0.65	0.62	0.59	0.55	1.0
MJ_{μ}	0.94	0.94	–	–	–
Total	1.1	1.08	1.09	1.06	1.0
	3-jet				
VH	1.3	1.3	1.29	1.27	1.31
VV	1.0	1.0	1.0	0.93	1.03
$t\bar{t}$	1.06	1.06	1.11	1.11	1.12
s-top	1.15	1.14	0.99	1.08	1.07
W+l	1.0	1.0	1.0	1.0	1.09
W+cl	1.14	1.17	1.11	1.16	1.18
W+hf	0.76	0.85	0.91	0.86	0.91
Z+l	1.0	1.0	1.0	1.0	1.0
Z+cl	0.87	0.87	0.87	0.87	0.87
Z+hf	1.07	1.07	1.07	1.07	1.07
MJ_{e}	0.95	1.11	1.25	1.45	–
MJ_{μ}	0.99	1.0	–	–	–
Total	1.04	1.05	1.08	1.07	1.06

Table 146: Table of post unconditional fit over prefit yields for 1-lepton 2 and 3-jet 2M-tag events in the dijet mass selection.

Sample	2T-tag				
	$p_{\mathrm{T}}^{V} < 90\ GeV$	$90 < p_{\mathrm{T}}^{V} < 120\ GeV$	$120 < p_{\mathrm{T}}^{V} < 160\ GeV$	$160 < p_{\mathrm{T}}^{V} < 200\ GeV$	$p_{\mathrm{T}}^{V} > 200\ GeV$
	2-jet				
VH	1.29	1.28	1.28	1.27	1.28
VV	1.05	1.08	1.11	1.14	1.2
$t\bar{t}$	1.18	1.2	1.23	1.19	1.19
s-top	1.41	1.39	1.22	1.2	1.16
W+l	1.0	1.0	1.0	1.0	1.0
W+cl	1.18	1.2	1.21	1.09	1.01
W+hf	0.88	0.82	0.77	0.75	0.74
Z+l	1.0	1.0	1.0	1.0	1.0
Z+cl	0.87	0.87	0.87	0.87	–
Z+hf	1.13	1.12	1.13	1.14	1.03
MJ_{e}	0.68	0.66	0.64	0.52	0.62
MJ_{μ}	1.31	1.28	–	–	–
Total	1.15	1.12	1.11	1.02	0.92
	3-jet				
VH	1.29	1.3	1.29	1.26	1.28
VV	1.0	1.0	1.0	0.95	0.95
$t\bar{t}$	1.05	1.06	1.12	1.09	1.01
s-top	1.16	1.16	0.97	1.0	0.99
W+l	1.0	1.0	1.0	1.0	1.0
W+cl	1.12	1.12	1.12	1.16	1.16
W+hf	0.8	0.85	0.88	0.9	0.92
Z+l	1.0	1.0	1.0	1.0	1.0
Z+cl	0.87	0.87	0.87	0.87	0.87
Z+hf	1.07	1.07	1.07	1.06	1.27
MJ_{e}	0.98	1.14	1.21	1.5	1.75
MJ_{μ}	0.99	–	–	0.99	–
Total	1.05	1.06	1.09	1.04	0.98

Table 147: Table of post unconditional fit over prefit yields for 1-lepton 2 and 3-jet 2T-tag events in the dijet mass selection.

Sample	1-tag	
	$p_{\mathrm{T}}^{V} < 120\ GeV$	$p_{\mathrm{T}}^{V} > 120\ GeV$
	2-jet	
VH	1.24	1.21
VV	1.0	1.1
$t\bar{t}$	1.19	1.17
s-top	1.0	1.0
W+l	1.0	1.0
W+cl	1.12	1.12
W+hf	0.84	0.84
Z+l	1.02	1.01
Z+cl	0.89	0.88
Z+hf	1.11	1.11
MJ	0.2	0.2
Total	1.01	1.01
	3-jet	
VH	1.24	1.22
VV	0.98	0.95
$t\bar{t}$	1.24	1.24
s-top	1.0	1.0
W+l	1.0	1.0
W+cl	1.12	1.12
W+hf	0.84	0.84
Z+l	0.98	0.93
Z+cl	1.1	1.04
Z+hf	0.97	0.93
MJ	0.2	0.2
Total	1.0	0.96

Table 148: Table of post unconditional fit over prefit yields for 2-lepton 2 and 3-jet 1-tag events in the dijet mass selection.

Sample	2L-tag				
	$p_T^V < 90\ GeV$	$90 < p_T^V < 120\ GeV$	$120 < p_T^V < 160\ GeV$	$160 < p_T^V < 200\ GeV$	$p_T^V > 200\ GeV$
	2-jet				
VH	1.31	1.3	1.28	1.29	1.29
VV	1.08	1.08	1.08	1.13	1.13
$t\bar{t}$	1.24	1.21	1.29	1.23	1.17
s-top	1.0	1.0	1.0	1.0	1.02
W+l	1.0	1.0	1.0	1.0	1.0
W+cl	1.12	1.12	1.12	1.12	1.12
W+hf	0.84	0.84	0.84	0.8	0.84
Z+l	1.06	1.06	1.05	1.04	1.03
Z+cl	0.92	0.91	0.92	0.91	0.91
Z+hf	1.19	1.18	1.17	1.16	1.11
MJ	0.2	0.2	1.0	1.0	–
Total	1.09	1.11	1.1	1.09	1.06
	3-jet				
VH	1.31	1.3	1.29	1.28	1.28
VV	0.99	1.01	0.99	1.03	0.97
$t\bar{t}$	1.28	1.32	1.34	1.24	–
s-top	1.0	1.0	1.0	1.0	–
W+l	1.0	1.0	1.0	1.0	1.0
W+cl	1.12	1.12	1.12	1.12	1.12
W+hf	0.84	0.84	0.84	0.84	0.84
Z+l	1.02	0.99	0.97	0.97	0.96
Z+cl	1.15	1.09	1.09	1.08	1.06
Z+hf	1.13	1.08	1.05	1.02	1.02
MJ	0.2	1.0	0.2	–	–
Total	1.11	1.08	1.05	1.03	1.01

Table 149: Table of post unconditional fit over prefit yields for 2-lepton 2 and 3-jet 2L-tag events in the dijet mass selection.

Sample	2M-tag				
	$p_T^V < 90\ GeV$	$90 < p_T^V < 120\ GeV$	$120 < p_T^V < 160\ GeV$	$160 < p_T^V < 200\ GeV$	$p_T^V > 200\ GeV$
	2-jet				
VH	1.3	1.29	1.28	1.27	1.29
VV	1.05	1.06	1.08	1.1	1.16
$t\bar{t}$	1.22	1.2	1.29	1.19	1.17
s-top	1.0	0.98	0.98	1.0	–
W+l	1.0	1.0	1.0	1.0	1.0
W+cl	1.12	1.12	1.12	1.12	1.12
W+hf	0.84	0.84	0.82	–	0.84
Z+l	1.15	1.14	1.14	1.13	1.09
Z+cl	0.91	0.93	0.96	0.94	0.97
Z+hf	1.16	1.14	1.13	1.13	1.13
MJ	0.2	0.2	1.0	–	–
Total	1.14	1.14	1.14	1.12	1.13
	3-jet				
VH	1.3	1.3	1.28	1.28	1.31
VV	0.97	1.01	0.96	0.95	0.99
$t\bar{t}$	1.28	1.31	1.26	1.24	1.36
s-top	1.0	1.01	1.03	–	1.02
W+l	1.0	1.0	1.0	1.0	1.0
W+cl	1.12	1.12	1.12	1.12	1.12
W+hf	0.84	0.84	0.84	0.84	0.84
Z+l	1.11	1.07	1.07	1.07	1.05
Z+cl	1.18	1.1	1.14	1.12	1.16
Z+hf	1.16	1.12	1.08	1.09	1.06
MJ	0.2	1.0	–	–	–
Total	1.17	1.15	1.1	1.09	1.07

Table 150: Table of post unconditional fit over prefit yields for 2-lepton 2 and 3-jet 2M-tag events in the dijet mass selection.

Sample	2T-tag				
	$p_{\mathrm{T}}^{V} < 90\ GeV$	$90 < p_{\mathrm{T}}^{V} < 120\ GeV$	$120 < p_{\mathrm{T}}^{V} < 160\ GeV$	$160 < p_{\mathrm{T}}^{V} < 200\ GeV$	$p_{\mathrm{T}}^{V} > 200\ GeV$
	2-jet				
VH	1.28	1.27	1.26	1.25	1.27
VV	1.05	1.05	1.06	1.08	1.13
$t\bar{t}$	1.21	1.21	1.27	1.28	–
s-top	1.0	1.0	1.14	1.29	1.1
W+l	1.0	–	–	–	–
W+hf	0.84	0.83	0.84	0.84	–
Z+l	1.0	1.0	1.0	1.0	1.0
Z+cl	0.87	0.87	0.93	0.87	0.87
Z+hf	1.13	1.12	1.11	1.09	1.1
MJ	0.2	0.2	0.2	–	–
Total	1.14	1.13	1.12	1.1	1.12
	3-jet				
VH	1.29	1.29	1.27	1.26	1.28
VV	0.99	0.97	0.97	0.95	0.97
$t\bar{t}$	1.28	1.28	1.31	1.17	1.32
s-top	1.0	1.0	0.97	1.0	–
W+l	1.0	–	–	–	–
W+hf	0.84	–	0.84	0.84	–
Z+l	1.0	1.0	1.0	1.0	1.0
Z+cl	0.87	0.87	0.87	0.87	0.87
Z+hf	1.15	1.09	1.08	1.06	1.06
MJ	0.2	1.0	–	–	–
Total	1.18	1.14	1.11	1.06	1.07

Table 151: Table of post unconditional fit over prefit yields for 2-lepton 2 and 3-jet 2T-tag events in the dijet mass selection.

AJ.4 MVA Analysis: Prefit

Sample	1-tag		2L-tag		2M-tag	2M+2T-tag	2T-tag
	$100 < p_{\mathrm{T}}^{V} < 120\ GeV$	$p_{\mathrm{T}}^{V} > 120\ GeV$	$100 < p_{\mathrm{T}}^{V} < 120\ GeV$	$p_{\mathrm{T}}^{V} > 120\ GeV$	$100 < p_{\mathrm{T}}^{V} < 120\ GeV$	$p_{\mathrm{T}}^{V} > 120\ GeV$	$100 < p_{\mathrm{T}}^{V} < 120\ GeV$
	2-jet						
VH	7.9 ± 0.7	22.8 ± 2.3	2.2 ± 0.2	6.9 ± 0.8	3.5 ± 0.3	23.4 ± 2.5	4.0 ± 0.4
VV	233.5 ± 6.5	631.8 ± 17.7	16.8 ± 0.9	47.8 ± 6.4	13.9 ± 1.5	78.2 ± 12.1	12.4 ± 1.6
$t\bar{t}$	596.6 ± 53.3	1163.6 ± 118.7	78.2 ± 7.4	133.2 ± 15.6	90.1 ± 7.8	236.1 ± 29.3	81.4 ± 9.3
s-top	443.2 ± 155.8	666.6 ± 117.3	34.4 ± 10.3	51.5 ± 8.2	27.2 ± 6.2	58.9 ± 9.6	18.8 ± 4.1
W+l	5290.0 ± 844.1	7371.0 ± 1249.3	159.0 ± 32.5	210.5 ± 47.3	13.2 ± 3.0	14.7 ± 4.1	0.2 ± 0.0
W+cl	1975.9 ± 184.1	3408.2 ± 337.3	93.9 ± 11.8	144.2 ± 19.1	20.9 ± 2.9	24.3 ± 3.9	0.9 ± 0.1
W+hf	883.2 ± 246.4	1967.2 ± 574.2	64.4 ± 12.1	159.4 ± 39.2	39.1 ± 7.0	162.1 ± 34.6	26.2 ± 3.8
Z+l	3709.6 ± 498.0	10805.1 ± 1490.5	89.1 ± 18.3	266.4 ± 56.0	5.2 ± 1.5	14.8 ± 4.2	0.1 ± 0.0
Z+cl	1741.4 ± 206.8	4571.6 ± 459.5	63.8 ± 8.5	180.9 ± 24.6	9.9 ± 1.8	26.1 ± 4.5	0.3 ± 0.0
Z+hf	2236.6 ± 242.3	5909.2 ± 684.5	187.7 ± 15.8	525.5 ± 54.7	155.9 ± 10.3	752.4 ± 69.7	129.2 ± 9.1
Total	17528.5 ± 1477.1	36860.0 ± 3070.9	808.4 ± 77.6	1742.6 ± 179.7	387.9 ± 25.7	1405.1 ± 113.7	279.9 ± 18.4
Data	18343.0 ± 135.4	36903.0 ± 192.1	887.0 ± 29.8	1860.0 ± 43.1	477.0 ± 21.8	1592.0 ± 39.9	306.0 ± 17.5
	3-jet						
VH	–	8.1 ± 1.1	–	2.0 ± 0.3	–	6.6 ± 0.8	–
VV	–	261.1 ± 7.3	–	15.8 ± 2.0	–	19.1 ± 3.0	–
$t\bar{t}$	–	1497.2 ± 326.8	–	157.2 ± 35.4	–	263.9 ± 62.6	–
s-top	–	329.4 ± 33.9	–	25.1 ± 3.6	–	30.2 ± 4.8	–
W+l	–	2536.7 ± 541.2	–	63.8 ± 16.3	–	4.2 ± 0.8	–
W+cl	–	1206.5 ± 198.6	–	50.6 ± 9.2	–	8.4 ± 1.7	–
W+hf	–	757.6 ± 242.4	–	56.4 ± 16.3	–	55.2 ± 13.2	–
Z+l	–	3347.7 ± 561.5	–	80.8 ± 18.0	–	4.3 ± 0.9	–
Z+cl	–	1571.8 ± 459.0	–	62.1 ± 18.7	–	9.1 ± 2.9	–
Z+hf	–	1913.7 ± 438.0	–	156.1 ± 35.3	–	220.0 ± 49.6	–
Total	–	13496.9 ± 1443.4	–	673.4 ± 83.2	–	624.4 ± 90.2	–
Data	–	13344.0 ± 115.5	–	657.0 ± 25.6	–	710.0 ± 26.6	–

Table 152: Table of prefit yields for 0-lepton 2 and 3-jet events in the MVA selection. The uncertainties are from the full prefit nusicance parameters (NPs) except the floating normalizations under the assumption that each NP is independent (uncorrelated).

DRAFT

Sample	1-tag		2L-tag		2M-tag		2T-tag	
	$p_{\mathrm{T}}^{V} < 120\ GeV$	$p_{\mathrm{T}}^{V} > 120\ GeV$	$p_{\mathrm{T}}^{V} < 120\ GeV$	$p_{\mathrm{T}}^{V} > 120\ GeV$	$p_{\mathrm{T}}^{V} < 120\ GeV$	$p_{\mathrm{T}}^{V} > 120\ GeV$	$p_{\mathrm{T}}^{V} < 120\ GeV$	$p_{\mathrm{T}}^{V} > 120\ GeV$
	2-jet							
VH	74.3 ± 5.6	28.1 ± 2.5	20.6 ± 1.9	10.3 ± 1.1	32.1 ± 2.7	16.0 ± 1.6	35.7 ± 3.3	18.4 ± 1.9
VV	3661.6 ± 102.5	928.9 ± 116.0	191.8 ± 5.4	69.0 ± 7.1	116.2 ± 3.3	39.5 ± 7.4	91.0 ± 9.3	31.4 ± 7.0
$t\bar{t}$	19624.1 ± 1776.3	5917.1 ± 537.5	3210.3 ± 318.1	980.7 ± 102.9	4009.6 ± 395.3	994.9 ± 108.6	3785.1 ± 370.6	813.2 ± 94.3
s-top	21755.7 ± 8260.9	3486.1 ± 552.5	1772.6 ± 581.5	392.1 ± 59.5	1505.9 ± 425.9	294.5 ± 42.0	1155.7 ± 311.3	208.9 ± 33.2
W+l	123372.0 ± 18342.2	23658.0 ± 3742.3	2909.5 ± 619.0	759.5 ± 171.4	206.5 ± 59.5	48.6 ± 14.4	6.1 ± 0.2	1.0 ± 0.0
W+cl	121663.4 ± 9259.4	19678.5 ± 1857.3	4346.8 ± 521.0	962.5 ± 126.4	746.4 ± 121.5	149.7 ± 24.9	36.4 ± 7.8	6.7 ± 1.4
W+hf	40061.1 ± 9410.4	7979.0 ± 2246.6	3374.7 ± 472.9	918.5 ± 218.2	2139.6 ± 201.8	561.6 ± 120.5	1104.1 ± 71.6	325.5 ± 68.9
Z+l	7880.2 ± 868.6	1221.2 ± 158.4	195.2 ± 34.5	41.4 ± 1.2	14.4 ± 0.4	3.1 ± 0.1	0.3 ± 0.0	0.0 ± 0.0
Z+cl	3061.3 ± 0.3	380.0 ± 0.0	118.9 ± 0.0	22.2 ± 0.0	21.9 ± 0.0	3.9 ± 0.0	1.0 ± 0.0	0.2 ± 0.0
Z+hf	3797.1 ± 0.4	436.9 ± 0.0	276.4 ± 0.0	44.8 ± 0.0	199.7 ± 8.1	31.1 ± 0.0	131.2 ± 6.8	21.6 ± 2.2
MJ_e	27450.6 ± 1428.9	2113.9 ± 891.2	1613.0 ± 213.6	136.5 ± 56.1	728.1 ± 102.2	70.1 ± 33.2	370.3 ± 81.6	32.9 ± 21.8
MJ_μ	11042.7 ± 1407.0	61.3	825.1 ± 234.9	7.5 ± 0.0	441.9 ± 186.1	–	189.0 ± 113.7	–
Total	383444.0 ± 27422.6	65889.0 ± 5745.7	18854.7 ± 1557.0	4345.0 ± 440.8	10162.4 ± 728.9	2212.9 ± 200.8	6906.0 ± 554.6	1459.9 ± 145.
Data	396213.0 ± 629.5	67603.0 ± 260.0	19974.0 ± 141.3	4561.0 ± 67.5	10948.0 ± 104.6	2446.0 ± 49.5	7720.0 ± 87.9	1551.0 ± 39.
	3-jet							
VH	29.6 ± 2.4	14.0 ± 1.4	6.1 ± 0.6	4.2 ± 0.5	9.1 ± 0.9	6.5 ± 0.7	10.4 ± 1.0	7.3 ± 0.8
VV	2077.8 ± 58.2	676.5 ± 84.9	94.0 ± 2.6	43.9 ± 1.2	41.7 ± 1.2	20.0 ± 2.3	26.2 ± 0.7	15.3 ± 2.3
$t\bar{t}$	36782.2 ± 7690.1	10937.5 ± 2365.7	5992.6 ± 1303.2	1749.5 ± 395.2	7659.2 ± 1682.4	1788.7 ± 410.9	7724.5 ± 1713.3	1470.2 ± 347.5
s-top	13636.1 ± 1155.0	2967.9 ± 392.3	1171.4 ± 109.4	359.9 ± 48.4	1053.3 ± 102.9	281.0 ± 38.8	848.9 ± 93.0	199.3 ± 29.0
W+l	51231.8 ± 9506.7	11958.2 ± 2306.0	1174.5 ± 284.5	372.0 ± 92.5	77.5 ± 2.2	21.9 ± 6.3	2.0 ± 0.1	0.5 ± 0.0
W+cl	46422.0 ± 6375.0	9640.6 ± 1407.6	1670.3 ± 275.5	479.5 ± 81.7	272.4 ± 55.6	70.4 ± 13.9	12.8 ± 0.0	3.1 ± 0.0
W+hf	18368.7 ± 5072.6	4613.7 ± 1448.5	1464.9 ± 290.9	493.8 ± 134.9	848.3 ± 134.6	294.8 ± 71.6	423.5 ± 49.4	160.7 ± 38.1
Z+l	3626.4 ± 487.1	594.8 ± 88.4	86.6 ± 2.4	19.9 ± 0.6	5.7 ± 0.2	1.5 ± 0.0	0.1 ± 0.0	0.0 ± 0.0
Z+cl	1566.2 ± 0.2	219.7 ± 0.0	60.4 ± 0.0	12.3 ± 0.0	10.6 ± 0.0	2.0 ± 0.0	0.4 ± 0.0	0.1 ± 0.0
Z+hf	1855.0 ± 0.2	250.3 ± 0.0	133.3 ± 0.0	26.2 ± 0.0	98.6 ± 0.0	18.5 ± 2.6	65.7 ± 0.0	13.6 ± 2.5
MJ_e	13137.4 ± 560.0	1199.9 ± 567.0	609.8 ± 36.6	54.6 ± 24.9	305.8 ± 19.0	29.7 ± 16.5	158.5 ± 10.7	12.4 ± 5.9
MJ_μ	6061.8 ± 1741.2	57.1	322.0 ± 45.1	–	166.1 ± 56.4	3.7	82.8 ± 23.2	–
Total	194795.0 ± 15819.9	43130.2 ± 4399.5	12785.8 ± 1475.1	3615.8 ± 485.4	10548.3 ± 1711.8	2538.6 ± 431.9	9355.7 ± 1738.3	1882.5 ± 361.1
Data	186860.0 ± 432.3	42557.0 ± 206.3	12691.0 ± 112.7	3895.0 ± 62.4	10965.0 ± 104.7	2640.0 ± 51.4	9866.0 ± 99.3	2057.0 ± 45.4

Table 153: Table of prefit yields for 1-lepton 2 and 3-jet events in the MVA selection. The uncertainties are from the full prefit nusicance parameters (NPs) except the floating normalizations under the assumption that each NP is independent (uncorrelated).

DRAFT

Sample	1-tag		2L-tag		2M+2T-tag	
	$p_{\mathrm{T}}^{V} < 120\ GeV$	$p_{\mathrm{T}}^{V} > 120\ GeV$	$p_{\mathrm{T}}^{V} < 120\ GeV$	$p_{\mathrm{T}}^{V} > 120\ GeV$	$p_{\mathrm{T}}^{V} < 120\ GeV$	$p_{\mathrm{T}}^{V} > 120\ GeV$
	2-jet					
VH	20.4 ± 1.6	7.4 ± 0.8	5.5 ± 0.5	2.0 ± 0.2	18.6 ± 1.6	7.0 ± 0.8
VV	793.0 ± 22.2	134.5 ± 3.8	67.7 ± 5.1	11.8 ± 1.5	122.5 ± 10.5	21.2 ± 2.7
$t\bar{t}$	3570.7 ± 134.7	221.9 ± 20.3	947.4 ± 57.3	47.2 ± 5.0	3026.1 ± 163.0	135.5 ± 13.3
s-top	383.3 ± 10.7	43.9 ± 1.2	40.0 ± 1.1	5.3 ± 0.5	89.5 ± 9.0	11.2 ± 1.4
W+l	244.1 ± 6.8	11.4 ± 0.3	3.7 ± 0.1	0.4 ± 0.0	0.3 ± 0.0	0.0 ± 0.0
W+cl	146.7 ± 0.0	15.5 ± 0.0	5.1 ± 0.0	0.5 ± 0.0	0.9 ± 0.0	0.1 ± 0.0
W+hf	107.9 ± 0.0	15.7 ± 0.0	9.0 ± 0.0	0.8 ± 0.0	5.9 ± 0.0	0.7 ± 0.1
Z+l	28159.8 ± 3610.2	4107.0 ± 482.0	612.2 ± 119.5	97.4 ± 19.3	39.5 ± 8.7	5.5 ± 1.5
Z+cl	13802.3 ± 1165.7	1832.7 ± 134.4	472.8 ± 60.1	70.2 ± 8.2	78.0 ± 12.9	10.5 ± 1.7
Z+hf	19252.5 ± 1906.3	2590.5 ± 270.5	1658.4 ± 133.6	247.8 ± 22.4	2519.2 ± 138.7	360.9 ± 27.2
Total	68583.4 ± 5529.1	9020.6 ± 624.0	3997.4 ± 326.7	486.2 ± 42.7	6008.0 ± 276.2	554.2 ± 36.5
Data	69313.0 ± 263.3	9150.0 ± 95.7	4313.0 ± 65.7	517.0 ± 22.7	6501.0 ± 80.6	570.0 ± 23.9
	3-jet					
VH	7.4 ± 0.7	3.9 ± 0.6	1.5 ± 0.2	0.9 ± 0.1	4.9 ± 0.5	2.8 ± 0.4
VV	345.4 ± 9.7	97.5 ± 9.6	21.3 ± 2.0	6.5 ± 1.1	26.2 ± 3.7	8.1 ± 1.2
$t\bar{t}$	2025.4 ± 409.9	172.7 ± 37.7	412.2 ± 85.0	25.2 ± 5.6	1273.2 ± 261.1	65.0 ± 14.5
s-top	143.5 ± 4.0	21.5 ± 0.6	16.4 ± 1.8	2.9 ± 0.5	38.2 ± 4.0	6.3 ± 1.1
W+l	75.6 ± 2.1	7.1 ± 0.2	1.3 ± 0.0	0.2 ± 0.0	0.1 ± 0.0	0.0 ± 0.0
W+cl	50.3 ± 0.0	7.9 ± 0.0	2.0 ± 0.0	0.3 ± 0.0	0.4 ± 0.0	0.0 ± 0.0
W+hf	47.6 ± 0.0	7.7 ± 0.0	3.7 ± 0.0	0.9 ± 0.0	0.9 ± 0.0	0.5 ± 0.0
Z+l	8854.2 ± 1293.5	1963.5 ± 251.4	187.3 ± 39.0	45.5 ± 9.3	11.5 ± 0.3	2.5 ± 0.7
Z+cl	4709.3 ± 1300.3	929.9 ± 250.4	162.9 ± 47.7	36.0 ± 10.2	24.1 ± 7.5	5.3 ± 1.6
Z+hf	6126.9 ± 1421.0	1252.9 ± 283.2	466.6 ± 103.9	110.3 ± 24.1	672.6 ± 142.4	153.6 ± 32.5
Total	23159.7 ± 2754.3	4488.1 ± 470.4	1300.6 ± 167.8	229.3 ± 31.7	2069.0 ± 305.1	244.7 ± 36.4
Data	22662.0 ± 150.5	4436.0 ± 66.6	1428.0 ± 37.8	253.0 ± 15.9	2394.0 ± 48.9	283.0 ± 16.8

Table 154: Table of prefit yields for 2-lepton 2 and 3-jet events in the MVA selection. The uncertainties are from the full prefit nusicance parameters (NPs) except the floating normalizations under the assumption that each NP is independent (uncorrelated).

AJ.5 MVA Analysis: Prefit

Sample	1-tag $100 < p_T^V < 120\ GeV$	1-tag $p_T^V > 120\ GeV$	2L-tag $100 < p_T^V < 120\ GeV$	2L-tag $p_T^V > 120\ GeV$	2M-tag $100 < p_T^V < 120\ GeV$	2M+2T-tag $p_T^V > 120\ GeV$	2T-tag $100 < p_T^V < 120\ GeV$
	2-jet						
VH	7.6 ± 3.2	21.1 ± 9.0	2.3 ± 1.0	7.0 ± 3.0	3.5 ± 1.5	23.0 ± 9.6	3.9 ± 1.6
VV	234.9 ± 6.0	635.6 ± 16.1	17.6 ± 0.8	48.4 ± 5.9	14.9 ± 1.3	80.2 ± 10.8	13.3 ± 1.4
$t\bar{t}$	833.2 ± 78.9	1553.3 ± 155.5	113.8 ± 10.2	188.2 ± 17.3	126.6 ± 11.7	344.1 ± 29.3	114.3 ± 10.5
s-top	568.6 ± 80.2	725.3 ± 59.4	42.7 ± 5.3	57.7 ± 4.9	34.3 ± 3.8	69.5 ± 7.6	24.3 ± 2.8
W+l	5370.9 ± 304.0	7009.7 ± 411.7	156.1 ± 11.7	202.6 ± 16.9	14.0 ± 1.6	15.3 ± 2.0	0.2 ± 0.0
W+cl	2305.8 ± 164.2	3841.9 ± 295.1	109.2 ± 8.1	165.4 ± 11.7	23.5 ± 1.7	27.5 ± 2.0	1.2 ± 0.1
W+hf	685.5 ± 168.0	1472.9 ± 240.9	49.0 ± 9.8	111.9 ± 19.4	29.9 ± 5.8	108.8 ± 21.3	19.2 ± 3.7
Z+l	3879.2 ± 195.7	10625.4 ± 488.6	96.2 ± 7.9	270.9 ± 21.4	6.0 ± 0.9	16.3 ± 2.2	0.1 ± 0.0
Z+cl	1616.8 ± 206.4	4068.5 ± 516.1	60.9 ± 7.0	165.9 ± 18.8	9.6 ± 0.9	24.1 ± 2.2	0.3 ± 0.0
Z+hf	2566.8 ± 100.1	6530.0 ± 237.2	229.0 ± 9.6	609.8 ± 24.4	186.5 ± 7.1	877.6 ± 32.0	151.9 ± 5.4
Total	18336.0 ± 144.2	36893.5 ± 193.5	889.5 ± 17.1	1846.9 ± 24.1	454.8 ± 9.7	1603.0 ± 27.8	333.0 ± 8.2
Data	18343.0 ± 135.4	36903.0 ± 192.1	887.0 ± 29.8	1860.0 ± 43.1	477.0 ± 21.8	1592.0 ± 39.9	306.0 ± 17.5
$\frac{\text{Sim}-\text{Data}}{\sigma}$	-0.04	-0.03	0.07	-0.27	-0.95	0.23	1.35
	3-jet						
VH	–	7.5 ± 3.2	–	2.0 ± 0.9	–	6.5 ± 2.7	–
VV	–	262.7 ± 6.7	–	16.6 ± 2.0	–	20.2 ± 2.9	–
$t\bar{t}$	–	1686.2 ± 150.0	–	189.6 ± 14.8	–	320.9 ± 22.7	–
s-top	–	319.6 ± 29.6	–	24.5 ± 2.6	–	30.5 ± 3.4	–
W+l	–	2200.5 ± 141.6	–	58.0 ± 5.1	–	4.4 ± 0.5	–
W+cl	–	1265.2 ± 101.0	–	54.3 ± 3.9	–	8.9 ± 0.7	–
W+hf	–	725.9 ± 121.7	–	52.9 ± 9.4	–	52.7 ± 10.0	–
Z+l	–	3148.4 ± 173.6	–	78.3 ± 6.6	–	4.5 ± 0.6	–
Z+cl	–	1686.8 ± 198.8	–	67.8 ± 7.3	–	9.9 ± 1.0	–
Z+hf	–	1909.2 ± 99.6	–	174.0 ± 9.2	–	257.0 ± 14.2	–
Total	–	13294.4 ± 105.6	–	719.0 ± 11.7	–	716.7 ± 17.2	–
Data	–	13344.0 ± 115.5	–	657.0 ± 25.6	–	710.0 ± 26.6	–
$\frac{\text{Sim}-\text{Data}}{\sigma}$	–	-0.32	–	2.12	–	0.21	–

Table 155: Table of post unconditional fit yields for 0-lepton 2 and 3-jet events in the MVA selection. The uncertainties are the full postfit errors including all nusicance parameters with priors, floating normalizations, and the correlations deduced from the data. The difference in the data and the postfit simulation is compared to σ which is obtained from the sum in simulation as the sum in quadrature of the postfit and Poissonian error.

DRAFT

Sample	1-tag		2L-tag		2M-tag		2T-tag	
	$p_T^V < 120\ GeV$	$p_T^V > 120\ GeV$	$p_T^V < 120\ GeV$	$p_T^V > 120\ GeV$	$p_T^V < 120\ GeV$	$p_T^V > 120\ GeV$	$p_T^V < 120\ GeV$	$p_T^V > 120\ GeV$
	2-jet							
VH	70.4 ± 30.0	26.2 ± 11.2	21.3 ± 9.1	10.7 ± 4.5	32.4 ± 13.7	16.0 ± 6.7	35.6 ± 15.0	18.2 ± 7.6
VV	3683.7 ± 93.5	921.7 ± 102.1	192.9 ± 4.9	68.6 ± 6.5	117.0 ± 3.0	40.5 ± 6.8	97.0 ± 8.2	32.6 ± 6.5
$t\bar{t}$	22454.2 ± 1401.9	6920.2 ± 488.6	3897.5 ± 224.2	1218.7 ± 75.8	4718.3 ± 263.4	1241.1 ± 71.9	4437.7 ± 243.6	1023.4 ± 57.1
s-top	28670.4 ± 4318.5	3846.3 ± 303.1	2405.7 ± 326.3	463.0 ± 37.0	2003.9 ± 244.8	350.7 ± 29.9	1521.4 ± 183.4	251.8 ± 25.6
W+l	122859.4 ± 7518.9	23301.3 ± 1402.8	2946.8 ± 268.1	768.1 ± 70.9	219.4 ± 33.6	51.6 ± 7.5	6.1 ± 0.2	1.0 ± 0.0
W+cl	140195.0 ± 8426.1	22354.9 ± 1500.0	5093.7 ± 284.3	1114.0 ± 68.6	887.0 ± 58.7	171.7 ± 12.0	45.4 ± 7.2	7.1 ± 1.1
W+hf	26010.4 ± 5459.1	5775.7 ± 945.1	2577.2 ± 470.4	647.5 ± 118.1	1700.5 ± 303.3	380.5 ± 73.1	912.8 ± 170.9	207.3 ± 42.9
Z+l	8131.4 ± 375.3	1204.1 ± 69.3	203.2 ± 14.5	41.7 ± 1.1	14.5 ± 0.4	3.1 ± 0.1	0.3 ± 0.0	0.0 ± 0.0
Z+cl	2737.6 ± 356.8	339.8 ± 44.3	106.4 ± 13.9	19.9 ± 2.6	19.6 ± 2.6	3.5 ± 0.5	0.9 ± 0.1	0.2 ± 0.0
Z+hf	4138.3 ± 185.2	476.1 ± 21.3	301.2 ± 13.5	48.8 ± 2.2	227.1 ± 8.1	33.9 ± 1.5	146.5 ± 5.4	25.9 ± 1.3
MJ_e	26707.1 ± 1243.9	2382.6 ± 732.0	1520.6 ± 159.3	152.4 ± 46.5	700.0 ± 93.2	85.5 ± 31.1	345.2 ± 73.4	39.7 ± 19.2
MJ_μ	10588.2 ± 1310.8	61.3	648.7 ± 154.9	7.6 ± 0.0	382.4 ± 113.9	–	125.5 ± 74.6	–
Total	396245.9 ± 660.4	67610.4 ± 279.7	19915.3 ± 128.3	4560.8 ± 49.6	11022.1 ± 91.7	2378.0 ± 32.2	7674.5 ± 77.0	1607.3 ± 26.8
Data	396213.0 ± 629.5	67603.0 ± 260.0	19974.0 ± 141.3	4561.0 ± 67.5	10948.0 ± 104.6	2446.0 ± 49.5	7720.0 ± 87.9	1551.0 ± 39.4
$\frac{\text{Sim}-\text{Data}}{\sigma}$	0.04	0.02	-0.31	-0.0	0.53	-1.16	-0.39	1.17
	3-jet							
VH	28.8 ± 12.3	13.5 ± 5.8	6.3 ± 2.7	4.3 ± 1.8	9.2 ± 3.9	6.4 ± 2.7	10.5 ± 4.4	7.3 ± 3.1
VV	2090.3 ± 53.0	686.0 ± 78.3	94.6 ± 2.4	44.1 ± 1.1	42.0 ± 1.1	21.0 ± 2.2	26.3 ± 0.7	15.5 ± 2.2
$t\bar{t}$	36443.2 ± 1277.4	10806.1 ± 609.5	6350.5 ± 148.8	1872.7 ± 78.0	8069.5 ± 142.3	1913.1 ± 64.6	8162.5 ± 129.2	1580.4 ± 47.2
s-top	14756.9 ± 890.3	2776.4 ± 292.5	1337.4 ± 78.7	351.4 ± 36.9	1233.3 ± 76.6	291.2 ± 31.7	1000.9 ± 64.3	207.5 ± 22.6
W+l	46814.0 ± 2813.0	11178.3 ± 682.0	1088.9 ± 98.2	355.9 ± 33.2	78.0 ± 2.0	23.0 ± 3.4	2.0 ± 0.0	0.5 ± 0.0
W+cl	49761.2 ± 3144.1	10393.8 ± 760.4	1822.6 ± 106.5	526.8 ± 35.6	309.6 ± 22.1	81.3 ± 6.4	15.3 ± 1.2	3.7 ± 0.3
W+hf	10153.9 ± 2211.4	4426.6 ± 754.8	957.1 ± 183.3	486.1 ± 88.2	589.3 ± 112.3	285.5 ± 54.0	320.8 ± 62.4	158.0 ± 32.7
Z+l	3533.4 ± 202.7	561.0 ± 31.1	87.2 ± 2.2	20.0 ± 0.5	5.7 ± 0.1	1.5 ± 0.0	0.1 ± 0.0	0.0 ± 0.0
Z+cl	1400.6 ± 182.5	196.5 ± 25.6	54.0 ± 7.0	11.0 ± 1.4	9.4 ± 1.2	1.8 ± 0.2	0.3 ± 0.0	0.1 ± 0.0
Z+hf	2021.7 ± 90.5	272.7 ± 12.2	145.3 ± 6.5	28.6 ± 1.3	107.5 ± 4.8	20.2 ± 1.0	71.6 ± 3.2	14.8 ± 0.8
MJ_e	13168.8 ± 535.6	1191.6 ± 358.9	604.5 ± 36.0	100.1 ± 36.1	294.9 ± 18.0	61.0 ± 26.6	165.4 ± 11.1	24.9 ± 11.8
MJ_μ	6667.4 ± 1558.0	57.1	300.0 ± 41.3	–	159.8 ± 59.9	3.7	85.2 ± 27.2	–
Total	186840.1 ± 472.1	42559.7 ± 203.6	12848.3 ± 92.1	3801.1 ± 43.9	10908.2 ± 76.9	2709.8 ± 35.2	9860.8 ± 80.5	2012.7 ± 31.6
Data	186860.0 ± 432.3	42557.0 ± 206.3	12691.0 ± 112.7	3895.0 ± 62.4	10965.0 ± 104.7	2640.0 ± 51.4	9866.0 ± 99.3	2057.0 ± 45.4
$\frac{\text{Sim}-\text{Data}}{\sigma}$	-0.03	0.01	1.08	-1.24	-0.44	1.11	-0.04	-0.81

Table 156: Table of post unconditional fit yields for 1-lepton 2 and 3-jet events in the MVA selection. The uncertainties are the full postfit errors including all nusicance parameters with priors, floating normalizations, and the correlations deduced from the data. The difference in the data and the postfit simulation is compared to σ which is obtained from the sum in simulation as the sum in quadrature of the postfit and Poissonian error.

DRAFT

Sample	1-tag		2L-tag		2M+2T-tag	
	$p_{\mathrm{T}}^{V} < 120\ GeV$	$p_{\mathrm{T}}^{V} > 120\ GeV$	$p_{\mathrm{T}}^{V} < 120\ GeV$	$p_{\mathrm{T}}^{V} > 120\ GeV$	$p_{\mathrm{T}}^{V} < 120\ GeV$	$p_{\mathrm{T}}^{V} > 120\ GeV$
	2-jet					
VH	19.3 ± 8.2	6.8 ± 2.9	5.7 ± 2.4	2.0 ± 0.9	18.6 ± 7.8	6.8 ± 2.8
VV	797.7 ± 20.2	135.3 ± 3.4	73.7 ± 4.0	12.2 ± 1.4	130.2 ± 8.5	21.5 ± 2.5
$t\bar{t}$	3518.8 ± 177.4	219.3 ± 14.6	1031.5 ± 40.4	50.7 ± 2.9	3177.8 ± 95.6	138.8 ± 7.3
s-top	385.6 ± 9.8	44.1 ± 1.1	40.2 ± 1.0	5.9 ± 0.5	98.2 ± 8.5	12.0 ± 1.0
W+l	245.6 ± 6.2	11.5 ± 0.3	3.7 ± 0.1	0.4 ± 0.0	0.3 ± 0.0	0.0 ± 0.0
W+cl	175.4 ± 13.7	18.5 ± 1.4	6.1 ± 0.5	0.7 ± 0.1	1.1 ± 0.1	0.1 ± 0.0
W+hf	84.3 ± 15.8	12.3 ± 2.3	7.0 ± 1.3	0.6 ± 0.1	4.6 ± 0.9	0.5 ± 0.1
Z+l	29175.7 ± 1403.4	4138.4 ± 188.8	644.1 ± 51.6	100.5 ± 8.0	41.4 ± 5.3	6.1 ± 0.8
Z+cl	12409.4 ± 1535.3	1653.7 ± 205.8	430.0 ± 47.9	65.2 ± 7.3	71.3 ± 6.3	9.8 ± 0.9
Z+hf	21170.3 ± 840.8	2846.9 ± 86.4	1925.2 ± 79.4	288.9 ± 9.5	2849.6 ± 93.6	410.1 ± 12.7
Total	69356.2 ± 281.3	9113.1 ± 86.0	4282.1 ± 48.9	528.9 ± 7.8	6463.4 ± 76.1	606.9 ± 12.4
Data	69313.0 ± 263.3	9150.0 ± 95.7	4313.0 ± 65.7	517.0 ± 22.7	6501.0 ± 80.6	570.0 ± 23.9
$\frac{\text{Sim}-\text{Data}}{\sigma}$	0.11	-0.29	-0.38	0.49	-0.34	1.34
	3-jet					
VH	6.9 ± 2.9	3.6 ± 1.5	1.6 ± 0.7	0.9 ± 0.4	4.9 ± 2.1	2.8 ± 1.2
VV	347.5 ± 8.8	99.4 ± 9.2	22.4 ± 1.8	6.9 ± 1.0	29.0 ± 3.3	8.6 ± 1.2
$t\bar{t}$	2189.2 ± 113.7	187.3 ± 13.3	490.9 ± 18.9	29.9 ± 1.8	1475.4 ± 49.9	76.4 ± 4.3
s-top	144.4 ± 3.7	21.6 ± 0.5	18.5 ± 1.7	3.0 ± 0.5	41.4 ± 3.8	6.4 ± 1.0
W+l	76.1 ± 1.9	7.1 ± 0.2	1.4 ± 0.0	0.2 ± 0.0	0.1 ± 0.0	0.0 ± 0.0
W+cl	60.1 ± 4.7	9.4 ± 0.7	2.4 ± 0.2	0.4 ± 0.0	0.4 ± 0.0	0.1 ± 0.0
W+hf	37.2 ± 7.0	6.0 ± 1.1	2.9 ± 0.5	0.7 ± 0.1	0.7 ± 0.1	0.4 ± 0.1
Z+l	8723.7 ± 495.4	1883.2 ± 100.0	187.1 ± 16.0	44.9 ± 3.9	11.6 ± 0.3	2.6 ± 0.4
Z+cl	4812.0 ± 574.2	982.1 ± 115.0	169.9 ± 18.6	39.1 ± 4.2	25.6 ± 2.4	5.8 ± 0.6
Z+hf	5818.6 ± 304.9	1223.5 ± 52.9	499.9 ± 25.0	120.4 ± 5.5	760.8 ± 38.5	176.5 ± 9.0
Total	22721.5 ± 150.2	4438.6 ± 56.0	1413.5 ± 19.3	247.0 ± 5.2	2360.9 ± 42.3	280.2 ± 8.3
Data	22662.0 ± 150.5	4436.0 ± 66.6	1428.0 ± 37.8	253.0 ± 15.9	2394.0 ± 48.9	283.0 ± 16.8
$\frac{\text{Sim}-\text{Data}}{\sigma}$	0.28	0.03	-0.34	-0.36	-0.51	-0.15

Table 157: Table of post unconditional fit yields for 2-lepton 2 and 3-jet events in the MVA selection. The uncertainties are the full postfit errors including all nusicance parameters with priors, floating normalizations, and the correlations deduced from the data. The difference in the data and the postfit simulation is compared to σ which is obtained from the sum in simulation as the sum in quadrature of the postfit and Poissonian error.

AJ.6 MVA Analysis: Postfit over Preft

Sample	1-tag		2L-tag		2M-tag	2M+2T-tag	2T-tag
	$100 < p_{\mathrm{T}}^{V} < 120\ GeV$	$p_{\mathrm{T}}^{V} > 120\ GeV$	$100 < p_{\mathrm{T}}^{V} < 120\ GeV$	$p_{\mathrm{T}}^{V} > 120\ GeV$	$100 < p_{\mathrm{T}}^{V} < 120\ GeV$	$p_{\mathrm{T}}^{V} > 120\ GeV$	$100 < p_{\mathrm{T}}^{V} < 120\ GeV$
				2-jet			
VH	0.96	0.93	1.05	1.01	1.0	0.98	0.99
VV	1.01	1.01	1.05	1.01	1.07	1.03	1.08
$t\bar{t}$	1.4	1.33	1.45	1.41	1.41	1.46	1.4
s-top	1.28	1.09	1.24	1.12	1.26	1.18	1.29
W+l	1.02	0.95	0.98	0.96	1.06	1.04	1.01
W+cl	1.17	1.13	1.16	1.15	1.12	1.13	1.35
W+hf	0.78	0.75	0.76	0.7	0.76	0.67	0.73
Z+l	1.05	0.98	1.08	1.02	1.16	1.1	1.01
Z+cl	0.93	0.89	0.95	0.92	0.97	0.93	0.89
Z+hf	1.15	1.11	1.22	1.16	1.2	1.17	1.18
Total	1.05	1.0	1.1	1.06	1.17	1.14	1.19
				3-jet			
VH	–	0.93	–	1.0	–	0.99	–
VV	–	1.01	–	1.05	–	1.06	–
$t\bar{t}$	–	1.13	–	1.21	–	1.22	–
s-top	–	0.97	–	0.98	–	1.01	–
W+l	–	0.87	–	0.91	–	1.04	–
W+cl	–	1.05	–	1.07	–	1.06	–
W+hf	–	0.96	–	0.94	–	0.96	–
Z+l	–	0.94	–	0.97	–	1.05	–
Z+cl	–	1.07	–	1.09	–	1.09	–
Z+hf	–	1.0	–	1.11	–	1.17	–
Total	–	0.98	–	1.07	–	1.15	–

Table 158: Table of post unconditional fit over prefit yields for 0-lepton 2 and 3-jet events in the MVA selection.

Sample	1-tag		2L-tag		2M-tag		2T-tag	
	$p_T^V < 120\ GeV$	$p_T^V > 120\ GeV$	$p_T^V < 120\ GeV$	$p_T^V > 120\ GeV$	$p_T^V < 120\ GeV$	$p_T^V > 120\ GeV$	$p_T^V < 120\ GeV$	$p_T^V > 120\ GeV$
	2-jet							
VH	0.95	0.93	1.04	1.03	1.01	1.0	1.0	0.99
VV	1.01	0.99	1.01	0.99	1.01	1.02	1.07	1.04
$t\bar{t}$	1.14	1.17	1.21	1.24	1.18	1.25	1.17	1.26
s-top	1.32	1.1	1.36	1.18	1.33	1.19	1.32	1.21
W+l	1.0	0.98	1.01	1.01	1.06	1.06	1.01	1.01
W+cl	1.15	1.14	1.17	1.16	1.19	1.15	1.25	1.05
W+hf	0.65	0.72	0.76	0.7	0.79	0.68	0.83	0.64
Z+l	1.03	0.99	1.04	1.01	1.01	1.01	1.01	1.01
Z+cl	0.89	0.89	0.89	0.89	0.89	0.89	0.89	0.89
Z+hf	1.09	1.09	1.09	1.09	1.14	1.09	1.12	1.2
MJ_e	0.97	1.13	0.94	1.12	0.96	1.22	0.93	1.21
MJ_μ	0.96	1.0	0.79	1.0	0.87	–	0.66	–
Total	1.03	1.03	1.06	1.05	1.08	1.07	1.11	1.1
	3-jet							
VH	0.97	0.96	1.03	1.02	1.01	1.0	1.01	1.01
VV	1.01	1.01	1.01	1.01	1.01	1.05	1.01	1.01
$t\bar{t}$	0.99	0.99	1.06	1.07	1.05	1.07	1.06	1.07
s-top	1.08	0.94	1.14	0.98	1.17	1.04	1.18	1.04
W+l	0.91	0.93	0.93	0.96	1.01	1.05	1.01	1.01
W+cl	1.07	1.08	1.09	1.1	1.14	1.15	1.2	1.2
W+hf	0.55	0.96	0.65	0.98	0.69	0.97	0.76	0.98
Z+l	0.97	0.94	1.01	1.01	1.01	1.01	1.01	1.01
Z+cl	0.89	0.89	0.89	0.89	0.89	0.89	0.89	0.89
Z+hf	1.09	1.09	1.09	1.09	1.09	1.09	1.09	1.09
MJ_e	1.0	0.99	0.99	1.83	0.96	2.06	1.04	2.0
MJ_μ	1.1	1.0	0.93	–	0.96	1.0	1.03	–
Total	0.96	0.99	1.0	1.05	1.03	1.07	1.05	1.07

Table 159: Table of post unconditional fit over prefit yields for 1-lepton 2 and 3-jet events in the MVA selection.

Sample	1-tag		2L-tag		2M+2T-tag	
	$p_{\mathrm{T}}^{V} < 120\ GeV$	$p_{\mathrm{T}}^{V} > 120\ GeV$	$p_{\mathrm{T}}^{V} < 120\ GeV$	$p_{\mathrm{T}}^{V} > 120\ GeV$	$p_{\mathrm{T}}^{V} < 120\ GeV$	$p_{\mathrm{T}}^{V} > 120\ GeV$
	2-jet					
VH	0.95	0.92	1.04	1.0	1.0	0.97
VV	1.01	1.01	1.09	1.03	1.06	1.02
$t\bar{t}$	0.99	0.99	1.09	1.07	1.05	1.02
s-top	1.01	1.01	1.01	1.12	1.1	1.08
W+l	1.01	1.01	1.01	1.01	1.01	1.01
W+cl	1.2	1.2	1.2	1.2	1.2	1.2
W+hf	0.78	0.78	0.78	0.78	0.78	0.7
Z+l	1.04	1.01	1.05	1.03	1.05	1.11
Z+cl	0.9	0.9	0.91	0.93	0.91	0.93
Z+hf	1.1	1.1	1.16	1.17	1.13	1.14
Total	1.01	1.01	1.07	1.09	1.08	1.1
	3-jet					
VH	0.93	0.92	1.04	1.01	1.01	0.98
VV	1.01	1.02	1.05	1.05	1.11	1.06
$t\bar{t}$	1.08	1.08	1.19	1.19	1.16	1.18
s-top	1.01	1.01	1.13	1.02	1.08	1.03
W+l	1.01	1.01	1.01	1.01	1.01	1.01
W+cl	1.2	1.2	1.2	1.2	1.2	1.2
W+hf	0.78	0.78	0.78	0.78	0.78	0.78
Z+l	0.99	0.96	1.0	0.99	1.01	1.06
Z+cl	1.02	1.06	1.04	1.09	1.06	1.1
Z+hf	0.95	0.98	1.07	1.09	1.13	1.15
Total	0.98	0.99	1.09	1.08	1.14	1.14

Table 160: Table of post unconditional fit over prefit yields for 2-lepton 2 and 3-jet events in the MVA selection.

AK Combining 7 TeV and 8 TeV results

This section describe the combination of the 7 TeV data and 8 TeV data to get the final results. For the 7 TeV data, we use the public results discussed in detail in [11] The 7 TeV dataset has not been re-analyzed following the new strategy described in the note, because some of the needed improvements in the understanding of the object performance (i.e. the pseudo-continuous b-tagging or the global sequential calibration) are not completely available/validated for 7 TeV data. The decision is to combine the new 8 TeV data, with the 7 TeV results described in [11]. To decide which correlation to keep across the 2 years, one should consider that among the two years:

- the jet calibration is different;
- the lepton identification algorithm is different
- the MET soft term is calculated in a slightly different way
- the b-tagging algorithm is different

so the decision is to keep all the systematic uncertainties on the reconstructed object as non correlated.

The extended phase space of the new 8 TeV analysis requested a more mature understanding of the background modeling, resulting in corrections and systematic uncertainties which are consistent but different from the ones used in the 7 TeV data. For this reason, it is hard to assume correlations across years for the nuisance parameters on the modeling of the backgrounds.

Given the conditions discussed above, the 2 analyses are treated as non correlated. In this section, we report the preliminary studies on the combination of the new 8 TeV analysis, with the 7 TeV results reported in [11]. The structure is the following:

- Consistency of the 2 results and expected final μ
- Checks on the pulls and correlations
- Post fit plots for 7 TeV distribution

The 7 TeV result is shown in Figure 512, 8 TeV in Figure 513, and the combination in Figure 514.

AK.1 Consistency of the results

The measured μ for the 7 TeV analysis in [11] is -2.1 ± 1.4. Let's assume that in the new 8 TeV analysis result we get a different μ, what would be the compatibility of the 2 results? In combining the 2 years, what is the expected final μ?

To answer these 2 questions, we generated Asimov datasets with different assumption on μ_{8TeV}, we combined these Asimov with the 7 TeV results, and we studied the compatibility of the two years results, and the final combined μ, as a function of μ_{8TeV}. The results are shown on Figure 515.

The consistency between the 2 years has been evaluated by studying the $\Delta \ln(L)$ when different nuisance parameters for the signal strength are used for each year, and when the 2 years have a common nuisance parameters for the signal strength. The probability is bigger than 4% if the 8 TeV result has a signal strength smaller than 1.6.

The combination of the two years follows the naive expectation coming from the weighted average of the two years, with a shift of more or less -0.3 if compared with the 8 TeV fit alone. Note that the final error on μ is of the order of 0.4, meaning a shift due to the 2011 data smaller than 1 standard deviation.

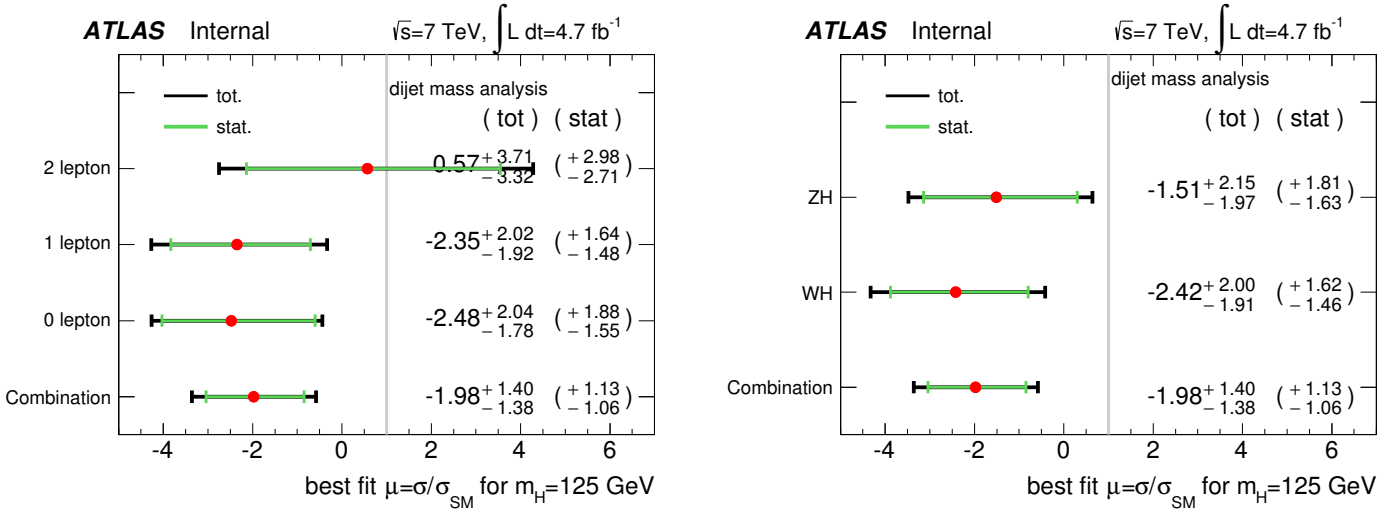

Figure 512: The fitted values of the Higgs-boson signal strength parameter μ for dijet mass 7 TeV result. Both plot have been created in the context on the full 0+1+2 lepton fit. The left plot was made fitting a signal strength in each lepton selection while the right was made fitting a signal strenght for WH and ZH separately.

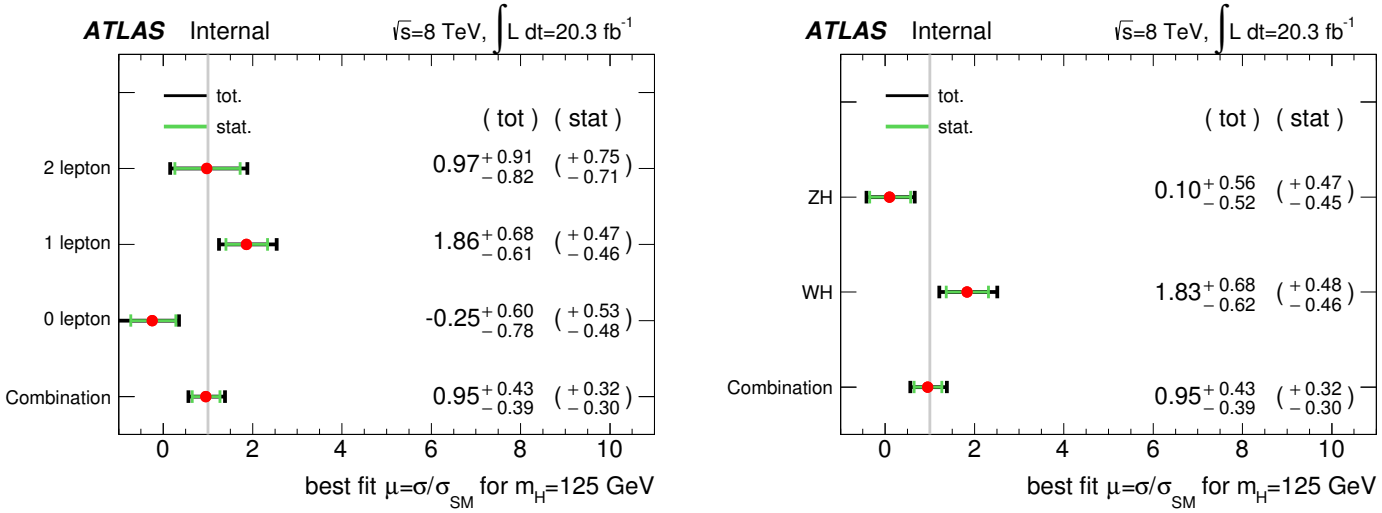

Figure 513: The fitted values of the Higgs-boson signal strength parameter μ for MVA 8 TeV result. Both plot have been created in the context on the full 0+1+2 lepton fit. The left plot was made fitting a signal strength in each lepton selection while the right was made fitting a signal strenght for WH and ZH separately.

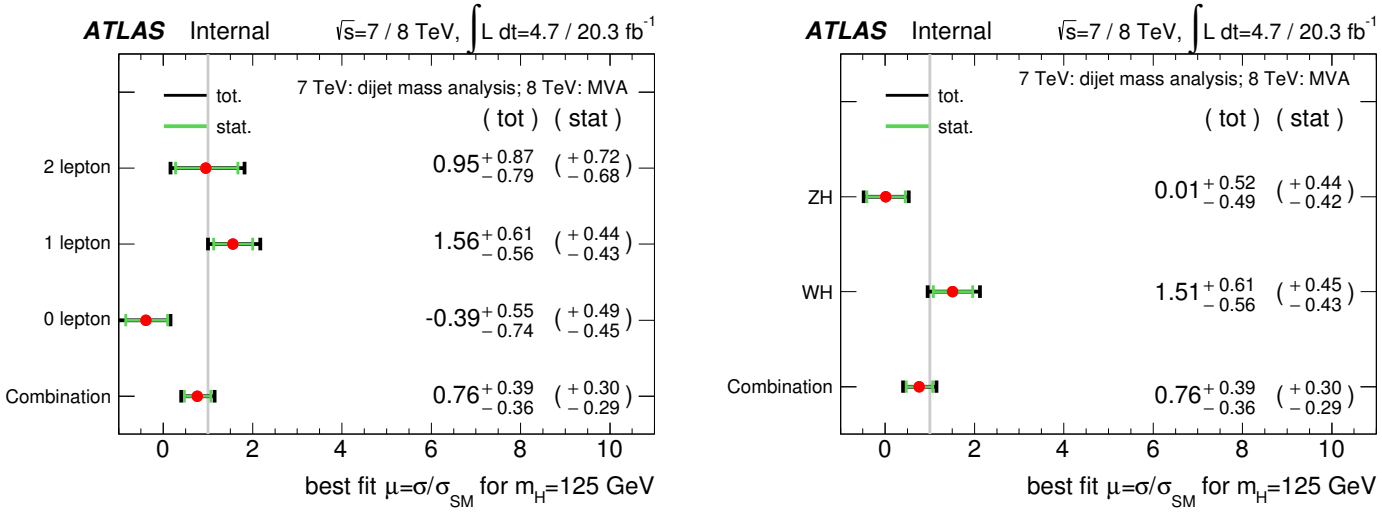

Figure 514: The fitted values of the Higgs-boson signal strength parameter μ for the combination of the 7 TeV dijet mass and MVA 8 TeV result. Both plot have been created in the context on the full 0+1+2 lepton fit. The left plot was made fitting a signal strength in each lepton selection while the right was made fitting a signal strenght for WH and ZH separately.

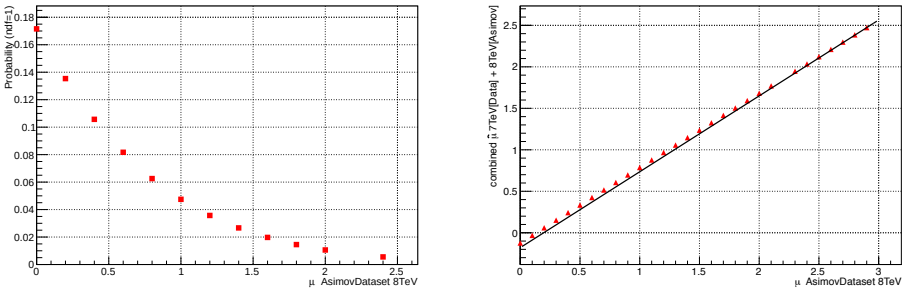

Figure 515: Left: Compatibility of the fit results in the 2 years, as a function of the injected signal in the Asimov dataset for the 8 TeV MVA analysis. Right: Final extracted μ as a function of the injected signal in the Asimov dataset for the 8 TeV MVA analysis. In red: fit result. In black: the expectation from the naive calculation.

AK.2 Pulls on the combination

Since we are fitting the two years as completely independent measurements, we expect that the pulls for the different NP in the combination follow identically their behavior in the individual fit. This is shown in Figures 516- 518. In these plots, we used the 2011 data, and the 2012 Asimov dataset, coherently with the rest of the studies in this section. As can be seen, the combined fit shows pulls and constrains which are coherent with the individual 7 TeV and 8 TeV fit (with minimal negligible deviations). NOTE: the plots on this section need to be updated.

Figure 519 shows the correlation induced by the fit between the 2011 and the 2012 NP. Correlation smaller than 0.3% are induced between NP of two years.

AK.3 Post-fit 2011 distributions

This part of the appendix contains the post-fit plots for the 7 TeV analysis from the new combined fit.

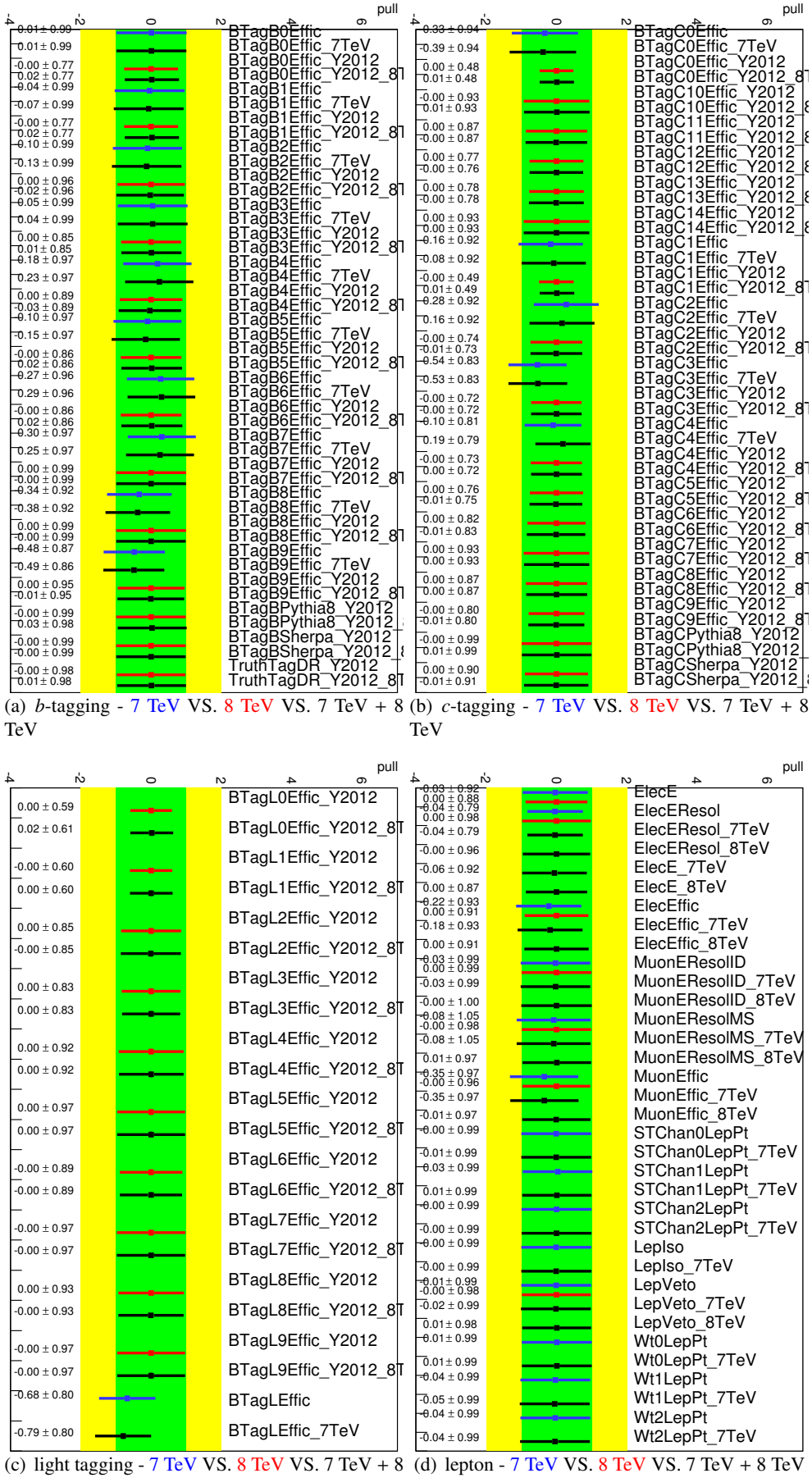

(a) *b*-tagging - 7 TeV VS. 8 TeV VS. 7 TeV + 8 TeV

(b) *c*-tagging - 7 TeV VS. 8 TeV VS. 7 TeV + 8 TeV

(c) light tagging - 7 TeV VS. 8 TeV VS. 7 TeV + 8 TeV

(d) lepton - 7 TeV VS. 8 TeV VS. 7 TeV + 8 TeV

Figure 516: Pull plots for *b*, *c*, light tagging and lepton systematics in the 0+1+2 lepton MVA fit. Comparison of the 7 TeV, 8 TeV and the combined fit.

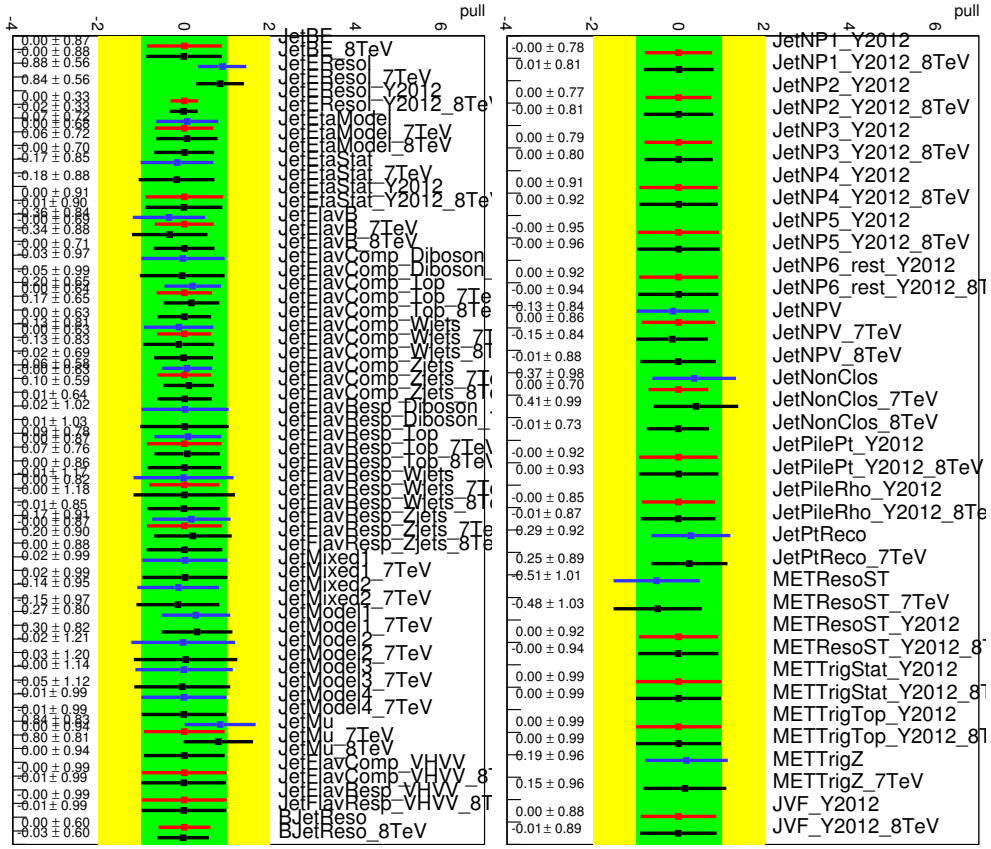

(a) JES 1 - 7 TeV VS. 8 TeV VS. 7 TeV + 8 TeV (b) JES 2 - 7 TeV VS. 8 TeV VS. 7 TeV + 8 TeV

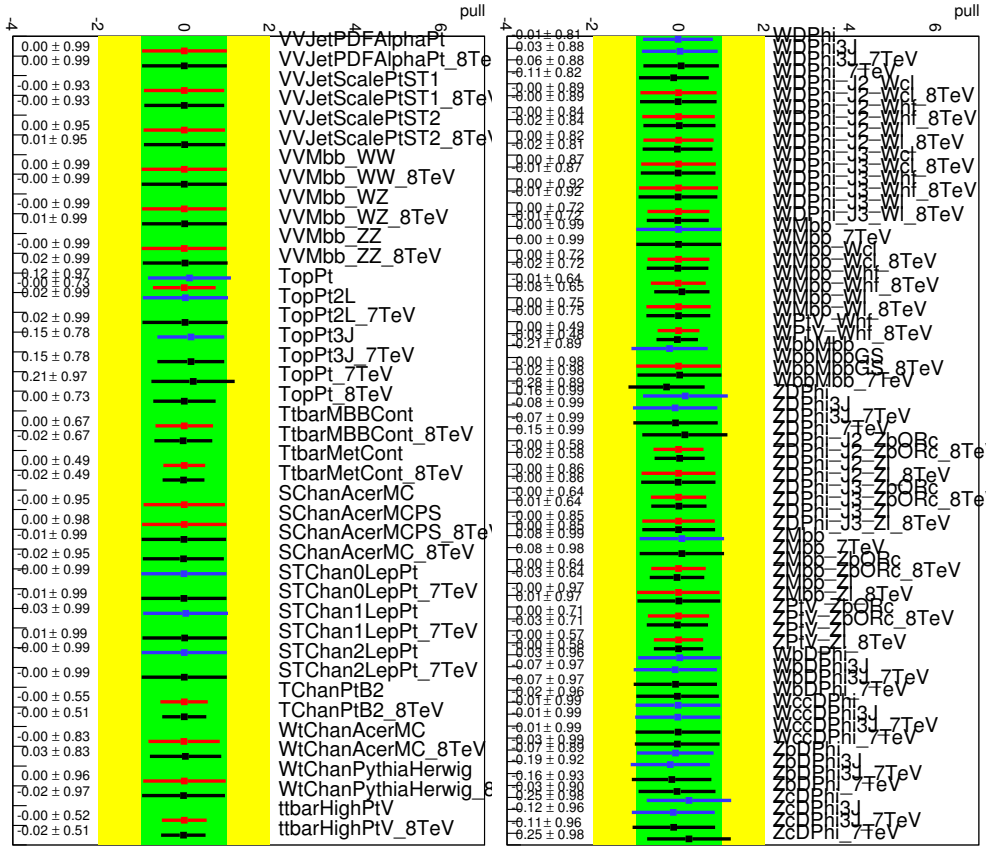

(c) Top and Diboson Modeling - 7 TeV VS. 8 TeV VS. 7 TeV + 8 TeV (d) W and Z Modeling - 7 TeV VS. 8 TeV VS. 7 TeV + 8 TeV

Figure 517: Pull plots for JES systematics, diboson/top and W/Z systematics in the 0+1+2 lepton MVA fit. Comparison of the 7 TeV, 8 TeV and the combined fit.

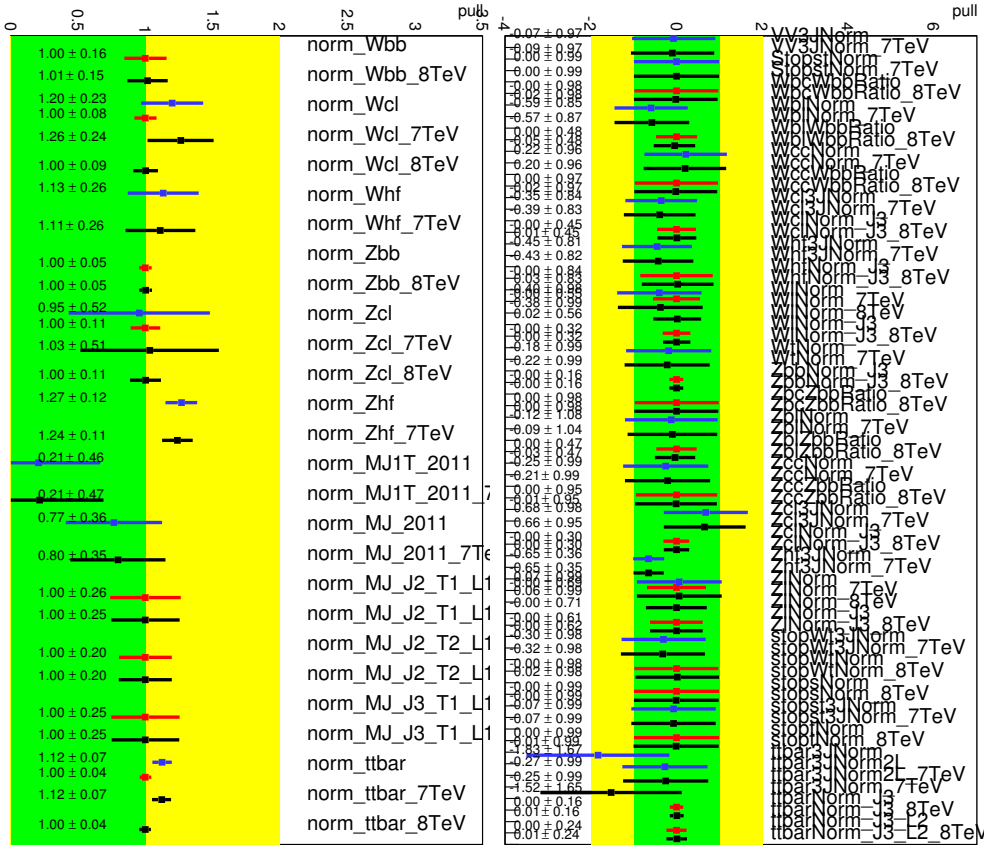

(a) Normalization - 7 TeV VS. 8 TeV VS. 7 TeV + 8 TeV

(b) Normalization systematics - 7 TeV VS. 8 TeV VS. 7 TeV + 8 TeV

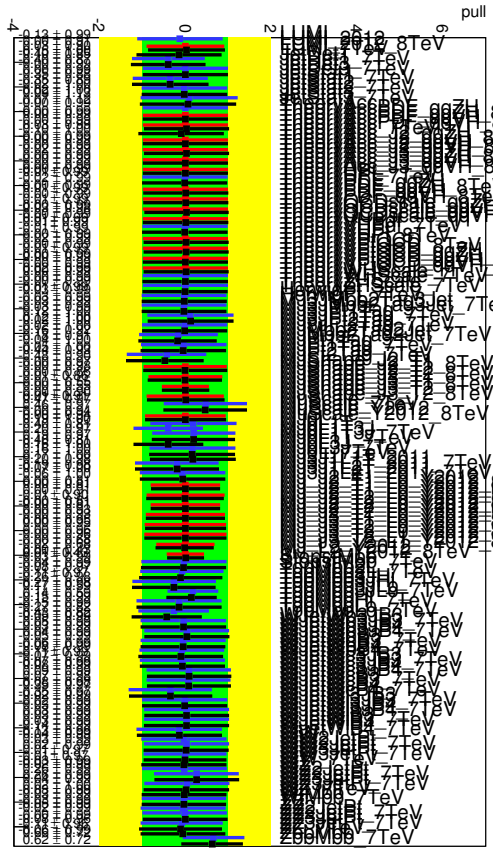

(c) Remaining NP - 7 TeV VS. 8 TeV VS. 7 TeV + 8 TeV

Figure 518: Pull plots for normalization NPs and remaining NPs in the 0+1+2 lepton MVA fit. Comparison of the 7 TeV, 8 TeV and the combined fit.

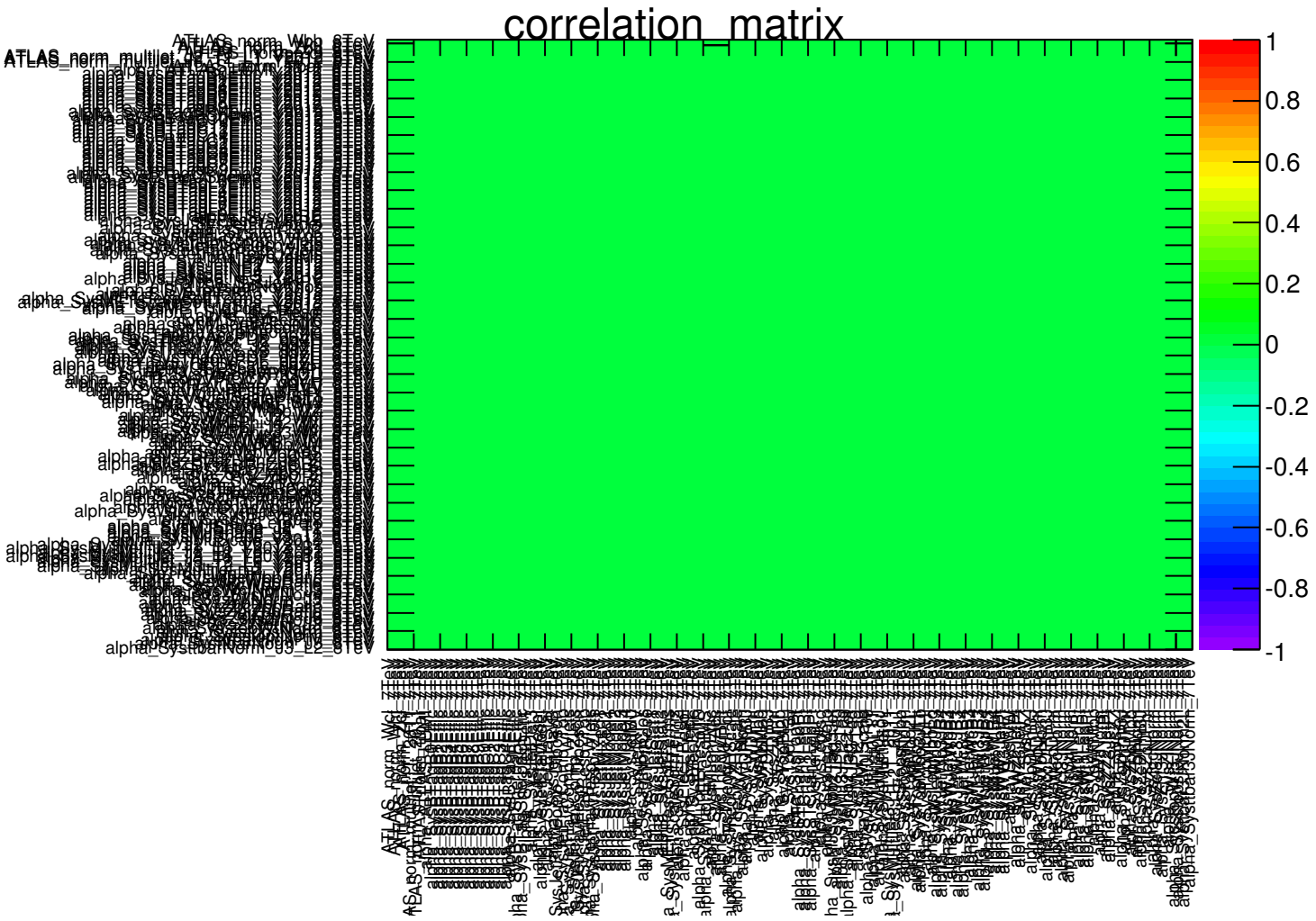

Figure 519: The correlation between 7 TeV NP and 8 TeV NP, induced by the fit. The maximum correlation induced by the fit is of the order of 0.3%.

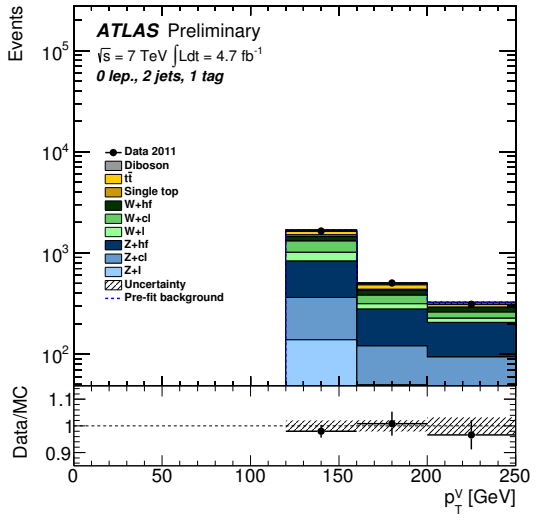

(a) 2 jets, 1 tag

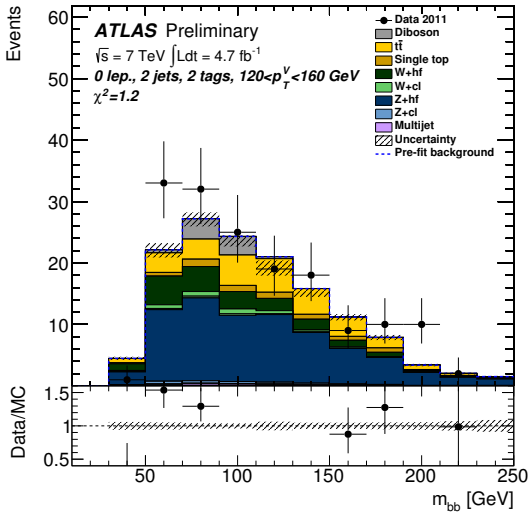

(b) $120 < p_{\mathrm{T}}^{V} < 160$ GeV, 2 jets, 2 tag

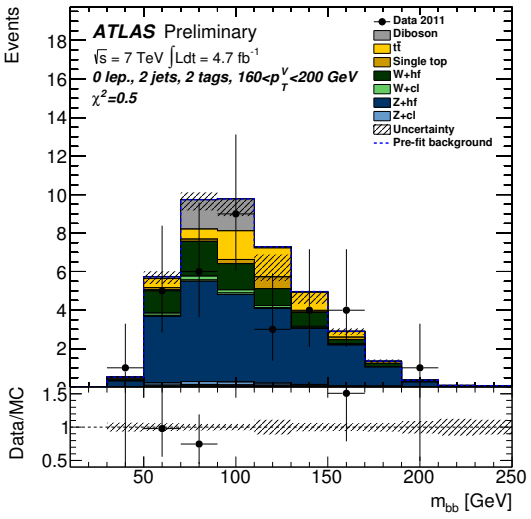

(c) $160 < p_{\mathrm{T}}^{V} < 200$ GeV, 2 jets, 2 tag

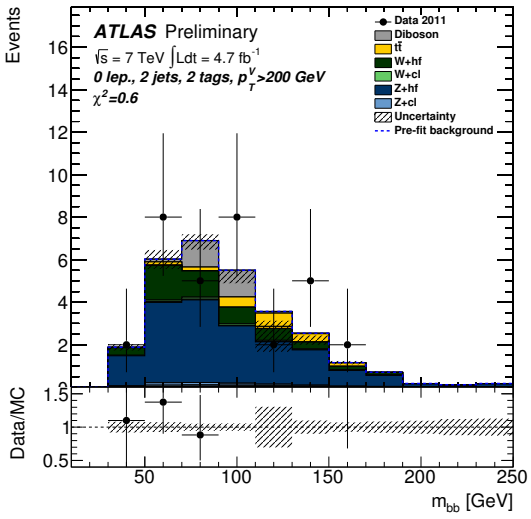

(d) $p_{\mathrm{T}}^{V} > 200$ GeV, 2 jets, 2 tag

Figure 520: Post-fit plots for m_{jj} distribution in 0-lepton events in the 1-tag (wherep_{T}^{V} is used in the fit) and 2-tag categories for the 2-jets events. Plots are shown for $120 < p_{\mathrm{T}}^{V} < 160$ GeVand $160 < p_{\mathrm{T}}^{V} < 200$ GeVand $p_{\mathrm{T}}^{V} > 200$ GeV. The pre-fit background expectation is indicated by the dashed blue line.

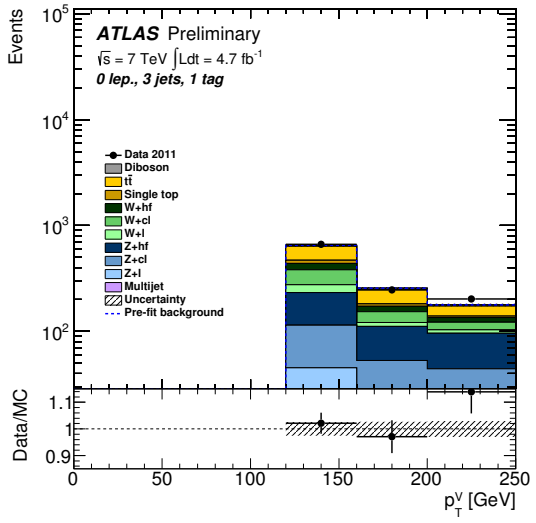

(a) 3 jets, 1 tag

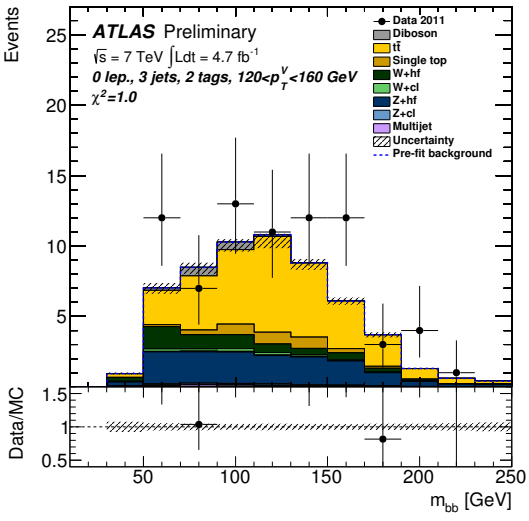

(b) $120 < p_{\mathrm{T}}^{V} < 160$ GeV, 3 jets, 2 tag

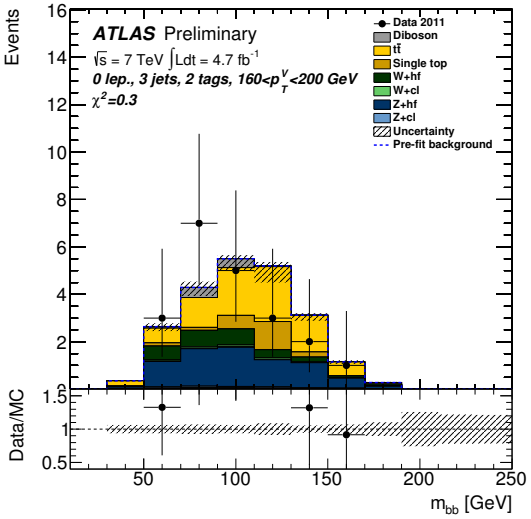

(c) $160 < p_{\mathrm{T}}^{V} < 200$ GeV, 3 jets, 2 tag

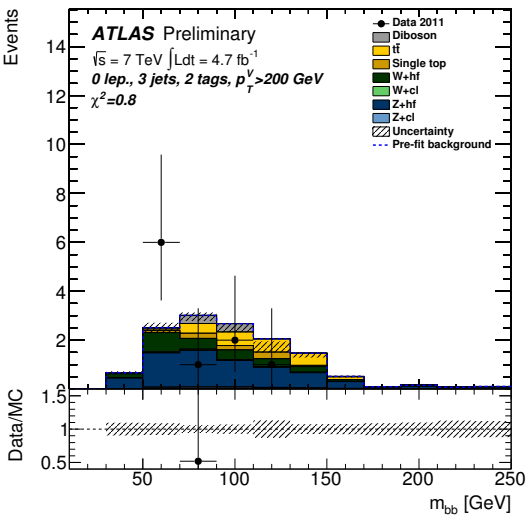

(d) $p_{\mathrm{T}}^{V} > 200$ GeV, 2 jets, 3 tag

Figure 521: Post-fit plots for m_{jj} distribution in 0-lepton events in the 1-tag (wherep_{T}^{V} is used in the fit) and 2-tag categories for the 3-jets events. Plots are shown for $p_{\mathrm{T}}^{V} < 90$ GeV, $90 < p_{\mathrm{T}}^{V} < 120$ GeV, $120 < p_{\mathrm{T}}^{V} < 160$ GeVand $160 < p_{\mathrm{T}}^{V} < 200$ GeVand $p_{\mathrm{T}}^{V} > 200$ GeV. The pre-fit background expectation is indicated by the dashed blue line.

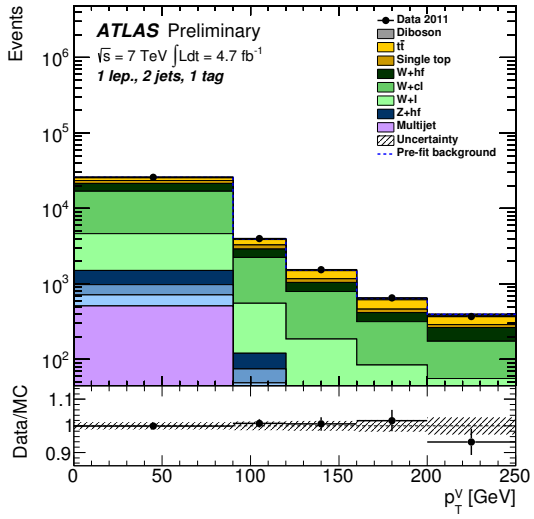

(a) 2 jets, 1 tag

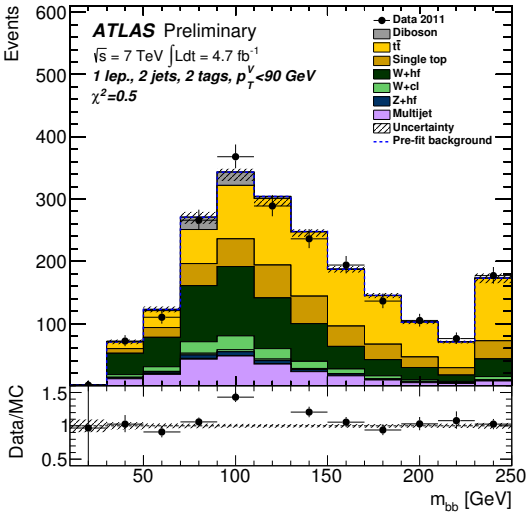

(b) $0 < p_{\mathrm{T}}^{V} < 90$ GeV, 2 jets, 2 tag

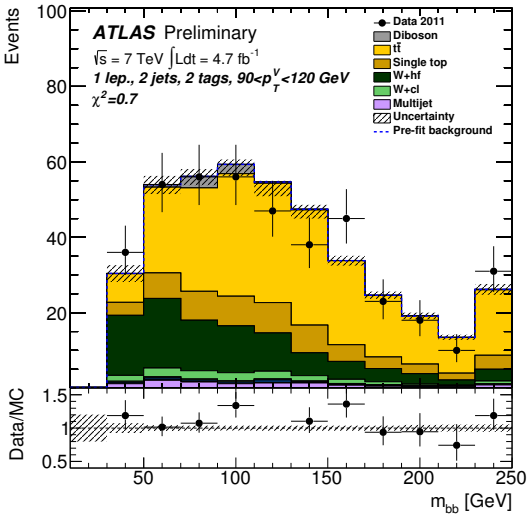

(c) $90 < p_{\mathrm{T}}^{V} < 120$ GeV, 2 jets, 2 tag

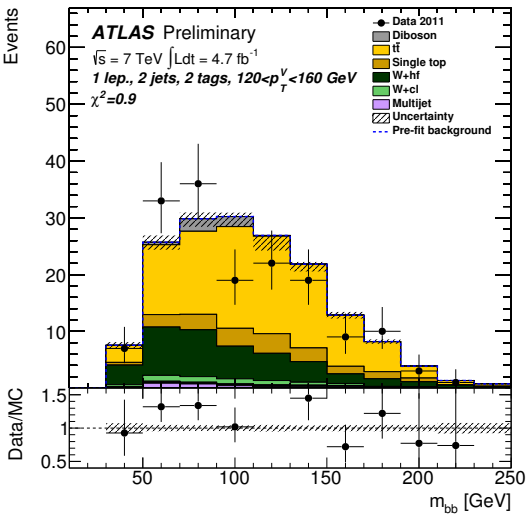

(d) $120 < p_{\mathrm{T}}^{V} < 160$ GeV, 2 jets, 2 tag

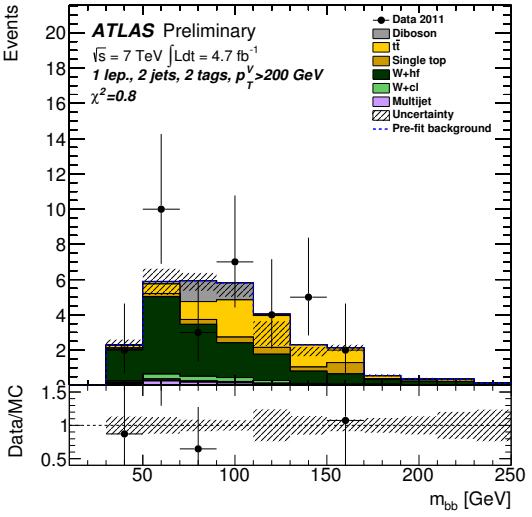

(e) $160 < p_{\mathrm{T}}^{V} < 200$ GeV, 2 jets, 2 tag

(f) $p_{\mathrm{T}}^{V} > 200$ GeV, 2 jets, 2 tag

Figure 522: Post-fit plots for m_{jj} distribution in 1-lepton events in the 1-tag (wherep_{T}^{V} is used in the fit) and 2-tag categories for the 2-jets events. Plots are shown for $p_{\mathrm{T}}^{V} < 90$ GeV, $90 < p_{\mathrm{T}}^{V} < 120$ GeV, $120 < p_{\mathrm{T}}^{V} < 160$ GeVand $160 < p_{\mathrm{T}}^{V} < 200$ GeVand $p_{\mathrm{T}}^{V} > 200$ GeV. The pre-fit background expectation is indicated by the dashed blue line.

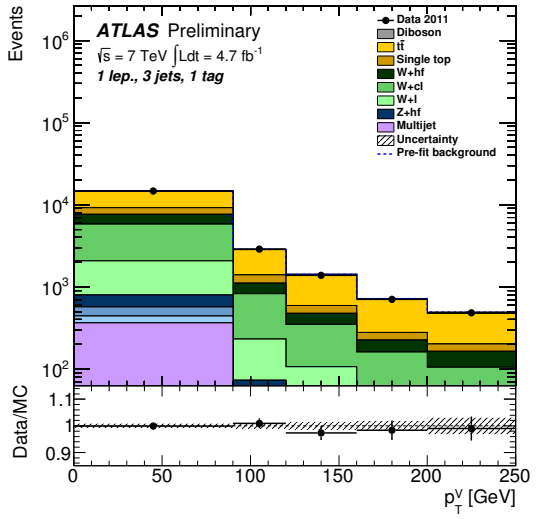

(a) 3 jets, 1 tag

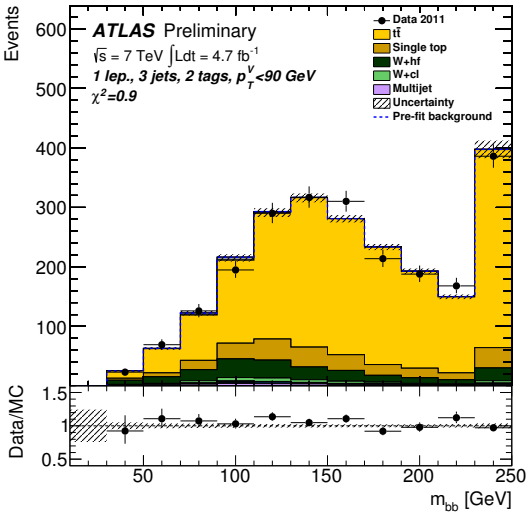

(b) $0 < p_{\mathrm{T}}^{V} < 90$ GeV, 3 jets, 2 tag

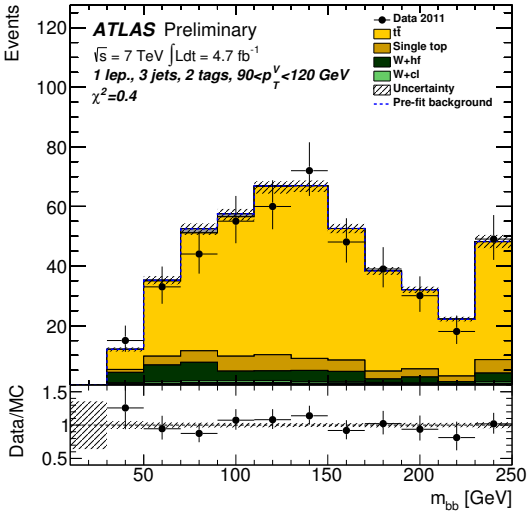

(c) $90 < p_{\mathrm{T}}^{V} < 120$ GeV, 3 jets, 2 tag

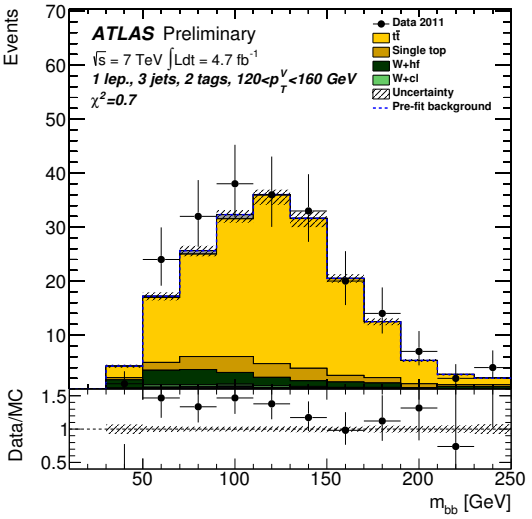

(d) $120 < p_{\mathrm{T}}^{V} < 160$ GeV, 3 jets, 2 tag

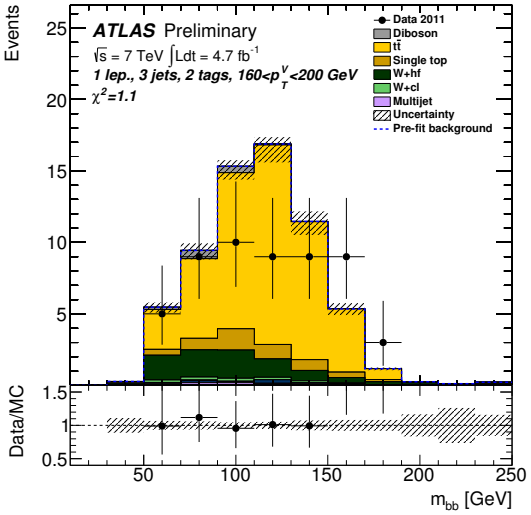

(e) $160 < p_{\mathrm{T}}^{V} < 200$ GeV, 3 jets, 2 tag

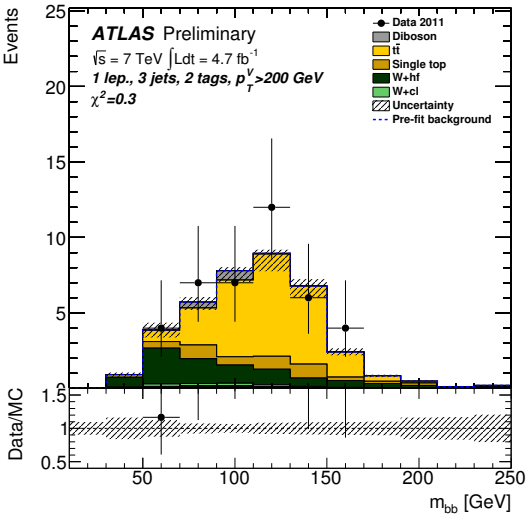

(f) $p_{\mathrm{T}}^{V} > 200$ GeV, 2 jets, 3 tag

Figure 523: Post-fit plots for m_{jj} distribution in 1-lepton events in the 1-tag (wherep_{T}^{V} is used in the fit) and 2-tag categories for the 3-jets events. Plots are shown for $p_{\mathrm{T}}^{V} < 90$ GeV, $90 < p_{\mathrm{T}}^{V} < 120$ GeV, $120 < p_{\mathrm{T}}^{V} < 160$ GeVand $160 < p_{\mathrm{T}}^{V} < 200$ GeVand $p_{\mathrm{T}}^{V} > 200$ GeV. The pre-fit background expectation is indicated by the dashed blue line.

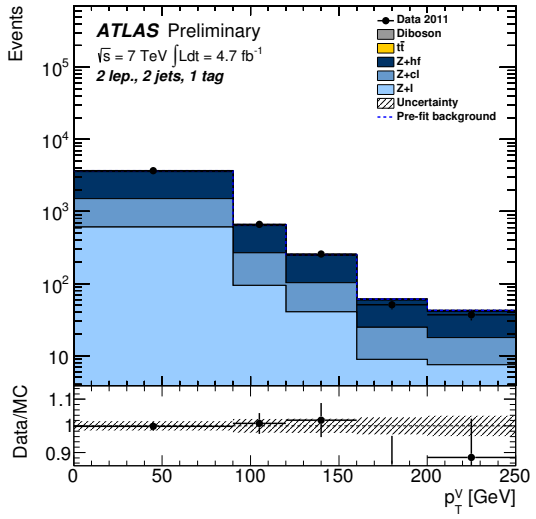

(a) 2 jets, 1 tag

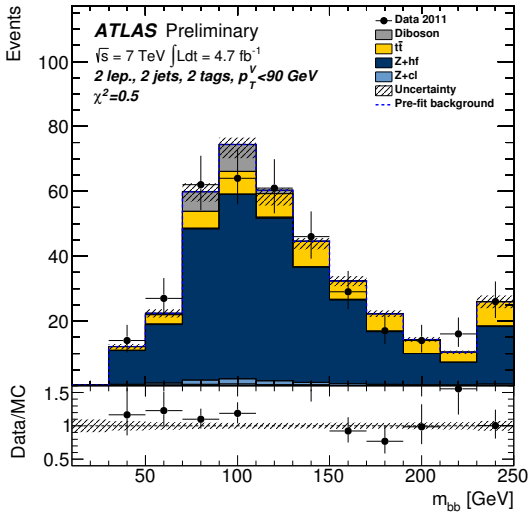

(b) $0 < p_{\mathrm{T}}^{V} < 90$ GeV, 2 jets, 2 tag

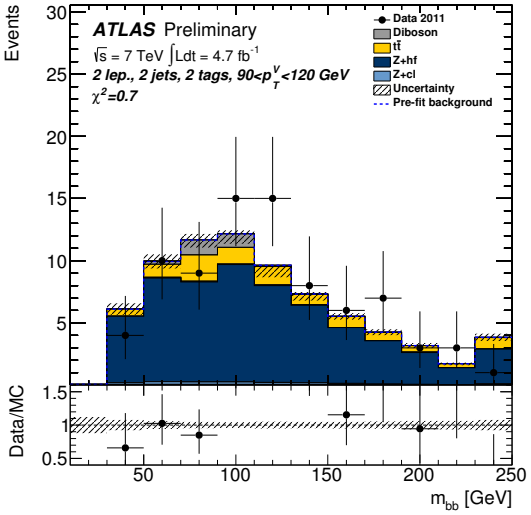

(c) $90 < p_{\mathrm{T}}^{V} < 120$ GeV, 2 jets, 2 tag

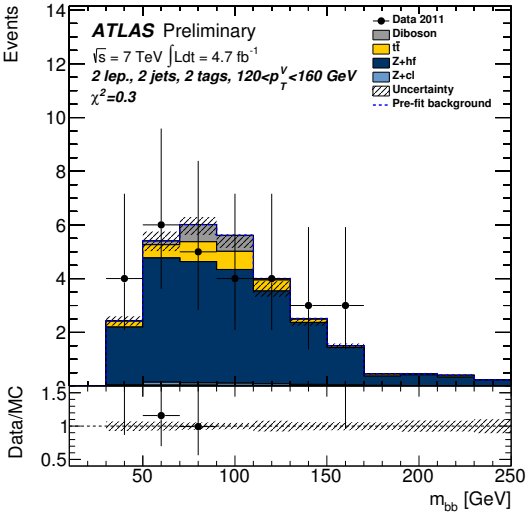

(d) $120 < p_{\mathrm{T}}^{V} < 160$ GeV, 2 jets, 2 tag

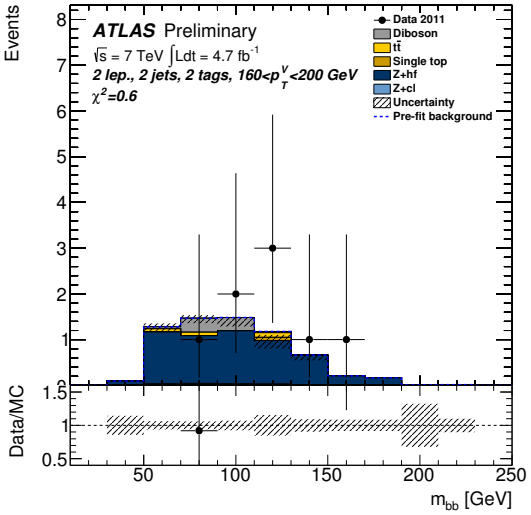

(e) $160 < p_{\mathrm{T}}^{V} < 200$ GeV, 2 jets, 2 tag

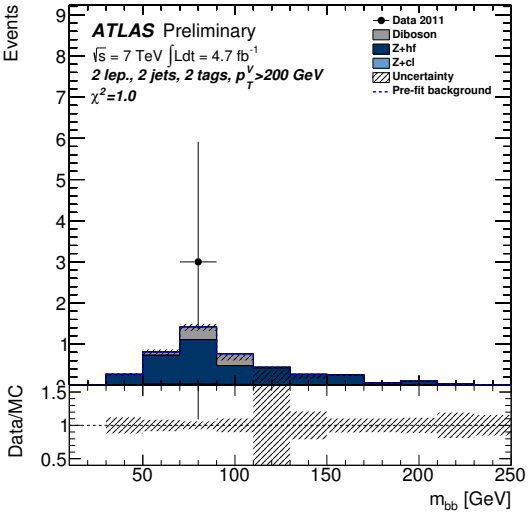

(f) $p_{\mathrm{T}}^{V} > 200$ GeV, 2 jets, 2 tag

Figure 524: Post-fit plots for m_{jj} distribution in 2-lepton events in the 1-tag (wherep_{T}^{V} is used in the fit) and 2-tag categories for the 2-jets events. Plots are shown for $p_{\mathrm{T}}^{V} < 90$ GeV, $90 < p_{\mathrm{T}}^{V} < 120$ GeV, $120 < p_{\mathrm{T}}^{V} < 160$ GeVand $160 < p_{\mathrm{T}}^{V} < 200$ GeVand $p_{\mathrm{T}}^{V} > 200$ GeV. The pre-fit background expectation is indicated by the dashed blue line.

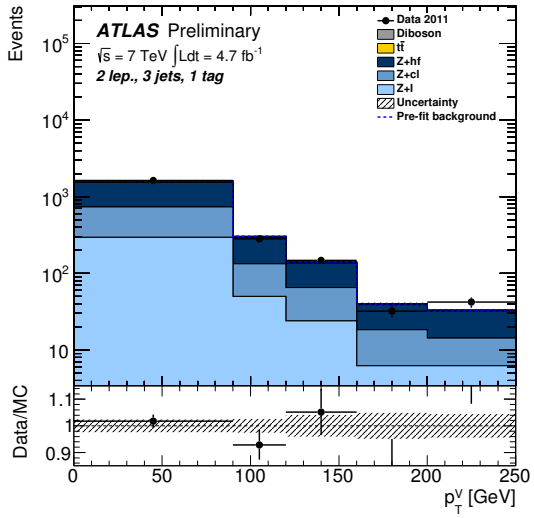

(a) 3 jets, 1 tag

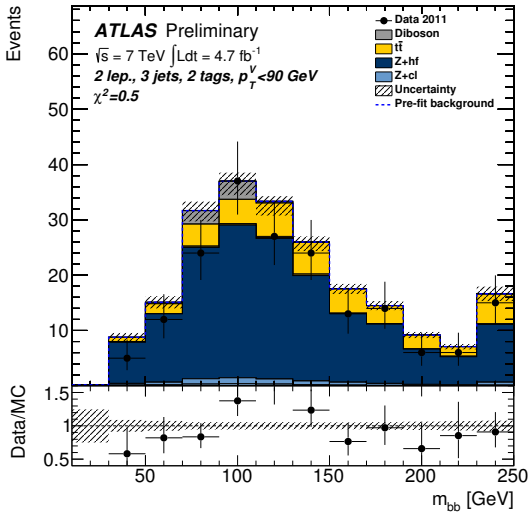

(b) $0 < p_{\mathrm{T}}^{V} < 90$ GeV, 3 jets, 2 tag

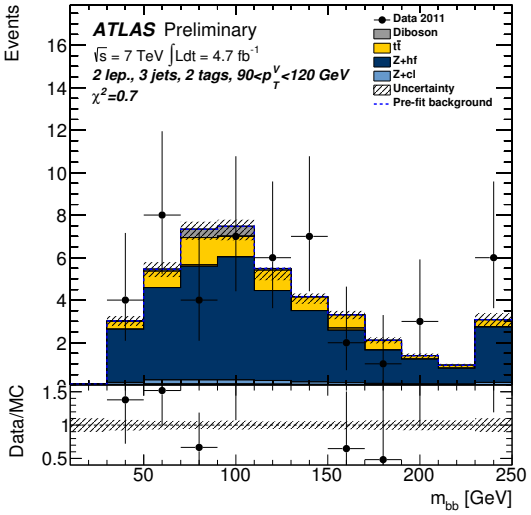

(c) $90 < p_{\mathrm{T}}^{V} < 120$ GeV, 3 jets, 2 tag

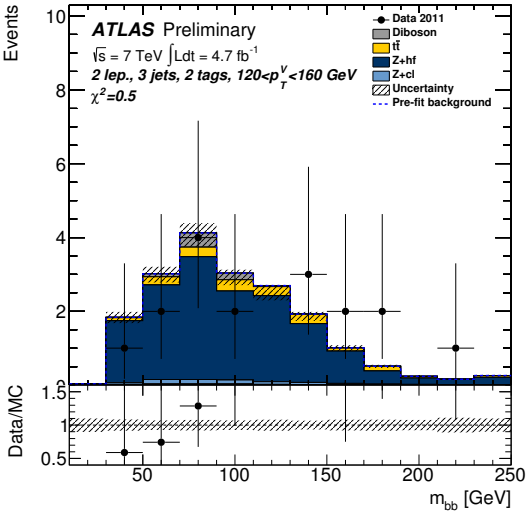

(d) $120 < p_{\mathrm{T}}^{V} < 160$ GeV, 3 jets, 2 tag

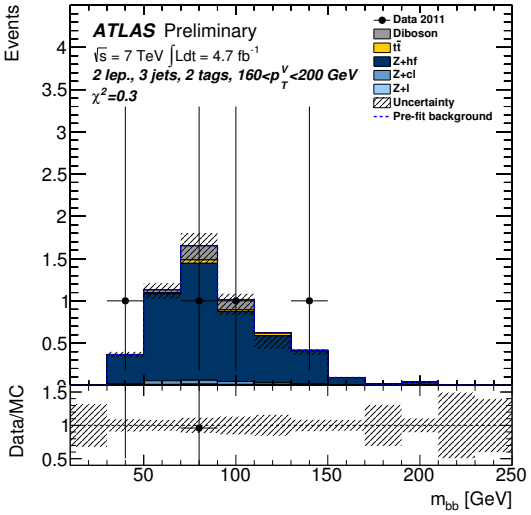

(e) $160 < p_{\mathrm{T}}^{V} < 200$ GeV, 3 jets, 2 tag

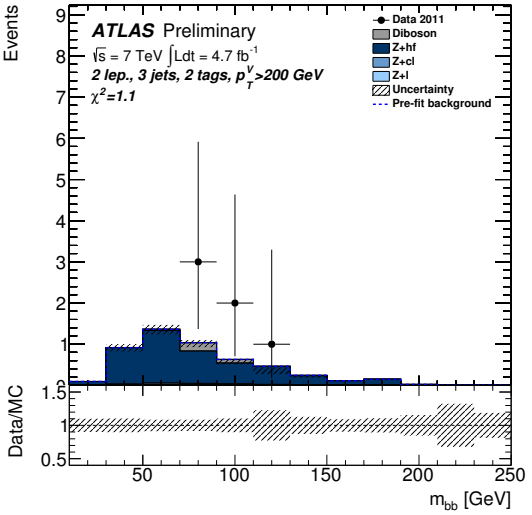

(f) $p_{\mathrm{T}}^{V} > 200$ GeV, 2 jets, 3 tag

Figure 525: Post-fit plots for m_{jj} distribution in 2-lepton events in the 1-tag (wherep_{T}^{V} is used in the fit) and 2-tag categories for the 3-jets events. Plots are shown for $p_{\mathrm{T}}^{V} < 90$ GeV, $90 < p_{\mathrm{T}}^{V} < 120$ GeV, $120 < p_{\mathrm{T}}^{V} < 160$ GeVand $160 < p_{\mathrm{T}}^{V} < 200$ GeVand $p_{\mathrm{T}}^{V} > 200$ GeV. The pre-fit background expectation is indicated by the dashed blue line.

AL Studies for the diboson VZ fit

This section contains the checks and the studies done for the diboson:

- Ranking plots;
- Pulls, comparing the Higgs analysis and the diboson analysis, an comparing the different lepton channels;
- Correlation among highly correlated variables;
- Correlation between diboson and Higgs signal.

Since the diboson fit is now unblindend, all the results on this section will show the results of the unblinded results. For the time being, particular attention is given to the MVA analysis, but in the future this appendix will contain the studies on the fit for both the m_{bb} shape analysis and the MVA shape analysis.

AL.1 Ranking plots for MVA diboson analysis

Figures 526 and 527 show the ranking plots on data. In general, the ranking plot show similarities with the Higgs fit described in the bulk of the note.

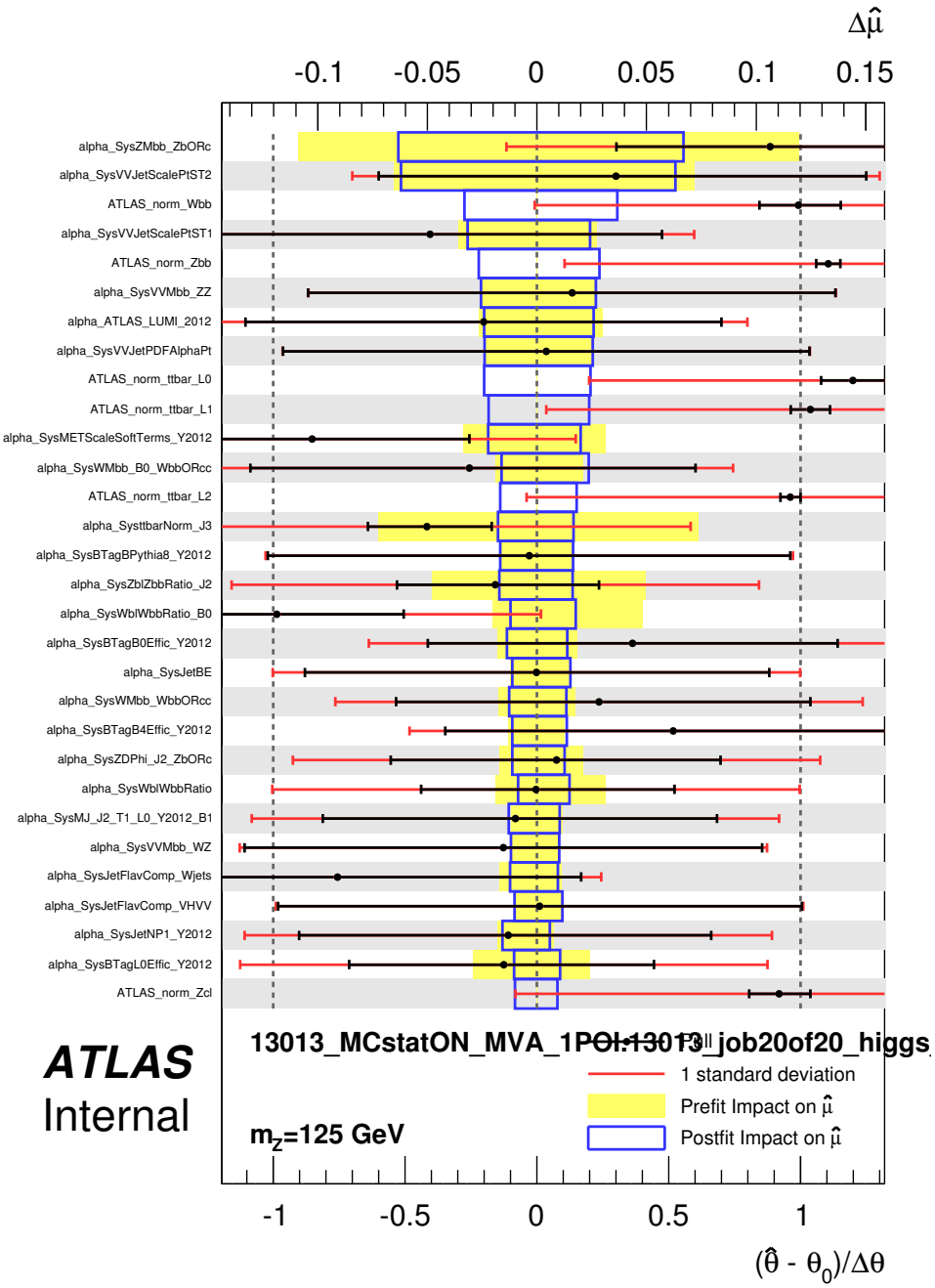

Figure 526: Ranking of systematic uncertainties in the MVA analysis for the combined fit.

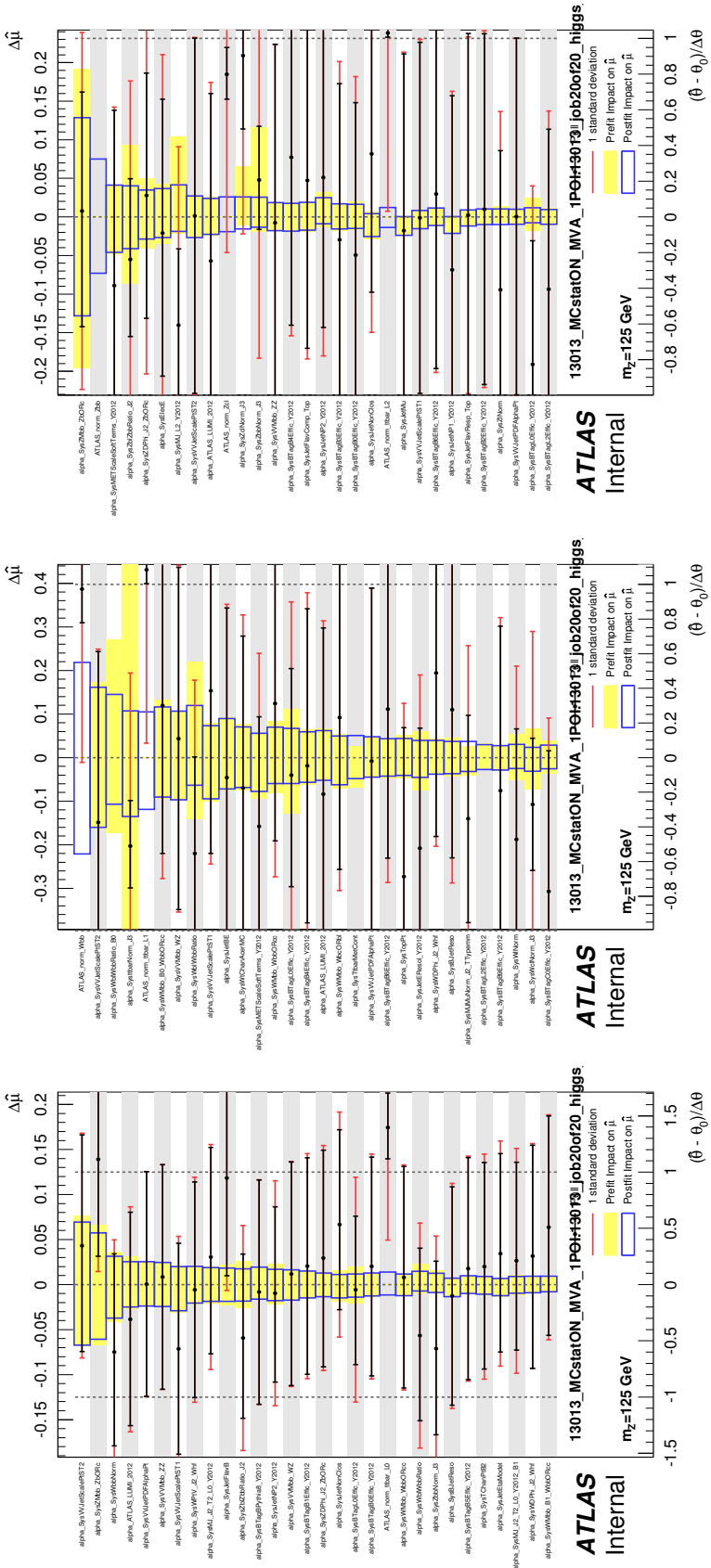

(a) 0-lepton, mva (b) 1-lepton, mva (c) 2-leptons, mva

Figure 527: Ranking of systematic uncertainties in the MVA analysis for the 0-lepton, 1 lepton and 2-leptons channels.

AL.2 Pulls for MVA diboson analysis

The pull plots for combined fit for the diboson MVA analysis are shown in Figures 528-533. Each plot compares the result from a fit to either the observed data in the diboson fit (black) and in the Higgs fit (red) on the left, and the result of the fit for each individual lepton channel on the right. Note that the BDT functions obtained for the diboson and for the Higgs are different.

AL.3 Correlation Plots for the MVA diboson fit

Figure 534 shows the largest correlations in the full MVA diboson analysis. This plot is produced by selecting all NP, which have a correlation larger than 20% with any another NP. Note that the parameter of interest, μ has been included by default not because it has particularly large correlations.

AL.4 Ranking plots for m_{jj} shape diboson analysis

Figures 535 and 536 show the ranking plots on data. In general, the ranking plot show similarities with the Higgs fit described in the bulk of the note.

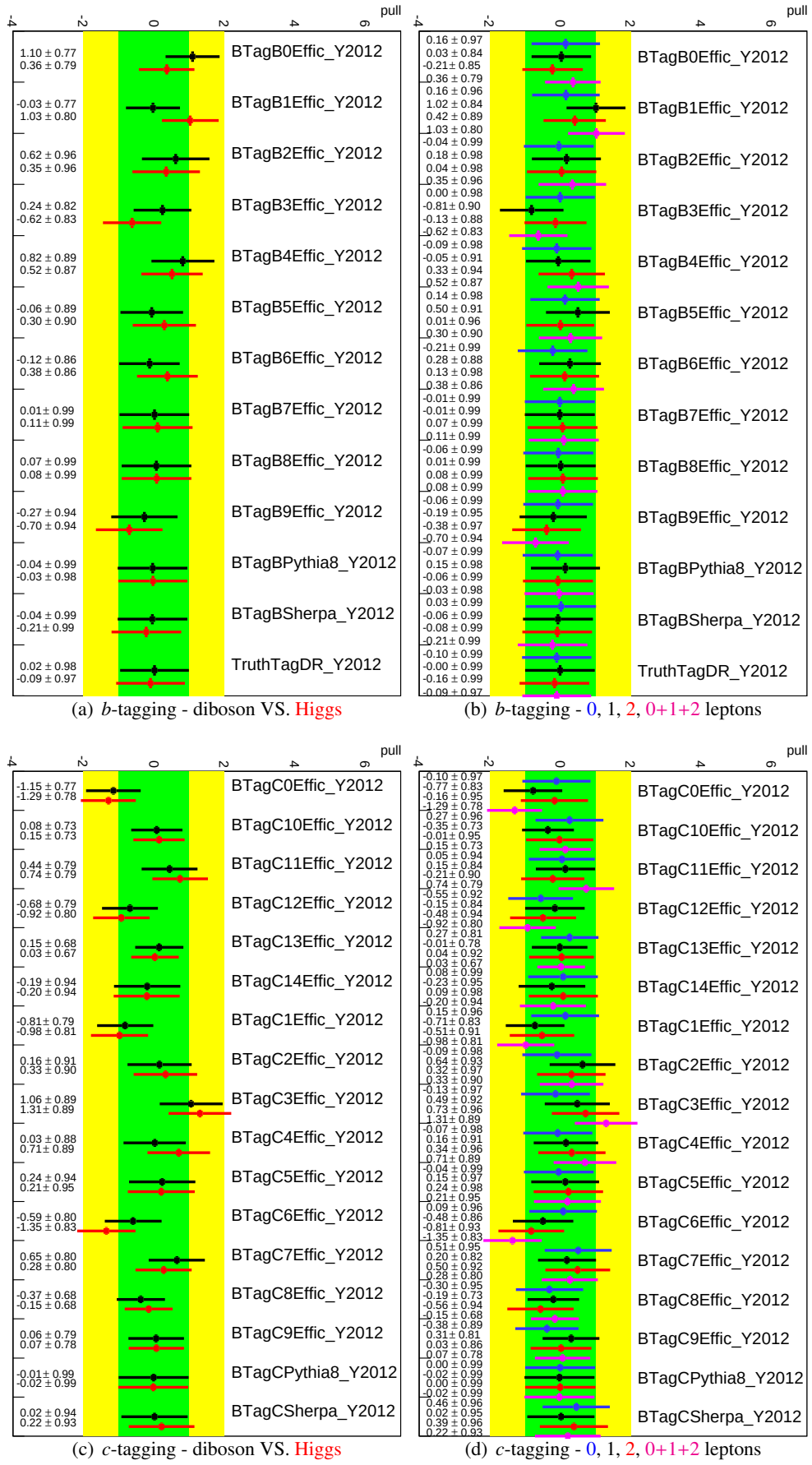

(a) *b*-tagging - diboson VS. Higgs

(b) *b*-tagging - 0, 1, 2, 0+1+2 leptons

(c) *c*-tagging - diboson VS. Higgs

(d) *c*-tagging - 0, 1, 2, 0+1+2 leptons

Figure 528: Pull plots for *b* and *c* tagging in the 0+1+2 lepton MVA diboson fit. The diboson fit in black is compared to the Higgs fit in red. Note that differnet BDT functions are used for the 2 fits. The fits to 0 lepton (blue), 1 lepton (black) and 2 leptons (red) data and the combined diboson fit to data (magenta) is shown on the right.

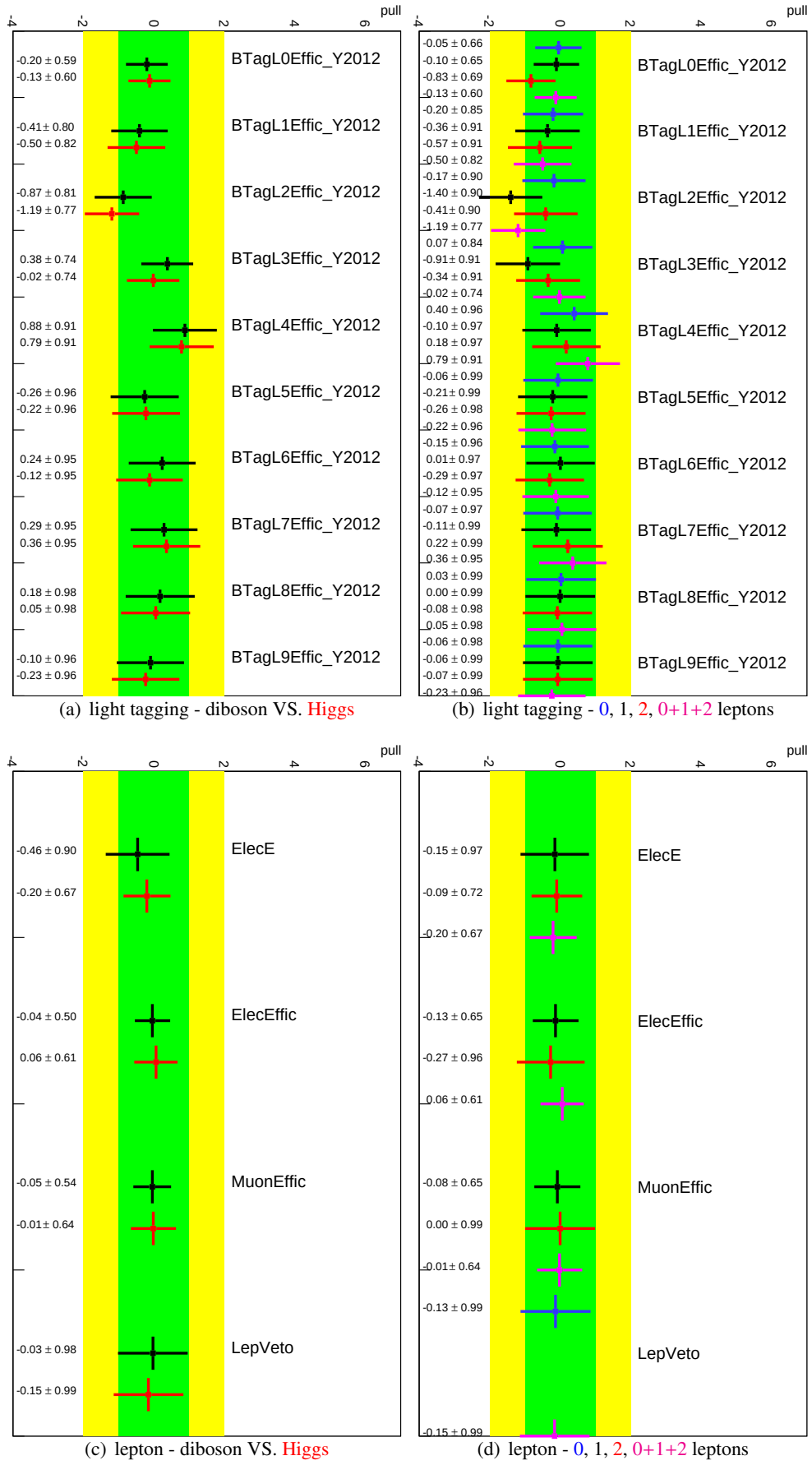

(a) light tagging - diboson VS. Higgs

(b) light tagging - 0, 1, 2, 0+1+2 leptons

(c) lepton - diboson VS. Higgs

(d) lepton - 0, 1, 2, 0+1+2 leptons

Figure 529: Pull plots for light-jet tagging and lepton related systematics in the 0+1+2 lepton MVA diboson fit. The diboson fit in black is compared to the Higgs fit in red. Note that differnet BDT functions are used for the 2 fits. The fits to 0 lepton (blue), 1 lepton (black) and 2 leptons (red) data and the combined diboson fit to data (magenta) is shown on the right.

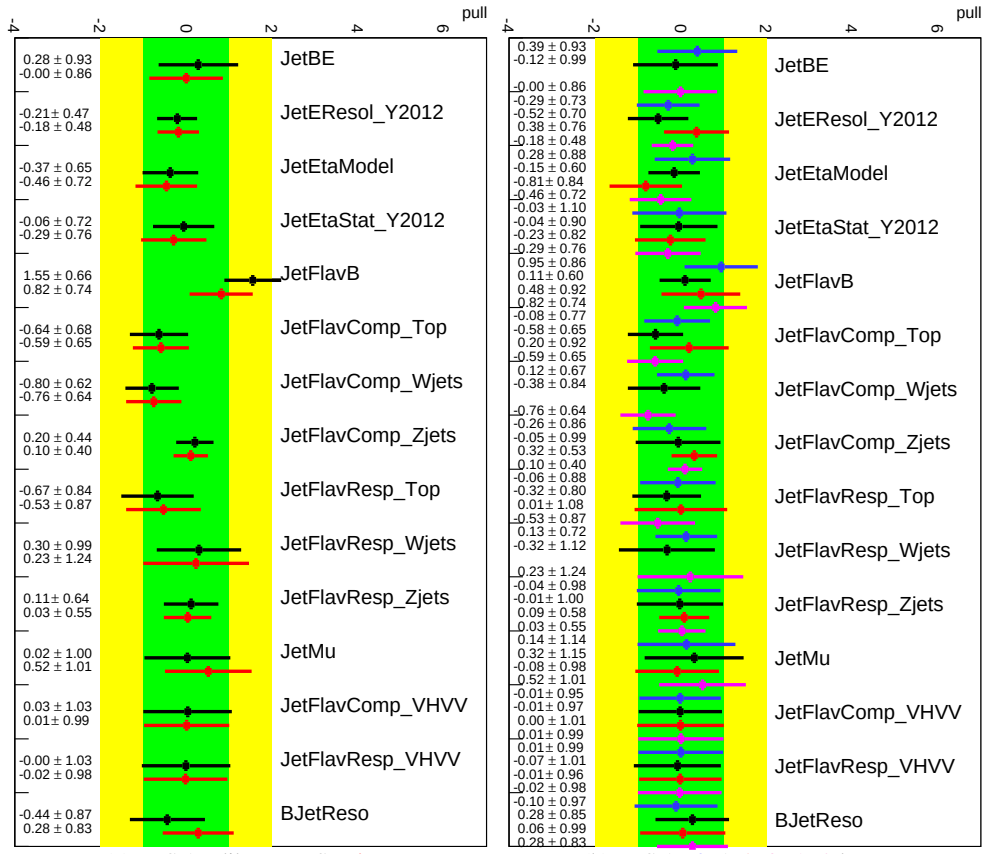

(a) JES 1 - diboson VS. Higgs (b) JES 1 - 0, 1, 2, 0+1+2 leptons

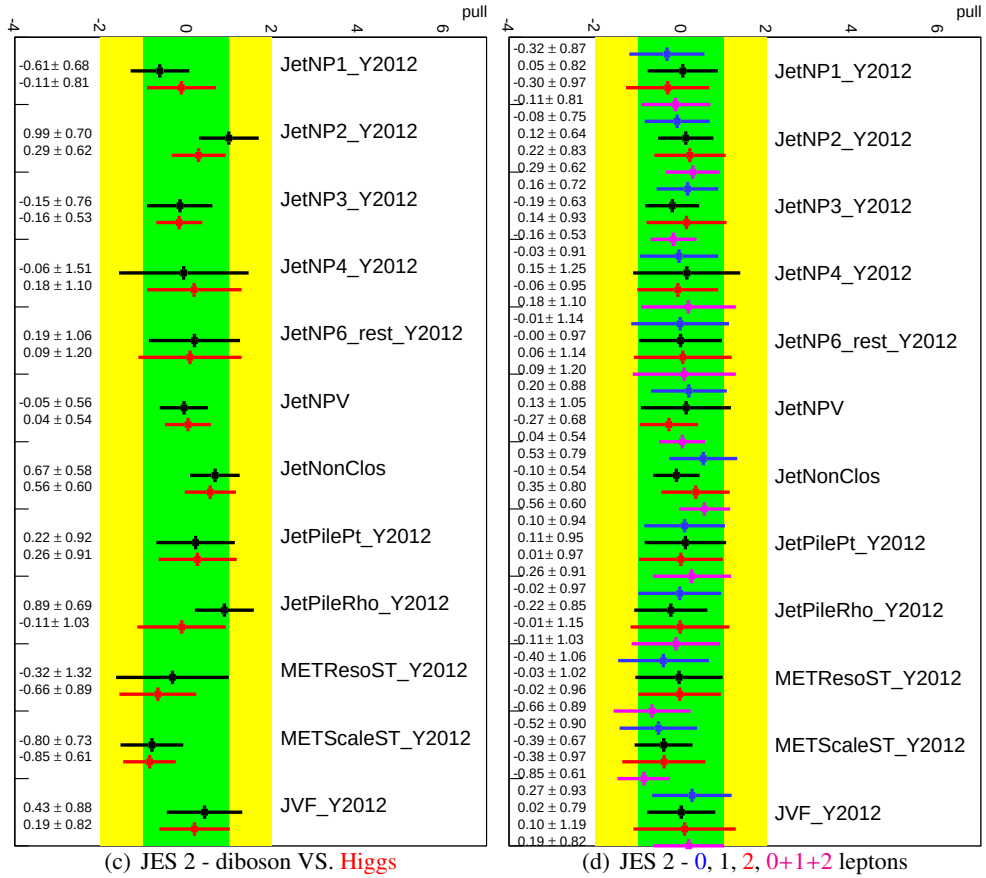

(c) JES 2 - diboson VS. Higgs (d) JES 2 - 0, 1, 2, 0+1+2 leptons

Figure 530: Pull plots for JES systematics in the 0+1+2 lepton MVA diboson fit. The diboson fit in black is compared to the Higgs fit in red. Note that differnet BDT functions are used for the 2 fits. The fits to 0 lepton (blue), 1 lepton (black) and 2 leptons (red) data and the combined diboson fit to data (magenta) is shown on the right.

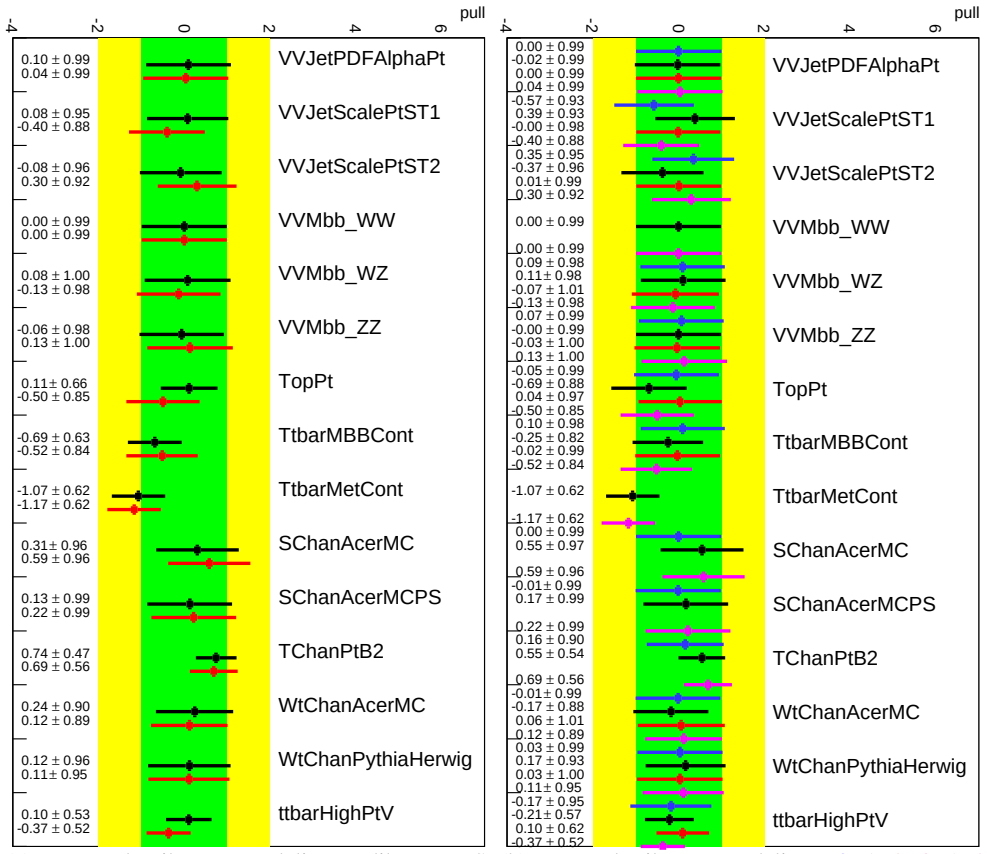

(a) Top and Diboson Modeling - diboson VS. Higgs

(b) Top and Diboson Modeling - 0, 1, 2, 0+1+2 leptons

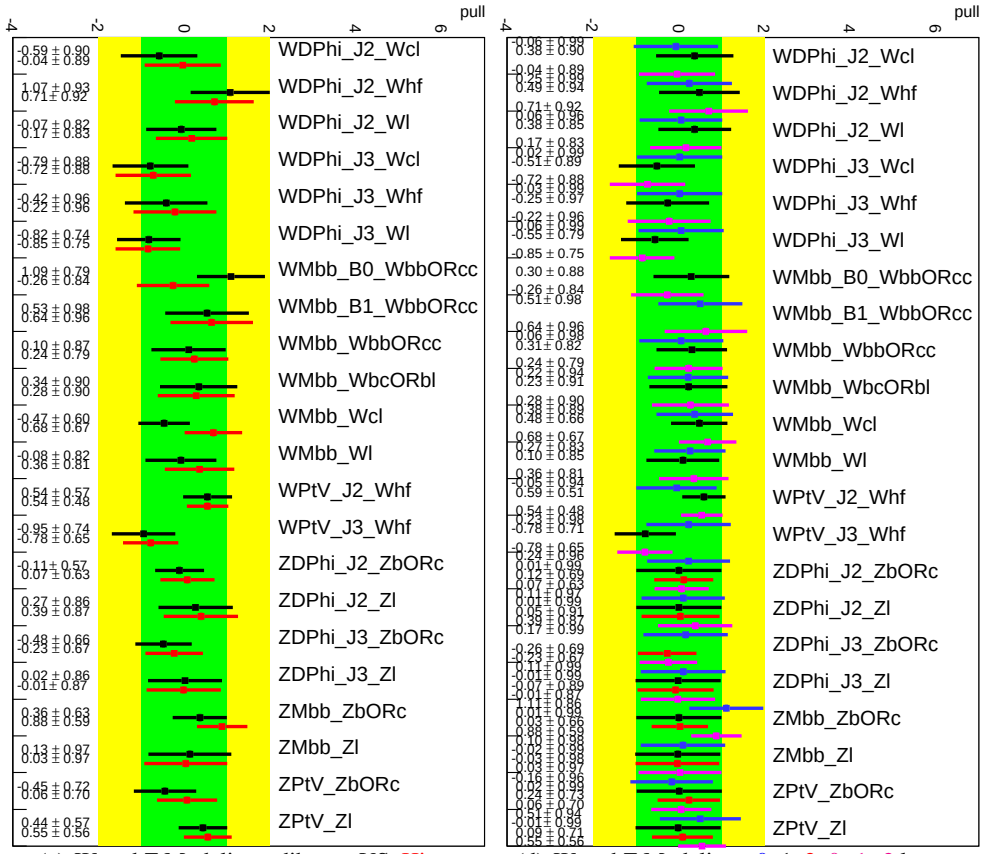

(c) W and Z Modeling - diboson VS. Higgs

(d) W and Z Modeling - 0, 1, 2, 0+1+2 leptons

Figure 531: Pull plots for diboson/top and W/Z systematics in the 0+1+2 lepton MVA diboson fit. The diboson fit in black is compared to the Higgs fit in red. Note that differnet BDT functions are used for the 2 fits. The fits to 0 lepton (blue), 1 lepton (black) and 2 leptons (red) data and the combined diboson fit to data (magenta) is shown on the right.

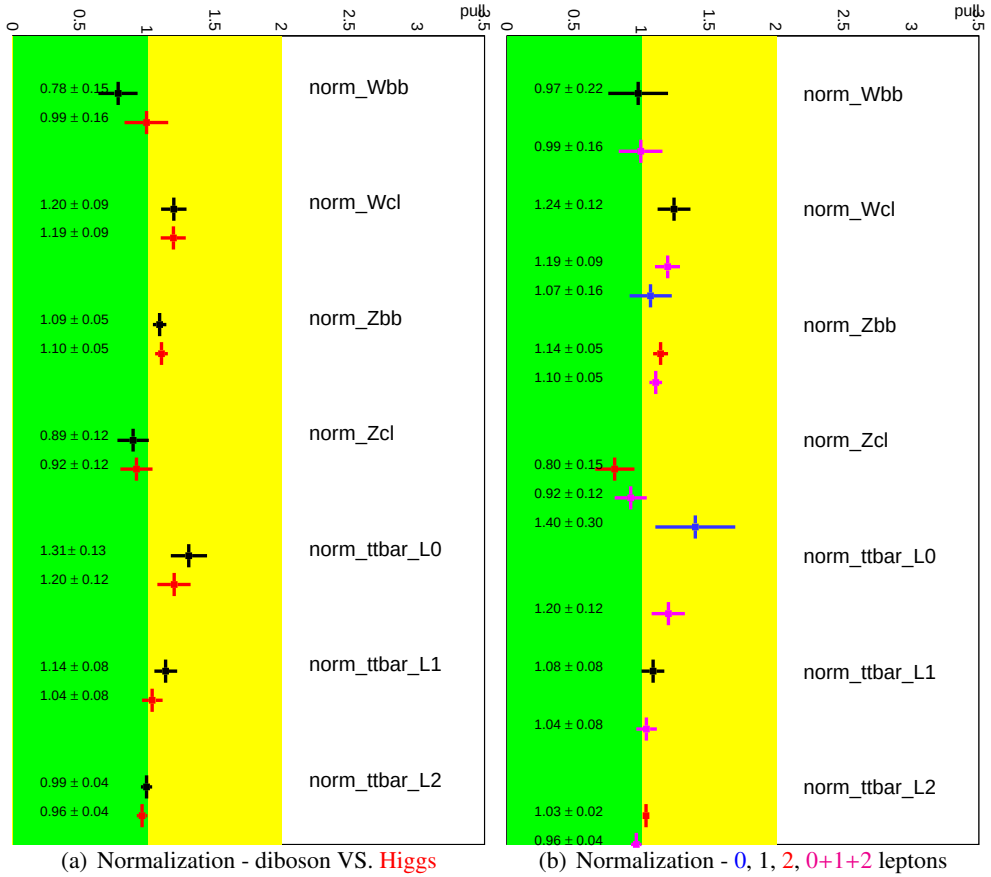

(a) Normalization - diboson VS. Higgs (b) Normalization - 0, 1, 2, 0+1+2 leptons

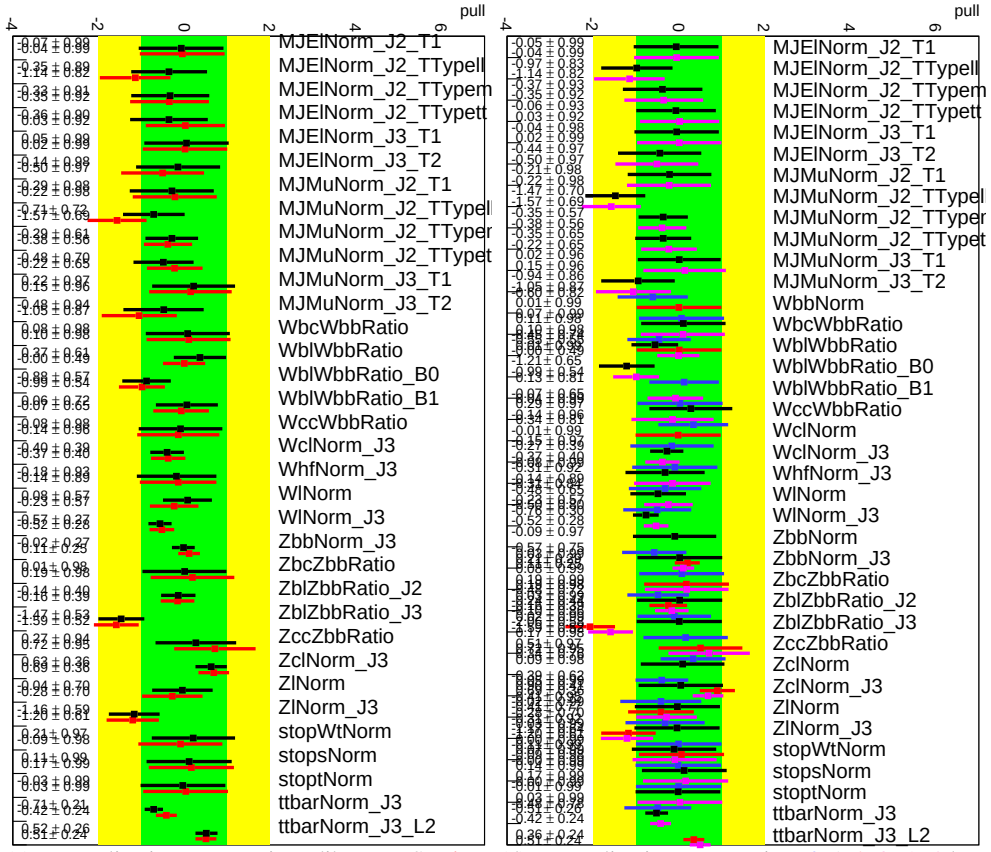

(c) Normalization systematics - diboson VS. Higgs (d) Normalization systematics - 0, 1, 2, 0+1+2 leptons

Figure 532: Pull plots for normalization in the 0+1+2 lepton MVA diboson fit. The diboson fit in black is compared to the Higgs fit in red. Note that differnet BDT functions are used for the 2 fits. The fits to 0 lepton (blue), 1 lepton (black) and 2 leptons (red) data and the combined diboson fit to data (magenta) is shown on the right.

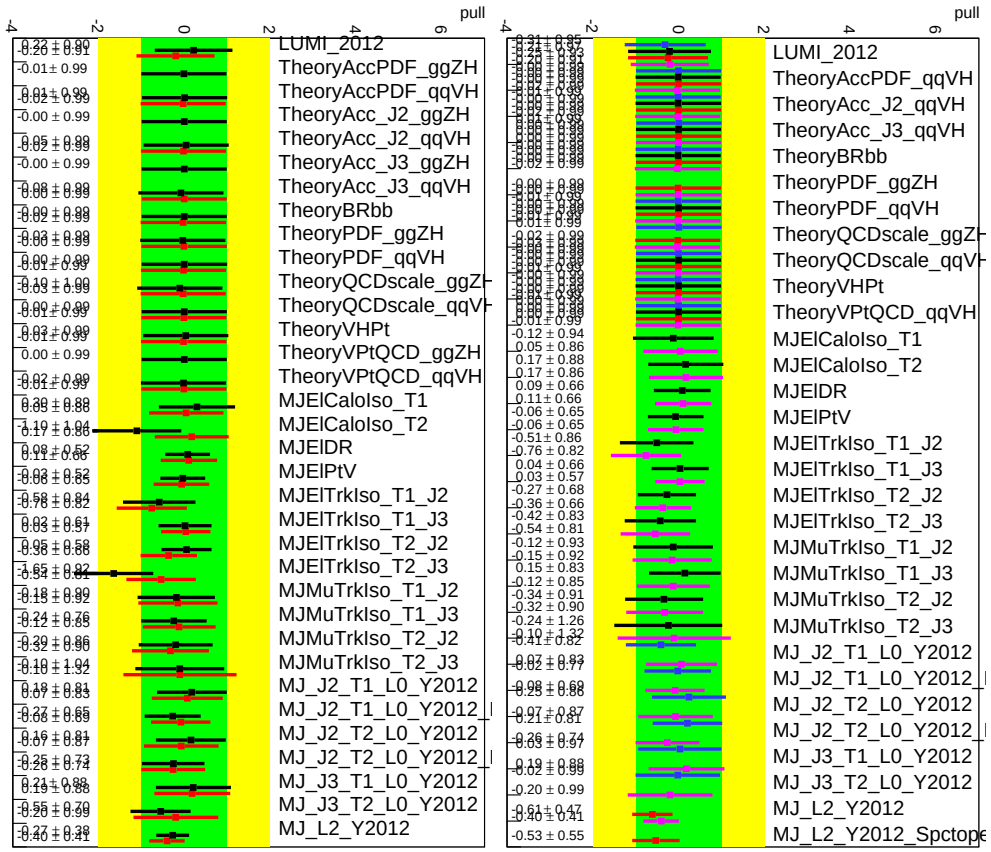

(a) Remaining NP - diboson VS. Higgs (b) Remaining NP - 0, 1, 2, 0+1+2 leptons

Figure 533: Pull plots for remaining systematics in the 0+1+2 lepton MVA diboson fit. The diboson fit in black is compared to the Higgs fit in red. Note that differnet BDT functions are used for the 2 fits. The fits to 0 lepton (blue), 1 lepton (black) and 2 leptons (red) data and the combined diboson fit to data (magenta) is shown on the right.

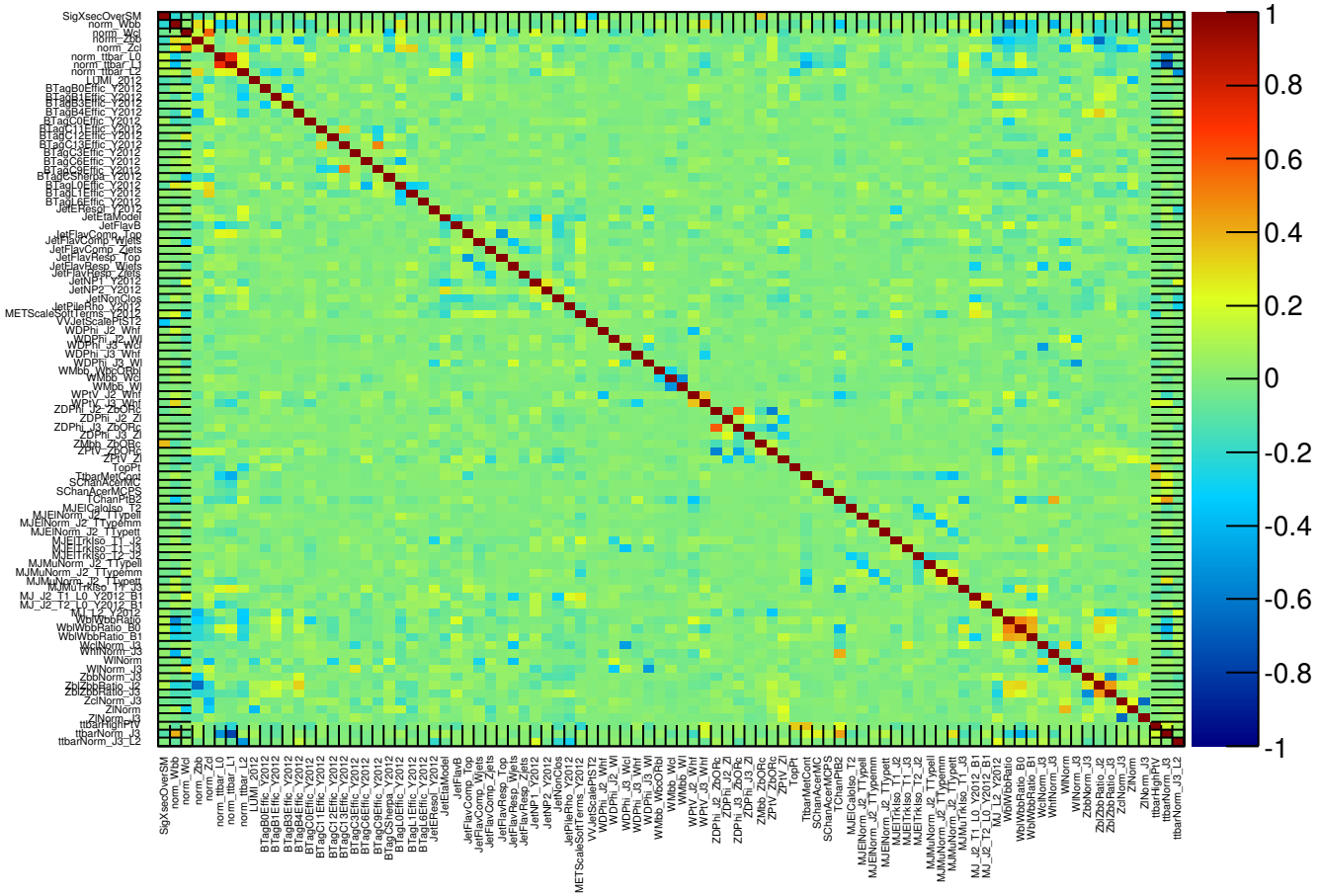

Figure 534: The correlation of all NP with a correlation larger than 20% in the 0+1+2 lepton MVA diboson fit. Note that the parameter of interest, μ has been included by default not because it has particularly large correlations.

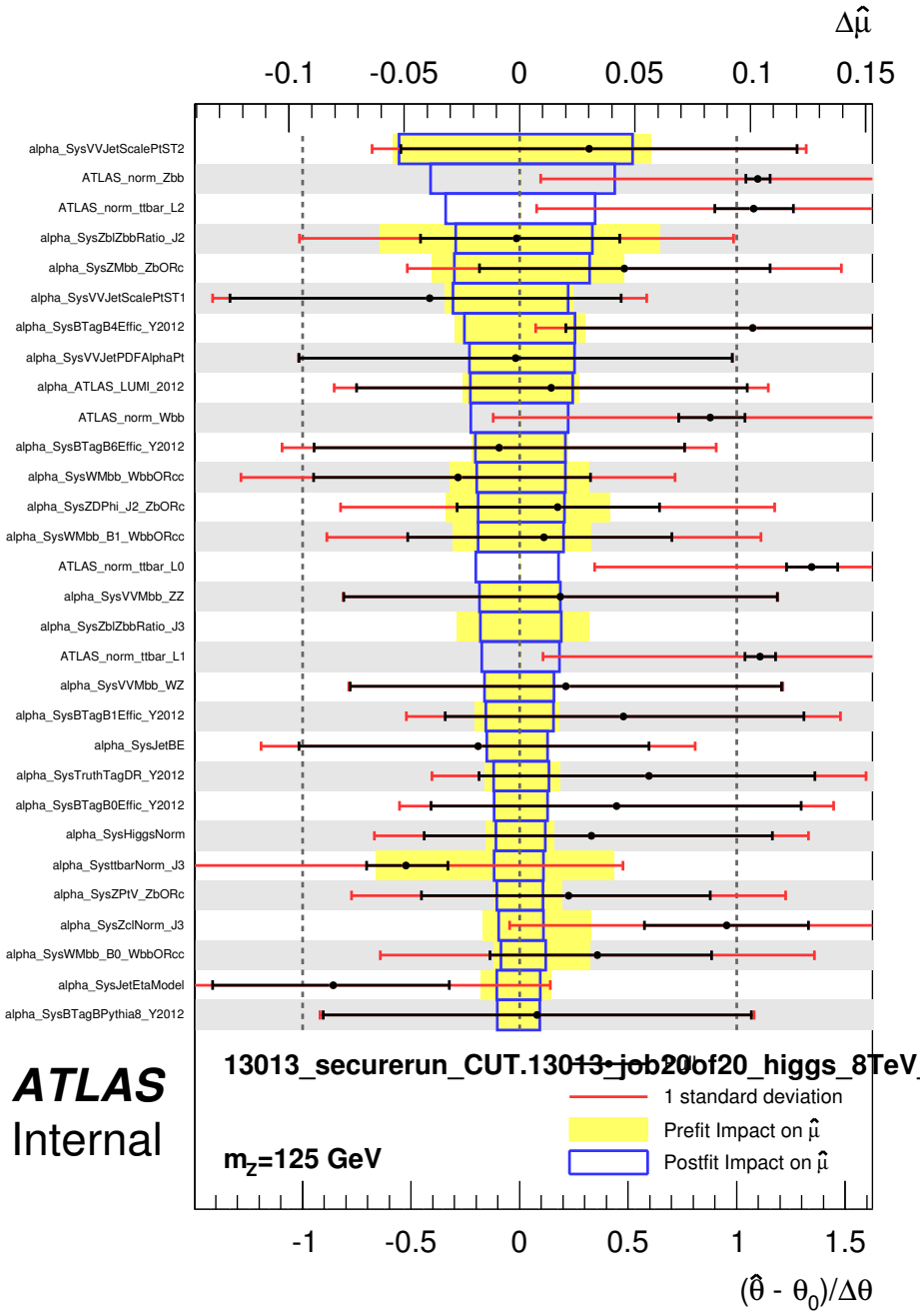

Figure 535: Ranking of systematic uncertainties in the m_{jj} shape analysis for the combined fit.

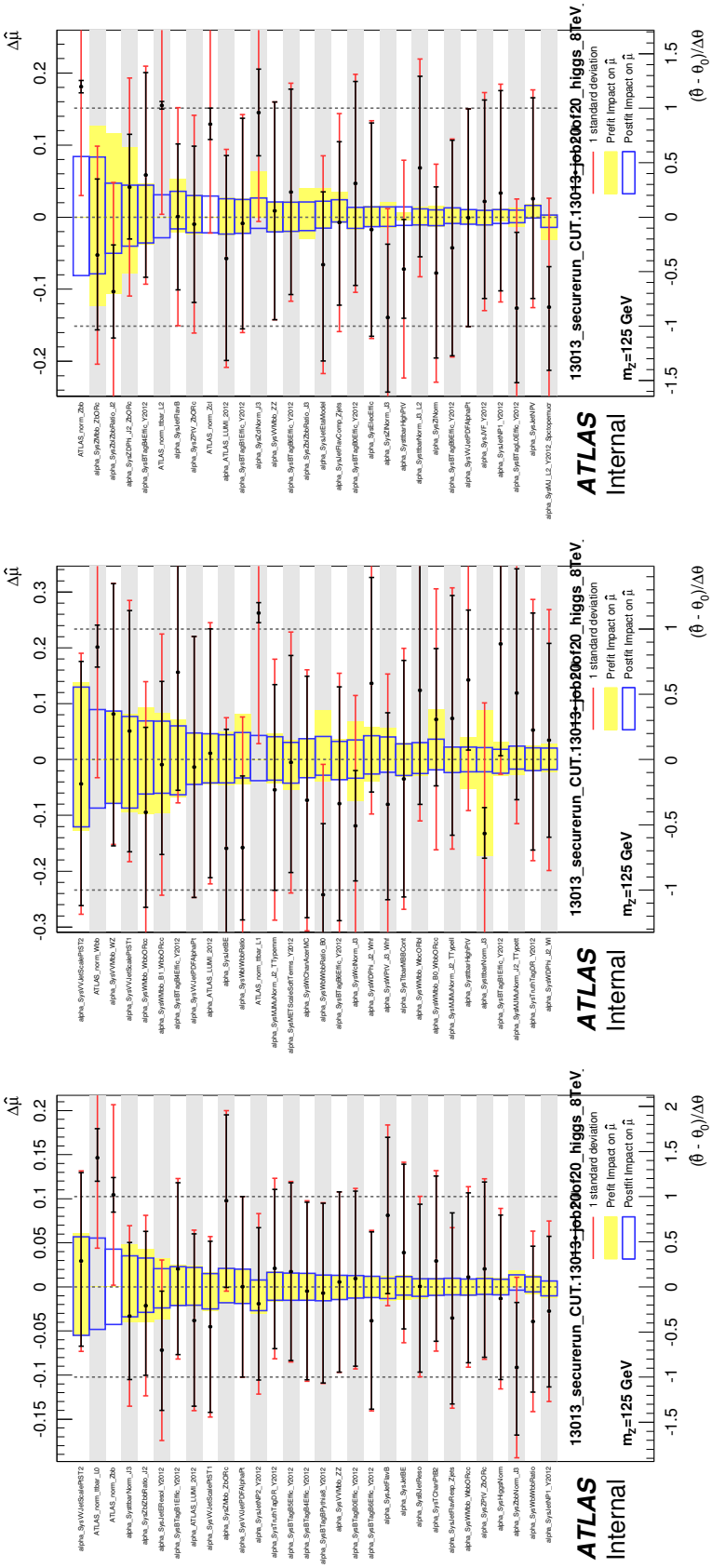

(a) 0-lepton, mva (b) 1-lepton, mva (c) 2-leptons, mva

Figure 536: Ranking of systematic uncertainties in the m_{jj} shape analysis for the 0-lepton, 1 lepton and 2-leptons channels.

AL.5 Pulls for m_{jj} shape diboson analysis

The pull plots for combined fit for the diboson m_{jj} shape analysis are shown in Figures 537-542. Each plot compares the result from a fit to either the observed data in the diboson fit (black) and in the Higgs fit (red) on the left, and the result of the fit for each individual lepton channel on the right. Note that as a result of the re-binning strategy, the histograms used in the diboson fit and the Higgs fit have different binning.

AL.6 Correlation Plots for the m_{jj} diboson fit

Figure 543 shows the largest correlations in the full m_{jj} shape diboson analysis. This plot is produced by selecting all NP, which have a correlation larger than 20% with any another NP. Note that the parameter of interest, μ has been included by default not because it has particularly large correlations.

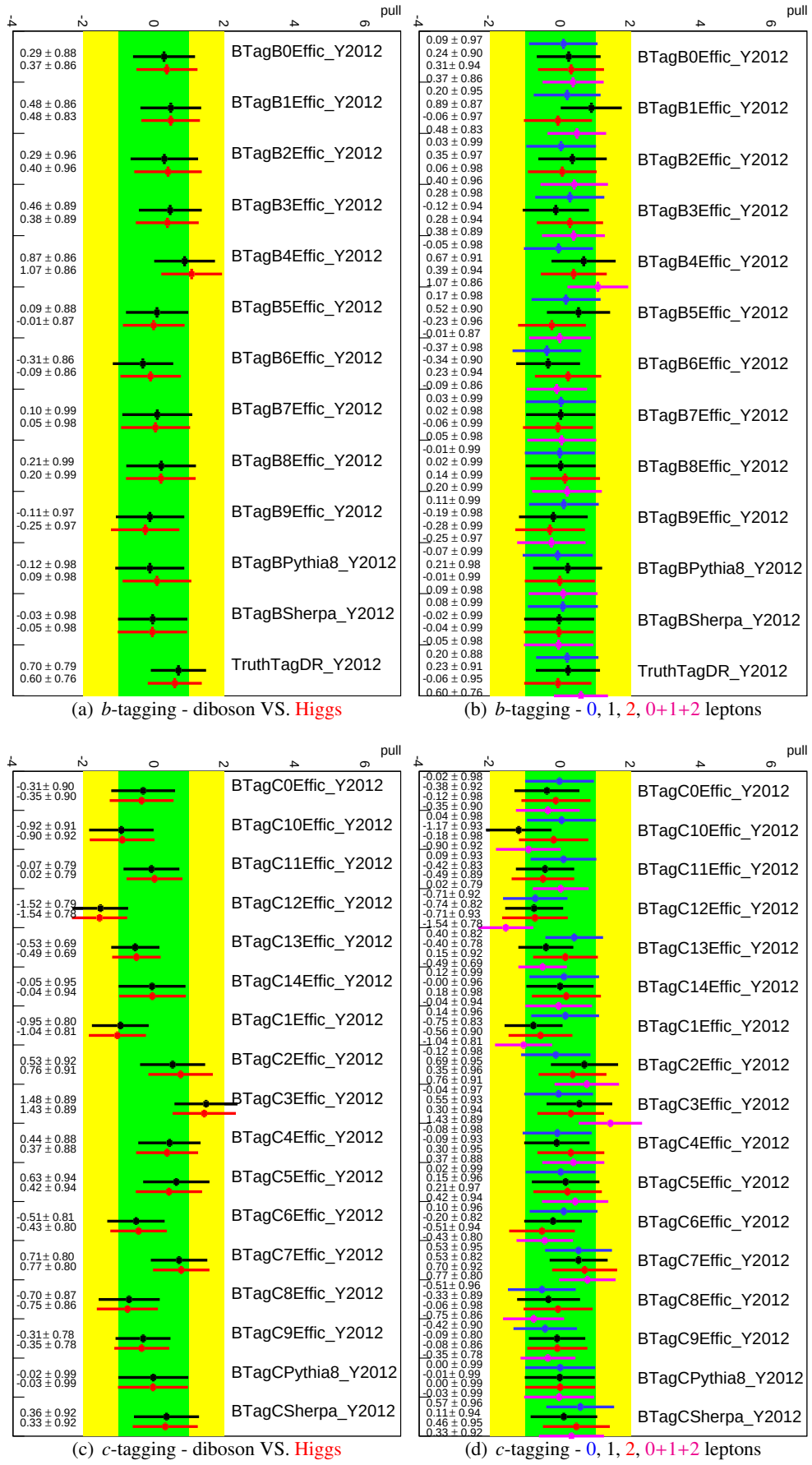

(a) *b*-tagging - diboson VS. Higgs

(b) *b*-tagging - 0, 1, 2, 0+1+2 leptons

(c) *c*-tagging - diboson VS. Higgs

(d) *c*-tagging - 0, 1, 2, 0+1+2 leptons

Figure 537: Pull plots for b and c tagging in the 0+1+2 lepton m_{jj} diboson fit. The diboson fit in black is compared to the Higgs fit in red. Note that differnet binnings are used for the 2 fits. The fits to 0 lepton (blue), 1 lepton (black) and 2 leptons (red) data and the combined diboson fit to data (magenta) is shown on the right.

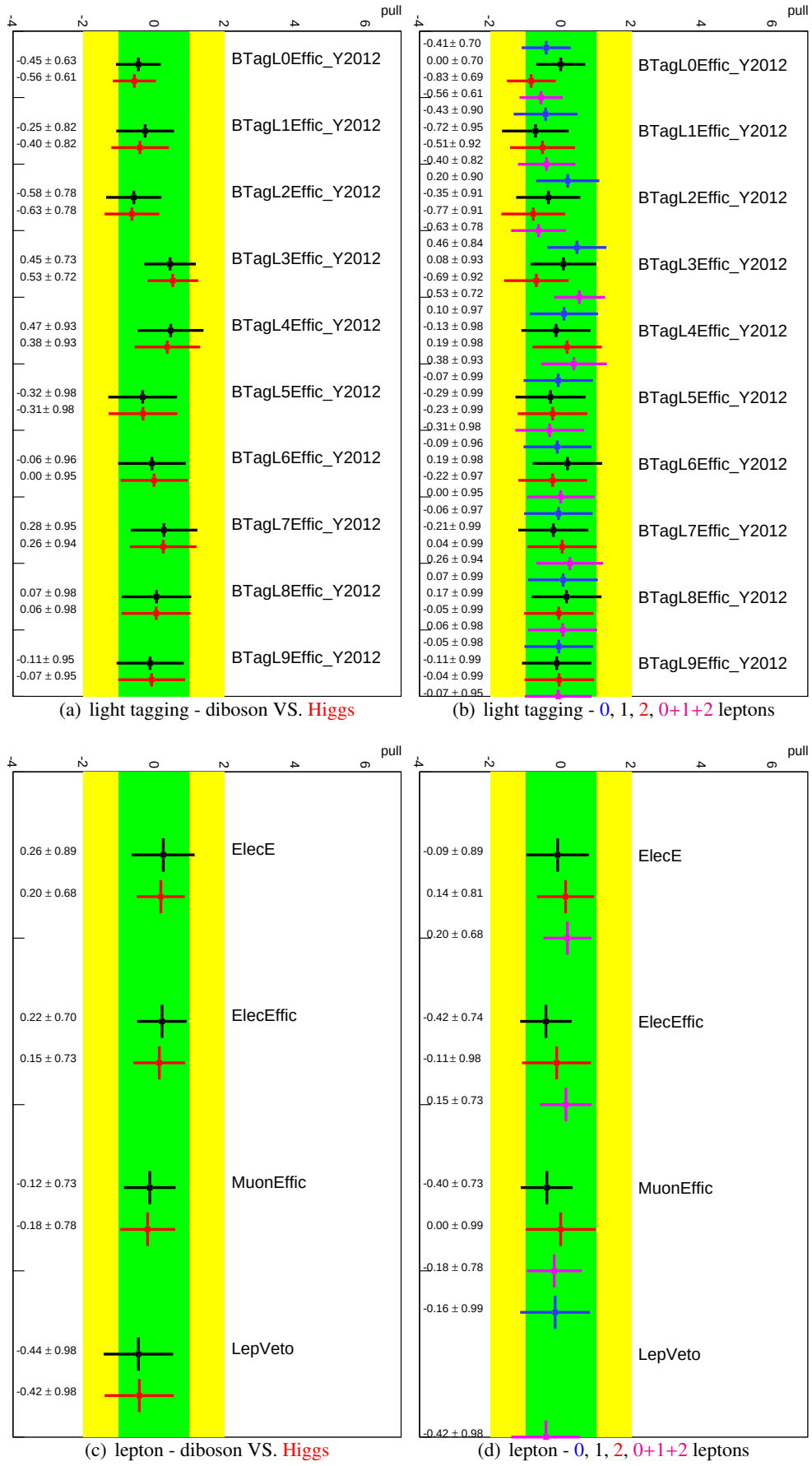

(a) light tagging - diboson VS. Higgs

(b) light tagging - 0, 1, 2, 0+1+2 leptons

(c) lepton - diboson VS. Higgs

(d) lepton - 0, 1, 2, 0+1+2 leptons

Figure 538: Pull plots for light-jet tagging and lepton related systematics in the 0+1+2 lepton m_{jj} shape diboson fit. The diboson fit in black is compared to the Higgs fit in red. Note that differnet binnings are used for the 2 fits. The fits to 0 lepton (blue), 1 lepton (black) and 2 leptons (red) data and the combined diboson fit to data (magenta) is shown on the right.

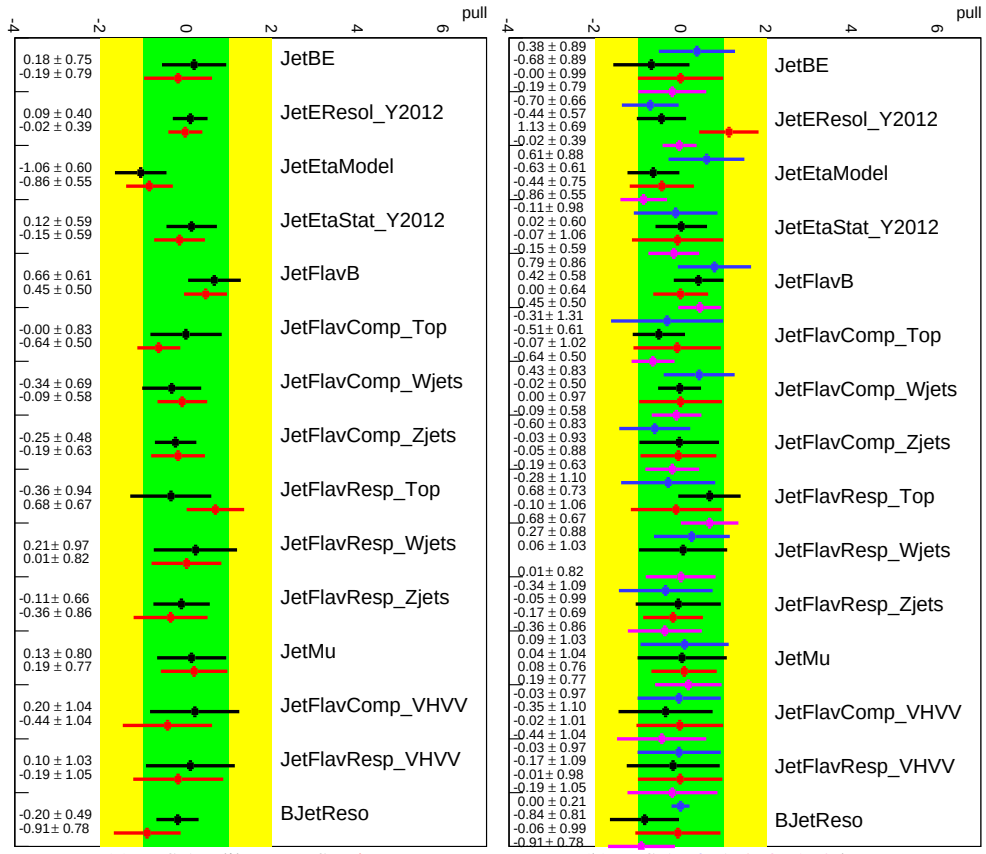

(a) JES 1 - diboson VS. Higgs (b) JES 1 - 0, 1, 2, 0+1+2 leptons

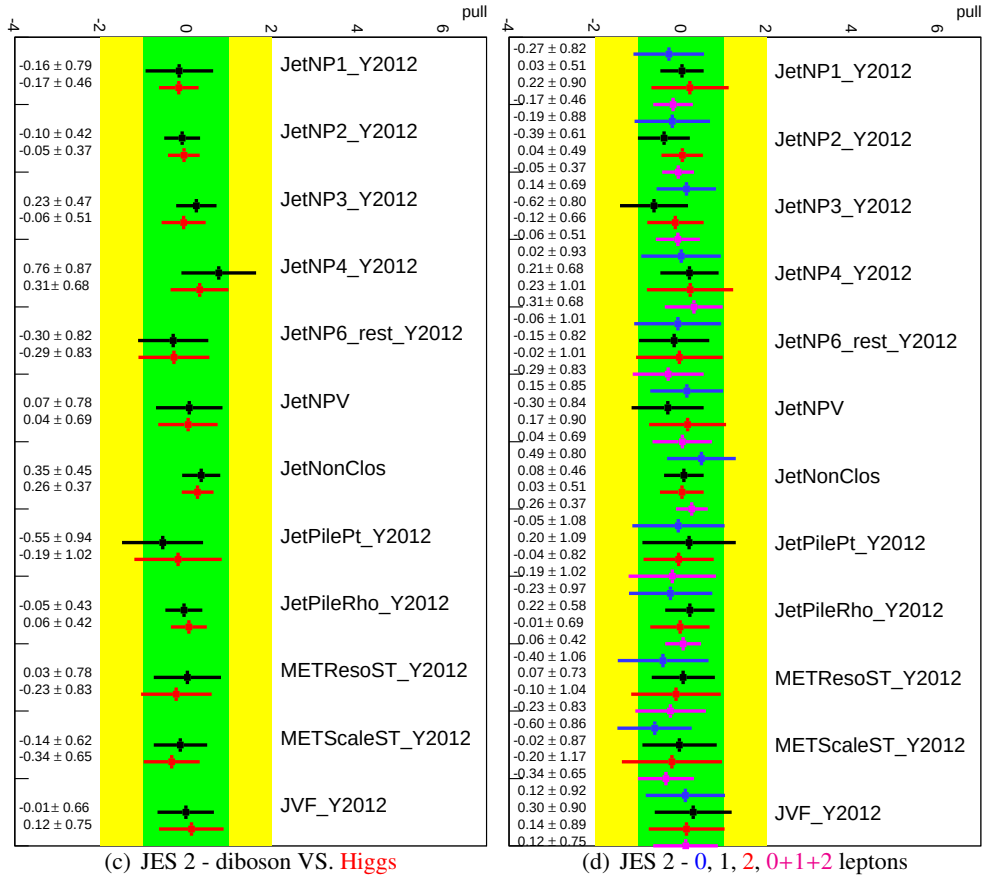

(c) JES 2 - diboson VS. Higgs (d) JES 2 - 0, 1, 2, 0+1+2 leptons

Figure 539: Pull plots for JES systematics in the 0+1+2 lepton m_{jj} shape diboson fit. The diboson fit in black is compared to the Higgs fit in red. Note that differnet binnings are used for the 2 fits. The fits to 0 lepton (blue), 1 lepton (black) and 2 leptons (red) data and the combined diboson fit to data (magenta) is shown on the right.

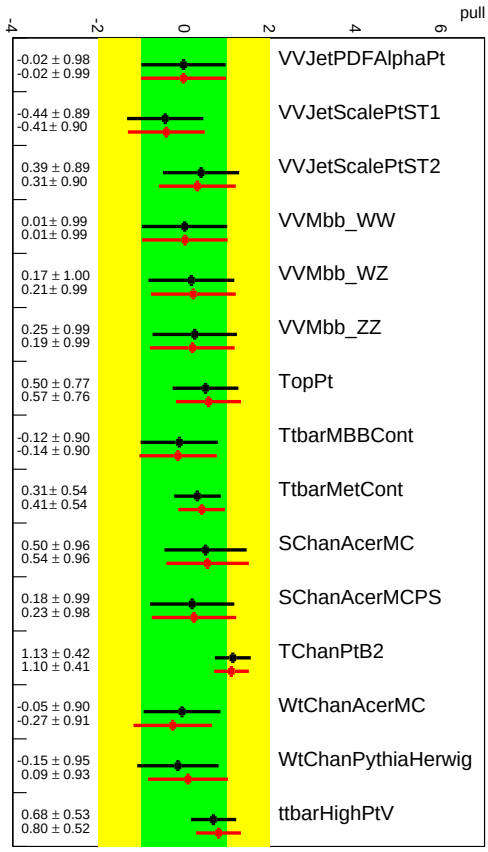

(a) Top and Diboson Modeling - diboson VS. Higgs

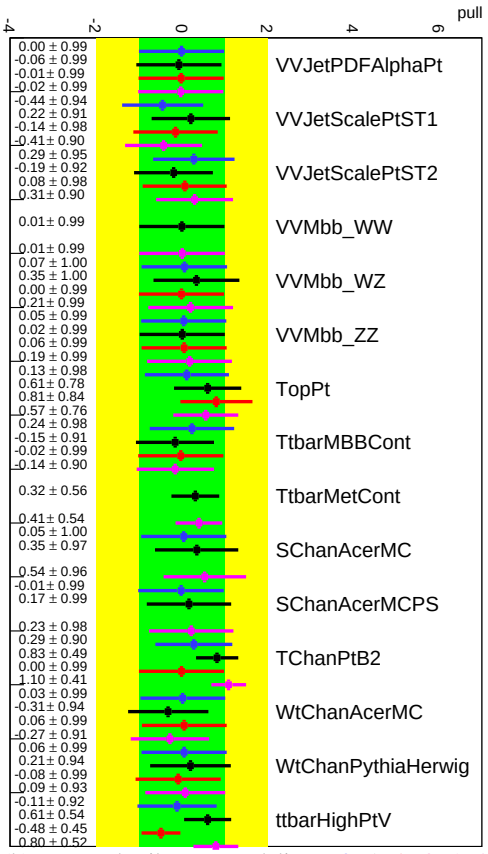

(b) Top and Diboson Modeling - 0, 1, 2, 0+1+2 leptons

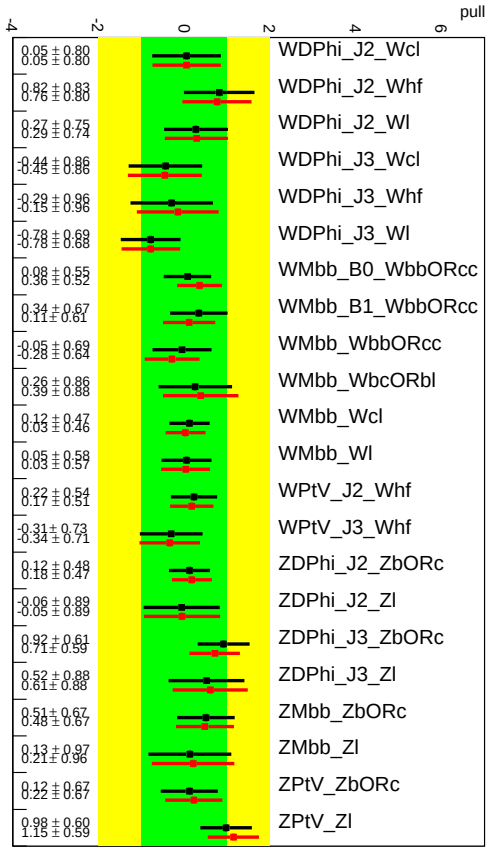

(c) W and Z Modeling - diboson VS. Higgs

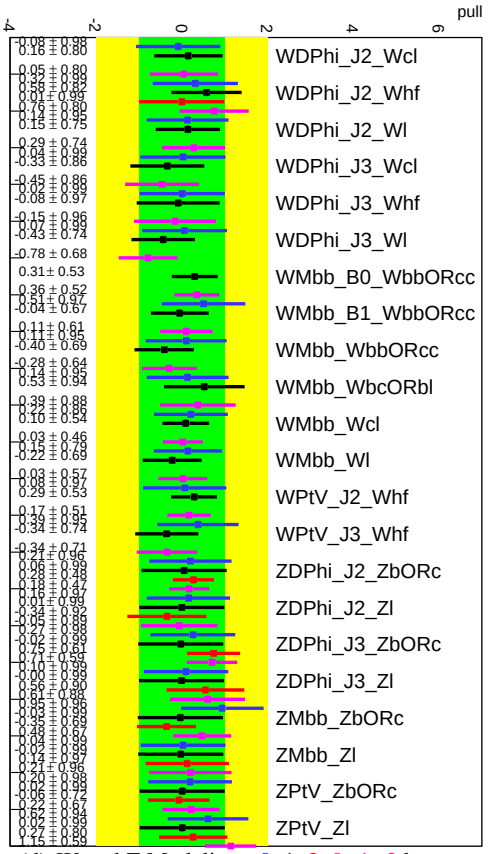

(d) W and Z Modeling - 0, 1, 2, 0+1+2 leptons

Figure 540: Pull plots for diboson/top and W/Z systematics in the 0+1+2 lepton m_{jj} shape diboson fit. The diboson fit in black is compared to the Higgs fit in red. Note that differnet binnings are used for the 2 fits. The fits to 0 lepton (blue), 1 lepton (black) and 2 leptons (red) data and the combined diboson fit to data (magenta) is shown on the right.

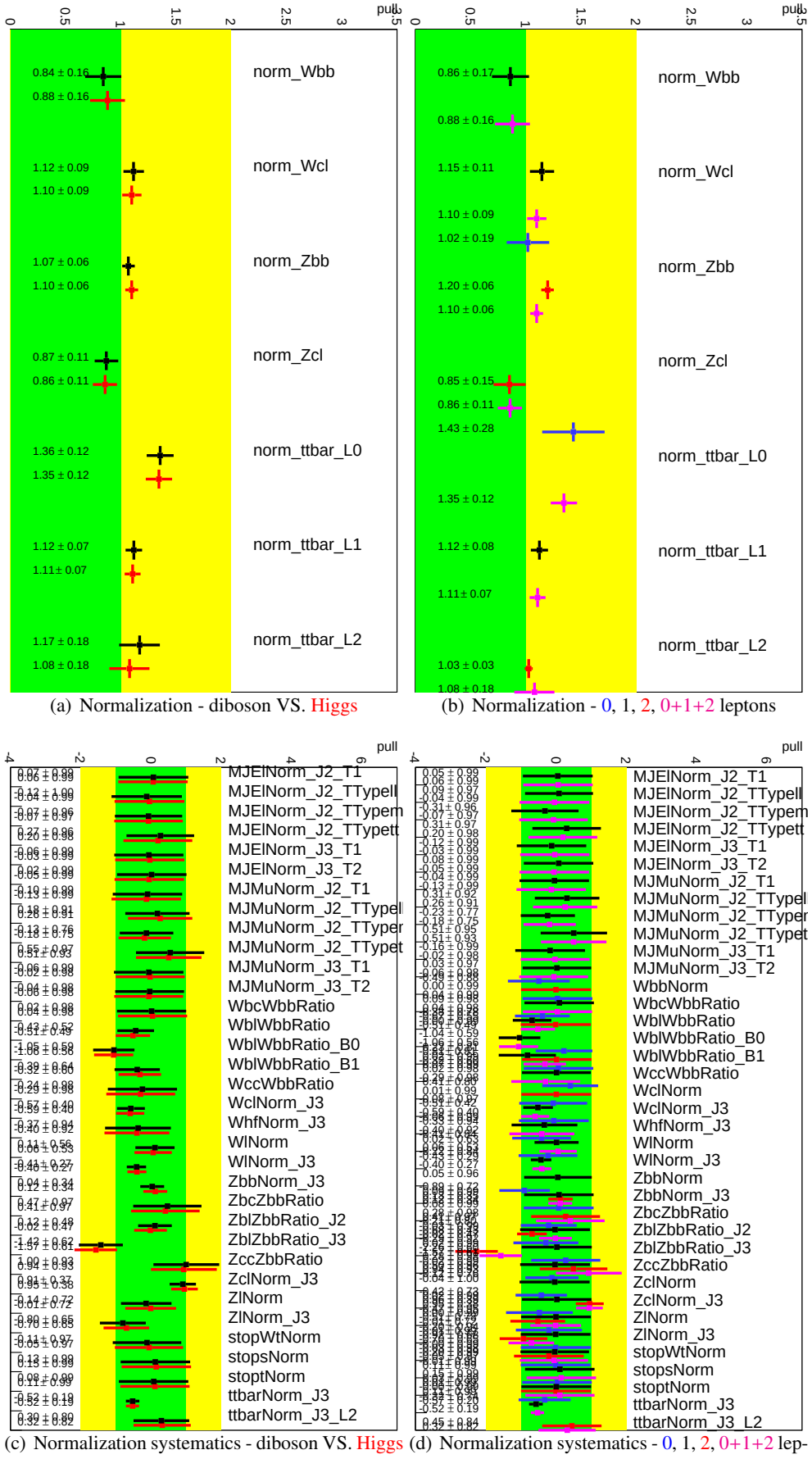

(a) Normalization - diboson VS. Higgs (b) Normalization - 0, 1, 2, 0+1+2 leptons

(c) Normalization systematics - diboson VS. Higgs (d) Normalization systematics - 0, 1, 2, 0+1+2 leptons

Figure 541: Pull plots for normalization in the 0+1+2 lepton m_{jj} shape diboson fit. The diboson fit in black is compared to the Higgs fit in red. Note that differnet binnings are used for the 2 fits. The fits to 0 lepton (blue), 1 lepton (black) and 2 leptons (red) data and the combined diboson fit to data (magenta) is shown on the right.

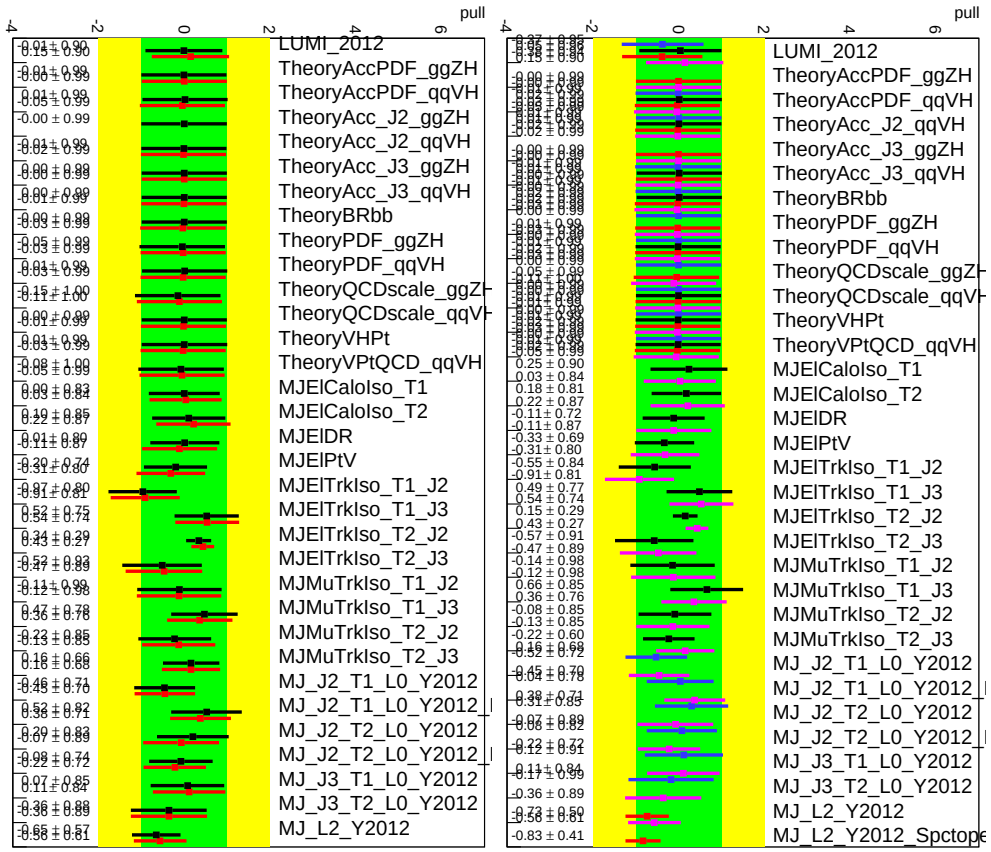

(a) Remaining NP - diboson VS. Higgs (b) Remaining NP - 0, 1, 2, 0+1+2 leptons

Figure 542: Pull plots for remaining systematics in the 0+1+2 lepton m_{jj} shape diboson fit. The diboson fit in black is compared to the Higgs fit in red. Note that differnet binnings are used for the 2 fits. The fits to 0 lepton (blue), 1 lepton (black) and 2 leptons (red) data and the combined diboson fit to data (magenta) is shown on the right.

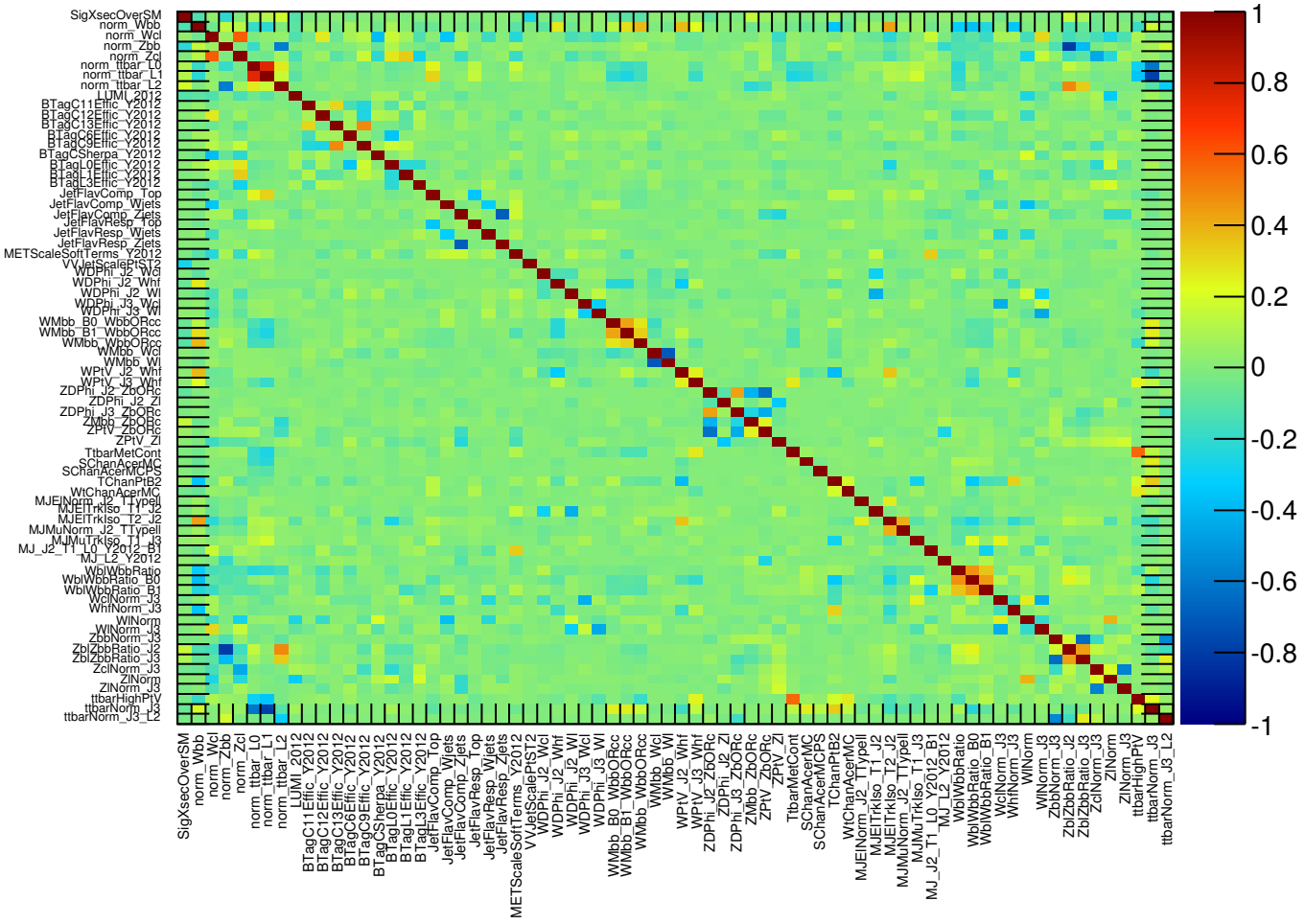

Figure 543: The correlation of all NP with a correlation larger than 20% in the 0+1+2 lepton m_{jj} shape diboson fit. Note that the parameter of interest, μ has been included by default not because it has particularly large correlations.

AL.7 Correlation between diboson and Higgs signal strength

To check the correlation between the Higgs and the diboson strength , we generate one workspace from the Higgs MVA distributions, in which both the Higgs and the diboson have floating normalization: μ_H and μ_{VZ}, and we perform fits on the Asimov dataset. The result, for each lepton channel, and for the combination 0+1+2 leptons is shown in Figure 545. In general the correlation is small.

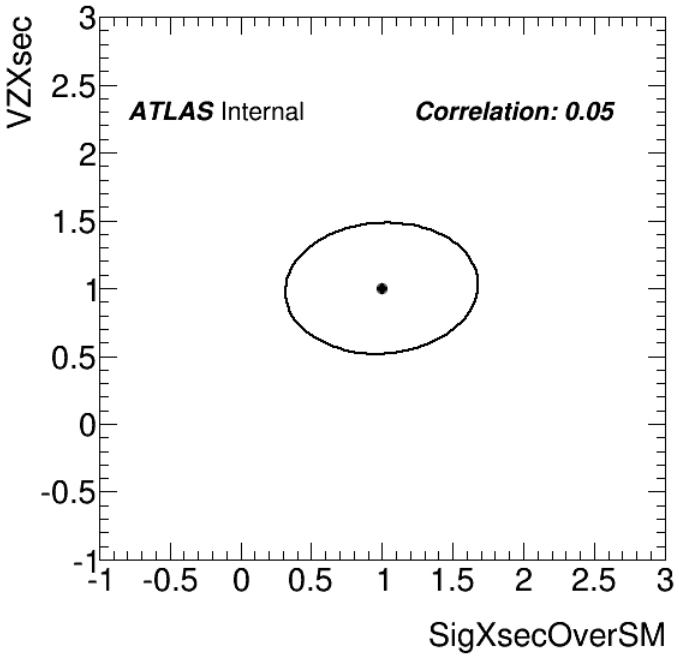

(a) 0-lepton

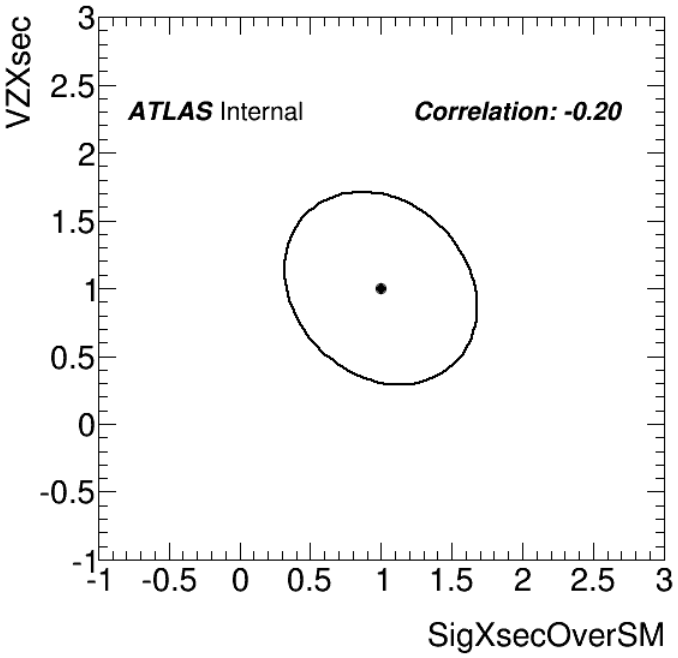

(b) 1-lepton

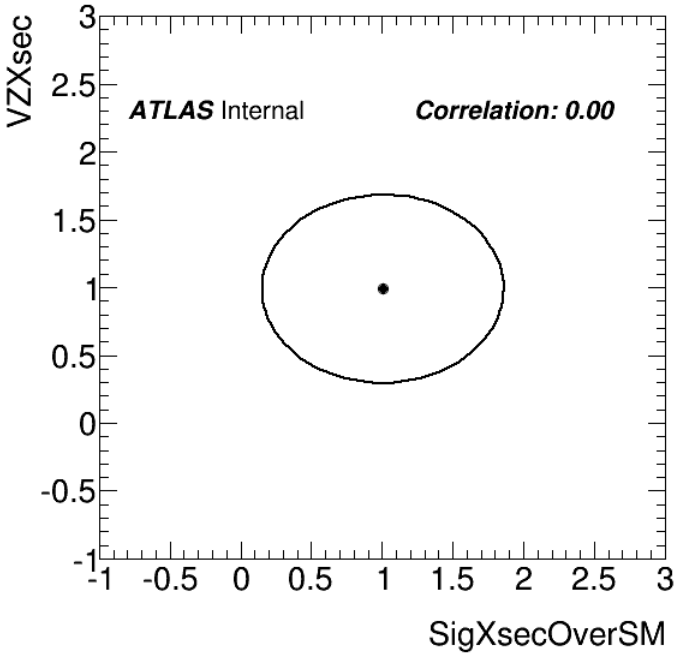

(c) 2-lepton

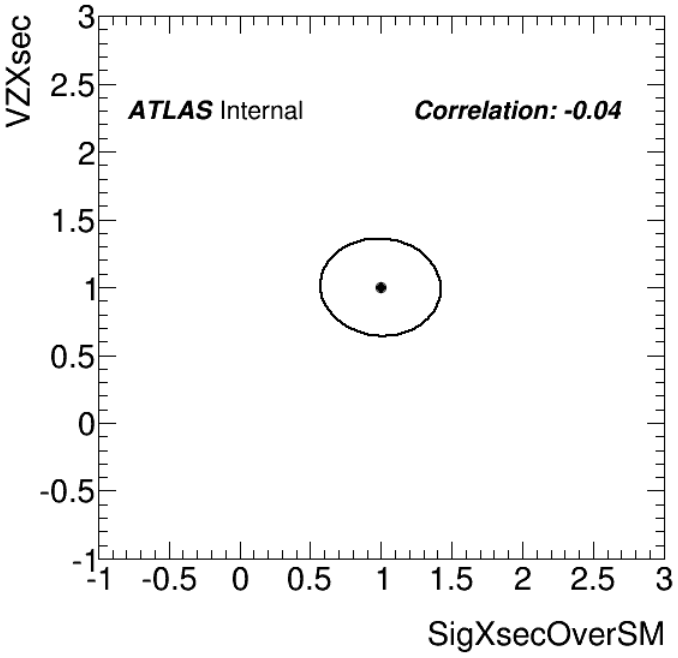

(d) 0+1+2-lepton

Figure 544: The correlation of Higgs and diboson *VZ* signal strength in the MVA fit for 0, 1, 2 and 0+1+2 lepton channels.

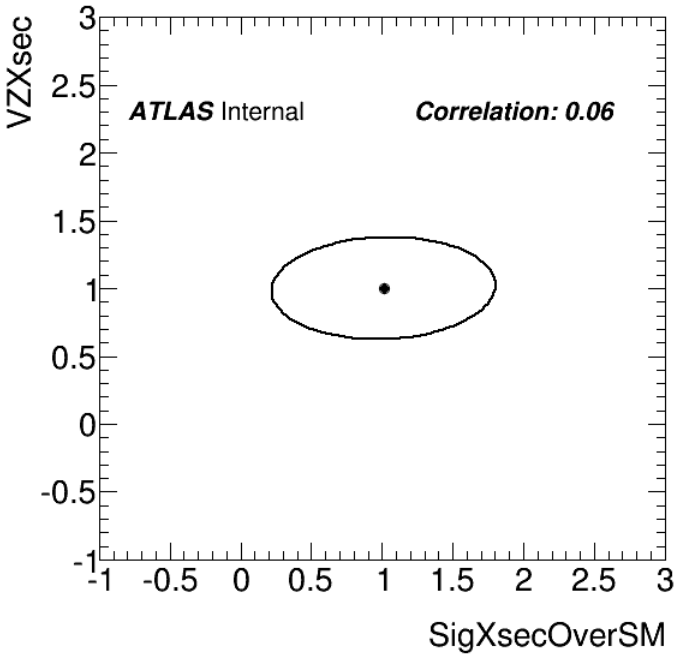

(a) 0-lepton

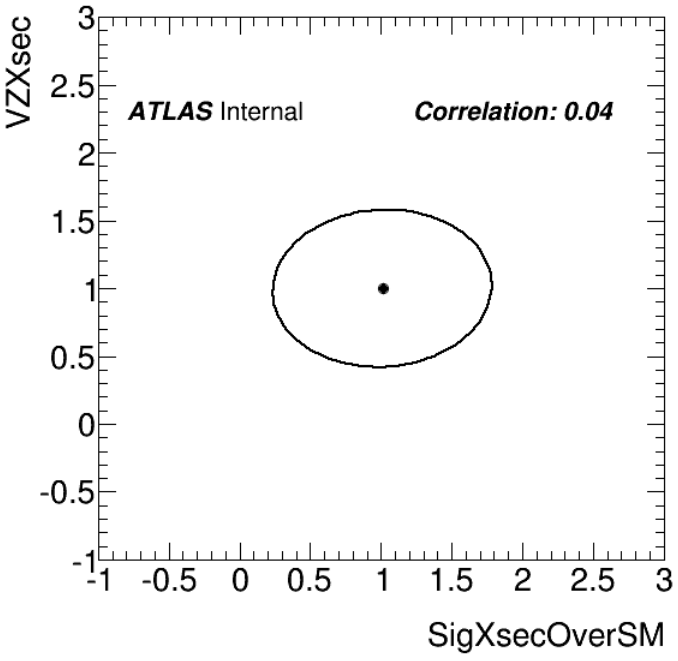

(b) 1-lepton

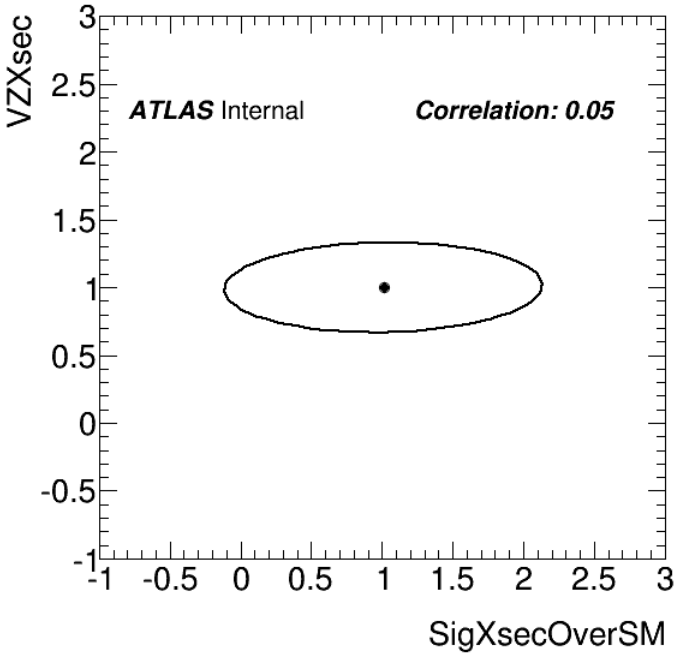

(c) 2-lepton

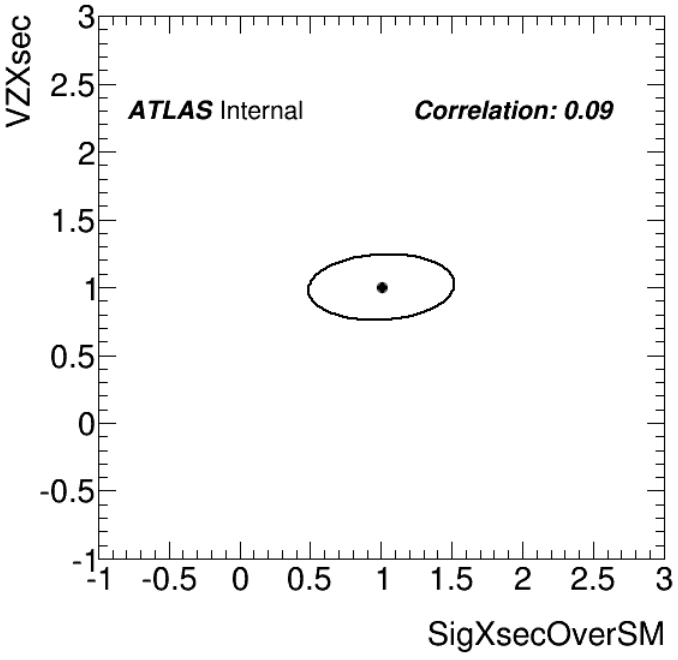

(d) 0+1+2-lepton

Figure 545: The correlation of Higgs and diboson VZ signal strength in the m_{jj} shape fit for 0, 1, 2 and 0+1+2 lepton channels.

AL.8 Diboson MVA post fit plots

In the following sections post-fit plots corresponding to fits to the data for the MVA analysis are presented. In all cases the MC expectations have been adapted to the pulls from the data in the combined 0+1+2 lepton fit. As a comparison, the total nominal background prediction is indicated by the dashed blue curve. Only statistical uncertainties are indicated.

In Figures 546, 547 and 548 shown the post-fit distribution for the variables used in the MVA shape analysis for the 0, 1 and 2-lepton channel respectively in the various 2-tag categories in different p_{T}^{V} bins.

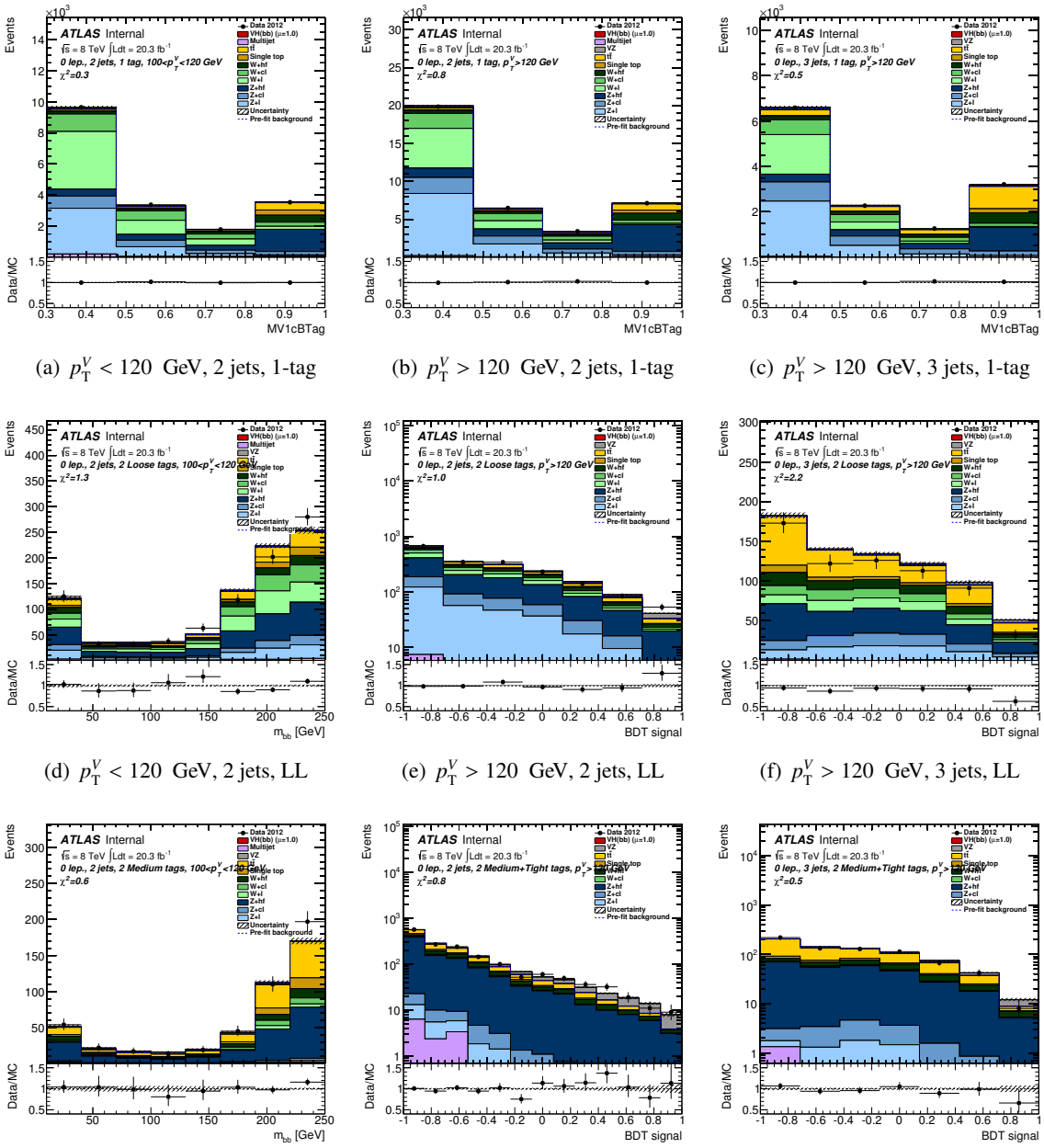

(a) $p_{\mathrm{T}}^{V} < 120$ GeV, 2 jets, 1-tag (b) $p_{\mathrm{T}}^{V} > 120$ GeV, 2 jets, 1-tag (c) $p_{\mathrm{T}}^{V} > 120$ GeV, 3 jets, 1-tag

(d) $p_{\mathrm{T}}^{V} < 120$ GeV, 2 jets, LL (e) $p_{\mathrm{T}}^{V} > 120$ GeV, 2 jets, LL (f) $p_{\mathrm{T}}^{V} > 120$ GeV, 3 jets, LL

(g) $p_{\mathrm{T}}^{V} < 120$ GeV, 2 jets, MM+TT (h) $p_{\mathrm{T}}^{V} > 120$ GeV, 2 jets, MM+TT (i) $p_{\mathrm{T}}^{V} > 120$ GeV, 3 jets, MM+TT

Figure 546: Post-fit plots for MVA distribution in 0-lepton events with 1 b-tag (MV1c is fit here), *LL* and $MM + TT$ b-tags in the 0+1+2 lepton fit. The pre-fit background expectation is indicated by the dashed blue line. Only statistical uncertainties are indicated.

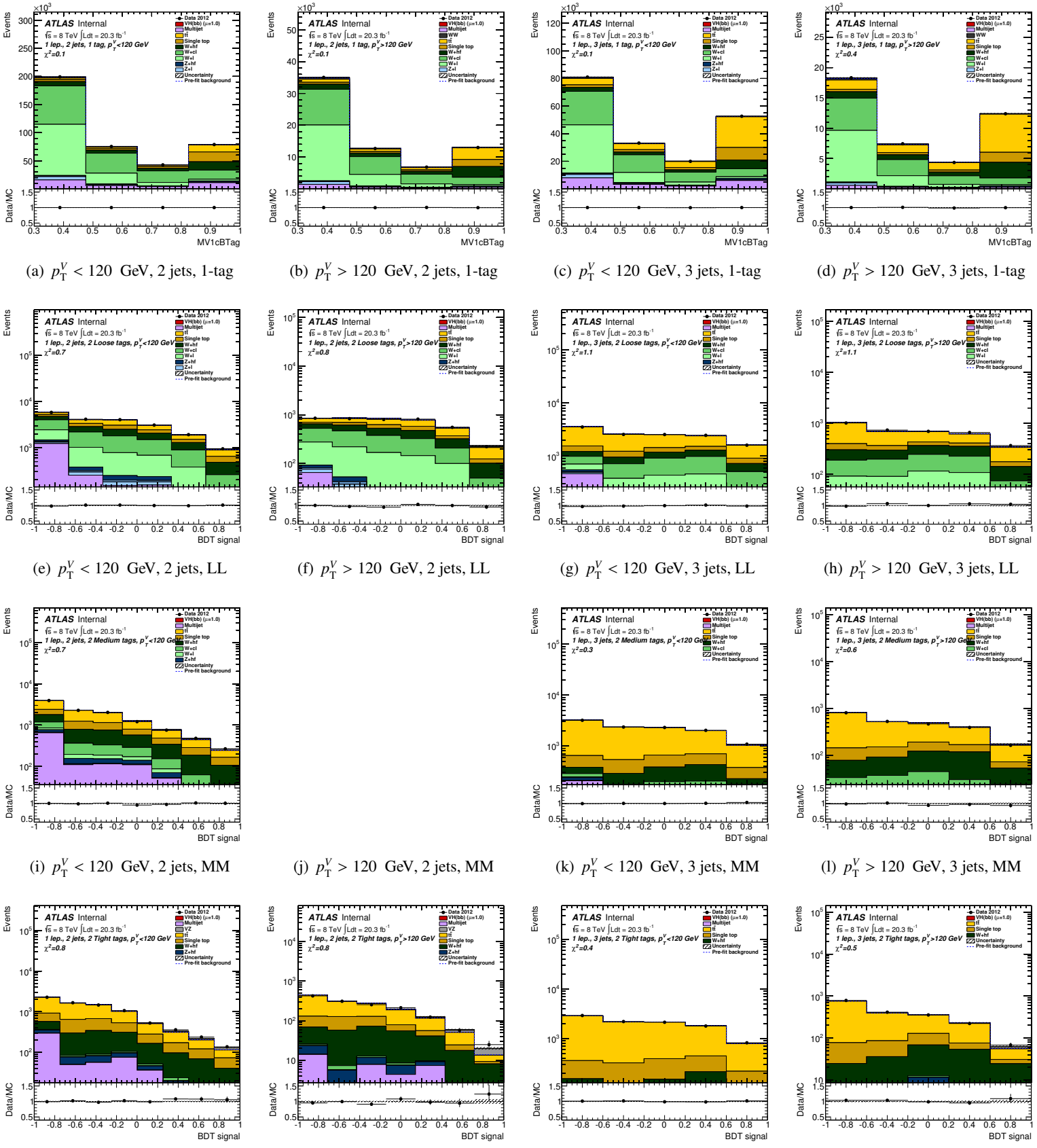

(a) $p_{\mathrm{T}}^{V} < 120$ GeV, 2 jets, 1-tag (b) $p_{\mathrm{T}}^{V} > 120$ GeV, 2 jets, 1-tag (c) $p_{\mathrm{T}}^{V} < 120$ GeV, 3 jets, 1-tag (d) $p_{\mathrm{T}}^{V} > 120$ GeV, 3 jets, 1-tag

(e) $p_{\mathrm{T}}^{V} < 120$ GeV, 2 jets, LL (f) $p_{\mathrm{T}}^{V} > 120$ GeV, 2 jets, LL (g) $p_{\mathrm{T}}^{V} < 120$ GeV, 3 jets, LL (h) $p_{\mathrm{T}}^{V} > 120$ GeV, 3 jets, LL

(i) $p_{\mathrm{T}}^{V} < 120$ GeV, 2 jets, MM (j) $p_{\mathrm{T}}^{V} > 120$ GeV, 2 jets, MM (k) $p_{\mathrm{T}}^{V} < 120$ GeV, 3 jets, MM (l) $p_{\mathrm{T}}^{V} > 120$ GeV, 3 jets, MM

(m) $p_{\mathrm{T}}^{V} < 120$ GeV, 2 jets, TT (n) $p_{\mathrm{T}}^{V} > 120$ GeV, 2 jets, TT (o) $p_{\mathrm{T}}^{V} < 120$ GeV, 3 jets, TT (p) $p_{\mathrm{T}}^{V} > 120$ GeV, 3 jets, TT

Figure 547: Post-fit plots for MVA distribution in 1-lepton 2-jet and 3-jets, $p_{\mathrm{T}}^{V} < 120$ GeV and $p_{\mathrm{T}}^{V} > 120$ GeV events with 1 b-tag (MV1c is fit here), *LL*, *MM* and *TT* b-tags in the 0+1+2 lepton fit. The pre-fit background expectation is indicated by the dashed blue line. Only statistical uncertainties are indicated.

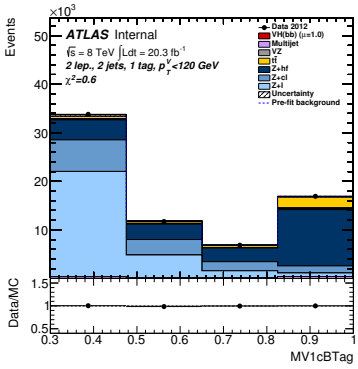

(a) $p_{\mathrm{T}}^{V} < 120$ GeV, 2 jets, 1-tag

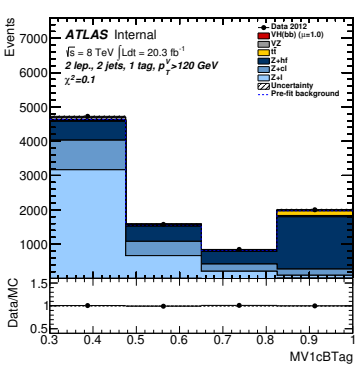

(b) $p_{\mathrm{T}}^{V} > 120$ GeV, 2 jets, 1-tag

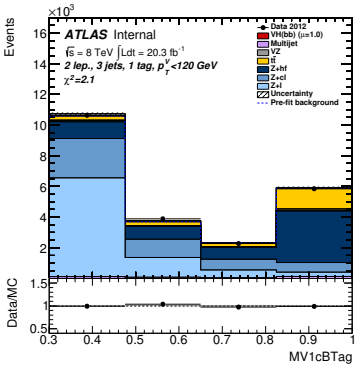

(c) $p_{\mathrm{T}}^{V} < 120$ GeV, 3 jets, 1-tag

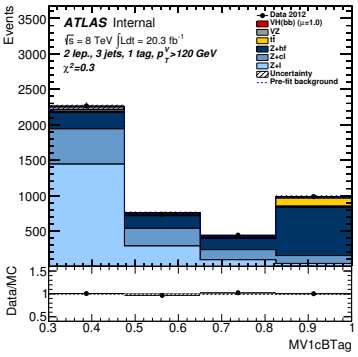

(d) $p_{\mathrm{T}}^{V} > 120$ GeV, 3 jets, 1-tag

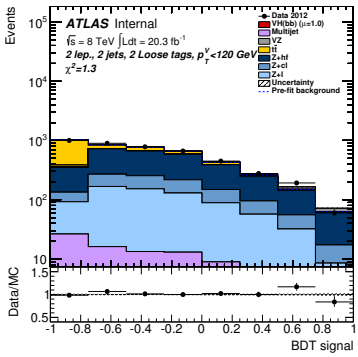

(e) $p_{\mathrm{T}}^{V} < 120$ GeV, 2 jets, LL

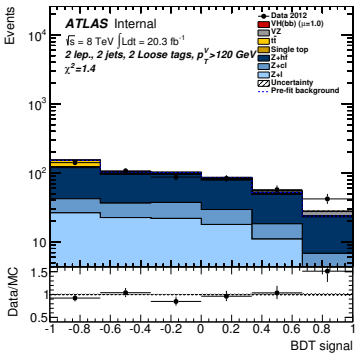

(f) $p_{\mathrm{T}}^{V} > 120$ GeV, 2 jets, LL

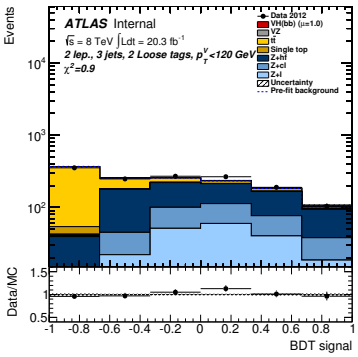

(g) $p_{\mathrm{T}}^{V} < 120$ GeV, 3 jets, LL

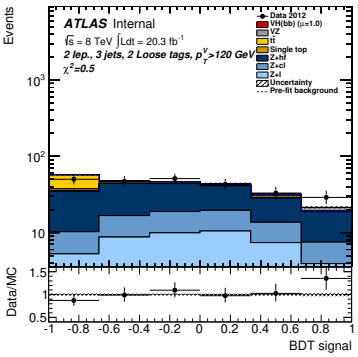

(h) $p_{\mathrm{T}}^{V} > 120$ GeV, 3 jets, LL

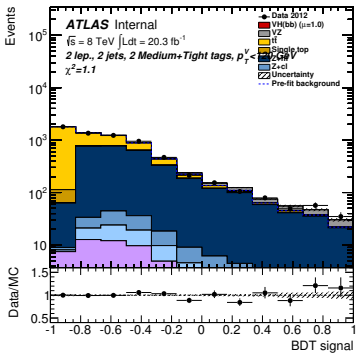

(i) $p_{\mathrm{T}}^{V} < 120$ GeV 2 jets, MM+TT

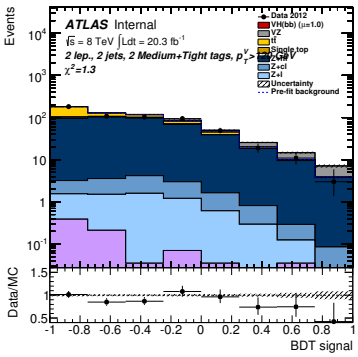

(j) $p_{\mathrm{T}}^{V} > 120$ GeV 2 jets, MM+TT

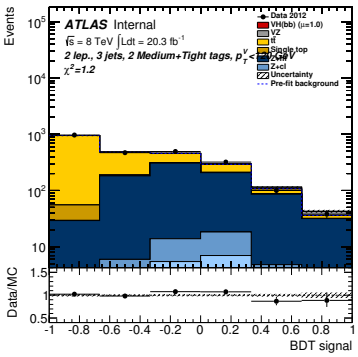

(k) $p_{\mathrm{T}}^{V} < 120$ GeV, 3 jets, MM+TT

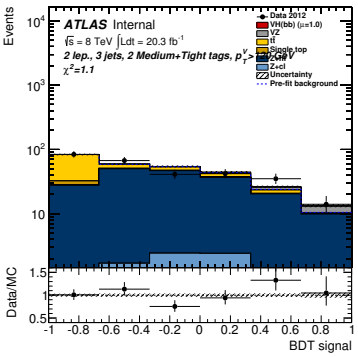

(l) $p_{\mathrm{T}}^{V} > 120$ GeV, 3 jets, MM+TT

Figure 548: Post-fit plots for MVA distribution in 2-lepton 2-jet and 3-jets , $p_{\mathrm{T}}^{V} < 120$ GeV (left) and $p_{\mathrm{T}}^{V} > 120$ GeV (right) events with 1 b-tag (MV1c is fit here), LL and $MM + TT$ b-tags in the 0+1+2 lepton fit. The pre-fit background expectation is indicated by the dashed blue line. Only statistical uncertainties are indicated.

AL.9 Diboson dijet Mass Analysis Post Fit Plots

In the following sections post-fit plots corresponding to unconditionnal μ fits to the data for the dijet mass analysis for the diboson search are presented. In all cases the MC expectations have been adapted to the pulls from the data in the combined 0+1+2 lepton fit. As a comparison, the total nominal background prediction is indicated by the dashed blue curve.

In Figures 549 - 551, 552 - 554, 555 - 74 post-fit plots for the m_{bb} shape analysis are shown for the 0, 1 and 2-lepton channel respectively in the various 1-tag and 2-tag categories in different p_{T}^{V} bins.

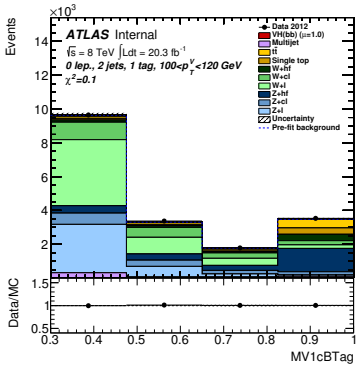

(a) $p_{\mathrm{T}}^{V} < 120$ GeV, 2 jets, 1-tag

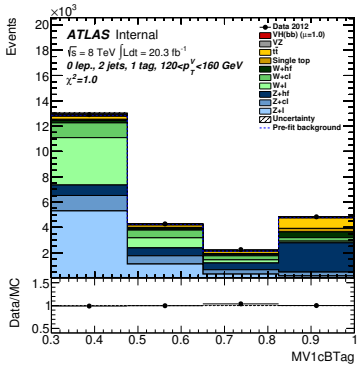

(b) $p_{\mathrm{T}}^{V} > 120$ GeV, 2 jets, 1-tag

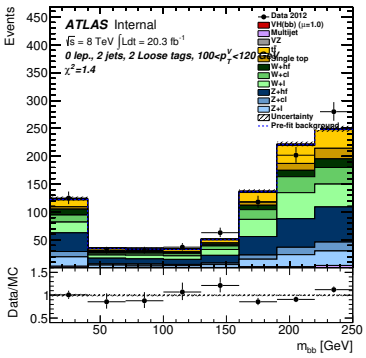

(c) $100 < p_{\mathrm{T}}^{V} < 120$ GeV, 2 jets, LL

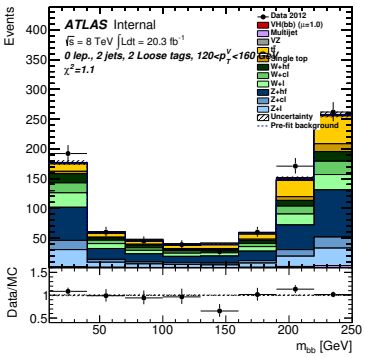

(d) $120 < p_{\mathrm{T}}^{V} < 160$ GeV, 2 jets, LL

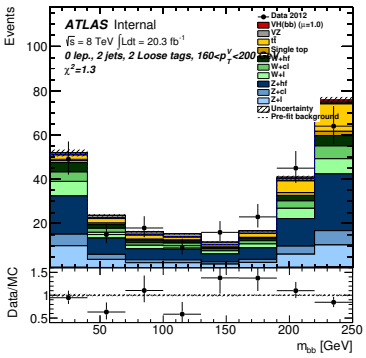

(e) $160 < p_{\mathrm{T}}^{V} < 200$ GeV, 2 jets, LL

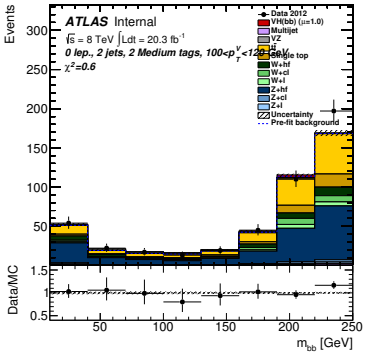

(f) $100 < p_{\mathrm{T}}^{V} < 120$ GeV, 2 jets, MM

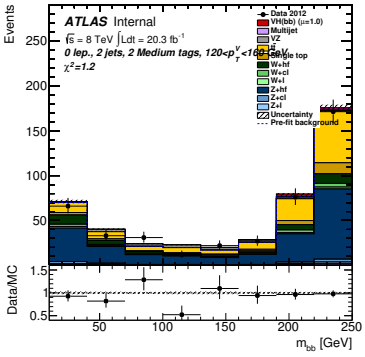

(g) $120 < p_{\mathrm{T}}^{V} < 160$ GeV, 2 jets, MM

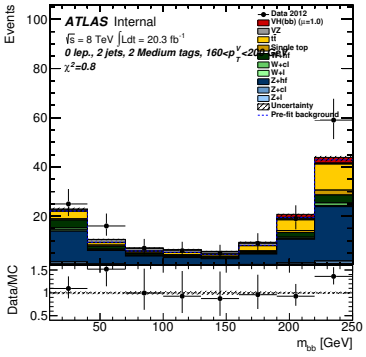

(h) $160 < p_{\mathrm{T}}^{V} < 200$ GeV, 2 jets, MM

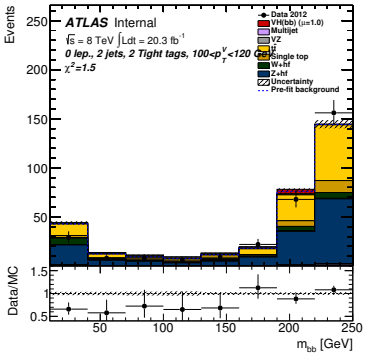

(i) $100 < p_{\mathrm{T}}^{V} < 120$ GeV, 2 jets, TT

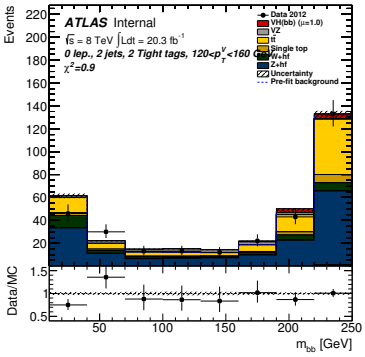

(j) $120 < p_{\mathrm{T}}^{V} < 160$ GeV, 2 jets, TT

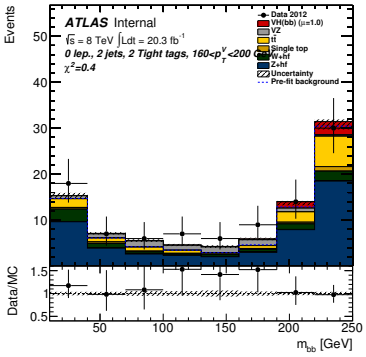

(k) $160 < p_{\mathrm{T}}^{V} < 200$ GeV, 2 jets, TT

Figure 549: Post diboson fit plots for m_{jj} distribution in 0-lepton events in the 1-tag (where mv1c is used in the fit) *LL*, *MM* and *TT* tag categories for the 2-jets events. Plots are shown for $100 < p_{\mathrm{T}}^{V} < 120$ GeV, $120 < p_{\mathrm{T}}^{V} < 160$ GeVand $160 < p_{\mathrm{T}}^{V} < 200$ GeV. The pre-fit background expectation is indicated by the dashed blue line.

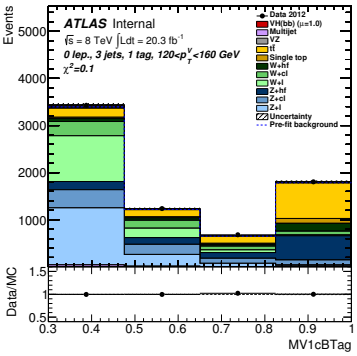

(a) $p_{\mathrm{T}}^{V} > 120$ GeV, 3 jets, 1-tag

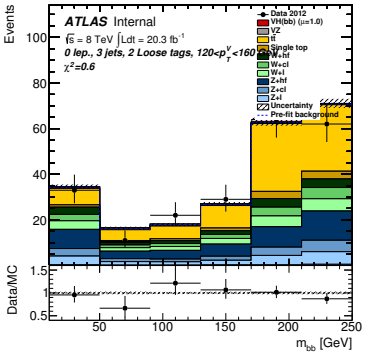

(b) $120 < p_{\mathrm{T}}^{V} < 160$ GeV, 3 jets, LL

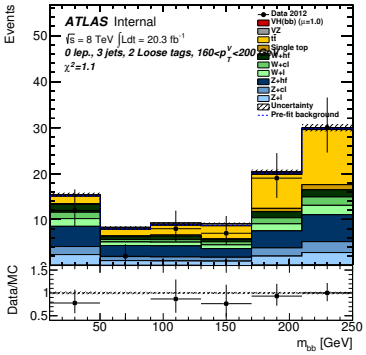

(c) $160 < p_{\mathrm{T}}^{V} < 200$ GeV, 3 jets, LL

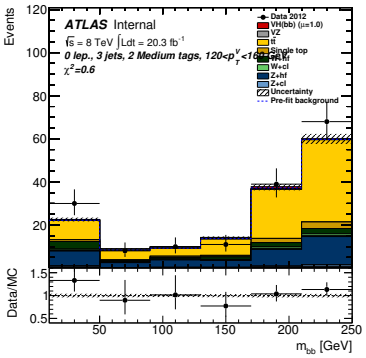

(d) $120 < p_{\mathrm{T}}^{V} < 160$ GeV, 3 jets, MM

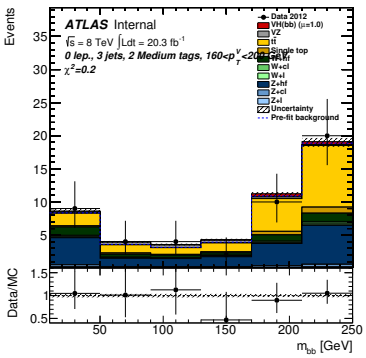

(e) $160 < p_{\mathrm{T}}^{V} < 200$ GeV, 3 jets, MM

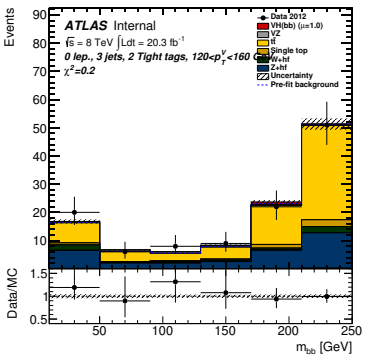

(f) $120 < p_{\mathrm{T}}^{V} < 160$ GeV, 3 jets, TT

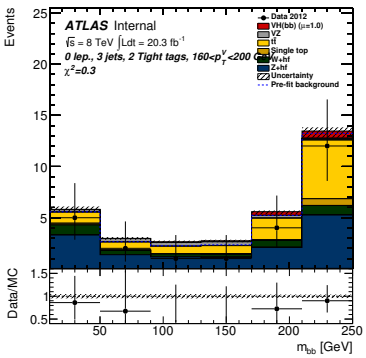

(g) $160 < p_{\mathrm{T}}^{V} < 200$ GeV, 3 jets, TT

Figure 550: Post diboson fit plots for m_{jj} distribution in 0-lepton events in the 1-tag (where mv1c is used in the fit) LL, MM and TT tag categories for the 3-jets events. Plots are shown for $120 < p_{\mathrm{T}}^{V} < 160$ GeVand $160 < p_{\mathrm{T}}^{V} < 200$ GeV. The pre-fit background expectation is indicated by the dashed blue line.

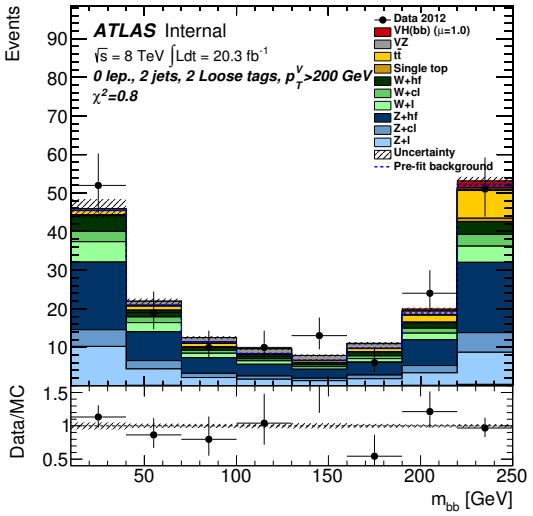

(a) p_{T}^{V} > 200 GeV, 2 jets, LL

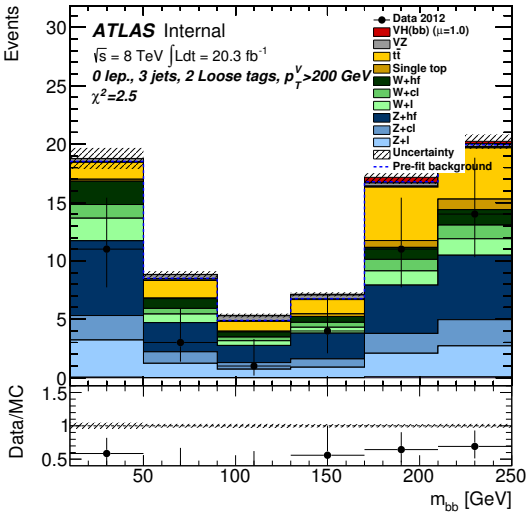

(b) p_{T}^{V} > 200 GeV, 3 jets, LL

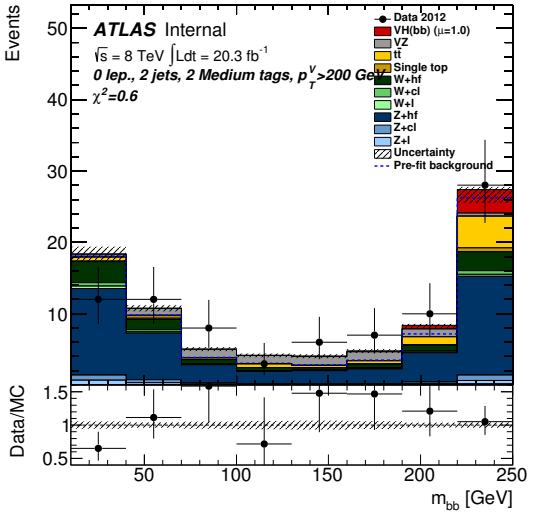

(c) p_{T}^{V} > 200 GeV, 2 jets, MM

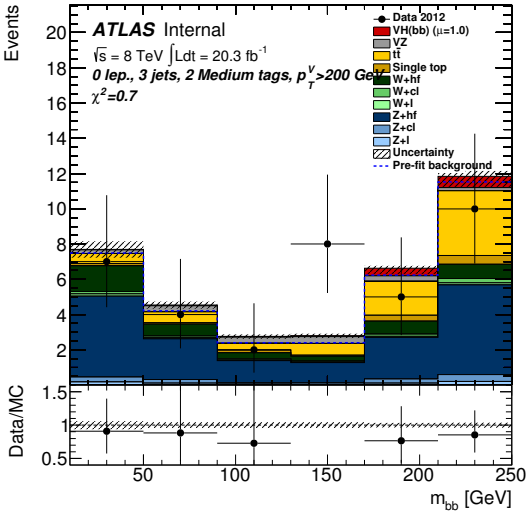

(d) p_{T}^{V} > 200 GeV, 3 jets, MM

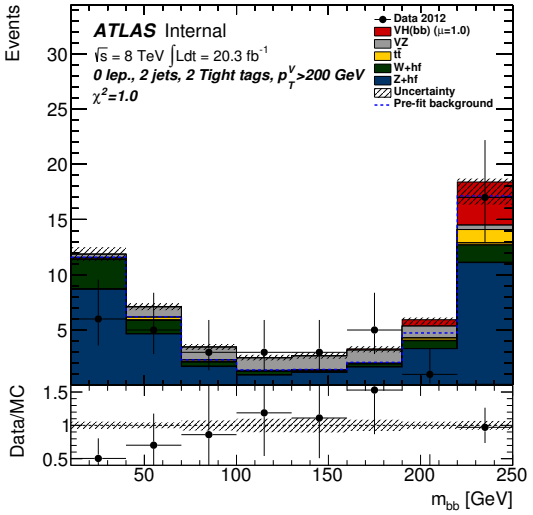

(e) p_{T}^{V} > 200 GeV, 2 jets, TT

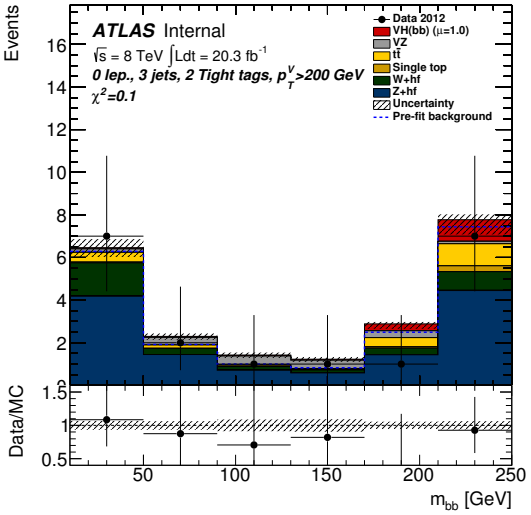

(f) p_{T}^{V} > 200 GeV, 3 jets, TT

Figure 551: Post diboson fit plots for m_{jj} distribution in 0-lepton events in the *LL*, *MM* and *TT* tag categories for the 2-jets and the 3-jets events. Plots are shown for $p_{\mathrm{T}}^{V} > 200$ GeV. The pre-fit background expectation is indicated by the dashed blue line.

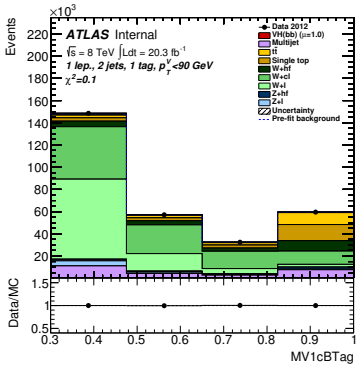

(a) $p_{\mathrm{T}}^{V} < 120$ GeV, 2 jets, 1-tag

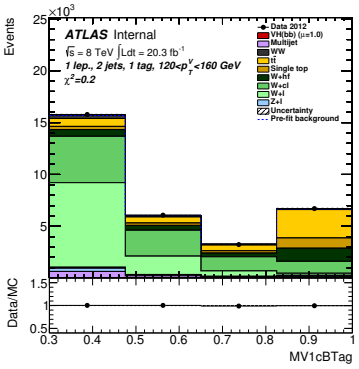

(b) $p_{\mathrm{T}}^{V} > 120$ GeV, 2 jets, 1-tag

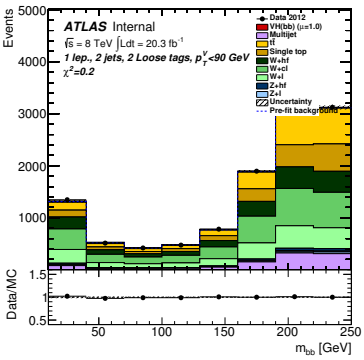

(c) $p_{\mathrm{T}}^{V} < 90$ GeV, 2 jets, LL

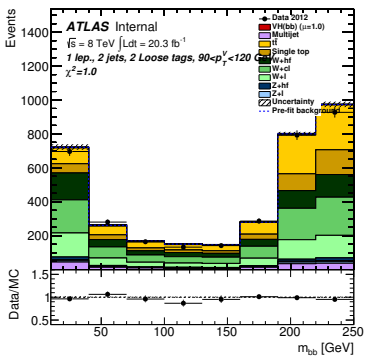

(d) $90 < p_{\mathrm{T}}^{V} < 120$ GeV, 2 jets, LL

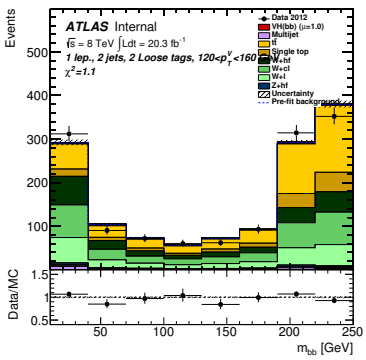

(e) $120 < p_{\mathrm{T}}^{V} < 160$ GeV, 2 jets, LL

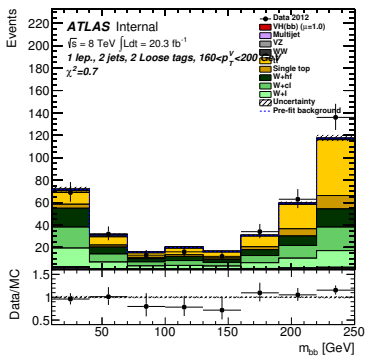

(f) $160 < p_{\mathrm{T}}^{V} < 200$ GeV, 2 jets, LL

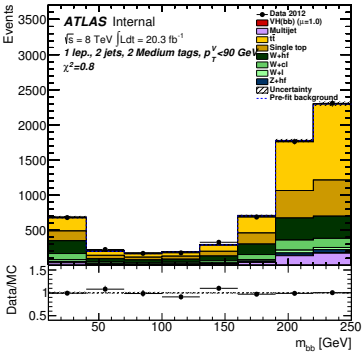

(g) $p_{\mathrm{T}}^{V} < 90$ GeV, 2 jets, MM

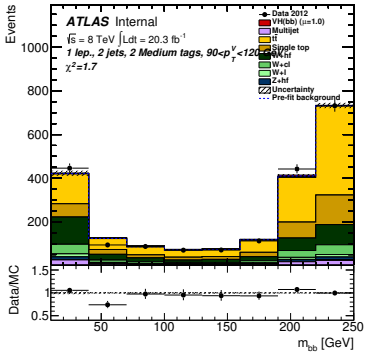

(h) $90 < p_{\mathrm{T}}^{V} < 120$ GeV, 2 jets, MM

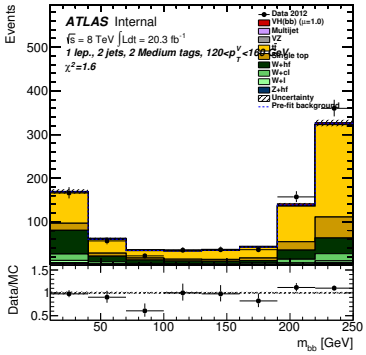

(i) $120 < p_{\mathrm{T}}^{V} < 160$ GeV, 2 jets, MM

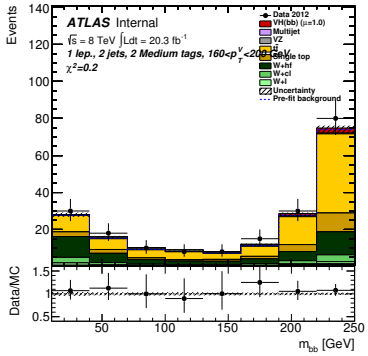

(j) $160 < p_{\mathrm{T}}^{V} < 200$ GeV, 2 jets, MM

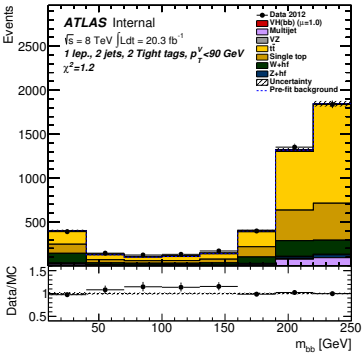

(k) $p_{\mathrm{T}}^{V} < 90$ GeV, 2 jets, TT

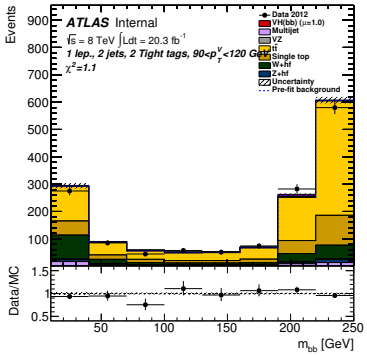

(l) $90 < p_{\mathrm{T}}^{V} < 120$ GeV, 2 jets, TT

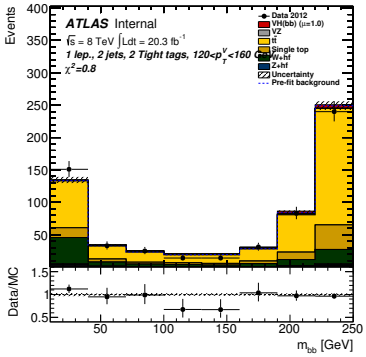

(m) $120 < p_{\mathrm{T}}^{V} < 160$ GeV, 2 jets, TT

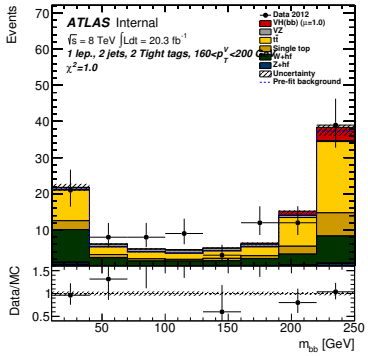

(n) $160 < p_{\mathrm{T}}^{V} < 200$ GeV, 2 jets, TT

Figure 552: Post diboson fit plots for m_{jj} distribution in 1-lepton events in the 1-tag (where mv1c is used in the fit) *LL*, *MM* and *TT* tag categories for the 2-jets events. Plots are shown for $p_{\mathrm{T}}^{V} < 90$ GeV, $90 < p_{\mathrm{T}}^{V} < 120$ GeV, $120 < p_{\mathrm{T}}^{V} < 160$ GeVand $160 < p_{\mathrm{T}}^{V} < 200$ GeV. The pre-fit background expectation is indicated by the dashed blue line.

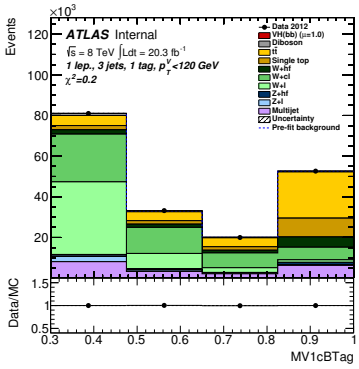

(a) $p_{\mathrm{T}}^{V} < 120$ GeV, 3 jets, 1-tag

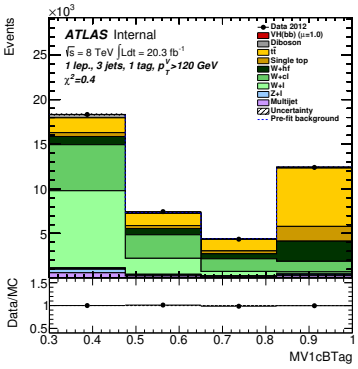

(b) $p_{\mathrm{T}}^{V} > 120$ GeV, 3 jets, 1-tag

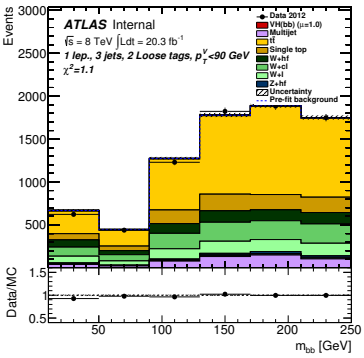

(c) $p_{\mathrm{T}}^{V} < 90$ GeV, 3 jets, LL

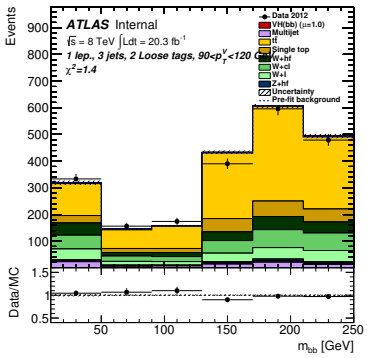

(d) $90 < p_{\mathrm{T}}^{V} < 120$ GeV, 3 jets, LL

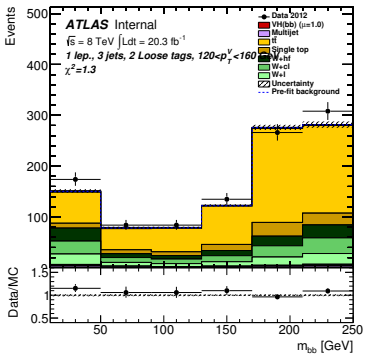

(e) $120 < p_{\mathrm{T}}^{V} < 160$ GeV, 3 jets, LL

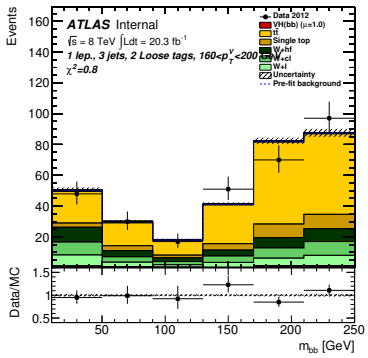

(f) $160 < p_{\mathrm{T}}^{V} < 200$ GeV, 3 jets, LL

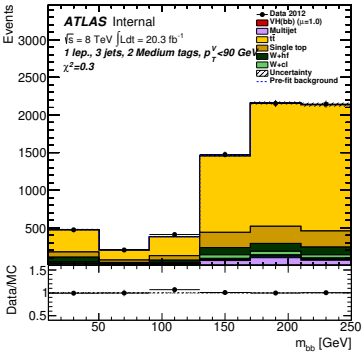

(g) $p_{\mathrm{T}}^{V} < 90$ GeV, 3 jets, MM

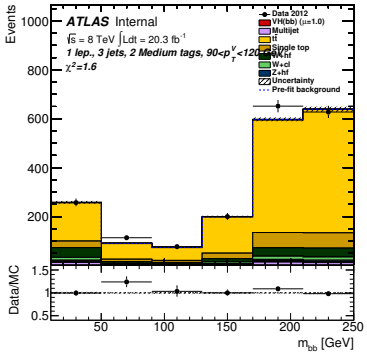

(h) $90 < p_{\mathrm{T}}^{V} < 120$ GeV, 3 jets, MM

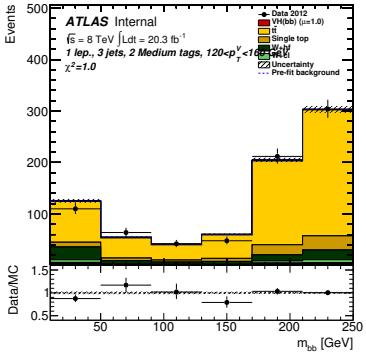

(i) $120 < p_{\mathrm{T}}^{V} < 160$ GeV, 3 jets, MM

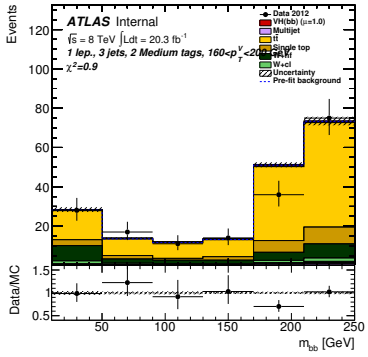

(j) $160 < p_{\mathrm{T}}^{V} < 200$ GeV, 3 jets, MM

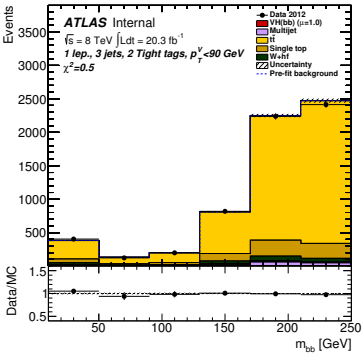

(k) $p_{\mathrm{T}}^{V} < 90$ GeV, 3 jets, TT

(l) $90 < p_{\mathrm{T}}^{V} < 120$ GeV, 3 jets, TT

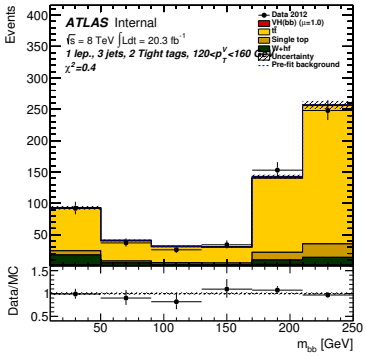

(m) $120 < p_{\mathrm{T}}^{V} < 160$ GeV, 3 jets, TT

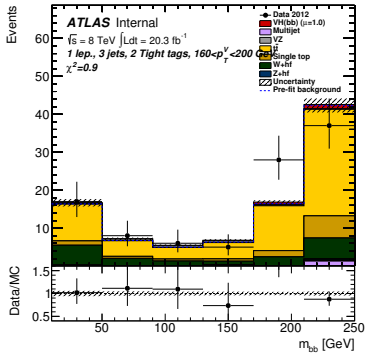

(n) $160 < p_{\mathrm{T}}^{V} < 200$ GeV, 3 jets, TT

Figure 553: Post diboson fit plots for m_{jj} distribution in 1-lepton events in the 1-tag (where mv1c is used in the fit) *LL*, *MM* and *TT* tag categories for the 3-jets events. Plots are shown for $p_{\mathrm{T}}^{V} < 90$ GeV, $90 < p_{\mathrm{T}}^{V} < 120$ GeV, $120 < p_{\mathrm{T}}^{V} < 160$ GeVand $160 < p_{\mathrm{T}}^{V} < 200$ GeV. The pre-fit background expectation is indicated by the dashed blue line.

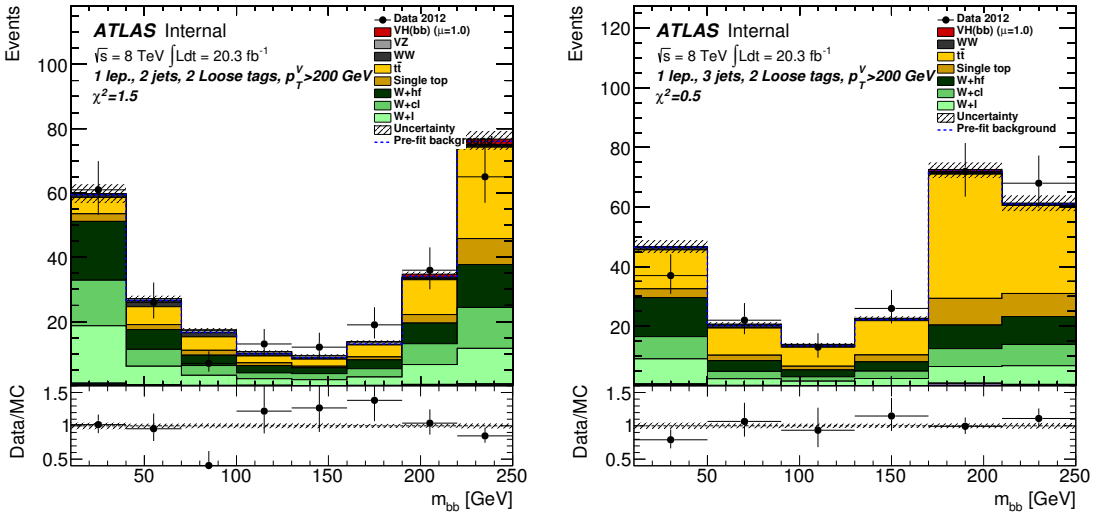

(a) $p_{\mathrm{T}}^{V} > 200$ GeV, 2 jets, LL

(b) $p_{\mathrm{T}}^{V} > 200$ GeV, 3 jets, LL

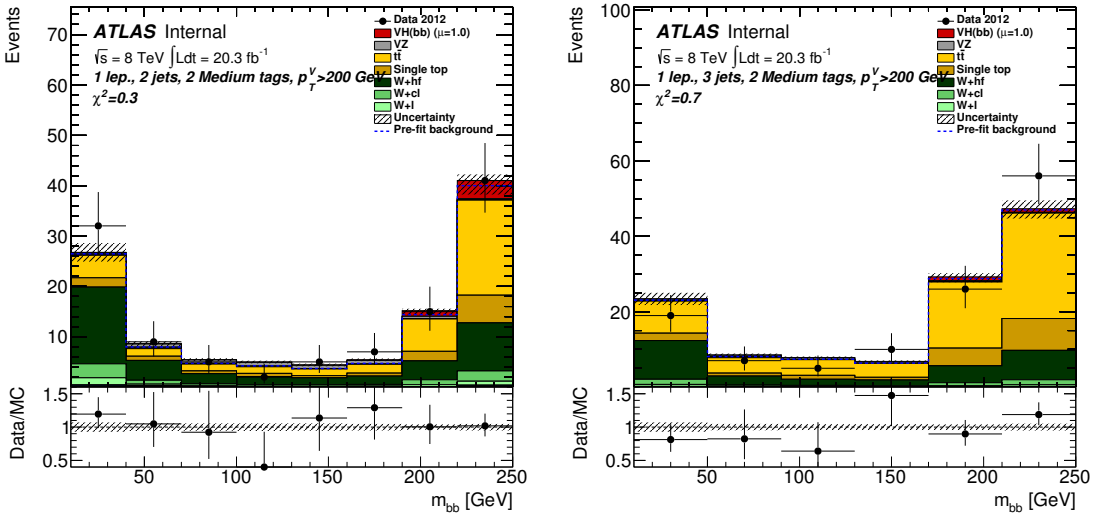

(c) $p_{\mathrm{T}}^{V} > 200$ GeV, 2 jets, MM

(d) $p_{\mathrm{T}}^{V} > 200$ GeV, 3 jets, MM

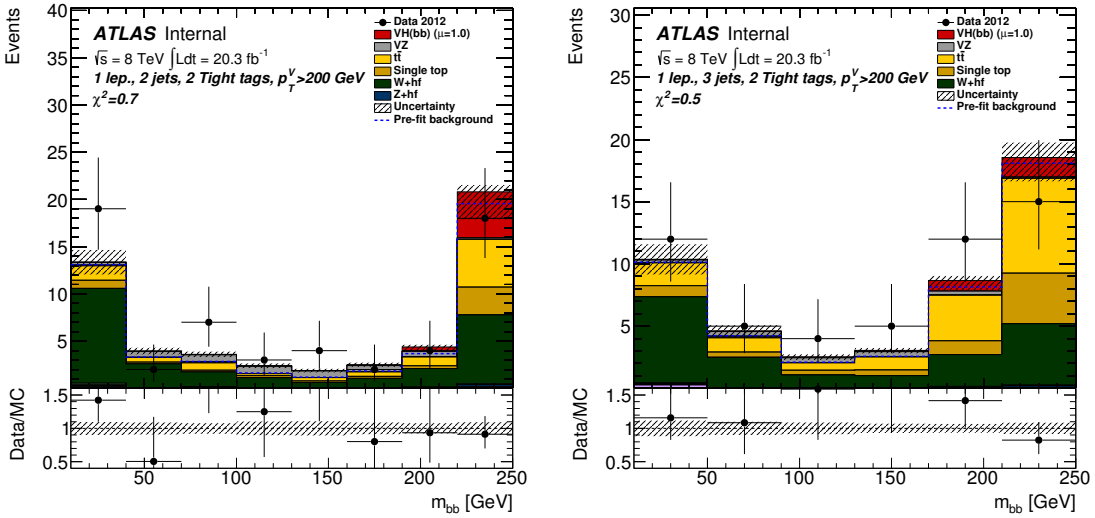

(e) $p_{\mathrm{T}}^{V} > 200$ GeV, 2 jets, TT

(f) $p_{\mathrm{T}}^{V} > 200$ GeV, 3 jets, TT

Figure 554: Post diboson fit plots for m_{jj} distribution in 1-lepton events in the *LL*, *MM* and *TT* tag categories for the 2-jets and the 3-jets events. Plots are shown for $p_{\mathrm{T}}^{V} > 200$ GeV. The pre-fit background expectation is indicated by the dashed blue line.

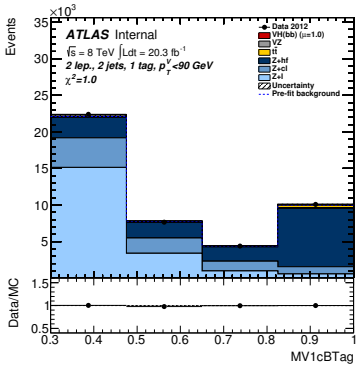

(a) $p_{\mathrm{T}}^{V} < 120$ GeV, 2 jets, 1-tag

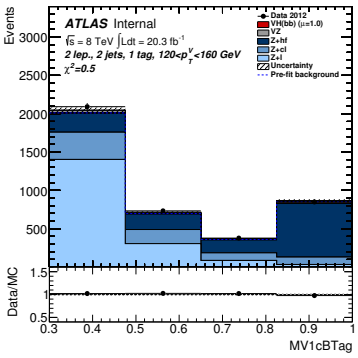

(b) $p_{\mathrm{T}}^{V} > 120$ GeV, 2 jets, 1-tag

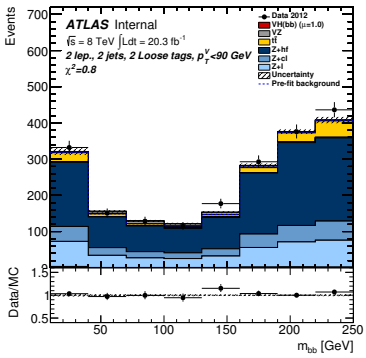

(c) $p_{\mathrm{T}}^{V} < 90$ GeV, 2 jets, LL

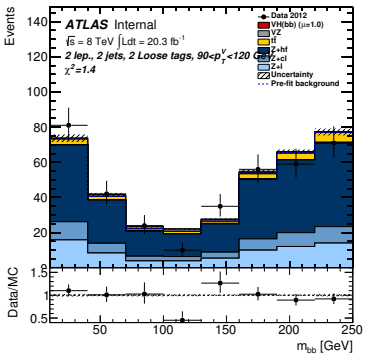

(d) $90 < p_{\mathrm{T}}^{V} < 120$ GeV, 2 jets, LL

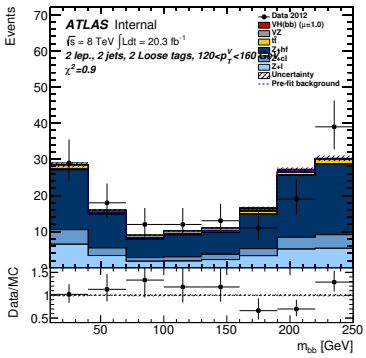

(e) $120 < p_{\mathrm{T}}^{V} < 160$ GeV, 2 jets, LL

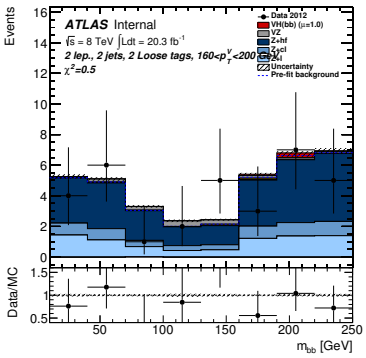

(f) $160 < p_{\mathrm{T}}^{V} < 200$ GeV, 2 jets, LL

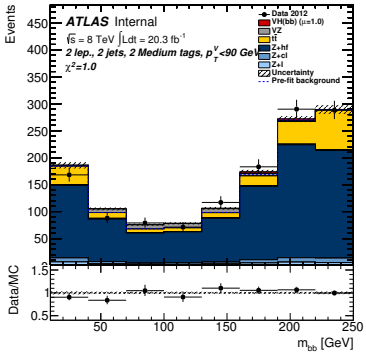

(g) $p_{\mathrm{T}}^{V} < 90$ GeV, 2 jets, MM

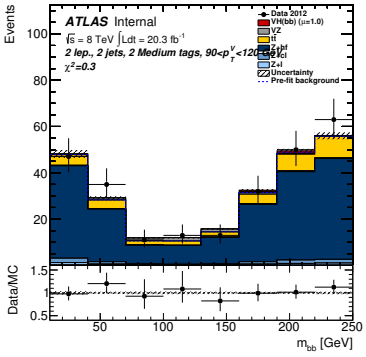

(h) $90 < p_{\mathrm{T}}^{V} < 120$ GeV, 2 jets, MM

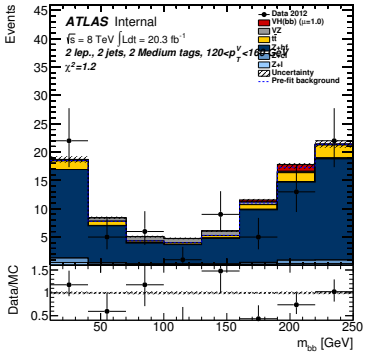

(i) $120 < p_{\mathrm{T}}^{V} < 160$ GeV, 2 jets, MM

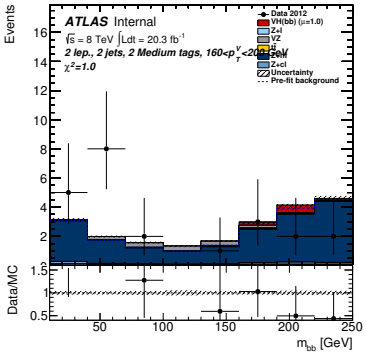

(j) $160 < p_{\mathrm{T}}^{V} < 200$ GeV, 2 jets, MM

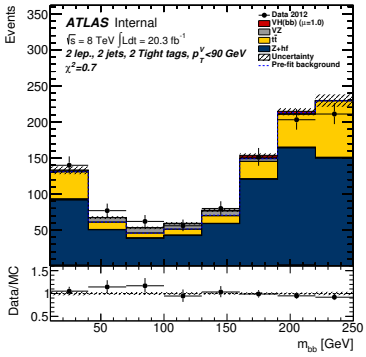

(k) $p_{\mathrm{T}}^{V} < 90$ GeV, 2 jets, TT

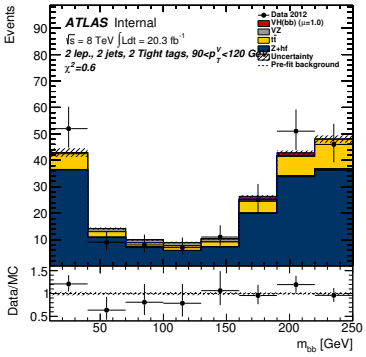

(l) $90 < p_{\mathrm{T}}^{V} < 120$ GeV, 2 jets, TT

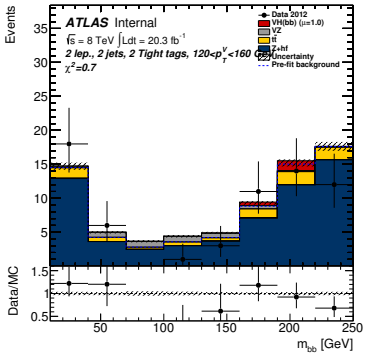

(m) $120 < p_{\mathrm{T}}^{V} < 160$ GeV, 2 jets, TT

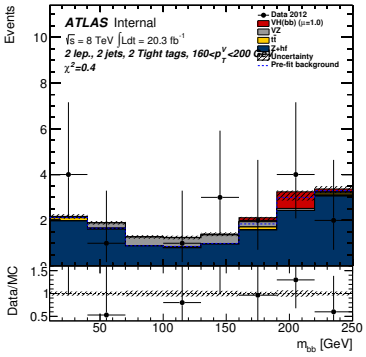

(n) $160 < p_{\mathrm{T}}^{V} < 200$ GeV, 2 jets, TT

Figure 555: Post diboson fit plots for m_{jj} distribution in 2-lepton events in the 1-tag (where mv1c is used in the fit) *LL*, *MM* and *TT* tag categories for the 2-jets events. Plots are shown for $p_{\mathrm{T}}^{V} < 90$ GeV, $90 < p_{\mathrm{T}}^{V} < 120$ GeV, $120 < p_{\mathrm{T}}^{V} < 160$ GeVand $160 < p_{\mathrm{T}}^{V} < 200$ GeV. The pre-fit background expectation is indicated by the dashed blue line.

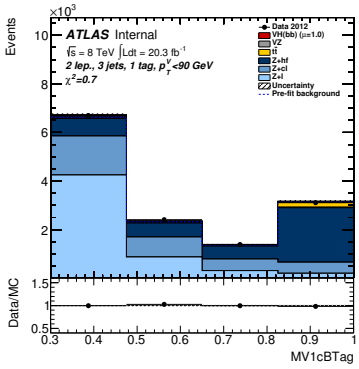

(a) $p_{\mathrm{T}}^{V} < 120$ GeV, 3 jets, 1-tag

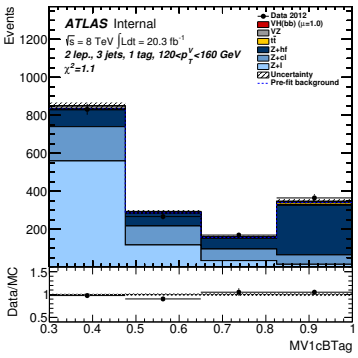

(b) $p_{\mathrm{T}}^{V} > 120$ GeV, 3 jets, 1-tag

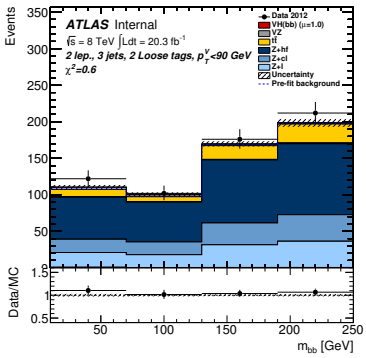

(c) $p_{\mathrm{T}}^{V} < 90$ GeV, 3 jets, LL

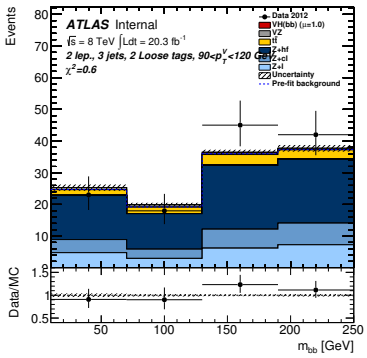

(d) $90 < p_{\mathrm{T}}^{V} < 120$ GeV, 3 jets, LL

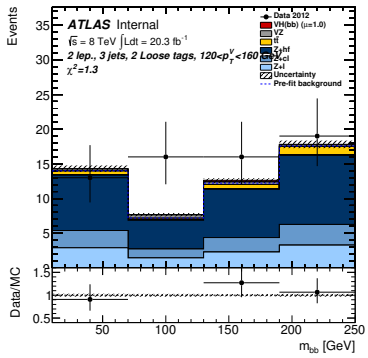

(e) $120 < p_{\mathrm{T}}^{V} < 160$ GeV, 3 jets, LL

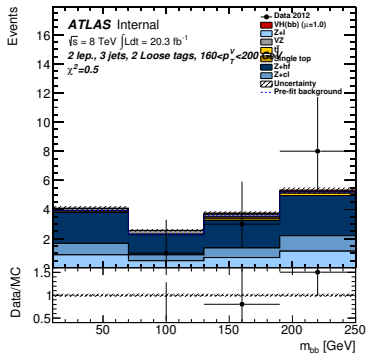

(f) $160 < p_{\mathrm{T}}^{V} < 200$ GeV, 3 jets, LL

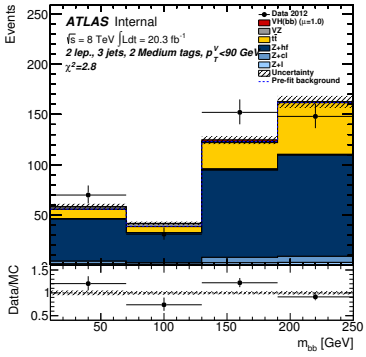

(g) $p_{\mathrm{T}}^{V} < 90$ GeV, 3 jets, MM

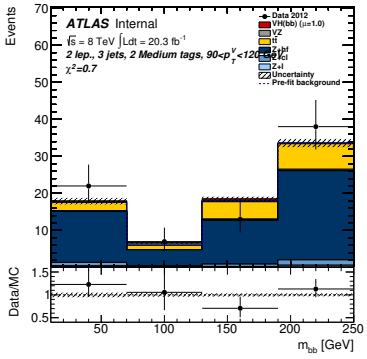

(h) $90 < p_{\mathrm{T}}^{V} < 120$ GeV, 3 jets, MM

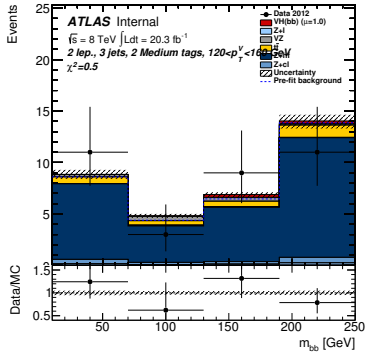

(i) $120 < p_{\mathrm{T}}^{V} < 160$ GeV, 3 jets, MM

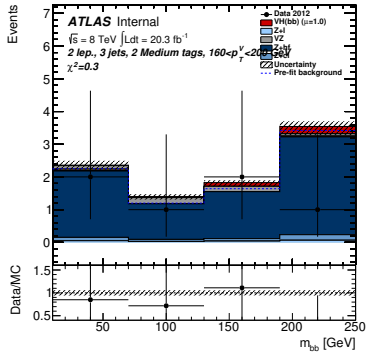

(j) $160 < p_{\mathrm{T}}^{V} < 200$ GeV, 3 jets, MM

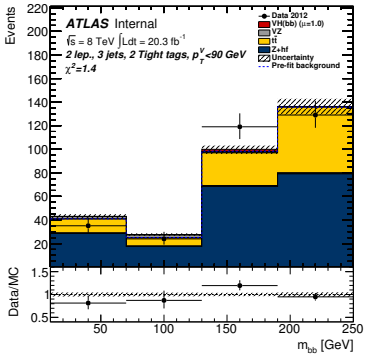

(k) $p_{\mathrm{T}}^{V} < 90$ GeV, 3 jets, TT

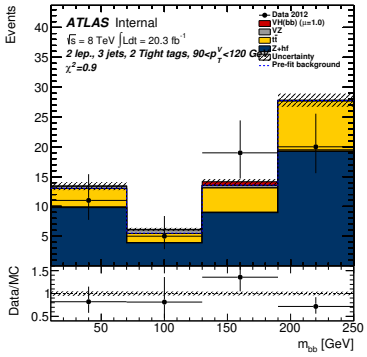

(l) $90 < p_{\mathrm{T}}^{V} < 120$ GeV, 3 jets, TT

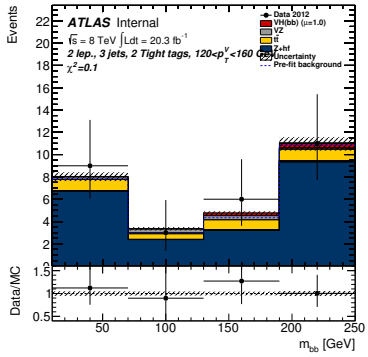

(m) $120 < p_{\mathrm{T}}^{V} < 160$ GeV, 3 jets, TT

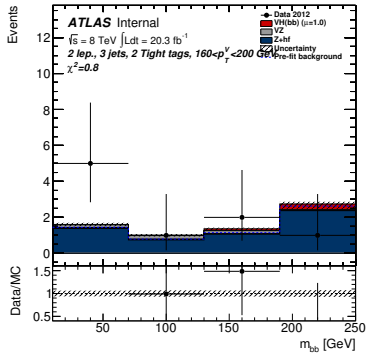

(n) $160 < p_{\mathrm{T}}^{V} < 200$ GeV, 3 jets, TT

Figure 556: Post diboson fit plots for m_{jj} distribution in 2-lepton events in the 1-tag (where mv1c is used in the fit) *LL*, *MM* and *TT* tag categories for the 3-jets events. Plots are shown for $p_{\mathrm{T}}^{V} < 90$ GeV, $90 < p_{\mathrm{T}}^{V} < 120$ GeV, $120 < p_{\mathrm{T}}^{V} < 160$ GeVand $160 < p_{\mathrm{T}}^{V} < 200$ GeV. The pre-fit background expectation is indicated by the dashed blue line.

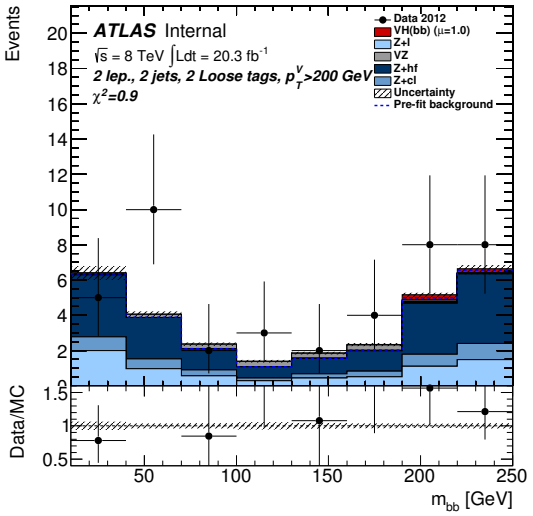

(a) $p_{\mathrm{T}}^{V} > 200$ GeV, 2 jets, LL

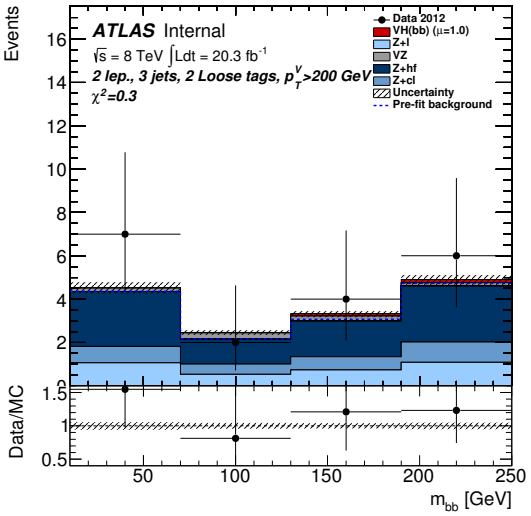

(b) $p_{\mathrm{T}}^{V} > 200$ GeV, 3 jets, LL

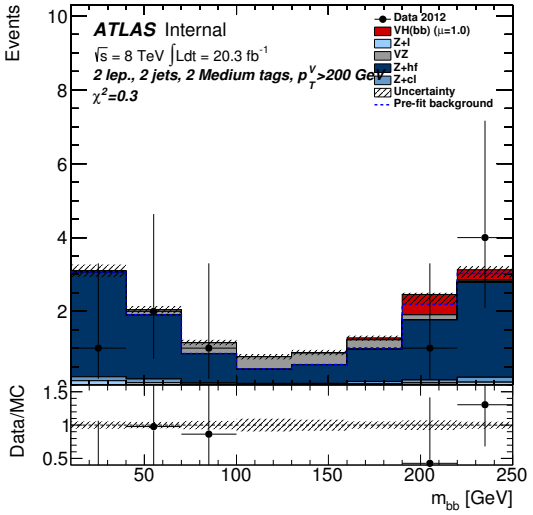

(c) $p_{\mathrm{T}}^{V} > 200$ GeV, 2 jets, MM

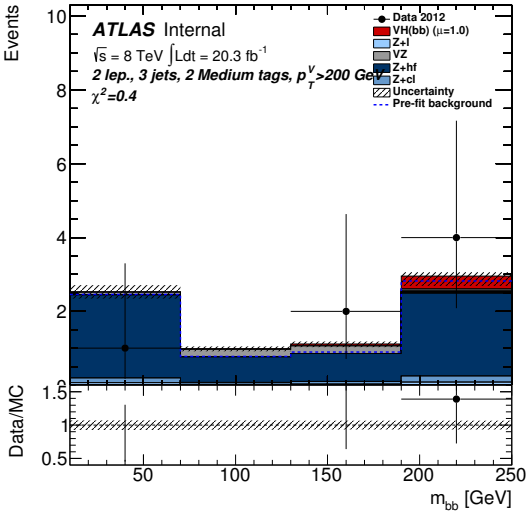

(d) $p_{\mathrm{T}}^{V} > 200$ GeV, 3 jets, MM

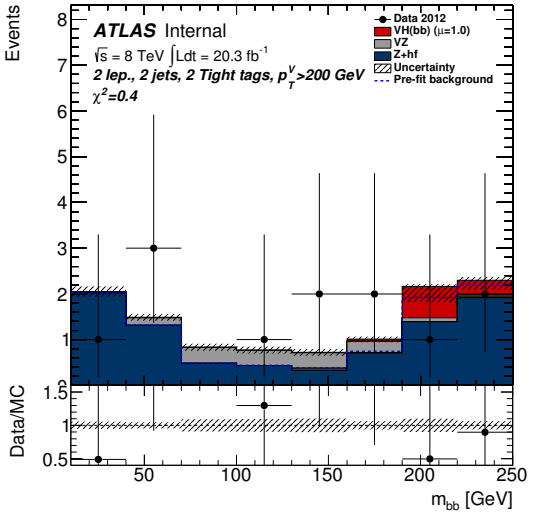

(e) $p_{\mathrm{T}}^{V} > 200$ GeV, 2 jets, TT

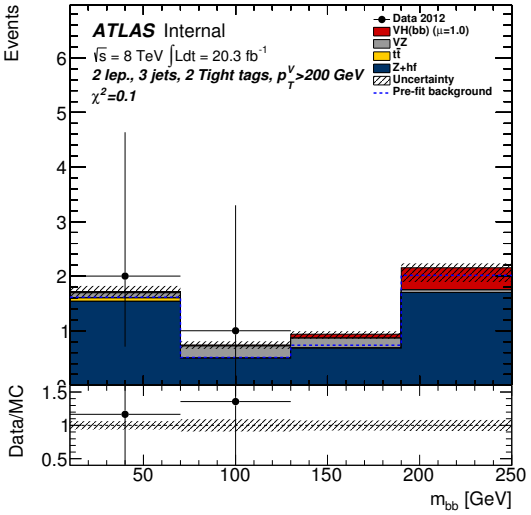

(f) $p_{\mathrm{T}}^{V} > 200$ GeV, 3 jets, TT

Figure 557: Post diboson fit plots for m_{jj} distribution in 2-lepton events in the *LL*, *MM* and *TT* tag categories for the 2-jets and the 3-jets events. Plots are shown for $p_{\mathrm{T}}^{V} > 200$ GeV. The pre-fit background expectation is indicated by the dashed blue line.

AM Impact of the BCH cleaning on the VH analysis

AM.1 BCH cleaning for dummies

During data taking, some tile modules were either temporarily or permanently masked. One of them, off in the full dataset, was masked in the MC production. A correction based on adjacent live modules was developed but it sometimes fails to properly estimate the lost energy. Jets in the masked modules (core region) tend to be undercorrected, while jets in adjacent modules (edge region) are overcorrected. The `BCHCleaningTool` [**?**] was developed to reject events with badly corrected jets, by picking random run and lumiblock numbers to emulate the data taking conditions of the full dataset.

The tool can run in two modes:

- *tight*: purely geometrical rejection of events with a jet in the core or edge regions;
- *medium*: rejection of events with jets in the core region, or jets in the edge region depending on their `emfrac` and `BCH_CORR_CELL` values.

AM.2 Samples used

Nominal signal samples for the 0 and 1 lepton analyses were used:

- $ZH \to \nu\nu bb$:
  `mc12_8TeV.161849.Pythia8_AU2CTEQ6L1_ZH125_nunubb.merge.NTUP_SMWZ.e1812_a188_a171_r3549_p1328_tid01219822_00`
- $WH \to \ell\nu bb$:
  `mc12_8TeV.161805.Pythia8_AU2CTEQ6L1_WH125_lnubb.merge.NTUP_SMWZ.e1812_a188_a171_r3549_p1328_tid01219824_00`

For data comparison the full `JetTauEtMiss` stream was processed.

Special signal samples were also produced, with all four problematic modules masked (worst data taking conditions). The $ZH \to \nu\nu bb$ sample was used in the following comparisons:
`mc12_8TeV.161849.Pythia8_AU2CTEQ6L1_ZH125_nunubb.merge.NTUP_SMWZ.e1812_a188_a249_r4540_p1328/`

AM.3 Impact on selection yield

In the 0-lepton analysis several triggers are used, with the following luminosities:

- EF_xe80T_tclcw_loose (1.91 fb^{-1}in periods A–B5)
- EF_xe80_tclcw (2.12 fb^{-1}in periods A–B5)
- EF_xe80_tclcw_loose (18.1 fb^{-1}in periods B6–End)

The impact on the yield after applying the full 0-lepton selection is shown in Table 161 for both signal MC and `JetTauEtMiss` stream, and it is very similar between data and MC. As expected the impact is smaller for the first two triggers, used during early data taking when fewer modules were problematic. For the remainder of this Appendix, only the EF_xe80_tclcw_loose trigger (representing 90% of the total luminosity) will be used.

The BCH cleaning acceptance loss is high for the tight selection (7–9%) and was deemed unacceptable for the analysis. In the following, medium cleaning is the only considered option.

The impact after the full 1-lepton selection on the $WH \to \ell\nu bb$ sample is reported in Table 162. It is very similar to the 0-lepton analysis.

	EF_xe80T_tclcw_loose		EF_xe80_tclcw		EF_xe80_tclcw_loose		Data
	Medium	Tight	Medium	Tight	Medium	Tight	Medium
Full selection	1.3%	4.0%	1.3%	4.1%	2.3%	7.4%	2.5%
Exactly 2 jets	1.3%	4.0%	1.3%	4.1%	2.1%	6.9%	2.3%
Exactly 3 jets	1.4%	4.0%	1.5%	4.4%	3.3%	9.7%	3.1%
Btagging TT	1.5%	4.3%	1.3%	4.3%	2.3%	7.7%	2.2%
Btagging MM	1.2%	4.2%	1.4%	4.3%	2.2%	7.0%	2.8%
Btagging LL	1.3%	3.1%	1.3%	3.6%	2.5%	7.5%	2.3%

Table 161: Impact of BCH cleaning on yield after the full 0-lepton selection in data (last column) and for the signal sample for all triggers. For MC both the medium and tight BCH cleaning are given.

	Medium
Full selection (2+3 jets)	2.7%
Exactly 2jets	2.4%
Exactly 3jets	3.7%

Table 162: Impact of BCH cleaning on signal yield after the full 1-lepton selection.

	All quarks	All gluons
Full selection	0.2%	-0.2%
Exactly 2 jets	0.1%	-0.2%
Exactly 3 jets	0.6%	-0.1%
Btagging TT	0.3%	-0.2%
Btagging MM	0.3%	-0.2%
Btagging LL	0.1%	-0.1%

Table 163: Impact of BCH cleaning systematic uncertainty on yield after the full 0-lepton selection for the signal sample. The percentages shown correspond to the difference between applying the nominal BCH cleaning and the all-quark or all-gluon BCH mode.

The `BCHCleaningTool` provides a systematic uncertainty associated to the quark/gluon content of jets. Variations when assuming an all-quark (`isUp`$= 1$) or all-gluon (`isUp`$= -1$) content are reported in Table 163 and show a negligible effect.

For the 0-lepton analysis, the BCH effect was also measured when not applying the $\Delta\phi_{min}(E_{\mathrm{T}}^{\mathrm{miss}}, jet)$ requirement, as this would enrich the sample in multijet-like events in a region used as a template for the multijet estimate. The impact was very similar to the full analysis, with a slightly more pronounced effect in data in the low $\Delta\phi_{min}(E_{\mathrm{T}}^{\mathrm{miss}}, jet)$ region. More details can be found in Ref. [**?**].

Finally the 0-lepton analysis was also run on the special sample with four masked modules. Results were found in complete agreement with the default sample.

AM.4 Impact on distribution shapes

The leading jet p_{T}, m_{bb}, $E_{\mathrm{T}}^{\mathrm{miss}}$, $\phi(E_{\mathrm{T}}^{\mathrm{miss}})$, $\Delta\phi_{min}(E_{\mathrm{T}}^{\mathrm{miss}}, jet)$ and $\Delta R(jj)$ distributions for events in the 0-lepton analysis that pass and fail BCH medium cleaning are shown in Fig. 558 for the signal sample and in Fig. 559 for the `JetTauEtMiss` stream. More distributions are available in Ref. [**?**], also split in $E_{\mathrm{T}}^{\mathrm{miss}}$ bins as in the analysis. Within the limited statistics of events failing the BCH cleaning, one can conclude that there is no particular impact on the kinematic distributions. The $\phi(E_{\mathrm{T}}^{\mathrm{miss}})$ distributions

do look different for pass and fail, as expected since the problematic modules are located at $\phi > 0$, generating $E_{\mathrm{T}}^{\mathrm{miss}}$ in the opposite direction.

The most important distribution in the end is the m_{bb} invariant mass. In data they look identical for pass and fail. In signal MC there may be a small shift observed, but even if it is indeed the case this would only affect a tiny fraction of the signal (2.5%) and the analysis would be insensitive to it.

AM.5 Impact on *b*-tagging

AM.6 Conclusion

Given the very limited impact the BCH cleaning has on all kinematic variables, both in signal MC and in data, it was decided to not apply this procedure in order to avoid losing 2.5% signal efficiency

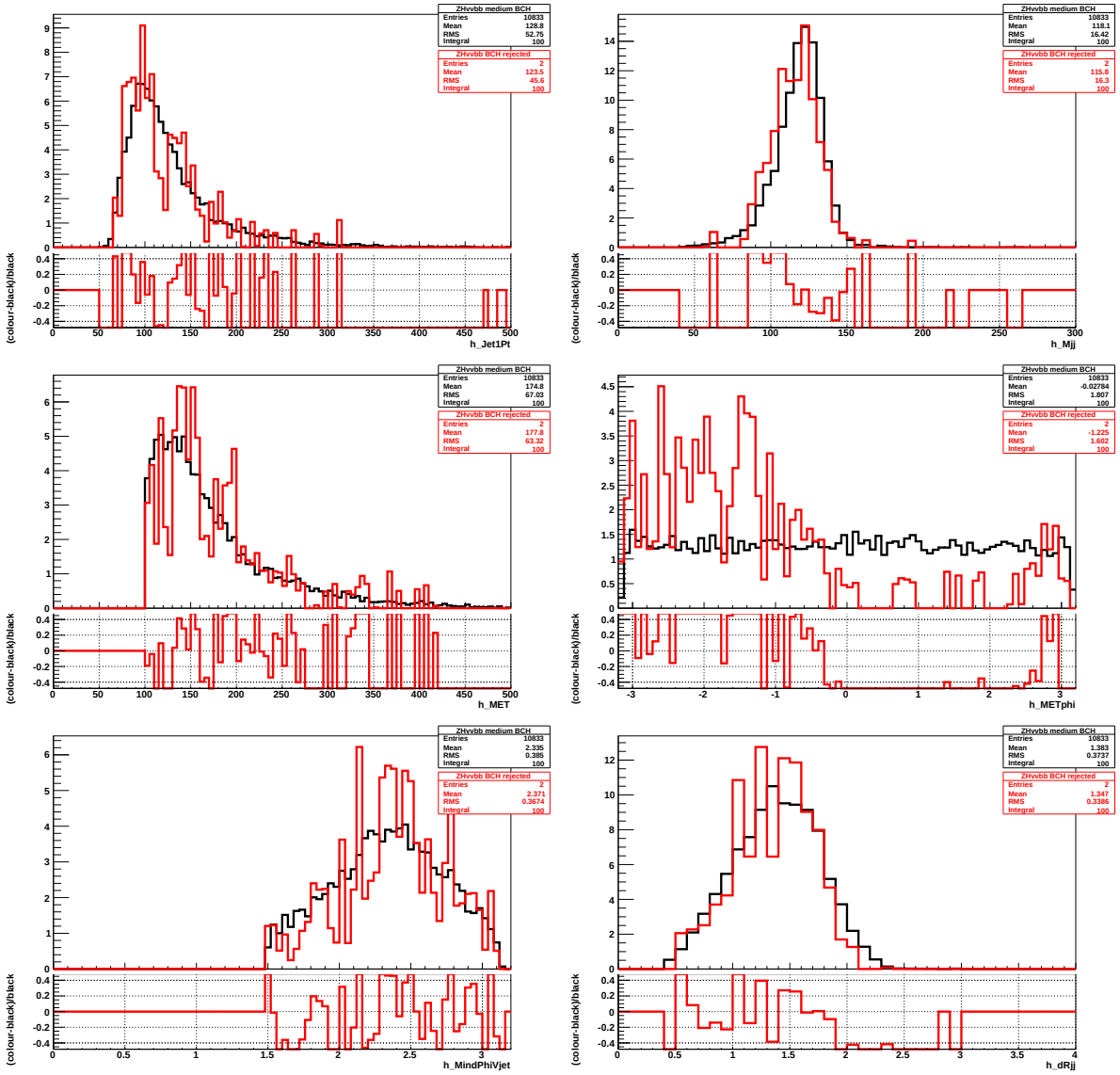

Figure 558: Leading jet p_{T}, m_{bb}, $E_{\mathrm{T}}^{\mathrm{miss}}$, $\phi(E_{\mathrm{T}}^{\mathrm{miss}})$, $\Delta\phi_{min}(E_{\mathrm{T}}^{\mathrm{miss}}, jet)$ and $\Delta R(jj)$ in the 0-lepton signal sample for events passing (black) and failing (red) BCH cleaning.

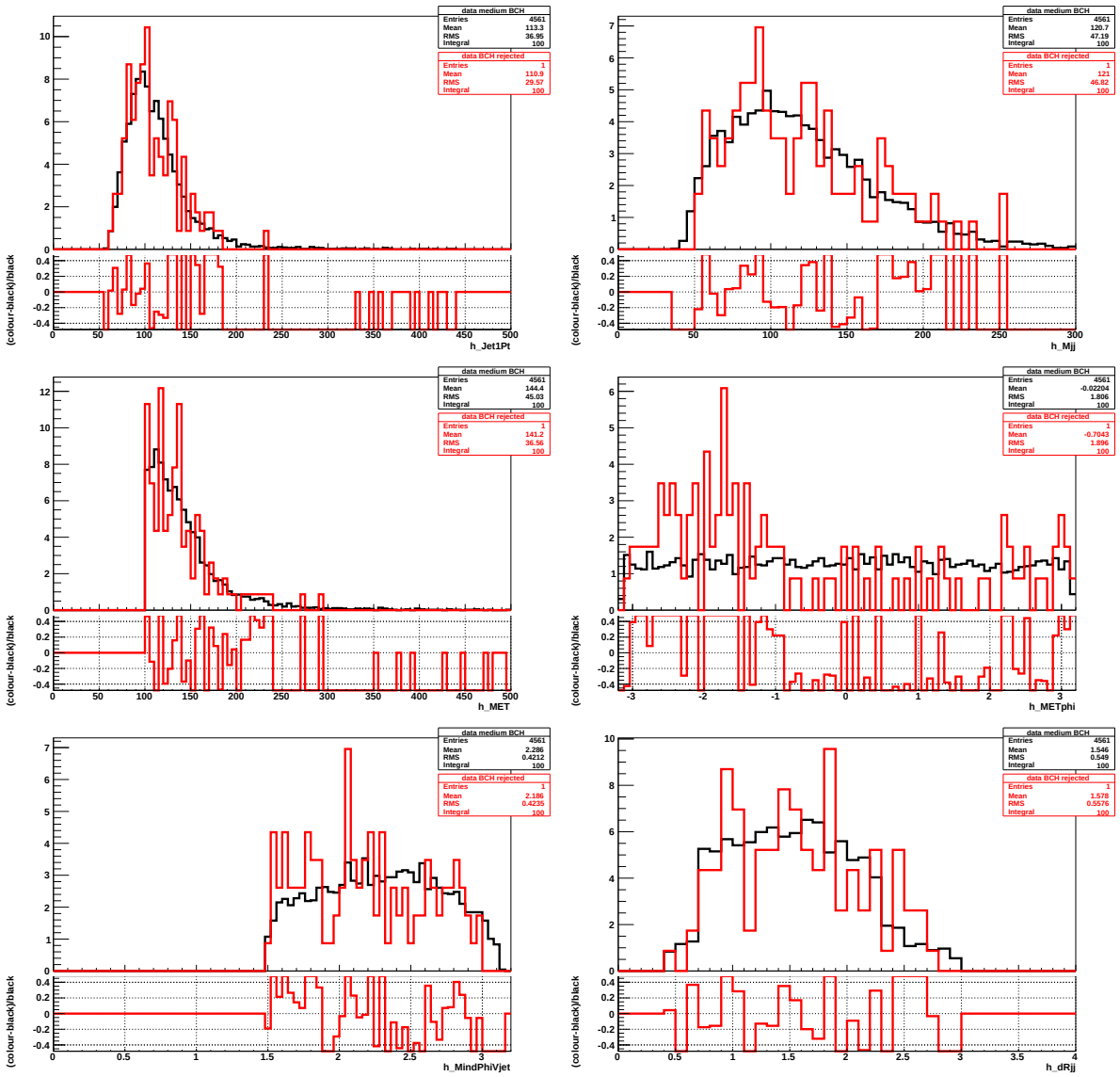

Figure 559: Leading jet p_{T}, m_{bb}, $E_{\mathrm{T}}^{\mathrm{miss}}$, $\phi(E_{\mathrm{T}}^{\mathrm{miss}})$, $\Delta\phi_{min}(E_{\mathrm{T}}^{\mathrm{miss}}, jet)$ and $\Delta R(jj)$ in the 0-lepton `JetTauEtMiss` sample for events passing (black) and failing (red) BCH cleaning.

AN Changes in different versions of this note

AN.1 v0.1

The object and event selections were included as well as a description of the MVA.

AN.2 v0.2

Changes included with respect to the previous version:

- small typographical errors and beautification
- replaced b-tagging cut table with a figure
- missing upper m_{T}^{W} cut in 1 lepton dijet mass analysis fixed
- major typo: iso_{calo} was tightened from EPS not iso_{track}
- added track selection for jet variables
- quantification of improvements from tightening $iso_{calo}$and 1-lepton event level cut changes
- more information about continuous tagging/calibration used
- p_{T}-reco correction plot
- appendices for plots of MVA input variables, MVA output and dijet mass, for low MET (90-120 GeV) bin in 0-lepton, 0-lepton delayed steam, 1 lepton in MET triggered events, GSC calibration, muon in jet overlap, package list and table with all pkgs

AN.3 v0.3

Changes included with respect to the previous version:

- small typographical errors and beautification
- included missing plots (still have a few outstanding)
- expanded modeling sections with specific references to EPS note and list of planned studies for MC specific systematics
- remove d0 significance cut in muon channel
- remove d0 cut in electron channel
- expanded MVA section including optimization studies plot and an appendix with training diagnostic plots
- 0-lepton multijet appendix
- MVA training plots appendix
- Switch H_{T} variable name to M_{eff} as it is a more accurate name.

AN.4 v0.4

Changes included with respect to the previous version:

- small typographical errors and beautification
- including an update for most of the modeling systematics for the background
- Brief W+jets systematic description and $t\bar{t}$ description
- expand the MVA section to include some of the 2 dimensional checks
- added experimental systematics section
- added first description of the statistical model
- added first draft of pulls, etc from the fit
- added new appendixes which will contain a complete description of the studies done to determine the modeling systematics
- update of the cut based histograms, including systematic bands. Multi variate input and output plots will come in the next version of the note.
- Added 2-lepton MJ estimate

AN.5 v0.5

Changes included with respect to the previous version:

- small typographical errors and beautification
- improved fit model section including links from tables of systematics back to sections describing the source
- HAWK MC NLO EW correction summary from EPS note
- Signal and background modeling sections were all revisited and revamped including summary tables
- kinematic fit mentioned in selection section
- Added appendices: kinematic fit, W+hf, $t\bar{t}$ modeling
- output transformation section has been expanded and moved into the statistical model section
- up-to-date description of re-binning procedure (moved to stat model section)
- update and additional post fit plots and fit diagnostic plots for the combined and individual fits
- ordered log(S/B) plots
- list of missing sections and appendices
- list of outstanding ed board requests

AN.6 v0.6

- add new NP pruning cuts since EPS(Section 8.5)
- replace p_{T}^{V} plots with MV1c for MVA 1tag as this is what is used in the fit (Figures **??-??**)

AN.7 v0.7

- Add closure test for truth tagging and dR correction
- Add b-tagging generator dependent scale factors
- Complete dedicated appendixes to describe the studies for the background modeling
- Reorganization of the plots in the stat model, to make the reading easier, showing for each fit the list of distribution used in the fit - NOTE, some of the plots could come from different fits, and they need to be updated again with the next set of fit results
- Add the unfolded post fit b-tagging scale factors
- Update the description of the binning transformation for the MVA, adding a dedicated section to show the optimization of the previously used algorithm
- Add a first preliminary version of the expected exclusion and local $p0$ for both the MVA and the m_{bb} shape analysis
- Add a first placeholder which will contain the description of the studies of important systematics or nuisance parameters.
- Update of the description of the MET trigger appendix
- Add Variations of MVA training including removing m_{bb} from input variables (example for 0 lepton)

AN.8 What we had foreseen from version v0.6 to version v0.7

- deeper description of the studies done to estimate the modeling systematic, in the dedicated appendixes Done
- Full set of plots to check the correlations between the variables entering in the multivariate analysis Some examples are given, but still looking for a convenient way to include them
- Update the plots for the pulls and fit results Done for MVA, but they need to be updated
- Update the multivariate input and output plots Done apart the 1 lepton channel, but they need to be updated
- Appendix for the diboson fit For the next version
- Expand 1-lepton MJ section/appendix as more studies are completed For the next version
- MV1c in the dijet mass analysis 1-tag region in all fit diagnostics and results Done, but the fits need to be updated

- signal systematic: show comparison for variables other than pTV and add comparisons to Powheg MINLO (Maria)Reply at the end of Section 4.2.2 with additional parton shower differences being checked.
- Wbb comparisons for MVA variables. Does assigned systematics cover all differences? Include MVA input variable comparisons to the appendix. (Maria)Appendix L.3

AN.9 v0.8.1

- Updates of alla the plots for the MVA analysis
- Appendix for the BCH
- Appendix for the MultiJet in 1-lepton
- Some more text on the result section.
- Implementation of most of the comments from the EdBoard of v7. For some of them some follow-up is ongoing.
- Add all the unfolded post fit b-tagging scale factors
- Update of the smoothing procedure
- Up-to-date input variable plots. The 1-lepton needs still an update.
- Appendix on the combination with the 7 TeV.

AO Package List

The list in table 164 show the version of the common packages used.

atlasoff/DataQuality/GoodRunsLists/tags/GoodRunsLists-00-01-03
atlasoff/PhysicsAnalysis/AnalysisCommon/PATCore/tags/PATCore-00-00-12
atlasoff/PhysicsAnalysis/TileID/TileTripReader/tags/TileTripReader-00-00-15
atlasoff/PhysicsAnalysis/AnalysisCommon/PileupReweighting/tags/PileupReweighting-00-02-11
atlasoff/Reconstruction/egamma/egammaEvent/tags/egammaEvent-03-06-41
atlasoff/Reconstruction/egamma/egammaAnalysis/egammaAnalysisUtils/tags/egammaAnalysisUtils-00-04-46
atlasoff/PhysicsAnalysis/ElectronPhotonID/ElectronEfficiencyCorrection/tags/ElectronEfficiencyCorrection-00-00-34
atlasoff/PhysicsAnalysis/ElectronPhotonID/ElectronPhotonSelectorTools/tags/ElectronPhotonSelectorTools-00-00-55
atlasoff/PhysicsAnalysis/MuonID/MuonIDAnalysis/MuonMomentumCorrections/tags/MuonMomentumCorrections-00-08-07
atlasoff/PhysicsAnalysis/MuonID/MuonIDAnalysis/MuonEfficiencyCorrections/tags/MuonEfficiencyCorrections-02-01-17
atlasoff/PhysicsAnalysis/MuonID/MuonIDAnalysis/MuonIsolationCorrection/tags/MuonIsolationCorrection-01-01
atlasoff/Trigger/TrigAnalysis/TrigMuonEfficiency/tags/TrigMuonEfficiency-00-02-42
atlasoff/Reconstruction/Jet/JetUncertainties/tags/JetUncertainties-00-08-07
atlasoff/Reconstruction/Jet/JetResolution/tags/JetResolution-02-00-02
atlasoff/Reconstruction/Jet/ApplyJetCalibration/tags/ApplyJetCalibration-00-03-18
atlasoff/Reconstruction/Jet/JetAnalysisTools/ApplyJetResolutionSmearing/tags/ApplyJetResolutionSmearing-00-01-02
atlasoff/Reconstruction/Jet/JetAnalysisTools/JVFUncertaintyTool/tags/JVFUncertaintyTool-00-00-04
atlasoff/PhysicsAnalysis/JetMissingEtID/JetSelectorTools/tags/JetSelectorTools-00-00-23
atlasoff/Reconstruction/MissingETUtility/tags/MissingETUtility-01-02-06
atlasoff/PhysicsAnalysis/JetTagging/JetTagPerformanceCalibration/CalibrationDataInterface/CalibrationDataInterface-00-03-06
atlasphys/Physics/Higgs/HSG5/Limits/InputPreparation/TrigMETEfficiency/tags/TrigMETEfficiency-00-00-10

Table 164: Complete list of packages used in the analysis

For the continuous b-tagging calibration the root file used is

`Summer2013_continuous_MV1c.root`

which comes from the file of the same name in
atlasperf/CombPerf/FlavorTag/JetTagPerformanceCalibration/Continuous/trunk/CDIfiles
from revision 296440 after the custom efficiency maps discussed in Appendix CITE have been added.Likelihood-based multijet rejection tool described in Appendix C can be obtained from this TWiki
https://twiki.cern.ch/twiki/bin/viewauth/AtlasProtected/LikelihoodForLowMETZHvvbb
Add SVN area.